HEAT TRANSFER - MATHEMATICAL MODELLING, NUMERICAL METHODS AND INFORMATION TECHNOLOGY

Edited by **Aziz Belmiloudi**

INTECHWEB.ORG

Heat Transfer - Mathematical Modelling,
Numerical Methods and Information Technology
Edited by Aziz Belmiloudi

Published by InTech
Janeza Trdine 9, 51000 Rijeka, Croatia

Copyright © 2011 InTech
All chapters are Open Access articles distributed under the Creative Commons Non Commercial Share Alike Attribution 3.0 license, which permits to copy, distribute, transmit, and adapt the work in any medium, so long as the original work is properly cited. After this work has been published by InTech, authors have the right to republish it, in whole or part, in any publication of which they are the author, and to make other personal use of the work. Any republication, referencing or personal use of the work must explicitly identify the original source.

Statements and opinions expressed in the chapters are these of the individual contributors and not necessarily those of the editors or publisher. No responsibility is accepted for the accuracy of information contained in the published articles. The publisher assumes no responsibility for any damage or injury to persons or property arising out of the use of any materials, instructions, methods or ideas contained in the book.

Publishing Process Manager Iva Lipovic
Technical Editor Teodora Smiljanic
Cover Designer Martina Sirotic
Image Copyright Zadiraka Evgenii, 2010. Used under license from Shutterstock.com

First published February, 2011
Printed in India

A free online edition of this book is available at www.intechopen.com
Additional hard copies can be obtained from orders@intechweb.org

Heat Transfer - Mathematical Modelling, Numerical Methods and Information Technology, Edited by Aziz Belmiloudi

p. cm.
ISBN 978-953-307-550-1

INTECH OPEN ACCESS PUBLISHER

INTECH open

free online editions of InTech
Books and Journals can be found at
www.intechopen.com

Contents

Preface IX

Part 1 Inverse, Stabilization and Optimization Problems 1

Chapter 1 **Optimum Fin Profile under Dry and Wet Surface Conditions 3**
Balaram Kundu and Somchai Wongwises

Chapter 2 **Thermal Therapy: Stabilization and Identification 33**
Aziz Belmiloudi

Chapter 3 **Direct and Inverse Heat Transfer Problems in Dynamics of Plate Fin and Tube Heat Exchangers 77**
Dawid Taler

Chapter 4 **Radiative Heat Transfer and Effective Transport Coefficients 101**
Thomas Christen, Frank Kassubek, and Rudolf Gati

Part 2 Numerical Methods and Calculations 127

Chapter 5 **Finite Volume Method Analysis of Heat Transfer in Multi-Block Grid During Solidification 129**
Eliseu Monteiro, Regina Almeida and Abel Rouboa

Chapter 6 **Lattice Boltzmann Numerical Approach to Predict Macroscale Thermal Fluid Flow Problem 151**
Nor Azwadi Che Sidik and Syahrullail Samion

Chapter 7 **Efficient Simulation of Transient Heat Transfer Problems in Civil Engineering 165**
Sebastian Bindick, Benjamin Ahrenholz, Manfred Krafczyk

Chapter 8 **Applications of Nonstandard Finite Difference Methods to Nonlinear Heat Transfer Problems 185**
Alaeddin Malek

Chapter 9 **Fast BEM Based Methods for Heat Transfer Simulation 209**
Jure Ravnik and Leopold Škerget

Chapter 10 **Aerodynamic Heating at Hypersonic Speed 233**
Andrey B. Gorshkov

Chapter 11 **Thermoelastic Stresses in FG-Cylinders 253**
Mohammad Azadi and Mahboobeh Azadi

Chapter 12 **Experimentally Validated Numerical Modeling of Heat Transfer in Granular Flow in Rotating Vessels 271**
Bodhisattwa Chaudhuri, Fernando J. Muzzio and M. Silvina Tomassone

Part 3 Heat Transfer in Mini/Micro Systems 303

Chapter 13 **Introduction to Nanoscale Thermal Conduction 305**
Patrick E. Hopkins and John C. Duda

Chapter 14 **Study of Hydrodynamics and Heat Transfer in the Fluidized Bed Reactors 331**
Mahdi Hamzehei

Chapter 15 **Particle Scale Simulation of Heat Transfer in Fluid Bed Reactors 383**
Zongyan Zhou, Qinfu Hou and Aibing Yu

Chapter 16 **Population Balance Model of Heat Transfer in Gas-Solid Processing Systems 409**
Béla G. Lakatos

Chapter 17 **Synthetic Jet-based Hybrid Heat Sink for Electronic Cooling 435**
Tilak T Chandratilleke, D Jagannatha and R Narayanaswamy

Chapter 18 **Turbulent Flow and Heat Transfer Characteristics of a Micro Combustor 455**
Tae Seon Park and Hang Seok Choi

Chapter 19 **Natural Circulation in Single and Two Phase Thermosyphon Loop with Conventional Tubes and Minichannels 475**
Henryk Bieliński and Jarosław Mikielewicz

Chapter 20 **Heat Transfer at Microscale 497**
Mohammad Hassan Saidi and Arman Sadeghi

Part 4 Energy Transfer and Solid Materials 527

Chapter 21 **Thermal Characterization of Solid Structures during Forced Convection Heating 529**
Balázs Illés and Gábor Harsányi

Chapter 22 **Analysis of the Conjugate Heat Transfer in a Multi-Layer Wall Including an Air Layer 553**
Armando Gallegos M., Christian Violante C., José A. Balderas B., Víctor H. Rangel H. and José M. Belman F.

Chapter 23 **An Analytical Solution for Transient Heat and Moisture Diffusion in a Double-Layer Plate 567**
Ryoichi Chiba

Chapter 24 **Frictional Heating in the Strip-Foundation Tribosystem 579**
Aleksander Yevtushenko and Michal Kuciej

Chapter 25 **Convective Heat Transfer Coefficients for Solar Chimney Power Plant Collectors 607**
Marco Aurélio dos Santos Bernardes

Chapter 26 **Thermal Aspects of Solar Air Collector 621**
Ehsan Mohseni Languri and Davood Domairry Ganji

Chapter 27 **Heat Transfer in Porous Media 631**
Ehsan Mohseni Languri and Davood Domairry Ganji

Preface

During the last years, spectacular progress has been made in all aspects of heat transfer. Heat transfer is a branch of engineering science and technology that deals with the analysis of the rate of transfer thermal energy. Its fundamental modes are conduction, convection, radiation, convection vs. conduction and mass transfer. It has a broad application to many different branches of science, technology and industry, ranging from biological, medical and chemical systems, to common practice of thermal engineering (e.g. residential and commercial buildings, common household appliances, etc), industrial and manufacturing processes, electronic devices, thermal energy storage, and agriculture and food process. In engineering practice, an understanding of the mechanisms of heat transfer is becoming increasingly important, since heat transfer plays a crucial role in the solar collector, power plants, thermal informatics, cooling of electronic equipment, refrigeration and freezing of foods, technologies for producing textiles, buildings and bridges, among other things. Engineers and scientists must have a strong basic knowledge in mathematical modelling, theoretical analysis, experimental investigations, industrial systems and information technology with the ability to quickly solve challenging problems by developing and using new, more powerful computational tools, in conjunction with experiments, to investigate design, parametric study, performance and optimization of real-world thermal systems.

In this book entitled ”Heat transfer - Mathematical Modelling, Numerical Methods and Information Technology”, the authors provide a useful treatise on the principal concepts, new trends and advances in technologies, and practical design engineering aspects of heat transfer, pertaining to powerful tools that are modelling, computational methodologies, simulation and information technology. These tools have become essential elements in engineering practice for solving problems. The present book contains a large number of studies in both fundamental and application approaches with various modern engineering applications.

These include ”Inverse, Stabilization and Optimization Problems” (chapters 1 to 4), which focus on modelling, stabilization, identification and shape optimization, with application to biomedical processes, electric arc radiation and heat exchanger systems; ”Numerical Methods and Calculations” (chapters 5 to 12), which concern finite-difference, finite-element and finite-volume methods, lattice Boltzmann numerical method, nonstandard finite difference methods, boundary element method and fast

multipole method, quadrature scheme and complex geometries, hermitian transfinite element, and numerical simulation with various applications as solidification, hypersonic speed, concert hall, porous media and nanofluids; "Heat Transfer in Mini/Micro Systems" (chapters 13 to 20) which cover miniscale and microscale processes with various applications such as fluidized beds reactors, flows conveying bubbles and particles, microchannel heat sinks, micro heat exchangers, micro combustors and semiconductors; "Energy Transfer and Solid Materials" (chapters 21 to 27) which concern heat transfer in furnaces and enclosures, solid structures, moisture diffusion behaviour, porous media with various applications such as tribosystems and solar thermal collectors.

The editor would like to express his thanks to all the authors for their contributions in different areas of their expertise. Their domain knowledge combined with their enthusiasm for scientific quality made the creation of this book possible.

The editor sincerely hopes that readers will find the present book interesting, valuable and current.

Aziz Belmiloudi
European University of Brittany (UEB),
National Institut of Applied Sciences of Rennes (INSA),
Mathematical Research Institute of Rennes (IRMAR),
Rennes, France.

Part 1

Inverse, Stabilization and Optimization Problems

1

Optimum Fin Profile under Dry and Wet Surface Conditions

Balaram Kundu[1] and Somchai Wongwises[2]
[1]*Department of Mechanical Engineering*
Jadavpur University, Kolkata – 700 032
[2]*Fluid Mechanics, Thermal Engineering and Multiphase*
Flow Research Lab (FUTURE), Department of Mechanical Engineering
King Mongkut's University of Technology Thonburi (KMUTT)
Bangmod,Bangkok 10140
[1]*India*
[2]*Thailand*

1. Introduction

Fins or extended surfaces are frequently employed in heat exchangers for effectively improving the overall heat transfer performance. The simple design of fins and their stability in different surface conditions have created them a popular augmentation device. The different fin shapes are available in the literature. The geometry of the fin may be dependent upon the primary surface also. For circular primary surface, the attachment of circumferential fins is a common choice. The longitudinal and pin fins are generally used to the flat primary surface. However, due to attachment of fins with the primary surface, the heat transfer augments but the volume, weight, and cost of the heat exchanger equipments increase as well. Hence, it is a challenge to the designer to minimize the cost for the attachment of fins. This can be done by determining the optimum shape of a fin satisfying the maximization of heat transfer rate for a given fin volume. In general, two different approaches are considered for the optimization of any fin design problem. Through a rigorous technique, the profile of a fin for a particular geometry (flat or curved primary surface) may be obtained such that the criteria of the maximum heat transfer for a given fin volume or equivalently minimum fin volume for a given heat transfer duty is satisfied. In a parallel activity, the optimum dimensions of a fin of given profile (rectangular, triangular etc.) are determined from the solution of the optimality criteria. The resulting profile obtained from the first case of optimum design is superior in respect to heat transfer rate per unit volume and thus it is very much important in fin design problems. However, it may be limited to use in actual practice because the resulting profile shape would be slightly difficult to manufacture and fabricate. Alternatively, such theoretical shape would first be calculated and then a triangular profile approximating the base two thirds of the fin would be used. Such a triangular fin transfers heat per unit weight, which is closer to that of the analytical optimum value.

Under a convective environmental condition, Schmidt (1926) was the first researcher to forward a systematic approach for the optimum design of fins. He proposed heuristically that for an optimum shape of a cooling fin, the fin temperature must be a linear function

with the fin length. Later, through the calculus of variation, Duffin (1959) exhibited a rigorous proof on the optimality criteria of Schmidt. Liu (1961) extended the variational principle to find out the optimum profile of fins with internal heat generation. Liu (1962) and Wilkins (1961) addressed for the optimization of radiating fins. Solov"ev (1968) determined the optimum radiator fin profile. The performance parameter of annular fins of different profiles subject to locally variable heat transfer coefficient had been investigated by Mokheimer (2002). From the above literature works, it can be indicated that the above works were formulated based on the "length of arc idealization (LAI)."

Maday (1974) was the first researcher to eliminate LAI and obtained the optimum profile through a numerical integration. It is interesting to note that an optimum convecting fin neither has a linear temperature profile nor possesses a concave parabolic shape suggested by Maday. The profile shape contains a number of ripples denoted as a "wavy fin". The same exercise was carried out for radial fins by Guceri and Maday (1975). Later Razelos and Imre (1983) applied Pontryagin's minimum principle to find out the minimum mass of convective fins with variable heat transfer coefficient. Zubair et al. (1996) determined the optimum dimensions of circular fins with variable profiles and temperature dependent thermal conductivity. They found an increasing heat transfer rate through the optimum profile fin by 20% as compare to the constant thickness fin.

A variational method was adopted by Kundu and Das (1998) to determine the optimum shape of three types of fins namely the longitudinal fin, spine and disc fin. A generalized approach of analysis based on a common form of differential equations and a set of boundary conditions had been described. For all the fin geometries, it was shown that the temperature gradient is constant and the excess temperature at the tip vanishes. By taking into account the LAI, Hanin and Campo (2003) forecasted a shape of a straight cooling fin for the minimum envelop. From the result, they have highlighted that the volume of the optimum circular fin with consideration of LAI found is 6.21-8 times smaller than the volume of the corresponding Schmidt's parabolic optimum fin. A new methodological determination for the optimum design of thin fins with uniform volumetric heat generation had been done by Kundu and Das (2005).

There are ample of practical applications in which extended surface heat transfer is involved in two-phase flow conditions. For example, when humid air encounter into a cold surface of cooling coils whose temperature is maintained below the dew point temperature, condensation of moisture will take place, and mass and heat transfer occur simultaneously. The fin-and-tube heat exchangers are widely used in conventional air conditioning systems for air cooling and dehumidifying. In the evaporator of air conditioning equipment, the fin surface becomes dry, partially or fully wet depending upon the thermogeometric and psychrometric conditions involved in the design process. If the temperature of the entire fin surface is lower than the dew point of the surrounding air, there may occur both sensible and latent heat transferred from the air to the fin and so the fin is fully wet. The fin is partially wet if the fin-base temperature is below the dew point while fin-tip temperature is above the dew point of the surrounding air. If the temperature of the entire fin surface is higher than the dew point, only sensible heat is transferred and so the fin is fully dry. For wet surface, the moisture is condensed on the fin surface, latent heat evolves and mass transfer occurs simultaneously with the heat transfer. Thermal performance of different surface conditions of a fin depends on the fin shape, thermophysical and psychrometric properties of air.

Many investigations have been devoted to analyze the effect of condensation on the performance of different geometric fins. It is noteworthy to mention that for each instance, a

suitable fin geometry has been selected a priory to make the analysis. For the combined heat and mass transfer, the mathematical formulation becomes complex to determine the overall performance analysis of a wet fin. Based on the dry fin formula, Threlkeld (1970) and McQuiston (1975) determined the one-dimensional fin efficiency of a rectangular longitudinal fin for a fully wet surface condition. An analytical solution for the efficiency of a longitudinal straight fin under dry, fully wet and partially wet surface conditions was introduced elaborately by Wu and Bong (1994) first with considering temperature and humidity ratio differences as the driving forces for heat and mass transfer. For the establishment of an analytical solution, a linear relationship between humidity ratio and the corresponding saturation temperature of air was taken. Later an extensive analytical works on the performance and optimization analysis of wet fins was carried out by applying this linear relationship. A technique to determine the performance and optimization of straight tapered longitudinal fins subject to simultaneous heat and mass transfer has been established analytically by Kundu (2002) and Kundu and Das (2004). The performance and optimum dimensions of a new fin, namely, SRC profile subject to simultaneous heat and mass transfer have been investigated by Kundu (2007a; 2009a). In his work, a comparative study has also been made between rectangular and SRC profile fins when they are operated in wet conditions. Hong and Web (1996) calculated the fin efficiency for wet and dry circular fins with a constant thickness. Kundu and Barman (2010) have studied a design analysis of annular fins under dehumidifying conditions with a polynomial relationship between humidity ratio and saturation temperature by using differential transform method. In case of longitudinal fins of rectangular geometry, approximate analytic solution for performances has been demonstrated by Kundu (2009b). Kundu and Miyara (2009) have established an analytical model for determination of the performance of a fin assembly under dehumidifying conditions. Kundu et al. (2008) have described analytically to predict the fin performance of longitudinal triangular fins subject to simultaneous heat and mass transfer.

The heat and mass transfer analysis for dehumidification of air on fin-and-tube heat exchangers was done experimentally by the few authors. The different techniques, namely, new reduction method, tinny circular fin method, finite circular fin method and review of data reduction method used for analyzing the heat and mass transfer characteristics of wavy fin-and-tube exchangers under dehumidifying conditions had been investigated by Pirompugd et al. (2007a; 2007b; 2008; 2009).

The above investigations had been focused on determination of the optimum profile subjected to convective environment. However a thorough research works have already been devoted for analyzing the performance and optimization of wet fins. To carryout these analyses, suitable fin geometry has been chosen a priory. However, the optimum profile fin may be employed in air conditioning apparatus, especially, in aircrafts where reduction of weight is always given an extra design attention. Kundu (2008) determined an optimum fin profile of thin fins under dehumidifying condition of practical interest formulated with the treatment by a calculus of variation. Recently, Kundu (2010) focused to determine the optimum fin profile for both fully and partially wet longitudinal fins with a nonlinear saturation curve.

In this book chapter, a mathematical theory has been developed for obtaining the optimum fin shape of three common types of fins, namely, longitudinal, spine and annular fins by satisfying the maximizing heat transfer duty for a given either fin volume or both fin volume and length. The analysis was formulated for the dry, partially and fully wet surface conditions. For the analytical solution of a wet fin equation, a relationship between humidity ratio and temperature of the saturation air is necessary and it is taken a linear variation. The influence of

wet fin surface conditions on the optimum profile shape and its dimensions has also been examined. From the analysis, it can be mentioned that whether a surface is dry, partially or fully wet at an optimum condition, the air relative humidity is a responsible factor. The optimum fin profile and design variables have been determined as a function of thermo-psychrometric parameters. The dry surface analysis can be possible from the present fully wet surface fin analysis with considering zero value of latent heat of condensation. From the analysis presented, it can be highlighted that unlike dry and partially wet fins, tip temperature for fully wet fins is below the ambient temperature for the minimum profile envelop fin.

2. Variational formulations for the optimum fin shape

For determination of the optimum fin shape, it can be assumed that the condensate thermal resistance to heat flow is negligibly small as the condensate film is much thinner than the boundary layer in the dehumidification process. Under such circumstances, it may follow that the heat transfer coefficient is not influenced significantly with the presence of condensation. The condensation takes place when fin surface temperature is below the dew point of the surrounding air and for its calculation, specific humidity of the saturated air on the wet surface is assumed to be a linear function with the local fin temperature. This assumption can be considered due to the smaller temperature range involved in the practical application between fin base and dew point temperatures and within this small range, saturation curve on the psychometric chart is possible to be an approximated by a straight line (Wu and Bong, 1994; Kundu, 2002; Kundu, 2007a; Kundu, 2007b; Kundu, 2008; Kundu, 2009). Owing to small temperature variation in the fin between fin-base and fin-tip, it can be assumed that the thermal conductivity of the fin material is a constant. The different types of fins, namely, longitudinal, spine and anuular fin are commonly used according to the shape of the primary surfaces. Depending upon the fin base, fin tip and dew point temperatures, fin-surface can be dry, partially and fully wet. The analysis for determination of an optimum profile of fully and partially wet fins for longitudinal, spine and annular fin geometries are described separately in the followings:

2.1 Fully wet longitudinal fins

The schematic diagram of an optimum shape of longitudinal fins is illustrated in Fig. 1. The governing energy equation for one-dimensional temperature distribution on fully wet surface fins can be written under steady state condition as follows:

$$\frac{d}{dx}\left(y\frac{dT}{dx}\right)=\frac{h}{k}\left[\left(T-T_a\right)+h_m\left(\omega-\omega_a\right)h_{fg}/h\right] \tag{1}$$

h_m is the average mass transfer coefficient based on the humidity ratio difference, ω is the humidity ratio of saturated air at temperature T, ω_a is the humidity ratio of the atmospheric air, and h_{jg} is the latent heat of condensation. For the mathematical simplicity, the following dimensionless variables and parameters can be introduced:

$$X=hx/k\ ;\ Y=hy/k\ ;\ L=hl/k\ ;\ \theta=\left(T_a-T\right)/\left(T_a-T_b\right)\ ;\ Le=\left(h/h_mC_p\right)^{3/2} \tag{2}$$

where, L_e is the Lewis number. The relationship between heat and mass transfer coefficients can be obtained from the Chilton-Colburn analogy (Chilton and Colburn, 1934). The relationship between the saturated water film temperature T and the corresponding

saturated humidity ratio ω is approximated by a linear function (Wu and Bong, 1994; Kundu, 2002; Kundu, 2007a; Kundu, 2007b; Kundu, 2008; Kundu, 2009) in this study:

$$\omega = a + bT \tag{3}$$

where, a and b are constants determined from the conditions of air at the fin base and fin tip. Eq. (1) is written in dimensionless form by using Eqs. (2) and (3) as follows:

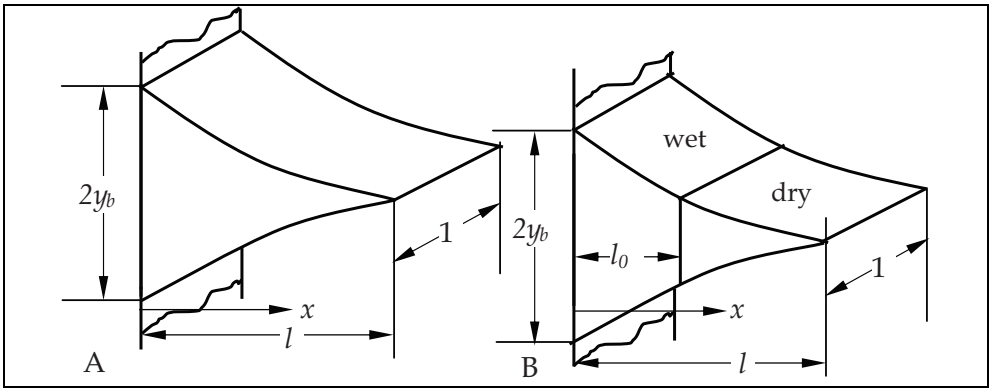

Fig. 1. Schematic diagram of an optimum longitudinal fin under dehumidifying conditions: A. Fully wet; and B. Partially wet.

$$d/dX\left(Y\, d\phi/dX\right) = \left(1 + b\xi\right)\phi \tag{4}$$

where

$$\phi = \theta + \theta_p;\ \theta_p = \left(\omega_a - a - bT_a\right)\Big/\left[\left(T_a - T_b\right)\left(1 + b\xi\right)\right];\ \xi = h_{fg}\Big/C_p Le^{2/3} \tag{5}$$

Eq. (4) is subjected to the following boundary conditions:

$$\text{at}\quad X = 0\ ,\ \phi = 1 + \theta_p = \phi_0 \tag{6a}$$

$$\text{at}\quad X = L\ ,\ Y d\phi/dX = 0 \tag{6b}$$

For determination of the heat transfer duty through fins, Eq. (4) is multiplied by ϕ, and then integrated, the following expression are obtained with the help of the corresponding boundary conditions:

$$-\left[Y\phi\, d\phi/dX\right]_{X=0} = \int_{X=0}^{L}\left[Y\left(d\phi/dX\right)^2 + \left(1 + b\xi\right)\phi^2\right]dX \tag{7}$$

The heat transfer rate through the fins can be calculated by applying the Fourier's law of heat conduction at the fin base:

$$Q = \frac{q}{2k\left(T_a - T_b\right)} = -\left[Y\, d\phi/dX\right]_{X=0} = \frac{1}{\phi_0}\int_{X=0}^{L}\left[Y\left(d\phi/dX\right)^2 + \left(1 + b\xi\right)\phi^2\right]dX \tag{8}$$

The fin volume is obtained from the following expression:

$$U = \frac{V\left(h/k\right)^2}{2} = \int_{X=0}^{L} Y\,dX \tag{9}$$

The profile shape of a fin has been determined from the variational principle after satisfying the maximization of heat transfer rate Q for a design condition. In the present study, either the fin volume or both the fin volume and length are considered as a constraint condition. A functional F may be constructed from Eqs. (8) and (9) by employing Lagrange multiplier λ:

$$F = Q - \lambda U = \frac{1}{\phi_0}\int_{X=0}^{L}\left[Y\left(d\phi/dX\right)^2 + \left(1+b\xi\right)\phi^2 - \lambda\phi_0 Y\right]dX \tag{10}$$

The relation between the variation of F and that of Y is obtained from the above equation and for maximum value of F, δF is zero for any admissible variation of δY. Thus

$$\delta F = \frac{1}{\phi_0}\int_{X=0}^{L} Y^{-1}\left[Y\left(d\phi/dX\right)^2 - \lambda\phi_0 Y\right]\delta Y\,dX = 0 \tag{11}$$

From the above equation, the following optimality criteria are obtained:

$$Y\left(d\phi/dX\right)^2 - \lambda\phi_0 Y = 0 \tag{12}$$

From Eq. (12), it is obvious that the temperature gradient in the longitudinal fin for the optimum condition is a constant.

2.1.1 Optimum longitudinal fin for the volume constraint

Here the fin length L is not a constant and thus it can be taken as a variable. From Eq. (10), the variation of function F with L is as follows:

$$\delta F = \frac{1}{\phi_0}\left[Y\left(d\phi/dX\right)^2 + \left(1+b\xi\right)\phi^2 - \lambda\,\phi_0 Y\right]\delta X\Big|_{X=0}^{L} = 0 \tag{13}$$

At $X = 0$, the above term vanishes as δX=0. At X=L, δX is not zero; therefore, at the tip, the following optimality conditions can be obtained:

$$Y\left(d\phi/dX\right)^2 + \left(1+b\xi\right)\phi^2 - \lambda\phi_0 Y = 0 \tag{14}$$

Combining Eqs. (4), (6), (12) and (14) , yields the tip condition $\phi = 0$. The tip thickness of a fin may be determined from the tip condition and the optimality criterion and boundary condition (Eqs. (12) and (6b)). It can be seen that the tip thickness is zero. The tip temperature for fully wet surface $\theta_t = -\theta_p$, which is slightly less than the ambient value and this temperature is obvious as a function of psychometric properties of the surrounding air.
From Eqs. (4) (6), (12) and tip condition, the temperature distribution and fin profile are written as follows:

$$\theta = 1 - \left(1 + \theta_p\right) X / L \tag{15}$$

and

$$Y = \frac{\left(1 + b\xi\right)}{2}\left(L - X\right)^2 \tag{16}$$

The optimum fin length L_{opt} can be obtained from Eqs. (9) and (16). The maximum heat transfer rate through the fin can be written by the design variables as follows:

$$\begin{bmatrix} L_{opt} \\ Q_{opt} \end{bmatrix} = \begin{bmatrix} \left\{6\,U/\left(1 + b\xi\right)\right\}^{1/3} \\ \phi_0 \left\{3U\left(1 + b\xi\right)^2/4\right\}^{1/3} \end{bmatrix} \tag{17a}$$

(17b)

2.1.2 Optimum longitudinal fin for both length and volume constraints

In fin design, some times the length of the fin is required to specify due to restricted space and ease of manufacturing. Under this design consideration, both length (fixed L) and volume may be adopted as a constraint. For obtaining the temperature distribution and fin profile, Eqs. (6), (9) and (12) can be combined:

$$\theta = 1 - \alpha X \tag{18}$$

and

$$Y = \frac{\left(1 + b\xi\right)}{2\alpha}\left[2\phi_0\left(L - X\right) - \alpha\left(L^2 - X^2\right)\right] \tag{19}$$

where

$$\alpha = \frac{3\,L^2\left(1 + b\xi\right)\phi_0}{6U + 2L^3\left(1 + b\xi\right)} \tag{20}$$

Here, it may be noted that the optimum fin shape for dry surface fins can be determined by using the above formula.

2.2 Partially wet longitudinal fins

There are two regions dry and wet in partially wet fins shown in Fig. 1B. For partially wet longitudinal fins, the energy equations are in the followings:

$$\begin{bmatrix} \frac{d}{dx}\left(y\frac{dT}{dx}\right) \\ \frac{d}{dx}\left(y\frac{dT}{dx}\right) \end{bmatrix} = \begin{bmatrix} \frac{h}{k}\left(T - T_a\right) \\ \frac{h}{k}\left\{\left(T - T_a\right) + h_m\left(\omega - \omega_a\right)h_{fg}/h\right\} \end{bmatrix} \quad \text{for dry surface } T > T_d \tag{21a}$$

$$\text{for wet surface } T \le T_d \tag{21b}$$

By using Eqs. (2) and (3), Eq. (21) is made in normalized form and it can be expressed as follows:

$$\begin{bmatrix} \frac{d}{dX}\left(Y\frac{d\theta}{dX}\right) \\ \frac{d}{dX}\left(Y\frac{d\phi}{dX}\right) \end{bmatrix} = \begin{bmatrix} \theta \\ (1+b\xi)\phi \end{bmatrix} \quad \begin{matrix} \text{for dry domain } \theta > \theta_d \\ \text{for wet domain } \theta \le \theta_d \end{matrix} \tag{22a, 22b}$$

The heat transfer through the tip is negligibly small in comparision to that through the lateral surfaces and fin base temperature is taken as a constant. In addition, continuity of temperature and heat conduction satisfies at the section where dry and wet separates. Thus, for solving Eq. (22) the following boundary conditions are taken:

$$\text{at} \quad X = 0\,, \ \phi = \phi_0 \tag{23a}$$

$$\text{at} \quad X = L_0\,, \begin{cases} \theta = \theta_d & (23b) \\ d\theta/dX = d\phi/dX & (23c) \end{cases}$$

$$\text{at} \quad X = L\,, \ Yd\theta/dX = 0 \tag{23d}$$

Eq. (22) are multiplied by respective variables θ and ϕ, and the following relationships are obtained by integration and using boundary conditions:

$$-\left[Y\phi\, d\phi/dX\right]_{X=0} = -\left[Y\phi\, d\phi/dX\right]_{X=L_0} + \int_{X=0}^{L_0}\left[Y\left(d\phi/dX\right)^2 + (1+b\xi)\phi^2\right]dX \tag{24a}$$

and

$$-\left[Y\theta\, d\theta/dX\right]_{X=L_0} = \int_{X=L_0}^{L}\left[Y\left(d\theta/dX\right)^2 + \theta^2\right]dX \tag{24b}$$

Combining Eqs. (24a) and (24b), one can get

$$-\left[Y\varphi\, d\varphi/dX\right]_{X=0} = \frac{\varphi_d}{\theta_d}\int_{X=L_0}^{L}\left[Y\left(d\theta/dX\right)^2 + \theta^2\right]dX + \int_{X=0}^{L_0}\left[Y\left(d\varphi/dX\right)^2 + (1+b\xi)\varphi^2\right]dX \tag{25}$$

The heat transfer rate through the fins is calculated by applying the Fourier's law of heat conduction at the fin base and it can be written by using Eq. (25) as

$$\begin{aligned} Q = \frac{q}{2k\left(T_a - T_b\right)} &= -\left(Y\frac{d\phi}{dX}\right)_{X=0} = \frac{\phi_d}{\phi_0\,\theta_d}\int_{X=L_0}^{L}\left[Y\left(d\theta/dX\right)^2 + \theta^2\right]dX \\ &+ \frac{1}{\phi_0}\int_{X=0}^{L_0}\left[Y\left(d\phi/dX\right)^2 + (1+b\xi)\phi^2\right]dX \end{aligned} \tag{26}$$

The fin volume per unit width can be obtained from the following expressions:

$$U = \frac{V(h/k)^2}{2} = \int_{X=0}^{L_0} Y dX + \int_{X=L_0}^{L} Y dX \tag{27}$$

The optimum profile shape of a fin can be determined from the variational principle by constructing a functional F from Eqs. (26) and (27) using Lagrange multiplier λ.

$$\begin{aligned} F = Q - \lambda U = \frac{1}{\phi_0} \int_{X=0}^{L_0} \left[Y(d\phi/dX)^2 + (1+b\xi)\phi^2 - \lambda \phi_0 Y \right] dX \\ + \frac{\phi_d}{\phi_0 \theta_d} \int_{X=L_0}^{L} \left[Y(d\theta/dX)^2 + \theta^2 - \lambda \phi_0 \theta_d Y/\phi_d \right] dX \end{aligned} \tag{28}$$

For maximizing value of F, the following condition is obtained from Eq. (28).

$$\begin{aligned} \delta F = \frac{1}{\phi_0} \int_{X=0}^{L_0} Y^{-1} \left[Y(d\phi/dX)^2 - \lambda \phi_0 Y \right] \delta Y dX \\ + \frac{\phi_d}{\phi_0 \theta_d} \int_{X=L_0}^{L} Y^{-1} \left[Y(d\theta/dX)^2 - \lambda \phi_0 \theta_d Y/\phi_d \right] \delta Y dX = 0 \end{aligned} \tag{29}$$

From Eq. (29), the optimality criterion is derived as follows:

$$\begin{bmatrix} Y(d\theta/dX)^2 - \lambda \phi_0 \theta_d Y/\phi_d \end{bmatrix} = \begin{bmatrix} 0 \end{bmatrix} \quad \theta > \theta_d \tag{30a}$$

$$\begin{bmatrix} Y(d\phi/dX)^2 - \lambda \phi_0 Y \end{bmatrix} = \begin{bmatrix} 0 \end{bmatrix} \quad \theta \le \theta_d \tag{30b}$$

2.2.1 Optimum longitudinal fin for volume constraint

The variation of F with a function of L and L_0 yields the following expressions from Eq. (29):

$$\begin{bmatrix} \delta F \end{bmatrix} = \begin{bmatrix} \frac{1}{\phi_0} \left\{ Y(d\phi/dX)^2 + (1+b\xi)\phi^2 - \lambda \phi_0 Y \right\} \delta X \Big|_{X=0}^{X=L_0} \end{bmatrix} = \begin{bmatrix} 0 \end{bmatrix} \quad \theta \le \theta_d \tag{31a}$$

$$\begin{bmatrix} \delta F \end{bmatrix} = \begin{bmatrix} \frac{\varphi_d}{\theta_d \phi_0} \left\{ Y(d\theta/dX)^2 + \theta^2 - \lambda Y \phi_0 \theta_d \ / \ \phi_d \right\} \delta X \Big|_{X=L_0}^{L} \end{bmatrix} = \begin{bmatrix} 0 \end{bmatrix} \quad \theta > \theta_d \tag{31b}$$

At $X = 0$, the above term should vanish as $\delta X=0$. At $X=L_0$ and X=L, δX is nonzero; thus, the location for both dry and wet surfaces coexist and the fin tip satisfies are the optimality conditions:

$$\begin{bmatrix} Y(d\theta/dX)^2 + \theta^2 - \lambda \theta_d \phi_0 Y/\phi_d \end{bmatrix} = \begin{bmatrix} 0 \end{bmatrix} \quad \text{at } X = L_0 \tag{32a}$$

$$\begin{bmatrix} Y(d\phi/dX)^2 + (1+b\xi)\phi^2 - \lambda \phi_0 Y \end{bmatrix} = \begin{bmatrix} 0 \end{bmatrix} \tag{32b}$$

and

$$Y(d\theta/dX)^2 + \theta^2 - \lambda \theta_d \phi_0 Y/\phi_d = 0 \quad \text{at } X = L \tag{33}$$

Combining Eqs. (4), (6b), (30), (32) and (33), the tip temperature vanishes. Using optimality criteria, the temperature distribution and fin profile can be expressed as

$$\theta = \begin{cases} 1-(1-\theta_d)X/L_0 & 0 \le X \le L_0 \quad (34a) \\ \theta_d (L-X)/(L-L_0) & L_0 \le X \le L \quad (34b) \end{cases}$$

and

$$Y = \frac{1}{2}\left[(L-L_0)^2 + \frac{(1+b\xi)}{(1-\theta_d)} \left\{ 2L_0\phi_0 (L_0 - X) - (1-\theta_d)\left(L_0^2 - X^2\right) \right\} \right] \quad \text{for } 0 \le X \le L_0 \quad (35a)$$

$$Y = \frac{1}{2}(L-X)^2 \quad \text{for } L_0 \le X \le L \quad (35b)$$

The length of the wet region L_0 can be determined by using an energy balance at that length where dry and wet sections live together.

$$L_0 = L(1-\theta_d) \quad (36)$$

Here L is not a constraint. L can be obtained from Eqs. (27), (35) and (36). The optimum length and the maximum heat transfer rate through a fin can be written as

$$L_{opt} = \frac{(6U)^{1/3}}{\left[\theta_d^2 (3-2\theta_d) + (1+b\xi)(1-\theta_d)^2 (3\phi_0 + 2\theta_d - 2) \right]^{1/3}} \quad (37a)$$

and

$$Q_{opt} = \frac{\left[\theta_d^2 + (1+b\xi)(2\phi_0 + \theta_d - 1)(1-\theta_d) \right]^2 (6U)^{1/3}}{\left[\theta_d^2 (3-2\theta_d) + (1+b\xi)(1-\theta_d)^2 (3\phi_0 + 2\theta_d - 2) \right]^{1/3}} \quad (37b)$$

2.2.2 Optimum longitudinal fin for both length and volume constraints

The temperature distribution and fin profile can be determined by using Eqs. (4), (6) and (13):

$$\begin{bmatrix} \theta \\ \theta \end{bmatrix} = \begin{bmatrix} 1-\alpha X \\ \theta_d - \alpha (X - L_0) \end{bmatrix} \begin{matrix} 0 \le X \le L_0 \quad (38a) \\ L_0 \le X \le L \quad (38b) \end{matrix}$$

and

$$Y = \frac{1}{2\alpha}\left[2(\theta_d + \alpha L_0)(L-L_0) - \alpha\left(L^2 - L_0^2\right) + (1+b\xi)\left\{ 2\phi_0 (L_0 - X) - \alpha\left(L_0^2 - X^2\right) \right\} \right] \quad (0 \le X \le L_0) \quad (39a)$$

$$Y = \frac{1}{2\alpha}\left[2(\theta_d + \alpha L_0)(L-X) - \alpha\left(L^2 - X^2\right) \right] \quad (L_0 \le X \le L) \quad (39b)$$

where

$$\alpha = \frac{3\theta_d\left(L^2 - L_0^2\right) + 3\phi_0\left(1 + b\xi\right)L_0^2}{6U + 2L_0^3\left(1 + b\xi\right) + 2L^3 - L_0\left(3L^2 - L_0^2\right) + 4\left(L^3 - L_0^3\right)} \tag{40}$$

and

$$L_0 = \left(1 - \theta_d\right)/\alpha \tag{41}$$

2.3 Fully wet annular fins

Figure 2a is drawn for a schematic representation of an optimum annular fin under condensation of saturated vapor on its surfaces. The energy equation for one-dimensional temperature distribution in fully wet annular fins can be written under steady state condition as

$$\frac{d}{dx}\left[y\left(r_i + x\right)\frac{dT}{dx}\right] = \frac{h}{k}\left(r_i + x\right)\left[\left(T - T_a\right) + h_m\left(\omega - \omega_a\right)h_{fg}/h\right] \tag{42}$$

Eq. (42) is made in dimensionless form by using Eqs. (2) and (3) as

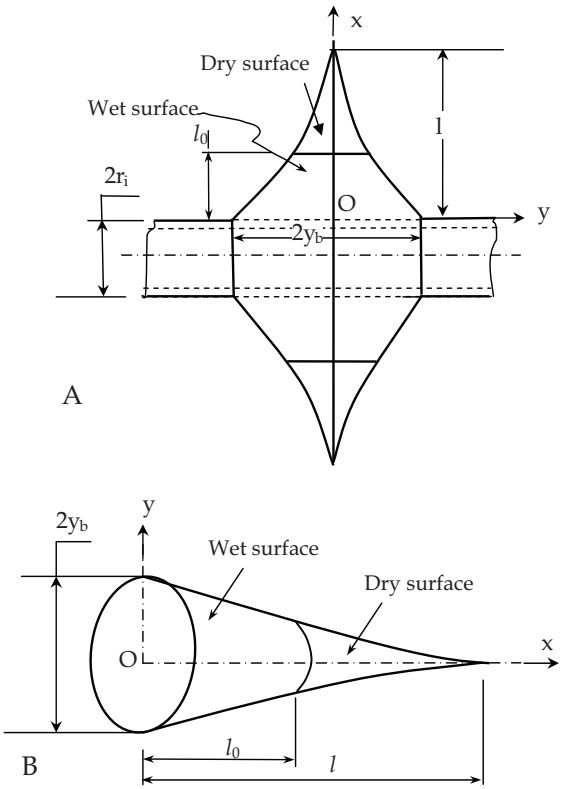

Fig. 2. Typical configuration of wet fins: A. Annular fin; and B. Spine

$$\frac{d}{dX}\left[Y\left(R_i+X\right)\frac{d\phi}{dX}\right]=\left(R_i+X\right)\left(1+b\xi\right)\phi;\quad R_i=h\,r_i/k \tag{43}$$

The boundary conditions for annular fins for temperature distribution are considered same as taken longitudinal fins described in Eq. (6). The actual nondimensional heat transfer rate is calculated from the following formula:

$$Q=\frac{q\left(h/\pi\right)}{4k^2\left(T_a-T_b\right)}=-\left[Y\left(R_i+X\right)\frac{d\phi}{dX}\right]_{X=0}=\frac{1}{\phi_0}\int_{X=0}^{L}\left(R_i+X\right)\left[Y\left(d\phi/dX\right)^2+\left(1+b\xi\right)\phi^2\right]dX \tag{44}$$

The fin volume in dimensionless form can be written as

$$U=\frac{V\left(h/k\right)^3}{4\pi^2}=\int_{X=0}^{L}\left(R_i+X\right)Y dX \tag{45}$$

For the application of variational principle, a function F can be constructed by using Lagrange multiplier λin the followings :

$$F=Q-\lambda U=\frac{1}{\phi_0}\int_{X=0}^{L}\left(R_i+X\right)\left[Y\left(d\phi/dX\right)^2+\left(1+b\xi\right)\phi^2-\lambda\phi_0 Y\right]dX \tag{46}$$

For maximizing value of F, Eq. (46) is differentiated with respect to Y and finally it becomes to zero.

$$\delta F=\frac{1}{\phi_0}\int_{X=0}^{L}Y^{-1}\left(R_i+X\right)\left[Y\left(d\phi/dX\right)^2-\lambda\phi_0 Y\right]\delta Y\,dX=0 \tag{47}$$

From Eq. (47), the following optimality condition for fully wet annular fins is obtained.

$$Y\left(d\phi/dX\right)^2-\lambda\phi_0 Y=0 \tag{48}$$

From the above optimality condition, it is to mention that the temperature gradient for fully wet anuular fins is a constant and it does not depend upon the wetness condition of the fin.

2.3.1 Optimum annular fin for volume constraint

For volume constraint, fin length is variable. The variation of function F with length L is determined from this expression.

$$\delta F=\frac{\left(R_i+X\right)}{\phi_0}\left[Y\left(d\phi/dX\right)^2+\left(1+b\xi\right)\phi^2-\lambda\,\phi_0 Y\right]\delta X\Big|_{X=0}^{L}=0 \tag{49}$$

At $X = L$, the following optimality conditions are obtained:

$$Y\left(d\phi/dX\right)^2+\left(1+b\xi\right)\phi^2-\lambda\phi_0 Y=0 \tag{50}$$

Using Eqs. (6), (43), (48) and (50), the condition for temperature at the tip is ϕ = 0. The thickness of fin profile at the tip is also zero. The temperature distribution and fin profile for the optimum annular fin for fully wet surface conditions is obtained from Eqs. (6), (43), (48) and optimum tip conditions as follows:

$$\theta = 1 - \left(1 + \theta_p\right) X \big/ L \tag{51}$$

and

$$Y = \frac{\left(1 + b\xi\right)}{6\left(R_i + X\right)}\left[\left(L^3 - 3LX^2 + 2X^3\right) + 3R_i\left(L - X\right)^2\right] \tag{52}$$

The optimum length and the maximum heat transfer rate through the fin can be determined as a function of design variables in the followings:

$$\begin{bmatrix} L_{opt} \\ Q_{opt} \end{bmatrix} = \begin{bmatrix} L_{opt}^4 + 2R_i L_{opt}^3 - 12U\big/\left(1 + b\xi\right) = 0 \\ \phi_0 L_{opt}\left(3R_i - L_{opt}\right)\left(1 + b\xi\right)\big/6 \end{bmatrix} \tag{53}$$

$$\tag{54}$$

The optimum length can be possible to calculate by a numerical technique. The Newton-Raphson method can be applied for the solution of Eq. (53) to determine the optimum fin length.

2.3.2 Optimum annular fin for both length and volume constraints

The temperature and fin profile for an optimum annular fin under length and volume constraints is determined from Eqs. (6), (43), (45) and (48) and they can be expressed as

$$\theta = 1 - \alpha X \tag{55}$$

and

$$Y = \frac{\left(1 + b\xi\right)}{6\alpha\left(R_i + X\right)}\left[6R_i\,\phi_0\left(L - X\right) + 3\left(\phi_0 - \alpha R_i\right)\left(L^2 - X^2\right) - 2\alpha\left(L^3 - X^3\right)\right] \tag{56}$$

where

$$\alpha = \frac{2\left(3R_i + 2L\right)L^2\left(1 + b\xi\right)\phi_0}{12U + L^3\left(1 + b\xi\right)\left(4R_i + 3L\right)} \tag{57}$$

2.4 Partially wet annular fins

The energy equations for dry and wet regions in partially wet fins can be written separately in the followings:

$$\begin{bmatrix} \frac{d}{dx}\left\{y\left(r_i + x\right)\frac{dT}{dx}\right\} \\ \frac{d}{dx}\left\{y\left(r_i + x\right)\frac{dT}{dx}\right\} \end{bmatrix} = \begin{bmatrix} \frac{h}{k}\left(r_i + x\right)\left(T - T_a\right) \\ \frac{h}{k}\left(r_i + x\right)\left\{\left(T - T_a\right) + h_m\left(\omega - \omega_a\right)h_{fg}\big/h\right\} \end{bmatrix} \tag{58}$$

dry domain $T > T_d$ (58a)

wet domain $T \le T_d$ (58b)

Eq. (58) can be expressed in normalized form as

$$\begin{bmatrix} \dfrac{d}{dX}\left\{Y\left(R_i+X\right)\dfrac{d\theta}{dX}\right\} \\ \dfrac{d}{dX}\left\{Y\left(R_i+X\right)\dfrac{d\phi}{dX}\right\} \end{bmatrix} = \begin{bmatrix} \left(R_i+X\right)\theta & \theta > \theta_d \\ \left(R_i+X\right)\left(1+b\xi\right)\phi & \theta \le \theta_d \end{bmatrix} \tag{59a}$$

$$\tag{59b}$$

For solving Eq. (59), four boundary conditions are required and these are already written in Eq. (23). Heat transfer equation is obtained from Eq. (59) and boundary conditions in the followings:

$$\begin{aligned} Q = \frac{q\left(h/\pi\right)}{4k^2\left(T_a-T_b\right)} &= -\left[Y\left(R_i+X\right)\frac{d\phi}{dX}\right]_{X=0} = \frac{\phi_d}{\phi_0\,\theta_d}\int_{X=L_0}^{L}\left(R_i+X\right)\left[Y\left(d\theta/dX\right)^2+\theta^2\right]dX \\ &+\frac{1}{\phi_0}\int_{X=0}^{L_0}\left(R_i+X\right)\left[Y\left(d\phi/dX\right)^2+\left(1+b\xi\right)\phi^2\right]dX \end{aligned} \tag{60}$$

The dimensionless fin volume for the partially wet fin can be formulated in the following:

$$U = \frac{V\left(h/k\right)^3}{4\pi} = \int_{X=0}^{L_0}\left(R_i+X\right)Y dX + \int_{X=L_0}^{L}\left(R_i+X\right)Y dX \tag{61}$$

To apply variational principle, a functional F is constructed by using heat transfer rate and fin volume expressions.

$$\begin{aligned} F = Q-\lambda U &= \frac{1}{\phi_0}\int_{X=0}^{L_0}\left(R_i+X\right)\left[Y\left(d\phi/dX\right)^2+\left(1+b\xi\right)\phi^2-\lambda\phi_0 Y\right]dX \\ &+\frac{\phi_d}{\phi_0\theta_d}\int_{X=L_0}^{L}\left(R_i+X\right)\left[Y\left(d\theta/dX\right)^2+\theta^2-\lambda\phi_0\theta_d Y/\phi_d\right]dX \end{aligned} \tag{62}$$

The optimality criterion can be derived by differentiating functional *F* with respect to *Y* and then equating to zero.

$$\begin{aligned} \delta F &= \frac{1}{\phi_0}\int_{X=0}^{L_0} Y^{-1}\left(R_i+X\right)\left[Y\left(d\phi/dX\right)^2-\lambda\phi_0 Y\right]\delta Y\,dX \\ &+\frac{\phi_d}{\phi_0\theta_d}\int_{X=L_0}^{L} Y^{-1}\left(R_i+X\right)\left[Y\left(d\theta/dX\right)^2-\lambda\varphi_0\theta_d Y/\phi_d\right]\delta Y\,dX = 0 \end{aligned} \tag{63}$$

Therefore from Eq. (63), the following optimality criterion is found:

$$\begin{bmatrix} \left(d\theta/dX\right)^2-\lambda\phi_0\,\theta_d/\phi_d \\ \left(d\phi/dX\right)^2-\lambda\phi_0 \end{bmatrix} = \begin{bmatrix} 0 & \theta > \theta_d \\ 0 & \theta \le \theta_d \end{bmatrix} \tag{64a}$$

$$\tag{64b}$$

2.4.1 Optimum annular fin for volume constraint

The following expression is obtained for variation of F with length L from Eq. (62)

$$\begin{bmatrix}\delta F\\ \delta F\end{bmatrix}=\begin{bmatrix}\dfrac{(R_i+X)}{\phi_0}\left\{Y\left(d\phi/dX\right)^2+\left(1+b\xi\right)\phi^2-\lambda\,\phi_0 Y\right\}\delta X\Big|_{X=0}^{X=L_0}\\ \dfrac{(R_i+X)\phi_d}{\theta_d\phi_0}\left\{Y\left(d\theta/dX\right)^2+\theta^2-\lambda Y\phi_0\theta_d/\phi_d\right\}\delta X\Big|_{X=L_0}^{L}\end{bmatrix}=\begin{bmatrix}0\\ 0\end{bmatrix}\quad\begin{matrix}\theta\le\theta_d\\ \theta>\theta_d\end{matrix} \tag{65a, 65b}$$

From Eq. (65), the following conditions are determined:

$$\begin{bmatrix}Y\left(d\theta/dX\right)^2+\theta^2-\lambda\,\theta_d\phi_0 Y/\phi_d\\ Y\left(d\phi/dX\right)^2+\left(1+b\xi\right)\phi^2-\lambda\phi_0 Y\end{bmatrix}=\begin{bmatrix}0\\ 0\end{bmatrix}\quad\text{at } X=L_0 \tag{66a, 66b}$$

and

$$Y\left(d\theta/dX\right)^2+\theta^2-\lambda\,\theta_d\varphi_0 Y/\phi_d=0\quad\text{at } X=L \tag{67}$$

From the above analysis, one can determine the dimensionless tip temperature and tip thickness, both are zero for the optimum design condition. The fin temperature and fin profile are obtained as follows:

$$\theta=\begin{cases}1-\left(1-\theta_d\right)X/L_0 & 0\le X\le L_0\\ \theta_d\left(L-X\right)/\left(L-L_0\right) & L_0\le X\le L\end{cases} \tag{68a, 68b}$$

and

$$\begin{aligned}Y=&\frac{1}{6\left(R_i+X\right)}\Big[6LR_i\left(L-L_0\right)+3\left(L-R_i\right)\left(L^2-L_0^2\right)-2\left(L^3-L_0^3\right)\\&+\frac{\left(1+b\xi\right)}{\left(1-\theta_d\right)}\left\{6R_iL_0\varphi_0\left(L_0-X\right)+3\left(\varphi_0L_0-\left(1-\theta_d\right)R_i\right)\left(L_0^2-X^2\right)-2\left(1-\theta_d\right)\left(L_0^3-X^3\right)\right\}\Big]\\&\text{for }\left(0\le X\le L_0\right)\end{aligned} \tag{69a}$$

$$Y=\frac{1}{6\left(R_i+X\right)}\Big[6LR_i\left(L-X\right)+3\left(L-R_i\right)\left(L^2-X^2\right)-2\left(L^3-X^3\right)\Big]\quad\text{for } L_0\le X\le L \tag{69b}$$

The length of the optimum annular fin can be determined from the following equation given below:

$$\begin{aligned}&\left[2\theta_d^2\left(1-\theta_d\right)+\left(1+b\xi\right)\left\{4\varphi_0-4\theta_d\varphi_0-3\left(1-\theta_d\right)^2\right\}\left(1-\theta_d\right)^2+\theta_d^3\left(2-\theta_d\right)\right]L^4\\&+\left[6\theta_d^2\left(1-\theta_d\right)+2\left(1+b\xi\right)\left(3\varphi_0+2\theta_d-2\right)\left(1-\theta_d\right)^2+2\theta_d^3\right]R_iL^3-12U=0\end{aligned} \tag{70}$$

Eq. (70) can be solved numerically. The Newton-Raphson iterative method can be employed to determine the optimum length of the fin after satisfying the necessary convergence criterion. After estimating L_{opt} value, one can calculate the maximum or optimum actual heat transfer rate which can be determined from the expression give below:

$$Q_{opt} = \frac{L_{opt}}{6}\Big[\, 6R_i\theta_d + 3\left(L_{opt} - R_i\right)\left\{1-\left(1-\theta_d\right)^2\right\} - 2L_{opt}\left\{1-\left(1-\theta_d\right)^3\right\} + \left(1-\theta_d\right)\left(1+b\xi\right)L_{opt}^2\left\{6R_i\phi_0 + 3\left(\phi_0 L_{opt} - R_i\right)\left(1-\theta_d\right) - 2L_{opt}\left(1-\theta_d\right)^2\right\}\Big] \tag{71}$$

2.4.2 Optimum annular fin for both length and volume constraints

The temperature distribution and fin profile for the annular fin can be determined by using Eqs. (6), (59), (61) and (64) as

$$\begin{bmatrix}\theta\end{bmatrix} = \begin{bmatrix}1-\alpha X\end{bmatrix} \quad 0 \le X \le L_0 \tag{72a}$$

$$\begin{bmatrix}\theta\end{bmatrix} = \begin{bmatrix}\theta_d - \alpha\left(X - L_0\right)\end{bmatrix} \quad L_0 \le X \le L \tag{72b}$$

and

$$Y = \frac{1}{6\alpha\left(R_i + X\right)}\Big[6R_i\left(\theta_d + \alpha L_0\right)\left(L - L_0\right) + 3\left(\theta_d - \alpha R_i + \alpha L_0\right)\left(L^2 - L_0^2\right) - 2\alpha\left(L^3 - L_0^3\right) + \left(1+b\xi\right)\left\{6\phi_0 R_i\left(L_0 - X\right) + 3\left(\phi_0 - \alpha R_i\right)\left(L_0^2 - X^2\right) - 2\alpha\left(L_0^3 - X^3\right)\right\}\Big] \quad \left(0 \le X \le L_0\right) \tag{73a}$$

$$Y = \frac{1}{6\alpha\left(R_i + X\right)}\Big[6\left(R_i\,\theta_d + \alpha R_i L_0\right)\left(L - X\right) + 3\,\left(\alpha L_0 - \alpha R_i + \theta_d\right)\left(L^2 - X^2\right) - 2\alpha\left(L^3 - X^3\right)\Big] \quad \left(L_0 \le X \le L\right) \tag{73b}$$

where

$$\alpha = \frac{6R_i\,\theta_d\left(L^2 - L_0^2\right) + 2\phi_0\left(1+b\xi\right)\left(3R_i + 2L_0\right)L_0^2 + 4\theta_d\left(L^3 - L_0^3\right)}{12U + L_0^3\left(1+b\xi\right)\left(4R_i + 3L_0\right) - 2R_i L_0\left(3L^2 - L_0^2\right) + L^3\left(4R_i + 3L\right) - L_0\left(4L^3 - L_0^3\right)} \tag{74a}$$

and

$$L_0 = \left(1-\theta_d\right)/\alpha \tag{74b}$$

Combining Eqs. (74a) and (74b), the following transcendental equation is obtained:

$$\Big[\left(1+b\xi\right)\left(3-3\theta_d-4\phi_0\right) + 3\theta_d + 1\Big]L_0^4 + 2R_i\Big[\left(1-\theta_d\right)\left(3+2b\xi\right) - 3\phi_0\left(1+b\xi\right) + 3\theta_d\Big]L_0^3 - 2L^2 L_0 + \left(1-\theta_d\right)\left(12U + 4R_i L^3 + 3L^4\right) = 0 \tag{75}$$

In order to determine the wet length in the fin L_0, Eq. (75) can be solved by using Newton-Raphson iterative technique.

2.5 Fully wet pin fins

A schematic diagram of a pin fin is shown in Fig. 2B. The energy equation for pin fins subject to condensation of vapor under fully wet condition is written below:

$$\frac{d}{dx}\left(y^2\frac{dT}{dx}\right)=\frac{2h}{k}y\left[\left(T-T_a\right)+h_m\left(\omega-\omega_a\right)h_{fg}/h\right] \tag{76}$$

Eq. (76) is expressed in nondimensional form as

$$\frac{d}{dX}\left(Y^2\frac{d\phi}{dX}\right)=2Y\left(1+b\xi\right)\phi \tag{77}$$

For the solution of Eq. (77), the boundary conditions expressed in Eq. (7) are taken. The actual heat transfer rate is calculated from the following expression:

$$Q=\frac{2q\left(h/\pi\right)}{2k^2\left(T_a-T_b\right)}=-\left[Y^2\frac{d\phi}{dX}\right]_{X=0}=\frac{1}{\phi_0}\int_{X=0}^{L}Y\left[Y\left(d\phi/dX\right)^2+2\left(1+b\xi\right)\phi^2\right]dX \tag{78}$$

The fin volume of a pin fin is written in dimensionless form as

$$U=\frac{V\left(h/k\right)^3}{\pi}=\int_{X=0}^{L}Y^2dX \tag{79}$$

For determination of the optimum shape, a functional F is defined as

$$F=Q-\lambda U=\frac{1}{\phi_0}\int_{X=0}^{L}Y\left[Y\left(d\phi/dX\right)^2+2\left(1+b\xi\right)\phi^2-\lambda\phi_0 Y\right]dX \tag{80}$$

The above equation gives a relationship between F and Y. The optimum condition can be obtained by differentiating functional F with respect to Y.

$$\delta F=\frac{1}{\phi_0}\int_{X=0}^{L}2\left[Y\left(d\phi/dX\right)^2+\left(1+b\xi\right)\phi^2-\lambda\phi_0 Y\right]\delta Y\,dX=0 \tag{81}$$

The following expression is obtained from Eq. (81).

$$Y\left(d\phi/dX\right)^2+\left(1+b\xi\right)\phi^2-\lambda\phi_0 Y=0 \tag{82}$$

Multiplying on both sides in Eq. (77) by $d\phi/dX$ yields the following expression after some manipulations:

$$d\left[Y^2\left(d\phi/dX\right)^2\right]\Big/dX+\left(d\phi/dX\right)^2 d\left(Y^2\right)\Big/dX=2\left(1+b\xi\right)Y\left(d\phi^2\right)\Big/dX \tag{83}$$

Eliminating ϕ^2 from Eq. (82) by using Eq. (83) and then integrating, the following expression is obtained.

$$3Y^2\left(d\phi/dX\right)^2-\lambda\phi_0 Y^2=C \tag{84}$$

where, C is an integration constant determined by using boundary conditions.

2.5.1 Optimum fully wet pin fin for volume constraint

The variation of F with a function of L yields from Eq. (80) as

$$\delta F=\frac{Y}{\phi_0}\left[Y\left(d\phi/dX\right)^2+2\left(1+b\xi\right)\phi^2-\lambda\,\phi_0 Y\right]\delta X\Big|_{X=0}^{L}=0 \tag{85}$$

As δX is nonzero at $X = L$, the following tip condition can be achieved :

$$Y\left(d\phi/dX\right)^2+2\left(1+b\xi\right)\phi^2-\lambda\phi_0 Y=0 \tag{86}$$

From Eqs. (6), (77), (82) and (86) the dimensionless temperature ϕ at the tip vanishes and it can be indicated that the same condition is obtained in the case of longitudinal and annular fins with fully wet condition. Using Eqs. (6), (77), (82) and (86), temperature distribution and fin profile for the optimum fin can be written as

$$\theta=1-\left(1+\theta_p\right)X/L \tag{87a}$$

and

$$Y=\frac{\left(1+b\xi\right)\left(L-X\right)^2}{2} \tag{87b}$$

The optimum fin length and heat transfer rate are determined as follows:

$$\begin{bmatrix}L_{opt}\\ Q_{\max}\end{bmatrix}=\begin{bmatrix}\left\{20\,U/\left(1+b\xi\right)^2\right\}^{1/5} & (88a)\\ \phi_0\left\{125U^3\left(1+b\xi\right)^4/8\right\}^{1/5} & (88b)\end{bmatrix}$$

2.5.2 Optimum fully wet pin fin for both length and volume constraints

The temperature distribution and fin profile can be found from Eqs. (6), (77) and (84) as

$$\phi=\phi_0\sqrt{Y_b\left(Y_t^2Y^{-1}+2Y\right)/\left(Y_t^2+2Y_b^2\right)},\quad Y_t\le Y\le Y_b \tag{89}$$

and

$$\int_{Y_t}^{Y}\frac{\left(2Y^2-Y_t^2\right)dY}{\sqrt{\left(Y^2-Y_t^2\right)\left(Y_t^2+2Y^2\right)Y}}=2\sqrt{\left(1+b\xi\right)}\,\left(L-X\right) \tag{90}$$

In order to determine the temperature profile and fin profile from the above two equations, the unknown variables Y_t and Y_b are required to calculate apriori. These can be determined by constructing two constraint equations as follows:

$$U = \int_{Y=Y_t}^{Y_b} \frac{\left(2Y^2 - Y_t^2\right)Y^2 dY}{2\sqrt{(1+b\xi)}\sqrt{\left(Y^2 - Y_t^2\right)\left(Y_t^2 + 2Y^2\right)Y}} \tag{91a}$$

and

$$\int_{Y=Y_t}^{Y_b} \frac{\left(2Y^2 - Y_t^2\right)dY}{\sqrt{\left(Y^2 - Y_t^2\right)\left(Y_t^2 + 2Y^2\right)Y}} = 2\sqrt{(1+b\xi)}\, L \tag{91b}$$

A simultaneous solution of Eqs. (91a) and (91b) is provided to get the fin thickness at the base and tip. The above all integration can be performed by Simson's 1/3 rule.

2.6 Partially wet pin fins

The energy equations for partially wet pin fins are written as

$$\left[\frac{d}{dx}\left(y^2\frac{dT}{dx}\right)\right] = \left[\frac{2h}{k}y\left(T - T_a\right)\right] \quad \text{for dry domain } T > T_d \tag{92a}$$

$$\left[\frac{d}{dx}\left(y^2\frac{dT}{dx}\right)\right] = \left[\frac{2h}{k}y\left\{\left(T - T_a\right) + h_m\left(\omega - \omega_a\right)h_{fg}/h\right\}\right] \quad \text{for wet domain } T \le T_d \tag{92b}$$

Eq. (92) can be expressed in dimensionless form as

$$\left[d\left(Y^2\, d\theta/dX\right)/dX\right] = \left[2Y\theta\right] \quad \text{dry domain } \theta > \theta_d \tag{93a}$$

$$\left[d\left(Y^2\, d\varphi/dX\right)/dX\right] = \left[2Y\left(1+b\xi\right)\phi\right] \quad \text{wet domain } \theta \le \theta_d \tag{93b}$$

Boundary conditions are reguired to solve Eq. (93) which can be taken as longitudinal fins expressed in Eq. (23). The actual heat transfer rate is calculated from the following equation:

$$\begin{aligned} Q = \frac{q\left(h/\pi\right)}{k^2\left(T_a - T_b\right)} &= -\left[Y^2\frac{d\phi}{dX}\right]_{X=0} = \frac{\phi_d}{\phi_0\,\theta_d}\int_{X=L_0}^{L} Y\left[Y\left(d\theta/dX\right)^2 + 2\theta^2\right]dX \\ &+ \frac{1}{\phi_0}\int_{X=0}^{L_0} Y\left[Y\left(d\phi/dX\right)^2 + 2\left(1+b\xi\right)\phi^2\right]dX \end{aligned} \tag{94}$$

The fin volume for a partially wet pin fin is written in an integral form as

$$U = \frac{V\left(h/k\right)^3}{\pi} = \int_{X=0}^{L_0} Y^2 dX + \int_{X=L_0}^{L} Y^2 dX \tag{95}$$

For the application of variational method, a functional F is constructed from heat transfer rate and fin volume expressions:

$$F = Q - \lambda U = \frac{1}{\phi_0}\int_{X=0}^{L_0} Y\left[Y\left(d\phi/dX\right)^2 + 2\left(1+b\xi\right)\phi^2 - \lambda\phi_0 Y\right]dX + \frac{\phi_d}{\phi_0\theta_d}\int_{X=L_0}^{L} Y\left[Y\left(d\theta/dX\right)^2 + 2\theta^2 - \lambda\phi_0\theta_d Y/\phi_d\right]dX \tag{96}$$

For maximizing value of F condition, the following expression is obtained:

$$\delta F = \frac{1}{\phi_0}\int_{X=0}^{L_0}\left[Y\left(d\phi/dX\right)^2 + \left(1+b\xi\right)\phi^2 - \lambda\phi_0 Y\right]\delta Y\,dX + \frac{\phi_d}{\phi_0\theta_d}\int_{X=L_0}^{L}\left[Y\left(d\theta/dX\right)^2 + \theta^2 - \lambda\phi_0\theta_d Y/\phi_d\right]\delta Y\,dX = 0 \tag{97}$$

Therefore, from Eq. (97), the following optimality criterion is derived:

$$\begin{bmatrix} Y\left(d\theta/dX\right)^2 + \theta^2 - \lambda\phi_0\,\theta_d\,Y/\phi_d \\ Y\left(d\phi/dX\right)^2 + \left(1+b\xi\right)\phi^2 - \lambda\phi_0\,Y \end{bmatrix} = \begin{bmatrix} 0 & \theta > \theta_d \\ 0 & \theta \le \theta_d \end{bmatrix} \tag{98a}$$

(98b)

The following expressions is obtained from Eq. (93) after multiplying on both sides of Eqs. (93a) and (93b) by $d\theta/dX$ and $d\phi/dX$, respectively.

$$\begin{bmatrix} d\left\{Y^2\left(d\theta/dX\right)^2\right\}/dX + \left(d\theta/dX\right)^2 d\left(Y^2\right)/dX \\ d\left\{Y^2\left(d\phi/dX\right)^2\right\}/dX + \left(d\phi/dX\right)^2 d\left(Y^2\right)/dX \end{bmatrix} = \begin{bmatrix} 2\,Y\,d\left(\theta^2\right)/dX & \theta > \theta_d \\ 2\left(1+b\xi\right)Yd\left(\phi^2\right)/dX & \theta \le \theta_d \end{bmatrix} \tag{99a}$$

(99b)

Eleminating θ^2 and ϕ^2 from Eq. (99) with the help of Eq. (98), the following equations are obtained:

$$\begin{bmatrix} 3Y^2\left(d\theta/dX\right)^2 - \lambda\phi_0\,\theta_d Y^2/\phi_d \\ 3Y^2\left(d\phi/dX\right)^2 - \lambda\phi_0 Y^2 \end{bmatrix} = \begin{bmatrix} C_1 & \theta > \theta_d \\ C_2 & \theta \le \theta_d \end{bmatrix} \tag{100a}$$

(100b)

The integration constants C_1 and C_2 are determined from the boundary conditions.

2.6.1 Optimum partially wet pin fin for volume constraint only

The variation of functional F with length parameter L for partially wet pin fins is given below:

$$\begin{bmatrix} \delta F \\ \delta F \end{bmatrix} = \begin{bmatrix} \dfrac{Y}{\phi_0}\left\{Y\left(d\phi/dX\right)^2 + 2\left(1+b\xi\right)\phi^2 - \lambda\,\phi_0\,Y\right\}\delta X\Big|_{X=0}^{X=L_0} \\ \dfrac{Y\phi_d}{\theta_d\phi_0}\left\{Y\left(d\theta/dX\right)^2 + 2\theta^2 - \lambda Y\varphi_0\theta_d/\phi_d\right\}\delta X\Big|_{X=L_0}^{L} \end{bmatrix} = \begin{bmatrix} 0 & \theta \le \theta_d \\ 0 & \theta > \theta_d \end{bmatrix} \tag{101a}$$

(101b)

For X=0, the above terms vanish as δX=0. For X=L_0 and X=L, δX is not zero; therefore, the location where dry and wet surfaces present, and the tip, the following optimality conditions are achieved:

$$\begin{bmatrix} Y\left(d\theta/dX\right)^2 + 2\theta^2 - \lambda\theta_d\phi_0 Y/\phi_d \\ Y\left(d\phi/dX\right)^2 + 2\left(1+b\xi\right)\phi^2 - \lambda\phi_0 Y \end{bmatrix} = \begin{bmatrix} 0 \\ 0 \end{bmatrix} \quad \text{at } X = L_0 \tag{102a}$$

(102b)

$$Y\left(d\theta/dX\right)^2 + 2\theta^2 - \lambda\theta_d\phi_0 Y/\phi_d = 0 \quad \text{at } X = L \tag{102c}$$

The temperature distribution and fin profile for an optimum pin fin for volume constraint only are same with that of the longitudinal fin. The fin length and heat transfer rate for the optimum profile fin is obtained from the following equations :

$$L_{opt} = \frac{\left(60U\right)^{1/5}}{\left[3\theta_d^4\left(5-2\theta_d\right) + Z_1\left\{Z_2 + 10\theta_d^2 + 1\right\}\left(3\phi_0 + 2\theta_d - 2\right)\right]^{1/5}} \tag{103a}$$

$$Q_{opt} = \frac{\left[\theta_d^2 + \left(1+b\xi\right)\left(2\varphi_0 + \theta_d - 1\right)\left(1-\theta_d\right)\right]^2\left(60U\right)^{3/5}}{\left[3\theta_d^4\left(5-2\theta_d\right) + Z_1\left\{Z_2 + 10\theta_d^2 + 1\right\}\left(3\phi_0 + 2\theta_d - 2\right)\right]^{3/5}} \tag{103b}$$

where

$$Z_1 = \left(1+b\xi\right)\left(1-\theta_d\right)^2 \tag{104a}$$

$$Z_2 = \left(1-\theta_d\right)\left(1+b\xi\right)\left\{5\left(2\phi_0 + \theta_d - 1\right)\left(5 - 6\phi_0 - 2\theta_d\right) + 5\phi_0\left(4\phi_0 + 3\theta_d - 3\right) + 3\left(1-\theta_d\right)^2\right\} \tag{104b}$$

2.6.2 Optimum partially wet pin fin for both length and volume constraints

The temperature distribution and fin profile can be found from Eqs. (6), (93), (95) and (100) for the partially wet conditions as follows:

$$\phi = \phi_0\sqrt{\frac{Y_b}{Y}\left[\frac{2\phi_d Y^2 + \left(\phi_d - \theta_d\right)Y_0^2 + \theta_d Y_t^2}{2\phi_d Y_b^2 + \left(\phi_d - \theta_d\right)Y_0^2 + \theta_d Y_t^2}\right]}, \quad Y_0 \le Y \le Y_b \tag{105a}$$

$$\theta = \theta_d\sqrt{Y_0\left({Y_t}^2 Y^{-1} + 2Y\right)\Big/\left({Y_t}^2 + 2{Y_0}^2\right)}, \quad Y_0 \le Y \le Y_t \tag{105b}$$

and

$$\int_{Y_0}^{Y} \frac{\left(2Y^2 - {Y_0}^2\right)dY}{\sqrt{\left(Y^2 - {Y_0}^2\right)\left({Y_0}^2 + 2Y^2\right)Y}} = 2\sqrt{\left(1+b\xi\right)}\left(L_0 - X\right) \tag{106a}$$

$$\int_{Y_t}^{Y} \frac{\left(2Y^2 - Y_t^2\right)dY}{\sqrt{\left(Y^2 - Y_t^2\right)\left(Y_t^2 + 2Y^2\right)Y}} = 2\left(L - X\right) \tag{106b}$$

From the above equations for obtaining temperature distribution and fin profile, it is worthy to mention that the design variables Y_0, Y_t, Y_b and L_0 are required to determine first. The Y_t and Y_b can be determined from the constraint equations taken in the design as

$$U = \int_{Y=Y_0}^{Y_b} \frac{\left(2Y^2 - Y_0^2\right)Y^2 dY}{2\sqrt{(1+b\xi)}\sqrt{\left(Y^2 - Y_0^2\right)\left(Y_0^2 + 2Y^2\right)Y}} + \int_{Y=Y_t}^{Y_0} \frac{\left(2Y^2 - Y_t^2\right)Y^2 dY}{2\sqrt{\left(Y^2 - Y_t^2\right)\left(Y_t^2 + 2Y^2\right)Y}} \tag{107a}$$

$$\int_{Y=Y_0}^{Y_b} \frac{\left(2Y^2 - Y_0^2\right)dY}{\sqrt{\left(Y^2 - Y_0^2\right)\left(Y_0^2 + 2Y^2\right)Y}} + \int_{Y=Y_t}^{Y_0} \frac{\left(2Y^2 - Y_t^2\right)dY}{\sqrt{\left(Y^2 - Y_t^2\right)\left(Y_t^2 + 2Y^2\right)Y}} = 2\sqrt{(1+b\xi)}L_0 + 2\left(L - L_0\right) \tag{107b}$$

The parameters L_0 and Y_0 are determined from the dewpoint temperature section where dry and wet part coexist and one can take the continuity of temperature and heat conduction at this section.

3. Results and discussion

The humid air is a mixture of dry air and water vapor. Three properties of air are used to calculate a thermodynamic state point to show the influence of dehumidification of air on the optimizing shape of three common type of fins, namely, Longitudinal, annular and pin fins. The air properties such as pressure, temperature, and relative humidity of air are used to determine a pychrometric state. The effect of the psychometric properties of air on the optimization study is investigated. Two constraints, namely, fin volume, and both fin volume and length have been adopted to furnish the result for any designed application.

Fig. 3 is depicted the profile shape and temperature distribution in an optimum fin under different surface conditions as a function of fin length for a constraint fin volume. For the dry surface fin, the optimum fin shape can be determined from the fully wet fin analysis presented above by taking zero value of latent heat parameter ξ. To make a comparison between dry and wet surface fins, the results for the dry surface fin has been plotted in the same figure. From the figure, it can be noticeable that the temperature distribution in the fin at an optimum condition under dry, partially wet, and fully wet surfaces varies linearly (Fig. 3A). For the same fin base temperature for all the surface conditions adopted here, temperature on the fin surface of wet fins differs from that of the dry surface fin and the difference increases gradually from the fin base to fin tip. The discrepancy in temperature occurs due to evolving of latent heat of condensation of moisture on the fin surface in the case of wet fins. This difference in temperature becomes maximum for the 100% relative humidity of air as the maximum value of latent heat released for this relative humidity. From the analysis, it can be highlighted that for the dry and partially wet fin at an optimum condition, the tip temperature equalizes to the ambient temperature. However, for fully wet fin, the tip temperature is sightly less than the ambient value. Figure 3B is illustrated the optimum fin profile for dry, partially wet and fully wet conditions. For the dry fin, the optimum length and

optimum base thickness are larger and smaller, respectively than that for the any wet fin for the same fin volume and the difference is maximum for the fully wet fin of 100% relative humidity of air. Nevertheless, the effect of relative humidity on the optimum fin profile for a wet fin is marginal. The same trend for temperature distribution and the optimum fin profile of the annular and pin fins, are found and they are displayed in Figs. 4 and 5, respectively. In the case of annular fins, it can be mentioned that the optimum temperature distribution and fin profile are also function of the tube outer radius parameter R_i.

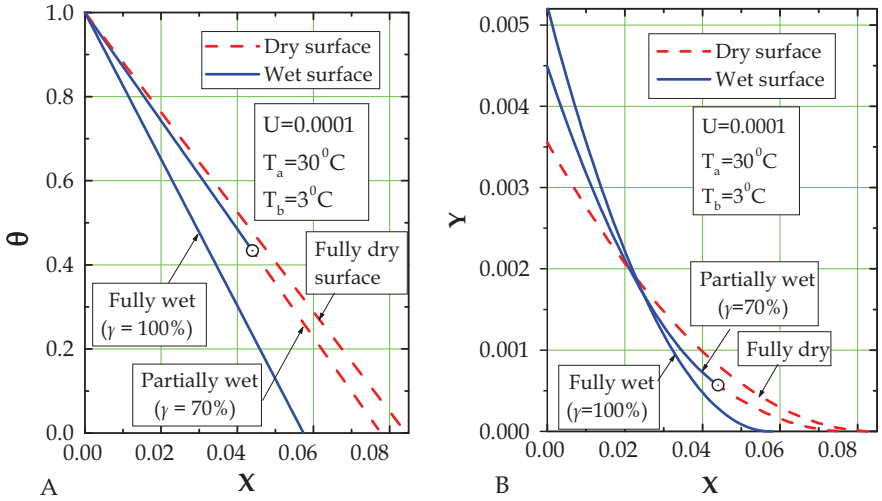

Fig. 3. Variation of temperature distribution and fin profile of an optimum longitudinal fin for the different surface conditions under a volume constraint: A. fin temperature; and B. fin profile

With satisfying either maximizing heat transfer rate for a given fin volume or minimizing fin volume for a given heat transfer duty, the optimization of any fin is studied. Depending upon the requirement of design, any one of these two constraints is used but they give the same result. The optimum profile shape is determined from the solution of the optimality criteria of the fin design and the constraint condition taken. The result from the optimization study of wet fins is depicted in Figs. 6, 7 and 8 as a function of fin volume for longitudinal, annular and spine, respectively. The optimum result for the dry surface condition of each fin, in comparison, is plotted in the corresponding figure. From these illustrations, it is understandable that the optimum parameters, namely, heat transfer rate, fin length, and fin thickness at the base, enhance continually with the fin volume. The maximum rate of heat transfer is not only as a function of the fin material but also as a function of the condition of the surface. A fully wet surface with 100% relative humidity predicts a maximum optimum heat transfer rate per unit volume in comparison with that transferred by any other surfaces. A partially wet surface transfers a less amount of heat per unit volume in comparison to that by fully wet surface fin and heat transfer rate decreases gradually with the decremented relative humidity. A dry surface fin at an optimum condition transfers least amount of heat per unit fin volume in comparison with the wet surface fin. This is happen due to latent heat evolved in wet fin heat transfer mechanism. For a lower value of fin volume, difference in heat transfer among fully wet, partially wet and dry surfaces may not so much important

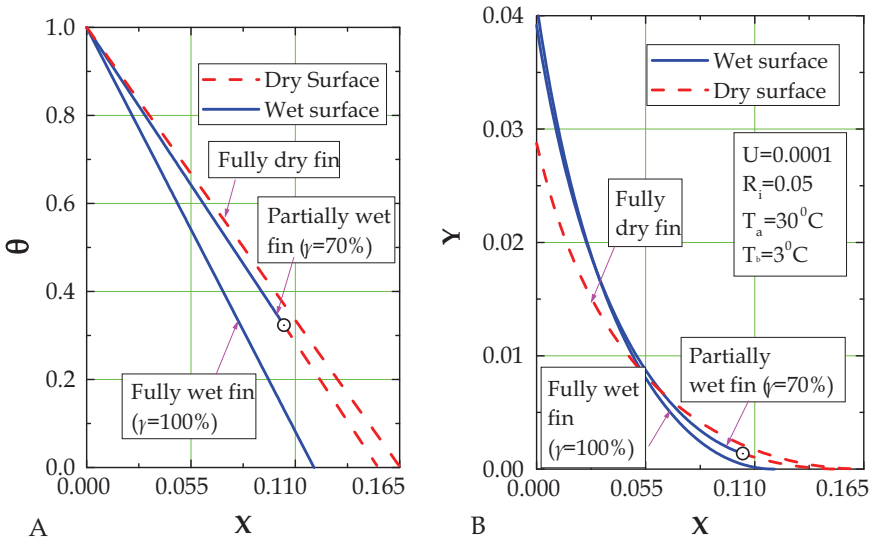

Fig. 4. Variation of temperature distribution and fin profile of an optimum annular fin for the different surface conditions for a volume constraint: A. fin temperature; and B. fin profile.

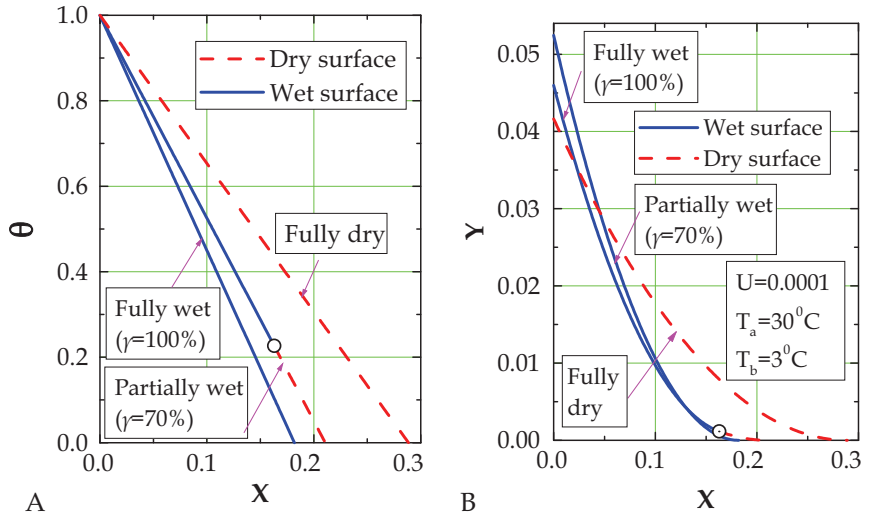

Fig. 5. Variation of temperature distribution and fin profile of an optimum spine for the different surface conditions under a volume constraint: A. fin temperature; and B. fin profile

than that for a higher value of fin volume as shown in Fig. 6A. Irrespective of any surface condition, the length and fin thickness at the base of an optimum fin increases with the fin volume. The optimum fin length for fully wet fins is always shorter than that for the partially wet as well as dry fins. The optimum length is a maximum for the dry surface condition under the same fin volume (Fig. 6B). Nevertheless, an opposite trend is noticed for

the variation of fin thickness at the base with the fin volume in comparison with the variation of fin length with volume for different surface condition as shown in Fig. 6C. A similar exercise has been made for the annular fin and spine by plotting Figs. 7 and 8. In the case of annular fin, the above parameters also function of the thermogeometric parameter R_i. With the increase in R_i, the optimum heat transfer rate increases as well as the optimum length and optimum base thickness decreases, separately with the same fin volume.

From the above optimum results, it can be emphasized to highlight that the optimum fin shape obtained from an optimization technique with the consideration of only one constraint either fin volume or heat transfer rate, is a complex in nature and fragile shape at the tip as already shown in Fig. 3 and hence, it is difficult surely in manufacturing process. To overcome this problem and to restrict the length of the fin, fin length can be taken as an additional constraint with the fin volume. In this case, the shape of the fin profile and fragile

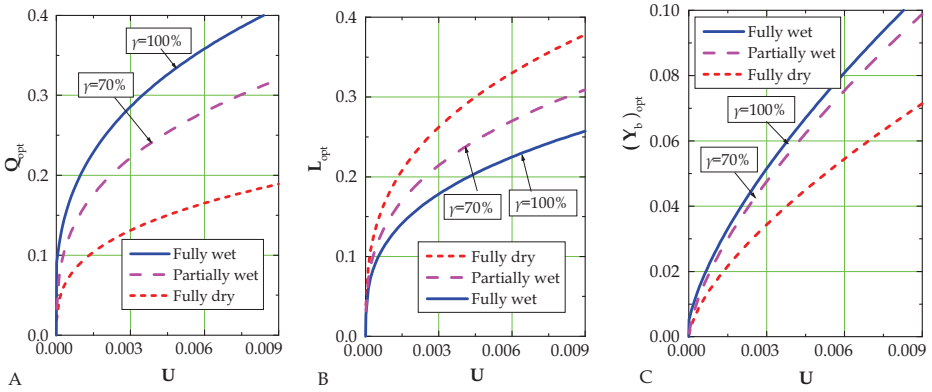

Fig. 6. Design parameters of an optimum longitudinal fin as a function of fin volume: A. maximum heat transfer rate; B. optimum length; and C. optimum semi-fin thickness at the base

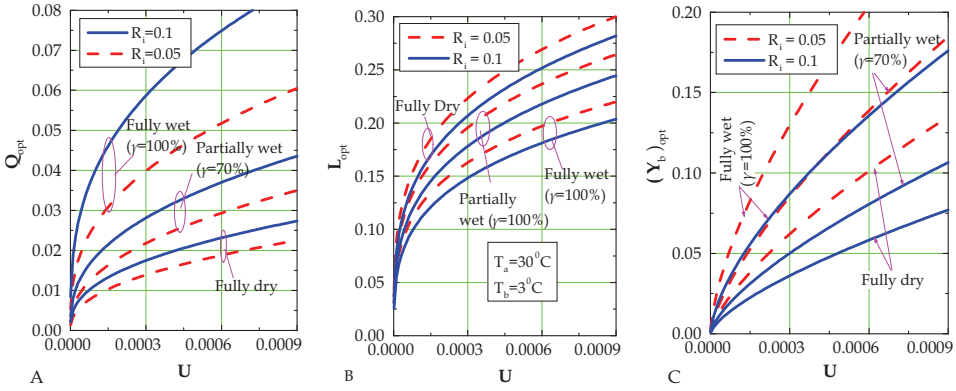

Fig. 7. Design parameters of an optimum annular fin as a function of fin volume: A. maximum heat transfer rate; B. optimum length; and C. optimum semi-fin thickness at the base

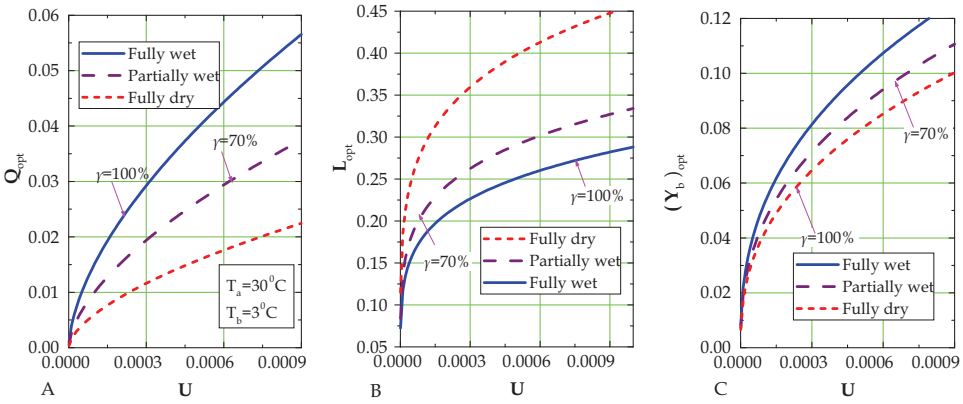

Fig. 8. Design parameters of an optimum pin fin as a function of fin volume: A. maximum heat transfer rate; B. optimum length; and C. optimum fin thickness at the base

geometry at the tip can be improved significantly. To avoid the same nature of the result, the optimum result under both volume and length constraint is illustrated only for the longitudinal fin. The variation of temperature and fin profile is determined under the aforementioned constraint, which is displayed in Fig. 9. From the temperature distribution, it can be mentioned that temperature at the tip of an optimum fin does not vanish and depends upon the magnitude of constraints chosen. For a fully wet surface, temperature at the tip may be closer to the ambient value in comparison with that for the partially and dry surface conditions. With the increase in relative humidity of air, condensation of moisture increases and as a result fin surface temperature increases. This observation can be found in Fig. 9A. The profile shape under both volume and length constraints for various surface conditions is illustrated as a function of dimensionless fin length shown in Fig. 9B. From this figure, it is clear that the profile shape is improved significantly with respect to a profile obtained from only volume constraint chosen, with the consideration of a suitable compatibility in the manufacturing technique. However, there is slightly different in shape between dry and wet surface optimum fin profiles under the same design constants.

4. Conclusions

The fin surface may be dry, fully wet or partially wet depending upon the psychometric conditions of the surrounding air participated as well as the constraints taken in the design. Owing to mass transfer occured with the heat transfer mechanism, the wet surface fin differs from that of dry surface fin. The optimum-envelop shape of wet fins is different with respect to that of dry surface fins. This deviation may be increased with the increase in relative humidity of air. In this chapter, the optimum profile shape of different fins, namely, longitudinal, spine and annular are evaluated for dry, fully wet, and partially wet surface conditions using variational principle. The analysis has also included for different constraint conditions, namely, fin volume and both fin length and fin volume presented for possible requirements of an optimum design. From the results, the optimum design variable for wet fins is not only function of the design constraints but also is a function of psychometric properties of air. Unlike dry and partially wet surface fins, tip temperature for the fully wet

optimum fins under the volume constraint is less than the surrounding temperature. A significant change in optimum design variables has been noticed with the design constants such as fin volume and surface conditions. In order to reduce the complexcity of the optimum profile fins under different surface conditions, the constraint fin length can be selected suitably with the constraint fin volume.

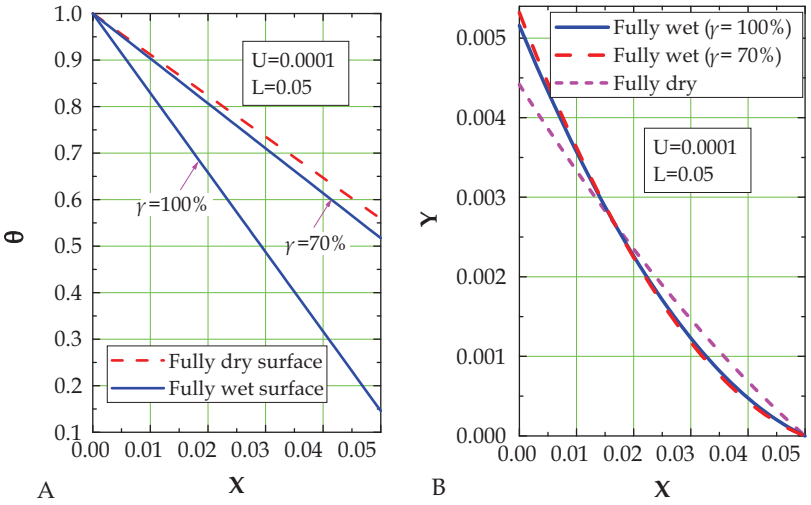

Fig. 9. Variation of temperature and fin profile in a longitudinal fin as a function of length for both volume and length constraints: A. Temperature distribution; and B. Fin profile

5. Acknowledgement

The authors would like to thank King Mongkut's University of Technology Thonburi (KMUTT), the Thailand Research Fund, the Office of Higher Education Commission and the National Research University Project for the financial support.

6. Nomenclatures

a constant determined from the conditions of humid air at the fin base and fin tip
b slop of a saturation line in the psychometric chart, K^{-1}
C non-dimensional integration constant used in Eq. (84)
C_p specific heat of humid air, J kg^{-1} K^{-1}
F functional defined in Eqs. (10), (28), (46), (62), (80) and (96)
h convective heat transfer coefficient, W $m^{-2}K^{-1}$
h_m mass transfer coefficient, kg m^{-2} S^{-1}
h_{fg} latent heat of condensation, J kg^{-1}
k thermal conductivity of the fin material, W $m^{-1}K^{-1}$
l fin length, m

l_0 wet length in partially wet fins, m
L dimensionless fin length, hl/k
L_0 dimensionless wet length in partially wet fins, hl_0/k
Le Lewis number
q heat transfer rate through a fin, W
Q dimensionless heat transfer rate
r_i base radius for annular fins, m
R_i dimensionless base radius, hr_i/k
T temperature, K
U dimensionless fin volume, see Eqs. (9), (27), (45), (61), (79), (91a) and (95)
V fin volume (volume per unit width for longitudinal fins), m^3
x, y coordinates, see Figs. 1 and 2, m
X, Y dimensionless coordinates, hx/k and hy/k, respectively
y_0 semi-thickness of a fin at which dry and wet parts separated, m
Y_0 dimensionless thickness, hy_0/k
Z_1, Z_2 dimensionless parameters defined in Eqs. (104a) and (104b), respectively

Greek Letters

α parameter defined in Eqs. (20), (40), (57) and (74a)
λ Lagrange multiplier
ω specific humidity of air, kg w. v. / kg. d. a.
ξ Latent heat parameter
ϕ dimensionless temperature, $\theta + \theta_p$
ϕ_0 dimensionless temperature at the fin base, $1 + \theta_p$
θ dimensionless fin temperature, $(T_a - T)/(T_a - T_b)$
θ_p dimensionless temperature parameter, see Eq. (5)
γ Relative humidity

Subscripts

a ambient
b base
d dewpoint
opt optimum
t tip

7. References

Chilton, T.H. & Colburn, A.P. (1934). Mass transfer (absorption) coefficients–prediction from data on heat transfer and fluid friction. *Ind. Eng. Chem.*, Vol. 26, 1183.

Duffin, R. J. (1959). A variational problem relating to cooling fins with heat generation. *Q. Appl. Math.*, Vol. 10, 19-29.

Guceri, S. & Maday, C. J. (1975). A least weight circular cooling fin. *ASME J. Eng. Ind.*, Vol. 97, 1190-1193.

Hanin, L. & Campo, A. (2003). A new minimum volume straight cooling fin taking into account the length of arc. *Int. J. Heat Mass Transfer*, Vol. 46, 5145-5152.

Hong, K. T. & Webb, R. L. (1996). Calculation of fin efficiency for wet and dry fins. *HVAC&R Research*, Vol. 2, 27-40.

Kundu, B. & Das, P.K. (1998). Profiles for optimum thin fins of different geometry - A unified approach. *J. Institution Engineers (India): Mechanical Engineering Division*, Vol. 78, No. 4, 215-218.

Kundu, B. (2002). Analytical study of the effect of dehumidification of air on the performance and optimization of straight tapered fins. *Int. Comm. Heat Mass Transfer*, Vol. 29, 269-278.

Kundu, B. & Das, P.K. (2004). Performance and optimization analysis of straight taper fins with simultaneous heat and mass transfer. *ASME J. Heat Transfer*, Vol. 126, 862-868.

Kundu, B. & Das, P. K. (2005). Optimum profile of thin fins with volumetric heat generation: a unified approach. *J. Heat Transfer*, Vol. 127, 945-948.

Kundu, B. (2007a). Performance and optimization analysis of SRC profile fins subject to simultaneous heat and mass transfer. *Int. J. Heat Mass Transfer*, Vol. 50, 1645-1655.

Kundu, B. (2007b). Performance and optimum design analysis of longitudinal and pin fins with simultaneous heat and mass transfer: Unified and comparative investigations. *Applied Thermal Engg.*, Vol. 27, Nos. 5-6, 976-987.

Kundu, B. (2008). Optimization of fins under wet conditions using variational principle. *J. Thermophysics Heat Transfer*, Vol. 22, No. 4, 604-616.

Kundu, B., Barman, D. & Debnath, S. (2008). An analytical approach for predicting fin performance of triangular fins subject to simultaneous heat and mass transfer, *Int. J. Refrigeration*, Vol. 31, No. 6, 1113-1120.

Kundu, B. (2009a). Analysis of thermal performance and optimization of concentric circular fins under dehumidifying conditions, *Int. J. Heat Mass Transfer*, Vol. 52, 2646-2659.

Kundu, B. (2009b). Approximate analytic solution for performances of wet fins with a polynomial relationship between humidity ratio and temperature, *Int. J. Thermal Sciences*, Vol. 48, No. 11, 2108-2118.

Kundu, B. & Miyara, A. (2009). An analytical method for determination of the performance of a fin assembly under dehumidifying conditions: A comparative study, *Int. J. Refrigeration*, Vol. 32, No. 2, 369-380.

Kundu, B. (2010). A new methodology for determination of an optimum fin shape under dehumidifying conditions. *Int. J. Refrigeration*, Vol. 33, No. 6, 1105-1117.

Kundu, B. & Barman, D. (2010). Analytical study on design analysis of annular fins under dehumidifying conditions with a polynomial relationship between humidity ratio and saturation temperature, *Int. J. Heat Fluid Flow*, Vol. 31, No. 4, 722-733.

Liu, C. Y. (1961). A variational problem relating to cooling fins with heat generation. *Q. Appl. Math.*, Vol. 19, 245-251.

Liu, C. Y. (1962). A variational problem with application to cooling fins. *J. Soc. Indust. Appl. Math.*, Vol. 10, 19-29.

Maday, C. J. (1974). The minimum weight one-dimensional straight fin. *ASME J. Eng. Ind.*, Vol. 96, 161-165.

McQuiston, F. C. (1975). Fin efficiency with combined heat and mass transfer. *ASHRAE Transaction*, Vol. 71, 350-355.

Mokheimer, E. M. A. (2002). Performance of annular fins with different profiles subject to variable heat transfer coefficient. *Int. J. Heat Mass Transfer*, Vol. 45, 3631-3642.

Pirompugd, W., Wang, C. C. & Wongwises, S. (2007a). Heat and mass transfer characteristics of finned tube heat exchangers with dehumidification. *J. Thermophysics Heat transfer*, Vol. 21, No. 2, 361-371.

Pirompugd, W., Wang, C. C. & Wongwises, S. (2007b). A fully wet and fully dry tiny circular fin method for heat and mass transfer characteristics for plain fin-and-tube heat exchangers under dehumidifying conditions. J. Heat Transfer, Vol. 129, No. 9, 1256-1267.

Pirompugd, W., Wang, C. C. & Wongwises, S. (2008). Finite circular fin method for wavy fin-and-tube heat exchangers under fully and partially wet surface conditions. *Int. J. Heat Mass Transfer*, Vol. 51, 4002-4017.

Pirompugd, W., Wang, C. C. & Wongwises, S. (2009). A review on reduction method for heat and mass transfer characteristics of fin-and-tube heat exchangers under dehumidifying conditions. *Int. J. Heat Mass Transfer*, Vol. 52, 2370-2378.

Razelos, P. & Imre, K. (1983). Minimum mass convective fins with variable heat transfer coefficient. *J. Franklin Institute*, Vol. 315, 269-282.

Schmidt, E. (1926). *Warmeubertragung durch Rippen. Z. Deustsh Ing*., Vol. 70, 885-951.

Solov"ev, B.A. (1968). An optimum radiator-fin profile. *Inzhenerno Fizicheskii Jhurnal*, Vol. 14, No. 3, 488-492.

Threlkeld, J. L. (1970). *Thermal environment engineering*. Prentice-Hall, New York.

Wilkins, J. E. Jr. (1961). Minimum mass thin fins with specified minimum thickness. *J. Soc. Ind. Appl. Math.*, Vol. 9, 194-206.

Wu, G. & Bong, T. Y. (1994). Overall efficiency of a straight fin with combined heat and mass transfer. *ASRAE Transation*, Vol. 100, No. 1, 365-374.

Zubair, S. M.; Al-Garni, A. Z. & Nizami, J. S. (1996). The optimum dimensions of circular fins with variable profile and temperature-dependent thermal conductivity. Vol. 39, No. 16, 3431-3439.

2

Thermal Therapy: Stabilization and Identification

Aziz Belmiloudi
Institut National des Sciences Appliquées de Rennes (INSA)
Institut de Recherche MAthématique de Rennes (IRMAR), Rennes
France

1. Introduction

1.1 Terminology and methods

The physicists, biologists or chemists control, in general, their experimental devices by using a certain number of functions or parameters of control which enable them to optimize and to stabilize the system. The work of the engineers consists in determining theses functions in an optimal and stable way in accordance with the desired performance. We can note that the three main steps in the area of research in control of dynamical systems are inextricably linked, as shown below:

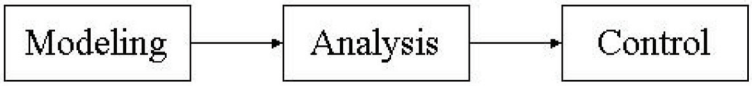

To predict the response of dynamic systems from given parameters, data and source terms requires a mathematical model of the behaviour of the process under investigation and a physical theory linking the state variables of the model to data and parameters. This prediction of the observation (i.e. modeling) constitutes the so-called **direct problem** (primal problem, prediction problem or also forward problem) and it is usually defined by one or more coupled integral, ordinary or partial differential systems and sufficient boundary and initial conditions for each of the main fields (such as temperature, concentration, velocity, pressure, wave, etc.). Initial and boundary conditions are essential for the design and characterization of any physical systems. For example, in a transient conduction heat transfer problem, in order to define a "direct heat conduction problem", in addition to the model which include thermal conductivity, specific heat, density, initial temperature and other data, temperature, flux or radiating boundary conditions are applied to each part of the boundary of the studied domain.

Direct problems are well-posed problem in the sense of Hadamard. Hadamard claims that a mathematical model for a physical problem has to be well-posed or properly problem in the sense that it is characterized by the existence of a unique solution that is stable (i.e. the solution depends continuously on the given data) to perturbations in the given data (material properties, boundary and initial conditions, etc.) under certain regularity conditions on data and additional properties. The requirement of stability is the most important one, because if this property is not valid, then the problem becomes very sensitive to small fluctuations and noises (chaotic situation) and consequently it is impossible to solve the problem.

If any of the conditions necessary to define a direct problem are unknown or rather badly known, an **inverse problem** (control problem or protection problem) results, typically when modeling physical situations where the model parameters (intervening either in the boundary conditions, or initial conditions or equations model itself) or material properties are unknown or partially known. Certain parameters or data can influence considerably the material behavior or modify phenomena in biological or medical matter; then their knowledge (e.g. parameter identification) is an invaluable help for the physicists, biologists or chemists who, in general, use a mathematical model for their problem, but with a great uncertainty on its parameters. The resolution of the inverse problems thus provides them essential informations which are necessary to the comprehension of the various processes which can intervene in these models. This resolution need some regularity and additional conditions, and partial informations of some unknown parameters and fields (observations) given, for example, by experiment measurements.

In all cases the inverse problem is ill-posed or improperly posed (as opposed to the well-posed or properly problem in the sense of Hadamard) in the sense that conditions of existence and uniqueness of the solution are not necessarily satisfied and that the solution may be **unstable** to perturbation in input data (see (Hadamard, 1923)). The inverse problem is used to determine the unknown parameters or control certain functions for problems where uncertainties (disturbances, noises, fluctuations, etc.) are neglected. Moreover the inverse problems are not always tolerant to changes in the control system or the environment. But it is well known that many uncertainties occur in the most realistic studies of physical, biological or chemical problems. The presence of these uncertainties may induce complex behaviors, e.g., oscillations, instability, bad performances, etc. Problems with uncertainties are the most challenging and difficult in control theory but their analysis are necessary and important for applications.

If uncertainties, stability and performance validation occur, a **robust control problem** results. The fundament of robust control theory, which is a generalization of the optimal control theory, is to take into account these uncertain behaviours and to analyze how the control system can deal with this problem. The uncertainty can be of two types: first, the errors (or imperfections) coming from the model (difference between the reality and the mathematical model, in particular if some parameters are badly known) and, second, the unmeasured noises and fluctuations that act on the physical, biological or chemical systems (e.g. in medical laser-induced thermotherapy (ILT), a small fluctuation of laser power can affect considerably the resulting temperature distribution and thus the cancer treatment). These uncertainty terms can have additive and/or multiplicative components and they often lead to great instability.

The goal of robust control theory is to control these instabilities, either by acting on some parameters to maintain the system in a desired state (target), or by calculating the limit of these parameters before the system becomes unstable (”predict to act”). In other words, the robust control allows engineers to analyze instabilities and their consequences and helps them to determine the most acceptable conditions for which a system remains stable. The goal is then to define the maximum of noises and fluctuations that can be accepted if we want to keep the system stable. Therefore, we can predict that if the disturbances exceed this threshold, the system becomes unstable. It also allows us, in a system where we can control the perturbations, to provide the threshold at which the system becomes unstable.

Our robust control approach consists in setting the problem in the worst-case disturbances which leads to the **game theory** in which the controls and the disturbances (which destabilize the dynamical behavior of the system) play antagonistic roles. For more details on this new

approach and its application to different models describing realistic physical and biological process, see the book (Belmiloudi, 2008).
We shall now present the process of our control robust approach.

1.2 General process of the robust control technique

In contrast with the inverse (or optimal control) problems[1], the relation between the problems of identification, regulation and optimization, lies in the fact that it acts, in these cases, to find a **saddle point** of a functional calculus depending on the control, the disturbance and the solution of the direct **perturbation problem**. Indeed, the problems of control can be formulated as the robust regulation of the deviation of the systems from the desired target; the considered control and disturbance variables, in this case, can be in the parameters or in the functions to be identified. This optimization problem (a **minimax problem**), depending on the solution of the direct problem, with respect to control and disturbance variables (intervening either in the initial conditions, or boundary conditions or equation itself), is the base of the robust control theory of partial differential equations (see (Belmiloudi, 2008)).
The essential data used in our robust control problem are the following.

- A known operator $\mathcal{F}$ which represents the dynamical system to be controlled i.e. $\mathcal{F}$ is the model of the studied boundary-value problem such that

$$\mathcal{F}(x,t,f,g,U) = 0, \tag{1}$$

  where (x,t) are the space-time variables, $(f,g) \in \mathcal{X}$ represents the input of the system (initial conditions, boundary conditions, source terms, parameters and others) and $U \in \mathcal{Z}$ represents the state or the output of the system (temperature, concentration, velocity, magnetic field, pressure, etc.), where $\mathcal{X}$ and $\mathcal{Z}$ are two spaces of input data and output solutions, respectively, which are assumed to be, for example, Hilbert and Banach spaces, respectively. We assume that the direct problem (1) is well-posed (or correctly-set) in Hadamard sense.

- A "control" variable φ in a set $U_{ad} \subset \mathcal{U}_1$ (known as set of "admissible controls") and a "disturbance" variable ψ in a set $V_{ad} \subset \mathcal{U}_2$ (known as set of "admissible disturbances"), where $\mathcal{U}_1$ and $\mathcal{U}_2$ are two spaces of controls and disturbances, respectively, which are assumed to be, for example, Hilbert spaces.

- For a chosen control-disturbance (φ,ψ), the **perturbation problem**, which models fluctuations (φ,ψ,u) to the desired target (f,g,U) (we assume that $(f+\mathcal{B}_1\varphi, g+\mathcal{B}_2\psi, U+u)$ is also solution of (1)) and which is given by

$$\tilde{\mathcal{F}}(x,t,\varphi,\psi,u) = \mathcal{F}(x,t,f+\mathcal{B}_1\varphi, g+\mathcal{B}_2\psi, U+u) - \mathcal{F}(x,t,f,g,U) = 0, \tag{2}$$

  where the operator $\tilde{\mathcal{F}}$, which depends on U, is the perturbation of the model $\mathcal{F}$ of the studied system and $\mathcal{B}_i$, for $i = 1,2$, are bounded linear operators from $\mathcal{U}_i$ into $\mathcal{Z}$. In the sequel we denote by $u = \mathcal{M}(x,t,\varphi,\psi)$ the solution of the direct problem (2).

- An "observation" u_{obs} which is supposed to be known exactly (for example the desired tolerance for the perturbation or the offset given by measurements).

[1] Inverse problem corresponds to minimize or maximize a calculus function depending on the control and the solution of the direct problem.

- A "cost" functional (or "objective" functional) $J(\varphi,\psi)$ which is defined from a real-valued and positive function $\mathcal{G}(X,Y)$ by (so-called the **reduced form**)

$$J(\varphi,\psi)=\mathcal{G}((\varphi,\psi),\mathcal{M}(.,\varphi,\psi)).$$

The goal is to find a saddle point of J, *i.e.*, a solution $(\varphi^*,\psi^*)\in U_{ad}\times V_{ad}$ of

$$J(\varphi,\psi^*)\leq J(\varphi^*,\psi^*)\leq J(\varphi^*,\psi)\quad\forall(\varphi,\psi)\in U_{ad}\times V_{ad},$$

i.e. find $(\varphi^*,\psi^*,u^*)\in U_{ad}\times V_{ad}\times\mathcal{Z}$ such that the cost functional J is minimized with respect to φ and maximized with respect to ψ subject to the problem (2) (i.e. $u^*(x,t)=\mathcal{M}(x,t,\varphi^*,\psi^*)$).

We lay stress upon the fact that there is no general method to analyse the problems of robust control (it is necessary to adapt it in each situation). On the other hand, we can define a process to be followed for each situation.

(i) solve the direct problem (existence of solutions, uniqueness, stability according to the data, regularity, *etc.*)

(ii) define the function or the parameter to be identified and the type of disturbance to be controlled

(iii) introduce and solve the perturbed problem which plays the role of the direct problem (existence of solutions, uniqueness, stability according to the data, regularity, differentiability of the operator solution, *etc.*)

(iv) define the cost (or objective) functional, which depends on control and disturbance functions

(v) obtain the existence of an optimal solution (as a saddle point of the cost functional) and analyse the necessary conditions of optimality

(vi) characterize the optimal solutions by introducing an **adjoint (dual or co-state)** model (the characterization include the direct problem coupled with the adjoint problem, linked by inequalities)

(vii) define an algorithm allowing to solve numerically the robust control problem.

Remark 1

1. *In nonlinear systems the analysis of robust control problems is more complicated than in the case of inverse problems, because we are interested in the robust regulation of the deviation of the systems from the desired target state variables (while the desired power level and adjustment costs are taken into consideration) by analyzing the* **full nonlinear** *systems which model large perturbations to the desired target. Consequently the perturbations of the initial models, which show additional operators (and then difficulties), generate new direct problem and then new adjoint problem which, often, seem of a new type.*
2. *If there are no noises (i.e., $\mathcal{B}_2$ vanishes), the problem becomes an inverse problem or model calibration, i.e., find φ in U_{ad} such that the cost functional $J_0(\varphi)$ (in reduced form i.e. in place of the form $\mathcal{G}_0(\varphi,U=M(.,\varphi))$) is minimized subject to the well-posed problem*

$$\mathcal{F}(x,t,f_0+\mathcal{B}_1\varphi,g,U)=0, \tag{3}$$

where data (f_0, g) *are known (we have supposed that* f *is decomposed into a known function* f_0 *and the control* φ*) and* $M(.,\varphi) = U$ *is the solution of (3), corresponding to* φ*. Precisely, the problem is : find* $(\varphi^*, U^*) \in U_{ad} \times \mathcal{Z}$ *solution of*

$$J_0(\varphi^*) = \inf_{\varphi \in U_{ad}} J_0(\varphi),$$

and $U^* = M(.,\varphi^*)$.

2. Statement of the problem

2.1 Problem definition

Motivated by topics and issues critical to human health and safety of treatment, the problem studied in this chapter derives from the modeling and stabilizing control of the transport of thermal energy in biological systems with porous structures.

The evaluation of thermal conductivities in living tissues is a very complex process which uses different phenomenological mechanisms including conduction, convection, radiation, metabolism, evaporation and others. Moreover blood flow and extracellular water affect considerably the heat transfer in the tissues and then the tissue thermal properties. The bioheat transfer process in tissues is also dependent on the behavior of blood perfusion along the vascular system. An analysis of thermal process and corresponding tissue damage taking into account theses parameters will be very beneficial for thermal destruction of the tumor in medical practices, for example for laser surgery and thermotherapy for treatment planning and optimal control of the treatment outcome, often used in treatment of cancer. The first model, taking account on the blood perfusion, was introduced by Pennes see (Pennes, 1948) (see also (Wissler, 1998) where the paper of Pennes is revisited). The model is based on the classical thermal diffusion system, by incorporating the effects of metabolism and blood perfusion. The Pennes model has been adapted per many biologists for the analysis of various heat transfer phenomena in a living body. Others, after evaluations of the Pennes model in specifical situations, have concluded that many of the hypotheses (foundational to the model) are not valid. Then these latter ones modified and generalized the model to adequate systems, see e.g. (Chen & Holmes, 1980a;b);(Chato, 1980); (Valvano et al., 1984); (Weinbaum & Jiji, 1985); (Arkin et al., 1986); (Hirst, 1989) (see also e.g. (Charney, 1992) for a review on mathematical modeling of the influence of blood perfusion). Recently, some studies have shown the important role of porous media in modeling flow and heat transfer in living body, and the pertinence of models including this parameter have been analyzed, see e.g. (Shih et al., 2002); (Khaled & Vafai, 2003); (Belmiloudi, 2010) and the references therein.

The goal of our contribution is to study time-dependent identification, regulation and stabilization problems related to the effects of thermal and physical properties on the transient temperature of biological tissues with porous structures. To treat the system of motion in living body, we have written the transient bioheat transfer type model in a generalized form by taking into account the nature of the porous medium. In paragraph 3.1, we have constructed a model for a specific problem which has allowed us to propose this generalized model as follows

$$\begin{aligned} c(\phi,x)\frac{\partial U}{\partial t} = & \, div(\kappa(\phi,U,x)\nabla U) - e(\phi,x)P(x,t)(U-U_a) \\ & -d(\phi,x)K_v(U) + r(\phi,x)g(x,t) + f(x,t) \quad in \;\; \mathcal{Q}, \end{aligned} \tag{4}$$

subjected to the boundary condition

$$(\kappa(\phi,U,x)\nabla U).\mathbf{n} = -q(x,t)(U-U_b) \\ -\lambda(x)(L(U)-L(U_b))+h(x,t) \quad in\ \Sigma,$$

and the initial condition

$$U(x,0) = U_0(x) \ \ in\ \Omega,$$

under the pointwise constraints

$$\begin{array}{l} a_1 \le P \le a_2 \ \ a.e.\ in\ \mathcal{Q}, \\ b_1 \le \phi \le b_2 \ \ a.e.\ in\ \Omega, \end{array} \tag{5}$$

where the state function U is the temperature distribution, the function K_v is the transport operator in $\vec{\vartheta}$ direction i.e. $K_v(U) = (\vec{\vartheta}.\nabla)U$, the function L is the radiative operator i.e. $L(U) = \mid U \mid^3 U$. The body Ω is an open bounded domain in $\mathbb{R}^m$, $m \le 3$ with a smooth boundary $\Gamma = \partial\Omega$ which is sufficiently regular, and Ω is totally on one side of Γ, the cylindre $\mathcal{Q}$ is $\mathcal{Q} = \Omega \times (0,T)$ with $T > 0$ a fixed constant (a given final time), $\Sigma = \partial\Omega \times (0,T)$, $\mathbf{n}$ is the unit outward normal to Γ and a_i, b_i, for $i = 1,2$, are given positive constants. The quantity P is the blood perfusion rate and $\phi \in L^\infty(\Omega)$ describes the porosity that is defined as the ratio of blood volume to the total volume (i.e. the sum of the tissue domain and the blood domain). The volumetric heat capacity type function $c(\phi,.)$ and the thermal conductivity type function of the tissue $\kappa(\phi,U,.)$ are assumed to be variable and satisfy $\nu \ge \kappa(\phi,U,.) = \sigma^2(\phi,U,.) \ge \mu > 0$, $M_1 \ge c(\phi,.) = \mathfrak{r}^2(\phi,.) \ge M_0 > 0$ (where ν, μ, M_0, M_1 are positive constants). The second term on the right of the state equation (4) describes the heat transport between the tissue and microcirculatory blood perfusion, the third term K_v is corresponding to the directional convective mechanism of heat transfer due to blood flow, the last terms are corresponding to the sum of the body heating function which describes the physical properties of material (depending on the thermal absorptivity, on the current density, on the electric field intensity, that can be calculated from the Maxwell equations, and others) and the source terms that describe a distributed energy source which can be generated through a variety of sources, such as focused ultrasound, radio-frequency, microwave, resistive heating, laser beams and others (depending on the difference between the energy generated by the metabolic processes and the heat exchanged between, for example, the electrode and the tissue). The first term in the right of the boundary condition in (4) describes the convective component and the second term is the radiative component. The term h is the heat flux due to evaporation. The function U_a is the arterial blood temperature, the function U_b is the bolus temperature and they are assumed to be in $L^\infty(\mathcal{Q})$ and in $L^\infty(\Sigma)$, respectively.
The function u_0 is the initial value and is assumed to be variable and $\lambda = \sigma_B\epsilon_e$ is assumed to be in $L^\infty(\Gamma)$ where σ_B ($Wm^{-2}K^{-4}$) is Stefan-Boltzmann's constant and ϵ_e is the effective emissivity. The vector function $\vec{\vartheta}$ is the flow velocity which is assumed to be sufficiently regular.

Remark 2

1. *Emissivity of a material is defined as the ratio of energy radiated by a particular material to energy radiated by a black body at the same temperature (the tissue is not a perfect black body). It is a dimensionless quantity (i.e. a quantity without a physical unit). The emissivity of human skin is in the range* $0.98 - 0.99$.

2. *We consider only the boundary effect of the process of radiation, since radiative heat transfer processes within the system are neglected.*
3. *In the physical case there is not absolute values under the boundary conditions (since the temperature is non negative). For real physical and biological data, we can prove by using the maximum principle that the temperature is positive and then we can remove the absolute values.*
4. *For all $\vec{\vartheta}$ sufficiently regular (such e.g. the condition (17)), the linear operator satisfies the following estimate:*

   there exists a constant $\gamma_v \geq 0$ (depending on the norm of $\vec{\vartheta}$) such that

$$\| K(\vec{\vartheta}, v) \|_{L^2(\Omega)} \leq \gamma_v \| v \|_{H^1(\Omega)}, \forall v \in H^1(\Omega). \tag{6}$$

5. *The nonlinear scalar function $L : \mathbb{R} \longrightarrow \mathbb{R}$ is a $C^1(\mathbb{R})$ function and its derivative is given by*

$$L'(v) = 4 \mid v \mid^3 . \tag{7}$$

2.2 Basis for thermal therapy

Cells, vasculature (which supply the tissue with nutrients and oxygen through the flow of blood) and extracellular matrix (which provides structural support to cells) are the main constituents of tissue. Most living cells and tissues can tolerate modest temperature elevations for limited time periods depending on the metabolic status of the individual cell (so-called thermotolerance). Contrariwise, when tissues are exposed to very high temperature conditions, this leads to cellular damage which can be irreversible.

Therapy by elevation of temperature is a thermal treatment in which pathological tissue is exposed to high temperatures to damage and destroy or kill malignant cells (directly or indirectly by the destruction of microvasculature) or to make malignant cells more sensitive to the effects of another therapeutic option, such as radiation therapy, chemotherapy or photodynamic therapy. Many scientists claim that this is due largely to the difference in blood circulation between tumor and normal tissues. Moreover, local tissue properties, in particular perfusion, have a significant impact on the size of treatment zone, for example, highly perfused tissue and large vessels act as a heat sink (this phenomenon makes normal tissue relatively more resilient to treatment than tumor tissue, since perfusion rates in tumors are generally less than those in normal tissues). Consequently, the knowledge of the thermal properties and blood perfusion of biological tissues is fundamental for accurately modeling the heat transfer process during thermal therapy. The most commonly used technique for heating of tumors is the interstitial thermal therapy, in which heating elements are implanted directly into the treated zone, because energy can be localized to the target region while surrounding healthy tissue is preserved. Different energy sources are employed to deliver local thermal energy including laser, microwaves, radiofrequency and ultrasound.

The traditional hyperthermia is defined as a temperature greater than $37.5 - 38.3^oC$, in general in the interval of about $41 - 47^oC$. This thermal therapy is only useful for certain kinds of cancer and is most effective when it is combined with the other conventional therapeutic modalities. Though temperatures are not very high and then cell death is not instantaneous, prolonged exposure leads to the thermal denaturation of non-stabilized proteins such as enzymes and to their destruction, which ultimately leads to cell death. There are various types of hyperthermia as alternative cancer therapy. These include: the regional (heats a larger part of the body, such as an entire affected organ) and local (heats a small area, such as the tumor

itself) hyperthermia, where temperatures reach between 42 and 44^oC and the whole body hyperthermia, where the entire body except for the head is overheated to a temperature of about 39 to 41^oC. Heat sensitivity of the tissue is lost at higher temperatures (above 44^oC) resulting in tumor and normal tissues destruction at the same rate. Consequently, in order to minimize damage to surrounding tissues and other adverse effects, we must keep local temperatures under 44^oC, but requires more treatment-time (between 1 and 3 hours). At these low temperatures damage can be reversible. Indeed damaged proteins can be repaired or degraded and replaced with new ones.
For a rapid destruction of tissue, it is necessary to make a temperature rise of at least exceed 50^oC. During thermotherapy, which employs higher temperatures over shorter times (seconds to minutes), than those used in hyperthermia treatment, several processes, as tissue vaporization, carbonization and molecular dissociation, occur which lead to the destruction or death of the tissue. At temperatures above 60^oC, proteins and other biological molecules of the tissue become severely denatured (irreversibly altered) and coagulate leading to cell and tissue death. Temperatures above 100^oC will cause vaporization from evaporation of water in the tissue and in the intracellular compartments and lead to rupture or explosion of cells or tissue components, and above 300^oC tissue carbonization occurs. At these temperatures, an elevated temperature front migrates through the tissue and structural proteins, such as fibrillar collagen and elastin, begin to damage irreversibly causing visible whitening of the tissue and then coagulation necrosis to the targeted tissue. Indeed, structural proteins are more thermally stable than the intracellular proteins and enzymes (involved in reversible heat damage), and consequently tissue coagulation signifies destruction of the lesion.
The actual level of thermal damage in cells and tissue is a function of both temperature and heating time. Using the temperature history, the accumulation of thermal damage, associated with injury of tissue, can be calculated by an approach (based on the well-known Arrhenius model see e.g. (Henriques, 1947)) characterizing tissue damage, including cell kill, microvascular stasis and protein coagulation. For this, we can use the Arrhenius damage integral formulation, which assumes that some thermal damage processes follow first-order irreversible rate reaction kinetics (from thermal chemical rate equations, see e.g. (Atkins, 1982)), for more details see e.g. (Tropea & Lee, 1992) and (Skinner et al., 1998):

$$\mathcal{D}(x,\tau_{exp}) = ln(\frac{C(0)}{C(\tau_{exp})}) = A\int_0^{\tau_{exp}} exp(\frac{-E}{RU(x,t)})dt, \tag{8}$$

where D is the nondimensional degree of tissue injury, U is the temperature of exposure (K), τ_{exp} is the duration of the exposure, $C(0)$ is the concentration of living cells before irradiation exposure and $C(\tau_{exp})$ is the concentration of living cells at the end of the exposure time. The parameter A is the molecular collision frequency (s^{-1}) i.e. damage rate, the parameter E is the denaturation activation energy ($J.mol^{-1}$) and R is the universal gaz constant equal to 8.314 $J.mol^{-1}K^{-1}$. The two kinetic parameters A and E are dependent on the type of tissue and must be determined by experiments a priori. The cumulative damage can be interpreted as the fraction of hypothetical indicator molecules that are denatured and can play an important role in the optimization of the treatment.
Other cell damage models are developed, in recent years, see for example the two-state model of Oden et al. in (Feng et al., 2008) (which is based on statistical thermodynamic principles) as follows:

$$\mathcal{D}(x,\tau_{exp}) = \int_0^{\tau_{exp}} \frac{1}{1+exp(\frac{-E_o(t,U(x,t))}{RU(x,t)})}dt, \tag{9}$$

with the activation energy function $E_0(t,U) = (\frac{\zeta}{U} + at + b)$, where ζ, a and b are known constants determined by in vitro cellular experiments.
In conclusion the cell damage model can be expressed by the following general form

$$\mathcal{D}(x,\tau_{exp}) = ln(\frac{C(0)}{C(\tau_{exp})}) = \int_0^{\tau_{exp}} \mathcal{H}(t,U(x,t))dt, \tag{10}$$

where $\mathcal{H}$ is differentiable on the variable U.

2.3 Outline

We give now the outline of the rest of the chapter. First, the modeling of thermal transport by perfusion within the framework of the theory of porous media is presented and the governing equations are established. The thermal processes within the tissues are predicted by using some generalized uncertain evolutive nonlinear bioheat transfer type models with nonlinear Robin boundary conditions (radiative type), by taking into account porous structures and directional blood flow. Afterwards the existence, the uniqueness and the regularity of the solution of the state equation are presented as well as stability and maximum principle under extra assumptions. Second, we introduce the initial perturbation problem and give the existence and uniqueness of the perturbation solution and obtain a stability result. Third, the real-time identification and robust stabilization problems are formulated, in different situations, in order to reconstitute simultaneously the blood perfusion rate, the porosity parameter, the heat transfer parameter, the distributed energy source terms and the heat flux due to the evaporation, which affect the effects of thermal physical properties on the transient temperature of biological tissues, and to control and stabilize the desired online temperature and thermal damage provided by MRI (Magnetic Resonance Imaging) measurements. Because, it is now well-known that a controlled and stabilized temperature field does not necessarily imply a controlled and stabilized tissue damage. This work includes results concerning the existence of the optimal solutions, the sensitivity problems, adjoint problems, necessary optimality conditions (necessary to develop numerical optimization methods) and optimization problems. Next, we analyse the case when data are measured in only some points in space-time domain, and the case where the body Ω is constituted by different tissue types which occupy finitely many disjointed subdomains. As in previous, we give the existence of an optimal solution and we derive necessary optimality conditions. Some numerical strategies, based on adjoint control optimization (combining the obtained optimal necessary conditions and gradient-iterative algorithms), in order to perform the robust control, are also discussed. Finally, control and stabilization problems for a coupled thermal, radiation transport and coagulation processes modeling the laser-induced thermotherapy in biological tissues, during cancer treatment, are analyzed.
In the sequel, we will always denoted by C some positive constant which can be different at each occurrence.

3. Mathematical modelling and motivation

3.1 Model development

3.1.1 Heat transfer equation

The blood-perfused tumor tissue volume, including blood flow in microvascular bed with the blood flow direction, contains many vessels and can be regarded as a porous medium consisting of a tumor tissue (a solid domain) fully filled with blood (a liquid domain), see

Figure 1. Consequently the temperature distribution in biological tissue can be modelized by analyzing a conjugate heat transfer problem with the porous medium theory. For the tumor tissue domain, we use the Pennes bioheat transfer equation by taking account on the blood perfusion in the energy balance for the blood phase. For the blood flow domain, we use the energy transport equation. The system of equations of the model is then

$$\begin{aligned} c_s(x)\rho_s(x)\frac{\partial U_s}{\partial t} &= div(\kappa_s(U_s,x)\nabla U_s) - c_l(x)w_l(x,t)(U_s - U_a) + Q_s(x,t) + Q_J(x,t), \\ c_l(x)\rho_l(x)(\frac{\partial U_l}{\partial t} + (\vec{\vartheta}.\nabla)U_l) &= div(\kappa_l(U_l,x)\nabla U_l) + Q_J(x,t), \end{aligned} \tag{11}$$

where c_l, c_s, ρ_l, ρ_s, U_l, U_s, κ_l, κ_s, Q_s, Q_J are the specific heat of blood, the specific heat of tissue, the density of blood, the density of tissue, the local blood temperature, local tissue temperature, blood effective thermal conductivity tensor, tissue effective thermal conductivity tensor, metabolic volumetric heat generation and energy source term (which is also called the specific absorption rate, SAR (Wm^{-3})), respectively, and U_a is the temperature in arterial blood. The term $div(\kappa_l(U_l)\nabla U_l)$ is corresponding to the enhancement of thermal conductivity in tissue due to the flow of blood within thermally significant blood vessels and the term $div(\kappa_s(U_s)\nabla U_s)$ is similar to Pennes model. The transport operator is $\vec{\vartheta}.\nabla$ and is corresponding to a directional convective term due to the net flux of the equilibrated blood.

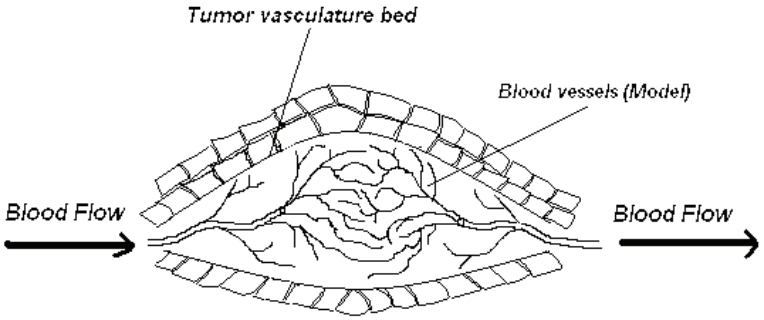

Fig. 1. : Relationship between tumor vascular and blood flow direction

The volumetric averaging of the energy conservation principle is achieved by combining and rearranging the first and the second part of the system (11) with the porous structure (regarded as a homogeneous medium). Under thermal equilibrium and according to the modelization of (Chen & Holmes, 1980a) (the model has been formulated after the analyzing of blood vessel thermal equilibration length) we have then by multiplying the first equation by $(1-\phi)$ and the second equation by ϕ

$$\begin{aligned} &((1-\phi)c_s(x)\rho_s(x) + \phi c_l(x)\rho_l(x))\frac{\partial U}{\partial t} + div(((1-\phi)\kappa_s(U,x) + \phi\kappa_l(U,x))\nabla U) \\ &+\phi c_l(x)\rho_l(x)(\vec{\vartheta}.\nabla)U + (1-\phi)c_l(x)w_l(x,t)(U - U_a) = (1-\phi)Q_s(x,t) + Q_J(x,t). \end{aligned} \tag{12}$$

Our model incorporates the effect of blood flow in the heat transfer equation in a way that captures the directionality of the blood flow and incorporates the convection features of the heat transfer between blood and solid tissue.

The model (12) is a particular case of the general equation in the system (4), by taking, in the first relation of (4), the heat capacity type function $c(\phi,x)$ as $(1-\phi)c_s\rho_s+\phi c_l\rho_l$, the thermal conductivity capacity type function $\kappa(\phi,U,x)$ as $(1-\phi)\kappa_s+\phi\kappa_l$, the function $e(\phi,x)P(x,t)$ as $(1-\phi)c_lw_l$, the function $d(\phi,x)$ as $\phi c_l\rho_l$, the function $r(\phi,x)$ as $1-\phi$, the function f as Q_J and the function g as Q_s .
To close the model, we must specify boundary conditions.

3.1.2 Boundary conditions

Every body emits electromagnetic radiation proportional to the fourth power of the absolute temperature of its surface. The total energy, emitted from a black body, E_R (Wm^{-2}) can be given by the following Stefan-Boltzmann-Law:

$$E_R=\sigma_B\epsilon_e(U^4-U_b^4), \tag{13}$$

where $\sigma_B=5.67.10^{-8}Wm^{-2}K^{-4}$ is the Stefan-Boltzmann constant, U and U_b (K) are the tissue surface temperature and surrouding temperature, respectively and $\epsilon<1$ (since tissue is not a perfect black body) is the emissivity coefficient.
Convection problems involve the exchange of heat between the surface of the body (the conducting) and the surrounding air (convecting). The thermal energy E_C (Wm^{-2}) can be given by Newton's law of cooling:

$$E_C=q(U-U_b), \tag{14}$$

where, the proportionality function q $(Wm^{-2}K^{-1})$ is the coefficient of local heat convection and U_b is the bulk temperature of the air (assumed to be similar as relation in (13)).
If we assume that the evaporation occurs mainly at the surface, the energy associated with the phase change occurring during evaporation (the heat flux due to evaporation) can be given by the following expression

$$E_V=h_{fg}m_w=-h(x,t), \tag{15}$$

where h_{fg} is the latent heat of vaporization and m_w is the mass flux of evaporating water.
According to the previous relations, the boundary condition can be imposed as follows:

$$-(\kappa(\phi,U,x)\nabla U).\mathbf{n}=E_R+E_C+E_V=q(U-U_b)+\lambda(x)(L(U)-L(U_b))-h(x,t), \tag{16}$$

where $\lambda=\sigma_B\epsilon_e$ and $L(v)=\mid v\mid^3 v=v^4$ for all positive functions.
We recall now some biological and medical background and motivations to analyse the identification, calibration and stabilization problem.

3.2 Background and motivation

Mathematical modeling of cancer treatments (chemotherapy, thermotherapy, etc) is an highly challenging frontier of applied mathematics. Recently, a large amount of studies and research related to the cancer treatments, in particular by chemotherapy or thermotherapy, have been the object of numerous developments.
As an alternative to the traditional surgical treatment or to enhance the effect of conventional chemotherapy, various problems associated with localized thermal therapy have been intensively studied (see e.g. (Pincombe & Smyth, 1991); (Hill & Pincombe, 1992); (Tropea & Lee, 1992); (Martin et al., 1992); (Seip & Ebbini, 1995); (Sturesson & Andersson-Engels, 1995); (Deuflhard & Seebass, 1998); (Xu et al.,

1998); (Liu et al., 2000); (Marchant & Lui, 2001); (Shih et al., 2002); (He & Bischof, 2003); (Zhou & Liu, 2004); (Zhang et al., 2005) and the references therein. In order to improve the treatments, several approaches have been proposed recently to control the temperature during thermal therapy. We can mention e.g. (Bohm et al., 1993); (Hutchinson et al., 1998); (Köhler et al., 2001); (Vanne & Hynynen, 2003); (Kowalski & Jin, 2004); (Malinen et al., 2006); (Belmiloudi, 2006; 2007) and the references therein. The essential of these contributions has been the numerical analysis, MRI-based optimization techniques and mathematical analysis. For the stabilization of the temperature treatment, see e.g. (Belmiloudi, 2008), in which the author develops nonlinear PDE robust control approach in order to stabilize and control the desired online temperature for a Pennes's type model with linear boundary conditions.
An important application of all bioheat transfer models in interdisciplinary research areas, in joining mathematical, biological and medical fields, is the analysis of the temperature field which develops in living tissue when a heat is applied to the tissue, especially in the clinical cancer therapy hyperthermia and in the accidental heating injury, such as burns (in hyperthermia, tissue is heated to enhance the effect of an accompanying radio or chemotherapy). Indeed the thermal therapy (performed with laser, focused ultrasound or microwaves) gives the possibility to destroy the pathological tissues with minimal damage to the surrounding tissues. Moreover, due to the self-regulating capability of the biological tissue, the blood perfusion and the porosity parameters depend on the evolution of the temperature and vary significantly between different patients, and between different therapy sessions (for the same patient). Consequently, in order to have a very optimal thermal diagnostics and so the result of the therapy being very beneficial to treatment of the patient, it is necessary to identify the value of these two parameters.
The new feature introduced in this work concerns the estimation of the evolution of the blood perfusion and the porosity parameters by using nonlinear optimal control methods, for some generalized evolutive bioheat transfer systems, where the observation is the online temperature control provided by Magnetic Resonance Imaging (*MRI*) measurements, see Figure2 (MRI is a new efficie

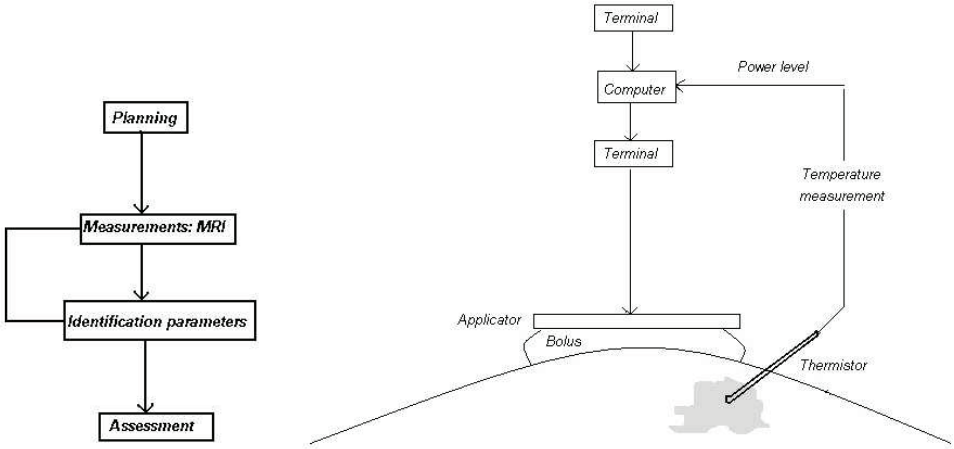

(a) Control process (b) Applicator and measurements

Fig. 2. : Laser-induced thermotherapy and identification

The introduction of the theory of porous media for heat transfer in biological tissues is very important because the physical properties of material have power law dependence on temperature (see e.g. (Marchant & Lui, 2001; Pincombe & Smyth, 1991)) and moreover the porosity is one of the crucial factors determining distribution of temperature during thermal therapies, for example in medical laser-induced thermotherapy (see e.g. the review of (Khaled & Vafai, 2003)). Consequently we cannot neglect the influence of the porosity in the model and then it is necessary to identify, in more of the blood perfusion, the porosity of the material during thermal therapy in order to maximize the efficiency and safety of the treatment. Moreover, the introduction of the nonlinear radiative operator including the cooling mechanism of water evaporation in the model is very important, because the heat exchange mechanisms at the body-air interface play a very important part on the total tissue temperature distribution and consequently we cannot also neglect the influence of the surface evaporation in the model (see e.g. (Sturesson & Andersson-Engels, 1995)). On the other hand we will consider that the source term f and the heat flux due to evaporation h (in the model (4)) are not accurately known.

4. Solvability of the state system

Now we give some assumptions, notations, results and an analysis of the state system (4) which are essential for the following investigations.

4.1 Assumptions and notations

We use the standard notation for Sobolev spaces (see (Adams, 1975)), denoting the norm of $W^{m,p}(\Omega)$ ($m \in \mathbb{N}$, $p \in [1,\infty]$) by $\| \ \|_{W^{m,p}(\Omega)}$. In the special case $p = 2$ we use $H^m(\Omega)$ instead of $W^{m,2}(\Omega)$. The duality pairing of a Banach space X with its dual space X' is given by $< .,. >_{X',X}$. For a Hilbert space Y the inner product is denoted by $(.,.)_Y$. For any pair of real numbers $r,s \geq 0$, we introduce the Sobolev space $H^{r,s}(\mathcal{Q})$ defined by $H^{r,s}(\mathcal{Q}) = L^2(0,T,H^r(\Omega)) \cap H^s(0,T,L^2(\Omega))$, which is a Hilbert space normed by

$$(\| v \|^2_{L^2(0,T,H^r(\Omega))} + \| v \|^2_{H^s(0,T,L^2(\Omega))})^{1/2},$$

where $H^s(0,T,L^2(\Omega))$ denotes the Sobolev space of order s of functions defined on $(0,T)$ and taking values in $L^2(\Omega)$, and defined by, for $\theta \in (0,1), s = (1-\theta)m$, m is an integer, (see e.g. (Lions & Magenes, 1968)) $H^s(0,T,L^2(\Omega)) = [H^m(0,T,L^2(\Omega)),L^2(\mathcal{Q})]_\theta$, $H^m(0,T,L^2(\Omega)) = \{v \in L^2(\mathcal{Q}) | \ \frac{\partial^j v}{\partial t^j} \in L^2(\mathcal{Q}), \forall j = 1,m\}$.

We denote by V the following space: $V = \{v \in H^1(\Omega) | \gamma_0 v \in L^5(\Gamma)\}$ equipped with the norm $\| v \| = \| v \|_{H^1(\Omega)} + \| \gamma_0 v \|_{L^5(\Gamma)}$ for $v \in V$, where γ_0 is the trace operator in Γ. The space V is a reflexive and separable Banach space and satisfies the following continuous embedding: $V \subset L^2(\Omega) \subset V'$ (see e.g. (Delfour et al., 1987)). For $\Omega \subset \mathbb{R}^2$, the space $H^1(\Omega)$ is compactly embedded in $L^5(\Gamma)$ and then $V = H^1(\Omega)$. We can now introduce the following spaces:
$\mathcal{H}(\mathcal{Q}) = L^\infty(0,T,L^2(\Omega)), \mathcal{V}(\mathcal{Q}) = L^2(0,T,V), \mathcal{W}(\mathcal{Q}) = \{w \in L^2(0,T,V) | \frac{\partial w}{\partial t} \in L^{5/4}(0,T,V')\}$
and $\tilde{\mathcal{W}}(\mathcal{Q}) = \{v \in \mathcal{W}(\mathcal{Q}) | v \in L^5(\Sigma)\}$.

Remark 3 *Let $\Omega \subset \mathbb{R}^m$, $m \geq 1$, be an open and bounded set with a smooth boundary and q be a nonnegative integer. We have the following results (see e.g. (Adams, 1975))*
(i) $H^q(\Omega) \subset L^p(\Omega)$, $\forall p \in [1, \frac{2m}{m-2q}]$, with continuous embedding (with the exception that if $2q = m$, then $p \in [1,+\infty[$ and if $2q > m$, then $p \in [1,+\infty]$).

(ii) (Gagliardo-Nirenberg inequalities) There exists $C > 0$ such that

$$\| v \|_{L^p} \leq C \| v \|_{H^q}^{\theta} \| v \|_{L^2}^{1-\theta}, \forall v \in H^q(\Omega),$$

where $0 \leq \theta < 1$ and $p = \frac{2m}{m-2\theta q}$ (with the exception that if $q - m/2$ is a nonnegative integer, then θ is restricted to 0).
2. If $u \in \mathcal{W}(\mathcal{Q}) \cap \mathcal{H}(\mathcal{Q})$, then u is a weakly continuous function on $[0,T]$ with values in $L^2(\Omega)$ i.e. $u \in \mathcal{C}_w([0,T], L^2(\Omega))$ (see e.g. (Lions, 1961)).

Definition 1 *A real valued function Φ defined on $\mathbb{R}^q \times D$, $q \geq 1$, is a Carathéodory function iff $\Phi(\mathbf{v},.)$ is measurable for all $\mathbf{v} \in \mathbb{R}^q$ and $\Phi(y,.)$ is continuous for almost all $y \in D$.*

We state the following hypotheses for the functions (or operators) c, d, e, r and κ appearing in the model (4) :

(**H1**) The functions $c = \mathfrak{r}^2 > 0$, $d > 0$, $e > 0$, r are Carathéodory functions from $\mathbb{R} \times \Omega$ into $\mathbb{R}^+$ and $c(.,x)$, $d(.,x)$, $e(.,x)$, $r(.,x)$ are Lipschitz and bounded functions for almost all $x \in \Omega$, where $M_1 \geq c(\phi,.) = \mathfrak{r}^2(\phi,.) \geq M_0 > 0$ (where M_0 and M_1 are positive constants).

(**H2**) The function $\kappa = \sigma^2 > 0$ is Carathéodory function from $\mathbb{R}^2 \times \Omega$ into $\mathbb{R}^+$ and $\kappa(.,x)$ is Lipschitz and bounded functions for almost all $x \in \Omega$,
where $\nu \geq \kappa(\phi,U,.) = \sigma^2(\phi,U,.) \geq \mu > 0$ (where ν and μ are positive constants).

(**H3**) The function c, d, e, r (resp. κ) are differentiable on φ (resp. on (ϕ,U)) and their partial derivatives are Lipschitz and bounded functions.

We assume that the flow velocities $\vec{\vartheta}$ satisfy the regularity :

$$\vec{\vartheta} \in L^{\infty}(0,T,W^{1,\infty}(\Omega)) \tag{17}$$

and we denote by K_v^* the adjoint operator of K_v i.e. $K_v^*(u) = -div(\vec{\vartheta}u)$ and we have:

$$\int_{\Omega} K_v(u)v dx = \int_{\Omega} K_v^*(v)u dx + \int_{\Gamma} uv\vec{\vartheta}.\mathbf{n} d\Gamma, \ \forall (u,v) \in (H^1(\Omega))^2. \tag{18}$$

Nota bene: For simplicity we denote the values $\mathfrak{h}(\varphi,.)$ by $\mathfrak{h}(\varphi)$, where the function $\mathfrak{h}$ plays the role of c, d, e or r, and the value $\kappa(\phi,U,.)$ by $\kappa(\phi,U)$.

4.2 Some fundamental inequalities and results

Our study involve the following fundamental inequalities, which are repeated here for review:
(i) *Hölder's inequality*

$$\int_D \Pi_{i=1,k} f_i dx \leq \Pi_{i=1,k} \| f_i \|_{L^{q_i}(D)}, \text{ where}$$
$$\| f_i \|_{L^{q_i}(D)} = \left(\int_D | f_i |^{q_i} dx\right)^{1/q_i} \text{ and } \sum_{i=1,k} \frac{1}{q_i} = 1.$$

(ii) *Young's inequality* ($\forall a,b > 0$ and $\epsilon > 0$)

$$ab \leq \frac{\epsilon}{p} a^p + \frac{\epsilon^{-q/p}}{q} b^q, \ for \ p,q \in]1,+\infty[\ and \ \frac{1}{p} + \frac{1}{q} = 1.$$

(iii) *Gronwall's Lemma*

$$\text{If } \frac{d\Phi}{dt} \leq g(t)\Phi(t) + h(t),\ \forall t \geq 0 \ \text{ then}$$
$$\Phi(t) \leq \Phi(0)exp(\int_0^t g(s)ds) + \int_0^t h(s)exp(\int_s^t g(\tau)d\tau)ds,\ \forall t \geq 0.$$

Lemma 1 *For u, v, w sufficiently regular functions and D positive and bounded function we have for all $r \geq 0$*
1. $(D(\mid u \mid^r u - \mid v \mid^r v), u - v)_\Gamma \geq 0$,
2. $\mid (D \mid u \mid^r u, v)_\Gamma \mid \leq C \parallel \mid u \mid^r u \parallel_{L^{\frac{r+2}{r+1}}(\Gamma)} \parallel v \parallel_{L^{r+2}(\Gamma)} = C \parallel u \parallel^{r+1}_{L^{r+2}(\Gamma)} \parallel v \parallel_{L^{r+2}(\Gamma)}$,
3. $\mid (D \mid u \mid^r w, v)_\Gamma \mid \leq C \parallel \mid u \mid^r w \parallel_{L^{\frac{r+2}{r+1}}(\Gamma)} \parallel v \parallel_{L^{r+2}(\Gamma)}$ *and*

$$\parallel \mid u \mid^r w \parallel_{L^{\frac{r+2}{r+1}}(\Gamma)} \leq C \parallel u \parallel^{\frac{r}{2}}_{L^{r+2}(\Gamma)} \parallel \mid u \mid^r w^2 \parallel^{\frac{1}{2}}_{L^1(\Gamma)}.$$

Proof. For the proof see (Belmiloudi, 2007).

Definition 2 *A function $U \in \mathcal{W}(\mathcal{Q})$ is a weak solution of system (4) provided*

$$\begin{aligned} &< c(\phi)\frac{\partial U}{\partial t}, v > + \int_\Omega \kappa(\phi, U)\nabla U.\nabla v dx + \int_\Omega d(\phi)K_v(U)v dx \\ &\quad + \int_\Omega e(\phi)P(U - U_a)v dx + \int_\Gamma q(U - U_b)v d\Gamma + \int_\Gamma \lambda(\mid U \mid^3 U - \mid U_b \mid^3 U_b)v d\Gamma \\ &\quad = \int_\Omega r(\phi)g v dx + \int_\Omega f v dx + \int_\Gamma h v d\Gamma \ \ \forall v \in V \text{and a.e. in} (0,T), \\ &U(0) = U_0 \ \text{in} \ \ \Omega, \end{aligned} \tag{19}$$

here $< .,. >$ denotes the duality between V' and V.

4.3 State system

The solvability (existence, uniqueness and stability) of the state system (4) and the boundedness of the solution are the content of the following results, where the existence is proved by compactness arguments and Faedo-Galerkin method, and the boundedness is derived from the maximum principle results. By using similar argument as in (Belmiloudi, 2007) and Lemma 1, combined with these of (Belmiloudi, 2010), we can prove the following results. So, we omit the details.

Theorem 1 *Let assumptions (H1)(H2) be fulfilled.*
(i) Let be given the initial condition U_0 in $L^2(\Omega)$ and source terms (P, ϕ, f, g, h) in $\mathcal{C}_{pt} \times (L^2(\mathcal{Q}))^2 \times L^2(\Sigma)$, where $\mathcal{C}_{pt} = \{(P, \phi) \in L^2(\mathcal{Q}) \times L^2(\Omega) \mid a_1 \leq P \leq a_2 \ \text{a.e. in} \ \mathcal{Q} \text{ and } b_1 \leq \phi \leq b_2 \ \text{a.e. in} \ \Omega\}$ is the set of functions describing the constraints (5). Then there exists a unique solution U in $\mathcal{W}(\mathcal{Q}) \cap \mathcal{H}(\mathcal{Q})$ of (4) satisfying the following regularity: $\mid U \mid^3 U \in L^{\frac{5}{4}}(\Sigma)$.

(ii) Let $(P_i, \phi_i, f_i, g_i, h_i, U_{0i})$, i=1,2 be two functions of $\mathcal{C}_{pt} \times (L^2(\mathcal{Q}))^2 \times L^2(\Sigma) \times L^2(\Omega)$. If $U_i \in \mathcal{W}(\mathcal{Q}) \cap \mathcal{H}(\mathcal{Q})$ is the solution of (4) corresponding to data $(p_i, \phi_i, f_i, g_i, h_i, U_{0i})$, i=1,2, then

$$\begin{aligned} \parallel U \parallel^2_{\mathcal{H}(\mathcal{Q}) \cap \mathcal{V}(\mathcal{Q})} \leq\ & C_1(\parallel P \parallel^2_{L^2(\mathcal{Q})} + \parallel f \parallel^2_{L^2(\mathcal{Q})} + \parallel g \parallel^2_{L^2(\mathcal{Q})}) \\ & + C_2(\parallel \phi \parallel^2_{L^2(\Omega)} + \parallel h \parallel^2_{L^2(\Sigma)} + \parallel U_0 \parallel^2_{L^2(\Omega)}), \end{aligned}$$

where $U = U_1 - U_2, P = P_1 - P_2, \phi = \phi_1 - \phi_2$, $f = f_1 - f_2$, $g = g_1 - g_2$, $h = h_1 - h_2$ and $U_0 = U_{01} - U_{02}$.

If we suppose now that the functions h, q and U_b satisfy the following hypotheses:

(**HS1**): h is in $\mathcal{R}_1(\Sigma) = \{h |\ h \in L^2(0,T,H^1(\Gamma)), \frac{\partial h}{\partial t} \in L^2(0,T,L^2(\Gamma))\}$,

(**HS2**): U_b and q are in $\mathcal{R}_2(\Sigma) = \{v |\ v \in L^\infty(\overline{\Sigma}), \frac{\partial v}{\partial t} \in L^2(0,T,L^2(\Gamma))\}$,

then the following theorem holds.

Theorem 2 *Let assumptions (H1)(H2)(HS1)(HS2) be fulfilled. Let be given the initial condition U_0 in $H^{3/2}(\Omega)$ and data (P,ϕ,f,g) in $\mathcal{C}_{pt} \times (L^2(\mathcal{Q}))^2$. Then the unique solution U of (4) satisfies the following regularity: $U \in \tilde{\mathcal{S}}(\mathcal{Q})$, where*

$$\begin{aligned} &\tilde{\mathcal{S}}(\mathcal{Q}) = \{v \in \mathcal{S}(\mathcal{Q}) \text{ such that } v \in L^\infty(0,T,L^5(\Gamma))\}, \text{with} \\ &\mathcal{S}(\mathcal{Q}) = \{v \in L^\infty(0,T,V) \text{ such that } \frac{\partial v}{\partial t} \in L^2(\mathcal{Q})\}. \end{aligned} \tag{20}$$

Remark 4 (**HS1**) *implies that $h \in C^0([0,T],L^2(\Gamma))$.*

Now, we establish a maximum principle under extra assumptions on the data. In addition to (H1)(H2), we suppose, for a constant u_s such that $0 \le u_s$, the following assumption:

(H4) $0 \le U_a \le u_s$ and $0 \le U_b \le u_s$ for all in $\mathcal{Q}$ and in Σ, respectively.

Then we have the following theorem.

Theorem 3 *Let (H1),(H2) and (H4) be fulfilled. Suppose that the initial data u_0 is such that $0 \le U_0 \le u_s$, a.e. in Ω and $f + r(\phi)g$ is a positive function and satisfies $0 \le f + r(\varphi)g \le M$, a.e. in $\mathcal{Q}$ and for all ϕ such that (5). Then, the weak solution $U \in \mathcal{W}(\mathcal{Q})$ of (4) satisfies, for all $t \in (0,T)$, $0 \le U(.,t) \le m_s = \max(u_s, M)$ a.e. in Ω.*

Proof: Let us consider the following notations: $r^+ = max(r,0)$, $r^- = (-r)^+$ and then $r = r^+ - r^-$.
We prove now that if $U_0 \ge 0$, a.e. in Ω then $U(.,t) \ge 0$, for all $t \in [0,T]$ and a.e. in Ω. According to (Gilbarg & Trudinger, 1983), we have that $U^- \in L^2(0,T,V)$ with $\frac{\partial U^-}{\partial x} = -\frac{\partial U}{\partial x}$ if $U > 0$ and $\frac{\partial U^-}{\partial x} = 0$ otherwise, a.e. in $\mathcal{Q}$. Then, taking $v = -U^-$ in the equation (19) we have (*a.e. in* $(0,T)$)

$$\begin{aligned} \frac{d}{2dt} \parallel \mathfrak{x}(\phi)U^- \parallel^2_{L^2(\Omega)} &+ \int_\Omega \kappa(\phi,U) \mid \nabla U^- \mid^2 dx + \int_\Omega d(\phi)K_v(U^-)U^- dx \\ &+ \int_\Omega e(\phi)pU_aU^- dx + \int_\Omega e(\phi)P(U^-)^2 dx = -\int_\Omega (f + r(\phi)g)U^- dx \\ &+ \int_\Gamma qU_bU^- d\Gamma + \int_\Gamma q(U^-)^2 d\Gamma \\ &+ \int_\Gamma \lambda \mid u \mid^3 (U^-)^2 d\Gamma + \int_\Gamma \lambda \mid U_b \mid^3 U_bU^- d\Gamma. \end{aligned}$$

According to the assumption $U_a, U_b \ge 0$ we find that

$$\frac{d}{2dt} \parallel \mathfrak{x}(\phi)U^- \parallel^2_{L^2(\Omega)} + \int_\Omega \kappa(\phi,U) \mid \nabla u^- \mid^2 dx \le -\int_\Omega d(\varphi)K_v(U^-)U^- dx$$

and then (according to (H1) and (6))

$$\frac{d}{2dt} \parallel \mathfrak{x}(\phi)U^- \parallel^2_{L^2(\Omega)} + \frac{\nu}{2} \int_\Omega \mid \nabla u^- \mid^2 dx \le C \parallel \mathfrak{x}(\phi)U^- \parallel^2_{L^2(\Omega)}.$$

Using the assumption $U_0 \geq 0$ (then $\| U_0^- \|^2_{L^2(\Omega)} = 0$) and Gronwall's lemma, we can deduce that $U(t,.) \geq 0$ for all $t \in (0,T)$ and a.e. in Ω.
To prove that, for all $t \in (0,T)$, $U(.,t) \leq m_s$ *a.e.* in Ω, we choose $v = (U - m_s)^+ \in V$ in the equation (19) and we use the same technique as before by using the following estimate:

$$\int_\Omega (f + r(\varphi)g)(U - m_s)^+ dx = \int_\Omega ((f + r(\varphi)g) - m_s)(U - m_s)^+ dx + \int_{[U \geq m_s]} m_s (U - m_s)^+ dx \leq C \| \mathfrak{x}(\phi)(U - m_s)^+ \|^2_{L^2(\Omega)} . \quad \square$$

5. Uncertainties and perturbation problems

In clinical practice, measurements, material data, behavior of patients and other process are highly disturbed and affected by noises and errors. Consequently, in order to obtain a solution robust to the noises and fluctuations in input data and parameters, it is necessary to incorporate these uncertainties in the modeling and to analyse the robust regulation of the deviation of the model from the desired temperature distribution target, due to fluctuations.
In the following, the solution U of problem (4) will be treated as the target function. We are then interested in the robust regulation of deviation of the problem from the desired target U. So, we now formulate the perturbation problem. Precisely, we develop the **full nonlinear perturbation** problem, which models fluctuations u to the target temperature therapy U, i.e. we assume that U satisfies the problem (4) with data $(U_0, P, \phi, f, g, h, U_a, U_b)$ and $U + u$ satisfies problem (4) with the data $(U_0 + u_0, P + p, \phi + \varphi, f + \xi, g + \eta, h + \pi, U_a + u_a, U_b + u_b)$.
Hence we consider the following system (for a given U sufficiently regular):

$$\begin{aligned} c(\phi+\varphi)\frac{\partial u}{\partial t} - div(\kappa(\phi+\varphi, U+u)\nabla u) - div((\kappa(\phi+\varphi, U+u) - \kappa(\phi, U))\nabla U) \\ = -e(\phi+\varphi)(p+P)(u-u_a) - d(\phi+\varphi)K_v(u) + r(\phi+\varphi)\eta + \xi \\ -(c(\phi+\varphi) - c(\phi))\frac{\partial U}{\partial t} - (e(\varphi+\phi)(p+P) - e(\phi)P)(U - U_a) \\ -(d(\varphi+\phi) - d(\phi))K_v(U) + (r(\varphi+\phi) - r(\phi))g \quad in \ \ \mathcal{Q}, \end{aligned}$$

subjected to the boundary condition (21)

$$\begin{aligned} (\kappa(\phi+\varphi, U+u)\nabla u).\mathbf{n} + ((\kappa(\phi+\varphi, U+u) - \kappa(\phi, U))\nabla U).\mathbf{n} = -q(u - u_b) \\ -\lambda(x)((L(U+u) - L(U)) - (L(U_b+u_b) - L(U_b))) + \pi \quad in \ \ \Sigma, \end{aligned}$$

and the initial condition

$$u(0) = u_0 \ \ in \ \ \Omega.$$

If we set : $\tilde{L}(u) = L(U+u) - L(U)$, $\tilde{L}^b(u_b) = L(U_b + u_b) - L(U_b)$, and $\tilde{\beta}(\varphi) = \beta(\phi + \varphi)$, $\tilde{\kappa}(\varphi, u) = \kappa(\phi + \varphi, U + u)$, where the function β plays the role of c, d, e or r, then System (21) reduces to

$$\begin{aligned} \tilde{c}(\varphi)\frac{\partial u}{\partial t} - div(\tilde{\kappa}(\varphi, u)\nabla u) - div((\tilde{\kappa}(\varphi, u) - \tilde{\kappa}(0,0))\nabla U) \\ = -\tilde{e}(\varphi)(p+P)(u-u_a) - \tilde{d}(\varphi)K_v(u) + \tilde{r}(\varphi)\eta + \xi \\ -(\tilde{c}(\varphi) - \tilde{c}(0))\frac{\partial U}{\partial t} - (\tilde{e}(\varphi)(p+P) - \tilde{e}(0)P)(U - U_a) \\ -(\tilde{d}(\varphi) - \tilde{d}(0))K_v(U) + (\tilde{r}(\varphi) - \tilde{r}(0))g \quad in \ \ \mathcal{Q}, \end{aligned} \tag{22}$$

subjected to the boundary condition

$$(\tilde{\kappa}(\varphi,u)\nabla u).\mathbf{n} + ((\tilde{\kappa}(\varphi,u) - \tilde{\kappa}(0,0))\nabla U).\mathbf{n} \\ = -q(u-u_b) - \lambda(x)(\tilde{L}(u) - \tilde{L}^b(u_b)) + \pi \quad in\ \Sigma,$$

and the initial condition

$$u(0) = u_0 \ in\ \Omega.$$

Remark 5 (i) *We can easily verify that $\tilde{c},\tilde{d},\tilde{e},\tilde{r}$ and $\tilde{\kappa}$ satisfy the same hypothesis that c,d,e,r and κ i.e. the assumptions (H1)-(H3).*

(ii) *For simplicity of future reference, we omit the " ~ " on $\tilde{L}$, $\tilde{L}^b$, $\tilde{c},\tilde{d},\tilde{e},\tilde{r}$ and $\tilde{\kappa}$ for the system (22).*

In the sequel we assume that

$$(U_a,\phi) \in L^\infty(\mathcal{Q}) \times L^\infty(\Omega),\ (U_b,q) \in \mathcal{R}_2(\Sigma) \ \text{ and } \ U \in \tilde{\mathcal{S}}(\mathcal{Q}). \tag{23}$$

Now we show the existence and uniqueness of the solution to the problem (22), and give some Lipschitz continuity results.

Theorem 4 *Let assumptions (H1)(H2) be fulfilled (with remark 5) and (U_a,ϕ,U_b,q) be given such that (23). We have the following results.*
(i) For the initial condition u_0 in $L^2(\Omega)$ and source terms (p,φ,ξ,η,π) in $L^\infty(\mathcal{Q}) \times L^\infty(\Omega) \times (L^2(\mathcal{Q}))^2 \times L^2(\Sigma)$. There exists a unique solution u in $\mathcal{W}(\mathcal{Q}) \cap \mathcal{H}(\mathcal{Q})$ of (22) satisfying the following regularity: $\mid u \mid^3 u \in L^{\frac{5}{4}}(\Sigma)$.
(ii) Let $(p_i,\varphi_i,\xi_i,\eta_i,\pi_i,u_{0i})$, i=1,2 be two functions of $L^\infty(\mathcal{Q}) \times L^\infty(\Sigma) \times (L^2(\mathcal{Q}))^2 \times L^2(\Sigma) \times L^2(\Omega)$. If $u_i \in \mathcal{W}(\mathcal{Q}) \cap \mathcal{H}(\mathcal{Q})$ is the solution of (22) corresponding to data $(p_i,\varphi_i,\xi_i,\eta_i,\pi_i,u_{0i})$, i=1,2, then

$$\begin{aligned} \| u \|^2_{\mathcal{H}(\mathcal{Q})\cap\mathcal{V}(\mathcal{Q})} \leq\ & C_1(\| p \|^2_{L^2(\mathcal{Q})} + \| \xi \|^2_{L^2(\mathcal{Q})}) \\ & + C_2(\| \varphi \|^2_{L^2(\Omega)} + \| \eta \|^2_{L^2(\mathcal{Q})} + \| \pi \|^2_{L^2(\Sigma)}) + C_3 \| u_0 \|^2_{L^2(\Omega)}, \end{aligned} \tag{24}$$

where $u = u_1 - u_2, p = p_1 - p_2, \varphi = \varphi_1 - \varphi_2$, $\xi = \xi_1 - \xi_2$, $\eta = \eta_1 - \eta_2$, $\pi = \pi_1 - \pi_2$ and $u_0 = u_{01} - u_{02}$.

Proof. The proof of this result can be obtained by using a similar technique as in the proof of Theorem 1. So, we omit the details.

6. Robust control and regulation problems

In this section we formulate the robust control problem and study the existence and necessary optimality conditions for an optimal solution.

6.1 Formulation of the control problem

Our problem in this section is to find the best admissible perfusion function p and distributed energy source ξ in the presence of the worst disturbance in the porosity function φ, in the evaporation term π and in the metabolic heat generation type term η. We then suppose that

the control is in $X=(p,\xi)$ and the disturbance is in $Y=(\varphi,\eta,\pi)$. Therefore, the function u is assumed to be related to the disturbance Y and control X through the problem

$$\begin{aligned} c(\varphi)\frac{\partial u}{\partial t} - div(\kappa(\varphi,u)\nabla u) + e(\varphi)(p+P)(u-w_a) + d(\varphi)K_v(u) \\ = div((\kappa(\varphi,u)-\kappa(0,0))\nabla U) + r(\varphi)\eta + \xi - (c(\varphi)-c(0))\frac{\partial U}{\partial t} \\ +e(0)Pv_a - (d(\varphi)-d(0))K_v(U) + (r(\varphi)-r(0))g \ \ in \ \ \mathcal{Q}, \end{aligned}$$

subjected to the boundary condition

$$\begin{aligned} (\kappa(\varphi,u)\nabla u).\mathbf{n} = -((\kappa(\varphi,u)-\kappa(0,0))\nabla U).\mathbf{n} \\ -q(u-u_b) - \lambda(x)(L(u)-L^b(u_b)) + \pi \ \ in \ \ \Sigma, \end{aligned} \tag{25}$$

and the initial condition

$$u(0) = u_0 \ \ in \ \ \Omega,$$

under pointwise constraints

$$\begin{aligned} \tau_1 \le p \le \tau_2 \ \ a.e. \ in \ \mathcal{Q}, \\ \delta_1 \le \varphi \le \delta_2 \ \ a.e. \ in \ \Omega, \end{aligned} \tag{26}$$

where $v_a = U - U_a$ and $w_a = u_a - v_a$, and $u_0 \in L^2(\Omega)$ is assumed to be given.
Let D_i, for $i=1,2$ be the sets of functions describing the constraints (26) such that

$$D_1 = \{p \in L^2(\mathcal{Q}) : \ \tau_1 \le p \le \tau_2 \ \ a.e. \ in \ \mathcal{Q}\} \ \text{ and } \ D_2 = \{\varphi \in L^2(\Omega) : \ \delta_1 \le \varphi \le \delta_2 \ \ a.e. \ in \ \Omega\},$$

and $\mathcal{K}_i$ for $i=1,2$ be convex, closed, non-empty and bounded subset of $L^2(\mathcal{Q})$ and $\mathcal{K}_3$ be convex, closed, non-empty and bounded subset of $L^2(\Sigma)$. The studied control problem is to find a saddle point of the cost function $\mathcal{J}$ which measures the distance between the known observations $\mathfrak{m}_{obs}$ and D_{obs} (or known offsets which are given by experiment measurements) , corresponding to the online temperature control and thermal damage via radiometric temperature measurement system, respectively, and the prognostic variables $\gamma u + \delta p$ (in practice the parameters γ and δ satisfy $\gamma \approx \delta$ in muscle and $\gamma \ll \delta$ in fat) and the variation of cell damage function $(\mathcal{D}(x,u+U) - \mathcal{D}(x,U))$ (see paragraph 2.2). Precisely we will study the following robust control problem (**SP**).

find $(X,Y) \in \mathcal{U}_{ad} \times \mathcal{V}_{ad}$ such that the cost functional (in the reduced form)

$$\begin{aligned} \mathcal{J}(X,Y) = \frac{a}{2} \parallel (\gamma u + \delta p) - \mathfrak{m}_{obs} \parallel^2_{L^2(\mathcal{Q})} + \frac{b}{2} \parallel \int_0^T \tilde{\mathcal{H}}(t,u(.,t))dt - D_{obs} \parallel^2_{L^2(\Omega)} \\ + \frac{\alpha}{2} \parallel \mathcal{N}X \parallel^2_{L^2(\mathcal{Q})\times L^2(\mathcal{Q})} - \frac{\beta}{2} \parallel \mathcal{M}Y \parallel^2_{L^2(\Omega)\times L^2(\mathcal{Q})\times L^2(\Sigma)} \end{aligned} \tag{27}$$

is minimized with respect to $X=(p,\xi)$ and maximized with respect to $Y=(\varphi,\eta,\pi)$ subject to the problem (25),

where $a+b>0$ and $a,b \ge 0$, $\tilde{\mathcal{H}}(t,u) = \mathcal{H}(t,u+U) - \mathcal{H}(t,U)$ with the cell damage function $D(x,u) = \int_0^T \mathcal{H}(t,u(.,t))dt$ (see paragraph 2.2), the matrix $\mathcal{N} = diag(\sqrt{n_1},\sqrt{n_2})$ and $\mathcal{M} =$

$diag(\sqrt{m_1},\sqrt{m_2},\sqrt{m_3})$, are predefined nonnegative weights such that $n_1+n_2\neq 0$ and $m_1+m_2+m_3\neq 0, \mathcal{U}_{ad}=D_1\times\mathcal{K}_1, \mathcal{V}_{ad}=D_2\times\mathcal{K}_2\times\mathcal{K}_3$ and $(\mathfrak{m}_{obs},D_{obs})$ is the target. The coefficient $\alpha>0$ can be interpreted as the measure of the price of the control (that the engineer can afford) and the coefficient $\beta>0$ can be interpreted as the measure of the price of the disturbance (that the environnement can afford). The parameters γ,δ are positive with space-time dependent entries and are in $L^\infty(\overline{\mathcal{Q}})$.

Remark 6 *Although D_1 (respectively D_2) is a subset of $L^\infty(\mathcal{Q})$ (respectively of $L^\infty(\Omega)$), we prefer to use the standard norms of the space $L^2(\mathcal{Q})$ (respectively of $L^2(\Omega)$). The reason is that we would like to take advantages of the differentiability of the latter norm away from the origin to perform our variational analysis.*

6.2 Fréchet differentiability and existence result

Let us introduce the following mapping $\mathcal{F}:\mathcal{U}_{ad}\times\mathcal{V}_{ad}\longrightarrow\mathcal{Z}=\tilde{\mathcal{W}}(\mathcal{Q})\cap\mathcal{H}(\mathcal{Q})$, which maps the source term $(X,Y)\in\mathcal{U}_{ad}\times\mathcal{V}_{ad}$ of (25) into the corresponding solution u in $\mathcal{Z}$, and assume, in addition, that the assumption (**H**3) holds.

Following the development in (Belmiloudi, 2008), we start by calculating the variation of the operator solution $\mathcal{F}$. For this we suppose that the operator solution $\mathcal{F}$ is continuously differentiable (in weak sense) on $\mathcal{U}_{ad}\times\mathcal{V}_{ad}$ and its derivative (at point $(X,Y)=(p,\xi,\varphi,\eta,\pi)$) $\mathcal{F}'(X,Y):(H,K)=(\mathfrak{y},\mathfrak{h},\psi,\mathfrak{e},\mathfrak{z})\in L^\infty(\mathcal{Q})\times L^2(\mathcal{Q})\times L^\infty(\Omega)\times L^2(\mathcal{Q})\times L^2(\Sigma)\longrightarrow w=\mathcal{F}'(X,Y).(H,K)=\lim\limits_{\epsilon\longrightarrow 0}\dfrac{\mathcal{F}(X+\epsilon H,Y+\epsilon K)}{\epsilon}$, where $(X+\epsilon H,Y+\epsilon K)\in\mathcal{U}_{ad}\times\mathcal{V}_{ad}$, is such that $w=\dfrac{\partial\mathcal{F}}{\partial X}(X,Y)H+\dfrac{\partial\mathcal{F}}{\partial Y}(X,Y)K$ is the unique weak solution of the following system

$$
\begin{aligned}
&c'(\varphi)\frac{\partial(u+U)}{\partial t}\psi+c(\varphi)\frac{\partial w}{\partial t}-div(\kappa(\varphi,u)\nabla w)\\
&\quad -div((\frac{\partial\kappa}{\partial\varphi}(\varphi,u)\psi+\frac{\partial\kappa}{\partial u}(\varphi,u)w)\nabla(u+U))\\
&\quad +e'(\varphi)\psi(p+P)(u-w_a)+e(\varphi)\mathfrak{y}(u-w_a)+e(\varphi)(p+P)w\\
&\quad +d'(\varphi)\psi K_v(u+U)+d(\varphi)K_v(w)=r'(\varphi)\psi(\eta+g)+r(\varphi)\mathfrak{e}+\mathfrak{h}\quad in\ \ \mathcal{Q},
\end{aligned}
$$

subjected to the boundary condition (28)

$$
\begin{aligned}
(\kappa(\varphi,u)\nabla w).\mathbf{n}=&-((\frac{\partial\kappa}{\partial\varphi}(\varphi,u)\psi+\frac{\partial\kappa}{\partial u}(\varphi,u)w)\nabla(U+u)).\mathbf{n}\\
&-qw-\lambda(x)L'(u)w+\mathfrak{z}\quad in\ \ \Sigma,
\end{aligned}
$$

and the initial condition

$$w(0)=0\ \ in\ \ \Omega,$$

where $u=\mathcal{F}(X,Y)$. If we put $U_1=u+U$, $P_1=p+P$, $V_a=u-w_a$ and $G_1=\eta-g$, the system (28) can be written as

$$
\begin{aligned}
c(\varphi)\frac{\partial w}{\partial t}&-div(\kappa(\varphi,u)\nabla w)-div((\frac{\partial\kappa}{\partial\varphi}(\varphi,u)\psi+\frac{\partial\kappa}{\partial u}(\varphi,u)w)\nabla U_1)+d(\varphi)K_v(w)\\
&+e(\varphi)P_1w+e'(\varphi)\psi P_1V_a+e(\varphi)\mathfrak{y}V_a\\
&+d'(\varphi)\psi K_v(U_1)=-c'(\varphi)\frac{\partial U_1}{\partial t}\psi+r'(\varphi)\psi G_1+r(\varphi)\mathfrak{e}+\mathfrak{h}\quad in\ \ \mathcal{Q},
\end{aligned}
\tag{29}
$$

subjected to the boundary condition

$$(\kappa(\varphi,u)\nabla w).\mathbf{n} = -((\frac{\partial \kappa}{\partial \varphi}(\varphi,u)\psi + \frac{\partial \kappa}{\partial u}(\varphi,u)w)\nabla U_1).\mathbf{n} \\ -qw - \lambda(x)L'(u)w + \mathfrak{z} \quad in\ \ \Sigma,$$

and the initial condition

$$w(0) = 0 \ \ in \ \ \Omega.$$

Definition 3 *The system (28) (or (29)) satisfied by w is called the tangent linear model (TLM) or sensitivity problem and w is called sensitivity temperature.*

Using the minimax formulation (of *Ky Fan-von Neumann*) in infinite dimensions presented in chapter 5 of (Belmiloudi, 2008) (see also (Ekeland & Temam, 1976)), we have the following sufficient and necessary conditions for the existence and characterisation of a saddle point.

1. Sufficient conditions for the objective functional $\mathcal{J}$ to admit a saddle point are :
   a) The mapping $\mathcal{P}_Y : \ X \longrightarrow \mathcal{J}(X,Y)$ is convex and lower semi-continuous (in a weak topology), for all $Y \in \mathcal{V}_{ad}$.
   b) The mapping $\mathcal{R}_X : \ Y \longrightarrow \mathcal{J}(X,Y)$ is concave and upper semi-continuous (in a weak topology), for all $X \in \mathcal{U}_{ad}$.
2. Necessary optimality conditions for a saddle point $(X^*,Y^*) \in \mathcal{U}_{ad} \times \mathcal{V}_{ad}$ of $\mathcal{J}$, if $\mathcal{P}_Y$ and $\mathcal{R}_X$ are Gâteaux differentiable, are

$$\begin{aligned} &\frac{\partial \mathcal{J}}{\partial X}(X^*,Y^*).(X - X^*) \geq 0 \quad \forall X \in \mathcal{U}_{ad}, \\ &\frac{\partial \mathcal{J}}{\partial Y}(X^*,Y^*).(Y - Y^*) \leq 0 \quad \forall Y \in \mathcal{V}_{ad}. \end{aligned} \tag{30}$$

From the expression of the cost functional $\mathcal{J}$, which is a composition of Gâteaux differentiable mappings, it follows that $\mathcal{P}_Y$ and $\mathcal{R}_X$ are Gâteaux differentiable. Consequently, in order to prove the convexity of $\mathcal{P}_Y$ (respectively the concavity of $\mathcal{R}_X$), it is sufficient to show that for all $(X_1,X_2) \in \mathcal{U}_{ad} \times \mathcal{U}_{ad}$ (respectively for all $(Y_1,Y_2) \in \mathcal{V}_{ad} \times \mathcal{V}_{ad}$), we have

$$(\mathcal{P}'_Y(X_1) - \mathcal{P}'_Y(X_2)).(X_1 - X_2) \geq 0 \ \ \text{(respectively } (\mathcal{R}'_X(Y_1) - \mathcal{R}'_X(Y_2)).(Y_1 - Y_2) \leq 0)),$$

where for $i = 1,2$ and for all $(H,K) \in \mathcal{U}_{ad} \times \mathcal{V}_{ad}$

$$\mathcal{P}'_Y(X_i)H = \lim_{\epsilon \longrightarrow 0} \frac{\mathcal{J}(X_i + \epsilon H, Y) - \mathcal{J}(X_i,Y)}{\epsilon}, \quad \mathcal{R}'_X(Y_i)K = \lim_{\epsilon \longrightarrow 0} \frac{\mathcal{J}(X,Y_i + \epsilon K) - \mathcal{J}(X,Y_i)}{\epsilon}.$$

Using similar arguments as in Chapter 8 of (Belmiloudi, 2008), we can prove that : *there exist constants α_l and β_l such that for all $\alpha \geq \alpha_l$ and $\beta \geq \beta_l$, the operators $\mathcal{P}_Y$ and $\mathcal{R}_X$ are convex and concave, respectively.* We shall prove now that $\mathcal{P}_Y$ (respectively $\mathcal{R}_X$) is lower (respectively

upper) semi-continuous for all $Y \in \mathcal{V}_{ad}$ (respectively $X \in \mathcal{U}_{ad}$). Let $X_k \in \mathcal{U}_{ad}$ be a minimizing sequence of $\mathcal{P}_Y$, i.e.,

$$\liminf_{k \longrightarrow \infty} \mathcal{J}(X_k, Y) = \inf_{X \in (L^2(\mathcal{Q}))^2} \mathcal{J}(X, Y).$$

Then, according to the nature of the cost function $\mathcal{J}$, we can deduce that X_k is uniformly bounded in $\mathcal{U}_{ad}$ and we can extract from X_k a subsequence also denoted by X_k such that $X_k \rightharpoonup X_Y$ weakly in $\mathcal{U}_{ad}$. Therefore, by using the same technique as to obtain the estimate (24), the function $u_k = \mathcal{F}(X_k, Y)$ is uniformly bounded in $\mathcal{W}(\mathcal{Q}) \cap \mathcal{H}(\mathcal{Q})$. Consequently, since the injection of $\mathcal{W}(\mathcal{Q})$ into $L^2(\mathcal{Q})$ is compact, these results make it possible to extract from u_k a subsequence also denoted by u_k such that

$$\begin{array}{l} u_k \rightharpoonup u_Y \textit{ weakly in } L^2(0,T;V), \\ u_k \longrightarrow u_Y \textit{ strongly in } L^2(\mathcal{Q}), \\ X_k \rightharpoonup X_Y \textit{ weakly in } L^2(\mathcal{Q}) \text{ and } X_Y \in \mathcal{U}_{ad}. \end{array} \tag{31}$$

It is easy to prove that u_Y is a solution of (25) with data (X_Y, Y) and according to the uniqueness of the solution of the direct problem (25), we have then $u_Y = \mathcal{F}(X_Y, Y)$. Therefore, since the norm is lower semi-continuous, we have that the map $\mathcal{P}_Y$ is lower semi-continuous for all $Y \in \mathcal{V}_{ad}$. By applying similar argument as in the proof of the previous result we obtain that $\mathcal{R}_X$ is upper semi-continuous for all $X \in \mathcal{U}_{ad}$ (in this case we consider a maximizing sequence $X_k \in \mathcal{U}_{ad}$ of $\mathcal{R}_X$, i.e., $\limsup_{k \longrightarrow \infty} \mathcal{J}(X_k, Y) = \sup_{Y \in \mathcal{Y}_2} \mathcal{J}(\mathcal{X}, \mathcal{Y})$, where $\mathcal{Y}_2 = L^2(\Omega) \times L^2(\mathcal{Q}) \times L^2(\Sigma)$).

In conclusion we have that: *for α and β sufficiently large there exists an optimal solution $(X^*, Y^*) \in \mathcal{U}_{ad} \times \mathcal{V}_{ad}$ and $u^* \in \mathcal{Z}$ such that (X^*, Y^*) is a saddle point of $\mathcal{J}$ and $u^* = \mathcal{F}(X^*, Y^*)$.*

Remark 7

- *To obtain the uniqueness of the optimal solution we can use similar assumption about sufficiently small final time T as e.g. in (Belmiloudi, 2005).*
- *If we assume in addition that the operator c, d, e, r and κ are twice differentiable, we can also derive the uniqueness result by proving the strict convexity of the functional $\mathcal{P}_Y$ and the strict convexity of the functional $\mathcal{R}_X$, which are equivalent to showing*

$$\Psi''_Y(\epsilon) > 0 \textit{ and } \Phi''_X(\epsilon) < 0 \quad \forall \epsilon \in [0,1],$$

where $\Psi(\epsilon) = \mathcal{J}(\epsilon X + (1-\epsilon)\overline{X}, Y)$, $\Phi(\epsilon) = \mathcal{J}(X, \epsilon Y + (1-\epsilon)\overline{Y})$, for $X, \overline{X}$ given in $\mathcal{U}_{ad}$ and $Y, \overline{Y}$ given in $\mathcal{V}_{ad}$. More precisely,

"If the coefficients α, β are sufficiently large, i.e. if there exists (α_L, β_L) such that $\alpha \geq \alpha_l \geq \alpha_L$ and $\beta \geq \beta_l \geq \beta_L$, then the robust control problem admits one unique solution."

- *According to the previous results, we can deduce that*

"If there exists (α_L, β_L) such that $\alpha \geq \alpha_l \geq \alpha_L$ and $\beta \geq \beta_l \geq \beta_L$, or if the final time T is sufficiently small, $\alpha \geq \alpha_l$ and $\beta \geq \beta_l$, then the robust control problem admits one unique solution."

In order to solve the saddle problem (27) it is necessary to derive the gradient $\mathcal{J}'(X, Y)$ of the cost functional $\mathcal{J}$ with respect to the control-disturbance (X, Y). To this end, let us introduce

the directional derivative $\mathcal{J}'(X,Y).(H,K)$, where $X=(p,\xi)$, $Y=(\varphi,\eta,\pi)$, $H=(\mathfrak{y},\mathfrak{h})$ and $K=(\psi,\mathfrak{e},\mathfrak{z})$ by

$$\begin{aligned}\mathcal{J}'(X,Y).(H,K) &= \frac{d}{d\mathfrak{s}}\mathcal{J}(X+\mathfrak{s}H,Y+\mathfrak{s}K)|_{\mathfrak{s}=0}\\ &= a\iint_{\mathcal{Q}}((\gamma u+\delta p)-\mathfrak{m}_{obs})(\gamma w+\delta\mathfrak{y})\,dxdt\\ &\quad +b\int_{\Omega}(\int_0^T\tilde{\mathcal{H}}(t,u(.,t))\,dt-D_{obs})(\int_0^T\tilde{\mathcal{H}}'(t,u(.,t))w\,dt)\,dx\\ &\quad +\alpha(n_1\iint_{\mathcal{Q}}p\mathfrak{y}\,dxdt+n_2\iint_{\mathcal{Q}}\xi\mathfrak{h}\,dxdt)\\ &\quad -\beta(m_1\int_{\Omega}\varphi\psi\,dx+m_2\iint_{\mathcal{Q}}\eta\mathfrak{e}\,dxdt+m_3\iint_{\Sigma}\pi\mathfrak{z}\,d\Gamma dt),\end{aligned}\tag{32}$$

where $w=\mathcal{F}'(X,Y).(H,K)$ is the solution of the sensitivity problem (6.2) and $\tilde{\mathcal{H}}'$ is the differential of $\tilde{\mathcal{H}}$ at the second variable u.

Remark 8 *Since $\tilde{\mathcal{H}}(t,u)=\mathcal{H}(t,U+u)-\mathcal{H}(t,U)$ then $\tilde{\mathcal{H}}'(t,u)=\mathcal{H}'(t,U+u)$. Consequently, for example in the case of Arrhenius model, we have that $\tilde{\mathcal{H}}'(t,u)=\dfrac{E}{R(U+u)^2}\mathcal{H}(t,U+u)$.*

It is clear from (32) that the main difficulty is the simplification of the directional derivative $\mathcal{J}'(X,Y).(H,K)$, which requires the introduction of the adjoint (or dual problem) to the sensitivity state corresponding to the direct problem (25). The adjoint model and the evaluation of the gradient of $\mathcal{J}$ are given in the next section.

6.3 Adjoint model and gradient

Let $\tilde{u}$ be a sufficiently regular function such that $\tilde{u}(T)=0$. Multiplying the first part of (29) by $\tilde{u}$ and integrating with respect to space and time, and using Green's formula, we obtain according to the second part of (29) (the boundary condition) that (since $c(\varphi)$ is independent on time)

$$\begin{aligned}&\iint_{\mathcal{Q}}-c(\varphi)\frac{\partial\tilde{u}}{\partial t}w\,dxdt+\int_{\Omega}(c(\varphi)(\tilde{u}(T)w(T)-\tilde{u}(0)w(0))\,dx\\ &\quad+\iint_{\Sigma}(qw+\lambda(x)L'(u)w-\mathfrak{z})\tilde{u}\,d\Gamma dt+\iint_{\Sigma}\kappa(\varphi,u)\nabla\tilde{u}.\mathbf{n}w\,d\Gamma dt\\ &\quad+\iint_{\mathcal{Q}}(\frac{\partial\kappa}{\partial\varphi}(\varphi,u)\psi+\frac{\partial\kappa}{\partial u}(\varphi,u)w)\nabla U_1.\nabla\tilde{u}\,dxdt-\iint_{\mathcal{Q}}div(\kappa(\varphi,u)\nabla\tilde{u})w\,dxdt\\ &\quad+\iint_{\mathcal{Q}}d(\varphi)K_v(w)\tilde{u}\,dxdt+\iint_{\mathcal{Q}}e(\varphi)P_1\tilde{u}w\,dxdt\\ &\qquad=-\iint_{\mathcal{Q}}(e'(\varphi)P_1V_a+c'(\varphi)\frac{\partial U_1}{\partial t}+d'(\varphi)K_v(U_1)-r'(\varphi)G_1)\psi\tilde{u}\,dxdt\\ &\qquad\quad-\iint_{\mathcal{Q}}e(\varphi)V_a\tilde{u}\mathfrak{y}\,dxdt+\iint_{\mathcal{Q}}r(\varphi)\tilde{u}\mathfrak{e}\,dxdt+\iint_{\mathcal{Q}}\tilde{u}\mathfrak{h}\,dxdt.\end{aligned}\tag{33}$$

According to (18) we can deduce that

$$\iint_{\mathcal{Q}}d(\varphi)K_v(w)\tilde{u}\,dxdt=\iint_{\mathcal{Q}}K_v^*(d(\varphi)\tilde{u})wdx+\iint_{\Sigma}d(\varphi)\tilde{u}\vec{\vartheta}.\mathbf{n}w\,d\Gamma dt.\tag{34}$$

Since $\tilde{u}(T)=0$, $w(0)=0$ and according to (34), we obtain (since ψ is independent on time)

$$\begin{aligned}
&\int\int_{\mathcal{Q}}\left(-c(\varphi)\frac{\partial\tilde{u}}{\partial t}-div(\kappa(\varphi,u)\nabla\tilde{u})+K_v^*(d(\varphi)\tilde{u})+e(\varphi)P_1\tilde{u}+\frac{\partial\kappa}{\partial u}(\varphi,u)\nabla U_1.\nabla\tilde{u}\right)w\,dxdt\\
&\quad+\int\int_{\Sigma}(q\tilde{u}+\lambda(x)L'(u)\tilde{u}+\kappa(\varphi,u)\nabla\tilde{u}.\mathbf{n}+d(\varphi)\tilde{u}\vec{\vartheta}.\mathbf{n})w\,d\Gamma dt\\
&\quad=-\int_{\Omega}\left(\int_0^T(e'(\varphi)P_1V_a+c'(\varphi)\frac{\partial U_1}{\partial t}+d'(\varphi)K_v(U_1)-r'(\varphi)G_1)\tilde{u}dt\right)\psi\,dx\\
&\quad-\int_{\Omega}\left(\int_0^T\frac{\partial\kappa}{\partial\varphi}(\varphi,u)\nabla U_1.\nabla\tilde{u}dt\right)\psi\,dx\\
&\quad-\int\int_{\mathcal{Q}}e(\varphi)V_a\tilde{u}\mathfrak{y}\,dxdt+\int\int_{\mathcal{Q}}r(\varphi)\tilde{u}\mathfrak{e}\,dxdt+\int\int_{\mathcal{Q}}\tilde{u}\mathfrak{h}\,dxdt+\int\int_{\Sigma}\mathfrak{z}\tilde{u}\,d\Gamma dt.
\end{aligned}\tag{35}$$

In order to simplify the problem (35), we assume that $\tilde{u}$ satisfies the following so-called adjoint problem (with initial value given at final time T)

$$\begin{aligned}
&-c(\varphi)\frac{\partial\tilde{u}}{\partial t}-div(\kappa(\varphi,u)\nabla\tilde{u})+K_v^*(d(\varphi)\tilde{u})+e(\varphi)P_1\tilde{u}+\frac{\partial\kappa}{\partial u}(\varphi,u)\nabla U_1.\nabla\tilde{u}\\
&\qquad+a\gamma(\gamma u+\delta p-\mathfrak{m}_{obs})+b(\int_0^T\tilde{\mathcal{H}}(t,u(.,t))\,dt-D_{obs})\tilde{\mathcal{H}}'(.,u)=0\quad in\ \ \mathcal{Q},\\
&\text{subjected to the boundary condition}\\
&-\kappa(\varphi,u)\nabla\tilde{u}.\mathbf{n}=q\tilde{u}+\lambda(x)L'(u)\tilde{u}+d(\varphi)\tilde{u}\vec{\vartheta}.\mathbf{n}\quad in\ \ \Sigma,\\
&\text{and the final condition}\\
&\tilde{u}(T)=0\ \ in\ \ \Omega.
\end{aligned}\tag{36}$$

Remark 9

1. *We point out that : if the function $\tilde{\mathcal{H}}$ is a Carathéodory function from $\mathbb{R}\times\mathbb{R}$ into $\mathbb{R}^+$ and $\tilde{\mathcal{H}}(t,.)$ is Lipschitz, differentiable, bounded function and its partial derivative is Lipschitz and bounded function (for almost all $t\in(0,T)$), the adjoint problem (36), which is backward in time, can be transformed into an initial-boundary value problem by the time transformation $t:=T-t$, which allows to employ similar argument as in the proof of Theorem 1 for the existence of a unique solution $\tilde{u}$ of (36) for a sufficiently regular data. So, we omit the details.*
2. *In the sequel we denote by $\mathcal{F}^{\perp}(X,Y)=\tilde{u}$ the solution of the adjoint problem (36) corresponding to the direct solution $u=\mathcal{F}(X,Y)$.*

Using the system (36), the problem (35) becomes

$$\begin{aligned}
&\int\int_{\mathcal{Q}}-\left(a\gamma(\gamma u+\delta p-\mathfrak{m}_{obs})+b(\int_0^T\tilde{\mathcal{H}}(t,u(.,t))\,dt-D_{obs})\tilde{\mathcal{H}}'(.,u)\right)w\,dxdt\\
&\quad=-\int_{\Omega}\left(\int_0^T(e'(\varphi)P_1V_a+c'(\varphi)\frac{\partial U_1}{\partial t}+d'(\varphi)K_v(U_1)-r'(\varphi)G_1)\tilde{u}dt\right)\psi\,dx\\
&\quad-\int_{\Omega}\left(\int_0^T\frac{\partial\kappa}{\partial\varphi}(\varphi,u)\nabla U_1.\nabla\tilde{u}dt\right)\psi\,dx\\
&\quad-\int\int_{\mathcal{Q}}e(\varphi)V_a\tilde{u}\mathfrak{y}\,dxdt+\int\int_{\mathcal{Q}}r(\varphi)\tilde{u}\mathfrak{e}\,dxdt+\int\int_{\mathcal{Q}}\tilde{u}\mathfrak{h}\,dxdt+\int\int_{\Sigma}\mathfrak{z}\tilde{u}\,d\Gamma dt.
\end{aligned}\tag{37}$$

According to the expression (32) of $\mathcal{J}'(X,Y)$ we can deduce that

$$\begin{aligned}\mathcal{J}'(X,Y).(H,K) &= \frac{\partial \mathcal{J}}{\partial X}(X,Y).H + \frac{\partial \mathcal{J}}{\partial Y}(X,Y).K \\ &= \iint_{\mathcal{Q}} (e(\varphi)V_a\tilde{u} + \alpha n_1 p + a\delta(\gamma u + \delta p - \mathfrak{m}_{obs}))\mathfrak{y}\, dxdt + \iint_{\mathcal{Q}} (n_2\xi - \tilde{u})\mathfrak{h}\, dxdt \\ &\quad + \int_{\Omega} (\mathcal{E}(\varphi, U_1, \tilde{u}) - \beta m_1 \varphi)\psi\, dx - \iint_{\mathcal{Q}} (r(\varphi)\tilde{u} + \beta m_2 \eta)\mathfrak{e}\, dxdt \\ &\quad - \iint_{\Sigma} (\tilde{u} + \beta m_3 \pi)\mathfrak{z}\, d\Gamma dt,\end{aligned} \tag{38}$$

where

$$\begin{aligned}\mathcal{E}(\varphi, U_1, \tilde{u}) = \int_0^T (e'(\varphi)P_1V_a + c'(\varphi)\frac{\partial U_1}{\partial t} + d'(\varphi)K_v(U_1) - r'(\varphi)G_1)\tilde{u}dt \\ + \int_0^T \frac{\partial \kappa}{\partial \varphi}(\varphi, u)\nabla U_1.\nabla \tilde{u} dt.\end{aligned} \tag{39}$$

Consequently the gradient of $\mathcal{J}$ at point (X,Y), in weak sense, is

$$\begin{aligned}\frac{\partial \mathcal{J}}{\partial X}(X,Y) &= \begin{pmatrix} e(\varphi)V_a\tilde{u} + \alpha n_1 p + a\delta(\gamma u + \delta p - \mathfrak{m}_{obs}) \\ n_2\xi - \tilde{u} \end{pmatrix}, \\ \frac{\partial \mathcal{J}}{\partial Y}(X,Y) &= \begin{pmatrix} \mathcal{E}(\varphi, U_1, \tilde{u}) - \beta m_1 \varphi \\ -(r(\varphi)\tilde{u} + \beta m_2 \eta) \\ -(\tilde{u} + \beta m_3 \pi) \end{pmatrix}.\end{aligned} \tag{40}$$

We next wish to show the appropriate first-order necessary optimality conditions of the saddle point (X^*, Y^*) of the functional $\mathcal{J}$, by using the characterization (30).

6.4 First-order optimality conditions

Let $(X^*, Y^*) \in \mathcal{U}_{ad} \times \mathcal{V}_{ad}$ and $u^* \in \mathcal{Z}$ be an optimal solution such that (X^*, Y^*) is a saddle point of $\mathcal{J}$ and $u^* = \mathcal{F}(X^*, Y^*)$ is the solution of (22). Then according to (30) and the expression (38) of $\mathcal{J}'$ we can deduce that, for all $(X,Y) \in \mathcal{U}_{ad} \times \mathcal{V}_{ad}$

$$\begin{aligned}\frac{\partial \mathcal{J}}{\partial X}(X^*, Y^*).(X - X^*) &= \iint_{\mathcal{Q}} (e(\varphi^*)V_a^*\tilde{u}^* + \alpha n_1 p^* + a\delta(\gamma u^* + \delta p^* - \mathfrak{m}_{obs}))(p - p^*)dxdt \\ &\quad + \iint_{\mathcal{Q}} (n_2\xi^* - \tilde{u}^*)(\xi - \xi^*)\, dxdt \geq 0 \\ \frac{\partial \mathcal{J}}{\partial Y}(X^*, Y^*).(Y - Y^*) &= \int_{\Omega} (\mathcal{E}(\varphi^*, U_1^*, \tilde{u}^*) - \beta m_1 \varphi^*)(\varphi - \varphi^*)\, dx \\ &\quad - \iint_{\mathcal{Q}} (r(\varphi^*)\tilde{u}^* + \beta m_2 \eta^*)(\eta - \eta^*)\, dxdt \\ &\quad - \iint_{\Sigma} (\tilde{u}^* + \beta m_3 \pi^*)(\pi - \pi^*)\, d\Gamma dt \leq 0\end{aligned} \tag{41}$$

where $U_1^* = u^* + U$, $P_1^* = p^* + P$, $V_a^* = u^* - w_a$, $G_1^* = \eta^* - g$ and $\tilde{u}^* = \mathcal{F}^{\perp}(X^*, Y^*)$ is the solution of the adjoint problem (36).

6.5 Optimization procedure

By using the successive resolutions of both the direct problem and the adjoint problem, we can therefore calculate the gradient of the objective function relative to the control-disturbance

functions X and Y. Once the gradient of the objective function $\mathcal{J}$, $\nabla\mathcal{J}$, is known, we can seek a saddle point of $\mathcal{J}$. For a given observation $(\mathfrak{m}_{obs}, D_{obs})$ for the outline temperature and thermal damage, the optimization algorithm is summarized in Table 1.

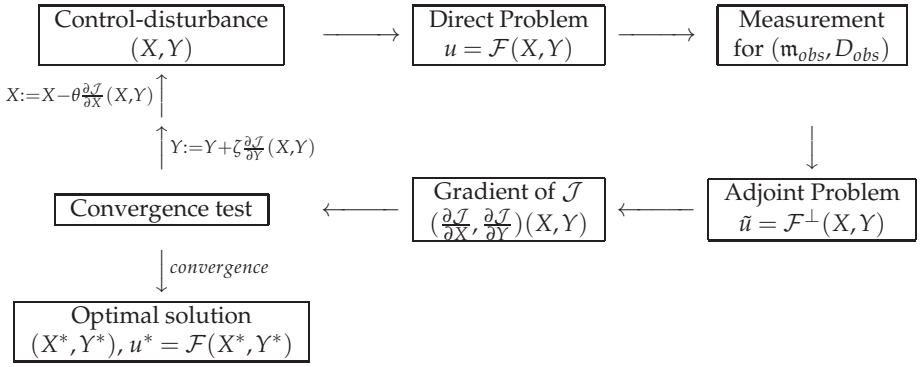

Table 1. Optimization algorithm : $\mathcal{J}$ is optimized until some convergence criteria are attained.

7. Finite number of measurements and different tissues

7.1 Finite number of measurements

In many situations, we can measure the online temperature $\mathfrak{m}_{obs}$ and the thermal damage D_{obs} in only some points in space-time domain. Let now some points be in $\Omega \times (0,T)$ where we assume that we can measure $(\mathfrak{m}_{obs}, D_{obs})$. Let $x_i \in \Omega, i = 1, \cdots l$ such that $x_i \neq x_j$ if $i \neq j$, $0 < t_1 < t_2 < \cdots < T$, and assume that we measure quantity ϵ_{ij} and $\mathfrak{d}_i$ which are meant to be the value of the functions $(\gamma u + \delta p)$ at point (x_i, t_j) and $\int_0^T \tilde{\mathcal{H}}(t, u(.,t))dt$ at point x_i denoted by $M(x_i,t_j)$, for $i = 1,\ldots,l$ and $j = 1,\ldots,N$ and $D(x_i)$, for $i = 1,\ldots,l$, respectively. Let $(\Omega_i)_{i=1,l}$ be a sequence of disjointed small ball in Ω such that $x_i \in \Omega_i$, $\forall i = 1,\ldots,l$. Let $(I_j)_{j=1,N}$ be also a sequence of disjoint intervals in $(0,T)$ such that $t_j \in I_j$, $\forall j = 1,\ldots,N$. We introduce the following average operators over the domains Ω_i and $\mathcal{Q}_{ij} = \Omega_i \times I_j$ (for $i = 1,\ldots,l$, $j = 1,\ldots,N$) by

$$< v >_{ij} = \frac{1}{meas(\mathcal{Q}_{ij})} \int_{\mathcal{Q}_{ij}} v(x,t)dxdt \quad \text{and} \quad < v >_i = \frac{1}{meas(\Omega_i)} \int_{\Omega_i} v(x)dx,$$

respectively, and we propose the following cost function ($(X,Y) \in \mathcal{U}_{ad} \times \mathcal{V}_{ad}$)

$$\begin{aligned} \mathcal{J}(X,Y) = \frac{a}{2} \sum_{i=1,l} \sum_{j=1,N} |< M >_{ij} - \epsilon_{ij}|^2 + \frac{b}{2} \sum_{i=1,l} |< D >_i - \mathfrak{d}_i|^2 \\ + \frac{\alpha}{2} \| \mathcal{N}X \|^2_{L^2(\mathcal{Q}) \times L^2(\mathcal{Q})} - \frac{\beta}{2} \| \mathcal{M}Y \|^2_{L^2(\Omega) \times L^2(\mathcal{Q}) \times L^2(\Sigma)} . \end{aligned} \tag{42}$$

Let χ_D be the usual characteristic function of a domain D i.e. $\chi_D = 1$ on D, and 0 outside of D. Let $\mathcal{L}_T : L^2(\mathcal{Q}) \longrightarrow L^2(\mathcal{Q})$ and $\mathcal{L}_D : L^2(\Omega) \longrightarrow L^2(\Omega)$ be defined by ($\forall v \in L^2(\mathcal{Q})$ and $w \in L^2(\Omega)$)

$$\mathcal{L}_T(v) = \sum_{i=1,l} \sum_{j=1,N} \frac{1}{meas(\mathcal{Q}_{ij})} \chi_{\mathcal{Q}_{ij}} < v >_{ij}, \quad \mathcal{L}_D(w) = \sum_{i=1,l} \frac{1}{meas(\Omega_i)} \chi_{\Omega_i} < w >_i \tag{43}$$

and

$$\epsilon = \sum_{i=1,l}\sum_{j=1,N} \frac{1}{meas(\mathcal{Q}_{ij})}\chi_{\mathcal{Q}_{ij}}\epsilon_{ij},\ \ \mathfrak{d} = \sum_{i=1,l} \frac{1}{meas(\Omega_i)}\chi_{\Omega_i}\mathfrak{d}_i. \tag{44}$$

By using the same technique as in the proof of the results of the previous section, we can prove the existence theorem of the control problem and obtain necessary optimality conditions as follows.

For α and β sufficiently large there exists an optimal solution $(X^*,Y^*) \in \mathcal{U}_{ad} \times \mathcal{V}_{ad}$ and $u^* \in \mathcal{Z}$ such that (X^*,Y^*) is a saddle point of $\mathcal{J}$ and $u^* = \mathcal{F}(X^*,Y^*)$ is the solution of (25). Moreover, the optimal solution (X^*,Y^*) is characterized by (for all $(X,Y) \in \mathcal{U}_{ad} \times \mathcal{V}_{ad}$)

$$\begin{aligned}
\frac{\partial \mathcal{J}}{\partial X}(X^*,Y^*).(X-X^*) &= \iint_{\mathcal{Q}} (e(\varphi^*)V_a^*\tilde{u}^* + \alpha n_1 p^* + a\delta(\mathcal{L}_T(M^*)-\epsilon))(p-p^*)dxdt \\
&\quad + \iint_{\mathcal{Q}} (n_2\xi^* - \tilde{u}^*)(\xi-\xi^*)\,dxdt \geq 0 \\
\frac{\partial \mathcal{J}}{\partial Y}(X^*,Y^*).(Y-Y^*) &= \int_{\Omega} (\mathcal{E}(\varphi^*,U_1^*,\tilde{u}^*) - \beta m_1\varphi^*)(\varphi-\varphi^*)\,dx \\
&\quad - \iint_{\mathcal{Q}} (r(\varphi^*)\tilde{u}^* + \beta m_2\eta^*)(\eta-\eta^*)\,dxdt \\
&\quad - \iint_{\Sigma} (\tilde{u}^* + \beta m_3\pi^*)(\pi-\pi^*)\,d\Gamma dt \leq 0
\end{aligned}$$

where $U_1^* = u^* + U$, $P_1^* = p^* + P$, $V_a^* = u^* - w_a$, $G_1^* = \eta^* - g$, $\mathcal{E}$ is given in (39) and $\tilde{u}^* = \mathcal{F}^{\perp}(X^*,Y^*)$ is the solution of the following adjoint problem

$$\begin{aligned}
-c(\varphi^*)\frac{\partial \tilde{u}^*}{\partial t} - div(\kappa(\varphi^*,u^*)\nabla\tilde{u}^*) + K_v^*(d(\varphi^*)\tilde{u}^*) + e(\varphi^*)P_1\tilde{u}^* + \frac{\partial \kappa}{\partial u}(\varphi^*,u^*)\nabla U_1^*.\nabla\tilde{u}^* \\
+a\gamma(\mathcal{L}_T(M^*)-\epsilon) + b(\mathcal{L}_D(D^*)-\mathfrak{d})\tilde{\mathcal{H}}'(.,u^*) = 0 \quad in\ \ \mathcal{Q},
\end{aligned}$$

subjected to the boundary condition

$$-\kappa(\varphi^*,u^*)\nabla\tilde{u}^*.\mathbf{n} = q\tilde{u}^* + \lambda(x)L'(u^*)\tilde{u}^* + d(\varphi^*)\tilde{u}^*\vec{\vartheta}.\mathbf{n} \quad in\ \ \Sigma,$$

and the final condition

$$\tilde{u}(T) = 0\ \ in\ \ \Omega.$$

7.2 Union of finite number of different tissue types

Suppose now that the body is constituted by different tissue types which occupy finitely many disjointed subdomains Ω_i, $i = 1,...,N_D$, of Ω, such that $\overline{\Omega} = \bigcup_{i=1,N_D}\overline{\Omega}_i$. Moreover we assume that the perfusion acts continuously according to the temperature in each domain Ω_i and discontinuously at tissue boundaries. We propose the following cost function

$$\begin{aligned}
\mathcal{J}(X,Y) = \frac{a}{2} \parallel (\gamma u + \delta p) - \mathfrak{m}_{obs} \parallel^2_{L^2(\mathcal{Q})} + \frac{b}{2} \parallel \int_0^T \tilde{\mathcal{H}}(t,u(.,t))dt - D_{obs} \parallel^2_{L^2(\Omega)} \\
+\frac{\alpha}{2} \parallel \mathcal{N}X \parallel^2_{L^2(0,T,\mathcal{R})\times L^2(\mathcal{Q})} - \frac{\beta}{2} \parallel \mathcal{M}Y \parallel^2_{L^2(\Omega)\times L^2(\mathcal{Q})\times L^2(\Sigma)}
\end{aligned}$$

where $(X,Y) \in \tilde{\mathcal{U}}_{ad} \times \mathcal{V}_{ad}$, $\tilde{\mathcal{U}}_{ad} = (L^2(0,T,\mathcal{R}) \cap D_1) \times \mathcal{K}_1$ and $\mathcal{R}$ is the Hilbert space

$$\{v \in L^2(\Omega), |v \in H^1(\Omega_i),\ for\ i = 1,...,N_D\}$$

equipped with the following norm and its corresponding scalar product:

$$\| v \|_{\mathcal{R}} = (\sum_{i=1,N_D} (\alpha_1 \| v \|^2_{L^2(\Omega_i)} + \alpha_2 \| \nabla v \|^2_{L^2(\Omega_i)}))^{1/2},$$

$$< v,w >_{\mathcal{R}} = \sum_{i=1,N_D} (\alpha_1 \int_{\Omega_i} vw \, d\Omega_i + \alpha_2 \int_{\Omega_i} \nabla v.\nabla w \, d\Omega_i),$$

with the fixed constants $\alpha_i > 0$ for $i = 1,2$.
Let the linear operator $\Lambda : L^2(\Omega) \longrightarrow \mathcal{R}$ be defined by $(\forall v \in L^2(\Omega))$ $\pi = \Lambda(v)$ is the solution of

$$\begin{aligned} -\alpha_2 \Delta \pi_i + \alpha_1 \pi_i &= v|_{\Omega_i}, \ \ in \ \Omega_i \\ \frac{\partial \pi_i}{\partial n} &= 0 \ \ on \ \partial\Omega_i, \end{aligned} \tag{45}$$

where $\pi_i = \pi$, *a.e. in* Ω_i and $v|_{\Omega_i}$ denotes the restriction of v on the subdomain Ω_i, for $i = 1,...,N_D$.
By using the same technique as in the previous section, we can derived the existence of an optimal solution and its necessary optimality conditions as follows.

For α and β sufficiently large there exists an optimal solution $(X^*,Y^*) \in \tilde{\mathcal{U}}_{ad} \times \mathcal{V}_{ad}$ and $u^* \in \mathcal{Z}$ such that (X^*,Y^*) is a saddle point of $\mathcal{J}$ and $u^* = \mathcal{F}(X^*,Y^*)$ is the solution of (25). Moreover, the optimal solution (X^*,Y^*) is characterized by (for all $(X,Y) \in \tilde{\mathcal{U}}_{ad} \times \mathcal{V}_{ad}$)

$$\begin{aligned} \frac{\partial \mathcal{J}}{\partial X}(X^*,Y^*).(X-X^*) = \int_0^T &< \Lambda(e(\varphi^*)V_a^*\tilde{u}^* + \alpha n_1 p^* + a\delta(M^* - \mathfrak{m}_{obs})), p - p^* >_{\mathcal{R}} \, dt \\ &+ \int\int_{\mathcal{Q}} (n_2\xi^* - \tilde{u}^*)(\xi - \xi^*) \, dxdt \geq 0 \\ \frac{\partial \mathcal{J}}{\partial Y}(X^*,Y^*).(Y-Y^*) = \int_\Omega &(\mathcal{E}(\varphi^*,U_1^*,\tilde{u}^*) - \beta m_1 \varphi^*)(\varphi - \varphi^*) \, dx \\ &- \int\int_{\mathcal{Q}} (r(\varphi^*)\tilde{u}^* + \beta m_2 \eta^*)(\eta - \eta^*) \, dxdt \\ &- \int\int_{\Sigma} (\tilde{u}^* + \beta m_3 \pi^*)(\pi - \pi^*) \, d\Gamma dt \leq 0 \end{aligned}$$

where $U_1^* = u^* + U$, $P_1^* = p^* + P$, $V_a^* = u^* - w_a$, $G_1^* = \eta^* - g$, $M^* = \gamma u^* + \delta p^*$, $\mathcal{E}$ is given in (39) and $\tilde{u}^* = \mathcal{F}^{\perp}(X^*,Y^*)$ is the solution of the following adjoint problem

$$\begin{aligned} -c(\varphi^*)\frac{\partial \tilde{u}^*}{\partial t} - div(\kappa(\varphi^*,u^*)\nabla\tilde{u}^*) + K_v^*(d(\varphi^*)\tilde{u}^*) + e(\varphi^*)P_1\tilde{u}^* + \frac{\partial \kappa}{\partial u}(\varphi^*,u^*)\nabla U_1^*.\nabla\tilde{u}^* \\ + a\gamma(M^* - \mathfrak{m}_{obs}) + b(D^* - D_{obs})\tilde{\mathcal{H}}'(.,u^*) = 0 \quad in \ \ \mathcal{Q}, \end{aligned}$$

subjected to the boundary condition

$$-\kappa(\varphi^*,u^*)\nabla\tilde{u}^*.\mathbf{n} = q\tilde{u}^* + \lambda(x)L'(u^*)\tilde{u}^* + d(\varphi^*)\tilde{u}^*\vec{\vartheta}.\mathbf{n} \quad in \ \ \Sigma,$$

and the final condition

$$\tilde{u}(T) = 0 \ \ in \ \ \Omega,$$

where $D^* = \int_0^T \tilde{\mathcal{H}}(t,u^*(.,t))dt$.

Remark 10 *We can also combine the results of this paragraph with the results of the previous paragraph, by replacing the first term of the function $\mathcal{J}$ as in (42), (M,D) by $(\mathcal{L}_T(M),\mathcal{L}_D(D))$ and $(\mathfrak{m}_{obs},D_{obs})$ by $(\epsilon,\mathfrak{d})$ (see (43) and (44), respectively).*

8. Stochastic robust control

In this section, we present formally a sketch of an extension of our robust control approach to the stochastic process. Consider then a complete probability space $\mathcal{T}=(\mathcal{D},\mathfrak{F},\mathcal{P})$, with $\mathcal{D}$ the sample space of elementary events, $\mathfrak{F}$ the minimal $\sigma-algebra$ of $\mathcal{D}$ and $\mathcal{P}$ a probability measure. In this context, a real-valued space-time stochastic process $v(x,t)$ with a known probability distribution can be written as a function $v(x,t;\mathfrak{f})$, where $\mathfrak{f}$ denotes the dependence on elementary events i.e. the process v can be interpreted as a function that maps each point $(x,t,\mathfrak{f})\in(\mathcal{Q},\mathcal{D})$ to a corresponding point $v(x,t;\mathfrak{f})$ according to the probability measure. For more details on the representation of random variables and stochastic processes see e.g. (Loeve, 1977; Prato & Zabczyk, 1992).
Assume that the stabilization and regulation process are with random temperature distribution, data, controls, disturbances and measurement. Then the perturbation problem with random corresponding to (25) can be written as

$$\begin{aligned} c(\varphi;\mathfrak{f})\frac{\partial u}{\partial t}-div(\kappa(\varphi,u;\mathfrak{f})\nabla u)+e(\varphi;\mathfrak{f})(p(x,t;\mathfrak{f})+P(x,t;\mathfrak{f}))(u-w_a(x,t;\mathfrak{f})\\ +d(\varphi;\mathfrak{f})K_v(u)=div((\kappa(\varphi,u;\mathfrak{f})-\kappa(0,0;\mathfrak{f}))\nabla U)+r(\varphi;\mathfrak{f})\eta(x,t;\mathfrak{f})+\xi(x,t;\mathfrak{f})\\ -(c(\varphi;\mathfrak{f})-c(0;\mathfrak{f}))\frac{\partial U}{\partial t}+e(0;\mathfrak{f})Pv_a(x,t;\mathfrak{f})\\ -(d(\varphi;\mathfrak{f})-d(0;\mathfrak{f}))K_v(U)\\ +(r(\varphi;\mathfrak{f})-r(0;\mathfrak{f}))g(x,t;\mathfrak{f})\ \ in\ \ \mathcal{Q}\times\mathcal{D}, \end{aligned}$$

subjected to the boundary condition (46)

$$\begin{aligned} (\kappa(\varphi,u;\mathfrak{f})\nabla u).\mathbf{n}=-((\kappa(\varphi,u;\mathfrak{f})-\kappa(0,0;\mathfrak{f}))\nabla U).\mathbf{n}-q(u-u_b(x,t;\mathfrak{f}))\\ -\lambda(x)(L(u)-L^b(u_b(x,t;\mathfrak{f})))+\pi(x,t;\mathfrak{f})\ \ in\ \ \Sigma\times\mathcal{D}, \end{aligned}$$

and the initial condition

$$u(x,0;\mathfrak{f})=u_0(x;\mathfrak{f})\ \ in\ \ \Omega\times\mathcal{D}.$$

We propose the following cost function

$$\begin{aligned} \mathcal{J}(X,Y)=\frac{a}{2}\int_{\mathcal{D}}\parallel(\gamma u(.\,;\mathfrak{f})+\delta p(.\,;\mathfrak{f}))-\mathfrak{m}_{obs}(.\,;\mathfrak{f})\parallel^2_{L^2(\mathcal{Q})}d\mathcal{P}\\ +\frac{b}{2}\int_{\mathcal{D}}\parallel\int_0^T\tilde{\mathcal{H}}(t,u(.,t);\mathfrak{f})dt-D_{obs}(.\,;\mathfrak{f})\parallel^2_{L^2(\Omega)}d\mathcal{P}\\ +\frac{\alpha}{2}\int_{\mathcal{D}}\parallel\mathcal{N}X(.\,;\mathfrak{f})\parallel^2_{L^2(0,T,\mathcal{R})\times L^2(\mathcal{Q})}d\mathcal{P}-\frac{\beta}{2}\int_{\mathcal{D}}\parallel\mathcal{M}Y(.\,;\mathfrak{f})\parallel^2_{L^2(\Omega)\times L^2(\mathcal{Q})\times L^2(\Sigma)}d\mathcal{P}, \end{aligned}$$

where $(X,Y)\in\tilde{\mathcal{U}}_{ad}\times\tilde{\mathcal{V}}_{ad}$, with $\tilde{\mathcal{U}}_{ad}=L^2(\mathcal{D};\mathcal{U}_{ad})$ and $\tilde{\mathcal{V}}_{ad}=L^2(\mathcal{D};\mathcal{V}_{ad})$, and $\int_{\mathcal{D}}.\,d\mathcal{P}$ is an integral with respect to the probability space $\mathcal{T}$.

If we assume that, for α and β sufficiently large, there exists an optimal solution $(X^*,Y^*) \in \tilde{\mathcal{U}}_{ad} \times \tilde{\mathcal{V}}_{ad}$ and $u^* \in L^2(\mathcal{D};\mathcal{Z})$ such that (X^*,Y^*) is a saddle point of $\mathcal{J}$ and $u^* = \mathcal{F}(X^*,Y^*)$ is the solution of (46), we can obtain, in the same way as to derive the necessary optimality conditions (41), the following result.

The optimal solution (X^*,Y^*) is characterized by (for all $(X,Y) \in \tilde{\mathcal{U}}_{ad} \times \tilde{\mathcal{V}}_{ad}$)

$$\frac{\partial \mathcal{J}}{\partial X}(X^*,Y^*).(X-X^*) = \int_{\mathcal{D}} \Big(\int\int_{\mathcal{Q}} (e(\varphi^*;\mathfrak{f}) V_a^* \tilde{u}^* + \alpha n_1 p^* + a\delta(M^* - \mathfrak{m}_{obs}))(p-p^*)\, dxdt \Big) d\mathcal{P} + \int_{\mathcal{D}} \Big(\int\int_{\mathcal{Q}} (n_2 \xi^* - \tilde{u}^*)(\xi - \xi^*)\, dxdt \Big) d\mathcal{P} \geq 0$$

$$\frac{\partial \mathcal{J}}{\partial Y}(X^*,Y^*).(Y-Y^*) = \int_{\mathcal{D}} \int_{\Omega} (\mathcal{E}_P(\varphi^*, U_1^*, \tilde{u}^*) - \beta m_1 \varphi^*)(\varphi - \varphi^*)\, dx d\mathcal{P} - \int_{\mathcal{D}} \Big(\int\int_{\mathcal{Q}} (r(\varphi^*;\mathfrak{f})\tilde{u}^* + \beta m_2 \eta^*)(\eta - \eta^*)\, dxdt \Big) d\mathcal{P} - \int_{\mathcal{D}} \Big(\int\int_{\Sigma} (\tilde{u}^* + \beta m_3 \pi^*)(\pi - \pi^*)\, d\Gamma dt \Big) d\mathcal{P} \leq 0$$

where $U_1^*(x,t;\mathfrak{f}) = u^* + U$, $P_1^*(x,t;\mathfrak{f}) = p^* + P$, $V_a^*(x,t;\mathfrak{f}) = u^* - w_a$, $G_1^*(x,t;\mathfrak{f}) = \eta^* - g$, $M^*(x,t;\mathfrak{f}) = \gamma u^* + \delta p^*$ and

$$\mathcal{E}_P(\varphi^*, U_1^*, \tilde{u}^*) = \int_0^T (e'(\varphi^*;\mathfrak{f}) P_1^* V_a^* + c'(\varphi^*;\mathfrak{f}) \frac{\partial U_1^*}{\partial t} + d'(\varphi^*;\mathfrak{f}) K_v(U_1^*) - r'(\varphi^*;\mathfrak{f}) G_1^*) \tilde{u}^* dt + \int_0^T \frac{\partial \kappa}{\partial \varphi}(\varphi^*, u^*;\mathfrak{f}) \nabla U_1^* . \nabla \tilde{u}^* dt,$$

with $\tilde{u}^*(x,t;\mathfrak{f}) = \mathcal{F}^{\perp}(X^*,Y^*)$ the solution of the following adjoint problem

$$\begin{aligned} -c(\varphi^*;\mathfrak{f}) \frac{\partial \tilde{u}^*}{\partial t} &- div(\kappa(\varphi^*, u^*;\mathfrak{f}) \nabla \tilde{u}^*) + K_v^*(d(\varphi^*;\mathfrak{f}) \tilde{u}^*) \\ &+ e(\varphi^*;\mathfrak{f}) P_1^* \tilde{u}^* + \frac{\partial \kappa}{\partial u}(\varphi^*, u^*;\mathfrak{f}) \nabla U_1^* . \nabla \tilde{u}^* \\ &+ a\gamma(M^* - \mathfrak{m}_{obs}(.;\mathfrak{f})) + b(D^* - D_{obs}(.;\mathfrak{f})) \tilde{\mathcal{H}}'(., u^*;\mathfrak{f}) = 0 \quad in \;\; \mathcal{Q} \times \mathcal{D}, \end{aligned}$$

subjected to the boundary condition

$$-\kappa(\varphi^*, u^*;\mathfrak{f}) \nabla \tilde{u}^* . \mathbf{n} = q \tilde{u}^* + \lambda(x) L'(u^*;\mathfrak{f}) \tilde{u}^* + d(\varphi^*;\mathfrak{f}) \tilde{u}^* \vec{\vartheta} . \mathbf{n} \quad in \;\; \Sigma \times \mathcal{D},$$

and the final condition

$$\tilde{u}(x,T;\mathfrak{f}) = 0 \;\; in \;\; \Omega \times \mathcal{D},$$

where $D^*(x;\mathfrak{f}) = \int_0^T \tilde{\mathcal{H}}(t, u^*(x,t;\mathfrak{f});\mathfrak{f}) dt.$

9. Radiation transport and coagulation process

In this section, we present formally the stabilization and regulation of the thermotherapy (by e.g. minimally invasive microwave or laser-induced thermal therapies) and radiation transport. During the treatment, the power energy provided by, for example, the laser or microwave, heats up the tumor to produce a coagulated region including the target cancer cells. As progression of tissue coagulation, physical properties of the tissue change, so, it is necessary to control the variation of the coagulated region.

9.1 Formulation and perturbation problem

We denote by Θ (which measures the fraction of native tissue) the concentration of living cells C which satisfy the relation (10) and we assume that the initial distribution of native tissue is given by $\Theta(x,t=0)=\Theta_0(x)$. So, the state Θ satisfies the following Cauchy equation (for a.e. $x\in\Omega$)

$$\begin{array}{l}\dfrac{\partial\Theta}{\partial t}(x,t)=\mathcal{H}(t,U(x,t))\Theta(x,t)\ \ in\ \ (0,T)\\ \Theta(x,t=0)=\Theta_0(x),\end{array} \tag{47}$$

where U is the temperature distribution.
We assume also that the sum of absorbed laser radiation, f, is given by

$$f(x,t)=\aleph(\theta(x,t),x)\Phi(x,t). \tag{48}$$

Here Φ ($W.m^{-2}$) is the irradiance and $\aleph=\aleph_a-\mathcal{B}$ where $\aleph_a$ is the absorption coefficient and $\mathcal{B}$ is the Planck emission function for the material. Then, according to (48), the problem (4) becomes

$$\begin{array}{l}c(\phi,x)\dfrac{\partial U}{\partial t}=div(\kappa(\phi,U,x)\nabla U)-e(\phi,x)P(x,t)(U-U_a)\\ \qquad\qquad -d(\phi,x)K_v(U)+r(\phi,x)g(x,t)+\aleph(\theta(x,t),x)\Phi(x,t)\ \ \ in\ \ \mathcal{Q},\end{array}$$

subjected to the boundary condition

$$\begin{array}{l}(\kappa(\phi,U,x)\nabla U).\mathbf{n}=-q(x,t)(U-U_b)\\ \qquad\qquad -\lambda(x)(L(U)-L(U_b))+h(x,t)\ \ \ in\ \ \Sigma,\end{array} \tag{49}$$

and the initial condition

$$U(x,0)=U_0(x)\ \ in\ \ \Omega.$$

The irradiance Φ, which corresponds to the radiation transport through the tissue, can be described by the following stationary diffusion equation (Niemz, 2002) (which is an approximation of more general radiation transport equation (Ishimaru, 1978; Pomraning, 1973))

$$-div(\mathfrak{X}(\Theta,x)\nabla\Phi)+\aleph(\Theta,x)\Phi=0\ \ in\ \ \Omega,$$

under the boundary conditions

$$\begin{array}{l}-\mathfrak{X}(\Theta,x)\nabla\Phi.\mathbf{n}+\mathfrak{s}\Phi=\mathfrak{J}\quad in\ \ \Gamma_r,\\ -\mathfrak{X}(\Theta,x)\nabla\Phi.\mathbf{n}+\mathfrak{s}\Phi=0\quad in\ \ \Gamma_{nr},\end{array} \tag{50}$$

where $\mathfrak{s}$ is a fixed constant, $\mathfrak{J}$ is the power of the applied laser source and $\Gamma=\Gamma_r\cup\Gamma_{nr}$ such that $\Gamma_r\cap\Gamma_{nr}=\emptyset$. Boundary Γ_r denotes the boundary through which radiation is emmitted and Γ_{nr} denotes the other boundary of the domain.
In the sequel, we assume that $\mathfrak{X}$ and $\aleph$ satisfy similar hypotheses as (**H1**)-(**H3**) and, for simplicity, we denote the values $\aleph(\Theta,.)$, $\mathfrak{X}(\Theta,.)$ and $\mathcal{H}(.,U)$ by $\aleph(\Theta)$, $\mathfrak{X}(\Theta)$ and $\mathcal{H}(U)$, respectively. In this context, we can formulate the perturbation problem as follows. We assume that (U,Φ,Θ) satisfies the problem (49),(47), (50) with data $(U_0,P,\phi,g,h,U_a,U_b,\Theta_0,\mathfrak{J})$ and $(U+u,\Phi+\Psi,\Theta+\theta)$ satisfies problem (49),(47), (50) with

data $(U_0+u_0, P+p, \phi+\varphi, g+\eta, h+\pi, U_a+u_a, U_b+u_b, \Theta_0+\theta_0, \mathfrak{J}+\xi)$. Hence we consider the following systems (for a given (U,Φ,Θ) sufficiently regular) as follows.

Perturbation of the transient bioheat transfer type problem

$$\begin{aligned} c(\phi+\varphi)\frac{\partial u}{\partial t} - div(\kappa(\phi+\varphi,U+u)\nabla u) - div((\kappa(\phi+\varphi,U+u)-\kappa(\phi,U))\nabla U) \\ = -e(\phi+\varphi)(p+P)(u-u_a) - d(\phi+\varphi)K_v(u) + r(\phi+\varphi)\eta + \aleph(\Theta+\theta)\Psi \\ -(c(\phi+\varphi)-c(\phi))\frac{\partial U}{\partial t} - (e(\varphi+\phi)(p+P)-e(\phi)P)(U-U_a) \\ -(d(\varphi+\phi)-d(\phi))K_v(U) + (r(\varphi+\phi)-r(\phi))g \\ +(\aleph(\Theta+\theta)-\aleph(\Theta))\Phi \quad in \ \ \mathcal{Q}, \end{aligned}$$

subjected to the boundary condition (51)

$$\begin{aligned} \kappa(\phi+\varphi,U+u)\nabla u.\mathbf{n} + (\kappa(\phi+\varphi,U+u)-\kappa(\phi,U))\nabla U.\mathbf{n} = -q(u-u_b) \\ -\lambda(x)((L(U+u)-L(U))-(L(U_b+u_b)-L(U_b))) + \pi \quad in \ \ \Sigma, \end{aligned}$$

and the initial condition

$$u(0) = u_0 \ \ in \ \ \Omega.$$

Perturbation of the coagulated region type model

$$\begin{aligned} &\frac{\partial \theta}{\partial t} = \mathcal{H}(U+u)\theta + (\mathcal{H}(U+u)-\mathcal{H}(U))\Theta \ \ in \ \ (0,T), \\ &\theta(.,t=0) = \theta_0. \end{aligned} \tag{52}$$

Perturbation of the radiation transport type problem

$$\begin{aligned} -div(\mathfrak{X}(\Theta+\theta)\nabla\Psi) - div((\mathfrak{X}(\Theta+\theta)-\mathfrak{X}(\Theta))\nabla\Phi) + \aleph(\Theta+\theta)\Psi \\ = -(\aleph(\Theta+\theta)-\aleph(\Theta))\Phi \ \ in \ \ \Omega, \end{aligned}$$

under the boundary condition (53)

$$\begin{aligned} -\mathfrak{X}(\Theta+\theta)\nabla\Psi.\mathbf{n} - (\mathfrak{X}(\Theta+\theta)-\mathfrak{X}(\Theta))\nabla\Phi.\mathbf{n} + \mathfrak{s}\Psi = \xi \quad in \ \ \Gamma_r, \\ -\mathfrak{X}(\Theta+\theta)\nabla\Psi.\mathbf{n} - (\mathfrak{X}(\Theta+\theta)-\mathfrak{X}(\Theta))\nabla\Phi.\mathbf{n} + \mathfrak{s}\Psi = 0 \quad in \ \ \Gamma_{nr}. \end{aligned}$$

If we set : $\tilde{L}(u) = L(U+u) - L(U)$, $\tilde{L}^b(u_b) = L(U_b+u_b) - L(U_b)$, $\tilde{\mathcal{H}}(u) = \mathcal{H}(U+u)$, $\tilde{\mathfrak{X}}(\theta) = \mathfrak{X}(\Theta+\theta)$, $\tilde{\aleph}(\theta) = \aleph(\Theta+\theta)$, $\tilde{\kappa}(\varphi,u) = \kappa(\phi+\varphi,U+u)$, and $\tilde{\beta}(\varphi) = \beta(\phi+\varphi)$, where the function β plays the role of c, d, e or r, then System (51),(52), (53) reduces to

$$\begin{aligned} \tilde{c}(\varphi)\frac{\partial u}{\partial t} - div(\tilde{\kappa}(\varphi,u)\nabla u) + \tilde{e}(\varphi)(p+P)(u-w_a) + \tilde{d}(\varphi)K_v(u) \\ = div((\tilde{\kappa}(\varphi,u)-\tilde{\kappa}(0,0))\nabla U) + \tilde{r}(\varphi)\eta + \tilde{\aleph}(\theta)\Psi \\ -(\tilde{c}(\varphi)-\tilde{c}(0))\frac{\partial U}{\partial t} + \tilde{e}(0)Pv_a - (\tilde{d}(\varphi)-\tilde{d}(0))K_v(U) \\ +(\tilde{r}(\varphi)-\tilde{r}(0))g + (\tilde{\aleph}(\theta)-\tilde{\aleph}(0))\Phi \quad in \ \ \mathcal{Q}, \end{aligned} \tag{54}$$

subjected to the boundary condition

$$\tilde{\kappa}(\varphi,u)\nabla u.\mathbf{n} + (\tilde{\kappa}(\varphi,u) - \tilde{\kappa}(0,0))\nabla U.\mathbf{n} \\ = -q(u-u_b) - \lambda(x)(\tilde{L}(u) - \tilde{L}^b(u_b)) + \pi \quad in\ \Sigma,$$

and the initial condition

$$u(0) = u_0 \ in\ \Omega,$$

$$\frac{\partial\theta}{\partial t} = \tilde{\mathcal{H}}(u)\theta + (\tilde{\mathcal{H}}(u) - \tilde{\mathcal{H}}(0))\Theta \ in\ (0,T), \\ \theta(.,t=0) = \theta_0 \tag{55}$$

and

$$-div(\tilde{\mathfrak{X}}(\theta)\nabla\Psi) - div((\tilde{\mathfrak{X}}(\theta) - \tilde{\mathfrak{X}}(0))\nabla\Phi) + \tilde{\aleph}(\theta)\Psi \\ = -(\tilde{\aleph}(\theta) - \tilde{\aleph}(0))\Phi \ in\ \Omega,$$

under the boundary conditions

$$-\tilde{\mathfrak{X}}(\theta)\nabla\Psi.\mathbf{n} - (\tilde{\mathfrak{X}}(\theta) - \tilde{\mathfrak{X}}(0))\nabla\Phi.\mathbf{n} + \mathfrak{s}\Psi = \xi \quad in\ \Gamma_r, \\ -\tilde{\mathfrak{X}}(\theta)\nabla\Psi.\mathbf{n} - (\tilde{\mathfrak{X}}(\theta) - \tilde{\mathfrak{X}}(0))\nabla\Phi.\mathbf{n} + \mathfrak{s}\Psi = 0 \quad in\ \Gamma_{nr}, \tag{56}$$

where $v_a = U - U_a$ and $w_a = u_a - v_a$.
For simplicity of future reference, we omit the " ˜ " on $\tilde{\mathfrak{X}}$,$\tilde{\aleph}$, $\tilde{L}$, $\tilde{L}^b$, $\tilde{c}$,$\tilde{d}$,$\tilde{e}$,$\tilde{r}$ and $\tilde{\kappa}$ for the system (54),(55), (56).

9.2 Robust control problem

Similarly as in the section 6, the problem is to find the best admissible perfusion function p and power of the applied laser source ξ in the presence of the worst disturbance in the porosity function φ, in the evaporation term π and in the metabolic heat generation type term η. We then suppose that the control is in $X = (p,\xi)$ and the disturbance is in $Y = (\varphi,\eta,\pi)$. Therefore, the function (u,θ,Ψ) is assumed to be related to the disturbance Y and control X through the problem (54),(55), (56) under the pointwise constraints (26).
Let $\mathcal{K}_1$ be convex, closed, non-empty and bounded subset of $L^2(\Sigma_r)$, $\mathcal{K}_2$ be convex, closed, non-empty and bounded subset of $L^2(\mathcal{Q})$ and $\mathcal{K}_3$ be convex, closed, non-empty and bounded subset of $L^2(\Sigma)$. The studied control problem is to find a saddle point of the cost function $\mathcal{J}$ which measures the distance between the known observation $\mathfrak{m}_{obs}$, corresponding to the online temperature control via radiometric temperature measurement system and the prognostic variables $\gamma u + \delta p$. Then we propose the following cost

$$\mathcal{J}(X,Y) = \frac{a}{2} \parallel (\gamma u + \delta p) - \mathfrak{m}_{obs} \parallel^2_{L^2(\mathcal{Q})} + \frac{\alpha}{2} \parallel \mathcal{N}X \parallel^2_{L^2(\mathcal{Q})\times L^2(\Sigma_r)} \\ - \frac{\beta}{2} \parallel \mathcal{M}Y \parallel^2_{L^2(\Omega)\times L^2(\mathcal{Q})\times L^2(\Sigma)} \tag{57}$$

where $a > 0$, $\alpha > 0$, $\beta > 0$, the matrix $\mathcal{N} = diag(\sqrt{n_1},\sqrt{n_2})$ and $\mathcal{M} = diag(\sqrt{m_1},\sqrt{m_2},\sqrt{m_3})$, are predefined nonnegative weights such that $n_1 + n_2 \neq 0$ and $m_1 + m_2 + m_3 \neq 0$, $\mathcal{U}_{ad} =$

$D_1 \times \mathcal{K}_1$, $\mathcal{V}_{ad} = D_2 \times \mathcal{K}_2 \times \mathcal{K}_3$ and $\mathfrak{m}_{obs}$ is the target. The parameters γ, δ are positive with space-time dependent entries and are in $L^\infty(\overline{\mathcal{Q}})$. Let us introduce the operator solution $\mathcal{F}$ which maps the source term $(X,Y) \in \mathcal{U}_{ad} \times \mathcal{V}_{ad}$ of (54),(55), (56) into the corresponding solution $(u,\theta,\Psi) = \mathcal{F}(X,Y)$. We suppose that the operator solution $\mathcal{F}$ is continuously differentiable (in weak sense) on $\mathcal{U}_{ad} \times \mathcal{V}_{ad}$ and its derivative (at point $(X,Y) = (p,\xi,\varphi,\eta,\pi)$) $\mathcal{F}'(X,Y) : (H,K) = (\mathfrak{y},\mathfrak{h},\psi,\mathfrak{e},\mathfrak{z}) \in L^\infty(\mathcal{Q}) \times L^2(\Sigma_r) \times L^\infty(\Omega) \times L^2(\mathcal{Q}) \times L^2(\Sigma) \longrightarrow (w,\varpi,\Pi) = \mathcal{F}'(X,Y).(H,K) = \lim_{\epsilon \longrightarrow 0} \dfrac{\mathcal{F}(X+\epsilon H, Y+\epsilon K)}{\epsilon}$, where $(X+\epsilon H, Y+\epsilon K) \in \mathcal{U}_{ad} \times \mathcal{V}_{ad}$, is such that $(w,\varpi,\Pi) = \dfrac{\partial \mathcal{F}}{\partial X}(X,Y)H + \dfrac{\partial \mathcal{F}}{\partial Y}(X,Y)K$ is the unique weak solution of the following system

$$
\begin{aligned}
c(\varphi)\frac{\partial w}{\partial t} - div(\kappa(\varphi,u)\nabla w) - div((\frac{\partial \kappa}{\partial \varphi}(\varphi,u)\psi + \frac{\partial \kappa}{\partial u}(\varphi,u)w)\nabla U_1) + d(\varphi)K_v(w) \\
+e(\varphi)P_1 w + e'(\varphi)\psi P_1 V_a + e(\varphi)\mathfrak{y}V_a + d'(\varphi)\psi K_v(U_1) \\
= -c'(\varphi)\frac{\partial U_1}{\partial t}\psi + r'(\varphi)\psi G_1 + r(\varphi)\mathfrak{e} + \aleph'(\theta)\varpi\Phi_1 + \aleph(\theta)\Pi \quad in \ \ \mathcal{Q},
\end{aligned}
$$

subjected to the boundary condition

$$
\begin{aligned}
(\kappa(\varphi,u)\nabla w).\mathbf{n} = -((\frac{\partial \kappa}{\partial \varphi}(\varphi,u)\psi + \frac{\partial \kappa}{\partial u}(\varphi,u)w)\nabla U_1).\mathbf{n} \\
-qw - \lambda(x)L'(u)w + \mathfrak{z} \quad in \ \ \Sigma,
\end{aligned}
\tag{58}
$$

and the initial condition

$$
w(0) = 0 \ \ in \ \ \Omega,
$$

$$
\begin{aligned}
\frac{\partial \varpi}{\partial t} = \mathcal{H}'(u)w\Theta_1 + \mathcal{H}(u)\varpi \ \ in \ \ (0,T), \\
\varpi(0) = 0
\end{aligned}
\tag{59}
$$

and

$$
-div(\mathfrak{X}(\theta)\nabla\Pi) - div(\mathfrak{X}'(\theta)\varpi\nabla\Phi_1) + \aleph'(\theta)\varpi\Phi_1 + \aleph(\theta)\Pi = 0 \ \ in \ \ \Omega,
$$

under the boundary condition

$$
\begin{aligned}
-\mathfrak{X}(\theta)\nabla\Pi.\mathbf{n} - \mathfrak{X}'(\theta)\varpi\nabla\Phi_1.\mathbf{n} + \mathfrak{s}\Pi = \mathfrak{h} \quad in \ \ \Gamma_r, \\
-\mathfrak{X}(\theta)\nabla\Pi.\mathbf{n} - \mathfrak{X}'(\theta)\varpi\nabla\Phi_1.\mathbf{n} + \mathfrak{s}\Pi = 0 \quad in \ \ \Gamma_{nr},
\end{aligned}
\tag{60}
$$

where $(u,\theta,\Psi) = \mathcal{F}(X,Y)$, $U_1 = u + U$, $\Theta_1 = \Theta + \theta$, $\Phi_1 = \Psi + \Phi$, $P_1 = p + P$, $V_a = u - w_a$ and $G_1 = \eta - g$. Moreover the derivative of $\mathcal{J}$ is given by

$$
\begin{aligned}
\mathcal{J}'(X,Y).(H,K) = \frac{d}{d\lambda}\mathcal{J}(X+\lambda H, Y+\lambda K)|_{\lambda=0} \\
= a\int\int_{\mathcal{Q}}((\gamma u + \delta p) - \mathfrak{m}_{obs})(\gamma w + \delta \mathfrak{y})\, dxdt \\
+\alpha(n_1\int\int_{\mathcal{Q}} p\mathfrak{y}\, dxdt + n_2\int\int_{\Sigma_r}\xi\mathfrak{h}\, d\Gamma dt) \\
-\beta(m_1\int_\Omega \varphi\psi\, dx + m_2\int\int_{\mathcal{Q}}\eta\mathfrak{e}\, dxdt + m_3\int\int_\Sigma \pi\mathfrak{z}\, d\Gamma dt),
\end{aligned}
\tag{61}
$$

where $(w,\varpi,\Pi) = \mathcal{F}'(X,Y).(H,K)$.

We assume that, for α and β sufficiently large, there exists an optimal solution $(X^*,Y^*)\in\mathcal{U}_{ad}\times\mathcal{V}_{ad}$ and (u^*,θ^*,Ψ^*) such that (X^*,Y^*) is a saddle point of $\mathcal{J}$ and $(u^*,\theta^*,\Psi^*)=\mathcal{F}(X^*,Y^*)$ is the solution of (54),(55), (56). In order to derive the necessary optimality conditions for the optimal solution (X^*,Y^*), we start by calculating the gradient of the cost $\mathcal{J}$. For this, consider a sufficiently regular function $(\tilde{u},\tilde{\theta},\tilde{\Phi})$ such that $(\tilde{u},\tilde{\theta})(T)=(0,0)$. Multiplying the system (58),(59) and (60) by $(\tilde{u},\tilde{\theta},\tilde{\Phi})$, respectively and integrating with respect to space and time, and using Green's formula, we obtain according to the boundary and initial conditions, and the relation (34) that (similarly as to obtain the relation (35))

$$\begin{aligned}
&\int\!\!\int_{\mathcal{Q}}\left(-c(\varphi)\frac{\partial\tilde{u}}{\partial t}-div(\kappa(\varphi,u)\nabla\tilde{u})+K_v^*(d(\varphi)\tilde{u})+e(\varphi)P_1\tilde{u}+\frac{\partial\kappa}{\partial u}(\varphi,u)\nabla U_1.\nabla\tilde{u}\right)w\,dxdt\\
&\quad+\int\!\!\int_{\Sigma}(q\tilde{u}+\lambda(x)L'(u)\tilde{u}+\kappa(\varphi,u)\nabla\tilde{u}.\mathbf{n}+d(\varphi)\tilde{u}\vec{\vartheta}.\mathbf{n})w\,d\Gamma dt\\
&\quad=-\int_{\Omega}\left(\int_0^T(e'(\varphi)P_1V_a+c'(\varphi)\frac{\partial U_1}{\partial t}+d'(\varphi)K_v(U_1)-r'(\varphi)G_1)\tilde{u}dt\right)\psi\,dx\\
&\quad-\int_{\Omega}\left(\int_0^T\frac{\partial\kappa}{\partial\varphi}(\varphi,u)\nabla U_1.\nabla\tilde{u}dt\right)\psi\,dx\\
&\quad-\int\!\!\int_{\mathcal{Q}}e(\varphi)V_a\tilde{u}\mathfrak{y}\,dxdt+\int\!\!\int_{\mathcal{Q}}r(\varphi)\tilde{u}\mathfrak{e}\,dxdt+\int\!\!\int_{\Sigma}\mathfrak{z}\tilde{u}\,d\Gamma dt\\
&\quad+\int\!\!\int_{\mathcal{Q}}(\tilde{u}\aleph'(\theta)\Phi_1)\varpi\,dxdt+\int\!\!\int_{\mathcal{Q}}(\tilde{u}\aleph(\theta))\Pi\,dxdt,
\end{aligned}\tag{62}$$

$$\int_0^T(-\frac{\partial\tilde{\theta}}{\partial t}-\mathcal{H}(u)\tilde{\theta})\varpi\,dt=\int_0^T(\mathcal{H}'(u)\tilde{\theta}\Theta_1)w\,dt\tag{63}$$

and

$$\begin{aligned}
\int_{\Omega}(-div(\mathfrak{X}(\theta)\nabla\tilde{\Phi})+\aleph(\theta)\tilde{\Phi})\Pi\,dx+\int_{\Gamma}(\mathfrak{X}(\theta)\nabla\tilde{\Phi}.\mathbf{n}-\mathfrak{s}\tilde{\Phi})\Pi\,d\Gamma\\
+\int_{\Gamma_r}\mathfrak{h}\tilde{\Phi}\,d\Gamma+\int_{\Omega}(\mathfrak{X}'(\theta)\nabla\Phi_1\nabla\tilde{\Phi}+\aleph'(\theta)\tilde{\Phi}\Phi_1)\varpi\,dx=0.
\end{aligned}\tag{64}$$

To simplify the relations (62), (63) and (64), we assume that $(\tilde{u},\tilde{\Phi},\tilde{\theta})$ satisfies the following adjoint system

$$\begin{aligned}
&-c(\varphi)\frac{\partial\tilde{u}}{\partial t}-div(\kappa(\varphi,u)\nabla\tilde{u})+K_v^*(d(\varphi)\tilde{u})+e(\varphi)P_1\tilde{u}+\frac{\partial\kappa}{\partial u}(\varphi,u)\nabla U_1.\nabla\tilde{u}\\
&\qquad+a\gamma(\gamma u+\delta p-\mathfrak{m}_{obs})+\mathcal{H}'(u)\tilde{\theta}\Theta_1=0\quad in\ \ \mathcal{Q},
\end{aligned}$$

subjected to the boundary condition

$$-\kappa(\varphi,u)\nabla\tilde{u}.\mathbf{n}=q\tilde{u}+\lambda(x)L'(u)\tilde{u}+d(\varphi)\tilde{u}\vec{\vartheta}.\mathbf{n}\quad in\ \ \Sigma,\tag{65}$$

and the final condition

$$\tilde{u}(T)=0\ \ in\ \ \Omega,$$

$$\begin{aligned}
&-\frac{\partial\tilde{\theta}}{\partial t}=\mathcal{H}(u)\tilde{\theta}+\tilde{u}\aleph'(\theta)\Phi_1+\mathfrak{X}'(\theta)\nabla\Phi_1\nabla\tilde{\Phi}+\aleph'(\theta)\tilde{\Phi}\Phi_1\ \ in\ \ (0,T)\\
&\tilde{\theta}(T)=0
\end{aligned}\tag{66}$$

and

$$-div(\mathfrak{X}(\theta)\nabla\tilde{\Phi}) + \aleph(\theta)\tilde{\Phi} + \tilde{u}\aleph(\theta) = 0 \ \ in \ \ \Omega,$$

under the boundary condition (67)

$$-\mathfrak{X}(\theta)\nabla\tilde{\Phi}.\mathbf{n} + \mathfrak{s}\tilde{\Phi} = 0 \quad in \ \ \Gamma.$$

Using the system (36), the problem (35) becomes

$$\begin{aligned}
&\iint_{\mathcal{Q}} -\left(a\gamma(\gamma u + \delta p - \mathfrak{m}_{obs}) + \mathcal{H}'(u)\tilde{\theta}\Theta_1\right) w \, dxdt \\
&\quad = -\int_\Omega \left(\int_0^T (e'(\varphi)P_1V_a + c'(\varphi)\frac{\partial U_1}{\partial t} + d'(\varphi)K_v(U_1) - r'(\varphi)G_1)\tilde{u}dt \right) \psi \, dx \\
&\qquad -\int_\Omega \left(\int_0^T \frac{\partial \kappa}{\partial \varphi}(\varphi, u)\nabla U_1.\nabla\tilde{u}dt \right) \psi \, dx \\
&\qquad -\iint_{\mathcal{Q}} e(\varphi)V_a\tilde{u}\mathfrak{y} \, dxdt + \iint_{\mathcal{Q}} r(\varphi)\tilde{u}\mathfrak{e} \, dxdt + \iint_\Sigma \mathfrak{z}\tilde{u} \, d\Gamma dt \\
&\qquad + \iint_{\mathcal{Q}} (\tilde{u}\aleph'(\theta)\Phi_1)\varpi \, dxdt + \iint_{\mathcal{Q}} (\tilde{u}\aleph(\theta))\Pi \, dxdt,
\end{aligned} \tag{68}$$

$$-\int_0^T (\mathcal{H}'(u)\tilde{\theta}\Theta_1)w \, dt + \int_0^T (\tilde{u}\aleph'(\theta)\Phi_1)\varpi \, dt = -\int_0^T (\mathfrak{X}'(\theta)\nabla\Phi_1\nabla\tilde{\Phi} + \aleph'(\theta)\tilde{\Phi}\Phi_1)\varpi \, dt,$$

$$\int_\Omega (\tilde{u}\aleph(\theta))\Pi \, dx = \int_{\Gamma_r} \mathfrak{h}\tilde{\Phi} \, d\Gamma + \int_\Omega (\mathfrak{X}'(\theta)\nabla\Phi_1\nabla\tilde{\Phi} + \aleph'(\theta)\tilde{\Phi}\Phi_1)\varpi \, dx.$$

Integrating by time the third part of (68) and by space the second part (68), and adding the first part, the second part and the third part of (68), we can deduce that

$$\begin{aligned}
&-\iint_{\mathcal{Q}} a\gamma(\gamma u + \delta p - \mathfrak{m}_{obs})w \, dxdt \\
&\quad = -\int_\Omega \left(\int_0^T (e'(\varphi)P_1V_a + c'(\varphi)\frac{\partial U_1}{\partial t} + d'(\varphi)K_v(U_1) - r'(\varphi)G_1)\tilde{u}dt \right) \psi \, dx \\
&\qquad -\int_\Omega \left(\int_0^T \frac{\partial \kappa}{\partial \varphi}(\varphi, u)\nabla U_1.\nabla\tilde{u}dt \right) \psi \, dx \\
&\qquad -\iint_{\mathcal{Q}} e(\varphi)V_a\tilde{u}\mathfrak{y} \, dxdt + \iint_{\mathcal{Q}} r(\varphi)\tilde{u}\mathfrak{e} \, dxdt + \iint_\Sigma \mathfrak{z}\tilde{u} \, d\Gamma dt + \int_{\Gamma_r} \mathfrak{h}\tilde{\Phi} \, d\Gamma.
\end{aligned} \tag{69}$$

According to the expression (61) of $\mathcal{J}'(X,Y)$ we can deduce that

$$\begin{aligned}
\mathcal{J}'(X,Y).(H,K) &= \frac{\partial \mathcal{J}}{\partial X}(X,Y).H + \frac{\partial \mathcal{J}}{\partial Y}(X,Y).K \\
&= \iint_{\mathcal{Q}} (e(\varphi)V_a\tilde{u} + \alpha n_1 p + a\delta(\gamma u + \delta p - \mathfrak{m}_{obs}))\mathfrak{y} \, dxdt + \int\int_{\Sigma_r} (n_2\xi - \tilde{\Phi})\mathfrak{h} \, dxdt \\
&\quad + \int_\Omega (\mathcal{E}(\varphi, U_1, \tilde{u}) - \beta m_1\varphi)\psi \, dx - \iint_{\mathcal{Q}} (r(\varphi)\tilde{u} + \beta m_2\eta)\mathfrak{e} \, dxdt \\
&\quad - \iint_\Sigma (\tilde{u} + \beta m_3\pi)\mathfrak{z} \, d\Gamma dt,
\end{aligned} \tag{70}$$

where

$$\begin{aligned}
\mathcal{E}(\varphi, U_1, \tilde{u}) = &\int_0^T (e'(\varphi)P_1V_a + c'(\varphi)\frac{\partial U_1}{\partial t} + d'(\varphi)K_v(U_1) - r'(\varphi)G_1)\tilde{u}dt \\
&+ \int_0^T \frac{\partial \kappa}{\partial \varphi}(\varphi, u)\nabla U_1.\nabla\tilde{u}dt.
\end{aligned} \tag{71}$$

Consequently the gradient of $\mathcal{J}$ at point (X,Y), in weak sense, is

$$\begin{aligned}\frac{\partial \mathcal{J}}{\partial X}(X,Y) &= \begin{pmatrix} e(\varphi)V_a\tilde{u} + \alpha n_1 p + a\delta(\gamma u + \delta p - \mathfrak{m}_{obs}) \\ n_2\xi - \tilde{\Phi} \end{pmatrix}, \\ \frac{\partial \mathcal{J}}{\partial Y}(X,Y) &= \begin{pmatrix} \mathcal{E}(\varphi, U_1, \tilde{u}) - \beta m_1 \varphi \\ -(r(\varphi)\tilde{u} + \beta m_2 \eta) \\ -(\tilde{u} + \beta m_3 \pi) \end{pmatrix}. \end{aligned} \tag{72}$$

We can now give the first-order optimality conditions for the robust control problem as follows.

The optimal solution (X^*,Y^*) is characterized by (for all $(X,Y) \in \mathcal{U}_{ad} \times \mathcal{V}_{ad}$)

$$\begin{aligned}\frac{\partial \mathcal{J}}{\partial X}(X^*,Y^*).(X-X^*) &= \int\!\!\int_{\mathcal{Q}} (e(\varphi^*)V_a^*\tilde{u}^* + \alpha n_1 p^* + a\delta(M^* - \mathfrak{m}_{obs}))(p-p^*)\,dxdt \\ &\quad + \int\!\!\int_{\Sigma_r} (n_2\xi^* - \tilde{\Phi}^*)(\xi - \xi^*)\,d\Gamma dt \geq 0 \\ \frac{\partial \mathcal{J}}{\partial Y}(X^*,Y^*).(Y-Y^*) &= \int_{\Omega} (\mathcal{E}(\varphi^*, U_1^*, \tilde{u}^*) - \beta m_1 \varphi^*)(\varphi - \varphi^*)\,dx \\ &\quad - \int\!\!\int_{\mathcal{Q}} (r(\varphi^*)\tilde{u}^* + \beta m_2 \eta^*)(\eta - \eta^*)\,dxdt \\ &\quad - \int\!\!\int_{\Sigma} (\tilde{u}^* + \beta m_3 \pi^*)(\pi - \pi^*)\,d\Gamma dt \leq 0\end{aligned}$$

where $(u^*,\theta^*,\Psi^*) = \mathcal{F}(X^*,Y^*)$, $U_1^* = u^* + U$, $\Theta_1^* = \Theta + \theta^*$, $\Phi_1^* = \Psi^* + \Phi$, $P_1^* = p^* + P$, $V_a^* = u^* - w_a$ and $G_1^* = \eta^* - g$, $M^*(x,t) = \gamma u^* + \delta p^*$ and $(\tilde{u}^*,\tilde{\theta}^*,\tilde{\Phi}^*) = \mathcal{F}^{\perp}(X^*,Y^*)$ is the solution of the adjoint problem (65),(66),(67).

Remark 11 *We can apply easily our stochastic robust control approach developed in the section 8 to the problem of coagulation process analyzed in the present section.*

To help the interested reader with the transition from theory to implementation, we also discuss some optimization strategies in order to solve the robust control problems, by using the adjoint model.

10. Minimax optimization algorithms and conclusion

We present algorithms where the descent direction is calculated by using the adjoint variables, particularly by choosing an admissible step size. The descent method is formulated in terms of the continuous variable such is independent of a specific discretization. The methods are valid for the continuous as well as random processes.

10.1 Gradient algorithm

The gradient algorithm for the resolution of treated saddle point problems is given by:
for k=1,..., (iteration index) we denote by (X_k,Y_k) the numerical approximation of the control-disturbance at the *kth* iteration of the algorithm.

(*Step*1) Initialization: (X_0,Y_0) (given initial guess).

(*Step*2) Resolution of the direct problem where the source term is (X_k,Y_k), gives $\mathcal{F}(X_k,Y_k)$.

(*Step*3) Resolution of the adjoint problem (based on $(X_k, Y_k, \mathcal{F}(X_k, Y_k))$, gives $\mathcal{F}^{\perp}(X_k, Y_k)$,

(*Step*4) Gradient of $\mathcal{J}$ at (X_k, Y_k):

$$(\mathbf{GJ}) \begin{cases} c_k \overset{def}{=} \dfrac{\partial \mathcal{J}}{\partial X}(X_k, Y_k), \\ \\ d_k \overset{def}{=} \dfrac{\partial \mathcal{J}}{\partial Y}(X_k, Y_k), \\ \\ G_k = (c_k, d_k). \end{cases}$$

(*Step*5) Determine X_{k+1}: $X_{k+1} = X_k - \gamma_k c_k$,

(*Step*6) Determine Y_{k+1}: $X_{k+1} = Y_k + \delta_k d_k$,
where $0 < m \leq \gamma_k, \delta \leq M$ are the sequences of step lengths.

(*Step*7) If the gradient is sufficiently small: end; else set $k := k + 1$ and goto (*Step*2).
Optimal Solution: $(X, Y) = (X_k, Y_k)$.

The convergence of the algorithm depends on the second Fréchet derivative of $\mathcal{J}$ (i.e. m, M depend on the second Fréchet derivative of $\mathcal{J}$) see e.g. (Ciarlet, 1989).

In order to obtain an algorithm which is numerically efficient, the best choice of γ_k, δ_k will be the result of a line minimization and maximization algorithm, respectively. Otherwise, at each iteration step k of the previous algorithm, we solve the one-dimensional optimization problem of the parameters γ_k and δ_k:

$$\begin{aligned} \gamma_k &= \min_{\lambda > 0} \mathcal{J}(X_k - \lambda c_k, Y_k), \\ \delta_k &= \min_{\lambda > 0} \mathcal{J}(X_k, Y_k + \lambda d_k), \end{aligned} \tag{73}$$

To derive an approximation for a pair (γ_k, δ_k) we can use a purely heuristic approach, for example, by taking $\gamma_k = min(1, \| c_k \|_{\infty}^{-1})$ and $\delta_k = min(1, \| d_k \|_{\infty}^{-1})$ or by using the linearization of $\mathcal{F}(X_k - \lambda c_k, Y_k)$ at X_k and $\mathcal{F}(X_k, Y_k - \lambda d_k)$ at Y_k by

$$\mathcal{F}(X_k - \lambda c_k, Y_k) \approx \mathcal{F}(X_k, Y_k) - \lambda \frac{\partial \mathcal{F}}{\partial X}(X_k, Y_k).c_k, \;\; \mathcal{F}(X_k, Y_k + \lambda d_k) \approx \mathcal{F}(X_k, Y_k) - \lambda \frac{\partial \mathcal{F}}{\partial Y}(X_k, Y_k).d_k,$$

where $\dfrac{\partial \mathcal{F}}{\partial X}(X_k, Y_k).c_k = \mathcal{F}'(X_k, Y_k).(c_k, 0)$ and $\dfrac{\partial \mathcal{F}}{\partial Y}(X_k, Y_k).d_k = \mathcal{F}'(X_k, Y_k).(0, d_k)$ are solutions of the sensitivity problem. According to the previous approximation, we can approximate the problem (73) by

$$\gamma_k = \min_{\lambda > 0} H(\lambda), \;\; \delta_k = \min_{\lambda > 0} R(\lambda), \tag{74}$$

where the functions H and R are polynomial functions of the degree 2 (since the functional $\mathcal{J}$ is quadratic), then the problem (74) can be solved exactly. Consequently, we obtain explicitly the value of the parameter λ_k.

10.2 Conjugate gradient algorithm:
Another strategy to solve numerically the treated saddle point problems, is to use a Conjugate Gradient type algorithm (CG-algorithm) combined with the Wolfe-Powell line search procedure for computing admissible step-sizes along the descent direction. The advantage of this method, compared to the gradient method, is that it performs a soft reset whenever the GC search direction yields no significant progress. In general, the method has the following form:

$$D_k = Dz = \begin{cases} -G_k \ \ for \ \ k = 0, \\ \\ -G_k + \xi_{k-1} D_{k-1} \ \ for \ \ k \geq 1, \end{cases}$$

$$z_{k+1} = z_k + \lambda_k D_k$$

where G_k denotes the gradient of the functional to be optimized at point z_k, λ_k is a step length obtained by a line search, D_k is the search direction and ξ_k is a constant. Several varieties of this method differ in the way of selecting ξ_k . Some well-known formula for ξ_k are given by Fletcher-Reeves, Polak-Ribière, Hestenes-Stiefel and Dai-Yuan.
The GC-algorithm for the resolution of the considered saddle point problems is given by:
for k=1,..., (iteration index) we denote by (X_k, Y_k) the numerical approximation of the control-disturbance at the *kth* iteration of the algorithm.

(*Step*1) Initialization: (X_0, Y_0) (given), $\xi_{-1} = 0$, $\eta_{-1} = 0$ and $C_{-1} = 0$, $D_{-1} = 0$,

(*Step*2) Resolution of the direct problem where the source term is (X_0, Y_0), gives $\mathcal{F}(X_0, Y_0)$,

(*Step*3) Resolution of the adjoint problem (based on (X_0, u_0)), gives $\mathcal{F}^{\perp}(X_0, Y_0)$,

(*Step*4) Gradient of $\mathcal{J}$ at (X_0, Y_0), the vector (c_0, d_0) is given by the system (GJ),

(*Step*5) Determine the direction: $C_0 = -c_0$, $D_0 = -d_0$

(*Step*6) Determine (X_1, Y_1): $X_1 = X_0 + \lambda_0 C_0$, $Y_1 = Y_0 - \delta_0 D_0$

(*Step*7) Resolution of the direct problem where the source term is (X_k, Y_k), gives $\mathcal{F}(X_k, Y_k)$,

(*Step*8) Resolution of the adjoint problem (based on (X_k, Y_k), gives $\mathcal{F}^{\perp}(X_k, Y_k)$,

(*Step*9) Gradient of $\mathcal{J}$ at (X_k, Y_k), the vector (c_k, d_k) is given by the system (GJ),

(*Step*10) Determine (ξ_{k-1}, η_{k-1}) by one of the following expressions:
$\xi_{k-1} = \dfrac{\| c_k \|^2_{U_{ad}}}{\| c_{k-1} \|^2_{U_{ad}}}$, $\eta_{k-1} = \dfrac{\| d_k \|^2_{V_{ad}}}{\| d_{k-1} \|^2_{V_{ad}}}$
(Fletcher-Reeves),

$\xi_{k-1} = \frac{< c_k - c_{k-1}, c_k >_{U_{ad}}}{\| c_{k-1} \|^2_{U_{ad}}}$, $\eta_{k-1} = \frac{< d_k - d_{k-1}, d_k >_{V_{ad}}}{\| d_{k-1} \|^2_{V_{ad}}}$
(Polak-Ribière),
$\xi_{k-1} = \frac{< c_k, c_k - c_{k-1} >_{U_{ad}}}{< C_{k-1}, c_k - c_{k-1} >_{U_{ad}}}$, $\eta_{k-1} = \frac{< d_k, d_k - d_{k-1} >_{V_{ad}}}{< D_{k-1}, d_k - d_{k-1} >_{V_{ad}}}$
(Hestenes-Stiefel),
$\xi_{k-1} = \frac{\| c_k \|^2_{U_{ad}}}{< C_{k-1}, c_k - c_{k-1} >_{U_{ad}}}$, $\eta_{k-1} = \frac{\| d_k \|^2_{V_{ad}}}{< D_{k-1}, d_k - d_{k-1} >_{V_{ad}}}$
(Dai-Yuan),

(*Step*11) Determine the direction: $C_k = -c_k + \xi_{k-1} C_{k-1}$, $D_k = -d_k + \eta_{k-1} D_{k-1}$,

(*Step*12) Determine (X_{k+1}, Y_{k+1}): $X_{k+1} = X_k + \lambda_k C_k$, $Y_{k+1} = Y_k - \delta_k D_k$,
where $0 < m \leq \lambda_k, \delta_k \leq M$ are the sequences of step lengths,

(*Step*13) If the gradient is sufficiently small (convergence): end; else set $k := k + 1$ and goto (*Step*7).

Optimal Solution: $(X, Y) = (X_k, Y_k)$.

Remark 12

1. *After derived the gradient $\mathcal{J}'$ of the cost functional $\mathcal{J}$, by using the adjoint model corresponding to the sensitivity state corresponding to the direct problem, we can use any other classical optimization strategies (see e.g (Gill et al., 1981)) to solve the robust/minimax control problems considered in this chapter.*
2. *For the discrete problem, the direct, sensitivity and adjoint problems can be discretized by a combination of Galerkin and the finite element methods for the space discretization and the classical first-order Euler method for the time discretization (see e.g. Chapter 9 of (Belmiloudi, 2008)).*

10.3 Conclusion

In ultrasound surgery, the best strategy to destroy the cancerous tissues is based on the rise in the temperature at the cytotoxic level (because the tumors are highly dependent on the temperature). Thus, in the clinical treatment of the tumors, it is very important to have enough complete knowledge about the behavior of the temperature in tissues. The mathematical models that we have used in this present work take account on the physical and thermal properties of the living tissues, in order to show the effects of living body exposure to variety energy sources (e.g. microwave and laser heating) on the thermal states of biological tissues.
For predicting and acting on the temperature distribution, we have discussed stabilization identification and regulation processes with and without randomness in data, parameters and, boundary and initial conditions, in order to reconstitute simultaneously the blood perfusion rate and the porosity parameter from MRI measurements (which are the desired online temperature distributions and thermal damages). In this context, we have considered two types of system of equations: a generalized form of the nonlinear transient bioheat transfer systems with nonlinear boundary conditions **(GNTB)** and the system (GNTB) coupled with a nonlinear radiation transport equation and a model of coagulation process.
The existence of the solution of the governing nonlinear system of equations is established and the Lipschitz continuity of the map solution is obtained. The differentiability and some

properties of the map solution are derived. Afterwards, robust control problems have been formulated. Under suitable hypotheses, it is shown that one has existence of an optimal solution, and the appropriate necessary optimality conditions for an optimal solution are derived. These conditions are obtained in a Lagrangian form. Some numerical methods, combining the obtained optimal necessary conditions and gradient-iterative algorithms, are presented in order to solve the robust control problems. We can apply the developed technic to other systems which couple the system **(GNTB)** with other processes, e.g. with a model calculating the SAR distribution in tissue during thermotherapy from the electrical potential as follows (Maxwell-type equation):

$$\begin{array}{l} \nabla \times B = \kappa_c E + J_{source}, \\ \nabla \times E = -i\omega\mu_c B, \end{array} \tag{75}$$

where $i^2 = -1$, $\kappa_c = \sigma + i\omega$ is the complex admittance, σ is the electrical conductivity, μ_c is the magnetic permeability type, J_{source} is the current density, E is the complex electric field vector, B is the complex magnetic field vector. The heat source term f can be taking as

$$f = SAR = \frac{1}{2}\sigma \mid E \mid^2 .$$

To derived the SAR distribution requires complex approach that is not discussed here : reader may refer e.g. to (Belmiloudi, 2006), for details on application complex robust control approach .
It is clear that we can consider other observations, controls and/or disturbances (which can appear in the boundary condition or in the state system) and we obtain similar results by using similar technique as used in this work (see (Belmiloudi, 2008)).

11. References

Adams, R. A. (1975). *Sobolev spaces*, Academic Press, New-York.

Arkin, H.; Holm, K.R.; Chen, M.M. & Bottje, W.G. (1986). Thermal pulse decay method for simultaneous measurement of local thermal conductivity and blood perfusion: A theoritical Analysis, *J. Biomech. Eng.*, 108, (1986), 208-214.

Atkins, P.W. (1982). *Physical chemistry*, Oxford University Press.

Belmiloudi, A. (2005). Nonlinear optimal control problems of degenerate parabolic equations with logistic time-varying delays of convolution type. *Nonlinear Anal.*, 63, (2005), 1126-1152.

Belmiloudi, A. (2006). Robust control problems of vortex dynamics in superconducting films with Ginzburg-Landau complex systems. *Abstr. Appl. Anal.*, 1-43, (2006) (Article ID 26724).

Belmiloudi, A. (2006). On some control problems for heat transfer systems in perfused biological tissues. *Wseas Translations on System*, 5, (2006), 17-25.

Belmiloudi, A. (2007). Analysis of the impact of nonlinear heat transfer laws on temperature distribution in irradiated biological tissues: Mathematical models and optimal controls. *J. Dynam. Control Systems*, 108, (2007), 217-254.

Belmiloudi, A. (2008). *Stabilization, optimal and robust control. Theory and applications in biological and physical sciences*, Communications and Control Engineering. Springer, London.

Belmiloudi, A. (2010). Parameter identification problems and analysis of the impact of porous media in biofluid heat transfer in biological tissues during thermal therapy. *Nonlinear Analysis: Real World Applications*, 11, (2010), 1345-1363.

Bohm, M.; Kremer, J. & Louis, A.K. (1993). Efficient algorithm for computing optimal control of antennas in hyperthermia. *Surveys Math. Indust.,* 3, (1993), 233-251.

Charney, C.K. (1992). Mathematical models of bioheat transfer. *Adv. Heat Trans.,* 22, (1992), 19-155.

Chato, J.C. (1980). Heat transfer to blood vessels. *J. Biomech. Eng.,* 102, (1980), 110-118.

Chen, M.M. & Holmes, K.R. (1980). Microvascular contributions in tissue heat transfer. *Annals N.Y. Acad. Sci.,* 335, (1980), 137-150.

Chen, M.M. & Holmes, K.R. (1980). In vivo tissue thermal conductivity and local blood perfusion measured with heat pulse-decay method. *Adv. Bioeng.,* (1980), 113-115.

Ciarlet, P.G. (1989). *Introduction to numerical linear algebra and optimization,* Cambridge Press.

Delfour, M.C.; Payre, C. & Zelesio, J.P. (1987). Approximation of nonlinear problems associated with radiating bodies in space. *SIAM J. Numer. Anal,* 24 (1987), 1077-1094.

Deuflhard, P. & Seebass, M. (1998). Adaptive multilevel FEM as decisive tools in clinical cancer therapy hyperthermia. *Konrad-Zuse-Zentrum fur informationstechnikl, Berlin Takustr.,* 7, (1998), D-14195 Berlin.

Ekeland, I. & Temam, R. (1976). *Convex analysis and variational problems,* North-Holland, Amsterdam.

Feng, Y.; Oden, J.T. & Rylander, M.N. (2008). A two-State cell damage model under hyperthermic conditions: theory and in vitro experiments. *J. Biomech. Engrg.,* 130, (2008), 1-10.

Gilbarg, D. & Trudinger, N.S. (1983). *Elliptic partial differential equations of second order*, Springer, Berlin.

Gill, P.E.; Murray, W. & Wright, M.H. (1981). *Pratical Optimization,* Academic Press, San Diago.

Hadamard, J. (1923). *Lectures on Cauchy problem in linear differential equations,* Yale University Press, New Haven, CT.

He, X. & Bischof, J. (2003). Quantification of temperature and injury response in thermal therapy and cryosurgery. *Crit. Rev. Biomed. Eng.,* 31, (2003), 355-421.

Henriques Jr, F.C. (1947). Studies of thermal injury: V. The predictability and the significance of thermally induced rate process leading to irreversible epidermal injury. *Arch. Pathol.,* 43, (1947), 489-502.

Hill, J. & Pincombe, A. (1992). Some similarity temperature profiles for the microwave heating of a half-space. *J. Austral. Math. Sco. Ser. B,* 33, (1992), 290-320.

Hirst, D.G. (1989). Tumor blood flow modification therapeutic benift: is this approach ready for clinical application? In: *Review. GrayLaboratory 1989 Annual Report.* Michael B and Hance M (eds). Cancer Research Campaign, London, (1989), 14-17.

Hutchinson, E.; Dahleh, M.A. & Hynynen, K. (1998). The feasibility of MRI Feedback Control for Intracavitary Phased Array Hyperthermia Treatments. *Int. J. Hyperthermia,* 14, (1998), 39-56.

Ishimaru, A. (1978). *Waves propagation and scattering in random media*, Vol. I, Academic Press, New York.

Khaled, A.R.A. & Vafai, K. (2003). The role of porous media in modeling flow and heat transfer in biological tissues. *Int. J. Heat. Mass transfer,* 46, (2003), 4989-5003.

Köhler, T.; Maass, P.; Wust, P. & Seebass, M. (2001). A fast algorithm to find optimal controls of multiantenna applicators in regional hyperthermia. *Phys. Med. Biol.,* 46, (2001), 2503-2514.

Kowalski, M.E. & Jin, J.M. (2004). Model-based optimization of phased arrays for electromagnetic hyperthermia. *IEEE Trans. Microwave Theory Tech.,* 52, (2004),

1964-1977.
Lions, J.L. (1961). *Equations differentielles operationnelles,* Springer-Verlag, New York.
Lions, J.L. & Magenes, E. (1968). *Problèmes aux limites non homogènes et applications,* Tome 1&2, Dunod, Paris.
Liu, J.; Zhu, L. & Xu, X.L. (2000). Studies on three-dimensional temperature transients in the canine prostate during transurethal microwave thermal therapy. *ASME J. Biomech. Eng.,* 122, (2000), 372-379.
Loève, M. (1977). *Probability theory*, Springer-Verlage, Berlin.
Marchant, T. & Lui, B. (2001). On the heating of a two-dimensional slab in a microwave cavity: aprature effects. *ANZIAM J.,* 43, (2001), 137-148.
Martin, G.T.; Bowman, H.F. & Newman, W.H. (1992). Basic element method for computing the temperature field during hyperthermia therapy planning. *Adv. bio. Heat Mass Transf.,* 23, (1992), 75-80.
Malinen, M.; Duncan, S.; Huttunen, T. & Kaipio, J. (2006). Feedforward and feedback control of ultrasound surgery. *Appl. Numer. Math.,* 56, (2006), 55-79 .
Niemz, M. (2002). *Laser-tissue Interactions. Fundamentals and Applications,* Springer, Berlin.
Pennes, H.H. (1948). Analysis of tissue and arterial blood temperatures in the resting human forearm. *J. Appl. Phys.,* 1, (1948), 93-122 (and 85, (1998), 5-34).
Pincombe, A.H. & Smyth, N.F. (1991). Microwave heating of materials with low conductivity. *Proc. R. Soc., A,* 433, (1991) ,479-498.
Pomraning, G. C. (1973). *The Equations of Radiation Hydrodynamics,* Pergamon, Oxford.
Prato, G.Da. & Zabczyk, J. (1992). *Stochastic equations in infinite dimension*, University Press, Cambridge.
Seip, R. & Ebbini, E.S. (1995). Studies on three-dimensional temperature response to heating fields using diagnostic ultrasound. *IEEE Trans. Biomed. Eng.,* 42, (1995), 828-839.
Shih, T.C.; Kou, H.S. & Lin, W.L. (2002). Effect of effective tissue conductivity on thermal dose distributions on living tissue with directional blood flow during thermal therapy, *Inter. Comm. Heat Mass transfer,* 29, (2002), 115-126.
Skinner, M.G.; Iizuka, M.N.; Kolios, M.C. & Sherar, M.D. (1998). A theoretical comparison of energy sources-microwave, ultrasound and laser-for interstitial thermal therapy. *Phys. Med. Biol.,* 43, (1998), 3535-3547.
Sturesson, C. & Andersson-Engels, S. (1995). A mathematical model for predicting the temperature distribution in laser-induced hyperthermia. Experimental evaluation and applications. *Phys. Med. Biol.,* 40, (1995), 2037-2052.
Tropea, B.I. & Lee, R.C. (1992). Thermal injury kinetics in electrical trauma. *J. Biomech. Eng.,* 114, (1992), 241-250.
Valvano, J.W. et al. (1984). An isolated rat liver model for the evaluation of thermal techniques to measure perfusion. *J. Biomech. Eng.,* 106, (1984), 187-191.
Vanne, A. & Hynynen, K. (2003). MRI feedback temperature control for focused ultrasound surgery. *Phys. Med. Biol.,* 48, (2003), 31-43.
Weinbaum, S. & Jiji, L.M. (1985). A two simplified bioheat equation for the effect of blood flow on average tissue temperature. *J. Biomech. Eng.,* 107, (1985) , 131-139.
Wissler, E.H. (1998). Pennes' 1948 paper revisited. *J. Appl. Phys.,* 85, (1998), 35-41.
Xu, L.; Zhu, L. & Holmes, K. (1998). Blood perfusion measurements in the canine prostate during transurethral hyperthermia. *Ann. New York Acad. Sci.,* 858, (1998), 21-29.
Zhang, J.; Sandison, G.; Murthy, J. & Xu, L. (2005). Numerical simulation for heat transfer in prostate cancer cryosurgery. *J. Biomech. Eng.,* 127, (2005), 279-293.

Zhou, J. & Liu, J. (2004). Numerical study on 3d light and heat transfer in biological tissue with large blood vessels during laser-induced thermotherapy. *Numer. Heat Transfer A,* 45, (2004), 415-449.

3

Direct and Inverse Heat Transfer Problems in Dynamics of Plate Fin and Tube Heat Exchangers

Dawid Taler
University of Science and Technology, Cracow
Poland

1. Introduction

Plate fin and tube heat exchangers can be manufactured from bare or individual finned tubes or from tubes with plate fins. Tubes can be circular, oval, rectangular or other shapes (Hesselgreaves, 2001; Kraus et al., 2001). The mathematical models of the heat exchanger were built on the basis of the principles of conservation of mass, momentum and energy, which were applied to the flow of fluids in the heat exchangers. The system of differential equations for the transient temperature of the both fluids and the tube wall was derived. Great emphasis was put on modelling of transient tube wall temperatures in thin and thick walled bare tubes and in individually finned tubes. Plate - fin and tube heat exchangers with oval tubes were also considered.

The general principles of mathematical modeling of transient heat transfer in cross-flow tube heat exchangers with complex flow arrangements which allow the simulation of multipass heat exchangers with many tube rows are presented.

At first, a mathematical model of the cross-flow plate-fin and tube heat exchanger with one row of tubes was developed. A set of partial nonlinear differential equations for the temperature of the both fluids and the wall, together with two boundary conditions for the fluids and initial boundary conditions for the fluids and the wall, were solved using Laplace Transforms and an explicit finite-difference method. The comparison of time variations of fluid and tube wall temperatures obtained by analytical and numerical solutions for step-wise water or air temperature increase at the heat exchanger inlets proves the numerical model of the heat exchanger is very accurate.

Based on the general rules, a mathematical model of the plate-fin and tube heat exchanger with the complex flow arrangement was developed. The analyzed heat exchanger has two passes with two tube rows in each pass. The number of tubes in the passes is different. In order to study the performance of plate-fin and tube heat exchangers under steady-state and transient conditions, and to validate the mathematical model of the heat exchanger, a test facility was built. The experimental set-up is an open wind tunnel.

First, tests for various air velocities and water volumetric flow rates were conducted at steady-state conditions to determine correlations for the air and water-side Nusselt numbers using the proposed method based on the weighted least squares method. Transient

experimental tests were carried out for sudden time changes of air velocity and water volumetric flow rate before the heat exchanger. The results obtained by numerical simulation using the developed mathematical model of the investigated heat exchanger were compared with the experimental data. The agreement between the numerical and experimental results is very satisfactory.
Then, a transient inverse heat transfer problem encountered in control of fluid temperature in heat exchangers was solved. The objective of the process control is to adjust the speed of fan rotation, measured in number of fan revolutions per minute, so that the water temperature at the heat exchanger outlet is equal to a time-dependant target value. The least squares method in conjunction with the first order regularization method was used for sequential determining the number of revolutions per minute. Future time steps were used to stabilize the inverse problem for small time steps. The transient temperature of the water at the outlet of the heat exchanger was calculated at every iteration step using a numerical mathematical model of the heat exchanger. The technique developed in the paper was validated by comparing the calculated and measured number of the fan revolutions. The discrepancies between the calculated and measured revolution numbers are small.

2. Dynamics of a cross-flow tube heat exchanger

Applications of cross-flow tubular heat exchangers are condensers and evaporators in air conditioners and heat pumps as well as air heaters in heating systems. They are also applied as water coolers in so called 'dry' water cooling systems of power plants, as well as in car radiators. There are analytical and numerical mathematical models of the cross-flow tube heat exchangers which enable to determine the steady state temperature distribution of fluids and the rate of heat transferred between fluids (Taler, 2002; Taler & Cebula, 2004; Taler, 2004). In view of the wide range of applications in practice, these heat exchangers were experimentally examined in steady-state conditions, mostly to determine the overall heat transfer coefficient or the correlation for the heat transfer coefficients on the air side and on the internal surface of the tubes (Taler, 2004; Wang, 2000). There exist many references on the transient response of heat exchangers. Most of them, however, focus on the unsteady-state heat transfer processes in parallel and counter flow heat exchangers (Tan, 1984; Li, 1986; Smith, 1997; Roetzel, 1998). In recent years, transient direct and inverse heat transfer problems in cross-flow tube heat exchangers have also been considered (Taler, 2006a; Taler, 2008; Taler, 2009). In this paper, the new equation set describing transient heat transfer process in tube and fin cross-flow tube exchanger is given and subsequently solved using the finite difference method (finite volume method). In order to assess the accuracy of the numerical solution, the differential equations are solved using the Laplace transform assuming constant thermo-physical properties of fluids and constant heat transfer coefficients. Then, the distributions of temperature of the fluids in time and along the length of the exchanger, found by both of the described methods, are compared. In order to assess the accuracy of the numerical model of the heat exchanger, a simulation by the finite difference method is validated by a comparison of the obtained temperature histories with the experimental results. The solutions presented in the paper can be used to analyze the operation of exchangers in transient conditions and can find application in systems of automatic control or in the operation of heat exchangers.

2.1 Mathematical model of one-row heat exchanger

A mathematical model of the cross flow tubular heat exchanger, in which air flows transversally through a row of tubes (Fig. 1), will be presented. The system of partial differential equations describing the space and time changes of: water T_1, tube wall T_w , and air T_2 temperatures are, respectively

$$\frac{1}{N_1}\frac{\partial T_1}{\partial x^+}+\tau_1\frac{\partial T_1}{\partial t}=-\left(T_1-T_w\right), \tag{1}$$

$$\tau_w\frac{\partial T_w}{\partial t}+\tau_f\frac{\partial T_{m2}}{\partial t}+T_w=\frac{h_1U_w}{h_1U_w+h_oU_z}T_1+\frac{h_oU_z}{h_1U_w+h_oU_z}T_{m2}, \tag{2}$$

$$\frac{1}{N_2}\frac{\partial T_2}{\partial y^+}+\tau_2\frac{\partial T_2}{\partial t}=T_w-T_2, \tag{3}$$

where T_{m2} denotes the mean air temperature over the row thickness, defined as

$$T_{m2}=\int_0^1 T_2\left(x^+,y^+,t\right)dy^+. \tag{4}$$

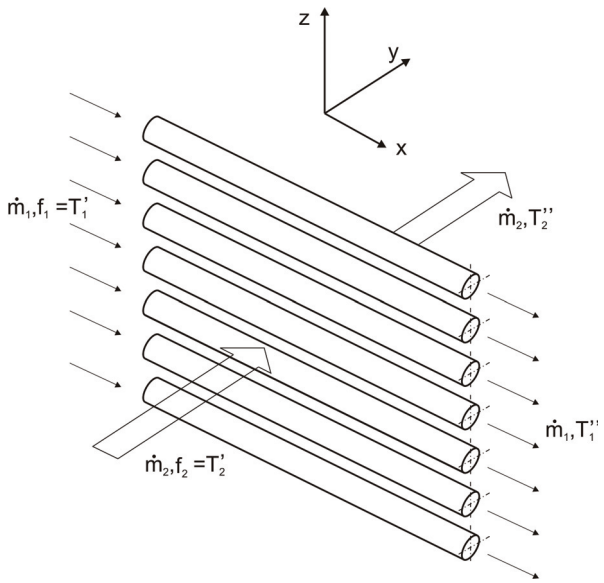

Fig. 1. One-row cross-flow tube heat exchanger

The numbers of heat transfer units N_1 and N_2 are given by

$$N_1=\frac{h_1A_{wrg}}{\dot{m}_1c_{p1}},\ N_2=\frac{h_oA_{zrg}}{\dot{m}_2c_{p2}},$$

The time constants τ_1, τ_w, τ_f, and τ_2 are

$$\tau_1 = \frac{m_1 c_{p1}}{h_1 A_{wrg}},\ \tau_w = \frac{\left(m_w + \eta_f m_f\right)c_w}{h_1 A_{wrg} + h_o A_{zrg}},\ \tau_f = \frac{\left(1-\eta_f\right)m_f c_w}{h_1 A_{wrg} + h_o A_{zrg}},\ \tau_2 = \frac{m_2 c_{p2}}{h_o A_{zrg}},$$

$$m_1 = n_{rg} A_w L_{ch} \rho_1,\ m_2 = n_{rg}\left(p_1 p_2 - A_{oval}\right)\left(s-\delta_f\right)n_f \rho_2,\ m_w = n_{rg} U_m \delta_w L_{ch} \rho_w$$

$$m_f = n_{rg} n_f \left(p_1 p_2 - A_{oval}\right)\delta_f \rho_w,\ A_w = \pi a b,\ A_{oval} = \pi\left(a+\delta_w\right)\left(b+\delta_w\right),\ U_m = \left(U_w + U_z\right)/2.$$

The weighted heat transfer coefficient h_o is defined by

$$h_o = h_2\left[\frac{A_{mf}}{A_{zrg}} + \frac{A_f}{A_{zrg}}\eta_f(\ h_2\ )\right] \quad . \tag{5}$$

The symbols in Equations (1-5) denote: a, b - minimum and maximum radius of the oval inner surface; A_f - fin surface area; A_{mf} - area of the tube outer surface between fins; A_{oval}, A_w - outside and inside cross section area of the oval tube; $A_{wrg} = n_{rg} U_w L_{ch}$, $A_{zrg} = n_{rg} U_z L_{ch}$ - inside and outside surface area of the bare tube; c_p - specific heat at constant pressure; c_w - specific heat of the tube and fin material; h_1 and h_2 - water and air side heat transfer coefficients, respectively; h_o - weighted heat transfer coefficient from the air side related to outer surface area of the bare tube; L_{ch} - tube length in the automotive radiator; m_1, m_2, m_f and m_w - mass of the water, air, fins, and tube walls in the heat exchanger, $\dot{m}_1$ - mass flow rate of cooling liquid flowing inside the tubes; $\dot{m}_2$ - air mass flow rate; n_f - number of fins on the tube length; n_{rg} - number of tubes in the heat exchanger; N_1 and N_2 – number of heat transfer units for water and air, respectively; p_1 - pitch of tubes in plane perpendicular to flow (height of fin); p_2 - pitch of tubes in direction of flow (width of fin); s - fin pitch; t - time; T_1, T_w and T_2 - water, tube wall and air temperature, respectively; U_w and U_z - inner and outer tube perimeter of the bare tube, η_f - fin efficiency, $x^+ = x/L_{ch}$, $y^+ = y/p_2$ - dimensionless Cartesian coordinates; δ_f and δ_w - fin and tube thickness, respectively; ρ - density; τ_1, τ_w, τ_f and τ_2 - time constants.
The initial temperature distributions of the both fluids $T_{1,0}\left(x^+\right)$, $T_{2,0}\left(x^+, y^+\right)$ and the wall $T_{w,0}\left(x^+\right)$ are known from measurements or from the steady-state calculations of the heat exchanger. The initial conditions are defined as follows

$$T_1\left(x^+, t\right)\big|_{t=0} = T_{1,0}\left(x^+\right), \tag{6}$$

$$T_w\left(x^+, t\right)\big|_{t=0} = T_{w,0}\left(x^+\right), \tag{7}$$

$$T_2\left(x^+, y^+, t\right)\big|_{t=0} = T_{2,0}\left(x^+, y^+\right). \tag{8}$$

The boundary conditions have the following form

$$T_1\left(x^+,t\right)\Big|_{x^+=0} = f_1(t)\,, \tag{9}$$

$$T_2\left(x^+,y^+,t\right)\Big|_{y^+=0} = f_2(t)\,, \tag{10}$$

where $f_1(t)$ and $f_2(t)$ are functions describing the variation of the temperatures of inlet liquid and air in time. The initial-boundary value problem formulated above (1–10) applies to heat exchangers made of smooth tubes and also from finned ones. The transient fluids and wall temperature distributions in the one row heat exchanger (Fig. 1) are then determined by the explicit finite difference method and by Laplace transform method.

2.1.1 Explicit finite difference method

When actual heat exchangers are calculated, the thermo-physical properties of the fluids and the heat transfer coefficients depend on the fluid temperature, and the initial boundary problem (1–10) is non-linear. In such cases, the Laplace transform cannot be applied. The temperature distribution $T_1\left(x^+,t\right)$, $T_w\left(x^+,t\right)$, and $T_2\left(x^+,y^+,t\right)$ can then be found by the explicit finite difference method. The time derivative is approximated by a forward difference, while the spatial derivatives are approximated by backward differences. The equations (1–3) are approximated using the explicit finite difference method

$$\frac{1}{N_1^n}\frac{T_{1,i+1}^n - T_{1,i}^n}{\Delta x^+} + \tau_1^n \frac{T_{1,i+1}^{n+1} - T_{1,i+1}^n}{\Delta t} = -\left(\frac{T_{1,i}^n + T_{1,i+1}^n}{2} - T_{w,i}^n\right), \tag{11}$$

$i = 1, \ldots, N$, $n = 0, 1, \ldots$

$$\tau_w^n \frac{T_{w,i}^{n+1} - T_{w,i}^n}{\Delta t} + \tau_f^n \frac{T_{m2,i}^{n+1} - T_{m2,i}^n}{\Delta t} + T_{w,i}^n = \frac{h_1^n U_w}{h_1^n U_w + h_o^n U_z}\frac{T_{1,i}^n + T_{1,i+1}^n}{2} + \frac{h_o^n U_z}{h_1^n U_w + h_o^n U_z} T_{m2,i}^n\,, \tag{12}$$

$i = 1, \ldots, N$, $n = 0, 1, \ldots$

$$\frac{1}{N_2^n}\frac{\left(T'_{2,i}\right)^n - \left(T''_{2,i}\right)^n}{1} + \tau_2^n \frac{\left(T''_{2,i}\right)^{n+1} - \left(T''_{2,i}\right)^n}{\Delta t} = T_{w,i}^n - \frac{\left(T'_{2,i}\right)^n + \left(T''_{2,i}\right)^n}{2}\,, \tag{13}$$

$i = 1, \ldots, N$, $n = 0, 1, \ldots$.

The nodes are shown in Fig. 2. The designations are as follows

$$W1(I) = T_{1,i}\,,\ P1(I) = T'_{2,i}\,,\ P2(I) = T''_{2,i}\,,\ R1(I) = T_{w,i}\,.$$

The unknown temperature $T_{1,i+1}^{n+1}$ is found from Eq. (11), $T_{w,i}^{n+1}$ from Eq. (12), and $\left(T''_{2,i}\right)^{n+1}$ from Eq. (13):

$$T_{1,i+1}^{n+1} = T_{1,i+1}^n - \frac{\Delta t}{N_1^n \tau_1^n}\frac{T_{1,i+1}^n - T_{1,i}^n}{\Delta x^+} - \frac{\Delta t}{\tau_1^n}\left(\frac{T_{1,i}^n + T_{1,i+1}^n}{2} - T_{w,i}^n\right), \tag{14}$$

$i = 1, \ldots, N$, $n = 0, 1, \ldots$

$$T_{w,i}^{n+1} = T_{w,i}^{n} + \frac{\Delta t}{\tau_w^n}\left\{ \frac{h_1^n A_{wrg}}{h_1^n A_{wrg} + h_o^n A_{zrg}} \frac{T_{1,i}^n + T_{1,i+1}^n}{2} + \frac{h_o^n A_{zrg}}{h_1^n A_{wrg} + h_o^n A_{zrg}} \frac{\left(T'_{2,i}\right)^n + \left(T''_{2,i}\right)^n}{2} - T_{w,i}^n - \right.$$

$$\left. - \frac{\tau_f^n}{\Delta t}\left[\frac{\left(T'_{2,i}\right)^{n+1} + \left(T''_{2,i}\right)^{n+1}}{2} - \frac{\left(T'_{2,i}\right)^n + \left(T''_{2,i}\right)^n}{2} \right] \right\}, \tag{15}$$

$i = 1, \ldots, N$, $n = 0, 1, \ldots$

$$\left(T''_{2,i}\right)^{n+1} = \left(T''_{2,i}\right)^n + \frac{\Delta t}{N_2^n \tau_2^n}\left[\left(T'_{2,i}\right)^n - \left(T''_{2,i}\right)^n\right] + \frac{\Delta t}{\tau_2^n}\left[T_{w,i}^n - \frac{\left(T'_{2,i}\right)^n + \left(T''_{2,i}\right)^n}{2} \right], \tag{16}$$

$i = 1, \ldots, N$, $n = 0, 1, \ldots$

where Δt is the time step and the dimensionless spatial step is: $\Delta x^+ = 1/N$.

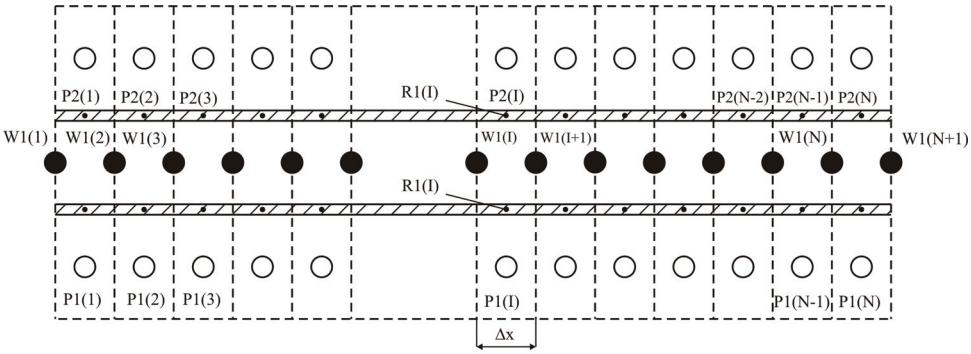

Fig. 2. Diagram of nodes in the calculation of temperature distribution by the finite difference method; P1(I)–inlet air temperature, R1(I)–tube wall temperature, P2(I)–outlet air temperature

The initial conditions (6–8) and the boundary conditions (9, 10) assume the form:

- initial conditions

$$T_{1,i}^0 = T_{1,0}\left(x_i^+\right), \; n = 0, \; i = 1,\ldots,N+1, \tag{17}$$

$$T_{w,i}^0 = T_{w,0}\left(x_i^+\right), \; i = 1,\ldots,N \tag{18}$$

$$\left(T'_{2,i}\right)^0 = T'_{2,0}\left(x_i^+\right), \; i = 1,\ldots,N, \tag{19}$$

$$\left(T''_{2,i}\right)^0 = T''_{2,0}\left(x_i^+\right), \; i = 1,\ldots,N, \tag{20}$$

where $x_i^+ = (i-1)\Delta x^+$, $i = 1,\ldots,N+1$.

- boundary conditions

$$T_{1,1}^n = f_1^n,\ n = 0,1,..., \tag{21}$$

$$\left(T'_{2,i} \right)^n = f_2^n,\ n = 0,1,..., \tag{22}$$

where $f_1^n = f_1\left(n\Delta t \right)$, $f_2^n = f_2\left(n\Delta t \right)$.
In order to ensure stability of the calculations by the explicit finite difference method, the conditions of Courant (Press et al. , 2006; Taler, 2009) must be satisfied

$$\frac{\Delta t}{N_1^n \tau_1^n \Delta x^+} \le 1, \tag{23}$$

$$\frac{\Delta t}{N_2^n \tau_2^n} \le 1. \tag{24}$$

Because of the high air flow velocity w_2, the time step Δt resulting from the condition (24) should be very small, in the range of tens of thousandths of a second. The temperature distribution is calculated using the formulas (14–16) taking into consideration the initial (17–20) and boundary conditions (21–22), and starting at n = 0.

2.1.2 Laplace transform method

Applying the Laplace transform for the time t in the initial boundary problem (1–10) leads to the following boundary problem

$$\frac{1}{N_1}\frac{d\overline{T}_1}{d x^+} + \tau_1\left(s\overline{T}_1 - T_{1,0} \right) = -\left(\overline{T}_1 - \overline{T}_w \right), \tag{25}$$

$$\tau_w\left(s\overline{T}_w - T_{w,0} \right) + \tau_f\left(s\overline{T}_{m2} - T_{m2,0} \right) + \overline{T}_w = \frac{h_1 U_w}{h_1 U_w + h_o U_z}\overline{T}_1 + \frac{h_o U_z}{h_1 U_w + h_o U_z}\overline{T}_{m2}, \tag{26}$$

$$\frac{1}{N_2}\frac{\partial \overline{T}_2}{\partial y^+} + \tau_2\left(s\overline{T}_2 - T_{2,0} \right) = \overline{T}_w - \overline{T}_2, \tag{27}$$

$$\overline{T}_1\left(x^+, s \right)\Big|_{x^+=0} = \overline{f}_1\left(s \right), \tag{28}$$

$$\overline{T}_2\left(x^+, y^+, s \right)\Big|_{y^+=0} = \overline{f}_2\left(s \right), \tag{29}$$

where the Laplace transform of the function $F(t)$ is defined as follows

$$\overline{F}\left(s \right) = \int_0^\infty e^{-st} F\left(t \right) dt. \tag{30}$$

The symbol s in Equations (25-30) denotes the complex variable.

Solving the equations (25–27) with boundary conditions (28–29) and the initial condition

$$T_{1,0} = T_{w,0} = T_{2,0} = T_{m2,0} = 0 \tag{31}$$

gives

$$\overline{T}_1 = (R/\tau)\left(1 - e^{-\tau N_1 x^+}\right) + \overline{f}_1(s)e^{-\tau N_1 x^+}, \tag{32}$$

$$\overline{T}_w = \frac{E\overline{T}_1 + \left[G\overline{f}_2(s)/H\right]\left(1-e^{-H}\right)}{1 - GN_2\left[1/H - \left(1/H^2\right)\left(1-e^{-H}\right)\right]}, \tag{33}$$

$$\overline{T}_2 = \overline{f}_2(s)e^{-(1+s\tau_2)N_2 y^+} + \frac{\overline{T}_w}{1+s\tau_2}\left[1 - e^{-(1+s\tau_2)N_2 y^+}\right], \tag{34}$$

where

$$\tau = s\tau_1 + 1 - \frac{E}{1 - GN_2\left[1/H - \left(1/H^2\right)\left(1-e^{-H}\right)\right]},$$

$$E = \frac{h_1 A_{wrg}}{h_1 A_{wrg} + h_o A_{zrg}} \cdot \frac{1}{\tau_w s + 1},$$

$$G = \left(\frac{h_0 A_{zrg}}{h_1 A_{wrg} + h_o A_{zrg}} - \tau_f s\right)\frac{1}{\tau_w s + 1},$$

$$H = (1 + s\tau_2)N_2,$$

$$R = \frac{\left[G\overline{f}_2(s)/H\right]\left(1-e^{-H}\right)}{1 - GN_2\left[1/H - \left(1/H^2\right)\left(1-e^{-H}\right)\right]}.$$

The transforms of the solutions $\overline{T}_1 = \overline{T}_1\left(x^+, s\right)$, $\overline{T}_w = \overline{T}_w(x^+, s)$ and $\overline{T}_2 = \overline{T}_2\left(x^+, y^+, s\right)$ are complex and therefore the inverse Laplace transforms of the functions $\overline{T}_1$ and $\overline{T}_2$ are determined numerically by the method of Crump (Crump, 1976) improved by De Hoog (De Hoog 1982). The transforms of the solutions $\overline{T}_1$, $\overline{T}_w$ and $\overline{T}_2$ are found under the assumption that the discussed problem is linear, i.e. that the coefficients N_1, τ_1, N_2, τ_2, τ_w and τ_f in the equations (1–3) are independent of temperature. In view of the high accuracy of the solution obtained by the Laplace transform, it can be applied to verify the approximate solutions obtained by the method of finite differences.

3. Test calculations

A step change of air inlet temperature in one tube row of the exchanger, from the initial temperature T_0 to $T_0 + \Delta T_2$ will be considered. The design of the exchanger is shown in the

paper (Taler 2002, Taler 2009). The discussed exchanger consists of ten oval tubes with external diameters $d_{\min} = 2 \cdot (a + \delta_w) = 6.35$ mm and $d_{\max} = 2 \cdot (b + \delta_w) = 11.82$ mm. The thickness of the aluminium wall is δ_w = 0.4 mm. The tubes are provided with smooth plate fins with a thickness of δ_f = 0.08 mm and width of p_2 = 17 mm. The height of the tube bank is $H = n_r\, p_1$ = 10 × 18.5 = 185 mm, where n_r = 10 denotes the number of tubes, and p_1 is the transverse tube spacing. Water flows inside the tubes and air on their outside, perpendicularly to their axis. The pipes are L_x = 0.52 m long. The initial temperature are: $T_{1,0} = T_{w,0} = T_{2,0}$ = 0°C. For time t > 0, the sudden temperature increase by ΔT_2 = 10°C occurs on the air-side before the heat exchanger. The water temperature f_1 at the inlet to the exchanger tubes is equal to the initial temperature T_0 = 0°C.

The flow rate of water is constant and amounts $\dot{V}_1$ = 1004 l/h. The air velocity in the duct before the exchanger is w_2 = 7.01 m/s and the velocity in the narrowest cross section between two tubes is $w_{\max}$ = 11.6 m/s. The mass of water in the tubes is m_1 = 0.245 kg and the mass of tubes including fins is (m_w + m_f) = 0.447 kg. The time constants are τ_1 = 5.68 s, τ_2 = 0.0078 s, τ_f = 0 s, τ_w = 1.0716 s and the numbers of heat transfer units N_1 and N_2 are equal to N_1 = 0.310, N_2 = 0.227. The heat transfer coefficients are: h_1 = 1297.1 W/(m²K), h_2 = 78.1 W/(m²K).

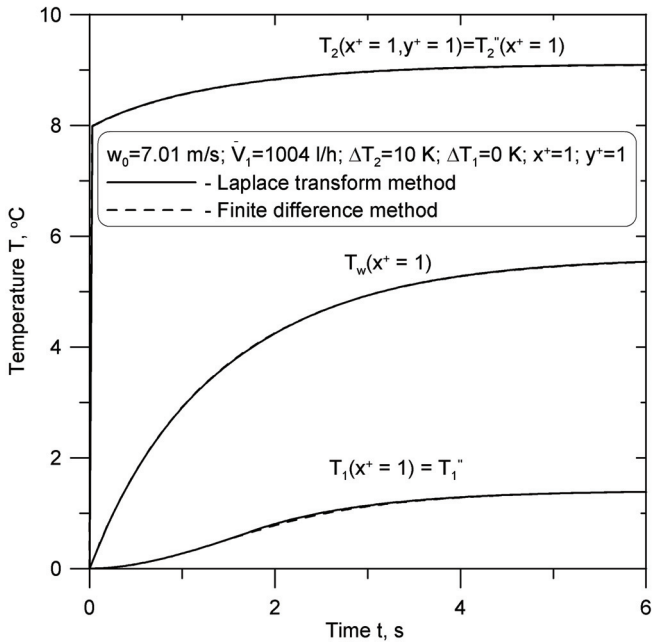

Fig. 3. Plot of temperatures of water $T_1(x^+ = 1)$, tube wall $T_w(x^+ = 1)$ and air $T_2(x^+ = 1, y^+ = 1)$ at the exchanger outlet ($x^+ = 1$, $y^+ = 1$)

The changes of the temperatures of water and air were determined by the method of Laplace transform and by the finite difference method. The water temperature on the tube length was determined in 21 nodes (N = 20, Δx^+ = 0.05). The time integration step was

assumed as Δt = 0.0001 s. The transients of water and air temperatures at the outlet of the exchanger (x^+ = 1, y^+ = 1) are presented in Fig. 3.
The water temperature distribution on the length of the exchanger at various time points is shown in Fig. 4. Comparing the plots of air, tube wall and water at the exchanger outlet indicates that the results obtained by the Laplace transform method and the finite difference method are very close. The air outlet temperature in the point x^+ = 1, y^+ = 1 is close to temperature in steady state already after the time t = 3.9 s. Figure 3 shows that the air temperature past the row of tubes (x^+ = 1, y^+ = 1) is already almost equal to the steady state temperature after a short time period when the inlet air arrives at the outlet of the heat exchanger. The steady-state water temperature increases almost linearly from the inlet of the heat exchanger to its outlet. It is evident that the accuracy of the results obtained by the finite difference method is quite acceptable.

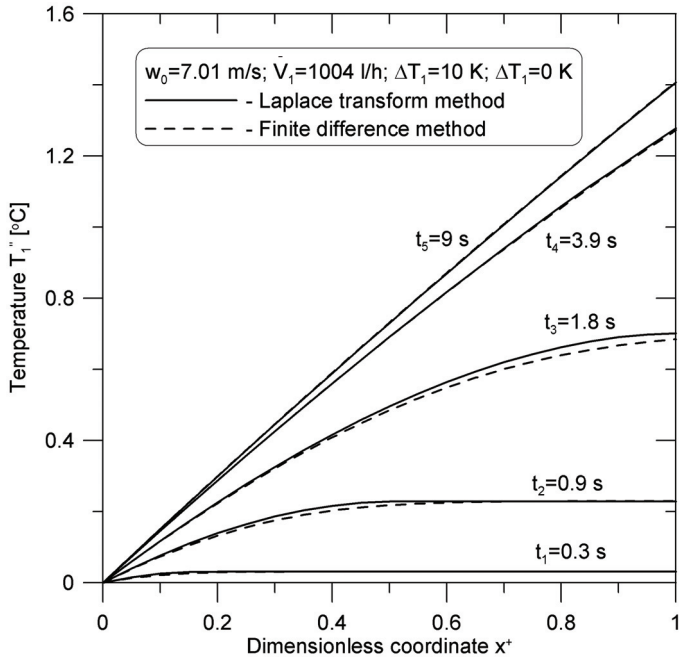

Fig. 4. Comparison of water temperatures on the tube length determined by the finite difference method and the Laplace transform method

4. The numerical model of the heat exchanger

The automotive radiator for the spark-ignition combustion engine with a cubic capacity of 1580 cm^3 is a double-row, two-pass plate-finned heat exchanger. The radiator consists of aluminium tubes of oval cross-section. The cooling liquid flows in parallel through both tube rows. Figures 5a-5c show a diagram of the two-pass cross-flow radiator with two rows of tubes. The heat exchanger consists of the aluminium tubes of oval cross-section.

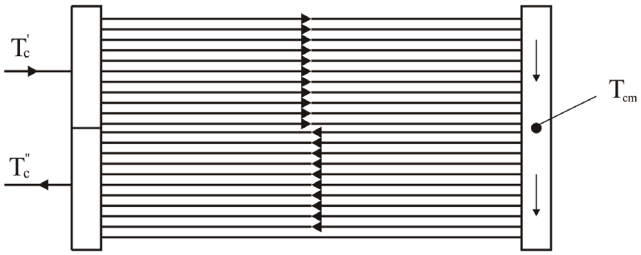

(a)

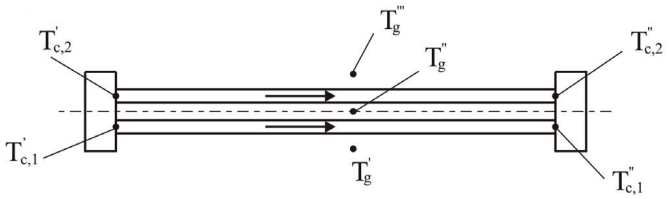

(b)

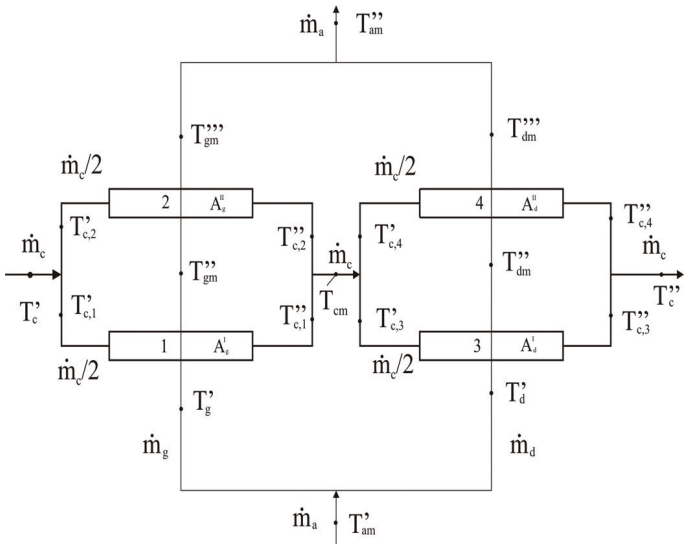

(c)

1 – first tube row in upper (first) pass, 2 – second tube row in upper pass; 3 – first tube row in lower (second) pass, 4 – second tube row in lower pass; T'_w and T''_w - inlet and outlet water temperature, respectively, T'_{am} and T''_{am} - inlet and outlet air mean temperature, respectively, $\dot{m}_a$, $\dot{m}_w$ - air and water mass flow rate at the inlet of the heat exchanger, respectively

Fig. 5. Two-pass plate-fin and tube heat exchanger with two in-line tube rows;

The outlets from the upper pass tubes converge into one manifold. Upon mixing the cooling liquid with the temperature $T'_1(t)$ from the first tube row and the cooling liquid with the

temperature T_2'' from the second tube row, the feeding liquid temperature of the second, lower pass is $T_{cm}(t)$. In the second, lower pass, the total mass flow rate splits into two equal flow rates $\dot{m}_c / 2$. On the outlet from the first tube row in the bottom pass the coolant temperature is $T_3''(t)$, and from the second row is $T_4''(t)$. Upon mixing the cooling liquid from the first and second row, the final temperature of the coolant exiting the radiator is $T_c''(t)$. The air stream with mass flow rate $\dot{m}_a(t)$ flows crosswise through both tube rows. Assuming that the air inlet velocity w_0 is in the upper and lower pass, the mass rate of air flow through the upper pass is $\dot{m}_g = \dot{m}_a n_g / n_t$, where n_g is the number of tubes in the first row of the upper pass and n_t is the total number of tubes in the first row of the upper and lower pass. The air mass flow rate across the tubes in the lower pass is $\dot{m}_d = \dot{m}_a n_d / n_t$, where n_d is the number of tubes in the first row of the lower pass. A discrete mathematical model, which defines the transient heat transfer was obtained using the control volume method. Figure 6a shows the division of the first pass (upper pass) into control volumes and Figure 6b the division of the second pass (lower pass).

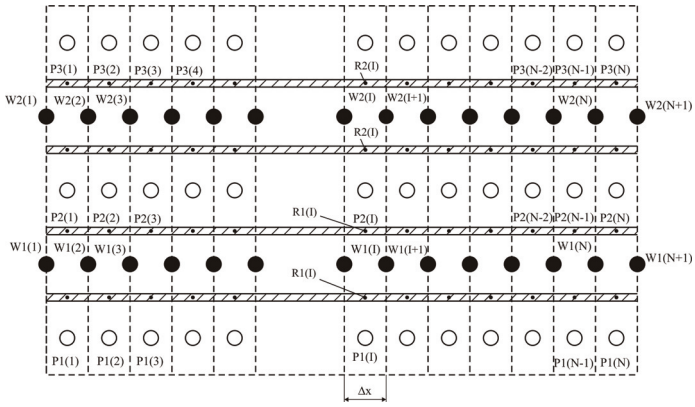

Fig. 6. Division of the first and second pass of the car radiator into control volumes; a) first pass, b) second pass, ◦ - air temperature, • - cooling liquid temperature

In order to increase the accuracy of the calculations, a staggered mesh will be applied. Liquid temperatures at the control volume nodes are denoted by W1(I) and W2(I) for the first and second rows of tubes, respectively. P1(I) denotes air temperature $T'_{g,i} = T'_{am}(t)$ in front of the radiator, P2(I) denotes air temperature $T''_{g,i}$ after the first row of tubes and P3(I) air temperature $T'''_{g,i}$ after the second row of tubes in the i -th control volume. The coolant temperature flowing through the first and second row, in the upper and lower pass, is a function of the coordinate x and time t, only. Temperatures $T'_{am}(t)$ and $T'''_{am}(t)$ denote the mean values of the radiator's inlet and outlet air temperatures, respectively. In order to determine transient temperature distribution of the water, tube wall and air, the finite difference method described in section 2.1 was used. For the analysis, the liquid temperature at the inlet to the first and second row of tubes in the upper pass was considered to be $T'_c(t)$ and $T_{cm}(t)$ in the lower pass. Using the notation shown in Figures 6a and 6b, the boundary conditions can be written in the following form

$$W1(1) = W2(1) = T'_1(t) = T'_2(t) = T'_c(t), \quad P1(I) = T'_{am}(t) = T'_{gm}(t) \quad I = 1,...,N \,. \tag{35}$$

The inlet air velocity w_0 and mass flow rate $\dot{m}_c$ are also functions of time. In the simulation program the time variations of: $T'_c(t)$, $T'_{am}(t)$, $w_0(t)$, and $\dot{m}_c(t)$ were interpolated using natural splines of the third degree.

The temperature $T_{cm}(t)$ is a temperature of the liquid at the outlet of the upper pass, where the liquid of temperature $W1(N+1)$ from the first row of tubes has been mixed with the liquid of temperature $W2(N+1)$ flowing out of the second row of tubes. In the case of the automotive radiator, temperature $T'_c(t)$ denotes the liquid temperature (of the engine coolant) at the inlet to the radiator whereas $T'_{am}(t)$ denotes air temperature in front of the radiator. Having determined the mean temperatures of the air T'''_{gm} and T'''_{dm} leaving the second row of tubes in the upper and lower pass, respectively, a mean temperature of the air behind the whole radiator $T'''_{am} = \left(n_g T'''_{gm} + n_d T'''_{dm} \right) / n_t$ was calculated. If the liquid and air temperatures are known, the heat transfer rate in the first and second rows of tubes in the upper and lower passes can be determined. The total heat transfer rate for the radiator was calculated using the formula $\dot{Q}_{chl} = \dot{m}_c \left[i_c(T'_c) - i_c(T''_c) \right] = \dot{m}_a \bar{c}_a \left(T'''_{am} - T'_{am} \right)$. The symbols i_c and $\bar{c}_a$ denote the water enthalpy and air mean specific capacity, respectively. The numerical model of the heat exchanger described briefly above is used to simulate its transient operation. Before starting transient simulation, the steady-state temperature distribution of water, tube wall and air was calculated using the steady-state mathematical model of the heat exchanger presented in (Taler, 2002; Taler, 2009).

5. Experimental verification

In order to validate the developed model of the heat exchanger, an experimental test stand was built. The measurements were carried out in an open aerodynamic tunnel.

The experimental setup was designed to obtain heat transfer and pressure drop data from commercially available automotive radiators. The test facility follows the general guidelines presented in ASHRAE Standards 33-798 (ASHRAE, 1978) and 84-1991 (ANSI/ASHRAE, 1982). Air is forced through the open-loop wind tunnel by a variable speed centrifugal fan. The air flow passed the whole front cross-section of the radiator. A straightener was used to provide better flow distribution. Air temperature measurements were made with multipoint (nickel-chromium)-(nickel-aluminium) thermocouple grids (K type sheath thermocouple

grids). The thermocouples were individually calibrated. The 95% uncertainty of the thermocouples estimated during the isothermal test was ±0.3 K. The air flow was determined at two cross sections from measurement of the velocity pressure obtained by Pitot traverses (Taler, 2006b). Additionally, the air flow was measured by the averaging Pitot tube device. The uncertainty in the measured air mass flow rate is ±1.0%. The static pressure drop across the radiator was measured with the four-tap piezometer rings using a precision differential pressure transducer with the 95% uncertainty of the order of ±1 Pa. The hot water is pumped from the thermostatically controlled tank through the radiator by the centrifugal pump with a frequency inverter. Water flow rates were measured with a turbine flowmeter that was calibrated using a weighting tank. The 95% uncertainty in the flow measurement was of ±0.004 L/s. Water solution temperatures at the inlet and outlet of the radiator were measured with calibrated platinum resistance thermometers (Pt 100 sensors). The 95% uncertainty in the temperature measurement is about ±0.05 K. Liquid pressure at the inlet and outlet of the radiator was measured with temperature compensated piezo-resistive sensors with an uncertainty of ±0.5 kPa. A personal computer-based data-acquisition system was used to measure, store and interpret the data. The relative difference between the air-side and liquid-side heat transfer rate was less than 3%. Extensive heat transfer measurements under steady-state conditions were conducted to find the correlations for the air- and water-side Nusselt numbers, which enable the calculation of heat transfer coefficients. Based on 21 measurement series, the following correlations were identified

$$Nu_c = \frac{(\xi/8)(\mathrm{Re}_c - 33.6625)\mathrm{Pr}_c}{(1+34.9622\sqrt{(\xi/8)}\left(\mathrm{Pr}_c^{2/3}-1\right)}\left[1+\left(\frac{d_r}{L_{ch}}\right)^{2/3}\right], \tag{36}$$

$$Nu_a = 0.01285\,\mathrm{Re}_a^{1.0755}\,\mathrm{Pr}_a^{1/3}, \tag{37}$$

where the friction factor ξ is given by

$$\xi = \frac{1}{(1.82\log\mathrm{Re}_c - 1.64)^2} = \frac{1}{(0.79\ln\mathrm{Re}_c - 1.64)^2}.$$

The water-side Reynolds number $\mathrm{Re}_c = w_c\, d_r / \nu_c$ is based on the hydraulic diameter $d_r = 4A_w / P_w$, where A_w denotes inside cross section area of the oval tube. The hydraulic diameter for the investigated radiator is: $d_r = 7.06\cdot 10^{-3}$ mm.

The physical properties of air and water were approximated using simple functions. The effect of temperature-dependent properties is accounted for by evaluating all the properties at the mean temperature of air and water, respectively. The method of prediction of heat transfer correlations for compact heat exchangers is described in details in (Taler, 2005). Measurement results are shown in Fig. 7. Then, the transient response of the heat exchanger was analyzed. Using the measured values of: inlet water temperature T_c', inlet air temperature T_{am}', air velocity in front of the radiator w_0, and water volumetric flow rate $\dot{V}_c$, the water, tube wall and air temperatures are determined using the explicit finite difference method, presented in the section 2.1. The calculation results and their comparison with experimental data are shown in Fig. 8. The agreement between the calculated and measured water temperature at the outlet of the heat exchanger is very good. In the case of

the outlet air temperature larger differences between calculated and measured values are observed (Fig. 8).

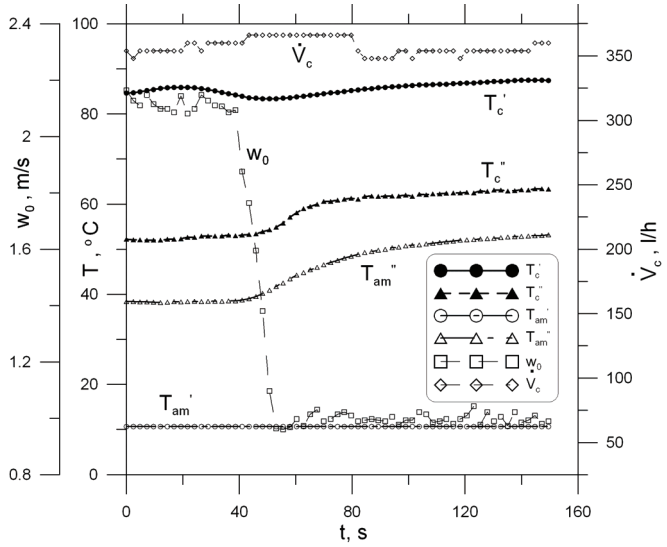

(a)

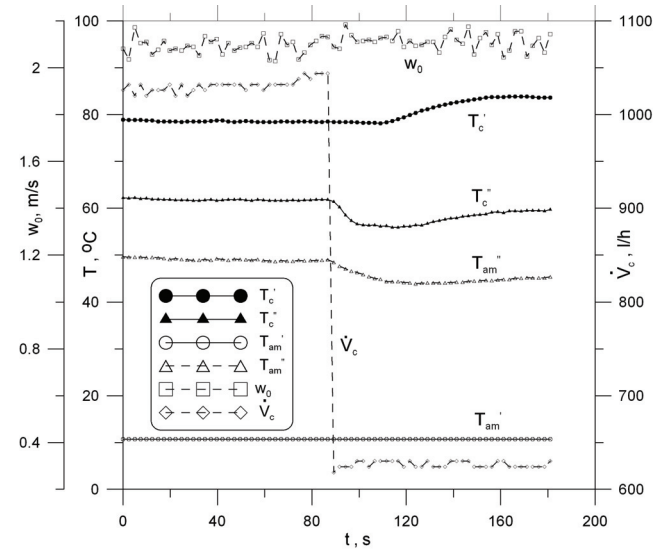

(b)

Fig. 7. Time variations of measured data: inlet water T_c' and air temperature T_{am}', respectively; outlet water T_c'' and air temperature T_{am}'', respectively; $\dot{V}_c$ - water mass flow rate, w_0 - air velocity before the heat exchanger

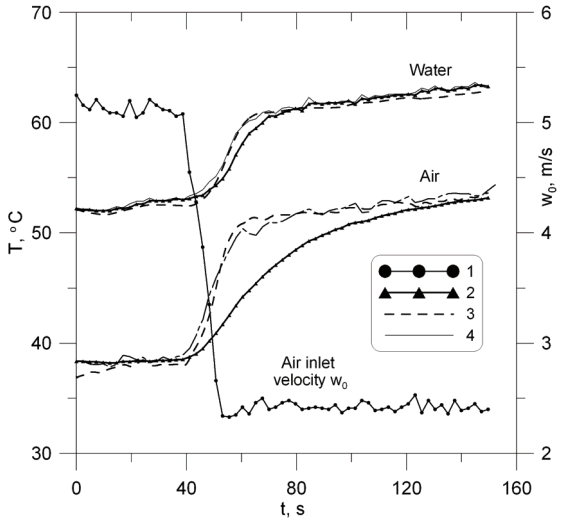

(a)

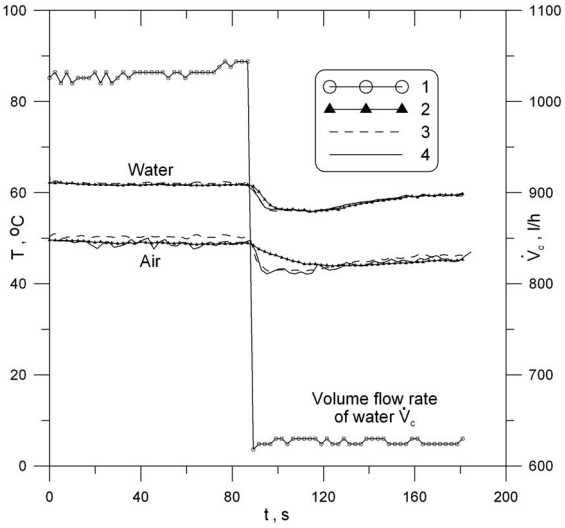

(b)

Fig. 8. Time variations of computed outlet water and air temperatures 1 - air velocity w_0 before the heat exchanger in Fig. a) and water volume flow rate $\dot{V}_c$ in Fig. b), 2 – outlet air and water temperatures indicated by thermocouples, 3 – computed air and water outlet temperatures, 4 – water and air outlet temperature calculated on the basis of measured value using the first order thermocouple model

This discrepancy is the result of damping and delay of air temperature changes by the sheath thermocouples of 1.5 mm diameter, used for the air temperature measurement. The

transient response of the thermocouple can be described by a simple first order differential equation

$$\tau_{th}\frac{dT_{th}}{dt}=T_f-T_{th}. \tag{38}$$

The symbols in equation (38) denote: T_f and T_{th} - fluid and thermocouple temperature, respectively, t - time, $\tau_{th}=m_{th}c_{th}/\left(h_{th}A_{th}\right)$ - time constant of the thermocouple, m_{th} - thermocouple mass, c_{th} - specific heat capacity of the thermocouple, h_{th} - heat transfer coefficient on the thermocouple surface, A_{th} - area of the outside surface of the thermocouple. Approximating time derivative in Eq. (38) by the central difference quotient and transforming Eq. (38) gives

$$T_f^n=T_{th}^n+\tau_{th}^n\frac{T_{th}^{n+1}-T_{th}^{n-1}}{2\Delta t_{th}}, \tag{39}$$

where the symbols in Eq. (39) stand for: $T_f^n=T_f\left(t\right)$, $T_{th}^n=T_{th}\left(t\right)$, $T_{th}^{n+1}=T_{th}\left(t+\Delta t_{th}\right)$, $T_{th}^{n-1}=T_{th}\left(t-\Delta t_{th}\right)$, Δt_{th} is the sampling time interval during temperature measurement by means of the data acquisition system. Taking into consideration that: τ_{th} = 20 s, Δt_{th} = 2.4 s, the air temperature is calculated using Eq. (39). An inspection of the results shown in Fig.8 indicates that the agreement between calculated and measured air temperature determined from Eq. (39) is very good. In the case of water temperature measurement, the time constant of the thermocouple is very small, since the heat transfer coefficient in the thermocouple surface is very high and the temperature indicated by the thermocouple and the real water temperature are very close.

6. Transient inverse heat transfer problem in control of plate fin and tube heat exchangers

In this section, a transient inverse heat transfer problem encountered in control of fluid temperature or heat transfer rate in a plate fin and tube heat exchanger was solved.

The water temperature $T_c''(t)$ at the outlet of the heat exchanger is known function of time. The problem to be solved is of great practical importance during start up and shut down processes of heat exchangers, internal combustion engines and in heating and ventilation systems. For example, the heat flow rate transferred from the internal combustion engine to cooling liquid is a function of time since it depends on the actual power of the engine, which in turn is a function of the car velocity and the slope of the road. Modern cooling systems are designed to maintain an even temperature at the outlet of the radiator despite of time dependent heat absorption by the engine coolant. This can be achieved by changing the fan rotating speed over time to keep the constant coolant temperature at the inlet of the engine. If the engine is operated at steady state conditions then its lifetime is much longer because thermal deformations and stresses are smaller.

The goal of the process control is to adjust the speed of fan rotation $n(t)$ in order that the water temperature $\left[T_c''(t)\right]^{cal}$ at the heat exchanger outlet is equal to a time-dependant target value (setpoint) $\left[T_c''(t)\right]^{set}$. The speed of rotation n is a function of time t and will be determined sequentially with a time step $\Delta t_B = t_M - t_{M-1}$. The method developed in the

paper can be easily extended to the control of heat flow rate transferred in the heat exchanger

$$\dot{Q}_c(t) = \dot{V}_c(t)\rho_c\left[T_c'(t)\right]\overline{c}_c\left[T_c'(t) - T_c''(t)\right], \tag{40}$$

where the symbols denote: $\dot{V}_c(t)$ - water volumetric flow rate at the heat exchanger inlet, ρ_c - water density, $\overline{c}_c$ - mean specific heat in the temperature range from $T_c''(t)$ to $T_c'(t)$. Solving equation (1) for $T_c''(t)$ gives

$$T_c''(t) = T_c'(t) - \frac{\dot{Q}_c(t)}{\dot{V}_c(t)\rho_c\left[T_c'(t)\right]\overline{c}_c}. \tag{41}$$

If the time changes of the heat flow rate $\dot{Q}_c(t)$ are prescribed as a function of time, then the inverse problem formulated with respect to the heat flow rate $\dot{Q}_c(t)$ is equivalent to the inverse problem formulated in terms of the water outlet temperature $T_c''(t)$.

6.1 Formulation of the inverse problem

The least squares method in conjunction with the first order regularization method are used for sequential determining the number of revolutions per minute

$$S(n_M) = \int_{t_{M-1}}^{t_{M+F}} \left[\left(T_{th,c}''\right)^{cal} - \left(T_{th,c}''\right)^{set} \right]^2 dt + w_r \left(\frac{dn}{dt}\Big|_{t=t_M} \right)^2 = \min, \tag{45}$$

where t is time, $\left(T_{th,c}''\right)^{cal}$ and $\left(T_{th,c}''\right)^{set}$ are the calculated and preset thermocouple temperature measuring water temperature at the outlet of the heat exchanger, w_r is the regularization parameter, and n denotes the speed of fan rotation. The sum (45) is minimized with respect to the number of fan revolutions per minute n_M at time t_M. Approximating the derivative in Eq. (45) by the forward difference quotient and the integral by the rectangle method gives

$$S(n_M) = \sum_{i=1}^{k_B(F+1)} \left\{ \left[T_{th,c}''(t_i)\right]^{cal} - \left[T_{th,c}''(t_i)\right]^{set} \right\}^2 + w_r \left(\frac{n_{M+F} - n_{M-1}}{t_{M+F} - t_{M-1}} \right)^2 = \min, \tag{46}$$

where (Fig. 1)

$$t_i = t_{M-1} + i\,\Delta t \;\;, i = 1,\ldots, k_B\,(F+1). \tag{47}$$

The symbol F denotes the number of future time intervals (Fig. 1). Future time steps are used to stabilize the inverse problem for small time steps. Since the outlet temperature changes $\left(T_{th,c}''\right)^{cal}$ are delayed with reference to the changes of the speed of fan rotation n, the time interval $t_M - t_{M-1}$ was artificially extended to the value: $t_{M+F} - t_{M-1}$.

The future time steps were introduced to the inverse analysis by Beck (Beck, 2003) in order to make it possible to determine the unknown parameters with higher frequency. At first, the searched number of fan revolutions n_M is assumed to be constant over the whole time

interval $t_{M+F} - t_{M-1}$. After determining n_M from Eq. (46), the time interval $t_{M+F} - t_M$ is rejected and the estimated parameter n_M is taken only for the basic time interval $t_M - t_{M-1}$. The estimation of n_{M+1} starts from the time point t_M .

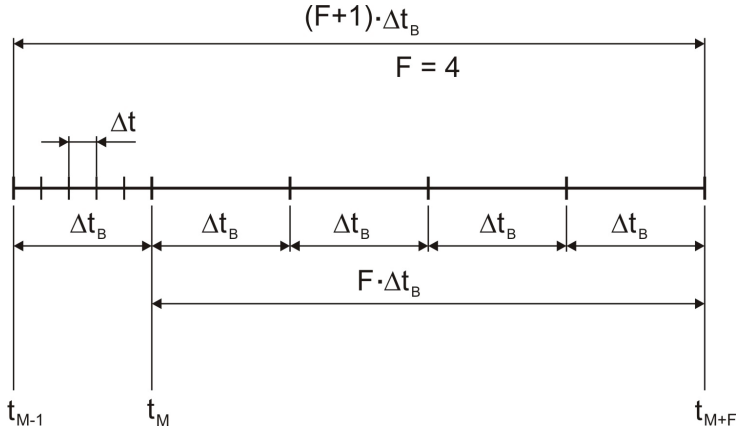

Fig. 9. Determination of speed of fan rotation n in the time interval $t_{M-1} \le t \le t_M$ using F future time intervals; Δt – time step in the finite difference method used in the mathematical model of the heat exchanger, $\Delta t_B = k_B \Delta t$ – basic time interval in the inverse analysis, F – number of future time intervals

The transient temperature of the thermocouple measuring the water temperature at the outlet of the heat exchanger $\left[T''_{th,c}(t_i)\right]^{cal}$ is calculated at every iteration step. The calculated thermocouple temperature $\left[T''_{th,c}(t_i)\right]^{cal}$ was determined from Eq. (38) using the explicit Euler method

$$\left[T''_{th,c}(t_i)\right]^{cal} = \left[T''_{th,c}(t_i - \Delta t_{th})\right]^{cal} + \left\{\left[T''_c(t_i - \Delta t_{th})\right]^{cal} - \left[T''_{th,c}(t_i - \Delta t_{th})\right]^{cal}\right\}\frac{\Delta t_{th}}{\tau_{th,c}}, \; n = 0,1,... \quad (48)$$

A finite difference model of the investigated cross-flow tube heat exchanger, which enables heat transfer simulation under transient condition has been developed in section 4. This model was used for calculating $\left[T''_c(t_i - \Delta t_{th})\right]^{cal}$. If the thermocouple time constant $\tau_{th,c}$ is small, then from Eq. (38) results that the thermocouple temperature $\left[T''_{th,c}(t_i)\right]^{cal}$ is equal the water temperature $\left[T''_c(t_i)\right]^{cal}$.

The initial temperature distributions of the both fluids $T_{c,0}(x^+)$, $T_{a,0}(x^+, y^+)$ and the wall $T_{w,0}(x^+)$ are known from measurements or from the steady-state calculations of the heat exchanger. The boundary conditions have the following form (Fig. 2)

$$T_c(x^+, t)\big|_{x^+=0} = T'_c(t), \quad (49)$$

$$T_a(x^+, y^+, t)\big|_{y^+=0} = T'_{am}(t), \quad (50)$$

where $T_c'(t)$ and $T_{am}'(t)$ are functions describing the variation of the inlet temperatures of the water and air in time. In section 4, similar equations with appropriate boundary and initial conditions were formulated for four rows of the two row heat exchanger with two passes and solved using an explicit finite difference method. The numerical model was validated by comparison of outlet water and air temperatures obtained from the numerical simulation with the experimental data. The discrepancy between numerical and experimental results was very small.

6.2 Results

In order to demonstrate the effectiveness of the method presented in the subsection 6.1, the water temperature $\left(T_c''\right)^{set}$ at the outlet of the automotive radiator for the spark-ignition combustion engine with a cubic capacity of 1580 cm^3 was prescribed

$$\left(T_c''\right)^{set} = 52.0 + \frac{77.0 - 52.0}{118.22}\, t\,,\ 0 \le t \le 118.22\,, \tag{51}$$

$$\left(T_c''\right)^{set} = 77.0 - \frac{77.0 - 64.0}{31.36}\left(t - 118.22\right),\ 118.22 \le t \le 150.0\,, \tag{52}$$

where $\left(T_c''\right)^{set}$ is in °C and t is time in s.

The radiator consists of aluminium tubes of oval cross-section. The cooling liquid flows in parallel through both tube rows. Fig. 5 shows a diagram of the two-pass cross-flow radiator with two rows of tubes. The time changes of the water volumetric flow rate $\dot{V}_c$, air and water inlet temperatures T_{am}' and T_c' are shown in Fig. 7a.

The speed of fun rotation n and water outlet temperature $\left[T_c''(t)\right]^{cal}$ obtained from the solution of the inverse problem are also shown in Fig. 10. The air velocity w_0 was calculated using the simple experimental correlation

$$w_o = 0.001566 \cdot n - 0.0551, \quad 250 \le n \le 1440 \tag{53}$$

where w_0 is expressed in m/s and n in number of revolutions per minute (rpm).

The proposed method works very well, since the calculated water outlet temperature $\left[T_c''(t)\right]^{cal}$ and the preset temperature $\left[T_c''(t)\right]^{set}$ coincide (Fig. 10).

In order to validate the developed inverse procedure, an experimental test stand was built. The measurements were carried out in an open aerodynamic tunnel which is presented in section 5. The experimental setup was designed to obtain heat transfer and pressure drop data from commercially available automotive radiators.

The experimental results for sudden decrease in air velocity w_0 are shown in Fig. 7a. The water and air inlet temperatures $T_c'(t)$ and $T_{am}'(t)$, water volumetric flow rate $\dot{V}_c(t)$, and temperature of the thermometer measuring the water temperature at the outlet of the heat exchanger $\left[T_{th,c}''(t)\right]^{set} = T_{th,c}''(t)$ were used as the input data for the inverse analysis. The sampling time interval was Δt = 2.4 s. The data acquisition readings were interpolated using cubic splines. The solutions of the inverse problem and their comparison with experimental data are shown in Fig. 11.

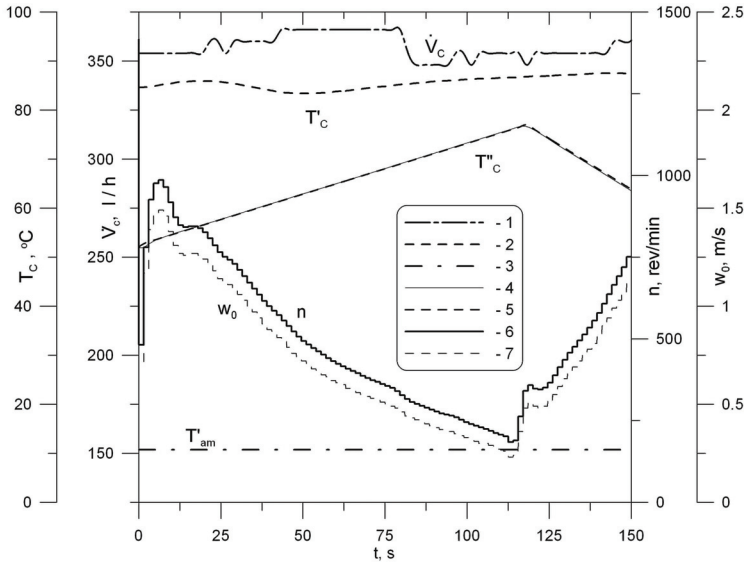

Fig. 10. Speed of fan rotation n (number of revolutions per minute), for which the calculated temperature $\left[T_c''(t)\right]^{cal}$ at the outlet of the heat exchanger is equal to preset temperature ; Δt = 0.05 s, k_B = 30, F = 2, w_r = 0; 1 – $\dot{V}_c$ - water mass flow rate at the inlet of the heat exchanger, 2 – T_c'' - water temperature at the inlet of the heat exchanger, 3 – T'_{am} - air temperature before the heat exchanger, 4 – calculated water temperature $\left[T_c''(t)\right]^{cal}$ obtained from the inverse solution, 5 – preset water temperature $\left[T_c''(t)\right]^{set}$ at the outlet of the heat exchanger, 6 – speed of fan rotation n determined from the inverse solution, 7 – air velocity before the heat exchanger based on the inverse solution for n

Despite different basic time intervals Δt_B and different number of future time intervals F very similar results are obtained (Fig. 11a and 11b). The agreement between the calculated and measured water temperature at the outlet of the heat exchanger is excellent.

7. Conclusions

The numerical models of cross-flow tube heat exchangers, which enable heat transfer simulation under transient condition were developed. First, the transient temperature distributions of fluids and tube wall in the one row tubular cross flow heat exchanger was determined using the finite difference method and the Laplace transform method. The results achieved by both methods were in good agreement. Then, the numerical model of the two row heat exchanger with two passes was presented. The numerical model was validated by comparison of outlet water and air temperatures obtained from the numerical simulation with the experimental data. The discrepancy between numerical and experimental results is very small.

In addition, a transient inverse heat transfer problem encountered in control of fluid temperature or heat transfer rate in a plate fin and tube heat exchanger was solved. The objective of the process control is to adjust the speed of fan rotation, measured in number of

fan revolutions per minute, so that the water temperature at the heat exchanger outlet is equal to a time-dependant target value (setpoint). The least squares method in conjunction with the first order regularization method was used for sequential determining the number of revolutions per minute. Future time steps are used to stabilize the inverse problem for small time steps. The transient temperature of the water at the outlet of the heat exchanger was calculated at every iteration step using a numerical mathematical model of the heat exchanger. The obtained solution, that is the speed of fan rotation, is very stable because of using future time steps and the first order regularization.

The method for solving the inverse problem developed in the paper was validated by comparing the calculated and measured number of fan revolutions per minute. The discrepancies between the calculated and measured revolution numbers are small.

The inverse method presented in the paper can be used for the solution of the inverse problems encountered in control of heat exchangers.

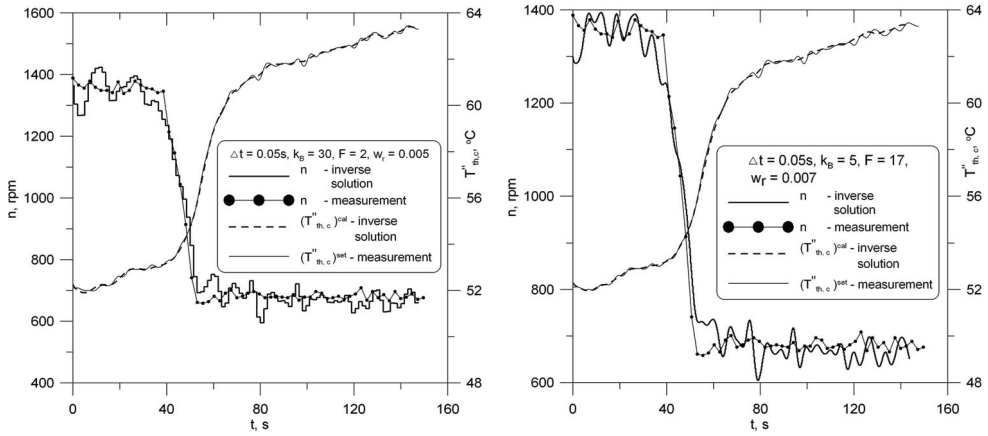

(a) (b)

Fig. 11. Speed of fan rotation n (number of revolutions per minute), for which the calculated temperature $\left[T''_{th,c}(t_i)\right]^{cal}$ at the outlet of the heat exchanger is equal to measured temperature $\left[T''_{th,c}(t_i)\right]^{set}$; a) $\Delta t = 0.05$ s, $k_B = 30$, $F = 2$, $w_r = 0.005$ $K^2s^2\,\mathrm{min}^2/rev^2$, b) $\Delta t = 0.05$ s , $k_B = 5$, $F = 17$, $w_r = 0.007$ $K^2s^2\,\mathrm{min}^2/rev^2$

8. References

ANSI/ASHRAE 84-1991. (1992). *Method of Testing Air-to-Air Heat Exchangers*. American Society of Heating, Refrigerating and Air-Conditioning Engineers, Inc., 1791 Tullie Circle, NE, Atlanta GA 30329, USA

ASHRAE Standard 33-798. (1978). *Methods of testing forced circulation air cooling and air heating coils.* American Society of Heating, Refrigerating and Air-Conditioning Engineers, Inc., Atlanta, USA

Beck, J. (2003). Sequential methods in parameter estimation, In: *Inverse Engineering Handbook*, Woodbury, K. A., (Ed.), 1-40, ISBN:0-8493-0861-5, CRC Press, Boca Raton, USA

Crump, K. S. (1976). Numerical inversion of Laplace transforms using a Fourier series approximation. *Journal of the Association of Computing Machinery*, Vol. 23, No. 1, 89-96, ISSN: 0004-5411

De Hoog, F. R.; Knight, J. H. & Stokes, A. N. (1982). An improved method for the numerical inversion of Laplace transforms. *SIAM Journal on Scientific and Statistical Computing*, Vol. 3, 357-366, ISSN: 0196-5204

Hesselgreaves, J. E. (2001) *Compact Heat Exchangers, Selection, Design and Operation*, Elsevier-Pergamon , ISBN: 0-08-042839-8, Oxford

Kraus A. D., Aziz A. & Welty J. (2001). *Extended Surface Heat Transfer*, Wiley & Sons, ISBN 0-471-39550-1, New York

Li, C.,H. (1986). Exact transient solutions of parallel-current transfer processes. *ASME Journal of Heat Transfer*, Vol. 108, 365-369, ISSN:0022-1481

Press, W. H.; Teukolsky, S. A., Vettering, W. T. & Flannery, B. P. (2006) *Numerical Recipes, The Art of Scientific Computing*. Second Edition, Cambridge University Press, ISBN: 0-521-43064-X, New York, USA

Roetzel, W. & Xuan, Y. (1998). *Dynamic behaviour of heat exchangers* , WIT Press/ Computational Mechanics Publications, ISBN: 1-85312-506-7, Southampton, UK.

Smith, E.,M. (1997): Thermal Design of Heat Exchanger, John Wiley & Sons, ISBN: 0-471-96566-9, Chichester, UK

Taler, D. (2002*). Theoretical and Experimental Analysis of Heat Exchangers with Extended Surfaces,* Vol. 25, Monograph 3, Polish Academy of Sciences Cracow Branch, ISBN: 83-915470-1-9, Cracow

Taler, D. & Cebula, A. (2004). Modeling of air flow and heat transfer in compact heat exchangers. *Chemical and Process Engineering*, Vol. 25, No. 4, 2331-2342, PL ISSN: 0208-6425 (in Polish)

Taler, D. (2004). Determination of heat transfer correlations for plate-fin-and-tube heat exchangers. *Heat and Mass Transfer*, Vol. 40, 809-822, ISSN: 0947-7411

Taler, D. (2005). Prediction of heat transfer correlations for compact heat exchangers. *Forschung im Ingenieurwesen* (*Engineering Research*), Vol. 69, No. 3, 137-150, ISSN 0015-7899

Taler, D. (2006a). *Dynamic response of a cross-flow tube heat exchanger*, Chemical and Process Engineering, Vol. 27, No. 3/2 , 1053-1071, PL ISSN 0208-64-25

Taler, D. (2006b). *Measurement of Pressure, Velocity and Flow Rate of Fluid*, ISBN 83-7464-037-5, AGH University of Science and Technology Press, Cracow, Poland (in Polish)

Taler, D. (2007). *Numerical and experimental analysis of transient heat transfer in compact tube-in-plate heat exchangers*, Proceedings of the XIII Conference on Heat and Mass Transfer, Koszalin-Darłówko, Vol. II, pp. 999-1008, ISBN 978-83-7365-128-9, September 2007, Publishing House of Koszalin University of Technology, Koszalin, Poland

Taler, D. (2008). Transient inverse heat transfer problem in control of plate fin and tube heat exchangers. *Archives of Thermodynamics*, Vol. 29, No. 4, 185-194, ISSN: 1231-0956

Taler, D. (2009). *Dynamics of Tube Heat Exchangers*, Monograph 193, AGH University of Science and Technology Press, ISSN 0867-6631, Cracow, Poland (in Polish)

Tan, K. S. & Spinner, I.,H. (1984). Numerical methods of solution for continuous countercurrent processes in the nonsteady state. *AIChE Journal*, Vol. 30, 770-786, ISSN: 0947-7411

Wang, C.C., Lin, Y.T. & Lee, C. (2000). An airside correlation for plain fin-and-tube heat exchangers in wet conditions. *Int. J. Heat Mass Transfer*, Vol. 43, 1869-1872, ISSN: 0017-9310

Yeoh, G. H. & Tu, J. (2010). *Computational Techniques for Multi-Phase Flows*, Elsevier-Butterworth-Heinemann, ISBN 978-0-08046-733-7, Oxford, UK

4

Radiative Heat Transfer and Effective Transport Coefficients

Thomas Christen, Frank Kassubek, and Rudolf Gati
ABB Schweiz AG, Corporate Research
Segelhofstrasse 1, CH-5405 Baden-Dättwil
Switzerland

1. Introduction

Heat radiation refers to electromagnetic radiation emitted by thermally excited degrees of freedom of matter. If both the matter and the radiation field are at thermodynamic equilibrium, well-known relations from thermodynamics exist between the temperature T, the characteristic radiation frequency ν, the energy density $E^{(eq)}$, and the pressure $p_{\rm rad}$ of the radiation field. These are Wien's displacement law, $\nu = 5.88 \cdot 10^{10} T$ (ν in Hz and T in K), the caloric equation of state, $E^{(eq)} = 7.57 \cdot 10^{-16} T^4$ (in J/m^3), and the thermal (or thermodynamic) equation of state, $p_{\rm rad} = E^{(eq)}/3$. It is then straight-forward to derive the Stefan-Boltzmann law for the power emitted by a black body, $Q = 5.67 \cdot 10^{-8} T^4$ in units of W/m^2 (cf. Landau & Lifshitz (2005)). In typical applications, heat radiation is relevant in the frequency range of $10^{11} - 10^{16}$ Hz, including the upper part of the microwave band, the infrared, the visible light, and the lower part of the ultra-violet band.

In many cases, be it for engineering purposes like electric arc radiation modelling, or related fundamental scientific problems like in stellar physics, radiation is usually not at thermal equilibrium. The present chapter of this book aims to give a focused overview on the theory of radiative heat transfer, i.e., energy transport by heat radiation that can be in a general nonequilibrium state, while matter is at local thermodynamic equilibrium. With emphasis on models based on partial differential equations for the radiation energy density, heat flux, and (if necessary) higher order moments, we will particularly discuss a powerful method for the determination of effective transport coefficients, which has been recently developed by Christen & Kassubek (2009). General monographs on radiative transfer are given by Chandrasekhar (1960), Siegel & Howell (1992), and Modest (2003), to mention a few.

In Sect. 2 the basic definitions and equations for radiative heat transfer will be introduced. There are two equivalent descriptions of radiation, either in terms of the *specific radiation intensity* (or *radiance*), $I_\nu(\mathbf{x},\mathbf{\Omega},t)$, or the *photon distribution function*, $f_\nu(\mathbf{x},\mathbf{\Omega},t)$. Here, t, $\mathbf{x}$, ν, and $\mathbf{\Omega}$ denote time, position, frequency, and direction (normalized wave-vector), respectively. Frequency dependence will always be indicated by an index ν. The associated transport equations for I_ν and f_ν are named the *radiative transfer equation (RTE)* and the *Boltzmann transport equation (BTE)*, respectively. The number of photons in the volume element $d^3\mathbf{x}$ at position $\mathbf{x}$ and time t, in the frequency band $d\nu$ at ν, and in direction $\mathbf{\Omega}$ within the solid angle $d\mathbf{\Omega}$ equals $f_\nu(\mathbf{x},\mathbf{\Omega},t)\, d^3\mathbf{x}\, d\nu\, d\mathbf{\Omega}$. The intensity is then given by $I_\nu(\mathbf{x},\mathbf{\Omega},t) = ch\nu f_\nu$, where $h\nu$ is the photon energy, $h = 6.626 \cdot 10^{-34}$ Js is Planck's constant, and $c = 2.998 \cdot 10^8$ m/s is the

vacuum velocity of light (cf. Tien (1968)). I_ν is the energy current density per solid angle in direction $\mathbf{\Omega}$.

The RTE (or BTE) is an integro-differential equation for I_ν (or f_ν) in the 6-dimensional phase space corresponding to position, frequency, and direction, and describes the temporal change of I_ν (or f_ν) due to emission, absorption, and scattering by the matter. Finding an appropriate solution is generally a highly sophisticated task, and can be significantly impeded by a complicated frequency dependence of the radiation-matter interaction. Moreover, radiation problems in science and engineering often require a self-consistent solution of the coupled equations for radiation and matter. For instance, a treatment of radiation in hot gases or plasma involves, besides the RTE, the gas-dynamic balance equations for mass, momentum, and energy (or temperature). Despite of the huge progress in computational technologies, an exact solution of the complete set of coupled equations is still unfeasible, except for some especially simple cases. As a consequence, in the course of time a number of methods for approximate solutions of the RTE have been developed. In Sect. 3, we will therefore briefly discuss a selected list of important approximation concepts. Methods based on truncated moment expansions will be emphasized, and the need of a reliable closure method for the determination of the transport coefficients occurring in these equations will be motivated.

In Sect. 4 we will argue that a recently introduced approach for the closure based on entropy production rate is superior to other closures used up to date. The theory of radiation in thermal equilibrium dates back to seminal work by Planck (1906). In chapter 5 of his book Planck emphasizes that, in modern language, photons, unlike a normal gas of massive particles, do not interact among themselves, but interaction with matter is needed for a relaxation to the thermal equilibrium state. As is often the case in many applications of radiative transport, we will assume that the medium, be it condensed matter, gas, or plasma, is at local thermodynamic equilibrium (LTE) and can thus be described locally by thermodynamic quantities like temperature, chemical potential, and the same. It is then the equilibration process of the photon gas to this LTE state that determines the details of the heat transfer by radiation in the medium. As is well-known from thermodynamics, equilibration is related to entropy production, which plays an important role in understanding the behavior of nonequilibrium radiation (cf. Oxenius (1966) and Kröll (1967)). In fact, various authors have shown that the state of radiation is often related to optima of the entropy production rate. Whether the optimum is a maximum or a minimum, depends on the specific details of the system under consideration, particularly on convexity properties of the optimization problem, and particularly, the constraints. For instance, Essex (1984) has shown that the entropy production rate is minimal in a gray atmosphere in local radiative equilibrium. Later on Essex (1997) applied his approach also to neutrino radiation. Würfel & Ruppel (1985) and Kabelac (1994) discussed entropy production rate maximization by introducing an effective chemical potential of the photons, related to their interaction with matter. Santillan et al. (1998) showed that for a constraint of fixed radiation power, black bodies maximize the entropy production rate.

The underlying reason for the success of entropy production rate principles has been recognized already by Kohler (1948), who has shown that the stationary solution of the BTE that is linearized at the equilibrium distribution, generally satisfies a variational principle for the entropy production rate. Kohler's principle has been widely used to determine linear transport coefficients (cf. Ziman (1956) and refs. cited in Martyushev (2006)). The important property of the RTE (or the BTE for photons) is its linearity over the *whole* nonequilibrium range, provided the interaction with the LTE-medium consists of single-photon processes

only. This linearity is thus not an approximation as it was in Kohler's work, but holds for arbitrarily large deviations from thermal equilibrium of the photon gas. The absence of interaction between photons is thus the reason for the success of the concept beyond small deviations of f_ν from equilibrium. Consequently, the entropy production rate is the appropriate basis for the determination of the nonequilibrium distribution I_ν (or f_ν) and the effective transport coefficients for radiative heat transfer in the framework of a truncated moment expansion. In Sect. 5 the transports coefficients, i.e., the effective absorption constants and the Eddington factor, are calculated for some specific examples. A practical reason for using moment equations for modelling radiative transfer is the convenience of having a set of structurally similar equations for the simulation of the complete radiation-hydrodynamics problem. Both the hydrodynamic equations for matter and the moment equations for radiation are hyperbolic partial differential equations and can thus be solved on the same footing. Sect. 5.4 gives some remarks on the requirement of hyperbolicity. For numerical simulations boundary conditions must be specified, these will be discussed in Sect. 6. Finally, Sect. 7 will then provide some simulation results for a simplified example of electric arc radiation.

2. Basics of radiative heat transfer in matter

The radiation intensity, $I_\nu(\mathbf{\Omega})$, is governed by the radiative transfer equation (RTE),

$$\frac{1}{c}\partial_t I_\nu + \mathbf{\Omega}\cdot\nabla I_\nu = \kappa_\nu(B_\nu - I_\nu) + \sigma_\nu\left(\frac{1}{4\pi}\int_{S^2} d\tilde{\Omega}\, p_\nu(\Omega,\tilde{\Omega})\, I_\nu(\tilde{\Omega}) - I_\nu\right) \ , \tag{1}$$

which has to be solved in a spatial region defined by the physical problem under consideration. Phase coherence and interference effects are disregarded when considering thermal radiation, and we will also neglect polarization effects. The BTE is simply obtained by a replacement of I_ν by f_ν in the RTE. The left hand side gives the total rate of change of $I_\nu(\mathbf{\Omega})$, divided by c, along the propagation direction $\mathbf{\Omega}$. This change must be equal to the expression on the right hand side, which consists of a sum of specific source and sink terms due to the radiation-matter interaction. In the absence of any interaction, e.g., in vacuum, the right hand side vanishes, which describes the so-called (free) streaming limit associated with a radiation beam, or the ballistic propagation of the photons. In the presence of interaction, however, photons are generated by emission and annihilated by absorption, described by $\kappa_\nu B_\nu$ and $-\kappa_\nu I_\nu$, respectively. Here, B_ν is the Planck function for thermal equilibrium,

$$B_\nu = \frac{2h\nu^3}{c^2} n^{(eq)} \ , \tag{2}$$

where

$$n_\nu^{(eq)} = \frac{1}{\exp(h\nu/k_B T) - 1} \tag{3}$$

is the Bose-Einstein distribution for thermal equilibrium photons (cf. Landau & Lifshitz (2005)) with the Boltzmann constant $k_B = 1.381\cdot 10^{-23} J/K$ and the local temperature $T = T(\mathbf{x})$ of the LTE medium. The coefficient κ_ν is the macroscopic spectral absorption coefficient in units of 1/m, and is generally a sum of products of particle densities, absorption cross-sections, factors $[1 - \exp(-h\nu/k_B T)]$, and depends thus not only on frequency but also on the partial pressures of the present particle species and the temperature. Often, opacities referring to κ_ν/ρ are discussed in the literature, where ρ is the mass density of

the matter. The macroscopic κ_ν includes spontaneous as well as induced emission (cf. Tien (1968)). Additionally to inelastic absorption-emission processes, Eq. (1) includes elastic (or so-called coherent or conservative) scattering. Incoming photons of frequency ν from all directions $\tilde{\Omega}$ are scattered with probability $p_\nu(\mathbf{\Omega},\tilde{\mathbf{\Omega}})$ into direction $\mathbf{\Omega}$. It is assumed that the phase-function $p_\nu(\Omega,\tilde{\Omega})$ obeys symmetry relations associated with reciprocity, depends only on the cosine between the directions $\tilde{\mathbf{\Omega}}$ and $\mathbf{\Omega}$ (cf. Chandrasekhar (1960)), and is normalized, $(4\pi)^{-1}\int_{S^2} d\tilde{\Omega}\, p_\nu(\Omega,\tilde{\Omega}) = 1$. Here, the Ω-Integration extends over S^2, which denotes the unit sphere associated with the full solid angle. The strength of the scattering process is quantified by the spectral scattering coefficient σ_ν in units of 1/m. The ratio $\sigma_\nu/(\kappa_\nu+\sigma_\nu)$ gives the probability that a collision event is a scattering process, and is sometimes called the *(single-scattering) albedo*. The mean free path of the photons is the inverse of $\kappa_\nu+\sigma_\nu$.
Because the bracket proportional to σ_ν in Eq. (1) vanishes for $\mathbf{\Omega}$-independent I_ν, the RTE can be written in the simple form

$$\frac{1}{c}\partial_t I_\nu + \mathbf{\Omega}\cdot\nabla I_\nu = \mathcal{L}(B_\nu - I_\nu)\ , \tag{4}$$

where the linear, self-adjoint, positive semi-definite[1] operator $\mathcal{L}$ is defined by the right hand side of Eq. (1) and consists of an algebraic term and an integral term.
The RTE has to be solved with appropriate initial conditions, $I_\nu(\mathbf{x},\mathbf{\Omega},t=0)$, and boundary conditions on the surface of the spatial domain under consideration. Because the RTE is a first order differential equation, the determination of each ray requires the knowledge of $I_\nu(\mathbf{\Omega})$ on the domain surface and in directions $\mathbf{\Omega}$ pointing into the domain. The behavior of the boundary is characterized by the radiation it emits, and the way it reflects impinging radiation. If one denotes the emittance of the boundary at position $\mathbf{x_w}$ by $\epsilon(\mathbf{x_w})$, the reflectivity by $r(\mathbf{x_w})$, and the normal vector of the boundary surface by $\mathbf{n}(\mathbf{x_w})$, the boundary condition generally reads (cf. Modest (2003))

$$I_\nu(\mathbf{x_w},\mathbf{\Omega},t) = \epsilon(\mathbf{x_w})B_\nu(\mathbf{x_w}) + \int_{\mathbf{n}(\mathbf{x_w})\cdot\tilde{\mathbf{\Omega}}\le 0} d\tilde{\mathbf{\Omega}}\mid \mathbf{n}(\mathbf{x_w})\cdot\tilde{\mathbf{\Omega}}\mid r(\mathbf{x_w},\mathbf{\Omega},\tilde{\mathbf{\Omega}})I_\nu(\mathbf{x_w},\tilde{\mathbf{\Omega}},t)\ . \tag{5}$$

The integration runs over all $\tilde{\mathbf{\Omega}}$ associated with radiation coming from the bulk domain towards the surface, while $\mathbf{\Omega}$ is pointing into the domain. For a smooth surface where a normal vector $\mathbf{n}(\mathbf{x_w})$ can be defined, this solid angle corresponds to half of the sphere S^2. This boundary condition can be simplified for special limit cases. For instance, a black surface has $r=0$ and $\epsilon=1$, a diffusively reflecting surface has $r(\mathbf{x_w},\mathbf{\Omega},\tilde{\mathbf{\Omega}}) = r(\mathbf{x_w})/\pi$, and a specularly reflecting surface has $r(\mathbf{x_w},\mathbf{\Omega},\tilde{\mathbf{\Omega}}) \propto \delta(\mathbf{\Omega_s}-\tilde{\mathbf{\Omega}})$, where $\mathbf{\Omega_s} = \mathbf{\Omega} - 2(\mathbf{\Omega}\cdot\mathbf{n})\mathbf{n}$ is the direction from which the ray must hit the surface in order to travel into the direction of $\mathbf{\Omega}$ after specular reflection.
We conclude this section by listing the basic equations for the LTE matter to which radiation is coupled. In general, LTE implies that at each point in space, the caloric and thermodynamic equations of state are locally valid. The respective equations relate the specific energy $e = e(\rho,T)$ and the pressure $p = p(\rho,T)$ to the mass density ρ and the temperature T of the matter. The spatio-temporal dynamics of the thermodynamic variables and, if relevant, the flow velocity $\mathbf{u}$, is then given by the hydrodynamic balance equations for mass, momentum,

[1] Note that a negative eigenvalue would immediately lead to an instability.

and energy. For a single component (non-relativistic) medium

$$\partial_t \rho + \nabla \cdot (\rho \mathbf{u}) = \dot{\rho}, \tag{6}$$

$$\partial_t (\rho \mathbf{u}) + \nabla \cdot \mathbf{\Pi}_{\mathrm{mat}} = \mathbf{f}, \tag{7}$$

$$\partial_t (\rho e_{\mathrm{tot}}) + \nabla \cdot \mathbf{j_e} = W, \tag{8}$$

where $\mathbf{\Pi}_{\mathrm{mat}}$, $\mathbf{j_e}$, and $e_{\mathrm{tot}} = e + \mathbf{u}^2/2$ are the momentum stress tensor, the energy flow density, and the total energy density. Together with the equations of state, Eqs. (6)-(8) constitute seven equations for the seven variables ρ, p, T, e, and $\mathbf{u}$. The right hand sides, $\dot{\rho}$, $\mathbf{f}$, and W are the mass source density, the force density, and the heat power density, respectively. The effect of radiation on matter may occur in these three source terms. For instance, a mass source may appear at a solid wall due to ablation by radiation (see, e.g. Christen (2007)), and the radiation pressure may act as a force (cf. Mihalas & Mihalas (1984)). These two effects are often negligible in engineering applications or are important only in special cases, like ablation arcs as discussed by Seeger et al. (2006). However, the heat exchange described by W can in general not be disregarded, and will play an important role in the theory below. The back-coupling of the matter on radiation, as mentioned before, occurs in the expressions on the right hand side of Eq. (1), which depend generally on ρ (or p) and T. An extensive monograph on radiation hydrodynamics is provided by Mihalas & Mihalas (1984), and a short introduction that fits well to the present chapter is given by the lecture notes of Pomraning (1982).

3. Approximation methods

The extreme difficulties to solve the RTE exactly for real systems caused the development of various approximation methods. There are two additional reasons for the use of approximations. First, in many cases the behavior of the matter is of interest, while it is sufficient to consider the radiation as a means of (nonlocal) interaction; hence only the radiative heat flux is needed, which enters the power balance equation for the matter via the heat power density W. As W equals the negative divergence of the radiation energy flux density, a radiation model would be convenient that is confined to this flux and to the lower order moments, which is here a single one, namely the radiation energy density. Secondly, radiation often behaves in two different specific ways. In a transparent medium absorption and scattering are weak, and radiation propagates as beams; full absence of interaction with matter refers to the so-called *free streaming limit*. In an opaque medium, on the other hand, absorption, emission and/or scattering is strong, and the radiation diffuses isotropically. In the extreme diffusive limit the *Rosseland diffusion approximation* applies, where radiative transfer is modelled by an effective heat conductivity of the matter (cf. Siegel & Howell (1992)) given by $16\sigma_{SB}T^3/3\sigma_F^{(\mathrm{eff})}$. Here $\sigma_{SB} = 2\pi^5 k_B^4/15h^3c^2 = 5.67 \cdot 10^{-8}\,\mathrm{W/m^2K^4}$ is the Stefan-Boltzmann constant and $\sigma_F^{(\mathrm{eff})}$ is the Rosseland mean absorption to be discussed later. For the two behaviors a ballistic (beam-like) and a diffusive description, respectively, are the appropriate 'zero order' models with effective transport coefficients, and deviations from the limits may be treated by corrections. Models based on one of these two limit cases can strongly reduce the computational effort. However, in many real systems radiative transfer is in between these limits such that more sophisticated methods must be involved.

In the following, a short list of some relevant approximation methods is given. The selection is not complete, as other approaches exist, like ray tracing and radiosity-irradiosity methods (Rey (2006)), or some rather heuristic methods like the $P_{1/3}$-approximation discussed by

Olson et al. (2000) and Simmons & Mihalas (2000). Furthermore, we will not discuss the issue of discretization methods concerning position space like finite differences, volumes, or elements; although this field would require special recognition (cf. Arridge et al. (2000) and Refs. cited therein), it is beyond the purpose of this chapter. Needless to say that there is not a unique best method, but every approach has its advantages and disadvantages for practical use, and the appropriate choice depends usually on the problem under consideration. Exhaustive overviews can be found, e.g., in Duderstadt & Martin (1979), Siegel & Howell (1992) and literature cited in the following three subsections. Subsequently, we will then focus in subsection 3.4 on approximations based on moment expansions, and particularly on the closure of the moment equations that will be discussed in Sect. 4.

3.1 Net emission

The *net emission approximation* is probably the most simplistic radiation model. It assumes a semi-empirical function $W(T,p,\boldsymbol{\zeta})$ in Eq. (8). Additionally to temperature and pressure, it depends on parameters $\boldsymbol{\zeta}$ of the radiating object. It is sometimes used, for instance, in computational fluid dynamics simulations of electrical arcs (cf. Lowke (1970), Zhang et al. (1987), Seeger et al. (2006)), where the only additional parameter ζ is the arc radius. Although such a description is very convenient in numerical simulations and sometimes even provides useful results, it is obviously oversimplifying and without any rigor. Furthermore, reliable accuracy requires, for the determination of the function $W(T,p,\zeta)$, a parameter study based on a more fundamental radiation model or on elaborate experiments.

3.2 Monte Carlo

Monte Carlo simulations refer to random sampling methods (see, for instance Yang et al. (1995) and Duderstadt & Martin (1979)), which are based on computer simulations of a number of photons. Their deterministic dynamics corresponds to the ballistic motion with speed of light. Emission, absorption, and scattering processes are simulated in a probabilistic way by appropriately determined random numbers for the various processes. Those include, of course, the interaction with boundaries of the spatial domain. Final results, like the radiation intensity, are determined by averages over many photon particles. The Monte Carlo concept is rather simple, which leads to a number of advantages of this method, as discussed by Yang et al. (1995). Efficient applications make use of specifically improved schemes like implicit Monte Carlo or special versions thereof (cf. Brooks & Fleck (1986) and Brooks et al. (2005)).

3.3 Discrete ordinates

The *discrete ordinates method* (*DOM*) considers a finite number of rays passing at every (discrete) space point. If a number N_D of direction vectors $\boldsymbol{\Omega}_k$, $k = 1,...,N_D$ is selected, one has $I_\nu = \Sigma_k I_\nu^{(k)} \delta(\boldsymbol{\Omega} - \boldsymbol{\Omega}_k)$, such that a set of N_D partially coupled RTE-equations for the different directions and frequencies must be solved. The right hand side of these equations, say $\tilde{\mathcal{L}}(B_\nu - I_\nu^{(k)})$, contains not an integral as Eq. (1) but a weighted sum. As reasonable values for N_D in 3-dimensional realistic geometries are at least of the order of 10, the computational effort is still large. For too small N_D an artifact called "ray effect" may occur, referring to spatial oscillations in the energy density. Another error known as "false scattering" or "false diffusion", is due to the discretization of position space and is linked in a certain way to the ray effect as discussed in Rey (2006).
Some further developments based on DOM exist, which make use of a decomposition and

discretization of the angular space into a finite set of directions, i.e. a finite partition of the unit sphere S^2. The methods of *partial characteristics* (Aubrecht & Lowke (1994)) and of *partial moments* (Frank et al. (2006)) are examples, the latter being mentioned again in the next section. Last but not least, we mention that it has been proven that the DOM is equivalent, under certain conditions, to the P-N method (cf. Barichello & Siewert (1998) and Cullen (2001)), which is a special kind of the moment approximations to be discussed in the next subsection.

3.4 Moment expansions

Radiation modelling in terms of moments of the distribution I_ν (or f_ν) is convenient because the radiation is coupled to the LTE matter in Eqs. (6)-(8) via the first three (angular) moments. Moment expansions can be formulated in a rather general manner (cf. Levermore (1996) and Struchtrup (1998)). In the following, we define moments based on I_ν by

$$E = \int_0^\infty d\nu\, E_\nu = \int_0^\infty d\nu \frac{1}{c} \int_{S^2} d\Omega\, I_\nu \ , \tag{9}$$

$$\mathbf{F} = \int_0^\infty d\nu\, \mathbf{F}_\nu = \int_0^\infty d\nu \frac{1}{c} \int_{S^2} d\Omega\, \mathbf{\Omega}\, I_\nu \ , \tag{10}$$

$$\mathbf{\Pi} = \int_0^\infty d\nu\, \mathbf{\Pi}_\nu = \int_0^\infty d\nu \frac{1}{c} \int_{S^2} d\Omega\, \mathbf{\Omega} : \mathbf{\Omega}\, I_\nu \ , \tag{11}$$

$$\ldots = \ldots \ ,$$

with $(\mathbf{\Omega} : \mathbf{\Omega})_{kl} = \Omega_k \Omega_l$. The last line indicates that an infinite number of moments exist in general. E_ν, $\mathbf{F}_\nu$, and $\mathbf{\Pi}_\nu$ are, respectively, the monochromatic energy density, radiative flux, and stress (or pressure) tensor of the radiation. For convenience, the prefactor (c^{-1}) is chosen in all definitions such that the moments have the same units of a spectral energy density. Similarly, E, $\mathbf{F}$, and $\mathbf{\Pi}$ are the spectrally integrated energy density, radiative flux, and pressure tensor. In the present units $F = \mid \mathbf{F} \mid$ has the meaning of energy density associated with the average directed motion of the photons, and E of the total energy density composed of directed and thermal fluctuation parts. Hence, $F \leq \mid E \mid$, which will be important below.
In thermal equilibrium all fluxes vanish. Then $\mathbf{F}_\nu = 0$, the stress tensor is proportional to the unit tensor with diagonal elements $E^{(eq)}/3$, and the energy density is given by

$$E^{(eq)} = \int_0^\infty 4\pi\, d\nu\, B_\nu = \frac{4\sigma_{SB}}{c} T^4 \ . \tag{12}$$

The purpose of a moment expansion is to derive from the RTE or BTE balance equations for the moments, either for each frequency ν, or for groups of frequencies or frequency bands, or for the full, integrated spectral range. Multiplication of the RTE with products and/or powers of Ω_k's, and integration over the solid angle gives for the moments E_ν, $\mathbf{F}_\nu$, etc.

$$\frac{1}{c}\partial_t E_\nu + \nabla \cdot \mathbf{F}_\nu = \frac{1}{c} \int_{S^2} d\Omega\, \mathcal{L}(B_\nu - I_\nu) \ , \tag{13}$$

$$\frac{1}{c}\partial_t \mathbf{F}_\nu + \nabla \cdot \mathbf{\Pi}_\nu = \frac{1}{c} \int_{S^2} d\Omega\, \mathbf{\Omega}\, \mathcal{L}(B_\nu - I_\nu) \ , \tag{14}$$

etc., where only the first two equations are listed for convenience, but the list still contains an infinite number for all moments and for all frequencies. Practical usability calls then for a two-fold approximation. First, the list of moments, and thus moment equations, should be truncated by considering only the N first moment equations. Secondly, the frequency space

should be discretized or partitioned in some way, in order to end up with a finite set. If the spectrum allows a division into a number of well defined frequency bands with approximately constant κ_ν and σ_ν, or a grouping of different frequencies together according to similar values of κ_ν and σ_ν, one can average the equations over such partitions. The associated methods are sometimes named multi-group, multi-band, or multi-bin methods. For details, we refer the reader to Turpault (2005), Ripoll & Wray (2008), Nordborg & Iordanidis (2008), and the literature cited therein. In the following we will consider the equations for the spectrally averaged quantities, which are obtained by integration of Eqs. (13), (14), etc., over frequency

$$\frac{1}{c}\partial_t E + \nabla \cdot \mathbf{F} = P_E = \frac{1}{c}\int_0^\infty d\nu \int_{S^2} d\Omega\, \mathcal{L}(B_\nu - I_\nu) \ , \tag{15}$$

$$\frac{1}{c}\partial_t \mathbf{F} + \nabla \cdot \mathbf{\Pi} = \mathbf{P_F} = \frac{1}{c}\int_0^\infty d\nu \int_{S^2} d\Omega \ , \mathbf{\Omega}\, \mathcal{L}(B_\nu - I_\nu), \tag{16}$$

etc., where the right hand sides define P_E and $\mathbf{P_F}$, etc. These quantities are still functionals of the unknown function I_ν. All moments, on the other hand, are variables that are determined by the full (still infinite) set of partial differential equations, provided reasonable initial and boundary conditions are given.

Now we perform a truncation by using only the first N moment equations. The first N moments would then be determined by the solution of these equations, if the right hand sides (P_E, $\mathbf{P_F}$, etc) and the $N+1$'th moment were known. In the following section we will discuss closure methods that determine these unknowns, which are supposed to be functions of the N moments. Prior, however, we remark that instead of using products of Cartesian coordinates of $\mathbf{\Omega}$, one may equivalently consider a representation in terms of spherical coordinates (θ, ϕ). The radiation density is then expanded in spherical harmonics $Y_l^m(\theta, \phi)$. If truncated, this approximation corresponds to the P-N approximation (cf. Siegel & Howell (1992)). The prominent P-1 approximation (cf. Siegel & Howell (1992)), for instance, refers to a truncation of the Eqs. (13) and (14) (or Eqs. (15) and (16)) after the second equation and considers an isotropic Π_ν (or Π) with diagonal elements equal to $E_\nu/3$ (or $E/3$).

We also mention again the partial moment approximation (cf. Frank et al. (2006)), where the approaches of DOM and moment expansion are combined in a smart way. As the DOM discretizes the angular space in different directions, the partial moment method selects partitions $\mathcal{A}$ of the unit sphere S^2 and defines partial moments $E_\nu^{(\mathcal{A})}$, $\mathbf{F}_\nu^{(\mathcal{A})}$, $\mathbf{\Pi}_\nu^{(\mathcal{A})}$, etc , where the solid angle integration is performed only over $\mathcal{A}$ instead of the whole S^2. The most simple but nontrivial partial moment model refers to the forward and backward traveling waves in a one-dimensional position space, where the integration occurs over the two half-spheres associated with forward and backward directions. According to Frank (2007), this method has several advantages, e.g., it is able to resolve a shock-wave artifact occurring for counter-propagating and interpenetrating radiation beams.

4. Closure approaches

The quality of the moment approximation depends on the number of moments taken into account, and on the specific closure concept. A closure of a truncated moment expansion requires in principle knowledge of I_ν. A simplification occurs if κ_ν, σ_ν, and p_ν are assumed to be constant (gray matter). The right hand sides of the moment equations strongly simplify as they can be directly expressed in terms of these constants and linear expressions of the moments. But in general matter is non-gray, and the absorption and scattering spectra can be extremely complex. Furthermore, the $N+1$'th moment remains still unknown even for gray

matter. In the sequel we will discuss a few practically relevant closure methods. We will then argue that the preferred closure is given by an entropy production principle.
For clarity we will consider the two-moment example; generalization to an arbitrary number of moments is straight-forward. The appropriate number of moments is influenced by the geometry and the optical density of the matter. For symmetric geometries, like plane, cylindrical, or spherical symmetry, less moments are needed than for complex arrangements with shadowing corners, slits, and the same. For optically dense matter, the photons behave diffusive, which can be modelled well by a low number of moments, as will be discussed below. For transparent media, beams, or even several beams that might cross and interpenetrate, may occur, which makes higher order or multipole moments necessary.

4.1 Two-moment example

The unknowns are P_E, $\mathbf{P_F}$, and $\mathbf{\Pi}$, which may be functions of the two moments E and $\mathbf{F}$. For convenience, we will write

$$P_E = \kappa_{\mathrm{E}}^{(\mathrm{eff})}(E^{(eq)} - E) \ , \tag{17}$$

$$\mathbf{P_F} = -\kappa_{\mathrm{F}}^{(\mathrm{eff})}\mathbf{F} \ , \tag{18}$$

where we introduced the effective absorption coefficients $\kappa_{\mathrm{E}}^{(\mathrm{eff})}$ and $\kappa_{\mathrm{F}}^{(\mathrm{eff})}$ that are generally functions of E and $\mathbf{F}$. Because the second rank tensor $\mathbf{\Pi}$ depends only on the scalar E and the vector $\mathbf{F}$, by symmetry reason it can be written in the form

$$\Pi_{nm} = E\left(\frac{1-\chi}{2}\delta_{nm} + \frac{3\chi-1}{2}\frac{F_n F_m}{F^2}\right) \ , \tag{19}$$

where the *variable Eddington factor (VEF)* χ is a function of E and $\mathbf{F}$ and where $\delta_{kl}(=0$ if $k \neq l$ and $\delta_{kl}=1$ if $k=l)$ is the Kronecker delta. Assuming that the underlying matter is isotropic, $\kappa_E^{(\mathrm{eff})}$, $\kappa_F^{(\mathrm{eff})}$, and χ can be expressed as functions of E and

$$v = \frac{F}{E} \tag{20}$$

with $F = \mid \mathbf{F} \mid$. Obviously it holds $0 \leq v \leq 1$, with $v = 1$ corresponding to a fully directed radiation beam (free streaming limit). According to Pomraning (1982), the additional E-dependence of suggested or derived VEFs often appears via an effective E-dependent single scattering albedo, which equals, e.g. for gray matter, $(\kappa E^{(eq)} + \sigma E)/(\kappa + \sigma)E$.
The task of a closure is to determine the *effective transport coefficients*, i.e., *effective mean absorption coefficients* $\kappa_E^{(\mathrm{eff})}$, $\kappa_F^{(\mathrm{eff})}$, and the VEF χ as functions of E and F (or v). This task is of high relevance in various scientific fields, from terrestrial atmosphere physics and astrophysics to engineering plasma physics.

4.2 Exact limits and interpolations

In limit cases of strongly opaque and strongly transparent matter, analytical expressions for the effective absorption coefficients are often used, which can be determined in principle from basic gas properties (see, e.g., AbuRomia & Tien (1967) and Fuss & Hamins (2002)). In an optically dense medium radiation behaves diffusive and isotropic, and is near equilibrium with respect to LTE-matter. The effective absorption coefficients are given by the so-called

Rosseland average or *Rosseland mean* (cf. Siegel & Howell (1992))

$$\kappa_E^{(\mathrm{eff})} = \langle \kappa_\nu \rangle_{\mathrm{Ro}} := \frac{\int_0^\infty d\nu\, \nu^4 \partial_\nu n_\nu^{(eq)}}{\int_0^\infty d\nu\, \nu^4 \kappa_\nu^{-1} \partial_\nu n_\nu^{(eq)}} \ , \tag{21}$$

where ∂_ν denotes differentiation with respect to frequency, and

$$\kappa_F^{(\mathrm{eff})} = \langle \kappa_\nu + \sigma_\nu \rangle_{\mathrm{Ro}} \ . \tag{22}$$

The Rosseland mean is an average of inverse rates, i.e., of scattering times, and must thus be associated with consecutive processes. A hand-waving explanation is based on the strong mixing between different frequency modes by the many absorption-emission processes in the optically dense medium due to the short photon mean free path.
Isotropy of $\mathbf{\Pi}$ implies for the Eddington factor $\chi = 1/3$. Indeed, because $\sum \Pi_{kk} = E$, one has then $\mathbf{\Pi}_{kl} = \delta_{kl} E/3$. With these stipulations, Eqs. (15) and (16) are completely defined and can be solved.
In a strongly scattering medium ($\sigma_\nu \gg \kappa_\nu$), where $\mathbf{F}$ relaxes quickly to its quasi-steady state, one may further assume $\mathbf{F} = -\nabla E/3\kappa_F^{(\mathrm{eff})}$ for appropriate time scales. Hence Eq. (15) becomes

$$\frac{1}{c}\partial_t E - \nabla \cdot \left(\frac{\nabla E}{3\kappa_F^{(\mathrm{eff})}} \right) = \kappa_E^{(\mathrm{eff})} (E^{(eq)} - E) \ , \tag{23}$$

which has the form of a reaction-diffusion equation. For engineering applications, E often relaxes much faster than all other hydrodynamic modes of the matter, such that the time derivative of Eq. (23) can be disregarded by assuming full quasi-steady state of the radiation. Equation (23) is then equivalent to an effective steady state gray-gas P-1 approximation.

For transparent media, in which the radiation beam interacts weakly with the matter, the Planck average is often used,

$$\langle \kappa_\nu \rangle_{\mathrm{Pl}} = \frac{\int_0^\infty d\nu\, \nu^3 \kappa_\nu n_\nu^{(eq)}}{\int_0^\infty d\nu\, \nu^3 n_\nu^{(eq)}} \ . \tag{24}$$

In contrast to the Rosseland mean, the Planck mean averages the rates and can thus be associated with parallel processes, because scattering is weak and there is low mixing between different frequency modes. In contrast to the Rosseland average, the Planck average is dominated by the largest values of the rates. Although in this case radiation is generally not isotropic, there are special cases where an isotropic $\mathbf{\Pi}$ can be justified; an example discussed below is the $v \to 0$ limit in the emission limit $E/E^{(eq)} \to 0$. But note that $\chi = 1$ often occurs in transparent media, and consideration of the VEF is necessary.

In the general case of intermediate situations between opaque and transparent media, heuristic interpolations between fully diffusive and beam radiation are sometimes performed. Effective absorption coefficients have been constructed heuristically by Patch (1967), or by Sampson (1965) by interpolating Rosseland and Planck averages.
The consideration of the correct stress tensor is even more relevant, because the simple $\chi = 1/3$ assumption can lead to the physical inconsistency $v > 1$. A common method to

solve this problem is the introduction of flux limiters in diffusion approximations, where the effective diffusion constant is assumed to be state-dependent (cf. Levermore & Pomraning (1981), Pomraning (1981), and Levermore (1984), and Refs. cited therein). A similar approach in the two-moment model is the use of a heuristically constructed VEF. A simple class of flux-limiting VEFs is given by

$$\chi = \frac{1+2v^j}{3} \ , \tag{25}$$

with positive j. These VEFs depend only on v, but not additionally separately on E. The cases $j = 1$ and $j = 2$ are attributed to Auer (1984) and Kershaw (1976), respectively. While the former strongly simplifies the moment equations by making them piecewise linear, the latter fits quite well to realistic Eddington factors, particularly for gray matter, but with the disadvantage of introducing numerical difficulties.

4.3 Maximum entropy closure

An often used closure is based on *entropy maximization* (cf. Minerbo (1978), Anile et al. (1991), Cernohorsky & Bludman (1994), and Ripoll et al. (2001)).[2] This closure considers the local radiation entropy as a functional of I_ν. The entropy of radiation is defined at each position $\mathbf{x}$ and is given by (cf. Landau & Lifshitz (2005), Oxenius (1966), and Kröll (1967))

$$S_{\mathrm{rad}}[I_\nu] = -k_B \int d\Omega\, d\nu \frac{2\nu^2}{c^3} \left(n_\nu \ln n_\nu - (1+n_\nu)\ln(1+n_\nu)\right), \tag{26}$$

where

$$n_\nu(\mathbf{x},\mathbf{\Omega}) = \frac{c^2 I_\nu}{2h\nu^3} \tag{27}$$

is the photon distribution for the state $(\nu,\mathbf{\Omega})$.[3] At equilibrium (27) is given by (3). I_ν is then determined by maximizing $S_{\mathrm{rad}}[I_\nu]$, subject to the constraints of fixed moments given by Eqs. (9), (10) etc. This provides I_ν as a function of ν, Ω, E and $\mathbf{F}$. If restricted to the two-moment approximation, the approach is sometimes called the M-1 closure. It is generally applicable to multigroup or multiband models (Cullen & Pomraning (1980), Ripoll (2004), Turpault (2005), Ripoll & Wray (2008)) and partial moments (Frank et al. (2006), Frank (2007)), as well as for an arbitrarily large number of (generalized) moments (Struchtrup (1998)). It is clear that this closure can equally be applied to particles obeying Fermi statistics (see Cernohorsky & Bludman (1994) and Anile et al. (2000)).

Advantages of the maximum entropy closure are the mathematical simplicity and the mitigation of fundamental physical inconsistencies (Levermore (1996) and Frank (2007)). In particular, there is a natural flux limitation by yielding a VEF with correct limit behavior in both isotropic radiation ($\chi \to 1/3$) and free streaming limit ($\chi \to 1$):

$$\chi_{\mathrm{ME}} = \frac{5}{3} - \frac{4}{3}\sqrt{1-\frac{3}{4}v^2} \tag{28}$$

that depends only on v. Furthermore, because the optimization problem is convex[4], the uniqueness of the solution is ensured and, as shown by Levermore (1996), the moment

[2] In part of the more mathematically oriented literature, the entropy is defined with different sign and the principle is called "minimum entropy closure".

[3] Note the simplified notation of a single integral symbol $\int$ in Eq. (26) and in the following, which is to be associated with full frequency and angular space.

[4] Convexity refers here to the mathematical entropy definition with a sign different from Eq. (26).

equations are hyperbolic, which is important because otherwise the radiation model would be physically meaningless. The main disadvantage is that the maximum entropy closure is unable to give the correct Rosseland mean in the near-equilibrium limit, and can thus not be correct. For example, for $\sigma_\nu \equiv 0$ the near-equilibrium effective absorption coefficients are given by (Struchtrup (1996))

$$\langle \kappa_\nu \rangle_{\mathrm{ME}} = \frac{\int_0^\infty d\nu\, \nu^4 \kappa_\nu \partial_\nu n_\nu^{(eq)}}{\int_0^\infty d\nu\, \nu^4 \partial_\nu n_\nu^{(eq)}} \ , \tag{29}$$

which is a Planck-like mean that averages κ_ν instead of averaging its inverse. It is only seemingly surprising that the maximum entropy closure is wrong even close to equilibrium. This closure concept must fail in general, as Kohler (1948) has proven that for the linearized BTE the *entropy production rate*, rather than the *entropy*, is the quantity that must be optimized. Both approaches lead of course to the correct equilibrium distribution. But the quantity responsible for transport is the first order deviation $\delta I_\nu = I_\nu - B_\nu$, which is determined by the entropy production and not by the entropy. Moreover, it is obvious that Eq. (26) is explicitly independent of the radiation-matter interaction. Consequently, the distribution resulting from entropy maximization cannot depend explicitly on the spectral details of κ_ν and σ_ν, which must be wrong in general. A critical discussion of the maximum entropy production closure was already given by Struchtrup (1998); he has shown that only a large number of moments generalized to higher powers in frequency up to order ν^4, are able to reproduce the correct result in the weak nonequilibrium case. Consequently, despite of its ostensible mathematical advantages, we propose to reject the maximum entropy closure for the moment expansion of radiative heat transfer. A physically superior method based on the entropy production rate will be discussed in the next subsection.

4.4 Minimum entropy production rate closure

As mentioned, Kohler (1948) has proven that a minimum entropy production rate principle holds for the linearized BTE. The application of this principle to moment expansions has been shown by Christen & Kassubek (2009) for the photon gas and by Christen (2010) for a gas of independent electrons. The formal procedure is fully analogous to the maximum entropy closure, but the functional to be minimized is in this case the *total entropy production rate*, which consist of two parts associated with the radiation field, i.e., the photon gas, and with the LTE matter. The latter acts as a thermal equilibrium bath. The two success factors of the application of this closure to radiative transfer are first that the RTE is linear not only near equilibrium but in the whole range of I_ν (or f_ν) values, and secondly that the entropy expression Eq. (26) is valid also far from equilibrium (cf. Landau & Lifshitz (2005)).

In order to derive the expression for the entropy production rate, $\dot{S}$, one can consider separately the two partial (and spatially local) rates $\dot{S}_{\mathrm{rad}}$ and $\dot{S}_{\mathrm{m}}$ of the radiation and the medium, respectively (cf. Struchtrup (1998)). $\dot{S}_{\mathrm{rad}}$ is obtained from the time-derivative of Eq. (26), use of Eq. (1), and writing the result in the form $\partial_t S_{\mathrm{rad}} + \nabla \cdot \mathbf{J}_S = \dot{S}_{\mathrm{rad}}$ with

$$\dot{S}_{\mathrm{rad}}[I_\nu] = -k_B \int d\nu\, d\Omega \frac{1}{h\nu} \ln\left(\frac{n_\nu}{1+n_\nu}\right) \mathcal{L}(B_\nu - I_\nu) \ , \tag{30}$$

where n_ν is given by Eq. (27). $\mathbf{J}_S$ is the entropy current density, which is not of further interest in the following. The entropy production rate of the LTE matter, $\dot{S}_{\mathrm{mat}}$, can be derived from the fact that the matter can be considered locally as an equilibrium bath with temperature $T(\mathbf{x})$.

Energy conservation implies that W in Eq. (8) is related to the radiation power density in Eq. (15) by $W = -P_E$. The entropy production rate (associated with radiation) in the local heat bath is thus $\dot{S}_{\rm mat} = W/T = -P_E/T$. Equation (3) implies $h\nu/k_BT = \ln(1+1/n_\nu^{(eq)})$, and one obtains

$$\dot{S}_{\rm mat}[I_\nu] = -k_B \int d\nu\, d\Omega \frac{1}{h\nu} \ln\left(\frac{1+n_\nu^{(eq)}}{n_\nu^{(eq)}}\right) \mathcal{L}(B_\nu - I_\nu) \ . \tag{31}$$

The total entropy production rate $\dot{S} = \dot{S}_{\rm rad} + \dot{S}_{\rm mat}$ is

$$\dot{S}[I_\nu] = \int_0^\infty d\nu\, \dot{S}_\nu = -k_B \int d\nu\, d\Omega \frac{1}{h\nu} \ln\left(\frac{n_\nu(1+n_\nu^{(eq)})}{n_\nu^{(eq)}(1+n_\nu)}\right) \mathcal{L}(B_\nu - I_\nu) \ . \tag{32}$$

The closure receipt prescribes to minimize $\dot{S}[I_\nu]$ by varying I_ν subject to the constraints that the moments E, $\mathbf{F}$, ... etc. are fixed. The solution I_ν of this constrained optimization problem depends on the values E, $\mathbf{F}$, ... The number N of moments to be taken into account is in principle arbitrary, but we still restrict the discussion to E and $\mathbf{F}$. After introducing Lagrange parameters λ_E and $\boldsymbol{\lambda}_F$, one has to solve

$$\delta_{I_\nu}\left[\dot{S}[I_\nu] - \lambda_E\left(E - \frac{1}{c}\int d\nu d\Omega\, I_\nu\right) - \boldsymbol{\lambda}_F \cdot \left(\mathbf{F} - \frac{1}{c}\int d\nu d\Omega\, \mathbf{\Omega}\, I_\nu\right)\right] = 0 \quad , \tag{33}$$

where δ_{I_ν} denotes the variation with respect to I_ν. The solution of this minimization problem provides the nonequilibrium state I_ν.

5. Effective transport coefficients

We will now calculate the effective transport coefficients $\kappa_E^{(\rm eff)}$, $\kappa_F^{(\rm eff)}$, and the Eddington factor χ with the help of the entropy production rate minimization closure. We assume $\mathbf{F} = (0,0,F)$ in x_3-direction, use spherical coordinates (θ,ϕ) in Ω-space, such that I_ν is independent of the azimuth angle ϕ. For simplicity, we consider isotropic scattering with $p(\mathbf{\Omega},\tilde{\mathbf{\Omega}}) = 1$, although it is straightforward to consider general randomly oriented scatterers with the phase function p_ν being a series in terms of Legendre polynomials $P_n(\mu)$. Here, we introduced the abbreviation $\mu = \cos(\theta)$. With $d\mathbf{\Omega} = 2\pi\sin(\theta)d\theta = -2\pi d\mu$, the linear operator $\mathcal{L}$, acting on a function $\varphi_\nu(\mu)$, can be written as

$$\mathcal{L}\varphi_\nu = \kappa_\nu\varphi_\nu(\mu) + \sigma_\nu\left(\varphi_\nu(\mu) - \frac{1}{2}\int_{-1}^{1} d\tilde{\mu}\, \varphi_\nu(\tilde{\mu})\right) \ , \tag{34}$$

which has an eigenvalue κ_ν with eigenfunction $P_0(\mu)$ and (degenerated) eigenvalues $\kappa_\nu + \sigma_\nu$ for all higher order Legendre polynomials $P_n(\mu)$, $n = 1,2,\ldots$. In the following two subsections we focus first on limit cases that can be analytically solved, namely radiation near equilibrium (leading order in $E - E^{(eq)}$ and F), and the emission limit (leading order in E, while $0 \le F \le E$). In the remaining subsections the general behavior obtained from numerical solutions and a few mathematically relevant issues will be discussed.

5.1 Radiation near equilibrium

Radiation at thermodynamic equilibrium obeys $I_\nu = B_\nu$ and $F = 0$. Near equilibrium, or weak nonequilibrium, refers to linear order in the deviation $\delta I_\nu = I_\nu - B_\nu$. Higher order corrections of the moments $E = E^{(eq)} + \delta E$ and $F = \delta F$ are neglected. Because the stress tensor is an

even function of δI_ν, $\chi = 1/3$ remains still valid in the linear nonequilibrium region (except for the singular case of Auer's VEF with $j = 1$). We will now show that, in contrast to the entropy maximization closure, the entropy production minimization closure yields the correct Rosseland radiation transport coefficients (cf. Christen & Kassubek (2009)).
For isotropic scattering it is sufficient to take into account the first two Legendre polynomials, 1 and μ: $\delta I_\nu = c_\nu^{(0)} + c_\nu^{(1)}\mu$, with μ-independent $c_\nu^{(0,1)}$ that must be determined. Equations (9) and (10) yield

$$\delta E_\nu = \frac{2\pi}{c}\int_{-1}^{1} d\mu\,(c_\nu^{(0)} + c_\nu^{(1)}\mu) = \frac{4\pi}{c}c_\nu^{(0)}, \tag{35}$$

$$\delta F_\nu = \frac{2\pi}{c}\int_{-1}^{1} d\mu\,(c_\nu^{(0)} + c_\nu^{(1)}\mu)\mu = \frac{4\pi}{3c}c_\nu^{(1)}, \tag{36}$$

and from Eq. (32)

$$\dot{S}_\nu = \frac{2k_B\pi c^2}{h^2\nu^4 n_\nu^{(eq)}(1+n_\nu^{(eq)})}\left(\kappa_\nu (c_\nu^{(0)})^2 + \frac{1}{3}(\kappa_\nu+\sigma_\nu)(c_\nu^{(1)})^2\right)\ . \tag{37}$$

Minimization of $\dot{S}_\nu$ with respect to $c_\nu^{(0,1)}$ with constraints $\delta E = \int d\nu \delta E_\nu$ and $\delta F = \int d\nu \delta F_\nu$ leads to

$$c_\nu^{(0)} = \frac{c\nu^4\partial_\nu n_\nu^{(eq)}}{4\pi\kappa_\nu\int d\nu\,\nu^4\kappa_\nu^{-1}\partial_\nu n_\nu^{(eq)}}\delta E, \tag{38}$$

$$c_\nu^{(1)} = \frac{3c\nu^4\partial_\nu n_\nu^{(eq)}}{4\pi(\kappa_\nu+\sigma_\nu)\int d\nu\,\nu^4(\kappa_\nu+\sigma_\nu)^{-1}\partial_\nu n_\nu^{(eq)}}\delta F\ , \tag{39}$$

where we made use of the relation $\partial_\nu n_\nu^{(eq)} = n_\nu^{(eq)}(1+n_\nu^{(eq)})h/k_BT$. As δI_ν is known to leading order in δE and δF, the transport coefficients can be calculated. One finds

$$\kappa_E^{(\mathrm{eff})} = \frac{2\pi}{c}\int d\nu d\mu\,\frac{\mathcal{L}(\delta I_\nu)}{\delta E} = \frac{4\pi}{c}\int d\nu\kappa_\nu\frac{c_\nu^{(0)}}{\delta E} = \langle\kappa_\nu\rangle_{\mathrm{Ro}}, \tag{40}$$

$$\kappa_F^{(\mathrm{eff})} = \frac{2\pi}{c}\int d\nu d\mu\,\mu\,\frac{\mathcal{L}(\delta I_\nu)}{\delta F} = \frac{4\pi}{c}\int d\nu(\kappa_\nu+\sigma_\nu)\frac{c_\nu^{(1)}}{3\delta F} = \langle\kappa_\nu+\sigma_\nu\rangle_{\mathrm{Ro}}\ , \tag{41}$$

hence the effective absorption coefficients are given by the Rosseland averages Eqs. (21) and (22). Similarly, it is shown that $\Pi_{kl} = (E/3)\delta_{kl}$. This proves that the minimum entropy production rate closure provides the correct radiative transport coefficients near equilibrium.

5.2 Emission limit

While the result of the previous subsection was expected due to the general proof by Kohler (1948), the emission limit is another analytically treatable case, which is, however, far from equilibrium. It is characterized by a photon density much smaller than the equilibrium density, hence $I_\nu \ll B_\nu$, i.e., $E \ll E^{(eq)}$, i.e., emission strongly predominates absorption. To leading order in n_ν, the entropy production rate becomes

$$\dot{S}_\nu = -2\pi k_B\int_{-1}^{1} d\mu\,\frac{\kappa_\nu B_\nu}{h\nu}\ln(n_\nu) \tag{42}$$

such that constrained optimization gives

$$I_\nu = \frac{2k_B}{c}\frac{\nu^2\kappa_\nu}{\lambda_E+\lambda_F\mu}n_\nu^{(eq)} \ , \tag{43}$$

with Lagrange parameters λ_E and λ_F. The μ-integration in Eqs. (9) and (10) can be performed analytically, yielding

$$E = \frac{k_B\mathcal{T}(\kappa_\nu)}{c^2\lambda_F}\ln\left(\frac{\lambda_E+\lambda_F}{\lambda_E-\lambda_F}\right), \tag{44}$$

$$F = \frac{k_B\mathcal{T}(\kappa_\nu)}{c^2\lambda_F}\left(2-\frac{\lambda_E}{\lambda_F}\ln\left(\frac{\lambda_E+\lambda_F}{\lambda_E-\lambda_F}\right)\right) \ , \tag{45}$$

where we introduced

$$\mathcal{T}(\kappa_\nu) = 4\pi\int_0^\infty d\nu\,\nu^2\kappa_\nu n_\nu^{(eq)} \ . \tag{46}$$

Up to leading order in I_ν, one finds by performing the integration analogous to Eqs. (40) and (41)

$$\kappa_E^{(\mathrm{eff})} = \langle\kappa_\nu\rangle_{\mathrm{Pl}} \quad \text{and} \quad \kappa_F^{(\mathrm{eff})} = \frac{\mathcal{T}(\kappa_\nu(\kappa_\nu+\sigma_\nu))}{\mathcal{T}(\kappa_\nu)} \ . \tag{47}$$

As one expects, in the emission limit the effective absorption coefficients are Planck-like, i.e., a direct average rather than an average of the inverse rates like Rosseland averages. The Eddington factor can be obtained from $\Pi_{33} = \chi E$ by calculating

$$\Pi_{33} = \frac{2\pi}{c}\int_0^\infty d\nu\int_{-1}^1 d\mu\,\mu^2 I_\nu \ , \tag{48}$$

which leads to

$$\chi(v) = -\frac{\lambda_E}{\lambda_F}v \ , \tag{49}$$

where the ratio of the Lagrange parameters, and thus also the VEF, depends only on $v = F/E$. This can be seen if one divides Eq. (44) by (45). For small v, the expansion of Eqs. (44) and (45) gives $\lambda_E/\lambda_F = -1/3v$, in accordance with the isotropic limit. In the free streaming limit, $v \to 1$ from below, it holds $\lambda_F \to -\lambda_E$, which follows from $\ln(Z) = 2 - \lambda_E\ln(Z)/\lambda_F$ with $Z = (\lambda_E+\lambda_F)/(\lambda_E-\lambda_F)$ obtained from equalizing (44) with (45).
For arbitrary v the Eddington factor in the emission limit can easily be numerically calculated by division of Eq. (44) by Eq. (45), and parameterizing v and χ with λ_F/λ_E. The result will be shown below in Fig. 4 a). It turns out that the difference to other VEFs often used in literature is quantitatively small.
While Christen & Kassubek (2009) disregarded scattering, it is included here. For strong scattering $\sigma_\nu \gg \kappa_\nu$, Eq. (47) implies that the effective absorption coefficient $\kappa_F^{(\mathrm{eff})}$ of the radiation flux is given by a special average of σ_ν where κ_ν enters in the weight function. In particular, for frequencies where κ_ν vanishes, there is no elastic scattering contribution to the average in this limit. This can be understood by the absence of photons with this frequency in the emission limit.

5.3 General nonequilibrium case

The purpose of this subsection is to illustrate how the entropy production rate closure treats strong nonequilibrium away from the just discussed limit cases. For convenience, we introduce the dimensionless frequency $\xi = h\nu/k_B T$. First, we consider gray-matter (frequency independent $\kappa_\nu \equiv \kappa$) without scattering ($\sigma_\nu = 0$). In Fig. 1 a) the quantity $\xi^3 n$, being proportional to I_ν, is plotted as a function of ξ for $F = 0$ and three values of E, namely $E = E^{(eq)}$, $E = E^{(eq)}/2$, and $E = 2E^{(eq)}$. The first case corresponds the thermal equilibrium with $I_\nu = B_\nu$, while the others must have nonequilibrium populations of photon states. The results show that the energy unbalance is mainly due to under- and overpopulation, respectively, and only to a small extent due to a shift of the frequency maximum.

Now, consider a non-gray medium, still without scattering, but with a frequency dependent κ_ν as follows: $\kappa = 2\kappa_1$ for $\xi < 4$, with constant κ_1, and $\kappa = \kappa_1$ for $\xi > 4$. The important property is that κ_ν is larger at low frequencies and smaller at high frequencies. The resulting distribution function, in terms of $\xi^3 n$, is shown in Fig. 1 b). For $E = E^{(eq)}$, the resulting distribution is of course still the Planck equilibrium distribution. However, for larger (smaller) energy density the radiation density differs from the gray-matter case. In particular, the distribution is directly influenced by the κ_ν-spectrum. This behavior is not possible if one applies the maximum entropy closure in the same framework of a single-band moment approximation. A qualitative explanation of such behavior is as follows. Equilibration of the photon gas is only possible via the interaction with matter. In frequency bands where the interaction strength, κ_ν, is larger ($\xi < 4$), the nonequilibrium distribution is pulled closer to the equilibrium distribution than for frequencies with smaller κ_ν. This simple argument explains qualitatively the principal behavior associated with entropy production rate principles: the strength of the irreversible processes determines the distance from thermal equilibrium in the presence of a stationary constraint pushing a system out of equilibrium.

Results for the effective absorption coefficients $\kappa_E^{(\mathrm{eff})}$ and $\kappa_F^{(\mathrm{eff})}$ are shown in Fig. 2. In Fig. 2 a) it is shown that the effective absorption coefficient $\kappa_E^{(\mathrm{eff})}$ is equal to the Planck mean ($1.6\kappa_1$, dashed-double-dotted) in the emission limit $E/E^{(eq)} \to 0$, and equal to the Rosseland mean ($1.26\kappa_1$, dashed-dotted) near equilibrium $E = E^{(eq)}$, and eventually goes slowly to the high frequency value κ_1 for large E. The effective absorption coefficient obtained from the maximum entropy closure is also plotted (dotted curve), and although correct for $E/E^{(eq)} \to 0$,

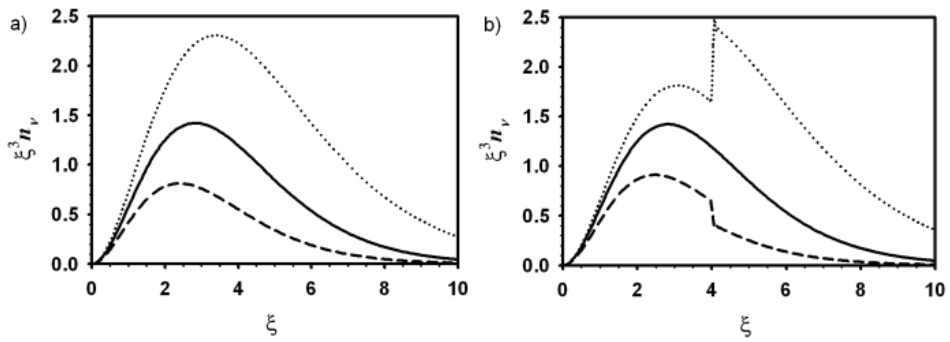

Fig. 1. Nonequilibrium distribution ($\xi^3 n_\nu \propto I_\nu$) as a function of $\xi = h\nu/k_B T$, without scattering, for $F = 0$ and $E = E^{(eq)}$ (solid), $E = E^{(eq)}/2$ (dashed), and $E = 2E^{(eq)}$ (dotted). a) gray matter; b) piecewise constant κ with $\kappa_{\xi<4} = 2\kappa_{\xi>4}$.

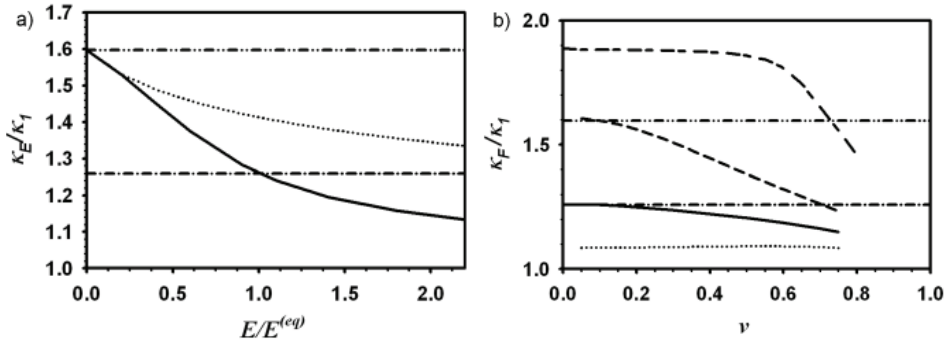

Fig. 2. a) Effective absorption coefficients for E as a function of E for $F = 0$, with the same spectrum as for Fig. 1 b). Dashed-dotted: Rosseland mean; dashed-double-dotted: Planck mean; solid: entropy production rate closure (correct at $E = E^{(eq)}$); dotted: entropy closure (wrong at $E = E^{(eq)}$). b) Effective absorption coefficients for **F** as a function of $v = F/E$ for different E-values (dotted: $E/E^{(eq)} = 2$; solid $E/E^{(eq)} = 1$; dashed: $E/E^{(eq)} = 0.5$; short-long dashed: $E/E^{(eq)} = 0.05$). Dashed-dotted and dashed-double dotted as in a).

it is wrong at equilibrium $E = E^{(eq)}$. For the present example the maximum entropy closure is strongly overestimating the values of $\kappa_E^{(\mathrm{eff})}$.

Figure 2 b) shows $\kappa_E^{(\mathrm{eff})}$ as a function v, for various values of E. As at constant E, increasing v corresponds to a shift of the distribution towards higher frequencies in direction of **F**, a decrease of $\kappa_E^{(\mathrm{eff})}$ must be expected, which is clearly observed in the figure.

In order to investigate the effect of scattering $\sigma_\nu \neq 0$, we consider the example of gray absorbing matter, i.e., constant $\kappa_\nu \equiv \kappa_1$, having a frequency dependent scattering rate $\sigma_{\xi<4} = 0$ and $\sigma_{\xi>4} = \kappa_1$. Scattering is only active for large frequencies. The distribution $\xi^3 n_\nu$ of radiation with $E = 2E^{(eq)}$, with finite flux $v = 0.25$ for different directions $\mu = \cos(\theta) = -1, -0.5, 0, 0.5, 1$ is plotted in Fig. 3 a). Since the total energy of the photon gas is twice the equilibrium energy, the curves are centered around about twice the equilibrium distribution. As one expects, the states in forward direction ($\mu = 1$) have the highest population, while the states propagating against the mean flux ($\mu = -1$) have lowest population. This behavior occurs, of course, also in the absence of scattering. One observes that scattering acts to decrease the anisotropy of the distribution, as for $\xi > 4$ the curves are pulled towards the state with $\mu \approx 0$. Hence, also the effect of elastic scattering to the distribution function can be understood in the framework of the entropy production, namely by the tendency to push the state towards equilibrium with a strength related to the interaction with the LTE matter.

The effective absorption coefficient $\kappa_F^{(\mathrm{eff})}$ is shown in Fig. 3 b) for two values of v; it is obvious that it must increase for increasing v and for increasing E. The Rosseland and Planck averages of $\kappa_\nu + \sigma_\nu$ are given by $1.42\kappa_1$ and $1.40\kappa_1$, while the emission limit for $\kappa_F^{(\mathrm{eff})}$ given in Eq. (47) is $1.20\kappa_1$.

The VEF will be discussed separately in the following subsection, because its behavior has not only quantitative physical, but also important qualitative mathematical consequences.

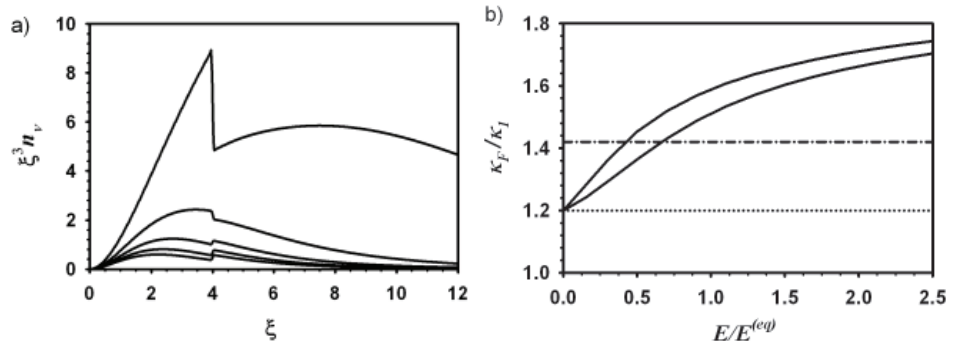

Fig. 3. a) Nonequilibrium distribution ($\xi^3 n_\nu \propto I_\nu$) as a function of $\xi = h\nu/k_B T$, for a medium with constant absorption $\kappa_\nu \equiv \kappa_1$ and piecewise constant scattering with $\sigma_{\xi<4} = 0$, and $\sigma_{\xi>4} = \kappa_1$. The different curves refer to different radiation directions of $\mu = -1, -0.5, 0, 0.5, 1$ (solid curves in ascending order) from photons counter-propagating to the mean drift **F** to photons in **F**-direction. b) Effective absorption coefficients $\kappa_F^{(\mathrm{eff})}$ as a function of $E/E^{(eq)}$ for $v = 0.25, 0.5$ (solid curves in ascending order); dashed-dotted: Rosseland mean, dashed: emission mean of $\kappa_F^{(\mathrm{eff})}$.

5.4 The variable Eddington factor and critical points

A detailed discussion of general mathematical properties and conventional closures is given by Levermore (1996). A necessary condition for a closure method is existence and uniqueness of the solution. It is well-known that convexity of a minimization problem is a crucial property in this context. One should note that convexity of the entropy production rate in nonequilibrium situations is often introduced as a presumption for further considerations rather than it is a proven property (cf. Martyushev (2006)). For the case without scattering, $\sigma_\nu \equiv 0$, Christen & Kassubek (2009) have shown that the entropy production rate (33) is strictly convex. A discussion of convexity for a finite scattering rate goes beyond the purpose of this chapter.

Besides uniqueness of the solution, the moment equations should be of hyperbolic type, in order to come up with a physically reasonable radiation model. It is an advantage of the entropy maximization closure that uniqueness and hyperbolicity are fulfilled and are related to the convexity properties of the entropy (cf. Levermore (1996)). In the following, we provide some basics needed for understanding the problem of hyperbolicity, its relation to the VEF and the occurrence of critical points. The latter is practically relevant because it affects the modelling of the boundary conditions, particularly in the context of numerical simulations. More details are provided by Körner & Janka (1992), Smit et al. (1997), and Pons et al. (2000).

A list of the properties that a reasonable VEF must have (cf. Pomraning (1982)) is: $\chi(v = 0) = 1/3$, $\chi(v = 1) = 1$, monotonously increasing $\chi(v)$, and the Schwarz inequality $v^2 \leq \chi(v)$. The latter follows from the fact that χ and v can be understood as averages of μ^2 and μ, respectively, with (positive) probability density $I_\nu(\mu)/E$. Hyperbolicity adds a further requirement to the list. Equations (13) and (14) form a set of quasilinear first order differential equations. For simplicity, we consider a one dimensional position space[5] with coordinate x with $0 \leq x \leq L$, and variables $E \geq 0$ and F. In this case we redefine F, such that it can have

[5]Momentum space remains three dimensional.

either sign, $-E \leq F \leq E$. We assume flux in positive direction, $F \geq 0$, and write the moment equations in the form

$$\frac{1}{c}\partial_t \begin{pmatrix} E \\ F \end{pmatrix} + \begin{pmatrix} 0 & 1 \\ \partial_E(\chi E) & E\partial_F \chi \end{pmatrix} \partial_x \begin{pmatrix} E \\ F \end{pmatrix} = \begin{pmatrix} P_E \\ P_F \end{pmatrix} . \tag{50}$$

For spatially constant E and F, small disturbances of δE and δF must propagate with well-defined speed, implying real characteristic velocities. Those are given by the eigenvalues of the matrix that appears in the second term on the left hand side of Eq. (50) and which we denote by $\mathbf{M}$:

$$w_\pm = \frac{\mathrm{Tr}\,\mathbf{M}}{2} \pm \sqrt{\frac{(\mathrm{Tr}\,\mathbf{M})^2}{4} - \det(\mathbf{M})} , \tag{51}$$

where "Tr" and "det" denote trace and determinant. Note that the $w_\pm$ are normalized to c, i.e. $-1 \leq w_- \leq w_+ \leq 1$ must hold. Hyperbolicity refers to real eigenvalues $w_\pm$ and to the existence of two independent eigenvectors. The condition for hyperbolicity reads $(\partial_F(\chi E))^2 + 4\partial_E(\chi E) > 0$.

Provided hyperbolicity is guaranteed, the sign of the velocities is an issue relevant for the boundary conditions. Indeed, the boundary condition, say at $x = L$, can only have an effect on the state in the domain if at least one of the characteristic velocities is negative. It is clear that a disturbance near equilibrium ($v = 0$) propagates in $\pm x$ direction since $w_+ = -w_-$ due to mirror symmetry. Hence $w_- < 0 < w_+$ for sufficiently small v. In this case boundary conditions to both boundaries $x = 0$ and $x = L$ have to be applied as in a usual boundary value problem. However, for finite v, reflection symmetry is broken and $w_+ \neq -w_-$. It turns out, that for sufficiently large v, either w_+ or w_- can change sign. For positive F, we denote the value of v where w_- becomes positive by v_c. This is called a *critical point* because $\det(\mathbf{M}) = w_+ w_-$ vanishes there. Beyond the critical point, all disturbances will propagate in positive direction, and a boundary condition at $x = L$ is not to be applied. This can introduce a problem in numerical simulations with fixed predefined boundary conditions. The rough physical meaning of the critical point is a cross-over from diffusion dominated to streaming dominated radiation. In the latter region it might be reasonable to improve the radiation model by involving higher order moments or partial moments, for example by decomposing the moments in backward and forward propagating components $E_\pm$ and $F_\pm$ (cf. sect. 3.1 in Frank (2007)).

In Fig. 4 a), different VEFs are shown. All of them exhibit the above mentioned properties, $\chi(v = 0) = 1/3$, monotonous increase, $\chi(v \to 1) = 1$, and the Schwarz inequality $v^2 \leq \chi$. In particular, the VEFs obtained from entropy production rate minimization is shown for $E = E^{(eq)}$ for gray matter with $\sigma_\nu \equiv 0$, as well as for the emission limit (cf. Eqs. (44) and (45)). Note that the latter $\chi(v)$ is a function of v only and is independent of the detailed properties of the absorption and scattering spectra. The similarity of the differently defined VEFs, combined with the error done anyhow by the two-moment approximation, makes it obvious that for practical purpose the simple Kershaw VEF ($j = 2$) may serve as a sufficient approximation. In Fig. 4 b) the characteristic velocities $w_\pm$ are plotted versus v for the various VEFs discussed above. It turns out that the VEF given by Eq. (25) has a critical point for $j > 3/2$ given by $v_c = 1/\sqrt[j]{2(j-1)}$, and that there is a minimum v_c value of 0.63 at $j = 3.16$. The VEF by Kershaw and maximum entropy have $v_c = 1/\sqrt{2}$ and $v_c = 2\sqrt{3}/5$, respectively. Also the VEF associated with the entropy production rate has generally a critical point, which depends on E. One has to expect a typical value of $v_c \approx 2/3$. For the VEF (25) with $j = 1$ a critical point does not

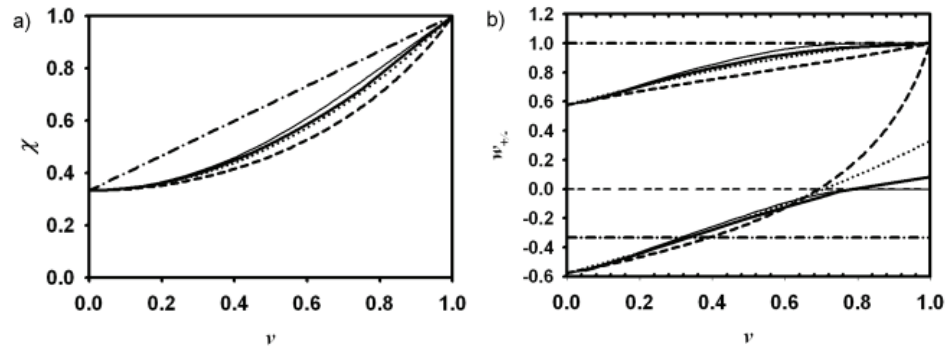

Fig. 4. a) Eddington Factors χ versus v and b) characteristic velocities $w_{\pm}$ for various cases. Minimum entropy production: $E = E^{(eq)}$ (thick solid curve) and emission limit $E \ll E^{(eq)}$ (thin solid curve); maximum entropy (dashed); Kershaw (dotted; $j = 2$ in Eq. (25)), and Auer (dashed-dotted; $j = 1$ in Eq. (25)).

appear. In the framework of numerical simulations, this advantage can outweigh in certain situations the disadvantage of the erroneous anisotropy in the $v \to 0$ limit.

6. Boundary conditions

In order to solve the moment equations, initial and boundary conditions are required. While the definition of initial conditions are usually unproblematic, the definition of boundary conditions is not straight-forward and deserves some remarks. In the sequel we will consider boundaries where the characteristic velocities are such that boundary conditions are needed. But note that the other case where boundary conditions are obsolete can also be important, for example in stellar physics where, beyond a certain distance from a star, freely streaming radiation completely escapes into the vacuum.

The mathematically general boundary condition for the two-moment model is of the form

$$aE + b\hat{\mathbf{n}} \cdot \mathbf{F} = \Gamma \ , \tag{52}$$

with the surface normal $\hat{\mathbf{n}}$, and where the coefficients a, b, and the inhomogeneity Γ must be determined from Eq. (5). There is a certain ambiguity to do this (cf. Duderstadt & Martin (1979)) and thus a number of different boundary conditions exist in the literature (cf. Su (2000)).

There may be simple cases where one can either apply Dirichlet boundary conditions $E(\mathbf{x}_{\mathrm{w}}) = E_{\mathrm{w}}$ to E, where E_{w} is the equilibrium value associated with the (local) wall temperature, and/or homogeneous Neumann boundary conditions to $\mathbf{F}$, $(\hat{\mathbf{n}} \cdot \nabla)\mathbf{F} = 0$, at $\mathbf{x}_{\mathrm{w}}$. This approach may be appropriate, if the boundaries do not significantly influence the physics in the region of interest, e.g., in the case where cold absorbing boundaries are far from a hot radiating object under investigation. It can also be convenient to include in the simulation, instead of using boundary conditions, the solid bulk material that forms the surface, and to describe it by its κ_ν and σ_ν. In the next section an example of this kind will be discussed. If necessary, thermal equilibrium boundary conditions deep inside the solid may be assumed. In this way, it is also possible to analytically calculate the Stefan-Boltzmann radiation law for a plane sandwich structure (hot solid body)-(vacuum gap)-(cold solid body), if an Eddington factor (25) with $j = 1$ is used and the solids are thick opaque gray bodies.

In general, however, one would like to have physically reasonable boundary conditions at a surface characterized by Eq. (5). For engineering applications, often boundary conditions by Marshak (1947) are used. In the following, we sketch the principle how these boundary conditions can be derived for a simple example (cf. Bayazitoglu & Higenyi (1979)). For other types, like Mark or modified Milne boundary conditions see, e.g. Su (2000). Let the coordinate $x \geq 0$ be normal to the surface at $x = 0$, and ask for the relation between the normal flux F, E, and $E_{\mathrm{w}}^{(eq)}$ at $x = 0$. The $\mathbf{F}$-components tangential to the boundary are assumed to vanish, and diffusive reflection with $r(\mathbf{x_w}, \mathbf{\Omega}, \tilde{\mathbf{\Omega}}) = r/\pi$ with $r = 1 - \epsilon$ is considered. In terms of moments, the radiation field is given by

$$I_\nu = \frac{c}{4\pi}\left(E_\nu P_0(\mu) + 3F_\nu P_1(\mu) + \frac{5}{2}(3\Pi_{\nu,11} - E_\nu)P_2(\mu) + ...\right) \ , \tag{53}$$

with Legendre polynomials $P_0 = 1$, $P_1 = \mu$, $P_2 = (3\mu^2 - 1)/2$. The exact solution contains also higher order Legendre polynomials, as indicated by the dots. The boundary condition (5) can be written as

$$I_\nu(\mu \geq 0) = \epsilon B_\nu + 2r \int_{-1}^{0} d\tilde{\mu} \mid \tilde{\mu} \mid I_\nu(\tilde{\mu}) \ . \tag{54}$$

By using Eq. (53), the integral can be calculated, such that the right hand side of Eq. (54) becomes a constant with respect to μ, while the left hand side is, according to Eq. (53), a function of μ defined for $0 \leq \mu \leq 1$. In order to obtain the required relation between F and E, one has to multiply Eq. (54) with a weight function $h(\mu)$ and integrate over μ from 0 to 1. The above mentioned ambiguity lies in the freedom of choice of $h(\mu)$. Marshak (1947) selected $h = P_1$. Provided P_n for $n > 3$ are neglected in Eq. (53), integration leads to an inward flux

$$F = \frac{\epsilon}{2(2-\epsilon)}\left(E_{\mathrm{w}} - \frac{(3E + 15\Pi_{11})}{8}\right) \ , \tag{55}$$

where $\Pi_{11} = \chi E$. If higher order moments are to be considered, additional projections have to be performed, in analogy to the procedure reported by Bayazitoglu & Higenyi (1979) for the P-3 approximation.[6] For isotropic radiation with $\chi = 1/3$, or $\Pi_{11} = E/3$, the prefactor of E becomes unity and Eq. (55) reduces to the well-known P-1-Marshak boundary condition. In the transparent limit with $\chi = 1$, the prefactor becomes $9/4$.

For the simple case of two parallel plane plates ($\epsilon = 1$) with temperatures associated with $E_{\mathrm{w},1}$ and $E_{\mathrm{w},2} < E_{\mathrm{w},1}$, and separated by a vacuum gap, both moments E and F are spatially constant and the Stefan-Boltzmann law $F = (E_1^{(eq)} - E_2^{(eq)})/4$ is recovered. But note that the energy density E between the plates is not equal to the expected average of $E_1^{(eq)}$ and $E_2^{(eq)}$, which is an artifact of the two-moment approximation with VEF.

7. A simulation example: electric arc radiation

The two-moment approximation will now be illustrated for the example of an electric arc. The extreme complexity of the full radiation hydrodynamics is obvious. Besides transonic and turbulent gas dynamics, which is likely supplemented with side effects like mass ablation and electrode erosion, a temperature range between room temperature and up to 30′000K

[6] Note that neither the series (53) stops after the N'th moment (even not for the P-N approximation, cf. Cullen (2001)), nor all higher order coefficients drop out after projection of Eq. (54) on P_n. A general discussion, however, goes beyond this chapter and will be published elsewhere.

is covered. In this range extremely complicated absorption spectra including all kinds of transitions occur, and the radiation is far from equilibrium although the plasma can often be considered at LTE. Last but not least, the geometries are usually of complicated three-dimensional nature without much symmetry, as for instance in a electric circuit breaker. More details are given by Jones & Fang (1980), Aubrecht & Lowke (1994), Eby et al. (1998), Godin et al. (2000), Dixon et al. (2004), and Nordborg & Iordanidis (2008).

It is sufficient for our purpose to restrict the considerations to the radiation part for a given temperature profile, for instance of a cylindrical electric arc in a gas in front of a plate with a slit (see Fig. 5). We may neglect scattering in the gas ($\sigma_\nu \equiv 0$) and mention that an electric arc consists of a very hot, emitting but transparent core surrounded by a cold gas, which is opaque for some frequencies and transparent for others. First, one has to determine the effective transport coefficients $\kappa_E^{(\mathrm{eff})}$, $\kappa_F^{(\mathrm{eff})}$, and $\chi(v)$, with the above introduced entropy production minimization method. For simplicity, we assume now that this is done and these functions are given simply by constant values listed in the caption of Fig. 5, and that $\chi(v)$ is well-approximated by Kershaw's VEF. Note that due to the low density in the hot arc core, the effective absorption coefficient there is smaller than in the surrounding cold gas. Therefore, one expects that the radiation in the arc center will exhibit stronger nonequilibrium than in the surrounding colder gas.

The energy density E and the velocity vectors $\mathbf{v} = \mathbf{F}/E$ obtained by a simulation with the commercial software ANSYS® FLUENT® are shown in Fig. 5. At the outer boundaries, homogeneous Neumann boundary conditions are used for all quantities. The wall defining the slit is modelled as a material with either a) high absorption coefficient or b) high scattering coefficient. The behavior of the velocity vector field clearly reflects these different boundary properties. The E-surface plot shows the shadowing effect of the wall when the arc radiation is focused through the slit. The energy densities E along the x-axis are shown in Fig. 6 a) for the two cases. One observes the enhanced E in the region of the slit for the scattering wall. The energy flux in physical units, i.e., cF, on the screen in front of the slit is shown in Fig. 6 b). The effect here is again what one expects: an enhanced and less focused power flux due to the absence of absorption in the constricting wall.

8. Summary and conclusion

After a short general overview on radiative heat transfer, this chapter has focused on truncated moment expansions of the RTE for radiation modelling. One reason for a preference of a moment based description is the occurrence of the moments directly in the hydrodynamic equations for the matter, and the equivalence of the type of hyperbolic partial differential equations for radiation and matter, which allows to set complete numerical simulations on an equal footing.

The truncation of the moment expansion requires a closure prescription, which determines the unknown transport coefficients and provides the nonequilibrium distribution as a function of the moments. It was the main goal of this chapter to introduce the minimum entropy production rate closure, and to illustrate with the help of the two-moment approximation that this closure is the one to be favored due to the following properties of the result:

- It is exact near thermodynamic equilibrium, and particularly leads to the Rosseland mean absorption coefficients.
- It exhibits the required flux limiting behavior by yielding reasonable variable Eddington factors.

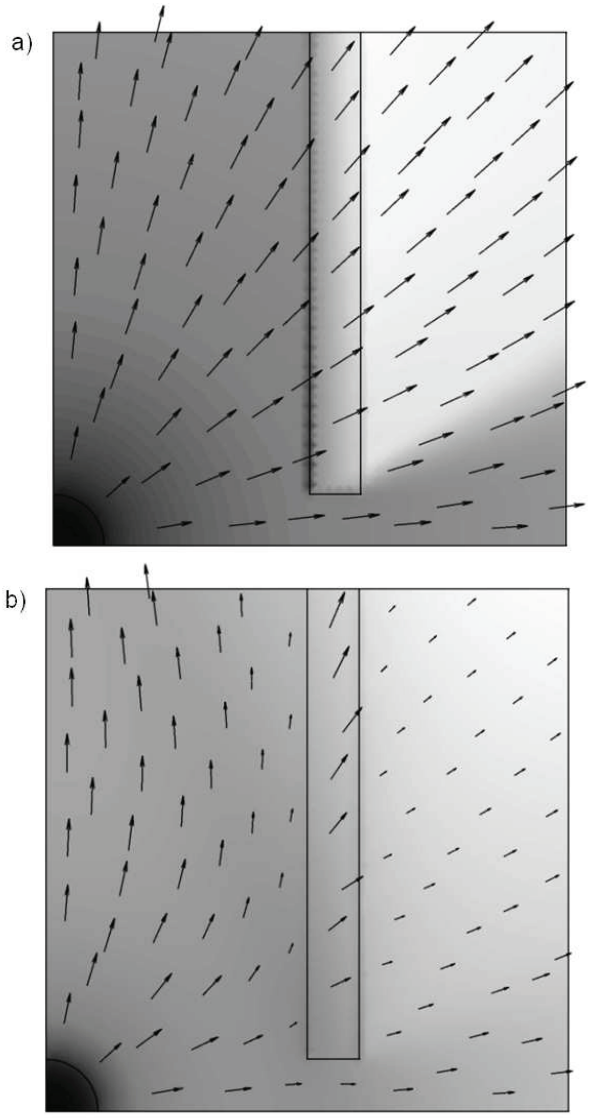

Fig. 5. Illustrative simulations of the moment equations with FLUENT® for a cylindrical electrical arc (radius 1 cm, temperature 10′000 K, $\kappa_E^{(\mathrm{eff})} = \kappa_F^{(\mathrm{eff})} = 1/\mathrm{m}$) in a gas (ambient temperature 300 K, $\kappa_E^{(\mathrm{eff})} = \kappa_F^{(\mathrm{eff})} = 5/\mathrm{m}$). A solid wall (a): only absorbing with $\kappa_E^{(\mathrm{eff})} = \kappa_F^{(\mathrm{eff})} \equiv 500/\mathrm{m}$; (b): wall with scattering coefficient, and $\kappa_E^{(\mathrm{eff})} = 5/\mathrm{m}$, $\kappa_F^{(\mathrm{eff})} \equiv 500/\mathrm{m}$ with a slit in front of the arc focusing the radiation towards a wall. Surface plot for E (dark: large, bright: small, logarithmic scale); arrows for $\mathbf{v}$ (not $\mathbf{F}$!). Only one quadrant of the symmetric arrangement is show.

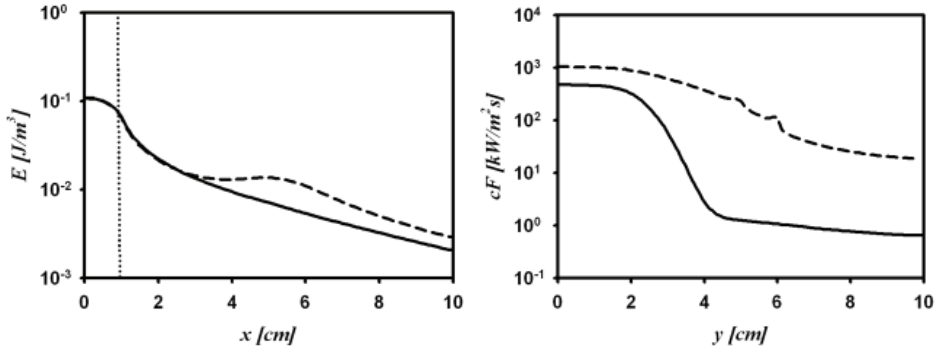

Fig. 6. a) Energy density along the x-axis (arc center at $x = 0$) and b) power flux along the screen ($x = 10$cm) for the two cases Fig. 5 a) (solid) and Fig. 5 b) (dashed).

- It gives the expected results in the emission limit, and particularly leads to the Planck mean absorption coefficient.
- It can be generalized to an arbitrary number and type of moments.
- It can be generalized to particles with arbitrary type of energy-momentum dispersion (e.g. massive particles) and statistics (Bosons and Fermions), as long as they are described by a linear BTE. In stellar physics, for instance, neutrons or even neutrinos can be included in the analogous way.

The main requirement of general applicability is that the particles be independent, i.e., they interact on the microscopic scale only with a heat bath but not among each other. On a macroscopic scale, long-range interaction (e.g., Coulomb interaction) via a mean field may be included for charged particles on the hydrodynamic level of the moment equations. Independency, i.e. linearity of the underlying Boltzmann equation, has the effect that on the level of the BTE (or RTE) nonequilibrium is always in the linear response regime. In this sense, all transport steady-states are near equilibrium even if f_ν strongly deviates from $f_\nu^{(eq)}$, and the entropy production rate optimization according to Kohler (1948) can be applied.

9. References

Abu-Romia M M and Tien C L, *J. Heat Transfer* 89, 321 (1967).
Anile A M, Pennisi S, and Sammartino M, *J. Math. Phys.* 32, 544 (1991).
Anile A, Romano V, and Russo G, *SIAM J. Appl. Math.* 61, 74 (2000).
Arridge S. R. et al., *Med. Phys.* 27, 252 (2000).
Aubrecht V, Lowke J J, *J. Phys. D: Appl. Phys.* 27, 2066 (1994).
Auer L H, in *Methods in radiative transfer*, ed. Kalkofen W, Cambridge University Press (1984).
Barichello L B and Siewert C E, *Nuclear Sci. and Eng.* 130,79 (1998).
Bayazitoglu Y and Higenyi J, *AIAA Journal* 17, 424 (1979).
Brooks E D and Fleck A, *J. Comp. Phys.* 67, 59 (1986).
Brooks E D et al. *J. Comp. Phys.* 205, 737 (2005).
Cernohorsky J and Bludman S A, *The Astrophys. Jour.* 443, 250 (1994).
Chandrasekhar S, *Radiative Transfer*, Dover Publ. Inc., N. Y. (1960).
Christen T, *J. Phys. D: Appl. Phys.* 40, 5719 (2007).
Christen T and Kassubek F, *J. Quant. Spectrosc. Radiat. Transfer.*110, 452 (2009).

Christen T *Entropy* 11, 1042 (2009).
Christen T, *Europhys. Lett.* 89, 57007 (2010).
Cullen D E and Pomraning G C, *J. Quant. Spectrosc. Radiat. Transfer.* 24, 97 (1980).
Cullen D E, *Why are the P-N and the S-N methods equivalent?*, UCRL-ID-145518 (2001).
Dixon C M, Yan J D, and Fang M T C, *J. Phys. D: Appl. Phys* 37, 3309 (2004).
Duderstadt J J and Martin W R, *Transport Theory*, Wiley Interscience, New York (1979).
Eby S D, Trepanier J Y, and Zhang X D, *J. Phys. D: Appl. Phys.* 31, 1578 (1998).
Essex C, *The Astrophys. Jeut.* 285, 279 (1984).
Essex C, *Minimum entropy production of neutrino radiation in the steady state*, Institute for fundamental theory, UFIFT HEP-97-7 (1997).
Fort J, *Physica A* 243, 275 (1997).
Frank M, Dubroca B, and Klar A, *J. Comput. Physics* 218, 1 (2006).
Frank M, *Bull. Inst. Math. Acad. Sinica* 2, 409 (2007).
Fuss S P and Hamins A, *J. Heat Transfer ASME* 124, 26 (2002).
Godin D et al., *J. Phys. D: Appl. Phys* 33, 2583 (2000).
Jones G R and Fang M T C, *Rep. Prog. Phys.* 43, 1415 (1980).
Kabelac S, *Thermodynamik der Strahlung* Vieweg, Braunschweig (1994).
Kershaw D, *Flux limiting nature's own way*, Lawrence Livermore Laboratory, UCRL-78378 (1976).
Kohler M, *Z. Physik* 124, 772 (1948).
Körner A and Janka H-T, *Astron. Astrophys.* 266, 613 (1992).
Kröll W, *J. Quant. Spectrosc. Radiat. Transfer.* 7, 715 (1967).
Landau L D and Lifshitz E M, *Statistical Physics*, Elsevier, Amsterdam (2005).
Levermore C D, *J. Quant. Spectrosc. Radiat. Transfer.* 31, 149 (1984).
Levermore C D, *J. Stat. Phys.* 83, 1021 (1996).
Levermore C D and Pomraning G C, *The Astrophys. Jou. Y* 248, 321 (1981).
Lowke J J, *J. Appl. Phys.* 41, 2588 (1970).
Marshak R E, *Phys. Rev.* 71, 443 (1947).
Martyushev L M and Seleznev V D, *Phys. Rep.* 426, 1 (2006).
Minerbo G N, *J. Quant. Spectrosc. Radiat. Transfer.* 20, 541 (1978).
Mihalas D and Mihalas B W, *Foundations of Radiation Hydrodynamics*, Oxford University Press, New York (1984).
Modest M, *Radiative Heat Transfer*, Elsevier Science, (San Diego, USA, 2003).
Nordborg H and Iordanidis A A, *J. Phys. D: Appl. Phys.* 41, 135205 (2008).
Olson G L, Auer L H, and Hall M L, *J. Quant. Spectrosc. Radiat. Transfer.* 64, 619 (2000).
Oxenius J, *J. Quant. Spectrosc. Radiat. Transfer.* 6, 65 (1966).
Patch R W, *J. Quant. Spectrosc. Radiat. Transfer.* 7, 611 (1967).
Planck M, *Vorlesungen über die Theorie der Wärmestrahlung*, Verlag J. A. Barth, Leipzig (1906).
Pons J A, Ibanez J M, and Miralles J A, *Mon. Not. Astron. Soc.* 317, 550 (2000).
Pomraning G C, *J. Quant. Spectrosc. Radiat. Transfer.* 26, 385 (1981).
Pomraning G C, *Radiation Hydrodynamics* Los Alamos National Laboratory, LA-UR-82-2625 (1982).
Rey C C, *Numerical Methods for radiative transfer*, PhD Thesis, Universitat Politecnica de Catalunya (2006).
Ripoll J-F, Dubroca B, and Duffa G, *Combustion Theory and Modelling* 5, 261 (2001).
Ripoll J-F , *J. Quant. Spectrosc. Radiat. Transfer.* 83, 493 (2004).
Ripoll J-F and Wray A A, *J. Comp. Phys.* 227, 2212 (2008).

Sampson D H, *J. Quant. Spectrosc. Radiat. Transfer.* 5, 211 (1965).
Santillan M, Ares de Parga G, and Angulo-Brown F, *Eur. J. Phys.* 19, 361 (1998).
Seeger M, et al. *J. Phys. D: Appl. Phys* 39, 2180 (2006).
Siegel R and Howell J R, *Thermal radiation heat transfer*, Washington, Philadelphia, London; Hemisphere Publ. Corp. (1992).
Simmons K H and Mihalas D, *J. Quant. Spectrosc. Radiat. Transfer.* 66, 263 (2000).
Smit J M, Cernohorsky J, and Dullemond C P *Astron. Astrophys.* 325, 203 (1997).
Struchtrup H, *Ph. D. Thesis* TU Berlin (1996).
Struchtrup H, in *Rational extended thermodynamics* ed. Müller I. and Ruggeri T., Springer, New. York, Second Edition, p. 308 (1998).
Su B, *J. Quant. Spectrosc. Radiat. Transfer.* 64, 409 (2000).
Tien C L, *Radiation properties of gases*, in *Advances in heat transfer*, Vol.5, Academic Press, New York (1968).
Turpault R, *J. Quant. Spectrosc. Radiat. Transfer.* 94, 357 (2005).
Würfel P and Ruppel W, *J. Phys. C: Solid State Phys.* 18, 2987 (1985).
Yang W-J, Taniguchi H, and Kudo K, *Radiative Heat Transfer by the Monte Carlo Method*, Academic Press, San Diego (1995).
Ziman J M, *Can. J. Phys.* 34, 1256 (1956).
Zhang J F, Fang M T C, and Newland D B, *J. Phys. D: Appl. Phys* 20, 368 (1987).

Part 2

Numerical Methods and Calculations

5

Finite Volume Method Analysis of Heat Transfer in Multi-Block Grid During Solidification

Eliseu Monteiro[1], Regina Almeida[2] and Abel Rouboa[3]
[1]*CITAB/UTAD - Engineering Department of University of Trás-os-Montes e Alto Douro, Vila Real*
[2]*CIDMA/UA - Mathematical Department of University of Trás-os-Montes e Alto Douro, Vila Real*
[3]*CITAB/UTAD - Department of Mechanical Engineering and Applied Mechanics of University of Pennsylvania, Philadelphia, PA*
[1,2]*Portugal*
[3]*USA*

1. Introduction

Solidification of an alloy has many industrial applications, such as foundry technology, crystal growth, coating and purification of materials, welding process, etc. Unlike the classical Stefan problem for pure metals, alloy solidification involves complex heat and mass transport phenomena. For most metal alloys, there could be three regions, namely, solid region, mushy zone (dendrite arms and interdendritic liquid) and liquid region in solidification process. Solidification of binary mixtures does not exhibit a distinct front separating solid and liquid phases. Instead, the solid is formed as a permeable, fluid saturated, crystal-line-like matrix. The structure and extent of this mushy region, depends on numerous factors, such as the specific boundary and initial conditions. During solidification, latent energy is released at the interfaces which separate the phases within the mushy region. The distribution of this energy therefore depends on the specific structure of the multiphase region. Latent energy released during solidification is transferred by conduction in the solid phase, as well as by the combined effects of conduction and convection in the liquid phase. To investigate the heat and mass transfer during the solidification process of an alloy, a few models have been proposed. They can be roughly classified into the continuum model and the volume-averaged model. Based on principles of classical mixture theory, Bennon & Incropera (1987) developed a continuum model for momentum, heat and species transport in the solidification process of a binary alloy. Voller et al. (1989) and Rappaz & Voller (1990) modified the continuum model by considering the solute distribution on microstructure, the so-called Scheil approach. Beckermann & Viskanta (1988) reported an experimental study on dendritic solidification of an ammonium chloride-water solution. A numerical simulation for the same physical configuration was also performed using a volumetric averaging technique. Subsequently, the volumetric averaging technique was systematically derived by Ganesan & Poirier (1990) and Ni & Beckermann (1991). Detailed discussions on microstructure formation and mathematical modelling of transport phenomenon during solidification of binary systems can be found in

the reviews of Rappaz (1989) and Viskanta (1990).
In the last few decades intensive studies have been made to model various problems, for example: to solve radiative transfer problem in triangular meshes, Feldheim & Lybaert (2004) used discrete transfer method (DTM can be see in the work of Lockwood & Shah (1981)), Galerkin finite element method was used by Wiwatanapataphee et al. (2004) and Tryggvason et al. (2005) to study the turbulent fluid flow and heat transfer problems in a domain with moving phase-change boundary and Dimova et al. (1998) also used Galerkin finite element method to solve nonlinear phenomena. Finite volume method for the calculation of solute transport in directional solidification has been studied and validated by Lan & Chen (1996). Finite element method to model the filling and solidification inside a permanent mold is performed by Shepel & Paolucci (2002). Three dimensional parallel simulation tool using a unstructured finite volume method with Jacobian-free Newton-Krylov solver, has been done by Knoll et al. (2001) for solidifying flow applications. Also arbitrary Lagrangian-Euler (ALE) formulation was develop by Bellet & Fachinotti (2004) to simulate casting processes, among others. One of the major challenges of heat transfer modelling of molten metal has been the phase change. To model such a phase change requires the strict imposition of boundary conditions. Normally, this could be achieved with a finite-element that is distorted to fit the interface. Since the solid-liquid phase boundaries are moving the use of level set methods are a recent trend (Sethian (1996)). However, both of these techniques are computationally expensive. The classical fixed mesh is computational less expensive but could not been able to maintain the correct boundary conditions. In this regard, Monteiro (1996) studied the application of the finite difference method to permanent mold casting using generalized curvilinear coordinates. A multi-block grid was applied to a complex geometry and the following boundary conditions: continuity condition to virtual interfaces and convective heat transfer to metal-mold and mold-environment interfaces. The reproduction of this simulation procedure using the finite volume method was made by Monteiro (2003). The agreement with experimental data was also good. Further developments of this work were made by Monteiro & Rouboa (2005) where more reliable initial conditions and two different kinds of boundary conditions were applied with an increase in agreement with the experimental data. In the present work we compare the finite difference and finite volume methods in terms of space discretization, boundary conditions definition, and results using a multi-block grid in combination with curvilinear coordinates. The multi-block grid technique allows artificially reducing the complexity of the geometry by breaking down the real domain into a number of subdomains with simpler geometry. However, this technique requires adapted solvers to a nine nodes computational cell instead of the five nodes computational cell used with cartesian coordinates for two dimensional cases. These developments are presented for the simple iterative methods Jacobi and Gauss-Seidel and also for the incomplete factorization method strongly implicit procedure.

2. Heat transfer and governing equations

Solidification modelling can be divided into three separate models, where each model is identified by the solution to a separate set of equations: *heat transfer modelling* which solves the energy equation; *fluid-flow modelling* which solves the continuity and momentum equations; and *free-surface modelling* which solves the surface boundary conditions. For a complete description of a casting solidification scenario, all these equations should be solved simultaneously, but under special circumstances they could be decoupled and modelled independently. This is the case for heat-transfer modelling, which has been widely used, and

its application has significantly improved casting quality (Swaminathan & Voller (1997)).

2.1 Mathematical model

The governing system equations is composed by the heat conservative equation, the boundary condition equations and the initial equation. In this section, differential equations of the heat conservative and adapted boundary conditions for the solidification phenomena will be presented.

2.1.1 Energy conservation equation

The energy conservation equation states that the rate of gain in energy per unit volume equals the energy gained by any source term, minus the energy lost by conduction, minus the rate of work done on the fluid by pressure and the viscous forces, per unit time. Assuming that: the fluid is isotropic and obeys Fourier's Law; the fluid is incompressible and obeys the continuity equation; the fluid conductivity is constant; viscous heating is negligible, and since the heat capacity of a liquid at constant volume is approximately equal to the heat capacity at constant pressure, then, the internal energy equation is reduced to the familiar heat equation, here shown in curvilinear coordinates (Monteiro et al. (2006), Monteiro & Rouboa (2005)). The governing differential equation for the solidification problem may be written in the following conservative form

$$\frac{\partial \left(\rho C_P \phi\right)}{\partial t} = \nabla \cdot \left(k \nabla \phi\right) + \dot{q}, \tag{1}$$

where $\frac{\partial(\rho C_P \phi)}{\partial t}$ represents the transient contribution to the conservative energy equation (ϕ temperature); $\nabla \cdot (k \nabla \phi)$ is the diffusive contribution to the energy equation and $\dot{q}$ represents the energy released during the phase change. The physical properties of the metal: the metal density ρ (kg/m^3), the heat capacity of constant pressure C_P (J/kg^oC) and the thermal conductivity k (W/m^oC) are considered to be constants analogously as done by Knoll et al. (2001), Monteiro (1996) and Shamsundar & Sparrow (1975).

The term $\dot{q}$ can be expressed as a function of effective solid (Monteiro (1996)), (*s solidus* or solidified metal) material fraction f_s, metal density ρ, and enthalpy variation during the phase change Δh_f called latent heat (Monteiro & Rouboa (2005), Monteiro et al. (2006)), by the following expression

$$\dot{q} = \frac{\partial \left(\rho \Delta h_f \, f_s\right)}{\partial t}. \tag{2}$$

One can also decompose f_s in the following way

$$\frac{\partial f_s}{\partial t} = \frac{\partial f_s}{\partial \phi} \frac{\partial \phi}{\partial t}. \tag{3}$$

Assuming that Δh_f is independent of temperature and the material is isotropic, one substitutes equations (2) and (3) in equation (1) and obtain

$$\frac{\partial \phi}{\partial t} \left(1 - \frac{\Delta h_f}{C_P} \frac{\partial f_s}{\partial \phi}\right) = a \left(\bigtriangledown^2 \phi\right), \tag{4}$$

where a is the thermal diffusivity which is equal to $a = \frac{k}{\rho C_p}$ (m^2/s).

The solid fraction can be determined, at each temperature, by the lever rule. When dealing

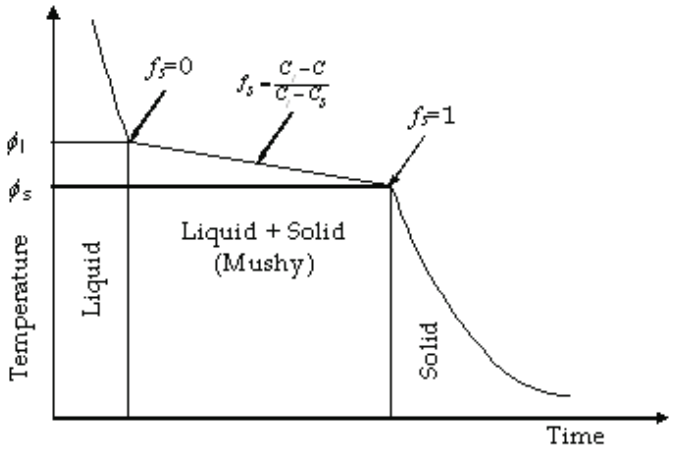

Fig. 1. Typical cooling diagram of alloys

with small temperature difference, a linear relationship between $f_s(\phi)$ and ϕ, is an acceptable approximation as shown in the Fig. 1. Thus, $\frac{\partial f_s}{\partial \phi}$ can be considered as constant. The constant ϕ_s is the solidus temperature, ϕ_l is the liquidus temperature and during the mushy phase the material fraction f_s is given by $f_s = \frac{C_l - C}{C_l - C_s}$, where C is the concentration, C_l and C_s are, respectively, the liquidus and solidus concentrations. This assumption allows the linearization of the source term of the energy equation.

One also uses the *curvilinear coordinates* which transforms the domain into rectangular and time independent. The calculation is given by a uniform mesh of squares in a two dimension, by the following transformation: $x_i = x_i(\xi_1, \xi_2)$, for $i = 1, 2$, characterized by the Jacobian J

$$J = \det\left[\frac{\partial x_i}{\partial \xi_j}\right]_{i,j}. \tag{5}$$

Therefore,

$$\frac{\partial \phi}{\partial x_i} = \frac{\partial \phi}{\partial \xi_j}\frac{\partial \xi_j}{\partial x_i} = \frac{\partial \phi}{\partial \xi_j}\frac{\beta^{ij}}{J}, \tag{6}$$

where $\beta^{ij} = (-1)^{i+j}\det(J_{ij})$ represents the cofactor in the Jacobian J, and J_{ij} is the Jacobian matrix taking out the line i and column j. Substituting the equation (6) in equation (4) one obtains

$$J\frac{\partial \phi}{\partial t}\left(1 - \frac{\Delta h_f}{C_P}\frac{\partial f_s}{\partial \phi}\right) = a\frac{\partial}{\partial \xi_j}\left[\frac{1}{J}\left(\frac{\partial \phi}{\partial \xi_m}B^{mj}\right)\right], \tag{7}$$

where the coefficient B^{mj} are defined by

$$B^{mj} = \beta^{kj}\beta^{km} = \beta^{1j}\beta^{1m} + \beta^{2j}\beta^{2m}. \tag{8}$$

The coefficient B^{mj} becomes zero when the grid is orthogonal, therefore the use of these coefficients in the equation (7).
The second term of equation (7) can be expressed by

$$J\frac{\partial\phi}{\partial t}\left(1-\frac{\Delta h_f}{C_P}\frac{\partial f_s}{\partial\phi}\right) = C_1\frac{\partial\phi}{\partial\xi_1}+C_2\frac{\partial\phi}{\partial\xi_2}+C_{11}\frac{\partial^2\phi}{\partial\xi_1^2}+C_{12}\frac{\partial^2\phi}{\partial\xi_1\partial\xi_2}+C_{22}\frac{\partial^2\phi}{\partial\xi_2^2}, \quad (9)$$

where

$$C_1 = \frac{\partial J^{-1}}{\partial\xi_1}B^{11}+\frac{\partial J^{-1}}{\partial\xi_2}B^{12}+J^{-1}\left(\frac{\partial B^{11}}{\partial\xi_1}+\frac{\partial B^{12}}{\partial\xi_2}\right),$$

$$C_2 = \frac{\partial J^{-1}}{\partial\xi_1}B^{21}+\frac{\partial J^{-1}}{\partial\xi_2}B^{22}+J^{-1}\left(\frac{\partial B^{21}}{\partial\xi_1}+\frac{\partial B^{22}}{\partial\xi_2}\right),$$

$$C_{11}=J^{-1}B^{11},\quad C_{12}=J^{-1}\left(B^{21}+B^{12}\right),\quad C_{22}=J^{-1}B^{22}.$$

2.1.2 Boundary conditions

In the present study heat transfer between cast part (p), mold (m) and environment (e) is investigated. The parameters of thermal behavior of the part/mold boundary govern the heat transfer, determining solidification progression. The heat flow through an interface will be the result of the combination of several modes of heat transfer. Furthermore, the value of the heat transfer coefficient varies with several factors. It is generally accepted that the heat transfer resistance at the interface originates from the imperfect contact or even separation of the cast part metal and the mold. It means a gap is formed between the casting and the mold during the casting (Wang & Matthys (2002), Lau et al. (1998)). Different possibilities must be considered for heat transfer conditions on the boundary:

i) Continuity condition

$$\left(\frac{\partial\phi}{\partial n}\right)_{m_1}=\left(\frac{\partial\phi}{\partial n}\right)_{m_2},\qquad \phi_{m_1}=\phi_{m_2} \quad (10)$$

is considered for the boundaries within continuous contact materials m_1 and m_2 (Monteiro (1996)). This means that the heat flux is fully transferred from the material m_1 to material m_2 without heat lost. These two materials are represented as blocks in the next sections.

ii) For the interface between different kind of materials, convective heat transfer is considered

$$k_m\left(\frac{\partial\phi}{\partial n}\right)_m = h^*\left(\phi_p-\phi_m\right), \quad (11)$$

where ϕ_m is the mold temperature, ϕ_p is the cast part temperature, h^* is the convective heat transfer coefficient and k_m in the thermal conductivity of the mold.

iii) For the exterior boundary in contact with the environment we have convection and radiation. From the work of Shi & Guo (2004) one has a mixed convection-radiation boundary condition given by

$$k_m\left(\frac{\partial\phi}{\partial n}\right)_m = h_{cr}\left(\phi_m-\phi_e\right), \quad (12)$$

here ϕ_e is the environment temperature and the convection-radiation heat transfer h_{cr} is calculated explicitly as follows

$$h_{cr} = \left(h_c + \varepsilon_r \sigma_r \left(\phi_m^3 - \phi_e^3\right)\right),$$

where ε_r is emissivity of the material, σ_r the Stefan-Boltzmann constant and the convective heat transfer coefficient h_c was considered equal to $150 W/m^{2^o}C$ (see Monteiro (1996)).

The governing system equations is composed by the heat conservative equation, the boundary condition equations and the initial equation. Despite the continuous efforts made by numerous studies, analytical solutions of such phase change problems are still limited to a few idealized situations. This is mainly because of the moving boundaries (interfaces) among different phases, the locations of which are essentially unknown. A comprehensive review of existing exact solutions can be found in the work of Carslaw & Jaeger (1959). On the other hand, numerous approximate methods including heat balance integral (Goodman (1958)), moving heat source (Lightfoot (1929)), and perturbation (Pedroso & Domoto (1973)) have been proposed to simplify the problem.

3. Numerical solution method

In this section, the discretization of the energy conservation equation coupling with convective boundary conditions using finite difference (FD), finite volume (FV) methods is presented. Furthermore, the development of the classical simple iterative methods: Jacobi and Gauss-Seidel and also for the incomplete factorization method strongly implicit procedure (SIP) is introduced in order to be used with curvilinear coordinates systems in a two dimensional domain.

3.1 Finite volume and finite difference

The most used approaches to discretization of the energy conservation equation coupling with convective boundary conditions are finite difference, finite volume and finite element methods. Here we use only the finite volume and finite difference methods. For the time discretization one uses the Crank-Nicholson semi implicit method (Ferziger & Peric (1999)).

3.1.1 Finite volume method

In the case of the FV method, two levels of approximation are needed for surface integrals: the integral is approximated in terms of the variables values at one location on the cell face, the midpoint point rule was used in this task; the cell face values are approximated in terms of the nodal values (control volume (CV) centers), the linear interpolation was used in this task. Fig. 2 shows the computational domain for FV discretization methods, using a geographical notation: E (east), N (north), S (south), W (west), NE (northeast), NW (northwest), SE (southeast), SW (southwest).

The volume integrals were approximated by a second-order approximation replacing the volume integral by the product of the mean value and the CV volume (Versteeg & Malalasekera (1995)). In this case, follows the expression for the first derivative

$$\int_V \frac{\partial \phi}{\partial \xi_i} dV = \frac{\phi_E - \phi_W}{2\Delta\xi_i} \Delta V, \tag{13}$$

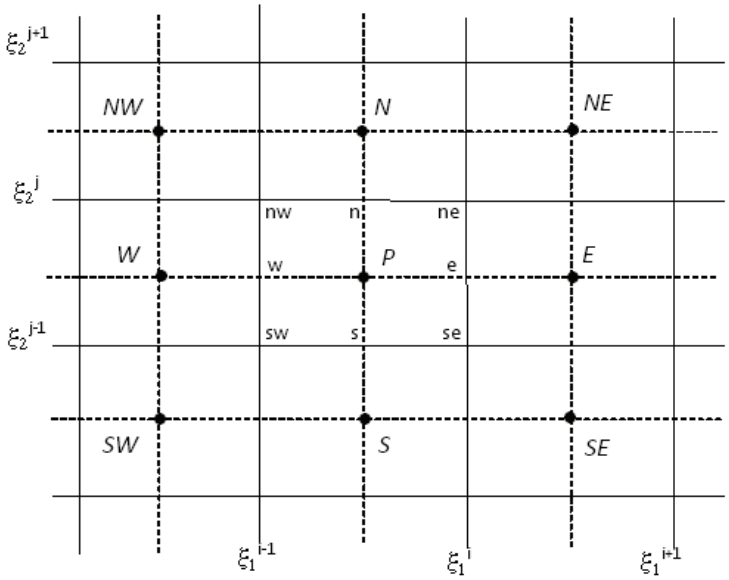

Fig. 2. Boundary condition treatment for finite volume method

and the second order derivatives are approximated as follows

$$\int_V \frac{\partial^2 \phi}{\partial \xi_i^2} dV = \int_S \frac{\partial \phi}{\partial \xi_i} \cdot \hat{n} dS = \left(\frac{\partial \phi}{\partial \xi_i}\right)_e S_e - \left(\frac{\partial \phi}{\partial \xi_i}\right)_w S_w, \tag{14}$$

$$\int_V \frac{\partial^2 \phi}{\partial \xi_i \partial \xi_j} dV = \int_V \frac{\partial}{\partial \xi_i}\left(\frac{\partial \phi}{\partial \xi_j}\right) dV = \frac{\left(\frac{\partial \phi}{\partial \xi_j}\right)_n S_n - \left(\frac{\partial \phi}{\partial \xi_j}\right)_s S_s}{\Delta \xi_i}. \tag{15}$$

Therefore, one can rewrite equation (9) as follows

$$\begin{aligned} & J\left(1 - \frac{\Delta h_f}{C_P}\frac{\partial f_s}{\partial \phi}\right)\left(\frac{\phi^{n+1} - \phi^n}{\triangle t}\right) \triangle V \\ = \; & \frac{1}{2}\left[\left(C_1 \frac{\partial \phi}{\partial \xi_1} + C_2 \frac{\partial \phi}{\partial \xi_2} + C_{11} \frac{\partial^2 \phi}{\partial \xi_1^2} + C_{12} \frac{\partial^2 \phi}{\partial \xi_1 \partial \xi_2} + C_{22} \frac{\partial^2 \phi}{\partial \xi_2^2}\right)^{n+1}\right. \\ + \; & \left.\left(C_1 \frac{\partial \phi}{\partial \xi_1} + C_2 \frac{\partial \phi}{\partial \xi_2} + C_{11} \frac{\partial^2 \phi}{\partial \xi_1^2} + C_{12} \frac{\partial^2 \phi}{\partial \xi_1 \partial \xi_2} + C_{22} \frac{\partial^2 \phi}{\partial \xi_2^2}\right)^{n}\right]. \end{aligned} \tag{16}$$

The discretization of the boundary condition derivatives are made by one side differences. The temperature value on each interface is computed considering the East surface interface of a general block 1 and the West surface interface a general block 2. One can see in Fig. 2 the boundary condition for FV methods, where P represents the node where the partial differential equation value is calculated.

The discretization of equation (10) allows us to obtain an explicit expression to determine the temperature on virtual interfaces, which is valid for FV discretization method and is given by

$$\phi_{m_1}(n,j) = \phi_{m_2}(0,j) = \frac{1}{2}\left(\phi_{m_1}(n-1,j) + \phi_{m_2}(1,j)\right). \tag{17}$$

The interface metal-mold using the FV method, is computed by

$$\phi_{m_1}(n,j) = \phi_{m_1}(n-1,j) + \frac{h_{m_1}}{2k\triangle\xi_1}\left(\phi^{old}_{m_1}(n,j) - \phi^{old}_{m_2}(0,j)\right), \tag{18}$$

$$\phi_{m_2}(0,j) = \phi_{m_2}(1,j) + \frac{h_{m_1}}{2k_m\triangle\xi_1}\left(\phi^{old}_{m_2}(0,j) - \phi^{old}_{m_1}(n,j)\right), \tag{19}$$

where $\phi^{old}_{m_l}$, for $l = 1,2$, is the previous iteration. For the interface mold-environment we have

$$\phi_{m_1}(n,j) = \phi_{m_1}(n-1,j) + \frac{h_{cr}}{2k_m\triangle\xi_1}\left(\phi_e - \phi^{old}_{m_2}(0,j)\right). \tag{20}$$

3.1.2 Finite difference method

Using a geographical notation, Fig. 3 shows the computational domain for FD discretization method.
In this case, the derivatives are approximated using the central difference scheme as follows

$$\frac{\partial\phi}{\partial\xi_i} = \frac{\phi_E - \phi_W}{2\Delta\xi_i}, \tag{21}$$

and the second order derivatives are approximated as follows

$$\frac{\partial^2\phi}{\partial\xi_i^2} = \frac{\phi_E - 2\phi_P - \phi_W}{2\Delta\xi_i^2}, \tag{22}$$

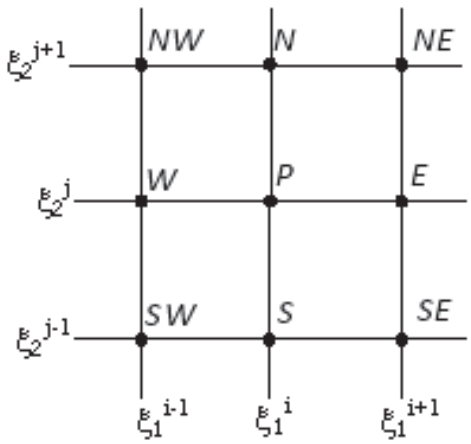

Fig. 3. Boundary condition treatment for finite difference method

$$\frac{\partial^2\phi}{\partial\xi_i\partial\xi_j} = \frac{\phi_{NE}-\phi_{SE}-\phi_{NW}+\phi_{SW}}{4\Delta\xi_i\Delta\xi_j}. \tag{23}$$

Therefore, one can rewrite equation (9) as follows

$$\begin{aligned} & J\left(1-\frac{\Delta h_f}{C_P}\frac{\partial f_s}{\partial\phi}\right)\left(\frac{\phi^{n-1}-\phi^n}{\triangle t}\right) \\ = \; & \frac{1}{2}\left[\left(C_1\frac{\partial\phi}{\partial\xi_1}+C_2\frac{\partial\phi}{\partial\xi_2}+C_{11}\frac{\partial^2\phi}{\partial\xi_1^2}+C_{12}\frac{\partial^2\phi}{\partial\xi_1\partial\xi_2}+C_{22}\frac{\partial^2\phi}{\partial\xi_2^2}\right)^{n+1}\right. \\ + \; & \left.\left(C_1\frac{\partial\phi}{\partial\xi_1}+C_2\frac{\partial\phi}{\partial\xi_2}+C_{11}\frac{\partial^2\phi}{\partial\xi_1^2}+C_{12}\frac{\partial^2\phi}{\partial\xi_1\partial\xi_2}+C_{22}\frac{\partial^2\phi}{\partial\xi_2^2}\right)^{n}\right]. \end{aligned} \tag{24}$$

The discretization of the boundary condition derivatives are made by one side differences. The temperature value on each interface is computed considering the East surface interface of a general block 1 and the West surface interface a general block 2.
The discretization of equation (10) allows us to obtain an explicit expression to determine the temperature on virtual interfaces, which is valid for both FV and FD discretization methods and is given by

$$\phi_{m_1}(n,j)=\phi_{m_2}(0,j)=\frac{1}{2}\left(\phi_{m_1}(n-1,j)+\phi_{m_2}(1,j)\right). \tag{25}$$

The interface metal-mold using the FD method, is computed by

$$\phi_{m_1}(n,j) = \phi_{m_1}(n-1,j)+\frac{h_{m_1}\triangle\xi_2}{k}\left(\phi_{m_1}^{old}(n,j)-\phi_{m_2}^{old}(0,j)\right), \tag{26}$$

$$\phi_{m_2}(0,j) = \phi_{m_2}(1,j)+\frac{h_{m_1}\triangle\xi_2}{k_m}\left(\phi_{m_2}^{old}(0,j)-\phi_{m_1}^{old}(n,j)\right), \tag{27}$$

where the first equation is related to the metal block and the second is related to the mold block. For the interface mold-environment we have

$$\phi_{m_1}(n,j) = \phi_{m_1}(n-1,j)+\frac{h_{cr}\triangle\xi_2}{k_m}\left(\phi_e-\phi_{m_2}^{old}(0,j)\right). \tag{28}$$

3.2 Jacobi, Gauss-Seidel and Stone's methods

Here, the development of the classical solvers (*Jacobi*,*Gauss-Seidel*) and *Stone's* solver also known as *strongly implicit procedure (SIP)* is presented in the way to be used with curvilinear coordinates in two dimensional domains. The aim is to apply these methods to non-orthogonal grid.

From the FV or FD discretisation procedure one obtains a linear system of the form

$$A\Theta = Q, \tag{29}$$

where A is a sparse matrix, Θ the variable in computation and Q a vector of independent terms (see e.g. Ferziger & Peric (1999), Pina (1995), Tannehill (1997)). The coefficient matrix will typically take on a hepta diagonal structure, with the non-zero components occupying only seven diagonals of the matrix. For a two dimensional partial differential equations there will

be only five diagonals which are non-zero. For unstructured meshes, the coefficient matrix will also take a diagonal structure, with the non-zero components occupying nine diagonals of the matrix for two dimensional. This regular structure enables a considerable reduction in memory use and the number of operations performed.
The structure of the matrix A depends on the ordering of the variables in the vector Θ. As in the work of Ferziger & Peric (1999), one orders the entries in the vector Θ starting at the southwest corner of the domain, proceeding northwards along each grid and then eastward across the domain. The algebraic equation for a particular control volume in a two dimensional domain, see Fig. 2, using curvilinear coordinates, is of the form

$$A_P\Theta_p + \sum_{nb} A_{np}\Theta_{np} = Q_p, \tag{30}$$

where P represents the node where the partial differential equation value is calculated and the index nb represents the neighborhood nodes involved in the approach. Using a geographical notation: E (east), N (north), S (south), W (west), NE (northeast), NW (northwest), SE (southeast), SW (southwest), the sum is extended in the following form

$$\begin{aligned}\sum_{nb} A_{np}\Theta_{np} &= A_E\Theta_E + A_W\Theta_W + A_N\Theta_N + A_S\Theta_S \\ &+ A_{NE}\Theta_{NE} + A_{SE}\Theta_{SE} + A_{NW}\Theta_{NW} + A_{SW}\Theta_{SW}.\end{aligned} \tag{31}$$

The properties of the linear system (29) are important when setting up an iteration method for its solutions. Let us present some of the classical iteration methods modified to the problem treated here.

3.2.1 Jacobi's method

In the Jacobi method the resulting equations from the discretisation process are determined separately. Equation (31) is modified assuming the following form

$$\Theta_P = (A_P)^{-1}\left(Q_P - \sum_{nb\neq P} A_{nb}\Theta_{nb}\right). \tag{32}$$

Having the following iterative method defined as

$$\Theta_P^{(k)} = (A_P)^{-1}\left(Q_P - \sum_{nb\neq P} A_{nb}\Theta_{nb}^{(k-1)}\right), \tag{33}$$

where all the terms of the equation (33) are related to the last iteration release. In the Jacobi method the used values are of the previous iteration in the way to get the values of the following iteration. However, when we are calculating the new, the actual value is already known.

3.2.2 Gauss-Seidel's method

The Gauss-Seidel method, in contrast with the Jacobi method, uses the actual values in detriment of the ones of the previous iteration (see Pina (1995), Norris (2001)). This idea leads to the following modification of equation (33)

$$\Theta_P^{(k)} = (A_P)^{-1}\left(Q_P - \sum_{nb\in\{SW,W,NE,S\}} A_{nb}\Theta_{nb}^{(k)} - \sum_{nb\in\{N,NE,E,SE\}} A_{nb}\Theta_{nb}^{(k-1)}\right).$$

Usually, this method converges faster than the Jacobi method.

3.2.3 Stone's method

The *strongly implicit procedure (SIP)*, also known as the Stone's method (Stone (1968)), is known for solving the system of algebraic equations that arises, for instance, in the finite differences or finite analytic description of field problems (Schneider & Zedan (1981)). This procedure was also used in multi-phase fluid flow and heat transfer problems (Peric (1987)). The SIP solver is an advanced version of the incomplete LU decomposition

$$M = LU,$$

where M is the iterative matrix, L (lower triangular) and U (upper triangular) matrices. The matrix M is given by the splitting of the matrix A in the form $M = A + N$, such that M is a good approximation to A.

This method will be described for a nine-point computational cell (see Fig. 2). The L (lower) and U (upper) matrices have non-zero elements only on diagonals on which A has non-zero elements. The product of lower and upper triangular matrices with these structures has more non-zero diagonals than A.

For the nine-point computational cell there are four diagonals (corresponding to nodes NN (north-north), NNW (nor-norwest) , SS (south-south), SSE (sud-southeast), SS (south-south)) as can be seen in Fig. 4.

The nine sets of elements (five in L and four in U) are determined using the rules of multiplication matrix as follows

$$\begin{aligned}
M_{SW} &= L_{SW} \\
M_W &= L_{SW}U_N + L_W \\
M_{NW} &= L_W U_N + L_{NW} \\
M_{NNW} &= L_{NW}U_N \\
M_{SS} &= L_{SW}U_{SE} \\
M_S &= L_{SW}U_E + L_W U_{SE} + L_S \\
M_P &= L_{SW}U_{NE} + L_W U_E + L_{NW}U_{SE} + L_S U_N + L_P \\
M_N &= L_W U_{NE} + L_{NW}U_E + L_P U_N \\
M_{NN} &= L_{NW}U_{NE} \\
M_{SSE} &= L_S U_{SE} \\
M_{SE} &= L_S U_E + L_P U_E \\
M_E &= L_S U_{NE} + L_P U_E \\
M_{NE} &= L_P U_{NE},
\end{aligned} \tag{34}$$

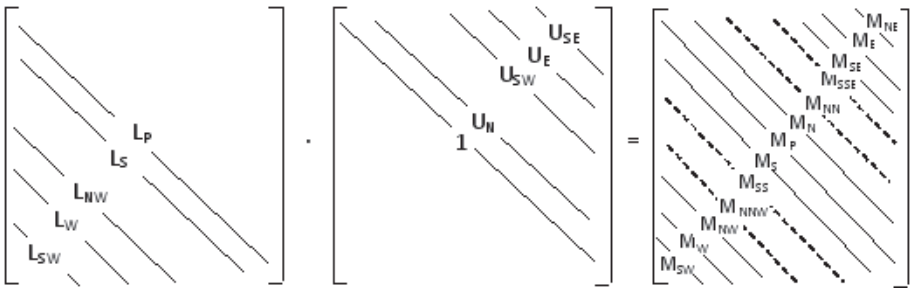

Fig. 4. Schematic presentation of the matrices L (Lower), U (Upper) and the product matrix M; diagonals of M not found in A are shown by dashed lines

we consider M_X to be the matrix with only the diagonal M_X non-zero as for L_X and U_X.
We wish to select matrices L and U, in order to obtain M as a good approximation to A and consequently has a faster convergence of the method. For this reason the matrix N must contain, at least, the four diagonals of the matrix M which correspond to zero diagonals of A. Furthermore, N has to have non-zero elements only on these diagonals. Therefore, the other diagonals of matrix M has the corresponding diagonals of A.
Stone (1968) recognized that convergence can be improved by allowing matrix N to have non-zero elements on the diagonal corresponding to all thirteen non-zero diagonals of LU.
Considering the vector $M\Theta$, the method can be easily derived

$$\begin{array}{rcl}(M\Theta)_P & = & M_P\Theta_P + M_S\Theta_S + M_N\Theta_N + M_E\Theta_E + M_W\Theta_W \\ & + & M_{NE}\Theta_{NE} + M_{NW}\Theta_{NW} + M_{SE}\Theta_{SE} + M_{SW}\Theta_{SW} \\ & + & M_{NNW}\Theta_{NNW} + M_{SSE}\Theta_{SSE} + M_{NN}\Theta_{NN} + M_{SS}\Theta_{SS}.\end{array} \tag{35}$$

Each term in this equation corresponds to a diagonal of $M = LU$. The matrix N must contain the four last terms which are the extra diagonals of M, and the elements on the remaining diagonals, are chosen so that $N\Theta \approx 0$, this is,

$$\begin{array}{l}N_P\Theta_P + N_S\Theta_S + N_N\Theta_N + N_E\Theta_E + N_W\Theta_W \\ +N_{NE}\Theta_{NE} + N_{NW}\Theta_{NW} + N_{SE}\Theta_{SE} + N_{SW}\Theta_{SW} \\ +N_{NNW}\Theta_{NNW} + N_{SSE}\Theta_{SSE} + N_{NN}\Theta_{NN} + N_{SS}\Theta_{SS} \quad \approx \quad 0.\end{array} \tag{36}$$

This requires that the contribution of the four extra terms, in the above equation, have to be nearly canceled by the contribution of other diagonals, i.e., equation (35) should be reduce to the following expression

$$\begin{array}{l}M_{NNW}\left(\Theta_{NNW} - \Theta^*_{NNW}\right) + M_{SSE}\left(\Theta_{SSE} - \Theta^*_{SSE}\right) \\ +M_{NN}\left(\Theta_{NN} - \Theta^*_{NN}\right) + M_{SS}\left(\Theta_{SS} - \Theta^*_{SS}\right) \quad \approx \quad 0,\end{array} \tag{37}$$

where $\Theta^*_{NNW}, \Theta^*_{SSE}, \Theta^*_{NN}, \Theta^*_{SS}$ are approximations of $\Theta_{NNW}, \Theta_{SSE}, \Theta_{NN}, \Theta_{SS}$, respectively.
Rouboa et al. (2009) considered the following possible approximation

$$\begin{array}{rcl}\Theta^*_{NNW} & = & \alpha\left(\Theta_{NW} + \Theta_N + \Theta_W - 2\Theta_P\right) \\ \Theta^*_{NN} & = & \alpha\left(\Theta_N + \Theta_{NE} + \Theta_{NW} - 2\Theta_P\right) \\ \Theta^*_{SS} & = & \alpha\left(\Theta_S + \Theta_{SW} + \Theta_{SE} - 2\Theta_P\right) \\ \Theta^*_{SSE} & = & \alpha\left(\Theta_S + \Theta_{SE} + \Theta_E - 2\Theta_P\right),\end{array} \tag{38}$$

where $\alpha < 1$ for stability reasons.
Substituting (38) into equation (37) and comparing the result with equation (36), we obtain all elements of matrix N as linear combinations of M_{NNW}, M_{SSE}, M_{NN} and M_{SS}. Elements of the matrix M can be set equal to the sum of matrix elements of A and N.
The resulting equations are not only sufficient to determine all of the elements of the matrix L and U, but they can be solved in sequential order beginning at the southwest corner of the grid

$$L^{ij}_{SW} \quad = \quad \frac{A^{ij}_{SW}}{1 + \alpha U^{(i-1),(j-1)}_{SE}}$$

$$
\begin{aligned}
L_W^{ij} &= A_W^{ij} + L_{SW}^{ij} U_N^{ij} - \alpha L_{NW}^{ij} U_N^{(i-1),(j+1)} \\
L_{NW}^{ij} &= \frac{A_S^{ij} - L_W^{ij} U_N^{i-1,j}}{1 + \alpha \left(U_N^{(i-1),(j+1)} + U_{NE}^{i-1,j+1} \right)} \\
L_S^{ij} &= \frac{A_S^{ij} - L_{SW}^{ij} U_E^{i-1,j-1} - L_W^{ij} U_{SE}^{i-1,j} - \alpha L_{SW}^{ij} U_{SE}^{i-1,j-1}}{1 + \alpha U_{SE}^{i,j-1}} \\
L_P^{ij} &= A_P^{ij} - L_{SW}^{ij} U_{NE}^{i-1,j-1} - L_W^{ij} U_E^{i-1,j} - L_{NW}^{ij} U_{SE}^{i-1,j+1} - L_S^{ij} U_N^{i,j-1} \\
&+ 2\alpha \left(L_{SW}^{ij} U_{SE}^{i-1,j-1} + L_S^{ij} U_{SE}^{i-1,j+1} + L_{NW}^{ij} \left(U_{NE}^{i-1,j+1} + U_N^{i-1,j+1} \right) \right) \\
U_N^{ij} &= \frac{A_N^{ij} - L_W^{ij} U_{NE}^{i-1,j} - L_{NW}^{ij} U_E^{i-1,j+1} - \alpha L_{NW}^{ij} U_{NE}^{i-1,j+1}}{L_P^{ij} + \alpha L_{NW}^{ij}} \\
U_{SE}^{ij} &= \frac{A_{SE}^{ij} - L_S^{ij} U_E^{i,j-1}}{L_P^{ij} + \alpha \left(L_{SW}^{ij} - L_S^{ij} \right)} \\
U_E^{ij} &= \frac{A_E^{ij} - L_S^{ij} U_{NE}^{i,j-1} - \alpha L_S^{ij} U_{SE}^{i,j-1}}{L_P^{ij}} \\
U_{NE}^{ij} &= \frac{A_{NE}^{ij}}{L_P^{ij} + \alpha L_{NW}^{ij}}.
\end{aligned}
\tag{39}
$$

One considers that any matrix element that carries the index of a boundary node is zero. The equation system using this approximation is solved by iteration. The updated residual is calculated by the following equation

$$L U \delta^{n+1} = \rho^n.$$

The multiplication of the above equation by L^{-1} leads to

$$\delta^{n+1} = \quad L^{-1} \rho^n =: \quad R^n \tag{40}$$

where R is computed by

$$R^{ij} = \frac{\rho^{ij} - L_{SW}^{ij} R^{i-1,j-1} - L_S^{ij} R^{i,j-1} - L_{NW}^{ij} R^{i-1,j+1} - L_W^{ij} R^{i-1,j}}{L_P^{ij}}. \tag{41}$$

When the computation of R is complete, we need to solve equation (40) using

$$\delta^{ij} = R^{ij} - U_N^{ij} \delta^{i,j+1} - U_{NE}^{ij} \delta^{i+1,j+1} + U_E^{ij} \delta^{i+1,j} + U_{SE}^{ij} \delta^{i+1,j-1}, \tag{42}$$

in order of decreasing the i,j indexes.

4. Numerical applications

The aim of these present experiments is to validate the developed numerical code. We start by developing the classical solvers (Jacobi, Gauss-Seidel) and Stone method in order to use them with curvilinear coordinates systems in two dimensional domains. Furthermore, we compare the finite volume and finite difference methods in terms of space discretization, boundary conditions definition and results using a multi-block grid in combination with curvilinear coordinates.

The numerical simulation was carried out on a two dimensional domain constituted by the cross-section defined by the middle plane of the test part. In Fig. 5 the $D1$ domain is constituted by the cross-section of the part including the filling channel, the $D2$ domain is constituted by the cross-section of the inferior part of the mold, $D3$ and $D4$ correspond to superior part of the mold and both domains are fixed to each other.

Grid generation was carried out by bilinear interpolation (Thompson et al. (1985)) and each domain was subdivided in simpler subdomains, see Fig. 6.

The use of curvilinear formulation in conjunction with a multi-block grid could be an excellent method to test every kind of curvilinear link of piping in a single simulation. The part (domain $D1$) is filled in with the aluminium alloy ($Al12Si$) cast in a grey cast iron mold (domains $D2$, $D3$ and $D4$). The physical characteristics of the materials involved in the numerical simulation are shown in Table 1 (Monteiro (1996), Sciama & Visconte (1987)).

Property	Metalic alloy AI 12Si	Mold Grey cast-iron
Density (kg/m^3)	2670	7230
Thermal conductivity ($W/m°C$)	185	38
Thermal heat capacity ($J/kg°C$)	1260	750
Latent heat (kJ/kg)	395	···
Liquidus temperature ($°C$)	585	···
Solidus temperature ($°C$)	575	···

Table 1. Physical properties

The liquidus and solidus temperatures were experimentally determined by a 50 KV high frequency induction furnace to melt the aluminium/silicon alloy used. K type thermocouples, constituted by the pair 5%Al Ni and 10%Cr-Ni with a total diameter of 1 mm, were used in the temperature measurements. A data acquisition board connected to a microcomputer was used to temperature recording. This board is responsible for the digitalization of the analogical signal produced by the thermocouples. The tested alloy is composed by aluminium with 12% of silicon (Al 12Si). The obtained cooling curve is represented in Fig. 7, from which is possible to determine that the liquidus temperature is 585^0C and the solidus temperature is 575^0C.

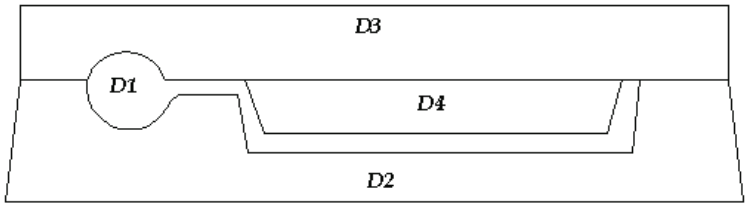

Fig. 5. Cross section of the mold/part set

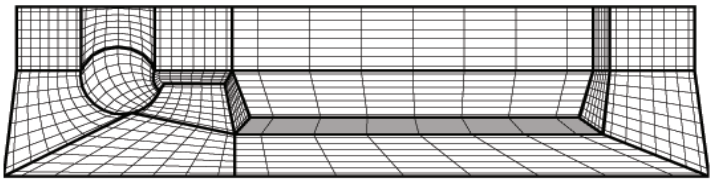

Fig. 6. Representation of the mesh used to discretize each of the subdomains

Fig. 8 shows the cross section of the studied domain and thermocouples locations. Due to the high temperature it was difficult to obtain stable values by thermocouples.
The environment temperature was considered to be constant, at 20^0C. During the filling of the mold by a gravity-fed system a significant volume of metal may solidify before the end of the process. To prevent the filling from being interrupted by premature solidification, the metal is usually cast into a hot mold. During the solidification process the initial temperature of the mold is considered uniform, as assumed in the previous works of Radovic & Lalovic (2005), Santos et al. (2003) and Shi & Guo (2004). For this reason the initial temperature field in the mold, considered uniform, was set to 300^0C. The initial temperature field in the part, considered also uniform, was set to 585^0C (liquidus temperature). The end of phase change is determined by the solidus temperature. The mold was divided into 17 polygons, Fig. 9 (Monteiro et al. (2006), Monteiro & Rouboa (2005)).
This phenomenon was applied on the outer wall of the mold. The convective heat transfer phenomena was adapted as boundary conditions between the following blocks

- block 1 with block 7, block 10, block 11, block 12;
- block 2 with block 7 and block 13;
- block 3 with block 7 and block 6;
- block 4 with block 6 and block 9;

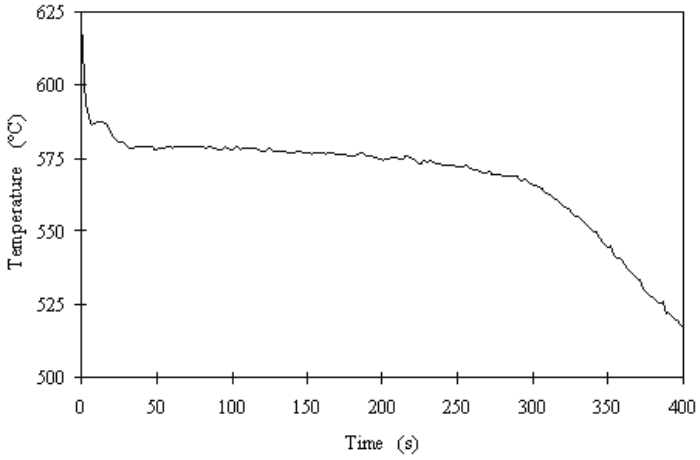

Fig. 7. Temperature profile during solidification of Al 12Si

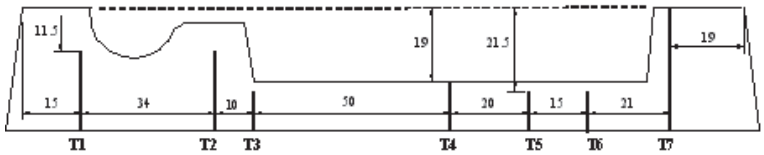

Fig. 8. Thermocouples (T1–T7) location (in mm) on the mold crosss-section

- block 5 with block 6 and block 8.

The convective heat transfer coefficients in Table 2 were determined using the inverse heat conduction problem of Beck (1970), which the basic principle is to assume that the heat flux is a constant on a linear function of time within a given time interval. The whole description of this technique can be found in the work of Lau et al. (1998). The definition of all coordinate

Interface	Convective heat transfer coefficient $[W/m^2\,^0C]$
Cast part/mold	$h_i = 2500$
Block 8/16	$h_i = 500$
Block 11/17	$h_i = 500$
Block 6/14	$h_i = 600$
Mold/environment	$h_i = 150$

Table 2. Convective heat transfer coefficients

lines in the interior of the domain is made by bilinear interpolation of the nodal position defined in the boundaries resulting in the grid showed in Fig. 6.
The physical characteristics of the material involved in the numerical simulation are shown in Table 1.

4.1 Performance of adapted solvers

In this study we adapt the simples iterative methods: Jacobi, Gauss-Seidel and the incomplete factorization method strongly implicit procedure (SIP) to generalized curvilinear coordinates and apply them to a complex geometry through the multi-block grid technique.
Since the analysis was made for each block, only some relevant block will be discussed further.

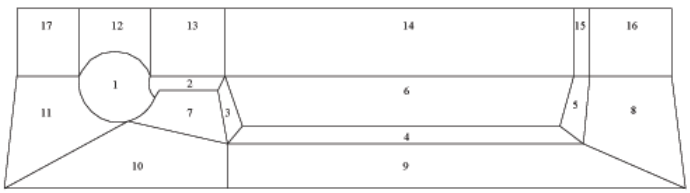

Fig. 9. Geometry division into 17 blocks

Subdomain	SIP		Gauss-Seidel		Jacobi	
Block	Iteration	Residue	Iteration	Residue	Iteration	Residue
1	1000	1.99×10^{-3}	1000	1.51	1000	1.51
2	2	8.90×10^{-4}	1000	0.46	1000	0.48
3	1000	1.05×10^{-3}	1000	0.33	1000	0.33
4	2	8.64×10^{-4}	1000	2.28	1000	2.28
5	2	9.18×10^{-4}	1000	0.53	1000	0.52
6	2	1.66×10^{-4}	1000	3.31	1000	3.32
7	2	1.54×10^{-4}	1000	0.57	1000	0.59
8	2	4.57×10^{-4}	1000	1.73	1000	1.65
9	2	6.41×10^{-5}	1000	1.66	1000	1.78
10	1000	1.91×10^{-3}	1000	1.59	1000	1.66
11	2	1.21×10^{-4}	1000	1.15	1000	1.27
12	2	4.44×10^{-5}	1000	0.34	1000	0.34
13	2	2.46×10^{-4}	1000	0.90	1000	1.05
14	1000	6.19×10^{-3}	1000	5.47	1000	5.36
15	2	2.85×10^{-4}	1000	0.25	1000	0.25
16	1000	3.07×10^{-3}	1000	0.78	1000	0.77
17	1000	1.31×10^{-3}	1000	0.37	1000	0.38

Table 3. Iterative performance

Consider Fig. 9, the block 1 which is the most complicated geometrical structure. After 1000 iterations it is observed, in Table 3, that the SIP method has better residual in comparison with the others two classical solvers.
For block 14 the same conclusion can be made after 1000 iterations, even though the regularity of its geometry and simplicity of its boundaries conditions. In fact, this block is submitted to natural convection on the top and conduction limit on the other three sides.
The block 7, that has more contact to the shape of the mold, converges after only 2 iterations for SIP solver. For the others cited solvers no convergence has been shown after 1000 iterations.
The block 9, presents the best residual result for the SIP solver, in relation to all block. Furthermore, its has a better residual result for the SIP methods only for 2 iterations compared to 1000 iteration made for the Jacobi and Gauss-Seidel methods.

4.1.1 Concluding remarks on numerical solvers

Adaptations of simple iterative methods (Jacobi and Gauss-Seidel) and the incomplete factorization method strongly implicit procedure (SIP) to generalized curvilinear coordinates was presented and its applicability in complex geometries through the multi-block grid technique was performed.
The complexity of the geometry, results showed that Jacobi and Gauss-Seidel solvers are not suitable. However, SIP method continues to have a reasonable performance. In conclusion strongly implicit procedure method, when combined with generalized curvilinear coordinates and multi-block grid technique, can be used in complex geometry problems when high precision results are not required.

4.2 Performance of finite differences and finite volume methods

The most used approaches to discretization of the energy conservation equation coupling with convective boundary conditions are finite difference, finite volume and finite element methods. For finer grid mesh, these methods yields the same approximately solution (Ferziger & Peric (1999), Versteeg & Malalasekera (1995)). Here we compare the FV and FD methods in terms of space discretization, boundary conditions definition and results using a multi-block grid in combination with curvilinear coordinates.

In this study the FV method is programmed using a multi-block grid applied in the case of heat transfer phenomena during solidification. Fig. 9 shows subdomains (blocks) of casting (block 1 to 5) and mold (block 6 to 17). The multi-block grid is generated by bilinear interpolation (Thompson et al. (1985)) with increased concentration of cells near the geometrical singularities where the thermal gradients are expected to be higher.

Due to the use of generalized curvilinear coordinates the calculations in each bock could be performed in a fixed square. Fig. 2 and Fig. 3 shows the computational domain for the FV and FD methods, respectively. In the FV method the domain is divided into a finite number of control volumes, which in opposite to the FD method defines the control volume limit and not the computational nodes.

4.2.1 Results and discussion

In this study, an analysis of heat transfer for the casting process in two dimensions was made for the nonlinear case during solidification taking into account the phase change. The time step used was 10^{-3} seconds. The result of the heat transfer is shown in two dimensions, as well as the cooling curves in different points in the cast metal and mold. The final step consists in solving the problem of heat transfer of the mold - cast metal system, using linearized equation (9) and controlled by the convergence criteria (10^{-5} for temperature). The SIP solver of Stone (1968) was used in this task. Numerical results calculated using FD and FV discretization methods were overlapped with experimental values, measured by the thermocouples $T1$, $T2$, $T3$, $T4$, $T5$, $T6$ and $T7$, shown in Fig. 10.

4.3 Concluding remarks

A multi-block grid generated by bilinear interpolation was successfully applied in combination with a generalized curvilinear coordinates system to a complex geometry in a casting solidification scenario. To model the phase change a simplified two dimensional mathematical model was used based on the energy differential equation. Two discretization methods: finite differences and finite volume were applied in order to determine, by comparison with experimental measurements, which works better in these conditions. For this reason a coarse grid was used. A good agreement between both discretization methods was obtained with a slight advantage for the finite volume method. This could be explained due to the use of more information by the finite volume method to compute each temperature value than the finite differences method. The multi-block grid in combination with a generalized curvilinear coordinates system has considerably advantages such as:

- better capacity to describe the contours through a lesser number of elements, which considerably reduces the computational time;
- any physical feature of the cast part or mold can be straightforwardly defined and obtained in a specific zone of the domain;
- the difficulty of the several virtual interfaces created by the geometry division are easily overcome by the continuity condition;

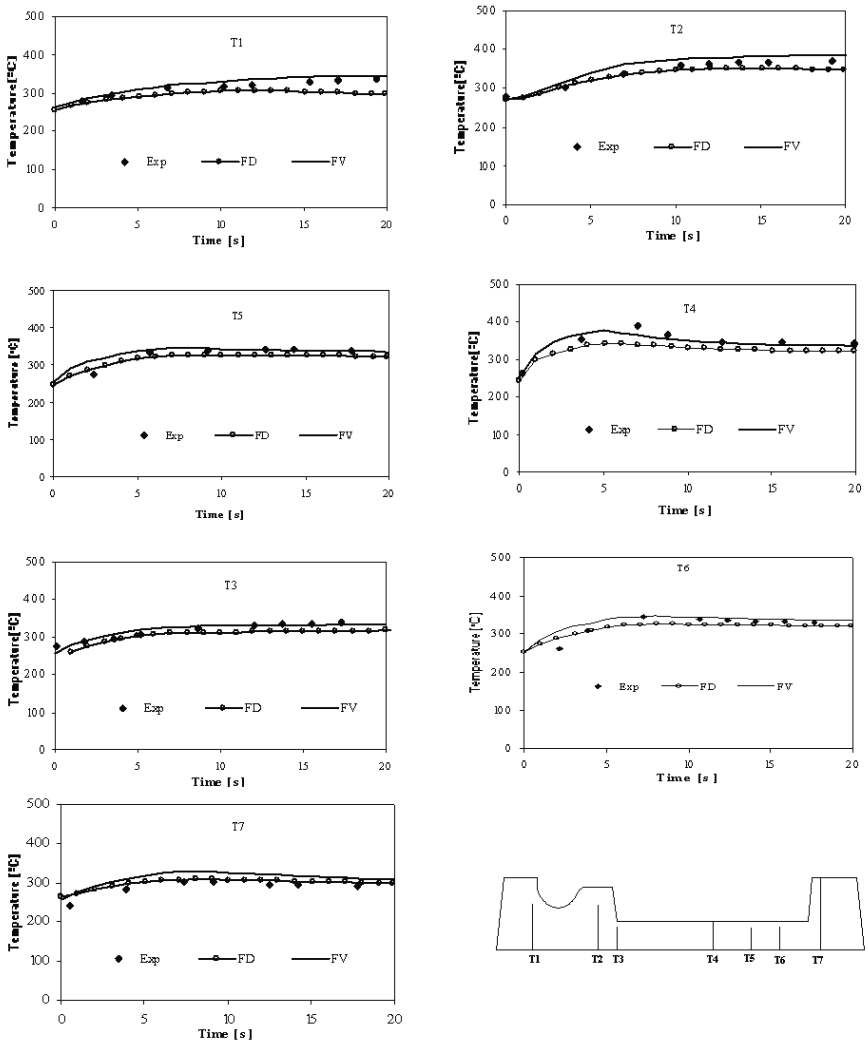

Fig. 10. Temperature results in seven points of the mold: Experimental measurement (Exp), Finite Differences numerical results (FD), Finite Volume numerical results (FV)

- straightforwardly programming.

In order to get even better results one could explore the grid refinement. However, special care must be taking in order to keep an acceptable computational time. This technique could also be an excellent choice for parallel computation, being each block or blocks affected to a physical processor.

While models can do a lot they are not yet transportable, meaning that considerable calibration is required for the conditions specific to the particular foundry. This is because nucleation

model are still highly empirical, and many physical properties are poorly known. Thus, we believe that the field has still potential for further development.

5. References

Beck, J.V. (1970). Nonlinear estimation applied to the nonlinear inverse heat conduction problem, *Int. J. Heat Mass Transfer*, 13, 703–716.

Beckermann, C. & Viskanta, R. (1988). Double-diffusion convection during dendritic solidification of a binary mixture, *Physicochem. Hydrodyn.*, 10, 195–213.

Bellet, M. & Fachinotti, V.D. (2004). ALE method for solidification modelling, *Comput. Methods. Appl. Mech. Engrg.*, 193, 4355–4381.

Bennon, W.D. & Incropera, F.P. (1987). A continuum model for momentum, heat and species transport in binary solid-liquid phase change systems-II. Application to solidification in a rectangular cavity, *Int. J. Heat Mass Transfer*, 30, 2171–2187.

Carslaw, H.S. & Jaeger, J.C. (1959). *Conduction of Heat in Solids*. Clarendon Press, Oxford.

Dimova, S.; Kaschiev, M.; Koleva, M. & Vasileva, D. (1998). Numerical analysis of radially nonsymmetric blow-up solutions of a nonlinear parabolic problem, *Journal of Computational and Applied Mathematics*, 97, 81–97.

Feldheim, V. & Lybaert, P. (2004). Solution of radial heat transfer problems with discrite transfer method applied to triangular meshes, *Journal of Computational and Applied Mathematics*, 168, 179–190.

Ferziger, J.H. & Peric, M. (1999). *Computational Methods for Fluid Dynamics*, 2nd edition, Springer Verlag, Berlin, Heidelberg, New York.

Ganesan, S. & Poirier, D.R. (1990). Conservation of mass and momentum for the flow of interdendritic liquid during 14. solidification, *Metall. Trans.*, 21B, 173–181.

Goodman, T.R. (1958). The heat balance integral and its applications to problems involving change of phase, *J. Heat Transf.*, 80(3), 335-341.

Knoll, D.A.; Vanderheyden, W.B.; Mousseau, V.A. & Kothe, D.B. (2001). On preconditioning Newton-Krylov methods in solidifying flow application, *SIAM, J. Appl. Math.*, 23(2), 381–397.

Lan, C.W. & Chen, F.C. (1996). A finite volume method for solute segregation in directional solidification and comparison with a finite element method, *Comput. Methods Appl. Mech. Engrg.*, 131(1–2), 191–207.

Lau, F.; Lee, W.B.; Xiong, S.M.; Liu, B.C. (1998). A study of the interface heat transfer between an iron casting and a metallic mould, *J. Mat. Process. Technol.*, 79 , 25–29.

Lightfoot, N.M.H. (1929). The solidification of molten steel, *Proc. Lond. Math. Soc.*, 31(2), 97-116.

Lockwood, F.C. & Shah, N.G. (1981). A new radiation solution method for incorporation in general combustion prediction procedures, *18th International Symposium on Combustion, The Combustion Institute, Pittsburgh, PA*, 1405–1414.

Monteiro, A.A.C. (1996). *Estudos do Comportamento Térmico de Moldações Metálicas para a Fundição Aplicando o Método das Diferenças Finitas Generalizadas*, Ph.D. Thesis, University of Minho, Braga, Portugal.

Monteiro, E. (2003). *Numerical study of the casting process using finite volume method*, M.Sc. Dissertation. University of Trás-dos-Montes e Alto Douro, Vila Real, Portugal.

Monteiro, E.; Monteiro, A.A.C. & Rouboa, A. (2006). Heat transfer simulation in the mould with generalize curvilinear formulation, *Journal of Pressure Vessel Technology*, 128, 462–466.

Monteiro, E. & Rouboa, A. (2005). Numerical simulation of the aluminium alloys solidification

in complex geometries, *J. Mech. Sci. Tech.*, 19(9), 1773–1780.
Ni, J. & Beckermann, C. (1991). A volume-averaged two-phase model for transport phenomena during solidification, *Metall. Trans.*, 22B, 349–361.
Norris, S.E. (2001). *A Parallel Navier Stokes Solver for Natural convection and Free Surface Flow*, Ph.D Thesis, Faculty of Mechanical Engineering, University of Sydney, Australia.
Pedroso, R.I. & Domoto, G.A. (1973). Inward spherical solidification-solution by the method of strained coordinates, *Int. J. Heat Mass Transf.*, 16, 1037-1043.
Peric, M. (1987). Efficient semi-implicit solving algorithm for nine-diagonal coefficient matrix, *Numer. Heat Transfer*, 11(3), 251–279.
Pina, H. (1995). *Métodos Numéricos*, McGraw-Hill.
Radovic, Z. & Lalovic, M. (2005). Numerical simulation of steel ingot solidification process, *J. Mater. Process. Technol.*, 160, 156–159.
Rappaz, M. (1989). Modelling of microstructure formation in solidification processes, *Int. Mater. Rev.*, 34, 93–123.
Rappaz, M. & Voller, V. (1990). Modeling of micro-macrosegregation in solidification process, *Metal. Trans.*, 21A, 749–753.
Rouboa, A.; Monteiro, E. & Almeida, R. (2009). Finite volume method analysis of heat transfer problem using adapted strongly implicit procedure, *J. Mech. Sci. Tech.*, 23, 1–10.
Santos, C.A.; Spim, J.A. & Garcia, J.A. (2003). Mathematical modelling and optimization strategies (genetic algorithm and knowledge base) applied to the continuous casting of steel, *Eng. Appl. Artif. Intelligence*, 16, 511–527.
Schneider, G.E. & Zedan, M. (1981). A modified Strongly Implicit procedure for the numerical solution of field problems, *Numer. Heat Transfer*, 4(1), 1–19.
Sciama, G. & Visconte, D. (1987). Modélisation des Transferts Thermiques Puor la Coulée en Coquillede Pièces de Robinetterie Sanitaire, *Foundarie, Fondeur d'Aujourd'hui,* 70, 11–26.
Sethian, J.A. (1996). *Level set methods and fast marching methods: evolving interfaces in computational geometry, fluid mechanics, computer vision and materials science*, Cambridge University Press.
Shamsundar, N. & Sparrow, E.M. (1975). Analysis of multidimentional condution phase change via the enthalpy model, *J. Heat Transfer*, 97, 333–340.
Shepel, S.E. & Paolucci, S. (2002). Numerical simulation of filling and solidification of permanent mold casting, *Applied Thermal Engineering*, 22, 229–248.
Shi, Z. & Guo, Z.X. (2004). Numerical heat transfer modelling for wire casting, *Mater. Sci. Eng.*, A265, 311–317.
Stone, H.L. (1968). Iterative solution of implicit approximations of multidimensional partial differential equations, *SIAM, J. Numer. Anal.*, 5, 530–558.
Swaminathan, C.R. & Voller, V.R. (1997). Towards a general numerical scheme for solidification systems, *Int. J. Heat MassTransfer*, 40, 2859 – 2868.
Tannehill, J.C.; Anderson, D.A. & Pletcher, R.H. (1997). *Computational Fluid Mechanics and Heat Transfer*, 2nd edition, Taylor & Francis Ltd.
Thompson, J.F.; Warsi, Z.U.A. & Mastin, C.W. (1985). *Numerical Grid Generation, Foundations and Applications*, Elsevier Science Publishing Co., Amsterdam.
Tryggvason, G.; Esmaeeli, A. & Al-Rawahi, N. (2005). Direct numerical simulations of flows with phase change, *Computers & Structures*, 83, 445–453.
Versteeg, H.K. & Malalasekera, W. (1995). *An Introduction to Computational Fluid Dynamics: The Finite Volume Method Approach*, Prentice Hall.

Viskanta, R. (1990). Mathematical modeling of transport processes during solidification of binary systems, *JSME Int. J.*, 33, 409–423.

Voller,V. R.; Brent, A. D. & Prakash, C. (1989). The modelling of heat, mass and solute transport in solidification systems, *Int. J. Heat Mass Transfer*, 32, 1719–1731.

Wang, G.X. & Matthys, E.F. (2002). Experimental ditermination of the interfacial heat transfer during cooling and solidification of molten metal droplets impacting on a metallic substrate: effect of roughness and superheat, *Int. J. Heat Mass Transfer*, 45, 4967–4981.

Wiwatanapataphee, B.; Wu, Y.H.; Archapitak, J.; Siew, P.F. & Unyong, B. (2004). A numerical study of the turbulent flow of molten steel in a domain with a phase-change boundary, *Journal of Computational and Applied Mathematics*, 166, 307–319.

6

Lattice Boltzmann Numerical Approach to Predict Macroscale Thermal Fluid Flow Problem

Nor Azwadi Che Sidik and Syahrullail Samion
Universiti Teknologi Malaysia
Malaysia

1. Introduction

Flow in an enclosure driven by buoyancy force is a fundamental problem in fluid mechanics. This type of flow is encountered in certain engineering applications within electronic cooling technologies, in everyday situation such as roof ventilation or in academic research where it may be used as a benchmark problem for testing newly developed numerical methods. A classic example is the case where the flow is induced by differentially heated walls of the cavity boundaries. Two vertical walls with constant hot and cold temperature is the most well defined geometry and was studied extensively in the literature. A comprehensive review was presented by Davis (1983). Other examples are the work by Azwadi and Tanahashi (2006) and Tric (2000).

The analysis of flow and heat transfer in a differentially heated side walls was extended to the inclusion of the inclination of the enclosure to the direction of gravity by Rasoul and Prinos (1997). This study performed numerical investigations in two-dimensional thermal fluid flows which are induced by the buoyancy force when the two facing sides of the cavity are heated to different temperatures. The cavity was inclined at angles from 20° to 160°, Rayleigh numbers from 10^3 to 10^6 and Prandtl numbers from 0.02 to 4000. Their results indicated that the mean and local heat flux at the hot wall were significantly depend on the inclination angle. They also found that this dependence becomes stronger for the inclination angle greater than 90°.

Hart (1971) performed a theoretical and experimental study of thermal fluid flow in a rectangular cavity at small aspect ratio and investigated the stability of the flow inside the system. Ozoe et al. (1974) conducted numerical analysis using finite different method of two-dimensional natural circulation in four types of rectangular cavity at inclination angles from 0° to 180°. Kuyper et al. (1993) provided a wide range of numerical predictions of flow in an inclined square cavity, covered from laminar to turbulent regions of the flow behavior. They applied k - ε turbulence model and performed detailed analysis for Rayleigh numbers of 10^6 to 10^{10}.

A thorough search of the literature has revealed that no work has been reported for free convection in an inclined square cavity with Neumann typed of boundary conditions. The type of boundary condition applied on the bottom and top boundaries of the cavity strongly affects the heat transfer mechanism in the system (Azwadi et al., 2010). Therefore, it is the purpose of present study to investigate the fluid flow behaviour and heat transfer mechanism in an inclined square cavity, differentially heated sidewalls and perfectly conducting boundary condition for top and bottom walls.

The current study is summarized as follow: two dimensional fluid flow and heat transfer in an inclined square cavity is investigated numerically. The two sidewalls are maintained at different temperatures while the top and bottom walls are set as a perfectly conducting wall. In current study, we fix the aspect ratio to unity. The flow structures and heat transfer mechanism are highly dependent upon the inclination angle of the cavity. By also adopting the Rayleigh number as a continuation parameter, the flow structure and heat transfers mechanism represented by the streamlines and isotherms lines can be identified as function of inclination angle. The computed average Nusselt number is also plotted to demonstrate the effect of inclination angle on the thermal behaviour in the system. Section two of this paper presents the governing equations for the case study in hand and introduces the numerical method which will be adopted for its solution. Meanwhile section three presents the computed results and provides a detailed discussion. The final section of this paper concludes the current study.

2. Numerical formulation

In present research, the incompressible viscous fluid flow and heat transfer are studied in a differentially heated side walls and perfectly conducting boundary conditions for top and bottom walls. Then the square enclosure is inclined from 20° to 160° to investigate the effect of inclination angles on thermal and fluid flow characteristics in the system. The governing equations are solved indirectly: i. e. using the lattice Boltzmann mesoscale method (LBM) with second order accuracy in space and time.

Our literature study found that there were several investigations have been conducted using the LBM to understand the phenomenon of free convection in an enclosure (Azwadi & Tanahashi, 2007; Azwadi & Tanahashi, 2008; Onishi et al., 2001). However, most of them considered an enclosure at 90^0 inclination angle and adiabatic boundary conditions at top and bottom walls. To the best of authors' knowledge, only Jami et al. (2006) predicted the natural convection in an inclined enclosure at two Rayleigh numbers and two aspect ratios. In their study, they investigated the fluid flow and heat transfer when an inclined partition is attached to the hot wall enclosure and assumed adiabatic boundary condition at the top and bottom walls. Due to lack of knowledge on the problem in hand, therefore, the objective of present paper is to gain better understanding for the current case study by using the lattice Boltzmann numerical method. To see this, we start with the evolution equations of the density and temperature distribution functions, given as (He et al., 1998)

$$f_i\left(\mathbf{x}+\mathbf{c}_i\Delta t, t+\Delta t\right)-f_i\left(\mathbf{x},t\right)=-\frac{1}{\tau_f}\left(f_i\left(\mathbf{x},t\right)-f_i^{eq}\left(\mathbf{x},t\right)\right)+F_i \tag{1}$$

$$g_i\left(\mathbf{x}+\mathbf{c}_i\Delta t, t+\Delta t\right)-g_i\left(\mathbf{x},t\right)=-\frac{1}{\tau_g}\left(g_i\left(\mathbf{x},t\right)-g_i^{eq}\left(\mathbf{x},t\right)\right) \tag{2}$$

where the density distribution function $f=f\left(\mathbf{x},t\right)$ is used to calculate the density and velocity fields and the temperature distribution function $g=g\left(\mathbf{x},t\right)$ is used to calculate the macroscopic temperature field. Note that Bhatnagar-Gross-Krook (BGK) collision model (Bhatnagar et al., 1954) with a single relaxation time is used for the collision term. For the D2Q9 model (two-dimension nine-lattice velocity model), the discrete lattice velocities are defined by

$$\begin{aligned}
&\mathbf{c}_0 = (0,0) \\
&\mathbf{c}_i = c\left(\cos\left((i-1)\pi/2\right), \sin\left((i-1)\pi/2\right)\right), i = 1,2,3,4 \\
&\mathbf{c}_i = \sqrt{2}c\left(\cos\left((i-5)\pi/2+\pi/4\right), \sin\left((i-5)\pi/2+\pi/4\right)\right), i = 5,6,7,8
\end{aligned} \tag{3}$$

Here, c is the lattice spacing. In LBM, the magnitude of $\mathbf{c}_i$ is set up so that in each time step Δt, the distribution function propagates in a distance of lattice nodes spacing Δx. This will ensure that the distribution function arrives exactly at the lattice nodes after Δt. The equilibrium function for the density distribution function f_i^{eq} for the D2Q9 model is given by

$$f_i^{eq} = \rho\omega_i\left[1 + 3\mathbf{c}_i \cdot \mathbf{u} + \frac{9}{2}(\mathbf{c}_i \cdot \mathbf{u})^2 - \frac{3}{2}\mathbf{u}^2\right] \tag{4}$$

where the weights are $\omega_0 = 4/9$, $\omega_i = 1/9$ for i =1 - 4 and $\omega_i = 1/36$ for i =5 - 8.
According to Azwadi and Tanahashi (2006) and He et al. (1998), the expression for equilibrium function of temperature distribution can be written as

$$\begin{aligned}
g^{eq} = \rho T\left(\frac{1}{2\pi RT}\right)^{D/2} \exp\left\{-\frac{\mathbf{c}^2}{2RT}\right\}\left[\frac{\mathbf{c}^2}{DRT} + \left(\frac{\mathbf{c}^2}{DRT} - \frac{2}{D}\right)\frac{\mathbf{c}\cdot\mathbf{u}}{RT}\right. \\
\left.\left(\frac{\mathbf{c}^2}{DRT} - \frac{4}{D}\right)\frac{(\mathbf{c}\cdot\mathbf{u})^2}{2(RT)^2} - \left(\frac{\mathbf{c}^2}{DRT} - \frac{2}{D}\right)\frac{\mathbf{u}^2}{2RT}\right]
\end{aligned} \tag{5}$$

Regroup Eq. (5) to avoid higher order quadrature gives

$$\begin{aligned}
&g^{eq} = \rho T\left(\frac{1}{2\pi RT}\right)^{D/2} \exp\left\{-\frac{\mathbf{c}^2}{2RT}\right\}\left[1 + \frac{\mathbf{c}\cdot\mathbf{u}}{RT} + \frac{(\mathbf{c}\cdot\mathbf{u})^2}{2(RT)^2} - \frac{\mathbf{u}^2}{2RT}\right] + \\
&\rho T\left(\frac{1}{2\pi RT}\right)^{D/2} \exp\left\{-\frac{\mathbf{c}^2}{2RT}\right\}\left[\frac{\mathbf{c}^2}{DRT} - 1\right] + \\
&\rho T\left(\frac{1}{2\pi RT}\right)^{D/2} \exp\left\{-\frac{\mathbf{c}^2}{2RT}\right\}\left[\left(\frac{\mathbf{c}^2}{DRT} - \frac{2+D}{D}\right)\frac{\mathbf{c}\cdot\mathbf{u}}{RT} + \right. \\
&\left.\left(\frac{\mathbf{c}^2}{DRT} - \frac{4+D}{D}\right)\frac{(\mathbf{c}_i\cdot\mathbf{u})^2}{2(RT)^2} - \left(\frac{\mathbf{c}^2}{DRT} - \frac{2+D}{D}\right)\frac{\mathbf{u}^2}{2RT}\right]
\end{aligned} \tag{6}$$

It has been proved by Shi et al. (2004) that the zeroth through second order moments in the last square bracket and the zeroth and first order moments in the second square bracket in the right hand side of Eq. (6) vanish. The exclusion of the second order moments in the second square bracket in Eq. (6) only related to the constant parameter in the thermal conductivity which can be absorbed by manipulating the parameter τ_f in the computation. Therefore, by dropping the terms in the last two square brackets on the right hand side of Eq. (6) gives

$$g^{eq} = \rho T\left(\frac{1}{2\pi RT}\right)^{D/2} \exp\left\{-\frac{\mathbf{c}^2}{2RT}\right\}\left[1 + \frac{\mathbf{c}\cdot\mathbf{u}}{RT} + \frac{(\mathbf{c}\cdot\mathbf{u})^2}{2(RT)^2} - \frac{\mathbf{u}^2}{2RT}\right] \tag{7}$$

After some modifications in order to satisfy the macroscopic energy equation via the Chapmann-Enskog expansion procedure, the discretised equilibrium function for the temperature distribution can be expressed as

$$g_i^{eq} = T\omega_i\left[1 + 3\mathbf{c}_i \cdot \mathbf{u} + \frac{9}{2}\left(\mathbf{c}_i \cdot \mathbf{u}\right)^2 - \frac{3}{2}\mathbf{u}^2\right] \tag{8}$$

where the weights are $\omega_0 = 4/9$, $\omega_i = 1/9$ for i =1 - 4 and $\omega_i = 1/36$ for i =5 - 8.
The macroscopic variables, density ρ , and temperature T can thus be evaluated as the moment to the equilibrium distribution functions as

$$\rho = \sum_i f_i^{eq}, T = \sum_i g_i^{eq} \tag{9}$$

Through a multiscaling expansion, the mass and momentum equations can be derived for D2Q9 model. The detail derivation of this is given by He and Luo (1997) and will not be shown here. The kinematic viscosity of fluid is given by

$$\upsilon = \frac{2\tau_f - 1}{6} \tag{10}$$

The energy equation at the macroscopic level can be expressed as follow

$$\frac{\partial}{\partial t}\rho T + \nabla \cdot \rho \mathbf{u} T = \chi \nabla^2\left(\rho T\right) \tag{11}$$

where χ is the thermal diffusivity. Thermal diffusivity and the relaxation time of temperature distribution function is related as

$$\chi = \frac{2\tau_g - 1}{6} \tag{12}$$

3. Problem physics and numerical results

The physical domain of the problem is represented in Fig. 1. The conventional no-slip boundary conditions (Peng et al., 2003) are imposed on all the walls of the cavity. The thermal conditions applied on the left and right walls are $T(x = 0, y) = T_H$ and $T(x = L, y) = T_C$. The top and bottom walls being perfectly conducted, $T = T_H - (x/L)(T_H - T_C)$, where T_H and T_C are hot and cold temperature, and L is the width of the enclosure. The temperature difference between the left and right walls introduces a temperature gradient in a fluid, and the consequent density difference induces a fluid motion, that is, convection.
The Boussinesq approximation is applied to the buoyancy force term. With this approximation, it is assumed that all fluid properties can be considered as constant in the body force term except for the temperature dependence of the density in the gravity term. So the external force in Eq. (1) is

$$F_i = 3\mathbf{G}\left(\mathbf{c} - \mathbf{u}\right) f_i^{eq} \tag{13}$$

where **G** is the contribution from buoyancy force.

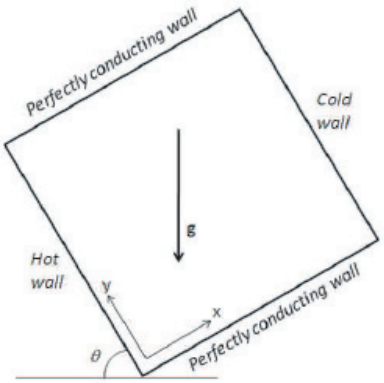

Fig. 1. Physical domain of the problem

The dynamical similarity depends on two dimensionless parameters: the Prandtl number Pr and the Rayleigh number Ra,

$$\mathrm{Pr} = \frac{\upsilon}{\chi}, \mathrm{Ra} = \frac{g_0 \beta \Delta T L^3}{\upsilon \chi} \tag{14}$$

We carefully choose the characteristic speed $v_c = \sqrt{g_0 LT}$ so that the low-Mach-number approximation is hold. Nusselt number, Nu is one of the most important dimensionless numbers in describing the convective transport. The average Nusselt number in the system is defined by

$$\mathrm{Nu} = \frac{H}{\chi \Delta T} \frac{1}{H^2} \int_0^H \int_0^H q_x(x,y)\mathrm{dxdy} \tag{15}$$

where $q_x(x,y) = uT(x,y) - \chi(\partial/\partial x)T(x,y)$ is the local heat flux in x-direction.
In all simulations, Pr is set to be 7.0 to represent the circulation of water in the system. Through the grid dependence study, the grid sizes of 251 × 251 is suitable for Rayleigh numbers from 10^5 to 10^6. The convergence criterion for all the tested cases is

$$\mathrm{Max}\left| \left(\left(u^2 + v^2 \right)^{n+1} \right)^{\frac{1}{2}} - \left(\left(u^2 + v^2 \right)^{n} \right)^{\frac{1}{2}} \right| \le 10^{-7} \tag{16}$$

$$\mathrm{Max}\left| T^{n+1} - T^{n} \right| \le 10^{-7} \tag{17}$$

where the calculation is carried out over the entire system.
Streamlines and isotherms predicted for flows at Ra = 10^5 and different inclination angles are shown in Figures 2 and 3. As can be seen from the figures of streamline plots, the liquid near the hot wall is heated and goes up due to the buoyancy effect before it hits the corner with the perfectly conducting walls and spread to a wide top wall. Then as it is cooled by the cold wall, the liquid gets heavier and goes downwards to complete the cycle. At low value of inclination angle, θ = 20, two small vortices are formed at the upper corner and lower corner of the enclosure indicates high magnitude of flow velocity near these regions. The presence of

these two corner vortices compressed the central cell to form an elongated vortex. The isotherms show a good mixing occurring in the center and relatively small gradient indicating small value of the local Nusselt number along the differentially heated walls.

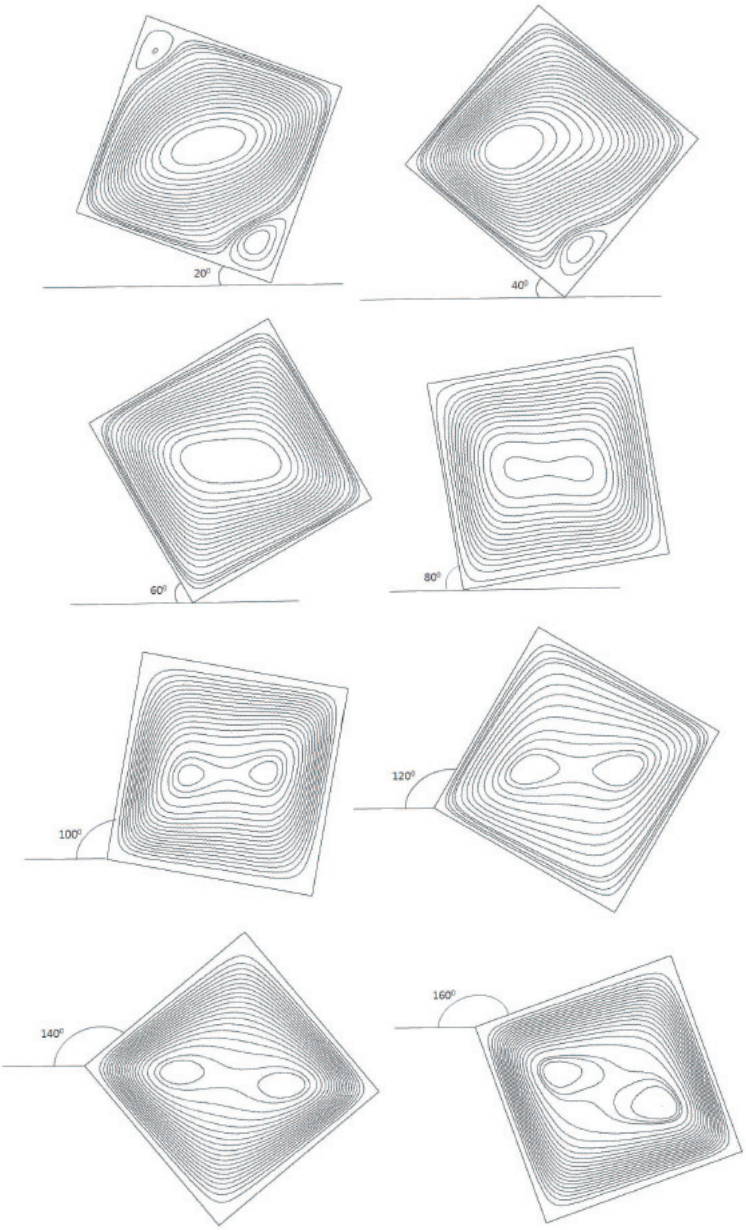

Fig. 2. Streamlines plots at Ra = 10^5

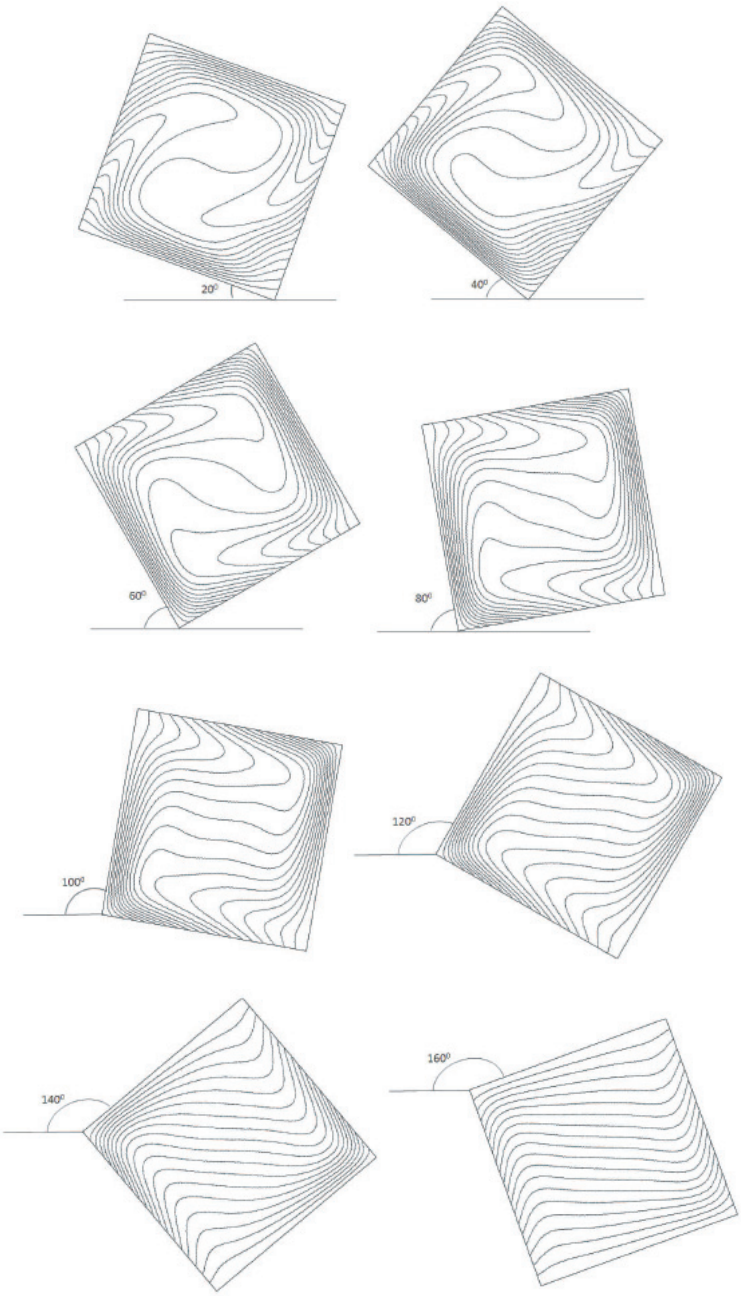

Fig. 3. Isotherms plots at Ra = 10^5.

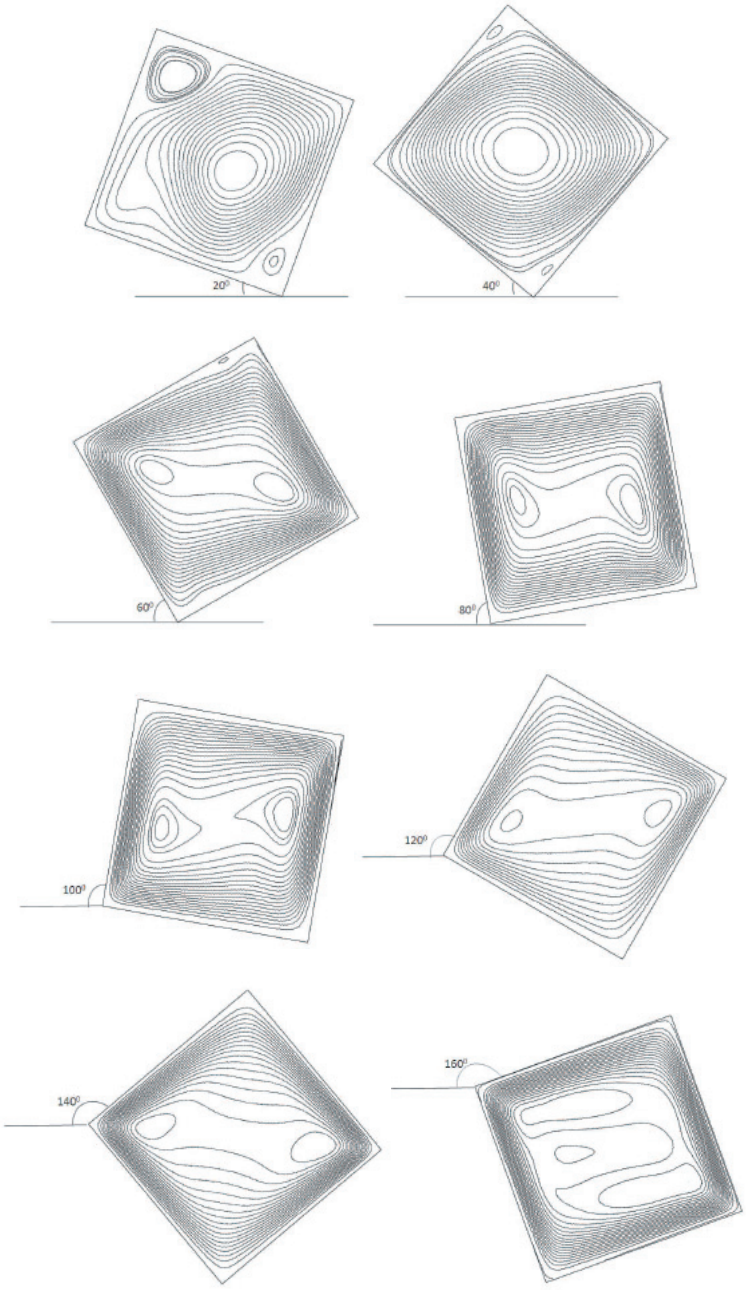

Fig. 4. Streamlines plots at Ra = 5×10^5.

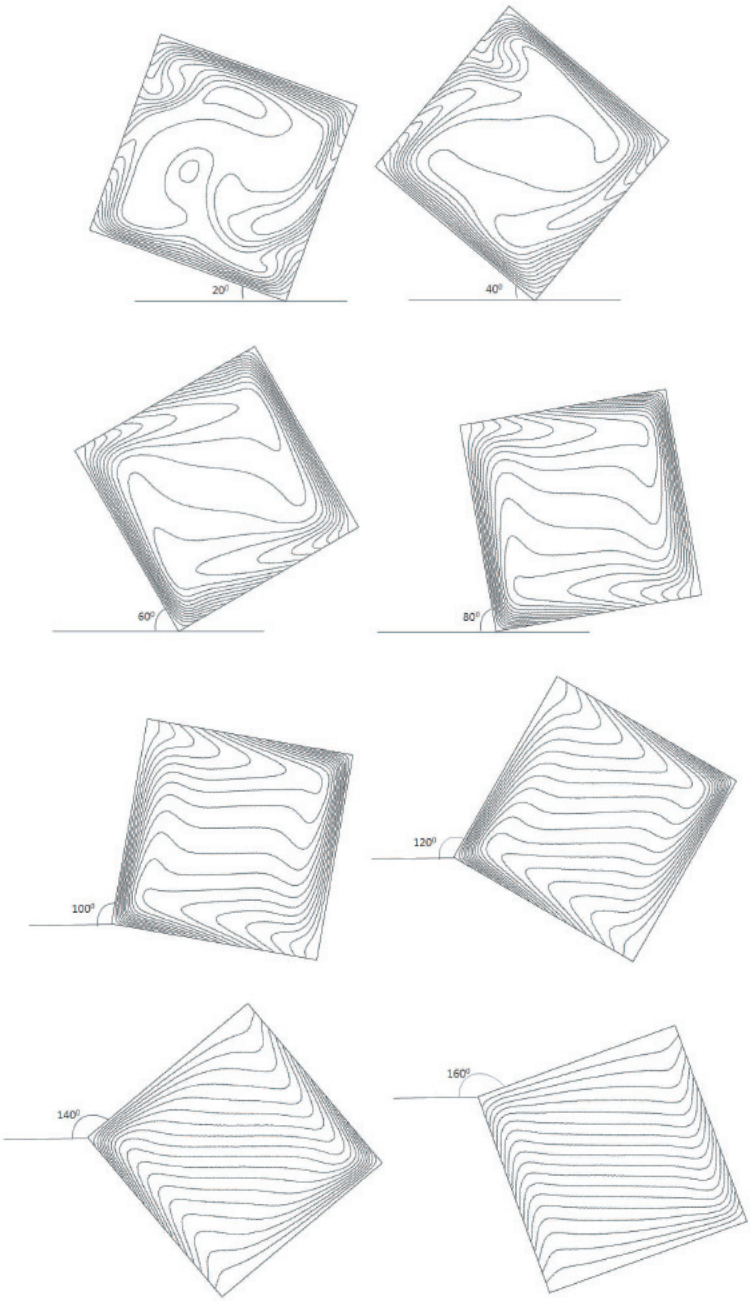

Fig. 5. Isotherms plots at Ra = 5×10^5.

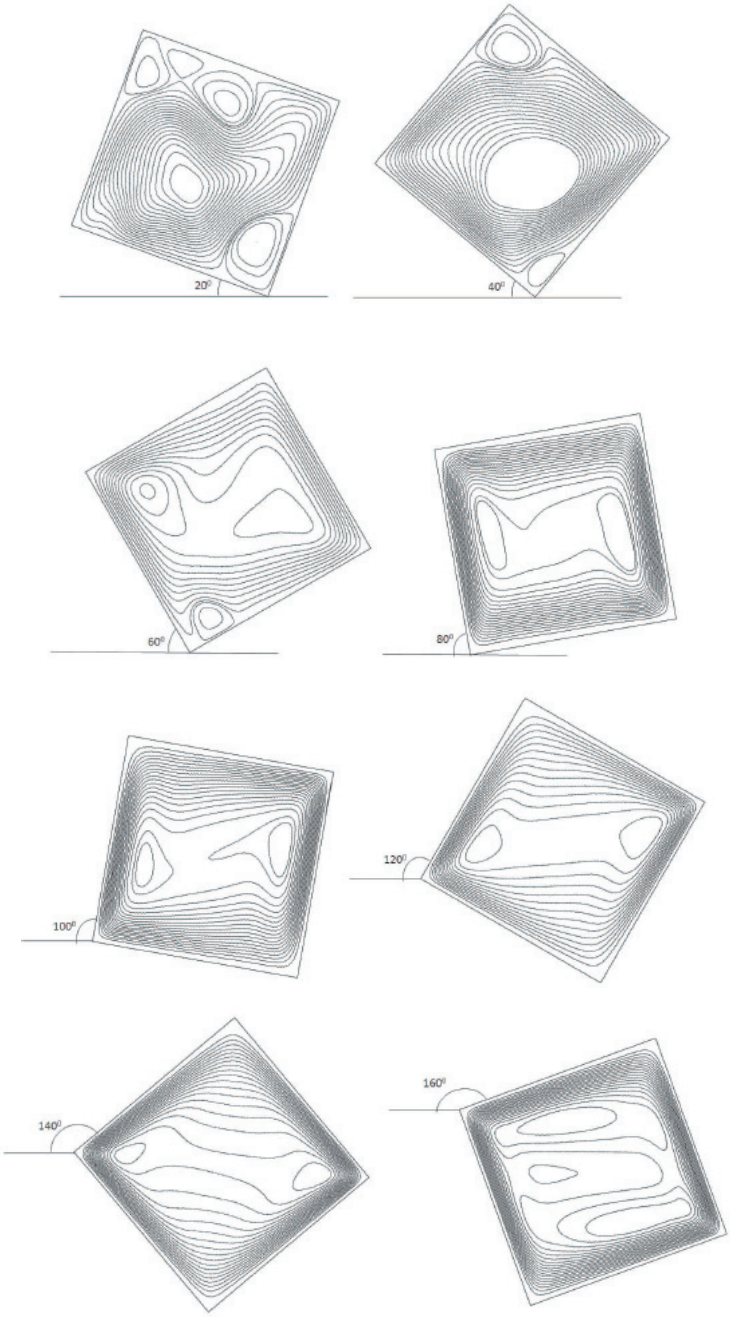

Fig. 6. Streamlines plots at Ra = 10^6.

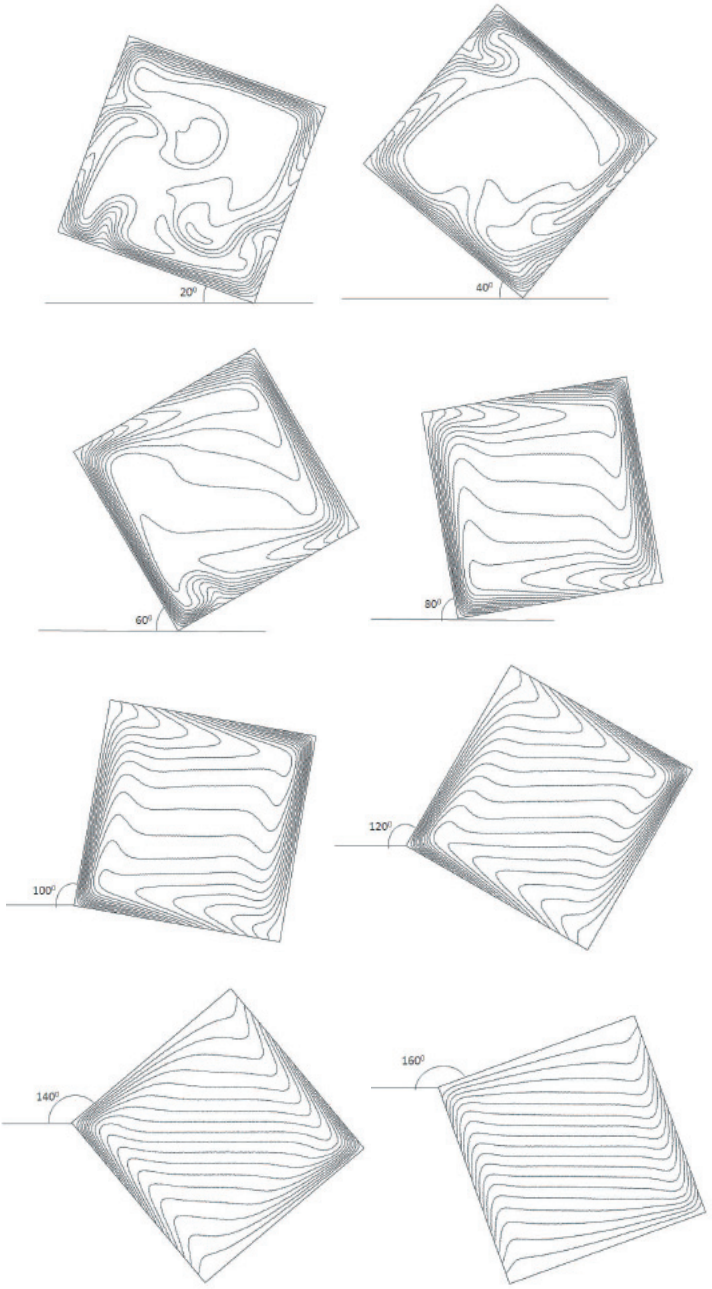

Fig. 7. Isotherms plots at Ra = 10^6.

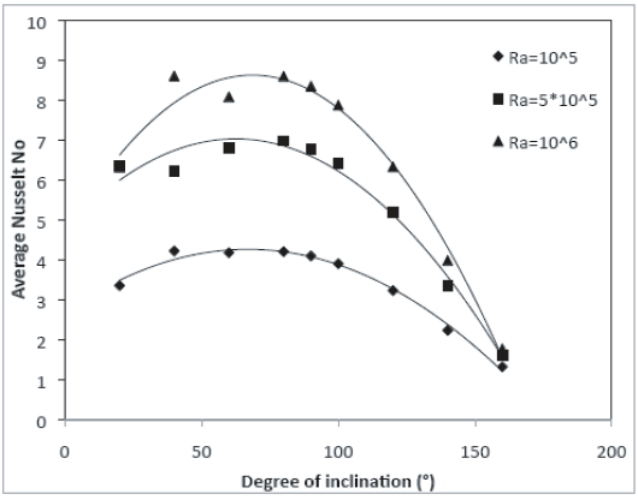

Fig. 8. Effect of inclination angles on averaged Nusselt number

Further increment of inclination angle θ = 40° leads to the size reduction of small corner vortices. At θ = 60°, the small corner vortices completely disappear and the central cell pointing towards the corners because high magnitude of gravity vector drag the outer vortex along the vertical walls of the enclosure. Denser isotherms lines can be seen from the figure indicate higher value of local and average Nusselt number compared to previous inclination angles. Further inclination of enclosure separates the main central vortex into two smaller vortices. As we increase the inclination angle, these two vortices grow in size indicates that some fluid from the hot or cold wall returns back to the same wall. For inclination angles of θ = 80° to θ = 120°, the isotherms line are parallel to the perfectly conducting walls indicates that the main heat transfer mechanism is by convection. Denser isotherms lines can be seen near the bottom left and top right corners demonstrate high local Nusselt number near these regions. However, at high inclination angles, $\theta \geq 140°$, the isotherms lines are equally spaced indicates low averages Nusselt number in the system.

For Rayleigh number equals to 5×10^5 and low inclination angles, the central vortex is more rounded indicates equal magnitude of flow velocity near all four enclosure walls. At angle equals to θ = 60°, the central cells splits into two before the corner vortices disappear. The velocity boundary layer can be clearly seen for inclination angles of θ = 60° and above. The isotherm patterns are similar to those for Ra = 10^5 at all angles. However, the thermal boundary layers are thicker indicating higher local and average Nusselt number along the cold and hot walls.

For the simulation at the highest Rayleigh number in the present study Ra = 10^6, the formation of corner vortices can be clearly seen at low value of inclination angles. At angle equals to θ = 20°, the complex structure of upper corner vortices indicates the instability of the flow in the system. This flow instability is confirmed when we were unable to obtain a steady solution even for a very high iteration number. The isotherms plots also display a complex thermal behavior and good mixing of temperature in the system. The flow becomes steady again when we increase the inclination angle to θ = 60°. The central vortex is separated into two smaller vortices and vertically elongated shaped indicates relatively high

value of flow velocity near the differentially heated walls. Most of the isotherms lines becomes parallel to the perfectly conducting walls indicates the convection type dominates the heat transfer mechanism in the system.

For $\theta > 80°$, the central vortex is stretched from corner to corner of the enclosure and perpendicular to the gravitational vector, developed denser streamlines near these corners, indicating the position of maximum flow velocity for the current condition. On the other hand, similar features of isotherms to those at lower Ra are observed.

The effect of the inclination angle on the average Nusselt number is shown in Figure 8 for all values of Rayleigh numbers. One common characteristic which can be drawn from the figure; the Nusselt number increases with increasing the Rayleigh number. However, the computed Nusselt numbers are lower than those for the case of adiabatic types of boundary condition (Peng et al., 2003) because the heat is allowed to pass through the top and bottom walls. Interestingly, the minimum value of average Nusselt number is found converging to the same value and when the inclination angle approaching $\theta = 180°$ for every Rayleigh number. On the other hand, the maximum value of average Nusselt number is determined at inclination angle between $\theta = 60°$ to $\theta = 80°$. These can be explained by analyzing the isotherms plots which demonstrating relatively denser lines near hot and cold walls leading to high temperature gradient near these regions. Lower value of average Nusselt number at lower inclination angle was due to the presence of small corner vortices which contributes smaller local heat transfer along the hot and cold walls. For the computation at higher inclination angles, where the hot wall is close to the top position, the magnitude of the gravity vector is reduced results in low magnitude of flow velocity along the hot wall. Due to this reason, the heat transfer rates are small resulted from the reduction in the driving potential for free convection.

4. Conclusion

The free convection in an inclined cavity has been simulated using the mesoscale numerical scheme where the Navier Stokes equation was solved indirectly using the lattice Boltzmann method. The result of streamlines plots clearly depicting the flow pattern and vortex structure in the cavity. The primary vortex is transformed from a single cellular to a double cellular as the inclination angle increases. These demonstrate the lattice Boltzmann numerical scheme of passive-scalar thermal lattice Boltzmann model is a very efficient numerical method to study flow and heat transfer in a differentially heated inclined enclosure.

5. Acknowledgement

The authors would like to acknowledge Universiti Teknologi Malaysia and Malaysia Government for supporting these research activities. This research is supported by research grant No. 78604

6. References

Bhatnagar, P. L.; Gross, E. P. & Krook, M. (1954). A Model for Collision Process in Gases. 1. Small Amplitude Processes in Charged and Neutral One-Component System, *Physical Review*, Vol. 94, No. 3, 511-525.

Davis, D. V. (1983). Natural Convection of Air in a Square Cavity; A Benchmark Numerical Solution, *International Journal for Numerical Methods in Fluids*, Vol. 3, No. 3, 249-264, ISSN 1097-0363.

Hart, J. E. (1971). Stability of the Flow in a Differentially Heated Inclined Box, *Journal of Fluid Mechanics*, Vol. 47, No. 3, 547-576, ISSN 0022-1120.

He, X. & Luo, L. S. (1997). Lattice Boltzmann Model for the Incompressible Navier-Stokes Equation, *Journal of Statistical Physics*, Vol. 88, No. 3, 927-944, ISSN 0022-4715.

He, X.; Shan, S. & Doolen, G. (1998). A Novel Thermal Model for Lattice Boltzmann Method in Incompressible Limit, *Journal of Computational Physics*, Vol. 146, No. 1, 282-300, ISSN 0021-9991.

Jami, M.; Mezrhab, A.; Bouzidi, M. & Lallemand, P. (2006). Lattice-Boltzmann Computation of Natural Convection in a Partitioned Enclosure with Inclined Partitions Attached to its Hot Wall, *Physica A*, Vol. 368, No. 2, 481-494.

Kuyper, R. A.; Meer, V. D.; Hoogendoorn, C. J. & Henkes, R. A. W. (1993). Numerical Study of Laminar and Turbulent Natural Convection in an Inclined Square Cavity, *International Journal of Heat Mass Transfer*, Vol. 36, No. 11, 2899-2911, ISSN 0017-9310.

Nor Azwadi, C. S. & Tanahashi, T. (2006). Simplified Thermal Lattice Boltzmann in Incompressible Limit, *International Journal of Modern Physics B*, Vol. 20, No. 17, 2437-2449, ISSN 0217-9792.

Nor Azwadi, C. S. & Tanahashi, T. (2007). Three-Dimensional Thermal Lattice Boltzmann Simulation of Natural Convection in a Cubic Cavity, *International Journal of Modern Physics B*, Vol. 21, No. 1, 87-96, ISSN 0217-9792.

Nor Azwadi, C. S. & Tanahashi, T. (2008). Simplified Finite Difference Thermal Lattice Boltzmann Method, *International Journal of Modern Physics B*, Vol. 22, No. 22, 3865-3876, ISSN 0217-9792.

Nor Azwadi, C. S.; Mohd Fairus, M. Y. & Samion, S. (2010). Virtual Study of Natural Convection Heat Transfer in an Inclined Square Cavity, *Journal of Applied Sciences*, Vol. 10, No. 4, 331-336, ISSN 1812-5654.

Onishi, J.; Chen, Y. & Ohashi, H. (2001). Lattice Boltzmann Simulation of Natural Convection in a Square Cavity, *JSME International Journal Series B*, Vol. 44, No. 1, 53-62.

Ozoe, H.; Yamamoto, K.; Sagama, H. & Churchill, S. W. (1974). Natural Circulation in an Inclined Rectangular Channel Heated on One Side and Cooled on the Opposing Side, *International Journal of Heat Mass Transfer*, Vol. 17, No. 10, 1209-1217, ISSN 0017-9310.

Peng, Y.; Shu, C. & Chew, Y. T. (2003). Simplified thermal lattice Boltzmann model for incompressible thermal flows, *Physical Review E*, Vol. 68, No. 1, 020671/1-20671/8, ISSN 1539-3755.

Rasoul, J. & Prinos, P. (1997). Natural Convection in an Inclined Enclosure, *International Journal of Numerical Methods for Heat and Fluid Flow*, Vol. 7, No. 5, 438-478, ISSN 0961-5539.

Shi, Y.; Zhao, T. S. & Guo, Z. L. (2004). Thermal lattice Bhatnagar-Gross-Krook model for flows with viscous heat dissipation in the incompressible limit, *Physical Review E*, Vol. 70, No. 6, 066310/1-066310/10, ISSN 1539-3755.

Tric, E.; Labrosse, G. & Betrouni, M. (2000). A First Incursion into the 3D Structure of Natural Convection of Air in a Differentially Heated Cubic Cavity, from Accurate Numerical Solutions, *International Journal of Heat and Mass Transfer*, Vol. 43, No. 21, 4043-4056, ISSN 0017-9310

7

Efficient Simulation of Transient Heat Transfer Problems in Civil Engineering

Sebastian Bindick, Benjamin Ahrenholz, Manfred Krafczyk
Institute for Computational Modeling in Civil Engineering, Technische Universitet Braunschweig
Germany

1. Introduction

Heat transport problems arise in many fields of civil engineering e.g. indoor climate comfort, building insulation, HVAC (heating, ventilating, and air conditioning) or fire prevention to name a few. An a priori and precise knowledge of the thermal behavior is indispensable for an efficient optimization and planning process. The complex space-time behavior of heat transfer in 3D domains can only be achieved with extensive computer simulations (or prohibitively complex experiments). In this article we describe approaches to simulate the transient coupled modes of heat transfer (convection, conduction and radiation) applicable to many fields in civil engineering. The numerical simulation of these coupled multi-scale, multi-physics problems are still very challenging and require great care in modeling the different spatio-temporal scales of the problem. One approach in this direction is offered by the Lattice-Boltzmann method (LBM) which is known to be a viable Ansatz for simulating physically complex problems. For the simulation of radiation a radiosity method is used which also has already proven its suitability for modeling radiation based heat transfer. The coupling and some typical applications of both methods are discussed in this chapter.

2. Modeling thermal flows with Lattice-Boltzmann

In the last two decades the Lattice-Boltzmann-Methods (LBM) has matured as an efficient alternative to discretizing macroscopic transport equations such as the Navier-Stokes equations describing coupled transport problems such as thermal flows. The Boltzmann equation describes the dynamics of a propability distribution function of particles with a microscopic particle velocity under the influence of a collision operator. Macroscopic quantities such as the fields of density, flow velocities, energy or heat fluxes are consistently computed as moments of ascending order from the solution. For flow problems the Boltzmann equation can be drastically simplified by discretizing the microscopic velocity space and by using a simplified collision operator. A non-trivial yet algorithmically straight forward Finite Difference discretization for this set of PDEs results in the Lattice-Boltzmann equations. For the simulation of thermal driven flows using the LB method a hybrid thermal LB model (Hybrid TLBE) has been established, i.e. an explicit coupling between an athermal LBE scheme for the flow part and a separate Lattice-Boltzmann equation for the temperature equation.

2.1 An overview of the physical background of lattice Boltzmann models

The origin of the physical modeling process is the fact that the physical scope of validity of the Boltzmann equation includes the Navier-Stokes equations as well. In the framework of the kinetic gas theory it can be shown that the Navier-Stokes equations can be derived from the Boltzmann equation in the limit of small Knudsen numbers if the hydrodynamic momentum and pressure fields are described as low order moments of the primary variables of the Boltzmann equation (i.e. probability distributions). This implies that approximate solutions of the Boltzmann equations and their resulting moments can be used to calculate approximate solutions for the corresponding Navier-Stokes equations (Succi, 2001; He & Luo, 1997b; Bhatnagar et al., 1954). A direct discretization of the full Boltzmann equation is neither useful nor necessary for most macroscopic flow problems; therefore, the following simplifications are typically made: First, the collision operator in the so-called BGK or Multiple-Relaxation-Time (MRT) approximation is considered, which assumes that the particle system is statistically close to a kinetic equilibrium. Furthermore, the microscopic velocity space is discretized to develop a system of discrete Boltzmann equations, instead of the Boltzmann equation in BGK-approximation. These discrete equations contain a constant prefactor in the convective term, which suggests a discretization along the corresponding characteristics. This system of discrete Boltzmann equations can be numerically discretized in different ways. The model relationships are outlined in Figure 1.

Historically, LBM originated from the lattice gas automata [LGA], which can be considered as a simplified, fictitious molecular dynamics in which space, time, and particle velocities are all discrete. However, it was discovered that LGA suffers from several inherent defects including

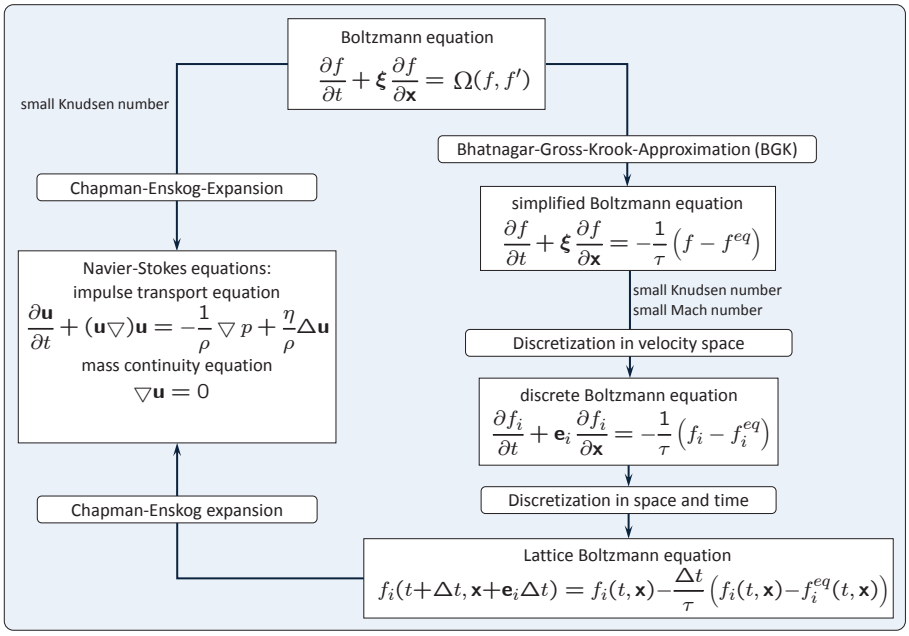

Fig. 1. From the Boltzmann equation to Navier-Stokes

the lack of Galilean invariance (except for $\rho = constant$), the presence of statistical noise and the absence of exponential complexity for three-dimensional lattices. The main motivation for the transition from LGA to LBM was the desire to remove statistical noise by replacing the Boolean particle number in a lattice direction with its ensemble average, the so-called density distribution function. Accompanying this replacement, the discrete collision rules also have to be modified as a continuous function - the collision operator. The first LBM has been proposed by (McNamara & Zanetti, 1988) and improved by (Higuera & Jiménez, 1989; Higuera et al., 1989). However, the connection to the Boltzmann equation (introduced by the Austrian physicist Ludwig Boltzmann in 1872) has been proven afterwards (He & Luo, 1997b; Sterling & Chen, 1996). The Boltzmann equation describes the statistical distribution of one particle in a fluid and the probability to encounter this particle at time t with velocity $\boldsymbol{\xi}$ at location x (Cercignani et al., 1994; Cercignani & Penrose, 1998):

$$\frac{\partial f}{\partial t} + \boldsymbol{\xi} \cdot \frac{\partial f}{\partial \mathsf{x}} + \mathsf{F} \cdot \frac{\partial f}{\partial \boldsymbol{\xi}} = \Omega(f, f') \tag{1}$$

In the LBM development, an important simplification is the approximation of the collision operator with the Bhatnagar-Gross-Krook (BGK) relaxation term. This lattice BGK (LBGK) model renders simulations more efficient and allows flexibility of the transport coefficients. On the other hand, it has been shown that the LBM scheme can also be considered as a special discretized form of the continuous Boltzmann equation. Through a Chapman-Enskog expansion (Frisch et al., 1987; Qian et al., 1992) or an asymptotic analysis (Junk et al., 2005), one can recover the governing continuity and Navier-Stokes equations (Equation 2) from the LBM algorithm (Qian et al., 1992).

$$\frac{\partial \mathsf{u}}{\partial t} + (\mathsf{u}\nabla)\mathsf{u} = -\frac{1}{\rho}\nabla p + \frac{\mu}{\rho}\Delta \mathsf{u}, \tag{2a}$$

$$\nabla \mathsf{u} = 0 \tag{2b}$$

In addition, the pressure field is also directly available from the density distributions as $p = c_S^2\, \rho$ where c_s is the speed of sound and hence there is no additional Poisson equation to be solved as in traditional CFD methods.

A particularly effective form of discretization is obtained if the spatial grid is being chosen so that the advection of the distribution functions follows exactly the characteristics defined by the microscopic particle velocities, i.e. if the physical discretization of the microscopic velocity space (after multiplying it with the appropriate local time step) is congruent with the numerical grid. This leads to a relatively simple Finite-difference approach. With the help of an appropriate multi-scale expansion it can be shown that the moments of zero to second order are approximate solutions of the velocity and pressure tensor of the Navier-Stokes equations, given that the relaxation time included in the BGK-operator is defined as a linear function of the kinematic viscosity. Yet, this scheme would not be competitive without further modifications. Theoretical analysis allows to determine a global constant numerical viscosity, which can be eliminated by appropriate scaling, resulting in a method of quadratic accuracy in space for the Navier-Stokes equations. A detailed description of the underlying derivations can be found in (Qian et al., 1992; Chen & Doolen, 1998; Succi, 2001; Dellar, 2003; He & Luo, 1997a;b; Bhatnagar et al., 1954) The accuracy of the method in the fluid depends, like for all transport problems mainly on the quality of the boundary conditions. In contrast to the direct discretization of the Navier-Stokes equations corresponding initial- and boundary conditions must be specified for the probability distributions within LBM.

Different approaches have been developed regarding accuracy and consistency and have been analyzed in the corresponding literature see e.g. (Junk et al., 2005; Ginzburg & d'Humières, 1996; d'Humières et al., 2002). Since typical LBM discretizations are based on Cartesian grids, it represents a curved surface only with first order accuracy. For second order accurate fluid/wall boundary conditions it is necessary to compute the projection of the node links to the surface of the geometry and incorporate them into the discretization scheme for the boundary conditions. If MRT approaches (d'Humières et al., 2002) are used, boundary conditions for pressure and velocities can be enforced with second order accuracy. The application of hierarchical Cartesian grid allows the use of tree type data structures and enables a hierarchical time-step procedure with an optimal Courant number of one at each grid level, i.e. on coarse grid cells only a correspondingly coarser time step is necessary (Tlke et al., 2006). The issue of efficiency of the LB method in direct comparison with state-of-the-art FE and FV-discretizations of the Navier-Stokes equations is discussed e.g. in (Geller et al., 2006).

Unlike the traditional computational fluid dynamics (CFD), which numerically solves the conservation equations of macroscopic properties (i. e., mass, momentum, and energy), LBM models the fluid consisting of fictitious particles, which perform consecutive propagation and collision processes over a discrete lattice. Due to its particulate nature and local dynamics, LBM is very efficient when dealing with complex boundaries and the incorporation of microscopic interactions.

2.2 A short introduction to the lattice Boltzmann method

The LB method is a numerical method to solve the Navier-Stokes equations Frisch et al. (1987); Benzi et al. (1992); Chen & Doolen (1998), where density distributions propagate and collide on a regular lattice. A common labeling for different lattice Boltzmann models is DdQq (Qian et al., 1992), where d is the space dimension and q the number of microscopic velocities. Besides the most common D3Q19 models (Figure 2) one can often find D3Q15 stencils (Figure 2) in 3D and D2Q9 in 2D (Figure 3) as well as non local stencils like D3Q27 or D3Q39. D3Q13 uses a reduced set of velocities, however it is very promising due to an excellent ratio between accuracy and computational requirements (d'Humières et al., 2001; Tlke & Krafczyk, 2008).

In the following section x represents a 3D vector in space and $\boldsymbol{f}$ a b-dimensional vector, where

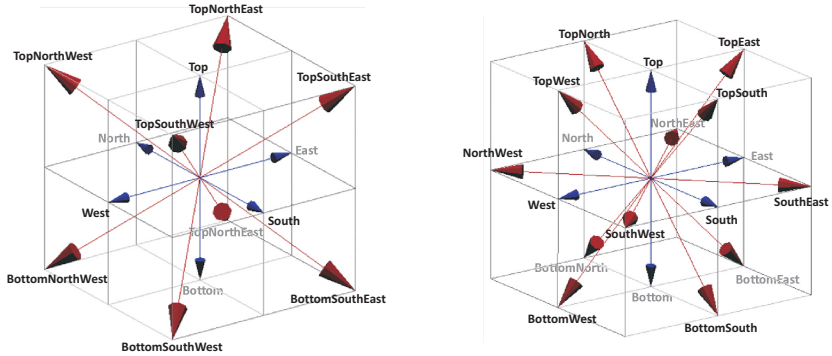

Fig. 2. D3Q19- and D3Q15 stencils, the most common representatives in 3D

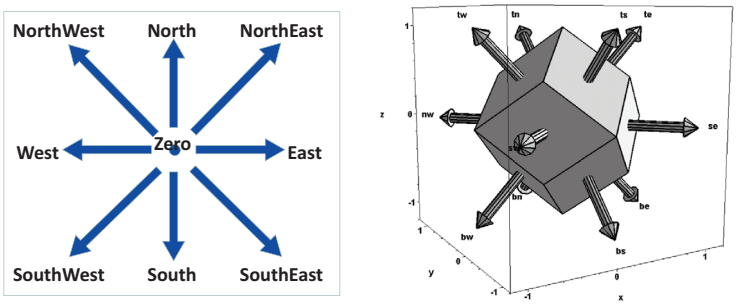

Fig. 3. D2Q9 stencil commonly used for 2D LBM and D3Q13 - the smallest stencil for a space filling grid in 3D

b is the number of microscopic velocities. The 19 velocities are given as

$$\mathsf{e}_i, i = 0,\ldots,18\} = \begin{pmatrix} 0 & c & -c & 0 & 0 & 0 & 0 & c & -c & c & -c & c & -c & c & -c & 0 & 0 & 0 & 0 \\ 0 & 0 & 0 & c & -c & 0 & 0 & c & -c & -c & c & 0 & 0 & 0 & 0 & c & -c & c & -c \\ 0 & 0 & 0 & 0 & 0 & c & -c & 0 & 0 & 0 & 0 & c & -c & -c & c & c & -c & -c & c \end{pmatrix}$$

where c is a constant microscopic reference velocity related to the speed of sound by $c_s^2 = c^2/3$. The microscopic velocities define a space-filling computational lattice where a node is connected to the neighboring nodes through the vectors $\{\Delta t\, \mathsf{e}_i, i = 0,\ldots,18\}$. The generalized lattice Boltzmann equation (GLBE) using the Multiple-Relaxation-Time model introduced by (d'Humières, 1992; Lallemand & Luo, 2000) is given by

$$f_i(t + \Delta t, \mathsf{x} + \mathsf{e}_i \Delta t) = f_i(t, \mathsf{x}) + \Omega_i, \quad i = 0,\ldots,b-1, \tag{3}$$

where f_i are mass fractions (unit kg m^{-3}) propagating with velocities e_i, Δt is the time step, the grid spacing is $\Delta x = c\Delta t$, and the collision operator of the Multiple-Relaxation-Time model (MRT) is given by

$$\Omega = \mathsf{M}^{-1}\mathsf{S}\left((\mathsf{M}\boldsymbol{f}) - \boldsymbol{m}^{eq}\right). \tag{4}$$

The matrix M is used to transform the distributions into moment space. The resulting moments $\boldsymbol{m} = \mathsf{M}\boldsymbol{f}$ are labeled as

$$\boldsymbol{m} = (\delta\rho, e, \epsilon, j_x, q_x, j_y, q_y, j_z, q_z, 3p_{xx}, 3\pi_{xx}, p_{ww}, \pi_{ww}, p_{xy}, p_{yz}, p_{xz}, m_x, m_y, m_z),$$

where $\delta\rho$ is a density variation related to the pressure variation δp by

$$\delta p = \frac{c^2}{3}\delta\rho. \tag{5}$$

and where $(j_x, j_y, j_z) = \rho_0(u_x, u_y, u_z)$ is the momentum and ρ_0 is a constant reference density. The moments $e, p_{xx}, p_{ww}, p_{xy}, p_{yz}, p_{xz}$ of second order are related to the stress tensor (Equation 6). The other moments of higher order are related to higher order derivatives of the flow field and have no direct physical impact with respect to the incompressible Navier-Stokes equations.

$$\sigma_{\alpha\beta} = -p\delta_{\alpha\beta} + \rho\nu(\frac{\partial u_\alpha}{\partial x_\beta} + \frac{\partial u_\beta}{\partial x_\alpha}) \tag{6}$$

The matrix S is a diagonal collision matrix composed of relaxation rates $\{s_{i,i}, \ldots, b-1\}$, also called the eigenvalues of the collision matrix $\mathsf{M}^{-1}\,\mathsf{S}\,\mathsf{M}$. The rates different from zero are

$$\begin{aligned}
s_{1,1} &= -s_e \\
s_{2,2} &= -s_\epsilon \\
s_{4,4} = s_{6,6} &= s_{8,8} = -s_q \\
s_{10,10} = s_{12,12} &= -s_\pi \\
s_{9,9} = s_{11,11} = s_{13,13} &= s_{14,14} = s_{15,15} = -s_\nu \\
s_{16,16} = s_{17,17} &= s_{18,18} = -s_m.
\end{aligned}$$

The relaxation rate s_ν is related to the kinematic viscosity ν by

$$s_\nu = \frac{1}{3\frac{\nu}{c^2\Delta t} + \frac{1}{2}}. \tag{7}$$

The remaining relaxation rates $s_e, s_\epsilon, s_q, s_\pi$ and s_m can be freely chosen in the range of $[0,2]$ and may be tuned to improve accuracy as well as stability (Lallemand & Luo, 2000) of the model. The optimum values depend on the specific system under consideration (geometry, initial, and boundary conditions) and can therefore not be computed in advance for general cases.
In summary it may be noted that if one uses either a Chapman-Enskog expansion (Frisch et al., 1987) or an asymptotic expansion using the diffusive scaling (Junk et al., 2005), it can be shown that the lattice Boltzmann method is a scheme of first order in time and second order in space for the incompressible Navier-Stokes equations.

2.3 Thermal flows

During the last decade different approaches for the simulation of thermal driven flows using the LB method have been developed (Alexander et al., 1993; Vahala et al., 2000; Shan, 1997; Qian, 1993; Filippova & Hänel, 2000; Lallemand & Luo, 2003). Energy conserving thermal LB equation models (TLBE) use a larger set of discrete velocities than the standard method (Qian et al., 1992) to include a thermal variable, such as temperature. The internal energy is defined by a second-order moment of the distribution function, and the collision operator is chosen to satisfy local energy conservation. However, these thermal flow simulations utilizing the thermal lattice Boltzmann equation (TLBE) are hampered by numerical instabilities caused by an algebraic coupling among different modes of the linearized collision operator, independently of the number of discrete velocities used in the model (Lallemand & Luo, 2003). To avoid the limitations of TLBE a hybrid scheme was developed in (Lallemand & Luo, 2003) by coupling the energy mode of the athermal LB model to the temperature field. This method has been extended for turbulent flows by (van Treeck et al., 2006) and is usually referred to as hybrid thermal lattice Boltzmann equation (HTLBE).
In this work the temperature equation is discretized by the following finite difference (FD) scheme:

$$\frac{T_{i,j,k}(t+\Delta t^{FD}) - T_{i,j,k}(t)}{\Delta t^{FD}} = -\vec{j}_{i,j,k}(t)\nabla^{(h)}_{i,j,k} T_{i,j,k}(t) + \alpha \triangle^{(h)}_{i,j,k} T_{i,j,k}(t) \tag{8}$$

where α is the thermal diffusivity. For computing the difference operators $\nabla^{(h)}_{i,j,k}$ and $\triangle^{(h)}_{i,j,k}$ a 6 point stencil is used. The coupling of both schemes is explicit, meaning that the velocity field obtained by the MRT scheme is inserted into the energy equation while the solution of the latter is used to compute the buoyant force $F_z(\vec{x},t)$ in the sense of a Boussinesq approximation. For a given Rayleigh number

$$Ra = \frac{Pr g_z \beta \Delta T L^3}{\nu^2} \tag{9}$$

and Prandtl number $Pr = \nu/\alpha$ and by setting $\beta = 1/T_0$, the parameters viscosity ν and diffusivity α are obtained and the relaxation coefficients can be determined with the formulae given in (Lallemand & Luo, 2003), while ν has to fulfill the stability constraints of the MRT scheme. L is a characteristic length scale of the dimensionless system, i.e. given in lattice units. The coupling of the temperature field to the energy mode of the LB model is done by inserting the temperature into the equilibrium moments (Tlke, 2006):

$$m_1^{eq} = ((3T-1) + (u_x^2 + u_y^2 + u_z^2))\rho_0 \tag{10}$$

$$m_2^{eq} = (1 - 1.8T)\rho_0 \tag{11}$$

where $T = T(t,i,j,k)$ is a dimensionless temperature varying in space and time.
In order to simulate more realistic engineering applications, such as convective heat transport in buildings, simulations with Reynolds numbers of more than 10^6 have to be performed. At this scale DNS simulations become too expensive and therefore it is necessary to extend the standard HTLBE by a turbulence model. Large-eddy (LES) approaches are regarded as a promising compromise between explicit modeling of all scales of the turbulent spectrum and direct numerical simulation (DNS). In LES the large scale motions of the flow are calculated, while the effect of the smaller universal scales (the so called sub-grid scales) are modeled using a sub-grid scale (SGS) model. The most commonly used SGS model is the Smagorinsky model. It compensates for the unresolved turbulent scales through the addition of a so-called eddy viscosity into the governing equations.
In the context of lattice Boltzmann, the LES approach has first been used by (Hou et al., 1994) in 2D and in (Krafczyk et al., 2003) in 3D. As an inherent property of the LBE scheme, components of the momentum flux tensor, here expressed in terms of moments,

$$\Pi_{\alpha\beta} = \sum_i e_{i\alpha} e_{i\beta} f_i \tag{12}$$

are given as local quantities and do not have to be computed from derivatives of hydrodynamic quantities. Therefore, the local strain tensor is obtained by the relation

$$\tilde{\epsilon}_{\alpha\beta} = \frac{s_{xx}}{2\rho C_s^2}(C_s^2 \rho \delta_{\alpha\beta} + \rho u_\alpha u_\beta - \Pi_{\alpha\beta}) \tag{13}$$

as previously shown by (Krafczyk et al., 2003). Consequently, the molecular and turbulent viscosities can be added to form a total viscosity $\nu_{total} = \nu_0 + \nu_T$ which substitutes the material property by a space and time-dependent quantity. Having computed a local value for ν_T, the relaxation parameter s'_{xx} for the second order moments related to the stress tensor components $p_{xx}, p_{ww}, p_{xy}, p_{yz}$ and p_{zx} can be determined by

$$s'_{xx} = \frac{1}{3(\nu_0 + \nu_T) + \frac{1}{2}} \quad , \tag{14}$$

where ν_T is either related to the same time step or the last time step before propagation of the explicit scheme. Due to consistency reasons a subgrid model is also used for heat flux as proposed in (van Treeck et al., 2006).

3. Radiative heat transfer using the Radiosity-method

In this section an approach for radiative heat transfer in 3d domains based on the hierarchical radiosity method coupled to the LB method is presented. The radiosity method assumes radiative exchange between gray, diffuse surfaces in a radiatively non-participating medium. The idea is to hierarchically subdivide surfaces forming a quad-tree structure until a refinement criterion is reached. The fundamental underlying operation of the radiosity method is visibility detection which can be solved efficiently by using a space partitioning approach for the input surfaces. For this reason a kd-tree is chosen which is the most efficient method for visibility detection on irregularly distributed surfaces. These approaches dramatically decrease the complexity of the radiation problem from $O(n^3)$ to $O((k^2+n)\log k)$, where k is the number of input surfaces and n is the number of refined surfaces. For validations of these approach for several non-trivial examples, demonstrating that this scheme is second-order accurate see (Bindick et al., 2010).

3.1 Modeling radiative heat transfer

Heat flux from a body induced by thermal radiation solely depends on the local surface temperature and is not bound to molecular transport. This implies that every body is not only interacting with its direct neighbors but with all visible elements. Thermal radiation incident to a surface may be partially absorbed, reflected or transmitted. Here the absorbed part will be transformed into thermal energy. The complex radiative processes at a solid body are depicted in Fig.4.

The energy flux $M(\lambda, T)$ emitted from a surface with the temperature T and the wavelength λ can be described through the Planck's law of black-body radiation:

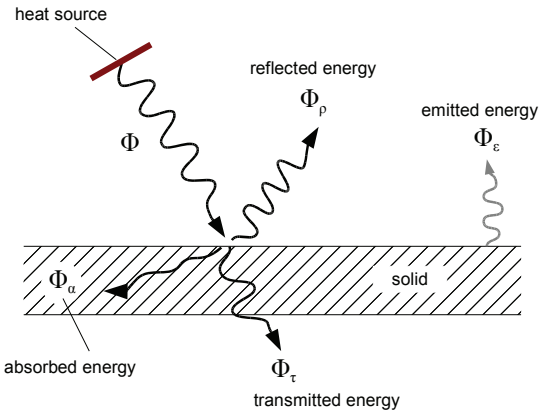

Fig. 4. Radiative processes at a solid body

$$M(\lambda, T) = \frac{2\pi c_0^2}{h^4} \frac{A}{e^{(hc_0/k\lambda T)} - 1} d\lambda \quad [W], \tag{15}$$

with the Planck constant $h = 6,626 \cdot 10^{-34}\ J \cdot s$, the speed of light c_0 and the Boltzmann constant $k = 1,381 \cdot 10^{-23}\ J/K$. This energy distribution is not constant over the spectrum and rises with increasing wavelength until a maximum at λ_{max} is reached (Siegel & Howell, 2002).
The energy flux leaving or entering a body depending on the direction in space can be described by the irradiance (E), the radiant energy arriving at a surface:

$$E = \int_\Omega I_a \cos(\Theta)\ d\Omega \quad \left[\frac{W}{m^2}\right] \tag{16}$$

with the radiative intensity I_a depending on the wavelength and $\cos(\Theta)\ d\Omega$ representing the projection of the solid angle. Analogously, the radiosity B (the radiant energy leaving a surface) can be written as:

$$B = \int_\Omega I_l \cos(\Theta)\ d\Omega \quad \left[\frac{W}{m^2}\right]. \tag{17}$$

In the following sections we describe how to solve the corresponding equations for a full radiant energy exchange in an enclosed 3d domain using the radiosity method (Goral et al., 1984).
The fundamentals of radiative heat transfer are explained in detail in e.g. (Siegel & Howell, 2002), (Modest, 2003), (Baehr & Stephan, 2006) and (Welty et al., 2001).

3.2 The classical radiosity method

The full energy exchange between diffuse surfaces can be calculated by forming an energy equilibrium for Eq. (16) and Eq. (17) in an enclosed environment. This approach leads to the radiosity method (based on the zonal method (Hottel & Cohen, 1958)) often used in the field of computer graphics to compute the inter-reflections of light (global illumination) (Goral et al., 1984). The radiosity method has long been an active field of research and many improvements could be found to reduce the algorithmic complexity of the problem. The radiosity method comes with the assumption that all bodies are gray diffusive reflectors, emitters and absorbers, (i.e. the same amount of radiant energy is reflected, emitted and absorbed in all directions) which is a common approximations for real bodies. Another assumption is that the radiative heat transfer between surfaces is separated by vacuum (radiatively nonparticipating), without considering the absorbing, scattering and emitting effects of the medium. This is a common approach for the relatively low pressures and temperatures that occur in many engineering applications. By subdividing the geometry surfaces into small planar patches, with homogeneous material properties, the discrete radiosity equation can be written as the sum of the patch radiation E_i and the radiosity B_j of all other n patches multiplied with the diffuse reflectivity ρ_d:

$$B_i = E_i + \rho_d \sum_{j=1}^{n} B_j F_{ij}, \tag{18}$$

with the configuration factor F_{ij} depending on the geometrical relation between two patches (see Fig.5).

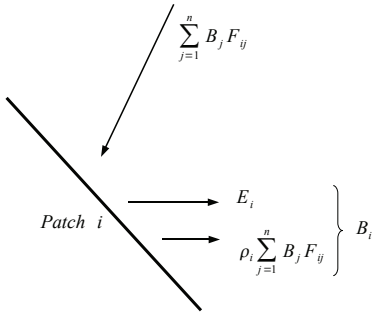

Fig. 5. Radiosity method

The configuration factor F_{ij} (also known as form factor or view factor) appearing in Eq. (18) describes the fraction of diffuse energy leaving a surface and directly reaching another surface (Goral et al., 1984). The configuration factor can be calculated by the following double integral which describes the relative position and orientation between two patches p_i and p_j:

$$F_{ij} = \frac{1}{A_i} \int_{A_i} \int_{A_j} \frac{\cos(\Theta_i)\cos(\Theta_j)}{\pi r^2} \, V(p_i, p_j) \, dA_i \, dA_j, \tag{19}$$

with the approximation of the solid angle $\frac{\cos(\Theta_i)\cos(\Theta_j)}{\pi r^2}$, the area A_i and A_j of surface i and j and a binary visibility function $V(p_i, p_j)$ to describe the visibility between two surfaces:

$$V(p_i, p_j) \quad \begin{cases} 1 \text{ if } p_i \text{ and } p_j \text{ are visible to each other} \\ 0 \text{ else} \end{cases}. \tag{20}$$

An analytic solution for Eq. 19 can only be found for very simple geometric configurations. A catalog of 300 known radiation configuration factors was published by Howell (Howell, 1982). The configuration factors for complex 3d geometries can not be determined analytically and in general have to be computed numerically as described below.
The kernel of Eq. (19), which is called differential form of the configuration factor, corresponds to the differential area of two patches, illustrated in Figure 6:

$$F_{ij} = \frac{\cos(\Theta_i)\cos(\Theta_j)}{\pi r^2} \, dA_j. \tag{21}$$

This expression represents the simplest approximation of the configuration factor and is only applicable for small patches with large distances to other patches and causes singularity problems.
Finding a general and accurate solution for the configuration factor F_{ij} has long been an active field of research (Tampieri, 1992; Cohen & Greenberg, 1985; Pianykh et al., 1998; Siegel & Howell, 2002). For this reason several numerical approaches to approximately solve the configuration factor integral exist. Early methods used a hemicube (Cohen & Greenberg, 1985) which comes with high memory requirements and makes it unusable for simulations with complex geometry models. A better approach combines adaptive mesh refinement (explained in detail in the following Sec. 3.3) with a point-to-disk approximation of the configuration factor (Wallace et al., 1989; Pianykh et al., 1998; Pellegrini, 1995; Siegel & Howell, 2002). Considering the configuration factor between a differential area and an arbitrarily oriented

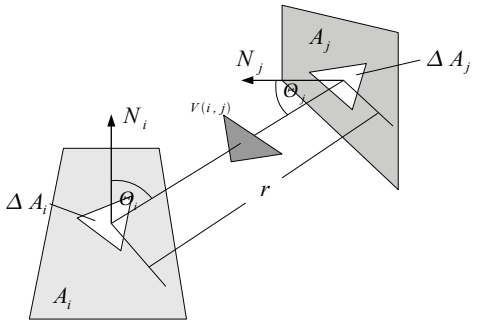

Fig. 6. Notation for configuration factor

disk Eq. (19) changes to:

$$F_{ij} = V(p_i, p_j)\ \frac{\cos(\Theta_i)\cos(\Theta_j)A_j}{\pi r^2 + A_i}, \tag{22}$$

where r is the distance between the patches. This approach was first introduced by Wallace (Wallace et al., 1989) and has been established as a practical approximation technique to solve the form factor double integral. Here we use the ray tracing algorithm to compute the visibility between two surfaces $V(p_i, p_j)$ where a ray is shot from the center point of the emitter to the center point of the receiver. Each ray must be tested for intersections with all objects in the environment. The ray tracing process can be accelerated substantially by using optimized hierarchical data structures based on kd-trees (see Sec. 3.4), so that logarithmic complexity as a function of the number of scene primitives can be achieved.
For a full radiative exchange in a closed environment Eq. (18) has to be solved simultaneously for all patches. These n equations form the following system of linear equations:

$$\begin{pmatrix} 1-\rho_1 F_{11} & -\rho_1 F_{12} & ... & -\rho_1 F_{1n} \\ -\rho_2 F_{21} & 1-\rho_2 F_{22} & ... & -\rho_2 F_{2n} \\ ... & ... & ... & ... \\ -\rho_n F_{n1} & -\rho_n F_{n2} & ... & 1-\rho_n F_{nn} \end{pmatrix} \begin{pmatrix} B_1 \\ B_2 \\ ... \\ B_n \end{pmatrix} = \begin{pmatrix} E_1 \\ E_2 \\ ... \\ E_n \end{pmatrix} \tag{23}$$

Solving this equation system yields the average radiosity value for each patch. Here an efficient solution technique called progressive refinement has been established, where the energy from a single patch is iteratively shot to the rest of the domain (Cohen et al., 1988). After the first iteration step only the patches in direct line of sight of an emitting patch will be affected. With every further step the indirectly irradiated patches will receive more energy. The shooting method utilizes the diagonal dominance of the interaction matrix and has proven to be an efficient solution technique (Cohen et al., 1988).

3.3 Hierarchical radiosity

The adaptive hierarchical radiosity method reduces the complexity of the standard radiosity method $O(n^2)$ (where all patches are in interaction with each other) to $O(k^2 + n)$ (where k is the number of input (root) patches and n is the number of refined patches) (Hanrahan et al., 1991). The basic idea of this approach is to use fewer and coarser interactions between patches depending on a specified solution accuracy. Receiver and emitter patches are hierarchically subdivided forming a quad-tree structure until a refinement criterion (often called oracle) is

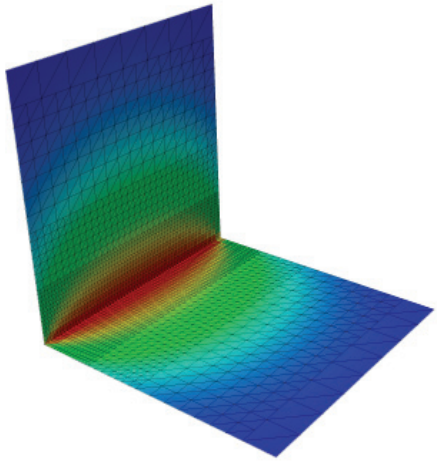

Fig. 7. Adaptive hierarchical subdivision for surfaces with high energy gradients

reached (see Fig.7). The goal is to establish links between patches that can be used for the energy transfer.
The hierarchical radiosity algorithm consists of three steps:

1. Initial linking: The configuration factor (using the disk approximation of Eq. 22) is evaluated for each pair of input patches. If the configuration factor is greater than a specified form factor threshold (F_ε) and a defined area threshold (E_ε) (depending on the required solution accuracy) a recursive subdivision routine is applied for the patch with the larger area. Here the subdivision process increases the accuracy of the solution. Otherwise, if the configuration factor is less than the thresholds a link is created which represents the energy transfer between these two patches. Links can be established between different levels and represent the interactions between groups of patches. This approach decreases the number of patches interacting with each other to $O(k^2 + n)$ where the visibility procedure is defined in section 3.4).
2. Energy gathering: For each patch the energy is repeatedly gathered over the incoming links until a convergence criterion is reached.
3. Push-pull: Energy arriving at a patch has to be propagated through the complete patch hierarchy to reach a consistent state after each iteration step. This can be achieved by pushing down the energy from the upper nodes to the leaf nodes and then pulling the weighted energy of the leafs to the upper ones.

A more detailed description of the hierarchical radiosity method can be found in, e.g. (Shaw, 1997) and (Schäfer, 2000) and for parallel approaches in, e.g. (Bohn & Garmann, 1995), (Podehl et al., 1998) and (Sinop et al., 2005).

3.4 Fast visibility computations based on kd-trees

The ray tracing algorithm is a fundamental operation in the radiosity method for visibility detection between surfaces and is the critical factor to develop a fast radiative heat transport method. Ray tracing can be solved efficiently by using a space partitioning data structure generated in a preprocessing step. Over the past few decades different space subdivision

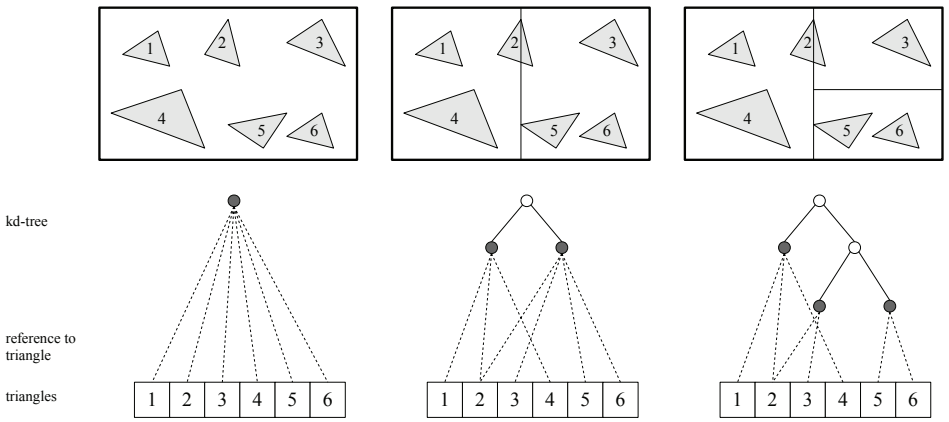

Fig. 8. Kd-tree example in 2D

schemes e.g. regular grids (Fujimoto et al., 1986), octrees (Glassner, 1984) or kd-trees (Havran, 2000) have been examined. Meanwhile kd-trees for ray tracing even for animated scenes have been established as the best known acceleration structure (Havran, 2000; Szirmay-Kalos et al., 2002; Shevtsov et al., 2007).

A kd-tree is a particular form of a Binary Space Partitioning (BSP) tree which always splits the space in axis-aligned cuboids. Each tree node is associated with such a cuboid and stores informations about its physical position in space (center point and length of the edges). The kd-tree root node contains all patches of the scene. The kd-tree is built over the bounding boxes of the surface polygons (mostly triangles or rectangles), often called *patches*). In each recursive construction step, two child nodes of the current node are created. The cuboid associated with the current node is split into two parts, which are then associated with the child nodes, a long with all the patches that overlap them (see Figure 8). A child node with no patches will be deleted immediately. The ray tracing algorithm on a kd-tree runs in $log\ n$ time (where n is the number of primitives) and uses linear memory space.

This process is repeated down to the leaf nodes until a termination criterion is reached (e.g. a maximum tree depth, a minimum number of leaf patches or an automatic termination criteria (based on a heuristic cost function)).

The main benefit of the kd-tree structure compared to other space subdivision schemes is the improved adaptability to the geometry. The tree quality can be influenced significantly by the position of the splitting plane. Here a heuristic approach called surface area heuristic (SAH) has been established for the kd-tree splitting (Havran, 2000; Havran & Bittner, 2002). This method maximizes the empty space to construct an optimal kd-tree by minimizing a cost function (MacDonald & Booth, 1990). The cost function is based on the fact that the geometric probability of a ray intersecting any tree node $P(V'|V)$ is equal to the surface area of the node $SA(V')$ divided by the surface area of the upper node $SA(V)$:

$$P(V'|V) = \frac{SA(V')}{SA(V)}, \tag{24}$$

where V' is the child node of V and the corresponding surface area SA. The cost function

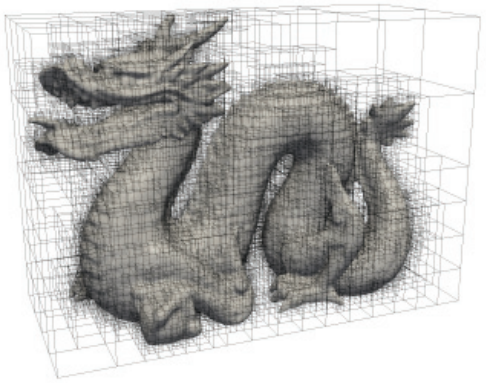

Fig. 9. Kd-tree example in 3D

is based on the following assumptions that the ray origins and directions are uniformly distributed, the cost of a traversal step C_t and a patch intersection C_i are known and the cost of intersecting n patches is directly proportional to the number of patches. Thus, the costs $C_N(V)$ for an inner tree node V can be calculated with the following equation:

$$\begin{aligned} C_N(V) &= C_t + n_l C_i P(V_l|V) + n_r C_i P(V_r|V) \\ &= C_t + C_i \left(n_l \frac{SA(V_l)}{SA(V)} + n_r \frac{SA(V_r)}{SA(V)} \right), \end{aligned} \tag{25}$$

where n_l is the number of patches overlapping the left node and analogously n_r is the number of patches overlapping the right node. In each recursive construction step, the cost function Eq. (25) can be evaluated for a certain number of possible split candidates. Here the best split position is coincident with the bounding box projection of the patch. So the cost function only needs to be evaluated at the triangle boundaries. With this approach the number of checked possible split candidates can be decreased dramatically. The best split position minimizes $C_N(V)$ Eq. (25). Fig.9 shows a three dimensional (3d) kd-tree example.
For the fast construction of heuristic optimized kd-trees a technique based on the sweeping algorithm has established, which works with a complexity of $O(n\ log^2\ n)$ (Szécsi, 2003; Pharr & Humphreys, 2004). This approach also includes an automatic termination criterion (ATC), based on the cost model, to decide whether to stop splitting or to continue subdividing a tree node (Havran & Bittner, 2002). An optimal kd-tree can thus be built without ad hoc defined constants.
The visibility detection between patches is processed by shooting rays on the kd-tree. As the traversal process starts at the root node, the child nodes are recursively tested for intersection with the ray until a leaf node is reached. All patches referenced from this leaf node are checked iteratively for intersection (fast ray-triangle and ray-box intersection tests can be found in e.g. (Badouel, 1990; Möller & Trumbore, 1997; Wald et al., 2001)). This approach allows to solve the visibility problem in $O(log\ n)$.

4. Preliminary applications

In this section some results of heat transfer and coupled heat transport simulations are shown. In the first application the energy distribution in porous asphalt induced by solar radiation is

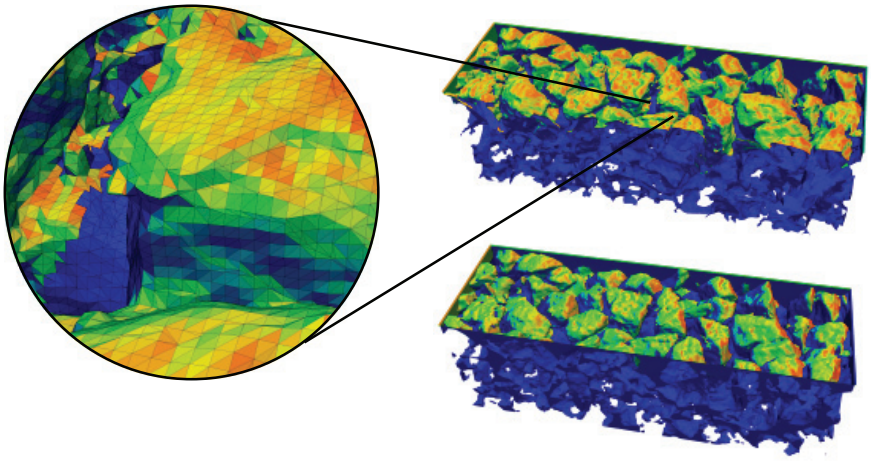

Fig. 10. Radiative energy distribution for different sun positions in a sample of porous asphalt with 50 million leaf triangles

simulated for different positions of the sun. Simulating the thermal behavior can help to optimize the composition and characteristics of asphalt. The geometric model is obtained by using a tomography scanner, which leads to complex models with very high resolutions (Ahrenholz, 2009). In this case a scan with 400x400x350 voxels is used, which is triangulated to a surface mesh (using e.g. the marching cubes method) with 10 million triangles. These high resolutions are necessary to represent the fine porous structure of the asphalt. The input surface mesh is adaptively refined during the hierarchical radiosity process to 50 million leaf triangles. Fig.10 shows the energy distribution over the surfaces for an equilibrium condition for two different sun position. The CPU time for this setup was about 700 seconds on an Intel Core2 Q9550 Quad-Cores, 8GB DDR2 Memory and Windows 7 64-bit.

A coupled variant is shown in Figure 11. Here, the surface temperatures are computed using the radiosity method introduced in section 3. These parameters are used as input values for the hTLBM simulation described in subsection 2.3. In this example the temperature distribution in a machine hall housing a server farm is simulated. This setup aims on the optimization of cooling and the identification of hot spots which can cause an overheating which potentially leads to malfunctioning server devices.

Another example demonstrating a combined simulation of radiation induced thermal energy and the resulting flow pattern also known as convection is shown in Figure 12. The aim of this simulation was to estimate the efficiency of three different versions of fassade constructions The simulation of the three different variants have been performed assuming worst case scenarios of the weather conditions (35° Celsius outside temperature, no wind). In order to obtain reasonable input data relative to the initial temperature distribution and the insertion of thermal energy into the system, the radiative heat transfer simulation section 3 has been performed in advance. Here, the surface temperature of all materials exposed to direct sunlight is determined and used as input data for LB simulations.

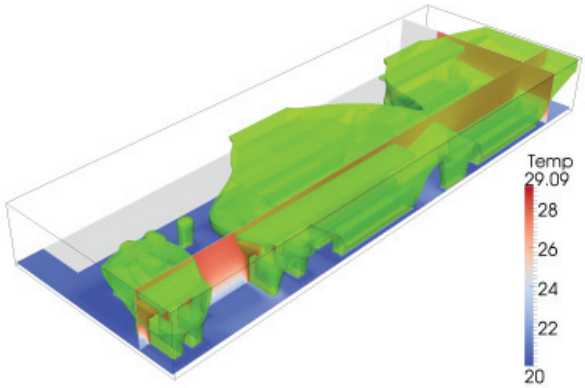

Fig. 11. Temperature distribution isosurfaces in a machine hall; the contours show the temperature boundary of 28° Celsius

5. Conclusion and outlook

With the radiosity-method the radiative heat transfer problem especially for applications in civil engineering can be efficiently and accurately simulated. Here, the hierarchical adaptive subdivision of the surfaces combined with a kd-tree based acceleration structure for the visibility detection dramatically decreases the runtime complexity of the radiation problem. Lattice Boltzmann fluid dynamics have been established as an alternative tool to solve different transport problems, including turbulent thermal flows. Its explicit numerical approach allows a straightforward coupling to other models representing structural dynamics or radiation and an efficient parallel implementation. The coupling between LBM and a radiation driven problem like convection has been succesfully demonstrated in the examples above.

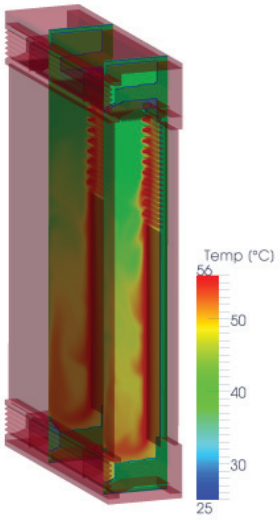

Fig. 12. Convection inside one floor of a buildings double fassade

Presently the bidirectional coupling of radiation induced heat and heat transport in fluid and solid is under investigation. Also the adaptation to special purpose hardware like GPUs is planed which is expected to deliver the accuracy of 3D transient transport simulations without the use of expensive supercomputers.

6. References

Ahrenholz, B. (2009). *Massively parallel simulations of multiphase- and multicomponent flows using lattice Boltzmann methods*, PhD thesis, Technischen Universität Carolo-Wilhelmina zu Braunschweig.

Alexander, F., Chen, S. & Sterling, J. (1993). Lattice Boltzmann thermohydrodynamics, *Physical Review E* 47: R2249.

Badouel, D. (1990). *An efficient ray-polygon intersection*, Academic Press Professional, Inc., San Diego, CA, USA.

Baehr, H. & Stephan, K. (2006). *Heat and Mass Transfer*, Springer Verlag.

Benzi, R., Succi, S. & Vergassola, M. (1992). The lattice Boltzmann equation: theory and applications, *Physics Reports* 222(3): 147–197.

Bhatnagar, P. L., Gross, E. P. & Krook, M. (1954). A Model for Collision Processes in Gases. I. Small Amplitude Processes in Charged and Neutral One-Component Systems, *Physical Review* 94: 511–525.

Bindick, S., Stiebler, M. & Krafczyk, M. (2010). Fast kd-tree based hierarchical radiosity for radiative heat transport problems, *submitted to: International Journal for Numerical Methods in Engineering* -: –.

Bohn, C.-A. & Garmann, R. (1995). A parallel approach to hierarchical radiosity, *University of West Bohemia*, pp. 26–35.

Cercignani, C., Illner, R. & Pulvirenti, M. (1994). *The Mathematical Theory of Dilute Gases*, Vol. 106 of *Applied Mathematical Sciences*, Springer Verlag, Berlin, Germany; New York, U.S.A.

Cercignani, C. & Penrose, R. (1998). *Ludwig Boltzmann: The Man Who Trusted Atoms*, Oxford University Press.

Chen, S. & Doolen, G. (1998). Lattice Boltzmann method for fluid flows, *Annual Review of Fluid Mechanics* 30: 329–364.

Cohen, M. F., Chen, S. E., Wallace, J. R. & Greenberg, D. P. (1988). A progressive refinement approach to fast radiosity image generation, *SIGGRAPH Comput. Graph.* 22(4): 75–84.

Cohen, M. F. & Greenberg, D. P. (1985). The hemi-cube: a radiosity solution for complex environments, *SIGGRAPH '85: Proceedings of the 12th annual conference on Computer graphics and interactive techniques*, ACM, New York, NY, USA, pp. 31–40.

d'Humières, D., Bouzidi, M. & Lallemand, P. (2001). Thirteen-velocity three-dimensional lattice boltzmann model, *Physical Review E* 63(6): 066702.

Dellar, P. (2003). Incompressible limits of lattice boltzmann equations using multiple relaxation times, *Journal of Computational Physics* 190: 351–370.

d'Humières, D. (1992). Generalized lattice-Boltzmann equations, *in* B. D. Shizgal & D. P. Weave (eds), *Rarefied Gas Dynamics: Theory and Simulations*, Vol. 159 of *Prog. Astronaut. Aeronaut.*, AIAA, Washington DC, pp. 450–458.

d'Humières, D., Ginzburg, I., Krafczyk, M., Lallemand, P. & Luo, L.-S. (2002). Multiple-relaxation-time lattice Boltzmann models in three dimensions, *Philosophical Transactions of the Royal Society A-Mathematical, Physical and Engineering Sciences* 360: 437–451.

Filippova, O. & Hänel, D. (2000). A novel lattice BGK approach for low Mach number combustion, *Journal of Computational Physics* 158: 139.

Frisch, U., d'Humières, D., Hasslacher, B., Lallemand, P., Pomeau, Y. & Rivet, J.-P. (1987). Lattice gas hydrodynamics in two and three dimensions, *Complex Systems* pp. 75–136.

Fujimoto, A., Tanaka, T. & Iwata, K. (1986). Arts: Accelerated ray-tracing system, *IEEE Comput. Graph. Appl.* 6(4): 16–26.

Geller, S., Krafczyk, M., Tölke, J., Turek, S. & Hron, J. (2006). Benchmark computations based on Lattice-Boltzmann, Finite Element and Finite Volume Methods for laminar Flows, *Computers & Fluids* 35: 888–897.

Ginzburg, I. & d'Humières, D. (1996). Local second-order boundary methods for lattice Boltzmann models, *Journal of Statistical Physics* 84: 927–971.

Glassner, A. S. (1984). Space subdivision for fast ray tracing, *IEEE Computer Graphics & Applications* 4(10): 15–22.

Goral, C. M., Torrance, K. E., Greenberg, D. P. & Battaile, B. (1984). Modeling the interaction of light between diffuse surfaces, *SIGGRAPH Comput. Graph.* 18(3): 213–222.

Hanrahan, P., Salzman, D. & Aupperle, L. (1991). A rapid hierarchical radiosity algorithm, *SIGGRAPH '91: Proceedings of the 18th annual conference on Computer graphics and interactive techniques*, ACM, New York, NY, USA, pp. 197–206.

Havran, V. (2000). *Heuristic Ray Shooting Algorithms*, Ph.d. thesis, Department of Computer Science and Engineering, Faculty of Electrical Engineering, Czech Technical University in Prague.

Havran, V. & Bittner, J. (2002). On Improving KD-Trees for Ray Shooting, *In Proc. of WSCG 2002 Conference*, pp. 209–217.

He, X. & Luo, L. S. (1997a). A priori derivation of the lattice boltzmann equation, *Physical Review E* 55(6): R6333–R6336.

He, X. & Luo, L.-S. (1997b). Theory of the lattice Boltzmann method: from the Boltzmann equation to the lattice Boltzmann equation, *Physical Review E* 56: 6811.

Higuera, F. J., Succi, S. & Benzi, R. (1989). Lattice Gas Dynamics with Enhanced Collisions, *Europhysics Letters* 9(4): 345–349.

Higuera, F. & Jiménez, J. (1989). Boltzmann approach to lattice gas simulations, *Europhysics Letters* 9: 663–668.

Hottel, H. C. & Cohen, E. S. (1958). Radiant heat exchange in a gas-filled enclosure: allowance for non-uniformity of gas temperature, *AIChE Journal* 4: 3–14.

Hou, S., Sterling, J., Chen, S. & Doolen, G. D. (1994). A Lattice Boltzmann Subgrid Model for High Reynolds Number Flows, *Contributions to Mineralogy and Petrology* pp. 1004–+.

Howell, J. R. (1982). *A Catalog of Radiation Configuration Factors*, McGraw-Hill, New York.

Junk, M., Klar, A. & Luo, L. (2005). Asymptotic analysis of the lattice Boltzmann equation, *jcp* 210: 676.

Krafczyk, M., Tölke, J. & Luo, L.-S. (2003). Large-Eddy Simulations with a Multiple-Relaxation-Time LBE Model, *APS Meeting Abstracts* pp. J7+.

Lallemand, P. & Luo, L.-S. (2000). Theory of the lattice Boltzmann method: Dispersion, dissipation, isotropy, Galilean invariance, and stability, *Physical Review E* 61: 6546–6562.

Lallemand, P. & Luo, L.-S. (2003). Theory of the lattice Boltzmann method: Acoustic and thermal properties in two and three dimensions, *Physical Review E* 68(3): 036706–+.

MacDonald, D. J. & Booth, K. S. (1990). Heuristics for ray tracing using space subdivision, *Vis. Comput.* 6(3): 153–166.

McNamara, G. & Zanetti, G. (1988). Use of the Boltzmann equation to simulate lattice-gas automata, *Physical Review Letters* 61: 2332–2335.

Modest, M. F. (2003). *Radiative Heat Transfer*, second edn, Academic Press, An imprint of Elsevier Science.

Möller, T. & Trumbore, B. (1997). Fast, Minimum Storage Ray-Triangle Intersection, *journal of graphics, gpu, and game tools* 2(1): 21–28.

Pellegrini, M. (1995). Monte carlo approximation of form factors with error bounded a priori, *SCG '95: Proceedings of the eleventh annual symposium on Computational geometry*, ACM, New York, NY, USA, pp. 287–296.

Pharr, M. & Humphreys, G. (2004). *Physically Based Rendering: From Theory to Implementation*, Morgan Kaufmann Publishers Inc., San Francisco, CA, USA.

Pianykh, O. S., Tyler, J. M. & Jr., W. N. W. (1998). Improved monte carlo form factor integration, *Computers & Graphics* 22(6): 723–734.

Podehl, A., Rauber, T. & Rünger, G. (1998). A shared-memory implementation of the hierarchical radiosity method, *Theor. Comput. Sci.* 196(1-2): 215–240.

Qian, Y. H. (1993). Simulating thermohydrodynamics with lattice BGK models, *Journal of Scientific Computing* 8: 231.

Qian, Y. H., d'Humières, D. & Lallemand, P. (1992). Lattice BGK models for Navier-Stokes equation, *Europhysics Letters* 17: 479–484.

Schäfer, S. (2000). *Efficient Object-Based Hierarchical Radiosity Methods*, PhD thesis, Technische Universität Braunschweig.

Shan, X. (1997). Simulation of Rayleigh-Bernard convection using the lattice Boltzmann method, *Physical Review E* 55: 2780.

Shaw, E. (1997). Hierarchical radiosity for dynamic environments, *Computer Graphics Forum* 16: 107–118.

Shevtsov, M., Soupikov, A. & Kapustin, A. (2007). Highly Parallel Fast KD-tree Construction for Interactive Ray Tracing of Dynamic Scenes, *Comput. Graph. Forum* 26(3): 395–404.

Siegel, R. & Howell, J. R. (2002). *Thermal radiation heat transfer*, third edn, Taylor & Francis Inc.

Sinop, A. K., Abaci, T., Akkuş, U., Gürsoy, A. & Güdükbay, U. (2005). Phr: A parallel hierarchical radiosity system with dynamic load balancing, *J. Supercomput.* 31(3): 249–263.

Sterling, J. D. & Chen, S. (1996). Stability analysis of lattice Boltzmann methods, *Journal of Computational Physics* 123(1): 196–206.

Succi, S. (2001). *The Lattice Boltzmann Equation for Fluid Dynamics and Beyond*, Oxford University Press, Oxford.

Szécsi, L. (2003). *Graphics programming methods*, Charles River Media, Inc., Rockland, MA, USA, chapter An effective implementation of the k-D tree, pp. 315–326.

Szirmay-Kalos, L., Havran, V., Balázs, B. & Szécsi, L. (2002). On the Efficiency of Ray-shooting Acceleration Schemes, *in* A. Chalmers (ed.), *Proceedings of the 18th Spring Conference on Computer Graphics (SCCG 2002)*, ACM Siggraph, Budmerice, Slovakia, pp. 89–98.

Tampieri, F. (1992). *Accurate form-factor computation*, Academic Press Professional, Inc., San Diego, CA, USA.

Tlke, J. (2006). A thermal model based on the lattice boltzmann method for low mach number compressible flows, *Journal of Computational and Theoretical Nanoscience* 3(4): 579–587.

Tlke, J. & Krafczyk, M. (2008). Teraflop computing on a desktop pc with gpus for 3d cfd, *International Journal of Computational Fluid Dynamics* 22(7): 443–456.
URL: *http://dx.doi.org/10.1080/10618560802238275*

Vahala, L., Wah, D., Vahala, G., Carter, J. & Pavlo, P. (2000). Thermal Lattice Boltzmann Simulation for Multispecies Fluid Equilibration, *Physical Review E* 62: 507.

van Treeck, C., Rank, E., Krafczyk, M., Tölke, J. & Nachtwey, B. (2006). Extension of a hybrid thermal LBE scheme for Large-Eddy simulations of turbulent convective flows, *Computers & Fluids* 35(8–9): 863–871.

Wald, I., Slusallek, P., Benthin, C. & Wagner, M. (2001). Interactive Rendering with Coherent Ray Tracing, *Computer Graphics Forum*, pp. 153–164.

Wallace, J. R., Elmquist, K. A. & Haines, E. A. (1989). A ray tracing algorithm for progressive radiosity, *SIGGRAPH Comput. Graph.* 23(3): 315–324.

Welty, J. R., Wicks, C. E., Wilson, R. E. & Rorrer, G. (2001). *Fundamentals of Momentum, Heat and Mass Transfer*, John Wiley & Sons, Inc.

8

Applications of Nonstandard Finite Difference Methods to Nonlinear Heat Transfer Problems

Alaeddin Malek
Department of Applied Mathematics, Faculty of Mathematical Sciences, Tarbiat Modares University, P.O. Box 14115-134, Tehran, Iran

1. Introduction

This chapter presents some applications of nonstandard finite difference methods to general nonlinear heat transfer problems. Nonlinearity in heat transfer problems arises when

i. Some properties in the problem are temperature dependent
ii. Boundary conditions are described by nonlinear functions
iii. The interface energy equation in phase change problems is nonlinear.

Free convection and surface radiation are famous examples of nonlinear boundary conditions. The temperature distribution in multi phase regions is governed by various heat equations, for example in two phase region the temperature is governed by two different heat equation, one for solid phase, and the other one for liquid phase. Conservation of energy at a phase change interface usually yields to the nonlinear boundary condition.

While particular problems presented in this research relates to nonlinear heat transfer in a thin finite rod, I fell that the methodology by which one solves these problems by nonstandard finite difference methods are quite general. I hope that these bits and pieces will be taken as both a response to a specific problem and a general method.

It is common to model the nonlinear heat transfer problems by parabolic time dependent nonlinear partial differential equations. The model assumes a certain separation between time and space which is present in parabolic heat transfer problems. There are two approaches for the solution of nonlinear parabolic PDEs. One is the closed analytical form solution based on the separation of variables. Although the method of separation of variables has wide applicability, it is most often limited to linear problems. The second approach is numerical approach based on the discretization of the region. There are various approaches for performing the discretization, such as finite difference (M. Necati Ozisik et al., 1994; D. R. Croft & D. G. Lilly, 1977), finite element (R. W. Lewis, et al., 2005; J. M. Bergheau, 2010), finite volume (S. V. Patankar, 1980; H. K. Versteeg & W. Malalasekera, 1996), and spectral methods (G. Ben-Yu, 1998; O. P. Le Maitre & O. M. Knio, 2010). Here we concentrate on both standard and nonstandard finite difference methods. Standard FDs are usually used for linear part of the problem while the nonstandard FDs are used to deal with nonlinearity. Since corresponding PDEs in the heat transformation are some time dependent equations, in general one need to consider both discretizations in time and in the space. There are two typical discretization techniques in the literature. First is the semi-

discertization scheme and the second is fully discertization formulation. In semi-discertization, we treat the time variable t as a specific variable among the independent variables, i.e., for a fixed t we discretize the spatial domain and derivatives first. This usually yields to a system of initial value ordinary differential equations. After this stage any of the ODE methods and software may be used to solve the problem. Some of the well known methods in this context are method of lines, Euler and Runge-Kutta methods. An obvious process to obtain a full discretization scheme for the time dependent PDEs such as parabolic equations is to discretize in time the corresponding semi-discretization scheme.

Nonlinear partial differential equations are defined as the mathematical representation of real world problems concerned with the determination of a solution of a function of several variables, which are required to satisfy a number of initial and boundary conditions. Such function computations are sought in diverse fields, including heat transform, fluid mechanics, electrical and industrial engineering, medical sciences and denoising a noisy image.

Although many classical numerical algorithms such as finite difference, finite element, control volume, boundary element and spectral methods are given to solve linear and nonlinear heat transfer problems, in many applications, it is easier and desire to have nonstandard FD discretization for the corresponding nonlinear terms. However, traditional standard finite difference algorithms are not suitable for nonlinear heat transfer problems. In the present work we will show that the nonstandard finite difference approach is one of the promising approaches that can handle the nonlinearity and perform an accurate numerical solution to the problem.

In the recent years many nonstandard FD models developed to solve nonlinear heat transfer problems. Several basic and advance questions associated with these models have motivated the studies presented in this chapter.

The goal of this chapter is threefold. First we consider the nonlinear conduction problems and discuss the sources of nonlinearity in these problems. Second, the theoretical areas of interest include fundamental methods, models and algorithms for solving general nonlinear heat transfer problems using various implicit and explicit nonstandard finite difference methods is discussed. Third, we will try to present and discuss the numerical analysis for the corresponding models, simulations and applications of nonstandard methods that solve various practical heat transfer problems.

Nonstandard finite difference methods are an area of finite difference methods which is one of the fundamental topics of the subject that coup with the nonlinearity of the problem very well. This subject combines many mathematical concepts like ordinary and partial differential equations, nonlinear boundary conditions, consistency, convergence, stability and error analysis of the corresponding algorithms. Students are often familiar with the steady and time dependent ODEs with one variable before embarking on an undergraduate course, and in practical way will have function derivatives which they cannot express in numerical form. Here we must compute the solution for the nonlinear time dependent PDEs with one dependent and of several independent variables. From mathematical point of the view convergence of the solution, consistency and stability of the method has quiet importance, while as an engineer one might look for an efficient algorithm that works for many different real life problems.

The numerical analysis and mathematical techniques considered here are some service industry in order to write some reliable codes to solve nonlinear heat transfer problems. The

theoretical analysis forms a tool to determine bounds on various kinds of errors and levels of stability. These error bounds form the basis of a theoretical justification for the solution convergence of the corresponding numerical algorithm to the actual solution of the original nonlinear heat transfer model. Whichever numerical algorithm is used, one should take care of the consistency between the nonstandard FD model and the original heat transfer problem.

The chapter covers a range of topics from undergraduate work on standard finite difference solution to ODEs and PDEs through to recent research on nonstandard finite difference schemes for nonlinear heat transfer problems. The source of the standard finite difference work is the lecture notes for graduate students participated in my advance course in the numerical solution to PDEs. The notes have grown in nineteen years of teaching the subject. The work on nonstandard finite difference models is based partly on my own research. Part of this research started in the year 2000 during the time that I was in university of Pretoria, South Africa in the sabbatical leave from Tarbiat Modares University, Tehran, Iran. It has taken annual updates as new models have proposed in some of the thesis of my postgraduate students during the last six years. This research is enriched by the literature published with Mickens and his co-author during the last fifteen years.

I am grateful to the applied mathematics department in the faculty of mathematical sciences at Tarbiat Modares University which has made available the technical equipment and environment for the research. The novel models and numerical programs have been tested, compared and improved using the different computers which have been installed over the years.

In the next section we study general concepts introductory in the heat transfer problems. Then, under the assumption that there exists a solution we try to seek an efficient numerical solution using nonstandard FD methods.

2. Heat transfer preliminaries

Definition 2.1:

In general, the process by which molecules spread from areas of high concentration, to areas of low concentration is called diffusion.

In the following we give some ideas and examples representing heat convection, conduction and radiation. These facts or events in the real world as they are experienced by the human senses are three physical concepts that heat transfer problems engage one or some combinations of them.

2.1 Conduction

Conduction is the transfer of energy through matter from particle to particle. It is a heat transfer directly through materials, occurring when mass of material stays in place. It is the transfer and distribution of heat energy from atom to atom within a substance. For example, a spoon in a cup of hot soup becomes warmer because the heat from the soup is conducted along the spoon. Conduction is most effective in solids but it can happen in fluids.

Have you ever noticed that metals tend to feel cold? They are not colder. They only feel colder because they conduct heat away from your hand. The human being recognizes the heat that is leaving his hand as cold. This makes it clear that: what identifies heat is temperature difference and not temperature.

Conduction heat transfer phenomenon is encountered in many real life problems. One may consider the following few examples among the broad range of conduction problems.

- Electronic Devices Design: An electronic package is to be cooled by conduction. A heat sink consisting of small devices is recommended to maintain the electronic components below a specified temperature. How many devices of what size and material and configuration are necessitated?
- Liquid in Glass Thermometer: Liquids like mercury and alcohol are used to measure temperature by the technique of putting the liquid in glass. Determine the minimum and maximum temperature that mercury and alcohol can measure by this technique of thermometer manufacturing.
- Heat Loss of an Aluminum Alloy Plate: An aluminum alloy plate is suddenly quenched into liquid oxygen. Find the heat loss by the plate. Calculate the required time for the plate to reach to specific temperature.
- Nuclear Reactor Coolant Pump: The temperature of some nuclear elements begins to rise, if the coolant pump fails. Determine the required time that engineers need to fix the pump before meltdown happens.
- Space Vehicle Reentry Safeguard: A heat guard is used to protect a space vehicle during reentry. The shield ablates as it passes through the atmosphere. Specify the required safeguard thickness and material to protect a space vehicle during reentry.
- Supersonic Rocket Nozzle Protection: The throat of a supersonic rocket nozzle is protected by inserting a porous ring at the throat. Injection of helium through the ring lowers the temperature and protects the nozzle. Determine the amount of helium needed to protect a rocket nozzle during a specified trajectory.

2.1.1 Classical heat conduction theory (linear)

In the case of classical heat conduction it has been demonstrated many times that if two parallel plates of the same area A and different constant temperatures T_1 and T_2 respectively, are separated by a small distance d, an amount of heat per unit time will pass from the warmer to cooler. This amount of heat is proportional to the area A, the temperature difference $\left| T_1 - T_2 \right|$, and inversely proportional to the separation distance d. Thus

$$\text{amount of heat per unit time} = \kappa A \frac{\left| T_1 - T_2 \right|}{d},$$

where the positive factor κ the material conductivity depends only on the material between the two plates. This is a physical law called Newton's low of cooling and has often been verified by careful experiment. Although, it is an experimental theory, it is the basis of the mathematical theory of classical heat conduction. This is a reason that in the classical theory of diffusion, Fourier's equation relates the heat flux to temperature according to the equation:

$$q(r,\tau) = -\kappa \nabla T(r,\tau), \tag{2.1}$$

where $q(r,\tau)$ is the heat flux, τ stands for time, r is a position vector that has heat flux components in the x, y and z directions and κ is the material conductivity. In this theory the medium is of macroscale and it is assumed that the heat flux vector and temperature gradient across a material volume occur at the same instant of time.

The simple linear diffusion problem in one space variable x and time τ, for $(x,\tau)\in(0,l)\times(0,\infty)$, is (J. D. Smith, 1985)

$$\frac{\partial T}{\partial \tau}=\kappa\frac{\partial^2 T}{\partial X^2} \tag{2.2}$$

The non-dimensionalizing process is illustrated below with the parabolic heat conduction equation (2.2).

Work Example 1: (Involves only heat conduction)

The solution of Eq. (2.2) gives the temperature T at a distance X from one end of a thin uniform wire after a time τ. This assumes the rod is ideally heat insulated along its length and heat transfers at its ends. Let l represent the length of the wire and T_0 some particular non negative constant temperature such as the maximum or minimum temperature at zero time.
Using the following dimensionless variables

$$u=T/T_0,\quad x=X/l,\qquad t=\kappa\tau/l^2, \tag{2.3}$$

equation (2.2) with the general boundary condition and specific initial temperature distribution, can be rewritten in the following dimensionless form

$$\begin{cases} u_t=u_{xx}, & (x,t)\in(0,1)\times(0,\infty);\\ u(0,t)=U_1, & u(1,t)=U_2, \quad t>0;\\ u(x,0)=2x, & x\in[0,1/2];\\ u(x,0)=2(1-x), & x\in[0,1/2]; \end{cases} \tag{2.4}$$

where U_1 and U_2 are the dimensionless forms of T_1 and T_2, respectively.

In other word we are seeking a numerical solution of $\frac{\partial u}{\partial t}=\frac{\partial^2 u}{\partial x^2}$ which satisfies

Case I:

i. $u=0 \;\; at \;\; x=0 \;\; and \;\; u=0 \;\; at \;\; x=l \;\; for \;\; all \;\; t>0$.

ii. $for \;\; t=0: \;\; u=2x \;\; for \;\; 0\le x\le 1/2 \;\; and \;\; u=2(1-x) \;\; for \;\; 1/2\le x\le 1,$

Case II:

iii. $u=0 \;\; at \;\; x=0 \;\; and \;\; u=0 \;\; at \;\; x=l \;\; for \;\; all \;\; t>0$.

iv. $for \;\; t=0: \;\; u=\sin\pi x \;\; for \;\; 0\le x\le 1.$

where (i), (iii) and (ii), (iv) are called the boundary condition and the initial condition respectively.

2.2 Convection

Convection is the transfer of heat by the actual movement of the warmed matter. It is a heat transfer through moving fluid, where the fluid carries the heat from the source to destination. For example heat leaves the coffee cup as the currents of steam and air rise. Convection is the transfer of heat energy in a gas or liquid by movement of currents. It can

also happen in some solids, like sand. More clearly, convection is effective in gas and fluids but it can happen in solids too. The heat current moves with the gas and fluid in the most of the food cooking. Convection is responsible for making macaroni rise and fall in a pot of heated water. The warmer portions of the water are less dense and therefore, they rise. Meanwhile, the cooler portions of the water fall because they are denser.
While heat convection and conduction require a medium to transfer energy, heat radiation does not. The energy travels through nothingness (vacuum) in the heat radiation.

2.3 Radiation

Electromagnetic waves that directly transport energy through space is called radiation. Heat radiation transmits by electromagnetic waves that travel best in a vacuum. It is a heat transfer due to emission and absorption of electromagnetic waves. It usually happens within the infrared/visible/ultraviolet portion of the spectrum. Some examples are: heating elements on top of toaster, incandescent filament heats glass bulb and sun heats earth. Sunlight is a form of radiation that is radiated through space to our planet without the aid of fluids or solids. The sun transfers heat through 93 million miles of space. There are no solids like a huge spoon touching the sun and our planet. Thus conduction is not responsible for bringing heat to Earth. Since there are no fluids like air and water in space, convection is not responsible for transferring the heat. Therefore, radiation brings heat to our planet.
Heat excites the black surface of the vanes more than it heats the white surface. Black is a good absorber and a good radiator. Think of black as a large doorway that allows heat to pass through easily. In contrast, white is a poor absorber and a poor radiator of energy. White is like a small doorway and will not allow heat to pass easily.
Note that heat transfer problems involve temperature distribution not just temperature. Heat transfer rates are determined knowing the temperature distribution. While Fourier's law of conduction provides the rate of heat transfer related to heat distribution, temperature distribution in a medium governs with the principle of conservation of energy.

2.3.1 Stefan-Boltzmann radiation law

If a solid with an absolute surface temperature of T is surrounded by a gas at temperature T_∞, then heat transfer between the surface of the solid and the surrounding medium will take place primarily by means of thermal radiation if $\left| T - T_\infty \right|$ is sufficiently large (P. M. Jordan, 2003). Mathematically, the rate of heat transfer across the solid-gas interface is given by the Stefan-Boltzmann radiation law

$$\kappa(\partial T / \partial n)_s = -\sigma\varepsilon A(T^4 - T_\infty^4), \tag{2.5}$$

where $(\partial T / \partial n)_s$ the thermal gradient at the surface of the solid is evaluated in the direction of the outward-pointing normal to the surface, A is radiating area and $\kappa > 0$ is the thermal conductivity of the solid (assumed constant). The constants $\varepsilon \in [0,1]$, ($\varepsilon = 1$ for ideal radiator while for a prefect insulator $\varepsilon = 0$) and $\sigma \approx 5.67 \times 10^{-8}$ W / ($\mathrm{m^2K^4}$) are, respectively, the emissivity of the surface and the Stefan-Boltzmann constant (P. M. Jordan, 2003). Mathematically, the rate of heat transfer across the solid-gas interface is given by the Newton's law of cooling (H. S. Carslaw & J. C. Jaeger, 1959; R. Siegel & J. H. Howell, 1972)

$$\kappa(\partial T / \partial n)_s = -hA(T - T_\infty), \tag{2.6}$$

where h is the convection heat transfer coefficient and A is cooloing area.
The applications of thermal radiation with/without conduction can be observed in a good number of science and engineering fields including aerospace engineering/design, power generation, glass manufacturing and astrophysics (R. Siegel & J. H. Howell, 1972; L. C. Burmeister, 1993; M. N. Ozisik, 1989; J. C. Jaeger, 1950; E. Battaner, 1996).
In the following Work Examples we consider two problems that involve various heat transfer properties in a thin finite rod (A. Mohammadi & A. Malek, 2009).

3. Nonlinear heat transfer in a finite thin wire

3.1 Heat transfer involving both conduction and radiation

In the following example we consider a problem that involves both conduction and radiation and no convection.
Consider a very thin, homogeneous, thermally conducting solid rod of constant cross-sectional area A, perimeter p, length l and constant thermal diffusivity $\kappa > 0$ that occupies the open interval $(0,l)$ along the X **-** axis of a Cartesian coordinate system. That T the temperature distribution of the rod, is $T(X,\tau)$, and $T_0 \sin(\pi X / l)$ is initial temperature of the rod, and let the ends at $X = 0, l$ be maintained at the constant temperatures T_1 and T_2 respectively and T_∞ the surrounding temperature. The parabolic one-dimensional unsteady heat conduction model in a thin finite rod that is radiating heat across its lateral surface into a medium of constant temperature is the mathematical model of this physical system consists of the following initial boundary value problem (P. M. Jordan, 2003; W. Dai & S. Su, 2004)

$$\begin{cases} T_\tau = \kappa T_{XX} - \beta_0 (T^4 - T_\infty^4), & (X,\tau) \in (0,l) \times (0,\infty); \\ T(0,\tau) = T_1, \quad T(l,\tau) = T_2, & \tau > 0; \\ T(X,0) = T_0 \sin(\pi X / l), & X \in (0,l); \end{cases} \tag{3.1}$$

where time τ is a non-negative variable, $\beta_0 = \kappa\sigma\varepsilon p / KA$ in wich K is relative thermal diffusivity constant and A stands for radiation area, and based on physical considerations, T is assumed to be nonnegative.

Work Example 2: (Involves heat conduction and heat radiation)

Using the following dimensionless variables

$$\begin{aligned} &u = T / T_0, \quad x = X / l, \quad t = \kappa\tau / l^2, \\ &\beta = T_0^3 l^2 \sigma\varepsilon p / KA, \quad u_\infty = T_\infty / T_0, \end{aligned} \tag{3.2}$$

where $T_0 > 0$ is taken as constant, problem (3.1) can be rewritten in dimensionless form as follows (P. M. Jordan, 2003; W. Dai & S. Su, 2004):

$$\begin{cases} u_t = u_{xx} - \beta(u^4 - u_\infty^4), & (x,t) \in (0,1) \times (0,\infty); \\ u(0,t) = U_1, \quad u(1,t) = U_2, & t > 0; \\ u(x,0) = \sin \pi x, & x \in (0,1); \end{cases} \tag{3.3}$$

where U_1 and U_2 are the dimensionless forms of T_1 and T_2, respectively.

3.2 Heat transfer in a finite thin rod with additional convection term

Problem (3.1) with additional convection term becomes:

$$\begin{cases} T_\tau = \kappa T_{XX} - \beta_0(T^4 - T_\infty^4) - \alpha_0(T - T_\infty), \ (X,\tau) \in (0,l) \times (0,\infty); \\ T(0,\tau) = T_1, \quad T(l,\tau) = T_2, \quad \tau > 0; \\ T(X,0) = T_0 \sin(\pi X / l), \quad X \in (0,l); \end{cases} \tag{3.4}$$

where τ the temporal is a non-negative variable, $\beta_0 = \kappa\sigma\varepsilon p / KA$, $\alpha_0 = \kappa hp / KA$, and based on physical considerations, T is assumed to be nonnegative.

Work Example 3: (Involve conduction, radiation and convection terms)

Using the following dimensionless variables,

$$\begin{aligned} u = T / T_0, \quad x = X / l, \quad t = \kappa\tau / l^2, \quad \beta = T_0^3 l^2 \sigma\varepsilon p / KA, \\ \alpha = l^2 hp / KA, \quad u_\infty = T_\infty / T_0, \end{aligned} \tag{3.5}$$

where $T_0 > 0$ is taken as constant, problem (3.4) can be rewritten in dimensionless form as follows:

$$\begin{cases} u_t = u_{xx} - \beta(u^4 - u_\infty^4) - \alpha(u - u_\infty), \ (x,t) \in (0,1) \times (0,\infty); \\ u(0,t) = U_1, \quad u(1,t) = U_2, \quad t > 0; \\ u(x,0) = \sin \pi x, \qquad x \in (0,1); \end{cases} \tag{3.6}$$

where U_1 and U_2 are the dimensionless forms of T_1 and T_2, respectively.
In the following we propose six nonstandard explicit and implicit schemes for problem (3.6).

Novel heat theory (Microscale)

Tzou (D. Y. Tzou, 1997) has shown that if the scale in one direction is at the microscale (of order 0.1 micrometer) then the heat flux and temperature gradient occur in this direction at different times. Thus the heat conduction equations used to describe the microstructure thermodynamic behavior are:

$$-\nabla . q + Q = \rho c_p \frac{\partial T}{\partial \tau} \text{ and } Q(r, \tau + \tau_Q) = -\kappa \nabla T(r, \tau + \tau_T),$$

where ρ, c_p and Q are density, a specific heat and a heat source, τ_Q and τ_T are the time lags of the heat flux and temperature gradient which are positive constants.
Now we can introduce (A. Malek & S. H. Momeni-Masuleh, 2008) the novel heat equation as:

$$\frac{\rho c_p}{\kappa}\left(\frac{\partial T}{\partial \tau} + \tau_q \frac{\partial^2 T}{\partial \tau^2}\right) = \nabla^2 T + \tau_q \left(\frac{\partial^3 T}{\partial \tau \partial x^2} + \frac{\partial^3 T}{\partial \tau \partial y^2}\right) + \tau_T \frac{\partial^3 T}{\partial \tau \partial z^2} + \frac{\left(Q + \tau_q \frac{\partial Q}{\partial \tau}\right)}{\kappa} \tag{3.7}$$

Malek and Momeni-Masuleh in years 2007 and 2008 used various hybrid spectral-FD methods to solve Eq. (3.7) efficiently. H. Heidari and A. Malek, studied null boundary controllability for hyperdiffusion equation in year 2009. Heidari, H. Zwart, and Malek, in year 2010 discussed

controllability and stability of the 3D novel heat conduction equation in a submicroscale thin film. In this Chapter we consider the heat theory for macroscale objects. Thus we do not consider the numerical solution for Eq. (3.7) that is out of the scope of this chapter.

4. Finite difference methods

4.1 Standard finite difference methods

In this section, we shall first consider two well known standard finite difference methods and their general discretization forms. Second, we shall introduce semi-discretization and fully discretization formulas. Third we will consider consistency, convergence and stability of the schemes. We will consider the nonlinear heat transfer problems in the next section during the study of nonstandard FD methods. This, as we shall see, leads to discovering some efficient algorithms that exists for corresponding class of nonlinear heat transfer problems.
Among the class of standard finite difference schemes, two important and richly studied subclasses are explicit and implicit approaches.

Notation

It is useful to introduce the following difference notation for the first derivative of a function u in the x direction at discrete point j throughout this Chapter.

$$(\frac{\partial u}{\partial x})_j = \frac{u_{j+1} - u_j}{\Delta x} \qquad \textit{Forward Finite Difference}$$

$$(\frac{\partial u}{\partial x})_j = \frac{u_j - u_{j-1}}{\Delta x} \qquad \textit{Backward Finite Difference}$$

$$(\frac{\partial u}{\partial x})_j = \frac{u_{j+1/2} - u_{j-1/2}}{\Delta x} \qquad \textit{Central Finite Difference}$$

The equation $\frac{\partial u}{\partial t} = \frac{\partial^2 u}{\partial x^2}$ may be approximated at the point $(i\Delta x, j\Delta t)$ by the difference equation:

$$\frac{u_{i,j+1} - u_{i,j}}{\Delta t} = \frac{\theta(u_{i+1,j+1} - 2u_{i,j+1} + u_{i-1,j+1}) + (1-\theta)(u_{i+1,j} - 2u_{i,j} + u_{i-1,j})}{(\Delta x)^2},$$

for $0 \le \theta \le 1$, where $u_{i,j} = u(i\Delta x, j\Delta t)$ for $i = 1,...N$ and $j = 1,...,J$ in the $x-t$ plane. Note that $\theta = 0$ gives the explicit scheme and $\theta = 1/2$ represents the Crank-Nicolson method that is one of the famous implicit FD schemes.

4.1.1 Explicit standard FD scheme ($\theta = 0$)

We calculate an explicit standard finite difference solution of the problem given in Work Example 1 for both Cases I and II, where the closed analytical form solutions are

$$U = \frac{8}{\pi^2}\sum_{n=0}^{\infty}\frac{1}{n^2}(\sin\frac{1}{2}n\pi)(\sin n\pi x)e^{-n^2\pi^2 t} \text{ and } U = e^{-\pi^2 t}\sin\pi x \text{ respectively.}$$

Figs. 1, 2, 3 and 4 display the power of both numerical schemes (Explicit and Crank-Nicolson) for the calculation of the solution for problems given in Work Example 1.

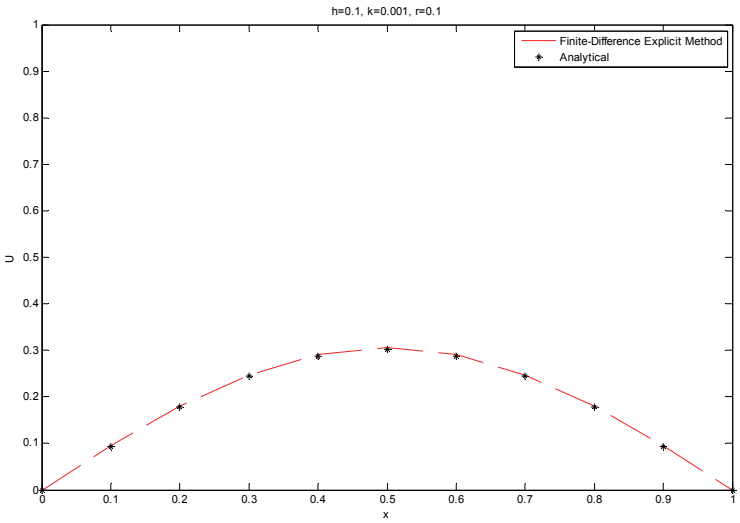

Fig. 1. Standard explicit FD solution of Work Example 1, Case I.

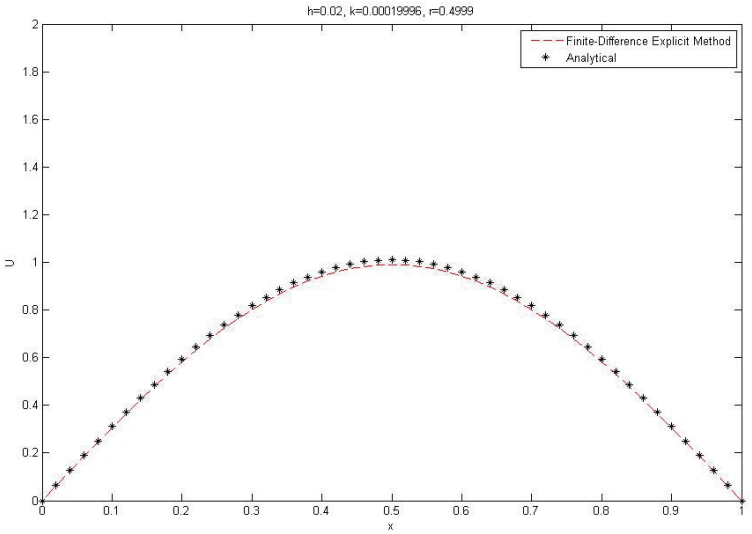

Fig. 2. Standard explicit FD solution of Work Example 1, Case II.

4.1.2 Crank-Nicolson standard FD scheme ($\theta = 1/2$)

We calculate a Crank-Nicolson implicit solution of the problem given in Work Example 1 for Case I and Case II.

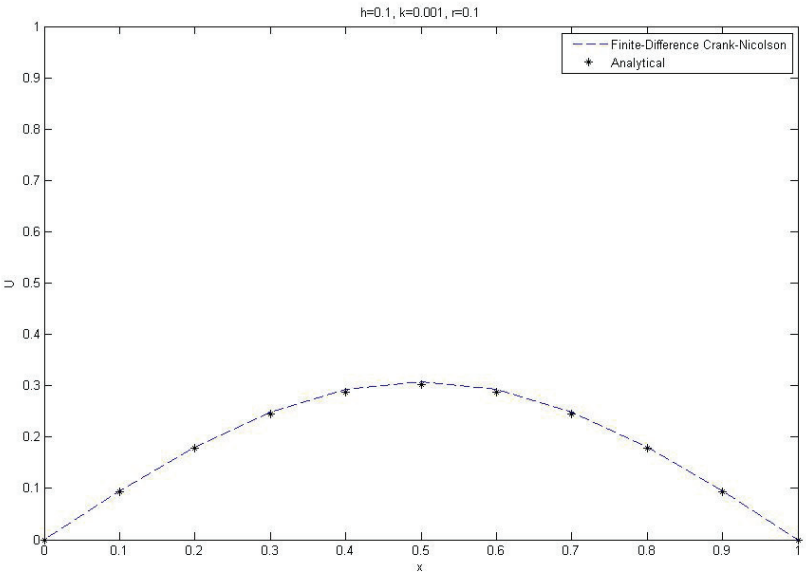

Fig. 3. Crank-Nicolson implicit FD solution for Work Example 1, Case I.

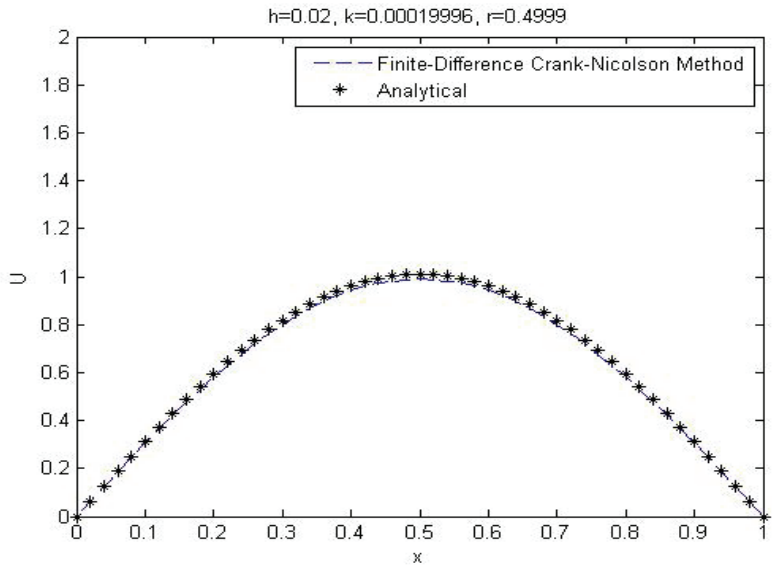

Fig. 4. Crank-Nicolson implicit FD solution of Work Example 1, Case II.

Up to this point most of our discussion has dealt with standard finite difference methods for solving differential equations. We have considered linear equations for which there is a well-designed and extensive theory. Some simple diffusion problems without nonlinear

terms were considered in Section 4.1. Now we must face the fact that it is usually very difficult, if not impossible, to find a solution of a given differential equation in a reasonably suitable and unambiguous form, especially if it involves the nonlinear terms. Therefore, it is important to consider what qualitative information can be obtained about the solutions of differential equation, particularly nonlinear terms, without actually solving the equations.

4.2 Nonstandard finite difference methods

Nonstandard finite difference methods for the numerical integration of nonlinear differential equations have been constructed for a wide range of nonlinear dynamical systems (P. M. Jordan, 2003; W. Dai & S. Su, 2004; H. S. Carslaw & J. C. Jaeger, 1959; R. Siegel & J. H. Howell, 1972; L. C. Burmeister, 1993). The basic rules and regulations to construct such schemes (R. E. Mickens, 1994), are:

Regulation 1. To do not face numerical instabilities, the orders of the discrete derivatives should be equal to the orders of the corresponding derivatives appearing in the differential equations.

Regulation 2. Discrete representations for derivatives must have nontrivial denominator functions.

Regulation 3. Nonlinear terms should be replaced by nonlocal discrete representations.

Regulation 4. Any particular properties that hold for the differential equation should also hold for the nonstandard finite difference scheme, otherwise numerical instability will happen.

Positivity, boundedness, existence of special solutions and monotonicity are some properties of particular importance in many engineering problems that usually model with differential equations. Regulation number four restricts one to force the nonstandard scheme satisfying properties of differential equation.

In the last two decays, several nonstandard finite difference schemes have been developed for solving nonlinear partial differential equations by Mickens and his co-authors. Particularly, Jordan and Dai considered a problem of one-dimensional unsteady heat conduction in a thin finite rod that is radiating heat across its lateral surface into a medium of constant temperature. The most fundamental modes of heat transfer are conduction and thermal radiation. In the former, physical contact is required for heat flow to occur and the heat flux is given by Fourier's heat law. In the latter, a body may lose or gain heat without the need of a transport medium, the transfer of heat taking place by means of electromagnetic waves or photons.

In the reminder of this Chapter, we consider twelve nonstandard implicit and explicit difference schemes for nonlinear heat transfer problems involving conductions and radiation with or without convection term. Specifically, we employ the highly successful nonstandard finite difference methods (A. Mohammadi, & A. Malek, 2009) to solve the nonlinear initial-boundary value problems in Work Examples 2 and 3 (see Section 3). We show that the third implicit schemes are unconditionally stable for large value of the equation parameters with or without convection term. It is observed that the rod reaches steady state sooner when it is exposed both to the radiation heat and convection.

4.1 Explicit nonstandard FD schemes

4.1.1 Nonstandard FD explicit schemes for Work Example 2

In Ref. (P. M. Jordan, 2003; W. Dai & S. Su, 2004), three nonstandard explicit finite difference schemes for Eq. (3.3) are developed as follows:

$$u_{i,j+1} = \frac{u_{i,j}(1-2r) + r(u_{i-1,j} + u_{i+1,j}) + \beta(\Delta t)u_\infty^4}{1 + \beta(\Delta t)(u_{i,j}^3)}, \tag{4.1}$$

$$u_{i,j+1} = \frac{u_{i,j}(1-2r) + r(u_{i-1,j} + u_{i+1,j}) + \beta(\Delta t)u_\infty^4}{1 + \beta(\Delta t)(u_{i-1,j}^3 + u_{i+1,j}^3)/2}, \tag{4.2}$$

and

$$u_{i,j+1} = \frac{u_{i,j}(1-2r) + r(u_{i-1,j} + u_{i+1,j}) + \beta(\Delta t)(u_{i,j}^2 + u_\infty^2)(u_{i,j} + u_\infty)u_\infty}{1 + \beta(\Delta t)(u_{i,j}^2 + u_\infty^2)(u_{i,j} + u_\infty)}, \tag{4.3}$$

where $r \equiv \Delta t / (\Delta x)^2$, and $u_{i,j} = u(i\Delta x, j\Delta t)$, Δx is the grid size and Δt is the time increment. While these three schemes differ in the way of dealing with the nonlinear terms, truncation errors for all of them are of the order $O\left[\Delta t + (\Delta x)^2\right]$.
Equation (4.3) has better stability property than Eq. (4.1) and (4.2), (for more details see A. Mohammadi, & A. Malek, 2009). This scheme satisfies the positivity condition, i.e., we can conclude that if $u_{i,j} > 0 \Rightarrow u_{i,j+1} > 0$, whenever $r \le \frac{1}{2}$. Moreover this scheme is stable for large values of the equation parameters comparing with the nonstandard schemes (4.1) and (4.2).

4.1.2 Nonstandard FD explicit schemes for Work Example 3

Three nonstandard explicit finite difference schemes are introduced (A. Mohammadi, & A. Malek, 2009) with additional convection heat transfer phenomenon as follows:

$$u_{i,j+1} = \frac{u_{i,j}(1-2r) + r(u_{i-1,j} + u_{i+1,j}) + \beta(\Delta t)u_\infty^4 + \alpha(\Delta t)u_\infty}{\left(1 + \beta(\Delta t)(u_{i,j}^3) + \alpha(\Delta t)\right)}, \tag{4.4}$$

$$u_{i,j+1} = \frac{u_{i,j}(1-2r) + r(u_{i-1,j} + u_{i+1,j}) + \beta(\Delta t)u_\infty^4 + \alpha(\Delta t)u_\infty}{\left(1 + \left(\beta(\Delta t)(u_{i-1,j}^3 + u_{i+1,j}^3)/2\right) + \alpha(\Delta t)\right)}, \tag{4.5}$$

and

$$\frac{u_{i,j}(1-2r) + r(u_{i-1,j} + u_{i+1,j}) + \beta(\Delta t)(u_{i,j}^2 + u_\infty^2)(u_{i,j} + u_\infty)u_\infty + \alpha(\Delta t)u_\infty}{\left(1 + \beta(\Delta t)(u_{i,j}^2 + u_\infty^2)(u_{i,j} + u_\infty) + \alpha(\Delta t)\right)}. \tag{4.6}$$

4.2 Implicit nonstandard FD schemes

4.2.1 Nonstandard FD implicit schemes for Work Example 2

Finite differencing methods can be employed to solve the system of equations and determine approximate temperatures at discrete time intervals and nodal points. Problem (3.3) is solved numerically using the non-standard Crank-Nicholson method. To provide accuracy, difference approximations are developed at the midpoint of the time increment.

A second derivative in space is evaluated by an average of two central difference equations, one evaluated at the present time increment j and the other at the future time increment j+1:

$$\frac{\partial^2 u}{\partial x^2} = \frac{1}{2}\left(\frac{u_{i-1,j+1} - 2u_{i,j+1} + u_{i+1,j+1}}{(\Delta x)^2} + \frac{u_{i-1,j} - 2u_{i,j} + u_{i+1,j}}{(\Delta x)^2} \right), \tag{4.7}$$

where j represents a temporal node and i represents a spatial node.
Making these substitutions into Eq. (3.3), gives

$$\frac{u_{i,j+1} - u_{i,j}}{\Delta t} = \frac{1}{2}\left(\frac{u_{i-1,j+1} - 2u_{i,j+1} + u_{i+1,j+1}}{(\Delta x)^2} + \frac{u_{i-1,j} - 2u_{i,j} + u_{i+1,j}}{(\Delta x)^2} \right) - \beta(u^4 - u_\infty^4). \tag{4.8}$$

Now define

$$\begin{aligned} &u^4 \to u_{i,j}^3 u_{i,j+1}, \quad u_{i,j}^3 \equiv (u_{i-1,j}^3 + u_{i+1,j}^3)/2, \\ &\beta(u^4 - u_\infty^4) \to \beta(u_{i,j}^2 + u_\infty^2)(u_{i,j} + u_\infty)(u_{i,j+1} - u_\infty). \end{aligned} \tag{4.9}$$

In this study, three nonstandard implicit finite difference schemes are developed as follows (A. Mohammadi, & A. Malek, 2009)

$$\begin{aligned} &-ru_{i-1,j+1} + \left(2 + 2r + \beta(\Delta t)u_{i,j}^3\right)u_{i,j+1} - ru_{i+1,j+1} = \\ &ru_{i-1,j} + (2 - 2r)u_{i,j} + ru_{i+1,j} + \beta(\Delta t)u_\infty^4 \ , \end{aligned} \tag{4.10}$$

$$\begin{aligned} &-ru_{i-1,j+1} + \left(2 + 2r + \beta(\Delta t)(u_{i-1,j}^3 + u_{i+1,j}^3)/2\right)u_{i,j+1} - ru_{i+1,j+1} = \\ &ru_{i-1,j} + (2 - 2r)u_{i,j} + ru_{i+1,j} + \beta(\Delta t)u_\infty^4 \ , \end{aligned} \tag{4.11}$$

and

$$\begin{aligned} &-ru_{i-1,j+1} + \left(2 + 2r + \beta(\Delta t)(u_{i,j}^2 + u_\infty^2)(u_{i,j} + u_\infty)\right)u_{i,j+1} - ru_{i+1,j+1} = \\ &ru_{i-1,j} + \left(2 - 2r + \beta(\Delta t)u_\infty(u_{i,j}^2 + u_\infty u_{i,j} + u_\infty^2)\right)u_{i,j} + ru_{i+1,j} + \beta(\Delta t)u_\infty^4 \ , \end{aligned} \tag{4.12}$$

where $t \to t_k = (\Delta t)k, \quad x \to x_m = (\Delta x)m.$ It can be seen that the truncation errors are of the order $O\left[(\Delta t)^2 + (\Delta x)^2\right]$. In the Section 4.3, we prove that the scheme (4.12) is stable.

4.2.2 Nonstandard FD implicit schemes for Work Example 3

Three nonstandard implicit finite difference schemes are proposed (A. Mohammadi, & A. Malek, 2009) with regard to convection heat transfer as follows:

$$\begin{aligned} &-ru_{i-1,j+1} + \left(2 + 2r + \beta(\Delta t)u_{i,j}^3 + \alpha(\Delta t)\right)u_{i,j+1} - ru_{i+1,j+1} = \\ &ru_{i-1,j} + (2 - 2r)u_{i,j} + ru_{i+1,j} + \beta(\Delta t)u_\infty^4 + \alpha(\Delta t)u_\infty \ , \end{aligned} \tag{4.13}$$

$$\begin{aligned} &-ru_{i-1,j+1} + \left(2 + 2r + \left(\beta(\Delta t)(u_{i-1,j}^3 + u_{i+1,j}^3)/2\right) + \alpha(\Delta t)\right)u_{i,j+1} - ru_{i+1,j+1} = \\ &ru_{i-1,j} + (2 - 2r)u_{i,j} + ru_{i+1,j} + \beta(\Delta t)u_\infty^4 + \alpha(\Delta t)u_\infty \ , \end{aligned} \tag{4.14}$$

and

$$\begin{aligned} &-ru_{i-1,j+1}+\left(2+2r+\beta(\Delta t)(u_{i,j}^2+u_\infty^2)(u_{i,j}+u_\infty)+\alpha(\Delta t)\right)u_{i,j+1}-ru_{i+1,j+1}= \\ &ru_{i-1,j}+\left(2-2r+\beta(\Delta t)u_\infty(u_{i,j}^2+u_\infty u_{i,j}+u_\infty^2)\right)u_{i,j}+ru_{i+1,j}+\beta(\Delta t)u_\infty^4+\alpha(\Delta t)u_\infty\ . \end{aligned} \tag{4.15}$$

4.3 Stability analysis for nonstandard FD implicit schems

The questions considered in this section are mainly associated with the idea of stability of a solution. In the simplest form it makes it clear that: is whether small changes in the initial conditions (inputs) lead to small changes (stability) or to large changes (instability) in the computed solution (output).

Consider the stability of the nonstandard implicit finite difference scheme (4.12) where the coefficients are constant values. If the boundary values at $i=0$ and N, for $j>0$, are known, these $(N-1)$ equations for $i=1\ ...\ N-1$ can be written in matrix form as

$$\begin{bmatrix} M & -r & & & & & \\ -r & M & -r & & & & \\ & \cdot & \cdot & \cdot & & & \\ & & \cdot & \cdot & \cdot & & \\ & & & \cdot & \cdot & \cdot & \\ & & & & -r & M & -r \\ & & & & & -r & M \end{bmatrix} \begin{bmatrix} u_{1,j+1} \\ u_{2,j+1} \\ \cdot \\ \cdot \\ \cdot \\ u_{N-2,j+1} \\ u_{N-1,j+1} \end{bmatrix} =$$

$$\begin{bmatrix} Q & r & & & & & \\ r & Q & r & & & & \\ & \cdot & \cdot & \cdot & & & \\ & & \cdot & \cdot & \cdot & & \\ & & & \cdot & \cdot & \cdot & \\ & & & & r & Q & r \\ & & & & & r & Q \end{bmatrix} \begin{bmatrix} u_{1,j} \\ u_{2,j} \\ \cdot \\ \cdot \\ \cdot \\ u_{N-2,j} \\ u_{N-1,j} \end{bmatrix} + \begin{bmatrix} \beta(\Delta t)u_\infty^4+ru_{0,j}-ru_{0,j+1} \\ \beta(\Delta t)u_\infty^4+0 \\ \cdot \\ \cdot \\ \cdot \\ \beta(\Delta t)u_\infty^4+0 \\ \beta(\Delta t)u_\infty^4+ru_{N,j}-ru_{N,j+1} \end{bmatrix}, \tag{4.16}$$

where

$$M=\left(2+2r+\beta(\Delta t)(u_{i,j}^2+u_\infty^2)(u_{i,j}+u_\infty)\right), \tag{4.17}$$

and

$$Q=\left(2-2r+\beta(\Delta t)u_\infty(u_{i,j}^2+u_\infty u_{i,j}+u_\infty^2)\right) \tag{4.18}$$

i.e. $\mathbf{Au}_{j+1}=\mathbf{Bu}_j+\mathbf{d}_j$, where the matrices $\mathbf{A}$ and $\mathbf{B}$ of order $(N-1)$ are as shown in (4.16), $\mathbf{u}_{j+1}$ denotes the column vector with components $u_{1,j+1},u_{2,j+1},...,u_{N-1,j+1}$, and $\mathbf{d}_j$ denotes the column vector of known boundary values and zeros. Hence,

$$\mathbf{u}_{j+1} = \mathbf{A}^{-1}\mathbf{B}\mathbf{u}_j + \mathbf{A}^{-1}\mathbf{d}_j, \tag{4.19}$$

that may be expressed more conveniently as

$$\mathbf{u}_{j+1} = \mathbf{C}\mathbf{u}_j + \mathbf{f}_j, \tag{4.20}$$

in which $\mathbf{C} = \mathbf{A}^{-1}\mathbf{B}$ and $\mathbf{f}_j = \mathbf{A}^{-1}\mathbf{d}_j$.

Theorem 4.1: For the scheme (4.12) norm of the error for j th time step is less than or equal to $\|\mathbf{C}\|^j \|\mathbf{e}_0\|$, where $\mathbf{e}_0$ is the error of the initial values.
Proof : Applying recursively from (4.20) leads to

$$\begin{aligned} \mathbf{u}_j &= \mathbf{C}\mathbf{u}_{j-1} + \mathbf{f}_{j-1} = \mathbf{C}(\mathbf{C}\mathbf{u}_{j-2} + \mathbf{f}_{j-2}) + \mathbf{f}_{j-1} = \\ &= \mathbf{C}^2\mathbf{u}_{j-2} + \mathbf{C}\mathbf{f}_{j-2} + \mathbf{f}_{j-1} = \\ &= \ldots \\ &= \mathbf{C}^j\mathbf{u}_0 + \mathbf{C}^{j-1}\mathbf{f}_0 + \mathbf{C}^{j-2}\mathbf{f}_1 + \ldots + \mathbf{f}_{j-1}. \end{aligned} \tag{4.21}$$

Perturb the vector of initial values u_0 to u_0^*. The exact solution at the j th time-row will then be

$$\mathbf{u}_j^* = \mathbf{C}^j\mathbf{u}_0^* + \mathbf{C}^{j-1}\mathbf{f}_0 + \mathbf{C}^{j-2}\mathbf{f}_1 + \ldots + \mathbf{f}_{j-1}. \tag{4.22}$$

If the perturbation or error vector $\mathbf{e}$ is defined by $\mathbf{e} = \mathbf{u}^* - \mathbf{u}$, it follows by Eqs. (4.21) and (4.22) that

$$\mathbf{e}_j = \mathbf{u}_j^* - \mathbf{u}_j = \mathbf{C}^j(\mathbf{u}_0^* - \mathbf{u}_0) = \mathbf{C}^j\mathbf{e}_0, \quad j = 1 \ldots J \tag{4.23}$$

Hence, for compatible matrix and vector norms,

$$\|\mathbf{e}_j\| \le \|\mathbf{C}^j\|\|\mathbf{e}_0\| \le \|\mathbf{C}\|^j\|\mathbf{e}_0\|. \tag{4.24}$$

Since the necessary and sufficient condition for the difference equations to be stable when the solution for the partial differential equation does not increase as t increases (J. D. Smith, 1985), is $\|\mathbf{C}\| \le 1$, in the following theorem we prove it for the scheme (4.12).
Theorem 4.2: The following three statements for the non-standard implicit scheme (4.12) satisfy

i. Matrix C in Eq. (4.20) is symmetric with real values.
ii. $\|\mathbf{C}\| < 1$
iii. The nonstandard implicit scheme (4.12) is unconditionally stable.

Proof (i) From matrix equation (4.16) it is obvious that matrix $\mathbf{C}$ is a real tridiagonal matrix. Since $\mathbf{A}$ and $\mathbf{B}$ are both symmetric and commute, matrix $\mathbf{C}$ is symmetric with real values, (J. D. Smith, 1985).
Proof (ii) Since matrix $\mathbf{C}$ is real and symmetric, $\|\mathbf{C}\|_2 = \rho(\mathbf{C}) = \max_s |\mu_s|$, therefore the scheme (4.12) will be stable when $\|\mathbf{C}\|_2 = \max_s |\mu_s| \le 1$, where μ_s, for $s = 1,\ldots,N$, are eigenvalues of the matrix $\mathbf{C}$. On the other hand the eigenvalues of matrix $\mathbf{C}$ are in the following form

$$\mu_s = \left(\frac{Q + 2r\cos s\pi/(N+1)}{M + 2r\cos s\pi/(N+1)} \right) \qquad s = 1,...,N. \tag{4.25}$$

Thus from (4.17) and (4.18) we have

$$\|\mathbf{C}\|_2 = \rho(\mathbf{C}) = \max_s \left| \frac{Q + 2r\cos s\pi/(N+1)}{M + 2r\cos s\pi/(N+1)} \right| < 1 \text{ for all } r > 0. \tag{4.26}$$

Now using Theorem 4.1, equation (4.24) leads to $\lim_{j\to\infty} \|\mathbf{e}_j\| \le \lim_{j\to\infty} \|\mathbf{C}\|^j \|\mathbf{e}_0\| = 0$. This proves statement (iii).

5. Numerical results

5.1 Numerical solutions for Work Example 2

Explicit and implicit schemes for equations (4.1)-(4.3), and (4.10)-(4.12) are numerically integrated. We computed and plotted the approximate solution to the problem (3.3), for $U_1 = U_2 = 0$ and various values of $\beta = u_\infty = 2$, $\beta = u_\infty = 6$, and $\beta = u_\infty = 20$, where $\Delta x = 0.02$ and $\Delta t = 1/5001$. We first chose $\beta = u_\infty = 2$, figures 5(a) and 6(a) show temperature profiles obtained based on three schemes for explicit models introduced by (P. M. Jordan, 2003; W. Dai & S. Su, 2004), and three schemes of this work, respectively. It can be seen from figure 6(a) that all of our schemes in figure 6(a) are stable while the scheme (1) in figure 5(a) of Ref. (P. M. Jordan, 2003; W. Dai & S. Su, 2004) is unstable.

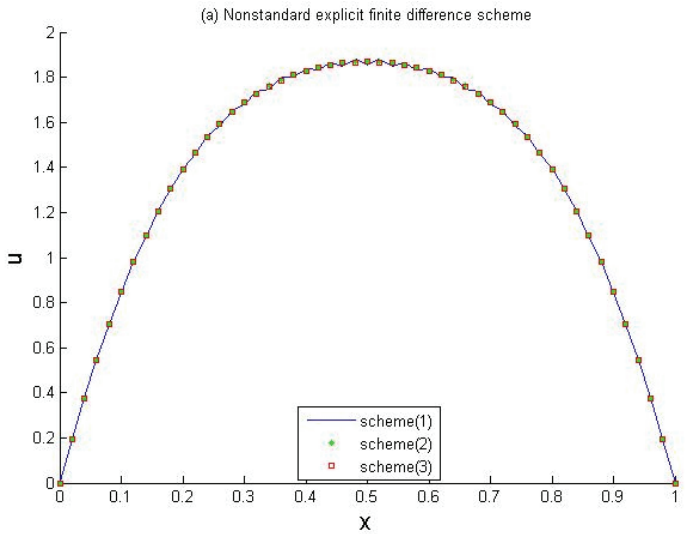

Fig. 5(a). For $\beta = u_\infty = 2$, scheme (1) There explicit nonstandard finite difference scheme given by Jordan (2003) is plotted in Eq. (4.1) is not stable, while schemes (2) and (3) given in Eqs. (4.2) and (4.3) are stable.

We then chose $\beta = u_\infty = 6$, and the results were plotted in figures 5(b), 5(c) and 6(b). The solution obtained based on Eq. (4.1) is not convergent as shown in figure 5(b), while the three implicit schemes of us are stable as shown in figure 6(b).

Finally, $\beta = u_\infty = 20$, it can be seen from figures 5(d) and 5(e) and figures 6(c) and 6(d) that neither of the solutions based on Eqs. (4.1), (4.2) and (4.10), (4.11) converge to the correct solution, while the schemes, in Eqs. (4.3) and (4.12) are still stable and convergent.

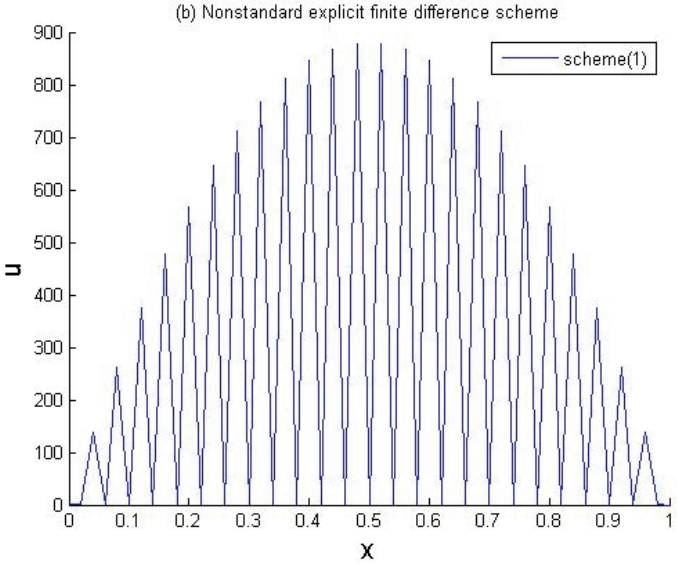

Fig. 5(b). For $\beta = u_\infty = 6$, scheme (1), given in Eq. (4.1), by Jordan (2003) does not converge.

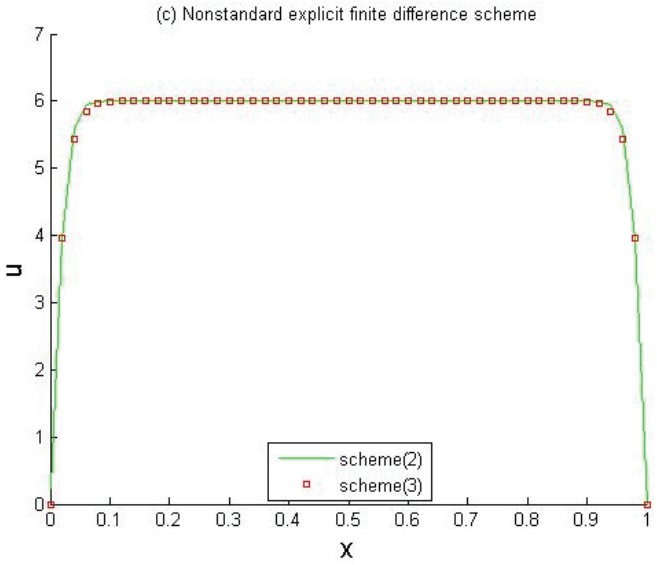

Fig. 5(c). For $\beta = u_\infty = 6$, schemes (2) and (3), given in Eqs. (4.2) and (4.3), converge to the correct solution.

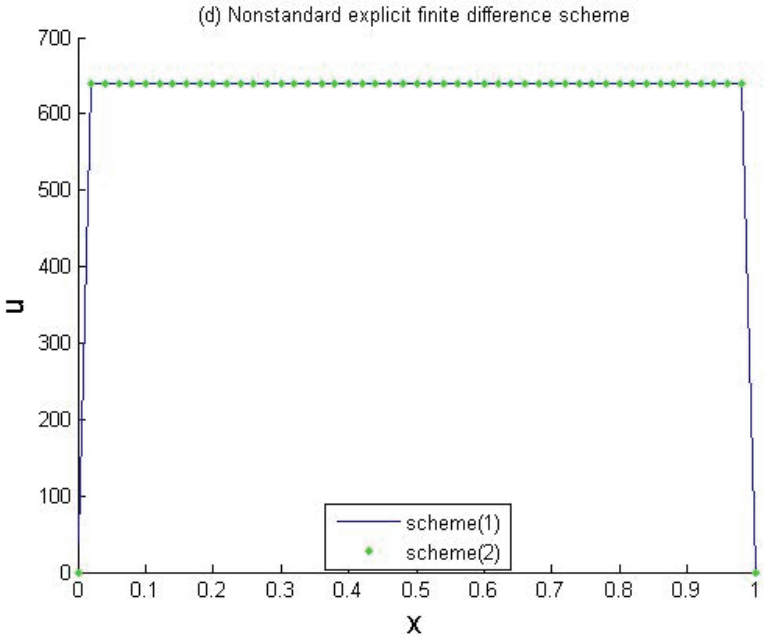

Fig. 5(d). For $\beta = u_\infty = 20$, schemes (1) and (2), given in Eqs. (4.1) and (4.2), converge but do not converge to the correct solution.

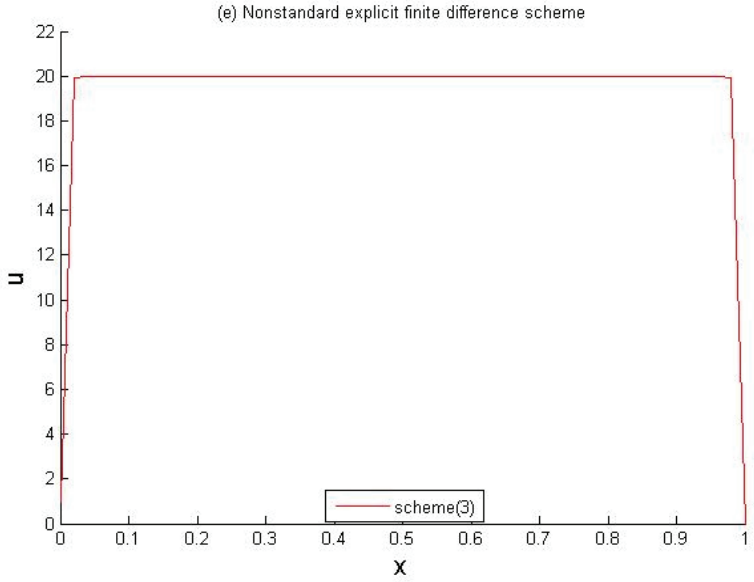

Fig. 5(e). For $\beta = u_\infty = 20$, scheme (3), given in Eq. (4.3), converge to the correct solution.

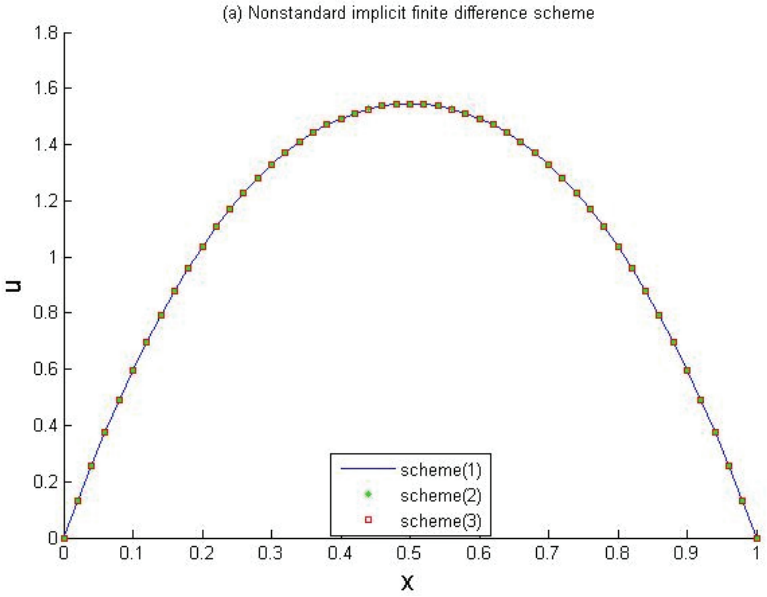

Fig. 6(a). For $\beta = u_\infty = 2,$ three schemes given by Eqs. (4.10), (4.11) and (4.12) converge to the correct solution.

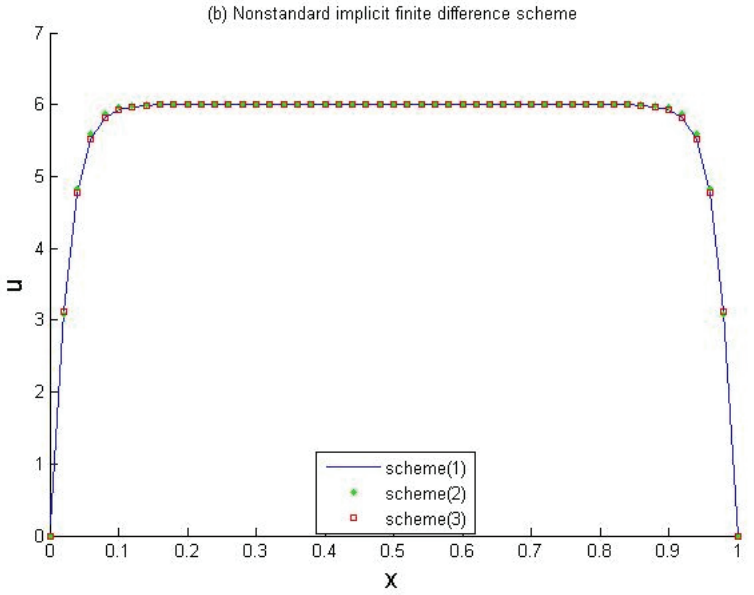

Fig. 6(b). For $\beta = u_\infty = 6,$ schemes (1), (2) and (3) based on Eqs. (4.10), (4.11) and (4.12), for Work Example 2 are shown. All of three implicit schemes are stable.

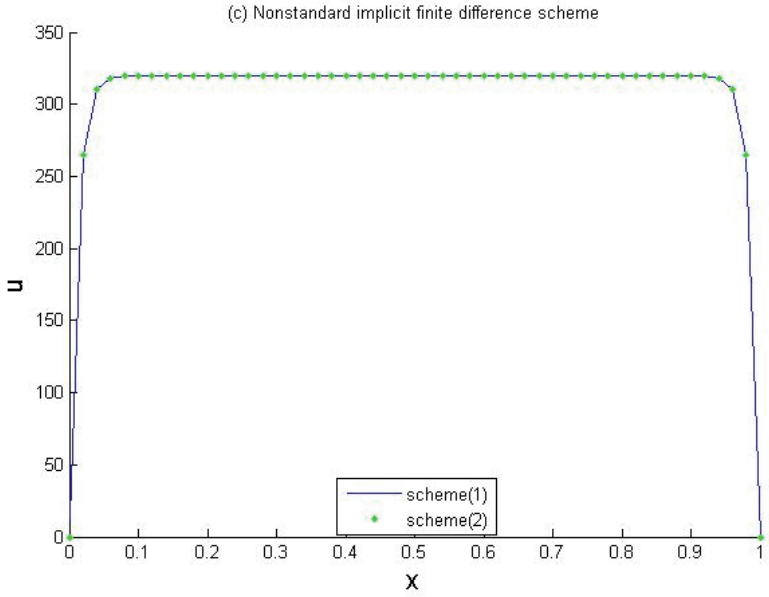

Fig. 6(c). For $\beta = u_\infty = 20$, schemes (1) and (2), given in Eqs. (4.10) and (4.11), converge but do not converge to the correct solution.

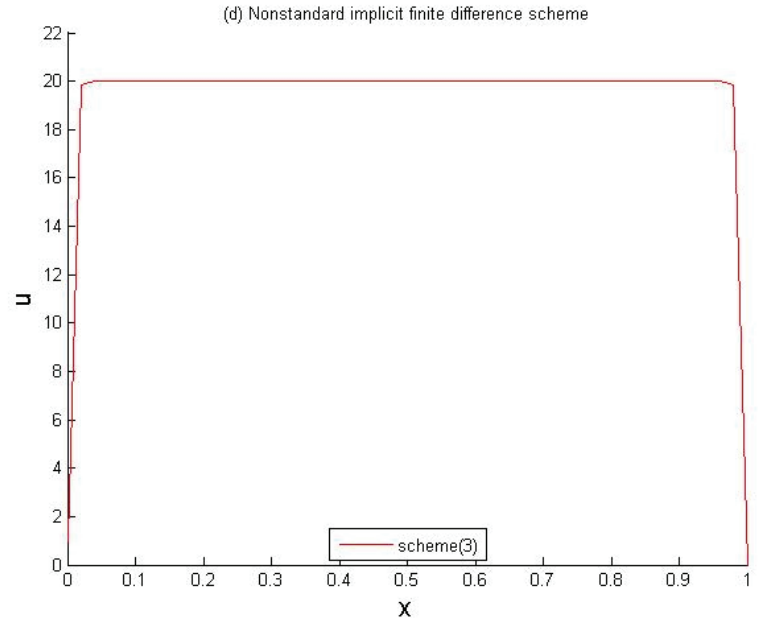

Fig. 6(d). For $\beta = u_\infty = 20$, scheme (3), given in Eq. (4.12) is stable and converges to the correct solution.

5.2 Numerical solutions for Work Example 3

The approximate solutions to the problem (3.6) are computed and plotted using the finite difference schemes given in Eqs. (4.4)-(4.6) and (4.13)-(4.15) for t =1, $U_1 = U_2 = 0$ with $\beta = u_\infty = 2$, in Work Example 2 and $\beta = u_\infty = 2$, $\alpha = 4$ in Work Example 3, where $\Delta x = 0.02$, $\Delta t = 1/5001$.

Figure 7(a) shows the temporal evolution of the temperature profiles corresponding to initial boundary value problem (3.3) and (3.6), for $\beta = u_\infty = 2$, and $\alpha = 4$, where numerical results for explicit schemes are plotted. It can be seen from figure 7(a) that the solution of problem without convection term in scheme (1) begun to oscillate, while all of the solution profiles for problem (3.6) are stable.

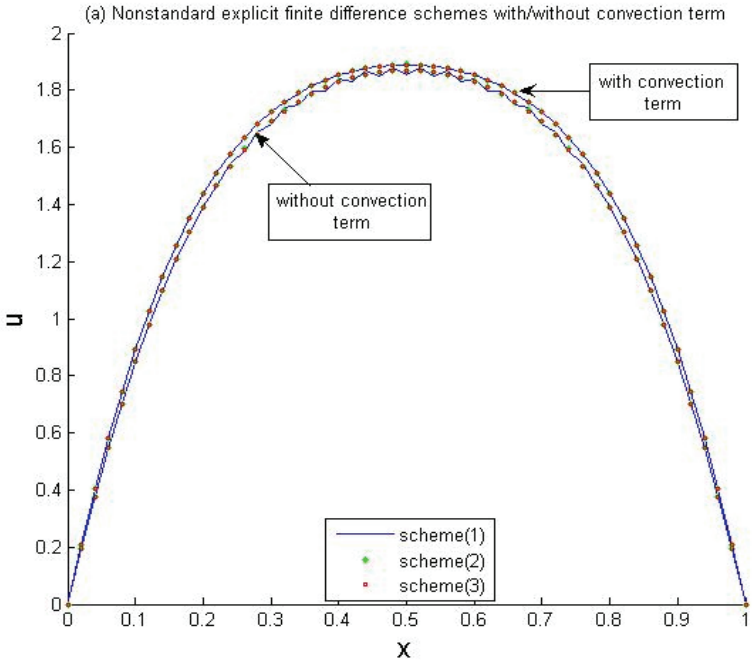

Fig. 7(a). For $\beta = u_\infty = 2$, plots of explicit schemes (1), (2) and (3) with convection term $(\alpha = 4)$ and without convection term are shown.

Figure 7(b) shows the temperature profiles corresponding to initial boundary value problem (3.3) and (3.6), for $\beta = u_\infty = 2$, $\alpha = 4$ where numerical results for implicit schemes are plotted. All the proposed schemes with/without convection terms are stable when implicit schemes are used.

Numerical results show that solution profile for implicit schemes are unconditionally stable for small values as well as the large values of the equation parameters. The theoretical stability analysis in Section 4.3 for implicit scheme (4.13) supports our numerical conclusions. The theoretical stability analysis for implicit schemes (4.14) and (4.15) may be done in the similar way. The convection term's effect is considered in Figs. 7(a) and 7(b) for explicit and implicit schemes respectively. It is shown that the schemes with convection term reach the steady state sooner.

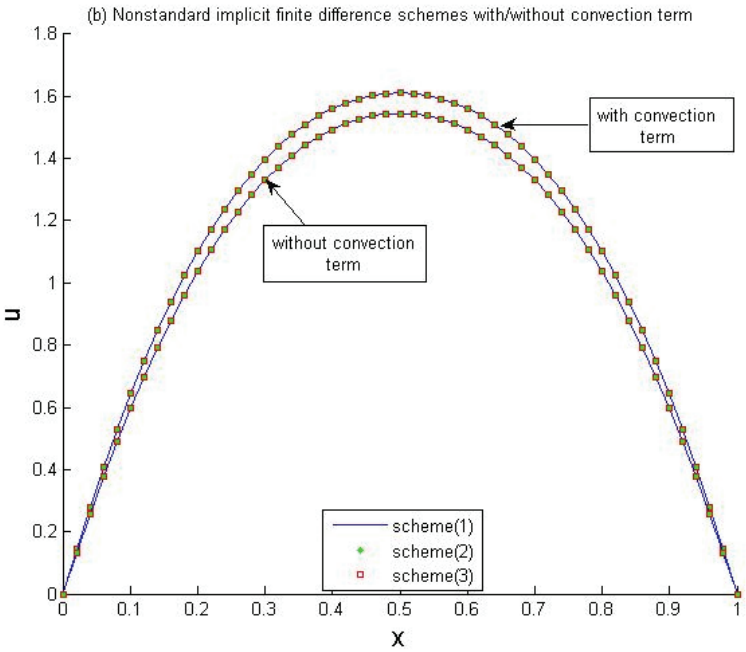

Fig. 7(b). For $\beta = u_\infty = 2,$ implicit schemes (1), (2) and (3) with convection term $(\alpha = 4)$ and without convection term is shown.

Our findings suggest that Regulation 4 is a serious property for a general nonstandard finite difference scheme because, otherwise it leads to instability. i.e. either the scheme does not converge or it converges to a wrong solution.

6. References

A. Malek, S. H. Momeni-Masuleh, A mixed collocation-finite difference method for 3D microscopic heat transport problems. J. Comput. Appl. Math. 217 (2008), no. 1, 137-147.

A. Mohammadi, A. Malek, Stable non-standard implicit finite difference schemes for non-linear heat transfer in a thin finite rod. J. Difference Equ. Appl. 15 (2009), no. 7, 719-728.

D. R. Croft, D. G. Lilly, Heat transfer calculations using finite difference equations. Applied Science Publishers, 1977.

D. Y. Tzou, Macro-To Micro-Scale Heat Transfer: The Lagging Behavior (Chemical and Mechanical Engineering Series). Taylor & Francis, 1997.

E. Battaner, Astrophysical Fluid Dynamics, Cambridge University Press, Cambridge, 1996.

G. Ben-Yu, Spectral Methods and Their Applications. World Scientific, 1998.

H. K. Versteeg, W. Malalasekera, An Introduction to Computational Fluid Dynamics: The Finite Volume Method. Addison-Wesley. 1996.

H. Heidari, A. Malek, Null boundary controllability for hyperdiffusion equation. Int. J. Appl. Math. 22 (2009), no. 4, 615-626.

H. Heidari; H. Zwart, A. Malek, Controllability and Stability of 3D Heat Conduction Equation in a Submicroscale Thin Film. Department of Applied Matematics, University of Twente, Netherlands, 2010, 1-21.

H. S. Carslaw and J. C. Jaeger, Conduction of Heat in Solids, 2nd Ed., Oxford University Press, New York, 1959.

J. C. Jaeger, Conduction of heat in a solid with a power law of heat transfer at its surface, Proc. Camb. Phil. Soc., 46 (1950), 634-641.

J. D. Smith, Numerical Solution of Partial Differential Equation, Clarendon Press, Oxford, 1985.

J. M. Bergheau, R. Fortunier, Finite Element Simulation of Heat Transfer. ISTE Ltd, 2010.

L. C. Burmeister, Convective Heat Transfer, 2nd Ed., Wiley, New York, 1993.

M. N. Ozisik, Boundary Value Problems of Heat Conduction, Dover, New York, 1989.

M. Necati Ozisik, M. Necati Czisik, Necati Ozisik. Finite Difference Methods in Heat Transfer, Crc Press, 1994.

O. P. Le Maitre, O. M. Knio, Spectral Methods for Uncertainty Quantification: With Applications to Computational Fluid Dynamics. Springer, 2010.

P. M. Jordan, A nonstandard finite difference scheme for a nonlinear heat transfer in a thin finite rod, J. Diff. Eqs. Appl., 9 (2003), 1015-1021.

R. E. Mickens, Nonstandard finite difference schemes for differential equations, J. Diff. Eqs. Appl., 8 (2002), 823-857.

R. E. Mickens, Nonstandard Finite Difference Models of Differential Equations. World Scientific, Singapore, 1994.

R. E. Mickens, Nonstandard finite difference schemes for reaction-diffusion equations, Numer Methods Partial Diff. Eqs. 15(1999), 201-214.

R. E. Mickens, and A.B Gumel, Construction and analysis of a nonstandard finite difference scheme for the Burgers-Fisher equation. J. Sound Vib. 257 (2002), 791-797.

R. E. Mickens, Advances in the applications of nonstandard finite difference schemes. World Scientific, London, 2005.

R. Siegel and J. H. Howell, Thermal Radiation Heat Transfer, McGraw-Hill, New York, 1972.

R. W. Lewis, P. Nithiarasu, K. N. Seetharamu, Fundamentals of the Finite Element Method for Heat and Fluid Flow, John Wiley & Sons Ltd, 2005.

S. H. Momeni-Masuleh, A. Malek, Hybrid pseudospectral-finite difference method for solving a 3D heat conduction equation in a submicroscale thin film. Numer. Methods Partial Differential Equations 23 (2007), no. 5, 1139-1148.

S. H. Momeni-Masuleh, A. Malek, Pseudospectral Methods for Thermodynamics of Thin Films at Nanoscale. African Physical Review, 2007, 35-36.

S. V. Patankar, Numerical Heat Transfer and Fluid Flow (Hemisphere Series on Computational Methods in Mechanics and Thermal Science). T & F / Routledge, 1980.

W. Dai and S. Su, "A nonstandard finite difference scheme for solving one dimensional nonlinear heat transfer," Journal of Difference Equations and Applications 10 (2004), 1025-1032.

9

Fast BEM Based Methods for Heat Transfer Simulation

Jure Ravnik and Leopold Škerget
University of Maribor, Faculty of Mechanical Engineering
Slovenia

1. Introduction

Development of numerical techniques for simulation of fluid flow and heat transfer has a long standing tradition. Computational fluid dynamics has evolved to a point where new methods are needed only for special cases. In this chapter we introduce a Fast Boundary Element Method (BEM), which enables accurate prediction of vorticity fields. Vorticity field is defined as a curl of the velocity field and is an important quantity in wall bounded flows. Vorticity is generated on the walls and diffused and advected into the flow field. Using BEM, we are able to accurately predict boundary values of vorticity as a part of the nonlinear system of equations, without the use of finite difference approximations of derivatives of the velocity field. The generation of vorticity on the walls is important for the development of the flow field, shear strain, shear velocity and heat transfer.
The developed method will be used to simulate natural convection of pure fluids and nanofluids. Over the last few decades buoyancy driven flows have been widely investigated. Cavities under different inclination angles with respect to gravity, heated either differentially on two opposite sides or via a hotstrip in the centre, are usually the target of research. Natural convection is used in many industrial applications, such as cooling of electronic circuitry, nuclear reactor insulation and ventilation of rooms.
Research of the natural convection phenomena started with the two-dimensional approach and has been recently extended to three dimensions. A benchmark solution for two-dimensional flow and heat transfer of an incompressible fluid in a square differentially heated cavity was presented by Davies (1983). Stream function-vorticity formulation was used. Vierendeels et al. (2001; 2004) and Škerget & Samec (2005) simulated compressible fluid in a square differentially heated cavity using multigrid and BEM methods. Rayleigh numbers between $Ra = 10^2$ and $Ra = 10^7$ were considered. Weisman et al. (2001) studied the transition from steady to unsteady flow for compressible fluid in a $1:4$ cavity. They found that the transition occurs at $Ra \approx 2 \times 10^5$. Ingber (2003) used the vorticity formulation to simulate flow in both square and $1:8$ differentially heated cavities. Tric et al. (2000) studied natural convection in a 3D cubic cavity using a pseudo-spectra Chebyshev algorithm based on the projection-diffusion method with spatial resolution supplied by polynomial expansions. Lo et al. (2007) also studied a 3D cubic cavity under five different inclinations $\vartheta = 0^o, 15^o, 30^o, 45^o, 60^o$. They used a differential quadrature method to solve the velocity-vorticity formulation of Navier-Stokes equations employing higher order polynomials to approximate differential operators. Ravnik et al. (2008) used a combination of single domain and sub domain BEM to solve the velocity-vorticity formulation of Navier-Stokes equations for fluid

flow and heat transfer.
Simulations as well as experiments of turbulent flow were also extensively investigated. Hsieh & Lien (2004) considered numerical modelling of buoyancy-driven turbulent flows in cavities using RANS approach. 2D DNS was performed by Xin & Quéré (1995) for an cavity with aspect ratio 4 up to Rayleigh number, based on the cavity height, 10^{10} using expansions in series of Chebyshev polynomials. Ravnik et al. (2006) confirmed these results using a 2D LES model based on combination of BEM and FEM using the classical Smagorinsky model with Van Driest damping. Peng & Davidson (2001) performed a LES study of turbulent buoyant flow in a $1:1$ cavity at $Ra = 1.59 \cdot 10^9$ using a dynamic Smagorinsky model as well as the classical Smagorinsky model with Van Driest damping.
Low thermal conductivity of working fluids such as water, oil or ethylene glycol led to the introduction of nanofluids. Nanofluid is a suspension consisting of uniformly dispersed and suspended nanometre-sized (10–50 *nm*) particles in base fluid, pioneered by Choi (1995). Nanofluids have very high thermal conductivities at very low nanoparticle concentrations and exhibit considerable enhancement of convection (Yang et al., 2005). Intensive research in the field of nanofluids started only recently. A wide variety of experimental and theoretical investigations have been performed, as well as several nanofluid preparation techniques have been proposed (Wang & Mujumdar, 2007).
Several researchers have been focusing on buoyant flow of nanofluids. Oztop & Abu-Nada (2008) performed a 2D study of natural convection of various nanofluids in partially heated rectangular cavities, reporting that the type of nanofluid is a key factor for heat transfer enhancement. They obtained best results with Cu nanoparticles. The same researchers (Abu-Nada & Oztop, 2009) examined the effects of inclination angle on natural convection in cavities filled with Cu–water nanofluid. They reported that the effect of nanofluid on heat enhancement is more pronounced at low Rayleigh numbers. Hwang et al. (2007) studied natural convection of a water based Al_2O_3 nanofluid in a rectangular cavity heated from below. They investigated convective instability of the flow and heat transfer and reported that the natural convection of a nanofluid becomes more stable when the volume fraction of nanoparticles increases. Ho et al. (2008) studied effects on nanofluid heat transfer due to uncertainties of viscosity and thermal conductivity in a buoyant cavity. They demonstrated that usage of different models for viscosity and thermal conductivity does indeed have a significant impact on heat transfer. Natural convection of nanofluids in an inclined differentially heated square cavity was studied by Ögüt (2009), using polynomial differential quadrature method. Stream function-vorticity formulation was used for simulation of nanofluids in two dimensions by Gümgüm & Tezer-Sezgin (2010).
Forced and mixed convection studies were also performed. Abu-Nada (2008) studied the application of nanofluids for heat transfer enhancement of separated flows encountered in a backward facing step. He found that the high heat transfer inside the recirculation zone depends mainly on thermophysical properties of nanoparticles and that it is independent of Reynolds number. Mirmasoumi & Behzadmehr (2008) numerically studied the effect of nanoparticle mean diameter on mixed convection heat transfer of a nanofluid in a horizontal tube using a two-phase mixture model. They showed that the convective heat transfer could be significantly increased by using particles with smaller mean diameter. Akbarinia & Behzadmehr (2007) numerically studied laminar mixed convection of a nanofluid in horizontal curved tubes. Tiwari & Das (2007) studied heat transfer in a lid-driven differentially heated square cavity. They reported that the relationship between heat transfer and the volume fraction of solid particles in a nanofluid is nonlinear. Torii (2010) experimentally

studied turbulent heat transfer behaviour of nanofluid in a circular tube, heated under constant heat flux. He reported that the relative viscosity of nanofluids increases with concentration of nanoparticles, pressure loss of nanofluids is slightly larger than that of pure fluid and that heat transfer enhancement is affected by occurrence of particle aggregation.

Development of numerical algorithms capable of simulating fluid flow and heat transfer has a long standing tradition. A vast variety of methods was developed and their characteristics were examined. In this work we are presenting an algorithm, which is able to simulate 3D laminar viscous flow coupled with heat transfer by solving the velocity-vorticity formulation of Navier-Stokes equations using fast BEM. The velocity-vorticity formulation is an alternative form of the Navier-Stokes equation, which does not include pressure. The unknown field functions are the velocity and vorticity. In an incompressible flow, both are divergence free. Daube (1992) pointed out that the correct evaluation of boundary vorticity values is essential for conservation of mass. Thus, the main challenge of velocity-vorticity formulation lies in the determination of boundary vorticity values. Several different approaches have been proposed for the determination of vorticity on the boundary. Wong & Baker (2002) used a second-order Taylor series to determine the boundary vorticity values explicitly. Daube (1992) used an influence matrix technique to enforce both the continuity equation and the definition of the vorticity in the treatment of the 2D incompressible Navier-Stokes equations. Liu (2001) recognised that the problem is even more severe when he extended it to three dimensions. Lo et al. (2007) used the differential quadrature method. Sellountos & Sequeira (2008) proposed a hybrid multi BEM scheme in combination with local boundary integral equations and radial basis functions for 2D fluid flow. Škerget et al. (2003) proposed the usage of single domain BEM to obtain a solution of the kinematics equation in tangential form for the unknown boundary vorticity values and used it in 2D. This work was extended into 3D using a linear interpolation in combination with FEM by Žunič et al. (2007) and using quadratic interpolation by Ravnik et al. (2009a) for uncoupled flow problems.

The BEM uses the fundamental solution of the differential operator and the Green's theorem to rewrite a partial differential equation into an equivalent boundary integral equation. After discretization of only the boundary of the problem domain, a fully populated system of equations emerges. The number of degrees of freedom is equal to the number of boundary nodes. This reduction of the dimensionality of the problem is a major advantage over the volume based methods. Fundamental solutions are known for a wide variety of differential operators (Wrobel, 2002), making BEM applicable for solving a wide range of problems.

Unfortunately, integral equations of nonhomogeneous and nonlinear problems, such as heat transfer in fluid flow, include a domain term. In this work, we solve the velocity-vorticity formulation of incompressible Navier-Stokes equations. The formulation joins the Poisson type kinematics equation with diffusion advection type equations of vorticity and heat transport. These equations are nonhomogenous and nonlinear. In order to write discrete systems of linear equations for such equations, matrices of domain integrals must be evaluated. Such domain matrices, since they are full and unsymmetrical, require a lot of storage space and algebraic operations with them require a lot of CPU time. Thus the domain matrices present a bottleneck for any BEM based algorithm effectively limiting the maximal usable mesh size through their cost in storage and CPU time.

The dual reciprocity BEM (Partridge et al. (1992), Jumarhon et al. (1997)) is one of the most popular techniques to eliminate the domain integrals. It uses expansion of the nonhomogenous term in terms of radial basis functions. Several other approaches that enable construction of data sparse approximations of fully populated matrices are also

known. Hackbusch & Nowak (1989) developed a panel clustering method, which also enables approximate matrix vector multiplications with decreased amount of arithmetical work. A class of hierarchical matrices was introduced by Hackbusch (1999) with the aim of reducing the complexity of matrix-vector multiplications. Bebendorf & Rjasanow (2003) developed an algebraic approach for solving integral equations using collocation methods with almost linear complexity. Methods based on the expansion of the integral kernel (Bebendorf, 2000) have been proposed as well. Fata (2010) proposed treatment of domain integrals by rewriting them as a combination of surface integrals whose kernels are line integrals. Ravnik et al. (2004) developed a wavelet compression method and used it for compression of single domain BEM in 2D. Compression of single domain full matrices has also been the subject of research of Eppler & Harbrecht (2005).

The algorithm proposed in this chapter tackles the domain integral problem using two techniques: a kernel expansion method based single domain BEM is employed for fast solution of the kinematics equation and subdomain BEM is used for diffusion-advection type equations.

In the subdomain BEM (Popov et al., 2007), integral equations are written for each subdomain (mesh element) separately. We use continuous quadratic boundary elements for the discretization of function and discontinuous linear boundary element for the discretization of flux. By the use of discontinuous discretization of flux, all flux nodes are within boundary elements where the normal and the flux are unambiguously defined. The corners and edges, where the normal is not well defined, are avoided. The singularities of corners and edges were dealt with special singular shape functions by Ong & Lim (2005) and by the use of additional nodes by Gao & Davies (2000). By the use of a collocation scheme, a single linear equation is written for every function and flux node in every boundary element. By using compatibility conditions between subdomains, we obtain an over-determined system of linear equations, which may be solved in a least squares manner. The governing matrices are sparse and have similar storage requirements as the finite element method. Subdomain BEM was applied on the Laplace equation by Ramšak & Škerget (2007) and on the velocity-vorticity formulation of Navier-Stokes equations by Ravnik et al. (2008; 2009a).

The second part of the algorithm uses fast kernel expansion based single domain BEM. The method is used to provide a sparse approximation of the fully populated BEM domain matrices. The storage requirements of the sparse approximations scale linearly with the number of nodes in the domain, which is a major improvement over the quadratic complexity of the full BEM matrices. The technique eliminates the storage and CPU time problems associated with application of BEM on nonhomogenous partial differential equations.

The origins of the method can be found in a fast multipole algorithm (FMM) for particle simulations developed by Greengard & Rokhlin (1987). The algorithm decreases the amount of work required to evaluate mutual interaction of particles by reducing the complexity of the problem from quadratic to linear. Ever since, the method was used by many authors for a wide variety of problems using different expansion strategies. Recently, Bui et al. (2006) combined FMM with the Fourier transform to study multiple bubbles dynamics. Gumerov & Duraiswami (2006) applied the FMM for the biharmonic equation in three dimensions. The boundary integral Laplace equation was accelerated with FMM by Popov et al. (2003). In contrast to the contribution of this paper, where the subject of study is the application of FMM to obtain a sparse approximation of the domain matrix, the majority of work done by other authors dealt with coupling BEM with FMM for the boundary matrices. Ravnik et al. (2009b) compared wavelet and fast data sparse approximations for boundary - domain

integral equations of Poisson type.

2. Governing equations

In this work, we will present a numerical algorithm and simulation results for heat transfer in pure fluids and in nanofluids. We present the governing equations for nanofluids, since they can be, by choosing the correct parameter values, used for pure fluids as well. We assume the pure fluid and nanofluid to be incompressible. Flow in our simulations is laminar and steady. Effective properties of the nanofluid are: density ρ_{nf}, dynamic viscosity μ_{nf}, heat capacitance $(c_p)_{nf}$, thermal expansion coefficient β_{nf} and thermal conductivity k_{nf}, where subscript nf is used to denote effective i.e. nanofluid properties. The properties are all assumed constant throughout the flow domain. The mass conservation law for an incompressible fluid may be stated as

$$\vec{\nabla} \cdot \vec{v} = 0. \tag{1}$$

Considering constant nanofluid material properties and taking density variation into account within the Boussinesq approximation we write the momentum equation as

$$\frac{\partial \vec{v}}{\partial t} + (\vec{v} \cdot \vec{\nabla})\vec{v} = -\beta_{nf}(T - T_0)\vec{g} - \frac{1}{\rho_{nf}}\vec{\nabla} p + \frac{\mu_{nf}}{\rho_{nf}}\nabla^2 \vec{v}. \tag{2}$$

We assume that no internal energy sources are present in the fluid. We will not deal with high velocity flow of highly viscous fluid, hence we will neglect irreversible viscous dissipation. With this, the internal energy conservation law, written with temperature as the unknown variable, reads as:

$$\frac{\partial T}{\partial t} + (\vec{v} \cdot \vec{\nabla})T = \frac{k_{nf}}{(\rho c_p)_{nf}}\nabla^2 T. \tag{3}$$

Relationships between properties of nanofluid to those of pure fluid and pure solid are provided with the models. Density of the nanofluid is calculated using particle volume fraction φ and densities of pure fluid ρ_f and of solid nanoparticles ρ_s as:

$$\rho_{nf} = (1 - \varphi)\rho_f + \varphi\rho_s \tag{4}$$

The effective dynamic viscosity of a fluid of dynamic viscosity μ_f containing a dilute suspension of small rigid spherical particles, is given by Brinkman (1952) as

$$\mu_{nf} = \frac{\mu_f}{(1 - \varphi)^{2.5}}. \tag{5}$$

The effective viscosity is independent of nanoparticle type, thus the differences in heat transfer between different nanofluids will be caused by heat related physical parameters only. The heat capacitance of the nanofluid can be expressed as (Khanafer et al., 2003):

$$(\rho c_p)_{nf} = (1 - \varphi)(\rho c_p)_f + \varphi(\rho c_p)_s. \tag{6}$$

Similarly, the nanofluid thermal expansion coefficient can be written as $(\rho\beta)_{nf} = (1 - \varphi)(\rho\beta)_f + \varphi(\rho\beta)_s$, which may be, by taking into account the definition of ρ_{nf} in equation (4), written as:

$$\beta_{nf} = \beta_f \left[\frac{1}{1 + \frac{(1-\varphi)\rho_f}{\varphi\rho_s}} \frac{\beta_s}{\beta_f} + \frac{1}{1 + \frac{\varphi}{1-\varphi}\frac{\rho_s}{\rho_f}} \right]. \tag{7}$$

The effective thermal conductivity of the nanofluid is approximated by the Maxwell-Garnett formula

$$k_{nf} = k_f \frac{k_s + 2k_f - 2\varphi(k_f - k_s)}{k_s + 2k_f + \varphi(k_f - k_s)}. \tag{8}$$

This formula is valid only for spherical particles (Shukla & Dhir, 2005), since it does not take into account the shape of particles. Our macroscopic modelling of nanofluids is restricted to spherical nanoparticles and it is suitable for small temperature gradients.

2.1 Nondimensional equations in velocity-vorticity form

Vorticity, $\vec{\omega}$, is defined as a curl of velocity. By taking the curl of the mass conservation law (1) and of the momentum transport equation (2) and taking into account that by definition vorticity is solenodial, $\vec{\nabla} \cdot \vec{\omega} = 0$, we derive the velocity-vorticity formulation of Navier-Stokes equations. The equations are rewritten into nondimensional form using

$$\vec{v} \to \frac{\vec{v}}{v_0}, \vec{r} \to \frac{\vec{r}}{L}, \omega \to \frac{\omega L}{v_0}, t \to \frac{v_0 t}{L}, T \to \frac{T - T_0}{\Delta T}, \vec{g} \to \frac{\vec{g}}{g_0}, v_0 = \frac{k_f}{(\rho c_p)_f L}, \tag{9}$$

where T_0 and L are characteristic temperature and length scale. Characteristic temperature difference is ΔT, while $g_0 = 9.81 m/s^2$. We define pure fluid Rayleigh and Prandtl number values as

$$Ra = \frac{g_0 \beta_f \Delta T L^3 \rho_f (\rho c_p)_f}{\mu_f k_f}, \qquad Pr = \frac{\mu_f c_p}{k_f}. \tag{10}$$

The choice for characteristic velocity v_0 in (9) is common for buoyant flow simulations. It ensures that the Reynolds number is eliminated for the governing equations, since its value multiplied by Prandtl number equals one. With this the nondimensional velocity-vorticity formulation of Navier-Stokes equations for simulation of nanofluids consists of the kinematics equation, the vorticity transport equation and the energy equation:

$$\nabla^2 \vec{v} + \vec{\nabla} \times \vec{\omega} = 0, \tag{11}$$

$$\frac{\partial \vec{\omega}}{\partial t} + (\vec{v} \cdot \vec{\nabla})\vec{\omega} = (\vec{\omega} \cdot \vec{\nabla})\vec{v} + PrN_a \nabla^2 \vec{\omega} - PrRaN_b \vec{\nabla} \times T\vec{g}, \tag{12}$$

$$\frac{\partial T}{\partial t} + (\vec{v} \cdot \vec{\nabla})T = N_c \nabla^2 T, \tag{13}$$

$$N_a = \frac{\mu_{nf}}{\mu_f} \frac{\rho_f}{\rho_{nf}}, \qquad N_b = \frac{\beta_{nf}}{\beta_f}, \qquad N_c = \frac{k_{nf}}{k_f} \frac{(\rho c_p)_f}{(\rho c_p)_{nf}}. \tag{14}$$

The flow and heat transfer of a nanofluid is thus defined by specifying the pure fluid Rayleigh and Prandtl number values. The nanofluid properties are evaluated using the following models: ρ_{nf}/ρ_f from (4), μ_{nf}/μ_f from (5), $(\rho c_p)_{nf}/(\rho c_p)_f$ from (6), β_{nf}/β_f from (7) and k_{nf}/k_f from (8). The system of equations (11)-(13) can be used to simulate pure fluids by taking $N_a = N_b = N_c = 1$.

3. Numerical method

We will apply a combination of subdomain BEM and fast single domain BEM for the solution of the governing equations. The Dirichlet and/or Neumann boundary conditions for velocity and temperature are given. They are used to obtain solutions of the kinematics equation (11)

for domain velocity values and energy equation (13) for domain temperature values. The boundary conditions for vorticity, which are needed to solve the vorticity transport equation (12), are unknown. We will use the single domain BEM on the kinematics equation to obtain the unknown boundary vorticity values. The outline of the algorithm is as follows:

– initialization, calculate integrals
– begin nonlinear loop
  a) calculate boundary vorticity values by solving the kinematics equation (11) by fast single domain BEM (see section 3.4)
  a) calculate domain velocity values by solving the kinematics equation (11) by subdomain BEM (see section 3.3)
  a) solve the energy equation (3) using the new velocity field for domain temperature values by subdomain BEM (see section 3.2)
  a) solve vorticity transport equation (12) by subdomain BEM for domain vorticity values using the boundary values from the solution of the kinematics equation and new velocity and temperature fields (see section 3.1)
  a) check convergence - repeat steps in the nonlinear loop until convergence of all field functions is achieved
– end nonlinear loop

3.1 Subdomain BEM solution of the vorticity transport equation

Let us consider a domain Ω with a position vector $\vec{r} \in \mathbb{R}^3$. The boundary of the domain is $\Gamma = \partial\Omega$. In this work we are simulating steady flow fields, thus we may write $\partial\vec{\omega}/\partial t = 0$. The integral form of the steady vorticity transport equation (12) is (Wrobel, 2002):

$$c(\vec{\theta})\vec{\omega}(\vec{\theta}) + \int_\Gamma \vec{\omega}\vec{\nabla}u^\star \cdot \vec{n}d\Gamma = \int_\Gamma u^\star \vec{q}d\Gamma$$
$$+\frac{1}{PrN_a}\int_\Omega u^\star \left\{(\vec{v}\cdot\vec{\nabla})\vec{\omega} - (\vec{\omega}\cdot\vec{\nabla})\vec{v}\right\}d\Omega + Ra\frac{N_b}{N_a}\int_\Omega u^\star\vec{\nabla}\times T\vec{g}d\Omega, \tag{15}$$

where $\vec{\theta}$ is the source or collocation point, $\vec{n}$ is a vector normal to the boundary, pointing out of the domain and $u^\star$ is the fundamental solution for the diffusion operator:

$$u^\star = \frac{1}{4\pi|\vec{\theta} - \vec{r}|}. \tag{16}$$

$c(\vec{\theta})$ is the geometric factor defined as $c(\vec{\theta}) = \alpha/4\pi$, where α is the inner angle with origin in $\vec{\theta}$. If $\vec{\theta}$ lies inside of the domain then $c(\vec{\theta}) = 1$; $c(\vec{\theta}) = 1/2$, if $\vec{\theta}$ lies on a smooth boundary. Vorticity on the boundary $\vec{\omega}(\vec{r})$ or vorticity flux on the boundary $\vec{q}(\vec{r}) = \vec{\nabla}\vec{\omega}(\vec{r})\cdot\vec{n}$ can be prescribed as boundary conditions.

Both domain integrals on the right hand side of equation (15) include derivatives of the unknown field functions. In the following we will use algebraic relations to move the derivative from the unknown field function to the fundamental solution. Let us first write the first domain integral alone for j^{th} component of vorticity only:

$$\frac{1}{PrN_a}\int_\Omega \left\{(\vec{v}\cdot\vec{\nabla})\omega_j - (\vec{\omega}\cdot\vec{\nabla})v_j\right\}u^\star\Omega. \tag{17}$$

Due to the solenoidality of the velocity and vorticity fields, we may use $(\vec{\omega}\cdot\vec{\nabla})v_j = \vec{\nabla}\cdot(\vec{\omega}v_j)$ and $(\vec{v}\cdot\vec{\nabla})\omega_j = \vec{\nabla}\cdot(\vec{v}\omega_j)$ to transform eqaution (17) into

$$\frac{1}{PrN_a}\int_\Omega \left\{\vec{\nabla}\cdot(\vec{v}\omega_j - \vec{\omega}v_j)\right\} u^\star d\Omega. \tag{18}$$

In order to move the derivative towards the fundamental solution, the following algebraic relation $\vec{\nabla}\cdot\left\{u^*(\vec{v}\omega_j - \vec{\omega}v_j)\right\} = u^*\vec{\nabla}\cdot(\vec{v}\omega_j - \vec{\omega}v_j) + (\vec{v}\omega_j - \vec{\omega}v_j)\cdot\vec{\nabla}u^*$ is used to obtain two integrals

$$\frac{1}{PrN_a}\int_\Omega \vec{\nabla}\cdot\left\{u^*(\vec{v}\omega_j - \vec{\omega}v_j)\right\} d\Omega - \frac{1}{PrN_a}\int_\Omega (\vec{v}\omega_j - \vec{\omega}v_j)\cdot\vec{\nabla}u^\star d\Omega. \tag{19}$$

The first integral may be converted to a boundary integral using a Gauss divergence clause. Thus, the final form of the first domain integral of equation (15) for j^{th} vorticity component without derivatives of field functions may be stated as:

$$\frac{1}{PrN_a}\int_\Gamma \vec{n}\cdot\left\{u^*(\vec{v}\omega_j - \vec{\omega}v_j)\right\} d\Gamma - \frac{1}{PrN_a}\int_\Omega (\vec{v}\omega_j - \vec{\omega}v_j)\cdot\vec{\nabla}u^* d\Omega. \tag{20}$$

In order to remove the derivative of temperature from the second domain integral of equation (15), we make use of the following algebraic relation: $\vec{\nabla}\times(u^\star T\vec{g}) = u^\star\vec{\nabla}\times T\vec{g} + T\vec{\nabla}\times u^\star\vec{g}$, which gives

$$+ Ra\frac{N_b}{N_a}\int_\Omega \vec{\nabla}\times(u^\star T\vec{g})d\Omega - Ra\frac{N_b}{N_a}\int_\Omega T\vec{\nabla}\times u^\star\vec{g}d\Omega. \tag{21}$$

With the aid of the Gauss clause we are able to transform the first domain integral of equation (21) into a boundary integral:

$$- Ra\frac{N_b}{N_a}\int_\Gamma u^\star T\vec{g}\times\vec{n}d\Gamma - Ra\frac{N_b}{N_a}\int_\Omega T\vec{\nabla}\times u^\star\vec{g}d\Omega, \tag{22}$$

yielding an expression without derivatives of the temperature field. Using expressions (20) and (22) instead of the domain integrals in equation (15), we may write the final integral form of the vorticity transport equation as:

$$\begin{aligned} c(\vec{\theta})\omega_j(\vec{\theta}) + \int_\Gamma \omega_j\vec{\nabla}u^*\cdot\vec{n}d\Gamma &= \int_\Gamma u^* q_j d\Gamma \\ + \frac{1}{PrN_a}\int_\Gamma \vec{n}\cdot\left\{u^*(\vec{v}\omega_j - \vec{\omega}v_j)\right\} d\Gamma - \frac{1}{PrN_a}\int_\Omega (\vec{v}\omega_j - \vec{\omega}v_j)\cdot\vec{\nabla}u^* d\Omega & \\ -Ra\frac{N_b}{N_a}\int_\Gamma (u^\star T\vec{g}\times\vec{n})_j d\Gamma - Ra\frac{N_b}{N_a}\int_\Omega (T\vec{\nabla}\times u^\star\vec{g})_j d\Omega. & \end{aligned} \tag{23}$$

In the subdomain BEM method we make a mesh of the entire domain Ω and name each mesh element a subdomain. Equation (23) is written for each of the subdomains. In order to obtain a discrete version of (23) we use shape functions to interpolate field functions and flux. We used hexahedral subdomains with 27 nodes, which enable continuous quadratic interpolation of field functions. On each boundary element we interpolate the flux using discontinuous linear interpolation scheme with 4 nodes. By using discontinuous interpolation we avoid flux definition problems in corners and edges. A subdomain and one boundary element are sketched in Figure 1. A function, e.g. temperature, is interpolated over a boundary elements

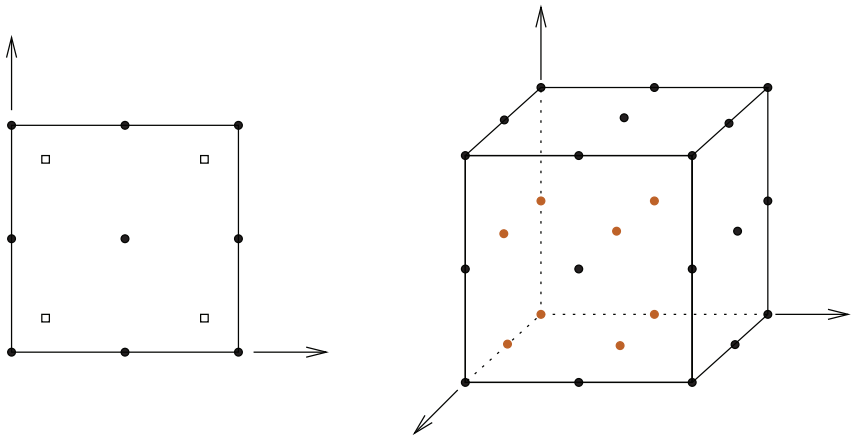

Fig. 1. A boundary element with function (circles) and flux (squares) nodes is shown on the left. A hexahedral subdomain with function nodes is shown on the right.

as $T = \sum \varphi_i T_i$, inside each subdomain as $T = \sum \Phi_i T_i$, while flux is interpolated over boundary elements as $q = \sum \phi_i q_i$.
The following integrals must be calculated:

$$[H] = \int_\Gamma \varphi_i \vec{\nabla} u^\star \cdot \vec{n} d\Gamma, \quad [G] = \int_\Gamma \phi_i u^\star d\Gamma, \quad [\vec{A}] = \int_\Gamma \varphi_i \vec{n} u^\star d\Gamma, \quad [\vec{D}] = \int_\Omega \Phi_i \vec{\nabla} u^\star d\Omega. \tag{24}$$

The square brackets denote integral matrices. Each source point location yields one row in these matrices. In order to calculate the integrals, a Gaussian quadrature algorithm is used. Calculation of the free coefficient $c(\vec{\theta})$ is preformed indirectly using a rigid body movement solution. The calculated $c(\vec{\theta})$ are added to the diagonal terms of the $[H]$ matrix.
The source point is set to all function and flux nodes in each subdomain. That makes the number of rows of each matrix 51 times the number of subdomains. By letting curly brackets denote vectors of nodal values of field functions, we may write the discrete vorticity transport equation in component form as:

$$\begin{aligned}[H]\{\omega_x\} = [G]\{q_x\} &+ \frac{1}{PrN_a}[A_y]\{v_y\omega_x - \omega_y v_x\} + \frac{1}{PrN_a}[A_z]\{v_z\omega_x - \omega_z v_x\} \\ &- \frac{1}{PrN_a}[D_y]\{v_y\omega_x - \omega_y v_x\} - \frac{1}{PrN_a}[D_z]\{v_z\omega_x - \omega_z v_x\} \\ &+ Ra\frac{N_b}{N_a}\left(g_z[A_y]\{T\} - g_y[A_z]\{T\} - g_z[D_y]\{T\} + g_y[D_z]\{T\}\right), \end{aligned} \tag{25}$$

$$\begin{aligned}[H]\{\omega_y\} = [G]\{q_y\} &+ \frac{1}{PrN_a}[A_x]\{v_x\omega_y - \omega_x v_y\} + \frac{1}{PrN_a}[A_z]\{v_z\omega_y - \omega_z v_y\} \\ &- \frac{1}{PrN_a}[D_x]\{v_x\omega_y - \omega_x v_y\} - \frac{1}{PrN_a}[D_z]\{v_z\omega_y - \omega_z v_y\} \\ &+ Ra\frac{N_b}{N_a}\left(g_x[A_z]\{T\} - g_z[A_x]\{T\} + g_z[D_x]\{T\} - g_x[D_z]\{T\}\right), \end{aligned} \tag{26}$$

$$[H]\{\omega_z\} = [G]\{q_z\} + \frac{1}{PrN_a}[A_x]\{v_x\omega_z - \omega_x v_z\} + \frac{1}{PrN_a}[A_y]\{v_y\omega_z - \omega_y v_z\}$$
$$- \frac{1}{PrN_a}[D_x]\{v_x\omega_z - \omega_x v_z\} - \frac{1}{PrN_a}[D_y]\{v_y\omega_z - \omega_y v_z\}$$
$$+ Ra\frac{N_b}{N_a}\left(g_y[A_x]\{T\} - g_x[A_y]\{T\} - g_y[D_x]\{T\} + g_x[D_y]\{T\}\right). \quad (27)$$

Since neighbouring subdomains share nodes, the systems of linear equations (25), (26) and (27) are over-determined. After taking into account the boundary conditions, we solve them using a least squares solver (Paige & Saunders, 1982).

3.2 Subdomain BEM solution of the energy equation

The energy equation (13) is also of a diffusion convection type. The solution of (13) is thus obtained in the same manner than the solution of the vorticity transfer equation. The discrete counterpart of the energy equation (13) is:

$$[H]\{T\} = [G]\{q_T\} +$$
$$+\frac{1}{N_c}\left([A_x]\{v_x T\} + [A_y]\{v_y T\} + [A_z]\{v_z T\} - [D_x]\{v_x T\} - [D_y]\{v_y T\} - [D_z]\{v_z T\}\right), \quad (28)$$

where $\{q_T\}$ is a nodal vector of temperature flux. Boundary conditions are either known temperature or temperature flux on the boundary. The system matrix is sparse and as such it is stored efficiently in a compressed row storage format. The system is solved in a least squares manner (Paige & Saunders, 1982).

3.3 Subdomain BEM solution of the kinematics equation

The kinematics equation (11) is an elliptic Poisson type equation. Its integral form (Wrobel, 2002) is

$$c(\xi)\vec{v}(\xi) + \int_\Gamma \vec{v}(\vec{n}\cdot\vec{\nabla})u^\star d\Gamma = \int_\Gamma u^\star(\vec{n}\cdot\vec{\nabla})\vec{v}d\Gamma + \int_\Omega(\vec{\nabla}\times\vec{\omega})u^\star d\Omega, \quad \xi\in\Gamma \quad (29)$$

The domain integral on the right hand side of equation (29) includes derivatives of vorticity. The equation is reformulated to transfer the derivative from the vorticity to the fundamental solution. We use the the definition of a curl of a product, i.e. $\vec{\nabla}\times(\vec{\omega}u^\star) = (\vec{\nabla}\times\vec{\omega})u^\star - \vec{\omega}\times\vec{\nabla}u^\star$ and obtain

$$\int_\Omega(\vec{\nabla}\times\vec{\omega})u^\star d\Omega = \int_\Omega(\vec{\nabla}\times(\vec{\omega}u^\star))d\Omega + \int_\Omega(\vec{\omega}\times\vec{\nabla}u^\star)d\Omega. \quad (30)$$

Using a derived form of the Gauss divergence clause, $\int_\Omega\vec{\nabla}\times\vec{F}d\Omega = -\int_\Gamma\vec{F}\times\vec{n}d\Gamma$, to change the first domain integral on the right hand side of (30) into a boundary integral, yields

$$\int_\Omega(\vec{\nabla}\times\vec{\omega})u^\star d\Omega = -\int_\Gamma(\vec{\omega}u^\star)\times\vec{n}d\Gamma + \int_\Omega(\vec{\omega}\times\vec{\nabla}u^\star)d\Omega. \quad (31)$$

Equation (31) is inserted into (29) and a new integral form of kinematics equation is obtained

$$c(\xi)\vec{v}(\xi) + \int_\Gamma\vec{v}(\vec{n}\cdot\vec{\nabla})u^\star d\Gamma = \int_\Gamma u^\star\left\{(\vec{n}\cdot\vec{\nabla})\vec{v} - \vec{\omega}\times\vec{n}\right\}d\Gamma + \int_\Omega(\vec{\omega}\times\vec{\nabla}u^\star)d\Omega. \quad (32)$$

The term in curly brackets in the boundary integral on the right hand side of equation (32) is for solenoidal fluid equal to $(\vec{n}\cdot\vec{\nabla})\vec{v}-\vec{\omega}\times\vec{n}=(\vec{n}\times\vec{\nabla})\times\vec{v}$. Using this relationship in equation (32) one can further rewrite the boundary integral as

$$\int_\Gamma u^\star(\vec{n}\times\vec{\nabla})\times\vec{v}d\Gamma=\int_\Gamma(\vec{n}\times\vec{\nabla})\times(\vec{v}u^\star)d\Gamma+\int_\Gamma\vec{v}\times(\vec{n}\times\vec{\nabla})u^\star d\Gamma \tag{33}$$

The first integral on the right hand side of the above equation represents an integral over a closed surface of a tangential derivative of a vector function. For a continuous function, such integral is always equal to zero. Inserting equation (33) into (32) we obtain an integral kinematics equation without derivatives of the velocity or vorticity fields:

$$c(\xi)\vec{v}(\xi)+\int_\Gamma\vec{v}(\vec{n}\cdot\vec{\nabla})u^\star d\Gamma=\int_\Gamma\vec{v}\times(\vec{n}\times\vec{\nabla})u^\star d\Gamma+\int_\Omega(\vec{\omega}\times\vec{\nabla}u^\star)d\Omega. \tag{34}$$

The boundary integrals on the left hand side are stored in the $[H]$ matrix, the domain integrals on the right hand side are the $[\vec{D}]$ matrices. We define the boundary integral on the right hand side as $[\vec{H}^t]$ integrals in the following manner:

$$[\vec{H}^t]=\int_\Gamma\varphi_i(\vec{n}\times\vec{\nabla})u^\star d\Gamma. \tag{35}$$

Since there are no fluxes in the equation, the source point is set to function nodes only. The discrete kinematics equation written in component wise form is:

$$[H]\{v_x\}=[H_z^t]\{v_y\}-[H_y^t]\{v_z\}+[D_z]\{\omega_y\}-[D_y]\{\omega_z\}, \tag{36}$$

$$[H]\{v_y\}=[H_x^t]\{v_z\}-[H_z^t]\{v_x\}-[D_z]\{\omega_x\}+[D_x]\{\omega_z\}, \tag{37}$$

$$[H]\{v_z\}=[H_y^t]\{v_x\}-[H_x^t]\{v_y\}+[D_y]\{\omega_x\}-[D_x]\{\omega_y\}. \tag{38}$$

The kinematics equation takes the same form for fluid flow problems and for coupled fluid flow - heat transfer problems. This form is used on every subdomain of the mesh to evaluate velocity flow field.

3.4 Fast Single domain BEM solution of the kinematics equation

In order to use the kinematics equation to obtain boundary vorticity values, we must rewrite the equation (34) in a tangential form by multiplying the system with a normal in the source point $\vec{n}(\vec{\theta})$:

$$\begin{aligned}c(\vec{\theta})\vec{n}(\vec{\theta})\times\vec{v}(\vec{\theta})+\vec{n}(\vec{\theta})\times\int_\Gamma\vec{v}\vec{\nabla}u^\star\cdot\vec{n}d\Gamma\\ =\vec{n}(\vec{\theta})\times\int_\Gamma\vec{v}\times(\vec{n}\times\vec{\nabla})u^\star d\Gamma+\vec{n}(\vec{\theta})\times\int_\Omega(\vec{\omega}\times\vec{\nabla}u^\star)d\Omega.\end{aligned} \tag{39}$$

This approach has been proposed by Škerget and used in $2D$ by Škerget et al. (2003) and in 3D by Žunič et al. (2007) and Ravnik et al. (2009a). The discrete form of the equations is

$$\begin{aligned}\{n_y\}[H]\{v_z\}-\{n_z\}[H]\{v_y\}=\{n_y\}([H_y^t]\{v_x\}-[H_x^t]\{v_y\}+[D_y]\{\omega_x\}-[D_x]\{\omega_y\})-\\ -\{n_z\}([H_x^t]\{v_z\}-[H_z^t]\{v_x\}-[D_z]\{\omega_x\}+[D_x]\{\omega_z\}),\end{aligned} \tag{40}$$

$$\{n_z\}[H]\{v_x\} - \{n_x\}[H]\{v_z\} = \{n_z\}([H_z^t]\{v_y\} - [H_y^t]\{v_z\} + [D_z]\{\omega_y\} - [D_y]\{\omega_z\}) - \\ -\{n_x\}([H_y^t]\{v_x\} - [H_x^t]\{v_y\} + [D_y]\{\omega_x\} - [D_x]\{\omega_y\}), \quad (41)$$

$$\{n_x\}[H]\{v_y\} - \{n_y\}[H]\{v_x\} = \{n_x\}([H_x^t]\{v_z\} - [H_z^t]\{v_x\} - [D_z]\{\omega_x\} + [D_x]\{\omega_z\}) - \\ -\{n_y\}([H_z^t]\{v_y\} - [H_y^t]\{v_z\} + [D_z]\{\omega_y\} - [D_y]\{\omega_z\}). \quad (42)$$

In order to write a system of equations for boundary vorticity, we decompose the vorticity nodal vectors in two parts. In the boundary part $\{\omega_i^\Gamma\}$ only boundary nodes are included, in the domain part $\{\omega_i^{\Omega\setminus\Gamma}\}$ the domain nodes are listed. The corresponding columns of the domain integral matrices are also separated into boudnary $[D_i^\Gamma]$ and domain $[D_i^{\Omega\setminus\Gamma}]$ parts. With this, the final form of the system of equation for the unknown boundary vorticity $\{\omega_x^\Gamma\}$, $\{\omega_y^\Gamma\}$, $\{\omega_z^\Gamma\}$ is

$$(\{n_x\}[D_x^\Gamma] + \{n_y\}[D_y^\Gamma] + \{n_z\}[D_z^\Gamma])\{\omega_x^\Gamma\} = \\ \{n_x\}[D_x^\Gamma]\{\omega_x^\Gamma\} - \{n_y\}[D_y^{\Omega\setminus\Gamma}]\{\omega_x^{\Omega\setminus\Gamma}\} - \{n_z\}[D_z^{\Omega\setminus\Gamma}])\{\omega_x^{\Omega\setminus\Gamma}\} + \\ \{n_y\}[H]\{v_z\} - \{n_z\}[H]\{v_y\} - \{n_y\}([H_y^t]\{v_x\} - [H_x^t]\{v_y\} - [D_x]\{\omega_y\}) + \\ \{n_z\}([H_x^t]\{v_z\} - [H_z^t]\{v_x\} + [D_x]\{\omega_z\}), \quad (43)$$

$$(\{n_x\}[D_x^\Gamma] + \{n_y\}[D_y^\Gamma] + \{n_z\}[D_z^\Gamma])\{\omega_y^\Gamma\} = \\ \{n_y\}[D_y^\Gamma]\{\omega_y^\Gamma\} - \{n_z\}[D_z^{\Omega\setminus\Gamma}]\{\omega_y^{\Omega\setminus\Gamma}\} - \{n_x\}[D_x^{\Omega\setminus\Gamma}])\{\omega_y^{\Omega\setminus\Gamma}\} + \\ \{n_z\}[H]\{v_x\} - \{n_x\}[H]\{v_z\} - \{n_z\}([H_z^t]\{v_y\} - [H_y^t]\{v_z\} - [D_y]\{\omega_z\}) + \\ \{n_x\}([H_y^t]\{v_x\} - [H_x^t]\{v_y\} + [D_y]\{\omega_x\}), \quad (44)$$

$$(\{n_x\}[D_x^\Gamma] + \{n_y\}[D_y^\Gamma] + \{n_z\}[D_z^\Gamma])\{\omega_z^\Gamma\} = \\ \{n_z\}[D_z^\Gamma]\{\omega_z^\Gamma\} - \{n_x\}[D_x^{\Omega\setminus\Gamma}]\{\omega_z^{\Omega\setminus\Gamma}\} - \{n_y\}[D_y^{\Omega\setminus\Gamma}])\{\omega_z^{\Omega\setminus\Gamma}\} + \\ \{n_x\}[H]\{v_y\} - \{n_y\}[H]\{v_x\} - \{n_x\}([H_x^t]\{v_z\} - [H_z^t]\{v_x\} - [D_z]\{\omega_x\}) + \\ \{n_y\}([H_z^t]\{v_y\} - [H_y^t]\{v_z\} + [D_z]\{\omega_y\}). \quad (45)$$

We set the source point into every boundary node of the whole computational domain. This yields a full system matrix with number of boundary nodes rows and columns. It is solved using a LU decomposition method. The domain matrices have the number of columns equal to the number of domain nodes. In order to reduce storage requirements and to make algebraic operation with domain matrices fast, we introduce a kernel expansion based approximation technique (Ravnik et al., 2009c).

3.4.1 Series expansion

The approximation method is based on the fact that it is possible to separate the variables (i.e. the collocation point $\vec{\theta}$ and the domain integration point $\vec{r}$) of the integral kernel of equation

(24) by series expansion. The gradient of the Laplace fundamental solution is expanded into a spherical harmonics series in the following manner:

$$\vec{\nabla}u^{\star} = \sum_{l=0}^{\infty}\sum_{m=-l}^{l}\frac{(-1)^m}{2l+1}\frac{1}{\xi^{l+1}}Y_l^{-m}(\theta_{\vec{\xi}},\varphi_{\vec{\xi}})\left\{lY_l^m(\theta_r,\varphi_r)r^{l-2}\vec{r}+r^l\vec{\nabla}Y_l^m(\theta_r,\varphi_r)\right\}, \tag{46}$$

where Y_l^m are spherical harmonics in polar coordinate system; $\vec{r}=(r,\varphi_r,\theta_r)$ and $\vec{\theta}=(\xi,\varphi_{\vec{\xi}},\theta_{\vec{\xi}})$. The gradient of spherical harmonics is expressed using associated Legendre polynomials P_l^m as

$$\vec{\nabla}Y_l^m(\theta,\varphi) = \sqrt{\frac{2l+1}{4\pi}\frac{(l-m)!}{(l+m)!}}\vec{\nabla}\left\{P_l^m(\cos\theta)\frac{\partial e^{im\varphi}}{\partial\varphi}\vec{\nabla}\varphi-\sin(\theta)\frac{\partial P_l^m(\cos\theta)}{\partial\cos\theta}\vec{\nabla}\theta\right\}. \tag{47}$$

The associated Legendre polynomials are evaluated using recurrence relations as described in Press et al. (1997). The derivatives of associated Legendre polynomials are obtained using the following recurrence relation:

$$\frac{\partial P_l^m(x)}{\partial x} = \frac{lxP_l^m(x)-(l+m)P_{l-1}^m(x)}{x^2-1}. \tag{48}$$

The derivatives of the polar angles written in Cartesian coordinate system are

$$\vec{\nabla}\theta = \frac{\sqrt{x^2+y^2}}{x^2+y^2+z^2}\left(\frac{zx}{x^2+y^2},\frac{zy}{x^2+y^2},-1\right), \qquad \vec{\nabla}\varphi = \frac{1}{x^2+y^2}(-y,x,0). \tag{49}$$

The origin of the coordinate system is set in such locations that the series convergence is improved. Using the above expansion, the domain integrals of equation (24) may now be written with separate variables. We are able to approximately calculate each entry in the domain matrices with the above sum. The number of expansion terms $n_{exp}=(L+1)^2$ in the series controls the accuracy of the approximation. Using the series instead of the direct evaluation of the integral kernel does not by itself bring a reduction of memory. Only when the expansion is used on a cluster of collocation points and domain cells it is possible to form a data sparse approximation of a part of the domain matrix. The clusters are formed and organized in a hierarchical tree-like structure, which is described below.

3.4.2 Cluster trees

Let us consider a cluster of n_r nearby collocation points and a cluster of n_c nearby domain cells, as illustrated in Figure 2.

These correspond to a $n_r \times n_c$ matrix block, which is a part of the domain matrix. Since the variables in the series are separated, it is possible to evaluate two lower order matrix blocks ($n_r \times n_{exp}$) and ($n_{exp} \times n_c$) instead of the full matrix block ($n_r \times n_c$). In the first lower order matrix block expansion terms that depend on source point location are evaluated for all collocation points. In the second one integrals of expansion terms that depend on domain location are evaluated for all domain cells. Multiplication of the two lower order matrix blocks gives the full $n_r \times n_c$ matrix block up to an expansion error. This technique saves memory if the amount of data, that must be stored in the two lower order matrices, is smaller than the amount of data in the full matrix block. As long as the collocation node cluster and the domain cells cluster are far apart this technique can be used. When the clusters coincide, i.e. the collocation nodes are a part of the integration cells, the kernels are singular. Such

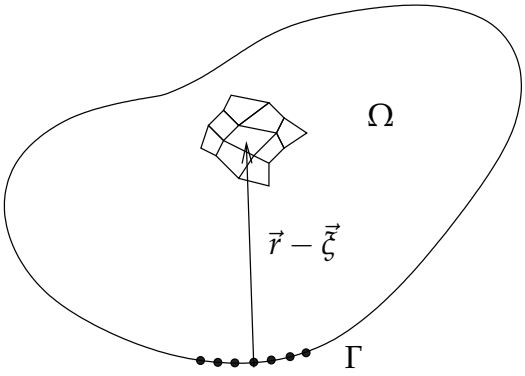

Fig. 2. A problem domain shown with a cluster of collocation points $\vec{\theta}$ and a cluster of domain cells.

cluster pairs are called inadmissible and the corresponding matrix block is evaluated in full, not approximated with two lower order matrices.
We constructed a tree of collocation point clusters and a tree of clusters of domain cells. The trees were constructed in a recursive hierarchical manner. The problem domain was enclosed by a parallelepiped. The parallelepiped is cut in half by a plane, breaking the root clusters into two. The cutting process is repeated recursively, so the clusters on each level have less and less collocation points and domain cells. The cutting sequence is stopped, when memory can no longer be saved.
Each branch of the collocation tree is paired with each branch of the domain cells tree on the same level and with each branch of the domain cells tree on the next level thus forming branches on the tree of pairs of clusters. For each pair a decision is taken based on the admissibility criterion whether a sparse approximation for this cluster pair is possible or not. If the pair is admissible, the branch on the tree becomes an admissible leaf, where the two low order matrices will be calculated. If admissibility criterion is not reached until the last level of the tree, such cluster pairs are inadmissible and will be calculated in full and not with the sparse approximation.
To illustrate the algorithm, a cubic domain is considered meshed by 12^3 domain cells having in total 25^3 nodes. Admissible and inadmissible blocks are shown in Figure 3.

4. Test cases

The developed numerical scheme was used to simulate fluid flow and heat transfer of pure fluids and nanofluids. Two configurations were considered: the hotstrip and the differentially heated cavity. Sketches and boundary conditions for both cases are shown in Figure 4.
Applying a temperature difference on two opposite walls of an otherwise insulated cavity starts up natural convection producing a large vortex in the main part of the cavity. At low Rayleigh number values the vortex is weak and the heat is transferred predominately with conduction. Convection dominates at $Ra = 10^6$ where temperature stratification may be observed. The flow becomes unsteady for higher Ra values with vortices forming along the hot and cold walls. Natural convection of air and other pure fluids in a differentially heated cavity has been under intense investigation in the past. Recently several authors simulated

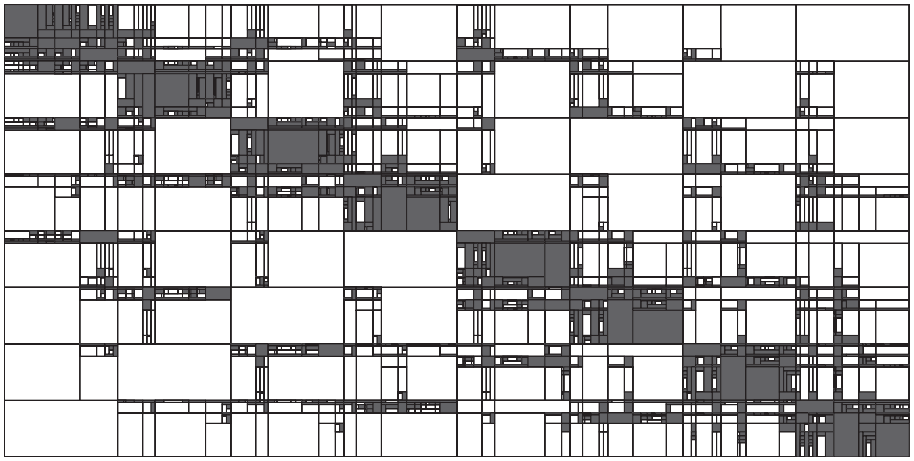

Fig. 3. Matrix structure of a cubic mesh (12^3 cells, 25^3 nodes). Filled areas show inadmissible matrix blocks, white areas are admissible matrix blocks obtained using an admissibility criteria of $\epsilon = 10^{-4}$.

nanofluids in this case (Abu-Nada & Oztop, 2009; Hwang et al., 2007; Ho et al., 2008; Tiwari & Das, 2007; Ravnik et al., 2010).
The hotstrip heats the surrounding fluid inducing two large main vortices. When the hotstrip is located in the centre of the cavity, the flow field is symmetric and the fluid rises from the centre of the hotstrip. If the hotstrip is placed off-centre, the flow symmetry is lost. Corvaro & Paroncini (2009; 2008) performed a 2D PIV experiment on a hotstrip problem, using air as the working fluid. Simulations of natural convection around the hotstrip were presented by Ravnik & Škerget (2009) and Ravnik et al. (2010).

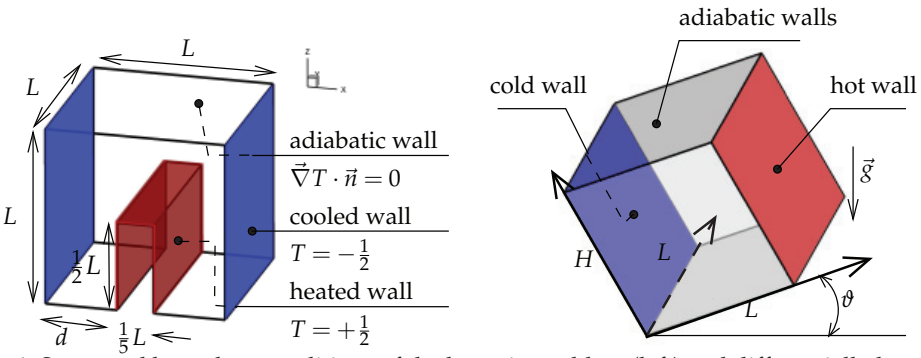

Fig. 4. Setup and boundary conditions of the hotstrip problem (left) and differentially heated cavity problem (right). Hotstrip of height $0.5L$ and width $0.2L$ is located at distance d from the left cold wall. The hotstrip is heated to $T = +0.5$, while the walls at $x = 0$ and $x = L$ are cooled to $T = -0.5$. There is no temperature flux through all other walls. In differentially heated cavity we keep two opposite vertical walls cold and hot, while all other walls are adiabatic. The height of the cavity is H, while its width and length are L. No-slip velocity boundary conditions are applied on all walls.

Both cases were investigated for air ($Pr = 0.71$), water ($Pr = 6.2$) and water based nanofluids (Table 1) for several Rayleigh number values. The hotstrip was positioned in the centre of the cavity ($d = 0.4H$) and off-centre ($d = 0.5H$). Aspect ratio of the differentially heated cavity was $H/L = 1$ and $H/L = 2$.
Normally, the heat flux $\dot{Q}$ is expressed in terms of pure fluid thermal conductivity, characteristic flow scales and a nondimensional Nusselt number, i.e. $\dot{Q} = k_f L \Delta T \cdot Nu$. The Nusselt number, Nu, is defined as the integral of the temperature flux through a wall. For a nanofluid, it is written as

$$Nu = \frac{k_{nf}}{k_f} \frac{1}{\Gamma_0} \int_\Gamma \vec{\nabla} T \cdot \vec{n} d\Gamma, \tag{50}$$

where Γ is the surface through which we calculate the heat flux and $\vec{n}$ is a unit normal to this surface. The area of the surface is Γ_0. The same definition may be used to pure fluids, since there $k_{nf}/k_f = 1$.

4.1 Natural convection in a differentially heated cavity

The domain was discretizised using 41^3 nodes. Nodes were concentrated towards the hot and cold walls in such a way that the ratio between the largest and the smallest element length was 7. First, we examine the flow structure with air as the working fluid. Figure 5 shows temperature contour plots on the $y = 0.5$ plane for Rayleigh number $Ra = 10^5$ and different inclination angles for cubic and $H/L = 2$ cavity. We observe temperature stratification in all cases. When the cavity is inclined, the thermal boundary layers widen and the heat transfer decreases. Tables 2 and 3 provide the Nusselt number values. We observe a decrease of the values with increasing inclination angle and an increase of heat transfer with increasing Rayleigh number. Present values compare well with the solution provided by Lo et al. (2007) and Tric et al. (2000). Nusselt number values for $H/L = 2$ cavity are given in Table 4.
Comparison of pure fluids and nanofluids is given in Figure 6, where temperature contours for water and water based nanofluids on the central $y = 0.5L$ plane are shown. Two solid volume fractions are compared. We observe that the change in nano particle volume fraction changes the temperature field considerably, thus changing the heat transfer. Nusselt number values for the natural convection of nanofluids in a cubical cavity are given in Table 5. Using water based nanofluids instead of pure water increases heat transfer in all cases. For low Rayleigh number, where conduction is the predominant heat transfer mechanism, the enhancement is the largest. For Cu nanofluid at $Ra = 10^3$ we observe an 27.2% increase in heat transfer for $\varphi = 0.1$ and 64.1% for $\varphi = 0.2$. TiO_2 nanofluid exhibits lower heat transfer enhancement, since its thermal conductivity is lower than that of Cu and Al_2O_3 nanofluids. Al_2O_3 and Cu nanofluid exhibit approximately the same heat transfer enhancement. As the Rayleigh number increases, convection becomes the dominant heat transfer mechanism, while conduction is negligible. Thus, the increased thermal conductivity of nanofluids plays a less important role in the overall heat balance. All nanofluids exhibit smaller heat transfer

	pure water	Cu	Al_2O_3	TiO_2
$c_p[J/kgK]$	4179	385	765	686.2
$\rho[kg/m^3]$	997.1	8933	3970	4250
$k[W/mK]$	0.613	400	40	8.9538
$\beta[\cdot 10^{-5} K^{-1}]$	21	1.67	0.85	0.9
$\alpha[\cdot 10^{-7} m^2/s]$	1.47	1163	131.7	30.7

Table 1. Thermophysical properties of water based nanofluids (Oztop & Abu-Nada, 2008).

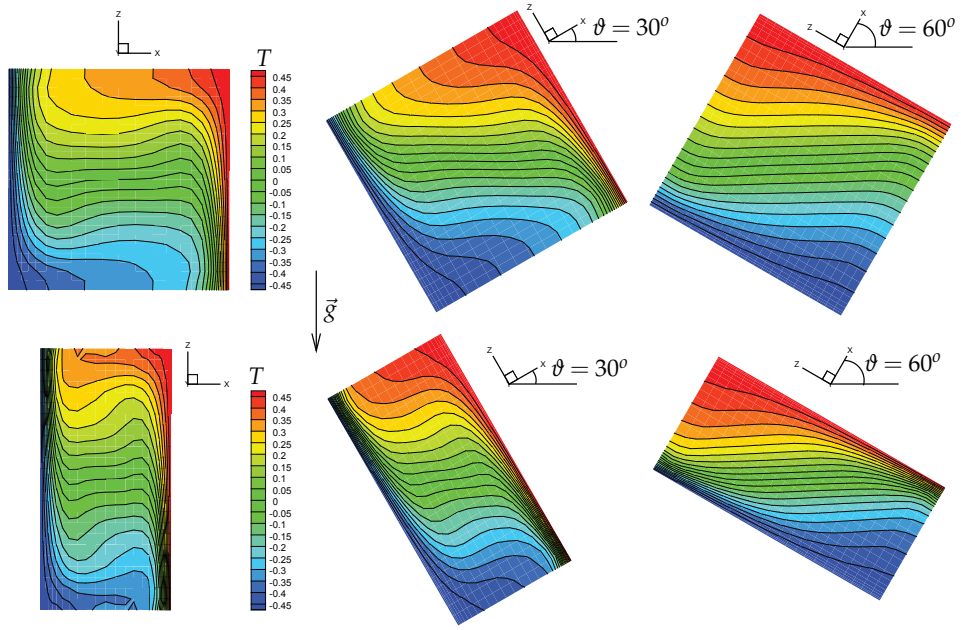

Fig. 5. Natural convection of air in a differentaily heat cavity. Temperature contour plots on the $y = 0.5$ plane for Rayleigh number $Ra = 10^5$; $\vartheta = 0^o$ (left), $\vartheta = 15^o$ (middle) and $\vartheta = 30^o$ (right). Top row: cubic cavity, bottom row $H/L = 2$ cavity. Gravity points downward in all cases.

enhancement as compared to the low Rayleigh number case. At $Ra = 10^6$ Cu nanofluid increases heat transfer at $\varphi = 0.1$ for 11.6% and at $\varphi = 0.2$ for 21.6%.

4.2 Natural convection around a hotstrip

Natural convection of air, water and water based nanofluids was simulated around the hotstrip. Two position of the hotstrip were considered - in the centre of the cavity ($d = 0.4L$) and off-centre ($d = 0.5L$). The mesh used for simulation had $61 \times 49 \times 19$ nodes in hexahedral cells. The nodes were concentrated towards the hot and cold walls.

Looking at the flow field of air in Figures 7 and 8 we observe that the hotstrip heats the surrounding fluid inducing two main vortices - one on each side. Hot fluid from the sides of the hotstrip is transported upwards by convection making the thermal boundary layer thin

	Air			Water
Ra	Lo et al. (2007)	Tric et al. (2000)	present	present
10^3	1.0710	1.0700	1.0712	1.071
10^4	2.0537	2.0542	2.0564	2.078
10^5	4.3329	4.3371	4.3432	4.510
10^6	8.6678	8.6407	8.6792	9.032

Table 2. Natural convection of air and water in a cubic cavity without inclination, $\vartheta = 0$. Present Nusselt number values are compared with the benchmark results of Lo et al. (2007) and Tric et al. (2000).

ϑ	Lo et al. (2007)			present		
	$Ra = 10^3$	$Ra = 10^4$	$Ra = 10^5$	$Ra = 10^3$	$Ra = 10^4$	$Ra = 10^5$
15^o	1.0590	1.8425	3.7731	1.0592	1.8464	3.7881
30^o	1.0432	1.5894	2.9014	1.0433	1.5916	2.9071
45^o	1.0268	1.3434	1.9791	1.0268	1.3443	1.9782
60^o	1.0127	1.1524	1.3623	1.0127	1.1526	1.3600

Table 3. Natural convection of air in a cubic cavity under inclination ϑ. Present Nusselt number values are compared with the benchmark results of Lo et al. (2007).

and thus resulting in high heat transfer. Upon reaching the top of the hotstrip the fluid flows over the top ultimately colliding with the fluid from the other side and rising upwards. When the hotstrip is located in the centre of the cavity, the flow field is symmetric and the fluid rises from the centre of the hotstrip. If the hotstrip is placed off-centre, the flow symmetry is lost. The sizes of large vortices on each side of the hotstrip are different. The flow does not rise above the centre of the hotstrip. Mixing of the fluid from both sides of the hotstrip occurs, which does not happen in the symmetric case.

We measured heat transfer in terms of the Nusselt number values over the whole surface of the hostrip (two vertical wall and a top wall). The values are shown in Table 6 for Rayleigh number values ranging from $Ra = 10^3$ to $Ra = 10^5$. We observe that the addition of nanoparticles increases heat transfer in all cases. The increase is the largest in the low Rayleigh number case and the smallest in the case of high Rayleigh values. This is expected, since at low Rayleigh number values conduction is the dominating heat transfer mechanism

ϑ	$Ra = 10^3$	$Ra = 10^4$	$Ra = 10^5$
0^o	1.111	2.163	4.177
15^o	1.096	2.029	3.892
30^o	1.073	1.839	3.430
45^o	1.047	1.594	2.774
60^o	1.023	1.317	1.915

Table 4. Natural convection of air in a $H/L = 2$ cavity. The Nusselt number values representing the heat flux through walls are shown for different inclination angles and Rayleigh numbers.

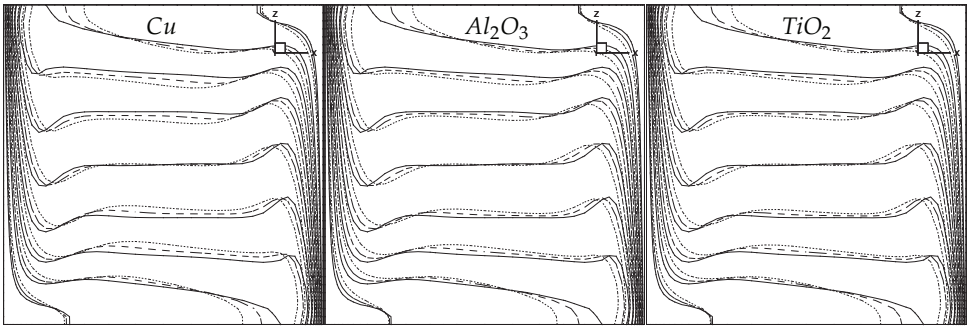

Fig. 6. Temperature contours on the central $y = 0.5H$ plane for natural convection in a differentially heated cubic cavity. Contour values are -0.4(0.1)0.4; $Ra = 10^6$. Solid line denotes pure water, dashed line $\varphi = 0.1$ nanofluid and dotted line $\varphi = 0.2$ nanofluid.

Ra	Water+Cu		Water+Al_2O_3		Water+TiO_2	
	$\varphi = 0.1$	$\varphi = 0.2$	$\varphi = 0.1$	$\varphi = 0.2$	$\varphi = 0.1$	$\varphi = 0.2$
10^3	1.363	1.758	1.345	1.718	1.297	1.598
10^4	2.237	2.381	2.168	2.244	2.115	2.132
10^5	4.946	5.278	4.806	4.968	4.684	4.732
10^6	10.08	10.98	9.817	10.39	9.556	9.871

Table 5. Nusselt number values for the natural convection of nanofluids in a cubical cavity. Solid particle volume fraction is denoted by φ.

and the improved nanofluid properties play an important role. At high Rayleigh number values convection dominates and improved thermal properties of nanofluids contribute at an lesser extent.

Ra	Air	Water	Water+Cu		Water+Al_2O_3		Water+TiO_2	
			$\varphi = 0.1$	$\varphi = 0.2$	$\varphi = 0.1$	$\varphi = 0.2$	$\varphi = 0.1$	$\varphi = 0.2$
				$d = 0.4L$				
10^3	3.781	3.781	5.030	6.591	4.974	6.451	4.788	5.997
10^4	4.233	4.251	5.232	6.667	5.153	6.511	4.974	6.060
10^5	8.331	8.542	9.434	10.05	9.157	9.435	8.926	8.983
				$d = 0.5L$				
10^3	3.985	3.982	5.296	6.941	5.237	6.793	5.042	6.313
10^4	4.542	4.538	5.571	7.051	5.481	6.877	5.294	6.403
10^5	7.597	8.336	9.255	10.21	9.001	9.673	8.762	9.162

Table 6. Nusselt number values for natural convection of nanofluids in a hotstrip. The values were obtained by integrating over the whole hotstrip.

5. Conclusions

We presented a method for solving coupled laminar viscous flow and heat transfer problems. The algorithm solves the velocity-vorticity formulation of Navier-Stokes equations. The boundary vorticity values are obtained by the single domain BEM solution of the kinematics equation, accelerated by kernel expansion based approximation technique. The solution of the vorticity equation for domain vorticity values, the energy equation for domain temperature values and the kinematics equation for domain velocity values are obtained by subdomain BEM.

The method was used to simulate natural convection phenomena in inclined parallelepiped shaped cavity as well as around a hotstrip. Working fluids were pure air, pure water and water based nanofluids: Cu, Al_2O_3 and TiO_2. The proposed numerical scheme was validated by comparing Nusselt number values with benchmark solutions.

By studying the temperature field in the differentially heated enclosure we observed, that in the central part the temperature field is stratified. The layers of constant temperature are set perpendicularly to the gravity direction regardless of the inclination angle as long as the hot wall lies above the cold wall. The velocity flow fields show that the flow is predominantly moving in a single vortex, up along the hot wall and down along the cold wall. The 3D nature of the flow may be observed in the corners of the enclosures. Comparing the cubic and $H/L = 2$ cavities we established that the Nusselt number values are higher in the case of $H/L = 2$ enclosure.

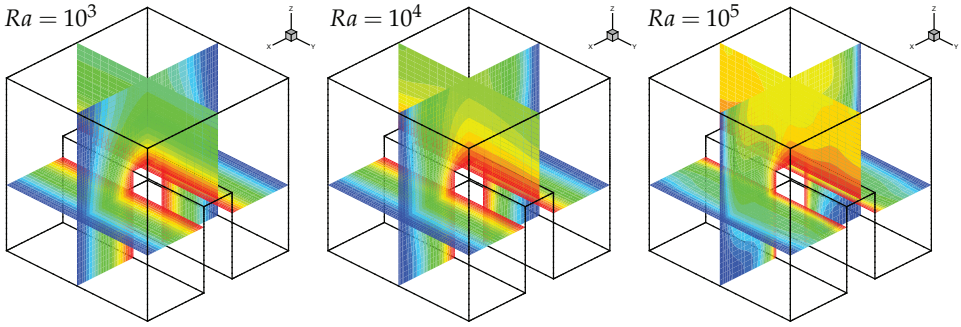

Fig. 7. Temperature contours for natural convection of air around a hotstrip; $d = 0.4L$. Contour values are -0.45(0.05)0.45.

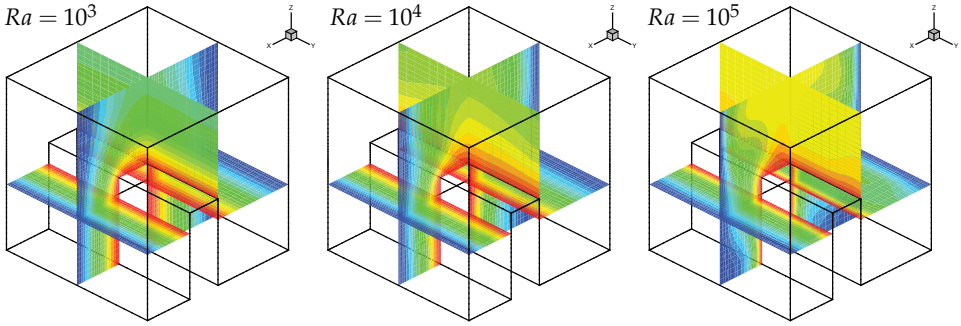

Fig. 8. Temperature contours for natural convection of air around a hotstrip; $d = 0.5L$. Contour values are -0.45(0.05)0.45.

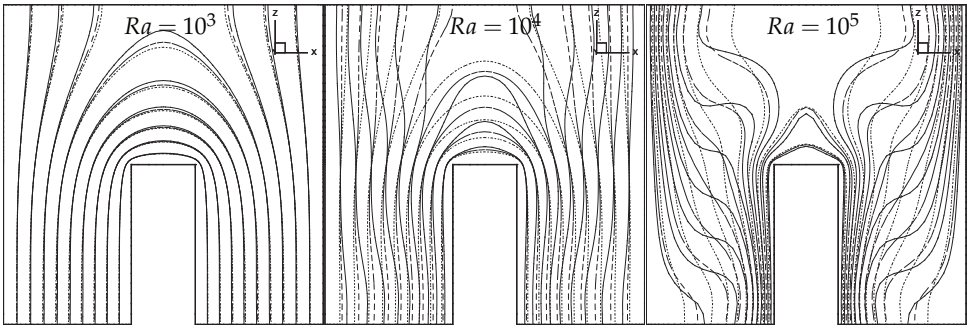

Fig. 9. Temperature contours on the central $y = 0.5H$ plane for natural convection around a hotstrip. Contour values are -0.4(0.1)0.4; Solid line denotes pure water, dashed line Al_2O_3 nanofluid with solid volume fraction $\varphi = 0.1$ and dotted line Al_2O_3 nanofluid with solid volume fraction $\varphi = 0.2$.

A hotstrip in a cavity produces two vortices, one on each side. For $Ra \leq 10^5$ the flow field is symmetric in the case of central placement of the hotstrip. Symmetry is lost when hotstrip is place off-centre. Most of the heat is transferred from the sides of the hotstrip and only a small part from the top wall.
Introduction of nanofluids leads to enhanced heat transfer in all cases. The enhancement is largest when conduction is the dominant heat transfer mechanism, since in this case the increased heat conductivity of the nanofluid is important. On the other hand, in convection dominated flows heat transfer enhancement is smaller. All considered nanofluids enhance heat transfer for approximately the same order of magnitude, Cu nanofluid yielding the highest values. Heat transfer enhancement grows with increasing solid particle volume fraction in the nanofluid. The differences between temperature fields when using different nanofluids with the same solid nanoparticle volume fraction are small.
In future the proposed method for simulating fluid flow and heat transfer will be expanded for simulation of unsteady phenomena and turbulence.

6. References

Abu-Nada, E. (2008). Application of nanofluids for heat transfer enhancement of separated flows encountered in a backward facing step, *Int. J. Heat Fluid Fl.* 29: 242–249.

Abu-Nada, E. & Oztop, H. F. (2009). Effects of inclination angle on natural convection in enclosures filled with cuwater nanofluid, *Int. J. Heat Fluid Fl.* 30: 669–678.

Akbarinia, A. & Behzadmehr, A. (2007). Numerical study of laminar mixed convection of a nanofluid in horizontal curved tubes, *Applied Thermal Engineering* 27: 1327–1337.

Bebendorf, M. (2000). Approximation of boundary element matrices, *Numer. Math* 86: 565–589.

Bebendorf, M. & Rjasanow, S. (2003). Adaptive low rank approximation of collocation matrices, *Computing* 70: 1–24.

Brinkman, H. C. (1952). The viscosity of concentrated suspensions and solutions, *J. Chem. Phys.* 20: 571–581.

Bui, T. T., Ong, E. T., Khoo, B. C., Klaseboer, E. & Hung, K. C. (2006). A fast algorithm for modeling multiple bubbles dynamics, *J. Comput. Phys.* 216: 430–453.

Choi, S. U. S. (1995). Enhancing thermal conductivity of fluids with nanoparticles, *Develop. Appl. Non Newtonian Flows* 66: 99–106.

Corvaro, F. & Paroncini, M. (2008). A numerical and experimental analysis on the natural convective heat transfer of a small heating strip located on the floor of a square cavity, *Applied Thermal Engineering* 28: 25–35.

Corvaro, F. & Paroncini, M. (2009). An experimental study of natural convection in a differentially heated cavity through a 2D-PIV system, *Int. J. Heat Mass Transfer* 52: 355–365.

Daube, O. (1992). Resolution of the 2D Navier-Stokes equations in velocity-vorticity form by means of an influence matrix technique, *J. Comput. Phys.* 103: 402–414.

Davies, G. D. V. (1983). Natural convection of air in a square cavity: a bench mark numerical solution, *Int. J. Numer. Meth. Fl.* 3: 249–264.

Eppler, K. & Harbrecht, H. (2005). Fast wavelet BEM for 3D electromagnetic shaping, *Applied Numerical Mathematics* 54: 537–554.

Fata, S. N. (2010). Treatment of domain integrals in boundary element methods, *Applied Numer. Math* .

Gao, X. W. & Davies, T. G. (2000). 3D multi-region BEM with corners and edges, *Int. J. Solids Struct.* 37: 1549–1560.

Greengard, L. & Rokhlin, V. (1987). A fast algorithm for particle simulations, *J. Comput. Phys.* 73: 325–348.

Gumerov, N. A. & Duraiswami, R. (2006). Fast multipole method for the biharmonic equation in three dimensions, *J. Comput. Phys.* 215: 363–383.

Gümgüm, S. & Tezer-Sezgin, M. (2010). DRBEM Solution of Natural Convection Flow of Nanofluids with a Heat Source, *Eng. Anal. Bound. Elem.* 34: 727–737.

Hackbusch, W. (1999). A sparse matrix arithmetic based on $\mathcal{H}$-matrices. Part I: Introduction to $\mathcal{H}$-matrices, *Computing* 62: 89–108.

Hackbusch, W. & Nowak, Z. P. (1989). On the fast multiplication in the boundary element method by panel clustering, *Numerische Mathematik* 54: 463–491.

Ho, C., Chen, M. & Li, Z. (2008). Numerical simulation of natural convection of nanofluid in a square enclosure: Effects due to uncertainties of viscosity and thermal conductivity, *Int. J. Heat Mass Transfer* 51: 4506–4516.

Hsieh, K. J. & Lien, F. S. (2004). Numerical modelling of buoyancy-driven turbulent flows in enclosures, *Int. J. Heat Fluid Fl.* 25(4): 659–670.

Hwang, K. S., Lee, J.-H. & Jang, S. P. (2007). Buoyancy-driven heat transfer of water-based Al_2O_3 nanofluids in a rectangular cavity, *Int. J. Heat Mass Transfer* 50: 4003–4010.

Ingber, M. S. (2003). A vorticity method for the solution of natural convection flows in enclosures, *Int. J. Num. Meth. Heat & Fluid Fl.* 13: 655–671.

Jumarhon, B., Amini, S. & Chen, K. (1997). On the boundary element dual reciprocity method, *Eng. Anal. Bound. Elem.* 20: 205–211.

Khanafer, K., Vafai, K. & Lightstone, M. (2003). Buoyancy-driven heat transfer enhancement in a two-dimensional enclosure utilizing nanofluids, *Int. J. Heat Mass Transfer* 46: 3639–3653.

Liu, C. H. (2001). Numerical solution of three-dimensional Navier Stokes equations by a velocity - vorticity method, *Int. J. Numer. Meth. Fl.* 35: 533–557.

Lo, D., Young, D., Murugesan, K., Tsai, C. & Gou, M. (2007). Velocity-vorticity formulation for 3D natural convection in an inclined cavity by DQ method, *Int. J. Heat Mass Transfer* 50: 479–491.

Mirmasoumi, S. & Behzadmehr, A. (2008). Effect of nanoparticles mean diameter on mixed convection heat transfer of a nanofluid in a horizontal tube, *Int. J. Heat Fluid Fl.* 29: 557–566.

Ögüt, E. B. (2009). Natural convection of water-based nanofluids in an inclined enclosure with a heat source, *International Journal of Thermal Sciences* 48: 2063–2073.

Ong, E. & Lim, K. (2005). Three-dimensional singular boundary element method for corner and edge singularities in potential problems, *Eng. Anal. Bound. Elem.* 29: 175–189.

Oztop, H. F. & Abu-Nada, E. (2008). Natural convection of water-based nanofluids in an inclined enclosure with a heat source, *Int. J. Heat Fluid Flow* 29: 1326–1336.

Paige, C. C. & Saunders, M. A. (1982). LSQR: An algorithm for sparse linear equations and sparse least squares, *ACM Transactions on Mathematical Software* 8: 43–71.

Partridge, P., Brebbia, C. & Wrobel, L. (1992). *The dual reciprocity boundary element method*, Computational Mechanics Publications Southampton, U.K. ; Boston : Computational Mechanics Publications ; London ; New York.

Peng, S. H. & Davidson, L. (2001). Large eddy simulation for turbulent buoyant flow in a confined cavity, *Int. J. Heat Fluid Fl.* 22: 323–331.

Popov, V., Power, H. & Škerget, L. (eds) (2007). *Domain Decomposition Techniques for Boundary Elements: Applications to fluid flow*, WIT press.

Popov, V., Power, H. & Walker, S. P. (2003). Numerical comparison between two possible multipole alternatives for the BEM solution of 3D elasticity problems based upon Taylor series expansions, *Eng. Anal. Bound. Elem.* 27: 521–531.

Press, W. H., Teukolsky, S. A., Vetterling, W. T. & Flannery, B. P. (1997). *Numerical Recipes - The Art of Scientific computing, Second Edition*, Cambridge University Press.

Ramšak, M. & Škerget, L. (2007). 3D multidomain BEM for solving the Laplace equation, *Eng. Anal. Bound. Elem.* 31: 528–538.

Ravnik, J. & Škerget, L. (2009). Natural convection around a 3D hotstrip simulated by BEM, *Mesh Reduction Methods BEM/MRM XXXI*, pp. 343–352.

Ravnik, J., Škerget, L. & Hriberšek, M. (2004). The wavelet transform for BEM computational fluid dynamics, *Eng. Anal. Bound. Elem.* 28: 1303–1314.

Ravnik, J., Škerget, L. & Hriberšek, M. (2006). 2D velocity vorticity based LES for the solution of natural convection in a differentially heated enclosure by wavelet transform based BEM and FEM, *Eng. Anal. Bound. Elem.* 30: 671–686.

Ravnik, J., Škerget, L. & Hriberšek, M. (2010). Analysis of three-dimensional natural convection of nanofluids by BEM, *Eng. Anal. Bound. Elem.* 34: 1018–1030.

Ravnik, J., Škerget, L. & Žunič, Z. (2008). Velocity-vorticity formulation for 3D natural convection in an inclined enclosure by BEM, *Int. J. Heat Mass Transfer* 51: 4517–4527.

Ravnik, J., Škerget, L. & Žunič, Z. (2009a). Combined single domain and subdomain BEM for 3D laminar viscous flow, *Eng. Anal. Bound. Elem.* 33: 420–424.

Ravnik, J., Škerget, L. & Žunič, Z. (2009b). Comparison between wavelet and fast multipole data sparse approximations for Poisson and kinematics boundary – domain integral equations, *Comput. Meth. Appl. Mech. Engrg.* 198: 1473–1485.

Ravnik, J., Škerget, L. & Žunič, Z. (2009c). Fast single domain–subdomain BEM algorithm for 3D incompressible fluid flow and heat transfer, *Int. J. Numer. Meth. Engng.* 77: 1627–1645.

Sellountos, E. & Sequeira, A. (2008). A Hybrid Multi-Region BEM / LBIE-RBF Velocity-Vorticity Scheme for the Two-Dimensional Navier-Stokes Equations, *CMES: Computer Methods in Engineering and Sciences* 23: 127–147.

Shukla, R. K. & Dhir, V. K. (2005). Numerical study of the effective thermal conductivity of nanofluids, *ASME Summer Heat Transfer Conference*.

Škerget, L., Hriberšek, M. & Žunič, Z. (2003). Natural convection flows in complex cavities by BEM, *Int. J. Num. Meth. Heat & Fluid Fl.* 13: 720–735.

Škerget, L. & Samec, N. (2005). BEM for the two-dimensional plane compressible fluid dynamics, *Eng. Anal. Bound. Elem.* 29: 41–57.

Tiwari, R. K. & Das, M. K. (2007). Heat transfer augmentation in a two-sided lid-driven differentially heated square cavity utilizing nanofluids, *Int. J. Heat Mass Transfer* 50: 2002–2018.

Torii, S. (2010). Turbulent Heat Transfer Behavior of Nanofluid in a Circular Tube Heated under Constant Heat Flux, *Advances in Mechanical Engineering* 2010: Article ID 917612, 7 pages.

Tric, E., Labrosse, G. & Betrouni, M. (2000). A first incursion into the 3D structure of natural convection of air in a differentially heated cubic cavity, from accurate numerical simulations, *Int. J. Heat Mass Transfer* 43: 4034–4056.

Vierendeels, J., Merci, B. & Dick, E. (2001). Numerical study of the natural convection heat transfer with large temperature differences, *Int. J. Num. Meth. Heat & Fluid Fl.* 11: 329–341.

Vierendeels, J., Merci, B. & Dick, E. (2004). A multigrid method for natural convective heat transfer with large temperature differences, *Int. J. Comput. Appl. Math.* 168: 509–517.

Wang, X.-Q. & Mujumdar, A. S. (2007). Heat transfer characteristics of nanofluids: a review, *International Journal of Thermal Sciences* 46: 1–19.

Weisman, C., Calsyn, L., Dubois, C. & Quéré, P. L. (2001). Sur la nature de la transition a l'instationare d'un ecoulement de convection naturelle en cavite differentiellement chauffee a grands ecarts de temperature, *Comptes rendus de l'academie des sciences Serie II b, Mecanique* pp. 343–350.

Wong, K. L. & Baker, A. J. (2002). A 3D incompressible Navier-Stokes velocity-vorticity weak form finite element algorithm, *Int. J. Num. Meth. Fluids* 38: 99–123.

Wrobel, L. C. (2002). *The Boundary Element Method*, John Willey & Sons, LTD.

Xin, S. & Quéré, P. L. (1995). Direct numerical simulations of two-dimensional chaotic natural convection in a differentially heated cavity of aspect ratio 4, *J. Fluid Mech.* 304: 87–118.

Yang, Y., Zhang, Z. G., Grulke, E. A., Anderson, W. B. & Wu, G. (2005). Heat transfer properties of nanoparticle-in-fluid dispersions (nanofluids) in laminar flow, *Int. J. Heat Mass Transfer* 48: 1107–1116.

Žunič, Z., Hriberšek, M., Škerget, L. & Ravnik, J. (2007). 3-D boundary element-finite element method for velocity-vorticity formulation of the Navier-Stokes equations, *Eng. Anal. Bound. Elem.* 31: 259–266.

10

Aerodynamic Heating at Hypersonic Speed

Andrey B. Gorshkov
Central Research Institute of Machine Building
Russia

1. Introduction

At designing and modernization of a reentry space vehicle it is required accurate and reliable data on the flow field, aerodynamic characteristics, heat transfer processes. Taking into account the wide range of flow conditions, realized at hypersonic flight of the vehicle in the atmosphere, it leads to the need to incorporate in employed theoretical models the effects of rarefaction, viscous-inviscid interaction, flow separation, laminar-turbulent transition and a variety of physical and chemical processes occurring in the gas phase and on the vehicle surface.

Getting the necessary information through laboratory and flight experiments requires considerable expenses. In addition, the reproduction of hypersonic flight conditions at ground experimental facilities is in many cases impossible. As a result the theoretical simulation of hypersonic flow past a spacecraft is of great importance. Use of numerical calculations with their relatively small cost provides with highly informative flow data and gives an opportunity to reproduce a wide range of flow conditions, including the conditions that cannot be reached in ground experimental facilities. Thus numerical simulation provides the transfer of experimental data obtained in laboratory tests on the flight conditions.

One of the main problems that arise at designing a spacecraft reentering the Earth's atmosphere with orbital velocity is the precise definition of high convective heat fluxes (aerodynamic heating) to the vehicle surface at hypersonic flight. In a dense atmosphere, where the assumption of continuity of gas medium is true, a detailed analysis of parameters of flow and heat transfer of a reentry vehicle may be made on the basis of numerical integration of the Navier-Stokes equations allowing for the physical and chemical processes in the shock layer at hypersonic flight conditions. Taking into account the increasing complexity of practical problems, a task of verification of employed physical models and numerical techniques arises by means of comparison of computed results with experimental data.

In this chapter some results are presented of calculations of perfect gas and real air flow, which have been obtained using a computer code developed by the author (Gorshkov, 1997). The code solves two- or three-dimensional Navier-Stokes equations cast in conservative form in arbitrary curvilinear coordinate system using the implicit iteration scheme (Yoon & Jameson, 1987). Three gas models have been used in the calculations: perfect gas, equilibrium and nonequilibrium chemically reacting air. Flow is supposed to be laminar.

The first two cases considered are hypersonic flow of a perfect gas at wind tunnel conditions. In experiments conducted at the Central Research Institute of Machine Building

(TsNIImash) (Gubanova et al, 1992), areas of elevated heat fluxes have been found on the windward side of a delta wing with blunt edges. Here results of computations are presented which have been made to numerically reproduce the observed experimental effect.
The second case is hypersonic flow over a test model of the Pre-X demonstrator (Baiocco et al., 2006), designed to glide in the Earth's atmosphere. A comparison between thermovision experimental data on heat flux obtained in TsNIImash and calculation results is made.
As the third case a flow of dissociating air at equilibrium and nonequilibrium conditions is considered. The characteristics of flow field and convective heat transfer are presented over a winged configuration of a small-scale reentry vehicle (Vaganov et al, 2006), which was developed in Russia, at some points of a reentry trajectory in the Earth's atmosphere.

2. Basic equations

For the three-dimensional flows of a chemically reacting nonequilibrium gas mixture in an arbitrary curvilinear coordinate system:

$$\xi = \xi(x,y,z,t), \quad \eta = \eta(x,y,z,t), \quad \zeta = \zeta(x,y,z,t), \quad \tau = t$$

the Navier-Stokes equations in conservative form can be written as follows (see eg. Hoffmann & Chiang, 2000):

$$\frac{\partial \mathbf{Q}}{\partial \tau} + \frac{\partial \mathbf{E}}{\partial \xi} + \frac{\partial \mathbf{F}}{\partial \eta} + \frac{\partial \mathbf{G}}{\partial \zeta} = \mathbf{S} \tag{1}$$

$$J^{-1} = \partial(x,y,z)/\partial(\xi,\eta,\zeta), \quad \mathbf{E} = J^{-1}\left(\xi_t \mathbf{Q} + \xi_x \mathbf{E}_c + \xi_y \mathbf{F}_c + \xi_z \mathbf{G}_c\right),$$

$$\mathbf{F} = J^{-1}\left(\eta_t \mathbf{Q} + \eta_x \mathbf{E}_c + \eta_y \mathbf{F}_c + \eta_z \mathbf{G}_c\right), \quad \mathbf{G} = J^{-1}\left(\zeta_t \mathbf{Q} + \zeta_x \mathbf{E}_c + \zeta_y \mathbf{F}_c + \zeta_z \mathbf{G}_c\right)$$

Here J – Jacobian of the coordinate transformation, and metric derivatives are related by:

$$\xi_x = J\left(y_\eta z_\zeta - y_\zeta z_\eta\right), \qquad \xi_t = -x_\tau \xi_x - y_\tau \xi_y - z_\tau \xi_z, \text{ etc.}$$

Q is a vector of the conservative variables, $\mathbf{E}_c$, $\mathbf{F}_c$ and $\mathbf{G}_c$ are x, y and z components of mass, momentum and energy in Cartesian coordinate system, **S** is a source term taking into account chemical processes:

$$\mathbf{Q} = \begin{pmatrix} \rho \\ \rho u \\ \rho v \\ \rho w \\ e \\ \rho_i \end{pmatrix}; \quad \mathbf{E}_c = \begin{pmatrix} \rho u \\ \rho u^2 + p - \tau_{xx} \\ \rho uv - \tau_{xy} \\ \rho uw - \tau_{xz} \\ (e+p)u - m_x \\ \rho_i u + d_{i,x} \end{pmatrix}; \mathbf{F}_c = \begin{pmatrix} \rho v \\ \rho vu - \tau_{xy} \\ \rho v^2 + p - \tau_{yy} \\ \rho vw - \tau_{yz} \\ (e+p)v - m_y \\ \rho_i v + d_{i,y} \end{pmatrix}; \quad \mathbf{G}_c = \begin{pmatrix} \rho w \\ \rho wu - \tau_{xz} \\ \rho wv - \tau_{yz} \\ \rho w^2 + p - \tau_{zz} \\ (e+p)w - m_z \\ \rho_i w + d_{i,z} \end{pmatrix}; \quad \mathbf{S} = \begin{pmatrix} 0 \\ 0 \\ 0 \\ 0 \\ 0 \\ \omega_i \end{pmatrix}$$

$$m_x = u\tau_{xx} + v\tau_{xy} + w\tau_{xz} - q_x; \quad m_y = u\tau_{xy} + v\tau_{yy} + w\tau_{yz} - q_y; \quad m_z = u\tau_{xz} + v\tau_{yz} + w\tau_{zz} - q_z$$

where ρ, ρ_i – densities of the gas mixture and chemical species i; u, v and w – Cartesian velocity components along the axes x, y and z respectively; the total energy of the gas mixture per unit volume e is the sum of internal ε and kinetic energies:

$$e = \rho\varepsilon + \rho(u^2 + v^2 + w^2)/2$$

The components of the viscous stress tensor are:

$$\tau_{xx} = 2\mu\frac{\partial u}{\partial x} + \lambda div\mathbf{V}, \quad \tau_{yy} = 2\mu\frac{\partial v}{\partial y} + \lambda div\mathbf{V}, \quad \tau_{zz} = 2\mu\frac{\partial w}{\partial z} + \lambda div\mathbf{V}$$

$$\tau_{xy} = \mu\left(\frac{\partial u}{\partial y} + \frac{\partial v}{\partial x}\right), \quad \tau_{xz} = \mu\left(\frac{\partial u}{\partial z} + \frac{\partial w}{\partial x}\right), \quad \tau_{yz} = \mu\left(\frac{\partial v}{\partial z} + \frac{\partial w}{\partial y}\right), \quad div\mathbf{V} = \frac{\partial u}{\partial x} + \frac{\partial v}{\partial y} + \frac{\partial w}{\partial z}$$

Inviscid parts of the fluxes $\mathbf{E} = \mathbf{E}_{inv} - \mathbf{E}_v$, $\mathbf{F} = \mathbf{F}_{inv} - \mathbf{F}_v$ и $\mathbf{G} = \mathbf{G}_{inv} - \mathbf{G}_v$ in a curvilinear coordinate system have the form:

$$\mathbf{E}_{inv} = J^{-1}\begin{pmatrix} \rho U \\ \rho Uu + \xi_x p \\ \rho Uv + \xi_y p \\ \rho Uw + \xi_z p \\ (e+p)U - \xi_t p \\ \rho_i U \end{pmatrix}; \quad \mathbf{F}_{inv} = J^{-1}\begin{pmatrix} \rho V \\ \rho Vu + \eta_x p \\ \rho Vv + \eta_y p \\ \rho Vw + \eta_z p \\ (e+p)V - \eta_t p \\ \rho_i V \end{pmatrix} \quad \mathbf{G}_{inv} = J^{-1}\begin{pmatrix} \rho W \\ \rho Wu + \zeta_x p \\ \rho Wv + \zeta_y p \\ \rho Ww + \zeta_z p \\ (e+p)W - \zeta_t p \\ \rho_i W \end{pmatrix}$$

where U, V and W – velocity components in the transformed coordinate system:

$$U = \xi_t + \xi_x u + \xi_y v + \xi_z w, \quad V = \eta_t + \eta_x u + \eta_y v + \eta_z w, \quad W = \zeta_t + \zeta_x u + \zeta_y v + \zeta_z w$$

Fluxes due to processes of molecular transport (viscosity, diffusion and thermal conductivity) $\mathbf{E}_v$, $\mathbf{F}_v$ и $\mathbf{G}_v$ in a curvilinear coordinate system

$$\mathbf{E}_v = J^{-1}\begin{pmatrix} 0 \\ \xi_x\tau_{xx} + \xi_y\tau_{xy} + \xi_z\tau_{xz} \\ \xi_x\tau_{xy} + \xi_y\tau_{yy} + \xi_z\tau_{yz} \\ \xi_x\tau_{xz} + \xi_y\tau_{yz} + \xi_z\tau_{zz} \\ \xi_x m_x + \xi_y m_y + \xi_z m_z \\ -\left(\xi_x d_{i,x} + \xi_y d_{i,y} + \xi_z d_{i,z}\right) \end{pmatrix}; \quad \mathbf{F}_v = J^{-1}\begin{pmatrix} 0 \\ \eta_x\tau_{xx} + \eta_y\tau_{xy} + \eta_z\tau_{xz} \\ \eta_x\tau_{xy} + \eta_y\tau_{yy} + \eta_z\tau_{yz} \\ \eta_x\tau_{xz} + \eta_y\tau_{yz} + \eta_z\tau_{zz} \\ \eta_x m_x + \eta_y m_y + \eta_z m_z \\ -\left(\eta_x d_{i,x} + \eta_y d_{i,y} + \eta_z d_{i,z}\right) \end{pmatrix}$$

$$\mathbf{G}_v = J^{-1}\begin{pmatrix} 0 \\ \zeta_x\tau_{xx} + \zeta_y\tau_{xy} + \zeta_z\tau_{xz} \\ \zeta_x\tau_{xy} + \zeta_y\tau_{yy} + \zeta_z\tau_{yz} \\ \zeta_x\tau_{xz} + \zeta_y\tau_{yz} + \zeta_z\tau_{zz} \\ \zeta_x m_x + \zeta_y m_y + \zeta_z m_z \\ -\left(\zeta_x d_{i,x} + \zeta_y d_{i,y} + \zeta_z d_{i,z}\right) \end{pmatrix}$$

Partial derivatives with respect to x, y and z in the components of the viscous stress tensor and in flux terms, describing diffusion $\boldsymbol{d}_i = (d_{ix}, d_{iy}, d_{iz})$ and thermal conductivity $\boldsymbol{q} = (q_x, q_y, q_z)$, are calculated according to the chain rule.

2.1 Chemically reacting nonequilibrium air

In the calculation results presented in this chapter air is assumed to consist of five chemical species: N_2, O_2, NO, N, O. Vibrational and rotational temperatures of molecules are equal to the translational temperature. Pressure is calculated according to Dalton's law for a mixture of ideal gases:

$$p = \frac{\rho RT}{M_{gm}} = \sum p_i = \sum \frac{\rho_i RT}{M_i}$$

where M_{gm}, M_i – molecular weights of the gas mixture and the i-th chemical species. The internal energy of the gas mixture per unit mass is:

$$\varepsilon = \sum_i c_i h_{fi} + \sum_i c_i C_{vi} T + \sum_i c_i \varepsilon_{ei}(T) + \sum_m c_i \varepsilon_{vm}(T)$$

Here $c_i = \rho_i/\rho$, h_{fi}, ε_{ei} – mass concentration, formation enthalpy and energy of electronic excitation of species i, C_{vi} – heat capacity at constant volume of the translational and rotational degrees of freedom of species i, equal to $3/2(R/M_i)$ for atoms and $5/2(R/M_i)$ for diatomic molecules. Vibrational energy ε_{vm} of the m-th molecular species is calculated in the approximation of the harmonic oscillator. The diffusion fluxes of the i-th chemical species are determined according to Fick's law and, for example, in the direction of the x-axis have the form:

$$d_{i,x} = -\rho D_i \frac{\partial c_i}{\partial x}$$

To determine diffusion coefficients D_i approximation of constant Schmidt numbers $Sc_i = \mu/\rho D_i$ is used, which are supposed to be equal to 0.75 for atoms and molecules. Total heat flux $\boldsymbol{q}$ is the sum of heat fluxes by thermal conductivity and diffusion of chemical species:

$$q_x = -\kappa \frac{\partial T}{\partial x} + \sum_i h_i d_{i,x}; \quad h_i = C_{pi} T + \varepsilon_{vi}(T) + \varepsilon_{ei}(T) + h_{fi}$$

where h_i, C_{pi} – enthalpy and heat capacity at constant pressure of translational and rotational degrees of freedom of the i-th chemical species per unit mass. Viscosity μ and thermal conductivity κ of nonequilibrium mixture of gases are found by formulas of Wilke (1950) and of Mason & Saxena (1958).

The values of the rate constants of chemical reactions were taken from (Vlasov et al., 1997) where they were selected on the basis of various theoretical and experimental data, in particular, as a result of comparison with flight data on electron density in the shock layer near the experimental vehicle RAM-C (Grantham, 1970). Later this model of nonequilibrium air was tested in (Vlasov & Gorshkov, 2001) for conditions of hypersonic flow past the reentry vehicle OREX (Inouye, 1995).

2.2 Perfect gas and equilibrium air

In the calculations using the models of perfect gas and equilibrium air mass conservation equations of chemical species in the system (1) are absent. For a perfect gas the viscosity is determined by Sutherland's formula, thermal conductivity is found from the assumption of the constant Prandtl number Pr = 0.72. For equilibrium air pressure, internal energy, viscosity and thermal conductivity are determined from the thermodynamic relations:

$$p = p(\rho, T); \quad \varepsilon = \varepsilon(\rho, T); \quad \mu = \mu(\rho, T); \quad \kappa = \kappa(\rho, T)$$

2.3 Boundary conditions

On the body surface a no-slip condition of the flow $u = v = w = 0$, fixed wall temperature T_w = const or adiabatic wall $q_w = \varepsilon_w \sigma T_w^4$ are specified, where q_w – total heat flux to the surface due to heat conduction and diffusion of chemical species (2), $\varepsilon_w = 0.8$ – emissivity of thermal protection material, σ - Stefan-Boltzmann's constant.

Concentrations of chemical species on the surface are found from equations of mass balance, which for atoms are of the form

$$d_{i,n} + K_{i,w}\rho_i = 0; \quad K_{i,w} = \frac{2\gamma_{i,w}}{2 - \gamma_{i,w}} \sqrt{\frac{1}{2\pi} \frac{RT}{M_i}} \tag{3}$$

where $\gamma_{i,w}$ – the probability of heterogeneous recombination of the i-th chemical species.

In hypersonic flow a shock wave is formed around a body. Shock-capturing or shock-fitting approach is used. In the latter case the shock wave is seen as a flow boundary with the implementation on it of the Rankine-Hugoniot conditions, which result from integration of the Navier-Stokes equations (1) across the shock, neglecting the source term S and the derivatives along it. Assuming that a coordinate line η = const coincides with the shock wave the Rankine-Hugoniot conditions can be represented in the form $\mathbf{F}_\infty = \mathbf{F}_s$ or in more details (for a perfect gas):

$$\begin{aligned}
&\rho_s (V_{ns} - D) = \rho_\infty (V_{n\infty} - D) \\
&\rho_s (V_{ns} - D)^2 + P_s = \rho_\infty (V_{n\infty} - D)^2 + P_\infty \\
&\rho_s (V_{ns} - D) V_{\tau s} = \rho_\infty (V_{n\infty} - D) V_{\tau\infty} \\
&h_s + \frac{(V_{ns} - D)^2}{2} + \frac{V_{\tau s}{}^2}{2} = h_\infty + \frac{(V_{n\infty} - D)^2}{2} + \frac{V_{\tau\infty}{}^2}{2}
\end{aligned} \tag{4}$$

here indices ∞ and s stand for parameters ahead and behind the shock, D – shock velocity, V_τ and V_n – projection of flow velocity on the directions of the tangent **τ** and the external normal **n** to the shock wave. In (4) terms are omitted responsible for the processes of viscosity and thermal conductivity, because in the calculation results presented below the shock wave fitting is used for flows at high Reynolds numbers.

2.4 Numerical method

An implicit finite-difference numerical scheme linearized with respect to the previous time step τ_n for the Navier-Stokes equations (1) in general form can be written as follows:

$$\left[\mathbf{I} + \Delta\tau \left\{ \delta_\xi \mathbf{A} + \delta_\eta \mathbf{B} + \delta_\zeta \mathbf{C} - \mathbf{T} \right\} \right] \Delta\mathbf{Q} = -\Delta\tau \mathbf{R}^n \tag{5}$$

$$\mathbf{R}^n = \delta_\xi \mathbf{E} + \delta_\eta \mathbf{F} + \delta_\zeta \mathbf{G} - \mathbf{S}; \quad \mathbf{A} = (\partial\mathbf{E}/\partial\mathbf{Q})^n; \quad \mathbf{B} = (\partial\mathbf{F}/\partial\mathbf{Q})^n; \quad \mathbf{C} = (\partial\mathbf{G}/\partial\mathbf{Q})^n; \quad \mathbf{T} = (\partial\mathbf{S}/\partial\mathbf{Q})^n$$

Here symbols δ_ξ, δ_η and δ_ζ denote finite-difference operators which approximate the partial derivatives $\partial/\partial\xi$, $\partial/\partial\eta$ and $\partial/\partial\zeta$, the index and indicates that the value is taken at time τ_n, **I** – identity matrix, $\Delta\mathbf{Q} = \mathbf{Q}^{n+1} - \mathbf{Q}^n$ – increment vector of the conservative variables at time-step $\Delta\tau = \tau_{n+1} - \tau_n$.

Let us consider first the inviscid flow. Yoon & Jameson (1987) have proposed a method of approximate factorization of the algebraic equations (5) – Lower-Upper Symmetric Successive OverRelaxation (LU-SSOR) scheme. Suppose that in the transformed coordinates (ξ, η, ζ) the grid is uniform and grid spacing in all directions is unity $\Delta\xi=\Delta\eta=\Delta\zeta=1$. Then the LU-SSOR scheme at a point (i,j,k) of a finite-difference grid can be written as:

$$\mathbf{L}\mathbf{D}^{-1}\mathbf{U}\Delta\mathbf{Q} = -\mathbf{R}^n \tag{6}$$

$$\mathbf{L} = \mathbf{D} + \mathbf{L}^*, \quad \mathbf{U} = \mathbf{D} + \mathbf{U}^*, \quad \mathbf{D} = \left\{ \frac{1}{\Delta\tau} + \beta(\rho_\mathbf{A} + \rho_\mathbf{B} + \rho_\mathbf{C}) \right\} \mathbf{I} - \mathbf{T}$$

$$\mathbf{L}^* = -\mathbf{A}^+_{i-1,j,k} - \mathbf{B}^+_{i,j-1,k} - \mathbf{C}^+_{i,j,k-1}, \quad \mathbf{U}^* = \mathbf{A}^-_{i+1,j,k} + \mathbf{B}^-_{i,j+1,k} + \mathbf{C}^-_{i,j,k+1}$$

where

$$\mathbf{A}^\pm = (\mathbf{A} \pm \beta\rho_\mathbf{A}\mathbf{I})/2; \qquad \rho_\mathbf{A} = U + a\sqrt{\xi_x^2 + \xi_y^2 + \xi_z^2}$$

$$\mathbf{B}^\pm = (\mathbf{B} \pm \beta\rho_\mathbf{B}\mathbf{I})/2; \qquad \rho_\mathbf{B} = V + a\sqrt{\eta_x^2 + \eta_y^2 + \eta_z^2}$$

$$\mathbf{C}^\pm = (\mathbf{C} \pm \beta\rho_\mathbf{C}\mathbf{I})/2; \qquad \rho_\mathbf{C} = W + a\sqrt{\zeta_x^2 + \zeta_y^2 + \zeta_z^2}$$

Here the indices of the quantities at the point (i,j,k) are omitted for brevity, $\beta \geq 1$ is a constant, ρ_A, ρ_B, ρ_C – the spectral radii of the "inviscid" parts of the Jacobians **A**, **B** и **C**, a – the speed of sound. Inversion of the equation system (6) is made in two steps:

$$\mathbf{L}\Delta\mathbf{Q}^* = -\mathbf{R}^n \tag{7a}$$

$$\mathbf{U}\Delta\mathbf{Q} = \mathbf{D}\Delta\mathbf{Q}^* \tag{7b}$$

It is seen from (6) that for non chemically reacting flows (**S**=0, **T**=0) LU-SSOR scheme does not require inversion of any matrices. For reacting flows due to the presence of the Jacobian of the chemical source **T**≠0, the "forward" and "back" steps in (7) require, generally speaking, matrix inversion. However, calculations have shown that if the conditions are not too close to equilibrium then in the "chemical" Jacobian **T** one can retain only diagonal terms which contain solely the partial derivatives with respect to concentrations of chemical species. In this approximation, scheme (6) leads to the scalar diagonal inversion also for the case of chemically reacting flows. Thus calculation time grows directly proportionally to the number of chemical species concentrations. This is important in calculations of complex flows of reacting gas mixtures, when the number of considered chemical species is large.

In the case of viscous flow, so as not to disrupt the diagonal structure of scheme (6), instead of the "viscous" Jacobians $\mathbf{A}_v$, $\mathbf{B}_v$ и $\mathbf{C}_v$ their spectral radii are used:

$$\rho_{\mathbf{A}v} = \frac{\gamma}{\mathrm{Pr}}\frac{\mu}{\rho}\left(\xi_x^2 + \xi_y^2 + \xi_z^2\right); \quad \rho_{\mathbf{B}v} = \frac{\gamma}{\mathrm{Pr}}\frac{\mu}{\rho}\left(\eta_x^2 + \eta_y^2 + \eta_z^2\right); \quad \rho_{\mathbf{C}v} = \frac{\gamma}{\mathrm{Pr}}\frac{\mu}{\rho}\left(\zeta_x^2 + \zeta_y^2 + \zeta_z^2\right)$$

In the finite-difference equation (6) central differences are employed, both for viscous and convective fluxes. The use of central differences to approximate the convective terms can cause non-physical oscillations of the flow parameters at high Reynolds numbers. To suppress such numerical oscillations artificial dissipation terms were added in the right part **R** of (6) according to Pulliam (1986). In calculations presented below it was assumed that the derivatives $\partial\xi/\partial t$, $\partial\eta/\partial t$ and $\partial\zeta/\partial t$ are zero and $\Delta\tau = \infty$. Since steady flow is considered, these assumptions do not affect the final result.

3. Calculation results

3.1 Flow and heat transfer on blunt delta wing

In thermovision experiments (Gubanova et al, 1992) in hypersonic flow past a delta wing with blunt nose and edges two regions of elevated heat were observed on its windward surface. At a distance of approximately 12-15 r from the nose of the wing (r – nose radius) there were narrow bands of high heat fluxes which extended almost parallel to the symmetry plane at a small interval (3-5 r) from it to the final section of the wing at $x \approx 100\,r$ (see Fig. 1, in which the calculated distribution of heat fluxes is shown at the experimental conditions). The level of heat fluxes in the bands was approximately twice the value of background heat transfer corresponding to the level for a delta plate with sharp edges under the same conditions. It turned out that this effect exists in a fairly narrow range of flow parameters. In particular, on the same wing but with a sharp tip a similar increase in heat flux was not observed. This effect was explained by the interaction of shock waves arising at the tip and on the blunt edges of the wing (Gubanova et al, 1992; Lesin & Lunev, 1994). In this section numerical results calculated for the experimental conditions are presented and compared with measured heat flux values (see also (Vlasov et al., 2009)).

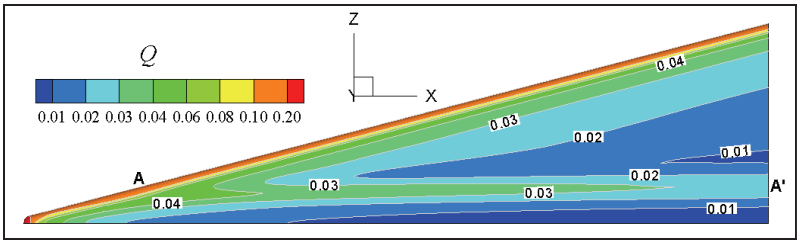

Fig. 1. Calculated distribution of non-dimensional heat flux $Q = q/q_0$ on the windward side of the blunt delta wing. q_0 – heat flux at the stagnation point of a sphere with a radius equal to the nose radius of the wing

Perfect gas hypersonic flow ($\gamma = 1.4$) past a delta wing with a spherical nose and cylindrical edges of the same radius is considered. Mach and Reynolds numbers calculated with free stream flow parameters and the wing nose radius are $M_\infty = 14$ and $Re_\infty = 1.4 \cdot 10^4$, angle of attack $\alpha = 10°$, wing sweep angle $\lambda = 75°$. The free stream stagnation temperature $T_{0\infty} = 1205$ K, the wall temperature $T_w = 300$ K. Due to the symmetry of flow, only half of the wing is computed. The flow calculation was performed with shock-fitting procedure, the computational grid is 120×40×119 (in the longitudinal, transverse and circumferential

directions, respectively, see Fig. 2). Below in this section all quantities with a dimension of length, unless otherwise specified, are normalized to the wing nose radius r.

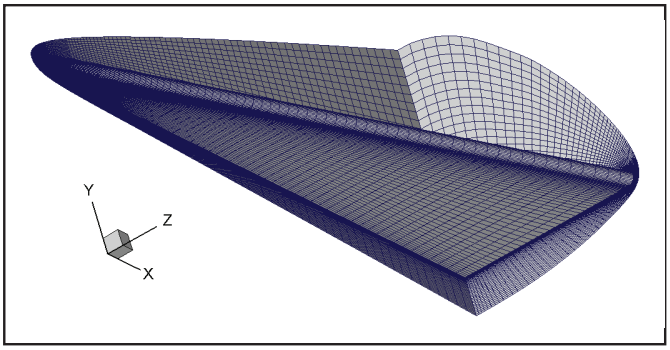

Fig. 2. The computational grid on the wing surface, in the plane of symmetry (z = 0) and in the exit section for the converged numerical solution

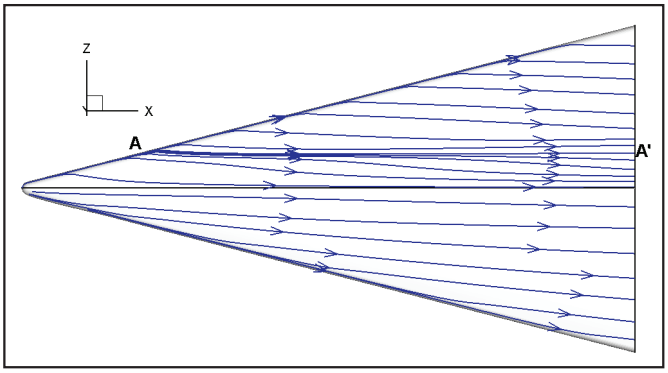

Fig. 3. Streamlines near the windward surface of the wing. Top – at a distance of one grid step from the wall, bottom – at the outer edge of the boundary layer

Calculated patterns of streamlines near the windward surface of the wing at a distance of one grid step from the wall and at the outer edge of the boundary layer are shown in Fig. 3. The streamlines, flowing down from the wing edge on the windward plane at almost constant pressure, form the line of diverging flow (line **A-A'**), along which there are bands of elevated heat fluxes. At the symmetry plane a line of converging streamlines is realized along the entire length of the wing, but upstream the shock interaction point **A** flow impinges on the symmetry plane from the edges, and downstream from **A** – from the diverging line **A-A'**. A characteristic feature of the considered case is that the distribution of heat fluxes on the windward side is mainly determined by the values of convergence and divergence of streamlines at almost constant pressure (see Fig. 4, which shows the distribution of pressure and heat flux on the windward side in several sections x = const). Local maxima of heat fluxes near symmetry plane appear only at x> 15 near the line z = 4 (after the nose shock wave intersects with the shock wave from the edges) and the relative intensity of these heat peaks grows with increasing distance from the nose (Fig. 4b).

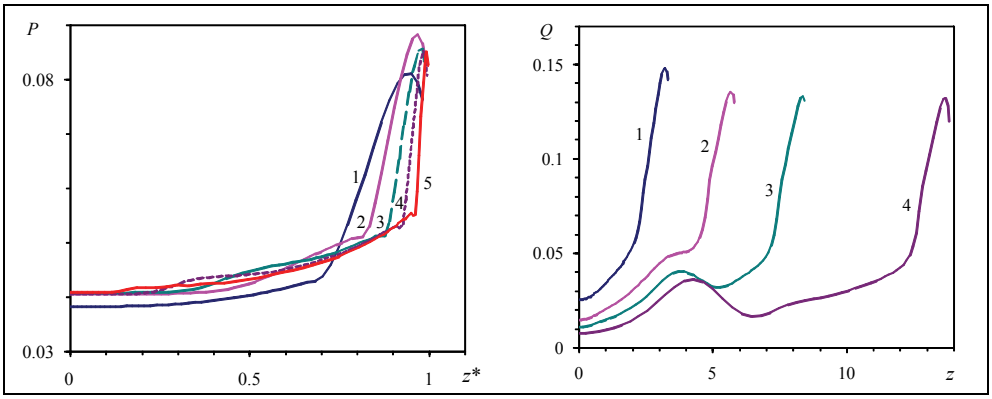

(a) (b)

Fig. 4. Pressure distribution $P = p/\rho_\infty V_\infty^2$ (a) and heat flux $Q = q/q_0$ (b) on windward side of wing in sections: 1-5 – x = 10, 20, 30, 50, 90, $z^* = z/z_{max}$, z_{max} – wingspan in section x = const

Comparison of the upper and lower parts of Fig. 3 shows that the flow near the wall and at the outer edge of the boundary layer are noticeably different, the streamlines near the wall are directed to the symmetry plane (converging), and in inviscid region – from it (diverging). It follows that the velocity component directed along the wing chord changes sign across the boundary layer, which indicates the existence of transverse vortex (cross separation flow) in the boundary layer. This is illustrated in Fig. 5a, which shows the projection of streamlines on the plane of the cross section at x = 90.

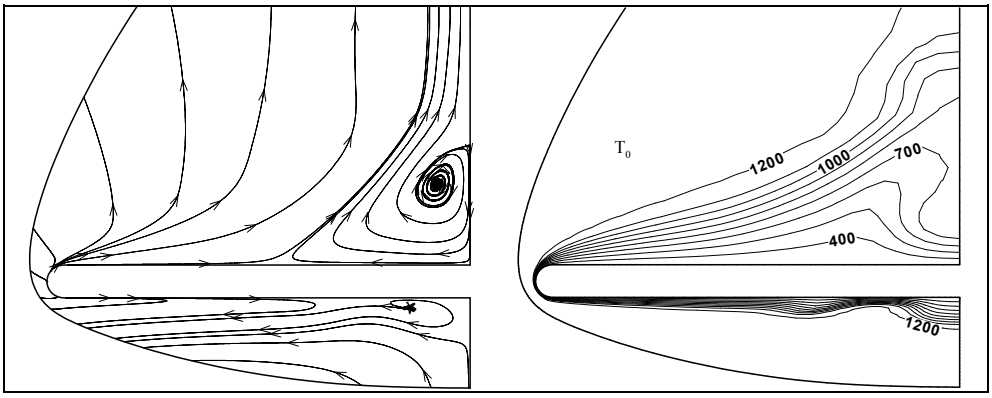

(a) (b)

Fig. 5. Projection of streamlines (a) and isolines of stagnation temperature T_0, K (b) in cross section x = 90

The distribution of the boundary layer thickness is clearly seen in Fig. 5b, which shows the contours of the stagnation temperature T_0 in the cross section x = 90. On the windward side of the wing minimum thickness of the boundary layer is located on the diverging line (line **A-A'** in Fig. 3). On the left and on the right sides of the diverging line there are converging lines with a thicker boundary layer (about 2 and 3 times respectively). One of the

converging lines is the symmetry plane. Here the boundary layer thickness on the windward side reaches a maximum, amounting to about one-third of the shock layer thickness.

Near the wing edge because of the expansion and acceleration of the flow the boundary layer thickness decreases sharply (at the edge it is almost 20 times less than at the symmetry plane on the windward side). On the leeward side of the wing flow separation occurs, and the concept of the boundary layer loses its meaning. Here scope of viscous flow is half the shock layer.

The shape of calculated shock wave in Fig. 6a, induced by the wing nose as a blunt body, is determined by the law of the explosive analogy, so that some front part of the wing $x \le x_A \approx 15$ will be located inside the initially axisymmetric shock wave. The coordinate of point **A** (x_A) is located in the vicinity of interaction region of shock waves induced by the nose and the edges of the wing. Here the profiles of pressure and heat flux along the edge are local maxima.

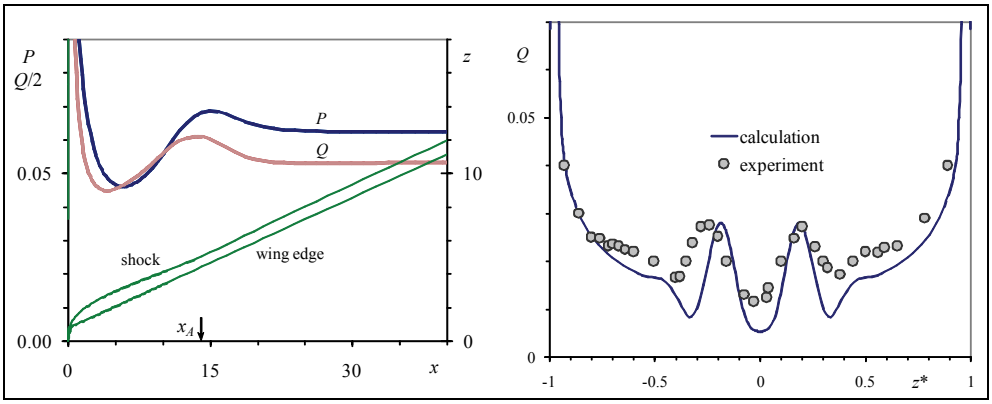

Fig. 6. Profiles of pressure, heat flux and the shock wave along the wing edge (a) and distribution of heat fluxes in cross section x = 90 (b)

In Fig. 6b the distribution of computed heat fluxes q/q_0 in the neighborhood of the wing end section at x = 90 is presented in comparison with the experiment of Gubanova et al. (1992) depending on the transverse coordinate z. On the whole the calculation correctly predicts the magnitude and position of local maximum of heat flux near the symmetry plane, taking into account the small asymmetry in the experimental data. Note that near the minima of heat fluxes calculated values are lower than experimental ones, probably due to effect of smoothing of experimental data in these narrow regions.

3.2 Heat transfer on test model of Pre-X space vehicle

Currently developed hypersonic aircraft have dimensions several times smaller than previously created space vehicles "Shuttle" and "Buran". This results in increase of heat load on a vehicle during flight, and therefore the problem of reliable calculation of heat fluxes on the surface for such relatively small bodies is particularly important. Thus the problem arises of verification of the employed physical models and numerical methods by comparing calculation results with experimental data.

In 2006-2007 on TsNIImash's experimental base in a piston gasdynamic wind tunnel PGU-7 a heat transfer study has been conducted on a small-scale model of Pre-X reentry demonstrator (Baiocco, 2006). This vehicle is designed to obtain in flight conditions experimental data pertaining to aerothermodynamic phenomena that are not modeled in ground tests, but they are critical for design of a vehicle returning from the Earth's orbit. In particular, Pre-X demonstrator is developed to test in a real flight and in specified locations on the vehicle surface samples of reusable thermal protection materials and to assess their durability.

During the study thermovision measurements have been conducted of heat fluxes on the model of scale 1/15 at various flow regimes – M = 10, Re = $1 \cdot 10^6$-$5 \cdot 10^6$ 1/m (Kovalev et al., 2009). Processing of thermovision measurements was carried out in accordance with standard technique and composed of determination of the model surface temperature during experiment, extraction from these data distributions of heat fluxes on the observed model surface and binding of the resulting thermovision frame to a three-dimensional CAD model of the demonstrator. The same CAD model has been used for numerical simulation of heat transfer on the Pre-X test model.

As a normalizing value the heat flux q_0 at the stagnation point of a sphere with radius of 70 mm is adopted, which is determined using the Fay-Riddell formula. Advantage of data presentation in this form is due to invariability of the relative values $Q = q/q_0$ on most model surface at variations of flow parameters.

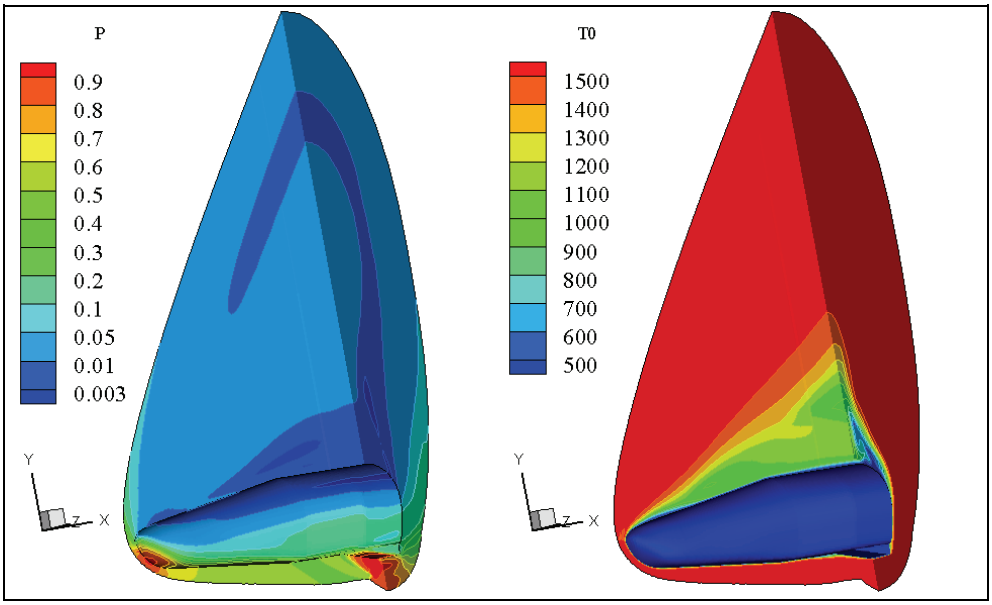

Fig. 7. Calculated distributions of pressure $P = p/\rho_\infty V_\infty^2$ (left) and stagnation temperature T_0, K (right) on surface and in shock layer (in symmetry plane and in exit section) for test model of Pre-X vehicle

On the base of the numerical solution of the Navier-Stokes equations a study was carried out of flow parameters and heat transfer for laminar flow over a test model of Pre-X space

vehicle for experimental conditions in the piston gasdynamic wind tunnel. Mach and Reynolds numbers, calculated from the free-stream parameters and the length of the model (330 mm), are $M_\infty = 10$ and $Re_\infty = 7 \cdot 10^5$. Angle of attack – 45°. The flap deflection angle was (as in the experiment) $\delta = 5$, 10 and 15°. The stagnation temperature of the free-stream flow and the wing surface temperature – $T_{0\infty} = 1000$ K and $T_w = 300$ K, respectively. An approximation of a perfect gas was used with ratio of specific heats $\gamma = 1.4$. The calculations were performed with a shock-fitting procedure, i.e. the bow shock was considered as a discontinuity with implementation of the Rankine-Hugoniot relations (4) across it. On the model surface no-slip and fixed temperature conditions were set. Note that in view of the flow symmetry computations were made only for a half of the model, although in the figures below for comparison with experiment the calculated data (upon reflection in the symmetry plane) are presented on the entire model.

The overall flow pattern obtained in the calculations over the test model of Pre-X space vehicle is shown in Fig. 7, where for the case of the flap deflection angle $\delta = 15°$ pressure and stagnation temperature T_0 isolines in the shock layer and on the model surface are shown. It is seen that there are two areas of high pressure: on the nose tip of the model ($P \approx 0.92$) and on the deflection flaps. In the latter case the pressure in the flow passing through the two shock waves reaches $P \approx 1.3$. Isolines of T_0 show the size of regions where viscous forces are significant: a thin boundary layer on the windward side of the model and an extensive separation zone on the leeward side. The small separation zone, appearing at deflection flaps, although about four times thicker than the boundary layer upstream of it is almost not visible in the scale of the figure.

Fig. 8 shows the distributions of relative heat flow Q on the windward side of the model obtained in the experiments and in the calculations at deflection angles of flaps $\delta = 5$, 10 and 15°. For the case $\delta = 5°$ it can be noted rather good agreement between experiment and calculation in the values of heat flux in the central part of the model and on the flaps. It is evident that before deflected flaps there is a region of low heat fluxes caused by near separation state (according to calculation results) of the boundary layer.

In analyzing the experimental data it should be taken into account the effect of "apparent" temperature reduction of the surface area with a large angle to the thermovision observation line. It is precisely this effect that explains the fact that in the nose part of the model the experimental values of heat flux are less than the calculated ones. Also narrow zones of high (at the sharp edges of the flaps) or low (in the separation zone at the root of the flaps) values of heat flux are smoothed or not visible in the experiment due to insufficient resolution of thermovision equipment. The resolution capability of thermovisor is clearly visible by the size of cells in the experimental isoline pattern of heat flux in Fig. 8. It should be noted that the calculations do not take into account a slit between the deflection flaps available on the test model, the presence of which should lead to a decrease in the separation region in front of the flaps.

At an angle of flap deflection $\delta = 10°$, as in the previous case $\delta = 5°$, there is fairly good agreement between calculation and experiment for the values of heat flux in the central part of the model and on the flaps. The calculations show that the growth of the flap deflection angle δ from 5° to 10° results in the formation of a large separation zone in front of the flaps and in a decrease in heat flux value Q from 0.2 to 0.1.

At the largest angle of flap deflection $\delta = 15°$ the maximum of calculated heat flux occurs in the zone of impingement of the separated boundary layer, where the level of Q is 2-3 times higher than its level on the undeflected flap. The coincidence of calculation results with

experimental data in the front part of the model up to the separation zone before the flaps is satisfactory. On the flaps the level of heat flux in the experiment is about one and a half times more than in the calculation. This difference in heat flux values is apparently due to laminar-turbulent transition in separation region induced by the deflected flaps which takes place in the experiment.

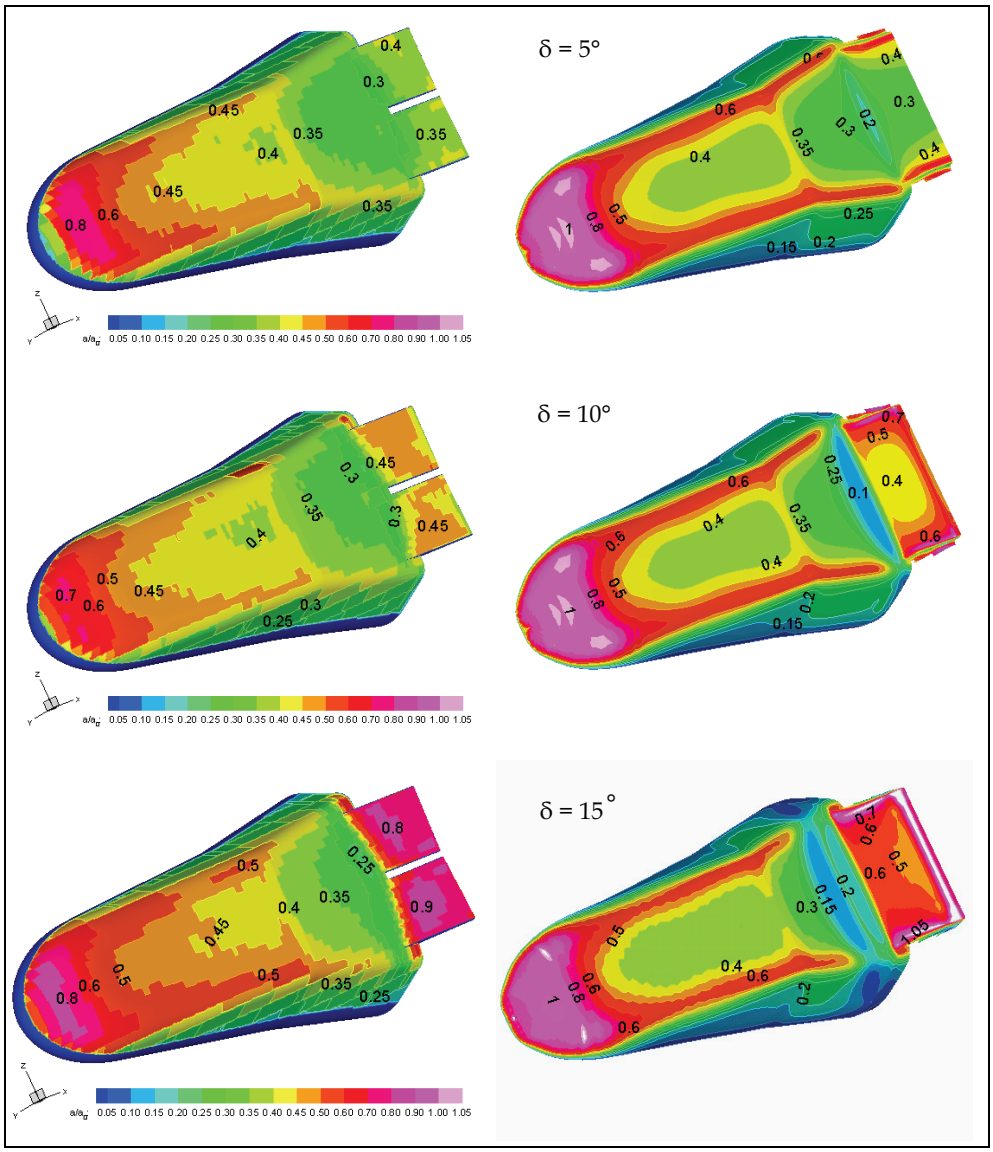

Fig. 8. Experimental (left) and calculated (right) heat fluxes $Q = q/q_0$ on windward side of test model of Pre-X space vehicle at different deflection angles of flaps δ.

3.3 Flow and heat transfer on a winged space vehicle at reentry to Earth's atmosphere

This section presents the results of numerical simulation of flow and heat transfer on a winged version of the small-scale reentry vehicle, being developed in TsAGI (Vaganov et al, 2006), moving at hypersonic speed in the Earth's atmosphere. Calculations were made using two physical-chemical models of the gas medium - equilibrium and non-equilibrium chemically reacting air.

The bow shock was captured in contrast to the previous two flow cases. Thus on the inflow boundary the free-stream conditions were specified. On the vehicle surface no-slip and adiabatic wall conditions were supposed. In calculations with use of the nonequilibrium air model the vehicle surface was supposed to be low catalytical with the probability of heterogeneous recombination of O and N atoms equal to $\gamma_A = 0.01$.

A computational grid was provided by Mikhalin V.A. (Dmitriev et al., 2007), and was taken from the inviscid flow calculation. The number of points in the direction normal to the vehicle surface has been increased to resolve the wall boundary layer. Part of the results presented below was reported in (Dmitriev et al., 2007; Gorshkov et al., 2008a).

Calculations were performed for two points of a reentry trajectory, for which thermal loads are close to maximum (Table 1). The angle of attack $\alpha = 35°$, the vehicle length $L = 9$m. A grid 93×50×101 in the longitudinal, transverse and circumferential directions respectively were used in the calculations. The surface grid of the vehicle is shown in Fig. 9.

H, km	V_∞, m/sec	$\mathbf{Re}_{\infty,L}$	$\mathbf{M}_\infty$	P_∞, atm	T_∞, K
70	5952	$3.46 \cdot 10^5$	20.0	$5.76 \cdot 10^{-5}$	219
63	5152	$6.84 \cdot 10^5$	16.6	$1.59 \cdot 10^{-4}$	243

Table 1. Parameters of trajectory points

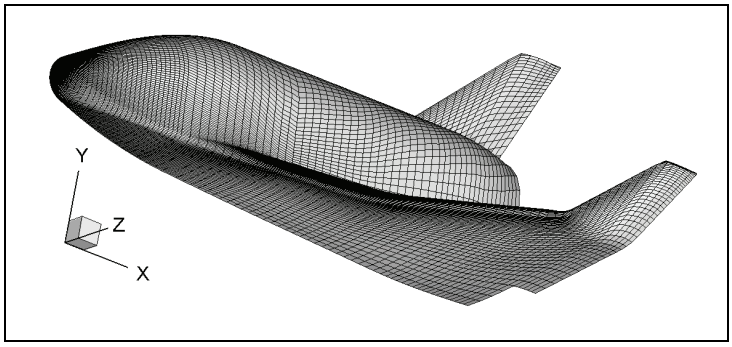

Fig. 9. Surface grid of the small-scale reentry vehicle

In Fig. 10a contours of total enthalpy H_0 on the surface and in the shock layer near the reentry vehicle are shown. On the windward side one can see the shock wave, the thin wall boundary layer and the inviscid flow between them, in which the values of H_0 are constant. In the calculations the shock wave is smeared upon 3-5 grid points and has a finite thickness due to the use of artificial dissipation. In particular, a local decrease in H_0 in a strong shock

wave on the windward side, which can be seen in the figure, has no physical meaning and is due to the influence of artificial dissipation. Recall that the Navier-Stokes equations do not correctly describe the shock structure at Mach numbers M> 1.5.

In the shock layer on the leeward side it is visible a large area with reduced values of total enthalpy $H_0<H_{0\infty}$ ($H_{0\infty}$ – total enthalpy in the free-stream), which arises as a result of boundary layer separation from the vehicle surface.

Chemical processes occurring in the shock layer over the vehicle are illustrated in Fig. 10b, which shows contours of mass concentrations of oxygen atoms c_o. Under the considered conditions in the vicinity of the vehicle nose behind the shock wave O_2 dissociation is complete. On the windward side downstream the nose in the shock layer and on the surface the recombination occurs and the concentration of O decreases. In contrast, on the leeward side where the flow is very rarefied, the level of c_o remains high, indicating that the process of recombination of atomic oxygen is frozen.

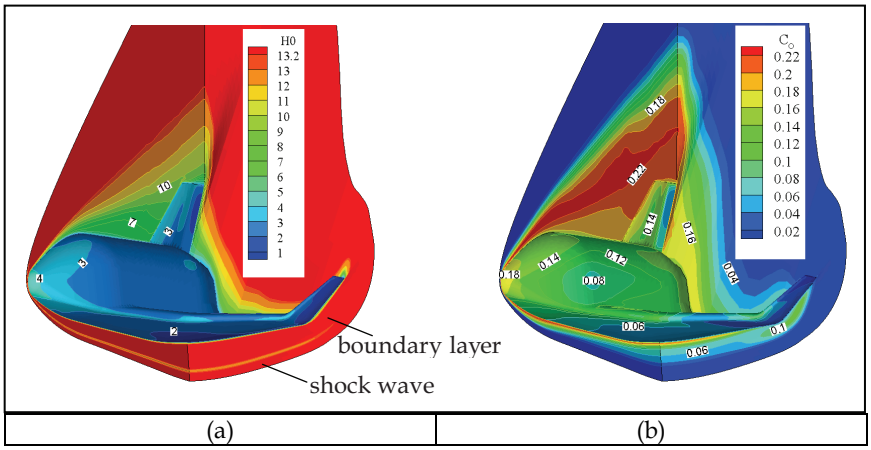

Fig. 10. Total enthalpy, MJ/kg (a), and mass concentration of oxygen atoms (b) on the surface and in the shock layer near the vehicle. H = 63 km

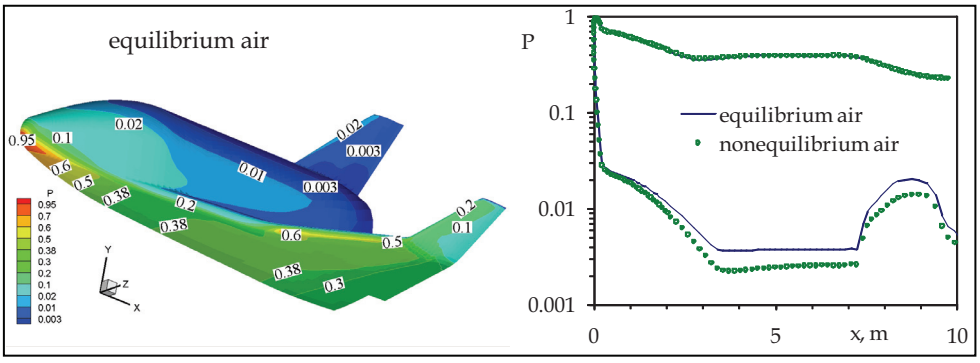

Fig. 11. Pressure distribution $P = p/\rho_\infty V_\infty^2$ on vehicle surface, overall view (left) and in symmetry plane (right), H = 63 km

In Fig. 11 and 12 isolines of pressure, heat flux q_w and equilibrium radiation temperature T_w on the vehicle surface are shown for cases of equilibrium and non-equilibrium dissociating air. Comparison of q_w and T_w distributions on the vehicle surface in the symmetry plane for two air models are depicted in Fig. 13.

Analysis of the calculation results shows that pressure distribution on the windward surface of the vehicle does not depend on physical-chemical model of the gas medium - the difference in pressure values for equilibrium and non-equilibrium air flow is 1 - 2%. On the leeward side pressure on the surface for nonequilibrium flow may be nearly two times lower than for equilibrium flow (e.g., in the vicinity of the tail). This is probably due to the fact that the effective ratio of specific heats for nonequilibrium air is greater than for equilibrium air, because in the shock layer on the leeward side nonequilibrium flow is chemically frozen, and here there is a sufficiently high concentration of atoms (see Fig. 10b).

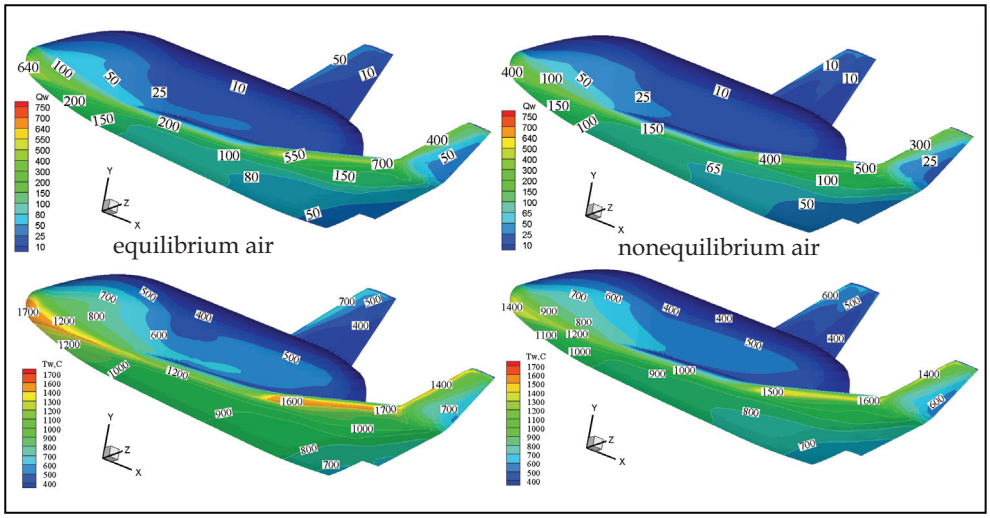

Fig. 12. Distributions of heat flux q_w, kW/m², (top) and equilibrium radiation temperature T_w,°C, (bottom) on the vehicle surface, H = 63 km

Nonequilibrium chemical processes in the shock layer and finite catalytic activity of the vehicle surface (γ_A = 0.01) significantly reduce the calculated levels of heat transfer in comparison with the case of equilibrium air flow. The most significant decrease in heat flux is observed on the vehicle nose part (for $x \le 1$ m) and in the vicinity of the tail. For example, at the nose stagnation point the level of heat flux decreases by about 40% – from 640 to 385 kW/m², while the surface temperature decreases by nearly 15% – from 1670 to 1430 °C.

Note a high heat flux level on the thin edge of the wing compared with one at the nose stagnation point. Particularly intense heating occurs at the sharp bend of the wing where the values of heat flux and surface temperature even slightly exceed their values at the front stagnation point. In the case of equilibrium air flow the exceeding for heat flux is about 10% (710 and 640 kW/m²), for temperature - 3% (1720 and 1670 °C). In the case of nonequilibrium air flow the exceeding is more significant, for heat flux - 30% (540 and 385 kW/m²), for temperature - 10% (1570 and 1430 ° C).

In other parts of the vehicle surface difference in heat flux levels for the two air models is somewhat less, and it decreases downstream, presumably due to gradual recombination of atoms in the boundary layer at flowing along the surface in case of non-equilibrium air.

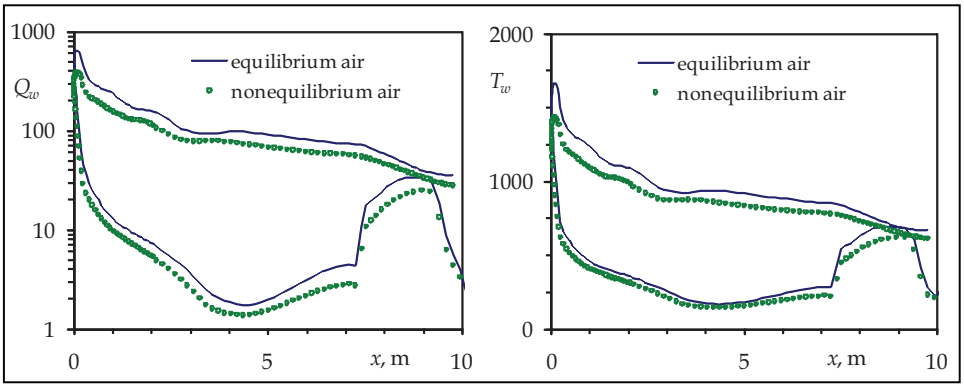

Fig. 13. Profiles of heat flux q_w, kW/m², (left) and equilibrium radiation temperature T_w,°C, (right) on vehicle surface in symmetry plane, H = 63 km

A similar flow and heat flux patterns are observed for the altitude H = 70 km, as seen in Fig. 14 where contours of heat flux and equilibrium radiation wall temperature are shown at this altitude for the two air models. For equilibrium air overall level of heat flux at 70 km is slightly higher than at 63 km. For example heat flux value at the nose stagnation point is increased by 5% (675 compared with 640 kW/m²). The opposite situation occurs for the model of nonequilibrium air, in this case the stagnation point heat flux value at 70 km is lower than at 63 km – by 7% (360 and 385 kW/m² respectively).

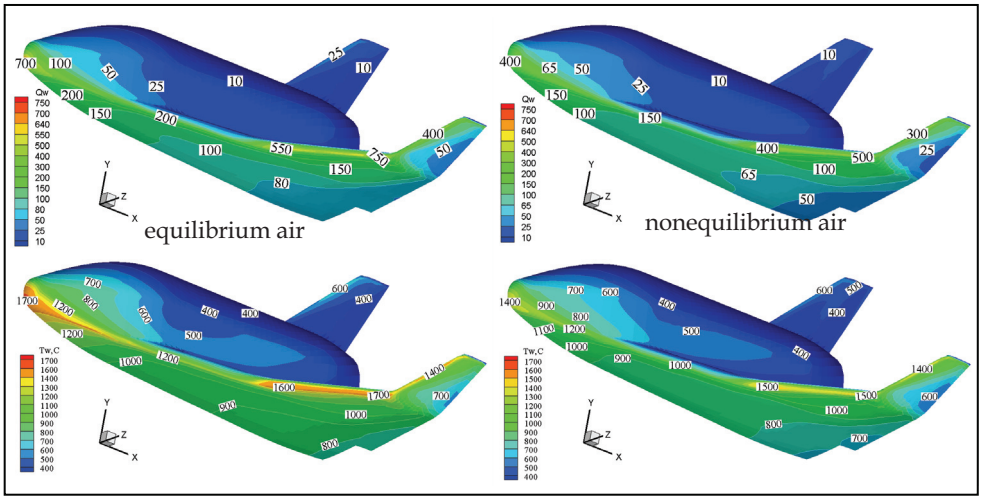

Fig. 14. Distributions of heat flux q_w, kW/m², (top) and equilibrium radiation temperature T_w,°C, (bottom) on the vehicle surface, H = 70 km

4. Conclusion

A three-dimensional stationary Navier–Stokes computer code for laminar flow, developed by the author, has been briefly described. The code is mainly intended to calculate super- and hypersonic flows over bodies accounting for high temperature real gas effects with special emphasis on convective heat transfer. Three gas models: perfect gas, equilibrium and nonequilibrium gas mixture can be used in the calculations.

In the chapter a comparison of code calculation results with experimental data is made for two perfect gas hypersonic flow cases at wind tunnel conditions. First case is a simulation of an anomalous heat transfer on the windward side a delta wing with blunt edges. On the whole the calculation correctly predicts the magnitude and position of local maximum of heat flux near the wing symmetry plane, taking into account a small asymmetry in the experimental data. Second case is a computation of heat transfer on a test model of the Pre-X demonstrator. Satisfactory agreement with thermovision heat fluxes on the smooth windward side and on the flaps is obtained, except for the largest deflection angle of flaps $\delta = 15°$ when the level of heat flux in the experiment is about one and a half times more than in the calculation. This discrepancy is apparently due to laminar-turbulent transition in separation region induced by the deflected flaps which takes place in the experiment.

Third flow case concerns chemically reacting air flow at equilibrium or nonequilibrium conditions. Flowfield and convective heat transfer parameters for a winged shape of a small-scale reentry vehicle are calculated for two points of a reentry trajectory in the Earth's atmosphere. Heat flux and equilibrium radiation temperature distributions on the vehicle surface are obtained. Also regions of maximal thermal loadings are localized.

Calculations show that for nonequilibrium air flow the use of a low catalytic coating (with probability of heterogeneous recombination of atoms $\gamma_A = 0.01$) on the vehicle surface enables to decrease considerably the level of heat fluxes in regions of maximal heat transfer in the nose part and on the wing edges in comparison with equilibrium air flow. For example for trajectory points with maximal thermal load a reduction of up to 40% in heat flux (which results in a 15% reduction of equilibrium radiation wall temperature) can be obtained at the vehicle nose.

5. Acknowledgments

The author is grateful to Kovalev R.V., Marinin V.P. and Vlasov V.I. for delivering thermovision data on test model of Pre-X vehicle, and also to Churakov D.A. and Mihalin V.A. for providing computational grids.

6. References

Baiocco, P.; Guedron, S.; Plotard, P. & Moulin, J. (2006). The Pre-X atmospheric re-entry experimental lifting body: Program status and system synthesis, *Proceedings of 57th International Astronautical Congress*, 2-6 October 2006. IAC-06-D2.P.2.2

Churakov, D.A.; Gorshkov, A.B.; Kovalev, R.V.; Vlasov, V.I.; Beloshitsky, A.V.; Dyadkin, A.A. & Zhurin, S.V. (2008). Heat Transfer of Reentry Vehicles during Atmosphere Flight, *Proceedings of 6-th* European *Symposium on Aerothermodynamics for Space Vehicles,* Versailles, France, 3 - 6 November 2008.

Dmitriev, V.G.; Vaganov, A.V.; Gorshkov, A.B.; Lapygin, V.I.; Galaktionov, A.Yu. & Mikhalin, V.A. (2007). Analysis of Aerothermodynamic Parameters of Reusable Space Wing Vehicle, *Proceedings of 2nd European Conference for Aero-Space Sciences,* Brussels, Belgium, July 1-6 2007

Gorshkov A.B. (1997) Calculation of Base Heat Transfer Behind Thin Cone-Shaped Bodies. *Cosmonautics and Rocket Engineering*, No. 11, (1997) pp. 13-20 (in Russian)

Gorshkov, A.B.; Kovalev, R. V.; Vlasov, V. I. & Zemlyanskiy, B. A. (2008a). Simulation of Heat Transfer to Space Vehicles during a Gliding Reentry into Earth's Atmosphere, *Proceedings of 14th International Conference on Methods of Aerophysical Research (ICMAR-2008),* Novosibirsk, Russia, 30 June - 06 July 2008

Gorshkov, A.B.; Kovalev, R. V.; Vlasov & V. I., Zemlyanskiy, B. A. (2008b). Heat Transfer Investigation for Hypersonic Flow over Experimental Model of Pre-X Reentry Vehicle, *Proceedings of 7th Sino-Russian High-Speed Flow Conference (SRHFC-7)*, Novosibirsk, Russia, 1 - 3 July 2008

Grantham W.L. (1970). Flight results of a 25,000 fps re-entry experiment, *NASA TN D 6062*.

Gubanova, O.I.; Zemlyansky, B.A.; Lessin, A.B.; Lunev, V.V.; Nikulin, A.N. & Syusin A.V. (1992). Anomalous heat transfer on the windward side of a delta wing with a blunt tip in hypersonic flow, In: *Aerothermodynamics of aerospace systems*, Pt. 1, pp. 188-196, Moscow, TsAGI (in Russian)

Hoffmann, K.A.; Chiang, S.T. (2000). *Computational fluid dynamics*, Vol. 2, Engineering Educational Systems, ISBN 0-9623731-3-3, Kansas, USA

Inouye, Y. (1995). OREX flight – quick report and lessons learned. *Proceedings of 2nd European Symposium on Aerothermodynamics for Space Vehicles,* pp. 271-279, ESTEC, Noordwik, The Netherlands, Europe Space Agency (November 1994).

Kovalev, R.V.; Kislykh, V.V.; Kolozezniy, A.E.; Kudryavtsev, V.V.; Marinin, V.P.; Vlasov, V.I. & Zemliansky, B.A. (2009). Experimental studies of Pre-X vehicle heat transfer in PGU-7 test facility, *3rd European Conference for Aerospace Sciences (EUCASS-2009)*, Versailles, France, 6-9 July 2009

Lesin, A.B. & Lunev, V.V. (1994). Heat transfer peaks on a blunt-nosed triangular plate in hypersonic flow. *Fluid Dynamics,* Vol. 29, No. 2, (April 1994) pp. 258-262, ISSN: 0015-4628

Mason, E.A. & Saxena, S.C. (1958). Approximate Formula for the Thermal Conductivity of Gas Mixtures. *Phys. Fluids*, Vol. 1, No. 5, (1958) pp. 361-369

Pulliam, T.H. (1986). Artificial dissipation models for the Euler equations. *AIAA Journal,* Vol.24, No. 12, (December 1986) pp. 1931-1940, ISSN: 0001-1452

Vaganov, A.V.; Dmitriev, V.G.; Zadonsky, S.M.; Kireev, A.Y.; Skuratov, A.S. & Stepanov, E.A. (2006). Estimations of low-sized winged reentry vehicle heat regimes on the stage of its designing. *Physico-chemical kinetics in gas dynamics*, www.chemphys.edu.ru/pdf/2006-11-20-002.pdf (in Russian)

Vlasov, V.I.; Gorshkov, A.B.; Kovalev, R.V. & Plastinin, Yu.A. (1997). Theoretical studies of air ionization and NO vibrational excitation in low density hypersonic flow around re-entry bodies. *AIAA Paper*. No. 97-2582 (1997)

Vlasov, V. I. & Gorshkov, A. B. (2001). Comparison of the Calculated Results for Hypersonic Flow Past Blunt Bodies with the OREX Flight Test Data. *Fluid Dynamics,* Vol. 36, No 5, (October 2001) pp. 812-819, ISSN: 0015-4628

Vlasov, V.I.; Gorshkov, A.B.; Kovalev, R.V. & Lunev, V.V. (2009). Thin triangular blunt-nosed plate in a viscous hypersonic flow. *Fluid Dynamics*, Vol. 44, No. 4 (August 2009) pp. 596-605, ISSN: 0015-4628

Wilke, *C.* (1950). A Viscosity Equation for Gas Mixtures. *J.Chem.Phys.,* Vol. 18, No. 4, (1950) pp.517-519

Yoon, S. & Jameson, A. *(*1987). An LU-SSOR Scheme for the Euler and Navier-Stokes Equations. *AIAA Paper*. No. 87-0600 (1987)

11

Thermoelastic Stresses in FG-Cylinders

Mohammad Azadi[1] and Mahboobeh Azadi[2]
[1]*Department of Mechanical Engineering, Sharif University of Technology*
[2]*Department of Material Engineering, Tarbiat Modares University*
Islamic Republic of Iran

1. Introduction

FGM components are generally constructed to sustain elevated temperatures and severe temperature gradients. Low thermal conductivity, low coefficient of thermal expansion and core ductility have enabled the FGM material to withstand higher temperature gradients for a given heat flux. Examples of structures undergo extremely high temperature gradients are plasma facing materials, propulsion system of planes, cutting tools, engine exhaust liners, aerospace skin structures, incinerator linings, thermal barrier coatings of turbine blades, thermal resistant tiles, and directional heat flux materials. Continuously varying the volume fraction of the mixture in the FGM materials eliminates the interface problems and mitigating thermal stress concentrations and causes a more smooth stress distribution.

Extensive thermal stress studies made by Noda reveal that the weakness of the fiber reinforced laminated composite materials, such as delamination, huge residual stress, and locally large plastic deformations, may be avoided or reduced in FGM materials (Noda, 1991). Tanigawa presented an extensive review that covered a wide range of topics from thermo-elastic to thermo-inelastic problems. He compiled a comprehensive list of papers on the analytical models of thermo-elastic behavior of FGM (Tanigawa, 1995). The analytical solution for the stresses of FGM in the one-dimensional case for spheres and cylinders are given by Lutz and Zimmerman (Lutz & Zimmerman, 1996 & 1999). These authors consider the non-homogeneous material properties as linear functions of radius. Obata presented the solution for thermal stresses of a thick hollow cylinder, under a two-dimensional transient temperature distribution, made of FGM (Obata et al., 1999). Sutradhar presented a Laplace transform Galerkin BEM for 3-D transient heat conduction analysis by using the Green's function approach where an exponential law for the FGMs was used (Sutradhar et al., 2002). Kim and Noda studied the unsteady-state thermal stress of FGM circular hollow cylinders by using of Green's function method (Kim & Noda, 2002). Reddy and co-workers carried out theoretical as well as finite element analyses of the thermo-mechanical behavior of FGM cylinders, plates and shells. Geometric non-linearity and effect of coupling item was considered for different thermal loading conditions (Praveen & Reddy, 1998, Reddy & Chin, 1998, Paraveen et al., 1999, Reddy, 2000, Reddy & Cheng, 2001). Shao and Wang studied the thermo-mechanical stresses of FGM hollow cylinders and cylindrical panels with the assumption that the material properties of FGM followed simple laws, e.g., exponential law,

power law or mixture law in thickness direction. An approximate static solution of FGM hollow cylinders with finite length was obtained by using of multi-layered method; analytical solution of FGM cylindrical panel was carried out by using the Frobinus method; and analytical solution of transient thermo-mechanical stresses of FGM hollow cylinders were derived by using the Laplace transform technique and the power series method, in which effects of material gradient and heat transfer coefficient on time-dependent thermal mechanical stresses were discussed in detail (Shao, 2005, Shao & Wang, 2006, Shao & Wang, 2007). Similarly, Ootao and Tanigawa obtained the analytical solutions of unsteady-state thermal stress of FGM plate and cylindrical panel due to non-uniform heat supply (Ootao & Tanigawa, 1999, 2004, 2005). Using the multi-layered method and through a novel limiting process, Liew obtained the analytical solutions of steady-state thermal stress in FGM hollow circular cylinder (Liew & et al., 2003). Using finite difference method, Awaji and Sivakuman studied the transient thermal stresses of a FGM hollow circular cylinder, which is cooled by surrounding medium (Awaji & Sivakuman, 2001). Ching and Yen evaluated the transient thermoelastic deformations of 2-D functionally graded beams under non-uniformly convective heat supply (Ching & Yen, 2006).

In this paper, by using the Hermitian transfinite element method, nonlinear transient heat transfer and thermoelastic stress analyses is performed for thick-walled FGM cylinder which materials are temperature-dependent. Time variations of the temperature, displacements, and stresses are obtained through a numerical Laplace inversion. Finally, results obtained considering the temperature-dependency of the material properties. Those results are the temperature distribution and the radial and circumferential stresses are investigated versus time, geometrical parameters and index of power law (N) and then they are compared with those derived based on temperature independency assumption.

Two main novelties of this research are incorporating the temperature-dependency of the material properties and proposing a numerical transfinite element procedure that may be used in Picard iterative algorithm to update the material properties in a highly nonlinear formulation. In contrast to before researches, second order elements are employed. Therefore, proposed transfinite element method may be adequately used in problems where time integration method is not recommended because of truncation errors (e.g. coupled thermo-elasticity problems with very small relaxation times) or where improper choice of time integration step may lead to loss of the higher frequencies in the dynamic response. Also, accumulated errors that are common in the time integration method and in many cases lead to remarkable errors, numerical oscillations, or instability, do not happen in this technique.

2. The governing equations

Geometric parameters of the thick-walled FGM cylinder are shown in Figure (1). The FGM cylinder is assumed to be made of a mixture of two constituent materials so that the inner layer ($r = r_i$) of the cylinder is ceramic-rich, whereas the external surface ($r = r_o$) is metal-rich. The properties can be expressed as follows:

$$P = P_0(P_{-1}T^{-1} + 1 + P_1T + P_2T^2 + P_3T^3) \tag{1}$$

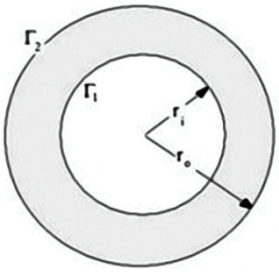

Fig. 1. FG Thick-walled Cylinder

Where P_0 , P_{-1} , P_1 , P_2 and P_3 are constants in the cubic fit of the materials property. The materials properties are expressed in this way so that higher order effects of the temperature on the material properties can be readily discernible. Volume fraction is a spatial function whereas the properties of the constituents are functions of temperature. The combination of these functions gives rise to the effective material properties of FGM and can be expressed by

$$P_{eff}(T,r) = P_m(T)V_m(r) + P_c(T)V_c(r) \tag{2}$$

Where P_{eff} is the effective material property of FGM, and P_m and P_c are the temperature dependent properties metal and ceramic, respectively. V_c is the volume fraction of the ceramic constituent of the FGM can be written by

$$V_c = \left(\frac{r_o - r}{r_o - r_i}\right)^N \quad , \; V_m = 1 - V_c \tag{3}$$

Where volume fraction index N dictates the material variation profile through the beam thickness and may be varied to obtain the optimum distribution of component materials ($0 \le N \le \infty$). From above equation, the effective Young's modulus E, Poisson ratio v, thermal expansion coefficient α and mass density ρ of an FGM cylinder can be written by

$$P_{eff} = (P_c - P_m)\left(\frac{r_o - r}{r_o - r_i}\right)^N + P_m \tag{4}$$

In this paper, only the effective Young's modulus and thermal expansion coefficient are dependent of temperature. The related equation is

$$P = P_{0c}(P_{-1c}T^{-1} + 1 + P_{1c}T + P_{2c}T^2 + P_{3c}T^3)V_c$$
$$+P_{0m}(P_{-1m}T^{-1} + 1 + P_{1m}T + P_{2m}T^2 + P_{3m}T^3)V_m \tag{5}$$

3. Finite element method

The equation of heat transfer is

$$-\frac{1}{r}\left[\frac{\partial T}{\partial r}\frac{\partial\left(\kappa r\right)}{\partial r} + \kappa r\frac{\partial^2 T}{\partial r^2}\right] + \rho\, C_v\frac{\partial T}{\partial t} = 0 \tag{6}$$

The boundary conditions are a heat flux in the internal layer and convection condition for external layer of FGM cylinder

$$\begin{cases} 2\pi\,\kappa\, r\dfrac{\partial T}{\partial r} + 2\pi\, r\, h\,(T - T_\infty) = 0 & at\ \ r = r_o \\ -\,\kappa\,\dfrac{\partial T}{\partial r} = \ q_0 & at\ \ r = r_i \end{cases} \tag{7}$$

The initial condition is $T(t = 0) = T_\infty$. Kantorovich approximation is

$$\{T(r,t)\} = \left[\widetilde{N}(r)\right]\{T^{(e)}(t)\} \tag{8}$$

$[\widetilde{N}]$ is the shape function matrix. For second order elements (with 3 nodes) which used in temperature field is

$$\left[\widetilde{N}\right] = \left[\frac{1}{2}\xi(\xi-1) \quad (1-\xi^2) \quad \frac{1}{2}\xi(\xi+1)\right] \tag{9}$$

ξ, natural coordinate which changes between -1 and 1 is used because of Gauss-Legendre numerical integration method. The relation between global and natural coordinate is

$$\left[\widetilde{N}\right]_{,r} = \left[\widetilde{N}\right]_{,\xi}\,\xi_{,r} = \ \left[\widetilde{N}\right]_{,\xi}\frac{\Delta\xi}{\Delta r} = \left[\widetilde{N}\right]_{,\xi}\frac{2n}{r_o - r_i} \tag{10}$$

n is number of elements. Residual integration form in Galerkin method is

$$\int_{\Omega}\left[\widetilde{N}\right]^T R\; d\,\Omega = 0 \tag{11}$$

For heat transfer problem, R is

$$R = \rho\; c\;[\widetilde{N}]\{\dot{T}^{(e)}\} - \frac{1}{r}\left[\left[\widetilde{N}\right]_{,r}\frac{\partial(\kappa\, r)}{\partial r} + \kappa r\left[\widetilde{N}\right]_{,rr}\right]\{T^{(e)}\} \tag{12}$$

Then the heat transfer problem can be written by

$$\left[C^{(e)}\right]\{\dot{T}^{(e)}\} + \left[A^{(e)}\right]\{T^{(e)}\} = \{q^{(e)}\} \tag{13}$$

Matrices C, A and q are damping and stiffness matrices and force vector, regularly.

$$\left[C^{(e)}\right] = \int_{\Omega}\left[\widetilde{N}\right]^T \rho\; c\;\left[\widetilde{N}\right] d\Omega \tag{14a}$$

$$\left[A^{(e)}\right] = -\int_{\Omega}\left[\widetilde{N}\right]^T \frac{1}{r}\frac{\partial(\kappa\, r)}{\partial r}\left[\widetilde{N}\right]_{,r} d\Omega + \int_{\Omega}\left[\left[\widetilde{N}\right]^T{}_{,r}\,\kappa + \left[\widetilde{N}\right]^T \kappa_{,r}\right]\left[\widetilde{N}\right]_{,r} d\Omega + \int_{\Gamma_2}\left[\widetilde{N}\right]^T h\,\left[\widetilde{N}\right] d\,\Gamma_2 \tag{14b}$$

$$\{q^{(e)}\} = \int_{\Gamma}\left[\widetilde{N}\right]^T \kappa\frac{\partial T}{\partial r}.n_r\; d\,\Gamma = \int_{\Gamma_1}\left[\widetilde{N}\right]^T q_0 d\,\Gamma_1 + \int_{\Gamma_2}\left[\widetilde{N}\right]^T h T_\infty d\,\Gamma_2 \tag{14c}$$

Strain can be written like below

$$\{\varepsilon\} = [d]\{u\} \tag{15}$$

$$\{\varepsilon\}^T = \langle \varepsilon_r \ \ \varepsilon_\theta \rangle \ \ , \ \ [d]^T = \begin{bmatrix} \frac{\partial}{\partial r} & \frac{1}{r} \end{bmatrix} \tag{16}$$

Energy function is

$$\pi = \frac{1}{2}\int_\Omega \{\varepsilon\}^T\{\sigma\}d\Omega + \int_\Omega \rho\,\{u\}^T\{\ddot{u}\}d\Omega - \int_\Gamma \{u\}^T\{\hat{p}\}\,d\Gamma \tag{17}$$

And so

$$\delta\pi = \int_\Omega \delta(\{\varepsilon\}^T).\{\sigma\}d\Omega + \int_\Omega \rho\,.\delta(\{u\}^T).\{\ddot{u}\}d\Omega - \int_\Gamma \delta(\{u\}^T).\{\hat{p}\}\,d\Gamma = 0 \tag{18}$$

Differential of strain is

$$\delta(\{\varepsilon\}^T) = \delta(\{u\}^T).[d]^T \tag{19}$$

Displacements in order to shape functions are

$$\{u\} = [N]\{U^{(e)}\} \tag{20}$$

[N] for displacement is a Hermitian shape function.

$$[N] = [N_1 \quad \bar{N}_1 \quad N_2 \quad \bar{N}_2] \tag{21a}$$

$$N_1 = \frac{1}{4}(\xi - 1)^2(2 + \xi) \tag{21b}$$

$$\bar{N}_1 = \frac{1}{4}(1 - \xi)^2(\xi + 1) \tag{21c}$$

$$N_2 = \frac{1}{4}(\xi + 1)^2(2 - \xi) \tag{21d}$$

$$\bar{N}_2 = \frac{1}{4}(1 + \xi)^2(\xi - 1) \tag{21e}$$

And displacement vector is

$$\{U^{(e)}\}^T = \langle {u_0}^{(1)} \ {u'_0}^{(1)} \ {u_0}^{(2)} \ {u'_0}^{(2)} \rangle \tag{22}$$

By defining of

$$[B] = [d][N] \tag{23}$$

In which

$$[B]=\begin{bmatrix} N_{1,r} & \bar{N}_{1,r} & N_{2,r} & \bar{N}_{2,r} \\ \frac{N_1}{r} & \frac{\bar{N}_1}{r} & \frac{N_2}{r} & \frac{\bar{N}_2}{r} \end{bmatrix} \tag{24}$$

And then, equation (18) is changed to

$$\begin{aligned}\delta\pi=\int_{\Omega}\delta\left(\{U^{(e)}\}^T\right)[B]^T.\{\sigma\}d\Omega+\int_{\Omega}\rho.\delta\left(\{U^{(e)}\}^T\right)[N]^T.\{\ddot{u}\}d\Omega \\ -\int_{\Gamma}\delta\left(\{U^{(e)}\}^T\right)[N]^T.\{\hat{p}\}\,d\Gamma\end{aligned} \tag{25}$$

And it's simplified to

$$\int_{\Omega}[B]^T.\{\sigma\}d\Omega+\int_{\Omega}\rho\,[N]^T\{\ddot{u}\}d\Omega-\int_{\Gamma}[N]^T.\{\hat{p}\}\,d\Gamma=0 \tag{26}$$

The relation between stress and strain is

$$\{\sigma\}=[D](\{\varepsilon\}-\{\varepsilon_T\}) \tag{27}$$

In which

$$\{\varepsilon_T\}^T=\langle\alpha\Delta T\ \ \alpha\Delta T\rangle \tag{28a}$$

$$[D]=\frac{E(r)}{1-\nu(r)^2}\begin{bmatrix}1 & \nu(r)\\ \nu(r) & 1\end{bmatrix} \tag{28a}$$

Then equation (26) becomes

$$\int_A\left([B]^T[D]\left([B]\{U^{(e)}\}-\{\varepsilon_T\}\right)\right)dA+\int_A\rho\,[N]^T[N]\{\ddot{U}^{(e)}\}dA-\int_S[N]^T.\{\hat{p}\}\,ds=0 \tag{29}$$

Thermo-elastic stress problem can be written like below

$$\left[M^{(e)}\right]\{\ddot{\Phi}^{(e)}\}+\left[K^{(e)}\right]\{\Phi^{(e)}\}=\{f^{(e)}\} \tag{30}$$

Matrices M, K and f are mass and stiffness matrices and force vector, regularly.

$$\left[M^{(e)}\right]=\int_A\rho\,[N]^T[N]dA \tag{31a}$$

$$\left[K^{(e)}\right]=\int_A[B]^T[D][B]dA \tag{31b}$$

$$\{f^{(e)}\}=\int_A[N]^T.\{\hat{p}\}\,dA+\int_A[B]^T[D]\{\varepsilon_T\}dA \tag{31c}$$

The general integral is

$$\int_{\Omega} L(r,\xi)d\,\Omega = \int 2\pi\, r\, L(r,\xi)dr = 2\pi \int_{-1}^{1} r\, L(r,\xi)\frac{\Delta r}{\Delta \xi}\, dz = \pi \int_{-1}^{1} r\, L(r,\xi)\frac{r_o - r_i}{n}\, dz \qquad (32)$$

To solve the above equations, a program which writes in MATLAB is used.
The geometrical characteristics and coefficients of properties of FGM cylinder are listed in Tables (1) and (2), regularly.

Characteristic	**Amount**
Heat Flux (q_0)	1000 ($\frac{kW}{m^2}$)
Coefficient of Conduction (h)	8 ($\frac{W}{m^2 °K}$)
Internal Radius (r_i)	12.7 (mm)
External Radius (r_o)	25.4 (mm)

Table 1. Geometrical Characteristics

Characteristics	Metal (Ti-6Al-4V)	Ceramic ($\mathbf{Si_3N_4}$)
$\rho\ (\frac{kg}{m^3})$	2370	4429
$C_v\ \left(\frac{j}{kg°K}\right)$	625.297	555.110
$\kappa\ (\frac{W}{m°K})$	13.723	1.209
E (GPa)	122.557	348.430
ν	0.29	0.24
$\alpha\ (\frac{1}{°K})$	7.579 e -6	5.872 e -6
P_{-1} (E, α)	0	0
P_1 (E)	-4.586 e -4	3.700 e-4
P_2 (E)	0	2.160 e -7
P_3 (E)	0	-8.948 e -11
P_1 (α)	6.500 e-4	9.095 e -4
P_2 (α)	0.313 e -6	0
P_3 (α)	0	0

Table 2. Coefficients of Properties of FG Material

4. Laplace transform

Making application of the Laplace transform, defined by

$$\Omega(s) = L[\omega(t)] = \int_0^{\infty} e^{-st}\omega(t)dt \qquad (33)$$

The governing equations become

$$\left(s\left[C^{(e)}\right]+\left[A^{(e)}\right]\right)\left\{T(s)^{(e)}\right\}=\left\{Q(s)^{(e)}\right\} \tag{34}$$

$$\left(s^2\left[M^{(e)}\right]+\left[K^{(e)}\right]\right)\left\{U(s)^{(e)}\right\}=\left\{F(s)^{(e)}\right\} \tag{35}$$

5. Numerical Laplace inversion

To obtain the distributions of the displacement and temperature in the physical domain, it is necessary to perform Laplace inversion for the transformed displacement and temperature obtained when a sequence of values of s is specified. In this paper an accurate and efficient numerical method is used to obtain the inversion of the Laplace transform.
The inversion of the Laplace transform is defined as

$$\omega(t)=L^{-1}[\Omega(s)]=\frac{1}{2\pi i}\int_{v-i\infty}^{v+i\infty}e^{st}\Omega(s)ds \tag{36}$$

The numerical inversion of the Laplace transform can be written

$$\omega_N(t)=\frac{1}{2}\lambda_0+\sum_{k=1}^{p}\lambda_k \tag{37}$$

$$\lambda_k=\frac{e^{-vt}}{T}\left\{Re\left[\Omega\left(v+i\frac{k\pi}{T}\right)\right]cos\frac{k\pi}{T}t\right\}-\frac{e^{-vt}}{T}\left\{Im\left[\Omega\left(v+i\frac{k\pi}{T}\right)\right]sin\frac{k\pi}{T}t\right\} \tag{38}$$

It should be noted that a good choice of the free parameters p and vT is not only important for the accuracy of the results but also for the application of the Korrektur method and the methods for the acceleration of convergence. The values of v and T are chosen according to the criteria outlined by Honig and Hirdes (Honig & Hirdes, 1984).
After choosing the optimal v, any nodal variables in physical domain can be calculated at any specific instant by using the Korrektur method and e-algorithm simultaneously to perform the numerical Laplace inversion (Honig & Hirdes, 1984).

6. Numerical results

6.1 Results for temperature distribution

Here are the dimensionless parameters which are used in numerical results

$$R=\frac{r-r_i}{r_o-r_i}\quad,\quad \bar{R}=\frac{r_o}{r_i}\quad,\quad \bar{t}=\frac{t}{T} \tag{39}$$

Results obtained in Figure (2) for different number of elements (n) shows that the results are convergent in $\bar{t}=0.5$. Hence, seven second order elements are chosen to perform the next analyses.
The distribution of temperature is drawn for N=1 in Figure (3). As it's expected, results of the consecutive times are convergent to each other and then the transient response vanishes and the steady-state response becomes the dominant.

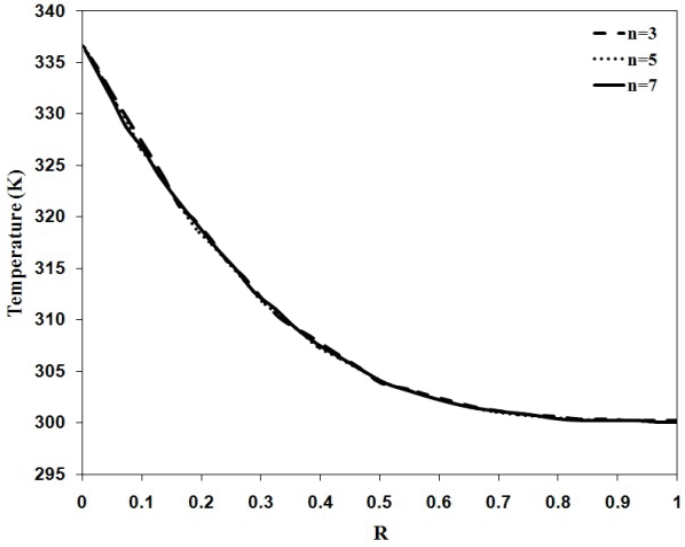

Fig. 2. Effect of element number on response of temperature for N=1 and $\bar{t} = 0.5$

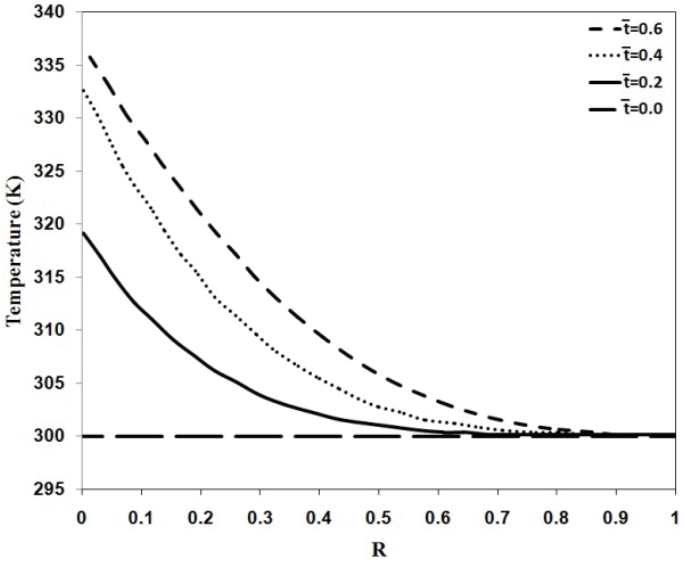

Fig. 3. Temperature distribution vs. dimensionless time for N=1

Effect of index of power law for $\bar{t} = 0.5$ is conducted in Figure (4). As the volume fraction index increases, the volume fraction of the ceramic material increases in the vicinity of the hot boundary surface (the inner surface). Therefore, higher temperatures, and subsequently higher temperature gradients are achieved in the neighborhood of the inner surface of the FGM cylinder. Furthermore, in this case, the temperature has converged asymptotically to the ambient temperature, in a higher rate.

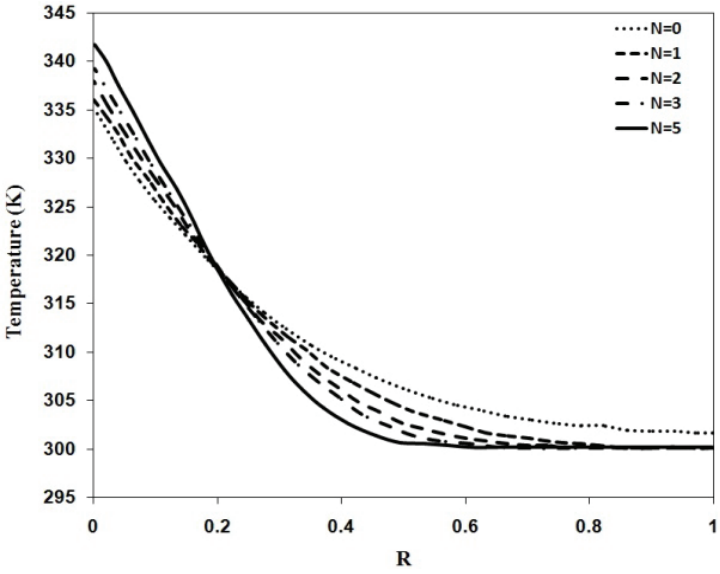

Fig. 4. N effect on temperature distribution for $\bar{t} = 0.5$

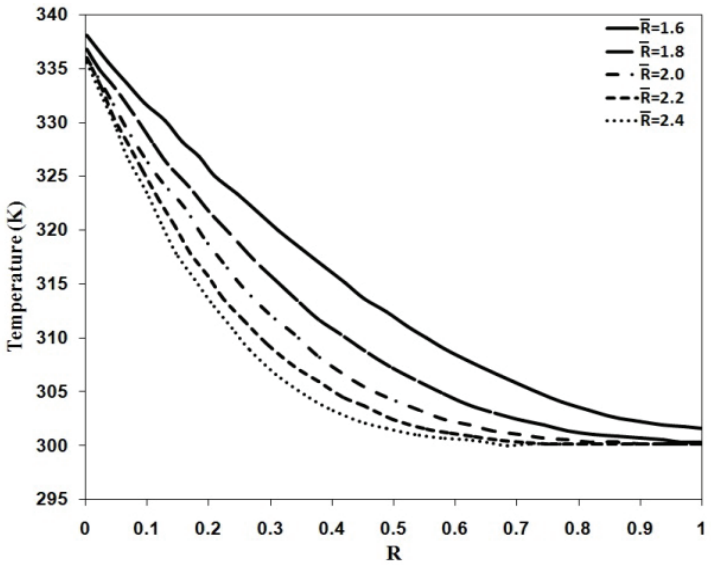

Fig. 5. Geometry effect on temperature distribution for N=1 and $\bar{t} = 0.5$

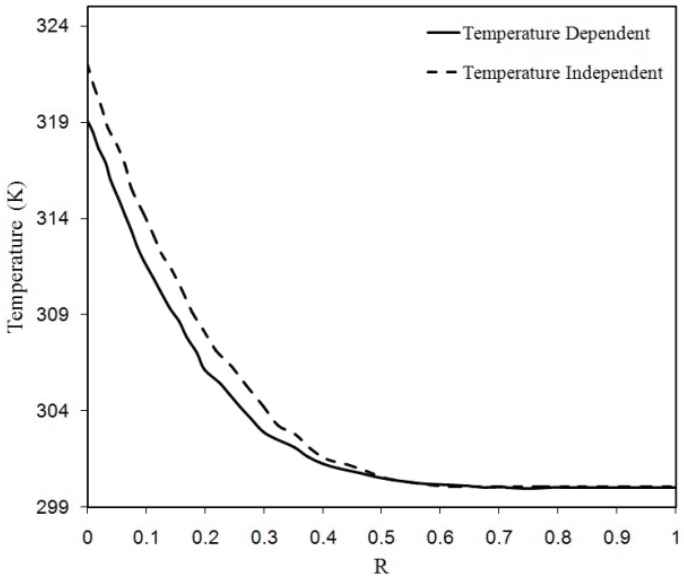

Fig. 6. Temperature distribution for N=1 and $\bar{t} = 0.5$

Then, Figure (5) shows the effect of change in geometry ($\bar{R} = r_o/r_i$) such as changing in internal and external radius, for $\bar{t} = 0.5$ and N=1. Temperatures of the thinner cylinders are generally higher. Therefore, temperature distribution with lower temperature gradient is constructed. In other words, for thinner cylinders, the response is more convergent to the steady-state one.

Influence of temperature-dependency on temperature distribution of FGM cylinder is drawn in Figure (6) for N=1, $\bar{t} = 0.2$ and $\bar{R} = 2$. This result shows that higher temperatures and temperature gradients are resulted when the temperature-dependency of the material properties is ignored. A difference up to 15 percent in temperature is observed. Since according to Figure (3), temperature values increase with the time, this difference is more remarkable for greater values of the dimensionless time ($\bar{t}$).

6.2 Results for thermo-elastic stresses

In Figures (7) and (8), radial and hoop stresses versus R and time for N=1. This result shows that radial and hoop stresses are increasing by time. In the inner layers of cylinder, stresses are higher because of higher temperature gradient. At both ends of cylinder (inner and outer layers) radial stress is to some extent zero (according to the numerical errors in FEM) due to free surface and having no pressure.

For various index of power law (N), radial and hoop stresses are drawn in Figures (9) and (10) for $\bar{t} = 0.4$. By increasing of N, as FGM material is become softer, both radial and hoop stresses reduced.

Figures (11) and (12) are shown for differences between dependency and independency of properties in temperature and then the changes in radial and hoop stresses for $\bar{t} = 0.4$ and N=1. This result shows that higher stresses are resulted when the temperature-dependency of material properties is ignored. A difference up to 15 percent in stresses is observed. Since

temperature values increase with the time (Figure 3), stresses increase too (Figure 7) and therefore this difference will be more remarkable for greater values of the dimensionless time ($\bar{t}$), consequently.

Geometry effect is shown in Figures (13) and (14) for both radial and hoop stress. By increasing of thickness, stresses decrease due to decreasing of temperature gradient.

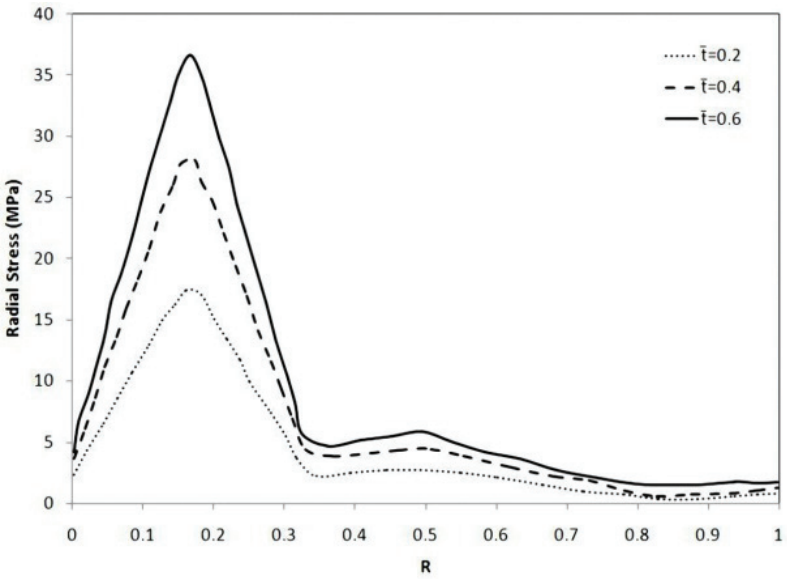

Fig. 7. Radial stress for N=1 versus R and dimensionless time

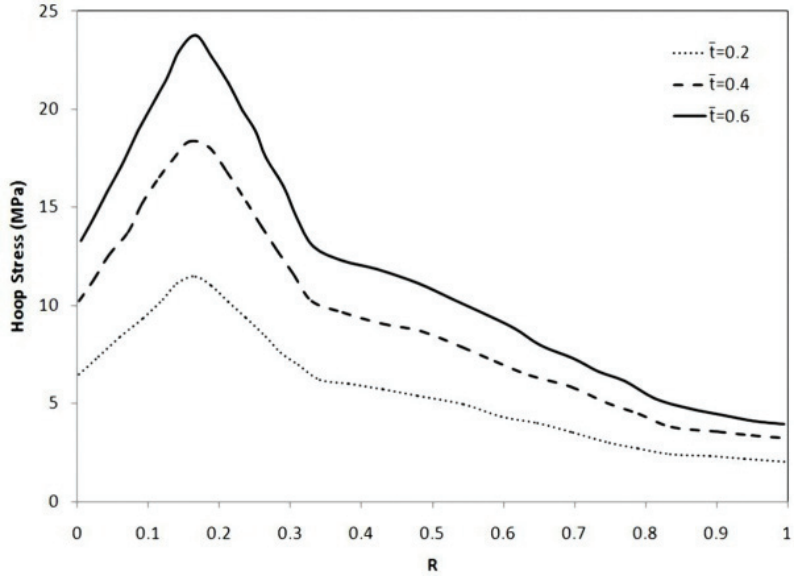

Fig. 8. Hoop stress for N=1 versus R and dimensionless time

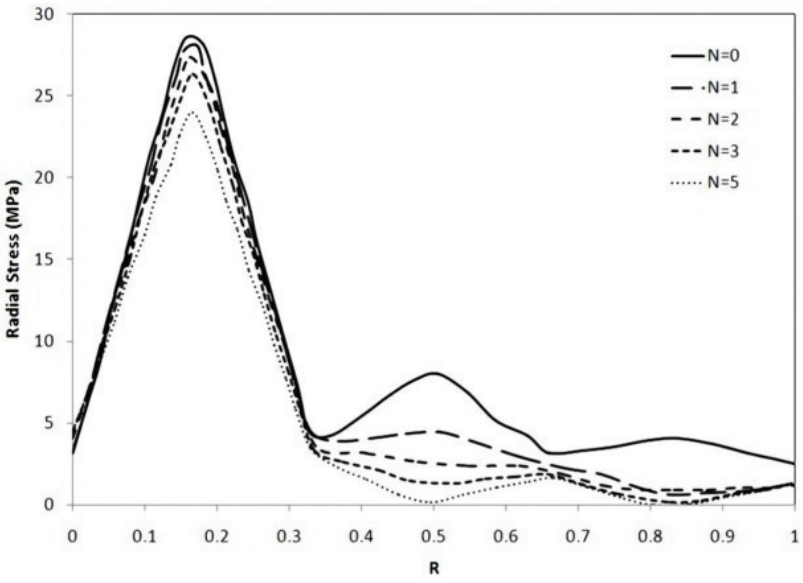

Fig. 9. Radial stress for $\bar{t} = 0.4$ versus R and N

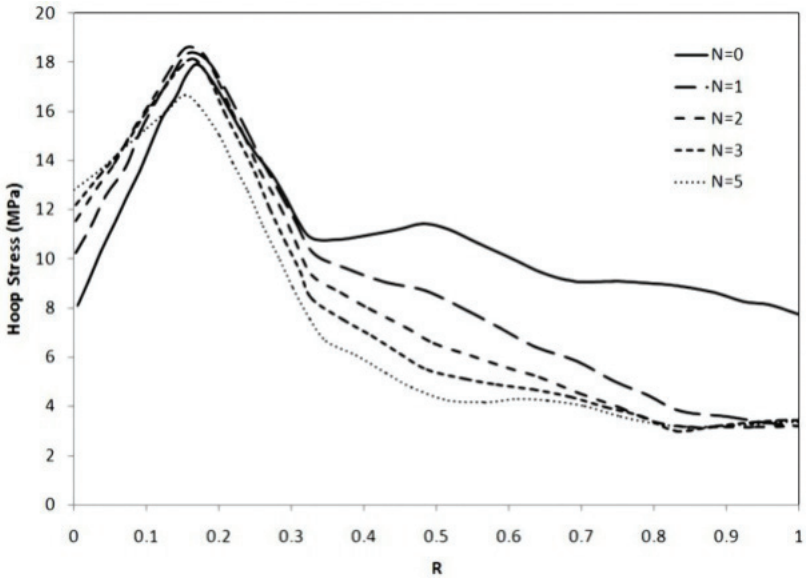

Fig. 10. Hoop Stress for $\bar{t} = 0.4$ versus R and N

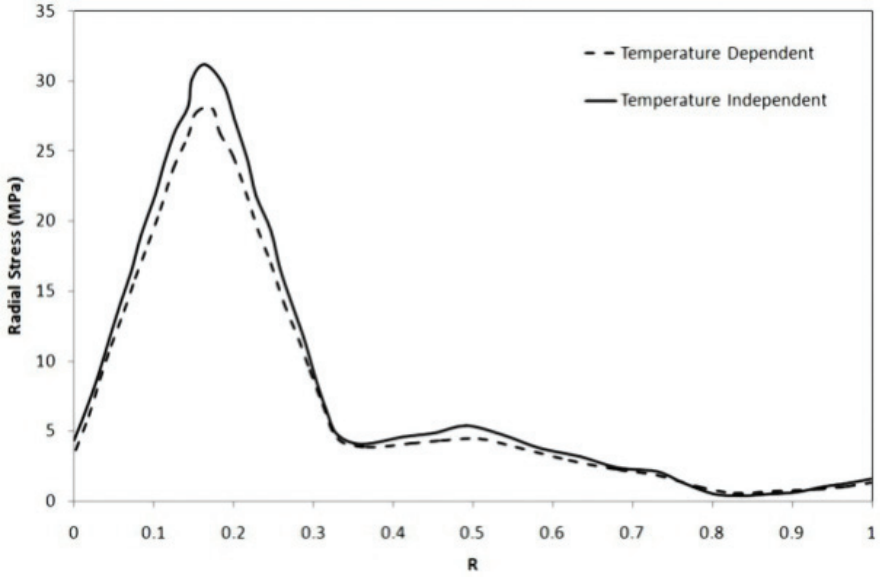

Fig. 11. Radial stress versus R in $\bar{t} = 0.4$ and N=1

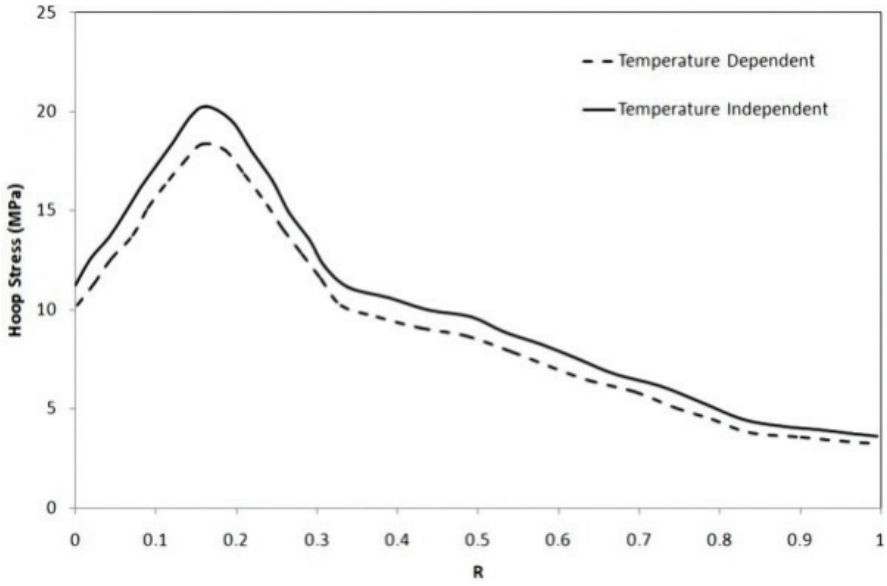

Fig. 12. Hoop stress versus R in $\bar{t} = 0.4$ and N=1

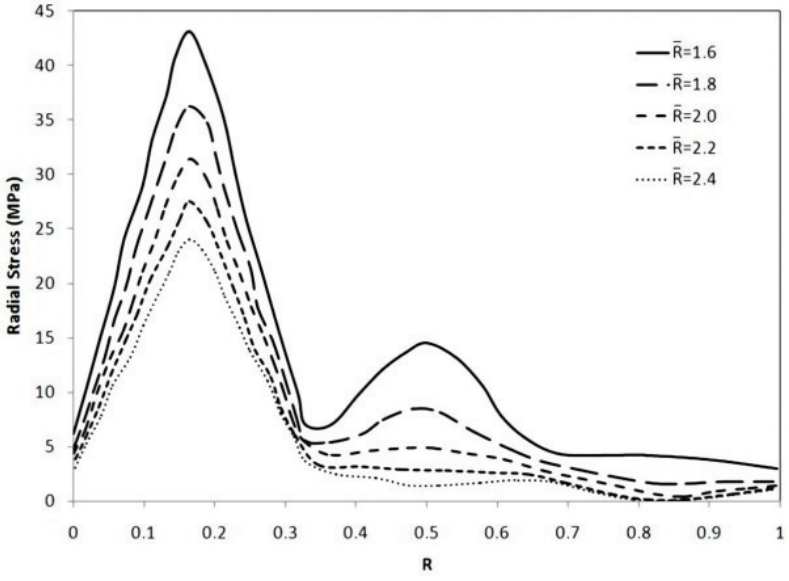

Fig. 13. Geometry effect on radial stress for N=1 and $\bar{t} = 0.4$

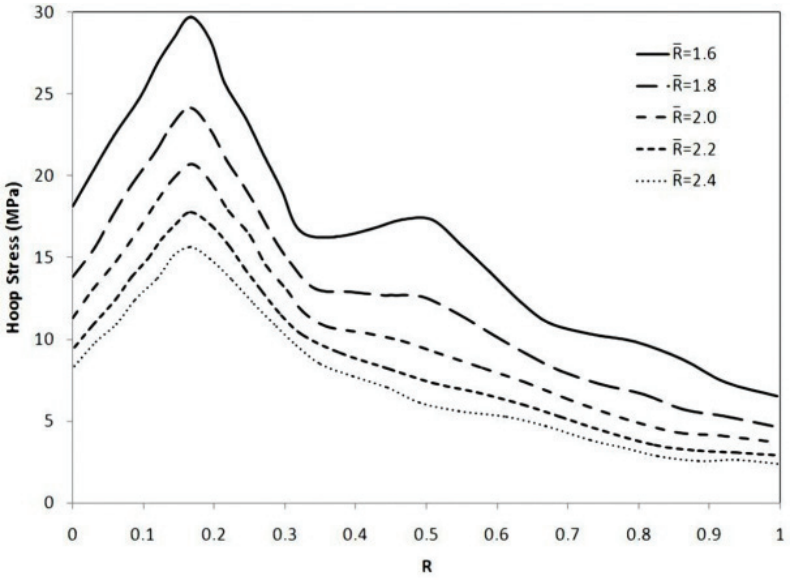

Fig. 14. Geometry effect on hoop stress for N=1 and $\bar{t} = 0.4$

7. Conclusion

In this paper, nonlinear transient heat transfer and thermo-elastic analysis of a thick-walled FGM cylinder is analyzed by using a transfinite element method that can be used in an updating and iterative solution scheme. Results also show that the temperature-dependency of the material properties may has significant influence (up to 15 percent) on the temperature distribution and gradient and also radial and hoop stresses that have remarkable effect on some critical behaviors such as thermal buckling or dynamic response, crack and wave propagation. Some other parameters such as index of power law (N) and geometrical parameter have also important affects on those mentioned results.

8. References

Noda, N. (1991). Thermal stresses in materials with temperature-dependent properties. *Journal of Applied Mechanics*, Vol. 44 (83-97)

Tanigawa, Y. (1995). Some basic thermo-elastic problems for non-homogeneous structural materials, *Journal of Applied Mechanics*, Vol. 48 (377-89)

Lutz, M.P. & Zimmerman, R.W. (1996). Thermal stresses and effective thermal expansion coefficient of a functionally graded sphere. *Journal of Thermal Stresses*, Vol. 19 (39-54)

Zimmerman, R.W. & Lutz, M.P. (1999). Thermal stress and thermal expansion in a uniformly heated functionally graded cylinder, *Journal of Thermal Stresses*, Vol. 22 (177-88)

Obata, Y.; Kanayama, K.; Ohji, T. & Noda, N. (1999). Two-dimensional unsteady thermal stresses in a partially heated circular cylinder made of functionally graded material, *Journal of Thermal Stresses*

Sutradhar, A.; Paulino, G.H. & Gray, L.J. (2002). Transient heat conduction in homogeneous and non-homogeneous materials by the Laplace transform Galerkin boundary element method, *Eng. Anal. Boundary Element*, Vol. 26 (119-32)

Kim, K.S. & Noda, N. (2002). Green's function approach to unsteady thermal stresses in an infinite hollow cylinder of functionally graded material, *Acta Mechanics*, Vol. 156 (145-61)

Praveen, G.N. & Reddy, J.N. (1998). Nonlinear transient thermo-elastic analysis of functionally graded ceramic–metal plates, *International Journal of Solids Structures*, Vol. 35 (4457–76)

Reddy, J.N. & Chin, C.D. (1998). Thermo-mechanical analysis of functionally graded cylinders and plates, *International Journal of Solids Structures*, Vol. 21 (593–626)

Praveen, G.N.; Chin, C.D. & Reddy, J.N. (1999) Thermo-elastic analysis of a functionally graded ceramic–metal cylinder, *ASCE Journal of Engineering Mechanics*, Vol. 125 (1259–67)

Reddy, J.N. (2000). Analysis of functionally graded plates, *International Journal of Numerical Meth. Eng.*, Vol. 47 (663–84)

Reddy, J.N. & Cheng, Z.Q. (2001). Three-dimensional thermo-mechanical deformations of functionally graded rectangular plates. *European Journal of Mechanics A/Solids*, Vol. 20 (841–60)

Reddy, J.N. & Cheng, Z.Q. (2003). Frequency of functionally graded plates with three-dimensional asymptotic approach, *Journal of Engineering Mechanics*, Vol. 129 (896–900)

Shao, Z.S. (2005). Mechanical and thermal stresses of a functionally graded hollow circular cylinder with finite length, *International Journal of Pressure Vessel Pipe*, Vol. 82 (155–63)

Shao, Z.S. & Wang, T.J. (2006). Three-dimensional solutions for the stress fields in functionally graded cylindrical panel with finite length and subjected to thermal/mechanical loads, *International Journal of Solids Structures*, Vol. 43 (3856–74)

Shao, Z.S.; Wang, T.J. & Ang, K.K. (2007). Transient thermo-mechanical analysis of functionally graded hollow circular cylinders, *Journal of Thermal Stresses*, Vol. 30 (81–104)

Ootao, Y. & Tanigawa, Y. (1999). Three-dimensional transient thermal stresses of functionally graded rectangular plate due to partial heating, *Journal of Thermal Stresses*, Vol. 22 (35–55)

Ootao, Y. & Tanigawa, Y. (2004). Transient thermo-elastic problem of functionally graded thick strip due to non-uniform heat supply, *Composite Structures*, Vol. 63, No. 2 (139–46)

Ootao, Y. & Tanigawa, Y. (2005). Two-dimensional thermo-elastic analysis of a functionally graded cylindrical panel due to non-uniform heat supply, *Mech. Res. Commun.*, Vol. 32 (429–43)

Liew, K.M.; Kitiporncai, S.; Zhang, X.Z. & Lim, C.W. (2003). Analysis of the thermal stress behavior of functionally graded hollow circular cylinders, *International Journal of Solids Structures*, Vol. 40 (2355–80)

Awaji, H. & Sivakuman, R. (2001) Temperature and stress distributions in a hollow cylinder of functionally graded material: the case of temperature-dependent material properties, *Journal of Am. Ceram. Soc.*, Vol. 84 (1059–65)

Ching, H.K.& Yen, S.C. (2006). Transient thermo-elastic deformations of 2-D functionally graded beams under non-uniformly convective heat supply, *Composite Structures*, Vol. 73, No. 4 (381–93)

Honig, G. & Hirdes, U. (1984) A method for the numerical inversion of Laplace transforms, *Journal of Computer Applied Mathematics*, Vol. 10 (113–132)

12

Experimentally Validated Numerical Modeling of Heat Transfer in Granular Flow in Rotating Vessels

Bodhisattwa Chaudhuri[1], Fernando J. Muzzio[2] and M. Silvina Tomassone[2]
[1]*Department of Pharmaceutical Sciences, University of Connecticut, Storrs, CT, 06269*
[2]*Department of Chemical and Biochemical Engineering, Rutgers University, Piscataway, NJ, 08854*
United States of America

1. Introduction

Heat transfer in particulate materials is a ubiquitous phenomenon in nature, affecting a great number of applications ranging from multi-phase reactors to kilns and calciners. The materials used in these type of applications are typically handled and stored in granular form, such as catalyst particles, coal, plastic pellets, metal ores, food products, mineral concentrates, detergents, fertilizers and many other dry and wet chemicals. Oftentimes, these materials need to be heated and cooled prior to or during processing. Rotary calciners are most commonly used mixing devices used in metallurgical and catalyst industries (Lee, 1984; Lekhal et. al., 2001). They are long and nearly horizontal rotating drums that can be equipped with internal flights (baffles) to process various types of feedstock. Double cone impregnators are utilized to incorporate metals or other components into porous carrier particles while developing supported catalysts. Subsequently, the impregnated catalysts are heated, dried and reacted in rotating calciners to achieve the desired final form. In these processes, heat is generally transferred by conduction and convection between a solid surface and particles that move relative to the surface. Over the last fifty years, there has been a continued interest in the role of system parameters and in the mechanisms of heat transfer between granular media and the boundary surfaces in fluidized beds (Mickey & Fairbanks, 1955; Basakov, 1964; Zeigler & Agarwal, 1969; Leong et.al., 2001; Barletta et. al., 2005), dense phase chutes, hoppers and packed beds (Schotte, 1960; Sullivan & Sabersky, 1975; Broughton & Kubie, 1976; Spelt et. al., 1982; Patton et. al., 1987; Buonanno & Carotenuto, 1996; Thomas et. al., 1998; Cheng et. al., 1999), dryers and rotary reactors and kilns (Wes et. al., 1976; Lehmberg et. al., 1977). More recently, experimental work on fluidized bed calciner and rotary calciners/kilns have been reported by LePage et.al, 1998; Spurling et.al., 2000, and Sudah. et al., 2002. In many of these studies, empirical correlations relating bed temperature to surface heat transfer coefficients for a range of operating variables have been proposed. Such correlations are of restricted validity because they cannot be easily generalized to different equipment geometries and it is risky to extrapolate their use outside the experimental range of variables studied. Moreover, most of these models do not capture particle-surface interactions or the detailed microstructure of the

granular bed. Since the early 1980s, several numerical approaches have been used to model granular heat transfer methods using (i) kinetic theory (Natarajan & Hunt, 1996) (ii) continuum approaches (Michaelides, 1986; Ferron & Singh, 1991; Cook & Cundy, 1995, Natarajan & Hunt, 1996, Hunt, 1997) and (iii) discrete element modeling (DEM) (Kaneko et. al., 1999; Li & Mason, 2000; Vargas & McCarthy, 2001; Skuratovsky et. al., 2005). The constitutive model based on kinetic theory incorporates assumptions such as isotropic radial distribution function, a continuum approximation and purely collisional interactions amongst particles, which are not completely appropriate in the context of actual granular flow. Continuum models neglect the discrete nature of the particles and assume a continuous variation of matter that obeys the laws of conservation of mass and momentum. To the best of our knowledge, among continuum approaches, only Cook and Cundy, 1995 modeled heat transfer of a moist granular bed inside a rotating vessel. Continuum-based models can yield accurate results for the time-averaged quantities such as velocity, density and temperature while simulating heat transfer in granular material, but fail to reveal the behavior of individual particles and do not consider inter-particle interactions.
In the discrete element model, each constituent particle is considered to be distinct. DEM explicitly considers inter-particle and particle-boundary interactions, providing an effective tool to solve the transient heat transfer equations. Most of the DEM-based heat transfer work has been either two-dimensional or in static granular beds. To the best of our knowledge no previous work has used three-dimensional DEM to study heat transfer in granular materials in rotary calciners (with flights attached) that are the subject of this study. Moreover, a laboratory scale rotary calciner is used to estimate the effect of various materials and system parameters on heat transfer, which also helps to validate the numerical predictions.

2. Experimental setup

A cylindrical tubing (8 inches outer diameter, 6 inches inner diameter and 3 inches long) of aluminum is used as the "calciner" for our experiments. The calciner rides on two thick Teflon wheels (10 inches diameter) placed at the two ends of the calciner, precluding the direct contact of the metal wall with the rollers used for rotating the calciner. The side and the lateral views of the calciner are shown in Figure 1a and 1b respectively. Figure 1a also shows how the ten thermocouples are inserted vertically into the calciner with their positions being secured at a constant relative position (within themselves) using a rectangular aluminum bar attached to the outer Teflon wall of the calciner. Twelve holes are made on the Teflon wall of the calciner where the two holes at the end are used to secure the aluminum bar with screws, whereas, the intermediate holes allow the insertion of 10 thermocouples (as shown in Fig 1c). The other end-wall of Teflon has a thick glass window embedded for viewing purpose. In Figure 1d, the internals of the calciner comprising the vertical alignment of 10 thermocouples is visible through the glass window. Thermocouples are arranged radially due to the radial variation of temperature during heat transfer in the granular bed as observed in our earlier simulations (Chaudhuri et.al, 2006). The thermocouples are connected to the Omega 10 channel datalogger that works in unison with the data acquisition software of the adjacent PC. 200 μm size alumina powder and cylindrical silica particles (2mm diameter and 3mm long) are the materials used in our experiments. The calciner is initially loaded with the material of interest. Twenty to fifty percent of the drum is filled with granular material during the experiments. At room

temperature, an industrial heat gun is used to uniformly heat the external wall of the calciner. The calciner is rotated using step motor controlled rollers, while the wall temperature is maintained at 100°C. At prescribed intervals, the "calciner" is stopped to insert the thermocouples inside the granular bed to take the temperature readings. Once temperature is recorded, the thermocouples are extracted and rotation is initiated again.

3. Numerical model and parameter used

The Discrete Element Method (DEM), originally developed by Cundall and Strack (1971, 1979), has been used successfully to simulate chute flow (Dippel, et.al., 1996), heap formation (Luding, 1997), hopper discharge (Thompson and Grest, 1991; Ristow and Hermann, 1994), blender segregation (Wightman, et.al, 1998; Shinbrot, 1999; Moakher, 2000) and flows in rotating drums (Ristow, 1996; Wightman, et.al., 1998). In the present study DEM is used to simulate the dynamic behavior of cohesive and non-cohesive powder in a rotating drum (calciner) and double cone (impregnator). Granular material is considered here as a collection of frictional inelastic spherical particles. Each particle may interact with its neighbors or with the boundary only at contact points through normal and tangential forces. The forces and torques acting on each of the particles are calculated as:

$$\sum F_i = m_i g + F_n + F_t + F_{cohes} \tag{1}$$

$$\sum T_i = r_i \times F_T \tag{2}$$

Thus, the force on each particle is given by the sum of gravitational, inter-particle (normal and tangential: F_N and F_T) and cohesive forces as indicated in Eq. (1). The corresponding torque on each particle is the sum of the moment of the tangential forces (F_T) arising from inter-particle contacts (Eq. (2)).

We use the "latching spring model" to calculate normal forces. This model, developed by Walton and Braun (1986, 1992, 1993), allows colliding particles to overlap slightly. The normal interaction force is a function of the overlap. The normal forces between pairs of particles in contact are defined using a spring with constants K_1 and K_2: $F_N=K_1\alpha_1$ (for compression), and $F_N = K_2\ (\alpha_1-\alpha_0)$ (for recovery). These spring constants are chosen to be large enough to ensure that the overlaps α_1 and α_0 remain small compared to the particles sizes. The degree of inelasticity of collisions is incorporated in this model by including a coefficient of restitution $e = (K_1/K_2)^{1/2}$ $(0<e<1$, where $e=1$ implies perfectly elastic collision with no energy dissipation and $e=0$ implies completely inelastic collision).

Tangential forces (F_T) in inter-particle or particle-wall collision are calculated with Walton's incrementally slipping model. After contact occurs, tangential forces build up, causing displacement in the tangential plane of contact. These forces are assumed to obey Coulomb's law. The initial tangential stiffness is considered to be proportional to the normal stiffness. If the magnitude of tangential forces is greater than the product of the normal force by the coefficient of static friction, (i.e. $T \geq \mu F_N$) sliding takes place with a constant coefficient of dynamic friction. The model also takes into account the elastic deformation that can occur in the tangential direction. The tangential force T is evaluated considering an effective tangential stiffness k_T associated with a linear spring. It is incremented at each time step as $T_{t+1} = T_t + k_t \Delta s$, where Δs is the relative tangential displacement between two time steps (for details on the definition of Δs see Walton (1993)). The described model was used

successfully to perform three-dimensional simulations of granular flow in realistic blender geometries, where it confirmed important experimental observations (Wightman, et.al., 1998, Moakher, et. al., 2000, Shinbrot, et.al., 1999; Sudah, et.al., 2005).

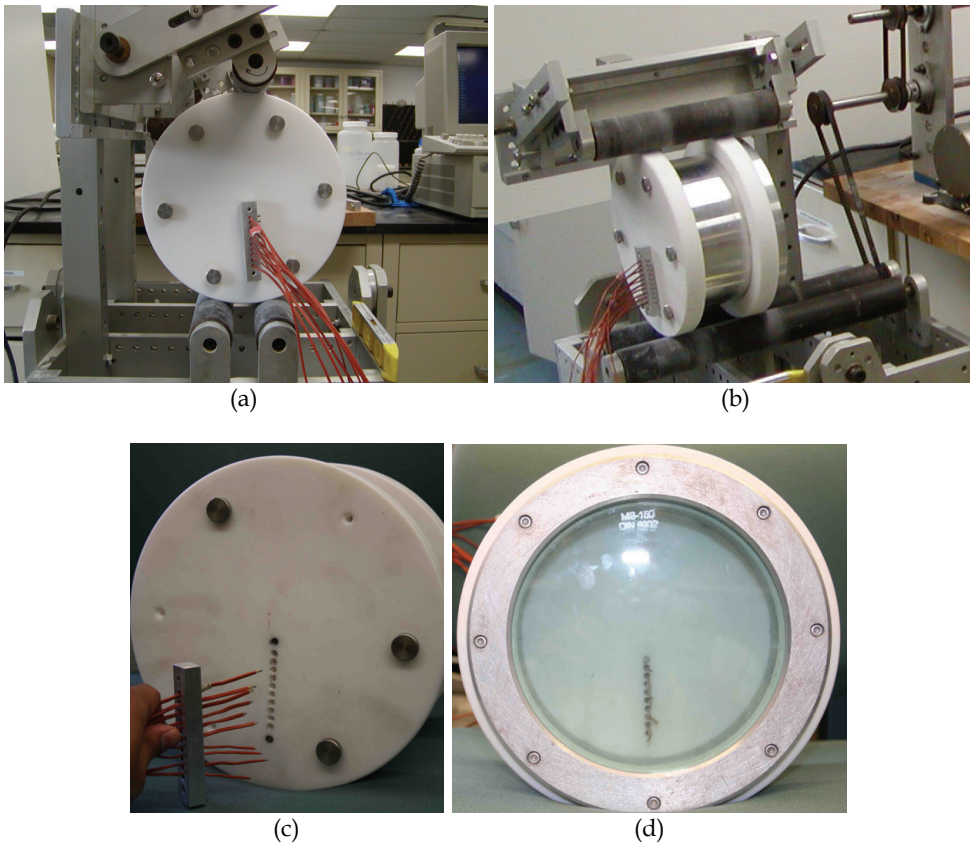

Fig. 1. (a) Aluminum calciner on rollers (side view) showing 10 thermocouples inserted within the calciner through the Teflon side-wall. (b) Lateral view of the calciner. (c) 10 thermocouples are tied up to the metal rod which is being attached to the teflon wall. Vertically located, ten holes are also shown in the teflon wall through which thermocouples are inserted inside the calciner. (d) Another side view showing the internals of the calciner and the vertical alignment of 10 thermocouples which are visible through the glass window.

We also incorporate cohesive forces between particles in our model using a square-well potential. In order to compare simulations considering different numbers of particles, the magnitude of the force was represented in terms of the dimensionless parameter $K = F_{cohes}/mg$[1], where K is called the bond number and is a measure of cohesiveness that is

[1] Notice that we are not claiming that cohesive forces depend on the particle weight. This is just a convenient way of defining how strong cohesion is, as compared to the particle weight (i.e. 20 times the weight, 30 times the weight, etc)

independent of particle size, F_{cohes} is the cohesive force between particles, and mg is the weight of the particles. Notice that this constant force may represent short range effects[2] such as electrostatic or van der Waals forces. In this model, the cohesive force (F_{cohes}) between two particles or between a particle and the wall is unambiguously defined in terms of K. Four friction coefficients need to be defined: particle-particle and particle-wall static and dynamic coefficients. Interestingly, (and unexpectedly to the authors) all four friction coefficients turn out to be important to the transport processes.

Heat transport within the granular bed may take place by: thermal conduction within the solid; thermal conduction through the contact area between two particles in contact; thermal conduction through the interstitial fluid; heat transfer by fluid convection; radiation heat transfer between the surfaces of particles. Our work is focused on the first two mechanisms of conduction which are expected to dominate when the interstitial medium is stagnant and composed of a material whose thermal conductivity is small compared to that of the particles. O'Brien (1977) estimated this assumption to be valid as long as ($k_S\ a / k_f\ r$) >> 1, where a is the contact radius, r is the particle radius of curvature, k_f denotes the fluid interstitial medium conductivity and k_S is the thermal conductivity of the solid granular material. This condition is identically true when k_f=0, that is in vacuum.

Heat transport processes are simulated accounting for initial material temperature, wall temperature, granular heat capacity, granular heat transfer coefficient, and granular flow properties (cohesion and friction). Heat transfer is simulated using a linear model, where the flux of heat transported across the mutual boundary between two particles i and j in contact is described as

$$Q_{ij} = H_c(T_j - T_i) \tag{3}$$

Here. T_i and T_j are the temperatures of the two particles and the inter-particle conductance H_c is:

$$H_c = 2k_S\left[\frac{3F_N r^*}{4E^*}\right]^{1/3} \tag{4}$$

where k_S is the thermal conductivity of the solid material, E* is the effective Young's modulus for the two particles, and r^* is the geometric mean of the particle radii (from Hertz's elastic contact theory). The evolution of temperature of particle i from its neighbor (j) is

$$\frac{dT_i}{dt} = \frac{Q_i}{\rho_i C_i V_i} \tag{5}$$

Here, Q_i is the sum of all heat fluxes involving particle i and $\rho_i C_i V_i$ is the thermal capacity of particle i.

Equations (3-5) can be used to predict the evolution of each particle's temperature for a flowing granular system in contact with hot or cold surfaces. The algorithm is used to examine the evolution of the particle temperature both in the calciner and the double cone impregnator. This numerical model is developed based on following assumptions:

[2] Improvement of this model can be achieved by including electrostatic forces explicitly. We are currently working on this extension, and the results will be published in a separate article.

1. Interstitial gas is neglected.
2. Physical properties such a heat capacity, thermal conductivity and Young Modulus are considered to be constant.
3. During each simulation time step, temperature is uniform in each particle (Biot Number well below unity).
4. Boundary wall temperature remains constant.

The major computational tasks at each time step are as follows: (i) add/delete contact between particles, thus updating neighbor lists, (ii) compute contact forces from contact properties, (iii) compute heat flux using thermal properties (iv) sum all forces and heat fluxes on particles and update particle position and temperatures, and (v) determine the trajectory of the particle by integrating Newton's laws of motion (second order scalar equations in three dimensions). A central difference scheme, Verlet's Leap Frog method, is used here.

The computational conditions and physical parameters considered are summarized in Table 1. Heat transport in alumina is simulated for the experimental validation work, and then copper is chosen as the material of interest for

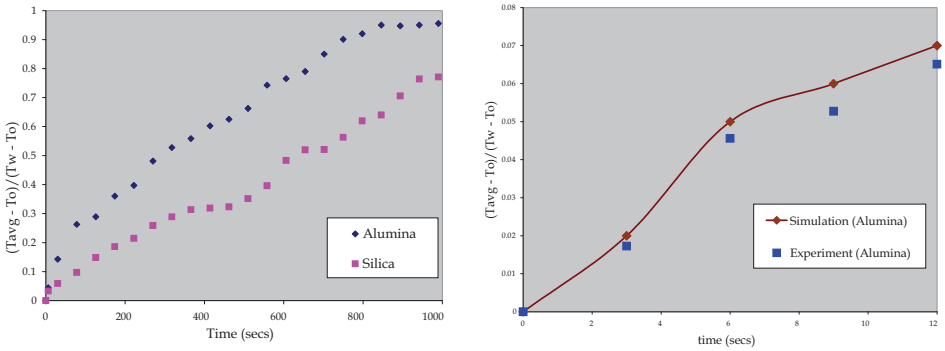

Fig. 2. (a) Variation of average bed temperature with time for alumina and silica; (b) Evolution of average bed temperature for simulation and experiments with alumina. The fill level of the calciner is 50% and is rotated at 20rpm in the experiments and simulations

further investigation on baffle size/orientation in calciners and impregnators.We simulated the flow and heat transfer of 20,000 particles of 1mm size rotated in the calciner equipped with or without baffle of variable shapes. The calciner consists of a cylindrical 6 inch diameter vessel with length of 0.6 inches, intentionally flanked with frictionless side walls to simulate a thin slice of the real calciner, devoid of end-wall effects. Two baffle sizes are considered (of thicknesses equal to 3cm and 6cm). The initial surface temperature of all the particles is considered to be 298 K (room temperature) whereas the temperature of the wall (and the baffle in the impregnator) is considered to be constant, uniform, and equal to 1298 K. The computational conditions and physical parameters considered are summarized in Table 1. Initially particles were loaded into the system and allowed to reach mechanical equilibrium. Subsequently, the temperature of the vessel was suddenly raised to a desired value, and the evolution of the temperature of each particle in the system was recorded as a function of time.

The double cone impregnator model considers flow and heat transfer of 18,000 particles of 3mm diameter in a vessel of 25 cm diameter and 30 cm length. The cylindrical portion of the impregnator is 25 cm diameter and 7.5 cm long. Each of the conical portions is 11.25 cm long and makes an angle of 45° with the vertical axis. The diameter at the top or bottom of the impregnator is 2.5cm The effect of baffle size is investigated in impregnators. Intuitively, the baffle is kept at an angle 45° with respect to the axis of rotation. The length of the baffle is 25cm, same as the diameter of the cylindrical portion of the impregnator. The width and thickness of the baffle are equal to one another (square cross section).
In order to describe quantitatively the dynamics of evolution of the granular temperature field, the following quantities were computed:

- Particle temperature fields vs. time
- Average bed temperature vs. time
- Variance of particle temperatures vs. time

These variables were examined as a function of relevant parameters, and used to examine heat transport mechanisms in both of the systems of interest here

4. Results and discussions

4.1 Effect of thermal properties in calciners

The effect of thermal conductivity in heat transfer is examined using alumina and silica particles separately, each occupying 50% of the calciner volume. The calciner is rotated at the speed of 20 rpm. The average bed temperature (T_{avg}) is estimated as the mean of the readings of the ten thermocouples and scaled with the average wall temperature (T_w) and the average initial condition (T_o) of the particle bed to quantify the effect of thermal conductivity. In Figure 2a, as expected, alumina with higher thermal conductivity warms up faster than silica. DEM simulations are performed with the same value for the physical and thermal properties of the material used in the experiments (for Alumina: thermal conductivity: k_s = 35 W/mK and heat capacity: Cp = 875 J/KgK, for Silica: K = 14 W/mK, Cp = 740 J/KgK). The initial surface temperature of all the particles is considered to be 298 K (room temperature) whereas the temperature of the wall is kept constant and equal to 398 K (in isothermal conditions). The DEM simulations predict the temperature of each of the particles in the system, thus the average bed temperature (T_{avg}) in simulation is the mean value of the predicted temperature of all the particles. Figure (2b) shows the variation of scaled average bed temperature for both simulation and experiments. The predictions of our simulation show a similar upward trend to the experimental findings.

4.2 Effect of vessel speed in the calciner

Alumina and silica powders are heated at varying vessel speed of 10, 20 and 30 rpm. The wall is heated and maintained at 100°C. Figure 3(a) and 3(b) show the evolution of average bed temperature with time as a function of vessel speed for alumina and silica respectively. The average bed temperatures for all the cases follow nearly identical trends. The external wall temperature is maintained at a constant temperature of 100°C. Figure (3c) shows the variation of scaled average bed temperature for simulation.
All experimental temperature measurements were performed every 30 seconds; with a running time of 1200 seconds. However, each of our simulation runs was performed for

only 12 seconds. Assuming a dispersion coefficient $E \sim \frac{L^2}{T}$ to be constant [Bird et. al., 1960; Crank, 1976], where L and T are the length and time scales, respectively, of the microscopic transitions that generate scalar transport, then the time required to achieve a certain progress of a temperature profile is proportional to the square of the transport microscale. The radial transport length scale used in the simulations, if measured in particle diameters, is much smaller than in the experiment, and correspondingly, the time scale needed to achieve a comparable progress of the temperature profile is much shorter, as presented in Figures 3a-c. In fact, the ratio of time scales between the experiment and the simulation probably is same to the ratio of length scales squared, shown by calculation below.

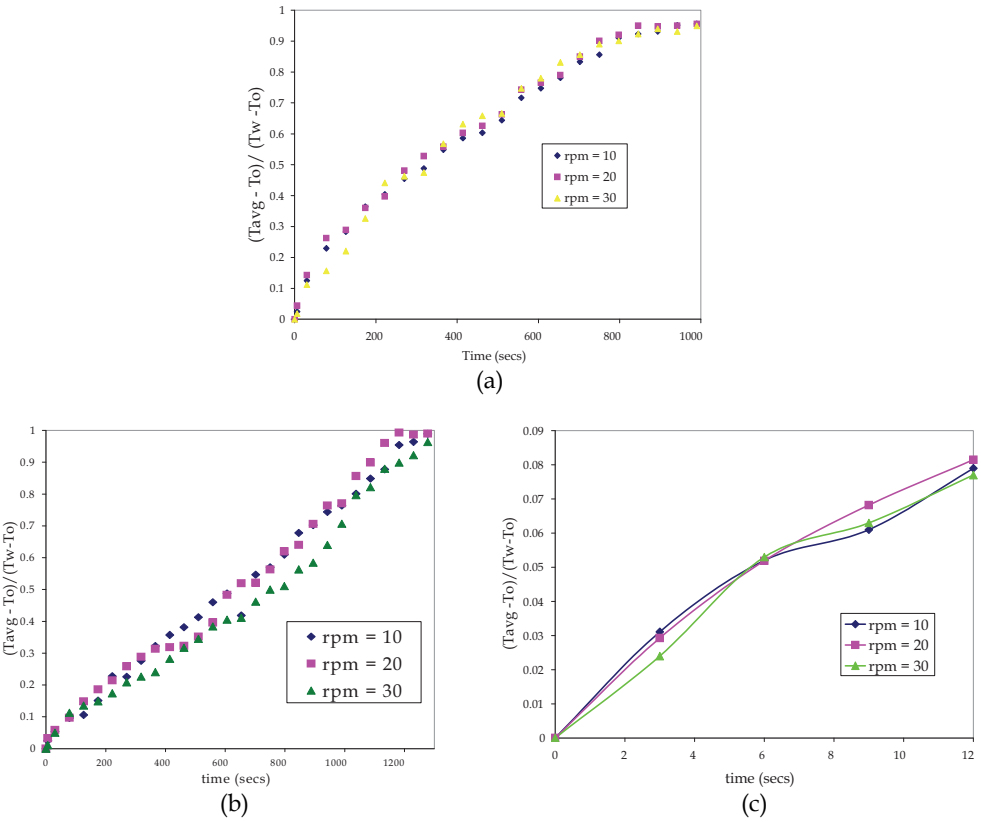

Fig. 3. Variation of temperature with time as a function of vessel speed for (a) Alumina (b) silica and (c) model with alumina.

In the experiments, the diameter of the vessel (*De*), duration of the experiment (*Te*) and particle size (*de*) are 6 inches, 1200 seconds and 200 microns (alumina) respectively. Whereas, in the simulations, the diameter of the vessel (*Ds*), time of the simulation (*Ts*) and particle size (*ds*) are 6 inches, 12 seconds and 2mm respectively. Ratios of time and length scales are estimated as below:

Ratio of time scales (R_T): $\frac{Te}{Ts} = \frac{1200}{12} = 100$

Ratio of length scales (R_L): $\frac{L_e}{L_s} = \frac{\frac{D_e}{d_e}}{\frac{D_s}{d_s}} = \frac{\frac{6}{0.2}}{\frac{6}{2}} = 10$

Therefore, $R_T = (R_L)^2$

Although there is a big difference in the time scale in the plots of our experiments (Fig. 3a or Fig. 3b) and simulations (Fig. 3c), they still exhibit the same transport phenomena in different time scales. The predictions of our simulation show the same upward trend similar to the experimental findings, even though, they are plotted in different time scales. The nominal effect of vessel speed on heat transfer was also observed by Lybaert, 1986, in his experiments with silica sand or glass beads heated in rotary drum heat exchangers.

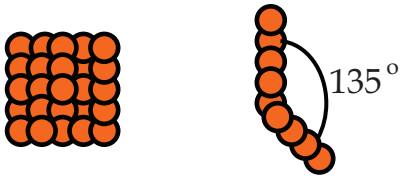

Fig. 4. Baffles are formed with particles glued together (a) square cross-section and (b) L-shaped cross section.

4.3 Effect of baffles on heat transfer in calciners using a DEM model

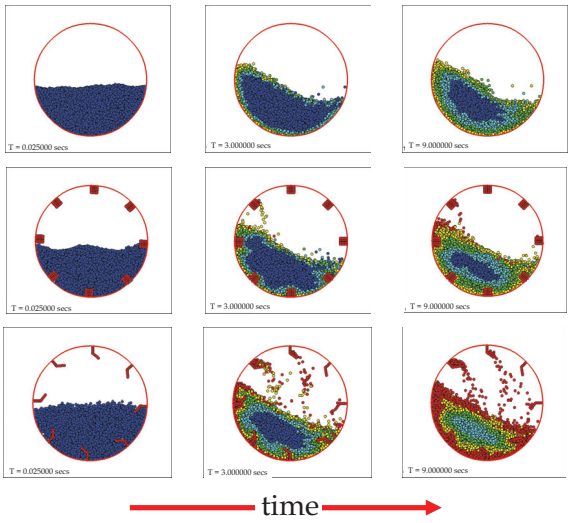

Fig. 5. Time sequence of axial snapshots

Section 4.3 is focused on our particle simulations only. After validation of the model, presented in last two subsections, a parametric study is conducted by varying the size and the orientation of the baffles of the calciner using the same DEM model. The evolution of particle temperature is visually track using color-coding. Particles with temperature lower than 350°K are colored blue; those with temperatures between 350°K and 550°K are painted cyan; those with temperatures between 550°K and 750°K are colored green and for temperatures between 750°K and 950°K, particles are colored yellow. Particles with temperatures higher than 950°K are colored red.
Figure 5 shows a time sequence of axial snapshots of color-coded particles in the calciner. Time increases from left to right (t = 0, 3 and 9 secs), while the baffle design vary from top to bottom.

4.3.1 Effect of baffle shape in heat transfer

In this section we study the effect of baffle shape in the calcination process. We do this by extending the DEM model of a calciner without baffles (which was previously validated) to one that which now effectively incorporates baffles. In our model, baffles or flights are attached to the inner wall of the calciner of radius 15cm and length of 1.6cm. Baffles run longitudinally along the axial direction of the calciner. We consider 8000 copper particles of radius 2mm heated in the calciner which rotates are 20 rpm for various baffle designs. The initial temperature of the particles is chosen to be at room temperature (298°K). We simulate baffles of two different cross sections, i.e. rectangular and L-shaped by rigidly grouping particles of 2mm size, which perform solid body rotation with the calciner wall. Fig 4 depicts the composition of the different baffles.
We construct the baffle particles purposely overlapping with each other by 10% of their diameter, to nullify any inter-particle gap which may cause smaller particles to percolate through the baffle. The square shaped baffle of cross sectional area of approximately 58mm^2 and 340 mm^2 are designed by arranging a matrix of 2 by 2 particles and 5 by 5 particles respectively. The L-shaped baffle is constructed by 9 particles bonded in a straight line until the 5th particle and then arranging the remaining 4 particles in an angle of 135°. Baffle particles also remain at the same temperature of the wall, i.e. 1298°K.
For visual representation, particles are color-coded based on their temperature. In Figure 5, the axial snapshots captured at time t= 0, 1 and 3 revolutions for 3 different baffle configurations: (i) no baffle (ii) baffles of each 400 mm^2 cross sectional area (iii) 8 L-shaped flights. The blue core displays the larger mass of particles at initial temperature. This cold core shrinks with time for all cases, however, the volume of the blue core shrinks faster for calciner with L shaped baffles. The number of red particles present in the bed increases for calciners with L-shaped baffles. Thus, increased surface area of the bigger baffle enhances in heat transfer within the calciners.
The effect of baffle configuration on heat transfer is quantified with our DEM model by measuring the average bed temperature as a function of time for all baffle configurations. Average bed temperature rises faster for calciners with L-shaped baffles, as seen in Figure 6(a). The uniformity of the temperature of the particle bed is quantified by estimating the standard deviation of the temperature of the bed. Figure 6(b) shows the effect of the baffle configuration on the uniformity of the bed temperature. The L-shaped baffles scoops up more particles in comparison to the square shaped baffle and helps in breaking the quasi-static zone in the center of the granular bed and redistributing the particles onto the cascading layer causing rapid mixing (uniformity) within the bed.

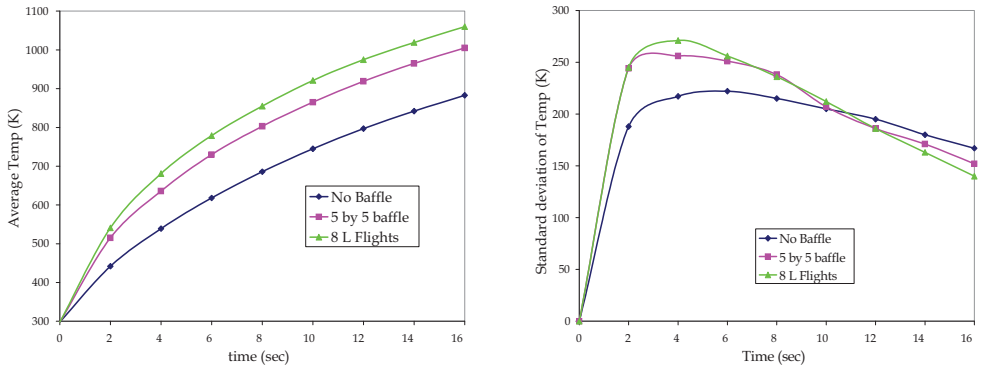

(a) (b)

Fig. 6. (a): Average temperature as function of time for different baffle configurations. (b): Standard deviation versus time for different baffle configurations.

4.3.2 Effect of baffle size on heat transfer in calciners

The effect of the size of the rectangular baffles/flights is investigated using DEM simulations. In Figure 7, the axial snapshots captured at time T= 0, 1 and 3 revolutions for 3 different baffle configurations: (i) no baffle (ii) 8 baffles of each 64 mm^2 cross sectional area (iii) 8 baffles of each 400 mm^2 cross sectional area. In our DEM model, four (2 by 2) and twenty-five (5 by 5) particles of radius 2 mm are glued together to form each of the baffles in case (ii) and (iii) respectively. The blue core signifies the mass of particles at initial temperature.

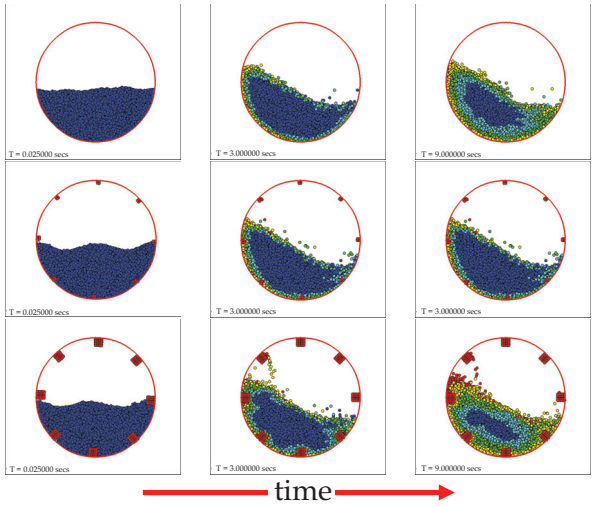

Fig. 7. shows a time sequence of axial snapshots of color-coded particles in the calciner. Time increases from left to right (t = 0, 3 and 9 secs), while the baffle size increases top to bottom

This cold core shrinks with time for all cases, but it shrinks faster for a calciner with bigger baffles. The number of red particles in the bed also increases for calciners with baffles of bigger sizes. Thus, increased surface area of the bigger baffle enhances heat transfer within the calciners. The effect of baffle size on heat transfer is quantified by calculating the average bed temperature as a function of time for all baffle configurations. Average bed temperature rises faster for calciners with bigger baffles, as seen in Figure 8(a). The uniformity of the temperature of the particle bed is quantified by estimating the standard deviation of the bed temperature. Figure 8(b) shows the effect of the baffle size on the uniformity of the bed temperature, systems with bigger baffles reach uniformity quicker.

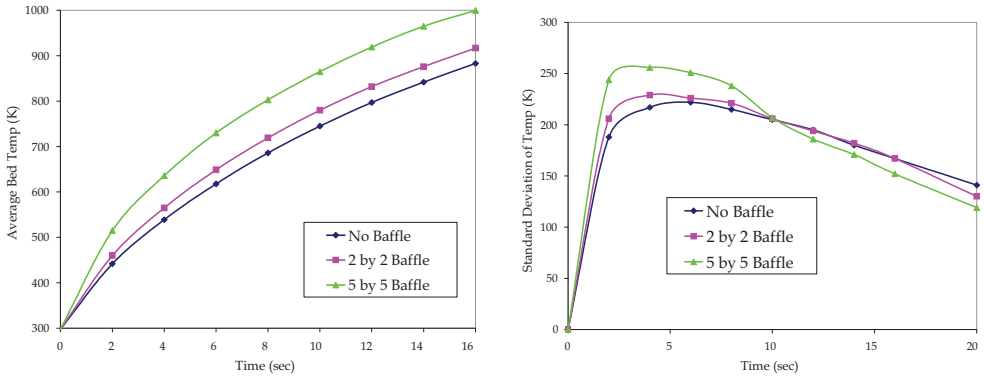

(a) (b)

Fig. 8. (a): Average bed temperature as a function of time for different sizes of rectangular baffles (b): The evolution of standard deviation versus time for different baffle configurations.

4.3.3 Effect of number of baffles/flights on heat transfer in calciners

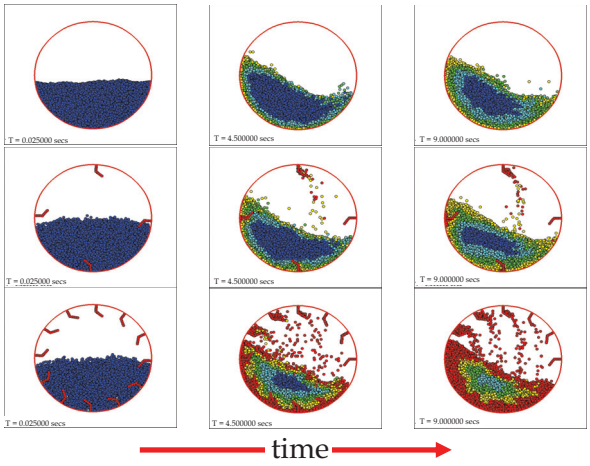

Fig. 9. Evolution of the temperature for non-baffled and baffled calciners (with 4 and 8 flights) at time = 0, 1.5 and 3 revs.

The number of baffles is an important geometric parameter for the rotary calciner. The effect of the parameter has been investigated with a calciner with L-shaped baffles. We calculated the evolution of the temperature depicted in successive snapshots for 0, 4 and 12 baffles in Fig 9. There is a cold core which shrinks with time for all the cases, and it shrinks faster for the calciner with larger number of baffles. The number of red particles present in the bed also increases for calciners with more baffles. Thus, increase in the number of baffles causes enhancement in heat transfer within the calciners. The effect of number of baffles on heat transfer is quantified by calculating the average bed temperature as a function of time for all baffle configurations. The average temperature of the bed rises faster for calciners with higher number of baffles. This can be seen in Figure 10(a). The uniformity of the temperature of the powder bed is quantified by estimating the standard deviation of the surface temperature of the bed and it is shown in Figure 10(b). It can be seen that the thermal uniformity of the bed is directly proportional to the number of baffles.

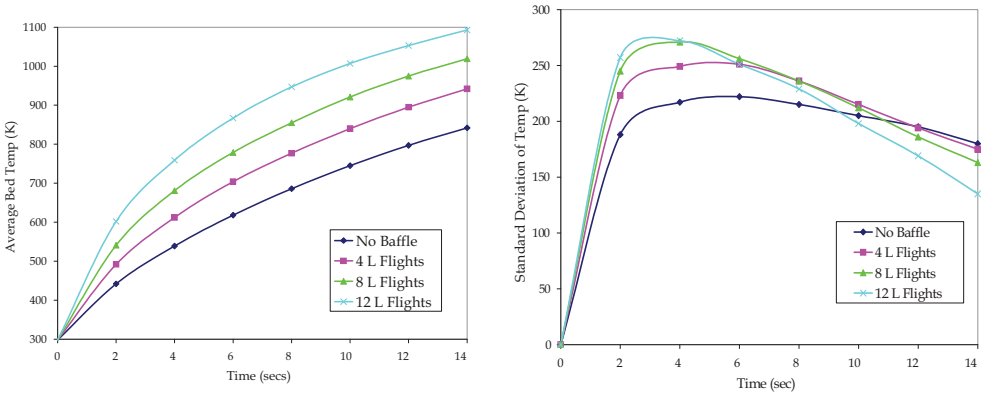

(a) (b)

Fig. 10. (a): Effect of number of L-Shaped baffles on heat transfer. (b): The evolution of standard deviation versus time for different baffle configurations

4.3.4 Effect of speed in baffled calciners:

Heat transfer as a function of vessel speed is examined for L-shaped baffles. The evolution of temperatures of the particles is estimated for calciners with 8 flights/baffles rotated at different speeds: 10, 20 and 30 rpm (shown in Fig 11). The cold core gets smaller with time for all the cases, but this reduction is faster for calciners rotated at higher speed. The number of red particles present in the bed also increases for calciners rotating with higher speed. Thus, an increase in the speed enhances heat transfer within the calciners. The effect of speed on heat transfer is quantified by means of the average bed temperature as a function of time for all baffle configurations. Average bed temperature rises faster for calciners with higher speeds, as seen in Figure 12(a). This observation contradicts previous observations for un-baffled calciners. The higher vessel speed ensures more scooping of the material inside the bed and redistribution of the particles per unit of time, by the L-shaped baffles. The uniformity of the temperature of the particle bed is quantified by estimating the standard deviation of the surface temperature of the bed. As expected, bed rotated at higher speed reaches thermal uniformity faster (see Fig. 12(b)).

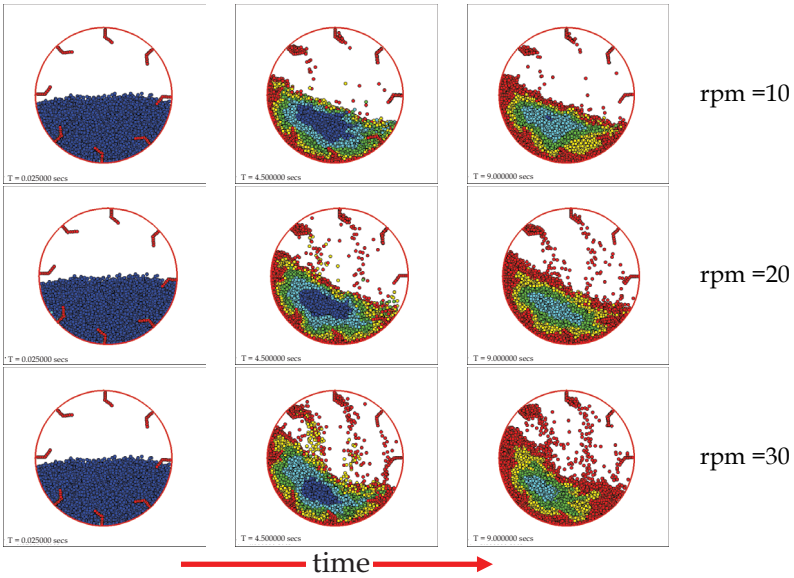

Fig. 11. Evolution of temperature for baffled calciners (8 flights) at different rotational speeds of 10, 20 and 30 rpm, for different values of time = 0, 4.5 and 9 secs.

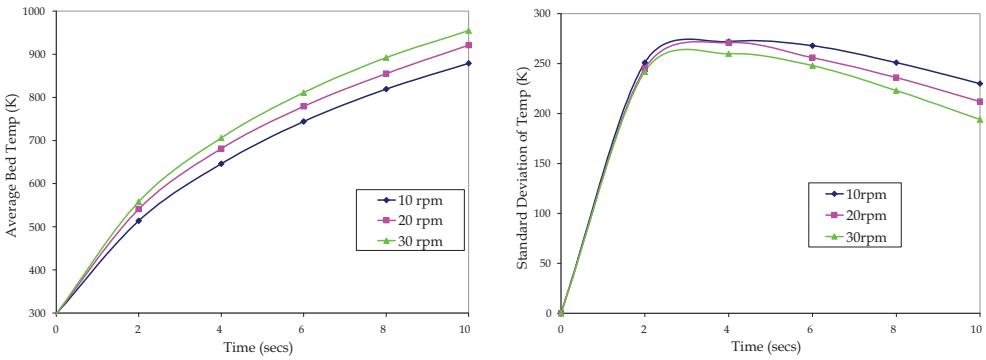

(a) (b)

Fig. 12. (a): Effect of speed on heat transfer for calciners with L-Shaped baffles. (b): The evolution of the standard deviation versus time for different vessel speeds.

4.3.5. Effect of adiabatic baffles on heat transfer in calciners

In the previous simulations all baffles were always at the wall temperature and enhanced the heat transfer and thermal uniformity (mixing) in the calciners. However, this can be due to two distinct effects. The flights not only scoop and redistribute particles enhancing convective transport, but also heat up the particles during the contact, increasing area for conductive transport. To nullify the conduction effect and check how flights affect convective heat transfer, L-shaped baffles were maintained at an adiabatic condition in a

particle-baffle contact, dQ = 0 is considered. The 8 flights are thus maintained at the room temperature (298K) whereas, the wall remains at 1298 K. In Figure 13, the axial snapshots are displayed at time T= 0, 4 secs and 8 seconds for 2 different baffle configurations: (i) 8 L-shaped baffles at room temperature (298K) (ii) 8 L-shaped flights at the wall temperature (1298 K). The blue core signifies the mass of particles at the initial temperature. This cold core shrinks with time for all the cases, but it shrinks faster for calciners with L-shaped baffles at wall temperature. The number of red particles present in the bed also increases for calciners with L-shaped baffles at wall temperature (shown in the left column in Fig 13).

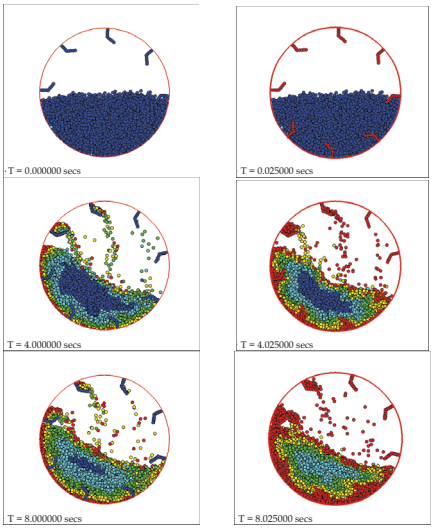

Fig. 13. The axial snapshots of the calciners with cold (left) and hot baffles (right) at different time intervals.

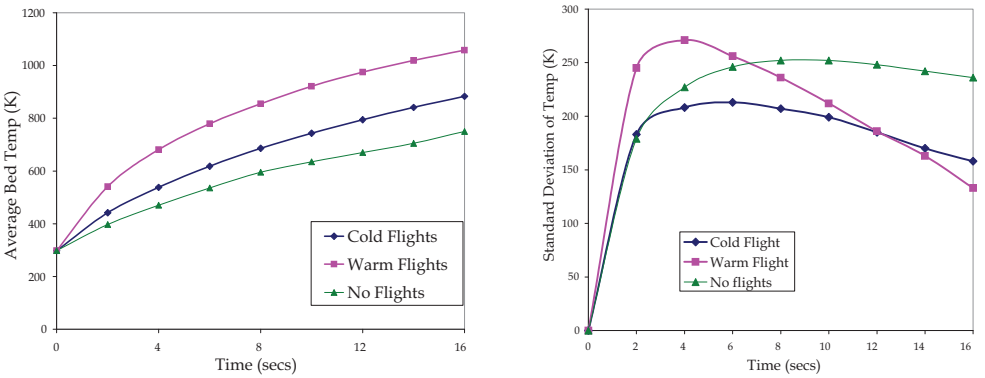

Fig. 14. (a): The evolution of average bed temperature for 8 L shaped cold and warm flights and unbaffled calciners. (b): The evolution of thermal uniformity for calciners with cold , warm baffled and unbaffled flights.

Thus, heated baffles enhance heat transfer within the calciners. The effect of the temperature of the baffle on heat transfer is quantified by calculating the average bed temperature as a function of time for all baffle configurations and comparing it with the temperature profile of the non-baffled calciner. The average bed temperature rises faster for calciners with L-shaped baffles at wall temperature, but the calciner with colder baffle shows faster heat transport than non-baffled calciners (see Figure 14(a)). In Figure 14b, the uniformity of the temperature of the particle bed is presented by estimating the standard deviation of the surface temperature of the bed. The calciners with flights are reaching thermal uniformity faster than the non-baffled calciners. The temperature of the baffle does not cause much difference in thermal uniformity as both the curves for baffled calciners are very close to each other (convective mixing effect is independent of baffle temperature)

4.4 Heat transfer of copper particles in the calciner

Initially, 16,000 particles are loaded into the system in a non-overlapping fashion and allowed to reach mechanical equilibrium under gravitational settling. Subsequently, the vessel is rotated at given rate, and the evolution of the position and temperature of each particle in the system is recorded as a function of time. The curved wall is considered to be frictional. To minimize the finite size effects the flat end walls are considered frictionless and not participating in heat transfer. A parametric study was conducted by varying thermal conductivity, particle heat capacity, granular cohesion, vessel fill ratio, and vessel speed of the calciner. A cohesive granular material (K_{cohes} = 75, μ_{SP} = 0.8, μ_{DP} = 0.6, μ_{SW} = 0.8, μ_{DW} = 0.8) is considered to examine the effect of thermal properties and the speed of the vessel. Particles with temperature lower than 350°K are colored blue; those with temperature in between 350°K and 550°K are considered cyan. Those with temperature between 550°K and 750°K are considered green and for temperatures between 750°K and 950°K are considered yellow. Those particles with temperature higher than 950°K are colored red.

4.4.1 Effect of thermal conductivity

Three values of thermal conductivity of the solid material are considered: 96.25, 192.5, 385 W/m°K. The calciner is rotated at the speed of 20 rpm. As the heat source is the wall, the particle bed warms up from the region in contact to the wall. Particle-wall contacts cause the transport of heat from the wall to the particle bed. With subsequent particle-particle contacts, heat is transported inside the bed. In Figure 15a, the axial snapshots captured at time T= 0, 0.5 and 1 revolutions for varying thermal conductivities are displayed. The combination of heat transfer and convective particle motion results in rings or striations as the temperature decrease from the wall to the core of the bed. The presence of these concentric striations signifies that under the conditions examined here, the dominant mechanism is radial conductive transport of heat from the wall to the core of the bed. The blue core signifies the mass of particles at initial temperature. This cold core shrinks with time, as expected; the volume of the blue core shrinks faster for higher particle conductivities. The average bed temperature is illustrated in Figure (15d). As conductivity increases, the system exhibits faster heating. The variation of the standard deviation of the temperature of the bed is illustrated on Fig. 15 (e). Uniformity in the bed temperature increases with conductivity until the end of 5 revolutions. Finally the bed with higher conductivity rapidly reaches a thermal equilibrium with the isothermal wall, where all the particles in bed reach the wall temperature and there is no more heat transfer.

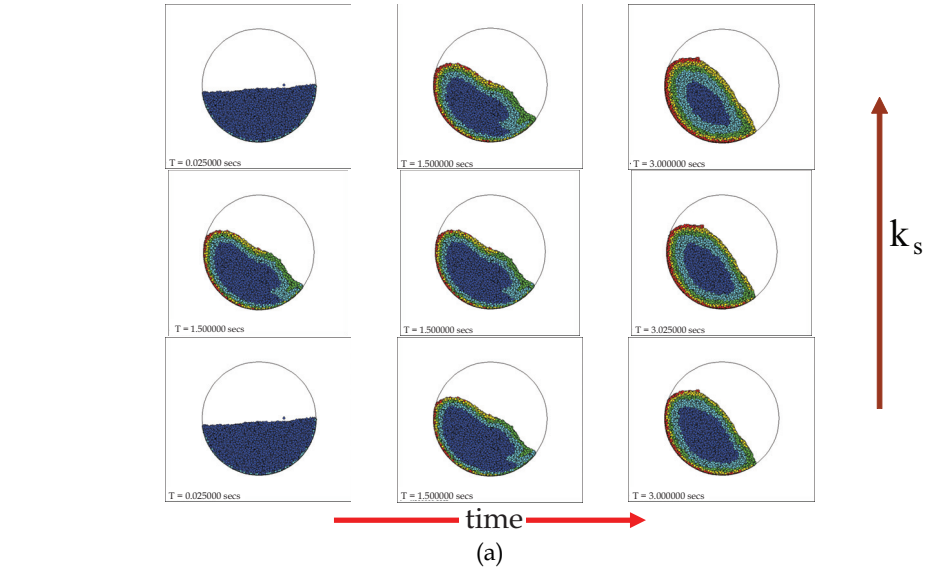

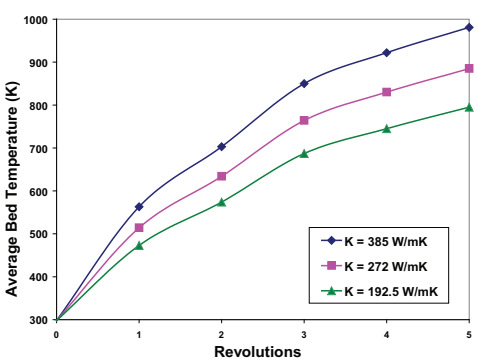

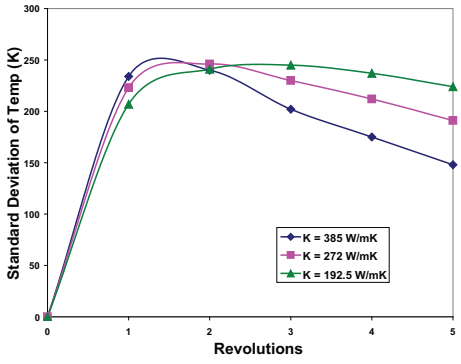

Fig. 15. (a) shows a time sequence of axial snapshots of color-coded particles in the calciner. Time increases from left to right (t = 0, 1.5 and 3 secs), while the thermal conductivity increases from bottom to top (k_s = 192.5, 272, 385 W/mK). (b) shows the growth of average bed temperature over time for materials with different conductivity. The granular bed heats up faster for material with higher conductivity. (c). illustrates the variation of the standard deviation of particle temperature over time for different conductivities. More uniformity of temperature in the bed for material of higher thermal conductivity.

A physical formula to fit the simulation prediction is derived based on the Levenberg-Marquardt method, which uses non-linear least square based regression techniques. This curve fitting method is employed for the average bed temperature data displayed in Fig 1 for the highest thermal conductivity (k_s = 385 W/mK). The 3rd order polynomial derived is as follows

$$T_{avg} = 301.92 + 288.624n - 45.05n^2 + 2.9n^3 \quad (6)$$

where T_{avg} and n are the average bed temperature and number of revolutions respectively. The vessel speed for this data is 20 rpm and so n=1 corresponds to 3 seconds. The correlation coefficient for this fit R = 0.9989. The simulation data and the 3rd order least square fit curve of the data are illustrated in Fig. 15d.To gather an insight of the evolution of average bed temperatures beyond 5 revolutions, the average bed temperatures at all time intervals for each of the cases in Fig. 15b is scaled by the corresponding average temperature at 5 revolutions. In Fig. 15e, almost all of the data points for different conductivity overlap showing the evolution of average temperature follow the same shape and will reach thermal equilibrium with the wall at the same rate shown in Fig. 15b.

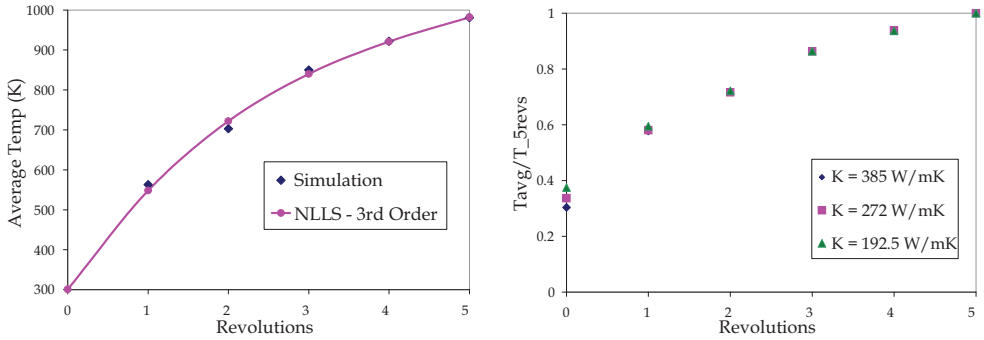

(d) (e)

Fig. 15. (d): Comparison of the simulation data (for k_s = 385 W/mK) and the non-linear least square fit, (e): Average bed temperature over time for materials with different conductivities.

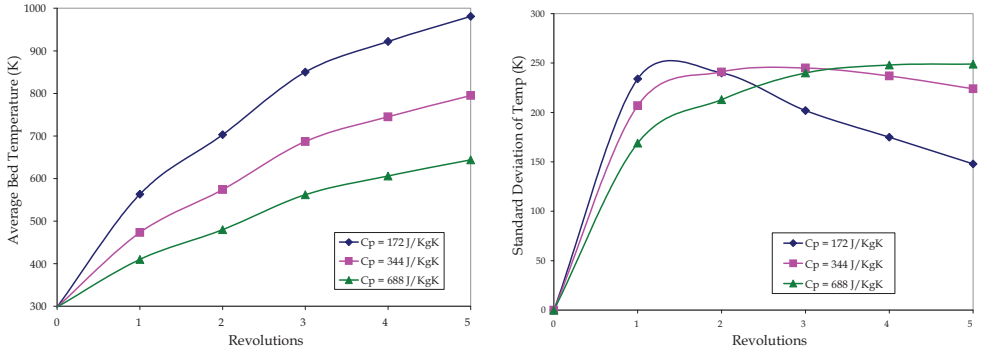

(a) (b)

Fig. 16. (a) Evolution of average bed temperature over time in a calciner, for material with different heat capacities (Cp= 172, 344, 688 J/KgK). Granular bed heats up faster for material with lower heat capacity (b) Variation of the standard deviation of particle temperature over time for different heat capacities. More uniformity of temperature is seen in the bed for materials of lower heat capacity.

4.4.2 Effect of heat capacity

After quantifying the effect of thermal conductivity, the other main thermal property of a material, heat capacity, is checked. Three values of heat capacity of the granular material are considered: 172, 344 and 688 J/Kg^{o}K, while keeping the thermal conductivity constant at 385 W/m^{o}K. Once again, the calciner is rotated at the speed of 20 rpm. Average bed temperatures are estimated as a function of time (Fig. (16a)). As expected, particles with lower heat capacity exhibit faster heating. The evolution of the standard deviation of temperature of the granular bed is illustrated in Figure 16(b). The variability in the bed temperature is larger for the material with lower heat capacity until 2 revolutions, but at the end of 5 revolutions, more uniform temperature is observed for the material of lower heat capacity.

4.4.3 Effect of granular cohesion and friction

The effect of granular cohesion on heat transfer is examined while keeping the thermal properties constant (k_s = 385 W/m*K and Cp = 172 J/Kg*K). As discussed in Section 2, to simulate different levels of cohesion and friction, the bond number K, the coefficients of static and dynamic friction between particles (μ_{SP} and μ_{DP}) and the coefficients of static and dynamic friction between particle and wall (μ_{SW} and μ_{DW}) are varied. Heat transfer in cohesionless particles (K_{cohes} = 0, μ_{SP} = 0.8, μ_{DP} = 0.1, μ_{SW} = 0.5, μ_{DW} = 0.5) is compared with a slightly cohesive (K_{cohes} = 45, μ_{SP} = 0.8, μ_{DP} = 0.1, μ_{SW} = 0.5, μ_{DW} = 0.5) and a very cohesive material (K_{cohes} = 75, μ_{SP} = 0.8, μ_{DP} = 0.6, μ_{SW} = 0.8, μ_{DW} = 0.8). The evolution of the average bed temperature over time is shown in Fig. 17a. For all cases examined here, cohesion does not cause a significant difference in the temperature profiles. The variability in bed temperature is quantified by the standard deviation of the particle temperature. In Figure 17b, the variation in standard deviation of temperature for the three values of cohesion is shown. Once again for the cases examined here, granular cohesion does not have a significant effect in the uniformity of the particle temperature of the bed.

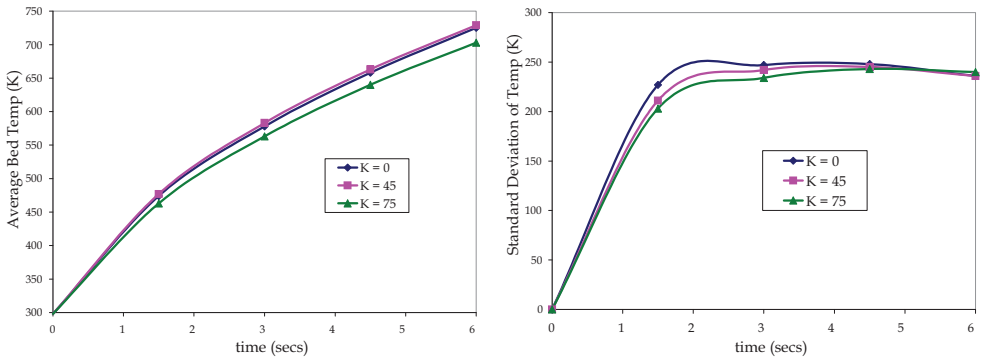

(a) (b)

Fig. 17. (a) shows the evolution of average bed temperature over time in the calciner, for materials with different granular cohesion (K_{cohes} = 0, 45, 75). (b) illustrates the variation of the standard deviation of particle temperature over time for different levels of granular cohesion. Granular cohesion has no significant effect in heat transfer.

4.4.4. Effect of vessel speed

In order to examine the effect of vessel speed, the most cohesive granular system (K_{cohes} = 75) is rotated at three different speeds: 12.5, 20 and 30 rpm, for thermal transport properties constant and equal to: k_s = 385 W/m^{o}K and C_p = 172 J/Kg^{o}K. Figure 18a displays snapshots captured at 0, 0.5 and 1 revolutions for varying vessel speeds. The higher vessel speed applies a higher shear rate to the granular system, causing significant differences in flow behavior, evident in the different dynamic angle of repose of the bed at each rotational speed.

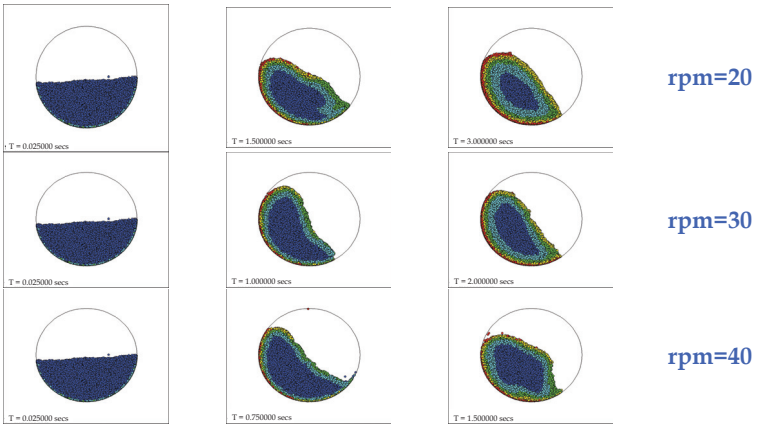

(a)

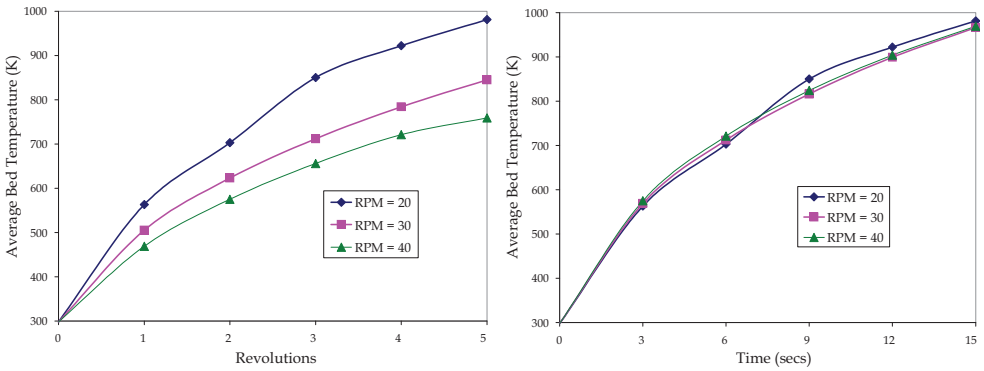

(b) (c)

Fig. 18. (a) shows the time sequence of axial snapshots of color-coded particles in the calciner. Time increase from left to right hand side (T = 0, 0.5 and 1 revolution), while the vessel speed increases from top to bottom (20, 30 and 40 rpm). (b) shows the evolution of average bed temperature versus vessel rotations for different vessel speeds. (c) shows the average bed temperature profile over real time for different vessel speeds. Rotation speed increases heat transfer in a per-revolution basis but the effect disappears on a per-time basis.

On a per-revolution basis, slower speed caused higher temperature rise (as shown in Fig. 18(b)). A thicker red band of particles (adjacent to the wall) and a smaller blue core are evident. At slower speeds, each particle has a more prolonged contact with the heated wall, which contributes to the rapid rise in the temperature. However, when analyzed on per absolute time basis, the effect of speed dissappers as the average bed temperatures for all the cases follows nearly identical trends (Fig 18(c)). The standard deviation of the temperature of the bed is also estimated in per-revolution and per-time basis. While the temperature of the bed is more uniform at slower speeds on a per revolution basis (Fig. 19(a)). This effect almost disappears on the real time basis (Fig 19(b)).

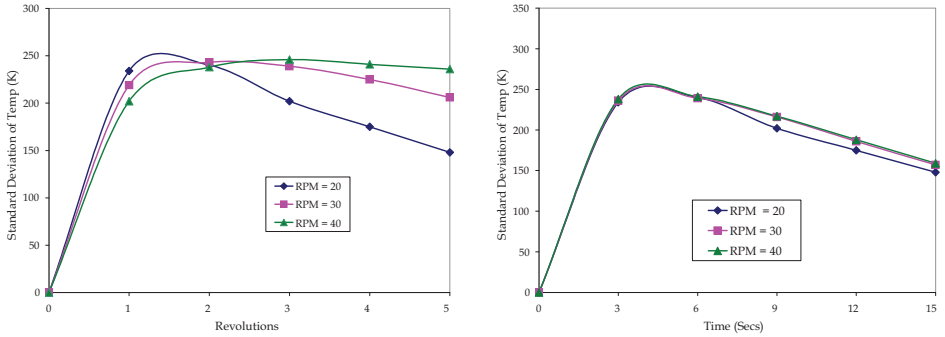

(a) (b)

Fig. 19. (a) shows the evolution of standard deviation of bed temperature versus vessel rotations for different vessel speeds. (b) shows the standard deviation of bed temperature over real time for different vessel speeds. Rotation speed increases the uniformity of bed temperature in a per revolution basis but the effect almost disappears on a per-time basis.

4.4.5. Effect of fill ratio

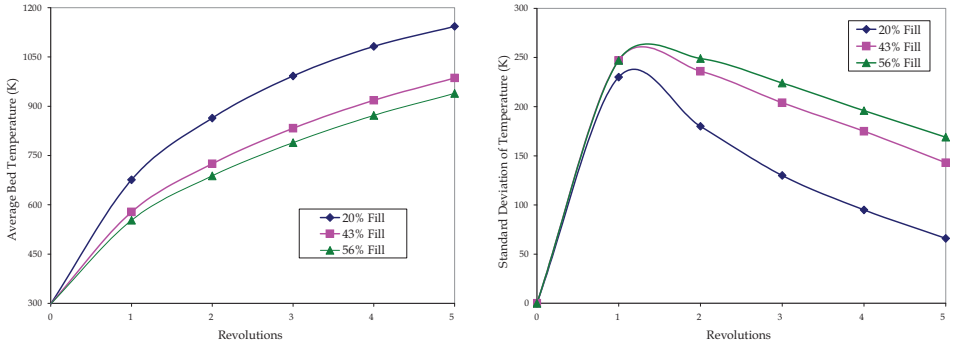

(a) (b)

Fig. 20. (a) shows the evolution of average bed temperature over time for granular bed of different volumes (fill % = 20, 43, 56). The granular bed heats up faster for lower fill fraction. (b) illustrates the variation of the standard deviation of particle temperature over time for different fill fractions. More uniformity of temperature in the bed of lower fill fraction.

Three different fill levels, 18%, 43% and 56%, are simulated using 7000, 16000 and 20,000 particles. Once again, the vessel is rotated at 20 rpm. Particle's thermal transport properties remain constant at k_s = 385 W/m°K and C_p = 172 J/Kg°K. Non-cohesive conditions are considered. In Fig. 20(a), the change in average bed temperature with time is shown as a function of the fill ratio. As expected, the granular bed with lower fill fraction heats up faster. Faster mixing is achieved for the lower fill fraction case, which causes rapid heat transfer from the vessel wall to the granular bed. The temperature is more uniform for lower fill fraction at the end of 5 revolutions (Fig 20(b)).

4.5 Heat transfer in a double cone impregnator

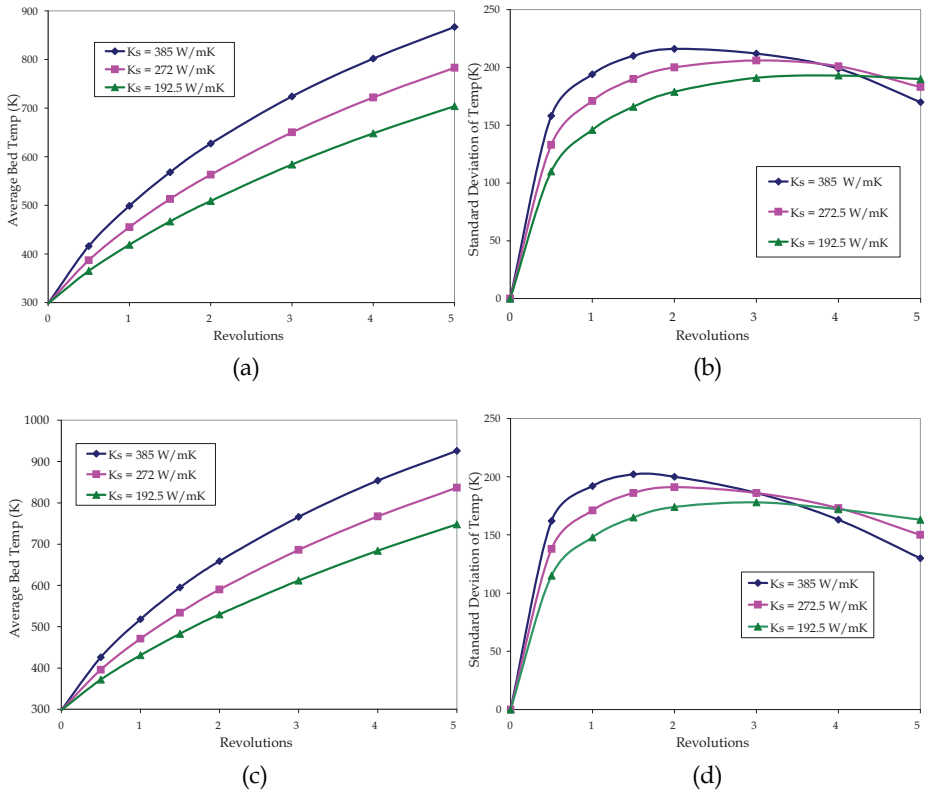

Fig. 21. (a) shows the growth of the average bed temperature over time in a non-baffled impregnator, for materials with different thermal conductivities (k_s = 192.5, 272, 385 W/mK). (b) shows the growth of the average temperature of the bed over time in baffled impregnator, for materials with different thermal conductivities (k_s = 192.5, 272, 385 W/mK). (c) illustrates the variation of the standard deviation of particle temperature in the non-baffled impregnator over time for different thermal conductivities. (d) illustrates the variation of the standard deviation of particle temperature over time for different thermal conductivities for a baffled vessel. Granular bed heats up faster for material with higher thermal conductivity.

We simulate the flow and heat transfer of 18,000 particles of 3mm size rotated in a double cone impregnator equipped with a baffle of variable size. Initially, particles are loaded into the system (with and without baffles) and allowed to reach mechanical equilibrium. Subsequently, the temperature of the vessel (and the baffle) is raised to the desired value of 1298°K, and the evolution of the temperature of each particle in the system is recorded as a function of time. All impregnator walls are considered to be frictional in the simulation. Coefficients of static friction between particles and particle-wall are considered to be 0.8 and 0.5 respectively. Coefficient of dynamic friction is considered to be the same as those of static friction for simplicity.
Firstly, the effects of thermal conductivity and heat capacity on temperature are examined. Subsequently, the impact of the vessel speed and baffle size on heat transfer rate and temperature field uniformity are examined. Three cases are considered: (a) no baffle, (b) baffle with 9 cm^2 cross-section (c) baffle with 36 cm^2 cross-section. Particles in all the impregnator simulations are considered non-cohesive. Once again, the initial temperature of all the particles are considered to be at 298°K (room temperature) whereas the temperature of the wall (and the baffle if present) is considered to be at 1298°K (and in isothermal condition). Particles with temperature lower than 400°K are colored blue, while those with temperature in between 400°K and 600°K are colored green; those with temperature in between 600°K and 900°K are colored yellow, and those with temperatures higher than 900°K are colored red.

4.5.1 Effect of thermal conductivity

Higher thermal conductivity favored the transfer of heat and enhanced temperature uniformity in calciner flows. Impregnators and calciners both tumble but have different shapes. The effect of thermal conductivity on granular bed temperature is quantified for non-baffled and baffled impregnators. Three values of thermal conductivity (k_s) of the material are considered: 96.25, 192.5 and 385 W/m°K. All three simulations are performed at 20 rpm. The evolution of the average bed temperature as a function of thermal conductivity is shown in Fig. 21a (un-baffled impregnator) and 21b (baffled impregnator with baffle cross-sectional area of 9 cm^2). More conductive particles exhibit faster heating in both cases. The standard deviation plots corresponding to particle temperature for the non-baffled and baffled impregnators are shown in Fig 21c and 21d. In the first three revolutions, we observe more uniform (lower standard deviation) temperature for the cases with lower conductivity. At later times, as most particles reach high temperatures, all the curves show low values of standard deviation (not shown). More uniform temperature is attained in the bed of highest conductivity (k_s = 385 W/mK) after 3 revolutions (Figs. 21c and 21d).

4.5.2 Effect of heat capacity

Similar to the transient heat transfer analysis of the calciner, the effect of heat capacity is also quantified for non-baffled and baffled impregnators. Three values of heat capacity are considered: 172, 344 and 688 J/Kg°K. The coefficient of thermal conductivity is kept constant at 385 W/m°K. These simulations are performed at a vessel speed of 20 rpm. The evolution of the average bed temperature over time is depicted in Fig. 22(a). As expected, the lower the heat capacity, the faster the rise in bed temperature. The variability of the bed temperature is higher for material with higher heat capacity (see Fig. 22(b)).

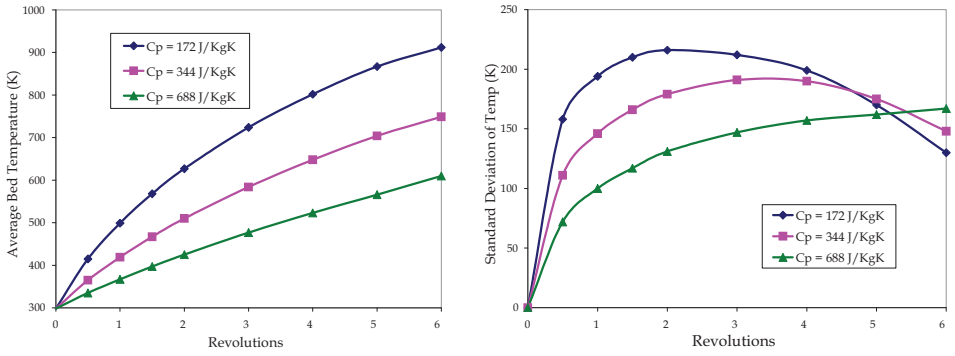

(a) (b)

Fig. 22. (a) shows the growth of average bed temperature over time for materials with different heat capacities (Cp =172,344,688 J/KgK). (b) illustrates the variation of the standard deviation of particle temperature over time for different baffle sizes. Granular bed heats up faster for material of lower heat capacity.

4.5.3 Effect of baffle size

The baffle size is a significant geometric parameter for the impregnator. The effects of baffle size on the motion and heat transfer of the granular bed are studied for three cases: (a) no baffle (b) baffle with 9 cm² cross-section (c) baffle with 36 cm² cross-section. Simulations are carried out for a vessel speed of 20 rpm. Thermal transport properties of the particles are k_s = 385 W/m°K and C_p = 172 J/Kg°K. Figure 23(a) displays snapshots captured at 0, 2.5 and 4 seconds for varying baffle sizes. The effect of the baffle is clearly seen at the snapshot corresponding to 2.5 seconds. Red particles (T > 900°K) group around the baffle boundary, whereas the un-baffled container barely contains any red particles. The average bed temperature and the standard deviation of the temperature are shown in Figs 23(b) and 23(c), respectively. The temperature increases at a faster rate (Fig. 23(b)) and more uniformly (Fig. 23(c)) for cases with baffles. The temperature rise is faster for larger baffles. Baffles enhance mixing, which increase the uniformity in the temperature field of the granular bed. This observation is line with the experimental finding by Brone, 2000 and the numerical mixing results of Muguruma, 1997, who found that an optimal baffle size and positioning enhances mixing in rotary vessels.

4.5.4 Effect of vessel seed

Numerical simulations of heat transfer in calciners (shown above), reveal that lower speed enhances heat transfer and temperature uniformity on a per-revolution basis. Heat transfer as a function of vessel speed is studied here for a baffled (36 cm² cross sectional area) impregnator at three different rotational speeds: 12.5, 20 and 30 rpm. Transport properties are: k_s = 385 W/m°K and C_p = 172 J/Kg°K, respectively. Figure 24(a) displays snapshots captured at 0, 0.5 and 1 revolutions for varying vessel speeds. At the end of 0.5 and 1 revolution, more red particles (T > 900°K) are seen for vessels rotating at lower speeds; once again, on a per-revolution basis, lower speed causes higher temperature rise (as shown in Fig. 24(b)). Again, at slower speeds, the particles have a more prolonged contact with the heated wall, which contributes to the rapid rise in the temperature. However, on a per-time basis, the effect of speed partially disappears, as the average bed temperatures rise in unison

for first 3 sec (Fig 24(c)) at all rotation speeds. However, after 3 seconds, temperature again rises faster for the vessel rotated at the slower speed of 12.5 rpm giving a counter-intuitive result. The standard deviation of the temperature of the granular bed is also estimated in per-revolution and per-time basis. The uniformity of the temperature of the bed significantly increases with slower speed of the calciner on a per-revolution basis (Fig. 25(a)). This effect also remains prominent on a real-time basis (Fig 25(b)).

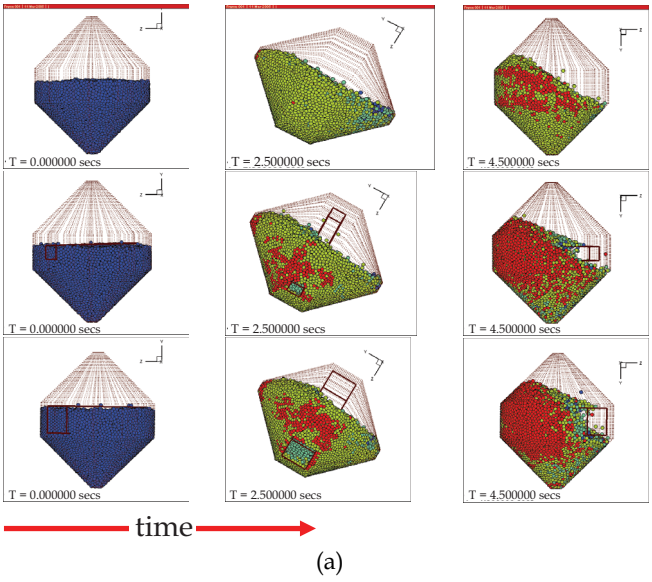

(a)

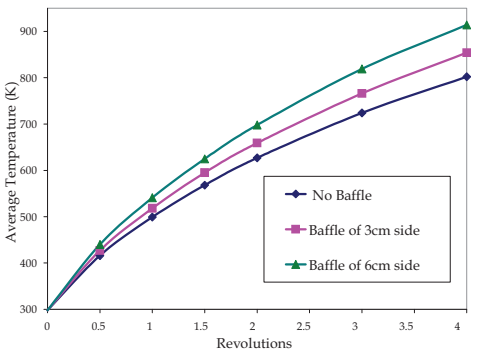

(b)

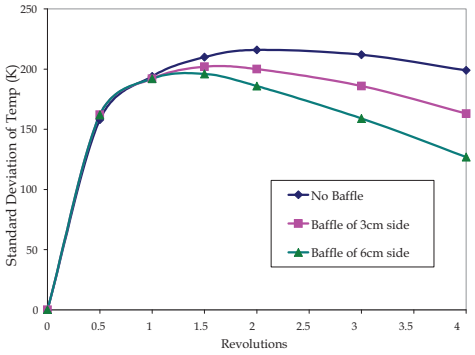

(c)

Fig. 23. (a) shows a time sequence of simulation snapshots of color-coded particles in the impregnator. Time increase from left to right hand side (T = 0, 2.5 and 4.5 secs), while the baffle size increases from top to bottom (no baffle, baffle of 3cm , baffle of 6cm). (b) shows the growth of average bed temperature over time for different sizes of baffle. Depending on size, baffles can either increase or decrease heat transfer. (c) shows the variation of the standard deviation of particle temperature over time for different baffle sizes. Uniformity in the bed temperature is more with bigger baffle.

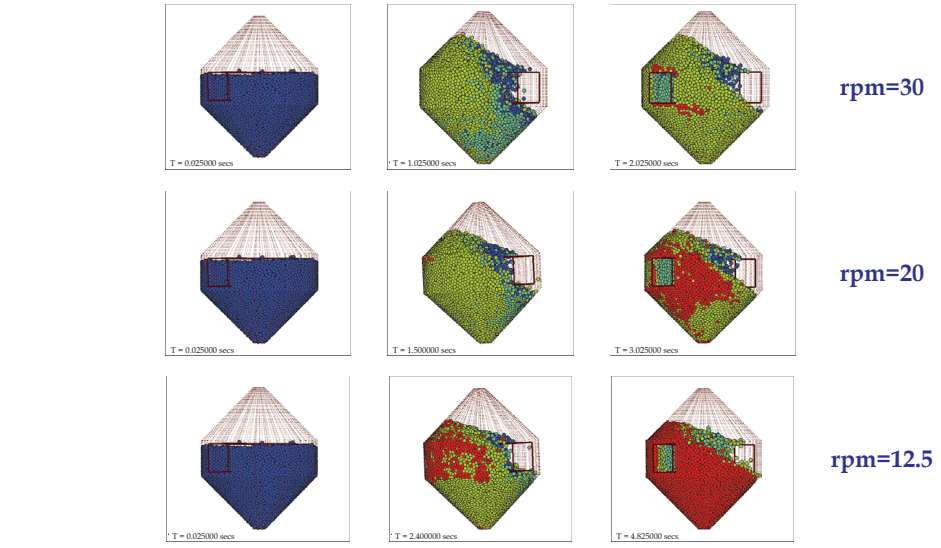

(a)

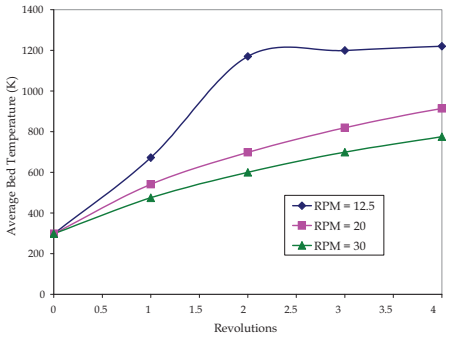

(b)

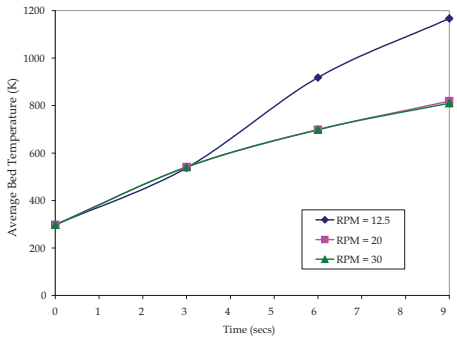

(c)

Fig. 24. (a) shows a time sequence of simulation snapshots of color coded particles in the impregnator. Time increases from left to right hand side (T = 0, 0.5 and 1 revolution), while the vessel speed increases from bottom to top (12.5, 20, 30 rpm). (b) shows the evolution of the average bed temperature versus the number of revolutions for different vessel speeds. (c) shows the growth of average bed temperature over real time for different vessel speeds. Lower rotational speed of the impregnators facilitates heat transfer if analyzed with respect to each revolution, but the effect disappears on a per-time basis.

5. Dimensionless analysis

Although conductivity and heat capacity of the material have similar effects in the heat transfer for both the calciner and impregnator, the vessel speed only affects the heat transfer

in impregnators. Thus for impregnators we could define a parameter **Π**, which is directly proportional to the thermal conductivity (k_s) but inversely proportional to the specific heat (C_p) and the rotational speed (N) of the vessel. The heat balance of the granular material could be expressed as:

$$\rho C_p \left[\frac{\delta T}{\delta t} + v \bullet \nabla T \right] = k_s \nabla^2 T$$

or

$$\rho C_p \frac{T^0}{\tau} \frac{\delta T^*}{\delta t^*} + \rho C_p \frac{U T^0}{L} v^* \bullet \nabla^* T^* = k_s \frac{T^0}{L^2} \nabla^{*2} T^*$$

or

$$\frac{\delta T^*}{\delta t^*} + \frac{U\tau}{L} v^* \bullet \nabla^* T^* = \frac{k_s \tau}{\rho C_p L^2} \nabla^{*2} T^*$$

T^o , U and L are the initial bed temperature, linear velocity and the length of the vessel respectively. If we consider $\tau = L/U$ (no independent time scale, i.e., Strouhal number = 1), the equation above becomes:

$$\frac{\delta T^*}{\delta t^*} + v^* \bullet \nabla^* T^* = \frac{k_s}{\rho C_p L U} \nabla^{*2} T^*$$

or

$$\frac{DT^*}{Dt^*} = \Pi \nabla^{*2} T^*$$

or

$$\frac{DT^*}{D(\Pi t^*)} = \nabla^{*2} T^*$$

The dimensionless parameter **Π** is expressed as follows:

$$\Pi = \frac{k_s}{\rho C_p L U} = \frac{k_s}{\rho C_p L (2\pi N L)} = \frac{k_s}{2\pi \rho C_p N L^2} \tag{7}$$

where N is rotational velocity in rotations per second. As per the dimensionless equation 6, the heat transfer in the granular bed is conduction controlled. Figure 26 illustrates the variation of the dimensionless average temperatures (T*) of the granular bed (in the impregnator with no baffle and a baffle with 36 cm^2 cross-section) with dimensionless time (**Π**t*) as a function of either thermal conductivity or heat capacity of the material. The set of five curves (3 for different thermal conductivities and constant heat capacity; and 2 for different heat capacities and constant thermal conductivity) remain very close to each other

justifying equation 6 for both the baffled and non-baffled impregnators. Thus, we observe two different groups of curves, one for baffled and one for non-baffled impregnators. The granular beds of baffled impregnator are heated faster in comparison to the non-baffled ones, which is in line to our observation in section 4.5.2. The presence of baffles, which causes a significant difference in the flow and heat transfer of granular material, brings in convective heat transport within the bed.

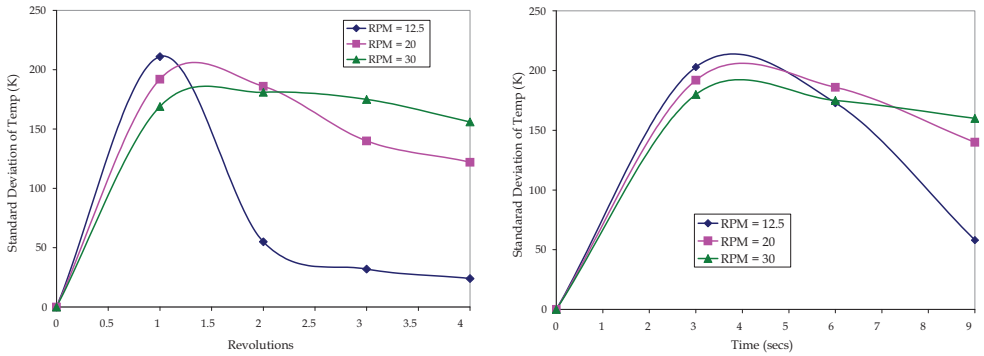

(a) (b)

Fig. 25. (a) shows the evolution of standard deviation of the bed temperature versus vessel rotations for different vessel speeds. (b) shows the standard deviation of the bed temperature over real time for different vessel speeds. Lower rotation speed increases the uniformity of bed temperature in both per revolution and real time basis.

6. Conclusions

We presented experimentally validated particle dynamics simulations of heat transfer in rotary calciners. Granular flow and heat transport properties of alumina and copper are taken into account in order to develop a fundamental understanding of their effect on calcination performance. Heat transport processes are simulated accounting for initial material temperature, wall temperature, granular heat capacity, granular heat transfer coefficient, and baffle configuration. Simulations and experiments show that the rotation speed has minimal impact on heat transfer. As expected, the material with higher thermal conductivity (alumina) warms up faster in experiments and simulations. We considered various baffle configurations (rectangular and L-shaped flights) in the calciner and their effect on the flow and heat transfer of granular material. Baffles or flights enhance heat transfer and thermal uniformity. L-shaped baffles are more effective than the square shaped baffles. The average wall-particles heat transfer coefficient of the granular system is also estimated from the experimental findings. Particle dynamics simulations were also used to examine heat transfer in granular materials rotated in the impregnators. While particle movement is quite different in the impregnators and calciners, both share similar heat transfer characteristics. We observe faster heating for materials with higher conductivity and lower heat capacity. Granular cohesion does not affect heat transfer rates. Increasing rotation speed decreases heat transfer and temperature uniformity on a per-revolution basis but the effect disappears on a per-time basis. Impregnator flows also exhibit faster heating of

the granular bed for material with higher conductivity and lower heat capacity. Baffles enhance temperature rise in the impregantors. Depending on size, baffles can either increase or decrease heat transfer in the impregnators. Lower rotational speed of the impregnators facilitates heat transfer both on a per-revolution and a per-time basis. A dimensionless parameter **Π** is derived for the heat transfer in the impregnators, coupling thermal conductivity, heat capacity of the material and the rotational speed of the vessel.

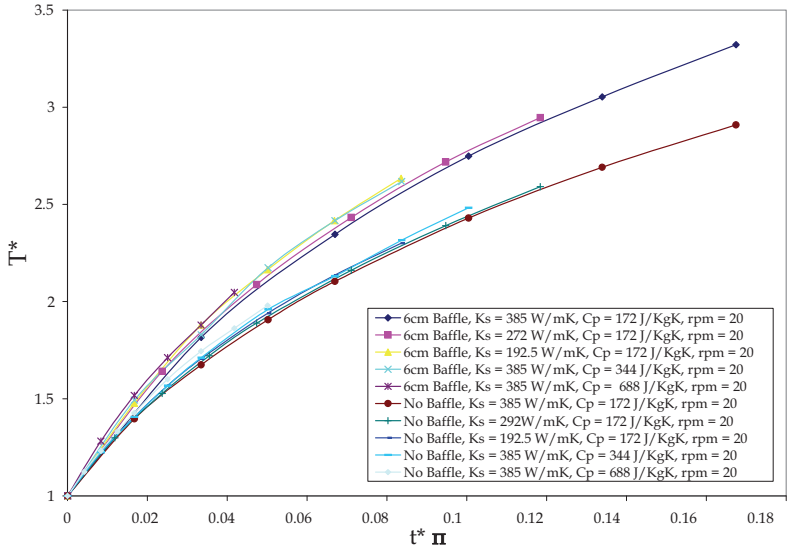

Fig. 26. The growth of dimensionless average bed temperature over dimensionless time in the baffled and non-baffled impregnators, for materials with different thermal conductivities (k_s = 192.5, 272, 385 W/mK) and heat capacities (Cp = 172 J/kgK, 344 J/KgK and 688 J/KgK).

	Notations	Copper	Alumina
Total number of particles	**N**	**8,000-20000**	**20,000**
Radius of the particles	**r**	**2 mm**	**1.0 mm**
Density of the particles	ρ	**8900 kg/m3**	**3900 kg/m3**
Specific Heat	C_p	**172 J/KgK**	**875 J/KgK**
Thermal Conductivity	k_s	**385 W/mK**	**36 W/mK**
Thermal Diffusivity	**α**	**2.5 x 10-7 m2/s**	**1.1 x 10-5 m2/s**
Coefficient of restitution	**e**		
Particle/particle		**0.8**	**0.8**
Particle/wall		**0.5**	**0.5**
Normal Stiffness Coefficient	**k**		
Particle/particle		**6000 N/m**	**6000 N/m**
Particle/wall		**6000 N/m**	**6000 N/m**
Time step	**Δt**	**1-3 x 10-6 sec**	**5 x 10-6 sec**

Table 1. Parameters employed in DEM simulations

7. Acknowledgements

We gratefully acknowledge the support of the Rutgers Consortium on Catalyst Manufacturing Science and Engineering and Pfizer Pharmaceuticals, both grants to FJM and MST. We also acknowledge under graduate students: Myo Kyaw, Dion Zhang and Daniel Carlson for helping with the experiments.

8. References:

Lee, H. H. (1984). Catalyst preparation by impregnation and activity distribution. *Chemical Engineering Science*, 39, 859.

Lekhal, A., Glasser, B.J., Khinast, J.G. (2001). Impact of drying on the catalyst profile in supported impregnation catalysts. *Chemical Engineering Science*, 56, 4473.

Mickey, H.S., Fairbanks, D.F., (1955). Mechanics of heat transfer to fluidized beds. *A.I.CH.E. Journal*, 1, 374.

Basakov, A.P. (1964) The mechanism of heat transfer between a fluidized bed and surface. *International Chemical Engineering*, 4, 320.

Zeigler, E.N., Agarwal, S. (1969). On the optimum heat transfer coefficient at an exchange surface in a gas fluidized bed, *Chemical Engineering Science*, 24, 1235.

Leong, K.C, Lu., G.Q., Rudolph, V. (2001). Modeling of heat transfer in fluidized bed coating of cylinders. *Chemical Engineering Science,* 56, 5189.

Barletta, M., Simone, G. Tagliaferri, , V. (2005). A FEM model of conventional hot dipping coating process by using fluidized bed. *Progress in Organic Coatings*, 54, 390.

W. Schotte, Thermal conductivity of packed beds. A.I.CH.E Journal, 6, (1960) 63.

Sullivan, W.N., Sabersky, R.H. (1975). Heat transfer to flowing granular media. *International Journal of Heat and Mass Transfer*, 18, 97.

Broughton, J., Kubie, J, (1976) A note on heat transfer mechanism as applied to flowing granular media. *International Journal of Heat and Mass Transfer*, 19, 232.

Spelt, J.K, Brennen, C.E., Sabersky, R.H. (1982). Heat transfer to flowing granular material. International Journal of Heat and Mass Transfer, 25, 791.

Patton, J.S., Sabersky, R.H., Brennen, C.E. (1987). Convective heat transfer to rapidly flowing granular materials. *International Journal of Heat and Mass Transfer*, 30, 1663.

Buoanno, G., Carotenuto, A. (1996). The effective thermal conductivity of a porous medium with interconnected particles, *International Journal of Heat and Mass Transfer*, 40, 393.

Thomas, B., Mason, M.O., Sprung, R., Liu, Y.A, Squires, A.M. (1998). Heat transfer in shallow vibrated beds. *Powder Technology*, 99, 293.

Cheng, G.J., Yu, A.B., Zulli, Y (1999). Evaluation of effective thermal conductivity from the structure of a packed bed. *Chemical Engineering Science*, 54, 4199.

Wes, G.W.J, Drinkenburg, A.A.H., Stemerding, S. (1976). Heat transfer in a horizontal rotary drum reactor. *Powder Technology*, 13, 185.

Lehmberg, J. , Hehl, M., Schugerl, K. (1977). Transverse mixing and heat transfer in horizontal rotary drum reactors. *Powder Technology*, 18, 149.

Perry, H.R., Chilton, C.H. (1984). C.H. *Chemical Engineers' Handbook*, McGraw-Hill New York, 6, 11-46.

Lybaert, P. (1986). Wall-particle heat transfer in rotating heat exchangers, *International Journal of Heat and Mass Transfer*, 29, 1263.

Boateng, A.A., Barr, P.V. (1998). A thermal model for the rotary kiln including heat transfer within the bed. *International Journal of Heat and Mass Transfer*, 41, 1929.

Le Page, G.P., Tade, M.O, Stone R.J. (1998). Comparitive evaluation of advanced process control techniques for alumina flash calciners. *Journal of Process Control*, 8, 287.

Spurling, R.J., Davidson, J.F., Scott, D.M. (2000). The no-flow problem for granular material in rotating kilns and dish granulators. *Chemical Engineering Science*, 55, 2303.

Sudha, O.S., Chester, A.W., Kowalski, J.A., Beekman, J.W., Muzzio, F.J. (2002). Quantitative characterization of mixing processes in rotary calciners. *Powder Technology*, 126, 166.

Natarajan, V.V.R., Hunt, M.L. (1996). Kinetic theory analysis of heat transfer in granular flows. *International Journal of Heat and Mass Transfer*, 39, 2131.

Michaelidies, E.E. (1986). Heat transfer in particulate flows. *International Journal of Heat and Mass Transfer*, 29, 265.

Ferron, J.R., Singh, D.K. (1991). Rotary kiln transport processes, *A.I.CH.E. Journal*, 37, 747.

Cook, C.A, Cundy, V.A. (1995). Heat transfer between a rotating cylinder and a moist granular bed. *International Journal of Heat and Mass Transfer*, 38, 419.

Cundall, P. A., (1971). A computer model for simulating progressive large-scale movements in blocky rock systems. *Proceedings of Symposium International Society of Rock Mechanics*, 2, 129.

Cundall, P. A., Strack, O. D. L., (1979). A discrete numerical model for granular assemblies. *Geotechnique*, 29, 47.

Dippel, S., Batrouni, G. G., Wolf, D. E., (1996). Collision-induced friction in the motion of a single particle on a bumpy inclined line. *Physical Review E*, 54, 6845.

Luding, S., (1997). Stress distribution in static two dimensional granular model media in the absence of friction. *Physical Review E*, 55, 4720

Thompson, P. S., Grest, G. S., (1991). Granular flow: friction and the dilatancy transition. *Physical Review Letters*, 67, 1751.

Ristow, G. H., Herrmann, H. J., (1994). Density patterns in two-dimensional hoppers. *Physical Review E*, 50, R5.

Wightman, C., Moakher, M., Muzzio, F. J., Walton, O., R., (1998). Simulation of Flow and Mixing of Particles in a Rotating and Rocking Cylinder, *A.I.CH.E. Journal*, 44, 1226.

Shinbrot, T., Alexander, A., Moakher, M., Muzzio, F. J. (1999). Chaotic granular mixing. *Chaos*, 9, 611.

Moakher, M., Shinbrot, T., Muzzio, F. J. (2000). Experimentally validated computations of flow, mixing and segregation of non-cohesive grains in 3D tumbling blenders. *Powder Technology,* 109, 58.

Ristow G. H (1996). Dynamics of granular material in a rotating drum. *Europhysics Letters*, 34, 263.

Walton, O. R., Braun, R. L., (1986). Viscosity, granular-temperature and stress calculations for shearing assemblies of inelastic, frictional disks. *Journal of Rheology*, 30, 949.

Walton, O. R., (1992). *Particulate Two-Phase Flow*, Butterworth-Heinemann, Boston.

Walton, O. R., (1993). Numerical simulation of inclined chute flows of mono disperse, inelastic, frictional spheres. *Mechanics of Materials*, 16, 239.

Sudah, O. S., Arratia, P. E., Alexander, A., Muzzio F. J. (2005). Simulation and experiments of mixing and segregation in a tote blender. *A.I.CH.E. Journal*, 51, 836.

O'Brien, R. W. O., Batchelor, G. K. (1977). Thermal or electrical conduction though granular material, Proc. R. Soc. Lond., 355, 313.

Bird, R. B., Stewart, W. E., Lightfoot, E. N. (1960). *Transport Phenomena*, John Wiley and Sons, New York.

Crank, J. (1976). *The mathematics of Diffusion*, Oxford University Press, UK.

Brone, D., Muzzio, F. J. (2000). Enhanced mixing in double-cone blenders. *Powder Technology*, 110, 179.

Muguruma, Y., Tanaka, T., Kawatake, S., Tsuji, Y. (1997). Discrete particle simulation of rotary vessel mixer with baffles. *Powder Technology*, 93, 261.

Part 3

Heat Transfer in Mini/Micro Systems

13

Introduction to Nanoscale Thermal Conduction

Patrick E. Hopkins[1,2] and John C. Duda[2]
[1]*Sandia National Laboratories, Albuquerque, New Mexico*
[2]*University of Virginia, Charlottesville, Virginia*
United States of America

1. Introduction

Thermal conduction in solids is governed by the well-established, phenomenological Fourier Law, which in one-dimension is expressed as

$$Q = -\kappa \frac{\partial T}{\partial z}, \tag{1}$$

where the thermal flux, Q, is related to the change in temperature, T, along the direction of thermal propagation, z, through the thermal conductivity, κ. The thermal conductivity is a temperature dependent material property that is unique to any given material. Figure 1 shows the measured thermal conductivity of two metals - Au and Pt - and two semiconductors - Si and Ge (Ho et al., 1972). In these bulk materials, the thermal conductivities span three orders of magnitude over the temperature range from 1 - 1,000 K. Temperature trends in the thermal conductivities are similar depending on the type of material, i.e., Si and Ge show similar thermal conductivity trends with temperature as do Au and Pt. These similarities arise due to the different thermal energy carriers in the different classes of materials.

In metals, heat is primarily carried by electrons, whereas in semiconductors, heat moves via atomic vibrations of the crystalline lattice. The macroscopic average of these carriers' scattering events, which is related to the thermal conductivity of the material, gives rise to the spatial temperature gradient in Eq. 1. This temperature gradient is established from the energy carriers traversing a certain distance, the mean free path, before scattering and losing their thermal energy. In bulk systems, this mean free path is related to the intrinsic properties of the materials. However, in material systems with engineered length scales on the order of the mean free path, additional scattering events arise due to energy carrier scattering with interfaces, inclusions, grain boundaries, etc. These scattering events can substantially change the thermal conductivity of nanostructured systems as compared to that of the bulk constituents (Cahill et al., 2003). In fact, in any given material in which the physical size is less than the mean free path, the carrier scattering events will only occur at the boundaries of the material. Therefore, there will be no temperature gradient established in the material and Eq. 1 will no longer be valid.

Typical carrier room temperature mean free paths in metals and semiconductors are about 10 - 100 nm, respectively (Tien et al., 1998). Clearly, with the wealth of technology and applications that rely on material systems with characteristic lengths scales in the sub-1.0 μm regime (Wolf, 2006), the need to understand thermal conduction at the nanoscale is immensely important for thermal management and engineering applications. In this chapter, the basic concepts of

nanoscale thermal conduction are introduced at the length scales of the fundamental energy carriers. This discussion will begin by introducing the kinetic theory of gases, specifically mean free path and scattering time, and how these concepts apply to thermal conductivity. Then, the properties of solids will be discussed and the concepts of lattice vibrations and density of states will be quantified. The link from this microscopic, individual energy carrier development to bulk properties will come with the discussion of statistical mechanics of the energy carriers. Finally, transport properties will be discussed by quantifying carrier scattering times in solids, which will lead to the derivation of the thermal conductivity from the individual energy carrier development in this chapter. In the final section, this expression for thermal conductivity will be used to model the thermal conductivity of nanosystems by accounting for energy carrier scattering times competing with boundary scattering effects.

2. Kinetic theory

Heat transfer involves the motion of particles, quasi-particles, or waves generated by temperature differences. Given the position and velocity of any of these energy carriers, their motion determines the heat transfer. If energy carriers are treated as particles, as will be the focus of this chapter, then the heat transfer can be analyzed through the Kinetic Theory of Gases (Vincenti & Kruger, 2002). For a discussion of nanoscale thermal conduction by waves, see Chapter 5 of Chen (2005).

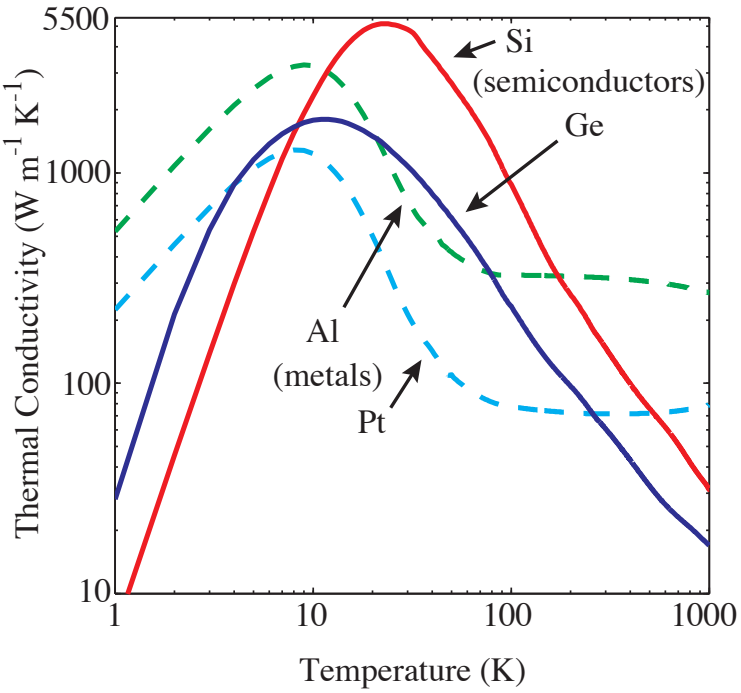

Fig. 1. Measured thermal conductivity of two metals (aluminum and platinum) and two semiconductors (silicon and germanium) (Ho et al., 1972).

Consider a one-dimensional flow of energy across an imaginary surface perpendicular to the energy flow direction. The net heat flux across this surface is the difference between the thermal fluxes of the carriers flowing in the positive and negative directions, Q_{+z} and Q_{-z} respectively. The carriers with energy ε will travel a distance before experiencing a scattering event that causes the carriers to change direction and/or transfer energy; this distance is called the mean free path, $\lambda = v_z\tau$, where v_z is the particle velocity in the z-direction (direction of heat flow) and τ is the relaxation time, or the average time a heat carrier travels before it is scattered and changes direction and/or transfers energy. Therefore, given a volumetric carrier number density, n, the net heat flux in the z-direction is

$$Q_z = Q_{+z} + Q_{-z} = \frac{1}{2}\left((n\epsilon v_z)|_{v_{z+\lambda}} + (-n\epsilon v_z)|_{v_{z-\lambda}} \right), \tag{2}$$

which can be re-expressed as

$$Q_z = -v_z\tau\frac{\partial(n\epsilon v_z)}{\partial z}. \tag{3}$$

Now, given an isotropic medium, the average velocity is $v_z^2 = v^2/3$, and thus, the average flux is given by

$$Q_z = -\frac{v^2}{3}\tau\frac{\partial(n\epsilon)}{\partial z}. \tag{4}$$

Defining a volumetric energy density, or internal energy, as $U = n\epsilon$, and applying the chain rule to the derivative in z yields

$$Q_z = -\frac{v^2}{3}\tau\frac{dU}{dT}\frac{dT}{dz}. \tag{5}$$

The temperature derivative of the internal energy is defined as the volumetric heat capacity, $C = dU/dT$, and with this, comparing Eq. 5 with Eq. 1 yields

$$\kappa = \frac{1}{3}Cv^2\tau = \frac{1}{3}Cv\lambda. \tag{6}$$

Equation 6 defines the thermal conductivity of a material based on the properties of the energy carriers in the solid. To calculate the thermal conductivity of the individual energy carriers in a solid, and therefore understand how κ changes on the nanoscale, the volumetric heat capacity, carrier velocity, and scattering times must be known. This will be the focus of the remainder of this chapter.

3. Energy states

The allowed energies of thermal carriers in solids are dictated by the periodicity of the atoms that comprise the solid. Atoms in a crystal are arranged in a basic primitive cell that is repeated throughout the crystalline volume. The atoms that comprise the primitive cell are called the basis of the crystal, and the arrangement in which this basis is repeated is called the lattice. As a full treatment of the solid state crystallography is beyond the scope of this chapter, the reader is directed to more information on crystallography and solid lattices in any introductory solid state physics (Kittel, 2005) or crystallography text (Ziman, 1972). However, the important thing to remember is that, for the development in this section, periodicity in the atomic arrangement gives rise to the available energy states in a solid.

At this point, the discussion is focused on the primary thermal energy carriers in a solid, i.e., electrons and lattice vibrations (phonons). In the subsections that follow, the fundamental

equations governing the motion of electron and lattice waves through a one-dimensional crystalline lattice will be introduced, and then the effects of periodicity will be discussed. This will give to rise the allowed energy states of the electrons and phonons, which are fundamental to determining κ.

3.1 Electrons

The starting point for describing the allowed motion of electrons through a solid is given by the Schrödinger Equation (Schrödinger, 1926)

$$-\frac{\hbar^2}{2m}\frac{\partial^2\Psi}{\partial z^2}+V\Phi=i\hbar\frac{\partial\Psi}{\partial t}, \tag{7}$$

where $\hbar$ is Planck's constant divided by 2π (Planck's constant is $h=6.6262\times10^{-34}$ J s), m is the mass of the electron, Ψ is the electron wavefunction which is dependent on time and space, V is the potential that is acting on the electron system, and t is the time. Equation 7 is the fundamental equation governing the field of quantum mechanics, and only a basic discussion of this equation will be provided in this chapter in order to understand introductory nanoscale thermal conduction. To delve more into this equation, the reader is encouraged to read any text on introductory quantum mechanics (Griffiths, 2000).

For the solid systems of interest in this chapter, the potential V is the interatomic potential, which is related to the force between the atoms in a crystal (or the "glue" that holds the lattice in a periodic arrangement), and can be assumed as independent of time. With this in mind, separation of variables can be performed on Eq. 7 to determine a spatial and temporal solution. The starting point of this is to assume that the wavefunction can be separated into independent spatial and temporal components (which, again, is valid since V is assumed as independent of time), $\Psi(z,t)=\psi(z)\phi(t)=\psi\phi$, where the functionality of the spatial and temporal solutions are dropped for convenience. Substituting this solution into Eq. 7 yields

$$\left[-\frac{\hbar^2}{2m}\frac{\partial^2\psi}{\partial z^2}+V\psi\right]\frac{1}{\psi}=i\hbar\frac{\partial\phi}{\partial t}\frac{1}{\phi}=\epsilon, \tag{8}$$

where ϵ is a constant eigenvalue solution to Eq. 8. Equation 8 can be immediately solved for ϕ yielding

$$\phi\propto\exp\left[-i\frac{\epsilon}{\hbar}t\right]. \tag{9}$$

It is interesting to note that the form of the expression describing a classical plane wave oscillating in time is given by $\exp[-i\omega t]$, where ω is the angular frequency of the wave defined as $\omega=2\pi f$, where f is the frequency of oscillation of the wave, which is of the same form as Eq. 9. From inspection, the Eigenvalues of the electron waves are $\epsilon\propto\hbar\omega$, i.e., the Eigenvalues are the electron energy states. The governing equation for the spatial component, which is called the time-independent Schrödinger Equation, is given by

$$-\frac{\hbar^2}{2m}\frac{\partial^2\psi}{\partial z^2}+(V-\epsilon)\psi=0. \tag{10}$$

Given that the solution to Eq. 7 is the solution to the steady state portion multiplied by Eq. 9, the solution of Eq. 10 contains all the pertinent information about the electronic energy states in a periodic crystal.

To understand the effects of a periodic interatomic potential acting on the electron waves, consider a simple, yet effective, model for the potential experienced by the electrons in a periodic lattice. This model, the Kronig-Penny Model, assumes there is one electron inside a square, periodic potential with a period distance equal to the interatomic distance, a, mathematically expressed as

$$V = \begin{cases} 0 & \text{for} \quad 0 < z \leq b \\ V_0 & \text{for} \quad -c \leq z \leq 0 \end{cases}, \tag{11}$$

subjected to the periodicity requirement given by $V(z+b+c) = V(z)$, where $a = b + c$. Solutions of Eq. 10 subjected to Eq. 11 are

$$\psi = \begin{cases} D_1 \exp[iMz] + D_2 \exp[-iMz] & \text{for} \quad 0 < z \leq b \\ D_3 \exp[iLz] + D_4 \exp[-iLz] & \text{for} \quad -c \leq z \leq 0 \end{cases}, \tag{12}$$

where D_1, D_2, D_3, and D_4 are constants determined from boundary conditions,

$$\epsilon = \frac{\hbar^2 M^2}{2m}, \tag{13}$$

and

$$V - \epsilon = \frac{\hbar^2 L^2}{2m}, \tag{14}$$

with M and L related to the electron energy.

Although the full mathematical derivation of the predicted allowed electron energies will not be pursued here (see, for example, Griffiths (2000)), one important part of this formalism is recognizing that the periodicity in the lattice gives rise to a periodic boundary condition of the wavefunction, given by

$$\psi(z + (b+c)) = \psi(z) \exp[iz(b+c)] = \psi(z) \exp[ika], \tag{15}$$

where k is called the wavevector. Equation 15 is an example of the Bloch Theorem. The wavevector is defined by the periodicity of the potential (i.e., the lattice), and therefore, the goal is to determine the allowed energies defined in Eq. 13 as a function of the wavevector. The relationship between energy and wavevector, $\epsilon(k)$, known as the dispersion relation, is the fundamental relationship needed to determine all thermal properties of interest in nanoscale thermal conduction.

After incorporating the Bloch Theorem and continuity equations for boundary conditions of Eq. 12 and making certain simplifying assumptions (Chen, 2005), the following dispersion relation is derived for an electron subjected to a periodic potential in a one-dimensional lattice:

$$\frac{A}{K} \sin[Mc] + \cos[Mc] = \cos[kc]. \tag{16}$$

Here, A is related to the electron energy and atomic potential V, and from Eq. 13

$$M = \sqrt{\frac{2m\epsilon}{\hbar^2}}, \tag{17}$$

such that Eq. 16 becomes

$$A\sqrt{\frac{\hbar^2}{2m\epsilon}} \sin\left[\sqrt{\frac{2m\epsilon}{\hbar^2}} c\right] + \cos\left[\sqrt{\frac{2m\epsilon}{\hbar^2}} c\right] = \cos[kc]. \tag{18}$$

Note that the right hand side of Eq. 18 restricts the solutions of the left hand side to only exist between -1 and 1. However, the left hand side of Eq. 18 is a continuous function that does in fact exist outside of this range. An energy-wavevector combination that results in the left hand side of Eq. 18 to evaluating to a number outside of the range from [-1,1] means that an electron cannot exist for that energy-wavevector combination, indicating that electrons can only exist at very specific energies related to the interatomic potential between the atoms in the crystalline lattice. In addition, there is periodicity in the solution to Eq. 18 that arises on an interval of $k = 2\pi/c$. If the interatomic potential is symmetric, then $b = c = 2a$, and the periodicity arises on a length scale of $k = \pi/a$ and is symmetric about $k = 0$. This length of periodicity is called a Brillouin Zone and, in a symmetric case as discussed here, only the first Brillouin Zone from $k = 0$ to $k = \pi/a$ need be considered due to symmetry and periodicity.
To simplify this picture, now consider the case where the electrons do not "see" the crystalline lattice, i.e., the electrons can be considered free from the interatomic potential. In this case, the electrons are called free electrons. For free electrons, Eqs. 13 and 14 are identical ($L = M$) and $A = 0$, thus Eq. 18 becomes

$$\cos\left[\sqrt{\frac{2m\epsilon}{\hbar^2}}c\right] = \cos[kc]. \tag{19}$$

From inspection, the free electron dispersion relation is given by

$$\epsilon = \frac{\hbar^2 k^2}{2m}. \tag{20}$$

This approach of deriving the free electron dispersion relation given by Eq. 20 is a bit involved, as the Schrödinger Equation was solved for some periodic potential, and the result was simplified to the free electron case by assuming the electrons did not "feel" any of the interatomic potential (i.e., $V = 0$). A bit more straightforward way of finding this free electron dispersion relation is to solve the Schrödinger Equation assuming $V = 0$. In this case, the time-independent version of the Schrödinger Equation (Eq. 10) is given by

$$-\frac{\hbar^2}{2m}\frac{\partial^2\psi}{\partial z^2} - \epsilon\psi = 0. \tag{21}$$

This ordinary differential equation is easily solvable. Rearranging Eq. 21 yields

$$\frac{\partial^2\psi}{\partial z^2} + \frac{2m\epsilon}{\hbar^2}\psi = 0. \tag{22}$$

The solution to the above equation takes the form

$$\psi = D_5 \exp\left[-i\sqrt{\frac{2m\epsilon}{\hbar^2}}z\right] + D_6 \exp\left[i\sqrt{\frac{2m\epsilon}{\hbar^2}}z\right], \tag{23}$$

where the wavevector of this plane wave solution is given by $k = \sqrt{2m\epsilon/\hbar^2}$, which yields the same dispersion relationship as given in Eq. 20. Note that the dispersion relationship for a free electron is parabolic ($\epsilon \propto k^2$). For every k in the dispersion relation, there are two electrons of the same energy with different spins. Although this is not discussed in detail in this development, it is important to realize that since two electrons can occupy the same energy at a given wavevector k (albeit with different spins), the electron energies are considered degenerate, or more specifically, doubly degenerate.

Although the mathematical development in this work focused on the free electron dispersion, it is important to note the role that the interatomic potential will have on the dispersion. Following the discussion below Eq. 18, the potential does not allow certain energy-wavevector combinations to exist. This manifests itself at the Brillouin zone edge and center as a discontinuity in the dispersion relation. This discontinuity is called a band gap. In practice, for electrons in a single band, the dispersion is often approximated by the free electron dispersion, since only at the zone center and edge does the electron dispersion feel the effect of the interatomic potential. This is a important consideration to remember in the discussion in Section 4.

Where the dispersion gives the allowed electronic energy states as a function of wavevector, how the electrons fill the states defines the material as either a metal or a semiconductor. At zero temperature, the filling rule for the electrons is that they always fill the lowest energy level first. Depending on the number of electrons in a given material, the electrons will fill up to some maximum energy level. This topmost energy level that is filled with electrons at zero Kelvin is called the Fermi level. Therefore, at zero temperature, all states with energies less than the Fermi energy are filled and all states with energies greater than the Fermi energy are empty. The location of the Fermi energy dictates whether the material is a metal or a semiconductor. In a metal, the Fermi energy lies in the middle of a band. Therefore, electrons are directly next to empty states in the same band and can freely flow throughout the crystal. This is why metals typically have a very high electrical conductivity. For this reason, the majority of the thermal energy in a metal is carried via free electrons. In a semiconductor, the Fermi energy lies in the middle of the band gap. Therefore, electrons in the band directly below the Fermi energy are not adjacent to any empty states and cannot flow freely. In order for electrons to freely flow, energy must be imparted into the semiconductor to case an electron to jump across the band gap into the higher energy band with all the empty states. This lack of free flowing electrons is the reason why semiconductors have intrinsically low electrical conductivity. For this reason, electrons are not the primary thermal carrier in semiconductors. In semiconductors, heat is carried by quantized vibrations of the crystalline lattice, or phonons.

3.2 Phonons

A phonon is formally defined as a quantized lattice vibration (elastic waves that can exist only at discrete energies). As will become evident in the following sections, it is often convenient to turn to the wave nature of phonons to first describe their available energy states, i.e., the phonon dispersion relationship, and later turn to the particle nature of phonons to describe their propagation through a crystal.

In order to derive the phonon dispersion relationship, first consider the equation(s) of motion of any given atom in a crystal. To simplify the derivation without losing generality, attention is given to the monatomic one-dimensional chain illustrated in Fig. 2a, where m is the mass of the atom j, K is the force constant between atoms, and a_1 is the lattice spacing. The displacement of atom m_j from its equilibrium position is given by,

$$u_j = x_j - x_j^o, \tag{24}$$

where x_j is the displaced position of the atom, and x_j^o is the equilibrium position of the atom. Likewise, considering similar displacements of nearest neighbor atoms along the chain and

applying Newtown's law, the net force on atom m_j is

$$F_j = K\left(u_{j+1} - u_j\right) + K\left(u_{j-1} - u_j\right). \tag{25}$$

Collecting like terms, the equation of motion of atom m_j becomes

$$m\ddot{u}_j = K\left(u_{j+1} - 2u_j + u_{j-1}\right), \tag{26}$$

where $\ddot{u}_j$ refers to the double derivative of u_j with respect to time. It is assumed that wavelike solutions satisfy this differential equation and are of the form

$$u_j \propto \exp\left[i\left(ka_1 - \omega t\right)\right], \tag{27}$$

where k is the wavevector. Substituting Eq. 27 into Eq. 26 and noting the identity $\cos x = 2(e^{ix} + e^{-ix})$ yields the expression

$$m\omega^2 = 2K\left(1 - \cos\left[ka_1\right]\right). \tag{28}$$

Finally, the dispersion relationship for a one-dimensional monatomic chain can be established by solving for ω,

$$\omega(k) = 2\sqrt{\frac{K}{m}}\left|\sin\left[\frac{1}{2}ka_1\right]\right|. \tag{29}$$

Just as was the case with electrons, attention is paid only to the solutions of Eq. 29 for $-\pi/a_1 \leq k \leq \pi/a_1$, i.e., within the boundaries of the first Brillouin zone. A plot of the dispersion relationship for a one-dimensional monatomic chain is shown in Fig. 3a. It is important to notice that the solution of Eq. 29 does not change if $k = k + 2\pi N/a_1$, where

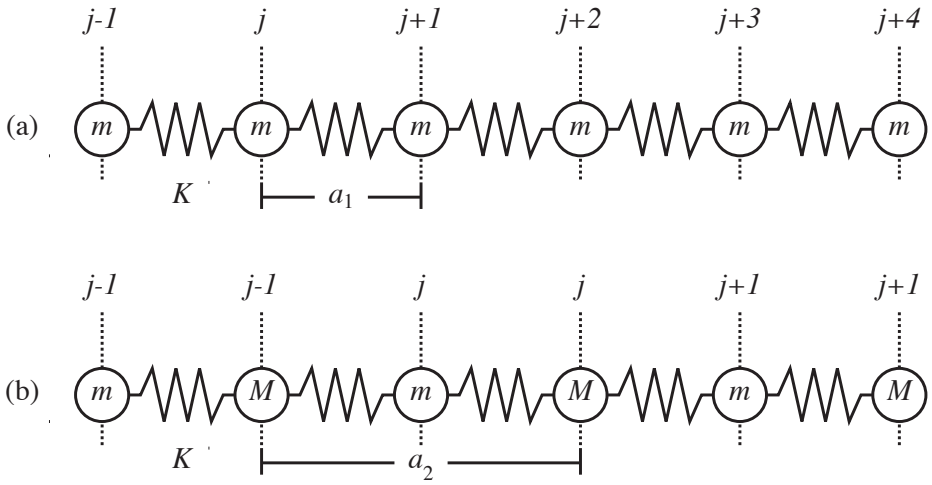

Fig. 2. Schematics representing (a) monatomic and (b) diatomic one-dimensional chains. Here, m and M are the masses of type-A and type-B atoms, a_1 and a_2 are the respective lattice constants of the monatomic and diatomic chains, and K is the interatomic force constant.

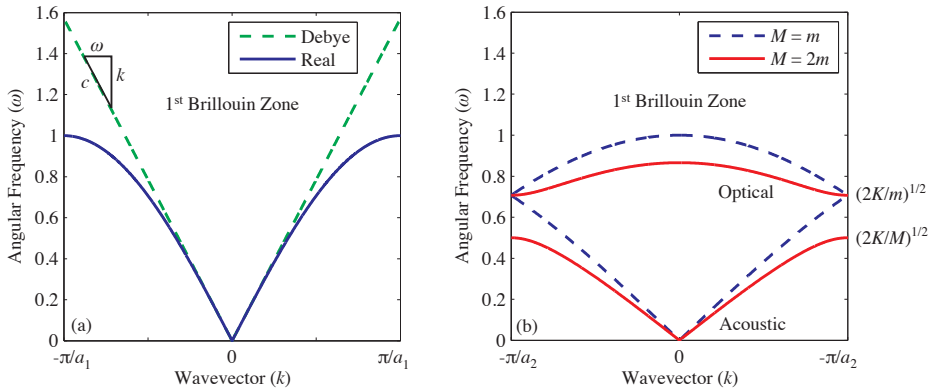

Fig. 3. (a) Phonon dispersion relationship of a one-dimensional monatomic chain as presented in Eq. 29. Also plotted is the corresponding Debye approximation. Note that not only does the Debye approximation over-predict the frequency of phonons near the zone edge, but it also predicts a non-zero slope, and thus, a non-zero phonon group velocity at the zone edge. (b) Phonon dispersion relationship of a one-dimensional diatomic chain as presented in Eq. 35. In the case where $M = m$, the dispersion is identical to that plotted in (a), but is represented in a "zone folded" scheme. The size of the phononic band gap depends directly on the difference between the atoms comprising the diatomic chain.

N is an integer. This indicates that all vibrational information is contained within the first Brillouin zone.

A phonon dispersion diagram concisely describes two essential pieces of information required to describe the propagation of lattice energy in a crystal. First, as is obvious from Eq. 29, the energy of a given phonon, $\hbar\omega$, is mapped to a distinct wavevector, k (in turn, this wavevector can be related to the phonon wavelength). As might be expected, longer wavelength phonons are associated with lower energies. Second, the group velocity, or speed at which a "packet" of phonons propagates, is described by the relationship

$$v_g = \frac{\partial \omega}{\partial k}, \tag{30}$$

where v_g is the phonon group velocity. Additional insight can be gained if focus is turned to two particular areas of the dispersion relationship: the zone center ($k = 0$) and the zone edge ($k = \pi / a_1$).

Discussion of phonons at the zone center is referred to as the long-wavelength limit. Evaluating the limit

$$\lim_{k \to 0} \frac{\partial \omega}{\partial k} = a_1 \sqrt{\frac{K}{m}}, \tag{31}$$

and noting that both ω and k equal 0 at the zone center, it is found that

$$\omega = a \sqrt{\frac{K}{m}} k = ck, \tag{32}$$

where c is the sound speed in the one-dimensional crystal. In this limit, the wavelength of the elastic waves propagating through the crystal are infinitely long compared to the lattice spacing, and thus, see the crystal as a continuous, rather than discrete medium.

Keeping this in mind, a common simplification can be made when considering phonon dispersion: the Debye approximation. The Debye approximation was developed under the assumption that a crystalline lattice could be approximated as an elastic continuum. While elastic waves can exist across a range of energies in such a medium, all waves propagate at the same speed. This description exactly mimics the zone center limit described in the previous paragraph, where phonons with wavelengths infinitely long relative to the lattice spacing travel at the sound speed within the crystal. Naturally, then, under the Debye approximation, Eq. 32 holds for phonons of all wavelengths, and hence, all wavevectors. The accuracy of the Debye approximation depends largely on the temperature regime one is working in. In Fig. 3a, both the slopes and the values of the Debye and real dispersion converge at the zone center. As a result, the Debye approximation is most accurate describing phonon transport in the low-temperature limit, where low energy, low frequency phonons dominate (to be discussed in Section 5).

At the zone edge, a second limit can be established and evaluated,

$$\lim_{k \to \pi/a} \frac{\partial \omega}{\partial k} = 0, \tag{33}$$

indicating that phonons at the zone edge do not propagate. In this short wavelength limit, the wavelengths of the elastic waves in the crystal are equal to twice the atomic spacing. Here, atoms vibrate entirely out-of-phase with each other, leading to the formation of a standing wave. Advanced texts address the formation of this standing wave further, noting that at $k = \pi/a$, the Bragg reflection condition is satisfied (Srivastava, 1990). Consequently, the coherent scattering and subsequent interference of the incoming wave creates the standing wave condition.

At this point, discussion has been limited to monatomic crystals. However, many materials of technological interest (semiconductors in particular) have polyatomic basis sets. Thus, attention is now given to the diatomic one-dimensional chain illustrated in Fig. 2b. Here, m is the mass of the "lighter" atom, and M is the mass of the "heavier" atom, such that $M > m$. Due to the diatomic nature of this system, equation(s) of motion must be formulated for each type of atom in the system,

$$m\ddot{u}_j = K\left(w_j - 2u_j + w_{j-1}\right) \tag{34a}$$

$$m\ddot{w}_j = K\left(u_{j+1} - 2w_j + u_j\right). \tag{34b}$$

Substituting wavelike solutions to these differential equations and isolating ω^2 yields

$$\omega^2 = K\left(\frac{1}{m} + \frac{1}{M}\right) \pm K\left(\left(\frac{1}{m} + \frac{1}{M}\right)^2 - \frac{4}{mM}\sin^2 ka_2\right). \tag{35}$$

Perhaps the most unique feature of Eq. 35 is that for each wavevector k, two unique values of ω satisfy the expression. As a result, as the two solutions ω_1 and ω_2 are plotted against each unique k, two distinct phonon branches form: the acoustic branch, and the optical branch.

The distinction between these branches is illustrated in Fig. 3. At the zone center, in the branch of lower energy, atoms m_j and M_j move in phase with each other, exhibiting the characteristic sound wave behavior discussed above. Thus, this branch is called the acoustic branch. On the other hand, in the branch of higher energy, atoms m_j and M_j move out of phase with each other. If these atoms had opposite charges on them, as would be the case in an ionic

crystal, this vibration could be excited by an electric field associated with the infrared edge of visible light spectrum (Srivastava, 1990). As such, this branch is called the optical branch. The phononic band gap between these branches at the zone edge is proportional to the difference in atomic masses (and the effective spring constants). In the unique case where $m = M$, the solution is identical to that of the monatomic chain.

Extending the one-dimensional cases described above to two or three dimensions is conceptually simple, but is often no trivial task. For each atom of the basis set, n equations of motion will be required, where n represents the dimensionality of the system. Generally, solutions for the resulting dispersion diagrams will yield n acoustic branches and $B(n-1)$ optical branches, where B is the number of atoms comprising the basis. While in the one-dimensional system above we considered only longitudinal modes (compression waves), in three-dimensional systems, two transverse modes will exist as well (shear waves due to atomic displacements in the two directions perpendicular to the direction of wave propagation). Rigorous treatments of such scenarios are presented explicitly in advanced solid-state texts (Srivastava, 1990; Dove, 1993).

4. Density of states

A convenient representation of the number of energy states in a solid is through the density of states formulation. The density of states represents the number of states per unit space per unit interval of wavevector or energy. For example, the one-dimensional density of states of electrons represents the number of electron states per unit length per dk or per $d\epsilon$ in the Brillouin zone. Similarly, the three dimensional density of states of phonons represents the number of phonon states per unit volume per dk or per $d\omega$ in the in the Brillouin zone (for phonons $\epsilon = \hbar\omega$). The general formulation of the density of states in n dimensions considers the number of states contained in the $n-1$ space of thickness dk per unit space L^n. Consequently, the density of states has units of states divided by length raised to the n divided by the differential wavevector or energy. For example, the density of states of a three-dimensional solid considers the number of states contained in the volume represented by the two-dimensional surface multiplied by the thickness dk per unit volume L^3, where L is a length, per dk or $d\epsilon$. In this section, the density of states will be derived for one-, two-, and three-dimensional isotropic solids. The representation of an isotropic solid implies that periodicity arises on a length scale of $k = \pi/a$ and is symmetric about $k = 0$, as discussed in the last section. This means, that for the isotropic case considered in this chapter, the total distance from one Brillouin Zone edge to the other is $2\pi/a$. This general derivation yields a density of states of the n-dimensional solid per interval of wavevector given by

$$D_{n\mathrm{D}} = \frac{(n\text{-1 surface of } n\text{-dimensional space})dk}{\left(\frac{2\pi}{a}\right)^n L^n dk}, \tag{36}$$

or per interval of energy given by

$$D_{n\mathrm{D}} = \frac{(n\text{-1 surface of } n\text{-dimensional space})dk}{\left(\frac{2\pi}{a}\right)^n L^n d\epsilon}, \tag{37}$$

where L^n is the "volume" of unit space n. Note that $a^n = L^n$. In practice, the density of states per interval of energy is more conceptually intuitive and is directly input into expressions for

the thermal properties, so the starting point for the examples discussed in the remainder of this section will be Eq. 37.
This general density of states formulation can then be recast into energy space via the electron or phonon dispersion relations. This is accomplished by solving the dispersion relation for k. For example, the electron dispersion relation, given by Eq. 20, can be rearranged as

$$k = \sqrt{\frac{2m\epsilon}{\hbar^2}}, \tag{38}$$

and from this

$$\partial k = \frac{1}{2}\sqrt{\frac{2m}{\hbar^2\epsilon}}\partial\epsilon. \tag{39}$$

Similarly, assuming the phonon dispersion relation given by Eq. 32 (i.e., the Debye relation) yields

$$k = \frac{\omega}{v_g}, \tag{40}$$

and from this

$$\partial k = \frac{\partial\omega}{v_g}. \tag{41}$$

Note that recasting Eq. 37 into energy space via a dispersion relation yields the number of states per unit L^n per energy interval. In the remainder of this section, the specific derivation of the one-, two- and three-dimensional electron and phonon density of states will be presented. This abstract discussion of the density of states will become much more clear with the specific examples.

4.1 One-dimensional density of states

The starting point for the density of states of a one-dimensional system, as generally discussed above, is to consider the number of states in contained in a zero dimensional space multiplied by dk divided by the one-dimensional space of distance $2\pi/a$. Therefore, the one-dimensional density of states is given by

$$D_{1\mathrm{D}} = \frac{dk}{\left(\frac{2\pi}{a}\right)Ld\epsilon}. \tag{42}$$

From Eq. 39, the one-dimensional electron density of states is given by

$$D_{\mathrm{e,1D}} = 2 \times \frac{a}{2\pi Ld\epsilon}\frac{1}{2}\sqrt{\frac{2m}{\hbar^2\epsilon}}d\epsilon = \frac{1}{2\pi}\sqrt{\frac{2m}{\hbar^2\epsilon}}, \tag{43}$$

where the subscript e denotes the electron system and the factor of 2 in front of the middle equation arises due to the double degeneracy of the electron states, as discussed in Section 3.1 . From Eq. 41, the one-dimensional phonon density of states is given by

$$D_{\mathrm{p,1D}} = \frac{a}{2\pi L\hbar d\omega}\frac{\hbar d\omega}{v_g} = \frac{1}{2\pi v_g}, \tag{44}$$

where the subscript p denotes the phonon system. Since a Debye model is assumed, the phonon group velocity is equal to the speed of sound (i.e., $v_g = c$), as discussed in Section 3.2.

4.2 Two-dimensional density of states

For the density of states in a two-dimensional (2D) system, the starting point is to consider the number of states along the surface of a circle with radius$k$ multiplied by dk divided by the 2D space of area $(2\pi/a)^2$. Therefore, the 2D density of states is given by

$$D_{2\mathrm{D}} = \frac{2\pi k dk}{\left(\frac{2\pi}{a}\right)^2 L^2 d\epsilon}. \tag{45}$$

From Eq. 38 and 39, the 2D electron density of states is given by

$$D_{\mathrm{e,2D}} = 2 \times \frac{a^2}{(2\pi)^2 L^2 d\epsilon} 2\pi \sqrt{\frac{2m\epsilon}{\hbar^2}} \frac{1}{2} \sqrt{\frac{2m}{\hbar^2 \epsilon}} d\epsilon = \frac{1}{\pi} \frac{m}{\hbar^2}. \tag{46}$$

Note that the 2D density of states for electrons is independent of energy. From Eq. 40 and 41, the 2D phonon density of states is given by

$$D_{\mathrm{p,2D}} = 2 \times \frac{a^2}{(2\pi)^2 L^2 \hbar d\omega} 2\pi \frac{\omega}{v_g} \frac{\hbar d\omega}{v_g} = \frac{\omega}{\pi v_g^2}. \tag{47}$$

where the factor of 2 in front of the middle equation arises due to the second dimension, which introduces a transverse polarization in addition to the longitudinal polarization, as discussed in Section 3.2. In the discussions in this chapter, equal phonon velocities and frequencies (i.e., dispersions) are assumed for each phonon polarization.

4.3 Three-dimensional density of states

The density of states in three-dimensions (3D) will be extensively used in the remainder of this chapter to discuss nanoscale thermal processes. Following the previous discussions in this section, the 3D density of states is formulated by considering the the number of states contained on the surface of a sphere in k-space multiplied by the thickness of the sphere dk divided by the 3D space of volume $(2\pi/a)^3$. Therefore, the 3D density of states is given by

$$D_{3\mathrm{D}} = \frac{4\pi k^2 dk}{\left(\frac{2\pi}{a}\right)^3 L^3 d\epsilon}. \tag{48}$$

From Eq. 38 and 39, the 3D electron density of states is given by

$$D_{\mathrm{e,3D}} = 2 \times \frac{a^3}{(2\pi)^3 L^3 d\epsilon} 4\pi \frac{2m\epsilon}{\hbar^2} \frac{1}{2} \sqrt{\frac{2m}{\hbar^2 \epsilon}} d\epsilon = \frac{1}{2\pi^2} \left(\frac{2m}{\hbar^2}\right)^{\frac{3}{2}} \epsilon^{\frac{1}{2}}. \tag{49}$$

From Eq. 40 and 41, the 3D phonon density of states is given by

$$D_{\mathrm{p,3D}} = 3 \times \frac{a^3}{(2\pi)^3 L^3 \hbar d\omega} 4\pi \frac{\omega^2}{v_g^2} \frac{\hbar d\omega}{v_g} = \frac{3\omega^2}{2\pi^2 v_g^3}, \tag{50}$$

where the factor of 3 in front of the middle equation arises due to the three dimensions, which introduces two additional transverse polarizations along with the longitudinal polarization, as discussed in Section 3.2.

5. Statistical mechanics

The principles of quantum mechanics discussed in the previous two sections give the allowable energy states of electrons and phonons. However, this development did not discuss the way in which these thermal energy carriers can occupy the quantum states. The bridge connecting the allowable and occupied quantum states to the collective behavior of the energy carriers in a nanosystem is provided by statistical mechanics. Through statistical mechanics, temperature enters into the picture and physical properties such as internal energy and heat capacity are defined.

It turns out that the thermal energy carriers in nature divide into two classes, fermions and bosons, which differ in the way they can occupy their respective density of states. Electrons are fermions that follow a rule that only one particle can occupy a fully described quantum state (where there are two quantum states with different spins per energy, as discussed in Section 3.1). This rule was first recognized by Pauli and is called the Pauli exclusion principle. In a system with many states and many fermion particles to fill these states, particles first fill the lowest energy states, increasing in energy until all particles are placed. As previously discussed in Section 3.1, the highest filled energy is called the Fermi energy, ϵ_F. Phonons are bosons and are not governed by the Pauli exclusion principle. Any number of phonons can fall into exactly the same quantum state.

When a nanophysical system is in equilibrium with a thermal environment at temperature T, then average occupation expectation values for the quantum states are found to exist. In the case of electrons (fermions), the occupation function is the Fermi-Dirac distribution function, given by

$$f_{FD} = \frac{1}{\exp\left[\frac{\epsilon-\epsilon_F}{k_B T}\right]+1}, \tag{51}$$

where k_B is Boltzmann's constant (Boltzmann's constant is $k_B = 1.3807 \times 10^{-23}\,\mathrm{J\,K^{-1}}$). For phonons (bosons), the corresponding occupation function is the Bose-Einstein distribution function, given by

$$f_{BE} = \frac{1}{\exp\left[\frac{\hbar\omega}{k_B T}\right]-1}. \tag{52}$$

Figure 4a and b show plots of Eqs. 51 as a function of electron energy and 52 as a function phonon frequency, respectively, for three different temperatures, $T = 10$, 500, and $1000K$.

Given the distribution of carriers, the number of electrons/phonons in a bulk solid at a given temperature is defined as

$$n_{e/p} = \int_{\epsilon} D_{e/p} f_{FD/BE}\, d\epsilon, \tag{53}$$

where the dimensionality of the system is driven by the dimensionality of the density of states of the electrons or phonons derived in Section 4. The total number of electrons and phonons is mathematically expressed by Eq. 53. The total number of electrons in a bulk solid is constant as the Fermi-Dirac distribution only varies between zero and one, as seen in Fig. 4a; this is also conceptually a consequence of the Pauli exclusion principle previously mentioned. Although the distribution of electron energies change, the number density stays the same. The phonon number density, however, which has no restriction on number of phonons per quantum states, continues to increase with increasing temperature. Note that at low temperatures, the majority of the phonons exist at low frequencies (low energy/long wavelengths). These phonons correspond to phonons near the center of the Brillouin zone ($k = 0$). As temperature

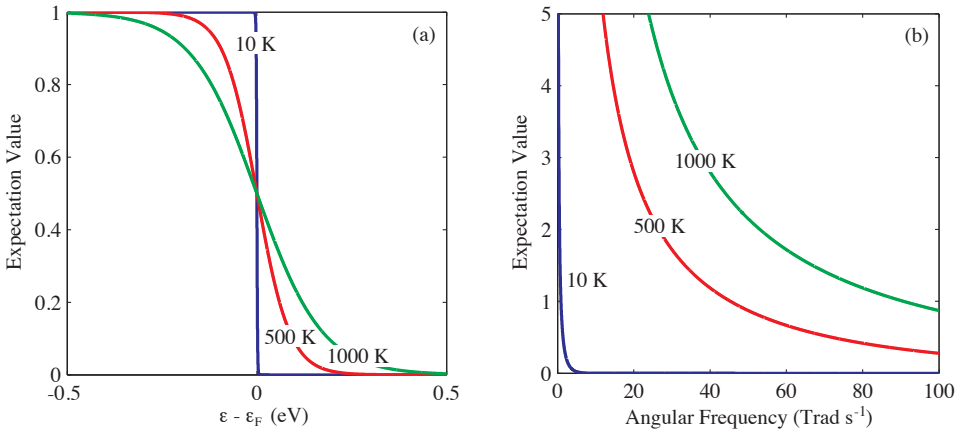

Fig. 4. (a) Fermi-Dirac and (b) Bose-Einstein expectation values calculated from Eqs. 51 and 52, respectively, for three different temperatures, $T = 10$, 500, and 1000K. Note that the expectations values of the Fermi-Dirac distribution function vary from zero to unity, and therefore represent the probability of an electron being at a certain energy state.

is increased, the proportion of higher frequency (higher energy/shorter wavelength) phonons that exist increases; these phonons correspond to phonons that are closer to the Brillouin zone edge ($k = \pi/a$). With the number of electrons/phonons defined in Eq. 53 and following the discussion in Section 2, the internal energy of the electron/phonon system is defined as

$$U_{\mathrm{e/p}} = \int_{\epsilon} \epsilon D_{\mathrm{e/p}} f_{\mathrm{FD/BE}}\, d\epsilon. \tag{54}$$

Now that the internal energies of the electrons and phonons are defined in terms of the properties of the individual energy carriers, their correspond heat capacities are given by the temperature derivative of the internal energies, as discussed in Section 2; that is,

$$C = \frac{\partial U}{\partial T}. \tag{55}$$

The heat capacities of electrons and phonons for one-, two-, and three-dimensional solids will be studied in the remainder of this section.

5.1 Electron heat capacity

Since the zero temperature state of a free electron gas does not correspond to a zero internal energy system (i.e., $U(T = 0) \neq 0$)), care must be taken when defining the integration limits in the calculation of the heat capacity. To begin, the internal energy of the $T = 0$ state of a free electron gas is given by

$$U_{\mathrm{e}}(T = 0) = \int_{0}^{\epsilon_{\mathrm{F}}} \epsilon D_{\mathrm{e}} f_{\mathrm{FD}}\, d\epsilon. \tag{56}$$

As temperature increases, the electrons redistribute themselves to higher energy levels and the internal energy is calculated by considering electrons over all energy states, given by

$$U_e(T=0) = \int_0^\infty \epsilon D_e f_{FD}\, d\epsilon. \tag{57}$$

Therefore, the change in internal energy of the electron system given some arbitrary δT is determined by subtracting Eq. 56 from 57, yielding

$$\delta U_e = \int_0^\infty (\epsilon - \epsilon_F)\, D_e(\delta f_{FD})\, d\epsilon. \tag{58}$$

Following Eq. 55, the electronic heat capacity is given by

$$C_e = \int_0^\infty (\epsilon - \epsilon_F)\, D_e \frac{\partial f_{FD}}{\partial T}\, d\epsilon. \tag{59}$$

At this point, the various electronic density of states defined in Section 4 will be inserted into Eq. 59 to study the effects of dimensionality on electronic thermal storage. For convenience, the electronic heat capacity discussion will be limited to metals since electrons are the dominant thermal carriers in metals and convenient simplifications in the heat capacity derivations can be made to elucidate the interesting thermophysics. Mainly, at low-to-moderate temperatures, the density of states in metals can be considered constant and evaluated at the Fermi energy. This simplifying assumption means that the density of states can be taken out of the integral in Eq. 59. Therefore, Eq. 59 can be rewritten as

$$C_e = D_e(\epsilon_F) \int_0^\infty (\epsilon - \epsilon_F) \frac{\partial f_{FD}}{\partial T}\, d\epsilon = D_e(\epsilon_F) \int_0^\infty \frac{(\epsilon - \epsilon_F)^2}{k_B T^2} \frac{\exp\left(\frac{\epsilon - \epsilon_F}{k_B T}\right)}{\left(\exp\left(\frac{\epsilon - \epsilon_F}{k_B T}\right) + 1\right)^2}\, d\epsilon. \tag{60}$$

Making the substitution of $x \equiv (\epsilon - \epsilon_F)/(k_B T)$, Eq. 60 can be re-expressed as

$$C_e = D_e(\epsilon = \epsilon_F) k_B T^2 \int_{-\frac{\epsilon_F}{k_B T}}^\infty x^2 \frac{\exp(x)}{(\exp(x)+1)^2}\, dx. \tag{61}$$

To simplify this integral, consider the lower bound of $-\epsilon_F/(k_B T)$. At low to moderate temperatures, the magnitude of this quantity is very large, meaning that this lower bound extends to very large negative numbers. Therefore, the lower bound of Eq. 61 can be approximated as negative infinity, so that Eq. 61 can be recast as

$$C_e = D_e(\epsilon = \epsilon_F) k_B T^2 \int_{-\infty}^\infty x^2 \frac{\exp(x)}{(\exp(x)+1)^2}\, dx. \tag{62}$$

This integral can now be solved exactly. By recognizing that

$$\int_{-\infty}^\infty x^2 \frac{\exp(x)}{(\exp(x)+1)^2}\, dx = \frac{\pi^2}{3}, \tag{63}$$

the electronic heat capacity is given by

$$C_{\mathrm{e}} = \frac{\pi^2}{3} k_{\mathrm{B}}^2 T D_{\mathrm{e}}(\epsilon = \epsilon_{\mathrm{F}}). \tag{64}$$

Now to study the electronic heat capacity of electronic systems with different dimensionalities, the various electronic densities of states derived in Section 4 just need be inserted into Eq. 64.
Consider the 3D electron density of states given by Eq. 49. Plugging this into Eq. 64 yields

$$C_{\mathrm{e,3D}} = \frac{\pi^2}{3} k_{\mathrm{B}}^2 T \frac{1}{2\pi^2} \left(\frac{2m}{\hbar^2}\right)^{\frac{3}{2}} \epsilon_{\mathrm{F}}^{\frac{1}{2}} = \frac{k_{\mathrm{B}}^2 T}{6} \left(\frac{2m}{\hbar^2}\right)^{\frac{3}{2}} \epsilon_{\mathrm{F}}^{\frac{1}{2}}. \tag{65}$$

To simplify this expression further, consider Eq. 53 for a 3D system of electrons. Since, as previously mentioned, Eq. 53 is constant for electrons, this expression can be evaluated exactly at $T = 0$ to give analytical expression for the electron number density. At zero temperature, Eq. 53 for electrons becomes

$$n_{\mathrm{e,3D}} = \int_0^{\epsilon_{\mathrm{F}}} D_{\mathrm{e,3D}} f_{\mathrm{FD}}(T=0)\, d\epsilon = \int_0^{\epsilon_{\mathrm{F}}} D_{\mathrm{e,3D}}\, d\epsilon = \frac{1}{3\pi^2} \left(\frac{2m}{\hbar^2}\right)^{\frac{3}{2}} \epsilon_{\mathrm{F}}^{\frac{3}{2}}. \tag{66}$$

and from this, it is apparent that for free electrons in a 3D metallic system

$$\left(\frac{2m}{\hbar^2}\right)^{\frac{3}{2}} = \frac{3\pi^2 n_{\mathrm{e,3D}}}{\epsilon_{\mathrm{F}}^{\frac{3}{2}}}. \tag{67}$$

Inserting Eq. 67 in 65 yields

$$C_{\mathrm{e,3D}} = \frac{\pi^2 k_{\mathrm{B}}^2 n_{\mathrm{e,3D}}}{2\epsilon_{\mathrm{F}}} T, \tag{68}$$

showing that for a 3D system of free electrons, the heat capacity is directly related to the temperature, where the proportionality constant is related to material properties. The electronic heat capacity of Au is plotted in Fig 5.
To examine the electronic heat capacity of a 2D electronic system, consider the 2D electron density of states given by Eq. 46. Substituting this 2D density of states into Eq. 64 yields

$$C_{\mathrm{e,2D}} = \frac{\pi^2}{3} k_{\mathrm{B}}^2 T \frac{1}{\pi} \frac{m}{\hbar^2} = \frac{\pi k_{\mathrm{B}}^2 T}{3} \frac{m}{\hbar^2}. \tag{69}$$

Following the development for the 3D heat capacity, Eq. 53 for a 2D system of electrons is given by

$$n_{\mathrm{e,2D}} = \int_0^{\epsilon_{\mathrm{F}}} D_{\mathrm{e,2D}} f_{\mathrm{FD}}(T=0)\, d\epsilon = \int_0^{\epsilon_{\mathrm{F}}} D_{\mathrm{e,2D}}\, d\epsilon = \frac{1}{\pi} \frac{m}{\hbar^2} \epsilon_{\mathrm{F}}. \tag{70}$$

From this, it is apparent that for free electrons in a 2D metallic system

$$\frac{m}{\hbar^2} = \frac{\pi n_{\mathrm{e,2D}}}{\epsilon_{\mathrm{F}}}. \tag{71}$$

Inserting Eq. 71 in 69 yields

$$C_{\mathrm{e,2D}} = \frac{\pi^2 k_{\mathrm{B}}^2 n_{\mathrm{e,2D}}}{3\epsilon_{\mathrm{F}}} T, \tag{72}$$

which has a similar dependence on temperature and material properties as the electronic heat capacity in 3D.
Finally, for a one-dimensional electronic system, consider the one-dimensional density of states given by Eq. 43. Plugging this into Eq. 64 yields

$$C_{\mathrm{e,1D}} = \frac{\pi^2}{3} k_{\mathrm{B}}^2 T \frac{1}{2\pi} \sqrt{\frac{2m}{\hbar^2 \epsilon_{\mathrm{F}}}} = \frac{\pi}{6} k_{\mathrm{B}}^2 T \sqrt{\frac{2m}{\hbar^2 \epsilon_{\mathrm{F}}}}. \tag{73}$$

The number density of a one-dimensional system of electrons is given by

$$n_{\mathrm{e,1D}} = \int_0^{\epsilon_{\mathrm{F}}} D_{\mathrm{e,1D}} f_{\mathrm{FD}}(T=0)\, d\epsilon = \int_0^{\epsilon_{\mathrm{F}}} D_{\mathrm{e,1D}}\, d\epsilon = \frac{1}{2\pi} \sqrt{\frac{2m\epsilon_{\mathrm{F}}}{\hbar^2}}. \tag{74}$$

From this

$$\sqrt{\frac{2m}{\hbar^2}} = \frac{2\pi n_{\mathrm{e,1D}}}{\sqrt{\epsilon_{\mathrm{F}}}}, \tag{75}$$

which yields

$$C_{\mathrm{e,1D}} = \frac{\pi^2 k_{\mathrm{B}}^2 n_{\mathrm{e,1D}}}{3\epsilon_{\mathrm{F}}} T, \tag{76}$$

which is also directly proportional to temperature. As apparent from the derivations of the electronic heat capacities in different dimensionalities of electron systems, the electronic heat capacity is always directly related to the temperature, regardless of the electron system dimension.

5.2 Phonon heat capacity

Unlike electrons (fermions), the zero temperature state of phonons (bosons) does not correspond to a zero internal energy state (i.e., $U(T=0) \neq 0$) since at $T=0$, the lattice is not vibrating so phonons do not exist. Therefore, the change in internal energy of the phonon system given some arbitrary δT is determined by evaluating

$$\delta U_{\mathrm{p}} = \int_0^{\omega_{\max}} \hbar\omega D_{\mathrm{p}} (\delta f_{\mathrm{BE}})\, d\omega. \tag{77}$$

Following Eq. 55, the phonon heat capacity is given by

$$C_{\mathrm{p}} = \int_0^{\omega_{\max}} \hbar\omega D_{\mathrm{p}} \frac{\partial f_{\mathrm{BE}}}{\partial T}\, d\omega = \int_0^{\omega_{\max}} \frac{\hbar^2\omega^2}{k_{\mathrm{B}} T^2} D_{\mathrm{p}} \frac{\exp\left[\frac{\hbar\omega}{k_{\mathrm{B}}T}\right]}{\left(\exp\left[\frac{\hbar\omega}{k_{\mathrm{B}}T}\right]-1\right)^2}\, d\omega. \tag{78}$$

Since the Debye assumption is employed for the phonon dispersion in these examples, the maximum phonon frequency is defined as $\omega_{\max} = v_g \pi / a_1$.

The 3D phonon heat capacity is derived by plugging in the expression for the 3D phonon density of states (Eq. 50) in Eq. 78 which gives

$$C_{\mathrm{p,3D}} = \int_0^{\omega_{\max}} \frac{\hbar^2\omega^2}{k_{\mathrm{B}}T^2}\frac{3\omega^2}{2\pi^2 v_g^3}\frac{\exp\left[\frac{\hbar\omega}{k_{\mathrm{B}}T}\right]}{\left(\exp\left[\frac{\hbar\omega}{k_{\mathrm{B}}T}\right]-1\right)^2}\,d\omega = \int_0^{\omega_{\max}} \frac{3\hbar^2\omega^4}{2\pi^2 v_g^3 k_{\mathrm{B}}T^2}\frac{\exp\left[\frac{\hbar\omega}{k_{\mathrm{B}}T}\right]}{\left(\exp\left[\frac{\hbar\omega}{k_{\mathrm{B}}T}\right]-1\right)^2}\,d\omega. \quad (79)$$

The 3D phonon heat capacity of Au is plotted in Fig. 5 along with the electronic heat capacity. Note that the phonon system heat capacity approaches a constant values at high temperatures. This limit of constant phonon heat capacity is called the Dulong and Petit limit. The onset of this Dulong and Petit limit (i.e., the onset of the constant phonon heat capacity) occurs around a material property called the Debye temperature. The Debye temperature is approximately the equivalent temperature in which all phonon modes in a solid are excited; this Debye temperature concept will be quantified in more detail below. Also, note that at very low temperatures ($T \approx 1$ K), the electron system heat capacity is larger than that of the phonon system. However, for the majority of the temperature range in which Au is solid (the melting temperature of gold is about 1,300 K), the phonon heat capacity is several orders of magnitude larger than that of the electrons. Note also the low temperature trend of the phonon heat capacity is different than the liner trend in temperature exhibited by the electron system. For the remainder of this section, the low temperature trends in the phonon heat capacity, and the effect of dimensionality on this trend, will be explored.

To examine the low temperature trends in phonon heat capacity, it is convenient to make the variable substitution $x \equiv \hbar\omega/(k_{\mathrm{B}}T)$. With this, the 3D phonon heat capacity becomes

$$C_{\mathrm{p,3D}} = \frac{3k_{\mathrm{B}}^4}{2\pi^2 v_g^3\hbar^3}T^3\int_0^{x_{\max}\equiv\theta_{\mathrm{D}}/T} x^4\frac{\exp[x]}{(\exp[x]-1)^2}\,dx, \quad (80)$$

where the upper limit is redefined as the Debye temperature, θ_{D}, divided by the temperature. Note that $\theta_{\mathrm{D}} = \hbar\omega_{\max}/k_{\mathrm{B}}$, which is, as previously conceptually discussed, directly related to the maximum phonon frequency in a solid. In this low temperature limit, $T \ll \theta_{\mathrm{D}}$ and $x_{\max} \longrightarrow \infty$, so that the integral in Eq. 80 can be evaluated exactly. Recognizing that

$$\int_0^{\infty} x^4\frac{\exp[x]}{(\exp[x]-1)^2}\,dx = \frac{4\pi^4}{15}, \quad (81)$$

the low temperature heat capacity in a 3D phonon system becomes

$$C_{\mathrm{p,3D}} = \frac{2\pi^2 k_{\mathrm{B}}^4}{5v_g^3\hbar^3}T^3, \quad (82)$$

showing that for a 3D system of phonons, the heat capacity is directly related to the cube of the temperature at low temperatures, where the proportionality constant is related to material properties.

Following a similar derivation for a 2D phonon system, plugging Eq. 47 in Eq. 78 gives

$$C_{\mathrm{p,2D}} = \int_0^{\omega_{\max}} \frac{\hbar^2\omega^2}{k_{\mathrm{B}}T^2}\frac{\omega}{\pi v_g^2}\frac{\exp\left[\frac{\hbar\omega}{k_{\mathrm{B}}T}\right]}{\left(\exp\left[\frac{\hbar\omega}{k_{\mathrm{B}}T}\right]-1\right)^2}\,d\omega = \int_0^{\omega_{\max}} \frac{\hbar^2\omega^3}{\pi v_g^2 k_{\mathrm{B}}T^2}\frac{\exp\left[\frac{\hbar\omega}{k_{\mathrm{B}}T}\right]}{\left(\exp\left[\frac{\hbar\omega}{k_{\mathrm{B}}T}\right]-1\right)^2}\,d\omega. \quad (83)$$

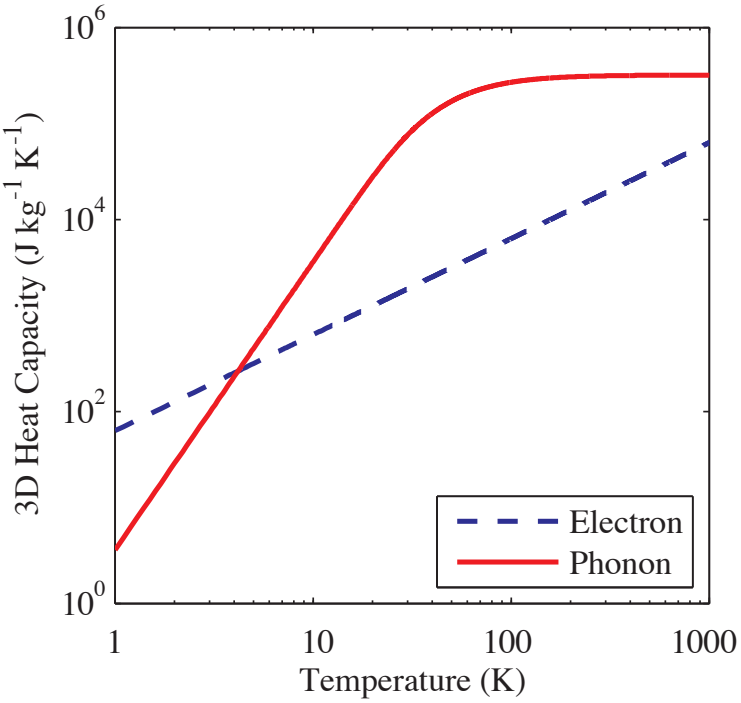

Fig. 5. 3D electron and phonon heat capacities of Au calculated from Eq. 68 and 80, respectively. For these calculations, the Au material parameters are assumed as $n_{e,3D} = 5.9 \times 10^{28}\,\mathrm{m}^{-3}$, $\epsilon_F = 5.5\,\mathrm{eV} = 8.811 \times 10^{-19}\,\mathrm{J}$, and $v_g = 3{,}240\,\mathrm{m\,s}^{-1}$.

Making the above mentioned x-substitution yields

$$C_{p,2D} = \frac{k_B^3}{piv_g^2\hbar^2} T^2 \int_0^{\theta_D/T} x^3 \frac{\exp[x]}{(\exp[x]-1)^2}\, dx, \tag{84}$$

As with the 3D case, at low temperatures, the integration can be extended to infinity. Recognizing that

$$\int_0^{\infty} x^3 \frac{\exp[x]}{(\exp[x]-1)^2}\, dx = 6\zeta[3], \tag{85}$$

where $\zeta[3]$ is the Zeta function evaluated at 3, the low temperature heat capacity in a 2D phonon system becomes

$$C_{p,2D} = \frac{6\zeta[3]k_B^3}{\pi v_g^2\hbar^2} T^2, \tag{86}$$

showing that for a 2D system of phonons, the heat capacity is directly related to the square of the temperature at low temperatures, where the proportionality constant is related to material properties.

Following a above derivations, the heat capacity of a one-dimensional phonon system is derived by plugging Eq. 44 in Eq. 78 which gives

$$C_{\mathrm{p,1D}} = \int_0^{\omega_{\max}} \frac{\hbar^2\omega^2}{k_{\mathrm{B}}T^2}\frac{1}{2\pi v_g}\frac{\exp\left[\frac{\hbar\omega}{k_{\mathrm{B}}T}\right]}{\left(\exp\left[\frac{\hbar\omega}{k_{\mathrm{B}}T}\right]-1\right)^2}d\omega = \int_0^{\omega_{\max}} \frac{\hbar^2\omega^2}{2\pi v_g k_{\mathrm{B}}T^2}\frac{\exp\left[\frac{\hbar\omega}{k_{\mathrm{B}}T}\right]}{\left(\exp\left[\frac{\hbar\omega}{k_{\mathrm{B}}T}\right]-1\right)^2}d\omega. \quad (87)$$

Making the above mentioned x-substitution yields

$$C_{\mathrm{p,1D}} = \frac{k_{\mathrm{B}}^2}{2\pi v_g\hbar}T\int_0^{\theta_{\mathrm{D}}/T} x^2\frac{\exp[x]}{(\exp[x]-1)^2}dx, \quad (88)$$

As with the previous cases, at low temperatures, the integration can be extended to infinity. Recognizing that

$$\int_0^{\infty} x^2\frac{\exp[x]}{(\exp[x]-1)^2}dx = \frac{\pi^2}{3}, \quad (89)$$

the low temperature heat capacity in a one-dimensional phonon system becomes

$$C_{\mathrm{p,1D}} = \frac{\pi k_{\mathrm{B}}^2}{6v_g\hbar}T, \quad (90)$$

showing that for a one-dimensional system of phonons, the heat capacity is directly and linearly related to the the temperature at low temperatures, where the proportionality constant is related to material properties. Note that, unlike the electron systems which in which the temperature trend in heat capacity does not change with dimensionality, an n-dimensional phonon system has a temperature dependency of T^n.

6. Thermal conductivity

In the preceding sections, the quantum energy states of electrons and phonons were derived, and from this, expressions for heat capacities of these thermal energy carriers were presented. With this, given a particle velocity and scattering time, the thermal conductivity can be calculated via Eq. 6. In this final section, the thermal conductivity of electrons and phonons will be calculated from the quantum derivations of heat capacity. The discussion will be limited to systems in which a 3D density of states can still be assumed and the electrons and phonons are treated as particles experiencing scattering events, as in the Kinetic Theory of Gases discussion in Section 2. This approximation of particle transport typical holds true until characteristic dimensions of nanosystems get below about 10 nm at elevated temperatures ($T > 50K$). Taking the particle approach, and referring to Eq. 6, the thermal conductivity is given by

$$\kappa_{\mathrm{e/p}} = \frac{1}{3}C_{\mathrm{e/p,3D}}v_{\mathrm{e/p}}^2\tau_{\mathrm{e/p}} = \int_{\epsilon}\epsilon D_{\mathrm{e/p}}\frac{\partial f_{\mathrm{FD/BE}}}{\partial T}v_{\mathrm{e/p}}^2\tau_{\mathrm{e/p}}\,d\epsilon. \quad (91)$$

As previously discussed, electrons are the dominant thermal carrier in metals where phonons are the dominant thermal carrier in semiconductors; therefore, the derivation of electron thermal conductivity will focus on gold for example calculations and the phonon thermal conductivity calculations will focus on silicon.

The final two quantities needed to determine the thermal conductivity of electrons and phonons are their respective scattering times and velocities. In our particle treatment, the electrons and phonons can scatter via several different mechanisms, which will be discussed in more detail later in this section. However, the total scattering rate used in Eq. 91 is related to the individual scattering processes of each thermal carrier via Matthiessen's Rule, given by (Kittel, 2005)

$$\frac{1}{\tau} = \sum_m \frac{1}{\tau_m}, \tag{92}$$

where m is an index representing a specific scattering process of an electron or a phonon. As for the velocities of the carriers, the phonon velocity was previous defined in Section 3.2, specifically Eq. 30. Typical phonon group velocities are on the order of $v_g = 10^3 - 10^4\,\mathrm{m\,s^{-1}}$. The electron velocities can be calculated from the Fermi energy. As the electronic thermal conductivity is related to the temperature derivative of the Fermi-Dirac distribution, only electrons around the Fermi energy will participate in transport. Approximating all the electrons participating in transport to have energies of about the Fermi energy, the velocity of the electrons at the Fermi energy, the Fermi velocity, can be calculated from the common expression for kinetic energy of a particle so that the electron Fermi velocity is given by

$$v_\mathrm{F} = \sqrt{\frac{2\epsilon_\mathrm{F}}{m}}. \tag{93}$$

Typical Fermi velocities in metals are on the order of $10^6\,\mathrm{m\,s^{-1}}$.

6.1 Electron thermal conductivity

To calculate the thermal conductivity of the electron system via Eq. 91, the final piece of information that must be known is the electron scattering time. At moderate temperatures, electrons can lose energy by scattering with other electrons and with the phonons. In metals, the electron-electron and electron-phonon scattering processes take the form $\tau_\mathrm{ee} = \left(A_\mathrm{ee}T^2\right)^{-1}$ and $\tau_\mathrm{ep} = \left(B_\mathrm{ep}T\right)^{-1}$, respectively, where A and B are material dependent constants related to the electrical resistivity (Kittel, 2005). From Eq. 94, the total scattering time at moderate temperatures in metals is given by

$$\frac{1}{\tau} = \left(\frac{1}{\tau_\mathrm{ee}} + \frac{1}{\tau_\mathrm{ep}}\right) = A_\mathrm{ee}T^2 + B_\mathrm{ep}T. \tag{94}$$

From this, the electron thermal conductivity is given by

$$\kappa_\mathrm{e} = \frac{v_\mathrm{F}^2}{A_\mathrm{ee}T^2 + B_\mathrm{ep}T}\int_{-\infty}^{\infty}(\epsilon - \epsilon_\mathrm{F})D_\mathrm{e,3D}(\epsilon_\mathrm{F})\frac{\partial f_\mathrm{FD}}{\partial T}\,d\epsilon = \frac{\pi^2 k_\mathrm{B}^2 n_\mathrm{e,3D} v_\mathrm{F}^2}{2\epsilon_\mathrm{F}\left(A_\mathrm{ee}T + B_\mathrm{ep}\right)}, \tag{95}$$

where the simplification on the right hand side comes from the development in Section 5.1.
The electron thermal conductivity of Au as a function of temperature predicted via Eq. 95 is shown in Fig. 6a along with the data from Fig. 1. Since the forms of the scattering times in metals discussed above are only valid for temperatures around and above the Debye temperature, the thermal conductivity is shown in the range from $100 - 1000$ K. Below this range, additional electron and phonon iterations affect the conductivity that are beyond the scope of this chapter. The scattering constants, A_ee and B_ep are used to fit the model in Eq. 95

to the data, and the resulting constants, listed in the figure caption, are in excellent agreement with previously published values (Ivanov & Zhigilei, 2003). In addition, the temperature trends agree remarkably well even with the simplified assumptions involved in the derivation of Eq. 95, showing the power of modeling electron thermal transport from a fundamental particle level.

With this approach, the effects of nanostructuring on thermal conductivity can now be calculated. When the sizes of a nanomaterial are on the same order as the mean free path of the thermal carriers, in the case of metals, the electrons, an additional scattering mechanism arises due to electron boundary scattering. This boundary scattering time is related to the length of the limiting dimension, d, in the nanosystem through $\tau_{eb} = d/v_F$. Using this with Matthiessen's Rule (Eq. 94), the thermal conductivity of a metallic nanosystem can be calculated by (Hopkins et al., 2008)

$$\kappa_e = \frac{\pi^2 k_B^2 n_{e,3D} v_F^2 T}{2\epsilon_F \left(A_{ee} T^2 + B_{ep} T + \frac{v_F}{d}\right)}. \tag{96}$$

Note that when d is very large, Eq. 96 reduces to Eq. 95. Fig. 6a shows the predicted thermal conductivity as a function of temperature for Au nanosystems with limiting d indicated in the figure. Due to electron-boundary scattering, the thermal conductivity of metallic nanosystems can be greatly reduced by nanostructuring.

6.2 Phonon thermal conductivity

As with the electron thermal conductivity, to calculate the thermal conductivity of the phonon system via Eq. 91, the phonon scattering times must be known. The major phonon scattering processes, valid at all temperatures, are phonon-phonon scattering, phonon-impurity scattering, and phonon-boundary scattering. Note that phonon boundary scattering exists even in bulk samples since phonons exist as a spectrum of wavelengths, some of which can be larger than bulk samples. These processes take the form of $\tau_{pp} = \left(AT\omega^2 \exp\left[-B/T\right]\right)^{-1}$ for phonon-phonon scattering, $\tau_{pi} = \left(C\omega^4\right)^{-1}$ for phonon-impurity scattering, and $\tau_{pb} = \left(v_g/d\right)^{-1}$ for phonon-boundary scattering. Note that this boundary scattering term represents the bulk boundaries. From this, the total scattering time for phonons is given by

$$\frac{1}{\tau} = \left(\frac{1}{\tau_{pp}} + \frac{1}{\tau_{pi}} + \frac{1}{\tau_{pb}}\right) = AT\omega^2 \exp\left[-\frac{B}{T}\right] + C\omega^4 + \frac{v_g}{d}. \tag{97}$$

and the phonon thermal conductivity can be calculated via

$$\begin{aligned}\kappa_e &= \int_0^{\omega_{max}} \hbar\omega D_{p,3D} \frac{\partial f_{BE}}{\partial T} v_g^2 \left(AT\omega^2 \exp\left[-\frac{B}{T}\right] + C\omega^4 + \frac{v_g}{d}\right)^{-1} d\omega \\ &= \int_0^{\omega_{max}} \frac{3\hbar^2\omega^4}{2\pi^2 v_g k_B T^2} \frac{\exp\left[\frac{\hbar\omega}{k_B T}\right]}{\left(\exp\left[\frac{\hbar\omega}{k_B T}\right] - 1\right)^2} \left(AT\omega^2 \exp\left[-\frac{B}{T}\right] + C\omega^4 + \frac{v_g}{d}\right)^{-1} d\omega. \end{aligned} \tag{98}$$

where the simplification on the right hand side comes from the development in Section 5.2.

The phonon thermal conductivity of Si as a function of temperature predicted via Eq. 98 is shown in Fig. 6b along with the data from Fig. 1. The scattering time coefficients A and

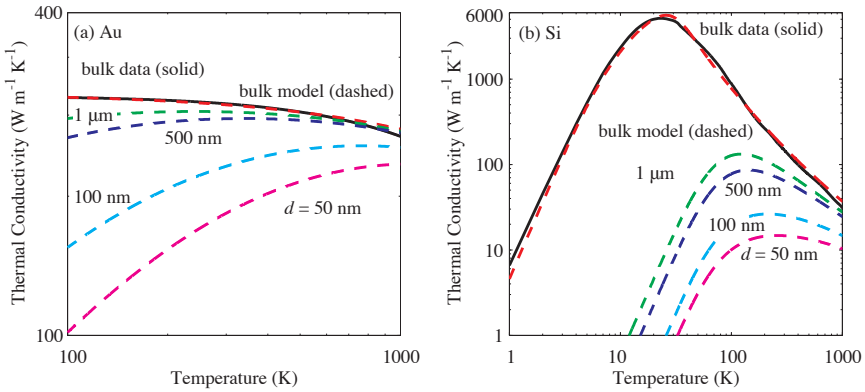

Fig. 6. (a) Electron thermal conductivity of Au as a function of temperature for bulk Au and for Au nanosystems of various limiting sizes indicated in the plot. The bulk model predictions, calculated via Eq. 95, are compared to the experimental data in Fig. 1. For these calculations, $A_{ee} = 2.4 \times 10^7\,\mathrm{K}^{-2}\,\mathrm{s}^{-1}$ and $B_{ep} = 1.23 \times 10^{11}\,\mathrm{K}^{-1}\,\mathrm{s}^{-1}$ were assumed, in excellent agreement with literature values (Ivanov & Zhigilei, 2003). Additional thermophysical parameters used for this calculation are listed in the caption of Fig. 5. The various Au nanosystem thermal conductivity is calculated via Eq. 96. (b) Phonon thermal conductivity of Si as a function of temperature for bulk Si and for Si nanoysstems of various limiting sizes in indicated in the plots. The bulk model predictions, calculated via Eq. 98, are compared to the experimental data in Fig. 1. For these calculations, the scattering coefficients were $A = 1.23 \times 10^{-19}\,\mathrm{s\,K}^{-1}$, $B = 140\,\mathrm{K}$, and $C = 1.32 \times 10^{-45}\,\mathrm{s}^3$. In addition, the group velocity of Si is taken as the speed of sound, $v_g = 8{,}433\,\mathrm{m\,s}^{-1}$, and the lattice parameter of Si is $a = 5.430 \times 10^{-10}\,\mathrm{m}$. To fit the bulk data, $d = 8.0 \times 10^{-3}\,\mathrm{m}$. To examine the effects of nanostructuring, d is varied as indicated in the plot.

B were iterated to match the data after the maximum and C was taken from the literature (Mingo, 2003). The boundary scattering constant, d, is used as a fitting parameter to match the data at temperatures lower than the maximum. The resulting coefficients were in excellent agreement with the literature values for bulk Si (Mingo, 2003). Note that the model using Eq. 98 fits the data and captures the temperature trends extremely well showing the power of modeling the bulk phonon thermal conductivity from a fundamental energy carrier level. To examine the effects of nanostructuring on the phonon thermal conductivity, d is varied to dimensions indicated in Fig. 6b. Nanostructruing greatly reduces the phonon thermal conductivity, especially at low temperatures where phonon mean free paths are long.

7. Summary

Modern devices, with feature sizes on the length scale of electron and phonon mean free paths, require thermal analyses different from that of the phenomenological Fourier Law. This is due to the fact that the scattering of electrons and phonons in such systems occurs predominantly at interfaces, inclusions, grain boundaries, etc., rather than within the materials comprising the device themselves. Here, electrons and phonons have been described in terms of their respective dispersion diagrams, calculated via the Schrödinger equation for electrons and atomic equations of motion for phonons. Using this information

and density of states expressions, energy storage properties, i.e., internal energy and heat capacity, have been formulated. Lastly, applying the Kinetic Theory of Gases, the thermal conductivity expressions for metals and semiconductors have been derived. It has been shown that limiting feature sizes can result in a significant reduction in thermal conductivity. This, then, once again reinforces the idea that thermal transport on the nanoscale requires an altogether different approach from that at the macroscale.

8. Acknowledgements

The authors would like to acknowledge Professor Pamela M. Norris at the University of Virginia for helpful advice and for recommending the writing of this book chapter. P.E.H. would like to thank Dr. Leslie M. Phinney at Sandia National Laboratories for guidance and support. P.E.H. is appreciative for funding from the LDRD program office through the Sandia National Laboratories Harry S. Truman Fellowship Program. J.C.D. is appreciative for funding from the National Science Foundation Graduate Research Fellowship Program. Sandia is a multiprogram laboratory operated by Sandia Corporation, a wholly owned subsidiary of Lockheed Martin Corporation, for the United States Department of Energy's National Nuclear Security Administration under Contract DE-AC04-94AL85000.

9. References

Cahill, D. G., Ford, W. K., Goodson, K. E., Mahan, G. D., Majumdar, A., Maris, H. J., Merlin, R. & Phillpot, S. R. (2003). Nanoscale thermal transport, *Journal of Applied Physics* 93(2): 793–818.

Chen, G. (2005). *Nanoscale Energy Transport and Conversion: A Parallel Treatment of Electrons, Molecules, Phonons, and Photons*, Oxford University Press, New York, New York.

Dove, M. T. (1993). *Introduction to Lattice Dynamics*, number 4 in *Cambridge Topics in Mineral Physics and Chemistry*, Cambridge University Press, Cambridge, England.

Griffiths, D. (2000). *Introduction to Quantum Mechanics*, 2nd edn, Prentice Hall, Upper Saddle River, New Jersey.

Ho, C. Y., Powell, R. W. & Liley, P. E. (1972). Thermal conductivity of the elements, *Journal of Physical and Chemical Reference Data* 1(2): 279–421.

Hopkins, P. E., Norris, P. M., Phinney, L. M., Policastro, S. A. & Kelly, R. G. (2008). Thermal conductivity in nanoporous gold films during electron-phonon nonequilibrium, *Journal of Nanomaterials* (418050).

Ivanov, D. S. & Zhigilei, L. V. (2003). Combined atomistic-continuum modeling of short-pulse laser melting and disintegration, *Physical Review B* 68: 064114.

Kittel, C. (2005). *Introduction to Solid State Physics*, 8th edn, Wiley, Hoboken, New Jersey.

Mingo, N. (2003). Calculation of Si nanowire thermal conductivity using complete phonon dispersion relations, *Physical Review B* 68(11): 113308.

Schrödinger, E. (1926). Quantisation as a problem of characteristic values, *Annalan der Physik* 79: 361–376, 489–527.

Srivastava, G. P. (1990). *The Physics of Phonons*, Adam Hilger, Bristol, England.

Tien, C.-L., Majumdar, A. & Gerner, F. M. (1998). *Microscale Energy Transport*, Taylor and Francis, Washington, D.C.

Vincenti, W. G. & Kruger, C. H. (2002). *Introduction to Physical Gas Dynamics*, Krieger Publishing Company, Malabar, Florida.

Wolf, E. L. (2006). *Nanophysics and Nanotechnology: An Introduction to Modern Concepts in*

Nanoscience, 2nd edn, WILEY-VCH Verlag GmbH & Co. KGaA, Weinheim, Germany.
Ziman, J. M. (1972). *Principles of the Theory of Solids*, 2nd edn, Cambridge University Press, Cambridge, England.

14

Study of Hydrodynamics and Heat Transfer in the Fluidized Bed Reactors

Mahdi Hamzehei
Islamic Azad University, Ahvaz Branch, Ahvaz
Iran

1. Introduction

Fluidized bed reactors are used in a wide range of applications in various industrial operations, including chemical, mechanical, petroleum, mineral, and pharmaceutical industries. Fluidized multiphase reactors are of increasing importance in nowadays chemical industries, even though their hydrodynamic behavior is complex and not yet fully understood. Especially the scale-up from laboratory towards industrial equipment is a problem. For example, equations describing the bubble behavior in gas-solid fluidized beds are (semi) empirical and often determined under laboratory conditions. For that reason there is little unifying theory describing the bubble behavior in fluidized beds.
Understanding the hydrodynamics of fluidized bed reactors is essential for choosing the correct operating parameters for the appropriate fluidization regime. Two-phase flows occur in many industrial and environmental processes. These include pharmaceutical, petrochemical, and mineral industries, energy conversion, gaseous and particulate pollutant transport in the atmosphere, heat exchangers and many other applications. The gas–solid fluidized bed reactor has been used extensively because of its capability to provide effective mixing and highly efficient transport processes. Understanding the hydrodynamics and heat transfer of fluidized bed reactors is essential for their proper design and efficient operation. The gas–solid flows at high concentration in these reactors are quite complex because of the coupling of the turbulent gas flow and fluctuation of particle motion dominated by inter-particle collisions. These complexities lead to considerable difficulties in designing, scaling up and optimizing the operation of these reactors [1-3].
Multiphase flow processes are key element of several important technologies. The presence of more than one phase raises several additional questions for the reactor engineer. Multiphase flow processes exhibit different flow regimes depending on the operating conditions and the geometry of the process equipment. Multiphase flows can be divided into variety of different flows. One of these flows in gas-solid flows. In some gas-solid reactors (fluidized reactors); gas is the continuous phase and solid particles are suspended within this continuous phase. Depending on the properties of the gas and solid phases, several different sub-regimes of dispersed two-phase flows may exist. For relatively small gas flow rates, the rector may contain a dense bed of fluidized solid particles. The bed may be homogenously fluidized or gas may pass through the bed in the form of large bubbles. Further increase in gas flow rate decreases the bed density and the gas-solid contacting pattern may change from dense bed to turbulent bed, then to fast-fluidized mode and ultimately to pneumatic conveying mode. In all these flow regimes the relative importance

of gas-particle, particle-particle, and wall interaction is different. It is, therefore necessary to identify these regimes to select an appropriate mathematical model. Apart from density and particle size as used in Geldart's classification, several other solid properties, including angularity, surface roughness and composition may also significantly affect quality of fluidization (Grace, 1992). However, Geldart's classification chart often provides a useful starting point to examine fluidization quality of a specific gas-solid system. Reactor configuration, gas superficial velocity and solids flux are other important parameters controlling the quality of fluidization. At low gas velocity, solids rest on the gas distributor and the regime is a fixed bed regime. The relationship between some flow regimes, type of solid particles and gas velocity is shown schematically in Fig.1. When superficial gas velocity increases, a point is reached beyond which the bed is fluidized. At this point all the particles are just suspended by upward flowing gas. The frictional force between particle and gas just counterbalances the weight of the particle.

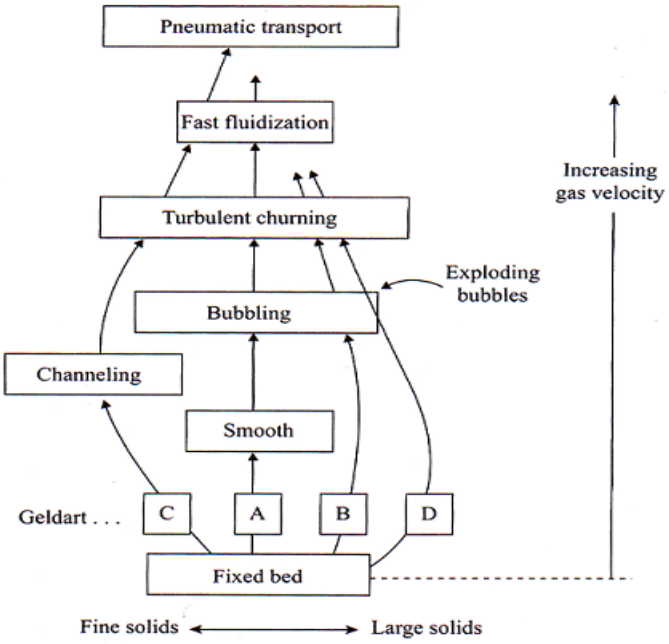

Fig. 1. Progressive change in gas-solid contact (flow regimes) with change on gas velocity

This gas velocity at which fluidization begins is known as minimum fluidization velocity (U_{mf}) the bed is considered to be just fluidized, and is referred to as a bed at minimum fluidization. If gas velocity increases beyond minimum fluidization velocity, homogeneous (or smooth) fluidization may exist for the case of fine solids up to a certain velocity limit. Beyond this limit (U_{mb} : minimum bubbling velocity), bubbling starts. For large solids, the bubbling regime starts immediately if the gas velocity is higher than minimum fluidization velocity ($U_{mb} = U_{mf}$). With an increase in velocity beyond minimum bubbling velocity, large instabilities with bubbling and channeling of gas are observed. At high gas velocities, the movement of solids becomes more vigorous. Such a bed is called a bubbling bed or

heterogeneous fluidized bed, in this regime; gas bubbles generated at the distributor coalesce and grow as they rise through the bed. For deep beds of small diameter, these bubbles eventually become large enough to spread across the diameter of the vessel. This is called a slugging bed regime. In large diameter columns, if gas velocity increases still further, then instead of slugs, turbulent motion of solid clusters and voids of gas of various size and shape are observed, Entrainment of solids becomes appreciable. This regime is called a turbulent fluidized bed regime. With further increase in gas velocity, solids entrainment becomes very high so that gas-solid separators (cyclones) become necessary. This regime is called a fast fluidization regime. For a pneumatic transport regime, even higher gas velocity is needed, which transports all the solids out of the bed. As one can imagine, the characteristics of gas-solid flows of these different regimes are strikingly different. It is, therefore, necessary to determine the prevailing flow regime in order to select an appropriate mathematical model to represent it.

Computational fluid dynamics (CFD) offers an approach to understanding the complex phenomena that occur between the gas phase and the particles. With the increased computational capabilities, computational fluid dynamics (CFD) has become an important tool for understanding the complex phenomena that occur between the gas phase and the particles in fluidized bed reactors [3, 4, 5]. As a result, a number of computational models for solving the non-linear equations governing the motion of interpenetrating continua that can be used for design and optimization of chemical processes were developed. Two different approaches have been developed for application of CFD to gas–solid flows, including the fluidized beds. One is the Eulerian-Lagrangian method where a discrete particle trajectory analysis method based on the molecular dynamics model is used which is coupled with the Eulerian gas flow model. The second approach is a multi-fluid Eulerian–Eulerian approach which is based on continuum mechanics treating the two phases as interpenetrating continua. The Lagrangian model solves the Newtonian equations of motion for each individual particle in the gas-solid system along with a collision model to handle the energy dissipation caused by inelastic particle-particle collision. The large number of particles involved in the analysis makes this approach computationally intensive and impractical for simulating fluidized bed reactors at high concentration. The Eulerian model treats different phases as interpenetrating and interacting continua. The approach then develops governing equations for each phase that resembles the Navier-Stokes equations. The Eulerian approach requires developing constitutive equations (closure models) to close the governing equations and to describe the rheology of the gas and solid phases.

For gas-solid flows modeling, usually, Eulerian-Lagrangian are called discrete particle models and Eulerian-Eulerian models are called granular flow models. Granular flow models (GFM) are continuum based and are more suitable for simulating large and complex industrial fluidized bed reactors containing billions of solid particles. These models, however, require information about solid phase rheology and particle-particle interaction laws. In principle, discrete particle models (DPM) can supply such information. DPMs in turn need closure laws to model fluid-particle interactions and particle-particle interaction parameters based on contact theory and material properties. In principle, it is possible to work our way upwards from direct solution of Navier-Stokes equations. Lattice-Boltzmann models and contact theory to obtain all the necessary closure laws and other parameters required for granular flow models. However, with the present state of knowledge, complete a priori simulations are not possible. It is necessary to use these different models judiciously. Combined with key experiments, to obtain the desired engineering information about

gas-solid flows in industrial equipment. Direct solution of Navier-Stokes equations or lattice Boltzmann methods are too computation intensive to simulate even thousands of solid particles. Rather than millions of particles, DPMs are usually used to gain an insight into various vexing issues such as bubble or cluster formations and their characteristics or segregation phenomena. A few hundred thousand particles can be considered in such DPMs.

The kinetic theory of granular flow that treats the kinetic energy of the fluctuating component of the particle velocity as the granular temperature has been used to guide the development of appropriate constitutive laws [3, 4]. In particular, solid pressure and effective viscosity of the particulate phase were successfully predicted from the kinetic theory of granular materials. Simulations of the hydrodynamics of gas-solid multiphase systems with the Eulerian models using different CFD codes have shown the suitability of the approach for modeling fluidized bed reactors [5, 6]. The reduced number of equations that need to be solved is the main advantage of the Eulerian approach in comparison with the Lagrangian method.

The fundamental problem encountered modeling of these reactors is the motion of two phases where the interface is unknown and transient, and the interaction is understood only for a limited range of conditions. Also, a large number of independent variables such as particle density, size and shape can influence hydrodynamic behavior [2,3,5]. Despite a significant amount of research on fluidized bed reactors, there are considerable uncertainties on their behavior. Part of the confusion is due to the presence of various complex flow regimes and their sensitivities to the operating conditions of these reactors. The fundamental problem encountered in modeling the hydrodynamics of a gas–solid fluidized bed is the strong interaction of the phases with unknown and transient interfaces. As a result, the interaction of the phases is understood only for a limited range of conditions. One additional important complexity is that in many of these industrial processes the gas flow is in a turbulent state of motion [2,3,5].

Recently, Nasr and Ahmadi [7] studied the turbulence modulation due to the presence of dispersed solid particles in a downward, fully developed channel flow. The Eulerian framework was used for the gas phase, whereas the modified Lagrangian approach was used for the particle-phase. The steady-state equations of conservation of mass and momentum were used for the gas phase, and the effect of turbulence was included via a $k-\varepsilon$ model. Taghipour et al. [8] have conducted experimental and computational studies of hydrodynamics of gas–solid flows in a fluidized bed reactor. The simulation results were compared with the experimental data. The model predicted bed expansion and gas–solid flow patterns reasonably well. Furthermore, the predicted instantaneous and time-average local voidage profiles showed trends similar to the experimental data. A multi fluid Eulerian model integrating the kinetic theory for solid particles was used of predicting the gas–solid behavior of a fluidized bed. Comparison of the model predictions, using the Syamlal–O'Brien, Gidaspow, and Wen–Yu drag functions, and experimental measurements on the time-average bed pressure drop, bed expansion, and qualitative gas–solid flow pattern indicated reasonable agreement for most operating conditions. Furthermore, the predicted instantaneous and time-average local voidage profiles showed similar trends with the experimental results.

Kaneko et al. [9] numerically analyzed temperature behavior of particles and gas in a fluidized bed reactor by applying a discrete element method, where heat transfer from particles to the gas was estimated using Ranz–Marshall equation. CFD simulation of a

fluidized bed reactor was also conducted by Rong et al. [10] focusing on the chemical kinetic aspects and taking into account the intra-particle heat and mass transfers, poly-disperse particle distributions, and multiphase fluid dynamics. Gas–solid heat and mass transfer, polymerization chemistry and population dynamic equations were developed and solved in a multi-fluid code (MFIX) in order to describe particle growth.

Behjat et al. [11] investigated unsteady state behavior of gas–solid fluidized beds. They showed that the model predictions of bubble size and gas–solid flow pattern using both Syamlal–O'Brien and Gidaspow drag models were similar. Also, when the bed containing two different solid phases was simulated, the results showed particles with smaller diameters had lower volume fraction at the bottom of the bed and higher volume fraction at the top of the reactor.

Gobin et al. [12] numerically simulated a fluidized bed using a two-phase flow method. In their study, time-dependent simulations were performed for industrial and pilot reactor operating conditions. Their numerical predictions were in qualitative agreement with the observed behavior in terms of bed height, pressure drop and mean flow regimes. Wachem et al. [13,14,15] verified experimentally their Eulerian-Eulerian gas-solid simulations of bubbling fluidized beds with existing correlations for bubble size or bubble velocity. A CFD model for a free bubbling fluidized bed was implemented in the commercial code CFX. This CFD model was based on a two-fluid model including the kinetic theory of granular flows.

Chiesa et al. [16] have presented a computational study of the flow behavior of a lab-scale fluidized bed. The results obtained from a 'discrete particle method' (DPM) were qualitatively compared with the results obtained from a multi-fluid computational fluid dynamic (CFD) model. They have also compared the experimental data for bubble formation with their computational results. The results obtained from the Eulerian - Lagrangian approach were found to show a much better agreement with the experimental data than those that were obtained by the Eulerian-Eulerian approach.

Mansoori et al. [17] investigated thermal interaction between a turbulent vertical gas flow and particles injected at two different temperatures experimentally and numerically. A two-phase $k-\tau$ and $k_\theta-\tau_\theta$ numerical model in four-way coupled simulation was used in a Eulerian-Lagrangian framework. In agreement with the numerical results, the experiments showed that the addition of hot particles to the suspension can cause an increase in the heat transfer coefficient. Also, in another paper [18] they used their four-way Eulerian-Lagrangian formulation to study the particle–particle heat transfer in turbulent gas–solid flows in a riser. Their formulation included the particle–particle collisions, in addition to the $k-\tau$ and the $k_\theta-\tau_\theta$ model equations. To examine the nature of inter-particle heat transfer, two groups of particles with different temperatures were fed into the flow field. Their numerical simulations included an inelastic soft sphere collision model, but unsteadiness and variation of gas velocity in the gas lens between two colliding particles and the non-continuum effects were neglected. Validations of the predicted velocity and heat transfer were also presented in [18]. Saffar-Avval et al. [19] performed simulations of gas–solid turbulent upward flows in a vertical pipe using the Eulerian–Lagrangian approach. Particle–particle and particle–wall collisions were simulated using a deterministic collision model. The influence of particle collisions on the particle concentration, mean temperature and fluctuating velocities was investigated. Numerical results were presented for different values of mass loading ratios. The profiles of particle concentration, mean velocity and temperature were shown to be flatter by considering inter-particle collisions, while this

effect on the gas mean velocity and temperature was not significant. It was demonstrated that the effect of inter-particle collisions had a dramatic influence on the particle fluctuation velocity.

Despite many studies on the modeling and model evaluation of fluidized-bed hydrodynamics, only a few works have been published on the CFD modeling and model validation of combined reactor hydrodynamics and heat transfer [1-50]. For example, Huilin et al. [28, 38] studied bubbling fluidized bed with the binary mixtures applying multi-fluid Eulerian CFD model according to the kinetic theory of granular flow. Their simulation results showed that hydrodynamics of gas bubbling fluidized bed are related with the distribution of particle sizes and the amount of dissipated energy in particle–particle interactions.

Also, Zhong et. al. [30, 31] studied the maximum spoutable bed heights of a spout-fluid bed packed with six kinds of Geldart group D particles were. They obtained the effects of particle size, spout nozzle size and fluidizing gas flow rate on the maximum spoutable bed height. Their results shown that the maximum spoutable bed height of spout-fluid bed decreases with increasing particle size and spout nozzle size, which appears the same trend to that of spouted beds. The increasing of fluidizing gas flow rate leads to a sharply decrease in the maximum spoutable bed height. CFD simulation of fluidized bed reactor has also been conducted by Fan et al. [43] focusing on the chemical kinetic aspects and taking into account the intra-particle heat and mass transfer rates, poly-disperse particle distributions and multiphase fluid dynamics. Gas–solid heat and mass transfer, polymerization chemistry and population balance equations were developed and solved in a multi-fluid code (MFIX) in order to describe particle growth. Lettieri et al. [44] used the Eulerian–Eulerian granular kinetic model available within the CFX-4 code to simulate the transition from bubbling to slugging fluidization for a typical Group B material at four fluidizing velocities. Results from simulations were analyzed in terms of voidage profiles and bubble size, which showed typical features of a slugging bed, and also good agreement between the simulated and predicted transition velocity.

In this study, the heat transfer and hydrodynamics of a two-dimensional non-reactive gas–solid fluidized bed reactor were studied experimentally and computationally. Particle size effects, superficial gas velocity and initial static bed height on hydrodynamics of a non-reactive gas–solid fluidized bed reactor were studied experimentally and computationally. Attention was given to the influence of gas temperature and gas velocity on gas-solid heat transfer and hydrodynamics. A multi-fluid Eulerian model incorporating the kinetic theory for solid particles with the standard $k-\varepsilon$ turbulence model was applied in order to simulate the gas–solid flow at different superficial gas velocities. It was assumed that inlet gas was hot and the initial solid particle was at ambient temperature. Simulation results were compared with the experimental data for model validation. The sensitivity of the simulation results to the use of the drag laws of Syamlal-O'Brien, Gidaspow and Cao-Ahmadi was also studied.

2. Governing equations

2.1 Basic equation

The governing equations of the gas-solid flow include the conservation of mass, momentum, and energy. The governing equations of solid and gas phases are based on the Eularian-Eularian model. By definition, the volume fractions of the phases must sum to one:

$$\alpha_g + \alpha_s = 1 \tag{1}$$

The continuity equation for gas and solid phases in the absence of inter-phase mass transfer are respectively given as

$$\frac{\partial}{\partial t}(\alpha_g \rho_g) + \nabla \cdot (\alpha_g \rho_g \overrightarrow{v_g}) = 0 \tag{2}$$

$$\frac{\partial}{\partial t}(\alpha_s \rho_s) + \nabla \cdot (\alpha_s \rho_s \overrightarrow{v_s}) = 0 \tag{3}$$

The conservation of momentum for the gas and solid phases are described by

$$\frac{\partial}{\partial t}(\alpha_g \rho_g \vec{v}_g) + \nabla.(\alpha_g \rho_g \vec{v}_g \vec{v}_g) = -\alpha_g \nabla p_g + \nabla.\overline{\overline{\tau_g}} + \alpha_g \rho_g \vec{g} + \beta_{gs}(\vec{v}_s - \vec{v}_g) \tag{4}$$

$$\frac{\partial}{\partial t}(\alpha_s \rho_s \vec{v}_s) + \nabla \cdot (\alpha_s \rho_s \vec{v}_s \vec{v}_s) = -\alpha_s \nabla p_g - \nabla p_s + \nabla.\overline{\overline{\tau_s}} + \alpha_s \rho_s \vec{g} + \beta_{gs}(\vec{v}_g - \vec{v}_s) \tag{5}$$

Here $\overline{\overline{\tau}}$ is Reynolds stress tensor, g is gravitational constant and $(-\alpha_s \nabla p + \beta_{gs}(\vec{v}_g - \vec{v}_s))$ is an interaction force (drag and buoyancy forces) representing the momentum transfer between gas and solid phases [1, 5, 6]. Several drag models for the gas-solid inter-phase exchange coefficient β_{gs} were reported in the literature. The drag model of Syamlal-O'Brien [20,21], Gidaspow [1] and Cao- Ahmadi [22, 23] were used in the present study. The drag model of Syamlal-O'Brien is based on the measurements of the terminal velocities of particles in fluidized or settling beds. The corresponding inter-phase exchange coefficient is expressed as

$$\beta_{gs} = \frac{3}{4}\frac{\alpha_s \alpha_g \rho_g}{\upsilon_{r,s}^2 d_s} C_D\left(\frac{\mathrm{Re}_s}{\upsilon_{r,s}}\right)\left|\vec{\upsilon}_s - \vec{\upsilon}_g\right| \tag{6}$$

where C_D, the drag coefficient, is given by

$$C_D = \left(\ 0.63 + \frac{4.8}{\sqrt{\mathrm{Re}_s / \upsilon_{r,s}}}\ \right)^2 \tag{7}$$

and $\upsilon_{r,s}$, a terminal velocity correlation, is expressed as

$$\upsilon_{r,s} = 0.5\left(A - 0.06\,\mathrm{Re}_s + \sqrt{(0.06\,\mathrm{Re}_s)^2 + 0.12\,\mathrm{Re}_s(2B - A) + A^2}\right) \tag{8}$$

$A = \alpha_g^{4.14}$ and $B = 0.8\alpha_g^{1.28}$ for $\varepsilon_g \le 0.85$ and $B = \alpha_g^{2.65}$ for $\alpha_g > 0.85$

The drag model of Gidaspow is a combination of the Wen and Yu model for dilute flow and the Ergun equation for dense flow. For $\alpha_g < 0.8$, β_{gs} is calculated with the equations from the Wen and Yu [24, 1, 5,8] model as

$$\beta_{gs,Wen-Yu} = \frac{3}{4} C_D \frac{\alpha_g \alpha_s \rho_g \left|\vec{v}_s - \vec{v}_g\right|}{d_s} \alpha_g^{-2.65} \tag{9}$$

where CD, the drag coefficient, is expressed as

$$C_D = \frac{24}{\mathrm{Re}_s}\left[1 + 0.15\mathrm{Re}_s^{0.687}\right] \text{ for } \mathrm{Re}_s \geq 1000 \text{ and } C_D = 0.44 \text{ for } \quad \mathrm{Re}_s > 1000 \tag{10}$$

For $\alpha_g \geq 0.8$, β_{gs} is calculated with the Ergun equation as

$$\beta_{gs,Ergun} = 150\frac{\alpha_s^2 \mu_g}{\alpha_g d_s^2} + 1.75\frac{\rho_g \alpha_s \left|\vec{v}_g - \vec{v}_s\right|}{d_s} \tag{11}$$

Cao- Ahmadi drag expression is given as

$$\beta_{gs} = \frac{18\mu_g \alpha_s}{d_s^2} \frac{[1 + 0.1(\mathrm{Re}_s)^{0.75}]}{\left(1 - (\frac{\alpha_s}{\alpha_{s,\max}})\right)^{2.5\alpha_{s,\max}}} \tag{12}$$

where solids Reynolds number, Re_s, is calculated as

$$\mathrm{Re}_s = \frac{\rho_g d_s \left|\vec{v}_g - \vec{v}_s\right|}{\mu_g} \tag{13}$$

Following Gidaspow, it is assumed that the gas and solid phases behave as Newtonian fluids. The constitutive equation for the solid phase stresses is assumed to be given as (Gidaspow, Cao and Ahmadi)

$$\overline{\overline{\tau}}_s = \alpha_s \mu_s \left[\nabla \vec{v}_s + (\nabla \vec{v}_s)^T\right] + \alpha_s \left(\lambda_s - \frac{2}{3}\mu_s\right) \nabla \vec{v}_s \overline{\overline{I}} \tag{14}$$

The granular temperature (Θ) of the solid phase is defined as one-third of the mean square particle velocity fluctuations. It should be emphasized that the granular temperature is proportional to the granular energy and is quite different from solid phase thermodynamic temperature. The transport equation for the solid phase granular temperature is given as [27, 29, 30].

$$\frac{3}{2}\frac{\partial}{\partial t}(\rho_s \alpha_s \Theta_s) + \nabla \cdot (\rho_s \alpha_s \vec{v}_s \Theta_s) = (-p_s \overline{\overline{I}} + \overline{\overline{\tau}}_s) : \nabla \cdot \vec{v}_s + \nabla \cdot (k_{\Theta_s} \nabla \Theta_s) - \gamma_{\Theta_s} + \phi_{gs} \tag{15}$$

where $(-p_s \overline{\overline{I}} + \overline{\overline{\tau}}_s) : \nabla . \vec{v}_s$ is the generation of energy by the solid stress tensor, $k_{\Theta_s} \nabla \Theta_s$ is the diffusion flux of granular energy (k_{Θ_s} is the diffusion coefficient), γ_{Θ_s} is the collisional dissipation of energy and φ_{gs} is the energy exchange between the gas and solid. The collision dissipation of energy, γ_{Θ_s}, representing the rate of energy dissipation within the solid phase due to inelastic particle collisions that was derived by Lun et al. [29] is given as

$$\gamma_{\Theta_s} = \frac{12(1-e_{ss}^2)g_{o,ss}}{d_s\sqrt{\pi}}\rho_s\alpha_s^2\Theta_s^{3/2} \tag{16}$$

The transfer of kinetic energy, φ_{gs}, due to random fluctuations in particle velocity is expressed as [1]

$$\varphi_{gs} = -3\beta_{gs}\Theta_s \tag{17}$$

A complete solution procedure of the above equation has not yet been developed. Jenkins and Mancini [30] have developed a theoretical description of a suspension with more than one particle size, employing the kinetic theory of granular flow. They predicted transport properties of binary mixture assuming equal granular temperature [9-11]. Gidaspow et al. [1, 11] have extended the kinetic theory of dense gases for binary granular mixture with unequal granular temperature between the particle phases. In the some researches [10, 14-16] the following algebraic granular temperature equation was used with the assumptions that the granular energy is dissipated locally, the convection and diffusion contributions are negligible and retaining only the generation and dissipation terms. Also van Wachem et al. [14-16] have shown that this assumption is feasible in the bubbling region of a fluidized bed. When using this algebraic equation in stead of solving the balance for the granular temperature, much faster convergence is obtained during simulations.

$$\Theta_s = \left\{ \frac{-K_1\alpha_s tr\left(\overline{\overline{D}}_s\right) + \sqrt{K_1{}^2 tr^2\left(\overline{\overline{D}}_s\right)\alpha_s^2 + 4K_4\alpha_s\left[K_2 tr^2\left(\overline{\overline{D}}_s\right) + 2K_s tr\left(\overline{\overline{D}}_s^{\,2}\right)\right]}}{2\alpha_s K_4} \right\}^2 \tag{18}$$

where $\overline{\overline{D}}_s$ is the solids strain rate tensor, and with the abbreviations :

$$\overline{\overline{D}}_s = \frac{1}{2}\left[\nabla\vec{v}_s + (\nabla\vec{v}_s)^T\right] \tag{19}$$

$$K_1 = 2(1+e_{ss})\rho_s g_{0,ss} \tag{20}$$

$$K_2 = \frac{4}{3\sqrt{\pi}}d_s\rho_s(1+e_{ss})\alpha_s g_{0,ss} - \frac{2}{3}K_3 \tag{21}$$

$$K_3 = \frac{d_s\rho_s}{2}\left\{\frac{\sqrt{\pi}}{3(3-e_{ss})}\left[1+0.4(1+e_{ss})(3e_{ss}-1)\alpha_s g_{0,ss}\right] + \frac{8\alpha_s g_{0,ss}(1+e_{ss})}{5\sqrt{\pi}}\right\} \tag{22}$$

$$K_4 = \frac{12\left(1-e_{ss}^2\right)\rho_s g_{0,ss}}{d_s\sqrt{\pi}} \tag{23}$$

For granular flows a solids pressure is calculated independently and used for the pressure gradient term, p_s, in the granular-phase momentum equation. Because a Maxwellian

velocity distribution is used for the particles, a granular temperature is introduced into the model and appears in the expression for the solid pressure and viscosities. The solid pressure is composed of a kinetic term and a second term due to particle collisions:

$$p_s = \alpha_s \rho_s \Theta_s + 2\rho_s (1 + e_{ss}) \alpha_s^2 g_{o,ss} \Theta_s \tag{24}$$

where e_{ss} is the coefficient of restitution for particle collisions. This coefficient is a measure of the elasticity of the collision between two particles, and relates to how much of the kinetic energy of the colliding particles before the collision remains after the collision. A perfectly elastic collision has a coefficient of restitution of 1. A perfectly plastic, or inelastic, collision has a coefficient of restitution of 0 [8, 9]. The coefficient of restitution is defined as the ratio of the difference in the velocities of the two colliding particles after the collision to that in their velocities before the collision, i.e.,

$$e_{ss} = \frac{\text{Speed of separation}}{\text{Speed of approaching}} \tag{25}$$

e_{ss} can be derived from Newton's equation of motion. It is a function of the material properties, impact velocity and hardness ratio. But, under near-elastic conditions the coefficient of restitution of a particle is approximately constant, and the assumption of a constant e_{ss} could greatly simplify mathematical manipulation of CFD simulation [8,9]. $g_{o,ss}$ is the radial distribution function that for one solids phase, use

$$g_{o,ss} = \left[1 - \left(\frac{\alpha_s}{\alpha_{s,\max}} \right)^{\frac{1}{3}} \right]^{-1} \tag{26}$$

At a packed state, the bed is crammed with particles, and hence the frictional force prevails over the other forces, while at a fluidized state, lasting contact gives way to free flight and brief collisions among particles. The competition and transformation of dominating forces lead to flow transition from the packed bed to fluidization. Subsequently, three mechanisms of the particle-phase transport result in two types of flow states, as shown in Fig. 2. The frictional transport determines the behaviors at a close packed state, while the kinetic collisional transports cause a two-phase flow. So, the total stress may be approximated as the sum of frictional and kinetic collisional contributions as if each of them acts alone. so, the solids stress tensor contains shear and bulk viscosities arising from particle momentum exchange due to translation and collision.

The solid stress tensor contains shear and bulk viscosities arising from particle momentum exchange due to translation and collision. A frictional component of viscosity can also be included to account for the viscous-plastic transition that occurs when particles of a solid phase reach the maximum solid volume fraction.

The collisional and kinetic parts, and the frictional part, were used to evaluate the solid shear viscosity. That is,

$$\mu_s = \mu_{s,col} + \mu_{s,kin} + \mu_{s,fr} \tag{27}$$

The collisional part of the shear viscosity is modeled as

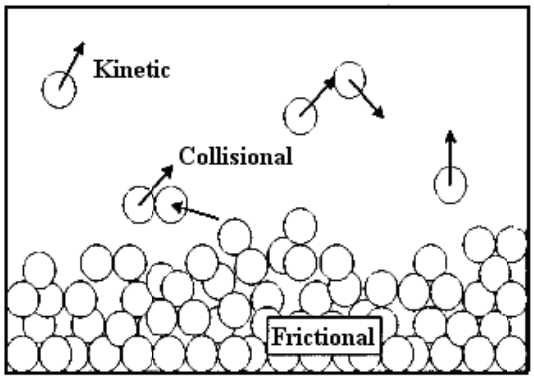

Fig. 2. Three particle transport mechanisms: kinetic, collisional, and frictional transport.

$$\mu_{s,col} = \frac{4}{5}\alpha_s \rho_s d_s g_{o,ss}(1+e_{ss})\left(\frac{\Theta_s}{\pi}\right)^{1/2} \tag{28}$$

The kinetic term is expressed in the Syamlal-O'Brien [20, 21] model as :

$$\mu_{s,kin} = \frac{\alpha_s \rho_s d_s \sqrt{\Theta_s \pi}}{6(3-e_{ss})}\left[1+\frac{2}{5}(1+e_{ss})(3e_{ss}-1)\alpha_s g_{o,ss}\right] \tag{29}$$

Gidaspow et al. suggested:

$$\mu_{s,kin} = \frac{10\rho_s d_s \sqrt{\Theta_s \pi}}{96(1+e_{ss})g_{o,ss}}\left[1+\frac{4}{5}g_{o,ss}\alpha_s(1+e_{ss})\right]^2 \tag{30}$$

Also Cao and Ahmadi [22, 23] suggested:

$$\begin{aligned}\mu_s = &\left[1+\left(\tau_g^t/\tau_{gs}^x\right)\left(1-\alpha_s/\alpha_{s,\max}\right)^3\right]^{-1}\times \\ &\left[0.1045\left(1/g_{0,ss}+3.2\alpha_s+12.1824 g_{0,ss}\alpha_s^2\right)\right]d_s\rho_s\sqrt{\Theta_s}\end{aligned} \tag{31}$$

where the particle relaxation time, τ_{gs}^x, and time-scale of turbulent eddies, τ_g^t, are given by

$$\tau_{gs}^x = \frac{\alpha_s \rho_s}{\beta_{gs}}, \quad \tau_g^t = \frac{3}{2}C_\mu \frac{k_g}{\varepsilon_g} \tag{32}$$

Here k_g is the turbulent kinetic energy of gas phase, C_μ is the constant in the gas turbulence model, and ε_g is the turbulent energy dissipation in the gas phase.
The friction stress plays a significant role when the solid-phase volume fraction gets close to the packing limit. For the contribution of the friction stress to the solid shear viscosity the expression suggested by Schaeffer [8] given as

$$\mu_{s,fr} = \frac{p_s \sin\varphi}{2\sqrt{I_{2D}}} \tag{33}$$

$$I_{2D} = \frac{1}{6}\left[\left(D_{s11} - D_{s22}\right)^2 + \left(D_{s22}\right)^2 + \left(D_{s11}\right)^2\right] + D_{s12}^2 \tag{34}$$

$$I_{2D} = \frac{1}{6}\left[\left(\frac{\partial u_s}{\partial x} - \frac{\partial v_s}{\partial y}\right) + \left(\frac{\partial v_s}{\partial y}\right)^2 + \left(\frac{\partial u_s}{\partial x}\right)^2\right] + \left[\frac{1}{2}\left(\frac{\partial u_s}{\partial y} + \frac{\partial v_s}{\partial x}\right)\right]^2 \tag{35}$$

is used. Here p_s is the solid pressure, φ is the angle of internal friction, and I_{2D} is the second invariant of the deviatoric stress tensor [5, 8, 11]. The solid bulk viscosity accounts for the resistance of the granular particles to compression and expansion. It has the following from Lun et al. [29]:

$$\lambda_s = \frac{4}{3}\alpha_s \rho_s d_s g_{o,ss}(1 + e_{ss})\sqrt{\frac{\Theta_s}{\pi}} \tag{36}$$

Also Cao and Ahmadi [22,23] suggested

$$\lambda_s = \frac{5}{3}\left[1 + \left(\tau_1^t / \tau_{12}^x\right)\left(1 - \alpha_s / \alpha_{s,\max}\right)^3\right]^{-1}\left[0.1045\left(12.1824 g_{0,ss}\alpha_s^2\right)\right] d_s \rho_s \sqrt{\Theta_s} \tag{37}$$

The diffusion coefficient for granular energy, k_{Θ_s} , is expressed by two different models. The Syamlal- O'Brien model expresses as [20, 21]

$$k_{\Theta_s} = \frac{15 d_s \rho_s \alpha_s \sqrt{\pi\Theta_s}}{4(41 - 33\eta)}\left[1 + \frac{12}{5}\eta^2(4\eta - 3)\alpha_s g_{o,ss} + \frac{16}{15\pi}(41 - 33\eta)\eta\alpha_s g_{o,ss}\right] \tag{38}$$

With $\eta = \frac{1}{2}(1 + e_{ss})$

and the Gidaspow model express k_{Θ_s} as [1]

$$k_{\Theta_s} = \frac{150\rho_s d_s \sqrt{\Theta_s \pi}}{384(1 + e_{ss}) g_{o,ss}}\left[1 + \frac{6}{5} g_{o,ss}\alpha_s(1 + e_{ss})\right]^2 + 2\alpha_s^2 \rho_s d_s g_{o,ss}(1 + e_{ss})\left(\frac{\Theta_s}{\pi}\right)^{1/2} \tag{39}$$

The minimum fluidization velocity is calculated from Ergun equation for spherical particles.

$$\frac{1.75}{\alpha_{s,\max}^3}\left(\frac{d_s U_{mf}\rho_g}{\mu_g}\right)^2 + \frac{150(1 - \alpha_{mf})}{\alpha_{s,\max}^3}\left(\frac{d_s U_{mf}\rho_g}{\mu_g}\right) = \frac{d_s^3 \rho_g(\rho_s - \rho_g)g}{\mu_g^2} \tag{40}$$

From equation (32) and parameters of Table.1, the minimum fluidization velocity (U_{mf}) for three particle sizes, 0.175, 0.275 and 0.375 mm, was calculated as 0.042, 0.065 and 0.078 m/s, respectively.

The internal energy balance for the gas phase can be written in terms of the gas temperature as follows:

$$\alpha_g \rho_g Cp_g \left(\frac{\partial T_g}{\partial t} + v_g . \nabla T_g \right) = -H_{gs} \tag{41}$$

The solid heat conductivity includes direct conduction through the fractional contact area and indirect conduction through a wedge of the gas that is trapped between the particles. Since the gas heat conductivity is negligible, the heat diffusion term has been ignored [11].
The thermal energy balance for the solid phases is given by

$$\alpha_s \rho_s Cp_s \left(\frac{\partial T_s}{\partial t} + v_s . \nabla T_s \right) = \nabla . \alpha_s K_s \nabla T_s + H_{gs} \tag{42}$$

Solid granular conductivity is obtained using the Ahmadi model

$$K_s = 0.1306 \rho_s d_s (1 + {e_{ss}}^2)(\frac{1}{g_{0,ss}} + 4.8\alpha_s + 12.1184 g_{0,ss} \alpha_s^2)\sqrt{\Theta_s} \tag{43}$$

The heat transfer between the gas and the solid is a function of the temperature difference between the gas and solid phases:

$$H_{gs} = -\gamma^0{}_{gs} \left(T_s - T_g \right) \tag{44}$$

The heat transfer coefficient is related to the particle Nusselt number using the following equation:

$$\gamma^0_{gs} = \frac{6 k^{'}{}_g \alpha_s Nu_s}{d_s^2} \tag{45}$$

Here $k^{'}{}_g$ is the thermal conductivity of the gas phase. The Nusselt number is determined applying the following correlation

$$\begin{aligned} Nu_s = &\left(7 - 10\alpha_g + 5\alpha_g^2\right)\left(1 + 0.7\,\mathrm{Re}_s{}^{0.2}\,\mathrm{Pr}^{1/3}\right) + \\ &\left(1.33 - 2.4\alpha_g + 1.2\alpha_g^2\right)\mathrm{Re}_s^{0.7}\,\mathrm{Pr}^{1/3} \end{aligned} \tag{46}$$

2.2 Turbulence model

The standard $k-\varepsilon$ model has become the workhorse of practical engineering flow calculations since it was proposed by Launder and Spalding. Robustness, economy, and reasonable accuracy for a wide range of turbulent flows explain its popularity in industrial flow and heat transfer simulations. The standard $k-\varepsilon$ model is a semi-empirical model based on model transport equations for the turbulence kinetic energy (k) and its dissipation rate (ε). The model transport equation for k is derived from the exact equation, while the model transport equation for ε was obtained using physical reasoning and bears little resemblance to its mathematically exact counterpart [30-34].
The Reynolds stress tensor for the gas phase is

$$\overline{\overline{\tau_g}} = -\frac{2}{3}(\rho_g k_g + \rho_g \mu_{t,g} \nabla . \overrightarrow{v_g}) \overline{\overline{I}} + \rho_g \mu_{t,g} \left[\nabla \overrightarrow{v_s} + (\nabla \overrightarrow{v_s})^T \right] \tag{47}$$

Symbol	Description	Value	Comment or reference
ρ_s	Solids density	1830 kg/m^3	Glass beads
ρ_g	Gas density	1.189 kg/m^3	Air at ambient conditions
d_s	Mean particle diameter	(Geldart B type)	Uniform distribution
e_{ss}	Coefficient of restitution	0.9	Fixed value
$\alpha_{\max}$	Maximum solids packing	0.61	Syamlal et al. [20,21]
φ	Angle of internal friction	25	Johnson and Jackson [33]
V_{mf}	Minimum fluidization velocity	5.5 cm/s	from Ergun [1,2]
D_t	Column diameter	25 cm	Fixed value
H_1	Fluidized bed height	100 cm	Fixed value
H_0	Initial static bed height	30, 40 cm	Specified
	Initial temperature of solids	300 K	Fixed value
	Inlet gas temperature	473 K	Fixed value
V_g	Superficial gas velocity	0- 1000 cm/s	A range was used
	Inlet boundary conditions	Velocity	Superficial gas velocity
	Outlet boundary conditions	Out flow	Fully developed flow
Δt	Time steps	0.001 s	Specified
	Maximum number of iterations	20	Specified
	Convergence criteria	10^{-3}	Specified

Table 1. Values of model parameters used in the simulations and experiments.

The turbulence kinetic energy, k, and its rate of dissipation, ε, are obtained from the following transport equations (modified $k-\varepsilon$ model):

$$\frac{\partial}{\partial t}(\alpha_g \rho_g k_g) + \nabla.(\alpha_g \rho_g \overrightarrow{v_g} k_g) = \nabla.(\alpha_g \frac{\mu_{t,g}}{\sigma_k} \nabla k_g) + \alpha_g G_{k,g} - \alpha_g \rho_g \varepsilon_g + \alpha_g \rho_g \prod_{k,g} \tag{48}$$

$$\begin{aligned} &\frac{\partial}{\partial t}(\alpha_g \rho_g \varepsilon_g) + \nabla.(\alpha_g \rho_g \overrightarrow{v_g} \varepsilon_g) = \nabla.(\alpha_g \frac{\mu_{t,g}}{\sigma_\varepsilon} \nabla \varepsilon_g) + \\ &\alpha_g \frac{\varepsilon_g}{k_g}(C_{1\varepsilon} C_{k,g} - C_{2\varepsilon} \rho_g \varepsilon_g) + \alpha_g \rho_g \prod_{\varepsilon,g} \end{aligned} \tag{49}$$

$\prod_{k,g}$ and $\prod_{\varepsilon,g}$ represent the influence of the dispersed phase on the continuous phase. Predictions of the turbulence quantities of the dispersed phase are obtained using the Tchen theory [7] of dispersion of discrete particles by homogeneous turbulence. In the transport equation for k, $G_{k,g}$ is the production of turbulence kinetic energy and is defined as

$$G_{k,g} = -\rho_g \overline{u_i' u_j'} \frac{\partial u_j}{\partial x_i} \tag{50}$$

The model constants $C_{1\varepsilon}, C_{2\varepsilon}, C_\mu, \sigma_k$, and σ_k have the values

$C_{1\varepsilon} = 1.44 \quad C_{2\varepsilon} = 1.92 \quad C_\mu = 0.09 \quad \sigma_k = 1.0 \quad \sigma_\varepsilon = 1.3$

For granular energy dissipation and turbulence interaction terms, Ahmadi suggested respectively

$$\varepsilon_s = 12(1-e_{ss}^2)\alpha_s^2 \rho_s g_{o,ss} \frac{\Theta_s^{3/2}}{d_s} \tag{51}$$

$$\Pi_{k,g} = \beta_{sg}(3\Theta_s - 2k_g) \ , \ \Pi_{\varepsilon,g} = 0 \ , \ \Pi_{k,s} = \beta_{sg}\left(\frac{2k_g}{1+\tau_{gs}^x / \tau_g} - 3\Theta_s\right) \tag{52}$$

Also, for gas turbulent viscosity, Ahmadi suggested

$$\mu_g^t = \rho_g C_\mu \left[1+\left(\tau_{sg}^x / \tau_g^t\right)\left(\alpha_s / \alpha_{s,\max}\right)^3\right]^{-1} \frac{k_g^2}{\varepsilon_g} \tag{53}$$

2.3 Initial and boundary conditions

The initial values of the variables for all the fields $(\alpha_g, \alpha_s, v_g, v_s)$ are specified for the entire computational domain. Initially, solid particle velocity was set at zero (in minimum fluidization), and gas velocity was assumed to have the same value everywhere in the bed. At the inlet, all velocities and volume fraction of all phases were specified. Outlet boundary condition was out flow and was assumed to be a fully developed flow. The other variables were subject to the Newmann boundary condition. The gas tangential normal velocities on the wall were set to zero (no slip condition). The normal velocity of the particles was also set at zero. The following boundary condition was applied for the tangential velocity of particles at the wall [28-35]

$$\vec{v}_{s,w} = -\frac{6\mu_s \alpha_{s,\max}}{\sqrt{3}\pi\rho_s \alpha_s g_{o,ss}\sqrt{\Theta_s}} \frac{\partial \vec{v}_{s,w}}{\partial n}. \tag{54}$$

The general boundary condition for granular temperature at the wall takes the form

$$\Theta_{s,w} = -\frac{k_s \Theta_s}{e_{ss,w}} \frac{\partial \Theta_{s,w}}{\partial n} + \frac{\sqrt{3}\pi\rho_s \alpha_s v_s^2 g_o \Theta_s^{3/2}}{6\alpha_{s,\max} e_{ss,w}} \tag{55}$$

Here $\vec{v}_{s,w}$ is the particle slip velocity, $e_{ss,w}$ is the restitution coefficient at the wall, and $\alpha_{s,\max}$ is the volume fraction for the particles at maximum packing. The boundary conditions for the energy equation are set such that the walls are adiabatic. Initial solid particles temperature is 300K and the inlet gas temperature is 473K.

3. Model solution procedure

Two-dimensional (2D) simulations of the fluidized bed with heat transfer under steady conditions were performed and the results are described in this section. The Eulerian multiphase model described earlier was used for the analysis. The 2D computational domain was discretized using 8600 rectangular cells. Typically, a time step of 0.001s with 20

iterations per time step was also used. This number of iterations was found to be adequate to achieve convergence for the majority of time steps. Table 1 shows values of model parameters that were used in the simulations.

The discretized governing equations were solved by the finite volume method employing the Semi Implicit Method for the Pressure Linked Equations (SIMPLE) algorithm that was developed by Patankar and Spalding for multiphase flow using the Partial Elimination Algorithm (PEA). Several research groups have used extensions of the SIMPLE method, which appears to be the method of choice in commercial CFD codes. Two modifications of the standard extensions of SIMPLE have been introduced in the present simulations to improve the stability and speed of computations. i) A solid volume fraction correction equation (instead of a solid pressure correction equation) was used. This appears to help the convergence when the solids are loosely packed. That equation also incorporates the effect of solid pressure that helps to stabilize the calculations in densely packed regions. ii) The automatic time-step adjustment was used to ensure that the run progresses with the highest execution speed. In this paper an approximate calculation of the normal velocity at the interfaces (defined by a small threshold value for the phase volume fraction) was used. Gas-solid flows are inherently unstable. For vast majority of gas-solid flows, a transient simulation analysis was conducted and the results were time-averaged. Transient simulations diverge if a large time-step is used. Using a very small time step makes the computations very slow. Therefore, the time step was automatically adjusted to reduce the computational time [39, 40].

The first order upwind scheme was used for discretization of the governing equations. The computational domain was divided into a finite number of control volumes. Volume fraction, density and turbulent kinetic energy were stored at the main grid points that were placed in the center of each control volume. A staggered grid arrangement was used, and the velocity components were solved at the control volume surfaces. The conservation equations were integrated in the space and time. The sets of resulting algebraic equations were solved iteratively [38-43].

The following steps were followed in the simulations:

1. Initially the physical properties and exchange coefficients are calculated.
2. Velocity fields based on the current pressure field and the corresponding u_m^*, v_m^* (m = 0, 1 for solid and gas phases) are evaluated.
3. The fluid pressure correction P_g' is calculated.
4. The fluid pressure field is updated applying an under-relaxation, $P_g = P_g^* + \omega_{sg} P_g'$.
5. The fluid velocity corrections from P_g' are evaluated, and the fluid velocity fields are updated using, $u_m = u_m^* + u_m'$.
   (Similarly the solid phase velocities u_s as denoted in step 9 are updated).
6. The pressure gradients, $\frac{\partial P_m}{\partial \alpha_m}$, are evaluated for use in the solid volume fraction correction equation.
7. The solid volume fraction correction α_m' is evaluated.
8. The solid volume fraction is updated. That is, $\alpha_m' = \alpha_m^* + \omega_{gs} \alpha_m'$.
9. The velocity corrections for the solid phase are estimated and the solid velocity fields are updated. That is, $u_s = u_s^* + u_s'$.

10. The solid pressure is evaluated.
11. The temperatures and the turbulence property are evaluated.

The normalized residuals calculated in Steps 2, 3, 5, and 9 are used to check for convergence [37, 39, 40, 41]. If the convergence criterion is not satisfied, then the iterations starting with Step 2 are repeated. The flowchart of the simulation algorithm for one time step is shown in Fig. 3.

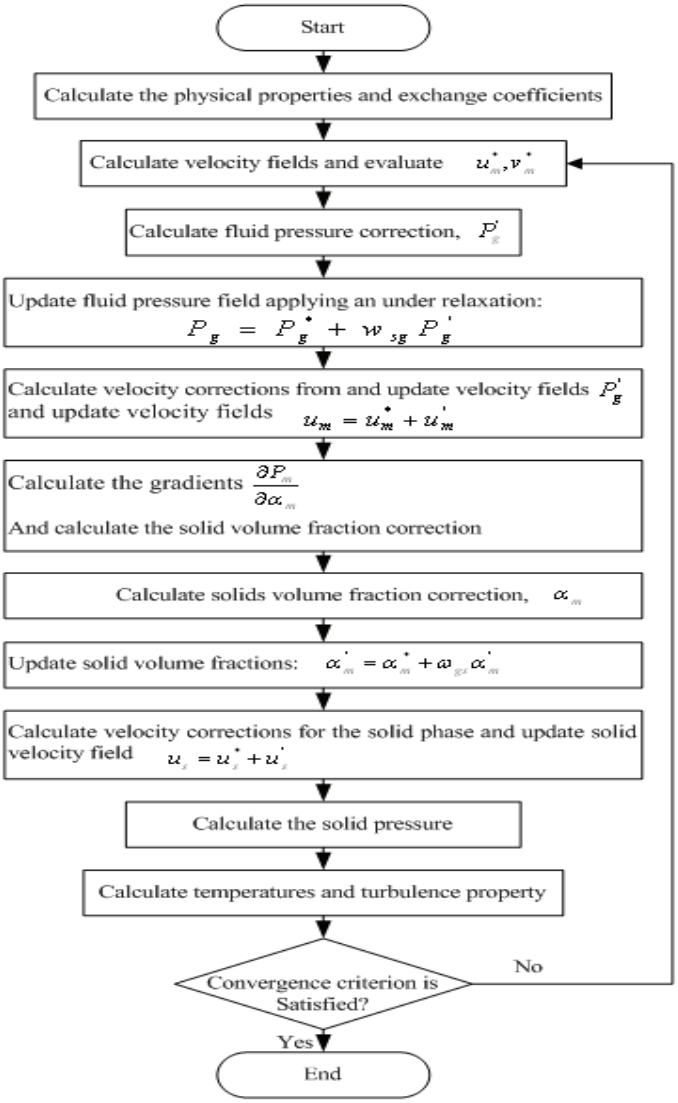

Fig. 3. Flowchart of the simulation procedure for one time step.

Sensitivity analysis of the effect of the time step, discretization schemes, and convergence criterion on the results was also studied. The simulated results for the solid volume fraction profile from the first-order discretization schemes for a time step of 0.001s with 10^{-3} convergence criterion (the typical numerical procedure for this study) were compared with those of first and second-order discretization schemes, for a time step of 0.0005s, and 10^{-4} convergence criterion with 50 iterations at each time step. (These high quality numerical procedures require additional computational time.) The simulation results show no noticeable difference in overall hydrodynamic behavior, temperature distribution and bubble shapes among these simulations; therefore, it is concluded that the selected numerical parameters are adequate for proper simulations of bed hydrodynamic with heat transfer.

4. Experimental setup

A bench scale experimental setup for studying gas-solid flows and heat transfer was designed and fabricated. The setup consists of a Pyrex cylinder with a height of 100cm and a diameter of 25 cm as shown schematically in Fig. 4. The air was injected through a

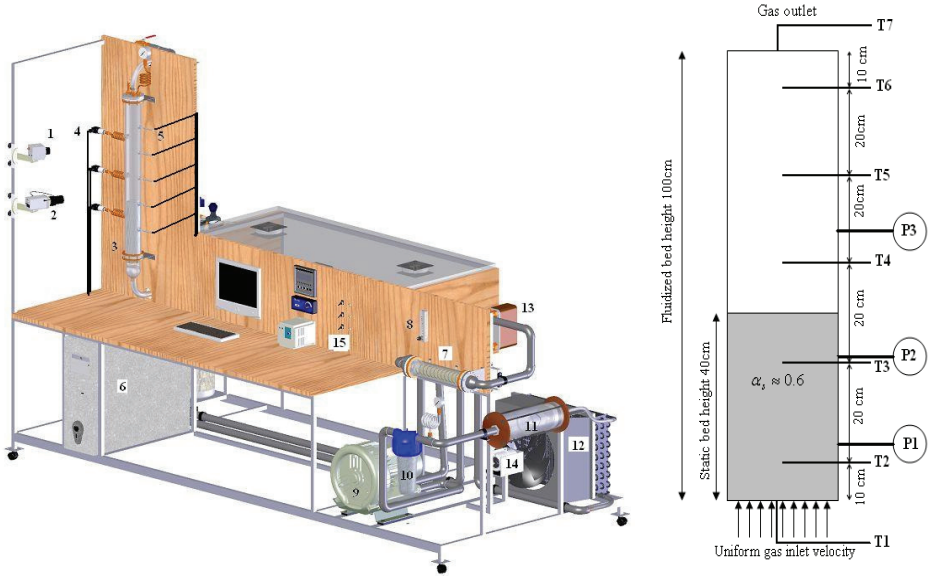

(A) (B)

Fig. 4. (A): A view of experimental set-up (1- digital camera, 2- digital video recorder, 3- Pyrex reactor, 4- pressure transducers, 5-thermocouples, 6- computer , A/D and DVR cards, 7- electrical heater, 8-rotameter, 9-blower, 10- filter, 11-14- cooling system, 15- controller system), (B) : pressure transducer and thermocouple positions in the fluidized bed reactor

perforated plate with an open area of 0.8 % and an orifice diameter of 2 cm. Under this plate there was a homogenization system to prevent the gas flow from generating asymmetrical effects inside the free board. This distribution belongs to group B in the Geldart

classification. Spherical particles with different diameter and a density of 1830 kg/m^3 were fluidized with air at ambient conditions. Typically, the static bed height was 30 and 40cm with a solid volume fraction of 0.6. A roots-type blower supplied the fluidizing gas. A pressure-reducing valve was installed to avoid pressure oscillations and achieve a steady gas flow. The airflow rate was measured using a gas flow meter (rotameter) placed between the blower and the inlet pipe to an electrical heater. Initial solid particle temperature was 300K. An electrical heater was used to increase the inlet gas temperature from ambient temperature to 473K. A cooling system was used to decrease the gas temperature that exited from the reactor in order to form a closed cycle. Fig. 4 (A) shows a schematic of experimental set-up and its equipments.

Pressure fluctuations in the bed were measured by three pressure transducers. The pressure transducers were installed in the fluidized bed column at different heights. Seven thermocouples (Type J) were installed in the center of the reactor to measure the variation of gas temperature at different locations. Also, three thermocouples were used in different positions in the set-up to control the gas temperature in the heat exchanger and cooling system. Fig. 4. (B) shows the locations of the pressure transducers and thermocouples. The pressure probes were used to convert fluctuation pressure signals to out-put voltage values proportional to the pressure. The output signal was amplified, digitized, and further processed on-line using a Dynamic Signal Analyzer. Analog signals from the pressure transducers were band pass filtered (0–25 Hz) to remove dc bias, prevent aliasing, and to remove 50 Hz noise associated with nearby ac equipment. The ratio of the distributor pressure drop to the bed pressure drop exceeded 11% for all operating conditions investigated. The overall pressure drop and bed expansion were monitored at different superficial gas velocities from 0 to 1 m/s.

For controlling and monitoring the fluidized bed operation process, A/D, DVR cards and other electronic controllers were applied. A video camera (25 frames per s) and a digital camera (Canon 5000) were used to photograph the flow regimes and bubble formation through the transparent wall (external photographs) during the experiments. The captured images were analyzed using image processing software. The viewing area was adjusted for each operating condition to observe the flow pattern in vertical cross sections (notably the bed height oscillations). Image processing was carried out on a power PC computer equipped with a CA image board and modular system software. Using this system, each image had a resolution of 340×270 pixels and 256 levels of gray scales. After a series of preprocessing procedures (e.g., filtering, smoothing, and digitization), the shape of the bed, voidage, and gas volume fraction were identified. Also, the binary system adjusted the pixels under the bed surface to 1 and those above the bed surface to 0. The area below the bed surface was thus calculated, and then divided by the side width of the column to determine the height of the bed and the mean gas and solid volume fraction.

Some of experiments were conducted in a Plexiyglas cylinder with 40cm height and 12 cm diameter (Fig. 5). At the lower end of this is a distribution chamber and air distributor which supports the bed when defluidized. This distributor has been designed to ensure uniform air flow into the bed without causing excessive pressure drop and is suitable for the granular material supplied. A Roots-type blower supplied the fluidizing gas. A pressure-reducing valve was installed to avoid pressure oscillations and to achieve a steady gas flow. Upon leaving the bed, the air passes through the chamber and escapes to the atmosphere through a filter. Installed in the bracket are probes for temperature and pressure

measurement, and a horizontal cylindrical heating element, all of which may move vertically to any level in the bed chamber.

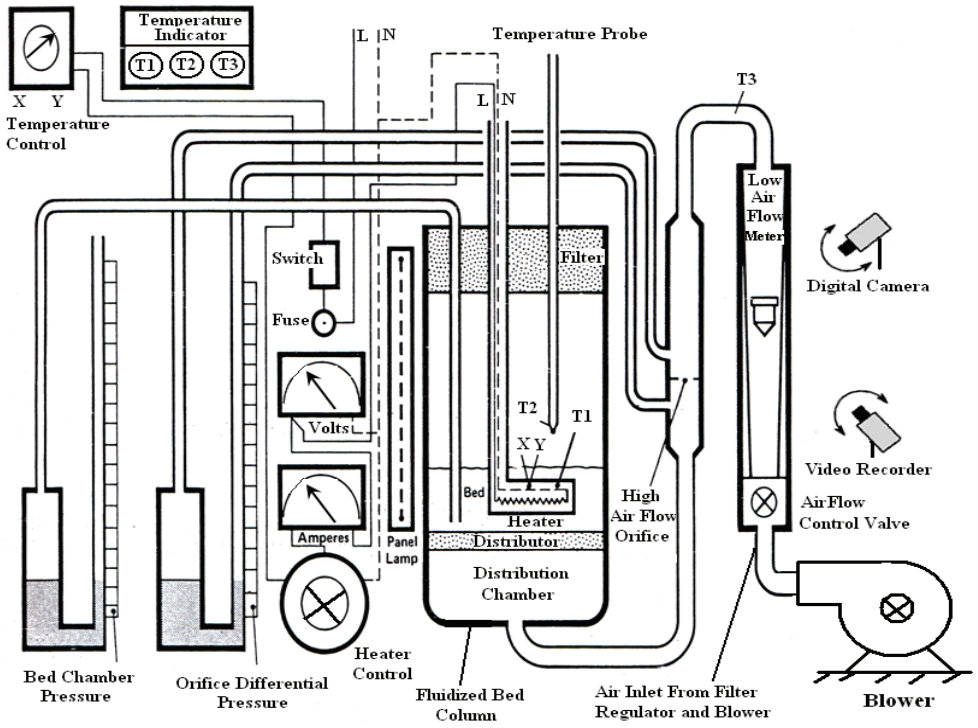

Fig. 5. A view of experimental set-up with its equipments.

Air is delivered through a filter, pressure regulator and an air flow meter fitted with a control valve and an orifice plate (to measure higher flow rates), to the distribution chamber. The heat transfer rate from the heating element is controlled by a variable transformer, and the voltage and current taken are displayed on the panel. Two thermocouples are embedded in the surface of the element. One of these indicates the surface temperature and the other, in conjunction with a controller, prevents the element temperature exceeding a set value. A digital temperature indicator with a selector displays the temperatures of the element, the air supply to the distributor, and the moveable probe in the bed chamber. Two liquid filled manometers are fitted. One displays the pressure of the air at any level in the bed chamber, and the other displays the orifice differential pressure, from which the higher air flow rates can be determined. Pressure fluctuations in the bed are obtained by two pressure transducers that are installed at the lower and upper level of the column. The electrical heater increases the solid particle temperature, so, initial solid particles temperature was 340K and for inlet air was 300K (atmospheric condition). The ratio of the distributor pressure drop to the bed pressure drop exceeded 14% for all operating conditions investigated.

5. Results and discussion

Simulation results were compared with the experimental data in order to validate the model. Pressure drop, Δp, bed expansion ratio, H/H_0, and voidage were measured experimentally for different superficial gas velocities; and the results were compared with those predicted by the CFD simulations. Fig. 6 compares the predicted bed pressure drop using different drag laws with the experimentally measured values.

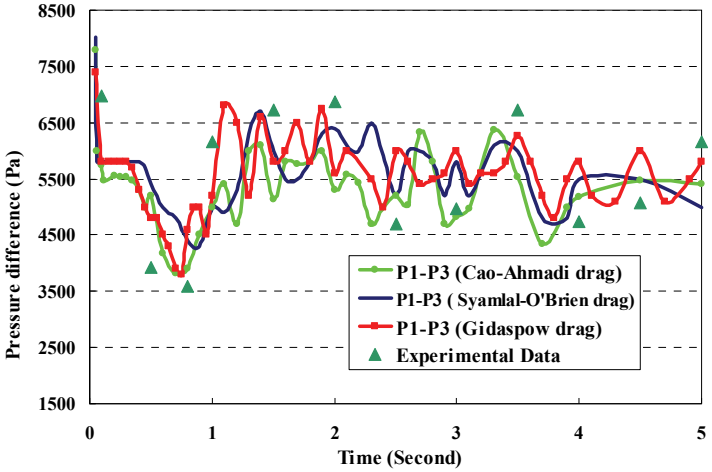

Fig. 6. Comparison of simulated bed pressure drop using different drag models with the experimental data for a superficial velocity of V_g = 50 cm/s.

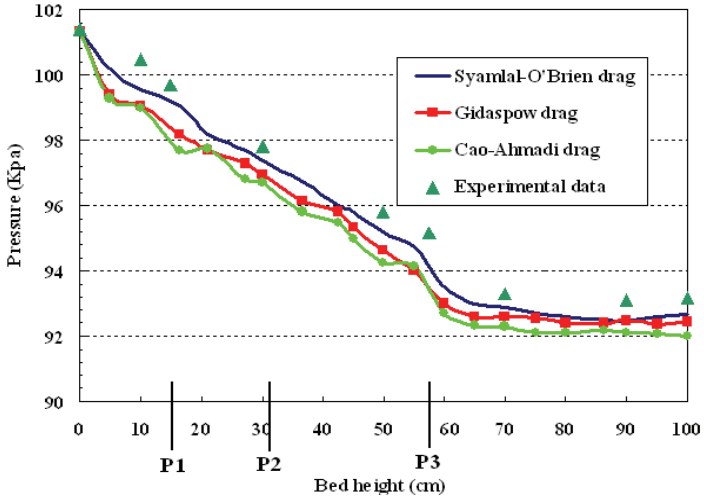

Fig. 7. Comparison of simulated pressure variation versus bed height using Cao-Ahmadi, Syamlal–O'Brien and Gidaspow drag models with the experimental data for a superficial velocity of V_g = 50 cm/s and position of pressure transducers (P1, P2 and P3).

Fig. 7 compares the simulated pressure variations versus the bed height for different drag laws with the experimentally measured values. The positions of pressure transducers (P1, P2 and P3) that were shown in Fig. 4(B) are identified in this Fig. To increase the number of experimental data for the pressure in the bed, five additional pressure transducers were installed at the thermocouple locations, and the corresponding pressures for a superficial velocity of V_g = 50 cm/s were measured. The air enters into the bed at atmospheric pressure and decreases roughly linearly from bottom up to a height of about 60 cm due to the presence of a high concentration of particles. At the bottom of the bed, the solid volume fraction (bed density) is large; therefore, the rate of pressure drop is larger. Beyond the height of 60cm (up to 100cm), there are essentially no solid particles, and the pressure is roughly constant. All three drag models considered show comparable decreasing pressure trends in the column. The predictions of these models are also in good agreement with the experimental measurements. Fig.s 6 and 7 indicate that there is no significant difference between the predicted pressure drops for different drag models for a superficial gas velocity of V_g = 50 cm/s.

Figs. 6 and 7 show that there is no significant difference between the predicted pressure drops and bed expansion ratio for the different drag models used. That is the fluidization behavior of relatively large Geldart B particles for the bed under study is reasonably well predicted, and all three drag models are suitable for predicting the hydrodynamics of gas–solid flows.

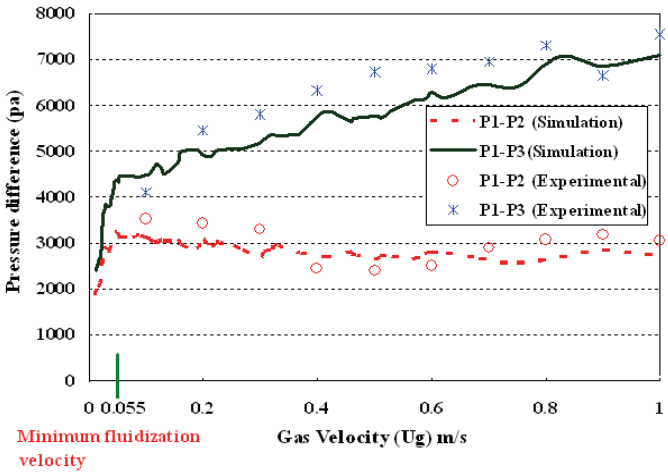

Fig. 8. Comparison of experimental and simulated bed pressure drop versus superficial gas velocity.

Fig. 8 compares the simulated time-averaged bed pressure drops, (P1-P2) and (P1-P3), against the superficial gas velocity with the experimental data. The Syamlal–O'Brien drag expression was used in these simulations. The locations of pressure transducers (P1, P2, P3) were shown in Fig. 4 (B). The simulation and experimental results show good agreement at velocities above $V_{mf.}$. For $V < V_{mf,}$ the solid is not fluidized, and the bed dynamic is dominated by inter-particle frictional forces, which is not considered by the multi-fluid models used. Fig. 8 shows that with increasing gas velocity, initially the pressure drops

(P1-P2 and P1-P3) increase, but the rate of increase for (P1-P3) is larger than that for (P1-P2). For $V > V_{mf}$ this Fig. shows that (P1-P3) increases with gas velocity, while (P1-P2) decreases slightly, stays roughly constant, and increases slightly. This trend is perhaps due to the expansion of the bed and the decrease in the amount of solids between ports 1 and 2. As the gas velocity increases further, the wall shear stress increases and the pressure drop begins to increase. Ports 1 and 3 cover the entire height of the dense bed in the column, and thus (P1-P3) increases with gas velocity.

As indicated in Fig. 9, the bed overall pressure drop decreased significantly at the beginning of fluidization and then fluctuated around a near steady-state value after about 3.5 s. Pressure drop fluctuations are expected as bubbles continuously split and coalesce in a transient manner in the fluidized bed. The results show with increasing the particles size, pressure drop increase. Comparison of the model predictions, using the Syamlal–O'Brien drag functions, and experimental measurements on pressure drop show good agreement for most operating conditions. These results (for d_s=0.275 mm) are the same with Tagipour et al. [8] and Behjat et al. [11] results.

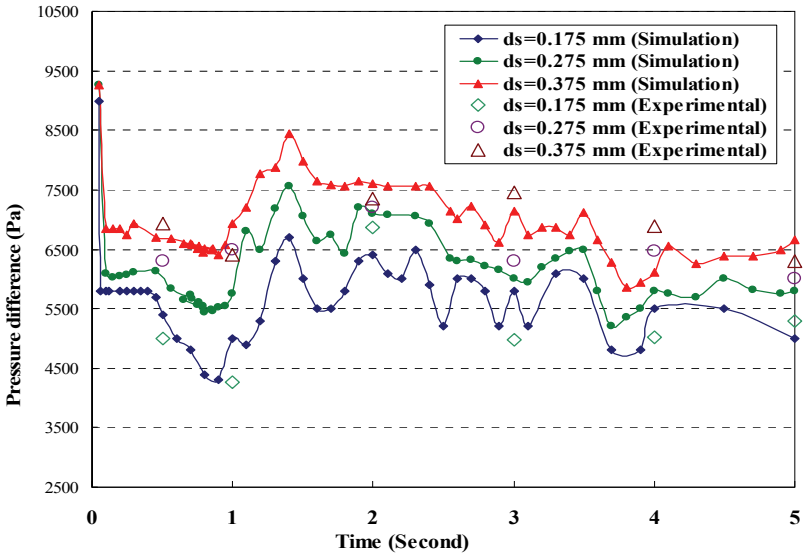

Fig. 9. Comparison of experimental and simulation bed pressure drop (P1-P2) at different solid particle sizes.

Comparison of experimental and simulated bed pressure drop (Pressure difference between two positions, P1-P2 and P1-P3) for two different particle sizes, d_s=0.175 mm and d_s=0.375 mm, at different superficial gas velocity are shown in Fig. 10. and Fig. 11. Pressure transducers positions (P1, P2, P3) also were shown in Fig. 4(B). The simulation and experimental results show better agreement at velocities above U_{mf}. The discrepancy for $U < U_{mf}$ may be attributed to the solids not being fluidized, thus being dominated by inter particle frictional forces, which are not predicted by the multi fluid model for simulating gas-solid phases.

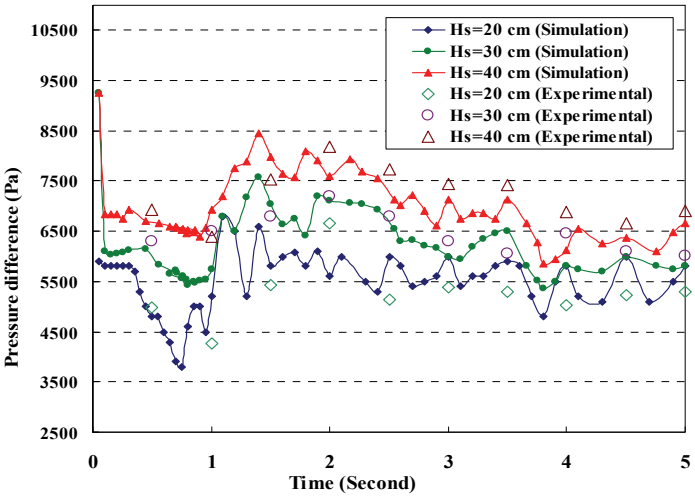

Fig. 10. Comparison of experimental and simulated bed pressure drop at different time

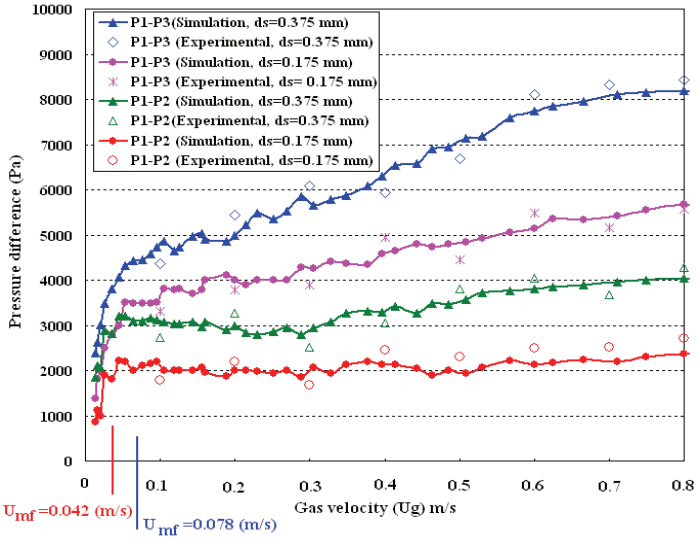

Fig. 11. Comparison of experimental and simulated bed pressure drop at different gas velocity and particle sizes.

Comparison of experimental and simulated bed pressure drop for two different initial bed height, H_s=30, H_s=40 cm, at different superficial gas velocity are shown in Fig. 11. The results show with increasing the initial static bed height and gas velocity, pressure drop (P1-P2 and P1-P3) increase but the rate of increasing for (P1-P3) is larger than (P1-P2). Comparison of the model predictions and experimental measurements on pressure drop (for both cases) show good agreement at different gas velocity.

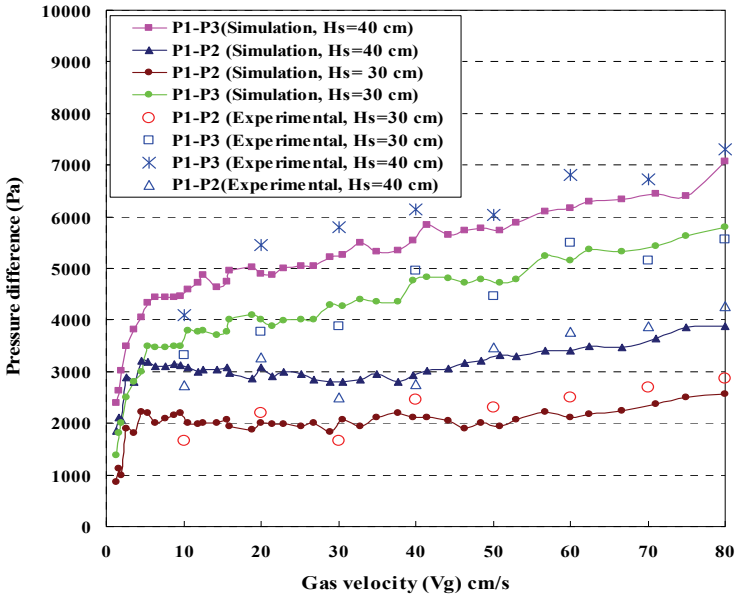

Fig. 12. Comparison of experimental and simulated bed pressure drop at different superficial gas velocity and static bed height.

These Figs. show that with increasing gas velocity, initially the pressure drops (P1-P2 and P1-P3) increase, but the rate of increase for (P1-P3) is larger than for (P1-P2). As indicated in Fig. 12. the bed overall pressure drop decreased significantly at the beginning of fluidization and then fluctuated around a near steady-state value after about 4 s. Pressure drop fluctuations are expected as bubbles continuously split and coalesce in a transient manner in the fluidized bed.

The results show with increasing the initial static bed height, pressure drop increase because of increasing the amount of particle, interaction between particle-particle and gas-particle. The results show with increasing the particle size, gas velocity and initial static bed height pressure drop (P1-P2 and P1-P3) increases. Comparison of the model predictions and experimental measurements on pressure drop (for both cases) show good agreement at different gas velocity.

The experimental data for time-averaged bed expansions as a function of superficial velocities are compared in Fig. 13 with the corresponding values predicted by the models using the Syamlal–O'Brien, Gidaspow and Cao-Ahmadi drag expressions. This Fig. shows that the models predict the correct increasing trend of the bed height with the increase of superficial gas velocity. There are, however, some deviations and the models slightly underpredict the experimental values. The amount of error for the bed expansion ratio for the Syamlal-O'Brien, the Gidaspow and Cao-Ahmadi models are, respectively, 6.7%, 8.7% and 8.8%. This Fig. suggests that the Syamlal–O'Brien drag function gives a somewhat better prediction when compared with the Gidaspow and Cao-Ahmadi models. In addition, the Syamlal–O'Brien drag law is able to more accurately predict the minimum fluidization velocity.

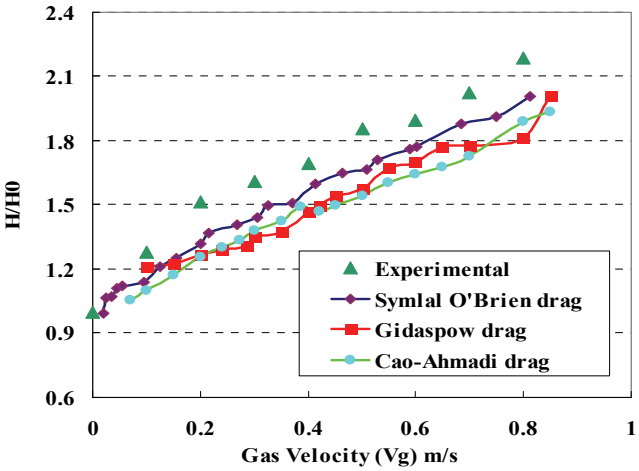

Fig. 13. Comparison of experimental and simulated bed expansion ratio.

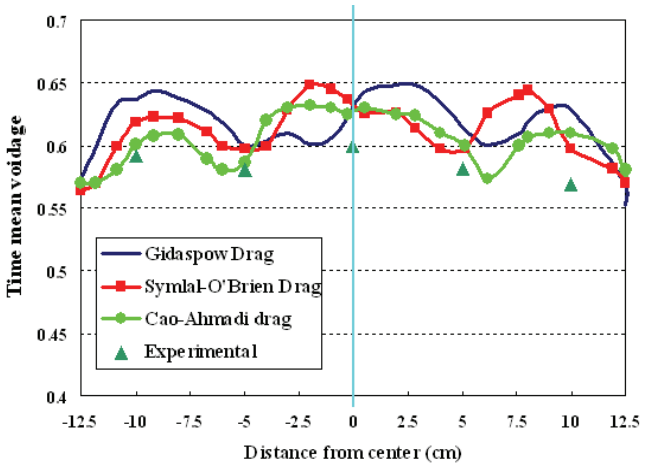

Fig. 14. Experimental and simulated time-averaged local voidage profiles at z=30 cm, Vg=50 cm/s.

The experimental data for the time-averaged voidage profile at a height of 30 cm is compared with the simulation results for the three different drag models in Fig. 14 for V_g=50 cm/s. This Fig. shows the profiles of time-averaged voidages for a time interval of 5 to 10 s. In this time duration, the majority of the bubbles move roughly in the bed mid-section toward the bed surface. This Fig. shows that the void fraction profile is roughly uniform in the core of the bed with a slight decrease near the walls. The fluctuation pattern in the void fraction profile is perhaps due to the development of the gas bubble flow pattern in the bed. Similar trends have been observed in the earlier CFD models of fluidized beds [8, 11]. The gas volume fraction average error between CFD simulations and the experimental data for the drag models of Gidaspow, Syamlal–O'Brien and Cao-Ahmadi are, respectively, about

12.7%, 7.6% and 7.2%. This observation is comparable to those of the earlier works [8, 11]. It can be seen that Cao- Ahmadi drag expression leads to a better prediction compared with those of Syamlal–O'Brien and Gidaspow drag models for the time averaged voidage.

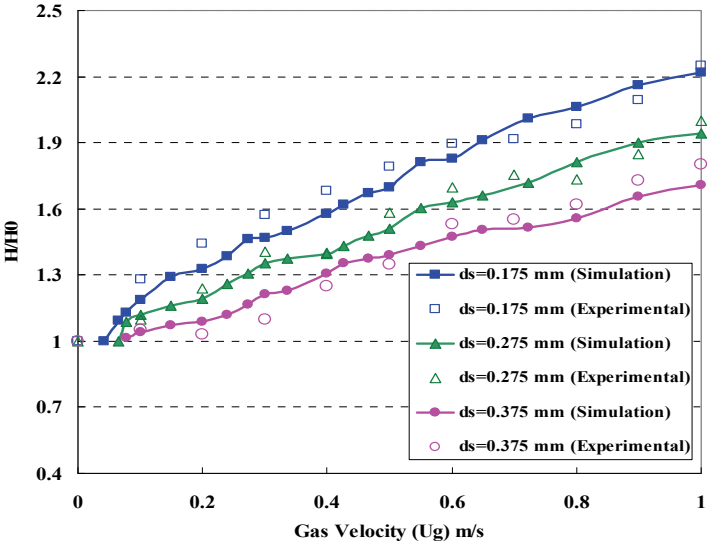

Fig. 15. Comparison of experimental and simulated bed expansion ratio for different solid particle sizes.

Time-averaged bed expansions as a function of superficial velocities are compared in Fig. 15. This Fig. shows that the model predicts the correct increasing trend of the bed height with the increase of superficial gas velocity. All cases demonstrate a consistent increase in bed expansion with gas velocity and predict the bed expansion reasonably well. There are, however, some deviations under predict the experimental values. This Fig. shows that with increasing the particles sizes, bed expansion ratio decreases. On the other hand, for the same gas velocity, bed expansion ratio is lager for smaller particles.

The experimental data of time-average bed expansion ratio were compared with corresponding values predicted for various velocities as depicted in Fig. 16. The time-average bed expansion ratio error between CFD simulation results and the experimental data for two different initial bed height, H_s=30, H_s=40 cm, are 6.7% and 8.7% respectively. Both cases demonstrate a consistent increase in bed expansion with gas velocity and predict the bed expansion reasonably well. It can be seen that Syamlal–O'Brien drag function gives a good prediction in terms of bed expansion and also, Syamlal–O'Brien drag law able to predict the minimum fluidization conditions correctly.

Simulation results for void fraction profile are show in Fig. 17. In this Fig. symmetry of the void fraction is observed at three different particle sizes. The slight asymmetry in the void fraction profile may result form the development of a certain flow pattern in the bed. Similar asymmetry has been observed in other CFD modeling of fluidized beds. Void fraction profile for large particle is flatter near the center of the bed. The simulation results of time-average cross-sectional void fraction at different solid particles diameter is shown in Fig. 18

for U_g=38 cm/s. This Fig. shows with increasing solid particles diameter, void fraction and bed height increase and steady state condition arrive rapidly.

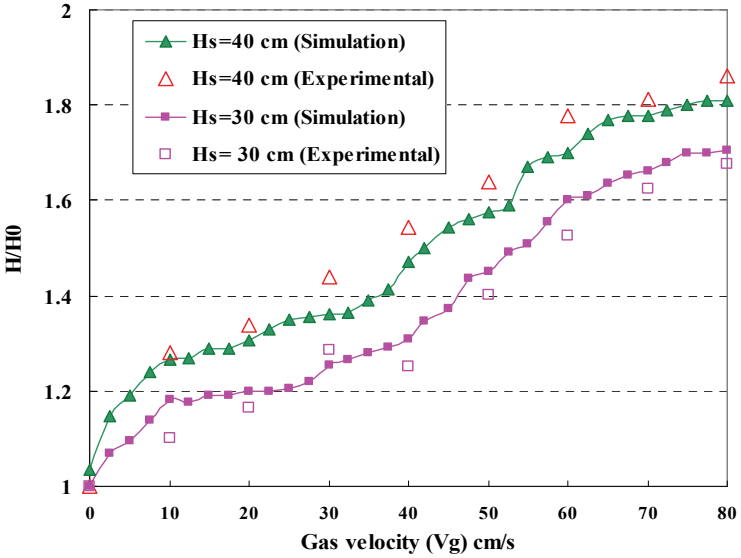

Fig. 16. Comparison of experimental and simulated bed expansion ratio for different initial static bed height.

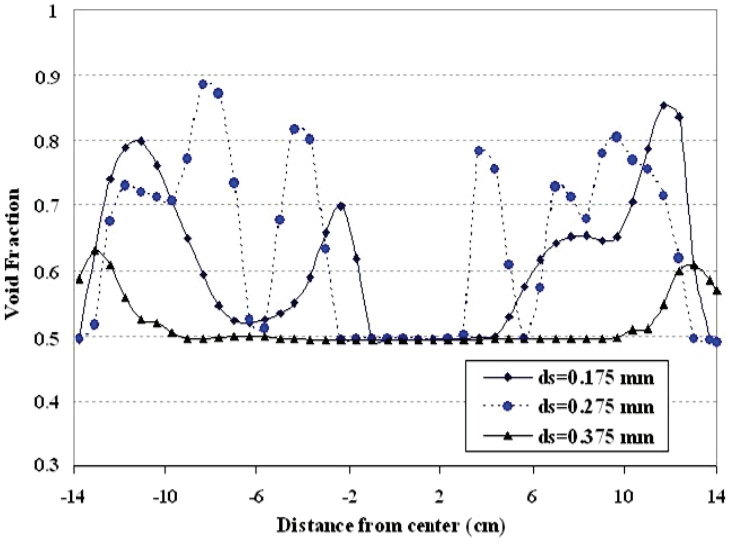

Fig. 17. Simulated void fraction at different solid particles diameter (at z=20 cm, Ug=38 cm/s, t=5.0s)

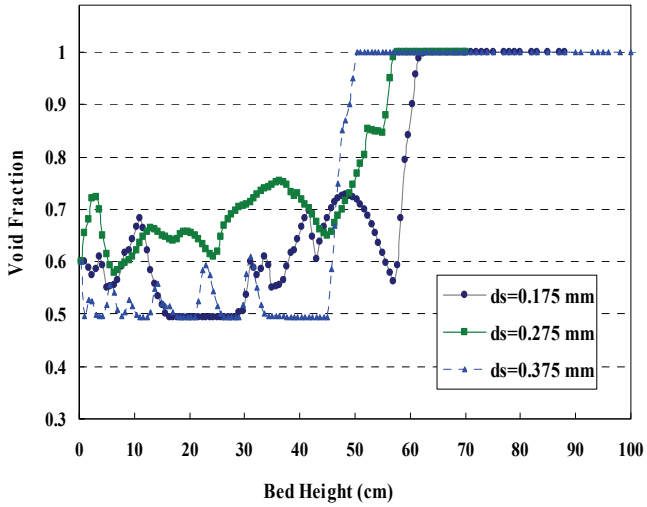

Fig. 18. Simulation results of time-average cross-sectional void fraction at different solid particles diameter (U_g=38cm/s)

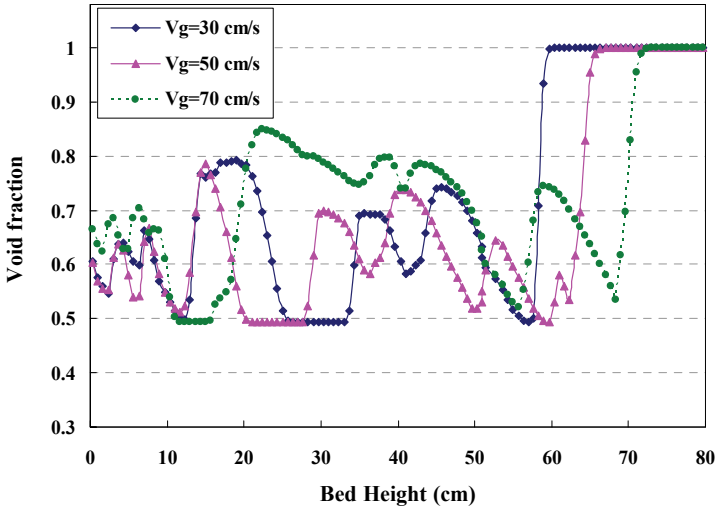

Fig. 19. Simulation results of time-average cross-sectional void fraction at different superficial gas velocity (H_s=40 cm)

Fig. 19 shows the simulation results of time-average cross-sectional void fraction, gas volume fraction, at different superficial gas velocity. This Fig. shows with increasing superficial gas velocity, void fraction also increase and bed arrive to steady state condition rapidly. Also in some position the plot is flat, it is means that particle distribution is uniform. When void fraction increase suddenly in the bed, it is means that the large bubble product in this position and when decrease, the bubble was collapsed.

Fig. 20 shows simulation results for void fraction contour plot, gas volume fraction, for U_g = 38 cm/s, d_s = 0.175 mm. The increase in bed expansion and variation of the fluid-bed voidage can be observed. At the start of the simulation, waves of voidage are created, which travel through the bed and subsequently break to form bubbles as the simulation progresses. Initially, the bed height increased with bubble formation until it leveled off at a steady-state bed height. The observed axisymmetry gave way to chaotic transient generation of bubble formation after 1.5 s. The bubbles coalesce as they move upwards producing bigger bubbles. The bubbles become stretched as a result of bed wall effects and interactions with other bubbles.

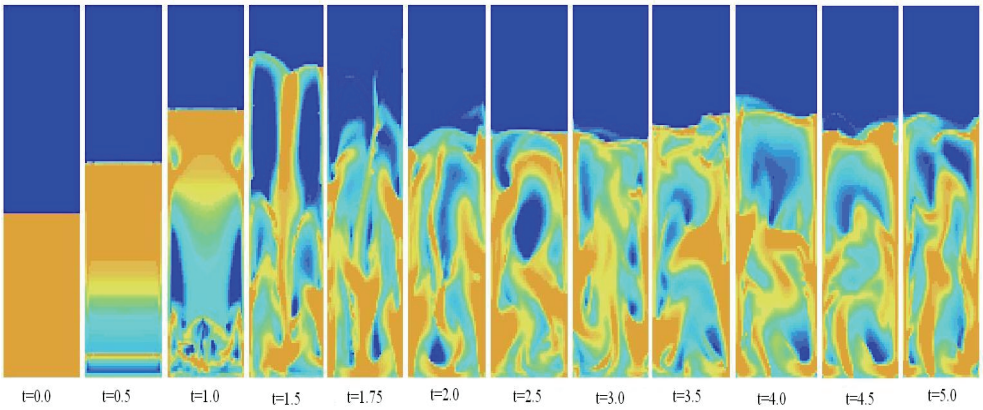

Fig. 20. Simulation void fraction profile of 2D bed (U_g= 38 cm/s, d_s = 0.175 mm)

The contour plots of solids fraction shown in Fig. 21 indicate similarities between the experimental and simulations for three particle sizes and at three different times. The results show that the bubbles at the bottom of the bed are relatively small. The experiments indicated small bubbles near the bottom of the bed; the bubbles grow as they rise to the top surface with coalescence. The elongation of the bubbles is due to wall effects and interaction with other bubbles. Syamlal–O'Brien drag model provided similar qualitative flow patterns. The size of the bubbles predicted by the CFD models are in general similar to those observed experimentally. Any discrepancy could be due to the effect of the gas distributor, which was not considered in the CFD modeling of fluid bed. In practice, jet penetration and hydrodynamics near the distributor are significantly affected by the distributor design.

The increase in bed expansion and the greater variation of the fluid-bed voidage can be observed in Fig. 20 and Fig. 21 for particles with d_s = 0.175 mm. According to experimental evidence, this type of solid particle should exhibit a bubbling behavior as soon as the gas velocity exceeds minimum fluidization conditions.

It is also worth noting that the computed bubbles show regions of voidage distribution at the bubble edge, as experimentally observed. In Fig. 21 symmetry of the void fraction is observed at three different particle sizes. The slight asymmetry in the void fraction profile may result form the development of a certain flow pattern in the bed. Similar asymmetry has been observed in other CFD modeling of fluidized beds [5, 8]. Void fraction profile for large particle is flatter near the center of the bed.

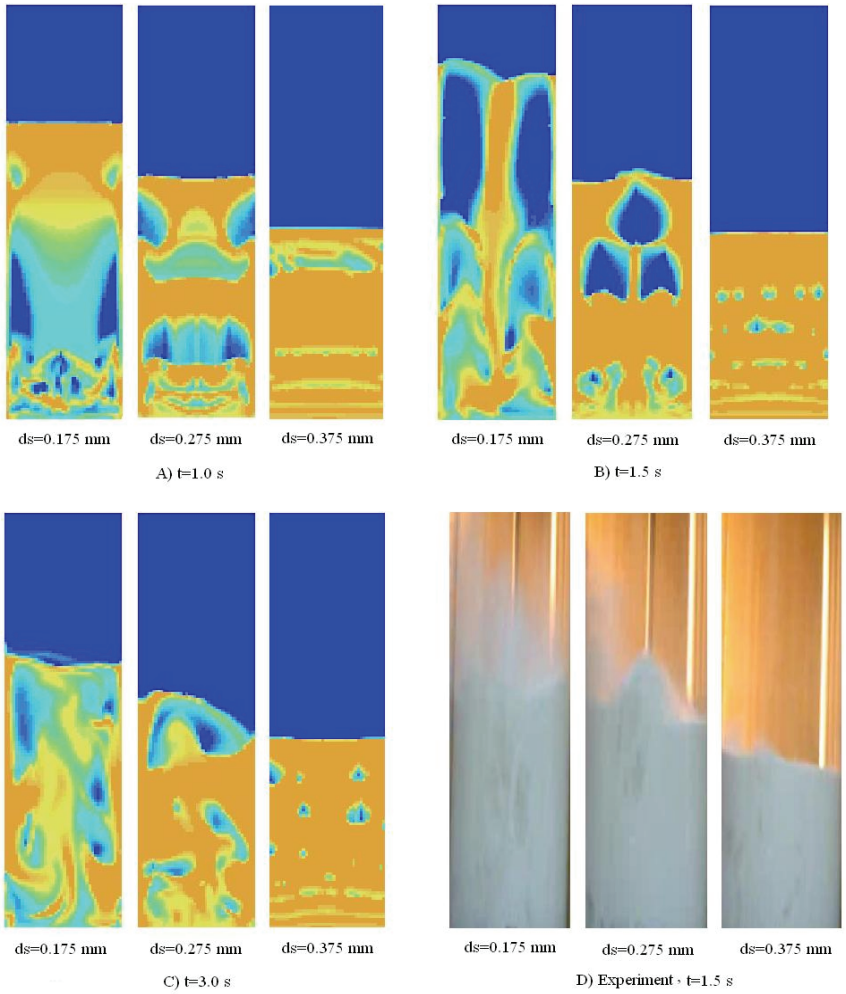

Fig. 21. Comparison of experiment and simulated void fraction and bobbles for three particle sizes and three different times

Fig. 22 shows simulated results for contour plot of solids volume fraction (U_g =38 cm/s, d_s=0.275 mm). Initially, the bed height increased with bubble formation until it leveled off at a steady-state bed height. The observed axisymmetry gave way to chaotic transient generation of bubble formation after 3 s. The results show that the bubbles at the bottom of the bed are relatively small. The bubbles coalesce as they move upwards producing bigger bubbles. The bubbles become stretched as a result of bed wall effects and interactions with other bubbles. Syamlal–O'Brien drag model provided similar qualitative flow patterns. The size of the bubbles predicted by the CFD models are in general similar to those observed experimentally. Any discrepancy could be due to the effect of the gas distributor, which was not considered in the CFD modeling of fluid bed. In practice, jet penetration and hydrodynamics near the distributor are significantly affected by the distributor design.

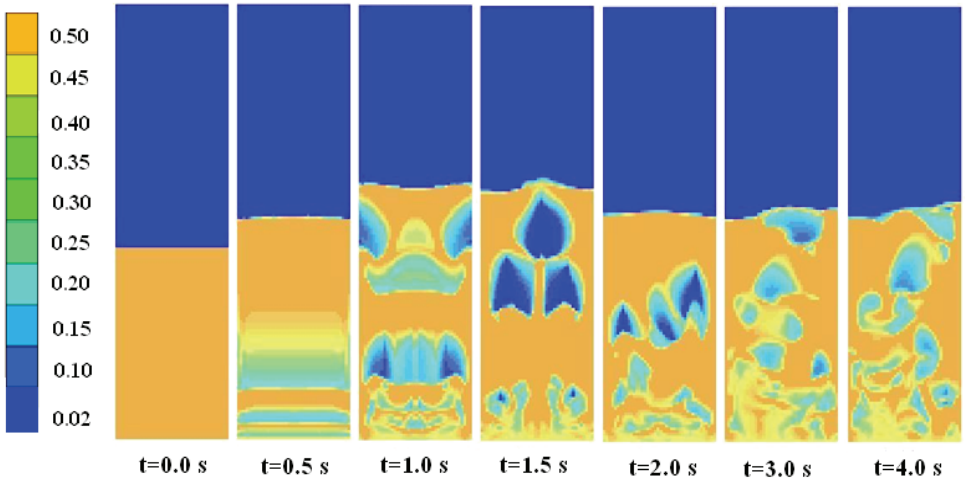

Fig. 22. Simulated solids volume fraction profile of 2D bed *(Ug*=38 cm/s, d_s=0.275 mm).

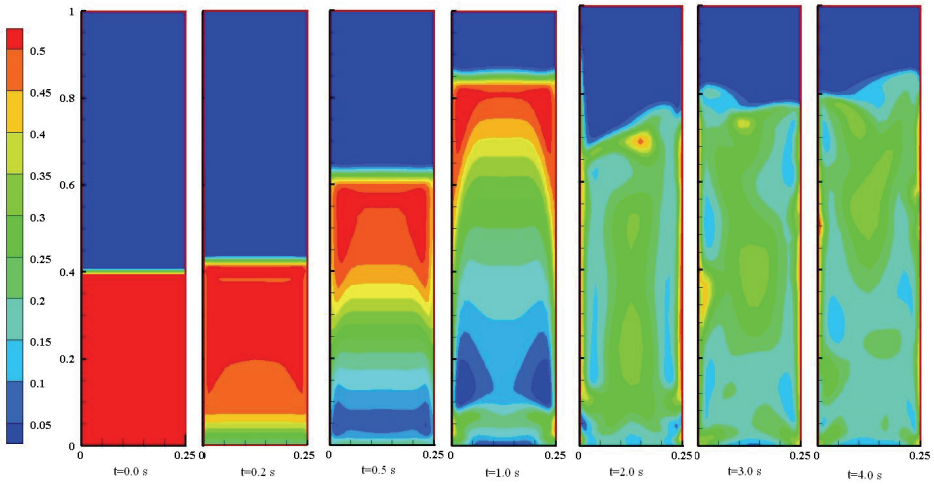

Fig. 23. Simulated solid volume fraction contours in the 2D bed *(Vg* =50 cm/s, drag function: Syamlal–O'Brien).

Simulation results for solid particle velocity vector fields at different times are shown in Fig. 24. This Fig. shows that initially the particles move vertically; at t= 0.7 s, two bubbles are formed in the bed that are moved to the upper part of the column. The bubbles collapse when they reach the top of the column, and solid particle velocity vector directions are changed as the particles move downward. The upward and downward movement of particles in the bed leads to strong mixing of the phases, which is the main reason for the effectiveness of the fluidized bed reactors.

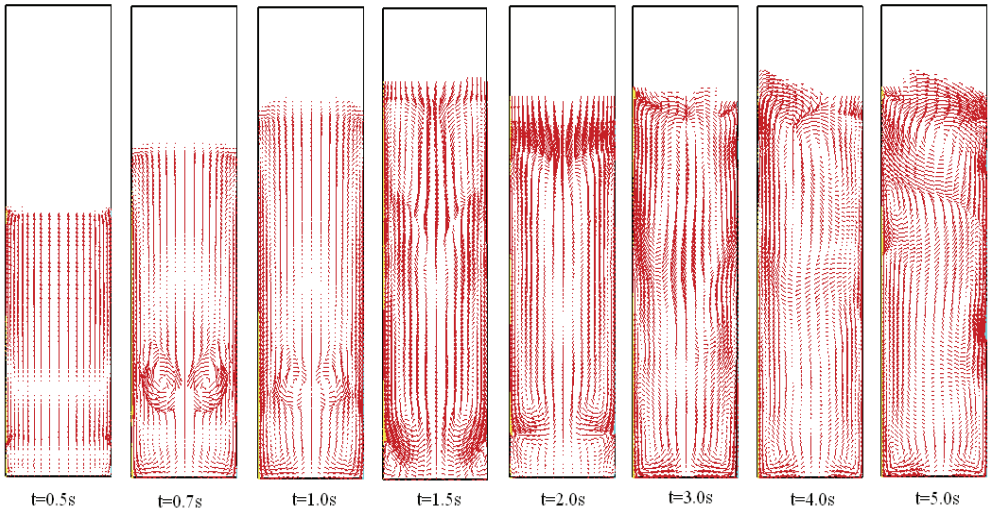

Fig. 24. Simulated solid particle velocity vector fields for different times, Vg=50 cm/s.

Fig. 25 compares the experimental results for bubble formation and bed expansion for different superficial gas velocities. At low gas velocities (lower than Vg=5.5 cm/s), the solids rest on the gas distributor, and the column is in the fixed bed regime. When superficial gas velocity reaches the fluidization velocity of 5.5 cm/s, all particles are entrained by the upward gas flow and the bed is fluidized. At this point, the gas drag force on the particles counterbalances the weight of the particles. When the gas velocity increases beyond the minimum fluidization velocity, a homogeneous (or smooth) fluidization regime forms in the bed. Beyond a gas velocity of 7 cm/s, a bubbling regime starts. With an increase in velocity beyond the minimum bubbling velocity, instabilities with bubbling and channeling of gas in the bed are observed. Vg=10 cm/s in Fig. 25 corresponds to this regime. At high gas velocities, the movement of solids becomes more vigorous. Such a bed condition is called a bubbling bed or heterogeneous fluidized bed, which corresponds to Vg=20-35 cm/s in Fig. 25. In this regime, gas bubbles generated at the distributor coalesce and grow as they rise through the bed. With further increase in the gas velocity (Vg=40-50 cm/s in Fig. 25), the intensity of bubble formation and collapse increases sharply. This in turn leads to an increase in the pressure drop as shown in Fig.s 8-11. At higher superficial gas velocities, groups of small bubbles break free from the distributor plate and coalesce, giving rise to small pockets of air. These air pockets travel upward through the particles and burst out at the free surface of the bed, creating the appearance of a boiling bed. As the gas bubbles rise, these pockets of gas interact and coalesce, so that the average gas bubble size increases with distance from the distributor. This bubbling regime for the type of powder studied occurs only over a narrow range of gas velocity values. These gas bubbles eventually become large enough to spread across the vessel. When this happens, the bed is said to be in the slugging regime. Vg=60 cm/s in Fig. 25 corresponds to the slugging regime. With further increase in the gas superficial velocity, the turbulent motion of solid clusters and gas bubbles of various size and shape are observed. This bed is then considered to be in a turbulent fluidization regime, which corresponds to Vg=70-100 cm/s in Fig. 25.

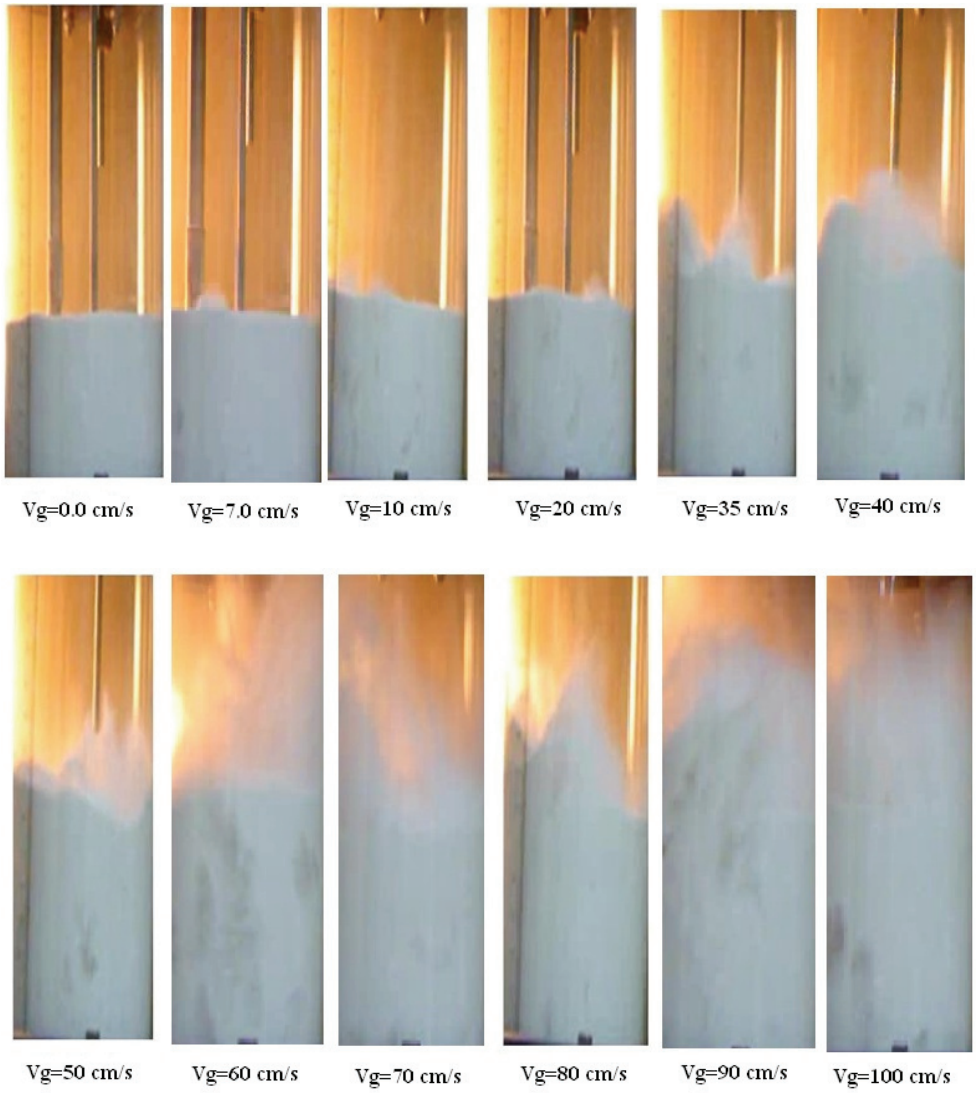

Fig. 25. Comparison of bubble formation and bed expansion for different superficial gas velocities.

Comparison of the contour plots of solid fractions in Fig. 24 and the experimental results for bubble formation and bed expansion in Fig. 25 for Vg=50 cm/s indicates qualitative similarities of the experimental observations and the simulation results. It should be pointed out that some discrepancies due to the effect of the gas distributor, which was not considered in the CFD model, should be expected.

Fig. 26 shows the simulation results of gas volume fraction for different superficial gas velocities. Initially, the bed height increases with bubble formation, so gas volume fraction

increases and levels off at a steady-state bed height. At the start of the simulation, waves of voidage are created, which travel through the bed and subsequently break to form bubbles as the simulation progresses. At the bottom of the column, particle concentration is larger than at the upper part. Therefore, the maximum gas volume fraction occurs at the top of the column. Clearly the gas volume fraction of 1 (at the top of the bed) corresponds to the region where the particles are absent. With increasing superficial gas velocity, Fig. 26 shows that the gas volume fraction generally increases in the bed up to the height of 50 to 60 cm. The gas volume fraction then increases sharply to reach to 1 at the top of the bed. Gas volume fraction approaches the saturation condition of 1 at the bed heights of 63cm, 70cm and 85 cm for Vg=30 cm/s, 50 cm/s and 80 cm/s, respectively. For higher gas velocities, Fig. 26 shows that the gas volume fraction is larger at the same height in the bed. This is because the amount of particles is constant and for higher gas velocity, the bed height is higher. Thus, the solid volume fraction is lower and gas volume fraction is higher. It should be noted here that the fluctuations of the curves in this Fig. are a result of bubble formation and collapse.

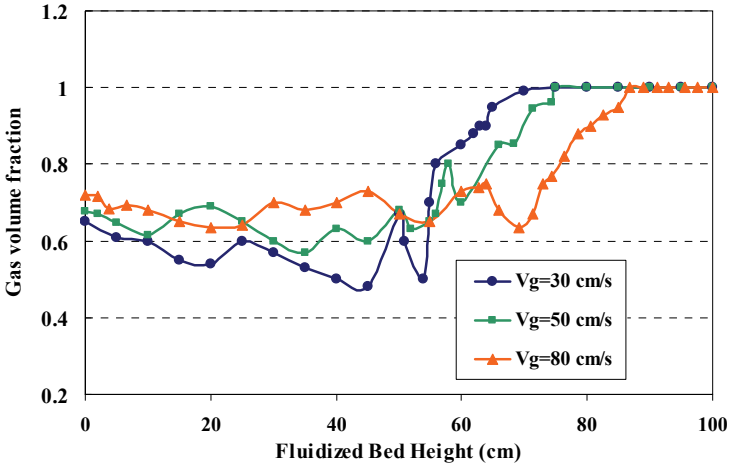

Fig. 26. Simulation results for gas volume fraction at t=5s (Syamlal–O'Brien drag model).

The influence of inlet gas velocity on the gas temperature is shown in Fig.s 27 and 28. As noted before, the gas enters the bed with a temperature of 473K, and particles are initially at 300K. Thermocouples are installed along the column as shown in Fig. 2(B). The thermocouple probes can be moved across the reactor for measuring the temperature at different radii. At each height, gas temperatures at five radii in the reactor were measured and averaged. The corresponding gas mean temperatures as function of height are presented in Fig.s 27 and 28. Fig. 29 shows that the gas temperature deceases with height because of the heat transfer between the cold particles and hot gas. Near the bottom of column, solid volume fraction is relatively high; therefore, gas temperature decreases rapidly and the rate of decrease is higher for the region near the bottom of the column. At top of the column, there are no particles (gas volume fraction is one) and the wall is adiabatic; therefore, the gas temperature is roughly constant. Also the results show that with increasing the gas velocity, as expected the gas temperature decreases. From Fig.s 22-25 it is seen that with increasing gas velocity, bed expansion height increases.

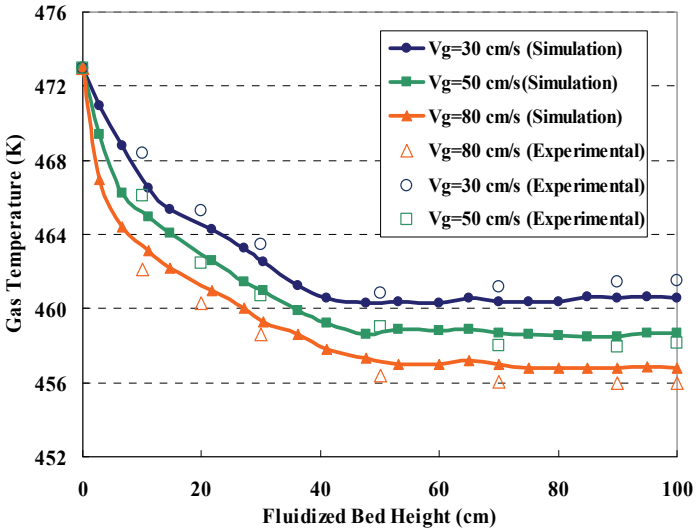

Fig. 27. Simulation and experimental results for inlet gas velocity effect on gas temperature in the bed (t=5 min).

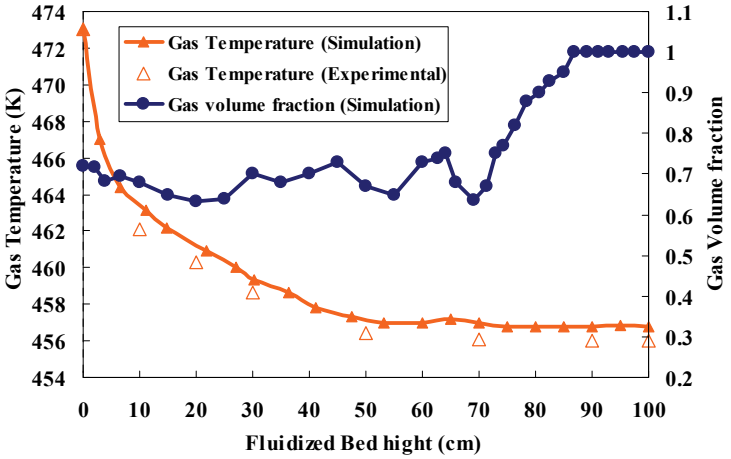

Fig. 28. Comparison of simulation and experimental gas temperature and gas volume fraction at t=5min for Vg=80 cm/s.

In addition, the gas temperature reaches to the uniform (constant temperature) condition in the upper region. When gas velocity is 30 cm/s, temperature reaches to its constant value at a height of about 40 cm; and for Vg=50 cm/s and Vg=80 cm/s, the corresponding gas temperatures reaching uniform state, respectively, at heights of 50 and 55 cm. Fig. 27 also shows that the simulation results are in good agreement with the experimental data. The small differences seen are the result of the slight heat loss from the wall in the experimental reactor. Fig. 28 shows the gas temperature and the gas volume fraction in the same graph.

This Fig. indicates that in the region where the gas volume fraction is highest, the gas temperature is lowest. Clearly in the free gas flow, there is little heat transfer. In the lower part of the reactor, the solid volume fraction is higher, so the rate of heat transfer with the cooler particles is higher and the temperature decreases faster.

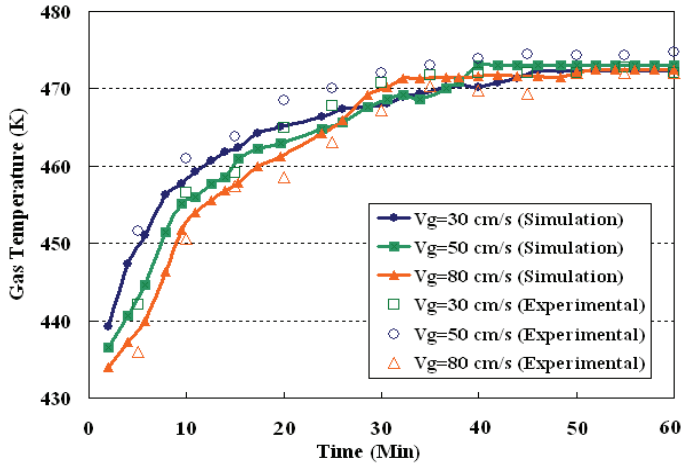

Fig. 29. Comparison of experimental and computational results for gas temperatures at different gas velocities (z=50 cm).

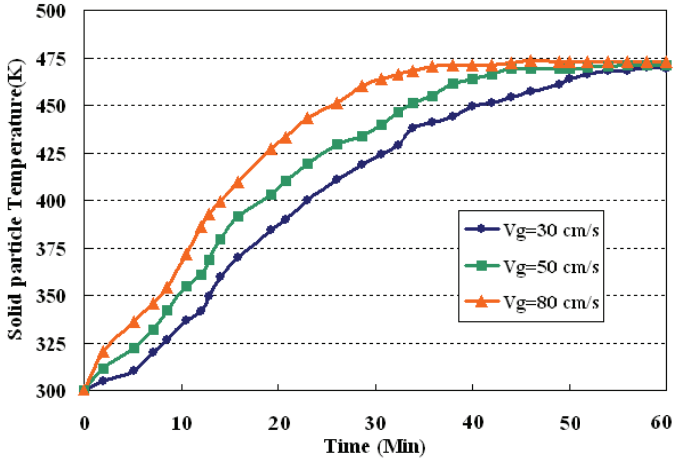

Fig. 30. Simulation results for variation of solid particle temperature with time at different gas velocities at z=50 cm

Fig. 29 compares the time variation of the simulated gas temperature at z=50 cm for different gas velocities with the experimental data. This Fig. shows that gas temperature increases with time and the rate of increase varies with somewhat with the gas velocity. The simulation results show that with increasing gas velocity, gas temperature reaches steady

state condition rapidly. For Vg=80 cm/s, gas temperature reaches steady state condition after about 30 min; but for Vg=50 and 30 cm/s temperature reaches to steady after 40 and 45min, respectively but there are a few difference between simulation and experimental results.

For different inlet gas velocities, time variations of the mean solid phase temperature at the height of z=50 cm are shown in Fig. 30. The corresponding variation of the averaged solid particle temperature with height is shown in Fig. 31. Note that, here, the averaged solid temperature shown is the mean of the particle temperatures averaged across the section of the column at a given height. It is seen that the particle temperature increases with time and with the distance from the bottom of the column. Fig. 30 also shows that at higher gas velocity, solid temperature more rapidly reaches the steady state condition. For Vg=80cm/s, solid temperature approaches the steady limit after about 30min; for Vg=50 and 30 cm/s, the steady state condition is reached, respectively, at about 40 and 45min. In addition, initially the temperature differences between solid and gas phases are higher; therefore, the rate of increase of solid temperature is higher. Fig. 31 shows that the rate of change of the solid temperature near the bottom of the bed is faster, which is due to a larger heat transfer rate compared to the top of the bed. These Fig.s also indicate that an increase in the gas velocity causes a higher heat transfer coefficient between gas and solid phases, and results in an increase in the solid particle temperature.

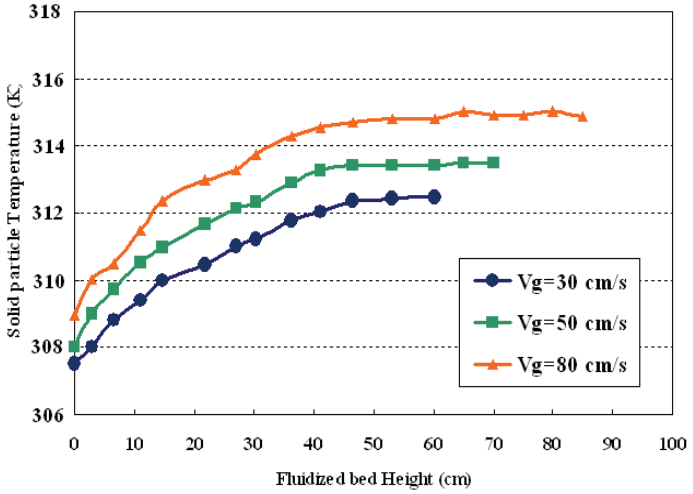

Fig. 31. Inlet gas velocity effect on the simulated solid particle temperatures in bed (t=5min).

The influence of initial bed height (particle amount) on the gas temperature at t=5s is shown in Fig. 32 experimentally and computationally. It indicates that with increasing the particle amount, due to a higher contact surfaces and heat transfer between hot gas and cold solid phase, gas temperature decreases.

The rate of gas temperature decreasing for H_s=40 cm is larger than H_s=20 cm because with increasing the particle amount, volume of cold solid particles and contact surface with hot gas increase. The effects of static initial bed height on solid phase temperature are shown in Fig. 33. It indicates that a decrease in particle amount causes a higher void fraction, gas volume fraction, and heat transfer coefficient between gas and solid phases (resulting in a

higher contact surface between hot gas and cold solid phase) that in turn leads to an increase in solid particle temperature. So with increasing the initial bed height from 20cm to 40cm, gas temperature decreases (Fig. 32) and solid phase temperature increases and rate of this increasing for Hs=40cm is larger than others (Fig. 33). Comparison of the model predictions and experimental measurements on mean gas temperature show good agreement for most operating conditions.

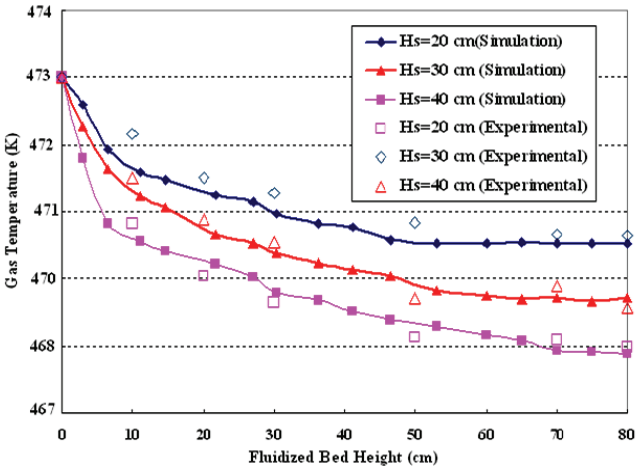

Fig. 32. Comparison of simulation and experimental results of bed height effect on gas temperature at t=5s (Vg=50 cm/s).

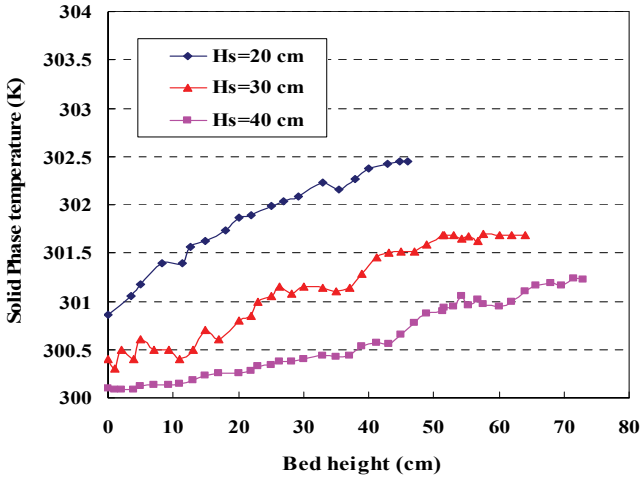

Fig. 33. Simulation results of initial bed height effect on solid particle temperature at t=5s (Vg=50 cm/s).

In addition, the temperature gradient between solid and gas phases is higher at the bed because inlet gas temperature is the highest and solid particles temperature is lowest in the

bed. The slope of temperature plots is higher at the top of the bed due to larger gas volume fraction that leads to a larger contact surfaces and heat transfer rate compared to the bottom of the bed. The influence of inlet gas velocity on the gas temperature is showed in Fig. 34. It indicates that with increasing the gas velocity, due to higher heat transfer coefficient between gas and solid phases, gas temperature decrease rapidly and also rate of this decreasing with increasing the gas velocity increase rapidly. The modeling predictions compared reasonably well with experimental data.

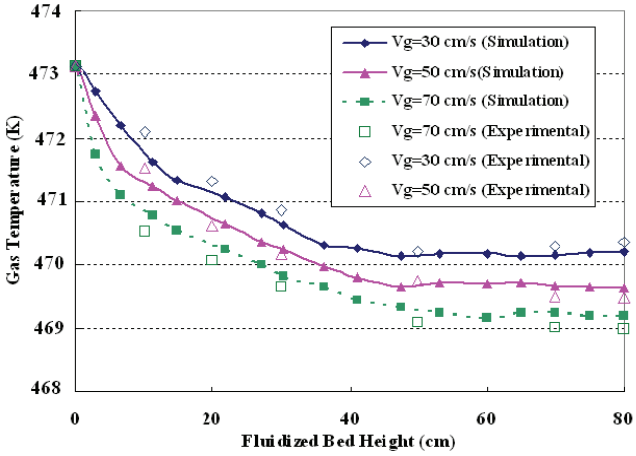

Fig. 34. Comparison of experimental and computational results of gas temperature at different gas velocity (H_s=40 cm, t=5s)

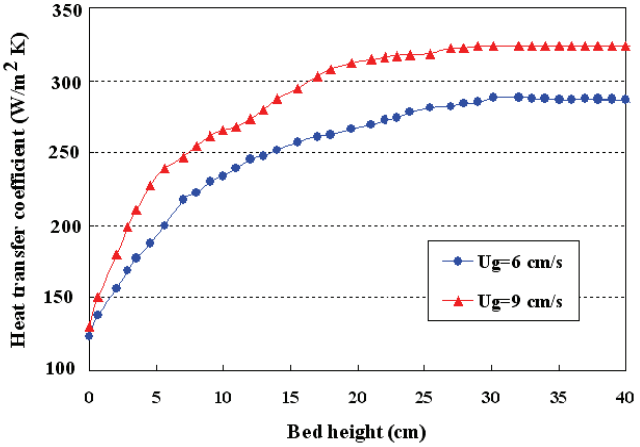

Fig. 35. Simulation results for heat transfer coefficient at different gas velocities (t=7 s).

Simulation results for heat transfer coefficient at different gas velocities at t=7s are shown in Fig. 35. From results of this Fig., heat transfer coefficient increases from bottom to top in the

column because with results of Fig. 35. gas volume fraction increases from bottom to top. This Fig. also indicates that an increase in the gas velocity causes a higher heat transfer coefficient between gas and solid phases.

6. Conclusions

In this chapter, unsteady flow and heat transfer in a gas–solid fluidized bed reactor was investigated. Effect of different parameters for example superficial gas velocity and temperature, initial static bed height and solid particles diameter on hydrodynamics of a two-dimensional gas–solid fluidized bed reactor was studied experimentally and computationally. The Eulerian-Eulerian model with the standard k - ε turbulence model was used for modeling the fluidized bed reactor. The model includes continuity, momentum equations, as well as energy equations for both phases and the equations for granular temperature of the solid particles. A suitable numerical method that employed finite volume method was applied to discritize the governing equations. In order to validate the model, an experimental setup was fabricated and a series of tests were performed. The predicted time-average bed expansion ratio, pressure drop and cross-sectional voidage profiles using Cao-Ahmadi, Syamlal–O'Brien and Gidaspow drag models were compared with corresponding values of experimentally measured data. The modeling predictions compared reasonably well with the experimental bed expansion ratio measurements and qualitative gas–solid flow patterns. Pressure drops predicted by the simulations were in relatively close agreement with the experimental measurements for superficial gas velocities higher than the minimum fluidization velocity. Results show that there is no significant difference for different drag models, so the results suggest that all three drag models are more suitable for predicting the hydrodynamics of gas–solid flows. The simulation results suggested that the Syamlal–O'Brien drag model can more realistically predict the hydrodynamics of gas–solid flows for the range of parameters used in this study. Moreover, gas and solid phase temperature distributions in the reactor were computed, considering the hydrodynamics and heat transfer of the fluidized bed using Syamlal–O'Brien drag expression. Experimental and numerical results for gas temperature showed that gas temperature decreases as it moves upwards in the reactor. The effects of inlet gas velocity, solid particles siizes and initial static bed height on gas and solid phase temperature was also investigated. The simulation showed that an increase in the gas velocity leads to a decrease in the gas and increase in the solid particle temperatures. Furthermore, comparison between experimental and computational simulation showed that the model can predict the hydrodynamic and heat transfer behavior of a gas-solid fluidized bed reasonably well.

7. Acknowledgments

The authors would like to express their gratitude to the Fluid Mechanics Research Center in Department of Mechanical Engineering of Amirkabir University, National Petrochemical company (NPC) and the Petrochemistry Research and Technology Company for providing financial support for this study.

8. Appendix

In this section drive an algebraic (discretized) equation from a partial differential equation [39, 40].

Continuity equation

For this demonstration the transport equation for a scalar ϕ is (m = 0, 1 for solid and gas phases):

$$\frac{\partial}{\partial t}(\alpha_m \rho_m \phi) + \frac{\partial}{\partial x_i}(\alpha_m \rho_m v_{mi} \phi) = 0 \tag{A1}$$

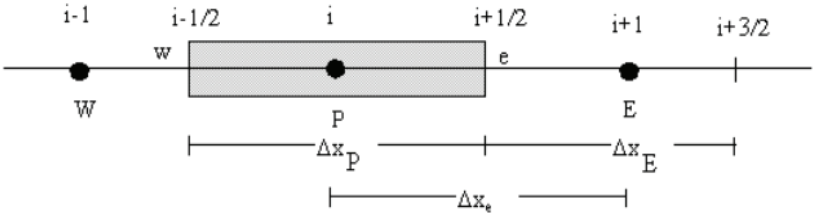

Fig. A1. Control volume and node locations in x-direction

With integrating this Equation over a control volume (Fig. A1) and write term by term, from left to right as follows:

Transient term

$$\int \frac{\partial}{\partial t}(\alpha_m \rho_m \phi) dV \approx [(\alpha_m \rho_m \phi)_P - (\alpha_m \rho_m \phi)_P^o] \frac{\Delta V}{\Delta t} \tag{A2}$$

where the superscript 'o' indicates old (previous) time step values.

Convection term

$$\begin{gathered}\int \frac{\partial}{\partial x_i}(\alpha_m \rho_m v_{mi} \phi)\, dV \approx \{\xi_e(\alpha_m \rho_m \phi)_E + \bar{\xi}_e(\alpha_m \rho_m \phi)_P\}(u_m)_e A_e \\ \{\xi_w(\alpha_m \rho_m \phi)_P + \bar{\xi}_w(\alpha_m \rho_m \phi)_W\}(u_m)_w A_w + \{\xi_n(\alpha_m \rho_m \phi)_N + \bar{\xi}_n(\alpha_m \rho_m \phi)_P\}(v_m)_n A_n \\ - \{\xi_s(\alpha_m \rho_m \phi)_P + \bar{\xi}_s(\alpha_m \rho_m \phi)_S\}(v_m)_s A_s\end{gathered} \tag{A3}$$

Combining the equations derived above Discretized Transport Equation is get

$$\begin{gathered}\left(\frac{(\rho'_m \phi)_P - (\rho'_m \phi)^0}{\Delta t}\right) \Delta V + \{\xi_e(\rho'_m \phi)_E + \bar{\xi}_e(\rho'_m \phi)_P\}(u_m)_e A_e - \\ \{\xi_w(\rho'_m \phi)_P + \bar{\xi}_w(\rho'_m \phi)_W\}(u_m)_w A_w + \{\xi_n(\rho'_m \phi)_N + \bar{\xi}_n(\rho'_m \phi)_P\}(v_m)_n A_n - \\ \{\xi_s(\rho'_m \phi)_P + \bar{\xi}_s(\rho'_m \phi)_S\}(v_m)_s A_s = 0\end{gathered} \tag{A4}$$

where the macroscopic densities define as $\rho'_m = \alpha_m \rho_m$

Equation (A4) may be rearranged to get the following linear equation for ϕ , where the subscript nb represents E, W, N and S [39, 40].

$$a_P \phi_P = \sum_{nb} a_{nb} \phi_{nb} + b \quad , \quad a_P = \sum_{nb} a_{nb} \tag{A5}$$

The discretized form of continuity equation can be easily by setting $\phi = 1$ and a linear equation of the form (A4), in which the coefficients are defined as follows:

$$a_E = -\xi_e(\alpha_m \rho_m)_E (u_m)_e A_e \quad a_W = \bar{\xi}_w(\alpha_m \rho_m)_W (u_m)_w A_w \tag{A6}$$

$$a_N = -\xi_n(\alpha_m\rho_m)_N(v_m)_n A_n \quad a_S = \bar{\xi}_s(\alpha_m\rho_m)_S(v_m)_s A_s \tag{A7}$$

$$a_P = \sum_{nb} a_{nb} + a_P^0 \quad a_P^0 = \frac{(\alpha_m\rho_m)^0}{\Delta t}\Delta V \quad b = a_P^0\phi_P^0 \tag{A8}$$

Momentum equation

The discretization of the momentum equations is similar to that of the scalar transport equation, except that the control volumes are staggered. As explained by Patankar, if the velocity components and pressure are stored at the same grid locations a checkerboard pressure field can develop as an acceptable solution. A staggered grid is used for preventing such unphysical pressure fields. As shown in Fig.A2, in relation to the scalar control volume centered around the filled circles, the x-momentum control volume is shifted east by half a cell. Similarly the y-momentum control volume is shifted north by half a cell, control volume is shifted top by half a cell.

For calculating the momentum convection, velocity components are required at the locations E, W, N, and S. They are calculated from an arithmetic average of the values at neighboring locations [39, 40]:

$$(u_m)_E = f_E(u_m)_P + (1 - f_E)(u_m)_e \tag{A9}$$

$$(v_m)_N = f_p(v_m)_{NW} + (1 - f_P)(v_m)_{NE} \tag{A10}$$

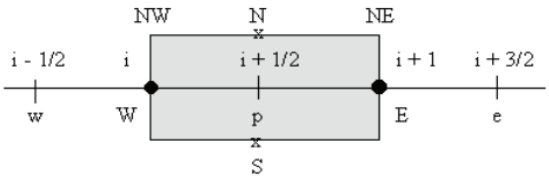

Fig. A2. X-momentum equation control volume

A volume fraction value required at the cell center denoted by *p* is similarly calculated.

$$(\alpha_m)_P = f_P(\alpha_m)_W + (1 - f_P)(\alpha_m)_E \tag{A11}$$

$$f_E = \frac{\Delta x_{Ee}}{\Delta x_P + \Delta x_e} \qquad f_P = \frac{\Delta x_E}{\Delta x_W + \Delta x_E} \tag{A12}$$

Now the discretized x-momentum equation can be written as

$$a_P(u_m)_P = \sum_{nb} a_{nb}(u_m)_{nb} + b_P - A_P(\alpha_m)_P\left(\left(P_g\right)_E - \left(P_g\right)_W\right) + (\beta_{gs}(u_g - u_s)_P)\Delta V_e \tag{A13}$$

The above equation is similar to the discretized scalar transport equation , except for the last two terms: The pressure gradient term is determined based on the current value of Pg and is added to the source term of the linear equation set. The interface transfer term couples all the equations for the same component.

The definitions for the rest of the terms in Equation (A13) are as follows:

$$a_e = D_E - \xi_E(\alpha_m\rho_m)_e(u_m)_E A_E \qquad a_w = D_W + \bar{\xi}_W(\alpha_m\rho_m)_w(u_m)_W A_W \tag{A14}$$

$$a_n = D_N - \xi_N(\alpha_m\rho_m)_n(v_m)_N A_N \qquad a_s = D_S + \bar{\xi}_S(\alpha_m\rho_m)_s(v_m)_S A_S \tag{A15}$$

$$a_P = \sum_{nb} a_{nb} + a_P^0 + S' \qquad b = a_P^0 u_m^0 + (\alpha_m\rho_m)_e g_x \Delta V_e + \bar{S} \tag{A16}$$

$$a_P^0 = \frac{(\alpha_m\rho_m)^0\Delta V_e}{\Delta t} \qquad D_E = \frac{(\mu_m)_E A_E}{\Delta x_E} \tag{A17}$$

The center coefficient *ap* and the source term *b* contain the extra terms S' and $\bar{S}$, which account for the sources arising from shear stress terms.

Fluid pressure correction equation

An important step in the algorithm is the derivation of a discretization equation for pressure, which is described in this section. As stated, first momentum equations are solved using the pressure field P_g^* and the void fraction field ϵ_0^* from the previous iteration to calculate tentative values of the velocity fields u_s^* and u_g^* and other velocity components. The actual values differ from the (starred) tentative values by the following corrections

$$\left(P_g\right)_E = \left(P_g^*\right)_E + \left(P_g'\right)_E \qquad (P_s)_E = (P_s^*)_E + (P_s')_E \tag{A18}$$

$$(u_0)_p = (u_0^*)_p + (u_0')_p \qquad (u_1)_p = (u_1^*)_p + (u_1')_p \tag{A19}$$

To develop an approximate equation for fluid pressure correction, the momentum convection and solids pressure terms are dropped to get (m = 0, 1 for solid and gas phases)

$$a_{0p}(u_0')_p = \sum_{nb} a_{0nb}(u_0')_{nb} - A_p(\alpha_0^*)_p\left(\left(P_g'\right)_E - \left(P_g'\right)_W\right) + \beta_{10}\left[(u_1')_p - (u_0')_p\right]\Delta V \tag{A20}$$

$$\begin{aligned} a_{1p}(u_1')_p = {} & \sum_{nb} a_{1nb}(u_1')_{nb} - A_p(\alpha_1^*)_p\left(\left(P_g'\right)_E - \left(P_g'\right)_W\right) \\ & + \beta_{10}\left[(u_0')_p - (u_1')_p\right]\Delta V - A_p((P_s')_E - (P_s')_W) \end{aligned} \tag{A21}$$

Substituting the above equation and similar equations for other components of velocity into the fluid continuity equation an equation for pressure correction get.

$$\begin{aligned} & \left(\frac{(\alpha_0\rho_0)_P - (\alpha_0\rho_0)_P^0}{\Delta t}\right)\Delta V + \left\{(\alpha_0\rho_0)_E\xi_e + (\alpha_0\rho_0)_P\bar{\xi}_e\right\}\left[(u_0^*)_e - d_{0e}\left(\left(P_g'\right)_E - \left(P_g'\right)_P\right)\right]A_e \\ & -\left\{(\alpha_0\rho_0)_P\xi_w + (\alpha_0\rho_0)_w\bar{\xi}_w\right\}\left[(u_0^*)_w - d_{0w}\left(\left(P_g'\right)_P - \left(P_g'\right)_W\right)\right]A_w \\ & +\left\{(\epsilon_0\rho_0)_N\xi_n + (\epsilon_0\rho_0)_p\bar{\xi}_n\right\}\left[(u_0^*)_n - d_{0n}\left(\left(P_g'\right)_N - \left(P_g'\right)_P\right)\right]A_n \\ & -\left\{(\alpha_0\rho_0)_P\xi_s + (\alpha_0\rho_0)_s\bar{\xi}_s\right\}\left[(u_0^*)_s - d_{0s}\left(\left(P_g'\right)_P - \left(P_g'\right)_S\right)\right]A_s = 0 \end{aligned} \tag{A22}$$

$$a_P\left(P_g'\right)_P = \sum_{nb} a_{nb}\left(P_g'\right)_{nb} + b \qquad a_P = a_E + a_W + a_N + a_S \tag{A23}$$

$$a_E = \left\{(\alpha_0\rho_0)_E\xi_e + (\alpha_0\rho_0)_P\bar{\xi}_e\right\}d_{0e}A_e \qquad a_W = \left\{(\alpha_0\rho_0)_P\xi_w + (\alpha_0\rho_0)_w\bar{\xi}_w\right\}d_{0w}A_w \tag{A24}$$

$$a_N = \{(\alpha_0\rho_0)_N\xi_n + (\alpha_0\rho_0)_p\bar{\bar{\xi}}_n\}d_{0n}A_n \qquad a_S = \{(\alpha_0\rho_0)_P\xi_s + (\alpha_0\rho_0)_s\bar{\bar{\xi}}_s\}d_{0s}A_s \tag{A25}$$

$$\begin{aligned} b = \Bigg\{\left(\frac{(\alpha_0\rho_0)_P - (\alpha_0\rho_0)_P^0}{\Delta t}\right)\Delta V\left[(\alpha_0\rho_0)_E\xi_e + (\alpha_0\rho_0)_P\bar{\bar{\xi}}_e\right]u_{0e}^*A_e \\ - \left[(\alpha_0\rho_0)_P\xi_w + (\alpha_0\rho_0)_w\bar{\bar{\xi}}_w\right]u_{0w}^*A_w + \left[(\alpha_0\rho_0)_N\xi_n + (\alpha_0\rho_0)_p\bar{\bar{\xi}}_n\right]u_{0n}^*A_n \\ - \left[(\alpha_0\rho_0)_P\xi_s + (\alpha_0\rho_0)_s\bar{\bar{\xi}}_s\right]u_{0s}^*A_s\Bigg\} \end{aligned} \tag{A26}$$

The discretization of energy balance equation is similar to that of the scalar transport equation described. The energy equations are coupled because of interphase heat transfer and are partially decoupled with the algorithm described.

Solids volume fraction correction equation

A small change in the solids pressure can be calculated as a function of the change in solids volume fraction:

$$P_m' = K_m\alpha_m' \ , \qquad K_m = \frac{\partial P_m}{\partial \alpha_m} \tag{A27}$$

Denote the solids velocity obtained from the tentative solids pressure field and solids volume fraction field as $(u_m^*)_e$

The actual solids velocity can be represented as

$$(u_m)_e = (u_m^*)_e + (u_m')_e \tag{A28}$$

where the correction $(u_m')_e$ is related to the correction in the solids pressure field as

$$(u_m')_e = e_e[(P_m')_P - (P_m')_E] \tag{A29}$$

Also, the volume fractions can be expressed as a sum of the current value plus a correction

$$(\alpha_m)_e = (\alpha_m^*)_e + (\alpha_m')_e \tag{A30}$$

So, the flux $(\rho_m\alpha_m u_m)_e$ in convection Term can be expressed as

$$\begin{aligned} (\rho_m)_e(\alpha_m)_e(u_m)_e \approx (\rho_m)_e(\alpha_m^*)_e(u_m^*)_e + (\rho_m)_e\left[\bar{\bar{\xi}}_e(u_m^*)_e + (\alpha_m^*)_e(K_m)_Pe_e\right](\alpha_m')_P \\ + (\rho_m)_e[\xi_e(u_m^*)_e - (\alpha_m^*)_e(K_m)_Ee_e](\alpha_m')_E \end{aligned} \tag{A31}$$

For transient term

$$\begin{aligned} \int\frac{\partial}{\partial t}(\alpha_m\rho_m)_P &= \frac{[(\alpha_m)_P(\rho_m)_P - (\alpha_m)_P^0(\rho_m)_P^0]}{\Delta t}\Delta V \\ &= \frac{[((\alpha_m^*)_P + (\alpha_m')_P)(\rho_m)_P - (\alpha_m)_P^0(\rho_m)_P^0]\Delta V}{\Delta t} \\ &= \frac{(\alpha_m')_P(\rho_m)_P\Delta V}{\Delta t} + \frac{[(\alpha_m^*)_P(\rho_m)_P - (\alpha_m)_P^0(\rho_m)_P^0]}{\Delta t}\Delta V \end{aligned} \tag{A32}$$

Collecting all the terms, a correction equation for volume fraction correction can be written as:

$$a_p(\alpha'_m)_P = \sum_{nb} a_{nb}(\alpha'_m)_{nb} + b \tag{A33}$$

$$\begin{aligned} a_E &= [(\rho_m\alpha_m)^*_e e_e (K_m)_E - \xi_e(\rho_m)_E(u_m)^*_e]A_e \\ a_W &= \left[(\rho_m\alpha_m)^*_w e_w (K_m)_W - \bar{\xi}_w(\rho_m)_W(u_m)^*_w\right]A_w \end{aligned} \tag{A34}$$

$$\begin{aligned} a_N &= \left[\left(\rho_m\alpha_m\right)^*_n e_n \left(K_m\right)_N - \xi_n\left(\rho_m\right)_N\left(u_m\right)^*_n\right]A_n \\ a_s &= \left[\left(\rho_m\alpha_m\right)^*_s e_s \left(K_m\right)_S - \bar{\xi}_s\left(\rho_m\right)_S\left(u_m\right)^*_s\right]A_s \end{aligned} \tag{A35}$$

$$\begin{aligned} a_P = {} & \left(\rho_m\right)_P\left[\bar{\xi}_e(u^*_m)_e A_e - \xi_W(u^*_m)_W A_W + \bar{\xi}_n(v^*_m)_n A_n - \bar{\xi}_s(v^*_m)_s A_s\right] \\ & +(K_m)_P\left[\left(\rho_m\alpha^*_m\right)_e e_e A_e + \left(\rho_m\alpha^*_m\right)_W e_W A_W + \left(\rho_m\alpha^*_m\right)_n e_n A_n + \left(\rho_m\alpha^*_m\right)_s e_s A_s\right] \\ & +\left(\rho_m\right)_P\frac{\Delta V}{\Delta t} \end{aligned} \tag{A36}$$

$$\begin{aligned} b = {} & -\left(\rho_m\alpha^*_m\right)_e (u^*_m)_e A_e + \left(\rho_m\alpha^*_m\right)_W (u^*_m)_W A_W \\ & -\left(\rho_m\alpha^*_m\right)_n (v^*_m)_n A_n + \left(\rho_m\alpha^*_m\right)_s (v^*_m)_s A_s \\ & -\left[\left(\rho_m\alpha^*_m\right)_P - \left(\rho_m\alpha^*_m\right)^0_P\right]\frac{\Delta V}{\Delta t} \end{aligned} \tag{A37}$$

Under relaxation

To ensure the stability of the calculations, it is necessary to under relax the changes in the field variables during iterations.

Where $0 \leq \omega_\phi \leq 1$ when $\omega_\phi = 0$ the old value remains unchanged.

Applying the under relaxation factor first the equations was solved and then applied Under relaxation as because of the better conditioning of the linear equation set and the consequent savings in the solution time.

Calculation of residuals

The convergence of iterations is judged from the residuals of various equations. The residuals are calculated before under relaxation is applied to the linear equation set. The standard form of the linear equation set is

$$a_P\phi_P = b + a_E\phi_E + a_W\phi_W + a_N\phi_N + a_S\phi_S + a_T\phi_T + a_B\phi_B \tag{A39}$$

Denoting the current value as ϕ^*, the residual at point P is given by

$$R_{\phi P} = b + a_E\phi^*_E + a_W\phi^*_W + a_N\phi^*_N + a_S\phi^*_S + a_T\phi^*_T + a_B\phi^*_B - a_P\phi^*_P \tag{A40}$$

Nomenclature

b, C_μ, C_3 C_V, C_β	Coefficients in turbulence model

C_D	Drag coefficient
Cp	Specific heat, J/(kg.k)
d_p	Solid diameter, mm
$Ds, D_{t,sg}$	Turbulent quantities for the dispersed phase
e_{ss}	Coefficient of restitution of particle
g	Gravitational constant, 9.81m/s^{-2}
$g_{0,ss}$	Radial distribution function
$G_{k,g}$	Production of turbulent kinetic energy
H	Expanded bed height, cm
H_0	Static bed height, cm
H_{gs}	Heat transfer between the gas and the solid, J/m^{3}s
I	Turbulent intensity
I_{2D}	Second invariant of the deviatoric stress, s^{-2}
$K_{\theta s}$	Diffusion coefficient for granular energy, Jkg^{-1}
$k^{'}$	Thermal conductivity, J/(m.K.s)
k	Turbulence kinetic energy tensor, dimensionless
$L_{t,g}$	Length scale of the turbulent eddies, m
Nu_s	Nusselt number, dimensionless
p	Pressure, Pa
P_r	Gas Prandtl number, dimensionless
R_e	Reynolds number, dimensionless
S	Modulus of the mean rate-of-strain tensor
T	Time, s
U, V	Superficial gas velocity, m/s
$\overrightarrow{Vi}$	Velocity, m/s
$\vec{v}_{dr}$	Drift velocity, m/s
$\overrightarrow{V_{s,\|\|}}$	Particle slip velocity parallel to the wall, m/s

Greek symbols

α	Volume fraction, dimensionless
β_{gs}	Gas-solid inter phase exchange coefficient, kgm^{-3}s^{-1}
ε	Turbulence dissipation rate, m^{2}s^{-3}
$\underline{\varepsilon}_{s,\max}$	Volume fraction for the particles at maximum packing
τ_x	Reynolds stress tensor, N/m^{-2}
τ_{12}	Particle relaxation time
τ_1^t	Time-scale of turbulent eddies
η_{sg}	Ratio between characteristic times
ϕ_{gs}	Gidaspow's switch function
φ	Angle of internal friction
Θ	Granular temperature, m^{2}s^{-2}
k_{Θ_s}	Diffusion coefficient
φ_{gs}	Transfer of kinetic energy, J/(m^3.s)
γ_{Θ_s}	Collision dissipation of energy, J/(m^3.K.s)

γ_{gs}^{0}	Heat transfer coefficient, J/(m^3.K.s)
$\mu_{t,g}$	Turbulent (or eddy) viscosity, Pa.s
$\prod_{k,g}$, $\prod_{\varepsilon,g}$	Influence of the dispersed phase on the continuous phase
κ	von Karman constant
η_{sg}	Ratio between characteristic times
φ	Specularity coefficient between the particle and the wall
$\tau_{F,sg}$	Characteristic particle relaxation time connected with the inertial effects, s
$\tau_{t,sg}$	Lagrangian integral time scale, s
$\mu_{s,fr}$	Shear viscosity, Pa.s
$\mu_{s,kin}$	Kinematics viscosity, m^2/s
$\mu_{s,col}$	Collisional part of the shear viscosity, Pa.s

Subscripts

g	gas
mf	minimum fluidization
s	solids
w	wall
t	turbulence

9. References

[1] Gidaspow, D., Multiphase Flow and Fluidization, First ed. Academic press, London, 1994.

[2] Kunii, D., Levenspiel ,O., Fluidization Engineering, Second ed. Butterworth-Heinemann, Boston, 1991.

[3] Ranade, V.V., Computational Flow Modeling for Chemical Reactor Engineering, First ed. Academic press, New York, 2002.

[4] Anderson T. B. and Jackson R. A Fluid Mechanical Description of Fluidized Beds. I & EC Fundam., 6,:527-534, 1967.

[5] Grace, J.R., Taghipour, F., Verification and validation of CFD models and dynamic similarity for fluidized beds. Powder Technology , 139, 99–110, 2004.

[6] Bird, R.B., Stewart, W.E., Lightfoot, E.N., Transport Phenomena. seconded. Wiley, New York, 2002.

[7] Nasr.H, Ahmadi.G, The effect of two-way coupling and inter-particle collisions on turbulence modulation in a vertical channel flow, International Journal of Heat and Fluid Flow, 28 ,1507–1517, 2007.

[8] Taghipour, F., Ellis, N., Wong, C., Experimental and computational study of gas–solid fluidized bed hydrodynamics, Chemical Engineering Science, 60, 6857–6867, 2005.

[9] Kaneko Y., Shiojima T., Horio M., DEM simulation of fluidized beds for gas-phase olefin polymerization, Chemical Engineering Science, 54, 5809–5821, 1999.

[10] Rong. F., Marchisio. D.L., Fox. R.O., CFD Simulation of Polydisperse Fluidized-Bed Polymerization Reactors, Department of Chemical Engineering, Iowa State

University, 2114 Sweeney Hall, Ames, IA 50010-2230, USA, Preprint submitted to Elsevier Science, August 2003.

[11] Behjat. Y, Shahhosseini.S, Hashemabadi.S.H, CFD modeling of hydrodynamic and heat transfer in fluidized bed reactors, International Communications in Heat and Mass Transfer, 35, 357–368, 2008.

[12] Gobin, H. Neau, O. Simonin, J. Llinas, V. Reiling, J.L. Selo, Fluid dynamic numerical simulation of a gas phase polymerization reactor, International Journal for Numerical Methods in Fluids, 43,1199–1220, 2003.

[13] Van Wachem, B.G.M., Schouten, J.C., Van den Bleek, C.M., Krishna, R., Sinclair, J.L., Comparative analysis of CFD models of dense gas–solid systems, AIChE Journal, 47, 1035–1051, 2001.

[14] Van Wachem, B.G.M., Schouten, J.C., Van den Bleek, C.M., Krishna, R., Sinclair, J.L., CFD modeling of gas-fluidized beds with a bimodal particle mixture, AIChE Journal, 47, 1292–1302, 2001.

[15] Wachem .V. B.G.M., Schouterf .J.C., Krishnab. R., and Bleek . van den.C.M., Eulerian Simulations of Bubbling Behaviour in Gas-Solid Fluidized Beds, Computers chcm. Engng , 22, 299-306, 1998.

[16] Chiesa, M., Mathiesen, V., Melheim, J.A.., Halvorsen, B., Numerical simulation of particulate flow by the Eulerian–Lagrangian and the Eulerian–Eulerian approach with application to a fluidized bed, Computers & Chemical Engineering, 29, 291–304, 2005.

[17] Mansoori, Z., Saffar-Avval, M., Basirat Tabrizi, H., Ahmadi, G., Modeling of heat transfer in turbulent gas–solid flow, Int. J. Heat Mass Transfer, 45, 1173, 2002.

[18] Mansoori, Z., Saffar-Avval, M., Basirat Tabrizi, H., Ahmadi, G., Lain, S., Thermo-mechanical modeling of turbulent heat transfer in gas–solid flows including particle collisions, Int. J. Heat Fluid Flow, 23, 792, 2002

[19] Saffar-Avval M., Basirat Tabrizi H., Mansoori Z., Ramezani P., Gas–solid turbulent flow and heat transfer with collision effect in a vertical pipe, Int. J. Thermal Sciences 46, 67–75, 2007.

[20] Syamlal, M., O'Brien, T.J., Computer simulation of bubbles in a fluidized bed. A.I.Ch.E. Symposium Series, 85, 22–31,1989.

[21] Syamlal, M., O'Brien, T.J., Fluid dynamic simulation of O3 decomposition in a bubbling fluidized bed. A.I.Ch.E. Journal 49, 2793–2801, 2003

[22] Cao. J., Ahmadi. G.,.Gas–particle two-phase turbulent flow in a vertical duct, Int. J. Multiphase Flows, 21,1203-1228, 1995.

[23] Cao. J., Ahmadi. G., Gas–particle two-phase flow in horizontal and inclined ducts, Int. J. Eng. Sci. 38, 1961-1981, 2000.

[24] Wen, C.-Y., Yu, Y.H.,. Mechanics of fluidization. Chemical Engineering Progress Symposium Series 62, 100–111, 1966.

[25] Abu-Zaid, S., Ahmadi, G., A rate dependent model for turbulent flows of dilute and dense two phase solid-liquid mixtures, powder Technology, 89, 45-56, 1996.

[26] Ding, J., Gidaspow, D., A bubbling fluidization model using kinetic theory of granular flow, A.I.Ch.E. Journal, 36, 523–538, 1990.

[27] Gelderbloom, S.J., Gidaspow, D., Lyczkowski, R.W., CFD simulations of bubbling/collapsing fluidized beds for three Geldart groups. A.I.Ch.E. Journal, 49, 844–858, 2003.

[28] Huilin, L., Yurong, H., Gidaspow, D., Hydrodynamic modeling of binary mixture in a gas bubbling fluidized bed using the kinetic theory of granular flow, Chemical Engineering Science, 58, 1197–1205, 2003.

[29] Lun, C.K.K., and Savage, S.B., A Simple Kinetic Theory for Granular Flow of Rough, Inelastic, Spherical Particles, J. Appl. Mech., 54, 47-53, 1987.

[30] Zhong.W, Zhang.M, Jin.B, Zhang.Y, Xiao.R, Huang.Y, Experimental investigation of particle mixing behavior in a large spout-fluid bed, Chemical Engineering and Processing, 2007.

[31] Zhong.W, Zhang.M, Jin.B, Maximum spoutable bed height of spout-fluid bed, Chemical Engineering Journal, 124, 55–62, 2006.

[32] Gamwo.I.K, Soong.Y, Lyczkowski.R.W, Numerical simulation and experimental validation of solids flows in a bubbling fluidized bed, Powder Technology, 103, 117–129, 1999.

[33] Pain, C., Mansoorzadeh, S., Oliveira, C.R.E.D., Goddard, A.J.H., Numerical modeling of gas–solid fluidized beds using the two-fluid approach, International Journal for Numerical Methods in Fluids, 36, 91–124, 2001.

[34] Du, W., Xiaojun, B.,, Jian, X.,Weisheng,W., computational fluid dynamics (CFD) modeling of spouted bed: influence of frictional stress, maximum packing limit and coefficient of restitution of particles, Chemical Engineering Science, 61, 4558-4570, 2006.

[35] Hui, K., Haff, P.K. and Jackson, R., Boundary Conditions for High-Shear Grain Flows. J.F.M. 145, 223-233, 1984.

[36] Johnson, P.C. and Jackson, R., Frictional-Collisional Constitutive Relations for Granular materials, with Application to Plane Shearing. J. Fluid Mech., 176, , 67-93, 1987.

[37] Patankar, S.V., Numerical heat transfer and fluid flow, First ed. Hemisphere Publishing, Washington, DC, 1980.

[38] Huilin, L., Wentie,L., Feng, L., Guangbo, Z., Huilin, H.L., Wentie, L., Feng, L., Guangbo, Z., Yurong, H., Eulerian simulations of bubble behavior in a two-dimensional gas–solid bubbling fluidized bed, International Journal of Energy Research, 26,1285–1293, 2002.

[39] Syamlal, M., W.A. Rogers, and T.J. O'Brien,. "MFIX Documentation, Theory Guide," Technical Note, DOE/METC-94/1004, NTIS/DE94000087, National Technical Information Service, Springfield, VA, 1993.

[40] Syamlal, M. December. MFIX Documentation: Numerical Techniques. DOE/MC-31346-5824. NTIS/DE98002029. National Technical Information Service, Springfield, VA, 1998

[41] Fluent, Fluent 6.3, User's Guide, 23, Modeling Multiphase Flows and 12, Modeling Turbulence, Fluent Inc, 2006.

[42] Gidaspow, D., Hydrodynamics of Fluidization and Heat Transfer: Supercomputer Modeling, Appl. Mech. Rev., 39, 1-23, 1986.

[43] Fan, R., Marchisio., D.L., Fox. R.O., CFD Simulation of Polydisperse Fluidized-Bed Polymerization Reactors, Department of Chemical Engineering, Iowa State University, 2114 Sweeney Hall, Ames, IA 50010-2230, USA, Preprint submitted to Elsevier Science, August 2003.

[44] Lettieri. P., Saccone. G., Cammarata. L., Predicting the Transition from Bubbling to Slugging Fluidization Using Computational Fluid Dynamics ,Trans IChemE, Part A, 2004 Chemical Engineering Research and Design, 82(A8): 939–944

[45] Algeri, C., Rovaglio, M., Dynamic Modeling of a Poly(ethylene terephthalate) Solid-State Polymerization Reactor I: Detailed Model Development, Ind. Eng. Chem. Res., 43, 4253-4266, 2004.

[46] Rovaglio M., Algeri, C., and Manca, D., Dynamic modeling of a poly(ethylene terephthalate) solid-state polymerization reactor II: Model predictive control, Ind. Eng. Chem. Res., 43, 4267-4277, 2004.

[47] Hamzehei, M., Rahimzadeh, H., Experimental and Numerical Study of Hydrodynamics with Heat Transfer in a Gas-Solid Fluidized bed Reactor at Different Particle Sizes, Ind. Eng. Chem. Res., 48, 3177–3186, 2009.

[48] Hamzehei, M., Rahimzadeh, H., Ahmadi, G., Computational and Experimental Study of Heat Transfer and Hydrodynamics in a 2D Gas-Solid Fluidized Bed Reactor, Ind. Eng. Chem. Res., (Special Issue) 49, 5110–5121, 2010.

[49] Hamzehei, M., Rahimzadeh, H., Ahmadi, G., Studies of gas velocity and particles size effects on fluidized bed hydrodynamics with CFD modeling and experimental investigation, Journal of Mechanics, 26, 113-124, 2010.

[50] Hamzehei, M. and Rahimzadeh, H., Investigation of a Fluidized Bed Chamber Hydrodynamics with Heat Transfer Numerically and Experimentally, Korean Journal of Chemical Engineering, 27, 355.363, 2010.

[51] Hamzehei, M., Rahimzadeh, H., Ahmadi, G., Study of Bed Height and Gas Velocity Effect on Hydrodynamics and Heat Transfer in a Gas-Solid Fluidized Bed Reactor Experimentally and Numerically, Heat Transfer Engineering, 2010, (Accepted).

[52] M., Hamzehei , H., Rahimzadeh, Study of Parameters Effect on Hydrodynamics of a Gas-Solid Chamber Experimentally and Numerically, Proceeding of Experimental Fluid Mechanics Conference, (EFM 2010), Liberec, Czech Republic November 24-26, 2010.

[53] Hamzehei, M., Rahimzadeh, H., Ahmadi, G., CFD Modeling and Simulation of Hydrodynamics in a Fluidized Bed Chamber with Experimental Validation, Proceeding of the *31st* IASTED International Conference on Modelling, Identification, and Control (*MIC* 2011) Innsbruck, Austria, February 14 – 16, 2011

[54] Hamzehei, M., Rahimzadeh., Study of Particle Size Effects on Hydrodynamics of a Fluidized Bed Chamber Experimentally and Computationally, Proceeding of 3rd Technology and Innovation for Sustainable conference (TISD2010) in Nong Khai, Thailand, March 4-6, (Best Paper and best presentation on the Topic E: Energy Technology, Thermal Systems and Applied Mechanics).

[55] Hamzehei, M., Rahimzadeh., Study of Hydrodynamics in a Two phase Fluidized Bed Reactor Experimentally and Numerically, Proceeding of Seventh South African Conference on Computational and Applied Mechanics (SACAM10), Pretoria, January 10–13, 2010.

15

Particle Scale Simulation of Heat Transfer in Fluid Bed Reactors

Zongyan Zhou, Qinfu Hou and Aibing Yu
Laboratory for Simulation and Modelling of Particulate Systems School of Materials Science and Engineering, The University of New South Wales, Sydney, NSW 2052, Australia

1. Introduction

Fluid bed reactors have been extensively used in chemical processes due to their high heat transfer efficiency (Kunii & Levenspiel, 1991). Typical examples are ironmaking blast furnace which involves complicated multiphase flow, heat transfer and chemical reactions in a packed bed (Omori, 1987; Dong et al., 2007), and fluidized bed combustors whose performance heavily depends on the hydrodynamics and thermal-chemical behavior of particles in interaction with gas (Avedesia & Davidson, 1973; Oka, 2004). To achieve optimal design and control of such a fluid bed reactor, it is important to understand the flow and heat transfer characteristics. The thermal behaviour of packed beds with a stagnant or dynamic fluid has been extensively investigated experimentally and theoretically in the past decades. Many empirical correlations have been formulated to determine the heat transfer coefficient (HTC), as respectively reviewed by various investigators (Botterill, 1975; Wakao & Kaguei, 1982; Kunii & Levenspiel, 1991; Molerus & Wirth, 1997). Those studies and resulting formulations are mainly macroscopic, focused on the overall heat transfer behaviour. They are very useful to the estimation of the thermal behaviour of process designs.

Physical experiments usually experience difficulty in quantifying the heat transfer mechanisms at a particle level identified many years ago (for example, Yagi & Kunii, 1957). To overcome this difficulty, in recent years, heat transfer behaviour in a fluidized bed at a microscopic, particle scale has been examined experimentally (Prins et al., 1985; Baskakov et al., 1987; Agarwal, 1991; Parmar & Hayhurst, 2002; Collier et al., 2004; Scott et al., 2004). In such a study, the transient temperature of a hot sphere immersed in the bed is measured using an attached thermocouple, and then its HTC can be determined. Such particle scale studies are useful but have limitations in exploring the fundamentals. For example, the heat transfer to a particle should be described by at least three mechanisms, e.g. convection from fluid, conduction from particles or wall, and radiation. However, the contribution of each of these mechanisms is difficult to quantify. Moreover, the heat transfer of a particle will be strongly affected by the local gas-solid flow structure, and hence varies spatially and temporally. The information derived for a single particle may not be reliable because of the difficulty in quantifying such local structures in a particle bed.

Alternatively, mathematical modeling has been increasingly accepted as an effective method to study the heat transfer phenomena in a particle-fluid system. Generally speaking, the existing approaches to modelling particle flow and thermal behaviour can be classified into two categories: the continuum approach at a macroscopic level, and the discrete approach at a microscopic/particle level. In the continuum approach, the macroscopic behavior is described by balance equations, e.g., mass, momentum and energy, closed with constitutive relations together with initial and boundary conditions (see, for example, Anderson & Jackson, 1967; Ishii, 1975; Gidaspow, 1994; Enwald et al., 1996). The so called two-fluid model (TFM) is widely used in this approach. In such a model, both fluid and solid phases are treated as interpenetrating continuum media in a computational cell which is much larger than individual particles but still small compared with the size of process equipment (Anderson & Jackson, 1967). However, its effective use heavily depends on the constitutive or closure relations for the solid phase and the momentum exchange between phases which are often difficult to obtain within its framework.

The discrete approach is based on the analysis of the motion of individual particles, typically by means of the discrete particle simualtion (DPS). The method considers a finite number of discrete particles interacting by means of contact and non-contact forces. When coupling with fluid flow, a coupled DPS-CFD (computatinal fluid dynamics) approached is often used. In this approach, the motion of discrete particles is obtained by solving Newton's second law of motion, and the flow of continuum fluid by solving the Navier-Stokes equations based on the concept of local average as used in CFD, with the coupling of CFD and DPS through particle-fluid interaction forces (Tsuji et al., 1992; Xu & Yu, 1997; 1998; Zhou et al., 2010b). The main advantage of DPS-CFD is that it can generate detailed particle-scale information, such as the trajectories of and forces acting on individual particles, which is key to elucidating the mechanisms governing the complicated flow behavior. With the rapid development of computer technology, the approach has been increasingly used by various investigators to study various particle-fluid flow systems as, for example, reviewed by Zhu *et al.* (2007; 2008).

Discrete approach has been extended to study heat transfer. In fact, mechanistic approach based on the packet model originally proposed by Mickley and Fairbanks (1955) is a typical one to study the heat transfer between bubbling beds and immersed objects. However, the problem associated with such early approaches is the lack of reliable estimation of parameters (Chen, 2003; Chen et al., 2005). This difficulty can be overcome by the newly developed discrete approach. With the DPS-CFD approach, information such as particle-particle or particle-wall contact, local voidage and local gas-solid flow structure can be produced. Such information is essential in determining the heat transfer behaviour of individual particles. The approach has been attempted by some investigators to study coal combustion (Rong & Horio, 1999; Peters, 2002; Zhou et al., 2003; Zhou et al., 2004), air drying (Li & Mason, 2000; Li & Mason, 2002), olefin polymerization (Kaneko et al., 1999), and inserts in a fluidized bed (Di Maio et al., 2009; Zhao et al., 2009). But in those studies, the heat transfer mode by particle-particle conduction is only partially considered. The analysis of heat transfer mechanisms has not been performed seriously.

More recently, Zhou et al. (2009; 2010a) proposed a comprehensive model taking into account most of the known heat transfer mechanisms. The approach considers the different heat transfer mechanisms in detail, for example, particle-fluid convection, particle-particle

conduction, and particle radiation. The extended DPS-CFD model offers a useful numerical technique to elucidate the fundamentals governing the heat transfer in packed/fluidized beds at a particle scale. This chapter aims to introduce this approach, and demonstrates its applications through some case studies.

2. Model description

2.1 Governing equations for solid particles

Various methods have been developed for DPS simulation, as reviewed by Zhu et al. (2007). The DPS model used here is based on the soft sphere model, i.e. discrete element method (DEM), originally proposed by Cundall and Strack (1979). Generally, a particle in a particle-fluid flow system can have two types of motion: translational and rotational, which are determined by Newton's second law of motion. The corresponding governing equations for particle i with radius R_i, mass m_i and moment of inertia I_i can be written as:

$$m_i \frac{d\mathrm{v}_i}{dt} = \mathrm{f}_{f,i} + \sum_{j=1}^{k_c} (\mathrm{f}_{c,ij} + \mathrm{f}_{d,ij}) + m_i \mathrm{g} \tag{1}$$

$$I_i \frac{d\omega_i}{dt} = \sum_{j=1}^{k_c} (\mathrm{M}_{t,ij} + \mathrm{M}_{r,ij}) \tag{2}$$

where $\mathbf{v}_i$ and $\boldsymbol{\omega}_i$ are respectively the translational and angular velocities of the particle. The forces involved are: particle-fluid interaction force $\mathbf{f}_{f,i}$, the gravitational force $m_i\mathbf{g}$, and inter-particle forces between particles which include elastic force $\mathbf{f}_{c,ij}$ and viscous damping force $\mathbf{f}_{d,ij}$. These inter-particle forces can be resolved into the normal and tangential components at a contact point. The torque acting on particle i by particle j includes two components: $\mathbf{M}_{t,ij}$ which is generated by tangential force and causes particle i to rotate, and $\mathbf{M}_{r,ij}$ commonly known as the rolling friction torque, is generated by asymmetric normal forces and slows down the relative rotation between particles. A particle may undergo multiple interactions, so the individual interaction forces and torques are summed over the k_c particles interacting with particle i.

Equations used to calculate the interaction forces and torques between two spheres have been well-established in the literature (Zhu et al., 2007). In our work, the determination of particle-particle interaction is based on the non-linear models, as listed in Table 1. This approach was also used by other investigators (Langston et al., 1994; 1995; Zhou et al., 1999; Yang et al., 2000). Particle-fluid interaction force $\mathbf{f}_{f,i}$ is a sum of fluid drag $\mathbf{f}_{d,i}$ and pressure gradient force $\mathbf{f}_{\nabla p,i}$. Many correlations are available in the literature to calculate the fluid drag acting on the individual particles, for example, Ergun equation (1952), Wen and Yu (1966), and Di Felice (1994). Particularly, Di Felice correlation (1994) has been widely used in the literature and also used in our work (see, for example, Xu & Yu, 1997; Xu et al., 2000; Feng & Yu, 2004; 2007; Zhou et al., 2009; 2010a; 2010b).

The heat transfer of particle i and its surroundings is considered to be controlled by three mechanisms: particle-fluid convection, particle-particle or particle-wall conduction, and radiation. According to the energy balance, the governing equation for particle i can be generally written as

$$m_i c_{p,i} \frac{dT_i}{dt} = \sum_{j=1}^{k_i} Q_{i,j} + Q_{i,f} + Q_{i,rad} + Q_{i,wall} \tag{3}$$

where k_i is the number of particles exchanging heat with particle i, $Q_{i,j}$ is the heat exchange rate between particles i and j due to conduction, $Q_{i,f}$ is the heat exchange rate between particle i and its local surrounding fluid, $Q_{i,rad}$ is the heat exchange rate between particle i and its surrounding environment by radiation, and $Q_{i,wall}$ is particle-wall heat exchange rate. $c_{p,i}$ is the particle specific heat. Different heat transfer models are adopted to determine the different heat exchange rates shown in Eq. (3), and described below.

Normal elastic force, $\mathbf{f}_{cn,ij}$	$-\frac{4}{3}E^*\sqrt{R^*}\delta_n^{3/2}\mathrm{n}$
Normal damping force, $\mathbf{f}_{dn,ij}$	$-c_n\left(8m_{ij}E^*\sqrt{R^*\delta_n}\right)^{1/2}\mathrm{v}_{n,ij}$
Tangential elastic force, $\mathbf{f}_{ct,ij}$	$-\mu_s\left\|\mathbf{f}_{cn,ij}\right\|(1-(1-\delta_t/\delta_{t,\max})^{3/2})\hat{\boldsymbol{\delta}}_t$
Tangential damping force, $\mathbf{f}_{dt,ij}$	$-c_t\left(6\mu_s m_{ij}\left\|\mathbf{f}_{cn,ij}\right\|\sqrt{1-\delta_t/\delta_{t,\max}}/\delta_{t,\max}\right)^{1/2}\mathrm{v}_{t,ij}$
Coulomb friction force, $\mathbf{f}_{t,ij}$	$-\mu_s\left\|\mathbf{f}_{cn,ij}\right\|\hat{\boldsymbol{\delta}}_t$
Torque by tangential forces, $\mathbf{T}_{t,ij}$	$\mathrm{R}_{ij}\times\left(\mathbf{f}_{ct,ij}+\mathbf{f}_{dt,ij}\right)$
Rolling friction torque, $\mathbf{T}_{r,ij}$	$\mu_{r,ij}\left\|\mathbf{f}_{n,ij}\right\|\hat{\boldsymbol{\omega}}_{ij}^n$
Particle-fluid drag force, $\mathbf{f}_{d,i}$	$0.125C_{d0,i}\rho_f\pi d_{pi}^2\varepsilon_i^2\left\|\mathrm{u}_i-\mathrm{v}_i\right\|(\mathrm{u}_i-\mathrm{v}_i)\varepsilon_i^{-\chi}$
Pressure gradient force, $\mathbf{f}_{\nabla p,i}$	$-V_{p,i}\nabla P_{d,i}$

where $1/m_{ij}=1/m_i+1/m_j$, $1/R^*=1/\left|\mathrm{R}_i\right|+1/\left|\mathrm{R}_j\right|$, $E^*=E/2(1-v^2)$,
$\hat{\boldsymbol{\omega}}_{ij}^n=\boldsymbol{\omega}_{ij}^n/\left|\boldsymbol{\omega}_{ij}^n\right|$, $\hat{\boldsymbol{\delta}}_t=\boldsymbol{\delta}_t/\left|\boldsymbol{\delta}_t\right|$, $\delta_{t,\max}=\mu_s\delta_n(2-v)/(2(1-v))$,
$\mathrm{v}_{ij}=\mathrm{v}_j-\mathrm{v}_i+\omega_j\times\mathrm{R}_j-\omega_i\times\mathrm{R}_i$, $\mathrm{v}_{n,ij}=(\mathrm{v}_{ij}\cdot\mathrm{n})\cdot\mathrm{n}$, $\mathrm{v}_{t,ij}=(\mathrm{v}_{ij}\times\mathrm{n})\times\mathrm{n}$,
$\chi=3.7-0.65\exp[-(1.5-\log_{10}\mathrm{Re}_i)^2/2]$, $C_{d0,i}=(0.63+4.8/\mathrm{Re}_i^{0.5})^2$,
$\mathrm{Re}_i=\rho_f d_{pi}\varepsilon_i\left|\mathbf{u}_i-\mathbf{v}_i\right|/\mu_f$.

Note that tangential forces ($\mathbf{f}_{ct,ij}$ + $\mathbf{f}_{dt,ij}$) should be replaced by $\mathbf{f}_{t,ij}$ when $\delta_t \geq \delta_{t,max}$.

Table 1. Components of forces and torques on particle i

Convective heat transfer

Convective heat transfer between particles and fluid has been extensively investigated since 1950s, and different equations have been proposed (Botterill, 1975; Wakao & Kaguei, 1982; Kunii & Levenspiel, 1991; Molerus & Wirth, 1997). Often, the convective heat transfer rate between particle i and fluid is calculated according to $Q_{i,f}=h_{i,conv}\cdot A_i\cdot(T_{f,i}-T_i)$, where A_i is the particle surface area, $T_{f,i}$ is fluid temperature in a computational cell where particle i is located, and $h_{i,conv}$ is the convective HTC. $h_{i,conv}$ is associated with the Nusselt number, which is a function of particle Reynolds number and gas Prandtl number, given by

$$Nu_i = h_{i,conv} d_{pi} / k_f = 2.0 + a \mathrm{Re}_i^b \mathrm{Pr}^{1/3} \quad (4)$$

where k_f and d_{pi} are the fluid thermal conductivity and particle diameter, respectively. Re_i is the local relative Reynolds number for particle i (Table 1). The gas (air) Prandtl number, Pr, is a material property. The constant, 2.0, represents the contribution by particle-fluid natural convection. a and b are two parameters that need to be evaluated. As suggested by Kunii and Levenspiel (1991), b=0.5, and a could range from 0.6 to 1.8, depending on the bed conditions.

For fluid-wall heat transfer, $Nu_D = h_{f,wall} D / k_f = 0.023 \mathrm{Re}^{0.8} \mathrm{Pr}^n$ is used to determine the heat transfer coefficient $h_{f,wall}$, where D is the hydraulic diameter, and the exponent n is 0.4 for heating, and 0.3 for cooling (Holman, 1981).

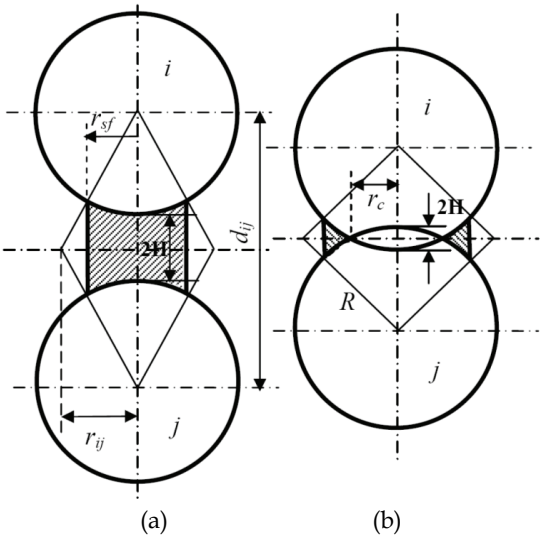

Fig. 1. Schematic of the relative positions of two spheres: (a) non-contact; and (b) contact with an overlap (Zhou et al., 2009)

Conductive heat transfer

Conduction between particles involves various mechanisms (Yagi & Kunii, 1957; Cheng et al., 1999), which mainly include (i) particle-fluid-particle conduction heat transfer; and (ii) particle-particle conduction heat transfer, as indicated in Fig. 1. The model details for those two mechanisms are described as follows.

Particle-fluid-particle heat transfer has been examined by various investigators (Delvosalle & Vanderschuren, 1985; Cheng et al., 1999). The model proposed by Cheng et al. (1999) is used here after some modification. According to this model, the heat transfer flux between spheres i and j is written as

$$Q_{i,j} = (T_j - T_i) \int_{r_{sij}}^{r_{sf}} \frac{2\pi \cdot r dr}{(\sqrt{R^2 - r^2} - r(R+H)/r_{ij}) \cdot \left(1/k_{pi} + 1/k_{pj}\right) + 2[(R+H) - \sqrt{R^2 - r^2}]/k_f} \quad (5)$$

where k_{pi} and k_{pj} are the thermal conductivities of particles i and j, respectively. For the details of parameters of H, r_{sf} and r_{ij}, see the reference of Zhou et al. (2009). The heat flux between two particles is ignored when the distance of 2H is greater than particle radius R.

Conduction heat transfer always occurs through the contacted area between particles or between particles and wall. Generally, such conduction heat transfer due to elastic deformation includes two mechanisms: conduction due to particle-particle static contact (particularly common in a packed bed) and conduction due to particle-particle collision, which occurs in a moving or fluidized bed. For conduction due to particle-particle static contact, the equation proposed by Batchelor and O'Brien (Batchelor & O'Brien, 1977) and modified by Cheng et al. (1999) is adopted. Thus, the heat flux $Q_{i,j}$ through the contact area between particles i and j can be calculated according to the equation below:

$$Q_{i,j} = \frac{4r_c(T_j - T_i)}{(1/k_{pi} + 1/k_{pj})} \tag{6}$$

Particle-particle heat transfer due to collision is normally determined by the model proposed by Sun and Chen (1988). Recently, Zhou et al. (2008) provided a modified equation that can be readily implemented in the DPS-CFD model:

$$Q_{i,j} = c' \frac{(T_j - T_i)\pi \ r_c^2 t_c^{-1/2}}{(\rho_{pi} c_{pi} k_{pi})^{-1/2} + (\rho_{pj} c_{pj} k_{pj})^{-1/2}} \tag{7}$$

where r_c and t_c are particle-particle contact radius and contact duration, respectively. To be consistent with the current model, r_c is obtained from the DEM simulation which is based on the Hertz elastic contact theory (see Table 1). For particle-wall static or collision contact, a wall can be treated as a particle with an infinite diameter and mass, as commonly used in the DEM work. Its properties are assumed to be the same as particles.

It should be noted that the two mechanisms represented by Eqs. (6) and (7) must be distinguished in computation (Zhou et al., 2009). For fixed beds, particle-particle contacts are all static. Thus only static contact heat transfer applies. For fluidized beds, two parameters are set: particle-particle collision time t_c, and particle-particle contact duration time t_d which can be obtained from simulation. For two colliding particles, if $t_c \geq t_d$, only collisional heat transfer applies. If $t_c < t_d$, two particles will keep in touch after collision. In such a case, collision heat transfer applies first during the time of t_c, and then static heat transfer during the time of $(t_d - t_c)$.

Radiative heat transfer

In a fixed or fluidized bed, a particle is surrounded by particles and fluid. In a specified enclosed cell, an environmental temperature is assumed to represent the enclosed surface temperature around such a particle. Thus, the equation used by Zhou et al. (2004) is slightly modified to calculate the heat flux due to radiation using a local environmental temperature to replace the bed temperature, and is written as (Zhou et al., 2009)

$$Q_{i,rad} = \sigma \varepsilon_{pi} A_i (T_{local,i}^4 - T_i^4) \tag{8}$$

where σ is the Stefan-Boltzmann constant, equal to 5.67×10^{-8} W/(m^2·K^4), and ε_{pi} is the sphere emissivity. Gas radiation is not considered due to low gas emissivities. The parameter $T_{local,i}$ is the averaged temperature of particles and fluid by volume fraction in a enclosed spherical domain Ω given by (Zhou et al., 2009)

$$T_{local,i} = \varepsilon_f T_{f,\Omega} + (1-\varepsilon_f)\frac{1}{k_\Omega}\sum_{j=1}^{k_\Omega} T_j (j \neq i) \tag{9}$$

where $T_{f,\Omega}$ and k_Ω are respectively the fluid temperature and the number of particles located in the domain Ω with its radius of $1.5d_p$. To be fully enclosed, a larger radius can be used.

2.2 Governing equations for fluid phase

The continuum fluid field is calculated from the continuity and Navier-Stokes equations based on the local mean variables over a computational cell, which can be written as (Xu et al., 2000)

$$\frac{\partial \varepsilon_f}{\partial t} + \nabla\cdot(\varepsilon_f \mathbf{u}) = 0 \tag{10}$$

$$\frac{\partial(\rho_f \varepsilon_f \mathbf{u})}{\partial t} + \nabla\cdot(\rho_f \varepsilon_f \mathbf{u}\mathbf{u}) = -\nabla p - \mathbf{F}_{fp} + \nabla\cdot\varepsilon_f\boldsymbol{\tau} + \rho_f \varepsilon_f \mathbf{g} \tag{11}$$

And by definition, the corresponding equation for heat transfer can be written as

$$\frac{\partial(\rho_f \varepsilon_f c_p T)}{\partial t} + \nabla\cdot(\rho_f \varepsilon_f \mathbf{u} c_p T) = \nabla\cdot(c_p \Gamma \nabla T) + \sum_{i=1}^{k_V} Q_{f,i} + Q_{f,wall} \tag{12}$$

where $\mathbf{u}$, ρ_f, p and $\mathbf{F}_{fp}\left(=(\sum_{i=1}^{k_V}\mathbf{f}_{f,i})/\Delta V\right)$ are the fluid velocity, density, pressure and volumetric fluid-particle interaction force, respectively, and k_V is the number of particles in a computational cell of volume ΔV. Γ is the fluid thermal diffusivity, defined by μ_e/σ_T, and σ_T the turbulence Prandtl number. $Q_{f,i}$ is the heat exchange rate between fluid and particle i which locates in a computational cell, and $Q_{f,wall}$ is the fluid-wall heat exchange rate.$\boldsymbol{\tau}$ $\left(=\mu_e[(\nabla\mathbf{u})+(\nabla\mathbf{u})^{-1}]\right)$ and ε_f $\left(=(1-(\sum_{i=1}^{k_V}V_{p,i})/\Delta V\right)$ are the fluid viscous stress tensor and porosity, respectively. $V_{p,i}$ is the volume of particle i (or part of the volume if the particle is not fully in the cell), μ_e the fluid effective viscosity determined by the standard k-ε turbulent model (Launder & Spalding, 1974).

2.3 Solutions and coupling schemes

The methods for numerical solution of DPS and CFD have been well established in the literature. For the DPS model, an explicit time integration method is used to solve the translational and rotational motions of discrete particles (Cundall & Strack, 1979). For the CFD model, the conventional SIMPLE method is used to solve the governing equations for the fluid phase (Patankar, 1980). The modelling of the solid flow by DPS is at the individual particle level, whilst the fluid flow by CFD is at the computational cell level. The coupling methodology of the two models at different length scales has been well documented (Xu & Yu, 1997; Feng & Yu, 2004; Zhu et al., 2007; Zhou et al., 2010b). The present model simply

extends that approach to include heat transfer, and more details can be seen in the reference of Zhou et al. (2009).

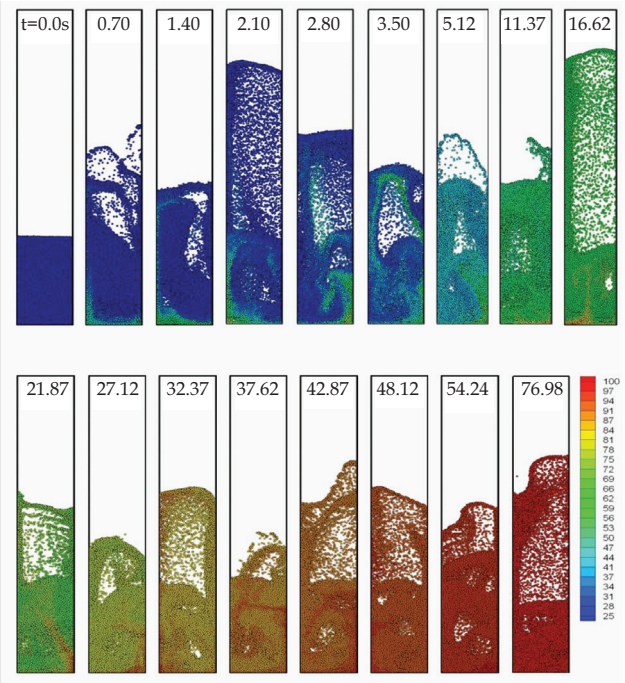

Fig. 2. Snapshots showing the heating process of fluidized bed by hot gas (1.2 m/s, 100°C) uniformly introduced from the bottom (Zhou et al., 2009).

3. Model application

3.1 Heat transfer in gas fluidization with non-cohesive particles

Gas fluidization is an operation by which solid particles are transformed into a fluid-like state through suspension in a gas (Kunii & Levenspiel, 1991). By varying gas velocity, different flow patterns can be generated from a fixed bed ($U<U_{mf}$) to a fluidzied bed. The solid flow patterns in a fluidized bed are transient and vary with time, as shown in Fig. 2, which also illustrates the variation of particle temperature. Particles located at the bottom are heated first, and flow upward dragged by gas. Particles with low temperatures descend and fill the space left by those hot particles. Due to the strong mixing and high gas-particle heat transfer rate, the whole bed is heated quickly, and reaches the gas inlet temperature at around 70 s. The general features observed are qualitatively in good agreement with those reported in the literature, confirming the predictability of the proposed DPS-CFD model in dealing with the gas-solid flow and heat transfer in gas fluidization.

The cooling of copper spheres at different initial locations in a gas fluidzied bed was examined by the model (Zhou et al., 2009). In physical experiments, the temperature of hot spheres is measured using thermocouples connected to the spheres (Collier et al., 2004; Scott

et al., 2004). But the cooling process of such hot spheres can be easily traced and recorded in the DPS-CFD simulations, as shown in Fig. 3a. The predicted temperature is comparable with the measured one. The cooling curves of 9 hot spheres are slightly different due to their different local fluid flow and particle structures. In the fixed bed, such a difference is mainly contributed to the difference in the local structures surrounding the hot sphere. But in the fluidized bed, it is mainly contributed to the transient local structure and particle-particle contacts or collisions. Those factors determine the variation of the time-averaged HTCs of hot spheres in a fluidized bed.

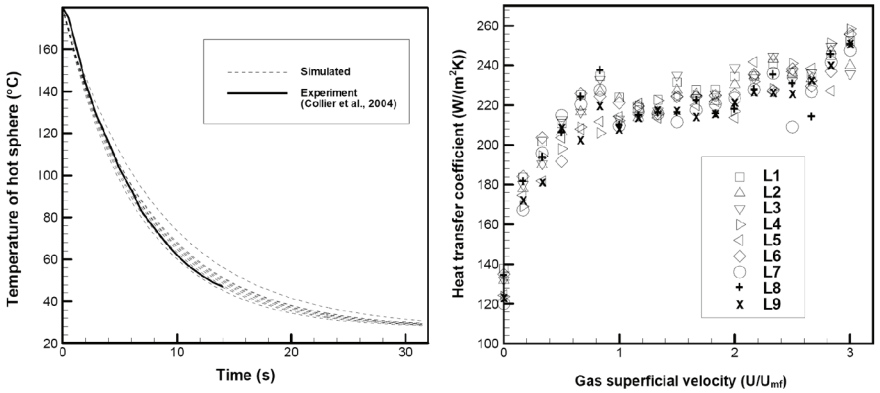

a) b)

Fig. 3. (a) Temperature evolution of 9 hot spheres when gas superficial velocity is 0.42 m/s; and (b) time-averaged heat transfer coefficients of the 9 hot spheres as a function of gas superficial velocity (Zhou et al., 2009).

The comparison of the HTC-U relationship between the simulated and the measured was made (Zhou et al., 2009). In physical experiments, Collier et al. (2004) and Scott et al. (2004) used different materials to examine the HTCs of hot spheres, and found that there is a general tendencyfor the HTC of hot sphere increasing first with gas superficial velocity in the fixed bed ($U<U_{mf}$), and then remaining constant, independent on the gas superficial velocities for fluidized beds ($U>U_{mf}$). The DPS-CFD simulation results also exhibit such a feature (Fig. 3b). For packed beds, the time-averaged HTC increases with gas superficial velocity, and reaches its maximum at around $U=U_{mf}$. After the bed is fluidized, the HTC is almost constant in a large range.

The HTC-U relationship is affected significantly by the thermal conductivity of bed particles (Zhou et al., 2009). The higher the k_p, the higher the HTC of hot spheres (Fig. 4). For exmaple, when k_p=30 W/(m·K), the predicted HTC in the fixed bed ($U/U_{mf}<1$) is so high that the trend of HTC-U relationship shown in Fig. 3b is totally changed. The HTC decreases with U in the fixed bed, then may reach a constant HTC in the fluidized bed. But when thermal conductivity of particles is low, the HTC always increases with U, independent of bed state (Fig. 4a). Fig. 4b further explains the variation trend of HTC with U. Generally, the convective HTC increases with U; but conductive HTC decreases with U. For a proper particle thermal conductivity, i.e. 0.84 W/(m·K), the two contributions (convective HTC and conductive HTC) could compensate each other, then the total HTC is nearly constant after

the bed is fluidized. So HTC independence of U is valid under this condition. But if particle thermal conductivity is too low or too high, the relationship of HTC and U can be different, as illustrated in Fig. 4a.

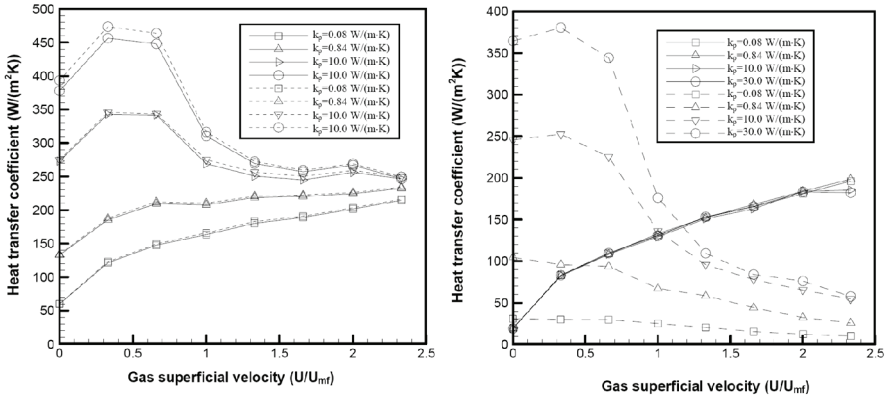

a) b)

Fig. 4. Time-averaged heat transfer coefficients of one hot sphere: (a) total HTC calculated by different equations; and (b) convective HTC (solid line) and conductive HTC (dashed line) for different thermal conductivities (Zhou et al., 2009).

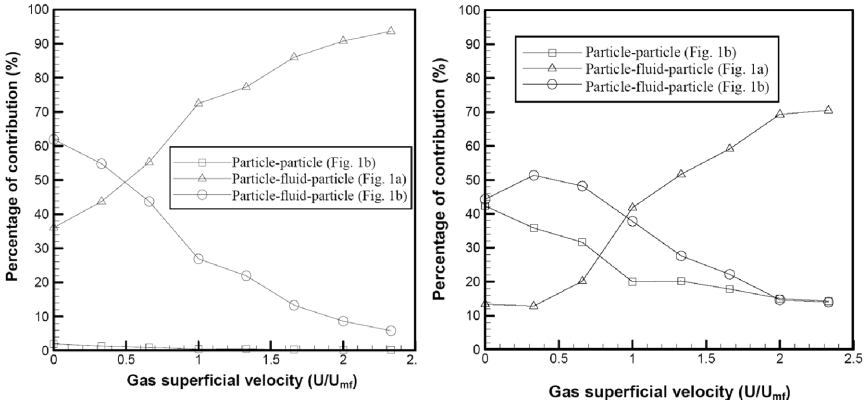

a) b)

Fig. 5. Contributions to conduction heat transfer by different heat transfer mechanisms when (a) k_p=0.08 W/(m·K); and (b) k_p=30 W/(m·K) (Zhou et al., 2009).

The proposed DPS-CFD model can be used to analyze the sub-mechanisms shown in Fig. 1a for conduction. The relative contributions by these heat transfer paths were quantified (Zhou et al., 2009). For example, when k_p=0.08 W/(m·K), particle-fluid-particle conduction always contributes more than particle-particle contact, but both vary with gas superficial velocity (Fig. 5a). For particle-fluid-particle conduction, particle-fluid-particle heat transfer with two contacting particles is far more important than that with two non-contacting

particles in the fixed bed. Zhou et al. (2009) explained that it is because the hot sphere contacts about 6 particles when $U<U_{mf}$. But such a feature changes in the fluidized bed ($U>U_{mf}$), where particle-fluid-particle conduction between non-contacting particles is relatively more important. This is because most of particle-particle contacts with an overlap are gradually destroyed with increasing gas superficial velocity, which significantly reduces the contribution by particle-fluid-particle between two contacting particles. However, particle-particle conduction through the contacting area becomes more important with an increase of particle thermal conductivity. The percentage of its contribution is up to 42% in the fixed bed when k_p=30 W/(m·K), then reduces to around 15% in the fluidized bed (Fig. 5b). Correspondingly, the contribution percentage by particle-fluid-particle heat transfer is lower, but the trend of variation with U is similar to that for k_p=0.08 W/(m·K).

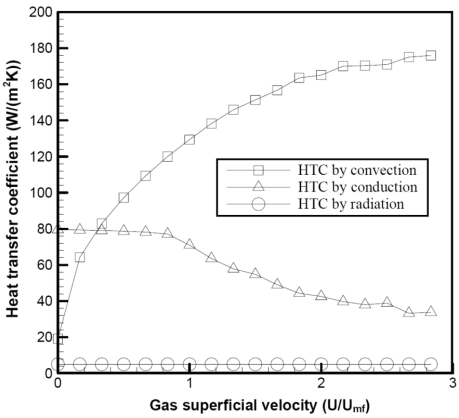

Fig. 6. Bed-averaged convective, conductive and radiative heat transfer coefficients as a function of gas superficial velocity (Zhou et al., 2009).

It should be noted that a fluid bed has many particles. A limited number of hot spheres cannot fully represent the averaged thermal behaviour of all particles in a bed. Thus, Zhou et al. (2009) further examined the HTCs of all the particles, and found that the features are similar to those observed for hot spheres (Fig. 6). The similarity illustrates that the hot sphere approach can, at least partially, represent the general features of particle thermal behaviour in a particle-fluid bed. Overall, the particles in a uniformly fluidized bed behave similarly. But a particle may behave differently from another at a given time. Zhou et al. (2009) examined the probability density distributions of time-averaged HTCs due to particle-fluid convection and particle conduction, respectively (Fig. 7). The convective HTC in the packed bed varies in a small range due to the stable particle structure. Then the distribution curve moves to the right as U increases, indicating the increase of convective HTC. The distribution curve also becomes wider. It is explained that, in a fluidized bed, clusters and bubbles can be formed, and the local flow structures surrounding particles vary in a large range. The density distribution of time-averaged HTCs by conduction shows that it has a wider distribution in a fixed bed (curves 1, 2 and 3) (Fig. 7b), indicating different local packing structures of particles. But curves 1 and 2 are similar. It is explained that, statistically, the two bed packing structures are similar, and do not vary much even if U is different. When $U>U_{mf}$ (e.g. $U=2.0U_{mf}$), the distribution curve moves to the left, indicating

the heat transfer due to interparticle conduction is reduced. The bed particles occasionally collide and contact each other. Statistically, the number of collisions and contacts are similar in fully fluidized beds, and not affected significantly by gas superficial velocities. Those features are consistent with those observed using the hot sphere approach. It confirms that hot sphere approach can represent the thermal behaviour of all bed particles to some degree.

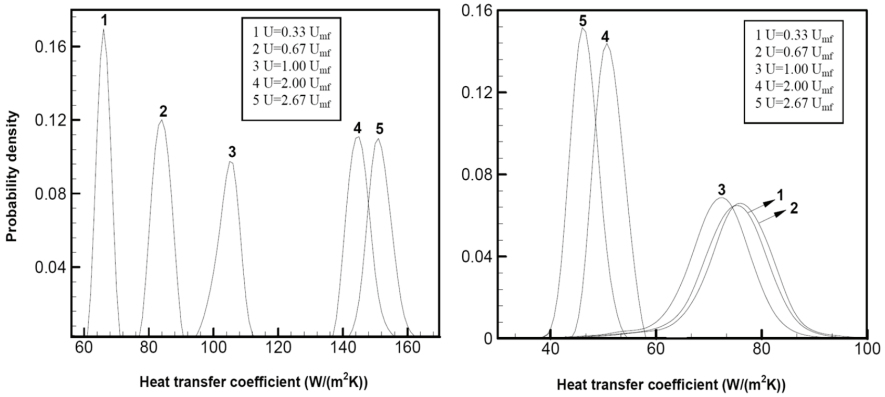

Fig. 7. Probability density distributions of time-averaged heat transfer coefficients of particles at different gas superficial velocities: (a), fluid convection; and (b), particle conduction (Zhou et al., 2009).

The particle thermal behaviour in a fluidized bed is affected by bed temperature. Zhou et al. (2009) carried out a simulation case at high tempertaure of 1000°C. It illustrated that the radiative HTC reaches 300 W/(m²·K), which is significantly larger than that for the case of hot gas with 100°C (around 5 W/(m²·K). The convective and radiative HTCs do not remain constant during the bed heating due to the variation of gas properties with temperature. The conductive heat transfer coefficient is not affected much by the bed temperature. This is because the conductive HTC is quite small in the fluidized bed, and only related to the gas and particle thermal conductivities.

3.2 Effective thermal conductivity in a packed bed.

Effective thermal conductivity (ETC) is an important parameter describing the thermal behaviour of packed beds with a stagnant or dynamic fluid, and has been extensively investigated experimentally and theoretically in the past. Various mathematical models, including continuum models and microscopic models, have been proposed to help solve this problem, but they are often limited by the homogeneity assumption in a continuum model (Zehner & Schlünder, 1970; Wakao & Kaguei, 1982) or the simple assumptions in a microscopic model (Kobayashi et al., 1991; Argento & Bouvard, 1996). Cheng et al. (1999; 2003) proposed a structure-based approach, and successfully predicted the ETC and analyzed the heat transfer mechanisms in a packed bed with stagnant fluid. Such efforts have also been made by other investigators (Vargas & McCarthy, 2001; Vargas & McCarthy, 2002a; b; Cheng, 2003; Siu & Lee, 2004; Feng et al., 2008). The proposed structured-based approach has been extended to account for the major heat transfer mechanisms in the calculation of ETC of a packed bed with a stagnant fluid (Cheng, 2003). But it is not so

adaptable or general due to the complexity in the determination of the packing structure and the ignorance of fluid flow in a packed bed. The proposed DPS-CFD model has shown a promising advantage in predicting the ETC under the different conditions (Zhou et al., 2009; 2010a).

Crane and Vachon (1977) summarized the experimental data in the literature, and some of them were further collected by Cheng et al. (1999) to validate their structure-based model (for example, see data from (Kannuluik & Martin, 1933; Schumann & Voss, 1934; Waddams, 1944; Wilhelm et al., 1948; Verschoor & Schuit, 1951; Preston, 1957; Yagi & Kunii, 1957; Gorring & Churchill, 1961; Krupiczka, 1967; Fountain & West, 1970)). Our work makes use of their collected data. In the structure-based approach (Cheng et al., 1999), it is confirmed that the ETC calculation is independent of the cube size sampled from a packed bed when each cube side is greater than 8 particle diameters. Zhou et al. (2009; 2010a) gave the details on how to determine the bed ETC. The size of the generated packed bed used is $13d_p \times 13d_p \times 16d_p$. 2,500 particles with diameter 2 mm and density 1000 kg/m^3 are packed to form a bed by gravity. Then the ETC of the bed is determined by the following method: the temperatures at the bed bottom and top are set constants, T_b=125°C and T_t=25°C, respectively. Then a uniform heat flux, q (W/m^2), is generated and passes from the bottom to the top. The side faces are assumed to be adiabatic to produce the un-directional heat flux. Thus, the bed ETC is calculated by $k_e = q \cdot H_b / (T_b - T_t)$, where H_b is the height between the two layers with two constant temperatures at the top and the bottom, respectively.

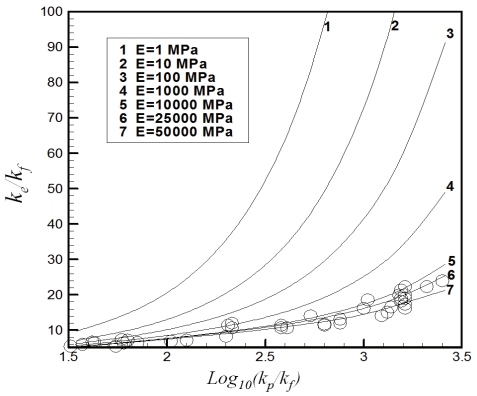

Fig. 8. Effect of Young's modulus E on the bed ETC (the experimental data represented by circles are from the collection of Cheng et al. (1999)) (Zhou et al., 2010a).

Young's modulus is an important parameter affecting the particle-particle overlap, hence the particle-particle heat transfer (Zhou et al., 2010a). Fig. 8 shows the predicted ETC for different Young's modulus varying from 1 MPa to 50 GPa. When E is around 50 GPa, which is in the range of real hard materials like glass beads, the predicted ETC are comparable with experiments. The high ETC for low Young's modulus is caused by the overestimated particle-particle overlap in the DPS based on the soft-sphere approach. A large overlap significantly increases the heat flux Q_{ij}. However, in the DPS, it is computationally very demanding to carry out the simulation using a real Young's modulus (often at an order of 10^3~10^5 MPa), particularly when involving a large number of particles. This is because a high Young's modulus requires extremely small time steps to obtain accurate results,

resulting in a high computational cost which may not be tolerated under the current computational capacity. The relationship often used for determining the time step is in the form of $\Delta t \propto \sqrt{m/k}$, where k is the particle stiffness. The higher the stiffness, the smaller the time step. It is therefore very helpful to have a method that can produce accurate results but does not have a high computational cost.

The calculation of heat fluxes for conduction heat transfer mechanisms is related to an important parameter: particle-particle contact radius r_c, as seen in Eqs. (6) and (7) Unfortunately, DPS simulation developed on the basis of soft-sphere approach usually overestimates r_c due to the use of low Young's modulus. The overestimation of r_c then significantly affects the calculation of conductive heat fluxes. To reduce such an over-prediction, a correction coefficient c is introduced, and then the particle-particle contact radius used to calculate the heat flux between particles through the contact area is written as

$$r_c{}' = c \cdot r_c \tag{13}$$

where r_c' is the reduced contact radius by correction coefficient c which varies between 0 and 1, depending on the magnitude of Young's modulus used in the DPS. The determination of c is based on the Hertzian theory, and can be written as (Zhou et al., 2010a)

$$c = r_{c,0}/r_c = (E_{ij}/E_{ij,0})^{1/5} \tag{14}$$

where $E_{ij} = 4/3[(1-\nu_i^2)/E_i + (1-\nu_j^2)/E_j]$, $E_{ij,0} = 4/3[(1-\nu_i^2)/E_{i,0} + (1-\nu_j^2)/E_{j,0}]$, ν is passion ratio, and E_i is the Young's modulus used in the DPS. It can be observed that, to determine the introduced correction coefficient c, two parameters are required: E_{ij}, the value of Young's modulus used in the DPS simulation and $E_{ij,0}$, the real value of Young's modulus of the materials considered. Different materials have different Young's modulus E_0. Then the obtained correction coefficients by Eq. (14) are also different, as shown in Fig. 9a. Fig. 9b further shows the applications of the otained correction coefficeints in some cases, where the particle thermal conductivity varied from 1.0 to 80 W/(m·K); gas thermal conductivities varied from 0.18 to 0.38 W/(m·K); Young's modulus used in the DPS varies from 1 MPa to 1 GPa, and the real value of Young's modulus is set to 50 GPa. The results show that the predicted ETCs are well comparable with experiments.

There are many factors influencing the ETC of a packed bed. The main factors are the thermal conductivities of the solid and fluid phases. Other factors include particle size, particle shape, packing method that gives different packing structures, bed temperature, fluid flow and other properties. Zhou et al. (2010a) examined the effects of some parameters on ETC, and revealed tha ETC is not sensitive to particle-particle sliding friction coefficient which varies from 0.1 to 0.8. ETC increases with the increase of bed average temperature, which is consistent with the observation in the literature (Wakao & Kaguei, 1982). The predicted ETC at 1475°C can be about 5 times larger than that at 75°C. The effect of particle size on ETC is more complicated. At low thermal conductivity ratios of k_p/k_f, the ETC varies little with particle size from 250 μm to 10 mm. But it is not the case for particles with high thermal conductivity ratios, where the ETC increases with particle size. The main reason could be that the particle-particle contact area is relatively large for large particles, and consequently, the increase of k_p/k_f enhances the conductive heat transfer between particles. However, that ETC is affected by particle size offers an explanation as to why the literature

data are so scattered. This is because different sized particles were used in experiments. For particles smaller than 500 μm, the predicted ETC is lower than that measured for high k_p/k_f ratios. This is because large particles were used in the reported experiments. Further studies are required to quantify the effect of particle size on the bed ETC under the complex conditions with moving fluid, size distributions or high bed temperature corresponding to those in experiments (Khraisha, 2002; Fjellerup et al., 2003; Moreira et al., 2005).

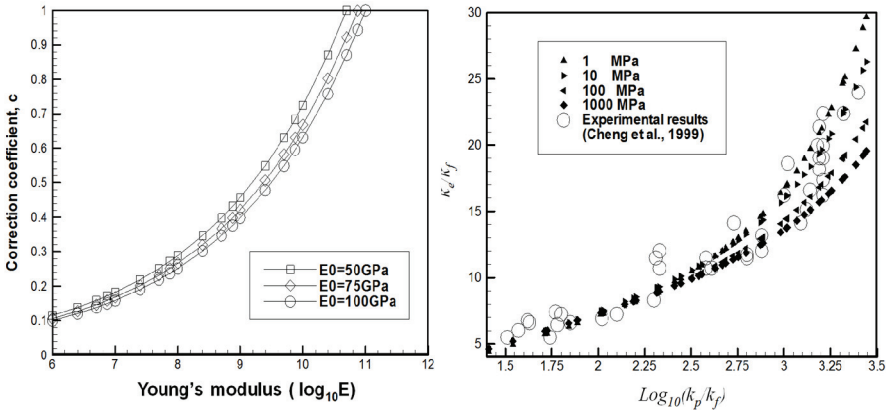

a) b)

Fig. 9. (a) Relationship between correction coefficient and Young's modulus E used in the DPS, and (b) the predicted ETCs as a function of k_p/k_f ratios for different E using the obtained correction coefficients according to Eq. (14) where E_0=50 GPa (Zhou et al., 2010a).

The approach of introduction of correction coefficient has also been applied to gas fluidization to test its applicability. An example of flow patterns has been shown in Fig. 2, which illustrates a heating process of the fluidized bed by hot gas (Zhou et al., 2009). The proposed modified model by an introduction of correction coefficient in this work can still reproduce those general features of solid flow patterns and temperature evolution with time using low Young's modulus, and the obtained results are comparable to those reported by Zhou et al. (2009) using a high Young's modulus. Zhou et al. (2010a) compared the obtained average convective and conductive heat transfer coefficients by three treatments: (1) $E=E_0$=50 GPa, and c=1.0; (2) E=10 MPa, and c=1.0; and (3) E=10 MPa, and c=0.182. Treatment 1 corresponds to the real materials, and its implementation requires a small time step. Treatments 2 and 3 reduce the Young's modulus so that a large time step is applicable. The difference between them is one with reduced contact radius (c=0.182 in treatment 3), and another not (c=1 in treatment 2). The results are shown in Fig. 10. The convective heat transfer coefficient is not affected by those treatments (Fig. 10a). Particle-particle contact only affects the conduction heat transfer (Fig. 10b). The results are very comparable and consistent between the models using treatments 1 and 3, but they are quite different from the model using the treatment 2. If the particle thermal conductivity is high, such difference becomes even more significant. The comparison in Fig. 10b indicates that the modified model by treatment 3 can be used in the study of heat transfer not only in packed beds but also in fluidization beds. It must be pointed out that the significance of proposed modified

model (treatment 3) is to save computational cost. For the current case shown in Fig. 10, the use of a low Young's modulus significantly reduces the computational time, i.e. 4~5 times faster with 16,000 particles. Such a reduction becomes more significant for a larger system involving a large number of particles.

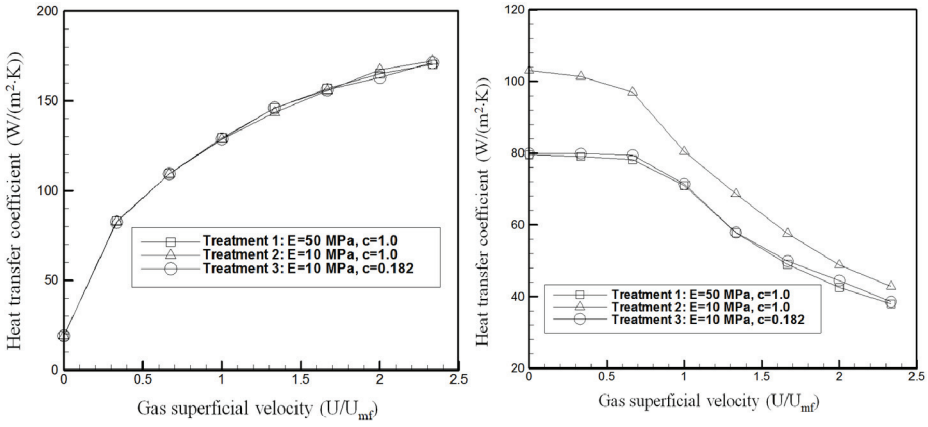

Fig. 10. Average convective heat transfer coefficient (a) and conductive heat transfer coefficient (b) of bed particles with different gas superficial velocities (k_p=0.84 W/(m·K)).

3.3 Heat transfer between a fluidized bed and an insert tube

Immersed surfaces such as horizontal/vertical tubes, fins and water walls are usually adopted in a fluidized bed to control the heat addition or extraction (Chen, 1998). Understanding the flow and heat transfer mechanisms is important to achieve its optimal design and control (Chen et al., 2005). The relation of the HTC of a tube and gas-solid flow characteristic in the vicinity of the tube such as particle residence time and porosity has been investigated experimentally using heat-transfer probe and positron emission particle tracking (PEPT) method or an optical probe (Kim et al., 2003; Wong & Seville, 2006; Masoumifard et al., 2008). The variations of HTC with probe positions and inlet gas superficial velocity are interpreted mechanistically. The observed angular variation of HTC is explained by the PEPT data.

Alternatively, the DPS-CFD approach has been used to study the flow and heat transfer in fluidization with an immersed tube in the literature (Wong & Seville, 2006; Di Maio et al., 2009; Zhao et al., 2009). Di Maio et al. (2009) compared different particle-to-particle heat transfer models and suggested that the formulation of these models are important to obtain comparable results to the experimental measurements. Zhao et al. (2009) used the unstructured mesh which is suitable for complex geometry and discussed the effects of particle diameter and superficial gas velocity. They obtained comparable prediction of HTC with experimental results at a low temperature. These studies show the applicability of the proposed DPS-CFD approach to a fluidized bed with an immersed tube. However, some important aspects are not considered in these studies. Firstly, their work is two dimensional with the bed thickness of one particle diameter. But as laterly pointed out by Feng and Yu (2010), three dimensional bed is more reliable to investigate the structure related

phenomena such as heat transfer. Secondly, the fluid properties such as fluid density and thermal conductivity are considered as constants. However, the variations of these properties have significant effect on the heat transfer process (Botterill et al., 1982; Pattipati & Wen, 1982). Thirdly, although the particle-particle heat transfer has proved to be critical for generation of sound results (Di Maio et al., 2009), the heat transfer through direct particle contact in these works simply combined static and collisional contacts mechanisms together, which are two important mechanisms particularly in a dynamic fluidized bed (Sun & Chen, 1988; Zhou et al., 2009). Finally, the radiative heat transfer mechanism is ignored, which is significant in a fluidized bed at high temperatures (Chen & Chen, 1981; Flamant & Arnaud, 1984; Chung & Welty, 1989; Flamant et al., 1992; Chen et al., 2005).

Recently, Hou et al. (2010a; 2010b) used the proposed DPS-CFD model to investigate the heat transfer in gas fluidization with an immersed horizontal tube in a three dimensional bed. The simulation conditions are similar to the experimental investigations by Wong and Seville (2006) except for the bed geometry. The predicted result of 0.27 m/s for minimum fluidization velocity (u_{mf}) is consistent with those experimental measurements (Chandran & Chen, 1982; Wong & Seville, 2006). Fig. 11 shows the snapshots of flow patterns obtained from the DPS-CFD simulation. The bubbling fluidized bed behaviour is significantly affected by the horizontal tube. Two main features can be identified: defluidized region in the downstream and the air film in the upstream (Glass & Harrison, 1964; Rong et al., 1999; Wong & Seville, 2006). Particles with small velocities tend to stay on the tube in the downstream and form the defluidized region intermittently. The thickness of the air film below the tube changes with time. There is no air film and the upstream section is fully filled with particles at some time intervals (e.g. t = 1.3 s and 3.0 s in Fig. 11).

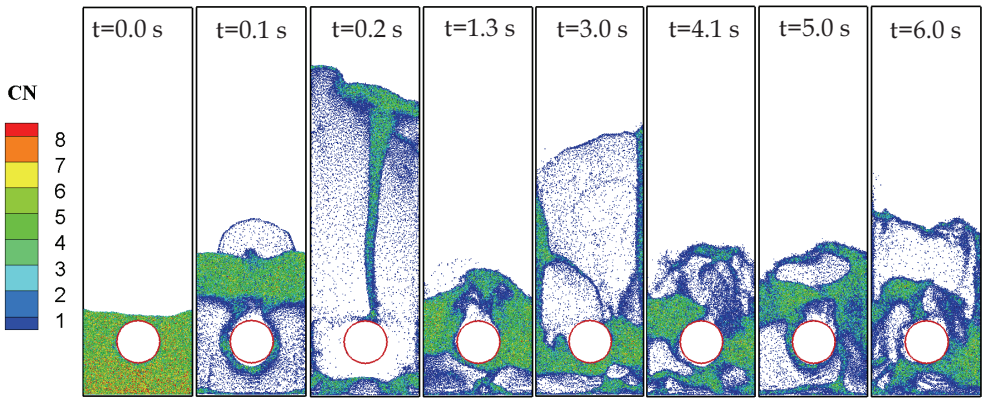

Fig. 11. Snapshots of solid flow pattern colored by coordination number of individual particles when u_{exc} = 0.50 m/s (Hou et al., 2010a).

The tube exchanges heat with its surrounding particles and fluid. The local HTC has a distribution closely related to these observed flow patterns. The distribution and magnitude of HTC are two factors commonly used to describe the heat transfer in such a system (Botterill et al., 1984; Schmidt & Renz, 2005; Wong & Seville, 2006). The effect of the gas velocity and the tube position are examined, showing consistent results with those reported in the literature (Botterill et al., 1984; Kim et al., 2003; Wong & Seville, 2006) (Fig. 12). The

local HTC is high at sides of the tube around 90° and 270° while it is low at the upstream and downstream of the tube around 0° and 180°. With the increase of gas velocity, the local HTC increases first and then decreases (Fig. 12a). The local HTC is also affected by tube positions, and increases with the increase of tube level within the bed static height as shown in Fig. 12b.

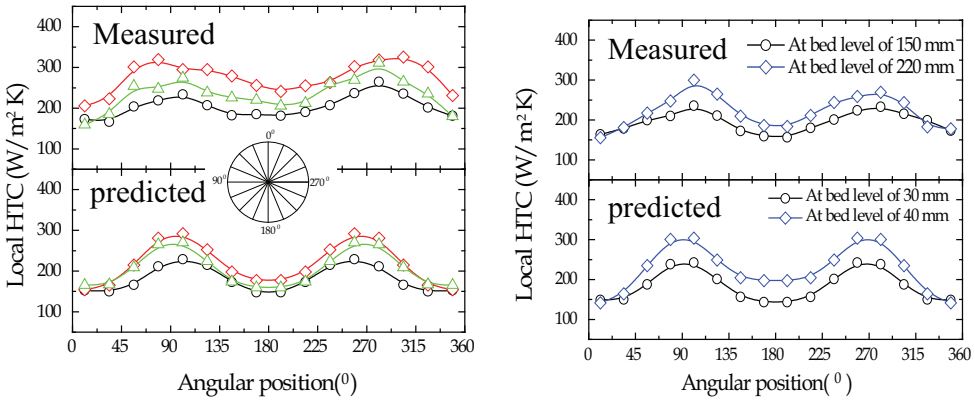

(a) (b)

Fig. 12. Comparison of local HTCs between the predicted (Hou et al., 2010a) and the measured (Wong & Seville, 2006): (a) local HTC distribution at different excess gas velocities (u_{exc}) (○, 0.08 m/s; ◊, 0.50 m/s; and Δ, 0.80 m/s); and (b) local HTC with different tube positions when u_{exc} = 0.20 m/s.

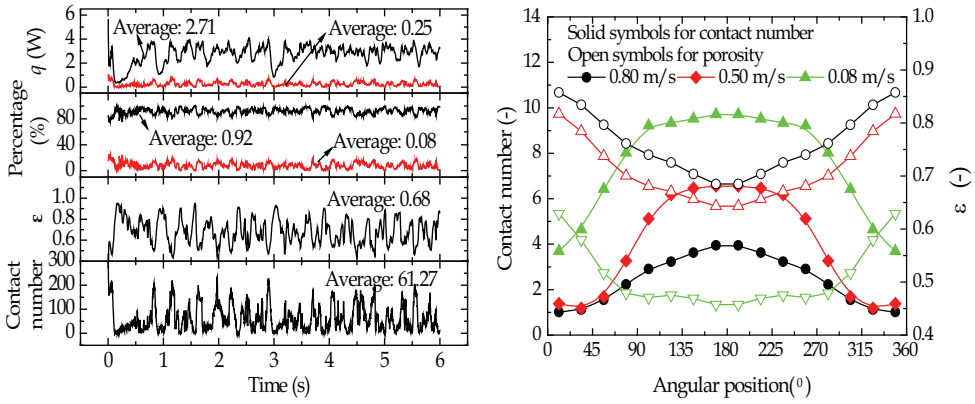

(a) (b)

Fig. 13. (a) Overall convective and conductive heat fluxes (q) and their percentages (—, convection; ⋯, conduction), overall contact number (CN) and overall porosity (ε) as a function of time, where u_{exc} = 0.40 m/s (the overall heat flux and CN are the sum of the corresponding values of each section and the overall porosity are the averaged value of all the sections), and (b) local porosity and CN with different u_{exc} (Hou et al., 2010a).

The heat is mainly transferred through convection between gas and particles and between gas and the tube, and conduction among particles and between particles and the tube at low temperature. As an example, Fig. 13a shows the total heat fluxes through convection and conduction (the radiative heat flux is quite small at low temperatures and is not discussed here). The convective and conductive heat fluxes vary temporally. Their percentages show that the convective heat transfer is dominant with a percentage over 90%. They are closely related to the microstructure around the tube, which can be indexed by the average porosity around the tube and by the contact number (CN) between the tube and the particles. The porosity and CN vary temporally depending on the complicated interactions between the particles and the tube and between the particles and fluid, which determine the flow pattern. Generally, a region with a larger CN corresponds to a defluidized region with a smaller porosity in the vicinity of the tube. Otherwise, it corresponds to a passing bubble where the porosity is larger and the CN is smaller. Fig. 13b further shows the distributuion of local porosity and CN. It can be seen that local porosity is larger in downstream sections and lower in upstream sections while local CN has an opposite distribution.

The heat transfer between an immersed tube and a fluidized bed depends on many factors, such as the contacts of particles with the tube, porosity and gas flow around the tube. These factors are affected by many variables related to operational conditions. Gas velocity is one of the most important parameters in affecting the heat transfer, which can be seen in Fig. 12. With the increase of u_{exc} from 0.08 to 0.50 m/s, the overall heat transfer coefficient increases. However, when the u_{exc} is further increased from 0.50 to 0.80 m/s, the heat transfer coefficient decreases. The effect of particle thermal conductivity k_p on the local HTC was also examined and shown in Fig. 14a (Hou et al., 2010a). The local HTC increases with the increase of k_p from 1.10 to 100 W/(m·K). However, such an increase is not significant for k_p from 100 to 300 W/(m·K). The variations of percentages of different heat transfer modes with k_p is further shown in Fig. 14b. When k_p is lower than 100 W/(m·K), the conductive heat transfer increases with the increase of k_p while the convective heat transfer decreases. Further increase of k_p has no significant effects.

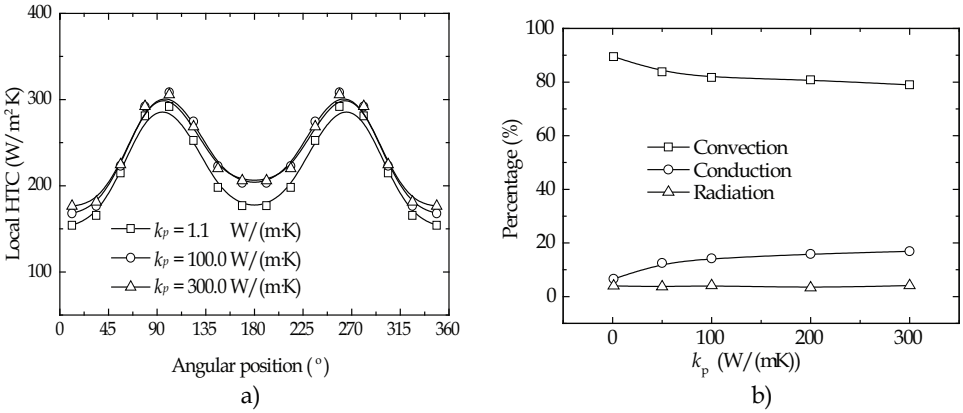

Fig. 14. Effect of k_p on: (a), local HTC; and (b), percentages of different heat fluxes; where u_{exc} = 0.50 m/s (Hou et al., 2010a).

The heat transfer by radiation is important in the considered system because the increase of environmental temperature of the tube, and its significance has already been pointed out in

the literature (see, for example, Mathur & Saxena, 1987; Chen et al., 2005). The effect of the tube temperature (T_s) on heat transfer characteristic was investigated in terms of the local HTC distribution and the heat fluxes by different heat transfer modes (Hou et al., 2010a). Fig. 15a shows that the local HTC increase with the increase of T_s. The increased trend of HTC agrees well with the results of the experiments (Botterill et al., 1984). The increase of gas thermal conductivity with temperature is one of the main reasons for the increase of HTC (Zhou et al., 2009). This manifests the importance of using the temperature related correlations of fluid properties. Variations of the heat fluxes with tube temperature T_s are shown in Fig. 15b. The conductive heat flux changes insignificantly. The convective heat flux increases linearly while the radiative heat fluxes increases exponentially with the increase of the T_s. Because of the increase of T_s, the difference between the environmental temperature (T_e) and the bed temperature (T_b) increases. The radiative heat flux increases more quickly than the convective heat flux according to the fourth power law of the temperature difference. The radiative heat flux becomes larger than that of conductive heat flux around T_s = 300°C and then, larger than that of the convective heat flux around T_s = 1200°C. These show that the radiation is an important heat transfer mode with high tube temperatures.

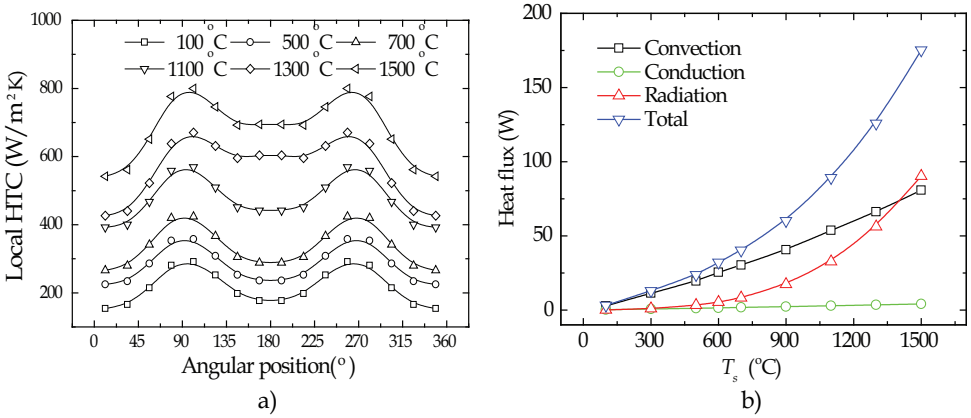

Fig. 15. Heat transfer behaviour at high tube temperatures: (a), variations of local HTC with different T_s, where u_{exc} = 0.50 m/s; and (b), convective, conductive, radiative and total heat fluxes as a function of T_s, where u_{exc} = 0.50 m/s (Hou et al., 2010a).

4. Conclusions

The DPS-CFD approach, originally applied to study the particle-fluid flow, has been extended to study the heat transfer in packed and bubbling fluidized beds at a particle scale. The proposed model is, either qualitatively or quantitatively depending on the observations in the literature, validated by comparing the predicted and measured results under different conditions. Three basic heat transfer modes (particle-fluid convection, particle conduction and radiation) are considered in the present model, and their contributions to the total heat transfer in a fixed or fluidized bed can be quantified and analyzed. The examples presented demonstrate that the DPS-CFD approach is very promising in quantifying the role of various heat transfer mechanisms in packed/fluidized beds, which is useful to the optimal design and control of fluid bed ractors.

5. References

Agarwal, P.K. (1991). Transport phenomena in multi-particle systems-IV. Heat transfer to a large freely moving particle in gas fluidized bed of smaller particles. *Chem. Eng. Sci.*, 46, 1115-1127

Anderson, T.B. & Jackson, R. (1967). Fluid mechanical description of fluidized beds-equations of motion. *Ind. Eng. Chem. Fund.*, 6, 527-539,0196-4313.

Argento, C. & Bouvard, D. (1996). Modeling the effective thermal conductivity of random packing of spheres through densification. *Int. J. Heat Mass Transfer*, 39, 1343-1350

Avedesia, M.M. & Davidson, J.F. (1973). Combustion of carbon particles in a fluidized-bed. *Trans. Inst. Chem. Eng.*, 51, 121-131,0046-9858.

Baskakov, A.P., Filippovskii, N.F., Munts, V.A. & Ashikhmin, A.A. (1987). Temperature of particles heated in a fluidized bed of inert material. *J. Eng. Phys.*, 52, 574-578,00220841.

Batchelor, G.K. & O'Brien, R.W. (1977). Thermal or electrical conduction through a granular material. *Proc. R. Soc. London, A*, 355, 313-333

Botterill, J.S.M. (1975). *Fluid-bed heat transfer*, Academic Press London, New York.

Botterill, J.S.M., Teoman, Y. & Yuregir, K.R. (1982). Minimum fluidization velocity at high-temperatures-comment. *Ind. Eng. Chem. Process Des. Dev.*, 21, 784-785,0196-4305.

Botterill, J.S.M., Teoman, Y. & Yuregir, K.R. (1984). Factors affecting heat transfer between gas-fluidized beds and immersed surfaces. *Powder Technol.*, 39, 177-189,0032-5910.

Chandran, R. & Chen, J.C. (1982). Bed-surface contact dynamics for horizontal tubes in fluidized beds. *AIChE J.*, 28, 907-914,0001-1541.

Chen, J.C. & Chen, K.L. (1981). Analysis of simultaneous radiative and conductive heat-transfer in fluidized-beds. *Chem. Eng. Commun.*, 9, 255-271,0098-6445.

Chen, J.C. (1998). Heat Transfer in Fluidized Beds. In: *Fluidization, Solids Handling, and Processing*, Y. Wen-Ching (Editor), pp. 153-208, William Andrew Publishing, 978-0-81-551427-5, Westwood, NJ.

Chen, J.C. (2003). Surface contact - Its significance for multiphase heat transfer: Diverse examples. *J. Heat Transfer-Trans. ASME*, 125, 549-566,0022-1481.

Chen, J.C., Grace, J.R. & Golriz, M.R. (2005). Heat transfer in fluidized beds: design methods. *Powder Technol.*, 150, 123-132

Cheng, G.J., Yu, A.B. & Zulli, P. (1999). Evaluation of effective thermal conductivity from the structure of a packed bed. *Chem. Eng. Sci.*, 54, 4199-4209

Cheng, G.J. (2003). Structural evaluation of the effective thermal conductivity of packed beds, the University of New South Wales.

Chung, T.Y. & Welty, J.R. (1989). Tube array heat transfer in fluidized beds- A study of particle size effects. *AIChE J.*, 35, 1170-1176,0001-1541.

Collier, A.P., Hayhurst, A.N., Richardson, J.L. & Scott, S.A. (2004). The heat transfer coefficient between a particle and a bed (packed or fluidised) of much larger particles. *Chem. Eng. Sci.*, 59, 4613-4620

Crane, R.A. & Vachon, R.I. (1977). A prediction of the bounds on the effective thermal conductivity of granular materials. *Int. J. Heat Mass Transfer*, 20, 711-723,0017-9310.

Cundall, P.A. & Strack, O.D.L. (1979). A discrete numerical-model for granular assemblies. *Geotechnique*, 29, 47-65,0016-8505.

Delvosalle, C. & Vanderschuren, J. (1985). Gas-to-particle and particle-to-particle heat transfer in fluidized beds of large particles. *Chem. Eng. Sci.*, 40, 769-779

Di Felice, R. (1994). The voidage function for fluid-particle interaction systems. *Int. J. Multiphase Flow*, 20, 153-159

Di Maio, F.P., Di Renzo, A. & Trevisan, D. (2009). Comparison of heat transfer models in DEM-CFD simulations of fluidized beds with an immersed probe. *Powder Technol.*, 193, 257-265,0032-5910.

Dong, X.F., Yu, A.B., Yagi, J.I. & Zulli, P. (2007). Modelling of multiphase flow in a blast furnace: Recent developments and future work. *ISIJ Int.*, 47, 1553-1570,0915-1559.

Enwald, H., Peirano, E. & Almstedt, A.E. (1996). Eulerian two-phase flow theory applied to fluidization. *Int. J. Multiphase Flow*, 22, 21-66

Ergun, S. (1952). Fluid flow through packed columns. *Chem. Eng. Prog.*, 48, 89-94,0360-7275.

Feng, Y.Q. & Yu, A.B. (2004). Assessment of model formulations in the discrete particle simulation of gas-solid flow. *Ind. Eng. Chem. Res.*, 43, 8378-8390,0888-5885.

Feng, Y.Q., Xu, B.H., Zhang, S.J., Yu, A.B. & Zulli, P. (2004). Discrete particle simulation of gas fluidization of particle mixtures. *AIChE J.*, 50, 1713-1728,1547-5905.

Feng, Y.Q. & Yu, A.B. (2007). Microdynamic modelling and analysis of the mixing and segregation of binary mixtures of particles in gas fluidization. *Chem. Eng. Sci.*, 62, 256-268,0009-2509.

Feng, Y.Q. & Yu, A.B. (2010). Effect of bed thickness on segregation behaviour of particle mixtures in a gas fluidized bed. *Ind. Eng. Chem. Res.*, 49, 3459–3468

Feng, Y.T., Han, K., Li, C.F. & Owen, D.R.J. (2008). Discrete thermal element modelling of heat conduction in particle systems: Basic formulations. *J. Comput. Phys.*, 227, 5072-5089,0021-9991.

Fjellerup, J., Henriksen, U., Jensen, A.D., Jensen, P.A. & Glarborg, P. (2003). Heat transfer in a fixed bed of straw char. *Energy Fuels*, 17, 1251-1258,0887-0624.

Flamant, G. & Arnaud, G. (1984). Analysis and theoretical study of high-temperature heat transfer between a wall and a fluidized bed. *Int. J. Heat Mass Transfer*, 27, 1725-1735

Flamant, G., Fatah, N. & Flitris, Y. (1992). Wall-to-bed heat transfer in gas--solid fluidized beds: Prediction of heat transfer regimes. *Powder Technol.*, 69, 223-230

Fountain, J.A. & West, E.A. (1970). Thermal conductivity of particulate basalt as a function of density in simulated lunar and martian environments. *J. Geophys. Res.*, 75, 4063-&,0148-0227.

Gidaspow, D. (1994). *Multiphase Flow and Fluidization*, Academic Press, San Diego.

Glass, D.H. & Harrison, D. (1964). Flow patterns near a solid obstacle in a fluidized bed. *Chem. Eng. Sci.*, 19, 1001-1002,0009-2509.

Gorring, R.L. & Churchill, S.W. (1961). Thermal conductivity of heterogeneous materials. *Chem. Eng. Prog.*, 57, 53-59

Holman, J.P. (1981). *Heat Transfer*, McGraw-Hill Company, 978-0070295988, New York.

Hou, Q.F., Zhou, Z.Y. & Yu, A.B. (2010a). Computational study of heat transfer in bubbling fluidized beds with a horizontal tube. AIChE J., submitted

Hou, Q.F., Zhou, Z.Y. & Yu, A.B. (2010b). Investigation of heat transfer in bubbling fluidization with an immersed tube. In: *6th International Symposium on Multiphase Flow, Heat Mass Transfer and Energy Conversion*, L.J. Guo, D.D. Joseph, Y. Matsumoto, M. Sommerfeld and Y.S. Wang (Editors), pp. 355-360, Amer Inst Physics, 978-0-7354-0744-2, Melville.

Ishii, M. (1975). *Thermo-fluid dynamic theory of two-phase flow*, Eyrolles, Paris.

Kaneko, Y., Shiojima, T. & Horio, M. (1999). DEM simulation of fluidized beds for gas-phase olefin polymerization. *Chem. Eng. Sci.*, 54, 5809-5821,0009-2509.

Kannuluik, W.G. & Martin, L.H. (1933). Conduction of heat in powders. *Proc. R. Soc. London, A-Containing Papers of a Mathematical and Physical Character*, 141, 144-158,0950-1207.

Khraisha, Y.H. (2002). Thermal conductivity of oil shale particles in a packed bed. *Energy Sources*, 24, 613-623,0090-8312.

Kim, S.W., Ahn, J.Y., Kim, S.D. & Lee, D.H. (2003). Heat transfer and bubble characteristics in a fluidized bed with immersed horizontal tube bundle. *Int. J. Heat Mass Transfer*, 46, 399-409,0017-9310.

Kobayashi, M., Maekwa, H., Nakamura, H. & Kondou, Y. (1991). Calculation of the mean thermal conductivity of heterogenious solid mixture with the Voronoi-Polyhedron element method. *Trans. Japan Soc. Mech. Eng. B*, 57, 1795-1801,03875016.

Krupiczka, R. (1967). Analysis of thermal conductivity in granular materials. *Int. Chem. Eng.*, 7, 122-144

Kunii, D. & Levenspiel, O. (1991). *Fluidization Engineering*, Butterworth-Heinemann, 978-0-409-90233-4, Boston.

Langston, P.A., Tuzun, U. & Heyes, D.M. (1994). Continuous potential discrete particle simulations of stress and velocity fields in hoppers: transition from fluid to granular flow. *Chem. Eng. Sci.*, 49, 1259-1275

Langston, P.A., Tuzun, U. & Heyes, D.M. (1995). Discrete Element Simulation of Internal-Stress and Flow-Fields in Funnel Flow Hoppers. *Powder Technol.*, 85, 153-169,0032-5910.

Launder, B.E. & Spalding, D.B. (1974). The numerical computation of turbulent flows. *Comput. Methods Appl. Mech. Eng.*, 3, 269-289

Li, J.T. & Mason, D.J. (2000). A computational investigation of transient heat transfer in pneumatic transport of granular particles. *Powder Technol.*, 112, 273-282,0032-5910.

Li, J.T. & Mason, D.J. (2002). Application of the discrete element modelling in air drying of particulate solids. *Drying Technol.*, 20, 255-282,0737-3937.

Masoumifard, N., Mostoufi, N., Hamidi, A.-A. & Sotudeh-Gharebagh, R. (2008). Investigation of heat transfer between a horizontal tube and gas-solid fluidized bed. *Int. J. Heat Fluid Flow*, 29, 1504-1511

Mathur, A. & Saxena, S.C. (1987). Total and radiative heat transfer to an immersed surface in a gas-fluidized bed. *AIChE J.*, 33, 1124-1135,0001-1541.

Mickley, H.S. & Fairbanks, D.F. (1955). Mechanism of heat transfer to fluidized beds. *AIChE J.*, 1, 374-384,0001-1541.

Molerus, O. & Wirth, K.E. (1997). *Heat transfer in fluidized beds*, Chapman and Hall, 978-0-412-60800-1, London.

Moreira, M.F.P., Thomeo, J.C. & Freire, J.T. (2005). Analysis of the heat transfer in a packed bed with cocurrent gas-liquid upflow. *Ind. Eng. Chem. Res.*, 44, 4142-4146,0888-5885.

Oka, S.N. (2004). *Fluidized bed combustion*, Marcel Dekker, Inc., New York.

Omori, Y. (1987). *Blast Furnace Phenomena and Modelling*, Elsevier Applied Science, 978-1-85166-057-5, London.

Parmar, M.S. & Hayhurst, A.N. (2002). The heat transfer coefficient for a freely moving sphere in a bubbling fluidised bed. *Chem. Eng. Sci.*, 57, 3485-3494

Patankar, S.V. (1980). *Numerical heat transfer and fluid flow*, Hemisphere, 978-0891165224, New York.

Pattipati, R.R. & Wen, C.Y. (1982). Minimum fluidization velocity at high-temperatures-response. *Ind. Eng. Chem. Process Des. Dev.*, 21, 785-786,0196-4305.

Peters, B. (2002). Measurements and application of a discrete particle model (DPM) to simulate combustion of a packed bed of individual fuel particles. *Combust. Flame*, 131, 132-146,0010-2180.

Preston, F.W. (1957). Mechanism of heat transfer in unconsolidated porous medi at low flow rates, Pennsylvania.

Prins, W., Draijer, W. & van Swaaij, W.P.M. (1985). Heat transfer to immersed spheres fixed or freely moving in a gas-fluidized bed, 20th Proceedings of the International Centre for Heat and Mass Transfer. Heat and mass transfer in fixed and fluidized beds. Washington: Hemisphere, pp. 317-331.

Rong, D.G. & Horio, M. (1999). DEM simulation of char combustion in a fluidized bed, Second International Conference on CFD in the Minerals and Process Industries,pp. 65-70, CD-ROM.

Rong, D.G., Mikami, T. & Horio, M. (1999). Particle and bubble movements around tubes immersed in fluidized beds - a numerical study. *Chem. Eng. Sci.*, 54, 5737-5754,0009-2509.

Schmidt, A. & Renz, U. (2005). Numerical prediction of heat transfer between a bubbling fluidized bed and an immersed tube bundle. *Heat Mass Transfer*, 41, 257-270,0947-7411.

Schumann, T.E.W. & Voss, V. (1934). Heat flow through granulated material. *Fuel*, 13, 249-256

Scott, S.A., Davidson, J.F., Dennis, J.S. & Hayhurst, A.N. (2004). Heat transfer to a single sphere immersed in beds of particles supplied by gas at rates above and below minimum fluidization. *Ind. Eng. Chem. Res.*, 43, 5632-5644,0888-5885.

Siu, W.W.M. & Lee, S.H.K. (2004). Transient temperature computation of spheres in three-dimensional random packings. *Int. J. Heat Mass Transfer*, 47, 887-898,0017-9310.

Sun, J. & Chen, M.M. (1988). A theoretical analysis of heat transfer due to particle impact. *Int. J. Heat Mass Transfer*, 31, 969-975

Tsuji, Y., Tanaka, T. & Ishida, T. (1992). Lagrangian numerical simulation of plug flow of cohesionless particles in a horizontal pipe. *Powder Technol.*, 71, 239-250

Vargas, W.L. & McCarthy, J.J. (2001). Heat conduction in granular materials. *AIChE J.*, 47, 1052-1059,1547-5905.

Vargas, W.L. & McCarthy, J.J. (2002a). Conductivity of granular media with stagnant interstitial fluids via thermal particle dynamics simulation. *Int. J. Heat Mass Transfer*, 45, 4847-4856,0017-9310.

Vargas, W.L. & McCarthy, J.J. (2002b). Stress effects on the conductivity of particulate beds. *Chem. Eng. Sci.*, 57, 3119-3131,0009-2509.

Verschoor, H. & Schuit, G. (1951). Heat transfer to fluids flowing through a bed of granular solids. *Appl. Sci. Res.*, 2, 97-119,0003-6994.

Waddams, A.L. (1944). The flow of heat through granular material. *J. Soc. Chem. Ind.*, 63, 337-340

Wakao, N. & Kaguei, S. (1982). *Heat and Mass Transfer in Packed Beds*, Gordon and Breach Science Publishers, New York.

Wen, C.Y. & Yu, Y.H. (1966). Mechanics of fluidization,pp. 100-111,

Wilhelm, R.H., Johnson, W.C., Wynkoop, R. & Collier, D.W. (1948). Reaction rate, heat transfer, and temperature distribution in fixed-bed catalytic converters - solution by electrical network. *Chem. Eng. Prog.*, 44, 105-116,0360-7275.

Wong, Y.S. & Seville, J.P.K. (2006). Single-particle motion and heat transfer in fluidized beds. *AIChE J.*, 52, 4099-4109,0001-1541.

Xu, B.H. & Yu, A.B. (1997). Numerical simulation of the gas-solid flow in a fluidized bed by combining discrete particle method with computational fluid dynamics. *Chem. Eng. Sci.*, 52, 2785-2809

Xu, B.H. & Yu, A.B. (1998). Comments on the paper "Numerical simulation of the gas-solid flow in a fluidized bed by combining discrete particle method with computational fluid dynamics" - Reply. *Chem. Eng. Sci.*, 53, 2646-2647,0009-2509.

Xu, B.H., Yu, A.B., Chew, S.J. & Zulli, P. (2000). Numerical simulation of the gas-solid flow in a bed with lateral gas blasting. *Powder Technol.*, 109, 13-26

Yagi, S. & Kunii, D. (1957). Studies on effective thermal conductivities in packed beds. *AIChE J.*, 3, 373-381,0001-1541.

Yang, R.Y., Zou, R.P. & Yu, A.B. (2000). Computer simulation of the packing of fine particles. *Phys. Rev. E*, 62, 3900-3908

Yu, A.B. & Xu, B.H. (2003). Particle-scale modelling of gas-solid flow in fluidisation. *J. Chem. Technol. Biotechnol.*, 78, 111-121,0268-2575.

Zehner, P. & Schlünder, E.U. (1970). Thermal conductivity of packed beds (in German). *Chem. Ing. Tech.*, 42, 933-941,1522-2640.

Zhao, Y.Z., Jiang, M.Q., Liu, Y.L. & Zheng, J.Y. (2009). Particle-scale simulation of the flow and heat transfer behaviors in fluidized bed with immersed tube. *AIChE J.*, 55, 3109-3124,1547-5905.

Zhou, H.S., Flamant, G., Gauthier, D. & Flitris, Y. (2003). Simulation of coal combustion in a bubbling fluidized bed by distinct element method. *Chem. Eng. Res. Des.*, 81, 1144-1149,0263-8762.

Zhou, H.S., Flamant, G. & Gauthier, D. (2004). DEM-LES simulation of coal combustion in a bubbling fluidized bed Part II: coal combustion at the particle level. *Chem. Eng. Sci.*, 59, 4205-4215,0009-2509.

Zhou, J.H., Yu, A.B. & Horio, M. (2008). Finite element modeling of the transient heat conduction between colliding particles. *Chem. Eng. J.*, 139, 510-516,1385-8947.

Zhou, Y.C., Wright, B.D., Yang, R.Y., Xu, B.H. & Yu, A.B. (1999). Rolling friction in the dynamic simulation of sandpile formation. *Physica A*, 269, 536-553

Zhou, Z.Y., Yu, A.B. & Zulli, P. (2009). Particle scale study of heat transfer in packed and bubbling fluidized beds. *AIChE J.*, 55, 868-884,1547-5905.

Zhou, Z.Y., Yu, A.B. & Zulli, P. (2010a). A new computational method for studying heat transfer in fluid bed reactors. *Powder Technol.*, 197, 102-110,0032-5910.

Zhou, Z.Y., Kuang, S.B., Chu, K.W. & Yu, A.B. (2010b). Discrete particle simulation of particle-fluid flow: Model formulations and their applicability. *J. Fluid Mech.*, 661, 482-510.

Zhu, H.P., Zhou, Z.Y., Yang, R.Y. & Yu, A.B. (2007). Discrete particle simulation of particulate systems: Theoretical developments. *Chem. Eng. Sci.*, 62, 3378-3396.

Zhu, H.P., Zhou, Z.Y., Yang, R.Y. & Yu, A.B. (2008). Discrete particle simulation of particulate systems: A review of major applications and findings. *Chem. Eng. Sci.*, 63, 5728-5770.

16

Population Balance Model of Heat Transfer in Gas-Solid Processing Systems

Béla G. Lakatos
University of Pannonia, Veszprém
Hungary

1. Introduction

In modeling heat transfer in gas-solid processing systems, five interphase thermal processes are to be considered: gas-particle, gas-wall, particle-particle, particle-wall and wall-environment. In systems with intensive motion of particles, the particle-particle and particle-wall heat transfers occur through inter-particle and particle-wall collisions so that both experimental and modeling study of these collision processes is of primary interest.
For modeling and simulation of collisional heat transfer processes in gas-solid systems, an Eulerian-Lagrangian approach, with Lagrangian tracking for the particle phase (Boulet *et al.,* 2000, Mansoori *et al.,* 2002, 2005, Chagras *et al.,* 2005), population balance models (Mihálykó *et al*., 2004, Lakatos *et al.,* 2006, 2008), and CFD simulation in the framework of Eulerian-Eulerian approach (Chang and Yang, 2010) have been applied.
The population balance equation is a widely used tool in modeling the disperse systems of process engineering (Ramkrishna, 2000) describing a number of fluid-particle and particle-particle interactions. This equation was extended by Lakatos *et al*. (2006) with terms describing also the direct exchange processes of extensive quantities, such as mass and heat between the disperse elements as well as between the disperse elements and solid surfaces by collisional interactions (Lakatos *et al.,* 2008).
The population balance model for describing the collisional particle-particle and particle-surface heat transfers was developed on the basis of a spatially homogeneous perfectly mixed system (Lakatos *et al.,* 2008). In order to take into consideration also the spatial inhomogeneities of particles in a processing system a compartment/population balance model was introduced (Süle *et al*., 2006) which has proved applicable to model turbulent fluidization and the gas-solid fluidized bed heat exchangers (Süle *et al*., 2008). However, the spatial transport of gas and particles in turbulent fluidized beds usually is modeled by continuous dispersion models (Bi *et al*., 2000) thus, in order to achieve easier correlations of the constitutive variables, it has appeared reasonable to formulate the population balance combining it with the axial dispersion model (Süle *et al.,* 2009 2010).
Particle-particle and particle-wall heat transfers may result from three mechanisms: heat transfers by radiation, heat conduction through the contact surface between the collided bodies, and heat transfers through the gas lens at the interfaces between the particles, as well as between the wall and particles collided with that. Heat conduction through the contact surface was modeled by Schlünder (1984), Martin (1984) and Sun and Chen (1988) developing analytical expressions for particle-particle and particle-wall contacts. Often, however, the conductive heat exchange can hardly be isolated from the mechanism

occurring through the gas lens at the interfaces of the colliding bodies. Based on this mechanism, Vanderschuren and Delvosalle (1980) and Delvosalle and Vanderschuren (1985) developed a deterministic model for describing particle-particle heat transfer, while a model for heat transfer through the gas lens between a surface and particles was derived by Molerus (1997). Mihálykó *et al.* (2004) and Lakatos *et al.* (2008), based on the assumption that most factors characterizing the simultaneous heat transfer through the contact point and the gas lens are stochastic quantities described the collisional interparticle heat transfer by means of an aggregative random parameter.

In this chapter, a generalized population balance model is formulated to analyze heat transfer processes in gas-solid processing systems with inter-particle and particle-wall interactions by collisions, taking into consideration the thermal effects of collisions and the gas-solid, gas-wall and wall-environment heat transfers. The population balance equation is developed for describing the spatial variation of temperature distribution of the particle population, and that of the gas and wall. The heat effects of energy change by collisions are included as a heat source in the particles. An infinite hierarchy of moment equations is derived, and a second order moment equation model is applied to analyze the thermal properties and behavior of bubbling fluidization by simulation.

2. The population balance approach

Consider a large population of solid particles being in intensive, turbulent motion in the physical space of a process vessel under the influence of some gas carrier. If the particulate phase is dense then particle collisions show significant effects on the behavior of the system therefore particle-particle and particle-surface heat transfer by collisions also may play important role in forming the thermal properties of system.

Let us assume that follow.

1) The two phase system is operated under developed hydrodynamic conditions.
2) Particles are mono-disperse and their size does not change during the course of the process.
3) Only thermal processes occur in the system without any mass transfer effects.
4) The temperature inside a particle can be taken homogeneous.
5) Heat transfer between the gas and particles, the wall and gas, as well as the wall and environment of the process vessel are continuous processes modeled by linear forces.
6) Heat transfer by radiation is negligible.

Under such conditions the state of a particle at time t is given by the vector $\left(\mathbf{x}_p, \mathbf{u}_p, T_p\right)$ where $\mathbf{x}_p$ denote the space coordinates, $\mathbf{u}_p$ are the velocities along the space coordinates, and T_p stands for the temperature of particles. The space coordinates, according to the nomenclature of population balance approach (Lakatos *et al.*, 2006) are external properties of particles, while the particle velocities and temperature are internal ones.

Since a dense gas-solid system consists of a sufficient number of particles in the vicinity of each space coordinate x therefore discontinuities can be smoothed out by introducing the population distribution function $(\mathbf{x},\mathbf{u},T,t) \to N(\mathbf{x},\mathbf{u},T,t)$ by the following

Definition. Let $\hat{N}(\mathbf{x},\mathbf{u},T,t)$ be a monotone non-decreasing function such that for every integrable and bounded function g: $\mathbf{X} \to \boldsymbol{R}$ the equality

$$\int_{\hat{\boldsymbol{X}}} g(\mathbf{x},\mathbf{u},T)\hat{N}(d\mathbf{x},d\mathbf{u},dT,t) = \sum_{n=1}^{n=N(t)} g\left(\mathbf{x}_p^n,\mathbf{u}_p^n,T_p^n\right),\ \left(\mathbf{x}_p^n,\mathbf{u}_p^n,T_p^n\right) \in \hat{\boldsymbol{X}} \tag{1}$$

holds where the triplet $\left(\mathbf{x}_p^n, \mathbf{u}_p^n, T_p^n\right)$ denotes the space coordinates, velocities and temperature of the n^{th} particle, $\hat{\boldsymbol{x}}$ stands for the state space of coordinates, velocities and temperature, and $N(t)$ is the total number of particles in a unit volume at the moment of time t.
For practical reasons, instead of the population distribution function usually the population density function $(\mathbf{x},\mathbf{u},T,t) \to \hat{n}(\mathbf{x},\mathbf{u},T,t)$ is applied that is determined as

$$\hat{n}(\mathbf{x},\mathbf{u},T,t) = \frac{\partial^7 \hat{N}(\mathbf{x},\mathbf{u},T,t)}{\partial\mathbf{x}\partial\mathbf{u}\partial T} \tag{2}$$

by means of which $\hat{n}(\mathbf{x},\mathbf{u},T,t)d\mathbf{x}d\mathbf{u}dT$ denotes the number of particles in the region $V(\mathbf{x},\delta\mathbf{x})$ of physical space from the domain $V(\mathbf{u},\delta\mathbf{u})$ of velocity and interval of temperature $(T, T+dT)$ at time t.
From the density function $\hat{n}(\mathbf{x},\mathbf{u},T,t)$ we obtain a reduced population density function

$$n(\mathbf{x},T,t) = \int_{U} \hat{n}(\mathbf{x},\mathbf{u},T,t)d\mathbf{u} \tag{3}$$

by means of which $n(\mathbf{x},T,t)d\mathbf{x}dT$ denotes the number of particles of all velocities in the region $V(\mathbf{x},\delta\mathbf{x})$ of physical space and interval of temperature $(T, T+dT)$ at time t.
The population density functions $\hat{n}(.,.,.,t)$ and $n(.,.,t)$, depending on the practical reasons, are interpreted as the states of particle populations.

3. Population balance equation

3.1 Integral forms with transition measures

According to the assumptions of former section particles are in intensive, stochastic motion in some domain $X \subseteq \boldsymbol{R}^7$ of the metric space $\boldsymbol{R}^7$ of external and internal properties therefore the time variation of particle state is described by the set of stochastic differential equations

$$d\mathbf{x}_p(t) = \mathbf{u}_p(t)dt \tag{3}$$

$$m_p d\mathbf{u}_p(t) = -\alpha\mathbf{u}_p(t)dt + \sum \mathbf{f}dt + \boldsymbol{\sigma}_{\mathbf{u},p}d\mathbf{W}(t) + \int_{\hat{\boldsymbol{x}}} \Xi_{\mathbf{u}_p}(\mathbf{u}_p)\mathcal{H}(t, d\mathbf{x}_p, d\mathbf{u}_p, dT_p) \tag{4}$$

$$m_p c_p dT_p(t) = \beta T_p(t)dt + \int_{\hat{\boldsymbol{x}}} \Xi_{T_p}(T_p)\mathcal{H}(t, d\mathbf{x}_p, d\mathbf{u}_p, dT_p) \tag{5}$$

subject to the appropriate initial conditions. In Eqs (3)-(5), $\sum \mathbf{f}$ are deterministic forces while $\mathbf{W}(t)$ is a Wiener process, inducing motion of particles in the physical space, a and β are deterministic functions characterizing the continuous motion in the physical and temperature subspace, while the integrals in Eqs (4) and (5) describe jump-like stochastic changes of internal properties. Here, function $\mathcal{H}_{(.)}$ determines the conditions of collisions of particles, while functions $\Xi_{\mathbf{u}_p}(\mathbf{u}_p)$ and $\Xi_{T_p}(T_p)$ denote, respectively, the velocity and temperature jumps induced by those.
The set of stochastic differential equations (3)-(5) describes the behavior of the population of particles entirely by tracking the time evolution of the state of each particle individually. However, numerical solution of Eqs (3)-(5) is a crucial problem although it would provide

detailed information about the life of each particle. Monte Carlo simulation means a good method for solving this system but to generate realistic results rather a large sample of particle population is required leading to long computer times.

However, for engineering purposes we usually are interested only in the behavior of the particle population as a whole. Naturally, this information would be generated also by solving the system of stochastic differential equations (3)-(5) but we can obtain it directly applying the population balance approach. Namely, taking into consideration that the system of stochastic equations (3)-(5) induces a Markov process $\left\{\mathbf{x}_p(t),\mathbf{u}_p(t),T_p(t)\right\}_{t\geq 0}$ having continuous sample paths with finite jumps (Gardiner,1983, Sobczyk,1991), the particulate system exhibits all the properties of interactive disperse systems (Lakatos *et al.*, 2006) for which we can derive a conditional transition measure $\hat{P}_c$ by means of which the variation of the state of population of particles is described by the transformation

$$\begin{aligned}\hat{n}(\mathbf{x},\mathbf{u},T,t)=&\frac{1}{N(s)}\int_{\hat{\boldsymbol{X}}}\int_{\hat{\boldsymbol{X}}}\hat{P}_c\left(s,\mathbf{x}',\mathbf{u}',T';t,\mathbf{x},\mathbf{u},T\middle|\mathbf{x}'',\mathbf{u}'',T''\right)\times\\ &\times\hat{n}(\mathbf{x}',\mathbf{u}',T',s)\hat{n}(\mathbf{x}'',\mathbf{u}'',T'',s)d\mathbf{x}'d\mathbf{x}''d\mathbf{u}'d\mathbf{u}''dT'dT''\\ &t>s;(\mathbf{x},\mathbf{u},T)\in\hat{\boldsymbol{X}}\end{aligned}\tag{6}$$

where $N(s)$ denotes the number of particles in the given domain at time s

$$N(s)=\int_{\hat{\boldsymbol{X}}}\hat{n}(\mathbf{x},\mathbf{u},T,s)d\mathbf{x}d\mathbf{u}dT\ .\tag{7}$$

In Eq.(6), expression

$$\frac{1}{N(s)}\hat{n}(\mathbf{x}'',\mathbf{u}'',T'',s)d\mathbf{x}''d\mathbf{u}''dT''\tag{8}$$

is interpreted as the probability that there exists a solid particle in the state domain $(\mathbf{x}'',\mathbf{u}'',T'',\mathbf{x}''+d\mathbf{x}'',\mathbf{u}''+d\mathbf{u}'',T''+dT'')$ possibly interacting with a particle of state $(\mathbf{x}',\mathbf{u}',T')$ and the result of this interaction event is expressed by the conditional transition measure $\hat{P}_c$. The properties of the conditional transition measure $\hat{P}_c$ are determined by the physical-chemical processes of the system that induce motion and/or formation of particles under given operational conditions. When the action of these processes can be described by means of some vector of random parameters $\boldsymbol{\theta}$ with distribution function $F_{\boldsymbol{\theta}}(.)$, and all particles are moved and/or formed under the same conditions then a lot of different realisations, described by the distribution function of the random parameters $\boldsymbol{\theta}$, can act on the particles. As a result, the final population is formed as expectation for the vector of parameters $\boldsymbol{\theta}$ so that Eq.(6) can be rewritten using randomization:

$$\begin{aligned}\hat{n}(\mathbf{x},\mathbf{u},T,t)=&\frac{1}{N(s)}\int_{\boldsymbol{\Theta}}\int_{\hat{\boldsymbol{X}}}\int_{\hat{\boldsymbol{X}}}\tilde{P}_c\left(s,\mathbf{x}',\mathbf{u}',T';t,\mathbf{x},\mathbf{u},\mathbf{c}\middle|\mathbf{x}'',\mathbf{u}'',T'',\boldsymbol{\theta}\right)\times\\ &\times\hat{n}(\mathbf{x}',\mathbf{u}',T',s)\hat{n}(\mathbf{x}'',\mathbf{u}'',T'',s)d\mathbf{x}'d\mathbf{x}''d\mathbf{u}'d\mathbf{u}''dT'dT''F_{\boldsymbol{\theta}}(d\boldsymbol{\theta})\\ &t>s;(\mathbf{x},\mathbf{u},T)\in\hat{\boldsymbol{X}}\end{aligned}\tag{9}$$

Eq.(9) is, in principle, a multidimensional, i.e. (3+4)D population balance equation written in integral form by means of the transition measure defined on the basis of transition probability of Markov processes. Here, indicating the dimension of the equation the first number denotes the external variables while the second one gives number of internal variables. The parameterized conditional transition measure $\tilde{P}_c$ of the particulate system involves, in principle, all information about the properties and behavior of the particle population and precision of the nature and components of motions along the property coordinates of population state makes possible to derive the corresponding population balance equation. However, this multidimensional population balance equation seems to be too complex; simplification is obtained by deriving a population balance equation for the ensemble of particles of all velocities

$$n(\mathbf{x},T,t)=\int_{\boldsymbol{U}}\hat{n}(\mathbf{x},\mathbf{u},T,t)d\mathbf{u} \tag{10}$$

modeling motion of particles in the physical space by using convection-dispersion models. Rewriting the population density function in the conditional form

$$\frac{1}{N(s)}\hat{n}(\mathbf{x},\mathbf{u},T,t)=\mathrm{Prob}\left(\mathbf{u}\middle|\mathbf{x},T\right)\frac{1}{N(s)}n(\mathbf{x},T,t) \tag{11}$$

where $\mathrm{Prob}\left(\mathbf{u}\middle|\mathbf{x},T\right)$ denotes the probability that a particle, residing at space coordinate x and having temperature T possesses velocity $\boldsymbol{u}$, introducing (11) into Eq.(9) and integrating both sides of Eq.(9) over variable $\boldsymbol{u}$ we obtain

$$\begin{aligned} n(\mathbf{x},T,t)=&\frac{1}{N(s)}\int_{\boldsymbol{X}}\int_{\boldsymbol{X}}P_c\left(s,\mathbf{x}',T';t,\mathbf{x},T\middle|\mathbf{x}'',T'',\boldsymbol{\theta}\right)\times\\ &\times n(\mathbf{x}',T',s)n(\mathbf{x}'',T'',s)d\mathbf{x}'d\mathbf{x}''dT'dT''F_{\boldsymbol{\theta}}(d\boldsymbol{\theta})\\ &t>s;(\mathbf{x},T)\in\boldsymbol{X} \end{aligned} \tag{12}$$

where

$$\begin{aligned} P_c\left(s,\mathbf{x}',T';t,\mathbf{x},T\middle|\mathbf{x}'',T'',\boldsymbol{\theta}\right)=&\int_{\boldsymbol{U}}\int_{\boldsymbol{U}}\int_{\boldsymbol{U}}\tilde{P}_c\left(s,\mathbf{x}',\mathbf{u}',T';t,\mathbf{x},\mathbf{u},T\middle|\mathbf{x}'',\mathbf{u}'',T'',\boldsymbol{\theta}\right)\times\\ &\times\mathrm{Prob}\left(\mathbf{u}'\middle|\mathbf{x}',T'\right)\mathrm{Prob}\left(\mathbf{u}''\middle|\mathbf{x}'',T''\right)d\mathbf{u}'d\mathbf{u}''d\mathbf{u} \end{aligned} \tag{13}$$

Here, expression (13) denotes the transition measure by means of which transformation (12) provides the amount of particles of all velocities which are converted into the state domain $(\mathbf{x},T,\mathbf{x}+d\mathbf{x},T+dT)$ to time t of particles of all velocities being in $\hat{\boldsymbol{X}}$ at time s under the conditions of interactions with particles of the same state domain of any velocities. As a consequence, transformation (12) describes motion of particles with possible heat exchange interactions in the 3+1 dimensional subspace of physical and temperature coordinates determined over a given, fully developed velocity field. Eq.(12) is a reduced form of the multidimensional population balance equation (9), given also in integral form.

3.2 Integral-differential equation form

Taking into account the conditions assumed and following the steps of derivation of the population balance equation of interactive disperse systems as it was presented by Lakatos *et al.*(2006), the population balance equation describing the behavior of population of the particles in the system is obtained from Eq.(9) in the form

$$\begin{aligned}
&\frac{\partial \hat{n}(\mathbf{x},\mathbf{u},T,t)}{\partial t}+\frac{\partial}{\partial T}\left[G_T\hat{n}(\mathbf{x},\mathbf{u},T,t)\right]+\nabla_{\mathbf{u}}\cdot\left[\mathbf{G}_{\mathbf{u}}\hat{n}(\mathbf{x},\mathbf{u},T,t)\right]=\\
&=\nabla_{\mathbf{x}}\cdot\mathbf{D}_{\mathbf{x}}\nabla_{\mathbf{x}}\hat{n}(\mathbf{x},\mathbf{u},T,t)-\nabla_{\mathbf{x}}\cdot\left[\mathbf{G}_{\mathbf{x}}\hat{n}(\mathbf{x},\mathbf{u},T,t)\right]-\\
&-\frac{\hat{n}(\mathbf{x},\mathbf{u},T,t)}{N(\mathbf{x},t)}\int_{\boldsymbol{U}}\int_{T_{\min}}^{T_{\max}}\hat{S}_{pp}(T,\mathbf{u}|T',\mathbf{u}')\hat{n}(\mathbf{x},\mathbf{u}',T',t)dT'd\mathbf{u}'+\\
&+\frac{1}{N(\mathbf{x},t)}\int_{\boldsymbol{\Theta}}\int_{\boldsymbol{U}}\int_{\boldsymbol{U}}\int_{T_{\min}}^{T_{\max}}\int_{T_{\min}}^{T_{\max}}\hat{S}_{pp}(T',\mathbf{u}'|T'',\mathbf{u}'')\hat{b}_{pp}(T',T,\mathbf{u}',\mathbf{u}|T'',\mathbf{u}'',\boldsymbol{\theta})\times\\
&\times\hat{n}(\mathbf{x},\mathbf{u}',T',t)\hat{n}(\mathbf{x},\mathbf{u}'',T'',t)dT'dT''d\mathbf{u}'d\mathbf{u}''\hat{F}_{\boldsymbol{\theta}}(d\boldsymbol{\theta})
\end{aligned} \tag{14}$$

subject to the appropriate boundary and initial conditions. Here, $N(\mathbf{x},t)$ denotes the total number of particles in the vicinity of position x of the physical space at the moment of time t.

The second and third terms on the left hand side of Eq.(14), next to the accumulation term describe variation of the population density function $\hat{n}$ due to continuous thermal and velocity interactions of particles with the carrier gas environment, respectively, while the first and second terms on the right hand side describe motion of particles in the physical space. Here, the rate expressions G_T, $\mathbf{G}_{\mathbf{u}}$ and $\mathbf{G}_{\mathbf{x}}$ are interpreted as convective terms of motion along the temperature, velocity and physical coordinates, and $\mathbf{D}_{\mathbf{x}}$ denotes the dispersion tensor of motion of particles in the physical space.

The last two terms on the right hand side of Eq.(14) describe the momentum and heat exchange between particles interacting with each other by collisions during their motion in the physical space. Namely, the third term describe the rate of decrease of number of particles of temperature T and velocity $\boldsymbol{u}$ collided with particles of temperature T' and velocity $\boldsymbol{u}'$, whereas the last term provides the rate of increase of number of particles having temperature T and velocity $\boldsymbol{u}$ resulted in collision interactions of particles of temperature T' and T'' as well as of velocity $\boldsymbol{u}'$ and $\boldsymbol{u}''$. The collision interactions are described by means of a product of two operators: the activity and conversion functions $\hat{S}_{pp}$ and $\hat{b}_{pp}$, respectively. In the present model, the activity function $\hat{S}_{pp}$ characterizes the intensity of collision interactions between the particles inducing temperature change, being, in turn, a product of the frequency of collisions $\hat{S}_{col}(T,\mathbf{u}|T',\mathbf{u}')$ and the efficiency term $\hat{S}_{ex}(T,\mathbf{u}|T',\mathbf{u}')$, written as $\hat{S}_{pp}(T,\mathbf{u}|T',\mathbf{u}')=\hat{S}_{col}(T,\mathbf{u}|T',\mathbf{u}')\cdot\hat{S}_{ex}(T,\mathbf{u}|T',\mathbf{u}')$. Here, $\hat{S}_{ex}(T,\mathbf{u}|T',\mathbf{u}')$ expresses the ratio of all events which are to be successful in inducing also heat and momentum exchange events. Naturally, since heat diffusion, deciding at this level on homogenization of temperature is a spontaneous process, while momentum exchange by collision of two solid bodies also occurs the efficiency term is equal to unity identically, i.e. $\hat{S}_{ex}(T,\mathbf{u}|T',\mathbf{u}')\equiv 1$. Finally, function $\hat{b}_{pp}(T',T,\mathbf{u}',\mathbf{u}|T'',\mathbf{u}'',\boldsymbol{\theta})$, called conversion density function, describes the results of events inducing changes of temperature and velocity of particles, i.e. $\hat{b}_{pp}(T',T,\mathbf{u}',\mathbf{u}|T'',\mathbf{u}'',\boldsymbol{\theta})dTd\mathbf{u}$ expresses the fraction of particles that become of temperature

$(T,T+dT)$ and $(\mathbf{u},\mathbf{u}+d\mathbf{u})$ as a result of interactions of all particles of temperature T' and T'' and velocity $\boldsymbol{u}'$ and $\boldsymbol{u}''$ in a unit time.

The (3+4) dimensional population balance equation (14) is a so called cognitive model that describes the behavior of particle population in detail taking into account also the velocity distribution of particles. However, a simplified population balance equation can be obtained from Eq.(12) for the population density function $n(\mathbf{x},T,t)$ not including the explicit velocity dependence into the model. Indeed, again following the steps of derivation of the population balance equation of interactive disperse systems we obtain

$$\begin{aligned}&\frac{\partial n(\mathbf{x},T,t)}{\partial t}+\frac{\partial}{\partial T}\left[G_T n(\mathbf{x},T,t)\right]=\nabla_{\mathbf{x}}\cdot\mathbf{D}_{\mathbf{x}}\nabla_{\mathbf{x}}n(\mathbf{x},T,t)-\nabla_{\mathbf{x}}\cdot\left[\mathbf{G}_{\mathbf{x}}n(\mathbf{x},T,t)\right]\\&-\frac{n(\mathbf{x},T,t)}{N(\mathbf{x},t)}\int_{T_{\min}}^{T_{\max}}S_{pp}(T|T')n(\mathbf{x},T',t)dT'+\\&+\frac{1}{N(\mathbf{x},t)}\int_{\Theta}\int_{T_{\min}}^{T_{\max}}\int_{T_{\min}}^{T_{\max}}b_{pp}(T',T|T'',\boldsymbol{\theta})S_{pp}(T'|T'')n(\mathbf{x},T',t)n(\mathbf{x},T'',t)dT'dT''F_{\boldsymbol{\theta}}(d\boldsymbol{\theta})\end{aligned}\tag{15}$$

subject to the appropriate boundary and initial conditions. Here, the constitutive expressions in Eq.(15) have similar meanings as it was described regarding Eq.(14) excluding the explicit velocity dependence. Note that in this simplified form the effects of collisions on motion of particles in the physical space can be taken into consideration by applying empirical models for the convective and dispersion terms $\mathbf{G}_{\mathbf{x}}$ and $\mathbf{D}_{\mathbf{x}}$, respectively.

In the context of the population balance equation (15), the particle-solid surface boundary condition is relevant that can be formulated as the heat exchange rate between the particle population and solid surface at a space coordinate $\boldsymbol{x}$ of surface S

$$\begin{aligned}&dQ_{wp}(\mathbf{x},t)\Big|_{\mathcal{S}}=-\int_{\Theta}\int_{T_{\min}}^{T_{\max}}S_{wp}\left(T_w(\mathbf{x},t)|T\right)b_{wp}\left(T_w(\mathbf{x},t),z|T,\boldsymbol{\theta}\right)n(\mathbf{x},z,t)dzF_{\boldsymbol{\theta}}(d\boldsymbol{\theta})\Big|_{\mathcal{S}}dt+\\&+\int_{\Theta}\int_{T_{\min}}^{T_{\max}}S_{wp}\left(T_w(\mathbf{x},t)|z\right)b_{wp}\left(T_w(\mathbf{x},t),T|z,\boldsymbol{\theta}\right)n(\mathbf{x},z,t)dzF_{\boldsymbol{\theta}}(d\boldsymbol{\theta})\Big|_{\mathcal{S}}dt\end{aligned}\tag{16}$$

where $T_w(\boldsymbol{x},t)$ denotes the temperature of surface S at position $\boldsymbol{x}$ at time t.

Eq.(15) with the boundary condition is an applicative or, in other words, a purpose-oriented partially distributed population balance model aimed for describing thermal processes in fluid-solid particulate systems. Introducing the constitutive expressions and making use of appropriate symmetric conditions it can be applied for determining spatially low dimensional population balance models. Here, the one-dimensional axial dispersion/population balance and the zero-dimensional well stirred vessel/population balance model will be presented to describe thermal processes in gas-solid particulate systems.

4. Constitutive equations for particle-particle heat transfer by collisions

4.1 Heat effects of particle-particle collisions

To close the population balance equation (15) the constitutive equations, first of all those characterizing the collision interactions are to be determined. In developing we consider

only binary collisions as it is shown schematically in Figs 1 and 2. Here we assumed that particles in the particulate system are of the same volume and mass but their shape usually are irregular. As a consequence, in this case the collision events are of random nature therefore practically all processes induced by collisions, among others the change of kinetic energy and exchange of extensive quantities between the colliding particles should be treated as random.

Let us now consider the encounter of two solid particles of mass m_j and m_k as it is shown in Fig.1. If the velocity vectors of these bodies are given by $\boldsymbol{u}_j$ and $\boldsymbol{u}_k$, and their difference is denoted by $\boldsymbol{u}_{jk}=\boldsymbol{u}_j-\boldsymbol{u}_k$ then the translational kinetic energy change during collision ΔE is

$$\Delta E = \frac{1}{2}\frac{m_j m_k}{m_j + m_k}\left(u_{jk}^{2\,\prime} - u_{jk}^2\right) = \frac{1}{2}\frac{m_j m_k}{m_j + m_k}\left(e^2 - 1\right)u_{jk}^2 \tag{17}$$

where e is assumed to be a random coefficient of restitution. If the two particles are of equal mass, i.e. $m_j=m_k=m_p$ then

$$\Delta E = \frac{m_p}{4}\left(e^2 - 1\right)u_{jk}^2 \tag{18}$$

,

and accounting for the probability that a particle is colliding with an another particle in the time interval $(t,t+\Delta t)$ the energy change is expressed as

$$\Delta E(\mathbf{x},t) = \frac{m_p\left(e^2-1\right)}{4N(\mathbf{x},t)} \iint\limits_{\boldsymbol{U}\times T} u_{jk}^2 \hat{n}(\mathbf{x},\mathbf{u}_{jk},T,t)\,d\mathbf{u}_{jk}\,dT\cdot\Delta t \tag{19}$$

Applying the Maxwellian distribution for particles

$$\hat{n}(\mathbf{x},\mathbf{u}_{jk},T,t) = \frac{n(\mathbf{x},T,t)}{\left(\frac{2}{3}\pi\left\langle\mathbf{u}^2\right\rangle\right)^{\frac{3}{2}}}\exp\left(-\frac{\mathbf{u}_{jk}^2}{\frac{2}{3}\left\langle\mathbf{u}^2\right\rangle}\right) \tag{20}$$

and taking into consideration that the coefficient of restitution is a random variable with the probability density function f_e, independent from the velocities, the mean value of energy change can be expressed as

$$\Delta E(\mathbf{x},t) = \frac{m_p\int_0^1\left(e^2-1\right)f_e(e)de}{4N(\mathbf{x},t)\left(\frac{2}{3}\pi\left\langle\mathbf{u}^2\right\rangle\right)^{\frac{3}{2}}} \iint\limits_{\boldsymbol{U}\times T} n(\mathbf{x},T,t)u_{jk}^2\exp\left(-\frac{\mathbf{u}_{jk}^2}{\frac{2}{3}\left\langle\mathbf{u}^2\right\rangle}\right)d\mathbf{u}_{jk}\,dT\cdot\Delta t\,. \tag{21}$$

With complete spherical symmetry

$$d\mathbf{u}_{jk} = 4\pi u_{jk}^2\,du_{jk} \tag{22}$$

we have

$$\Delta E(\mathbf{x},t)=\frac{4\pi m_p\int_0^1\left(e^2-1\right)f_e(e)de}{4N(\mathbf{x},t)\left(\frac{2}{3}\pi\left\langle\mathbf{u}^2\right\rangle\right)^{\frac{3}{2}}}\iint\limits_{U\times T}n(\mathbf{x},T,t)u_{jk}^4\exp\left(-\frac{\mathbf{u}_{jk}^2}{\frac{2}{3}\left\langle\mathbf{u}^2\right\rangle}\right)du_{jk}dT\cdot\Delta t \tag{23}$$

Making use of evaluation of the definite integral (Gidaspow, 1994)

$$\int_0^1 x^4\exp\left(-ax^2\right)dx=\frac{3\sqrt{\pi}}{8}\alpha^{-\frac{5}{2}} \tag{24}$$

we obtain

$$\Delta E(\mathbf{x},t)=\frac{m_p}{4N(\mathbf{x},t)}\left\langle\mathbf{u}^2\right\rangle\int_0^1\left(e^2-1\right)f_e(e)de\int_T n(\mathbf{x},T,t)dT\cdot\Delta t \tag{25}$$

As a consequence, assuming that this heat arise in particles as it was generated by an internal heat source we can write

$$c_p m_p\frac{dT}{dt}=\frac{1}{2}\frac{dE(\mathbf{x},t)}{dt}=\frac{m_p}{8}\left\langle\mathbf{u}^2\right\rangle\int_0^1\left(e^2-1\right)f_e(e)de \tag{26}$$

that results in the following rate of temperature change for a particle

$$\frac{dT}{dt}=\frac{\left\langle\mathbf{u}^2\right\rangle}{8c_p}\int_0^1\left(e^2-1\right)f_e(e)de\,. \tag{27}$$

4.2 Heat transfer by collisions of two particles

Let us consider the heat transfer process induced by collision of two solid bodies, shown schematically in Fig. 1, as described by the set of simple first order differential equations with linear driving forces

$$m_j c_j\frac{dT_j(t)}{dt}=\beta\left(T_k(t)-T_j(t)\right) \tag{28a}$$

and

$$m_k c_k\frac{dT_k(t)}{dt}=-\beta\left(T_k(t)-T_j(t)\right) \tag{28b}$$

subject to the initial conditions

$$T_j(0)=T_{j0},\qquad T_k(0)=T_{k0} \tag{29}$$

where β is a not specified aggregated heat transfer coefficient.

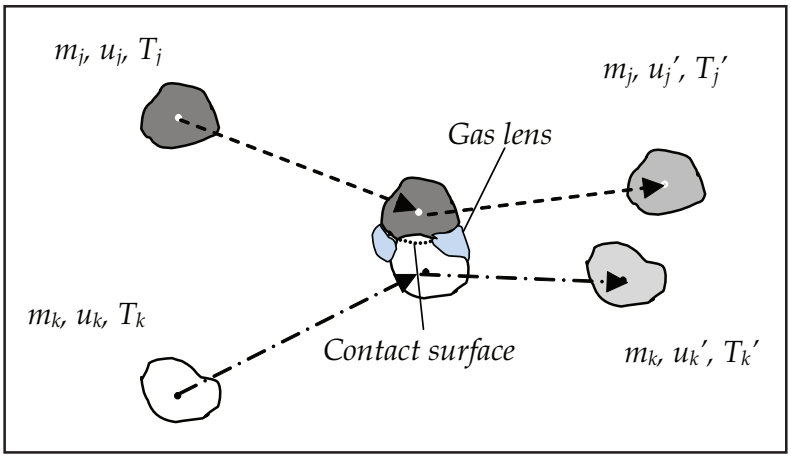

Fig. 1. Collision of two particles of irregular shape

Eqs (28) are of such forms as the temperature of particles would be uniform. However it is not the case so that these equations have to be interpreted as they were written for the mean values. In this case the variables are, in essence, mean values, i.e.

$$T_\iota(t) = \frac{1}{v_\iota}\int T_\iota dV, \quad \iota = j,k \tag{30}$$

Since the temperature of a particle is not uniform the actual temperature values in the driving force in Eq.(28) are uncertain so that this should be treated also as random. Therefore the left hand sides of Eq.(28) are random and we allocate this randomness into the β transfer coefficient.

The solutions of the first order differential equations (28) at time θ become

$$T_j(\theta) = T_{j0} + \frac{m_k c_k}{m_j c_j + m_k c_k}\left(T_{k0} - T_{j0}\right)\left\{1 - \exp\left[-\beta\theta\left(\frac{1}{m_j c_j} + \frac{1}{m_k c_k}\right)\right]\right\} = T_{j0} + p_j\omega\left(T_{k0} - T_{j0}\right) \tag{31a}$$

and

$$T_k(\theta) = T_{k0} - \frac{m_j c_j}{m_j c_j + m_k c_k}\left(T_{k0} - T_{j0}\right)\left\{1 - \exp\left[-\beta\theta\left(\frac{1}{m_j c_j} + \frac{1}{m_k c_k}\right)\right]\right\} = T_{k0} - p_k\omega\left(T_{k0} - T_{j0}\right) \tag{31b}$$

where

$$\omega := 1 - \exp\left[-\beta\theta\left(\frac{m_j c_j + m_k c_k}{m_j c_j m_k c_k}\right)\right],\ p_j = \frac{m_k c_k}{m_j c_j + m_k c_k},\ p_k = \frac{m_j c_j}{m_j c_j + m_k c_k}. \tag{32}$$

Here θ denotes the contact time which is, in principle, also a random quantity. As a consequence, parameter $\omega \in [0,1]$, characterizing the efficiency of heat exchange between the colliding bodies is a random function of variables β and θ, and its distribution is entirely determined by their distribution functions.

Let us now assume that the two bodies suffering collisions are two particles with equal masses and heat capacities. Then, $m_j c_j = m_k c_k = m_p c_p$ and $p_j = p_k = \frac{1}{2}$. Introducing the notation $T_{j0} = T_p'$, $T_{k0} = T_p''$ we can write

$$\omega = \omega_{pp} = 1 - \exp\left[\frac{-2h_{pp}a_{pp}\theta_{pp}}{m_p C_p}\right] \tag{33}$$

and

$$T_p(\theta) = T_p' + (T_p'' - T_p') \cdot \frac{\omega_{pp}}{2} \tag{34}$$

from which

$$\frac{2\left(T_p - T_p'\right)}{\omega_{pp}} + T_p' = T_p'' \tag{35}$$

Interpretation of Eq.(12) is that in heat transfer process characterized with parameter ω_{pp} a particle with temperature T_p' has to collide with particle of temperature T_p'' to achieve final temperature T_p. Taking now into consideration the definitions of conversion functions, the conversion distribution function of particle-particle heat transfer takes the form

$$B_{pp}\left(T_p', T_p \mid T_p'', \omega_{pp}\right) = 1_{T_p}\left[\left(\frac{2\left(T_p - T_p'\right)}{\omega_{pp}} + T_p'\right) - T_p''\right] \tag{36}$$

so that the corresponding density function is

$$b_{pp}\left(T_p', T_p \mid T_p'', \omega_{pp}\right) dT_p = \delta_{T_p}\left[\left(\frac{2\left(T_p - T_p'\right)}{\omega_{pp}} + T_p'\right) - T_p''\right] \frac{2}{\omega_{pp}} dT_p \tag{37}$$

4.3 Heat transfer through the gas lens and the contact surface

Heat transfer between two particles may be considered as a combination of transfers through the gas lens between the particles and through the contact surface as it is shown in Fig. 1. These processes depend strongly on the shapes and velocities of the colliding bodies that is why the parameters β and θ are treated as random variables. However, under symmetrical conditions for particles of regular spherical forms explicit expressions have been determined.

The heat flow rate through the gas lens between two particles with diameter d_p in the angle $\left(-\alpha_{\max},+\alpha_{\max}\right)$ was developed by Delvosalle and Vanderschuren (1985) in the form

$$q_h = \pi h d_p \left(T_k - T_j\right)\int_0^{\alpha_{\max}} \frac{\sin^2\alpha d\alpha}{2\left[\frac{s}{R}+\left(1-\left|\cos\alpha\right|\right)\right]\alpha} \tag{38}$$

where 2*s* denotes the width of the gas lens. At this flow rate the temperature of the j^{th} particle during the time interval (0, θ) increases to the value

$$T_j = T_{j0} + \Gamma(\theta)\left(T_{k0} - T_{j0}\right) \tag{39}$$

where

$$\Gamma(\theta) = 1 - \exp\left(\frac{3h}{\rho_p c_p d_p^2}\int_0^{\alpha_{\max}} \frac{\sin^2\alpha d\alpha}{2\left[\frac{s}{R}+\left(1-\left|\cos\alpha\right|\right)\right]\alpha}\theta\right) \tag{40}$$

In the case of intensive motion of particles, the parameters *h*, *s* and $a_{\max}$ in Eq.(38) as well as the contact time θ are, in principle, random quantities therefore Γ is also a random function of these arguments.

The heat flow rate through the contact surface was studied by Sun and Chen (1988) developing an approximate expression in the form

$$q_h = \frac{\sqrt{\rho_p c_p k_p}\, t^{-\frac{1}{2}}}{2\sqrt{\pi}}\left(T_k - T_j\right) \tag{41}$$

by means of which the total temperature increase in the *jth* particle during the time interval (0,θ) is expressed as

$$T_j(\theta) = T_{j0} + \frac{0.87\sqrt{\rho_p c_p k_p}\, a_c \theta^{\frac{1}{2}}}{2 m_p c_p}\left(T_{k0} - T_{j0}\right) \tag{42}$$

where a_c denotes the maximum contact area. Again, in Eq.(42) the maximum contact area and contact time depend on the velocities of collided particles so that these quantities are to be treated also as random variables.

Comparing the equations (31), (39) and (42) all these are expressed by linear driving forces so that the overall heat transfer flow can be given as superposition of the heat flows through the gas lens and the contact surface.

5. Constitutive equations for particle-wall heat transfer by collisions

5.1 Heat effects of particle-wall collisions

Let us consider again the encounter of two solid bodies of mass m_j and m_k as it is shown in Fig. 2 from which now the second is a no moving solid surface. In this case the velocity

vector $\boldsymbol{u}_k$=0 so that the velocity difference is $\boldsymbol{u}_{jk}$=$\boldsymbol{u}_j$ then the translational kinetic energy change ΔE is given as

$$\Delta E = \frac{1}{2}\frac{m_p m_w}{m_p + m_w}\left(u_j^{2\prime} - u_j^2\right) = \frac{m}{2}u_j^2\int_0^1\left(e^2 - 1\right)f_e(e)\,de \tag{43}$$

where, again, e is a random coefficient of restitution and $m = m_p m_w / \left(m_p + m_w\right)$.

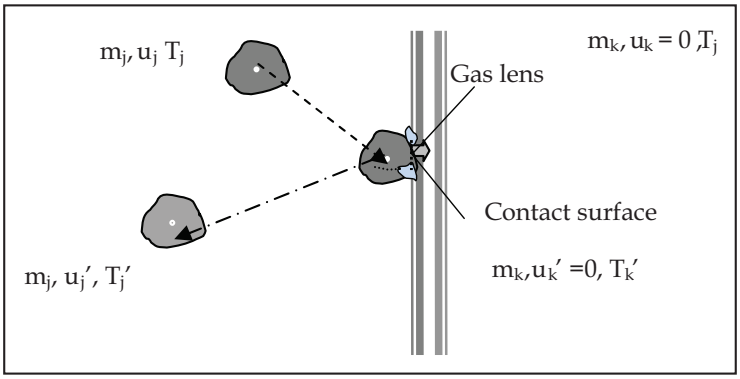

Fig. 2. Collision of an irregular particle with the wall

Now accounting for the probability that a particle is colliding with the surface in the time interval (t,t+Δt)

$$\Delta E(\mathbf{x},t) = \frac{m}{2N(\mathbf{x},t)}\int_0^1\left(e^2 - 1\right)f_e(e)\,de\iint_{\boldsymbol{U}\times T} u_j^2\hat{n}(\mathbf{x},\mathbf{u}_j,T,t)\,d\mathbf{u}_j\,dT\cdot\Delta t \tag{44}$$

Making use of the Maxwellian distribution and the hemi-spherical symmetry

$$d\mathbf{u}_j = 2\pi u_j^2\,du_j \tag{45}$$

we obtain

$$\Delta E(x,t) = \frac{\pi m\int_0^1\left(e^2 - 1\right)f_e(e)\,de}{N(x,t)\left(\frac{2}{3}\pi\left\langle u^2\right\rangle\right)^{\frac{3}{2}}}\iint_{U\times T} n(x,T,t)u_j^4\exp\left(-\frac{u_j^2}{\frac{2}{3}\left\langle u^2\right\rangle}\right)du_j\,dT\cdot\Delta t \tag{46}$$

that results in the following rate of temperature change for a particle and the wall

$$\frac{dT}{dt} = \frac{m\left\langle\mathbf{u}^2\right\rangle}{8m_\iota c_\iota}\int_0^1\left(e^2 - 1\right)f_e(e)de,\quad \iota = p,w \tag{47}$$

5.2 Particle-wall heat transfer by collisions

When a particle and the wall are two colliding bodies, as it shown in Fig. 2, then introducing the notation

$$m_j c_j = m_p c_p\,,\ m_k c_k = m_w c_w\,,\ p_j = p_p = \frac{m_w c_w}{m_p c_p + m_w c_w}\,,\ p_k = p_w = \frac{m_p c_p}{m_p c_p + m_w c_w} \tag{48}$$

as well as $T_{j0} = T_p'$ and $T_{k0} = T_w'$, we can write

$$\omega := \omega_{pw} := \omega_{wp} := 1 - \exp\left[\frac{-h_{pw} a_{pw} \theta_{pw}\left(m_p c_p + m_w c_w\right)}{m_p c_p m_w c_w}\right] \tag{49}$$

Now, instead of Eq. (34) we have

$$T_p(\theta) = p_w \omega_{pw}\left(T_w' - T_p'\right) + T_p' \tag{50}$$

from which

$$\frac{T_p - T_p'}{p_w \omega_{pw}} + T_p' = T_w' \tag{51}$$

Eq.(51) expresses the fact that in heat transfer process between a particle and the wall, characterized with parameter ω_{pw}, the temperature T_p' of the particle becomes T_p if the temperature of the wall was T_w'. As a consequence, the conversion distribution function of the particle-wall heat transfer for particles takes the form

$$B_{pw}\left(T_p', T_p \mid T_w', \omega_{pw}\right) = \mathbf{1}_{T_p}\left[\left(\frac{T_p - T_p'}{p_w \omega_{pw}} + T_p'\right) - T_w'\right] \tag{52}$$

thus the density function becomes

$$b_{pw}(T_p', T_p \mid T_w'', \omega_{pw}) dT_p = \delta_{T_p}\left[\left(\frac{T_p - T_p'}{p_w \omega_{pw}} + T_p'\right) - T_w'\right] \frac{1}{p_w \omega_{pw}} dT_p \tag{53}$$

Finally, in the particle-wall collisional heat transfer we consider the process from the side of the wall. Then Eq.(34) is rewritten as

$$\frac{T_w - T_w'}{p_p \omega_{pw}} + T_w' = T_p' \tag{54}$$

based on which, since the change of the wall temperature is related to $T_w(t)$ which is fixed at the moment t the conversion distribution function becomes

$$B_{wp}\left(T_w', T_w \mid T_p', \omega_{wp}\right) = \mathbf{1}_{T_w}\left[\left(\frac{T_w - T_w'}{p_p \omega_{wp}} + T_w'\right) - T_p'\right] \tag{55}$$

while the conversion density function

$$b_{wp}\left(T_w', T_w \mid T_p', \omega_{wp}\right) dT_w = \delta_{T_w}\left[\left(\frac{T_w - T_w'}{p_p \omega_{wp}} + T_w'\right) - T_p'\right]\frac{1}{p_p \omega_{wp}} dT_w \tag{56}$$

At this moment all collisional constitutive expressions have been derived and the heat balance model of the process, applying the population balance equation (15) can be determined.

6. Moment equation model

Substituting the constitutive equations into the (3+1)D population balance equation (15) we obtain

$$\begin{aligned}&\frac{\partial n(\mathbf{x},T,t)}{\partial t} + \frac{\partial}{\partial T}\left[\frac{dT}{dt} n(\mathbf{x},T,t)\right] = \nabla_{\mathbf{x}} \cdot \mathbf{D}_{\mathbf{x}} \nabla_{\mathbf{x}} n(\mathbf{x},T,t) - \nabla_{\mathbf{x}} \cdot \left[\mathbf{u}_{\mathbf{x}} n(\mathbf{x},T,t)\right] - \\ &- S_{pp} n(\mathbf{x},T,t) + \int_0^1 \frac{2S_{pp}}{\omega_{pp} N(x,t)} \int_{T_{\min}}^{T_{\max}} n\left[\mathbf{x}, \left(\frac{2(T-y)}{\omega_{pp}} + y\right), t\right] n(\mathbf{x},y,t) f_{\omega_{pp}}(\omega_{pp}) dy d\omega_{pp}\end{aligned} \tag{57}$$

where the second term describes the change of population density function due to continuous thermal interactions of particles with gas and energy dissipation generated by particle-particle collisions

$$\frac{dT}{dt} = \frac{a_{pg} h_{pg}}{m_p c_p}\left[T_g(\mathbf{x},t) - T\right] + \frac{\left\langle \mathbf{u}^2 \right\rangle}{8c_p} \int_0^1 \left(e^2 - 1\right) f_e(e) de \tag{58}$$

Similarly, for the solid surface the boundary condition (16) becomes

$$dQ_{pw}(\mathbf{x},t)\big|_{\mathcal{S}} = S_{pw} c_p m_p \left[-n(\mathbf{x},T,t)\big|_{\mathcal{S}} + \int_0^1 n\left(\frac{T - p_w \omega_{pw} T_w(\mathbf{x},t)}{1 - p_w \omega_{pw}}, t\right) \frac{f_{\omega_{pw}}(\omega_{pw})}{1 - p_w \omega_{pw}} d\omega_{pw}\right]_{\mathcal{S}} dt \tag{59}$$

while the boundary condition for surfaces playing the role of input and output of the system takes the form

$$\nu(\mathbf{x},T,t)\big|_{\mathcal{S}} = \mathbf{u}_{\mathbf{x}} n(\mathbf{x},T,t) - \mathbf{D}_{\mathbf{x}} \cdot \nabla_{\mathbf{x}} n(\mathbf{x},T,t)\big|_{\mathcal{S}} \tag{60}$$

where $\nu(\mathbf{x},T,t)$ is a given function stimulating the system or specifying the surface conditions.

This is a boundary value problem of the (3+1)D integral-differential equation (57). This is still a cognitive model and it appears to be too complex for numerical solution. However, accounting for the constitutive expressions of the collision heat transfer terms a useful closed moment equation hierarchy can be determined introducing the moments with respect to the temperature variable

$$\mu_k(\mathbf{x},t) = \int_{T_{\min}}^{T_{\max}} T^k n(\mathbf{x},T,t) dT, \quad k = 0,1,2... \tag{61}$$

where $N(\mathbf{x},t)=\mu_0(\mathbf{x},t)$ and $\langle T\rangle(\mathbf{x},t)=\mu_1(\mathbf{x},t)/\mu_0(\mathbf{x},t)$ denote, respectively, the total number and the mean temperature of particles in the vicinity of position x at time t. In this case the first two moments have physical meaning while by means of the higher order ones the temperature distribution can be specified more exactly.
The infinite set of moment equations becomes

$$\begin{aligned}&\frac{\partial\mu_k(\mathbf{x},t)}{\partial t}-\frac{ka_{pg}h_{pg}}{c_pm_p}\left[\mu_{k-1}(\mathbf{x},t)T_g(\mathbf{x},t)-\mu_k(\mathbf{x},t)\right]-\frac{k}{c_pm_p}\Delta H_{coll}^{pp}\mu_{k-1}(\mathbf{x},t)=\\&=\nabla_{\mathbf{x}}\cdot\mathbf{D}_{\mathbf{x}}\nabla_{\mathbf{x}}\mu_k(\mathbf{x},t)-\nabla_{\mathbf{x}}\cdot\left[\mathbf{u}_{\mathbf{x}}\mu_k(\mathbf{x},t)\right]-S_{pp}\mu_k(\mathbf{x},t)+\\&+\frac{S_{pp}}{\mu_0(\mathbf{x},t)}\sum_{j=0}^{k}b_{jk}^{pp}\mu_j(\mathbf{x},t)\mu_{k-j}(\mathbf{x},t),\quad k=0,1,2,...\end{aligned}\tag{62}$$

subject to the initial conditions

$$\mu_k(\mathbf{x},0)=\mu_{k,0}(\mathbf{x}),\quad k=0,1,2,...\tag{63}$$

In Eqs (62) ΔH_{coll}^{pp} denotes the internal heat source generated by particle-particle collisions, in correspondence with Eq.(27), and the coefficients of the collision terms are

$$b_{jk}^{pp}=\int_0^1\binom{k}{j}\left(\frac{\omega_{pp}}{2}\right)^j\left(1-\frac{\omega_{pp}}{2}\right)^{k-j}f_{\omega_{pp}}(\omega_{pp})d\omega_{pp},\quad k=0,1,2,...,\ j=1,2,...k\tag{64}$$

while the boundary conditions become

$$d\,\mu_k(\mathbf{x},t)\big|_{\mathcal{S}}=S_{pw}\sum_{j=0}^{k}b_{jk}^{pw}\mu_j(\mathbf{x},t)T_w^{k-j}(\mathbf{x},t)\Big|_{\mathcal{S}}\cdot dt,\quad k=0,1,2,...\tag{65}$$

and

$$\mu_k(\mathbf{x},t)\big|_{\mathcal{S}}=\mathbf{u}_{\mathbf{x}}\mu_k(\mathbf{x},t)-\mathbf{D}_{\mathbf{x}}\cdot\nabla_{\mathbf{x}}\mu_k(\mathbf{x},t)\big|_{\mathcal{S}}\tag{66}$$

where

$$b_{jk}^{pw}=\int_0^1\binom{k}{j}\left(1-p_w\omega_{pw}\right)^j\left(p_w\omega_{pw}\right)^{k-j}f_{\omega_{pw}}(\omega_{pw})d\omega_{pw},\quad k=0,1,2,...,\ j=1,2,...k\tag{67}$$

Here $\mu_k(\mathbf{x},t)$ denotes the k^{th} order moment of a given function stimulating the system across the inlet surface and that providing the outlet surface conditions.
Specifying the appropriate symmetry conditions for the spatial terms in Eq.(62) results in 3D, 2D and 1D applicative, i.e. purpose-oriented moment equation models for different gas-particle processing systems.
When applying the moment equation model, the computational results are assessed by means of the first three of the normalized moments

$$m_k(\mathbf{x},t)=\frac{\mu_k(\mathbf{x},t)}{\mu_0(\mathbf{x},t)},\ k=0,1,2\,.\tag{68}$$

Here, beside the zero order and the normalized first order moments, i.e. the total number and mean temperature of particles, the variance defined as

$$\sigma^2(\mathbf{x},t)=\frac{\mu_2(\mathbf{x},t)}{\mu_0(\mathbf{x},t)}-\left(\frac{\mu_1(\mathbf{x},t)}{\mu_0(\mathbf{x},t)}\right)^2=m_2(\mathbf{x},t)-m_1^2(\mathbf{x},t) \tag{69}$$

is used for characterizing the temperature distribution of particles.

7. Heat transfer in bubbling fluidized beds

Gas-solid fluidized beds may operate in several different flow regimes: bubbling, slug flow, turbulent and fast fluidization. With increasing superficial velocity there is a transition between the lower velocity bubbling and higher velocity turbulent fluidization states (Thompson *et al*., 1999, Bi *et al*., 2000). In the bubbling regime, as the gas flow rate increases the total volume of bubbles also increases and accounting for their coalescence and breakage, the bubble phase can be described by an axial dispersion model containing no particles. The bubbling regime, however, is characterized by intensive pressure fluctuations so that the dense emulsion phase, containing the particle population and being in intensive motion can be modeled as a perfectly stirred part of the bed as it is shown schematically in Fig. 3. At higher velocities, because of disappearance of bubbles the amplitudes of pressure fluctuations decrease significantly, and the distribution of particles along the height of the vessel becomes smoother. In this case the spatial distribution of particles is described by an axial dispersion model too, as it was analyzed by Süle *et al*. (2010).

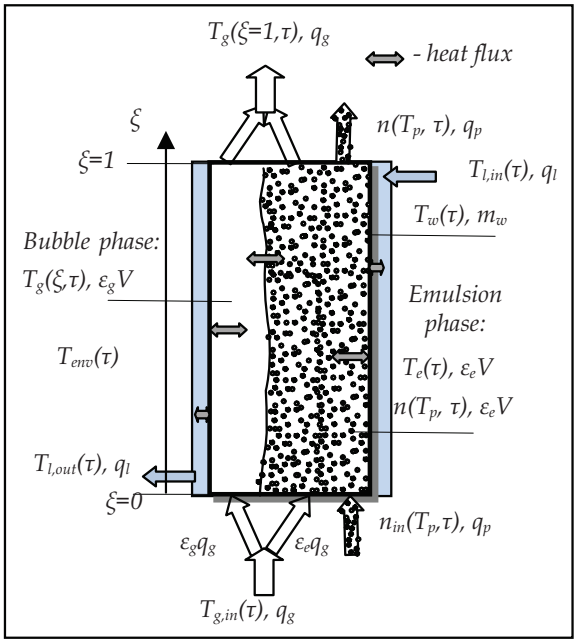

Fig. 3. Schematics of a bubbling fluidized bed

As regards the model of bubbling fluidization we start with the following assumptions.

- The bubble phase is described by an axial dispersion model, and is connected thermally with the emulsion phase through the gas and with the wall.
- The emulsion phase is a perfectly stirred cell containing the homogeneously distributed particle population. Inside the emulsion phase heat transfer occurs between the gas and particles, and there exists thermal connection of the gas and particles of the emulsion phase and the wall.
- Homogeneous temperature distribution is assumed in the wall through which the bed is connected thermally with the jacket filled with liquid.
- Liquid through the jacket flows with constant flow rate and is assumed to be thermally homogeneous.
- The bubbling fluidized bed is operated continuously.

Introducing the dimensionless variables and parameters

$$\xi = \frac{x}{X},\ \bar{t}_p = \frac{\varepsilon_e V}{q_p},\ \tau = \frac{t}{\bar{t}_p},\ Pe_b = \frac{u_b X}{D_b},\ \bar{t}_b = \frac{X}{u_b}$$

the axial dispersion model for the bubble phase is written as

$$\begin{aligned}\frac{\partial T_b(\xi,\tau)}{\partial \tau} &= \frac{\bar{t}_p}{\bar{t}_b}\frac{\partial}{\partial \xi}\left(\frac{1}{Pe_b}\frac{\partial T_b(\xi,\tau)}{\partial \xi} - T_b(\xi,\tau)\right) - K_{be}\bar{t}_p\int_0^1 \left(T_b(\xi,\tau) - T_e(\tau)\right)d\xi \\ &-K_{bw}\bar{t}_p\int_0^1 \left(T_b(\xi,\tau) - T_w(\xi,\tau)\right), \quad \tau > 0,\ \xi \in (0,1)\end{aligned} \tag{70}$$

while the corresponding boundary conditions take the forms

$$\frac{u_{b,in}}{u_b}T_{b,in}(\tau) = T_b(0+,\tau) - \frac{1}{Pe_b}\frac{\partial T_b(0+,\tau)}{\partial \xi},\ \ \frac{\partial T_b(1-,\tau)}{\partial \xi} = 0 \tag{71}$$

In Eq. (70)

$$K_{be} = \frac{a_{be}h_{be}}{\rho_g c_g} \text{ and } K_{bw} = \frac{a_{bw}h_{bw}}{\rho_g c_g}$$

denote the coefficients of heat transfers between the bubbles and, respectively, the emulsion phase and the wall.

Integrating both sides of Eq. (57) over the volume of the emulsion phase $\varepsilon_e V$ and taking into consideration the boundary conditions we obtain for the population of particles of the emulsion phase

$$\begin{aligned}&\frac{\partial n(T,t)}{\partial t} + \frac{\partial}{\partial T}\left[\frac{dT}{dt}n(T,t)\right] = \frac{q_p}{\varepsilon_e V}\left[n_{in}(T,t) - n(T,t)\right] - \left(S_{pp} + S_{pw}\right)n(T,t) \\ &+\frac{2}{N(t)}\int_0^1 \frac{S_{pp}}{\omega_{pp}}\int_{T_{\min}}^{T_{\max}} n\left[\left(\frac{2(T-y)}{\omega_{pp}} + y\right), t\right] n(y,t) f_{\omega_{pp}}(\omega_{pp})\,dy\,d\omega_{pp} + \\ &+\int_0^1 \frac{S_{pw}}{1 - p_w\omega_{pw}}\int_{T_{\min}}^{T_{\max}} n\left(\frac{y - p_w\omega_{pw}T_w(t)}{1 - p_w\omega_{pw}}, t\right) f_{\omega_{pw}}(\omega_{pw})\,dy\,d\omega_{pw}\end{aligned} \tag{72}$$

where

$$n(T,t)=\frac{1}{\varepsilon_e V}\int\limits_{\varepsilon_e V} n(x,T,t)dV \tag{73}$$

and

$$\frac{dT}{dt}=\frac{a_{pe}h_{pe}}{m_p c_p}\left[T_e(t)-T\right]+\frac{\Delta H}{m_p c_p} \tag{74}$$

where $\Delta H=\Delta H_{coll}^{pp}+\Delta H_{coll}^{pw}$ is the overall heat effects generated by the particle-particle and particle-wall collisions, in correspondence with Eqs. (27) and (47). Naturally, when the particles are homogeneously distributed in the emulsion phase then $n(T,t)\equiv n(\mathbf{x},T,t)$.
In this case the moment equations (62), taking into account Eq. (72) and written using the dimensionless variables and parameters are as follows.
Zero order moment:

$$\frac{d\mu_0(\tau)}{d\tau}=\mu_{0,in}(\tau)-\mu_0(\tau) \tag{75}$$

First order moment:

$$\begin{aligned}\frac{d\mu_1(\tau)}{d\tau}&=\mu_{1,in}(\tau)-\mu_1(\tau)+K_{pe}\overline{t}_p\left(\mu_0(\tau)T_e(\tau)-\mu_1(\tau)\right)+\\&+S_{pw}p_w m_{1,\omega_{pw}}\overline{t}_p\left(\mu_1(\tau)-T_w(\tau)\mu_0(\tau)\right)+\frac{\overline{t}_p}{m_p c_p}\Delta H\mu_0(\tau)\end{aligned} \tag{76}$$

Second order moment:

$$\begin{aligned}\frac{d\mu_2(\tau)}{d\tau}&=\mu_{2,in}(\tau)-\mu_2(\tau)+2K_{pe}\overline{t}_p\left(\mu_1(\tau)T_e(\tau)-\mu_2(\tau)\right)+\frac{2\overline{t}_p}{m_p c_p}\Delta H\mu_1(\tau)+\\&+S_{pp}\kappa_{pp}\overline{t}_p\left(\frac{\mu_1^2(\tau)}{\mu_0(\tau)}-\mu_2(\tau)\right)+2S_{pw}p_w m_{1,\omega_{pw}}\overline{t}_p\left[T_w(\tau)\mu_1(\tau)-\mu_2(\tau)\right]+\\&+S_{pw}p_w^2 m_{2,\omega_{pw}}\overline{t}_p\left(\mu_2(\tau)-2T_w(\tau)\mu_1(\tau)+T_w^2(\tau)\mu_0(\tau)\right)\end{aligned} \tag{77}$$

where the coefficients of terms representing the collision particle-particle and particle-wall heat transfers are expressed by means of expectations and variances of random parameters ω_{pp} and ω_{pw}. In Eqs. (75) and (76), we have

$$K_{pe}=\frac{a_{pe}h_{pe}}{m_p c_p}\ \text{ and }\ \kappa_{pp}=m_{1,\omega_{pp}}\left(1-\frac{m_{1,\omega_{pp}}}{2}\right)-\frac{\sigma^2_{\omega_{pp}}}{2} \tag{78}$$

The differential equation for the gas contents in the emulsion phase is given as

$$\frac{dT_e(\tau)}{d\tau} = \frac{\overline{t}_p}{\overline{t}_e}\left(T_{e,in}(\tau) - T_e(\tau)\right) - K_{we}\overline{t}_p\left(T_e(\tau) - T_w(\tau)\right) - K_{pe}\overline{t}_p\left(\mu_0(t)T_e(\tau) - \mu_1(\tau)\right)$$
$$+K_{be}\overline{t}_p\int_0^1\left(T_b(\xi,\tau) - T_e(\tau)\right)d\xi \tag{79}$$

where

$$K_{we} = \frac{h_{we}a_{we}}{\rho_g c_g},\quad K_{pe} = \frac{h_{pe}a_{pe}}{\rho_g c_g},\quad K_{be} = \frac{h_{be}a_{be}}{\rho_g c_g} \tag{80}$$

Finally the balance equation for the wall takes the form:

$$\frac{dT_w(\tau)}{d\tau} = K_{wb}\overline{t}_p\int_0^1\left(T_b(\xi,\tau) - T_w(\tau)\right) + K_{pw}\overline{t}_p\left(\mu_1(\tau) - T_w(t)\mu_0(\tau)\right) +$$
$$+K_{we}\overline{t}_p\left(T_e(\tau) - T_w(\tau)\right) - K_{wl}\overline{t}_p\left(T_w(\tau) - T_l(\tau)\right) \tag{81}$$

where

$$K_{wb} = \frac{a_{wb}h_{wb}}{\rho_w c_w},\quad K_{pw} = \frac{S_{pw}p_p m_{1,\omega_{pw}}}{\rho_w c_w},\quad K_{we} = \frac{a_{we}h_{we}}{\rho_w c_w},\quad K_{w,env} = \frac{a_{w,env}h_{w,env}}{\rho_w c_w} \tag{82}$$

while for the liquid we have:

$$\frac{dT_l(\tau)}{d\tau} = \frac{\overline{t}_p}{\overline{t}_l}\left(T_{l,in}(\tau) - T_l(\tau)\right) - K_{wl}\overline{t}_p\left(T_l(\tau) - T_w(\tau)\right) \tag{83}$$

where

$$K_{wl} = \frac{a_{wl}h_{wl}}{\rho_l c_l} \tag{84}$$

8. Simulation results and discussion

Numerical experiments for studying the behavior of bubbling fluidized bed were carried out in MATLAB environment. The basic process parameters and hydrodynamic properties of the fluidized bed were computed using the values and correlations given by Lakatos *et. al.* (2008) while the heat source generated by the energy loss due to collisions was taken constant. The details of numerical experimentation will be presented elsewhere.

Fig. 4. presents the time evolution and steady state values of the variance of temperature of particles, defined by Eq. (69), depending on the interparticle collision frequency S_{pp}. Initially the temperature of particle population was homogeneous but the particle temperature input was generated as a step function having two different temperatures $T_{p,in}^{(1)} = 20\,^{o}C$ and $T_{p,in}^{(2)} = 160\,^{o}C$, respectively, which were totally segregated from each other. Such temperature distribution is described by the input population density function having the form

$$n_{in}(T,\tau)=\phi M_{0,in}\delta\left(T-T_{in}^{(1)}\right)+(1-\phi)M_{0,in}\delta\left(T-T_{in}^{(2)}\right),\quad 0\le\varphi\le 1 \tag{85}$$

where $M_{0,in}=10^8/\mathrm{m}^3$ is the total number of particles in a unit volume, and $\varphi=0.6$ is the ratio of particles having different temperatures.

Fig. 4 shows that there may remain rather significant inhomogeneities in the temperature distribution of particles in the bed. These inhomogeneities are decreasing with increasing interparticle collision frequency therefore the particle-particle interaction play important role in homogenization of temperature inside the population of particles.

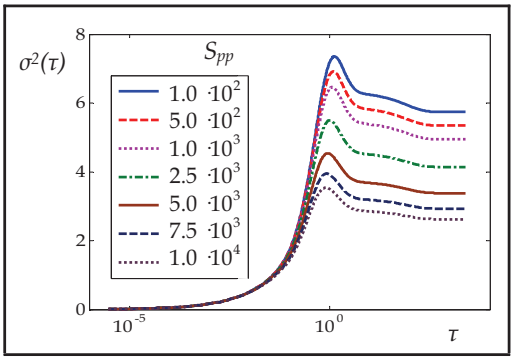

Fig. 4. Time evolution of the variance of temperature distribution of the particle population

Fig. 5 presents the time evolution of the temperatures of characteristic parts of the bubbling bed, i.e. mean temperature of particles, the temperatures of the bubble phase and the gas in the emulsion phase, as well as the temperatures of the wall and liquid in the jacket. In this case the input temperature of gas was 180 °C and the initial temperature of gas in the emulsion and bubble phases were of the same values. It is seen how the temperature profiles vary in interconnections of the different parts of the bed. In steady state, under the given heat transfer resistance conditions of the particle population, the wall and liquid is heated practically only by the gas in the emulsion phase while the bubbles flow through the bed without losing heat assuring only the well stirred state of the emulsion phase.

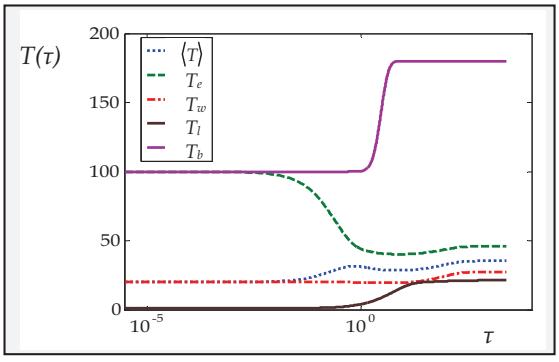

Fig. 5. Time evolution of the temperatures of characteristic parts of the bubbling bed in inter-relations with each other

In Fig. 5, bubble temperature transient is shown only for the bed output indicating here a rather sharp front. Naturally, the temperature front of bubbles evolves progressively along the bed as it shown in Fig. 6 at different axial coordinates showing that in transient states the bubble phase also plays role in the heating process.
However the bubble evolves transient states

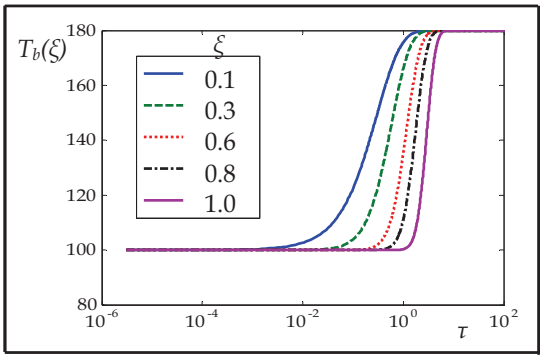

Fig. 6. Progression of evolution of the temperature front of the bubble phase along the axial coordinate of the bed

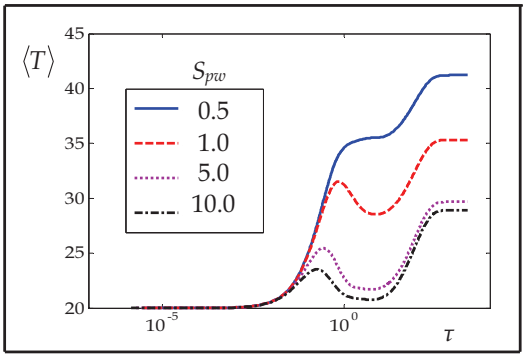

Fig. 7. Time evolution of the mean temperature of particle population as a function of the particle-wall collision frequency

Eq. (76) shows clearly that when the number of particles is constant, i.e. under steady state hydrodynamic conditions interparticle heat transfer does not influence the mean value of temperature of the particle population but, as it is demonstrated by Fig. 4, it affects the variance. However, as Fig. 7 gives an evidence of that the mean value of temperature of the particle population depends on the particle-wall collision frequency. This figure indicates also that because of the heat transfer interrelations of different parts of the bed oscillations may arise in the transient processes which becomes smoothed as the particle-wall collision frequency decreases. At the same time, in this case the particle-wall collision frequency affects also the variance of temperature distribution of the particle population as it is shown in Fig. 8. It is seen that with increasing particle-wall collision frequency the variance de-

creases. i.e. increasing particle-wall heat transfer intensity gives rise to smaller inhomogeneites in the temperature distribution of particles.

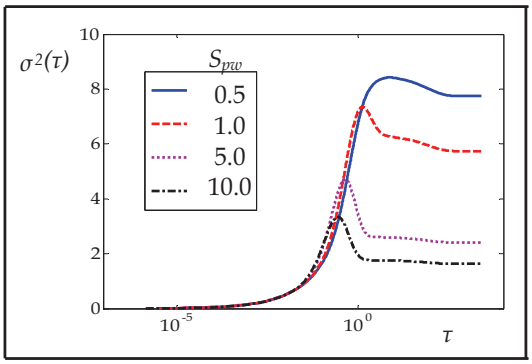

Fig. 8. Time evolution of the variance of temperature distribution of the particle population as a function of the particle-wall collision frequency

9. Conclusion

The spatially distributed population balance model presented in this chapter provides a tool of modeling heat transfer processes in gas-solid processing systems with interparticle and particle-wall interactions by collisions. Beside the gas-solid, gas-wall and wall-environment heat transfers the thermal effects of collisions have also been included into the model. The basic element of the model is the population density function of particle population the motion of which in the space of position and temperature variables is governed by the population balance equation.

The population density function provides an important and useful characterization of the temperature distribution of particles by means of which temperature inhomogeneities and developing of possible hot spots can be predicted in particulate processes. In generalized form the model can serve for cognitive purposes but by specifying appropriate symmetry conditions useful applicative, i.e. purpose-oriented models can be obtained.

The second order moment equation model, obtained from the infinite hierarchy of moment equations generated by the population balance equation, as an applicative model can be applied successfully for analyzing the thermal properties of gas-solid processing systems by simulation. The first two moments are required to formulate the heat balances of the particulate system while the higher order moments are of use for characterizing the process in more detail.

Applicability of the second order moment equation model was demonstrated by modeling and studying the behavior of bubbling fluidization by numerical experiments. It has proved that collision particle-particle and particle-wall heat transfers contribute to homogenization of the temperature of particle population to a large extent. The particle-particle heat transfer no affects the mean temperature of particle population and, in fact, no influences any of temperatures of the system whilst the particle-wall heat transfer collisions exhibits significant influence not only on the steady state temperatures but on the transient processes of the system as well. It has been demonstrated that the second order moment equation

model can be effectively used to analyze both the dynamical and steady state processes of bubbling fluidization

10. Acknowledgement

This work was supported by the Hungarian Scientific Research Fund under Grant K 77955.

11. Symbols

a	–	surface area, m^2
c	–	specific heat, J kg^{-1} K^{-1}
D	–	dispersion coefficient, m^2 s^{-1}, bed diameter, m
e	–	coefficient of restitution
f	–	probability density function
h	–	enthalpy, J; heat transfer coefficient W m^{-2} K^{-1}
K	–	aggregate rate coefficient of heat transfer
k	–	thermal conductivity, W m^{-1} K^{-1}
m	–	mass, kg
m_k	–	normalized k^{th} order moment of particle temperature
N	–	number of particles, no m^{-3}
n	–	population density function, no m^{-3} K^{-1}
p_p	–	weight parameter
p_w	–	weight parameter
Pe	–	Peclet number
q	–	volumetric flow rate, m^3 s^{-1}
S	–	frequency of collisions, s^{-1}
T	–	temperature, K
t	–	time, s
u	–	linear velocity, m s^{-1}
v	–	volume, m^3
V	–	volume, m^3
x	–	axial coordinate, m
$\bar{t}$		mean residence time, s
$\langle \cdot \rangle$		mean value
$\mathbf{1}$	-	Heaviside function

Greek symbols

β	–	aggregate heat transfer coefficient
ρ	–	density, kg m^{-3}
δ	–	Dirac delta function
κ	–	parameter
ω	–	random variable characterizing collision heat transfer
μ_k	–	k^{th} order moment of particle temperature
ε	–	volumetric fraction
ξ	–	dimensionless axial coordinate
τ	–	dimensionless time

σ^2 – variance of the temperature of particle population

Subscripts and superscripts

c – critical value
e – emulsion phase; coefficient of restitution
g – gas
in – input
b – bubble
max – maximal value
min – minimal value
p – particle
pg – particle-gas
pp – particle-particle
pw – particle-wall
w – wall
wb – wall-gas

12. References

Bi, H.T., Ellis, N., Abba, A. & Grace, J.R. (2000). A state-of-the-art review of gas-solid turbulent fluidization. *Chem. Eng. Sci.*, 55, 4789-4825.

Boulet, P, Moissette, S., Andreaux, R. & Osterlé, B., (2000). Test of an Eulerian–Lagrangian simulation of wall heat transfer in a gas–solid pipe flow. *Int. J. Heat Fluid Flow*, 21, 381-387.

Chagras, V., Osterlé, B. & Boulet, P. (2005). On heat transfer in gas-solid pipe flows: Effects of collision induced alterations on the flow dynamics. *Int. J. Heat Mass Transfer*, 48, 1649-1661.

Chang, J. & Yang, S. (2010). A particle-to-particle heat transfer model dense gas-solid fluidi-zed bed of binary mixtures. *Chem. Eng. Res. Des.*, doi:10.1018/j.cherd.2010.08.004

Delvosalle, C. & Vanderschuren, J., (1985). Gas-to-particle and particle-to-particle heat transfer in fluidized beds of large particles. *Chem. Eng. Sci*., 40, 769-779.

Gardiner, C.W.,(1983). *Handbook of Stochastic Methods*. Springer-Verlag, Berlin.

Gidaspow, D. (1994). *Multiphase Flow and Fluidization*. Boston: Academic Press.

Lakatos, B.G., Mihálykó, Cs. & Blickle, T. (2006). Modelling of interactive populations of disperse system. *Chem. Eng. Sci*., 61, 54-62.

Lakatos, B.G., Süle, Z. & Mihálykó, Cs. (2008). Population balance model of heat transfer in gas-solid particulate systems. *Int. J. Heat Mass Transfer*, 51, 1633-1645.

Mansoori, Z., Saffar-Avval, M., Basirat-Tabrizi, H., Ahmadi, G. & Lain, S. (2002). Thermomechanical modeling of turbulent heat transfer in gas-solid flows including particle col-lisions, *Int. J. Heat Fluid Flow Transfer*, 23, 792-806.

Mansoori, Z., Saffar-Avval, M., Basirat-Tabrizi, H., Dabir, B. & Ahmadi, G. (2005). Interparticle heat transfer in a riser of gas-solid turbulent flows. *Powder Technol*., 159, 35-45.

Martin, H., (1984). Heat transfer between gas fluidized bed of solid particles and the surfaces of immersed heat transfer exchanger elements. *Chem. Eng. Proc*. 18, 199-223.

Mihálykó, Cs., Lakatos, B.G., Matejdesz, A. & Blickle, T., (2004). Population balance model for particle-to-particle heat transfer in gas-solid systems. *Int. J. Heat Mass Transfer*, 47, 1325-1334.

Molerus, O., (1997). Heat transfer in moving beds with a stagnant interstitial gas. *Int. J. Heat Mass Transfer,* 40, 4151-4159.

Ramkrishna, D. (2000). Population Balances. *Theory and Applications to Particulate Systems in Engineering*. San Diego: Academic Press.

Schlünder, E.U., (1984). Heat transfer to packed and stirred beds from the surface of immersed bodies. *Chem. Eng. Proc.* 18, 31-53.

Sobczyk, K., (1991). *Stochastic Differential Equations with Applications to Physics and Engeneering.* Kluwer Academic, Amsterdam.

Süle, Z., Lakatos, B.G. & Mihálykó, Cs., (2009). Axial dispersion/population balance model of heat transfer in turbulent fluidization. in: Jeżowski J., and Thullie, J., (Eds) *Proc. 19th ESCAPE. Comp. Aided Chem. Eng. 26*, Elsevier, Amsterdam:, 815-820.

Süle, Z., Lakatos, B.G. & Mihálykó, Cs., (2010). Axial dispersion/population balance model of heat transfer in turbulent fluidization. *Comp. Chem. Eng.*, 34, 753-762.

Süle, Z., Mihálykó, Cs. & Lakatos, B.G. (2006). Modelling of heat transfer processes in particulate systems. in: W. Marquardt, C. Pantelides (Eds), Proc. *16th ESCAPE and 9th ISPSE. Comp-Aided Chem. Eng. 21A*, Elsevier, Amsterdam, 589-594.

Süle, Z., Mihálykó, Cs. & Lakatos, G.B., (2008). Population balance model of gas-solid fluidized bed heat exchangers. *Chem. Proc. Eng.,* 29, 201-213.

Sun, J. & Chen, M.M., (1988). A theoretical analysis of heat transfer due to particle impact. *Int. J. Heat Mass Transfer*, 31, 969-975.

Thompson, M.L., Bi, H. & Grace, J.R. (1999). A generalized bubbling/turbulent fluidized-bed reactor model. *Chem. Eng. Sci.*, 54, 2175-2185.

Vanderschuren, J. & Delvosalle, C., (1980). Particle-to-particle heat transfer in fluidized bed drying. *Chem. Eng. Sci.,* 35, 1741-1748

17

Synthetic Jet-based Hybrid Heat Sink for Electronic Cooling

Tilak T Chandratilleke, D Jagannatha and R Narayanaswamy
Curtin University
Australia

1. Introduction

Modern lifestyle is increasingly dependant on a myriad of microelectronic devices such as televisions, computers, mobile phones and navigation systems. When operating, these devices produce significant levels of internal heat that needs to be readily dissipated to the ambient to prevent excessive temperatures and resulting thermal failure. With inadequate cooling, internal heat builds up within electronic packages to raise microchip temperatures above permitted thermal thresholds causing irreparable damage to semiconductor material. Devices would then develop unreliable operation or undergo complete thermal breakdown from overheating with reduced working life. In electronic industry, 55 percent of failures are attributed to overheating of internal components. Therefore, effective dissipation of internally generated heat has always been a major technical consideration for microelectronic circuitry design in preventing overheating and subsequent device failure.
In recent years, the modern microelectronic industry has shown a dramatic growth in microprocessor operating power, circuit component density and functional complexity across the whole spectrum of electronic devices from small handheld units to powerful microprocessors, as evidenced by Figs. 1 and 2.

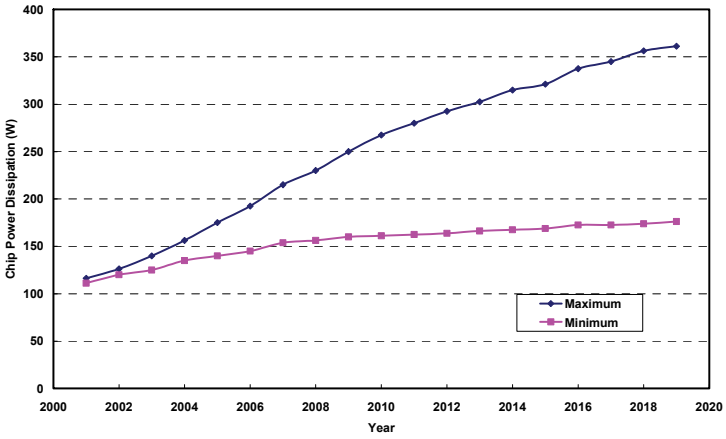

Fig. 1. Evolution of chip power dissipation (Chu, 2003)

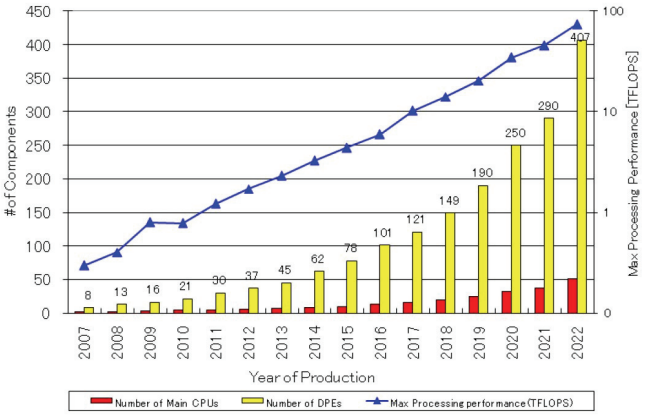

Fig. 2. Component density and maximum processing performance trends
Source: International Technology Roadmap for Semiconductors (ITRS)-2008

These industry trends into the future are very much poised to increase the microprocessor internal heat loads well beyond the capabilities of established cooling technologies making them rapidly inadequate to meet the predicted intense heat dissipation demand. For this, the future of electronic product design and development is critically hinged upon the availability of more enhanced or effective heat dissipation methods. This chapter presents a novel electronic cooling technique to address this current technological shortfall.

1.1 Thermal management techniques

In electronic system design, thermal management involves the use of appropriate heat transfer technology to remove internally generated heat as effectively as possible to retain component temperatures within safe operating limits. Literature identifies two specific stages for thermal management process. The first stage considers heat conduction from integrated circuit and to the encased package surface while the second stage deals with the global rejection of heat from the system to the ambient. Thus, the thermal management technologies can be broadly divided into two groups: (a) Technologies for enhancing heat flow integrated circuits to package surfaces, such as thermoelectric devices and heat pipes; (b) Technologies for enhancing heat exchange between the electronic package and the ambient, such as heat sinks, microchannels and fluid jet cooling. The work entailed in this chapter contributes to the latter group.

Thermal management techniques can be passive or active mechanisms. Passive techniques (e.g. convective heat sink, heat pipe) do not require additional energy input for operation; however their poor heat transfer capabilities overshadow this advantage. Intrinsically, active techniques (e.g. micro-refrigerator, microchannel heat sink) have better thermal performance, but are discredited by the extra operating power needs or higher pressure drop penalties. In spite of these limitations, active heat sinks firmly remain the most thermally effective and preferred option for future high-powered microcircuitry cooling applications, whilst passive heat sinks are being confined to low heat loads.

As an active thermal management technique, heat sinks utilising micro or mini fluid passages are highly regarded by the electronic industry to be the current frontier technology for meeting high heat dissipation demand. It has been estimated (Palm, 2001) that the

industry application of microchannel heat sinks would increase by 10 fold within the next 5 years in view of its high cooling potential achievable. A major drawback of microchannel heat sinks is their inherently high pressure drop characteristics, particularly at increased fluid flow rates necessary to deliver large cooling loads.

Motivated by the application needs of the electronic industry, the research on microchannel thermal behaviour has extensively progressed through numerical modelling and experimentation (Lee et al., 2005; Qu & Mudawar, 2002; Lee & Garimella, 2006). The primary focus of such research has been to predict and validate thermal performance. Much less attention has been directed for developing effective thermal enhancement strategies for micro-scale channels. The use of internal fins in microchannels has been identified to be a very promising passive enhancement option for single phase mini and microchannels (Steinke & Kandlikar, 2004) although the increased pressure drop is a design concern. This is well supported by a comprehensive treatment on such internal fins and possibilities for thermal optimisation (Narayanaswamy et al., 2008).

Whilst passive enhancement techniques have conceivable application potential, active methods are known to be more thermally effective and relevant for future cooling needs. Active heat sink systems can be made a more attractive proposition if an innovative approach could reduce operating power or pressure penalties without impacting on thermal performance. A hybrid heat sink incorporating a pulsating fluid jet offers a unique thermal enhancement option of this nature, as discussed below.

The proposed method utilises a special pulsing fluid jet mechanism called synthetic jet for enhancing convective heat transfer process in fluid flow channels of an active heat sink. This arrangement operates with unprecedented thermal performance but without the need for additional fluid circuits or incurring pressure drop, which are key features that set it apart from other traditional methods.

1.2 Synthetic (pulsed) jet mechanism and its behaviour

A synthetic jet is created when a fluid is periodically forced back and forth through a submerged orifice in such a way that the net mass discharged through the orifice is zero while generating large positive momentum in the jet fluid stream. A simple synthetic jet actuator is schematically shown in Fig. 3.

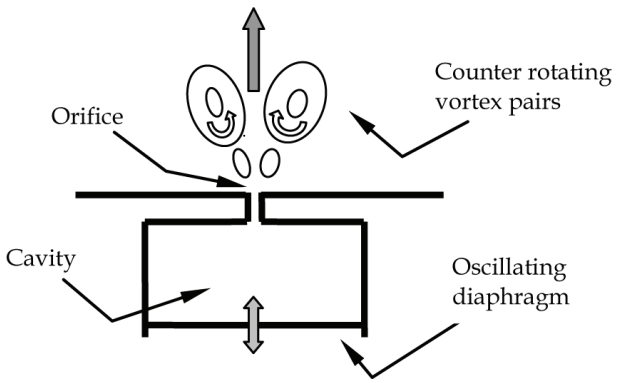

Fig. 3. Schematic diagram of a synthetic jet actuator

The actuator comprises of an oscillating diaphragm that resides within a cavity and induces a periodic fluid flow through a submerged orifice. In its upward motion, the diaphragm forces the fluid to be squirted out through the orifice with very large momentum. During downward motion, the diaphragm draws low-momentum fluid from the surroundings back into the cavity. Thus, over an operating cycle, the jet delivers very high net outflow of fluid momentum with no net change of fluid mass within the cavity. Owing to this unique feature, this jet flow is known as a synthetic jet or Zero-Net-Mass-Flux (ZNMF) jet (Smith & Glezer, 1998).

A synthetic jet impinging on a heated surface is capable of generating very high localised cooling because of the large fluid momentum imparted. As evident, this mechanism does not require additional fluid circuits to operate or introduce extra pressure drop to the flow field, which are major technical advantages. Synthetic jets are formed from the same working fluid in which they are deployed. This has significant benefits for microelectronic circuitry where air-cooling is preferred to prevent possible electrical short-circuiting and leakage faults. Smaller synthetic jet size permits high-flux clustered cooling without the need for fluid circulatory circuits unlike steady jets thereby reducing energy consumption and production cost. The diaphragm motion is practically achieved by a piston or acoustic loudspeaker or piezo-electric unit to obtain the desired amplitude or frequency.

Synthetic jets have been primarily studied in the context of pulsating jet actuators impinging on submerged surfaces in quiescent fluid media without any cross flow interactions. Such studies indicate outstanding thermal characteristics for localised cooling with synthetic jets. Significant examples of those are by (Campbell et al., 1998) who have demonstrated that synthetic air micro jets were effective cooling arrangements for laptop processors. (Mahalingam & Rumigny, 2004) illustrated the effectiveness of synthetic jets for high power electronic cooling by developing an integrated active heat sink based on this mechanism. (Gillespie et al., 2006) provide the results of an experimental investigation of a rectangular synthetic jet impinging on a unconfined heated plate exposed to the ambient where characteristics of the jet and plots of Nusselt numbers are available. (Pavlova & Amitay, 2006) have conducted experimental studies on impinging synthetic jets for constant heat flux surface cooling and compared its performance with a steady or continuous jet where there are no velocity fluctuations. They concluded that for the same Reynolds number, synthetic jets are three times more effective than the corresponding continuous jets.

(Utturkar et al., 2008) experimentally studied synthetic jet acting parallel to the flow within a duct. The synthetic jet was placed at the surface of a heated duct wall and aligned with the bulk flow such that the jet assisted the bulk flow. In a 100 mm square channel with a 30 mm synthetic jet, they obtained a 5.5 times enhancement for a bulk flow velocity 1 m/s. This enhancement reduced to approximately 3 times when the bulk velocity was increased to 2.0 m/s. Their numerical simulation matched reasonably well with only one test condition.

(Go & Mongia, 2008) experimentally studied the effect of introducing a synthetic jet into a low speed duct flow to emulate the confined flow within in a typical notebook. The interaction of these two flows was studied using particle image velocimetry (PIV) and measurements on the heated duct wall. They found that the synthetic jet tends to retard or block the duct flow while a 25 percent increase in thermal performance was observed.

Numerical studies on thermal performance of synthetic jet with cross flow interaction are also very limited in published literature. Such significant work is presented by (Timchenko et al., 2004) who investigated the use of a synthetic jet induced by a vibrating diaphragm to enhance the heat transfer in a 200 μm microchannel. Their two-dimensional (2-D) transient

simulation considered the jet acting in cross-flow to the bulk flow in a channel with the diaphragm executing a parabolic motion. They observed a 64 percent improvement in cooling at the impinging wall for the flow conditions used. Despite the recognised significance of flow turbulence in synthetic jet flows, their analysis however did not include an appropriate turbulence model in the simulation.

In a recent study, (Erbas & Baysal, 2009) conducted computational work of a synthetic jet actuator in a two-dimensional channel to assess its thermal effectiveness on a heated surface protruding into the fluid as a step. They varied the number of actuators, placement and phasing of the membrane concluding that the heat transfer rate would increase with the number of jets, appropriate jet spacing, the use of nozzle-type orifice geometry and 180^o out of phase jet operation. However, the investigation did not examine the influence of cross flow on the thermal performance.

Performing a detailed parametric study, the work presented in this chapter evaluates and quantifies the thermal enhancement benefits for fluid flow through an electronic heat sink from a synthetic jet actuator mechanism. This hybrid arrangement is numerically simulated to obtain heat and fluid flow characteristics from which unique behaviour of the jet and cross-flow interaction is analysed. The degree of thermal enhancement is with respect to a heat sink unassisted by synthetic jet flow.

2. Synthetic jet hybrid heat sink - numerical model development

2.1 Geometrical description and operation

The present study proposes a hybrid arrangement for electronic cooling utilising a synthetic jet intercating with conventional fluid stream in heat sink, as depicted in Fig. 4. The synthetic jet is induced by a cavity fitted with an oscillating diaphragm that is mounted on the heat sink. The oscilatory motion of the diaphragm injects a pulsating fluid jet through a small orifice into the fluid stream in the heat sink's flow passage. The diaphragm moving inwards, ejects a high-speed jet that creating a pair of counter-rotating vortices in the surrounding fluid. When retreating, the diaphragm draws fluid back into the cavity. The

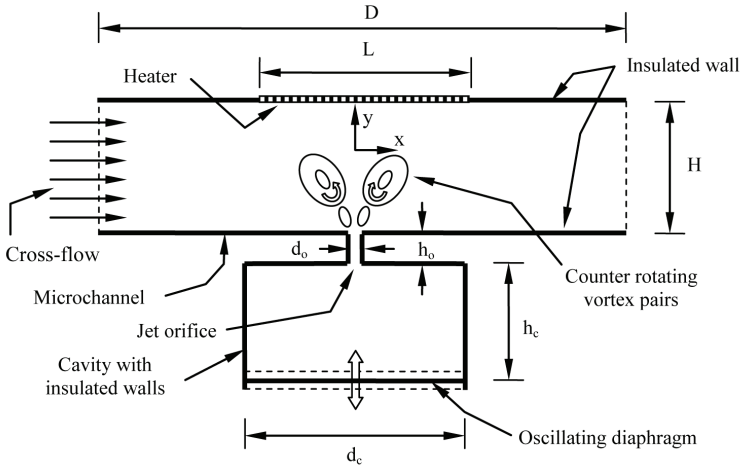

Fig. 4. Schematic diagram of synthetic jet mounted on heat sink in cross-flow configuration

fluid jet and its vortices interact in cross-flow manner with the fluid stream in heat sink's flow passage and perform periodic impingement on the heated wall. The operation over one diaphragm cycle is such, the jet delivers an intense momentum fluid outflow with zero net mass output through the orifice, hence complying with "synthetic jet" or Zero-Net-Mass-Flux jet condition.

The vortex formation associated with synthetic jet is governed by the non-dimensional groups Reynolds number (Re) and Stokes number (S), and occurs under the parametric condition of $Re/S^2>K$, where the constant $K \approx 1$ for two-dimensional jets and 0.16 for axi-symmetric synthetic jets (Holman et al., 2005). Through due consideration of this requirement, the geometrical dimensions were selected for the 2-dimensional analytical model attempted. They are: orifice width d_o = 50 μm, orifice length h_o = 50 μm, channel height H = 500 μm, channel length D = 2250 μm, heater length L = 750 μm, cavity width d_c = 750 μm and cavity height h_c = 500 μm. This selection was checked for its compliance with the continuum mechanics for the scale of the attempted problem using Knudsen number Kn, which is the ratio of the molecular free path length to representative length.

2.2 Governing equations

This study investigates the heat transfer characteristics of low Reynolds number turbulent synthetic jets operating in a confined region while interacting with fluid flow in heat sink. Applicable governing equations for the analysis are: the Navier-Stokes equations; the continuity equation and the energy equation subject to applied boundary conditions. Air is assumed to be an incompressible Newtonian fluid although compressibility effects are considered later. These equations are as follows:

Continuity
$$\frac{\partial u}{\partial x}+\frac{\partial v}{\partial y}=0 \tag{1}$$

x-momentum
$$\frac{\partial u}{\partial t}+u\frac{\partial u}{\partial x}+v\frac{\partial u}{\partial y}=-\frac{\partial p}{\partial x}+\mu\left(\frac{\partial^2 u}{\partial x^2}+\frac{\partial^2 u}{\partial y^2}\right) \tag{2}$$

y-momentum
$$\frac{\partial v}{\partial t}+u\frac{\partial v}{\partial x}+v\frac{\partial v}{\partial y}=-\frac{\partial p}{\partial y}+\mu\left(\frac{\partial^2 v}{\partial x^2}+\frac{\partial^2 v}{\partial y^2}\right) \tag{3}$$

Energy
$$\frac{\partial}{\partial t}(\rho E)=-\nabla\cdot\left(U(\rho E+p)\right)+k_{eff}\nabla^2 T \tag{4}$$

where k_{eff} is the effective conductivity and E is the total energy.

The local Nusselt number Nu (x,t) wherein the local wall heat transfer coefficient h is embedded, describes the convective heat transfer between the heated surface and the synthetic jet flow. Using orifice width d_o as the characteristic length, this is defined as,

$$Nu(x,t)=\frac{hd_o}{k_f}=\frac{\partial T}{\partial y}\frac{d_o}{\Delta T} \tag{5}$$

The Nusselt number is evaluated from the local surface normal temperature gradient, $\frac{\partial T}{\partial y}$ and the temperature difference $\Delta T = (T_w - T_b)$ where T_w is the local wall temperature and T_b is the average bulk fluid temperature the in the fluid domain.

2.3 Solution domain and boundary conditions

The 2-dimensional numerical simulation was formulated using the computational fluid dynamics software FLUENT. A structured mesh was used in the solution domain, as shown in Fig. 5 using GAMBIT mesh generation facility. The grid dependency of results was tested by observing the changes to the time-averaged velocity fields in the solution domain for varied grid sizes of 14000 (coarse), 48072 (medium) and 79000 (fine). In view of the moving mesh integrity and CPU time, the most appropriate grid size was found to be 48072 cells for a five percent tolerance between successive grid selections. In capturing intricate details of the jet formation and flow separation, the grid density in the vicinity of the orifice was refined to have 14 grid cells in the axial direction and 20 in the transverse direction.

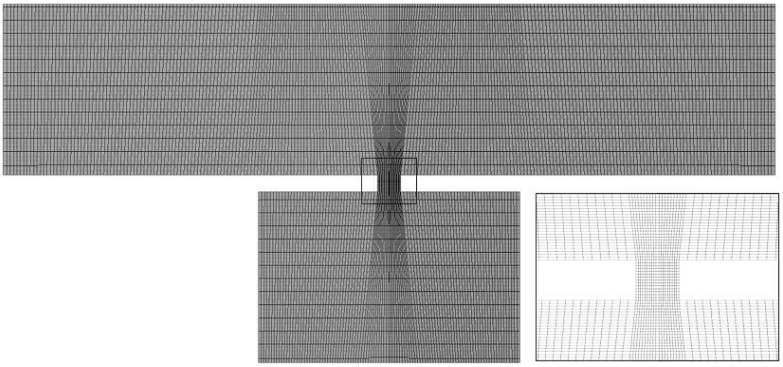

Fig. 5. Computational grid for solution domain (Inset shows enlarged view of the marked region)

Adiabatic conditions were applied at the cavity walls and the diaphragm while the heater surface was maintained at an isothermal temperature of 360 K. The (left) inlet to the heat sink flow passage was treated as a known constant velocity boundary while the (right) flow outlet was treated as pressure outlet boundary. It was assumed that the working fluid air is incompressible and has an inlet temperature of 300 K with constant thermodynamic properties under standard atmospheric conditions.

Arising from small geometrical length scales, synthetic jets generally tend to have small operating Reynolds numbers making flow turbulence seemingly unimportant. However, the oscillating nature of the flow may give rise to intense localised perturbations. In handling the wide flow variations, the Shear-Stress-Transport (SST) k-ω turbulence model was invoked in the model to provide an accurate representation of the near-wall region of wall-bounded turbulent flows. Initially, a 3 percent turbulence intensity was applied at the outlets, thereafter the flow was allowed to develop on its own through the inherent instabilities. The y+ and y* value in the wall region were found to be approximately 1, confirming that the near-wall mesh resolution is in the laminar sublayer.

2.4 Initial conditions and solution methodology

The initial (t = 0) position of the diaphragm was taken to be at the bottom of the cavity. A special User Defined Function (UDF) incorporating Dynamic-layering technique (FLUENT, 2004) was formulated and combined with the FLUENT solver to describe the periodic diaphragm movement. For this, the diaphragm displacement was expressed as y = A sin (ωt), where A is the diaphragm amplitude, ω is the angular frequency and t is time.

A segregated solution method with implicit solver formulation in FLUENT was used as the numerical algorithm while the Second-order discretisation schemes were employed for density, momentum, pressure, kinetic energy, specific dissipation rate and energy. The Pressure-Implicit with Splitting of Operators (PISO) scheme was used for pressure-velocity coupling. The bulk temperature of air at every time step was calculated using an UDF while the updated bulk temperature was fed back to the simulation for calculating local heat transfer coefficient and Nusselt number.

The jet Reynolds number (Re_c) was calculated based on the jet characteristic velocity U_c, which is defined by (Smith & Glezer, 1998) as,

$$U_c = L_s f = \frac{1}{T} \int_0^{T/2} u_0(t)\, dt \tag{6}$$

where $u_o(t)$ is the jet velocity at the orifice discharge plane, ½T is the jet discharge time or half period of diaphragm motion, and L_s is the stroke length (defined as the discharged fluid length through orifice during the inward diaphragm stroke).

Considering the operating range given in Table 1, the unsteady, Reynolds-averaged Navier-Stokes equations and the energy equation were solved to obtain the simulated thermal behaviour of the synthetic jet hybrid heat sink. The simulation was carried out using 720 time steps per cycle wherein 20 sub-iterations were performed within each time step.

Parameter	Range
Heat sink inlet flow velocity, V_i (m/s)	0, 0.5, 1.0, 2.0
Diaphragm frequency, f (kHz)	10
Diaphragm Amplitude, A (μm)	0,25,50,75,100
Jet Reynolds Number, Re_c	15, 30, 46, 62
Distance from orifice to heated wall, H/d_o	10

Table 1. Parametric range for numerical simulation

At each time step of a cycle, the internal iterations were continued until the residuals of mass, momentum, turbulence parameters (k and ω) were reduced below 10^{-3} and energy residuals were reduced below 10^{-6}, which is the convergence criterion for the computation. Data were extracted at every twentieth time step giving 36 data points per cycle. It was observed that 10 diaphragm cycles would be sufficient to achieve quasi-steady operating conditions in this flow geometry. To increase accuracy, a 2D-double precision solver was used to solve the governing equations for heat and fluid flow.

3. Results and discussion

3.1 Model validation

The model validation for the present simulation was carried out by formulating a separate synthetic jet model to match the dimensions used in the published work of (Yao et al., 2006). These results were extensively incorporated in NASA Langley Research Centre Workshop (CFDVAL2004) in assessing the suitability of turbulence models for synthetic jet flows. The results of this workshop concluded that the Shear-Stress-Transport (SST) k-ω turbulence model works best among the URANS models for jet flows.

For validation, the predicted axial (y-velocity) was compared with the experimental jet velocities measured by (Yao et al., 2006) using the techniques of Particle Image Velocimetry (PIV), Hot wire anemometry and Laser Doppler Velocimetry (LDV). This comparison is shown in Fig. 6, where it is seen that the present simulation agreed very well with the experimental data validating the model and its accuracy.

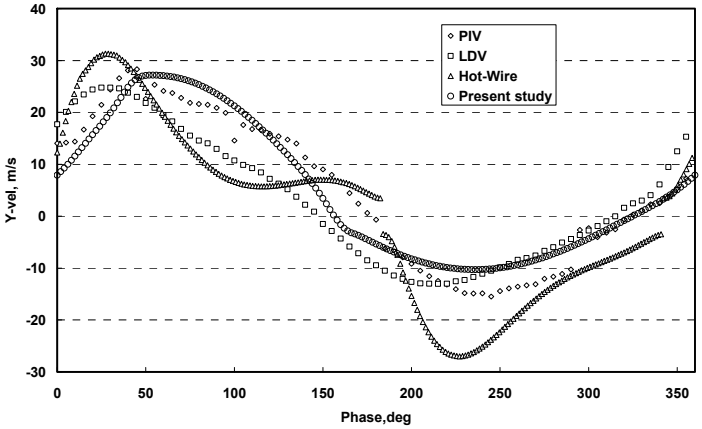

Fig. 6. Comparison of predicted axial/y-velocity of present work with the (PIV, LDV, Hot-wire) experimental data of (Yao et.al., 2006) at 0.1 mm from the orifice exit plane (f = 444.7 Hz, A=1.25 mm)

3.2 Velocity and fluid flow characteristics

For the synthetic jet operating frequency of 10 kHz and amplitude of 25 μm, Fig. 7 illustrates the diaphragm displacement and the jet discharge velocity over one cycle completed in 0.1 milliseconds. This jet velocity fluctuation resembles a sinusoidal pattern and verifies the net fluid mass discharge through the orifice to be zero for the synthetic jet operation.

Figs. 8 (a) and 8 (b) show typical time-lapsed velocity contours within the solution domain respectively for two separate cases of synthetic jet operation: (a) with stagnant fluid within heat sink (b) with flowing fluid in heat sink passages. It is seen that the simulation very well captures the intricate details of the synthetic jet discharge, subsequent vortex formation and the flow interaction between the jet and the cross-flow heat sink fluid stream.

During the diaphragm upward motion, a high-velocity fluid jet is discharged through the cavity orifice into the flow passage. Determined by diaphragm amplitude, sufficiently strong jet momentum enables the jet to penetrate the micro passage flow to reach the heated

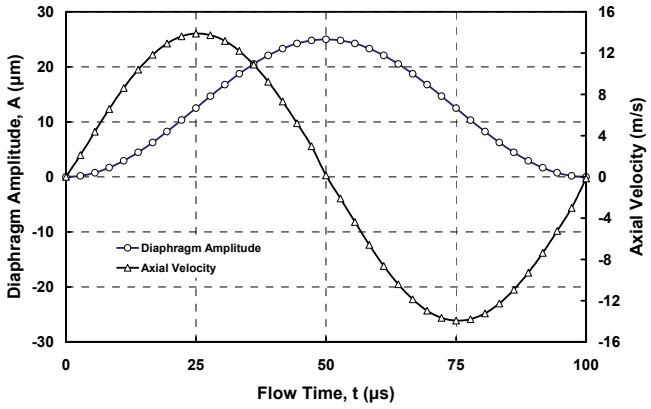

Fig. 7. Diaphragm displacement and jet velocity over one cycle at A = 25 μm and f = 10 kHz

(upper) wall within the time up to t = ½T at the peak diaphragm displacement. In the figures, the formation of synthetic jet vortices is clearly visible during this initial phase of sequence. The flow patterns exhibits symmetry in Fig. 8 (a) while the cross-flow drag imparted by the fluid stream in heat sink passage gives rise to asymmetry in Fig. 8 (b) where the jet is swayed in the streamwise direction. For t > ½T, the diaphragm retreats from its peak displacement to complete the cycle. During this final phase, the jet mechanism draws fluid back into the cavity. Meanwhile, already formed synthetic jet vortices are washed downstream by the fluid flow in heat sink passage.

Fig. 8(b) reveals that, even with the flow through heat sink, the synthetic jet still exhibits all of its fundamental characteristics corresponding to stagnant flow conditions. The synthetic jet periodically interrupts the flow through heat sink and breaks up the developing thermal and hydrodynamic boundary layers at the heated top wall. This cross-flow interaction creates steep velocity and temperature gradients at the heated surface as long as jet impingement occurs. This pulsating flow mechanism therefore leads to improved thermal characteristics in the synthetic jet-mounted heat sink.

The skewness in the jet discharge velocity profile is recognised as a prime factor in the process of synthetic jet vortex formation at the orifice. Fig. 9 shows the velocity vectors near jet orifice at t=T/2 (point of maximum jet expulsion) for two heat sink cross-flow velocities, V_i = 0.5 m/s and 2.0 m/s. The figure clearly indicates the existence of lateral flow velocities across the orifice mouth. This fluid motion induces fluid recirculation or entrainment within the orifice passage and its vicinity, encouraging the jet flow to diverge and form vortices. As illustrated, for higher heat sink cross-flow velocity, the fluid entrainment at the orifice becomes vigorous, hence producing stronger synthetic jet vortices.

The nature of synthetic jet movement through heat sink's cross flow is depicted in Fig. 10, where the axial jet velocity is plotted at several height elevations in the heat sink flow passage above the orifice plane. These velocity profiles are at t = T/2, where the diaphragm displacement is maximum with f = 10 kHz and A = 50 μm. The velocity profiles for a synthetic jet operating in stagnant fluid medium are also shown for comparison. These figures show that, the heat sink cross-flow drag shifts the point of impingement downstream of the flow passage with respect to jet operation in stagnant fluid. The jet impingement velocity is also somewhat attenuated with the increased cross-flow velocity.

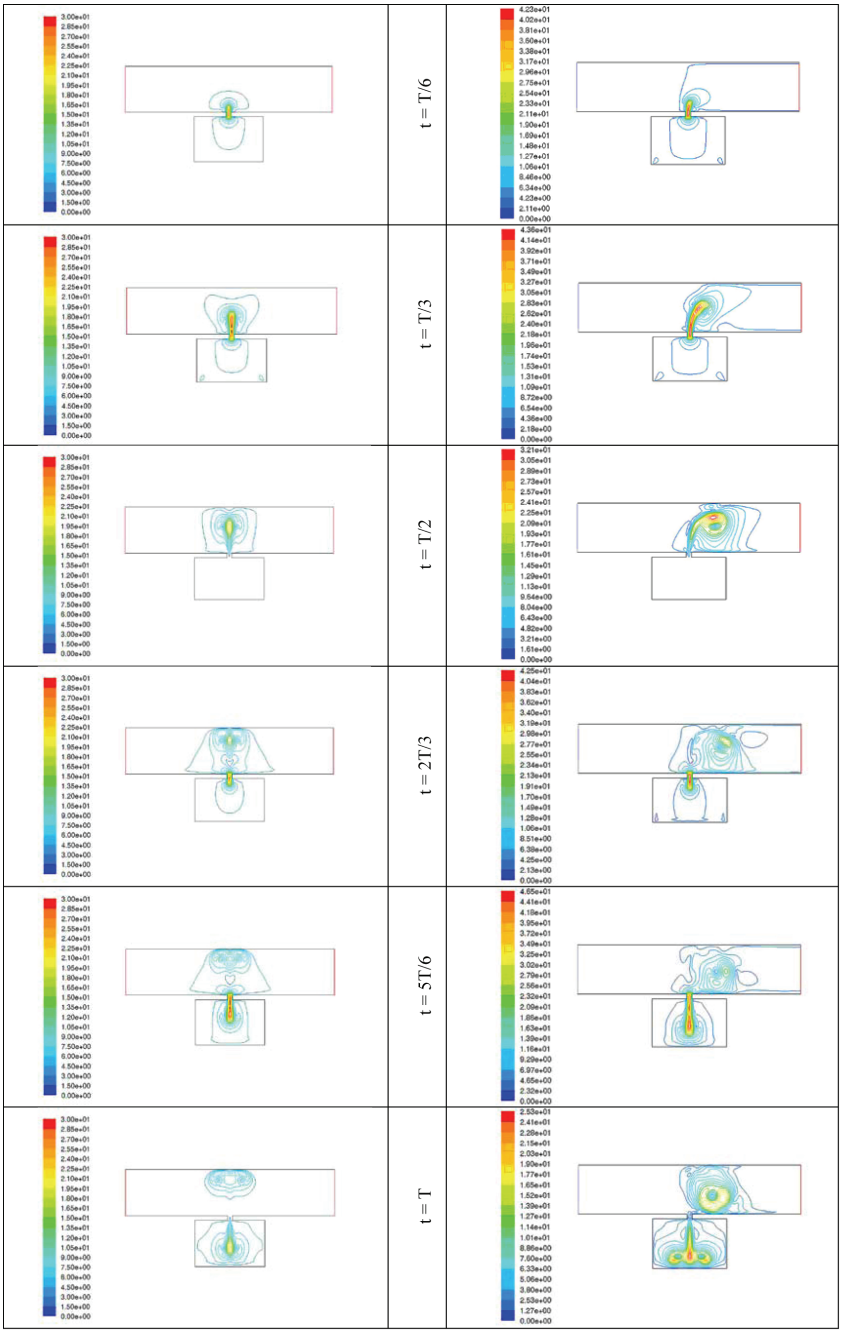

(a) V_i = 0 m/s A = 50 μm and f = 10 kHz (b) V_i = 0.5 m/s A = 75 μm and f = 10 kHz

Fig. 8. Time-lapsed velocity contours over one diaphragm cycle

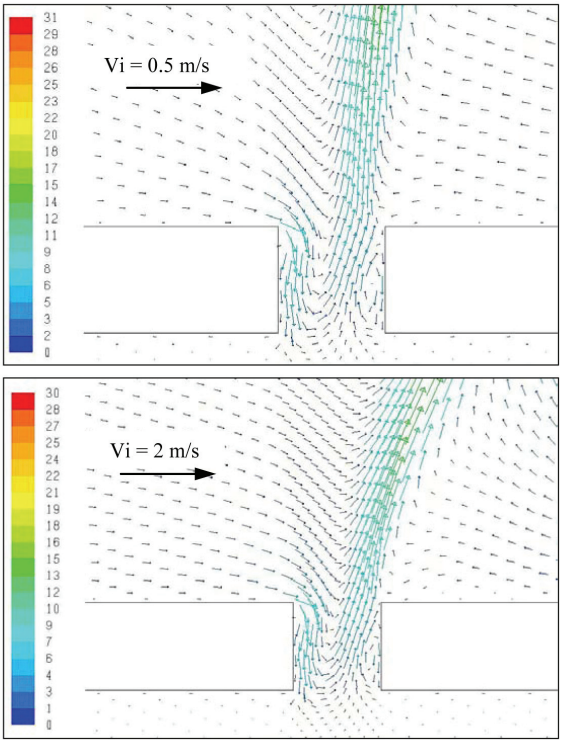

Fig. 9 Velocity vectors near the orifice at time t=T/2 (maximum expulsion)
f = 10 kHz, A = 50 μm *Note: Length of arrows and colours indicate velocity magnitude (m/s)*

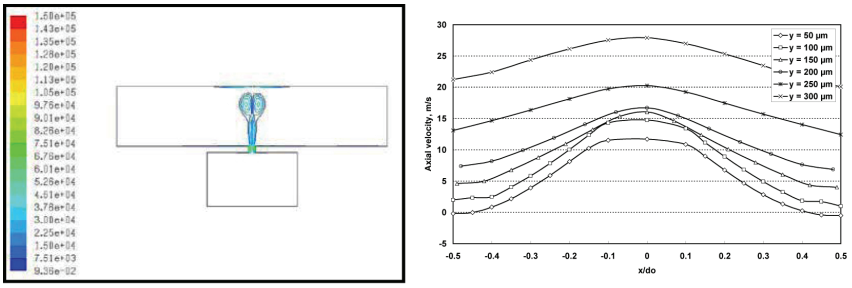

(a) V_i = 0 m/s (stagnant fluid)

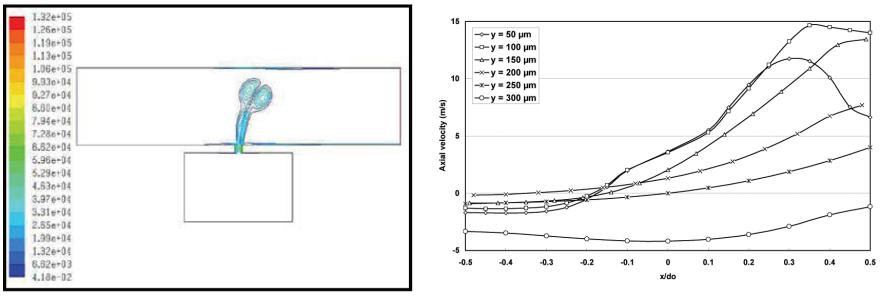

(b) V_i = 0.5 m/s

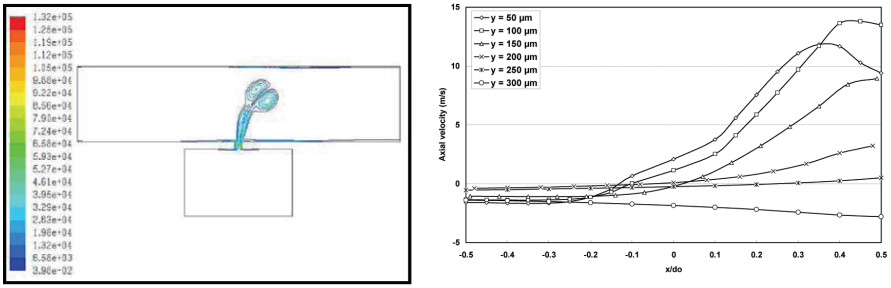

(c) V_i = 1.0 m/s

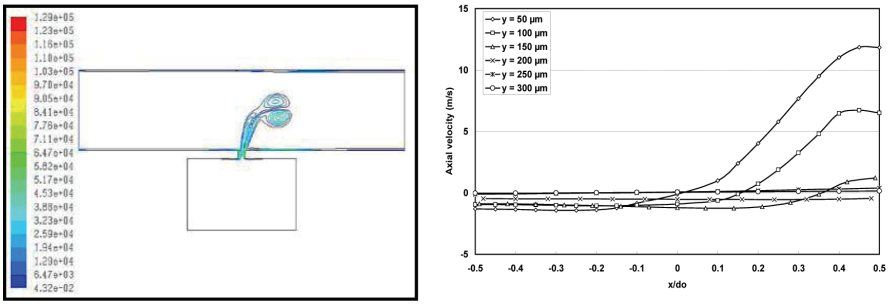

(d) V_i = 2.0 m/s

Fig. 10. Channel cross-flow effect on jet propagation at f = 10 kHz and A = 50 μm

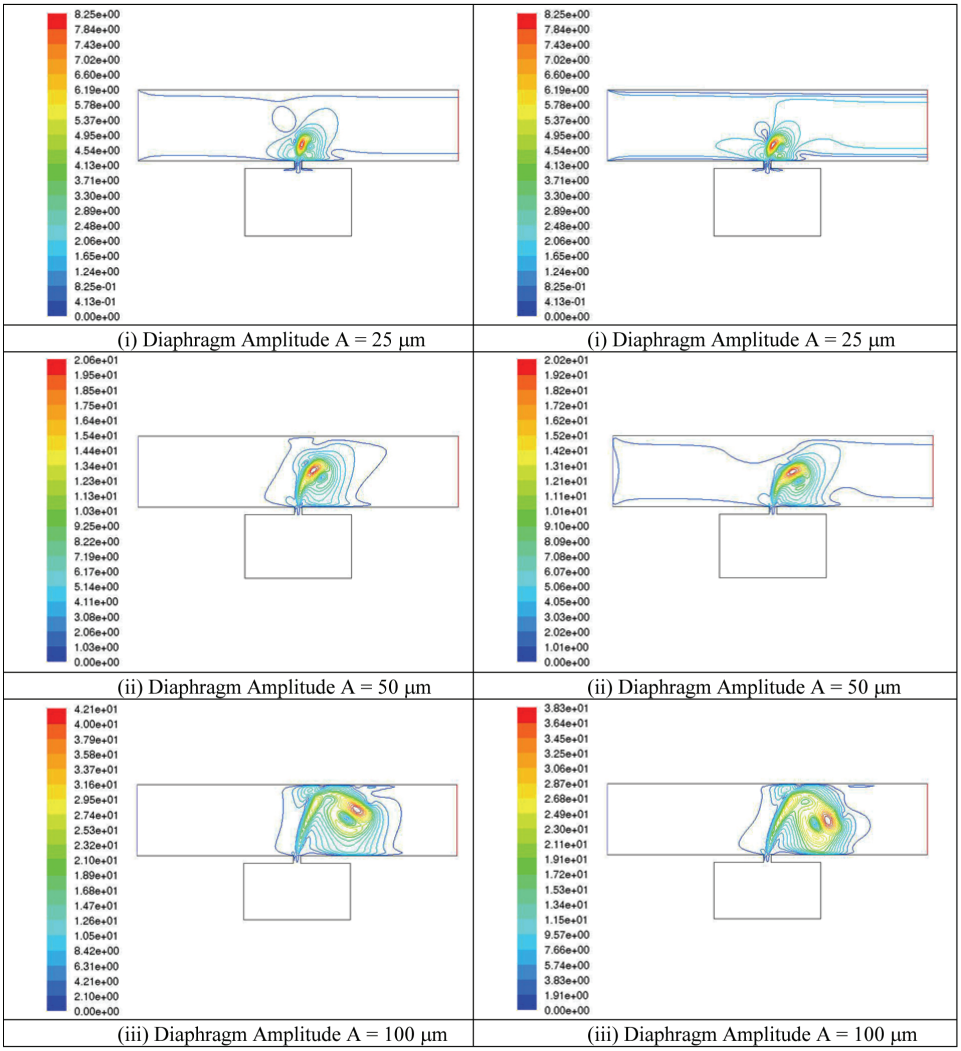

(a) V_i = 0.5 m/s, f = 10 kHz (b) V_i = 1.0 m/s, f = 10 kHz

Fig. 11. Effect of diaphragm amplitude illustrated by velocity contours at t = ½ T

Relative strengths of the synthetic jet and the channel flow drag determine the extent of cross-flow interference and the boundary layer disruption at the heated wall. This is illustrated in Figs. 11(a) and 11(b) for heat sink flow velocities of 0.5 m/s and 1.0 m/s. It is clearly evident that the increased cross-flow causes the jet to be swayed downstream impeding the jet's penetrating ability through the boundary layer to reach the heated wall. Although this may reduce thermal benefits from jet impingement, the steeper velocity gradients generated by the cross-flow and jet interaction at the heated wall may improve forced convection heat transfer, leading to an increase in overall thermal performance.

3.3 Thermal characteristics and heat transfer enhancement

The vortex generation process of the synthetic jet creates fluid flow structures very conducive for heat transfer at the heated wall. This is effected by two major mechanisms: (a) development of steep temperature gradients at the heated wall due to periodic thinning of the thermal boundary layer arising from the synthetic jet and vortex impingement, and (b) vigorous mixing of heated fluid layers at the wall with the bulk fluid, thus rapidly transferring heat from the wall to the fluid. The temperature contours in Fig. 12 clearly illustrate these two mechanisms. It is seen that, the regions of high fluid temperature are essentially near the heated wall giving extremely high temperature gradients in that vicinity and, it takes only a few cycles for the temperature dispersion into the bulk fluid.

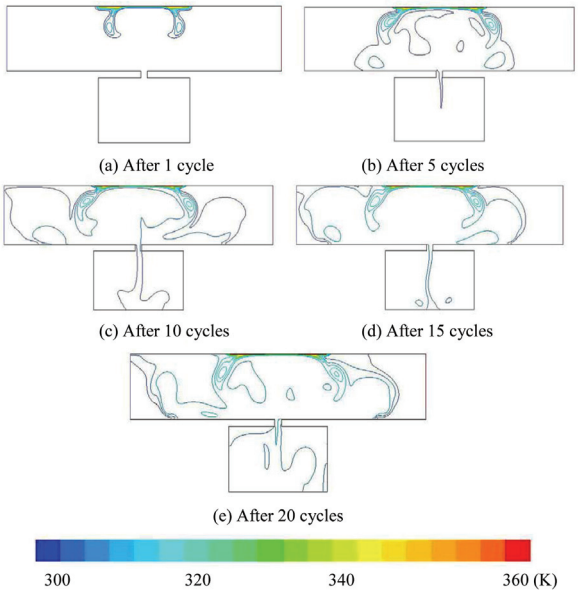

Fig. 12. Temperature contours within the solution domain after 1, 5, 10, 15 and 20 cycles

Over one diaphragm cycle, Figs. 13 and 14 show the distribution of local Nusselt numbers at the heated wall respectively, for the cases of with and without fluid flowing through the heat sink flow passage.

In Fig. 13 for $0 < t < \frac{1}{2}T$, the Nusselt number remains very low. This value is more or less similar to natural convection since the synthetic jet and vortices have yet to impinge on the heated surface. Nusselt number shows a very rapidly increase to about 23 when $t = 2T/3$, where the vortices begin to impinge on the heated surface. Subsequently, the Nusselt number gently declines for $t > 2T/3$ as the jet recedes and diaphragm descends. On the contrary, the variation of local Nusselt number in Fig. 14 shows a gentler rise over the entire heated wall during the cycle because of the forced convection due to the fluid flow in heat sink passage. At each time step, a peak is noticed in the distribution due to the jet and cross-flow fluid interaction. At $t = 2T/3$, the Nusselt number shows its highest value of about 13 in the cycle. The position of this peak is shifted downstream because of the cross-flow fluid drag swaying the impinging jet, as depicted in Figs. 8, 10 and 11.

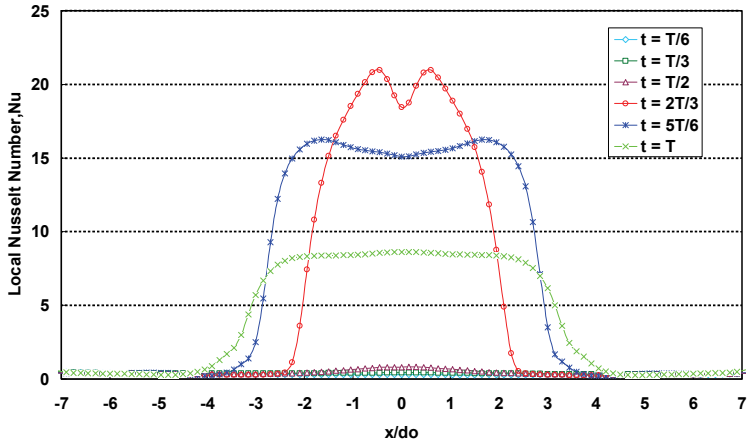

Fig. 13. Local Nusselt number at heated wall with stagnant flow in heat sink over one cycle V_i =0 m/s, f = 10 kHz and A = 50 μm

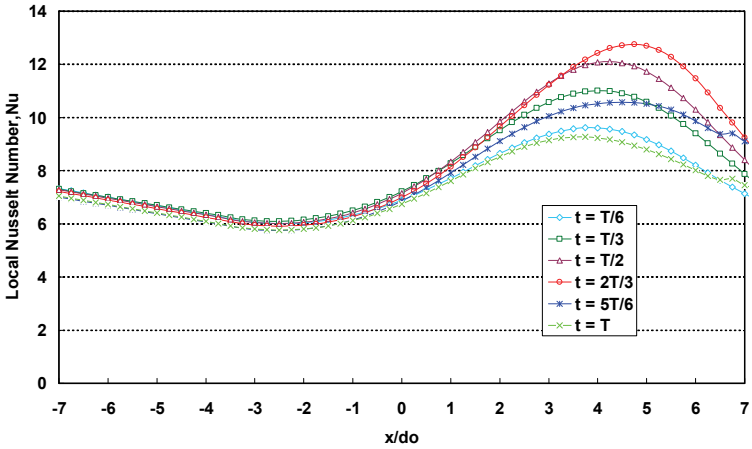

Fig. 14. Local Nusselt number at heated wall with flowing fluid in heat sink over one cycle V_i =1 m/s , f = 10 kHz and A = 50 μm

In evaluating thermal benefits delivered by the synthetic jet interaction to heat sink passage, a separate simulation was performed without the diaphragm movement while retaining all the other geometrical and boundary conditions, as described before. For this pure forced convection heat sink without the synthetic jet, Fig. 15 shows the variation of local Nusselt number over the heated wall. It is observed that the Nusselt number asymptotically decays from the leading edge of heated wall with the developing flow. Taking this pure forced convection Nusselt number as the datum, the relative thermal performance of the hybrid synthetic jet-heat sink is evaluated and presented in Fig. 16, where the degree of thermal enhancement is expressed as the ratio of average heat sink Nusselt number with and

without synthetic jet operation. It is evident that, for the tested parametric range, the synthetic jet-based hybrid heat sink arrangement is capable of delivering up to 4.3 times (V_i=0.5 m/s) more heat transfer than an identical pure forced convection heat sink. Because of the nature of synthetic jet mechanism, this degree of thermal enhancement is realised without introducing additional net mass flow into the heat sink flow passage or needing additional fluid circuits. These are recognised as major operational benefits of this hybrid heat sink mechanism. Fig. 16 further shows that, higher cross-flow velocity impairs thermal enhancement. This is a manifestation of channel flow drag swaying the synthetic jet downstream preventing jet impingement. As the jet Reynolds number (or jet velocity or diaphragm amplitude) is increased for a given cross-flow velocity, the thermal enhancement rapidly increases when the jet is able to penetrate and reach the heated surface.

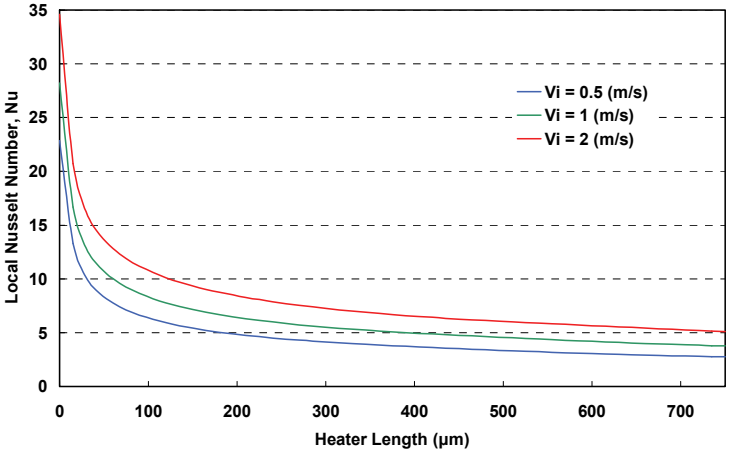

Fig. 15. Variation of Nusselt number along the heater surface without synthetic jet

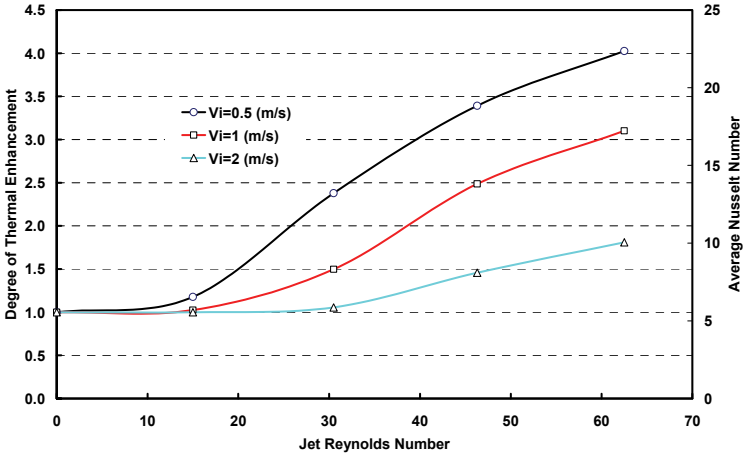

Fig. 16. Degree of thermal enhancement in heat sink due to synthetic jet mechanism

For increasing channel velocity, Fig. 17 shows the thermal performance and pressure drop of a heat sink without synthetic jet mechanism. If this heat sink were to deliver, for example, 4.3 times thermal enhancement, it would require a 40-fold high velocity from a datum value of 0.5 m/s. This would result in 70 times more channel pressure drop. On the other hand, the synthetic jet-based hybrid heat sink achieves 4.3-fold thermal enhancement with 0.5 m/s channel flow velocity with no increase in pressure drop. This clearly signifies the thermal enhancement potential of this hybrid arrangement and its operational benefits.

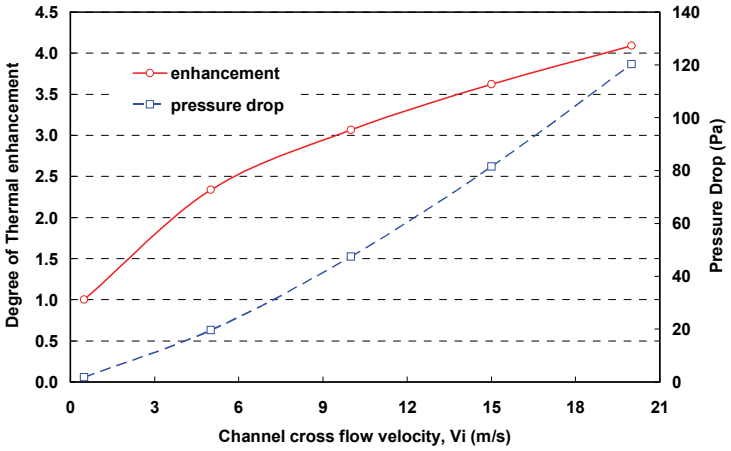

Fig. 17. Degree of thermal enhancement and pressure drop without synthetic jet mechanism

3.4 Fluid compressibility effects on synthetic jet performance

The compressibility of air mass within the cavity may affect the jet discharge, thus the heat sink performance, when the diaphragm operating frequency is varied. In examining this, two identical simulations are carried out and the results are compared. The first case is performed assuming constant air density, so that the fluid compressibility is totally eliminated. In the second case, the fluid density is taken to be dependant on local pressure in the solution domain with all the other simulation parameters being identical.

For the analyses with and without air compressibility, Fig. 18 illustrates the variation of Nusselt number with diaphragm frequency. The Nusselt numbers for both cases closely follow each other and increase almost linearly up to about 20 kHz. Beyond this, the Nusselt number predicted by the compressibility analysis quickly deviates and indicates a drop in magnitude while the incompressible Nusselt number continues to grow. The former behaviour shows a minimum at a frequency of around 80 kHz in heat sink with stagnant channel flow. At this frequency, the fluid discharge through the orifice is observed to cease. This is attributed to the simultaneous expulsion and ingestion of air neutralising the flow though the orifice or formation of standing waves. Therefore, a temporary breakdown occurs in the synthetic jet thermal effectiveness. However, the performance readily recovers beyond this critical diaphragm frequency. When the cross-flow is introduced, this limiting frequency is dramatically reduced to about 40 kHz at 0.5 m/s channel velocity. It is thought to be due to choking of the orifice arising from the increased flow entrainment at the orifice passage, as previously explained with respect to Fig. 9.

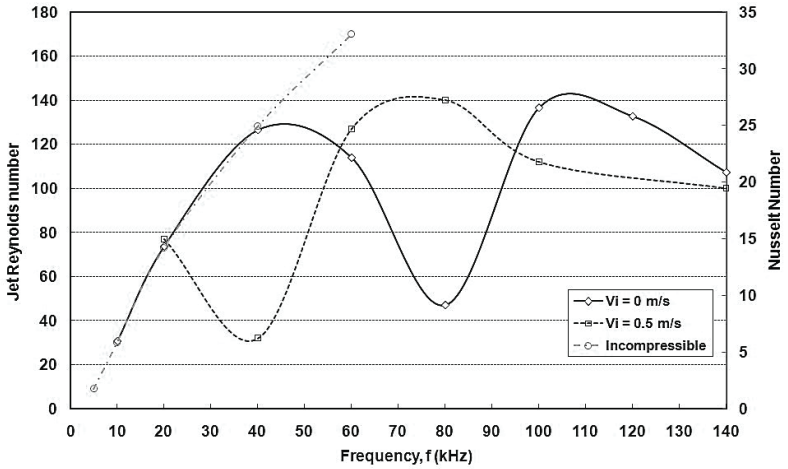

Fig. 18. Effect of compressibility on synthetic jet heat sink characteristics

4. Conclusions

This study has successfully demonstrated a novel technique for enhancing thermal performance of pure convective heat sinks in electronic cooling applications. The proposed method utilises a periodic fluid jet called "Synthetic Jet" that is injected into the heat sink's flow channel with a large fluid momentum but with zero averaged fluid mass discharge. The interaction between the jet and the fluid flow in channel creates excellent thermal characteristics at the heated wall thereby enhancing the heat sink's thermal performance. In the tested range, this synthetic jet-based heat sink delivers up to 4.3 times more wall heat transfer compared to an identical pure convection heat sink. Under incompressibility conditions, the thermal performance continues to grow with the increased diaphragm frequency. When the fluid compressibility is accounted for, the thermal performance temporarily falls upon reaching a certain frequency and then recovers with further frequency increase. This hybrid flow system has a unique ability to achieve excellent heat transfer rates without higher channel flow velocities in heat sink or causing pressure drop increases in flow passage. Also, this mechanism does not require additional fluid circuits to achieve such high heat transfer rates. These are identified as key operational attributes that set it apart from other thermal enhancement strategies.

5. References

Chu, R C. (2003). The Perpetual Challenges of Electronic Cooling Technology for Computer Product Applications-from laptop to supercomputers. *National Taiwan University Presentation*, November 12, 2003, Taipei, Taiwan.

Campbell, J S.; Black, W Z. & Glezer, A. (1998). Thermal Management of a laptop Computer with Synthetic Air Microjets, *InterSociety Conference on Thermal Phenomena, IEEE*, 43-50.

Erbas, N. & Baysal, O. (2009). Micron-level actuators for thermal management of microelectronic devices, *Heat Transfer Engineering*, Vol. 30, No. 1-2, 138-147.

FLUENT User Guide Manual 6.2.16, 2004.

Gillespie, M B.; Black, W Z.; Rinehart, C. & Glezer, A. (2006). Local Convective Heat Transfer From a Constant Heat Flux Flat Plate Cooled by Synthetic Air Jets, *Journal of Heat Transfer*, Vol. 128, 990-1000.

Go, D B. & Mongia, R K. (2008). Experimental studies on synthetic jet cooling enhancement for portable platforms. *IEEE*, 528-536.

Holman, R.; Utturkar, Y.; Mittal, R; Smith, B L. & Cattafesta, L. (2005). Formation criterion for synthetic jets. *AIAA Journal*, Vol. 43, No. 10, 2110-2116.

Lee, P S.; Garimella, S V. & Liu, D. (2005). Investigation of Heat Transfer in Rectangular Microchannels, *International Journal of Heat and Mass Transfer*, Vol. 48, No. 9, 1688-1704.

Lee, P S. & Garimella, S V. (2006). Thermally Developing Flow and Heat Transfer in Rectangular Mircochannels, *International Journal of Heat and Mass Transfer*, Vol. 49, No. 17, 3060-3067.

Mahalingam, R. & Rumigny, N. (2004). Thermal Management using synthetic jet ejectors. *IEEE,* Vol. 27, No. 3, 439-444.

Narayanaswamy, R.; Chandratilleke, T.T & Foong, J L. (2008). Laminar convective heat transfer in a microchannel with internal fins. *Proceedings of the 6th International ASME Conference on Nanochannels, Microchannels and Minichannels*, (ICNMM 2008-62044), Darmstadt, Germany.

Palm, B. (2001). Heat Transfer in Microchannels. *Microscale Thermophysical Engineering*, Vol. 5, 133-175.

Pavlova, A. & Amitay, M. (2006). Electronic Cooling Using Synthetic Jet Impingement, *Journal of Heat Transfer*, Vol. 128, No. 9, 897-907.

Qu, W. & Mudawar, I. (2002). Experimental and Numerical Study of Pressure Drop and Heat Transfer in a Single Phase Microchannel Heat Sink, *International Journal of Heat and Mass Transfer*, Vol. 45, No. 2, 2549-2565.

Steinke, M E. & Kandlikar, S G. (2004). Single Phase Heat Transfer Enhancement Technique in Microchannel and Minichannel Flows, *International conference of Microchannel and Minichannels*, ICMM 2004-2328, 141-148.

Smith, B L. & Glezer, A. (1998). The formation and evolution of synthetic jets. *Physics of fluids*, Vol. 10, No. 9, 2281-2297.

Timchenko, V.; Reizes, J. & Leonardi, E. (2004). A numerical study of enhanced micro-channel cooling using a synthetic jet actuator. *Proceedings of the 15th Australasian Fluid Mechanics Conference,* Sydney, Australia.

Utturkar, Y.; Arik, M. & Gursoy, M. (2007). Assessment of cooling enhancement of synthetic jet in conjunction with forced convection, *Proceedings of IMECE2007,* November 11-15, Seattle, USA.

Yao, C S.; Chen, F J. & Neuhart, D. (2006). Synthetic Jet Flowfeild Database for Computational Fluid Dynamics Validation, *AIAA*, Vol. 44, No. 12, 3153-3157.

18

Turbulent Flow and Heat Transfer Characteristics of a Micro Combustor

Tae Seon Park[1] and Hang Seok Choi[2]
[1]*School of Mechanical Engineering, Kyungpook National University*
[2]*Environment & Energy Systems Research Division,*
Korea Institute of Machinery and Materials
Republic of Korea

1. Introduction

Currently, a micro gas turbine (MGT) has been widely drawing attention as a distributed energy generation system for an individual household or a small community. In parallel to the progress of MGT technology, a fuel cell has been highlighted for its high efficiency and environmental advantages. For MGT, its efficiency can reach to 40% (Mcdonald, 2000), but it seems to be difficult to achieve higher efficiency than 40% (Kee et al., 2005; Suzuki et al., 2000). However, the efficiency of solid oxide fuel cell (SOFC) for electricity generation recently becomes 50% or higher. Therefore, a hybrid system with MGT and SOFC is promising because the MGT/SOFC hybrid system can provide higher efficiency over 70% (Massardo & Lubelli, 2000). Recently, (Suzuki et al., 2000) proposed the MGT/SOFC hybrid system having a micro combustor. In their system, the micro combustor is an important component to realize high system efficiency and low toxic exhausted gas. In a combustor of that kind, combustion efficiency may decrease by two critical issues, because combustion in a very small chamber may not simply resemble a scaled-down version of its large-scale counterpart (Choi & Park, 2009).

One is the incomplete mixing between oxidant and fuel, which is highly related to reliable ignition and flammable limits. As a combustor size decreases, Reynolds number becomes smaller. Such a small combustor may be suffering from incomplete mixing between fuel and oxidant, insufficient fuel residence time for complete combustion and high heat transfer rate to combustor outside because of high surface to volume ratio. In that situation, flow field is significantly stabilized by viscous effect and this may restrain active turbulent mixing. This mechanism is not favorable for small combustor. Therefore, mixing enhancement is a critical consideration to develop such a micro combustor. (Suzuki et al., 2000) suggested a baffle plate to enhance the slow mixing in low Reynolds number condition. Its effectiveness is evaluated by the succeeding studies by (Choi et al., 2001; Choi et al., 2005; Choi et al., 2006a; Choi et al., 2008) for turbulent mixing fields downstream of the baffle plate. Micro combustor of this type is expected to secure zero emission of toxic gases and to maintain a stable flame for burning the effluent of SOFC in an extraordinary fuel lean condition.

The other issue is the effect of heat loss to wall. This may be ignored in a large-scale combustor, but it is an important factor to a micro combustor. Heat generation depends on the combustor volume and mixing characteristics, while the heat loss is proportional to the surface area. In general, the surface-to-volume ratio for a micro combustor is larger than that

of a large-scale counterpart. For a can-type combustor, combustor volume and surface area are $V = \pi r^2 L$ and $A = 2\pi rL$, respectively. Here, r and L are radius and length of the combustor. Therefore, the heat loss increases more rapidly than the heat generation as the combustor size is reduced. As discussed by (Choi et al., 2001; Choi et al., 2006b), a heat loss has a critical influence on combustor efficiency. Excess enthalpy loss makes it difficult to sustain stable combustion by thermal quenching.

This chapter provides characteristics of turbulent flow and heat transfer in a micro can combustor (Choi et al., 2001; Choi et al., 2005; Choi et al., 2006a; Choi et al., 2006b; Choi et al., 2008; Choi et al., 2009). Three different shapes of baffle plates, leading to different values of oxidant to fuel velocity ratios, are selected and thermal quantities are scrutinized based on the flow structures. In particular, we are focused on investigating the heat loss of nonreacting flows in the micro combustor with baffle plate. For that purpose, conjugate heat transfer of the combustor is analyzed by using large eddy simulation (LES). As a result, peculiar characteristics of the heat transfer in the micro combustor with multiple jet flows are elucidated.

2. Numerical methods

2.1 Computational procedure

In LES method, small-scale or subgrid-scale quantities of governing equations are filtered out and then comparably large-scale ones are considered. The filtered forms of continuity and momentum equations for incompressible fluid are expressed as follows:

$$\frac{\partial \overline{u}_i}{\partial x_i} = 0, \tag{1}$$

$$\frac{\partial \overline{u}_i}{\partial t} + \overline{u}_j \frac{\partial \overline{u}_i}{\partial x_j} = -\frac{1}{\rho}\frac{\partial \overline{p}}{\partial x_j} - \frac{\partial \tau_{ij}}{\partial x_j} + \nu \frac{\partial^2 \overline{u}_i}{\partial x_j \partial x_j}, \tag{2}$$

where $\overline{u}_i$, $\overline{p}$ and $\overline{\tau}_{ij}$ are the filtered velocity, filtered pressure and the subgrid-scale stress tensor, respectively. In Equation (2), $\overline{\tau}_{ij}$ is defined as $\overline{\tau}_{ij} \equiv \overline{u_i u_j} - \overline{u}_i \overline{u}_j$ and the dynamic subgrid-scale model (Lilly, 1992) is adopted in the present study as follows:

$$\overline{\tau}_{ij} - 1/3\delta_{ij}\overline{\tau}_{kk} = -2\nu_t \overline{S}_{ij} \tag{3}$$

here $\overline{S}_{ij} = 0.5(\partial \overline{u}_i / \partial x_j + \partial \overline{u}_j / \partial x_i)$ and ν_t is the eddy viscosity to be obtained. The eddy viscosity is given by $\nu_t = C\overline{\Delta}^2 |\overline{S}|$ and $|\overline{S}| = \sqrt{2\overline{S}_{ij}\overline{S}_{ij}}$. Here, the width of grid filter is taken by $\overline{\Delta} = (\Delta x \Delta y \Delta z)^{1/3}$ and model constant C is obtained from the least square technique suggested by (Lilly, 1992).

For turbulent thermal field, the filtered governing equation of temperature, $\overline{\theta}$, is used to represent the evolution of thermal field.

$$\frac{\partial \overline{\theta}}{\partial t} + \overline{u}_j \frac{\partial \overline{\theta}}{\partial x_j} = \frac{\partial}{\partial x_j}\left[\frac{\nu}{\mathrm{Pr}}\frac{\partial \overline{\theta}}{\partial x_j} - \frac{\nu_t}{\mathrm{Pr}_t}\frac{\partial \overline{\theta}}{\partial x_j}\right], \tag{4}$$

here Pr_t is turbulent Prandtl number and its value is carefully selected (Moin et al., 1991; Andreopoulos, 1993). The Prandtl numbers are set constant as $\mathrm{Pr}=0.7$ and $\mathrm{Pr}_t=0.9$. Although more resonable value is possible, it is not important because this study aims to see how the geometrical variation is effective on the heat transfer variation.

The $k-\varepsilon-f_\mu$ model of (Park et al., 2003) is employed for comparison. The turbulent kinetic energy equation and its dissipation rate equation are

$$\frac{\partial k}{\partial t}+U_j\frac{\partial k}{\partial x_j}=\frac{\partial}{\partial x_j}\left[\left(\nu+\frac{\nu_t}{\sigma_k}\right)\frac{\partial k}{\partial x_j}\right]+P_k-\varepsilon, \tag{5}$$

$$\frac{\partial \varepsilon}{\partial t}+U_j\frac{\partial \varepsilon}{\partial x_j}=\frac{\partial}{\partial x_j}\left[\left(\nu+\frac{\nu_t}{\sigma_\varepsilon}\right)\frac{\partial \varepsilon}{\partial x_j}\right]+(C^*_{\varepsilon 1}P_k-C_{\varepsilon 2}f_2\varepsilon)/T+C_{\varepsilon 3}(1-f_W)\nu\nu_t\left(\frac{\partial^2 U_i}{\partial x_j\partial x_k}\right)^2. \tag{6}$$

Here, $f_2=1-(2/9)\exp(-0.33R_t^{1/2})$, $T=\sqrt{(k/\varepsilon)^2+36(\nu/\varepsilon)}$

and $C^*_{\varepsilon 1}=1.42+C_\mu/(1+5f_{\mu 2}(C_\mu\eta)^2)$.

The Reynolds stress can be expressed in a conventional form as

$$-\overline{u_iu_j}^{linear}=\nu_t\left(\frac{\partial U_i}{\partial x_j}+\frac{\partial U_j}{\partial x_i}\right)-\frac{2}{3}k\delta_{ij}, \tag{5}$$

$$-\overline{u_iu_j}=-\overline{u_iu_j}^{linear}-k\beta_2\left(S^*_{ik}S^*_{kj}-\frac{1}{3}S^{*2}\delta_{ij}\right)-k\beta_3\left(W^*_{ik}S^*_{kj}-S^*_{ik}W^*_{kj}\right) \tag{6}$$

$$-k\beta_4\left(S^*_{il}S^*_{lm}W^*_{mj}-W^*_{il}S^*_{lm}S^*_{mj}\right)-k\beta_5\left(W^*_{il}W^*_{lm}S^*_{mj}-S^*_{il}W^*_{lm}W^*_{mj}+0.5S^*_{ij}W^{*2}-\frac{2}{3}III_S\delta_{ij}\right),$$

where $\nu_t=C_\mu f_\mu k^2/\varepsilon$, $\beta_2=\tilde{\beta}_2+\tilde{\beta}_{2,wall}C_W$, $\beta_3=\tilde{\beta}_3+\tilde{\beta}_{3,wall}C_W$, $\beta_4=\tilde{\beta}_4$, $\beta_5=\tilde{\beta}_5$, $III_S=S^*_{lm}W^*_{mn}W^*_{nl}$, $S^*_{ij}=S_{ij}k/\varepsilon$, $W^*_{ij}=W_{ij}k/\varepsilon$, $S^*=\sqrt{2S^*_{ij}S^*_{ij}}$, $W^*=\sqrt{2W^*_{ij}W^*_{ij}}$. In the above, β_i represents the strain dependent coefficients and the model constant is set as $C_W=1$ for $i=j$ and $C_W=0$ for $i\neq j$. Further details regarding the formulation of the nonlinear stress-strain relation can be found in (Park et al., 2003). The variations of the eddy viscosity are allowed by decomposing f_μ into two parts, i.e., $f_\mu=f_{\mu 1}f_{\mu 2}$, where $f_{\mu 1}$ signifies the effect of wall-rpoximity in the near-wall region while $f_{\mu 2}$ represents the strain effects.

$$f_{\mu 1}=(1+f_DR_t^{-3/4})f_W^2,\ \frac{\partial^2 f_W}{\partial x_j\partial x_j}=\frac{R_t^{3/2}}{8.4^2L^2}(f_W-1) \tag{7}$$

$$f_{\mu 2}=\frac{5(1+g)}{g^2+C_\mu g^3+A_S}, \tag{8}$$

$$g=\begin{cases}\dfrac{C_0}{3}+(P_1+\sqrt{P_2})^{1/3}+\sin(P_1-\sqrt{P_2})\,|\,P_1-\sqrt{P_2}\,|^{1/3} & P_2\geq 0\\ \dfrac{C_0}{3}+2(P_1^2-P_2)^{1/6}\cos\left[\dfrac{1}{3}\arccos\left(\dfrac{P_1}{\sqrt{P_1^2-P}}\right)\right] & P_2<0\end{cases} \tag{9}$$

$$P_1=C_0\left[\frac{C_0^2}{27}-\frac{(A_S-\alpha_1\eta^2)}{6}+\frac{1}{2}\right],\ P_2=P_1^2-\left[\frac{C_0^2}{9}-\frac{(A_S-\alpha_1\eta^2)}{3}\right] \tag{10}$$

Here, $f_D=10\exp[-(R_t/120)^2]$, $L^2=k^3/\varepsilon^2+70^2\sqrt{\nu^3/\varepsilon}$, $A_S=\alpha_3^2\xi^2-\alpha_2^2\eta^2/3$, $\eta=f_W S^*$ and $\xi=f_W W^*$. The model constants are set as $C_\mu=0.09$, $C_0=2.5$, $\alpha_1=0.48$, $\alpha_2=0.375$, $\alpha_3=0.8$, $\sigma_k=1.1$, $\sigma_\varepsilon=1.3$, $C_{\varepsilon 2}=1.9$ and $C_{\varepsilon 3}=0.8$.

For the time integration of the governing equations, a PISO(Pressure Implicit with Splitting of Operator) algorithm (Issa, 1986) is adopted to Eqs. (1) through (4). Details regarding the solution procedure of the PISO algorithm can be found in (Issa, 1986) and (Park, 2006a; Park, 2006b). For the spatial discretization of the governing equations, the fourth-order COMPACT scheme (Lele, 1992) is used for the convective terms of the equations, and the fourth-order central differencing scheme is applied to the diffusion and other remaining terms. In the present study, a non-staggered grid is adopted in the generalized coordinate system. Therefore, to avoid the pressure-velocity decoupling a momentum interpolation technique is employed. The numerical method used in the present LES is fully validated as discussed in (Park, 2006a; Park, 2006b) for the turbulent channel flows and for a turbulent jet flow by (Choi et al., 2006a).

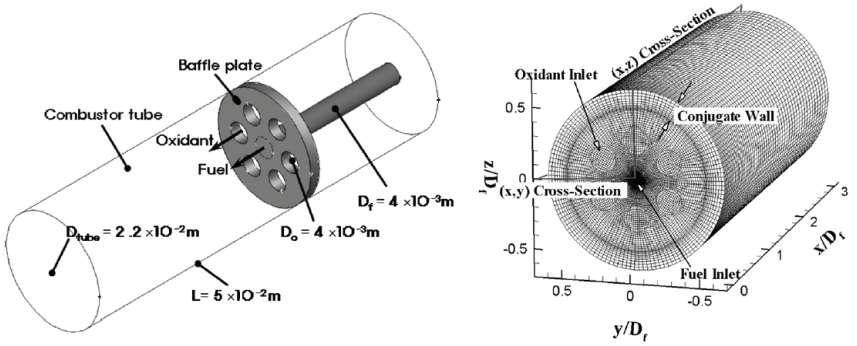

Fig. 1. A proposed micro combustor for case A. (a) configuration and (b) grid

2.2 Computational conditions

Figure 1 shows the configuration of the micro combustor, its computational domain and grid system, respectively and Table 1 describes calculation conditions for each baffle plate shape (Choi et al., 2008; Choi & Park 2009). In Fig. 1 (a), an injection nozzle for fuel is located in the center of the baffle plate and it is surrounded by six oxidant injection holes. The geometrical dimensions of the combustor are illustrated in Fig. 1 (a) for the case A. As shown in Table 1, velocity ratio is varied with the same baffle geometry or the diameter ratio, D_o/D_f, is changed so that the oxidant to fuel velocity ratio V_o/V_f is also changed. In the cases of A1, A2

and A3, Reynolds number is maintained in a similar level with the identical geometry, which is based on the total gas flow rate and the inner tube diameter of micro combustor, D_{tube}. On the other hand, Re_{tube} is kept constant as $\mathrm{Re}_{tube} = 3060$ for cases A2, B and C with different baffle plate configurations. This means that each flow rate for fuel and oxidant is kept constant but their velocities are changed. In Fig. 1 (b), x, y and z axes correspond to streamwise, transverse and spanwise directions, respectively for case A and the grid system consists of inner fluid and outer wall grids to solve conjugate heat transfer. The total grid number is set as $55 \times 52 \times 127$ through grid dependency test for all the cases of Table 1.

Case	D_o / D_f	V_o / V_f	Re_{tube}	$\theta_{inlet}(\mathrm{K})$	$\theta_{baffle}(K)$	$h_{tube}(W/m^2K)$
A1	1	1.4	3,147	800	300	20
A2	1	2	3,060	800	300	20
A3	1	2.8	2,981	800	300	20
B	2	0.5	3,060	800	300	20
C	0.5	8	3,060	800	300	20

Table 1. Calculation condition

Figure 2 shows the spectra of scalar fluctuation (E_f) for case A2 having grid numbers of $55 \times 52 \times 127$ and three different spectra along the streamwise direction are presented at a center point between fuel and oxidant jets. In fully-resolved LES results, the general relation of the energy spectrum is well reproduced by the present LES. The result shows that the spatial filtering cutoff lies outside the inertial range and higher frequency region representing scalar dissipation (Peng & Davision, 2002) is also resolved. Hence, it can be judged indirectly from the figure that the present grid allocation is enough for LES study.

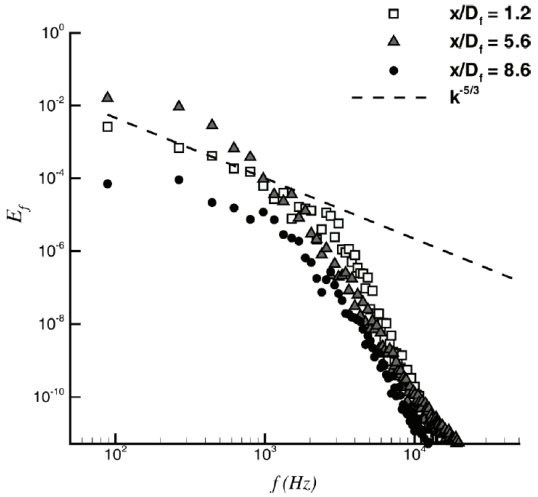

Fig. 2. Spectra of scalar fluctuation for case A2

Now, boundary conditions will be discussed as follows. For inlet boundary condition, three dimensional, unsteady nature of turbulence is considered as superposing random perturbation on streamwise velocity component as follows:

$$u = U_{inlet}(1 + I\Phi) \tag{11}$$

here Φ is a probability function which returns real number randomly in the range of $-1 \le \Phi \le 1$ and I is the fluctuation intensity. U_{inlet} is the fuel or oxidant inlet velocity described in Table 1 as V_f or V_o. For the temperature, the Dirichlet condition is applied to the fuel and oxidant inlets, respectively as presented in Table 1. For outlet boundary conditions, convective boundary condition is used as follows.

$$\frac{\partial u_i}{\partial t} + U_{exit}\frac{\partial u_i}{\partial x_j} = 0 \tag{12}$$

where U_{exit} is the mean velocity over the outflow boundary, and this convective boundary condition fulfils a correction on the streamwise velocity to ensure the global mass balance for mass flux of inlet and outlet boundaries (Ferziger & Peric, 2002). For temperature outlet boundary condition, the Neumann condition, $\partial\theta / \partial x = 0$, is adopted. In the wall boundary condition, no-slip and non-permeable conditions are adopted and for temperature the Dirichlet condition described in Table 1 is used for baffle plate. For the outer wall of combustor tube, a convective heat transfer boundary condition is applied and the heat transfer coefficient is set as in Table 1 considering the maximum limit of free convection of air. For the consistency condition of a fluid-solid interface to calculate conjugate heat transfer, the continuity of instantaneous temperature and heat flux is obtained as follows:

$$\theta|_f = \theta|_s\,,\ \kappa_f\left(\frac{\partial\theta}{\partial n}\right)_f = \kappa_s\left(\frac{\partial\theta}{\partial n}\right)_s \tag{13}$$

here subscripts f and s mean fluid and solid region at the interface and n represents the wall-normal direction.

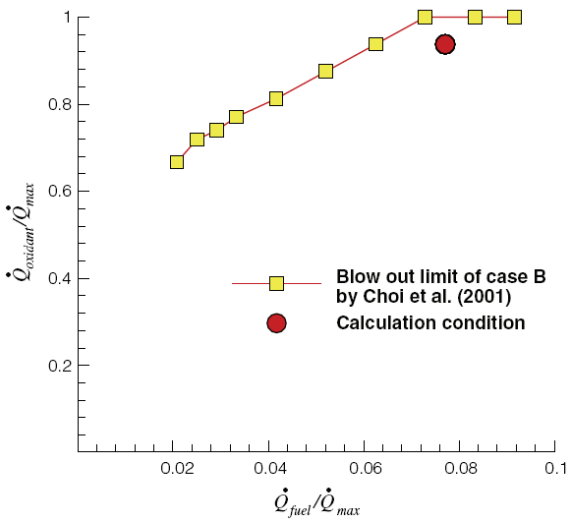

Fig. 3. Blowout limit of the flame in a micro can combustor in case B

To determine calculation condition for the mass flow rate of fuel and oxidant, experimental results (Choi et al., 2001) are used as follows. Figure 3 shows the blowout limit (Choi et al., 2001) of the flame experimentally obtained in a micro combustor with baffle plate B specified in Table 1. In case B, the mixing rate and flame stability are lower than those of other two cases. In the figure, $\dot{Q}_{oxidant}$ and $\dot{Q}_{fuel}$ mean the total volume flow rates of the oxidant and fuel which are entering into the combustor, respectively. The $\dot{Q}_{\max}$ indicates the maximum volume flow rate of oxidant below which blowout of the flame does not occur and its value is $\dot{Q}_{\max} = 8.0 \times 10^{-4} m^3 / s$.

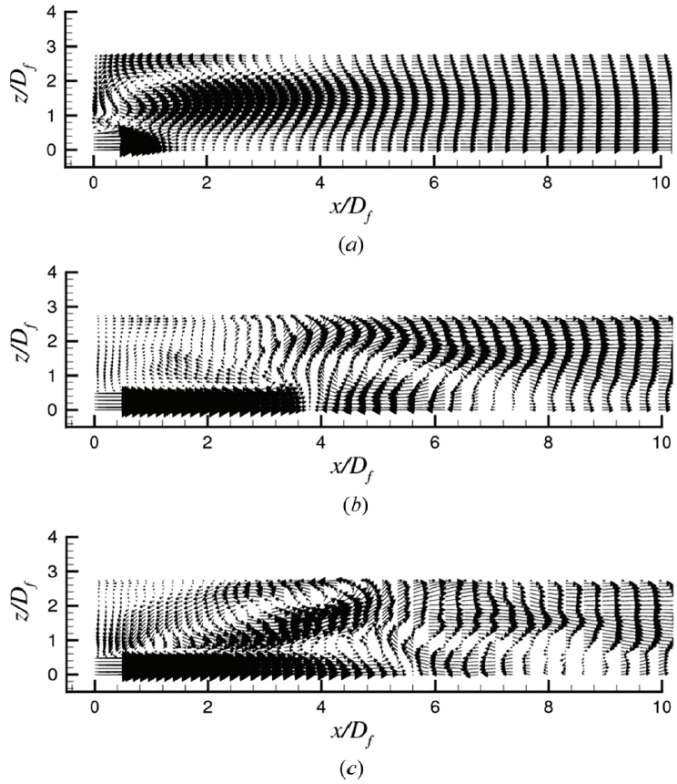

Fig. 4. Comparison of velocity vector map at (x, z) cross-section for case A2. (a) $k-\varepsilon$ model; (b) $k-\varepsilon-f_\mu$ model; and (c) the present LES

Figure 4 shows the comparison between the time-averaged results located at (x, z) plane of y = 0 obtained by using turbulence models and LES. Here, the fuel jet center is located at $x/D_f = 0$, $z/D_f = 0$, and the combustor wall is located along the top of the figure. For turbulence models, the standard $k-\varepsilon$ model and Park and Sung's low Reynolds number $k-\varepsilon-f_\mu$ one (Park et al., 2003) are used. In the case of the $k-\varepsilon$ model, the recirculation region between the fuel jet and wall appears but it cannot predict another flow recirculation region located in front of the fuel jet. However, the $k-\varepsilon-f_\mu$ model and LES predict the

flow recirculation region in front of the fuel jet but its size and location are different each other. Generally, for turbulence models it is hard to predict the turbulent flow fields with high fidelity having both free shear flow and wall bounded one according to its historical development. However, theoretically it is possible for LES to decompose the turbulence scale larger than the selected spatial filter (Benard & Wallace, 2002). Hence, in the present study, LES is selected to elucidate the turbulent and thermal fields of the micro combustor more accurately compared with turbulence models

3. Results and discussions

In the previous studies (Choi et al., 2005; Choi et al., 2006a; Choi et al., 2008), the characteristics of turbulent flow and turbulent mixing in confined multiple jet flows of a micro can combustor have been fully investigated for cases A2, B, and C by LES. It was proven that to control the fuel and oxidant jet velocities by the baffle geometry was very effective and practical for mixing in such a small combustor (Choi et al., 2001).

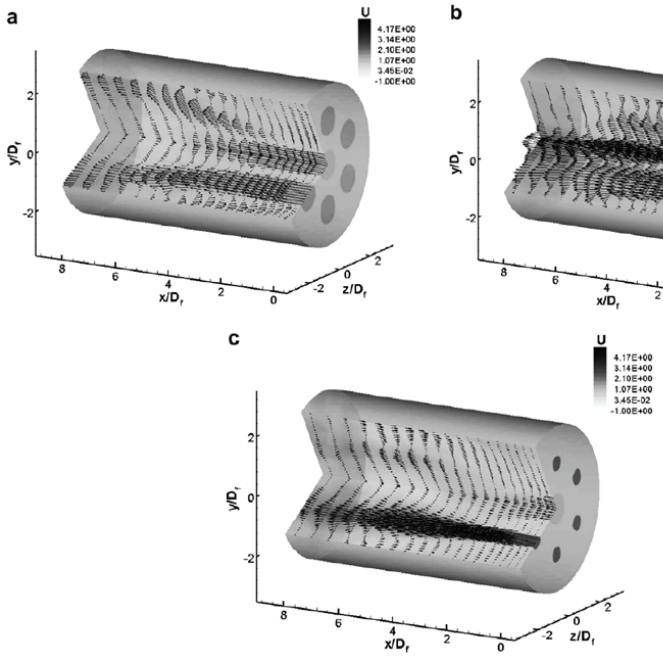

Fig. 5. Contour of streamwise velocity and velocity vector map in the two cross-sectional planes. (a)Case A2; (b) Case B; and (c) Case C

Figure 5 represents the vector map of time-averaged velocity and contour of time-averaged streamwise velocity in two different crosssectional planes for the three different baffle plate cases. This result explains the effect of baffle plate geometry on time-averaged velocity field. The upper cross-section shows the results in a plane slicing the middle of the space between the neighboring oxidant jets and the lower one shows the results in a plane slicing the center of a oxidant hole. In the figures, the magnitude of the velocity is non-dimensionalized by

fuel inlet velocity V_f of case A2. In all the three cases, large flow recirculation regions appear near the combustor wall, namely both between fuel jet and wall and between air jet and wall. These flow recirculation regions are called as near-wall flow recirculation regions in the following and the near-wall flow recirculation regions can be affected by the shape of baffle plate geometry like the one appearing downstream a backward facing step (Le et al., 1997). Peculiarity of the flow fields observed in two cases A and C is that, in addition to the near-wall flow recirculation regions, another flow recirculation region is formed downstream the fuel jet core region. This flow recirculation region is hereafter called as central flow recirculation region. This vortical flow can affect the mixing fields and actually is a key element of the enhanced mixing as will be discussed later. It may be worth to note that the central flow recirculation region is not found in case B. The central flow recirculation region ahead of the fuel jet originates from the lowering of fuel jet momentum due to the entrainment of fuel jet fluid into air jet.

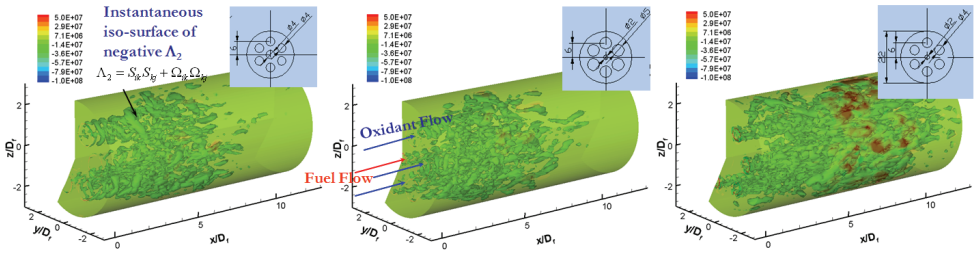

(a) Case A2 (b) Case B (c) Case C

Fig. 6. Visualization of instantaneous vortices generated in the micro combustor

Figure 6 shows the iso-surfaces of instantaneous negative Λ_2 value captured at an instant. As can be seen in the figure, the generation of ring vortices is noticeable in the brim of oxidant jets and they develop downstream and interact with each other., i.e. between neighboring vortices or between ring vortices and fuel jets. This vortical flow makes the flowfield more turbulent and significantly enhances the heat transport.

Figure 7 shows the contours of turbulent kinetic energy $k = 0.5(\overline{u_i' u_i'})$ in (y,z) cross-sectional planes at different streamwise positions for case A. As observed in Fig. 7a, higher turbulent regions are limited at the edge of each oxidant jet and of ring shape at the first two locations downstream the baffle plate. These regions overlap the regions where the appearance of ring vortex is identified in Fig. 6a, which means that the shear layer caused by the vortices may affect the turbulent kinetic energy. This distribution pattern of turbulent kinetic energy is vaguely still observed at $x / D_f = 5.5$ in Fig. 7c. Mixing and dissipation of turbulence proceed toward downstream. Turbulent kinetic energy is now lowered and distributes almost uniformly in the cross-section at $x / D_f = 7.5$. This suggests that mixing of the scalar quantity is almost completed at this position.

Now, heat loss will be discussed by analyzing conjugate heat transfer of the combustor numerically. It is noted that the (x,z) cross-sectional plane is slicing the middle of the fuel and oxidant nozzles as shown in Fig. 1, so the vigorous interaction between the oxidant jet and fuel jet or wall may be displayed clearly comparing with other cross-sectional plane containing only fuel jet flow. This can be found in Fig. 8. Accordingly, in the following figures, the only (x,z) cross-sectional plane will be presented.

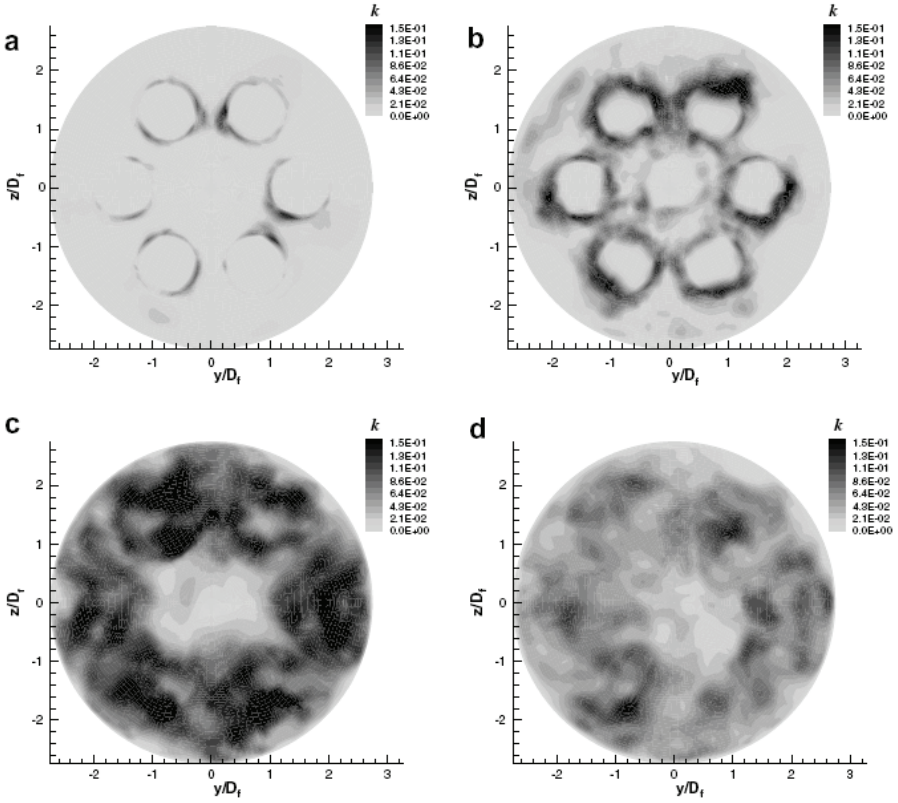

Fig. 7. Contour of turbulent kinetic energy at four different streamwise positions in case A2. (a) $x / D_f = 1.0$; (b) $x / D_f = 2.5$; (c) $x / D_f = 5.5$; and (d) $x / D_f = 7.5$

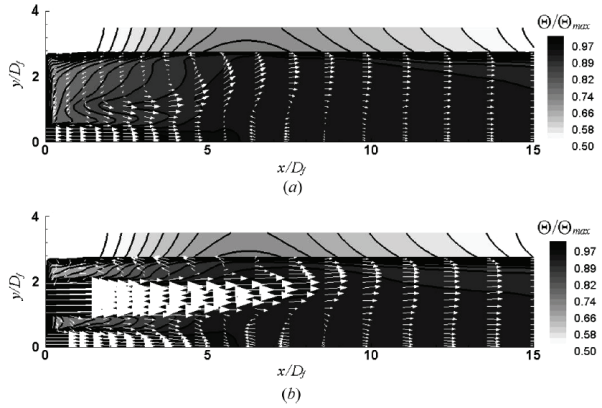

Fig. 8. Temperature contours with velocity vector map for case A2. (a) (x, y) cross-sectional plane and (b) (x, z) cross-sectional plane

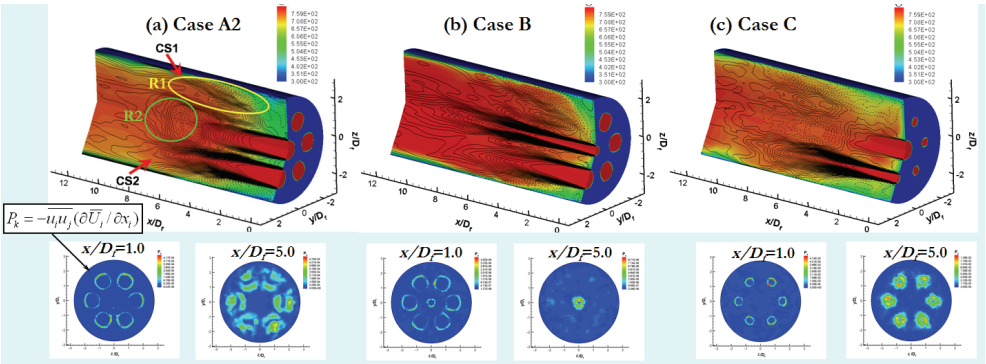

Fig. 9. Contours of time mean temperature, streamwise velocity and turbulent production

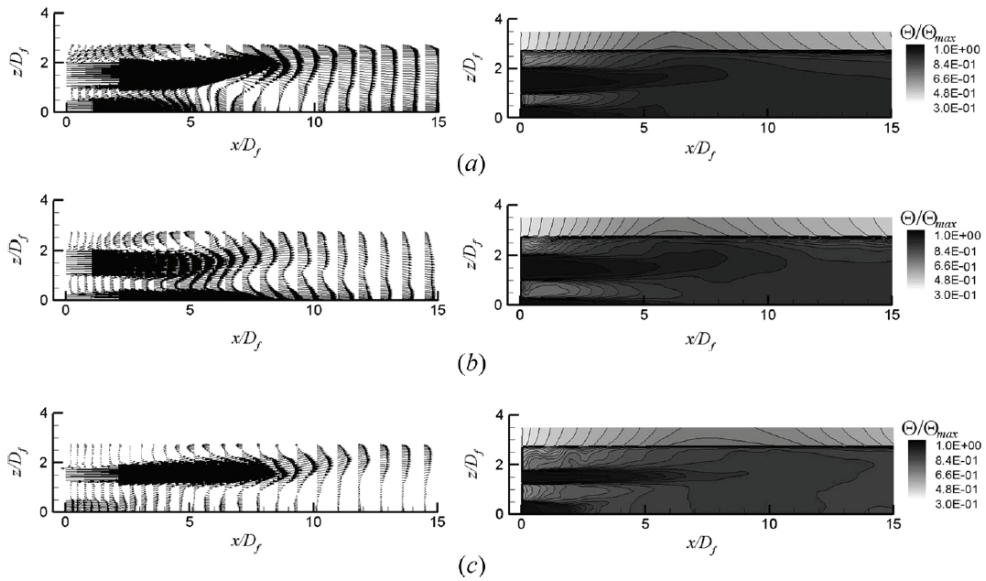

Fig. 10. Contour of Θ/Θmax and velocity vector fields at (x, z) cross-sectional plane. (a) Case A2; (b) case B; and (c) case C

Figure 9 shows contours of the time averaged temperature, streamwise velocity and turbulent production and the time averaged temperature and velocity vector fields are shown in Fig. 10. In the figures, two large vortical regions exist as discussed (Choi et al., 2008) and these are called as near-wall recirculation region and central recirculation region, respectively. It is noted that near-wall recirculation region appears between combustor tube wall and jet flows and central one is located in front of fuel jet flow downstream the baffle plate. The near-wall recirculation region appears in all the three cases and the central recirculation one is generated only in the cases A2 and C. The streamlines of the flows are different according to the dissimilar recirculation regions and these flow fields affect the

transport of the passive scalar, i.e. temperature. The steep temperature gradient region close to the tube wall is located around $x/D_f = 6$ for the cases A2 and B and $x/D_f = 8$ for the case C, where the distinct upward flow motion to the wall exists by near-wall recirculation region. Recirculation zone (R1) carries hot fluids from the jets onto the cooler wall, where temperature gradient becomes steeper resulting in high Nusselt number. Recirculation zone (R2) pumps up the cooler fluids near wall mixing them well with hot fluids from the jet.

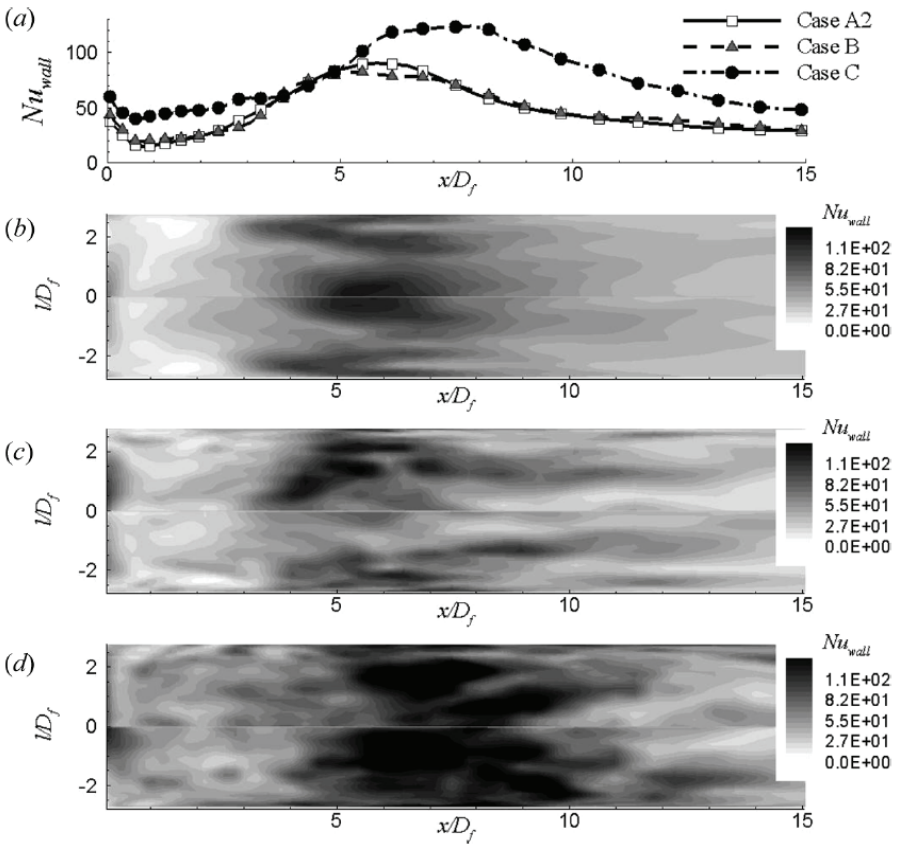

Fig. 11. Distributions of Nuwall along the streamwise direction. (a) Time and space averaged Nuwall; (b) case A2; (c) case B; and (d) case C

To analyze the effect of geometrical variations to the wall heat transfer, Nusselt number is displayed in Fig. 11. In Fig. 11 (a), the wall Nusselt number is averaged for time and space along the circumferential direction. As can be seen, the peak Nu_{wall} of the case C is the highest among the three cases. However, the wall heat transfer of the cases A2 and B is nearly same over the whole region. It is generally accepted that the evolution of a passive scalar is closely linked to the characteristics of the flow field. Therefore, the variation of the near-wall recirculation region can be considered as the source of the above Nu_{wall} feature.

This result suggests that the heat loss of the micro combustor with the baffle plate geometry depends on the baffle diameter ratio (D_o / D_f) and the oxidant to fuel velocity ratio (V_o / V_f).

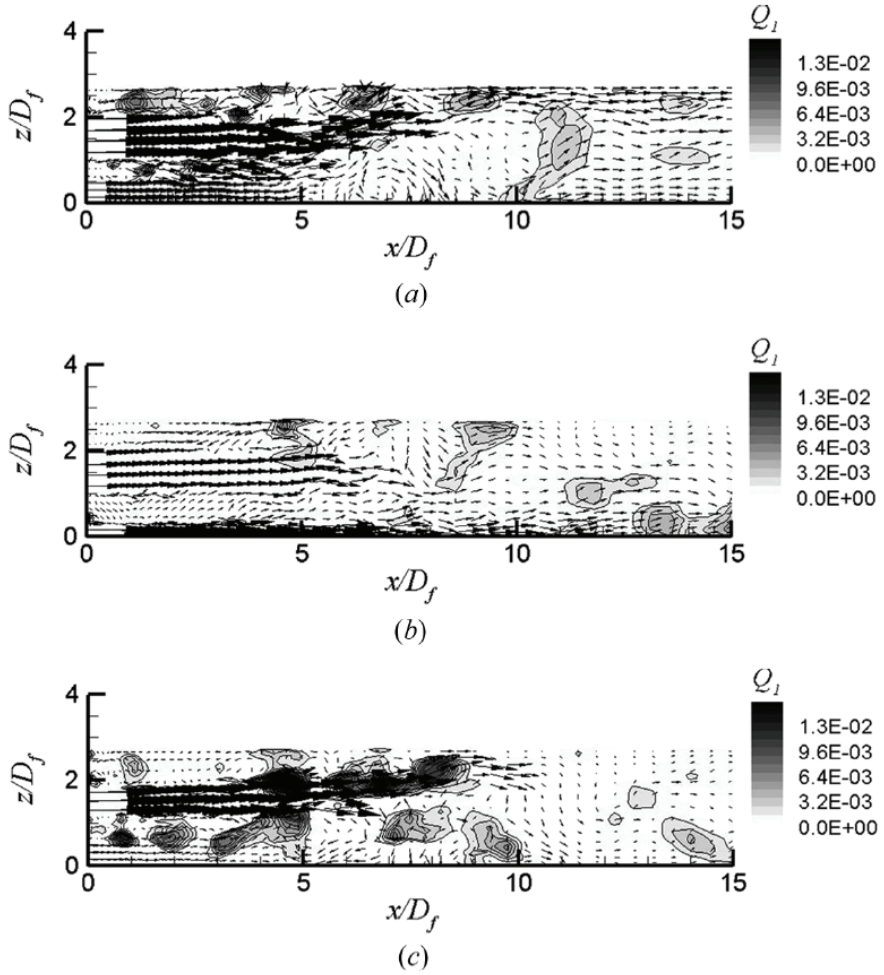

Fig. 12. Instantaneous contour of Q1 and velocity vector fields at (x, z) cross-sectional plane. (a) Case A2; (b) case B; and (c) case C

To show the effect of flow event as a contributor to the wall heat transfer, quadrant analysis is applied to the fluctuating components of velocity and temperature as follows. Figure 12 shows the instantaneous velocity vector fields and Q_1 contour normalized by V_o and Θ_{inlet} for each case, respectively. The Q_1 is defined as $Q_1 = w'\theta'$ when $\theta' > 0$ and $w' > 0$ for (x,z) plane representing hot sweep toward wall or hot wall-ward interaction. For all the three cases, the near-wall recirculation region appears at upstream very close to the wall. However, the central recirculation region is not formed in case B where the velocity ratio is

the lowest as shown in Table 1. For the three cases, the higher Q_1 region is created at the area where strong upward flow exists toward the wall near the reattachment point. In cases A2 and C, the central recirculation region makes the direction of oxidant flow more bent toward the wall and in case C inlet velocity of oxidant jet is the largest. As a result stronger wall-ward hot flow is generated. So, at that region the Q_1 is very high and moreover in case C the level of Q_1 is more raised than the case A2 by virtue of increased wall-ward velocity magnitude. However, in case B, owing to comparatively slow oxidant jet velocity and no augmented wall-ward fluid motion of it caused by the central recirculation region the level of Q_1 near the wall is much decreased. So, the variation of the baffle geometry finally has a great influence on the wall heat transfer and this will be confirmed with heat flux ratio H_j.

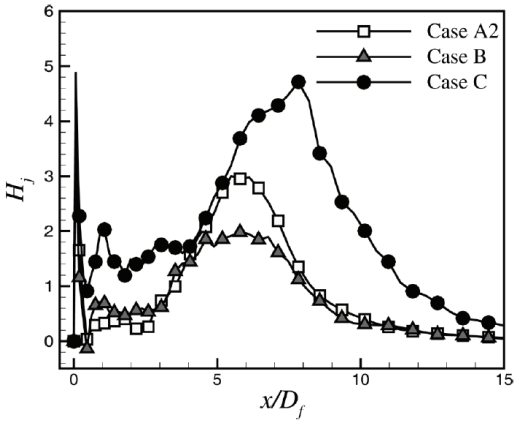

Fig. 13. Distributions of along the streamwise direction

Figure 13 shows the distribution of the heat flux ratio which is averaged for time and space along the circumferential direction at $1.3 < y^+ < 4.0$ very close to the wall. Here the heat flux ratio, H_j, represents the ratio of turbulent heat flux to molecular diffusion near the wall. For all the three cases, the higher magnitude of the heat flux ratio appears at the region of the strong upward flow motion generated by the near-wall flow recirculation region as illustrated in the previous figure. The peak value of the H_j is elevated in the order of the cases B, A2 and C. This indicates that the magnitude of the wall-normal turbulent heat flux is raised with increasing velocity ratio because the strength of the upward fluid motion to the wall is augmented as discussed before. The augmented turbulent heat flux makes the thermal boundary layer thinner resulting in steep temperature gradient near the wall, especially near the reattachment region. It should be noted that the case A2 has the significantly larger H_j values compared with case B only near the reattachment region. Except the reattachment region, the H_j of case B is slightly larger or same as that of the case A2. From the above results, the change of baffle configuration shows different characteristics of heat loss. Consequently, considering the heat loss, the cases A2 and B may be recommended for the micro combustor, but the central recirculation region does not exist in the case B. The central recirculation region greatly helps the mixing between fuel and oxidant and plays an important role for flame holder which becomes much significant in such a small combustor due to relatively larger heat loss. Therefore, the case B is not suitable for the micro combustor and the case A2 is recommended.

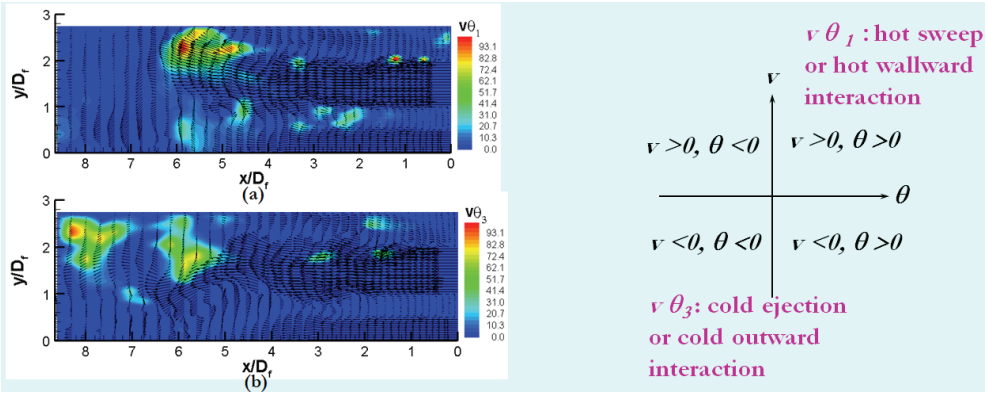

Fig. 14. Contours of instantaneous the 1st and 3rd quadrants of turbulent heat flux and velocity vector map at z=0 plane for case A2

Figure 14 shows contours of instantaneous the 1st and 3rd quadrants of turbulent heat flux and velocity vector map at z=0 plane for case A2. Strong wallward flow is generated inside the instantaneous flow recirculation region and this wallward motion carries hot fluid from the oxidant jet near the combustor wall resulting in a steep temperature gradients there. Cold fluid near the wall is drawn into the central recirculation zone consequently mixed well with hot fluids from fuel jet.

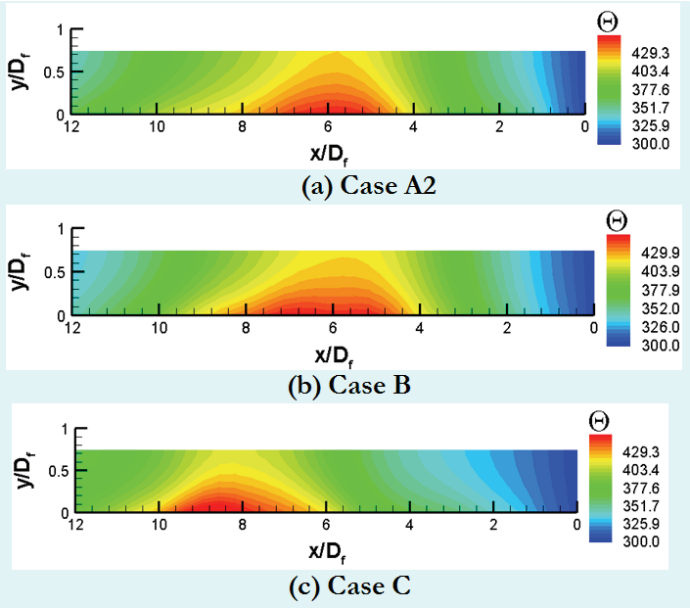

Fig. 15. Temperature distributions of the combustor wall

Figure 15 shows temperature distributions of the combustor wall. For the cases A2 and B, hot regions exist around the middle axial positions. In case C, the hot region is located

further downward axial position compared with cases A2 and B. These phenomena are matched well with the wall Nusselt number distributions. This may decrease the combustion efficiency because of big heat loss from the combustor inside. However, if hot gases are recirculated as in the case of the MGT proposed by (Suzuki et al., 2000), the effect of this heat loss may be mitigated.

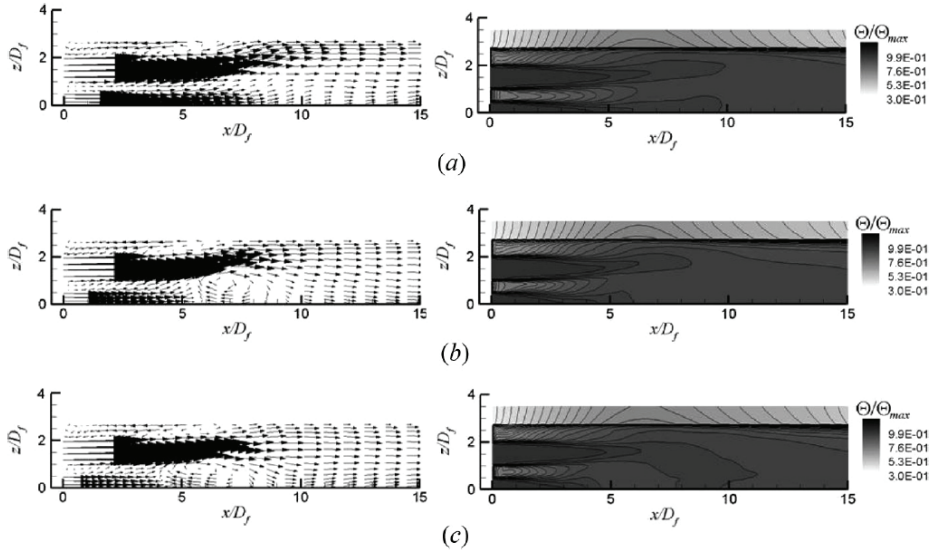

Fig. 16. Contour of Θ/Θmax and velocity vector fields at (x, z) cross-sectional plane. (a) Case A1; (b) case A2; and (c) case A3

To look into the effect of velocity or momentum ratio between fuel jet and oxidant jet flows for the recommended case A2, the cases A1, A2 and A3 are calculated as in Table 1 with the same geometry and similar Reynolds number. Figure 16 shows the contours of time averaged temperature both in the flow field and conjugate wall together with velocity vector fields. With increasing velocity ratio the central recirculation region is generated and the width(streamwise direction) and height(wall-normal direction) of the recirculation region are changed. This greatly affects the evolution of flow and thermal fields. In Figure 16, the near-wall recirculation region exists for the three cases and another tiny recirculation bubble is shown at upstream very close to the baffle plate. In case A1, the path of oxidant jet flow is going toward the wall following streamline of the near-wall recirculation region and at that region close to the wall temperature gradient becomes steep and the temperature gradient of the conjugated wall, too. For cases A2 and A3, the central recirculation region is generated but its configuration is different. In case A2, the central recirculation region looks circular in shape and above it the streamline is curved following it. So, the recirculation region pushes more the oxidant jet flow to upward compared with case A1 and this results in the thinnest thermal boundary layer among the three cases. In case A3 the central recirculation region resembles ellipsoidal shape. Furthermore, according to increased oxidant jet momentum the starting point of the recirculation region appears earlier compared with the case A2. This makes the streamline of the oxidant jet flow partly downward earlier toward the center of

the combustor tube. Therefore, the temperature gradient around $x / D_f = 6$ is the mildest among the three cases.

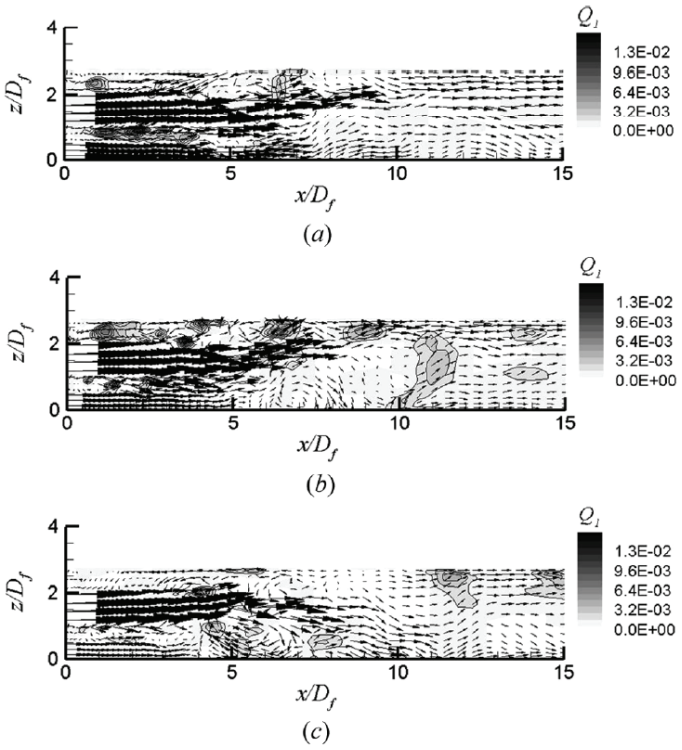

Fig. 17. Instantaneous contour of Q1 and velocity vector fields at (x, z) cross-sectional plane. (a) Case A1; (b) case A2; and (c) case A3

In Figure 17, for all the three cases the instantaneous near-wall recirculation region is generated, but the central flow recirculation region can be shown only in (b) and (c). In case A1, following the outer streamline of the near-wall recirculation region, the oxidant jet is bent toward the wall and the parcels of fuel jet fluids are entrained into the oxidant jet flow because of higher momentum of the oxidant jet. The Q_1 is higher at the regions between fuel and oxidant jets and around the upward flow of the near-wall recirculation region. With increasing velocity ratio in cases (b) and (c), the central recirculation region appears due to smaller fuel jet momentum and this deforms the direction of the oxidant jet flow. In case A2, the velocity of upward flow near the reattachment region is larger than that of case A1 because the passage of oxidant jet becomes narrower by the central flow recirculation region. The larger wall-ward velocity makes Q_1 higher at that region and the level of Q_1 is elevated than that of the region between fuel jet and oxidant jet flows. This makes the thermal boundary layer thinner resulting in steep temperature gradient close to the wall. However, in case A3, the location of the central recirculation region is pulled more upstream because of increased oxidant jet momentum compared with fuel jet one and the shape of the the central recirculation region becomes flatter as ellipsoid. Especially, at this instant of the

case, the direction of oxidant jet is changed toward the center region of the combustor tube. Therefore around the near-wall recirculation region the strength of wall-ward fluid motion is decreased. This results in the reduction of Q_1 at that region. These instantaneous thermal features are repeated and finally have an effect on time-averaged values as discussed before. From the above results, in case of the same baffle plate configuration, the variation of velocity ratio makes the heat loss different in quantity and from this point of view the case A3 might be recommended for a micro combustor.

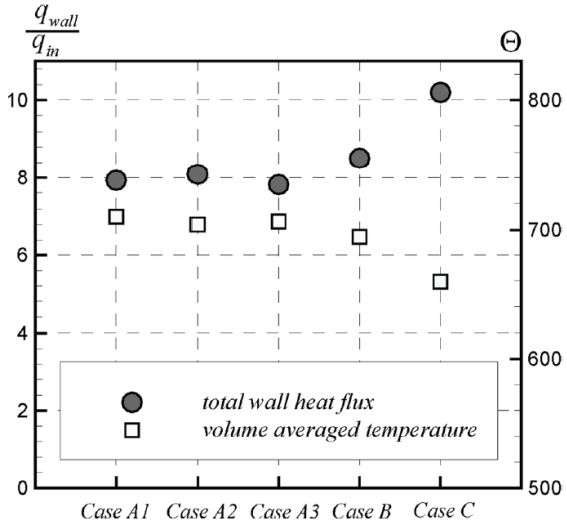

Fig. 18. Comparison of heat loss

Finally, Figure 18 shows the heat loss percentage of the combustor and volume averaged temperature of the fluid for all the cases. Here, the heat loss is defined as the total heat flux passing through the annular wall of the combustor. These are averaged over the combustor wall surface and normalized by heat input. As expected the previous figures, with varying baffle plate shape the total heat loss is increased in the order from the case A2 to B and finally case C. Also, with changing the velocity ratio case A3 has the lowest heat loss. So, the case A3 has the best thermal performance against the heat loss. From the results, for a method to reduce heat loss in the micro combustor, it is recommended that when the near-wall recirculation region exists, its momentum of negative streamwise direction should be decreased. It is noted that the heat generation by combustion should be considered for total thermal energy budget, which is closely connected with mixing efficiency and will be discussed in the future study and from the work of (Choi et al., 2005; Choi et al., 2006a; Choi et al., 2008), the flow recirculation regions can greatly help the mixing enhancement between fuel and oxidant. So, there should be the compromise between mixing enhancement and reduction of heat loss for stable and complete combustion.

4. Conclusion

In this chapter, heat transfer characteristics of multiple jet flows in a micro combustor is investigated by using Large Eddy Simulation (LES). The micro combustor is characterized

by a baffle plate having single fuel nozzle surrounded by six oxidant nozzles annularly and study was made in the three cases of different baffle plate configurations. The baffle plate is mounted to enhance the slow scalar mixing in the low Reynolds number condition of the micro combustor and to hold the flame stable.

With varying baffle plate shapes as the cases of A2, B, and C, the central and near-wall recirculation region appear differently according to the velocity ratio, which is controlled by the configuration and size of the nozzle. In cases with the baffle plates A2 and C, central flow recirculation region is generated and turbulent mixing proceeds more effectively than in the case with the baffle plate B where no central flow recirculation region appears. As a result, mixing is found to be greatly affected by the near-wall flow recirculation regions formed between jets and wall and the central flow recirculation region formed downstream the fuel jet flow. In case C, air jet velocity is high and ring vortices appear most noticeably, intermingling with each other and develop most effectively into turbulent vortices. Also, high momentum of air jet flow brings about the upstream movement of the central flow recirculation region and results in the completion of turbulent mixing within a shorter distance from the baffle plate.

The near-wall recirculation region plays an important role for wall heat transfer, especially near the reattachment region. The central recirculation region only appears in the cases A2 and C and helps turbulent heat transfer to the wall near the reattachment region affecting wall-ward flow. The reattachment flow pushes the hot fluid lumps into the combustor tube wall and this leads to the thinner thermal boundary layer representing higher wall heat transfer there. Among the three cases of different baffle geometry, the case A2 has the smallest wall heat loss, so the case A2 may be recommended for better design of the micro combustor. For this case, to investigate the velocity ratio effect on the same recommended geometry, numerical study is made for the three cases of A1, A2 and A3. With changing the velocity ratio for the cases A1, A2 and A3, the existence and the shape of the central and the near-wall recirculation regions are varied resulting in different heat loss characteristics. Among the three cases, the case A3 shows the minimum heat loss in the present study. It is noted that to prevent the big heat loss, the method of hot gas recirculation by (Suzuki et al., 2000) may be one solution so that the effect of the heat loss may be mitigated.

5. References

Andreopoulos, J. (1993). Heat Transfer Measurement in a Heated Jet-Pipe Flow Issuing into a Cold Cross Stream, *Phys. Fluids*, Vol. 26, pp. 3201-3210, ISSN:1070-6631.

Benard, P. S. & Wallace, J. M. (2002). *Turbulent Flow*, John Willey & Sons Inc., Hoboken, NJ.

Choi, H. S., Nakabe, K., Suzuki K. & Katsumoto, Y. (2001). An Experimental Investigation of Mixing and Combustion Characteristics on the Can-Type Micro Combustor with a Multi-Jet Baffle Plate, *Fluid Mechanics and Its Application*, Vol. 70, pp. 367-375, ISSN:0926-5112.

Choi, H. S., Park, T. S. & Suzuki, K. (2005). LES of Turbulent Flow and Mixing in a Micro Can Combustor, *Proc. 4th Int. Symposium Turbulence and Shear Flow Phenomena*, Vol. 2, pp. 389-394.

Choi, H. S., Park, T. S. & Suzuki, K. (2006a). Numerical Analysis on the Mixing of a Passive Scalar in the Turbulent Flow of a Small Combustor by Using Large Eddy Simulation, *Journal of Computational Fluid Engineering (Korean)*, Vol. 11, pp. 67-74, ISSN:1598-6071.

Choi, H. S., Park, T. S. & Suzuki, K. (2008). Turbulent Mixing of a Passive Scalar in Confined Multiple Jet Flows of a Micro Combustor, *Int. J. Heat Mass Transfer*, Vol. 51, pp. 4276-4286, ISSN:0017-9310.

Choi, H. S., Park, T. S. & Suzuki, K. (2006b). Large Eddy Simulation of Turbulent Convective Heat Transfer in a Micro Can Combustor with Multiple Jets, *Proc. 13th Int. Heat Transfer Conference*, Vol. 1, pp. TRB-22.

Choi, H. S. & Park, T. S. (2009). A Numerical Study for Heat Transfer Characteristics of a Micro Combustor by Large Eddy Simulation, *Numerical Heat Trnasfer Part A*, Vol. 56, pp. 230-245, ISSN:1040-7782

Ferziger, J. H. & Peric, M. (2002). *Computational Methods for Fluid Dynamics*, 3rd ed., Springer-Verlag, Berlin, ISBN:3-540-42074-6.

Issa, R. I. (1986). Solution of the Implicitly Discretized Fluid Flow Equations by Operating-Splitting, *J. Comput. Phys.*, Vol. 62, pp. 40-65, ISSN:0021-9991.

Kee, R. J., Zhu, H. & Goodwin, D. G. (2005). Solid-Oxide Fuel Cells with Hydrocarbon Fuels, *Proceedings of the Combustion Institute*, Vol. 30, pp. 2379-2404, ISSN:1540-7489.

Le, H., Moin, P. And Kim, J. (1997). Direct Numerical Simulation of Turbulent Flow over a Backward-Facing Step, *J. Fluid Mechacnics*, Vol. 330, pp. 349-374.

Lele, S. K. (1992). Compact Finite Difference Schemes with Spectral-Like Resolution, *J. Comput. Phys.*, Vol. 103, pp. 16-42, ISSN:0021-9991.

Lilly, D. K. (1992). A Proposed Modification of the Germano Subgrid-Scale Closure Model, *Phys. Fluids*, Vol. 4, pp. 633-635, ISSN:1070-6631.

Massardo, A. F. & Lubelli, F. (2000). Internal Reforming Solid Oxide Fuel Cell-Gas Turbine Combined Cycles(IRSOFCGT) :Part A-Cell Model and Cycle Thermodynamics Analysis, *ASME Journal of Engineering for Gas Turbine and Power*, Vol. 122, pp. 27-35, ISSN:0742-4795.

Mcdonald, C. F. (2000). Low Cost Compact Primary Surface Recuperator Concept for Microturbine, *Applied thermal Engineering*, Vol. 20, pp. 471-497, ISSN:1359-4311.

Moin, P., Squires, K., Cabot, W. & Lee, S. (1991). A Dynamic Subgrid-Scale Model for Compressible Turbulence and Scalar Transport, *Phys. Fluids*, Vol. 3, pp. 2746-2757, ISSN:1070-6631.

Park, T. S. (2006a). Effect of Time-Integration Method in a Large Eddy Simuation using PISO Algorithm: Part I-Flow Field, *Numerical Heat Trnasfer Part A*, Vol. 50, pp. 229-245, ISSN:1040-7782.

Park, T. S. (2006b). Effect of Time-Integration Method in a Large Eddy Simuation using PISO Algorithm: Part II-Thermal Field, *Numerical Heat Trnasfer Part A*, Vol. 50, pp. 247-262, ISSN:1040-7782.

Park, T. S., Sung, H. J. & Suzuki, K. (2003). Development of a Nonlinear Near-Wall Turbulence Model for Turbulent Flow and Heat Transfer, *Int. J. Heat Fluid Flow*, Vol. 24, pp. 29-40, ISSN:0142-727X.

Peng, S. H. & Davision, L. (2002). On a Subgrid-Scale Heat Flux Model for Large Eddy Simulation of Turbulent Flow, Stream, *Int. J. Heat Mass Transfer*, Vol. 45, pp. 1393-1405, ISSN:0017-9310.

Suzuki, K., Teshima, K. & Kim, J. H. (2000). Solid Oxide Fuel Cell and Micro Gas Turbine Hybrid Cycle for a Distributed Energy Generation System, *Proc. 4th JSME-KSME Thermal Engineering Conference*, Vol. 13, pp. 1-8.

19

Natural Circulation in Single and Two Phase Thermosyphon Loop with Conventional Tubes and Minichannels

Henryk Bieliński and Jarosław Mikielewicz
The Szewalski Institute of Fluid-Flow Machinery, Polish Academy of Sciences, Fiszera 14, 80-952 Gdańsk, Poland

1. Introduction

The primary function of a natural circulation loop (i.e. thermosyphon loop) is to transport heat from a source to a sink. Fluid flow in a thermosyphon loop is created by the buoyancy forces that evolve from the density gradients induced by temperature differences in the heating and cooling sections of the loop. An advanced thermosyphon loop consists of the evaporator, where the working liquid boils; and the condenser, where the vapour condenses back to liquid; the riser and the downcomer connect these two exchangers. Heat is transferred as the vaporization heat from the evaporator to the condenser. The thermosyphon is a passive heat transfer device, which makes use of gravity for returning the liquid to the evaporator. Thermosyphons are less expensive than other cooling devices because they feature no pump.

There are numerous engineering applications for thermosyphon loops such as, for example, solar water heaters, thermosyphon reboilers, geothermal systems, nuclear power plants, emergency cooling systems in nuclear reactor cores, electrical machine rotor cooling, gas turbine blade cooling, thermal diodes and electronic device cooling. The thermal diode is based on natural circulation of the fluid around the closed-loop thermosyphon (Bieliński & Mikielewicz, 1995, 2001), (Chen, 1998). The closed-loop thermosyphon is also known as a "liquid fin" (Madejski & Mikielewicz, 1971).

Many researchers focused their attention on the single-phase loop thermosyphons with conventional tubes, and the toroidal and the rectangular geometry of the loop. For example, Zvirin (Zvirin, 1981) presented results of theoretical and experimental studies concerned with natural circulation loops, and modeling methods describing steady state flows, transient and stability characteristics. Greif (Greif, 1988) reviewed basic experimental and theoretical work on natural circulation loops. Misale (Misale et al., 2007) reports an experimental investigations related to rectangular single-phase natural circulation mini-loop. Ramos (Ramos et al., 1985) performed the theoretical study of the steady state flow in the two-phase thermosyphon loop with conventional tube. Vijayan (Vijayan et al., 2005) compared the dynamic behaviour of the single-phase and two-phase thermosyphon loop with conventional tube and the different displacement of heater and cooler. The researcher found that the most stable configuration of the thermosyphon loop with conventional tube is the one with both vertical cooler and heater.

In the case of closed rectangular and toroidal loops with conventional tube, particular attention has to be devoted to both transient and steady state flows as well as to stability analysis of the system under various heating and cooling conditions.
The purpose of this chapter is to present a detailed analysis of heat transfer and fluid flow in a new generalized model of thermosyphon loop and its different variants. Each individual variant can be analyzed in terms of single- and two-phase flow in the thermosyphon loop with conventional tubes and minichannels. The new empirical correlations for the heat transfer coefficient in flow boiling and condensation, and two-phase friction factor in diabatic and adiabatic sectors in minichannels and conventional tube, are used to simulate the two-phase flow and heat transfer in the thermosyphon loop. The analysis of the thermosyphon loop is based on the one-dimensional model, which includes mass, momentum and energy balances.

2. A generalized model of the thermosyphon loop

A schematic diagram of a one-dimensional generalized model of the thermosyphon loop is shown in Fig. 1.

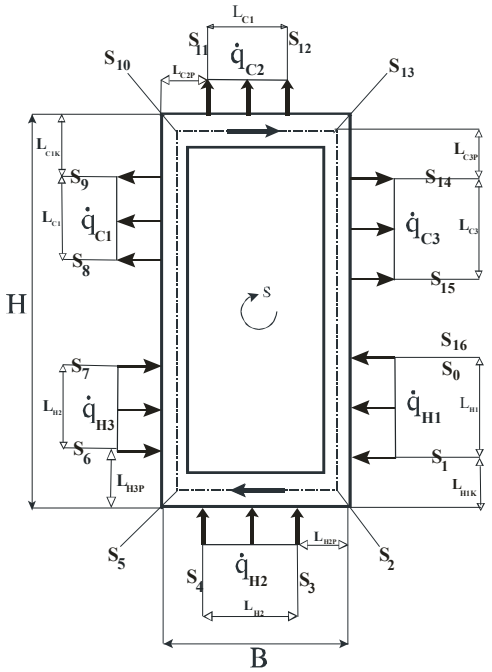

Fig. 1. A schematic diagram of a one-dimensional generalized model of the thermosyphon loop.

The loop has a provision for selecting one or two or three of the heat sources at any location, in the bottom horizontal pipe or in the vertical leg; similarly, the heat sink can be chosen in the top horizontal pipe or in the vertical leg. Therefore, any combination of heaters and coolers can be analyzed. The constant heat fluxes $\dot{q}_H$ and $\dot{q}_C$ are applied in the cross-

section area per heated and cooled length: L_H and L_C. The heated and cooled parts of the thermosyphon loop are connected by perfectly insulated channels. The coordinate s along the loop and the characteristic geometrical points on the loop are marked with s_j, as shown in Fig. 1. The total length of the loop is denoted by *L*, the cross-section area of the channel by *A* and the wetted perimeter by U. Thermal properties of fluid: ρ - density, c_p - heat capacity of constant pressure, λ - thermal conductivity.

The following assumptions are used in the theoretical model of natural circulation in the closed loop thermosyphon:

1. thermal equilibrium exists at any point of the loop,
2. incompressibility because the flow velocity in the natural circulation loop is relatively low compared with the acoustic speed of the fluid under current model conditions,
3. viscous dissipation in fluid is neglected in the energy equations,
4. heat losses in the thermosyphon loop are negligible,
5. $(D/L) << 1$; one-dimensional models are used and the flow is fully mixed. The velocity and temperature variation at any cross section is therefore neglected,
6. heat exchangers in the thermosyphon loop can be equipped by conventional tubes or minichannels,
7. fluid properties are constants, except density in the gravity term,
8. single- and two-phase fluid can be selected as the working fluid,
   a. if the Boussinsq approximation is valid for a single-phase system, then density is assumed to vary as $\rho = \rho_0 \cdot [1 - \beta \cdot (T - T_0)]$ in the gravity term where $\beta = \frac{1}{\upsilon_0} \cdot \left(\frac{\partial \upsilon}{\partial T}\right)_p$ (υ - specific volume, "0" is the reference of steady state),
   b. for the calculation of the frictional pressure loss in the heated, cooled and adiabatic two-phase sections, the two-phase friction factor multiplier $R = \phi_{L0}^2$ is used; the density in the gravity term can be approximated as follows: $\rho = \alpha \cdot \rho_V + (1 - \alpha) \cdot \rho_L$, where α is a void fraction,
   c. homogeneous model or separate model can be used to evaluate the friction pressure drop of two phase flow,
   d. quality of vapor in the two-phase regions is assumed to be a linear function of the coordinate around the loop,
9. the effect of superheating and subcooling are neglected,

Under the above assumptions, the governing equations for natural circulation systems can be written as follows:

- conservation of mass:

$$\frac{\partial \rho}{\partial \tau} + \frac{\partial}{\partial s}(\rho \cdot w) = 0; \tag{1}$$

where τ - time, w - velocity.

- conservation of momentum:

$$\rho \cdot \left(\frac{\partial w}{\partial \tau} + w \cdot \frac{\partial w}{\partial s}\right) = -\frac{\partial p}{\partial s} + \varepsilon \cdot \rho \cdot \tilde{g} - \tau_w \cdot \frac{U}{A}; \tag{2}$$

where $\varepsilon = 0$ for $\vec{e} \perp \vec{g}$; $\varepsilon = (+1)$ for $\vec{e} \uparrow \wedge \vec{g} \downarrow$; $\varepsilon = (-1)$ for $\vec{e} \downarrow \wedge \vec{g} \downarrow$; $\tilde{g} = \vec{e} \circ \vec{g} = 1 \cdot g \cdot \cos(\vec{e}, \vec{g})$; $|\vec{g}| = g$; $|\vec{e}| = 1$; and $\vec{e}$ is a versor of the coordinate around the loop, and τ_w - wall shear stress.

In order to eliminate the pressure gradient and the acceleration term, the momentum equation in Eq. (2) is integrated around the loop $\oint\left(\frac{\partial p}{\partial s}\right)ds = 0$.

- conservation of energy:

$$\frac{\partial T}{\partial \tau} + w \cdot \frac{\partial T}{\partial s} = a_0 \cdot \frac{\partial^2 T}{\partial s^2} \begin{cases} +0 & \text{for adiabatic section} \\ -\dfrac{q_C \cdot U}{c_{p_0} \cdot \rho_0 \cdot A} & \text{for cooled section} \\ +\dfrac{\dot{q}_H \cdot U}{c_{p_0} \cdot \rho_0 \cdot A} & \text{for heated section} \end{cases} \tag{3}$$

where $a_0 = \frac{\lambda_0}{\rho_0 \cdot c_{p_0}}$ - thermal diffusivity,

The flow in natural circulation systems which is driven by density distribution is also known as a gravity driven flow or thermosyphonic flow. In such flows, the momentum and the energy equations are coupled and for this reason they need to be simultaneously solved (Mikielewicz, 1995).

3. Thermosyphon loop Heated from below Horizontal side and Cooled from upper Horizontal side (HHCH).

In this paper, we present the case of the onset of motion of the single-phase fluid from a rest state, which occurs only for the (HHCH) variant. We have assumed that: $\dot{q}_C = \alpha_C \cdot (T - T_0)$. The heat transfer coefficient between the wall and environment α_C and the temperature of the environment T_0 are constant.

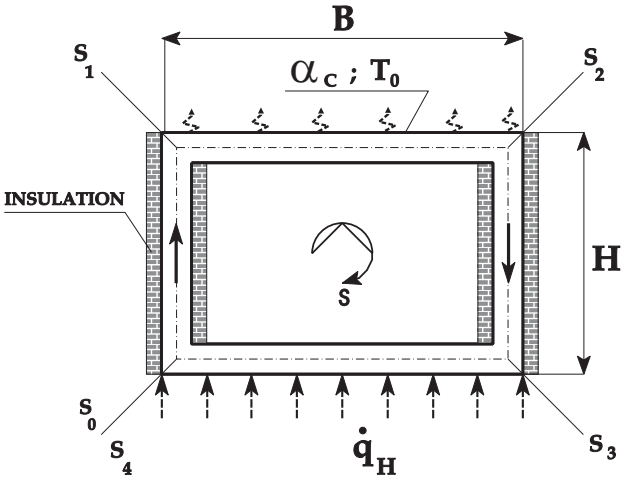

Fig. 2. The variant of HHCH.

The above governing equations can be transformed to their dimensionless forms by the following scaling:

$$\tau^+ = (a_0 \cdot \tau)/L^2; \quad s^+ = s/L; \quad \dot{m}^+ = (\dot{m} \cdot L)/(a_0 \cdot \rho_0 \cdot A); \quad T^+ = \frac{\lambda_0 \cdot (A/U_H) \cdot (T - T_0)}{(\dot{q}_H \cdot L^2)}; \quad (4)$$

The dimensionless momentum equation and the energy equation at the steady state for the thermosyphon loop heated from below can be written as follows:

- momentum equation (with: $K_j = s_j/L$;)

$$\dot{m}^+ = (Ra)^{**} \cdot \left(\int_0^{K_1} T^+ ds^+ - \int_{K_2}^{K_3} T^+ ds^+ \right); \quad (5)$$

- energy equation

$$\dot{m}^+ \frac{dT^+}{ds^+} = \frac{d^2T^+}{ds^{+2}} \begin{cases} +0 & \text{insulated sections} \\ -(Bi)^{**} \cdot T^+ & \text{for cooling section} \\ +1 & \text{heater section} \end{cases} \quad (6)$$

- with boundary conditions

$$\begin{aligned} &T^+_{A1}(0) = T^+_H(1); \quad T^+_{A1}(K_1) = T^+_C(K_1); \quad T^+_C(K_2) = T^+_{A2}(K_2); \quad T^+_{A2}(K_3) = T^+_H(K_3); \\ &\left.\frac{dT^+_{A1}}{ds^+}\right|_{s^+=0} = \left.\frac{dT^+_H}{ds^+}\right|_{s^+=1}; \quad \left.\frac{dT^+_{A1}}{ds^+}\right|_{s^+=K_1} = \left.\frac{dT^+_C}{ds^+}\right|_{s^+=K_1}; \\ &\left.\frac{dT^+_C}{ds^+}\right|_{s^+=K_2} = \left.\frac{dT^+_{A2}}{ds^+}\right|_{s^+=K_2}; \quad \left.\frac{dT^+_{A2}}{ds^+}\right|_{s^+=K_3} = \left.\frac{dT^+_H}{ds^+}\right|_{s^+=K_3}; \end{aligned} \quad (7)$$

The parameters appearing in the momentum and the energy equations are the modified Biot, Rayleigh and Prandtl numbers.

$$(Bi)^{**} = \frac{\alpha_C \cdot U_C}{\lambda_0} \cdot \frac{L^2}{A}; \quad (Ra)^{**} = \frac{g \cdot \beta_0 \cdot L^3 \cdot (\dot{q}_H/\lambda_0)}{\nu_0 \cdot a_0} \cdot \frac{A \cdot U_H}{2 \cdot U^2}; \quad (Pr)^{**} = 2 \cdot L^2 \cdot \left(\frac{U}{A}\right)^2 \cdot \left(\frac{\nu_0}{a_0}\right); \quad (8)$$

For the discussed case of laminar steady-state flow the dimensionless distributions of temperature around the loop can be obtained analytically from Eq. (6). Working fluid was the distilled water. The results of calculations are presented in Fig. 3.
It has been found that the Biot number has an influence on temperature and mass flow rate in the laminar flow. The results are shown in Figs. 3 and 4.
Substitution of the temperature distributions into the dimensionless equation of motion for the steady-state yields the relation for the dimensionless flow rate for laminar flow.
The presented numerical calculations are based on our new method for solution of the problem for the onset of motion in the fluid from the rest. Conditions for the onset of motion

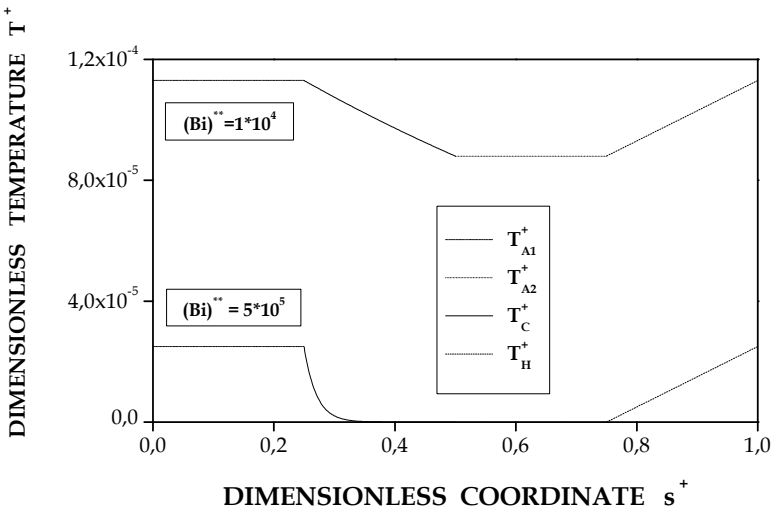

Fig. 3. The effect of Biot number on temperatures in laminar steady-state flow (HHCH).

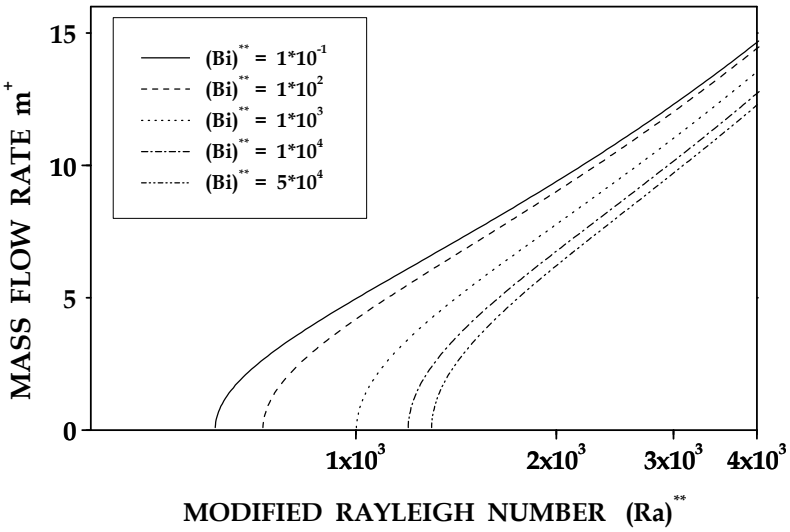

Fig. 4. The dimensionless mass flow rate $\dot{m}^+$ versus modified Rayleigh number $(Ra)^{**}$ with the modified Biot number $(Bi)^{**}$ used as a fixed parameter (HHCH) .

in the thermosyphon can be determined by considering the steady solutions with circulation for the limiting case of $\dot{m}_1^+ \to 0$. The analysis was based on the equations of motion and energy for the steady-state conditions. The heat conduction term has to be taken into account in this approach because the heat transfer due to conduction is becoming an increasingly important factor for decreasing mass flow rates.

It is shown that the geometrical and thermal parameters have an influence on the problem of global flow initiation from the rest (Figs. 4, 5 and 6).
Fig. 5 illustrates that the larger Biot numbers correspond to larger values of the critical Rayleigh number.

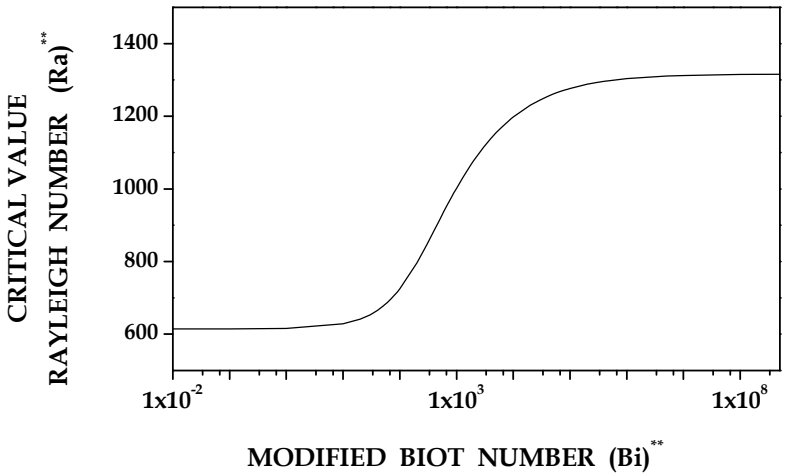

Fig. 5. The critical value of the modified Rayleigh number $(\mathrm{Ra})^{**}$ versus modified Biot number $(\mathrm{Bi})^{**}$ (HHCH).

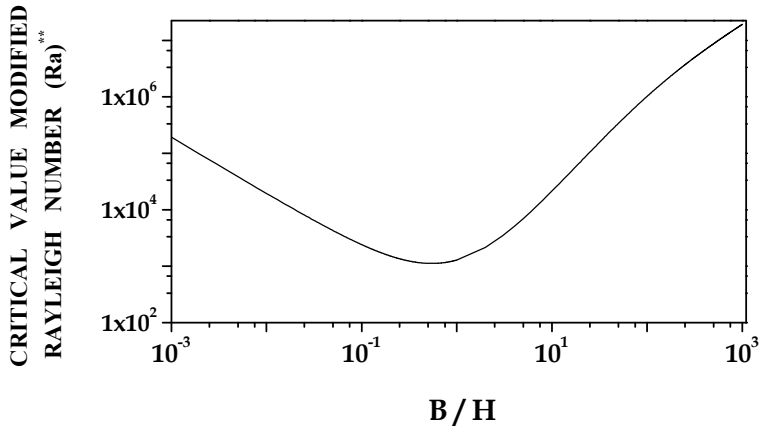

Fig. 6. The critical value of the modified Rayleigh number $(\mathrm{Ra})^{**}$ versus B/H ratio (HHCH).

It has been found that the minimum of the critical modified Rayleigh number $(\mathrm{Ra})^{**}$=1121, with $(\mathrm{Bi})^{**} = 2\times10^{5}$, appears for B/H=0.544.
The stability analysis shows that the loop heated from one side and cooled from the other one asymmetrically with respect to the gravity force is always unstable and any temperature gradient due to heating or cooling results in the onset of flow circulation.

4. Thermosyphon loop Heated from the lower part of Vertical side and Cooled from the upper part of the opposite Vertical side (HVCV).

The thermosyphon loop heated from the lower part of vertical leg and cooled from the upper part of the opposite vertical leg (HVCV) is chosen as an example to present the analysis of two-phase flow in conventional tubes. The Stomma (Stomma, 1979) correlation describing the void fraction, the Friedel (Friedel, 1979) correlation for the friction pressure drop of two-phase flow in adiabatic region, the Müller-Steinhagen & Heck (Müller-Steinhagen & Heck, 1986) correlation for the friction pressure drop of two-phase flow in diabatic region and the Mikielewicz correlation for the flow boiling heat transfer coefficient in conventional channels (Mikielewicz et al., 2007) are used to calculate two phase flow in the thermosyphon loop equipped with conventional tubes. Freon R-11 was chosen as a working fluid in the thermosyphon device. A schematic diagram of the analysed thermosyphon loop (HVCV) is shown in Fig. 7.

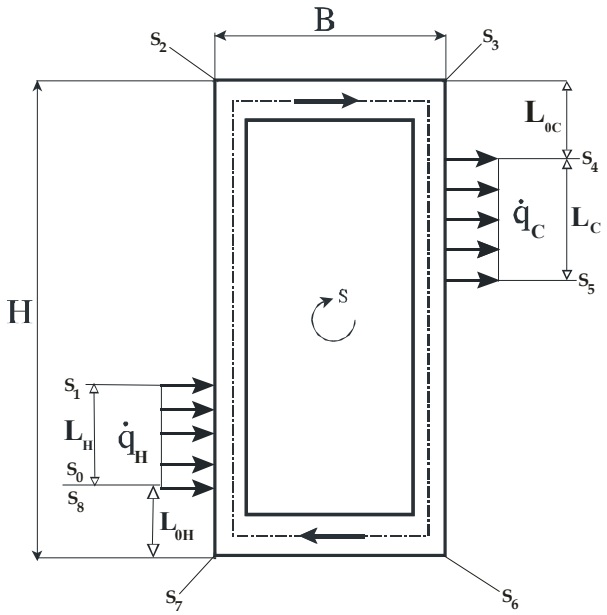

Fig. 7. The thermosyphon loop heated from the lower part of vertical side and cooled from the upper part of the opposite vertical side (HVCV).

After integrating the gravitational term in the momentum equation (2) around the loop, we obtain

$$\oint \left\{ \varepsilon \cdot g \cdot \left[(1-\alpha)\cdot \rho_L + \alpha \cdot \rho_V \right] \right\} ds = \\ = g \cdot (\rho_V - \rho_L) \times \left\{ \left[(s_2 - s_1) - (s_4 - s_3) \right] \cdot \bar{\alpha}_{\langle s_1 ; s_4 \rangle} + (s_1 - s_0) \cdot \bar{\alpha}_{\langle s_0 ; s_1 \rangle} - (s_5 - s_4) \cdot \bar{\alpha}_{\langle s_4 ; s_5 \rangle} \right\} ; \tag{9}$$

where $\bar{\alpha}_{\langle s_P ; s_K \rangle} = \dfrac{1}{(s_K - s_P)} \cdot \int_{s_P}^{s_K} \alpha_{\langle s_P ; s_K \rangle}(s) ds$.

The Stomma empirical correlation (Stomma, 1979) for the void fraction at low pressures is applied in the form

$$\alpha^{STOMMA} = 1 - \frac{\left[\left(\alpha_{HOM}\right)^2 - \left(x\right)^2 \right]}{2 \cdot \left[\ln\left(\frac{1-x}{1-\alpha_{HOM}} \right) - \left(\alpha_{HOM} - x\right) \right]} \tag{10}$$

where $\alpha_{HOM} = \frac{1}{1 + \frac{1-x}{x} \cdot \left(\frac{\rho_V}{\rho_L} \right)}$. (Subscripts: V – vapour, L – liquid, HOM - homogeneous).

The following additional assumptions are made in this study (HVCV): a) flows of liquid and vapour phases in the two-phase regions are both turbulent and flow of liquid in single phase region is also turbulent, b) friction coefficient is constant in each region of the loop and the frictional component of the pressure gradient in two-phase regions was calculated according to the two-phase separate model. Due to the friction of fluid, the pressure losses in two-phase regions can be calculated as

$$\frac{U}{A} \cdot \tau_w = \left(\frac{-dp}{ds} \right)_{2p} = R \cdot \left(\frac{-dp}{ds} \right)_{L0} \tag{11}$$

where: $\left(\frac{dp}{ds} \right)_{L0} = \frac{2 \cdot f_{L0}^{Chur} \cdot \left(\dot{G}\right)^2}{D \cdot \rho_L}$ is the liquid only frictional pressure gradient calculated for the total liquid mass velocity, $\dot{G} = \rho \cdot w$, f_{L0}^{Chur} is friction factor of the fluid (Churchill, 1977).

The local two-phase friction coefficient in two-phase adiabatic region was calculated using the Friedel formula (Friedel, 1979):

$$\left(\frac{dp}{ds} \right)_{2f,Frict}^{FRIEDEL} = \Phi_{L0}^2 \cdot \left(\frac{dp}{ds} \right)_{L0} ; \tag{12}$$

where

$$\Phi_{L0}^2 = E + \frac{3.24 \cdot F \cdot H}{\left(Fr\right)^{0.045} \cdot \left(We\right)^{0.035}} ;$$

and

$$E = \left(1-x\right)^2 + x^2 \cdot \frac{\rho_L \cdot f_{V0}}{\rho_V \cdot f_{L0}} ; \; F = \left(x\right)^{0.78} \cdot \left(1-x\right)^{0.224} ; \; H = \left(\frac{\rho_L}{\rho_V} \right)^{0.91} \cdot \left(\frac{\mu_V}{\mu_L} \right)^{0.19} \left(1 - \frac{\mu_V}{\mu_L} \right)^{0.7} ;$$

and (σ - surface tension)

$$\left(Fr\right) = \frac{\left(\dot{G}\right)^2}{g \cdot D \cdot \left(\rho_{HOM}\right)^2} ; \; \left(We\right) = \frac{\left(\dot{G}\right)^2 \cdot D}{\left(\rho_{HOM}\right) \cdot \sigma} ;$$

The local two-phase friction coefficient in two-phase diabatic regions was calculated using the Müller-Steinhagen & Heck formula (Müller-Steinhagen & Heck, 1986)

$$\left(\frac{dp}{ds}\right)_{2f,Frict}^{M-S} = F\cdot(1-x)^{\frac{1}{3}} + B\cdot x^3 \ ; \tag{13}$$

where

$$F = A + 2\cdot x\cdot(B-A)\ ;\ A = \left(\frac{dp}{ds}\right)_{L0}\ ;\quad B = \left(\frac{dp}{ds}\right)_{V0}\ ;$$

After integrating the friction term in Eq. (2) around the loop, we obtain

$$\oint\left(\frac{U}{A}\cdot\tau_w\right)ds = \left(\frac{dp}{ds}\right)_{L0}\cdot\left\{(s_1-s_0)\cdot\overline{R}_{\langle s_0;s_1\rangle} + (s_4-s_1)\cdot\overline{R}_{\langle s_1;s_4\rangle} + (s_5-s_4)\cdot\overline{R}_{\langle s_4;s_5\rangle} + (s_8-s_5)\right\}; \tag{14}$$

where: $\overline{R}_{\langle s_P;s_K\rangle} = \dfrac{1}{(s_K-s_P)}\cdot\int_{s_P}^{s_K} R(s)ds$.

Thus the momentum equation (2) for the two-phase thermosyphon loop (HVCV) can be written as

$$\begin{aligned}&\left(\frac{dp}{ds}\right)_{L0}\cdot\left\{(s_1-s_0)\cdot\overline{R}_{\langle s_0;s_1\rangle} + (s_4-s_1)\cdot\overline{R}_{\langle s_1;s_4\rangle} + (s_5-s_4)\cdot\overline{R}_{\langle s_4;s_5\rangle} + (s_8-s_5)\right\} + \\ &+ g\cdot(\rho_V-\rho_L)\cdot\left\{\left[(s_2-s_1)-(s_4-s_3)\right]\cdot\overline{\alpha}_{\langle s_1;s_4\rangle} + (s_1-s_0)\cdot\overline{\alpha}_{\langle s_0;s_1\rangle} - (s_5-s_4)\cdot\overline{\alpha}_{\langle s_4;s_5\rangle}\right\} = 0 \quad ;\end{aligned} \tag{15}$$

The mass flux distributions $\dot{G}$ versus heat flux $\dot{q}_H$ for the steady-state conditions and for the conventional tube case, is shown in Fig. 8. Calculations were carried out also using the homogeneous model of two-phase flow. The working fluid was freon R11.

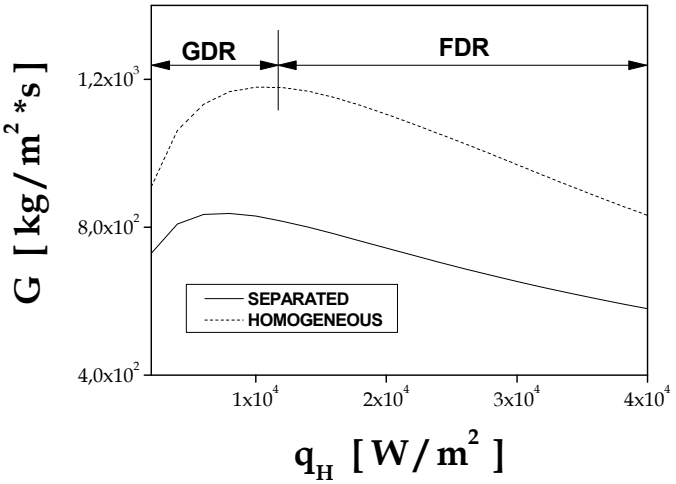

Fig. 8. Mass flux rate $\dot{G}$ as a function of $\dot{q}_H$ for homogeneous model and separate model of two-phase flow (HVCV), (L=2 [m], D=0.08 [m], H=0.9 [m], B=0.1 [m], L_H=L_C=0.2 [m], L_{HP}=L_{CP}=0.05 [m]).

Two flow regimes can be clearly identified in Fig. 8, namely GDR - gravity dominant regime and FDR – friction dominant regime. In the gravity dominant regime, for a small change in quality there is a large change in the void fraction and therefore density and buoyancy force. The increased buoyancy force can be balanced by a significant increase in the corresponding frictional force which is possible only at higher flow rates. As a result, the gravity dominant regime is characterized by an increase in the flow rate with heat flux $\dot{q}_H$. However, the continued conversion of high density water to low density steam due to increase in heat flux $\dot{q}_H$ requires that the mixture velocity must increase resulting in the increase of the frictional force and hence a decrease in flow rate. Thus the friction dominant regime is characterized by a decrease in flow rate with increase in heat flux $\dot{q}_H$ (Vijayan et al., 2005). As presented in Fig. 8 a comparison between two models of two-phase flow shows that the homogeneous and the separated flow models reveal relatively big differences.

4.1 The distributions of heat transfer coefficient in flow boiling.

The heat transfer coefficient in flow boiling in minichannels was calculated using the Mikielewicz general formula for conventional channels (Mikielewicz et al., 2007)

$$\frac{h_{TPB}^{JM}}{h_{REF}} = \sqrt{\left(R_{M-S}\right)^n + \frac{1}{1+P}\cdot\left(\frac{h_{PB}}{h_{REF}}\right)^2} \quad ; \tag{16}$$

where

$$R_{M-S} = \left[1+2\cdot\left(\frac{1}{f_1}-1\right)\cdot x\right]\cdot(1-x)^{\frac{1}{3}} + x^3\cdot\frac{1}{f_{1z}} \; ;$$

$$TUR \Rightarrow n = 0.76 \; ; \; h_{REF} = 0.023\cdot\frac{\lambda_L}{D}\cdot\left(Re_{L0}\right)^{0.8}\cdot\left(Pr_L\right)^{\frac{1}{3}} ;$$

$$f_1^{TUR} = \left(\frac{\mu_L}{\mu_V}\right)^{0.25}\cdot\left(\frac{\rho_V}{\rho_L}\right); \; f_{1z}^{TUR} = \left(\frac{\mu_V}{\mu_L}\right)^{\frac{7}{15}}\cdot\left(\frac{c_{pL}}{c_{pV}}\right)^{\frac{1}{3}}\cdot\left(\frac{\lambda_L}{\lambda_V}\right)^{\frac{3}{2}} ;$$

$$P = 2.53\times10^{(-3)}\cdot\left(Re_{L0}\right)^{1.17}\cdot(Bo)^{0.6}\cdot\left(R_{M-S}-1\right)^{(-0.65)} ;$$

$$h_{PB} = 55\cdot\dot{q}^{0.67}\cdot M^{(-0.5)}\cdot\left(\frac{P_n}{P_{CRIT}}\right)^{0.12}\cdot\left[-\log_{10}\left(\frac{P_n}{P_{CRIT}}\right)\right]^{(-0.55)} ; (Bo) = \frac{\dot{q}}{\dot{G}\cdot r} ; \left(Re_{L0}\right) = \frac{\dot{G}\cdot d}{\mu_L} ;$$

For comparison purposes the heat transfer coefficient for flow boiling in minichannels was also calculated using the Liu and Winterton formula (Liu & Winterton, 1991):

$$h_{TPB}^{L-W} = \sqrt{\left(F\cdot h_{REF}\right)^2 + \left(S\cdot h_{PB}\right)^2} \quad ; \tag{17}$$

where

$$F = \left[1+x\cdot\left(Pr_L\right)\cdot\left(\frac{\rho_L}{\rho_V}-1\right)\right]^{0.35} ; \; S = \left[\frac{1}{\left(1+0.055\cdot(F)^{0.1}\cdot\left(Re_{L0}\right)^{1.16}\right)}\right]; \; (Fr) = \frac{\dot{G}}{\rho_L^2\cdot g\cdot D} ;$$

The heat transfer coefficient distributions in flow boiling for minichannels h_{TPB} versus heat flux $\dot{q}_H$ for the steady-state conditions are presented in Fig. 9.

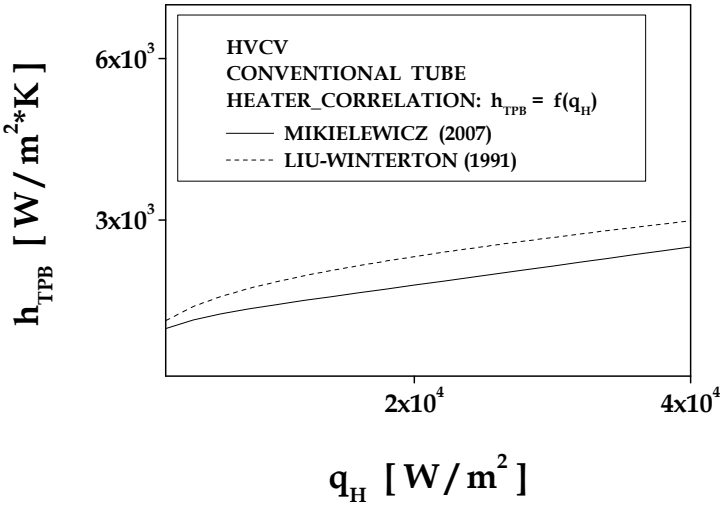

Fig. 9. Heat transfer coefficient h_{TPB} as a function of $\dot{q}_H$ (HVCV).

5. Thermosyphon Loop Heated from the Lower Part of Horizontal Side and Cooled from the Upper Part of Vertical Side (HHCV).

The thermosyphon loop heated from the lower part of horizontal side and cooled from the upper part of vertical side (HHCV) was analyzed for case of two-phase flow in minichannels. A schematic diagram of the analysed thermosyphon loop is shown in Fig. 10. In case of a thermosyphon loop with minichannels, it is necessary to apply some other correlations for void fraction and the local two-phase friction coefficient in the two-phase region, and local heat transfer coefficient for flow boiling and condensation. The following correlations have been used in calculations of the thermosyphon loop with minichannels: the El-Hajal correlation for void fraction (El-Hajal et al., 2003), the Zhang-Webb correlation for the friction pressure drop of two-phase flow in adiabatic region (Zhang & Webb, 2001), the Tran correlation for the friction pressure drop of two-phase flow in diabatic region (Tran et al. 2000), the Mikielewicz (Mikielewicz et al., 2007) and the Saitoh (Saitoh et al., 2007) correlations for the flow boiling heat transfer coefficient for minichannels, the Mikielewicz and the Tang (Tang et al., 2000) correlations for condensation heat transfer coefficient for minichannels.

After integrating momentum equation (2) for the two-phase thermosyphon loop with minichannels (HHCV) can be written in the form

$$\left(\frac{dp}{ds}\right)_{L0}\cdot\left\{(s_1-s_0)\cdot\bar{R}_{\langle s_0;s_1\rangle}+(s_5-s_1)\cdot\bar{R}_{\langle s_1;s_5\rangle}+(s_6-s_5)\cdot\bar{R}_{\langle s_5;s_6\rangle}+(s_8-s_6)\right\}+$$
$$+g\cdot(\rho_V-\rho_L)\cdot\left[\left[(s_3-s_2)-(s_5-s_4)\right]\cdot\bar{\alpha}_{\langle s_1;s_5\rangle}-(s_6-s_5)\cdot\bar{\alpha}_{\langle s_5;s_6\rangle}\right]=0\ ; \tag{18}$$

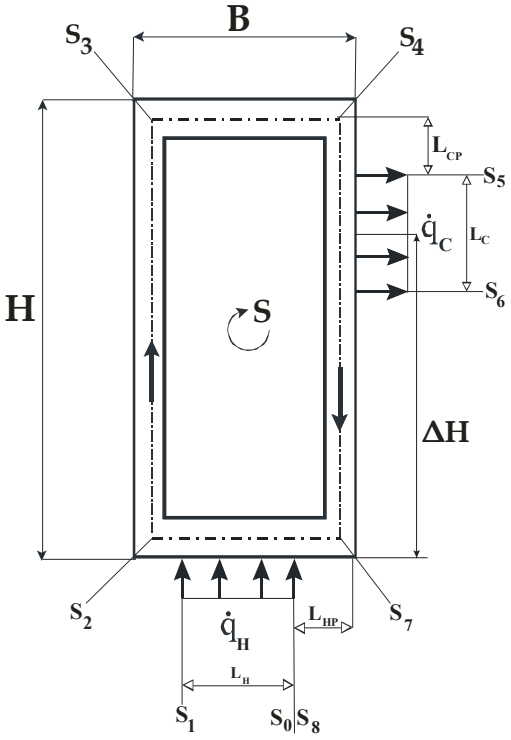

Fig. 10. The scheme of the two-phase thermosyphon loop heated from the lower part of horizontal side and cooled from the upper part of vertical side (HHCV).

The El-Hajal's empirical correlation (El-Hajal et al., 2003) for the void fraction at low pressures is used in calculations

$$\alpha_{\mathrm{HAJAL}} = \frac{\alpha_{\mathrm{HOM}} - \alpha_{\mathrm{STEINER}}}{\ln\left(\dfrac{\alpha_{\mathrm{HOM}}}{\alpha_{\mathrm{STEINER}}}\right)} \quad ; \tag{19}$$

where

$$\alpha_{\mathrm{STEINER}} = \left(\frac{x}{\rho_V}\right) \times$$

$$\times \left\{ \left[1 + 0.12 \cdot (1-x)\right] \cdot \left[\frac{x}{\rho_V} + \frac{1-x}{\rho_L}\right] + \frac{1.18 \cdot (1-x) \cdot \left[g \cdot \sigma \cdot (\rho_L - \rho_V)\right]^{0.25}}{\dot{G} \cdot (\rho_L)^{0.5}} \right\}^{(-1)} \quad ;$$

The local two-phase friction coefficient in two-phase adiabatic region was calculated using the Zhang & Webb formula (Zhang & Webb, 2001):

$$\left(\frac{dp}{dl}\right)_{2p}^{Z-W} = \Phi_{L0}^2 \cdot \left(\frac{dp}{dz}\right)_{L0} ;$$
$$\Phi_{L0}^2 = (1-x)^2 + 2.87 \cdot (x)^2 \cdot \left(\frac{P}{P_{CRIT}}\right)^{(-1)} + 1.68 \cdot (1-x)^{0.25} \cdot \left(\frac{P}{P_{CRIT}}\right)^{(-1.64)} ; \quad (20)$$

and the local two-phase friction coefficient in two-phase diabatic regions was calculated using the Tran formula (Tran et al., 2000):

$$\left(\frac{dp}{dl}\right)_{2p}^{TRAN} = \Phi_{L0}^2 \cdot \left(\frac{dp}{dz}\right)_{L0} ;$$
$$\Phi_{L0}^2 = 1 + \left(4.3 \cdot Y^2 - 1\right) \cdot \left[N_{CONF} \cdot (x)^{0.875} \cdot (1-x)^{0.875} + (x)^{1.75}\right]; \quad (21)$$
$$N_{CONF} = \frac{\left[\frac{\sigma}{g \cdot (\rho_L - \rho_V)}\right]^{0.5}}{D} ; Y = \sqrt{\left(\frac{dp}{dz}\right)_{V0} \Big/ \left(\frac{dp}{dz}\right)_{L0}} ;$$

The mass flux distributions $\dot{G}$ versus heat flux $\dot{q}_H$ were obtained numerically for the steady-state conditions for minichannels, as shown in Fig. 11. The working fluid was distilled water. Two flow regimes can be clearly identified in Fig. 11. GDR - gravity dominant regime and FDR – friction dominant regime.

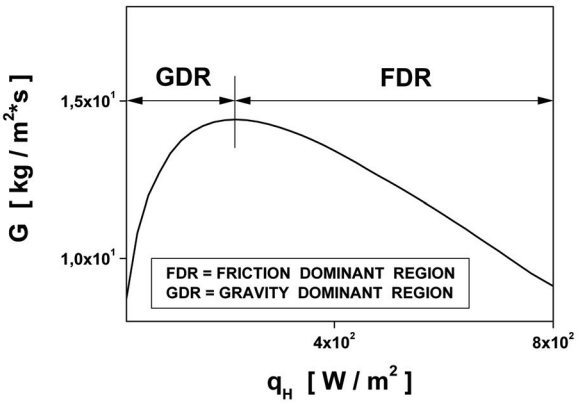

Fig. 11. Mass flux $\dot{G}$ as a function of $\dot{q}_H$ (HHCV), (L=0.2 [m], D=0.002 [m], H=0.07 [m], B=0.03 [m], L_H=L_C=0.025 [m], L_{HP}=L_{CP}=0.0001 [m]).

The gravity dominant regime is characterized by an increase in the flow rate with heat flux $\dot{q}_H$ contrary to the friction dominant regime, which is characterized by a decrease in flow rate with increase in heat flux $\dot{q}_H$ (Vijayan et al., 2005).

5.1 The effect of geometrical parameters on the mass flux distributions.

The effect of the internal diameter tube *D* on the mass flow rate for the steady-state conditions is presented in Fig. 12. The mass flow rate rapidly increases with increasing internal diameter tube *D*.

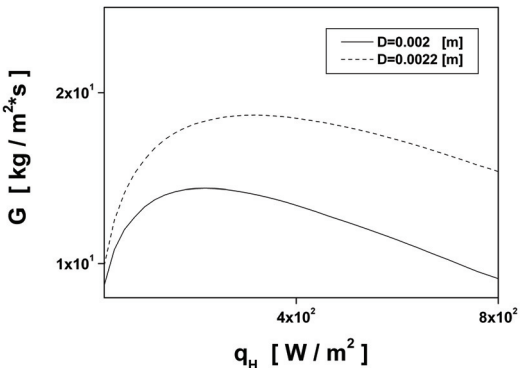

Fig. 12. Mass flux rate $\dot{G}$ as a function of $\dot{q}_H$ with internal diameter tube D as the parameter (HHCV).

The effect of the loop aspect ratio (height *H* to breadth *B*) on the mass flow rate for the steady-state conditions is presented in Fig. 13. The mass flow rate increases with increasing *H/B* aspect ratio, due to the increasing gravitational driving force. The friction force is not changed because the total length of the loop is assumed to be constant.

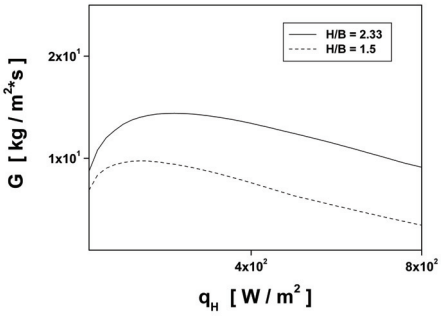

Fig. 13. Mass flux $\dot{G}$ as a function of $\dot{q}_H$ with aspect ratio *H/B* (height to breadth) as a parameter (HHCV).

The effect of the length of the heated section L_H on the mass flow rate is shown in Fig. 18. The length of FDR- friction dominant regime increases with increasing the length of the heated section L_H.

The effect of the length of preheated section L_{HP} on the mass flux rate was obtained and is demonstrated in Fig. 15. The mass flux rate increases with increasing length of preheated section L_{HP}, due to the decreasing length of insulated section $\langle s_1; s_5 \rangle$.

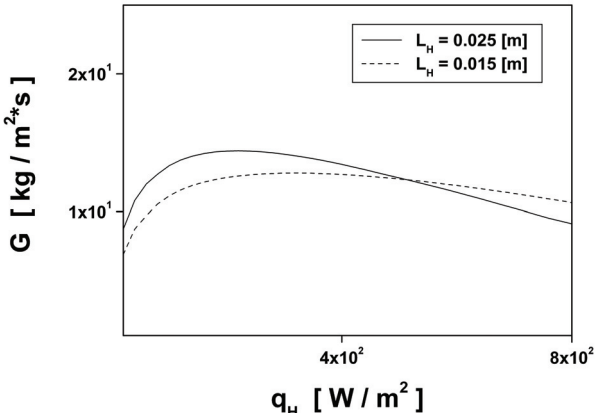

Fig. 14. Mass flux $\dot{G}$ as a function of $\dot{q}_H$ with parameter L_H (HHCV).

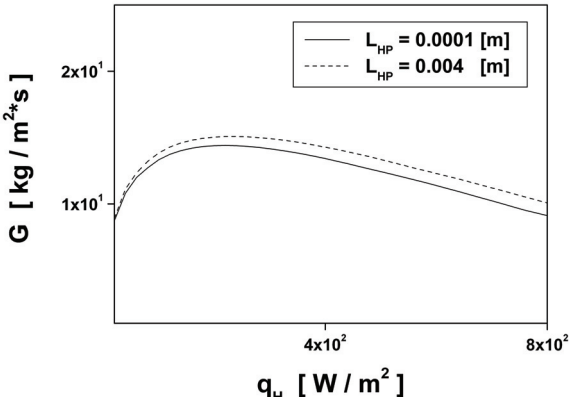

Fig. 15. Mass flux $\dot{G}$ as a function of $\dot{q}_H$ with parameter L_{HP} (HHCV).

The effect of the length of the cooled section L_C on the mass flux rate was also investigated and the results of calculations are presented in Fig. 16. The mass flux rate decreases with increasing length of the cooled section L_C, due to the decreasing gravitational driving force $\left(\Delta H \downarrow\right)$.

The effect of the length of precooled section L_{CP} on the mass flux rate is shown in Fig. 17. The mass flux rate increases with decreasing length of precooled section L_{CP} due to the decreasing length of insulated section $\langle s_1; s_5 \rangle$ and due to the increasing gravitational driving force $\left(\Delta H \uparrow\right)$. The decreasing value of the insulated two phase friction pressure drop $\left(\frac{dp}{ds}\right)^{2p,Friction}_{\langle s_1; s_5 \rangle}$ was caused by the decreasing length of insulated section $\langle s_1; s_5 \rangle$.

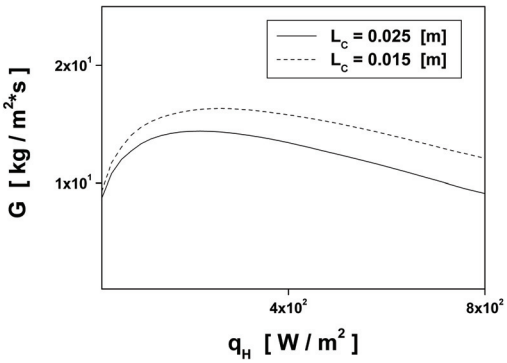

Fig. 16. Mass flux $\dot{G}$ as a function of $\dot{q}_H$ with parameter L_C (HHCV).

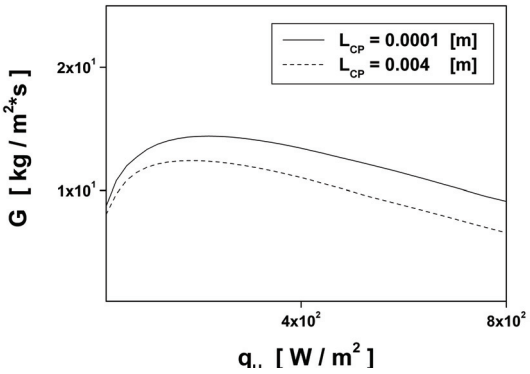

Fig. 17. Mass flux $\dot{G}$ as a function of $\dot{q}_H$ with L_{CP} as a parameter (HHCV)

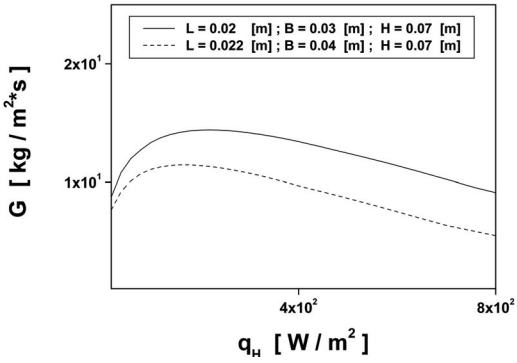

Fig. 18. Mass flux $\dot{G}$ as a function of $\dot{q}_H$ with parameter L (HHCV).

The effect of the total length of the loop L on the mass flow rate is shown in Fig. 18. The mass flow rate decreases with increasing total length of the loop L, due to the increasing frictional pressure drop. The gravitational pressure drop is not changed because the difference of height ΔH of the loop is constant.

5.2 The distributions of the heat transfer coefficient in flow boiling.

The heat transfer coefficient for flow boiling in minichannels was calculated using the Mikielewicz formula Eq. (16) with some modifications concerning the two-phase flow in minichannels, such as:

$$R_{M-S} = \left[1 + 2\cdot\left(\frac{1}{f_1} - 1\right)\cdot x\cdot\left(N_{CONF}\right)^{(-1)}\right]\cdot(1-x)^{\frac{1}{3}} + x^3\cdot\frac{1}{f_{1z}}\ ; \tag{22}$$

The heat transfer coefficient for flow boiling in minichannels was also calculated using the Saitoh formula (Saitoh et al., 2007).

$$h_{TPB}^{SAITOH} = E\cdot h_{REF} + S\cdot h_{POOL}\ ; \tag{23}$$

where

$$h_{POOL} = 207\cdot\left(\frac{\lambda_L}{d_b}\right)\cdot\left(\frac{q\cdot d_b}{\lambda_L\cdot T_{SAT}}\right)^{0.745}\cdot\left(\frac{\rho_G}{\rho_L}\right)^{0.581}\cdot\left(Pr_L\right)^{0.533}\ ;$$

$$h_{REF} = \begin{cases} (Nu)_{LAM}\cdot\left(\frac{\lambda_L}{D}\right)\ ; & \text{LAM} \\ 0.023\cdot\left(Re_L\right)^{\frac{4}{5}}\cdot\left(Pr_L\right)^{0.4}\cdot\left(\frac{\lambda_L}{D}\right)\ ; & \text{TUR} \end{cases}$$

$$E = 1 + \frac{\left(\frac{1}{X}\right)^{1.05}}{1+\left(We_V\right)^{(-0.4)}}\ ;\ \left(Re_V\right) = \frac{\dot{G}_V\cdot D}{\mu_V}\ ;\ \left(Re_L\right) = \frac{\dot{G}_L\cdot D}{\mu_L}\ ;$$

$$\left(We_V\right) = \frac{\dot{G}_V\cdot D}{\sigma\cdot\rho_V}\ ;\ S = \frac{1}{1+0.4\cdot\left[\left(10^{(-4)}\right)\cdot\left(Re_{TP}\right)\right]^{1.4}}\ ;\ d_b = 0.51\cdot\left(\frac{2\cdot\sigma}{g\cdot\left(\rho_L-\rho_V\right)}\right)0.5\ ;$$

$$\dot{G}_V = \dot{G}\cdot x\ ;\ \dot{G}_L = \dot{G}\cdot(1-x)\ ;\ \left(Re_{TP}\right) = \left(Re_L\right)\cdot\left(F\right)^{1.25}\ ;\ \left(Re_L\right) = \frac{\dot{G}_L\cdot D}{\mu_L}\ ;$$

$$X = \left(\frac{1-x}{x}\right)^{0.9}\cdot\left(\frac{\rho_G}{\rho_L}\right)^{0.5}\cdot\left(\frac{\mu_L}{\mu_G}\right)^{0.1} \quad \text{for} \quad \begin{cases}\left(Re_L\right) > 1000 \\ \left(Re_G\right) > 1000\end{cases};$$

$$C_V = 0.046\ ;\ \ C_L = 16\ ;$$

$$X = \left(\frac{C_L}{C_V}\right)^{0.5}\cdot\left(Re_G\right)^{(-0.4)}\cdot\left(\frac{G_L}{G_V}\right)^{0.5}\cdot\left(\frac{\rho_V}{\rho_L}\right)^{0.5}\cdot\left(\frac{\mu_L}{\mu_V}\right)^{0.5} \quad \text{for} \quad \begin{cases}\left(Re_L\right) < 1000 \\ \left(Re_V\right) > 1000\end{cases};$$

The heat transfer coefficient for flow boiling in minichannels h_{TPB} versus heat flux $\dot{q}_H$ is presented in Fig. 19.

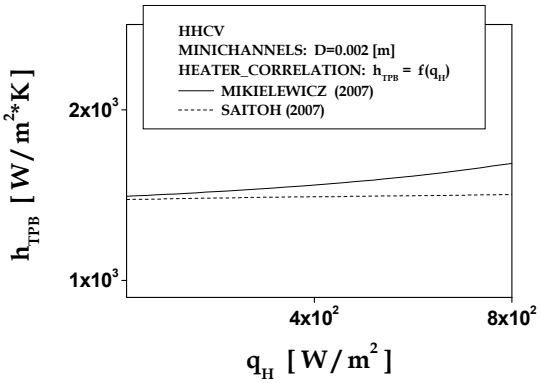

Fig. 19. Heat transfer coefficient α_{TPB} as a function of $\dot{q}_H$ (HHCV).

5.3 The heat transfer coefficient for condensation.

The heat transfer coefficient in condensation for minichannels was calculated using the general Mikielewicz formula Eq. (16). The term which describes nucleation process in that formula was neglected.

The heat transfer coefficient for condensation in minichannels was also calculated using the modified Tang formula (Tang et al., 2000)

$$h_{TPC}^{TANG} = (Nu)\cdot\left(\frac{\lambda_L}{D}\right)\cdot\left[1+4.863\cdot\left(\frac{(-x)\cdot\left[\ln\left(\frac{p_{SAT}}{p_{CRIT}}\right)\right]}{(1-x)}\right)^{0.836}\right]; \quad (24)$$

The heat transfer coefficient for condensation in minichannels h_{TPC} versus heat flux $\dot{q}_C$ is presented in Fig. 21.

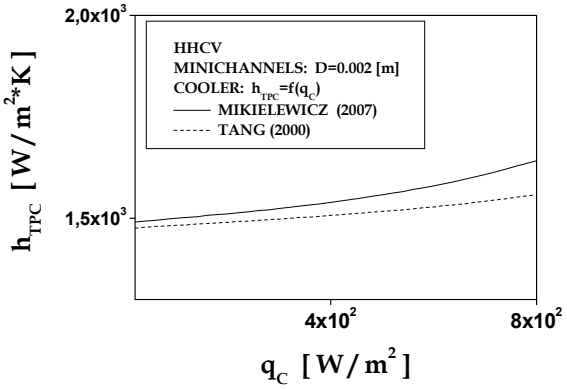

Fig. 20. Heat transfer coefficient h_{TPC} as a function of $\dot{q}_C$ (HHCV).

6. Conclusions

The presented variants (HHCH, HVCV, HHCV) of the thermosyphon loop can be analyzed using the conservation equations of mass, momentum and energy based on a generalized model of the thermosyphon loop. We have found a new and effective numerical method to solve the problem for the onset of motion in a fluid from the rest.

Our studies demonstrate that the best choice of the presented variants depends on specific technical conditions. The increasing integration of electronic systems requires improved cooling technologies. Because the progress in electronic equipment is due to the increased power levels and miniaturization of devices, the traditional cooling techniques are not able to cool effectively at high heat fluxes, so the thermosyphon cooling is an alternative technology allowing to dissipate high local heat fluxes.

The application of the complexity analysis for the various variants of a generalized model of the thermosyphon loop can support development of an alternative cooling technology.

The results show that the one-dimensional two-phase separate flow model can be used to describe heat transfer and fluid flow in the thermosyphon loop for conventional tube as well as minichannels. The Stomma correlation (Stomma, 1979) for void fraction, the Friedel correlation (Friedel, 1979) for the friction pressure drop of two-phase flow in adiabatic region, the Müller-Steinhagen & Heck correlation (Müller-Steinhagen & Heck, 1986) for the friction pressure drop of two-phase flow in diabatic region and the Mikielewicz correlation (Mikielewicz et al., 2007) for the flow boiling heat transfer coefficient in conventional channels can be used to evaluate the thermosyphon loop.

In order to evaluate the thermosyphon loop with minichannels the following correlations such as the El-Hajal correlation (El-Hajal et al., 2003) for void fraction, the Zhang-Webb correlation (Zhang & Webb, 2001) for the friction pressure drop of two-phase flow in adiabatic region, the Tran correlation (Tran et al., 2000) for the friction pressure drop of two-phase flow in diabatic region and the Mikielewicz correlation (Mikielewicz et al., 2007) for the heat transfer coefficient in evaporator, the Mikielewicz correlation for condensation heat transfer coefficient in minichannels, can be used in calculations.

The distribution of the mass flux against the heat flux approaches a maximum and then slowly decreases for minichannels, and two flow regimes can be clearly identified: GDR-gravity dominant regime and FDR – friction dominant regime as shown in Fig. 2.

The effect of geometrical parameters on the mass flux distributions was obtained numerically for the steady-state conditions as presented in Figs. 12-18. The mass flow rate increases with the following parameters: (a) increasing of the internal tube diameter, (b) increasing H/B aspect ratio, (c) decreasing length of preheated section L_{HP}, (d) decreasing length of cooled section L_C, (e) decreasing length of precooled section L_{CP}, (f) decreasing total length of the loop L. Fig. 19 and Fig. 20 respectively show that for minichannels the heat transfer coefficient in flow boiling increases with an increasing of the heat flux and the heat transfer coefficient in condensation against the heat flux approaches a maximum and then slowly decreases.

Future trends and developments in the application of mini-loops should be focused on employing complex geometries, such as parallel mini-channels, in order to maximize the heat transferred by the systems under condition of single- and two phase flows. Moreover, the transient analysis should be developed in order to characterize the dynamic behaviour of single- and two phase flow for different combination of boundary conditions. The next

design-step should also be the experimental verification of the theoretical models of thermosyphon loops with minichannels.

7. References

Bieliński, H.; Mikielewicz, J. (1995). Natural Convection of Thermal Diode., *Archives of Thermodynamics*, Vol. 16, No. 3-4.

Bieliński, H.; Mikielewicz, J. (2001). New solutions of thermal diode with natural laminar circulation., *Archives of Thermodynamics*, Vol. 22, pp. 89-106.

Bieliński, H.; Mikielewicz J. (2004). The effect of geometrical parameters on the mass flux in a two phase thermosyphon loop heated from one side., *Archives of Thermodynamics*, Vol. 29, No. 1, pp. 59-68.

Bieliński, H.; Mikielewicz J. (2004). Natural circulation in two-phase thermosyphon loop heated from below., *Archives of Thermodynamics*, Vol. 25, No. 3, pp. 15-26.

Bieliński, H.; Mikielewicz, J. (2005). A two-phase thermosyphon loop with side heating, *Inżynieria Chemiczna i Procesowa*., Vol. 26, pp. 339-351 (in Polish).

Chen, K. (1988). Design of Plane-Type Bi-directional Thermal Diode., *ASME J. of Solar Energy Engineering*, Vol. 110.

Churchill, S.W. (1977). Friction-Factor Equation Spans all Fluid Flow Regimes., *Chem. Eng.*, pp. 91-92.

El-Hajal, J.; Thome, J.R. & Cavalini A. (2003). Condensation in horizontal tubes, part 1; two-phase flow pattern map., *Int. J. Heat Mass Transfer*, Vol. 46, No. 18, pp. 3349-3363.

Friedel, L. (1979). Improved Friction Prresure Drop Correlations for Horizontal and Vertical Two-Phase Pipe Flow., Paper No. E2, European Two-Phase Flow Group Meeting, Ispra, Italy.

Greif, R. (1988). Natural Circulation Loops., *Journal of Heat Transfer*, Vol. 110, pp. 1243-1257.

Liu, Z.; Winterton, R.H.S. (1991). A general correlation for saturated and subcooled flow boiling in tubes and annuli,based on a nucleate pool boiling equation. *Int. J. Heat Mass Transfer*, Vol. 34, pp. 2759–2766.

Madejski, J.; Mikielewicz, J. (1971). Liquid Fin - a New Device for Heat Transfer Equipment, *Int. J. Heat Mass Transfer*, Vol. 14, pp. 357-363.

Mertol, A.; Greif, R. (1985). A review of natural circulation loops., In: *Natural Convection: Fundamentals and Applications*, pp. 1033-1071, 1985.

Mikielewicz, D.; Mikielewicz, J. & Tesmar J. (2007). Improved semi-empirical method for determination of heat transfer coefficient in flow boiling in conventional and small diameter tubes., *Inter. J. Heat Mass Transfer* , Vol. 50, pp. 3949-3956.

Mikielewicz J. (1995). Modelling of the heat-flow processes., *Polska Akademia Nauk Instytut Maszyn Przepływowych, Seria Cieplne Maszyny Przepływowe,* Vol. 17, Ossolineum.

Misale, M.; Garibaldi, P.; Passos, J.C.; Ghisi de Bitencourt, G. (2007). Experiments in a Single-Phase Natural Circulation Mini-Loop., *Experimental Thermal and Fluid Science*, Vol. 31, pp. 1111-1120.

Müller-Steinhagen, H.; Heck, K. (1986). A Simple Friction Pressure Drop Correlation for Two-Phase Flow Pipes., *Chem. Eng. Process*., Vol. 20, pp. 297-308.

Ramos, E.; Sen, M. & Trevino, C. (1985). A steady-state analysis for variable area one- and two-phase thermosyphon loops, *Int. J. Heat Mass Transfer*, Vol. 28, No. 9, pp. 1711-1719.

Saitoh, S.; Daiguji, H. & Hihara, E. (2007). Correlation for Boiling Heat Transfer of R-134a in Horizontal Tubes Including Effect of Tube Diameter., *Int. J. Heat Mass Tr.*, Vol. 50, pp. 5215-5225.

Stomma, Z., (1979). Two phase flows-pressure drop values determination." IBJ, Warszawa, INR 1819/IX/R/A.

Tang, L.; Ohadi, M.M. & Johnson, A.T. (2000). Flow condensation in smooth and microfin tubes with HCFC-22, HFC-134a, and HFC-410 refrigerants, Part II: Design equations. *Journal of Enhanced Heat Transfer*, Vol. 7, pp. 311-325.

Tran, T.N.; Chyu, M.C.; Wambsganss, M.W.; & France D.M. (2000). Two –phase pressure drop of refrigerants during flow boiling in small channels: an experimental investigations and correlation development., *Int. J. Multiphase Flow*, Vol. 26, No. 11, pp. 1739-1754.

Vijayan, P.K.; Gartia, M.R.; Pilkhwal, D.S.; Rao, G.S.S.P. & Saha D. (2005). Steady State Behaviour Of Single-Phase And Two-Phase Natural Circulation Loops. 2nd RCM on the IAEA CRP ,Corvallis, Oregon State University, USA.

Zhang, M.; Webb, R.L. (2001). Correlation of two-phase friction for refrigerants in small-diameter tubes. *Experimental Thermal and Fluid Science*, Vol. 25, pp. 131-139.

Zvirin, Y. (1981). A Review of Natural Circulation Loops in PWR and Other Systems., *Nuclear Engineering Design*, Vol. 67, pp. 203-225.

20

Heat Transfer at Microscale

Mohammad Hassan Saidi and Arman Sadeghi
Center of Excellence in Energy Conversion (CEEC), School of Mechanical Engineering, Sharif University of Technology, P.O. Box: 11155-9567, Tehran, Iran

1. Introduction

In the past two decades, Micro-Electro-Mechanical-Systems (MEMS) have been one of the major advances of industrial technologies because of their lower cost in spite of supplying higher performance. MEMS covers micron-sized, electrically and/or mechanically driven devices. Having been derived initially from the integrated circuit (IC) fabrication technologies, MEMS devices are already emerging as products in both commercial and defense markets such as automotive, aerospace, medical, industrial process control, electronic instrumentation, office equipment, appliances, and telecommunications. Current products include: airbag crash sensors, pressure sensors, inkjet printer heads, lab-on-a-chip devices, etc. The study of microfluidics is crucial in MEMS investigations. Microfluidics may be defined as the fluid flow and heat transfer in microgeometries which by microgeometry we mean the geometries with the characteristic length scales of the order of 1-100 μm. Transport phenomena at microscale reveal many features that are not observed in macroscale devices. These features are quite different for gas and liquid flows. In gas microflows we encounter four important effects: compressibility, viscous heating, thermal creep, and rarefaction (Karniadakis et al., 2005). Liquid flows are encountered with other microscale features such as surface tension and electrokinetic effects.
This chapter deals with the fundamentals of microfluidics and major developments in this area. The flow physics pertinent to microfluidics and their methods of simulation are numerous and there is not enough space to consider all of them. Therefore, we confine our presentation to gas slip flow and electrokinetics. Section 2 is devoted to gas slip flow in microchannels with special attention to its basic concepts along with emerging features such as slip velocity, temperature jump, thermal creep, viscous dissipation, and Shear work at solid boundaries. Section 3 deals with electrokinetic phenomena such as electroosmosis and streaming potential effects.

2. Gas flow in microchannels

Design and optimization of many microdevices involve the analysis of gas flow through microchannels, as an important part of these devices. When characteristic length scale of the device is comparable with gas mean free path, continuum approach may be no longer valid, since the rarefaction effects are important. The deviation of the state of the gas from continuum behavior is measured by the Knudsen Number (Kn). For a microchannel, the

Knudsen number is defined as $Kn = \lambda/D_h$, where D_h is the channel hydraulic diameter and λ is the mean free path of gas molecules, given by $\lambda = \mu\sqrt{\pi/2RT\rho^2}$, where μ is the dynamic viscosity, R is the gas constant and T and ρ are the temperature and density of the gas, respectively (Kandlikar et al., 2006). Based on a classification given by Beskok and Karniadakis (1994), gas flow can be categorized into four regimes according to its Knudsen number. For $Kn < 10^{-3}$, the gas is considered as a continuum, while for $Kn > 10$ it is considered as a free molecular flow. In the Knudsen number ranging between 10^{-3} and 10, two different regimes exist: slip flow ($10^{-3} \leq Kn \leq 0.1$) and transition flow ($0.1 < Kn \leq 10$). In general, there are several rarefaction effects, such as discontinuities of velocity and temperature on boundary, non-Newtonian components of stress tensor, non-Fourier heat flux and formation of Knudsen boundary layer (Taheri et al., 2009). In the slip flow regime, deviations from the state of continuum are relatively small and the Navier-Stokes equations are still valid, except at the region next to the boundary which is known as Knudsen boundary layer. The Knudsen boundary layer is significant only up to distances of the order of one mean free path from the wall (Hadjiconstantinou, 2006). So, besides velocity and temperature discontinuities at the wall, its effects are negligible in slip flow regime and the Navier-Stokes equations may be applied to the whole domain. The velocity and temperature discontinuities are incorporated into the solution as boundary conditions. In the next subsection, slip flow boundary conditions along with other phenomena associated with gas flow in microchannels are introduced.

2.1 Basic concepts

2.1.1 Slip velocity and temperature jump

In this subsection, an expression for the slip velocity given by Karniadakis et al. (2005) is derived and an expression will be introduced for the temperature jump. It should be pointed out that these expressions have been originally obtained for low pressure flows and we

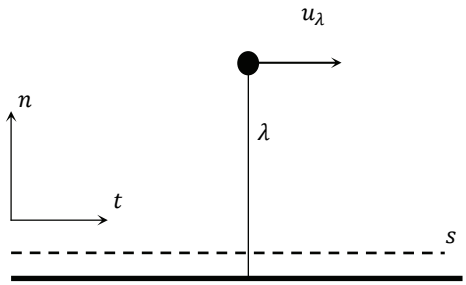

Fig. 1. Control surface for tangential momentum flux near a wall moving at velocity u_w

therefore use a similarity between fluid flow at microscale and that at low pressures. For validity of this similarity, it is necessary that the size of gas molecules be negligible compared with the characteristic length of the channel (Kandlikar et al., 2006). In slip flow regime, the minimum length scale corresponds to $Kn = 0.1$. The molecular diameter and the mean free path at atmospheric conditions for air are about 0.42 nm and 67 nm, respectively. Therefore, at $Kn = 0.1$, the characteristic length of the device is about 670 nm. So the ratio of the channel length to the gas molecular diameter is about 1595. Therefore, it seems that the

size of gas molecules is negligible compared with the characteristic length of the channel for slip flow regime and, consequently, the similarity may be used for this flow regime.
The tangential momentum flux on a surface s located near the wall shown in Fig. 1 is given by

$$\frac{1}{4}n_s m\bar{v}u_s \tag{1}$$

in which n_s is the number density of the molecules crossing surface s, m is the molecular mass, u_s is the tangential (slip) velocity of the gas on this surface, and $\bar{v}$ is the mean thermal speed given by (Kennard, 1938)

$$\bar{v} = (8RT/\pi)^{0.5} \tag{2}$$

We now assume that approximately half of the molecules passing through s are coming from a layer of gas at a distance proportional to one mean free path away from the surface. The tangential momentum flux of these incoming molecules is written as

$$\frac{1}{4}n_\lambda m\bar{v}_\lambda u_\lambda \tag{3}$$

where the subscript λ indicates quantities evaluated one mean free path away from the surface. Since we have assumed that half of the molecules passing through s are coming from λ away from this surface, therefore $n_\lambda = \frac{1}{2}n_s$. The other half of the molecules passing through s are reflected from the wall with a tangential momentum flux of

$$\frac{1}{4}n_w m\bar{v}_w u_r \tag{4}$$

where the subscript w indicates wall conditions, u_r shows the average tangential velocity of the molecules reflected from the wall, and the number density n_w is equal to $\frac{1}{2}n_s$. For determination of u_r, the definition of tangential momentum accommodation coefficient, F_m, should be used. Assuming that F_m fraction of the molecules are reflected from the wall with average tangential velocity corresponding to that of the wall, u_w, and $(1 - F_m)$ of the molecules are reflected from the wall conserving their average incoming tangential velocity, u_λ, we have

$$u_r = F_m u_w + (1 - F_m)u_\lambda \tag{5}$$

Therefore, the total tangential momentum flux on surface s is given by

$$\frac{1}{4}n_s m\bar{v}u_s = \frac{1}{4}n_\lambda m\bar{v}_\lambda u_\lambda + \frac{1}{4}n_w m\bar{v}_w[F_m u_w + (1 - F_m)u_\lambda] \tag{6}$$

We now assume that the temperatures of the fluid and the surface are the same. So the mean thermal speeds become identical, i.e., $\bar{v}_s = \bar{v}_\lambda = \bar{v}_w$. By applying the aforementioned assumptions to the above equation, the slip velocity, u_s, is obtained as follows

$$u_s = \frac{1}{2}[u_\lambda + (1 - F_m)u_\lambda + F_m u_w] \tag{7}$$

Using a Taylor series expansion for u_λ about u_s, results in

$$u_s = \frac{1}{2}\left[u_s + \lambda\left(\frac{\partial u}{\partial n}\right)_s + \frac{\lambda^2}{2}\left(\frac{\partial^2 u}{\partial n^2}\right)_s + \cdots\right] + \frac{1}{2}\left\{(1-F_m)\left[u_s + \lambda\left(\frac{\partial u}{\partial n}\right)_s + \frac{\lambda^2}{2}\left(\frac{\partial^2 u}{\partial n^2}\right)_s + \cdots\right] + F_m u_w\right\} \tag{8}$$

where n is the normal direction exiting the wall. This expansion ultimately results in the following slip relation on the boundaries

$$u_s - u_w = \frac{2-F_m}{F_m}\left[\lambda\left(\frac{\partial u}{\partial n}\right)_s + \frac{\lambda^2}{2}\left(\frac{\partial^2 u}{\partial n^2}\right)_s + \cdots\right] \tag{9}$$

The above relation may be written dimensionless based on appropriate scale velocity and reference length as

$$u_s^* - u_w^* = \frac{2-F_m}{F_m}\left[Kn\left(\frac{\partial u^*}{\partial n^*}\right)_s + \frac{Kn^2}{2}\left(\frac{\partial^2 u^*}{\partial n^{*2}}\right)_s + \cdots\right] \tag{10}$$

If we truncate the above equation to include only up to first order terms in Kn, we recover Maxwell's first order slip boundary condition (Maxwell, 1879)

$$u_s^* - u_w^* = \frac{2-F_m}{F_m} Kn\left(\frac{\partial u^*}{\partial n^*}\right)_s \tag{11}$$

Karniadakis et al. (2005) have proposed the following general slip velocity, instead of Eq. (11)

$$u_s^* - u_w^* = \frac{2-F_m}{F_m}\frac{Kn}{1-bKn}\left(\frac{\partial u^*}{\partial n^*}\right)_s \tag{12}$$

where b is a general slip coefficient. The value of b is determined such that maximum agreement between the calculated velocity profiles with Direct Simulation Monte Carlo (DSMC) results is obtained. For channel flow, it has been shown that $b = -1$ provides more accurate results. The above equations exclude the thermal creep effects, since they have been obtained based on isothermal condition. We will add the corresponding term due to the thermal creep to the above equation in the next sections.

For the temperature jump, the following expression is given by Kennard (1938) which is obtained based on the kinetic theory of gases

$$T_s^* - T_w^* = \frac{2-F_t}{F_t}\frac{2\gamma}{1+\gamma}\frac{Kn}{Pr}\left(\frac{\partial T^*}{\partial n^*}\right)_s \tag{13}$$

in which F_t is the thermal accommodation coefficient, γ is the specific heat capacity ratio, and Pr is the Prandtl number. Karniadakis et al. (2005) proposed the following form for the high order temperature jump condition by analogy with Eq. (10)

$$T_s^* - T_w^* = \frac{2-F_t}{F_t}\frac{2\gamma}{1+\gamma}\frac{1}{Pr}\left[Kn\left(\frac{\partial T^*}{\partial n^*}\right)_s + \frac{Kn^2}{2}\left(\frac{\partial^2 T^*}{\partial n^{*2}}\right)_s + \cdots\right] \tag{14}$$

2.1.2 Thermal creep

The term thermal creep points out to rarefied gas flow due to tangential temperature gradients along the channel walls, where the fluid starts creeping in the direction from cold

towards hot. This phenomenon may be explained by means of the following example used by Karniadakis et al. (2005): Let us consider two containers filled with the same gas that are kept at the same pressure

$$P_1 = P_2 \tag{15}$$

but at different temperatures

$$T_1 > T_2 \tag{16}$$

It is now assumed that these two containers are connected with a relatively thin channel having the height of $H \ll \lambda$. In this situation, the intermolecular collisions are negligible compared with the interaction of molecules with the surfaces of the channel. Then, the assumption of $F_m = 0$ will result in the validation of the following analysis. It is assumed that the density of the fluid is proportional to the number density

$$\rho \propto n \tag{17}$$

and the temperature of the fluid is proportional to the square of average molecular speed, $\bar{c}$

$$T \propto \bar{c}^2 \tag{18}$$

The mass fluxes at the hot and the cold ends of the channel are $mn_1\bar{c}_1$ and $mn_2\bar{c}_2$, respectively, with m being the mass of the gas molecules. Then

$$\frac{mn_1\bar{c}_1}{mn_2\bar{c}_2} \approx \frac{\rho_1}{\rho_2}\left(\frac{T_1}{T_2}\right)^{0.5} = \frac{P_1}{P_2}\left(\frac{T_2}{T_1}\right)^{0.5} = \left(\frac{T_2}{T_1}\right)^{0.5} \leq 1 \tag{19}$$

in which the equation of state of ideal gas has been used, i.e.,

$$P = \rho RT \tag{20}$$

The above analysis indicates a flow creeping from cold to hot. A detailed derivation of thermal creep boundary condition is given by Kennard (1938) and the resultant velocity which should be added to Eq. (9) is as follows

$$u_c = \frac{3}{4}\frac{\mu R}{P}\left(\frac{\partial T}{\partial t}\right)_s \tag{21}$$

where u_c is the creep velocity, and $(\partial T/\partial t)_s$ is the tangential temperature gradient along the surface. Using the equation of state of ideal gas and the relation $\lambda = \mu\sqrt{\pi/2RT\rho^2}$, Eq. (21) may be written as

$$u_c = \frac{3}{2\pi}\frac{R\rho\lambda^2}{\mu}\left(\frac{\partial T}{\partial t}\right)_s \tag{22}$$

and in dimensionless form as

$$u_c^* = \frac{3}{2\pi}\frac{\gamma - 1}{\gamma}\frac{ReKn^2}{Ec}\left(\frac{\partial T^*}{\partial t^*}\right)_s \tag{23}$$

in which $Re = \rho U D_h/\mu$ and $Ec = U^2/c_p\Delta T$ with U and ΔT being the reference velocity and temperature difference. Therefore, the complete expression for the slip velocity may be written as

$$u_s^* - u_w^* = \frac{2 - F_m}{F_m}\left[Kn\left(\frac{\partial u^*}{\partial n^*}\right)_s + \frac{Kn^2}{2}\left(\frac{\partial^2 u^*}{\partial n^{*2}}\right)_s + \cdots\right] + \frac{3}{2\pi}\frac{\gamma - 1}{\gamma}\frac{ReKn^2}{Ec}\left(\frac{\partial T^*}{\partial t^*}\right)_s \tag{24}$$

2.1.3 Viscous dissipation

Viscous dissipation effects are typically only significant for high viscous flows or in presence of high gradients in velocity distribution. In macroscale, such high gradients occur in high velocity flows. In microscale devices, however, because of small dimensions, such high gradients may occur even for low velocity flows. So, for microchannels the viscous dissipation should be taken into consideration. Viscous dissipation features as a source term in the fluid flow due to the conversion of the kinetic motion of the fluid to the thermal energy and causes variation in the temperature distribution. The effects of viscous dissipation on the temperature field and ultimately on the friction factor have been investigated by Koo and Kleinstreuer (2003, 2004), using dimensional analysis and experimentally validated computer simulations. It was found that ignoring viscous dissipation could affect accurate flow simulations and measurements in microconduits. The effect of viscous dissipation in convective heat transfer is characterized by the Brinkman number, Br, which is the ratio of energy generated by viscous heating to the energy transferred by conduction at the solid boundaries, i.e.,

$$Br = \frac{\mu U^2}{qH} \quad \text{or} \quad Br = \frac{\mu U^2}{k\Delta T} \tag{25}$$

where q is the wall heat flux and H is the channel height or radius. Some theoretical studies has been undertaken to investigate viscous dissipation effects on the heat transfer features of the gas flow in microchannels of different cross section such as circular channel (Aydin and Avci, 2006), parallel plate and annular channel (Sadeghi and Saidi, 2010), and rectangular channel (Rij et al., 2009).

2.1.4 Flow work and shear work at solid boundaries

In this section, we discuss the effects of flow work and shear work at the boundary in slip flow and how these affect convective heat transfer in small scale channels. Flow work and shear work at the boundary have been neglected in the majority of the recent studies of viscous dissipation in slip flow convective heat transfer. However, flow work is of the same order of magnitude as viscous dissipation (Ou and Cheng, 1973). Also Hadjiconstantinou (2003) showed that, for rarefied flows, the effect of shear work scales with the Brinkman number. The effect of shear work on boundary is due to the slip velocity and it is zero at macroscale. This effect causes smaller amounts of the streamwise temperature gradient at slip flow regime. Therefore, in order to take it into account, one should consider its effects in evaluating the axial temperature gradient. Let us show the effects of shear work by considering the fully developed slip flow forced convection in a parallel plate microchannel with the channel half height of H, which is shown in Fig. 2.

The energy equation including the effects of viscous dissipation and flow work is written as

$$\rho c_p u\frac{\partial T}{\partial x} = k\frac{\partial^2 T}{\partial y^2} + u\frac{\mathrm{d}P}{\mathrm{d}x} + \tau_{xy}\frac{\mathrm{d}u}{\mathrm{d}y} \tag{26}$$

In the above equation, $u\,\mathrm{d}P/\mathrm{d}x$ and $\tau_{xy}\,\mathrm{d}u/\mathrm{d}y$ denote the rate of energy absorbed by flow work and generated by viscous heating, respectively. It is noteworthy that for a constant

wall heat flux, which is the case in this example, the axial conduction term in the energy equation is zero. The integral form of the above equation in the transverse direction becomes

$$\rho c_p UH \frac{\mathrm{d}T_b}{\mathrm{d}x} = q + UH \frac{\mathrm{d}P}{\mathrm{d}x} + \int_0^H \tau_{xy} \frac{\mathrm{d}u}{\mathrm{d}y} \mathrm{d}y \tag{27}$$

in which q is the thermal energy transferred from the wall to the fluid, U is the mean velocity, and T_b is the bulk temperature defined as

$$T_b = \frac{\int_0^H uT \mathrm{d}y}{UH} \tag{28}$$

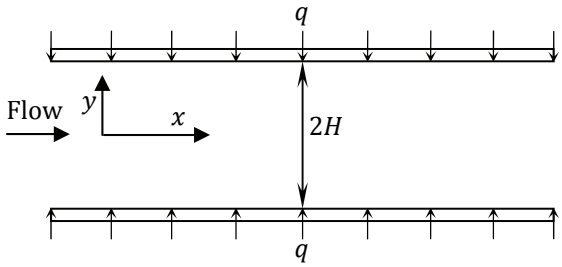

Fig. 2. Schematic of a parallel plate microchannel with coordinate system

In addition to the thermal energy transfer, there is also dissipation due to shear work between the wall and the slipping gas. It is the sum of these two contributions that is responsible for the axial temperature gradient as shown by the integral form of the total (mechanical plus thermal) energy equation (Hadjiconstantinou, 2003)

$$\rho c_p UH \frac{\mathrm{d}T_b}{\mathrm{d}x} = q + u_s \tau_{xy,s} \tag{29}$$

in which u_s is the slip velocity and $\tau_{xy,s} = \mu(\mathrm{d}u/\mathrm{d}y)_s$ is the wall shear stress. In Eq. (29), $u_s \tau_{xy,s}$ is the dissipation due to shear work between the wall and the slipping gas and it is zero at no slip condition. Equations (27) and (29) are linked by the mechanical energy balance

$$0 = -u \frac{\mathrm{d}P}{\mathrm{d}x} + u \frac{\mathrm{d}\tau_{xy}}{\mathrm{d}y} = -u \frac{\mathrm{d}P}{\mathrm{d}x} + \frac{\mathrm{d}\left(u\tau_{xy}\right)}{\mathrm{d}y} - \tau_{xy} \frac{\mathrm{d}u}{\mathrm{d}y} \tag{30}$$

which integrates to

$$u_s \tau_{xy,s} = UH \frac{\mathrm{d}P}{\mathrm{d}x} + \int_0^H \tau_{xy} \frac{\mathrm{d}u}{\mathrm{d}y} \mathrm{d}y \tag{31}$$

and shows that the viscous heating and flow work terms in Eq. (27) are, in effect, representing the contribution of the shear work at the wall. Hadjiconstantinou (2003) obtained the Nusselt number based on the total heat exchange between the wall and the flow, Nu_t, as

$$Nu_t = Nu + \frac{4Hu_s\tau_{xy,s}}{k(T_w - T_b)} \tag{32}$$

with $Nu = 4Hq/k(T_w - T_b)$ being the Nusselt number based on the thermal energy exchange. In spite of their importance, the effects of flow work and shear work at boundaries have rarely been investigated in the literature. The only work performed is by Rij et al (2009) which numerically investigated slip flow forced convection in rectangular microchannels.

2.2 Slip flow forced convection

In this section, we consider slip flow forced convection in microchannels. First, a solution is derived for forced convection with viscous dissipation in a parallel plate microchannel and, afterwards, the other progresses in the literature will shortly be presented. Let us consider fully developed forced convection in a parallel plate microchannel with constant wall heat fluxes which was shown in Fig. 2. The momentum equation in x-direction and relevant boundary conditions may be written as

$$\frac{\mathrm{d}^2u}{\mathrm{d}y^2} = \frac{1}{\mu}\frac{\mathrm{d}p}{\mathrm{d}z} = \text{const.}$$
$$u_{(H)} = -\frac{2-F_m}{F_m}KnD_h\left(\frac{\mathrm{d}u}{\mathrm{d}y}\right)_{(H)} \quad \text{and} \quad \left(\frac{\mathrm{d}u}{\mathrm{d}y}\right)_{(0)} = 0 \tag{33}$$

here $D_h = 4H$. The dimensionless velocity distribution will then be

$$u^* = \frac{3}{2}\left(\frac{1 - y^{*2} + 8\dfrac{2-F_m}{F_m}Kn}{1 + 12\dfrac{2-F_m}{F_m}Kn}\right) \tag{34}$$

in which $y^* = y/H$, $u^* = u/U$ and U is the mean velocity.

The energy equation including the effects of viscous dissipation and relevant boundary conditions are written as

$$u\frac{\partial T}{\partial z} = \alpha\frac{\partial^2 T}{\partial y^2} + \frac{\nu}{c_p}\left(\frac{\mathrm{d}u}{\mathrm{d}y}\right)^2$$
$$T_{(x,H)} - T_w = -\frac{2-F_t}{F_t}\frac{8\gamma}{1+\gamma}\frac{KnH}{Pr}\left(\frac{\partial T}{\partial y}\right)_{(x,H)} \quad \text{and} \quad \left(\frac{\partial T}{\partial y}\right)_{(x,0)} = 0 \tag{35}$$

We introduce dimensionless temperature as follows, which only depends on y for fully developed flow

$$\theta(y) = \frac{T - T_s}{\dfrac{qH}{k}} \tag{36}$$

in which T_s is the gas temperature at the wall. Taking differentiation of Eq. (36) with respect to x gives

$$\frac{\partial T}{\partial x} = \frac{\mathrm{d}T_s}{\mathrm{d}x} = \frac{\mathrm{d}T_b}{\mathrm{d}x} \tag{37}$$

From an energy balance on a length of duct $\mathrm{d}x$, the following expression is obtained for $\mathrm{d}T_b/\mathrm{d}x$

$$\frac{\mathrm{d}T_b}{\mathrm{d}x} = \frac{q}{\rho c_p U H}\left[1 + \frac{12Br}{\left(1 + 12\frac{2-F_m}{F_m}Kn\right)^2}\right] \tag{38}$$

in which $Br = \mu U^2/4qH$. The energy equation then is modified into the following dimensionless form

$$\frac{\mathrm{d}^2\theta}{\mathrm{d}y^{*2}} = a - by^{*2} \tag{39}$$

with the following coefficients

$$a = \frac{3(1 + 8\frac{2-F_m}{F_m}Kn)}{2\left(1 + 12\frac{2-F_m}{F_m}Kn\right)}\left[1 + \frac{12Br}{\left(1 + 12\frac{2-F_m}{F_m}Kn\right)^2}\right]$$
$$b = \frac{3}{2\left(1 + 12\frac{2-F_m}{F_m}Kn\right)} + \frac{36Br}{\left(1 + 12\frac{2-F_m}{F_m}Kn\right)^2} + \frac{18Br}{\left(1 + 12\frac{2-F_m}{F_m}Kn\right)^3} \tag{40}$$

The thermal boundary conditions in the dimensionless form are written as

$$\left(\frac{\mathrm{d}\theta}{\mathrm{d}y^*}\right)_{(0)} = 0 \quad , \quad \theta_{(1)} = 0 \tag{41}$$

Using Eq. (39) and applying boundary conditions (41), the dimensionless temperature distribution is obtained as

$$\theta(y^*) = -\frac{a}{2}\left(1 - y^{*2}\right) + \frac{b}{12}\left(1 - y^{*4}\right) \tag{42}$$

On the other hand, Eq. (42) which is in terms of T_s can be transformed into an equation in terms of T_w, using the following conversion formula

$$\frac{T_w - T_s}{\frac{qH}{k}} = \frac{2 - F_t}{F_t}\frac{8\gamma}{1+\gamma}\frac{Kn}{Pr} \tag{43}$$

So that Eq. (42) becomes

$$\theta^*(y^*) = \frac{T - T_w}{\frac{qH}{k}} = \frac{T - T_s}{\frac{qH}{k}} - \frac{T_w - T_s}{\frac{qH}{k}} = -\frac{a}{2}\left(1 - y^{*2}\right) + \frac{b}{12}\left(1 - y^{*4}\right) - \frac{2 - F_t}{F_t}\frac{8\gamma}{1+\gamma}\frac{Kn}{Pr} \tag{44}$$

To obtain the Nusselt number, first the dimensionless bulk temperature θ_b^* must be calculated, which is given by

$$\theta_b^* = \frac{\int_0^1 u^*\theta^* \mathrm{d}y^*}{\int_0^1 u^* \mathrm{d}y^*} = \frac{3}{4\left(1+12\frac{2-F_m}{F_m}Kn\right)}\left[\left(1+8\frac{2-F_m}{F_m}Kn\right)\left(2-\frac{8}{3}a+\frac{4}{5}b\right)-\frac{2}{3}+\frac{4}{5}a - \frac{16}{63}b\right]-\frac{2-F_t}{F_t}\frac{8\gamma}{1+\gamma}\frac{Kn}{Pr} \tag{45}$$

Based on definition, the Nusselt number is written as

$$Nu = \frac{hD_h}{k} = \frac{qD_h}{k(T_w - T_b)} = -\frac{4}{\theta_b^*} \tag{46}$$

Some of the results obtained for this example are now depicted using $F_m = F_t = 1$. Figure 3 depicts transverse distribution of dimensionless velocity at different values of Knudsen number. As a result of slip conditions, slip velocities occur at the walls. An increase in Kn results in an increase in the slip velocities at the walls, while according to mass conservation, the maximum velocity decreases. Note that as Knudsen number increases the velocity gradient becomes smaller, especially at the walls at which the maximum decrease occurs.

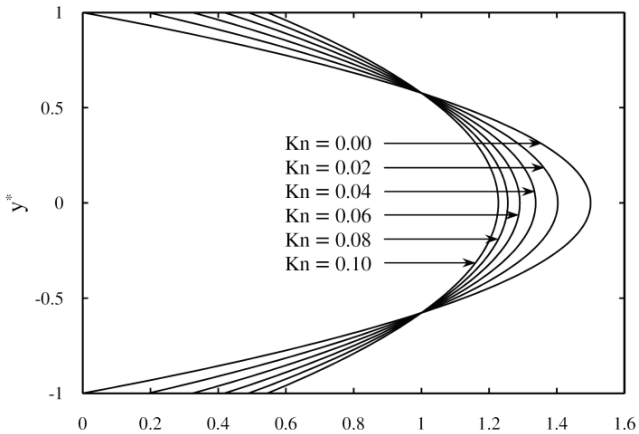

Fig. 3. Transverse distribution of dimensionless velocity at different values of Knudsen number

The effect of rarefaction on dimensionless temperature profile is illustrated in Fig. 4. As observed, to increase Knudsen number is to decrease dimensionless temperature as a result of temperature jump at the wall.

Figure 5 illustrates the Nusselt number values versus Knudsen number at different Brinkman numbers. Both positive and negative values of the heat fluxes at the walls are considered. Positive values of Brinkman number correspond to the wall cooling case where heat is transferred from the walls to the fluid, while the opposite is true for negative values of Brinkman number. For each case, the viscous dissipation behaves like an energy source increasing the temperature of the fluid especially near the wall since the highest shear rate occurs at this region while it is zero at the centerline. In the absence of viscous dissipation, the distribution of dimensionless temperature is independent of whether the wall is heated or cooled. As seen, for wall cooling case, which corresponds to positive values of Brinkman number, viscous dissipation decreases the Nusselt number. Viscous heating increases the

difference between the wall and the bulk temperatures. Thus for a constant value of wall heat flux, according to Eq. (46), the Nusselt number values decrease. For wall heating case, as expected, viscous heating leads to greater values of Nusselt number. Increasing values of Knudsen number result in decreasing the values of Nusselt number for wall cooling case and also for no viscous heating case. But for wall heating case at small values of Knudsen number, an increment of Knudsen number values leads to a larger amount of Nusselt, while the opposite is true for larger values of Knudsen. For all cases, the effect of Brinkman number on Nusselt number becomes insignificant at larger values of Knudsen number. This is due to the fact that the slip velocity tends to unify the velocity profile which leads to smaller velocity gradients and consequently smaller shear rates, which in the following reduces viscous heating effects.

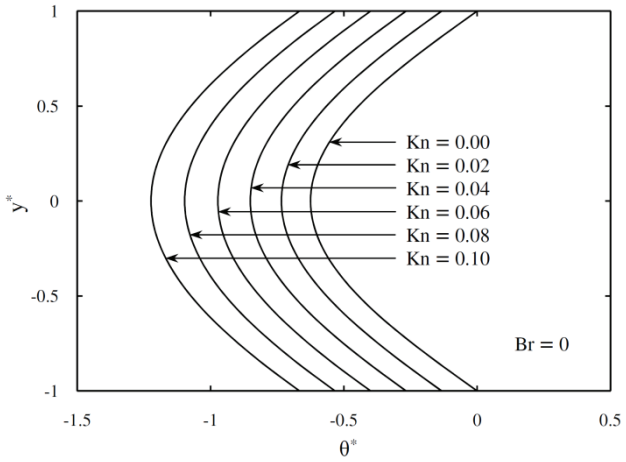

Fig. 4. Effect of rarefaction on dimensionless temperature profile for no viscous heating case

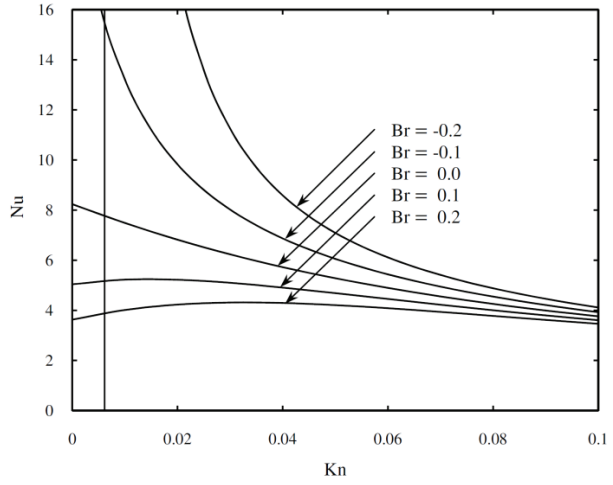

Fig. 5. Nusselt number values versus Knudsen number at different Brinkman numbers

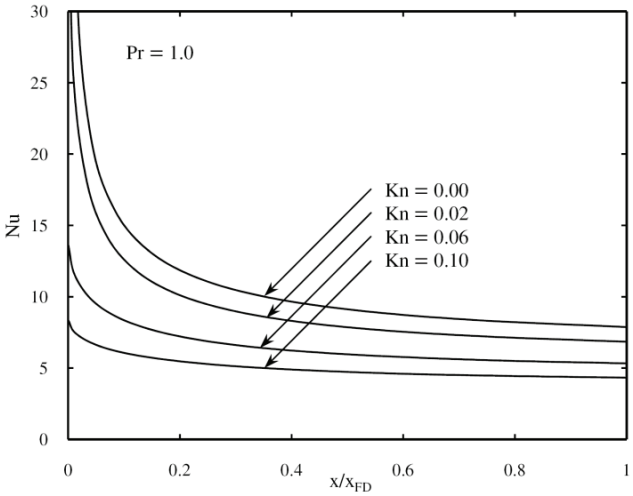

Fig. 6. Nusselt number in the entrance region for different Knudsen numbers (Sadeghi et al., 2009)

Slip flow forced convection in microchannels has widely been investigated in the literature. Aydin and Avci (2006, 2007) analytically studied fully developed laminar slip flow forced convection in a micropipe and microchannel between two parallel plates. The thermally developing cases have been studied by Jeong and Jeong (2006a, 2006b) by taking the effects of viscous dissipation and streamwise conduction into account. Fully developed laminar slip flow forced convection in a rectangular microchannel was studied by Tunc and Bayazitoglu (2002), using integral transform method. The thermally developing case has been studied by Yu and Ameel (2001) by applying a modified generalized integral transform technique to solve the energy equation, assuming hydrodynamically fully developed flow. Sadeghi et al. (2009) have performed a boundary layer analysis for simultaneously developing flow through parallel plate microchannels with constant wall temperatures. The results showed that an increment in Knudsen number leads to a larger amount of hydrodynamic entry length. They proposed the following correlation for Nusselt number in the entrance region

$$Nu = 3\left\{\frac{\delta}{D}+\frac{6\gamma}{1+\gamma}\frac{Kn}{Pr}-\frac{\left(3Kn+\frac{19}{60}\frac{\delta}{D}\right)\left(\frac{\delta}{D}\right)^2}{\left[8Kn\frac{\delta}{D}+\frac{4}{3}\left(\frac{\delta}{D}\right)^2+\left(1-2\frac{\delta}{D}\right)\left(4Kn+\frac{\delta}{D}\right)\right]}\right\}^{-1} \tag{47}$$

where D is the channel width and δ is the boundary layer thickness. Figure 6 depicts the above correlation for different Knudsen numbers at $Pr = 1$. It can be seen that the effects of rarefaction are more significant at the inlet.

2.3 Slip flow free convection

In comparison with forced convection, much less attention has been given to free convection slip flow in the literature. The first work in this field has been done by Chen and Weng

(2005), which analytically studied fully developed natural convection in an open-ended vertical parallel plate microchannel with asymmetric wall temperature distributions. They showed that the Nusselt number based on the channel width is given by

$$Nu = \frac{1 - \frac{T_2 - T_0}{T_1 - T_0}}{1 + 2\frac{2 - F_t}{F_t} Kn} \tag{48}$$

where T_1 and T_2 are the wall temperatures and T_0 is the free stream temperature. Chen and Weng afterwards extended their works by taking the effects of thermal creep (2008a) and variable physical properties (2008b) into account. Natural convection gaseous slip flow in a vertical parallel plate microchannel with isothermal wall conditions was numerically investigated by Biswal et al. (2007), in order to analyze the influence of the entrance region on the overall heat transfer characteristics. Chakraborty et al. (2008) performed a boundary layer integral analysis to investigate the heat transfer characteristics of natural convection gas flow in symmetrically heated vertical parallel plate microchannels. It was revealed that for low Rayleigh numbers, the entrance length is only a small fraction of the total channel extent.

2.4 Thermal creep effects

When the channel walls are subject to constant temperature, the thermal creep effects vanish at the fully developed conditions. However, for a constant heat flux boundary condition, the effects of thermal creep may become predominant for small Eckert numbers.

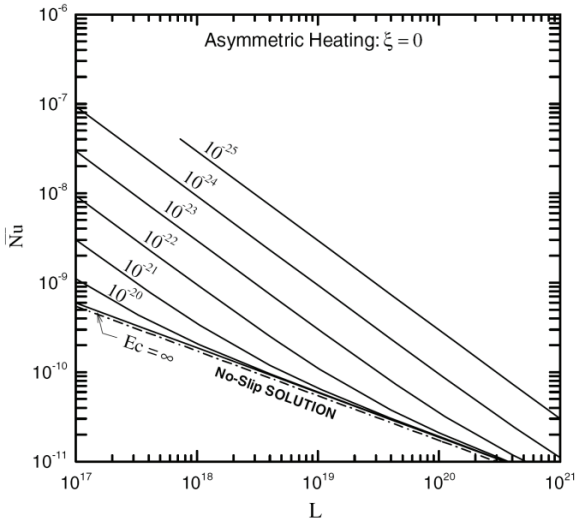

Fig. 7. Variation of average Nusselt number as a function of the channel length, L, for different values of Ec with $Kn = 0.03$ (Chen and Weng, 2008a)

The effects of thermal creep for parallel plate and rectangular microchannels have been investigated by Rij et al. (2007) and Niazmand et al. (2010), respectively. As mentioned before, Chen and Weng (2008a) studied the effects of creep flow in steady natural

convection in an open-ended vertical parallel plate microchannel with asymmetric wall heat fluxes. It was found that the thermal creep has a significant effect which is to unify the velocity and pressure and to elevate the temperature. Moreover, the effect of thermal creep was found to be enhancing the flow rate and heat transfer rate and reducing the maximum gas temperature and flow drag. Figure 7 shows the variation of average Nusselt number as a function of the channel length, L, for different values of Ec with $Kn = 0.03$. Note that ξ is the ratio of the wall heat fluxes. It can be seen that the thermal creep significantly increases the average Nusselt number.

3. Electrokinetics

In this section, we pay attention to electrokinetics. Electrokinetics is a general term associated with the relative motion between two charged phases (Masliyah and Bhattacharjee, 2006). According to Probstein (1994), the electrokinetic phenomena can be divided into the following four categories

- *Electroosmosis* is the motion of ionized liquid relative to the stationary charged surface by an applied electric field.
- *Streaming potential* is the electric field created by the motion of ionized fluid along stationary charged surfaces.
- *Electrophoresis* is the motion of the charged surfaces and macromolecules relative to the stationary liquid by an applied electric field.
- *Sedimentation potential* is the electric field created by the motion of charged particles relative to a stationary liquid.

Due to space limitations, only the first two effects are being considered here. The study of electrokinetics requires a basic knowledge of electrostatics and electric double layer. Therefore, the next section is devoted to these basic concepts.

3.1 Basic concepts

3.1.1 Electrostatics

Consider two stationary point charges of magnitude Q_1 and Q_2 in free space separated by a distance R. According to the Coulomb's law the mutual force between these two charges, $\mathbf{F}_{12}$, is given by

$$\mathbf{F}_{12} = \frac{Q_1 Q_2}{4\pi\varepsilon_0 R^2}\mathbf{r}_{12} \tag{49}$$

in which $\mathbf{r}_{12}$ is a unit vector directed from Q_1 towards Q_2. Here, ε_0 is the permittivity of vacuum which its value is $8.854 \times 10^{-12}\mathrm{CV^{-1}m^{-1}}$ with C (Coulomb) being the SI unit of electric charge. The electric field $\mathbf{E}$ at a point in space due to the point charge Q is defined as the electric force $\mathbf{F}$ acting on a positive test charge Q_t placed at that point divided by the magnitude of the test charge, i.e.,

$$\mathbf{E} = \frac{\mathbf{F}}{Q_t} = \frac{Q}{4\pi\varepsilon_0 R^2}\mathbf{r} \tag{50}$$

where $\mathbf{r}$ is a unit vector directed from Q towards Q_t. One can generalize Eq. (50) by replacing the discrete point charge by a continuous charge distribution. The electric field then becomes

$$\mathbf{E} = \frac{1}{4\pi\varepsilon_0}\int \frac{\mathrm{d}\rho_e}{R^2}\mathbf{r} \tag{51}$$

where the integration is over the entire charge distribution and ρ_e is the electrical charge density which may be per line, surface, or volume.

Let us pay attention to the Gauss's law, a useful tool which relates the electric field strength flux through a closed surface to the enclosed charge. To derive the Gauss's law, we consider a point charge Q located in some arbitrary volume, V, bounded by a surface S as shown in Fig. 8.

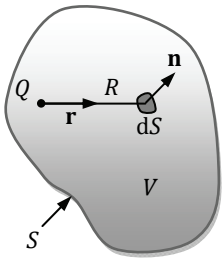

Fig. 8. Point charge Q bounded by a surface S.

The electric field strength at the element of surface dS due to the charge Q is given by

$$\mathbf{E} = \frac{Q}{4\pi\varepsilon_0 R^2}\mathbf{r} \tag{52}$$

where the unit vector $\mathbf{r}$ is directed from the point charge towards the surface element dS. Performing dot product for Eq. (52) using $\mathbf{n}\mathrm{d}S$ with $\mathbf{n}$ being the unit outward normal vector to the bounding surface and integrating over the bounding surface S, we come up with

$$\oint_S (\mathbf{E}\cdot\mathbf{n})\mathrm{d}S = \oint_S \frac{Q}{4\pi\varepsilon_0 R^2}(\mathbf{r}\cdot\mathbf{n})\mathrm{d}S \tag{53}$$

The term $(\mathbf{r}\cdot\mathbf{n})\mathrm{d}S/R^2$ represents the element of solid angle dΩ. Therefore, the above equation becomes

$$\oint_S (\mathbf{E}\cdot\mathbf{n})\mathrm{d}S = \frac{1}{4\pi\varepsilon_0}\int_0^{4\pi} Q\mathrm{d}\Omega \tag{54}$$

Upon integration, Eq. (54) gives

$$\oint_S (\mathbf{E}\cdot\mathbf{n})\mathrm{d}S = \frac{Q}{\varepsilon_0} \tag{55}$$

Equation (55) is the integral form of the Gauss's law or theorem. The differential form of the Gauss's law can be derived quite readily using the divergence theorem, which states that

$$\int_S (\mathbf{E}\cdot\mathbf{n})\mathrm{d}S = \int_V (\nabla\cdot\mathbf{E})\mathrm{d}V \tag{56}$$

and the total charge Q may be written based on the charge density as

$$Q = \int_V \rho_e \mathrm{d}V \tag{57}$$

The following equation is obtained, using Eqs. (55) to (57)

$$\int_V (\nabla \cdot \mathbf{E}) \mathrm{d}V = \frac{1}{\varepsilon_0} \int_V \rho_e \mathrm{d}V \tag{58}$$

Since the volume V is arbitrary, therefore

$$\nabla \cdot \mathbf{E} = \frac{\rho_e}{\varepsilon_0} \tag{59}$$

The above is the differential form of the Gauss's law.
Using Eq. (50), it is rather straightforward to show that

$$\nabla \times \mathbf{E} = 0 \tag{60}$$

From the above property, it may be considered that the electric field is the gradient of some scalar function, ψ, known as electric potential, i.e.,

$$\mathbf{E} = -\nabla \psi \tag{61}$$

By substituting the electric field from Eq. (61) into Eq. (59), we come up with the Poison equation:

$$\nabla^2 \psi = -\frac{\rho_e}{\varepsilon_0} \tag{62}$$

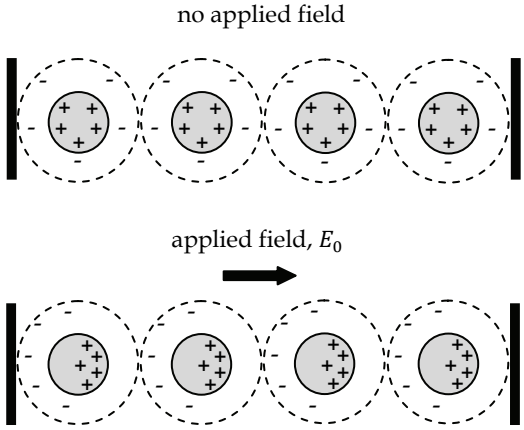

Fig. 9. Polarization of a dielectric material in presence of an electric field

All the previous results are pertinent to the free space and are not useful for practical applications. Therefore, we should modify them by taking into account the materials

electrical properties. It is worth mentioning that from the perspective of classical electrostatics, the materials are broadly categorized into two classes, namely, conductors and dielectrics. Conductors are materials that contain free electric charges. When an electrical potential difference is applied across such conducting materials, the free charges will move to the regions of different potentials depending on the type of charge they carry. On the other hand, dielectric materials do not have free or mobile charges. When a dielectric is placed in an electric field, electric charges do not flow through the material, as in a conductor, but only slightly shift from their average equilibrium positions causing dielectric polarization. Because of dielectric polarization, positive charges are displaced toward the field and negative charges shift in the opposite direction. This creates an internal electric field that partly compensates the external field inside the dielectric. The mechanism of polarization is schematically shown in Fig. 9.

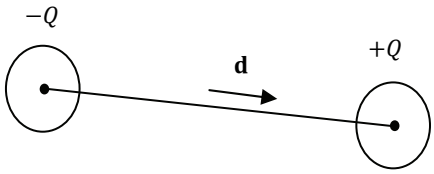

Fig. 10. Schematic of a dipole.

We should now derive the relevant electrostatic equations for a dielectric medium. In the presence of an electric field, the molecules of a dielectric material constitute dipoles. A dipole, which is shown in Fig. 10, comprises two equal and opposite charges, $+Q$ and $-Q$, separated by a distance d. Dipole moment, a vector quantity, is defined as $Q\mathbf{d}$, where $\mathbf{d}$ is the vector orientation between the two charges. The polarization density, $\mathbf{P}$, is defined as the dipole moment per unit volume. It is thus given by

$$\mathbf{P} = NQ\mathbf{d} \tag{63}$$

where N is the number of dipoles per unit volume. For homogeneous, linear, and isotropic dielectric medium, when the electric field is not too strong, the polarization is directly proportional to the applied field, and one can write

$$\mathbf{P} = \chi\varepsilon_0\mathbf{E} \tag{64}$$

Here χ is a dimensionless parameter known as electric susceptibility of the dielectric medium. The following relation exists between the polarization density and the volumetric polarization (or bound) charge density, ρ_p

$$\nabla \cdot \mathbf{P} = -\rho_p \tag{65}$$

Within a dielectric material, the total volumetric charge density is made up of two types of charge densities, a polarization and a free charge density

$$\rho_e = \rho_p + \rho_f \tag{66}$$

One can combine the definition of total charge density provided by Eq. (66) with the Gauss's law, Eq. (59), to get

$$\nabla \cdot \mathbf{E} = \frac{1}{\varepsilon_0}(\rho_p + \rho_f) \tag{67}$$

By substituting the polarization charge, from Eq. (65), the divergence of the electric field becomes

$$\nabla \cdot \mathbf{E} = \frac{1}{\varepsilon_0}(\nabla \cdot \mathbf{P} + \rho_f) \tag{68}$$

which may be rearranged as

$$\nabla \cdot (\varepsilon_0 \mathbf{E} + \mathbf{P}) = \rho_f \tag{69}$$

The polarization may be substituted from Eq. (64) and the outcome is the following

$$\nabla \cdot [\varepsilon_0(1 + \chi)\mathbf{E}] = \rho_f \tag{70}$$

Let

$$\varepsilon = \varepsilon_0(1 + \chi) \tag{71}$$

We will call ε the permittivity of the material. Therefore, Eq. (70) becomes

$$\nabla \cdot (\varepsilon \mathbf{E}) = \rho_f \tag{72}$$

For constant permittivity, Eq. (72) gives

$$\varepsilon \nabla \cdot \mathbf{E} = \rho_f \tag{73}$$

which is Maxwell's equation for a dielectric material. Equation (73) may be written as

$$\varepsilon_0 \varepsilon_r \nabla \cdot \mathbf{E} = \rho_f \tag{74}$$

with $\varepsilon_r = (1 + \chi)$ being the relative permittivity of the dielectric material. The minimum value of ε_r is unity for vacuum. Its value varies from near unity for most gases to about 80 for water. Substituting for the electric field from Eq. (61), Eq. (73) becomes

$$\nabla^2 \psi = -\frac{\rho_f}{\varepsilon} \tag{75}$$

Equation (75) represents the Poisson's equation for the electric potential distribution in a dielectric material.

3.1.2 Electric double layer

Generally, most substances will acquire a surface electric charge when brought into contact with an electrolyte medium. The magnitude and the sign of this charge depend on the physical properties of the surface and solution. The effect of any charged surface in an electrolyte solution will be to influence the distribution of nearby ions in the solution, and the outcome is the formation of an electric double layer (EDL). The electric double layer, which is shown in Fig. 11, is a region close to the charged surface in which there is an excess of counterions over coions to neutralize the surface charge. The EDL consists of an inner layer known as Stern layer and an outer diffuse layer. The plane separating the inner layer and outer diffuse layer is called the Stern plane. The potential at this plane, ψ_S, is close to the

electrokinetic potential or zeta (ζ) potential, which is defined as the potential at the shear surface between the charged surface and the electrolyte solution. Electrophoretic potential measurements give the zeta potential of a surface. Although one at times refers to a "surface potential", strictly speaking, it is the zeta potential that needs to be specified (Masliyah and Bhattacharjee, 2006). The shear surface itself is somewhat arbitrary but characterized as the plane at which the mobile portion of the diffuse layer can slip or flow past the charged surface (Probstein, 1994).

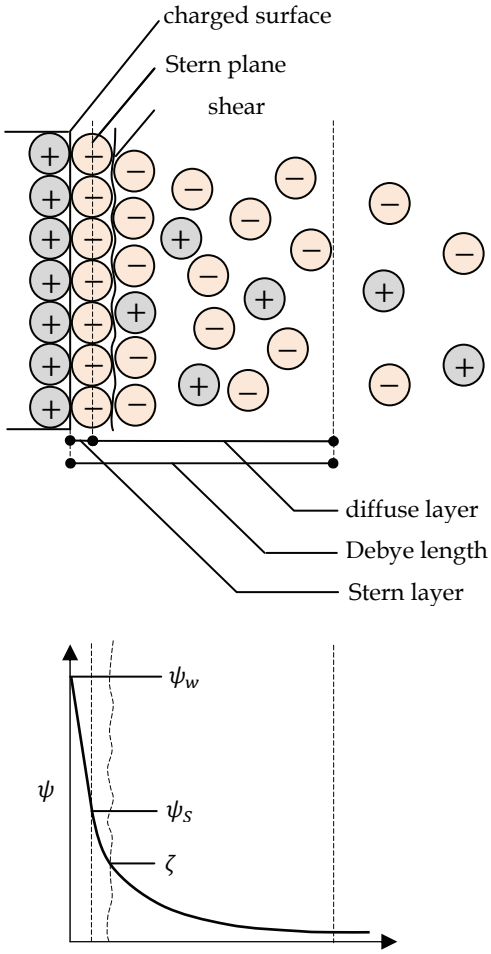

Fig. 11. Structure of electric double layer

The spatial distribution of the ions in the diffuse layer may be related to the electrostatic potential using Boltzmann distribution. It should be pointed out that the Boltzmann distribution assumes the thermodynamic equilibrium, implying that it may be no longer valid in the presence of the fluid flow. However, in most electrokinetic applications, the Peclet number is relatively low, suggesting that using this distribution does not lead to

significant error. At a thermodynamic equilibrium state, the probability that the system energy is confined within the range W and $W + \mathrm{d}W$ is proportional to $\mathrm{d}W$, and can be expressed as $\mathcal{P}(W)\mathrm{d}W$ with $\mathcal{P}(W)$ being the probability density, given by

$$\mathcal{P} \propto e^{\left(-\frac{W}{k_B T}\right)} \tag{76}$$

where T is the absolute temperature and $k_B = 1.38 \times 10^{-23}\,\mathrm{J/K}$ is the Boltzmann constant. Equation (76), initially derived by Boltzmann, follows from statistical considerations.

Here, W corresponds to a particular location of an ion relative to a suitable reference state. An appropriate choice may be the work W required to bring one ion of valence z_i from infinity, at which $\psi = 0$, to a given location r having a potential ψ. This ion, therefore, possess a charge of $z_i e$ with $e = 1.6 \times 10^{-19}\mathrm{C}$ being the proton charge. Consequently, the system energy will be $z_i e\psi$ and, as a result, the probability density of finding an ion at location x will be

$$\mathcal{P} \propto e^{\left(-\frac{z_i e\psi}{k_B T}\right)} \tag{77}$$

Similarly, the probability density of finding the ion at the neutral state at which $\psi = 0$ is

$$\mathcal{P}_0 \propto e^{(0)} \tag{78}$$

The ratio of $\mathcal{P}$ to $\mathcal{P}_0$ is taken as being equal to the ratio of the concentrations of the species i at the respective states. Combining Eqs. (77) and (78) results in

$$n_i = n_{i\infty} e^{\left(-\frac{z_i e\psi}{k_B T}\right)} \tag{79}$$

where $n_{i\infty}$ is the ionic concentration at the neutral state and n_i is the ionic concentration of the i^{th} ionic species at the state where the electric potential is ψ. The valence number z_i can be either positive or negative depending on whether the ion is a cation or an anion, respectively. As an example, for the case of $CaCl_2$ salt, z for the calcium ion is +2 and it is −1 for the chloride ion.

We are now ready to investigate the potential distribution throughout the EDL. The charge density of the free ions, ρ_f, can be written in terms of the ionic concentrations and the corresponding valances as

$$\rho_f = \sum_{i=1}^{N} z_i e n_i = \sum_{i=1}^{N} z_i e n_{i\infty} e^{\left(-\frac{z_i e\psi}{k_B T}\right)} \tag{80}$$

For the sake of simplicity, it is assumed that the liquid contains a single salt dissociating into cationic and anionic species, i.e., $N = 2$. It is also assumed that the salt is symmetric implying that both the cations and anions have the same valences, i.e.,

$$z_+ = -z_- = z \tag{81}$$

The charge density, thus, will be of the following form

$$\rho_f = z_+ e n_+ + z_- e n_- = z e n_\infty e^{\left(-\frac{ze\psi}{k_B T}\right)} - z e n_\infty e^{\left(\frac{ze\psi}{k_B T}\right)} \tag{82}$$

or

$$\rho_f = -2zen_\infty \sinh\left(\frac{ze\psi}{k_B T}\right) \tag{83}$$

in which $n_{+\infty} = n_{-\infty} = n_\infty$. Let us know consider the parallel plate microchannel which was shown in Fig. 2. By introducing Eq. (83) into the Poisson's equation, given by Eq. (75), the following differential equation is obtained for the electrostatic potential

$$\frac{\mathrm{d}^2\psi}{\mathrm{d}y^2} = -\frac{2zen_\infty}{\varepsilon}\sinh\left(\frac{ze\psi}{k_B T}\right) \tag{84}$$

The above nonlinear second order one dimensional equation is known as Poisson-Boltzmann equation. Yang et al. (1998) have shown with extensive numerical simulations that the effect of temperature on the potential distribution is negligible. Therefore, the potential field and the charge density may be calculated on the basis of an average temperature, T_{av}. Using this assumption, Eq. (84) in the dimensionless form becomes

$$\frac{\mathrm{d}^2\psi^*}{\mathrm{d}y^{*2}} = \frac{2n_\infty e^2 z^2}{\varepsilon k_B T_{av}} H^2 \sinh\psi^* \tag{85}$$

where $\psi^* = ez\psi/k_B T_{av}$ and $y^* = y/H$. The quantity $(2n_\infty e^2 z^2/\varepsilon k_B T_{av})^{-1/2}$ is the so-called Debye length, λ_D, which characterizes the EDL thickness. It is noteworthy that the general expression for the Debye length is written as $\left(2e^2\sum_{i=1}^{N} n_{i\infty} z_i^2/\varepsilon k_B T_{av}\right)^{-1/2}$. Defining Debye-Huckel parameter as $\kappa = 1/\lambda_D$, we come up with

$$\frac{\mathrm{d}^2\psi^*}{\mathrm{d}y^{*2}} - \kappa^2 H^2 \sinh\psi^* = 0 \tag{86}$$

If ψ^* is small enough, namely $\psi^* \leq 1$, the term $\sinh\psi^*$ can be approximated by ψ^*. This linearization is known as Debye-Huckel linearization. It is noted that for typical values of $T_{av} = 298\text{K}$ and $z = 1$, this approximation is valid for $\psi \leq 25.7\text{mV}$. Defining dimensionless Debye-Huckel parameter, $K = \kappa H$, and invoking Debye-Huckel linearization, Eq. (86) becomes

$$\frac{\mathrm{d}^2\psi^*}{\mathrm{d}y^{*2}} - K^2\psi^* = 0 \tag{87}$$

The boundary conditions for the above equation are

$$\left(\frac{\mathrm{d}\psi^*}{\mathrm{d}y^*}\right)_{(0)} = 0 \quad , \quad \psi^*{}_{(1)} = \zeta^* \tag{88}$$

in which ζ^* is the dimensionless wall zeta potential, i.e., $\zeta^* = ez\zeta/k_B T_{av}$. Using Eq. (87) and applying boundary conditions (88), the dimensionless potential distribution is obtained as follows

$$\psi^* = \zeta^* \frac{\cosh\,(Ky^*)}{\cosh K} \tag{89}$$

Figure 12 shows the transverse distribution of ψ^* at different values of ζ^*. The simplified cases are those pertinent to the Debye-Huckel linearization and the exact ones are the results of the Numerical solution of Eq. (86). The figure demonstrates that performing the Debye-Huckel linearization does not lead to significant error up to $\zeta^* \cong 2$ which corresponds to the value of about 51.4 mV for the zeta potential at standard conditions. This is due to the fact that for $\zeta^* = 2$, the dimensionless potential is lower than 1 over much of the duct cross section. According to Karniadakis et al. (2005), the zeta potential range for practical applications is $1 - 100$ mV, implying that the Debye-Huckel linearization may successfully be used to more than half of the practical applications range of the zeta potential.

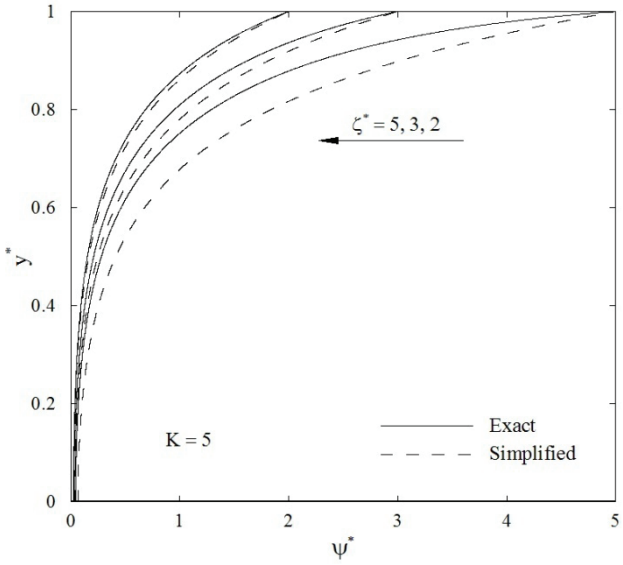

Fig. 12. Transverse distribution of ψ^* at different values of ζ^*

3.2 Electroosmosis

As mentioned previously, there is an excess of counterions over coions throughout the EDL. Suppose that the surface charge is negative, as shown in Fig. 13. If one applies an external electric field, the outcome will be a net migration toward the cathode of ions in the surface liquid layer. Due to viscous drag, the liquid is drawn by the ions and therefore flows through the channel. This is referred to as electroosmosis. Electroosmosis has many applications in sample collection, detection, mixing and separation of various biological and chemical species. Another and probably the most important application of electroosmosis is the fluid delivery in microscale at which the electroosmotic micropump has many advantages over other types of micropumps. Electroosmotic pumps are bi directional, can generate constant and pulse free flows with flow rates well suited to microsystems and can be readily integrated with lab on chip devices. Despite various advantages of the electroosmotic pumping systems, the pertinent Joule heating is an unfavorable phenomenon. Therefore, a pressure driven pumping system is sometimes added to the electroosmotic pumping systems in order to reduce the Joule heating effects, resulting in a combined electroosmotically and pressure driven pumping.

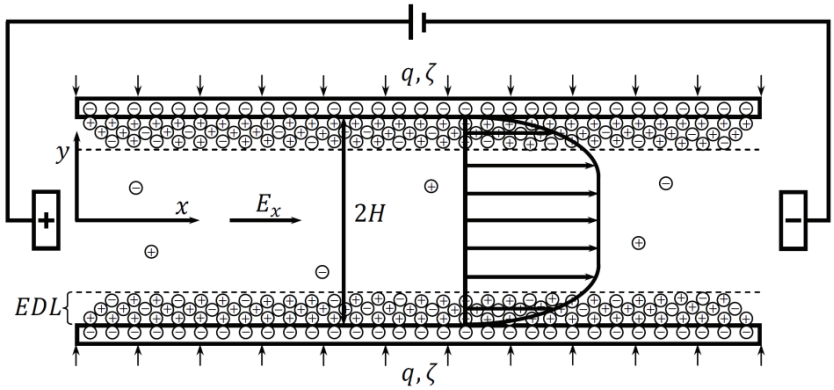

Fig. 13. A parallel plate microchannel with an external electric field

In the presence of external electric field, the poison equation becomes

$$\nabla^2\varphi = -\frac{\rho_f}{\varepsilon} \tag{90}$$

The potential φ is now due to combination of externally imposed field Φ and EDL potential ψ, namely

$$\varphi = \Phi + \psi \tag{91}$$

For a constant voltage gradient in the x direction, Eq. (90) is reduced to Eq. (84), and thus the potential distribution is again given by Eq. (89). The momentum exchange through the flow field is governed by the Cauchy's equation given as

$$\rho\frac{D\mathbf{u}}{Dt} = -\nabla p + \nabla\cdot\boldsymbol{\tau} + \mathbf{F} \tag{92}$$

in which p represents the pressure, $\mathbf{u}$ and $\mathbf{F}$ are the velocity and body force vectors, respectively, and $\boldsymbol{\tau}$ is the stress tensor. The body force is given by (Masliyah and Bhattacharjee, 2006)

$$\mathbf{F} = \rho_f\mathbf{E} - \frac{1}{2}\mathbf{E}\cdot\mathbf{E}\nabla\varepsilon + \frac{1}{2}\nabla\left[\left(\rho\frac{\partial\varepsilon}{\partial\rho}\right)_T\mathbf{E}\cdot\mathbf{E}\right] \tag{93}$$

Therefore, for the present case, the body force is reduced to $\rho_f E_x$, assuming a medium with constant permittivity. Regarding that $\mathrm{D}\mathbf{u}/\mathrm{D}t = 0$ at fully developed conditions, we come up with the following expression for the momentum equation in the x direction

$$\mu\frac{\mathrm{d}^2u}{\mathrm{d}y^2} = \frac{\mathrm{d}p}{\mathrm{d}x} + 2E_x n_0 ez\sinh\left(\frac{ez\psi}{k_B T_{av}}\right) \tag{94}$$

Invoking the Debye-Huckel linearization, the dimensionless form of the momentum equation becomes

$$\frac{\mathrm{d}^2u^*}{\mathrm{d}y^{*2}} = -2\Gamma - \frac{K^2}{\zeta^*}\psi^* = -2\Gamma - K^2\frac{\cosh(Ky^*)}{\cosh K} \tag{95}$$

in which $u^* = u/u_{HS}$ with $u_{HS} = -\varepsilon\zeta E_x/\mu$ being the maximum possible electroosmotic velocity for a given applied potential field, known as the Helmholtz-Smoluchowski

electroosmotic velocity. It is noteworthy that $\varepsilon\zeta/\mu$ is often termed the electroosmotic mobility of the liquid. Also Γ is the ratio of the pressure driven velocity scale to u_{HS}, namely $\Gamma = u_{PD}/u_{HS}$ where $u_{PD} = -H^2(\mathrm{d}p/\mathrm{d}x)/2\mu$. The boundary conditions for the momentum equation are the symmetry condition at centerline and no slip condition at the wall. The dimensionless velocity profile then is readily obtained as

$$u^* = \Gamma\left(1 - y^{*2}\right) + 1 - \frac{\cosh\left(Ky^*\right)}{\cosh K} \tag{96}$$

Dimensionless velocity profile for purely electroosmotic flow is depicted in Fig. 14. For a sufficiently small value of K such as $K = 1$, since EDL potential distribution over the duct cross section is nearly uniform which is the source term in momentum equation (94), so the velocity distribution is similar to Poiseuille flow. As dimensionless Debye-Huckel parameter increases the dimensionless velocity distribution shows a behavior which is different from Poiseuille flow limiting to a slug flow profile at sufficiently great values of K. This is due to the fact that at higher values of K, the body force is concentrated in the region near the wall.

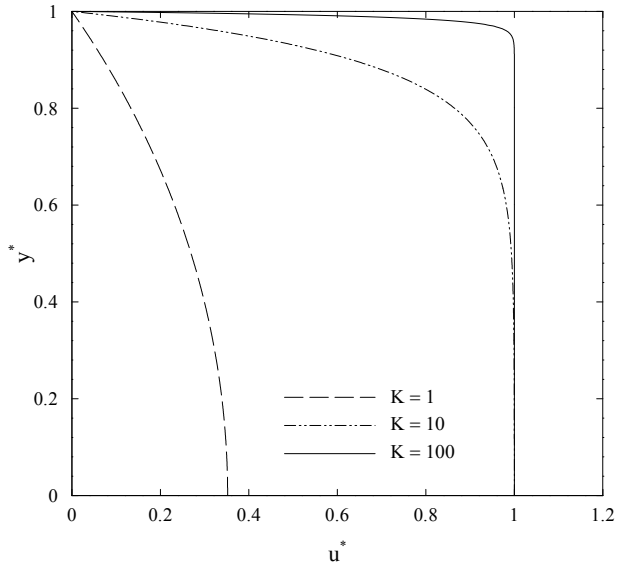

Fig. 14. Dimensionless velocity profile for purely electroosmotic flow

Dimensionless velocity profile at different values of Γ at $K = 100$ is illustrated in Fig. 15. As observed, the velocity profile for non zero values of Γ is the superposition of both purely electroosmotic and Poiseuille flows. Note that for sufficiently large amounts of the opposed pressure, reverse flow may occur at centerline.

Electrokinetic flow in ultrafine capillary slits was firstly analyzed by Burgreen and Nakache (1964). Rice and Whitehead (1965) investigated fully developed electroosmotic flow in a narrow cylindrical capillary for low zeta potentials, using the Debye-Huckel linearization. Levine et al. (1975) extended the Rice and Whitehead's work to high zeta potentials by means of an approximation method. More recently, an analytical solution for electroosmotic flow in a cylindrical capillary was derived by Kang et al. (2002a) by solving the complete

Poisson-Boltzmann equation for arbitrary zeta potentials. They (2002b) also analytically analyzed electroosmotic flow through an annulus under the situation when the two cylindrical walls carry high zeta potentials. Hydrodynamic characteristics of the fully developed electroosmotic flow in a rectangular microchannel were reported in a numerical study by Arulanandam and Li (2000).

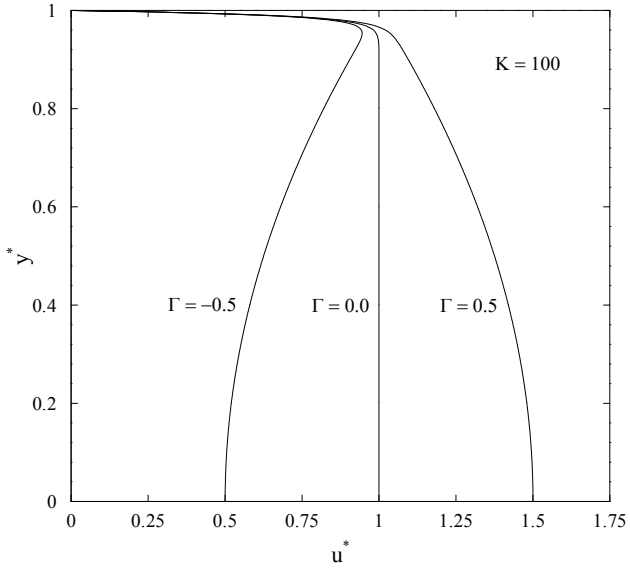

Fig. 15. Dimensionless velocity profile at different values of Γ

Let us now pay attention to the thermal features. Note that the passage of electrical current through the liquid generates a volumetric energy generation known as Joule heating. The conservation of energy including the effect of Joule heating requires

$$\rho c_p \frac{DT}{Dt} = \nabla \cdot (k \nabla T) + s \tag{97}$$

In the above equation, s denotes the rate of volumetric heat generation due to Joule heating and equals $s = E_x^2/\sigma$ with σ being the liquid electrical resistivity given by (Levine et al., 1975)

$$\sigma = \frac{\sigma_0}{\cosh\left(\frac{ez\psi}{k_B T_{av}}\right)} \tag{98}$$

in which σ_0 is the electrical resistivity of the neutral liquid. The hyperbolic term in the above equation accounts for the fact that the resistivity within the EDL is lower than that of the neutral liquid, due to an excess of ions close to the surface. For low zeta potentials, which is assumed here, $\cosh(ez\psi/k_B T_{av}) \to 1$ and, as a result, the Joule heating term may be considered as the constant value of $s = E_x^2/\sigma_0$. For steady fully developed flow $\mathrm{D}T/\mathrm{D}t = u(\partial T/\partial x)$, so energy equation (97) becomes

$$\rho c_p u \frac{\partial T}{\partial x} = k\left(\frac{\partial^2 T}{\partial x^2} + \frac{\partial^2 T}{\partial y^2}\right) + \frac{E_x^2}{\sigma_0} \tag{99}$$

and in dimensionless form

$$\frac{\mathrm{d}^2\theta}{\mathrm{d}y^{*2}} = (1+S)\frac{u^*}{u_m^*} - S \tag{100}$$

with the following dimensionless variables for a constant wall heat flux of q

$$\theta(y) = \frac{T - T_w}{\frac{qH}{k}} \quad , \quad S = \frac{E_x^2 H}{q\sigma_0} \quad , \quad u_m^* = \int_0^1 u^* \mathrm{d}y^* = 1 + \frac{2}{3}\Gamma - \frac{\tanh K}{K} \tag{101}$$

The corresponding non-dimensional boundary conditions for the energy equation are

$$\left(\frac{\mathrm{d}\theta}{\mathrm{d}y^*}\right)_{(0)} = 0 \quad , \quad \theta_{(1)} = 0 \tag{102}$$

The solution of Eq. (100) subject to boundary conditions (102) may be written as

$$\theta = \left[(1+\Gamma)\frac{1+S}{u_m^*} - S\right]\frac{y^{*2}}{2} - \frac{\Gamma(1+S)}{12u_m^*}y^{*4} - \frac{(1+S)}{u_m^*}\frac{\cosh(Ky^*)}{K^2\cosh K} + a \tag{103}$$

in which

$$a = \left(\frac{1}{K^2} - \frac{1}{2} - \frac{5}{12}\Gamma\right)\frac{1+S}{u_m^*} + \frac{S}{2} \tag{104}$$

The dimensionless mean temperature is given by

$$\theta_b = \frac{\int_0^1 u^*\theta \mathrm{d}y^*}{\int_0^1 u^* \mathrm{d}y^*} = \frac{\int_0^1 u^*\theta \mathrm{d}y^*}{u_m^*} \tag{105}$$

and the Nusselt number will be

$$Nu = \frac{hD_h}{k} = \frac{qD_h}{k(T_w - T_b)} = -\frac{4}{\theta_b} \tag{106}$$

The complete expression for the Nusselt number is given by Chen (2009) and it is

$$Nu = c_4 u_m^* \tag{107}$$

where

$$\begin{aligned} c_4^{-1} = \frac{1}{210}\Bigg\{ & 14\left[10c_1 + 12c_2 + 15c_3 - \frac{30}{K^2}(c_1 + 2c_2) - \frac{360}{K^4}c_2\right] \\ & + 4\left[28c_1 + 32c_2 + 35c_3\left(1 - \frac{3}{K^2}\right)\right]\Gamma\Bigg\} \\ & + \frac{1}{2}\Bigg\{c_3 \operatorname{sech}^2 K + \frac{\tanh K}{K}\left[\frac{4}{K^2}\left(c_1 + 6c_2 + 12\frac{c_2}{K^2}\right) - c_3\left(3 - 4\frac{\Gamma}{K^2}\right)\right]\Bigg\} \end{aligned} \tag{108}$$

with the following coefficients

$$c_1 = \frac{1}{8}\left[(1+\Gamma)\frac{1+S}{u_m^*} - S\right] \quad , \quad c_2 = -\Gamma\frac{1+S}{48u_m^*} \quad , \quad c_3 = -\frac{1+S}{4u_m^* K^2} \tag{109}$$

Figure 16 depicts the Nusselt number values versus $1/K$ for purely electroosmotic flow. It can be seen that to increase S is to decrease Nusselt number. Increasing the Joule heating effects results in more accumulation of energy near the wall and, consequently, higher wall temperatures. The ultimate outcome thus will be smaller values of Nusselt number, according to Eq. (106). As K goes to infinity, for all values of S, the Nusselt number approaches 12 which is the classical solution for slug flow (Burmeister, 1993).

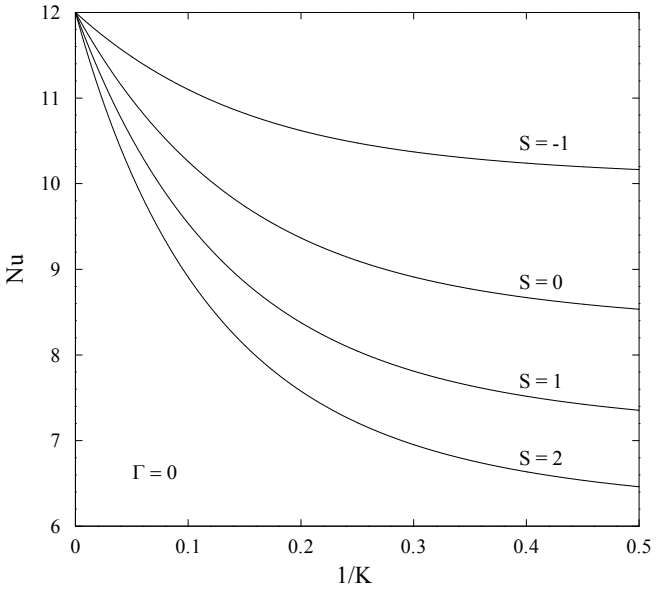

Fig. 16. Nusselt number versus $1/K$ for purely electroosmotic flow

Unlike hydrodynamic features, the study of thermal features of electroosmosis is recent. Maynes and Webb (2003) were the first who considered the thermal aspects of the electroosmotic flow due to an external electric field. They analytically studied fully developed electroosmotically generated convective transport for a parallel plate microchannel and circular microtube under imposed constant wall heat flux and constant wall temperature boundary conditions. Liechty et al. (2005) extended the above work to the high zeta potentials. It was determined that elevated values of wall zeta potential produce significant changes in the charge potential, electroosmotic flow field, temperature profile, and Nusselt number relative to previous results invoking the Debye-Huckel linearization. Also thermally developing electroosmotically generated flow in circular and rectangular microchannels have been considered by Broderick et al. (2005) and Iverson et al. (2004), respectively. The effect of viscous dissipation in fully developed electroosmotic heat transfer for a parallel plate microchannel and circular microtube under imposed constant wall heat flux and constant wall temperature boundary conditions was analyzed by Maynes and Webb (2004). In a recent study, Sadeghi and Saidi (2010) derived analytical solutions for thermal features of combined electroosmotically and pressure driven flow in a slit microchannel, by taking into account the effects of viscous heating.

3.3 Streaming potential

The EDL effects may be present even in the absence of an externally applied electric field. Consider the pressure driven flow of an ionized liquid in a channel with negatively charged surface. According to the Boltzmann distribution, there will be an excess of positive ions over negative ions in liquid. The ultimate effect thus will be an electrical current due to the liquid flow, called the streaming current, I_s. According to the definition of electrical current, the streaming current is of the form

$$I_s = \int u\rho_f \mathrm{d}A \tag{110}$$

where A is the channel cross sectional are and u is the streamwise velocity. The streaming current accumulates positive ions at the end of the channel. Consequently, a potential difference, called the streaming potential, Φ_s, is created between the two ends of the channel. The streaming potential generates the so-called conduction current, I_c, which carries charges and molecules in the opposite direction of the flow, creating extra impedance to the flow motion. The net electrical current, I, is the sum of the streaming current and the conduction current and in steady state should be zero

$$I = I_s + I_c = 0 \tag{111}$$

In order to study the effects of the EDL on a pressure driven flow, first the conduction current should be evaluated from Eqs. (110) and (111). Afterwards, the value of I_c is used to find out the electric field associated with the flow induced potential, E_s, using the following relationship

$$E_s = \frac{I_c \sigma}{A} \tag{112}$$

The flow induced electric field then is used to evaluate the body force in the momentum equation. It should be pointed out that since there is not any electrical current due to an external electric field, therefore, the Joule heating term does not appear in the energy equation.

4. References

Arulanandam, S. & Li, D. (2000). Liquid transport in rectangular microchannels by electroosmotic pumping. *Colloids and Surfaces A: Physicochemical and Engineering Aspects*, Vol. 161, pp. 89–102, 0927-7757

Aydin, O. & Avci, M. (2006). Heat and flow characteristics of gases in micropipes, *Int. J. Heat Mass Transfer,* Vol. 49, pp. 1723–1730, 0017-9310

Aydin, O. & Avci, M. (2007). Analysis of laminar heat transfer in micro-Poiseuille flow, *Int. J. Thermal Sciences,* Vol.46, pp. 30–37, 1290-0729

Beskok, A. & Karniadakis, G.E. (1994). Simulation of heat and momentum transfer in complex micro-geometries. *J. Thermophysics Heat Transfer*, Vol. 8, pp. 647–655, 0887-8722

Biswal, L.; Som, S.K. & Chakraborty, S. (2007). Effects of entrance region transport processes on free convection slip flow in vertical microchannels with isothermally heated walls. *Int. J. Heat Mass Transfer*, Vol. 50, pp. 1248–1254, 0017-9310

Broderick, S.L.; Webb, B.W. & Maynes, D. (2005). Thermally developing electro-osmotic convection in microchannels with finite Debye-layer thickness. *Numerical Heat Transfer, Part A*, Vol. 48, pp. 941–964, 1040-7782

Burgreen, D. & Nakache, F.R. (1964). Electrokinetic flow in ultrafine capillary slits. *J. Physical Chemistry*, Vol. 68, pp. 1084–1091, 1089-5639

Burmeister, L.C. (1993). *Convective heat transfer*, Wiley, 0471310204, New York

Chakraborty, S.; Som, S.K. & Rahul (2008). A boundary layer analysis for entrance region heat transfer in vertical microchannels within the slip flow regime. *Int. J. Heat Mass Transfer*, Vol. 51, pp. 3245–3250, 0017-9310

Chen, C.K. & Weng, H.C. (2005). Natural convection in a vertical microchannel. *J. Heat Transfer*, Vol. 127, pp. 1053–1056, 0022-1481

Chen, C.H. (2009). Thermal transport characteristics of mixed pressure and electroosmotically driven flow in micro- and nanochannels with Joule heating. *J. Heat Transfer*, Vol. 131, 022401, 0022-1481

Hadjiconstantinou, N.G. (2003). Dissipation in small scale gaseous flows. *J. Heat Transfer,* Vol. 125, pp. 944-947, 0022-1481

Hadjiconstantinou, N.G. (2006). The limits of Navier Stokes theory and kinetic extensions for describing small scale gaseous hydrodynamics. *Phys. Fluids*, Vol. 18, 111301, 1070-6631

Iverson, B.D.; Maynes, D. & Webb, B.W. (2004). Thermally developing electroosmotic convection in rectangular microchannels with vanishing Debye-layer thickness. *J. Thermophysics Heat Transfer*, Vol. 18, pp. 486–493, 0887-8722

Jeong, H.E. & Jeong, J.T. (2006a). Extended Graetz problem including axial conduction and viscous dissipation in microtube, *J. Mechanical Science Technology,* Vol. 20, pp. 158–166, 1976-3824

Jeong, H.E. & Jeong, J.T. (2006b). Extended Graetz problem including streamwise conduction and viscous dissipation in microchannel, *Int. J. Heat Mass Transfer,* Vol. 49, pp. 2151–2157, 0017-9310

Kandlikar, S.G.; Garimella, S.; Li, D.; Colin, S. & King, M.R. (2006). *Heat Transfer and Fluid Flow in Minichannels and Microchannels*, Elsevier, 0-0804-4527-6, Oxford

Kang, Y.; Yang, C. & Huang, X. (2002a). Dynamic aspects of electroosmotic flow in a cylindrical microcapillary. *Int. J. Engineering Science*, Vol. 40, pp. 2203–2221, 0020-7225

Kang, Y.; Yang, C. & Huang, X. (2002b). Electroosmotic flow in a capillary annulus with high zeta potentials. *J. Colloid Interface Science*, Vol. 253, pp. 285–294, 0021-9797

Karniadakis, G.; Beskok, A. & Aluru, N. (2005). *Microflows and Nanoflows, Fundamentals and Simulation*, Springer, 0-387-90819-6, New York

Kennard, E.H. (1938). *Kinetic Theory of Gases*, McGraw–Hill, New York

Koo, J. & Kleinstreuer, C. (2003). Liquid flow in microchannels: experimental observations and computational analyses of microfluidics effects. *J. Micromechanics and Microengineering,* Vol. 13, pp. 568–579, 1361-6439

Koo, J. & Kleinstreuer, C. (2004). Viscous dissipation effects in microtubes and microchannels, *Int. J. Heat Mass Transfer,* Vol. 47, pp. 3159–3169, 0017-9310

Levine, S.; Marriott, J.R.; Neale, G. & Epstein, N. (1975). Theory of electrokinetic flow in fine cylindrical capillaries at high zeta-potentials. *J. Colloid Interface Science*, Vol. 52, 136–149, 0021-9797

Liechty, B.C.; Webb, B.W. & Maynes, R.D. (2005). Convective heat transfer characteristics of electro-osmotically generated flow in microtubes at high wall potential. *Int. J. Heat Mass Transfer*, Vol. 48, pp. 2360–2371, 0017-9310

Masliyah J.H. & Bhattacharjee, S. (2006). *Electrokinetic and Colloid Transport Phenomena*, First ed., John Wiley, 0-471-78882-1, New Jersey.

Maxwell, J.C. (1879). On stresses in rarefied gases arising from inequalities of temperature, *Philos. Trans. Royal Soc.*, Vol. 170, pp. 231-256

Maynes, D. & Webb, B.W. (2003). Fully developed electroosmotic heat transfer in microchannels. *Int. J. Heat Mass Transfer*, Vol. 46, pp. 1359–1369, 0017-9310

Maynes, D. & Webb, B.W. (2004). The effect of viscous dissipation in thermally fully developed electroosmotic heat transfer in microchannels. *Int. J. Heat Mass Transfer*, Vol. 47, pp. 987–999, 0017-9310

Niazmand, H.; Jaghargh, A.A. & Renksizbulut, M. (2010). Slip-flow and heat transfer in isoflux rectangular microchannels with thermal creep effects. *J. Applied Fluid Mechanics*, Vol. 3, pp. 33-41, 1735-3645

Ou, J.W. & Cheng, K.C. (1973). Effects of flow work and viscous dissipation on Graetz problem for gas flows in parallel-plate channels, *Heat Mass Transfer*, Vol. 6, pp. 191–198, 0947-7411

Probstein, R.F. (1994). *Physicochemical Hydrodynamics*, 2nd ed. Wiley, 0471010111, New York

Rice, C.L. & Whitehead, R. (1965). Electrokinetic flow in a narrow cylindrical capillary. *J. Physical Chemistry*, Vol. 69, pp. 4017–4024, 1089-5639

Rij, J.V.; Harman, T. & Ameel, T. (2007). The effect of creep flow on two-dimensional isoflux microchannels. *Int. J. Thermal Sciences*, Vol. 46, pp. 1095–1103, 1290-0729

Rij, J.V.; Ameel, T. & Harman, T. (2009). The effect of viscous dissipation and rarefaction on rectangular microchannel convective heat transfer. *Int. J. Thermal Sciences,* Vol. 48, pp. 271–281, 1290-0729

Sadeghi, A.; Asgarshamsi, A. & Saidi M.H. (2009). Analysis of laminar flow in the entrance region of parallel plate microchannels for slip flow, *Proceedings of the Seventh International ASME Conference on Nanochannels, Microchannels and Minichannels, ICNMM2009,* S.G. Kandlikar (Ed.), Pohang, South Korea

Sadeghi, A. & Saidi, M.H. (2010). Viscous dissipation and rarefaction effects on laminar forced convection in microchannels. *J. Heat Transfer,* Vol. 132, 072401, 0022-1481

Sadeghi, A. & Saidi, M.H. (2010). Viscous dissipation effects on thermal transport characteristics of combined pressure and electroosmotically driven flow in microchannels. *Int. J. Heat Mass Transfer*, Vol. 53, pp. 3782–3791, 0017-9310

Taheri, P.; Torrilhon, M. & Struchtrup, H. (2009). Couette and Poiseuille microflows: analytical solutions for regularized 13-moment equations. *Phys. Fluids*, Vol. 21, 017102, 1070-6631

Tunc, G.& Bayazitoglu, Y. (2002). Heat transfer in rectangular microchannels. *Int. J. Heat Mass Transfer*, Vol. 45, pp. 765–773, 0017-9310

Weng, H.C. & Chen, C.K. (2008a). On the importance of thermal creep in natural convective gas microflow with wall heat fluxes. *J. Phys. D*, Vol. 41, 115501, 0022-3727

Weng, H.C. & Chen, C.K. (2008b). Variable physical properties in natural convective gas microflow. *J. Heat Transfer*, Vol. 130, 082401, 0022-1481

Yang, C.; Li, D. & Masliyah, J.H. (1998). Modeling forced liquid convection in rectangular microchannels with electrokinetic effects. *Int. J. Heat Mass Transfer*, Vol. 41, pp. 4229–4249, 0017-9310

Yu, S. & Ameel, T.A. (2001). Slip flow heat transfer in rectangular microchannels. *Int. J. Heat Mass Transfer*, Vol. 44, pp. 4225–4234, 0017-9310

Part 4

Energy Transfer and Solid Materials

21

Thermal Characterization of Solid Structures during Forced Convection Heating

Balázs Illés and Gábor Harsányi
Department of Electronics Technology,
Budapest University of Technology and Economic
Hungary

1. Introduction

By now the forced convection heating became an important part of our every day life. The success could be thanked to the well controllability, the fast response and the efficient heat transfer of this heating technology. We can meet a lot of different types of forced convection heating methods and equipments in the industry (such as convection soldering oven, convection thermal annealing, paint drying, etc.) and also in our household (such as air conditioning systems, convection fryers, hair dryers, etc.).
In every cases the aim of the mentioned applications are to heat or cool some kind of solid materials and structures. If we would like to examine this heating or cooling process with modeling and simulation, first we need to know the physical parameters of the forced convection heating such as the velocity, the pressure and the density space of the flow, together with the temperature distribution and the heat transfer coefficients on the different points of the heated structure. Therefore in this chapter, first we present the mathematical and physical basics of the fluid flow and the convection heating which are needed to the modeling and simulation. We show some models of gas flows trough typical examples in aspect of the heat transfer. We discuss the theory of free-streams, the vertical – radial transformation of gas flows and the radial gas flow layer formation on a plate. The models illustrate how we can study the velocity, pressure and density space in a fluid flow and we also point how these parameters effect on the heat transfer coefficient.
After it new types of measuring instrumentations and methods are presented to characterize the temperature distribution in a fluid flow. Calculation methods are also discussed which can determine the heat transfer coefficients according to the dynamic change of the temperature distribution. The ability of the measurements and calculations will be illustrated with two examples. In the first case we determine the heat transfer coefficient distribution under free gas streams. The change of the heat transfer coefficient is examined when the heated surface shoves out the gas stream. In the second case we study the direction characteristics of the heat transfer coefficient in the case of radial flow layers on a plate in function of the height above the plate. It is also studied how the blocking elements towards the flow direction affects on the formation of the radial flow layer.
In the last part of our chapter we present how the measured and calculated heat transfer coefficients can be applied during the thermal characterization of solid structures. The mathematical and physical description of a 3D thermal model is discussed. The model based

on the thermal (central) node theory and the calculations based on the Finite Difference Method (FDM). We present a new cell partition method, the Adaptive Interpolation and Decimation (AID) which can increase the resolution and the accuracy of the model in the investigated areas without increasing the model complexity. With the collective application of the thermal cell method, the FDM calculations and the AID cell partition, the model description is general and the calculation time of the thermal model is very short compared with the similar Finite Element Method (FEM) models.

2. Basics of convection heating and fluid flow

The phrase of "Convection" means the movement of molecules within fluids (i.e. liquids, gases and rheids). Convection is one of the major modes of heat transfer and mass transfer. Convective heat and mass transfer take place through both diffusion – the random Brownian motion of individual particles in the fluid – and by advection, in which matter or heat is transported by the larger-scale motion of currents in the fluid. In the context of heat and mass transfer, the term "convection" is used to refer to the sum of advective and diffusive transfer (Incropera & De Witt, 1990). There are two major types of heat convection:

1. Heat is carried passively by a fluid motion which would occur anyway without the heating process. This heat transfer process is often termed **forced convection** or occasionally heat advection.
2. Heat itself causes the fluid motion (via expansion and buoyancy force), while at the same time also causing heat to be transported by this bulk motion of the fluid. This process is called **natural convection**, or free convection.

Both forced and natural types of heat convection may occur together (in that case being termed mixed convection). Convective heat transfer can be contrasted with conductive heat transfer, which is the transfer of energy by vibrations at a molecular level through a solid or fluid, and radiative heat transfer, the transfer of energy through electromagnetic waves.

2.1 The convection heating

Convection heating is usually defined as a heat transfer process between a solid structure and a fluid (in the following we will use this type of interpretation). The performance of the convection heating mainly depends on the heat transfer coefficient and can be characterized by the convection heat flow rate from the heater fluid to the heated solid material (Newton's law) (Castell et al., 2008; Gao et al., 2003):

$$\frac{dQ_c}{dt} = F_c = h \cdot A \cdot (T_h(t) - T_t(t)) \qquad [\mathrm{w}] \tag{1}$$

where A is the heated area [m^2], $T_h(t)$ is the temperature of the fluid [K], $T_t(t)$ is the temperature of the solid material [K] and h is the heat transfer coefficient [W/m^{2}K] on the A area.

The heat transfer coefficient can be defined as some kind of "concentrated parameter" which is characterised by the density and the velocity filed of the fluid used for heating, the angle of incidence between the solid structure and the fluid, and finally the roughness of the heated surface (Kays et al., 2004). The value of the heat transfer coefficient can vary between wide ranges but it is typically between 5 and 500 [W/mK] in the case of gases. In a lot of application the material of the fluid and the roughness of the heated surface can be consider

to be constant. Therefore mainly the gas flow parameters (density and velocity) influence the heat transfer coefficient which can be characterized by the mass flow rate q_m (Tamás, 2004):

$$q_m = \int_A \rho \cdot v \cdot dA \qquad [\mathrm{kg/s}] \tag{2}$$

where ρ is the density of the fluid [kg/m³], v is the velocity of the fluid [m/s] and A is the are whereon q_m is defined.

As you can see in Eq. (1) the calculation of the convection heat transfer is very simple if we know the exact value of the heat transfer coefficient. The problem is that in most of the cases this value is not known. Although we know the influence parameters (velocity, density, etc.) on the heat transfer coefficient but the strength of dependence from the different parameters changes in every cases. There are not existed explicit formulas to determine the heat transfer coefficient only in some special cases.

Inoue (Inoue & Koyanagawa, 2005) has approximated the h parameter of the heater gas streams from the nozzle-matrix blower system with the followings:

$$h = \frac{\lambda}{d} \frac{\sqrt{(\pi/4)(D/l)^2}\left(1 - 2.2\sqrt{(\pi/4)(D/l)^2}\right)}{1 + 0.2(H/D - 6)\sqrt{(\pi/4)(D/l)^2}} \mathrm{Re}^{\frac{2}{3}} \mathrm{Pr}^{0.42} \left[1 + \left(\frac{H/d}{0.6/\sqrt{(\pi/4)(D/l)^2}}\right)^6\right]^{-0.05} \tag{3}$$

where λ is thermal conductivity of the gas [W/m.K], d is the diameter of the nozzles, H is the distance between nozzles and the target [m], r is the distance between the nozzles in the matrix [m], Re is the Reynolds number and Pr is the Prandtl number. The Eq. (3) shown above, has been derived from systematic series of experiments. But unfortunately this method only gives an average value of h and can not deal with the changes of the blower system (contamination, aging, etc.). In addition in many cases it is difficult to determine the exact value of some parameters e.g. the velocity and density of the gas which are needed for Re and Pr numbers.

The same problem occurs in case of other approximations e.g. Dittus–Boelter, Croft–Tebby, Soyars, etc. (a survey of these methods can be seen in (Guptaa et al, 2009)). The simplest way to approximate h is carried out with the linear combination of the velocity and some constants (Blocken et al., 2009), but it gives useful results only in case of big dimensions (e.g. buildings). Other methods calculate h from the mass flow (Bilen et al., 2009; Yin & Zhang, 2008; Dalkilic et al., 2009), but in this case determining the mass flow is also as difficult as determining the velocity.

Therefore in most of the cases the easiest way to determine the heat transfer coefficient is the measuring (see details in Section 4), however it is also important that we can study the effect of the environmental circumstances on the h parameter with gas flow models (see details in Section 3).

2.2. Basics of fluid dynamics

The main issue of this topic is the forced convection when the heat is transported by forced movement of a fluid. Therefore the fluid dynamics are important tools during the study of various forced convection heating methods. During the description of fluid movements, Newton 2nd axiom can be applied, which creates relation between the acting forces on the

fluid particles and the change of the momentum of the fluid particles. Take an elementary fluid particle which moves in the flowing space (Fig. 1.a).

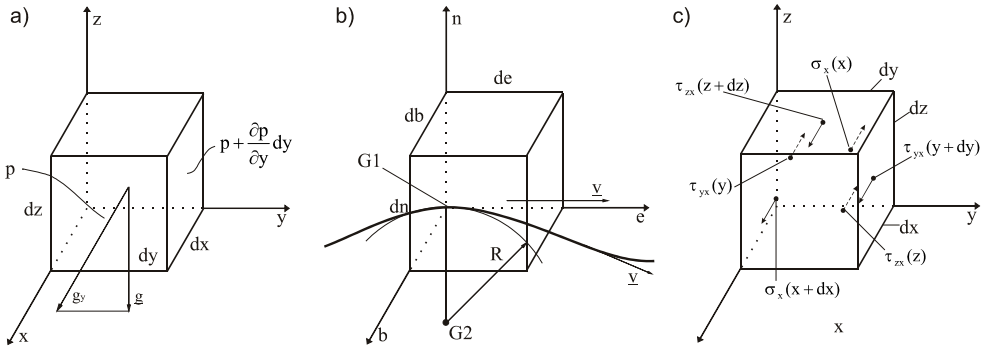

Fig. 1. a) Elementary fluid particle in the flowing phase; b) elementary fluid particle in the flowing phase (natural coordinate system); c) acting stresses towards the *x* direction.

The acting forces are originated from two different sources:

- forces acting on the mass of the fluid particles (e.g. gravity force),
- forces acting on the surface of the fluid particles (e.g. pressure force).

According to these the most common momentum equation – when the friction is neglected and the flow is stationer – is the Euler equation (Tamás, 2004):

$$v\frac{dv}{dr} = g - \frac{1}{\rho} gradp \tag{4}$$

where v is the velocity of the fluid [m/s], t is the time [s], g is the gravity force, ρ is the density [kg/m^3] and p is the pressure. Another important form of this equation – which is often used in the case of the vertical–radial transformation of fluid flows (see in Section 3.) – is defined in natural coordinate system (Fig. 1.b). The natural coordinate system is fixed to the streamline. The connection point is G1. The tangential (e) and the normal (n) coordinate axis are in one plan with the velocity vector (v). In the ambiance of G1 the streamline can be supplemented by an arc which has R radius and G2 center. In this natural coordinate system the Euler equation (vector form) is the following (Tamás, 2004):

$$v\frac{\partial v}{\partial e} = g_e - \frac{1}{\rho}\frac{\partial p}{\partial e} \text{ and } -\frac{v^2}{R} = g_n - \frac{1}{\rho}\frac{\partial p}{\partial n} \text{ and } 0 = g_b - \frac{1}{\rho}\frac{\partial p}{\partial b} \tag{5}$$

In the previous equations we have neglected the effect of friction. However in a lot of convection heating examples this is a non-accurate approach. In the area where the moving fluid touches a solid material the effect of friction can be considerable both form the point of the flowing and the heating. The effect of friction can be determined as some kind of force acting on the surfaces of the moving fluid particle such as the pressure. In Fig. 1.c the stresses acting towards the x direction is presented.

The sheer stresses (τ) [Pa] and the tensile stresses (σ) [Pa] usually changes in space and this changes cause the accelerating force on the fluid particle. The stress tensor is:

$$\underline{\underline{\Phi}} = \begin{bmatrix} \sigma_x & \tau_{yx} & \tau_{zx} \\ \tau_{xy} & \sigma_y & \tau_{zy} \\ \tau_{xz} & \tau_{yz} & \sigma_z \end{bmatrix} \tag{6.1}$$

In most of the cases the tensile stresses are caused by only the pressure, therefore:

$$\sigma = -p \tag{6.2}$$

and the sheer stresses can be defined according to the Newton's viscosity law:

$$\tau_{yx} = \mu\left(\frac{\partial v_y}{\partial x} + \frac{\partial v_x}{\partial y}\right) \tag{6.3}$$

where μ is the viscosity of the fluid [kg/m.s]. So τ_{yx} means the tensile stress towards the x direction on the plane with y normal. The other tensile stresses can be defined by the similar way. With the application of the stress tensor the momentum equation can be expressed (the flow is still stationer):

$$v\frac{dv}{dr} = g + \frac{1}{\rho}\underline{\underline{\Phi}}\underline{\nabla} \tag{7}$$

where $\underline{\nabla}$ is the nabla vector. The vector form of the momentum equation is more interesting and more often used which is:

$$v_x\frac{\partial v_x}{\partial x} + v_y\frac{\partial v_x}{\partial y} + v_z\frac{\partial v_x}{\partial z} = g_x + \frac{1}{\rho}\left(-\frac{\partial p}{\partial x} + \mu\left(\frac{\partial^2 v_y}{\partial x^2} + \frac{\partial^2 v_x}{\partial y \partial x}\right) + \mu\left(\frac{\partial^2 v_z}{\partial x^2} + \frac{\partial^2 v_x}{\partial z \partial x}\right)\right) \tag{8.1}$$

$$v_x\frac{\partial v_y}{\partial x} + v_y\frac{\partial v_y}{\partial y} + v_z\frac{\partial v_y}{\partial z} = g_y + \frac{1}{\rho}\left(\mu\left(\frac{\partial^2 v_x}{\partial y^2} + \frac{\partial^2 v_y}{\partial x \partial y}\right) - \frac{\partial p}{\partial y} + +\mu\left(\frac{\partial^2 v_z}{\partial y^2} + \frac{\partial^2 v_y}{\partial z \partial y}\right)\right) \tag{8.2}$$

$$v_x\frac{\partial v_z}{\partial x} + v_y\frac{\partial v_z}{\partial y} + v_z\frac{\partial v_z}{\partial z} = g_z + \frac{1}{\rho}\left(\mu\left(\frac{\partial^2 v_x}{\partial z^2} + \frac{\partial^2 v_z}{\partial x \partial z}\right) + \mu\left(\frac{\partial^2 v_y}{\partial z^2} + \frac{\partial^2 v_z}{\partial y \partial z}\right) - \frac{\partial p}{\partial z}\right) \tag{8.3}$$

3. Application examples of convection heating

In the followings we concentrate only for forced convection heating methods which apply some kind of gas flows. The gas flows can be usually considered to be laminar; therefore the analysis of them is much easier than other fluid flows where this condition is not existed. In this Section typical convection heating applications is studied from the point of gas flow. Simple gas flow models are presented to examine how the changes of the flow parameters effect on the value of the heat transfer coefficient.

The most common and widely used example for the convection heating is the heating with concentrated gas streams. The gas streams blow trough nozzles with d_0 diameter into a free space where the heat structure is placed. Before the deeper analysis, we will discus the basic of this technology which is the free-stream theory.

3.1 Free-stream theory

The free-stream is a single gas stream blown trough a nozzle into the free space (Fig. 2). There are no blocking objects facing to the stream. The free-streams can be studied according to simple and overall rules which are the followings: the initial velocity of the gas is v_0 – instead of the close ambience of the nozzle wall – and the flow is laminar. The out blowing free-stream contacts and interacts with the standing gas in the free space around the circuit of the stream. Therefore the free-stream budges and grips more and more from the standing gas while the radius of the circle where the stream velocity is still v_0 narrows due to the braking effect of the standing gas.

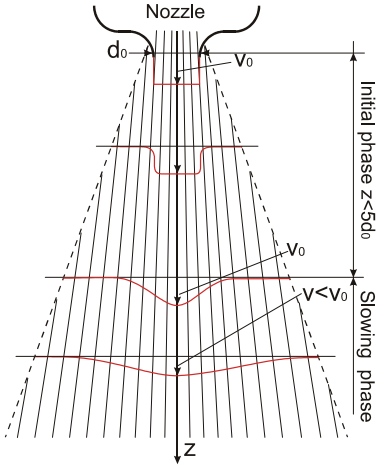

Fig. 2. Cylinder symmetrical free-stream.

The narrowing rate is proportional with distance from the nozzle. Around at $z \cong 5d_0$ distance the velocity of the stream is equal with v_0 only in the axis of the out blowing (Fig. 2). The distance between the out blowing and $z \cong 5d_0$ is the initial phase of the free-stream, if $z > 5d_0$ the stream is in the slowing phase.

The initial value of the heat transfer coefficient is h_0 at the out blowing, and this can be considered to be constant under the nozzle in the initial phase, since the mass flow rate is near constant (Eq. (2)). In the other parts of the stream the heat transfer coefficient increases from the out blowing, but in the initial phase it is smaller than h_0 at least with one order of magnitude. In the slowing phase the mass flow rate decreases exponentially under the nozzle with the heat transfer coefficient, and it is near equalized in the whole free-stream before the gas flow velocity becomes zero.

3.2 Heating with gas streams

Our basic case study is the following: we heat a brick-shape by gas streams from a nozzle-matrix (Fig. 3). We assume that the heated structure is closer to the nozzles than the boarder of the initial phase (defined in Section 3.1). The size of the nozzle-matrix is bigger than the heated structure; around and under the heated structure we defined free space. The nozzle-matrix generates numerous vertical gas streams. We consider the inlet gas streams to be laminar (inlet condition). The diameter of the nozzles are much smaller than the horizontal sizes of heated structure, hence the heated brick-shape effects on the gas streams as a

blocking element. Therefore we model the gas flow on the following criteria which is that the vertical gas streams from the nozzle-matrix turn and join into a continuous radial flow layer (outlet condition) above the brick-shape. At a given point on the surface of the brick-shape the flow direction of the radial layer is determined by a so called "balance line". The balance line marks that location where the main flow direction is changed.

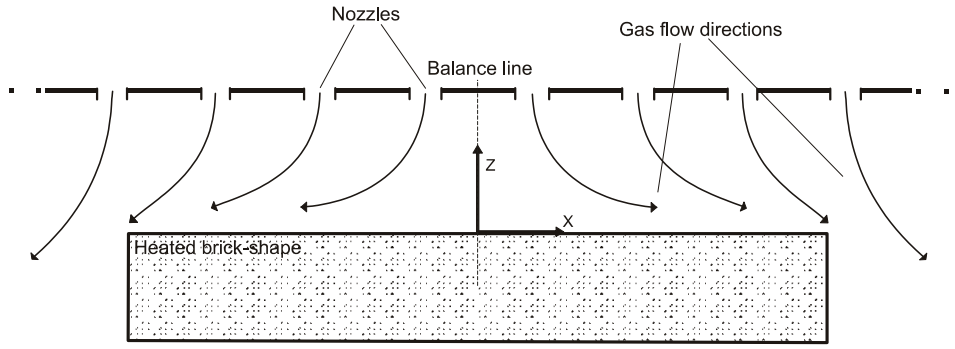

Fig. 3. Gas flows above the heated structure, cross-section, *x* axis.

The schematic view of the gas flow can be seen along the *x* axis in Fig. 3. The zero point of the coordinate system is placed onto the geometrical centre of the heated surface. The direction of a gas stream from a given nozzle depends on the position of the heat structure under the nozzle-matrix. If the system is symmetrical along the *x* axis, this enables us to assume that the transported mass and energy are nearly equal in the $-x$ and $+x$ directions.
However if the system is not symmetric, the balance line is shifted onto asymmetrical position. We have illustrated an example in Fig. 4 where a wall is placed near the heated structure perpendicular to the *y* axis. In this case due to the blocking effect of the wall on the radial flow layer, the transported mass and energy has to be smaller into the –y direction than into the y direction.
Henceforward we study the vertical–radial flow transformation (the radial flow layer formation) of a single gas stream and examine how the transformation effect on the *h* parameter. The model of an inlet vertical gas stream can be seen in Fig. 5. The changes of the flow parameters are much faster than the changes of the gas temperature.

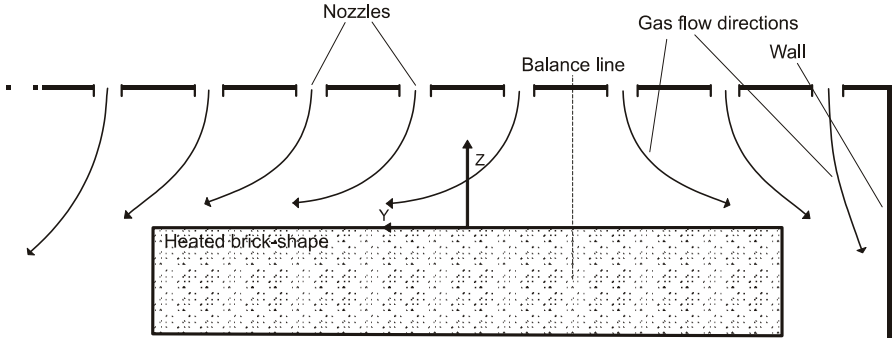

Fig. 4. Gas flows above the heated structure, cross-section, *y* axis.

Therefore the gas flow model of the radial layer formation can be considered as isothermal and stationary. The radial flow layer is separated into further layers from *L(1)* to *L(m)*. In these *L* layers, the velocity of the gas flow, the pressure and the density of the gas are considered to be constant. In Fig. 5 the broken lines represent the borders of *L* flow layers and not streamlines.

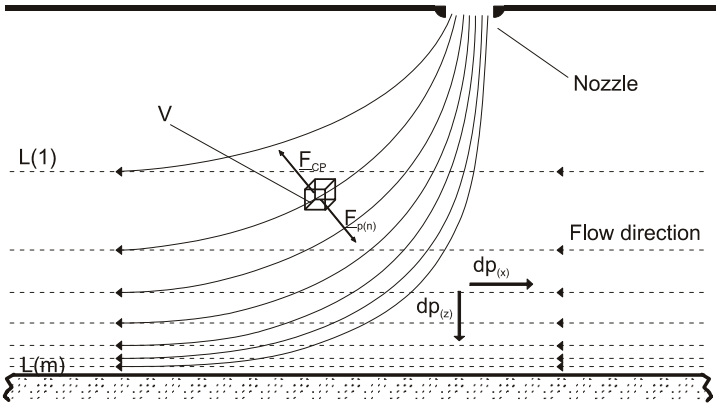

Fig. 5. Radial layer formation, cross-section *x* axis.

We examine the movement of an elemental amount of gas in a constant *V* volume. The m_g mass [kg] in the *V* volume [m³] passes to the radial layer along an arc. During this an F_{CP} centripetal force [N] and an $F_{p(n)}$ force [N] from the pressure change (normal to the movement orbit) acts on the m_g of *V*. The force of the pressure change is defined in a normal coordinate system by the simplified Euler equation (5.2):

$$\underline{F}_{p(n)} = m_g \cdot \frac{|\underline{v}|^2}{R_a} = m_g \cdot \frac{1}{\rho} \cdot \frac{\mathrm{d}p}{\mathrm{d}n} \tag{9}$$

The layer scaling effect of the entrance gas stream starts towards the direction of the radial flow layer. The radiuses of the arcs decrease from *L(1)* to *L(m)*. It occurs that $\mathrm{d}p_n(1) < \mathrm{d}p_n(2) < ... < \mathrm{d}p_n(m)$ and the density of the gas also grows towards the heated structure (caused by the isothermal condition).
The momentum equation system in the stationary model is described by Eq. (7):

$$\underline{v} \cdot \frac{\partial \underline{v}}{\partial \underline{r}} = \frac{1}{\rho} \cdot \underline{\underline{\Phi}} \cdot \underline{\nabla} \tag{10}$$

In case of gas flow the gravity force can be neglected. As we defined in Section 2, the $\underline{\underline{\Phi}}$ contains tensile σ [Pa] and shear τ [Pa] stresses. In the gas flow model the tensile stresses are $\sigma_{xx} = \sigma_{yy} = \sigma_{zz} = -p$ and the shear stresses are caused by the friction. Significant friction occurs only between the *L(m)* layer and the surface of the heated structure. Therefore, only

$$\sigma_{zx} = \mu \cdot (\partial v_x / \partial z) \text{ and } \sigma_{zy} = \mu \cdot (\partial v_y / \partial z) \tag{11}$$

have been considered (in both cases the change of the v_z component along the x and y axes can be neglected). So the stress tensor (Eq. (6.1)) can be reduced and this contains only the following elements:

$$\underline{\underline{\Phi}} = \begin{bmatrix} -p & 0 & \mu \cdot (\partial v_x / \partial z) \\ 0 & -p & \mu \cdot (\partial v_y / \partial z) \\ 0 & 0 & -p \end{bmatrix} \tag{12}$$

According to the reduced stress tensor (12) some members of the left side of the momentum Eq. (8) is reduced:

$$v_x \cdot \frac{\partial v_x}{\partial x} + v_z \cdot \frac{\partial v_x}{\partial z} = \frac{1}{\rho} \cdot \left(\mu \cdot \frac{\partial^2 v_x}{\partial z \partial x} - \frac{\partial p}{\partial x} \right) \tag{13.1}$$

$$v_y \cdot \frac{\partial v_y}{\partial y} + v_z \cdot \frac{\partial v_y}{\partial z} = \frac{1}{\rho} \cdot \left(\mu \cdot \frac{\partial^2 v_y}{\partial z \partial y} - \frac{\partial p}{\partial y} \right) \tag{13.2}$$

$$v_z \cdot \frac{\partial v_z}{\partial z} = \frac{1}{\rho} \cdot \left(-\frac{\partial p}{\partial z} \right) \tag{13.3}$$

The equations from (13.1) to (13.3) show that mainly the change of the pressure affects on the velocity. (Except of the *L(m)* layer where the friction is considerable). It was discussed that the pressure in the *L* flow layers increases when getting closer to the heated structure (Fig. 5). This results in that v_z decreases along the z direction towards the brick-shape and causes the decrease of heat transfer coefficient of the inlet gas streams along the z direction when getting closer to the heated structure. Besides the heat transfer coefficient of the radial flow layer has to increase when getting closer to the heated structure while the v_x and v_y velocity components and the density increase. The larger density and velocity should give larger mass flow (according to Eq. (2)) and heat transfer coefficient in the lower radial flow layers.

Consequently the heat transfer coefficients during the vertical-radial flow transformation changes in the following way: the h parameter of the inlet gas streams have to decrease towards the heated structure due to the slew of the velocity vector. Contrarily the h parameter of the radial flow layer has to increase towards the heated structure due to the velocity and density increase.

In the next Section, the effects of the vertical–radial flow transformation and the blocking elements on the heat transfer coefficient are examined and proved by measurements.

4. Measurement methods of the heat transfer coefficient

As we have discussed in Section 2, in most of the cases the only exact solution to determine the heat transfer coefficient is the measurement. Therefore in this section two measurement and calculation methods are presented; with these the h parameter can be determined in the previously discussed cases (Section 3.2).

4.1 Measurement methods

The *h* parameter can be directly calculated form Eq. (1), if we can measure the temperature changes during the convection heating. First we present a method to measure the heat transfer coefficient of the inlet gas streams in function of the height above the heated structure.

The temperature changes have to be measured with the minimum of disturbance to the gas streams. Therefore, point probes have to be used for this purpose. The K-Type rigid (steel coat) thermocouples are suitable with a 1mm diameter. An installation of the measuring can be seen in Fig. 6.

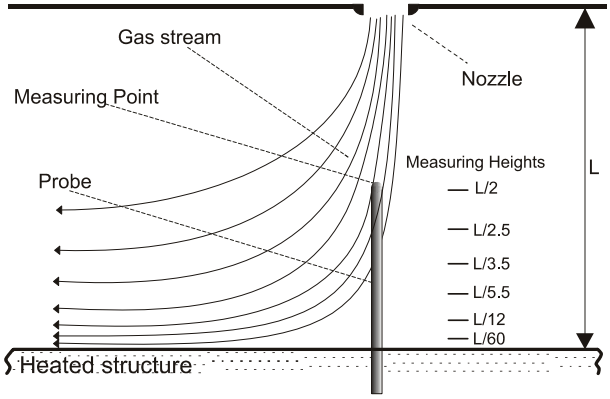

Fig. 6. Measuring installation (inlet gas streams, cross-sectional view).

Their rigid coating has ensured that the thermocouples are being kept in appropriate position during the measurements. The thermo-couple is pinned through a prepared hole of the heated structure. A model structure can be used instead of the real structure; the point is that the shape of the model and the real structure has to be similar. The measurements have to be done below the nozzles facing towards the entrance gas streams.

For the study of the *h* parameter changes of the inlet gas streams above the heated structure, the measurements has to be done at different measurement heights. The measurements have to start at that height where the velocity changes of the inlet gas streams start. The rule of thumb is that this point is near *L/2* (where *L* is the distance between the nozzle-matrix and the heated structure). In our case study we have chosen six measuring heights from the heated structure: *L/60, L/12, L/5.5, L/35, L/2.5* and *L/2* (but these are optional).

If the measurements are repeated at different locations under the nozzle-matrix, the distribution of the heat transfer coefficient can be determined in the function of the height above the heated structure. This kind of distribution measurements can be useful to investigate the inhomogeneity of the heater system (nozzle-matrix).

For the study of the heat transfer coefficient in the radial flow layer, the measurement installation can be seen in Fig. 7.a. The probes are fixed in a measuring gate (measuring box) which held them in position. The front and the rear end of the gate were opened so the radial flow could pass through it, but the roof of the gate protected the probes from the disturbing effect of the inlet gas streams. The probes can be put into the gate through holes on the lateral sides. The gate can be made from any heat insulator material. The size of the gate depends on the diameter of the nozzles and the distance between the nozzle-matrix and

the heated structure. The suitable gate is enough narrow to ensure exact sampling but enough wide to not cause turbulence in the radial flow layer and enough length to protect the probes the from the disturbing effect of the inlet gas streams; optimal width and length is $5...6 \cdot d_{nozzle}$. The height is dedicated by the measurement heights.

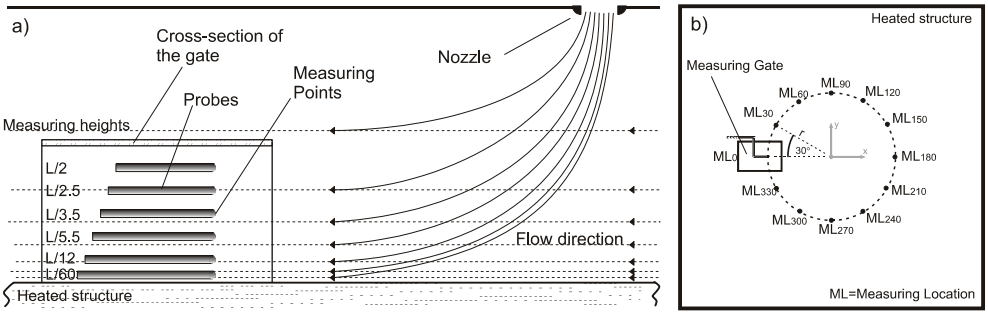

Fig. 7. a) Measuring installation (radial flow layer, cross-sectional view); b) measuring locations (MLs) on the heated structure (upper view).

An advantage of this arrangement was that the probes only obstruct the flow at the measuring points because they were parallel to the radial flow layer. The obstruction and measuring points were overlapped and the disturbance of the radial layer was minimal. During the measurements the same measuring heights are practical to use than in the case of the vertical measurements. With this method the heat transfer coefficient of the radial flow layer can be determined in function of height above the heated structure.

The nature of the radial flow layer can cause that the heat transfer coefficient depends not only on the height but also on the flow direction (as we have seen it in the case of blocking elements, Fig. 4). Therefore the measurements of the *h* parameter in the radial flow layer have to be done as some kind of direction characteristic measurements. We have to measure the temperature changes at different locations in the radial flow layer. The Measuring Locations (MLs) are located equally around a circle whose centre aligned with the centre of the heated structure (Fig. 7.b). The measuring gate was positioned at the MLs facing towards the centre of the heated structure. The radius of the circle is about the quarter of the smaller plane dimension of the heated structure. For our case study we have chosen 12 MLs.

4.2 Calculation method

The *h* parameters can be calculated using the heat equation of the investigated thermal system:

$$Q_a = Q_c - Q_k \tag{14}$$

where Q_a is the absorbed thermal energy [J], Q_c is the convection thermal energy [J] and Q_k is a parasite conduction thermal energy [J] caused by measurement system. During the measurements the data logger system is usually colder than the measurement probes; therefore some of the convection heat flows towards the data logger trough the thermo-couples. In most cases of the convection heating the infra-radiation can be neglected.

The measured curves (the temperature changes) showed exponential saturation. Analytical curves have to be fitted to the measured curves for to calculate the h parameter. The temperature changes are modeled with exponential saturation:

$$T(t) = (T_h - T(t_0)) \cdot (1 - e^{-t/\tau}) \tag{15.1}$$

where T_h is the heater (gas) temperature, $T(t_0)$ is the initial temperature of the probe, t is the time and τ is the time coefficient of the heating:

$$\tau = t \,/\, \ln\left(1 - (T(t_r) - T(t_0)) \,/\, (T_h - T(t_0))\right) \tag{15.2}$$

where $T(t_r)$ is the maximum temperature reached at the end of the heating.
Although we know the set temperatures in during the heating, but these are not equal to T_h as in most of the cases the measuring device has a cooling effect on the heater system. This effect depends on the size (thermal capacity) and the temperature differences between the measurement system and the heater gas. In addition the heater system often tries to hold the set temperatures with some kind of temperature control system. Therefore, the exact T_h values of the measured curves are not known, they have to be calculated. This task can be carried out by an iteration curve fitting method.
The T_h is iterated from the value of $T(t_r)$ using a 0.01°C temperature step up. In each iteration steps, the model curves are fitted onto the measured curve. The iteration stops when the fitting failure reaches the minimal value. In Fig. 8, the dashed curve is calculated with only one T_h value (one fitting curve) for the whole curve. But T_h is changing during the measurement. If two T_h values are applied (two fitting curves) – one for the first part $[t_0, t_1]$ and one for the second part $[t_1, t_r]$ of the curve – the matching is much better (continuous line). In other cases more than two T_h values can be also applied in order to reach the best fitting of the analytical curve. Typically in those cases when the heating takes a long time or contrariwise the gradient of the heating is high and the heat capacity of the heated structure is large.

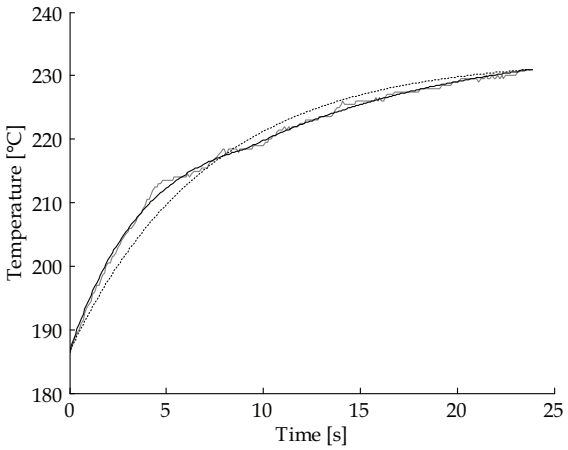

Fig. 8. Analytical curve fitting.

According to the foregoing Eq. (15) has to be modified:

$$T(t) = (T_h(t) - T(t_0)) \cdot (1 - e^{-t/\tau(t)}) \tag{16.1}$$

where

$$T_h(t) = \left[T_{h1}\big|_{0-t_1} ; T_{h2}\big|_{t_1-t_2} ; ...; T_{hn}\big|_{t_{n-1}-t_r} \right] \tag{16.2}$$

and

$$\tau(t) = \left[\tau_1\big|_{0-t_1} ; \tau_2\big|_{t_1-t2} ; ...; \tau_n\big|_{t_{n-1}-tr} \right] \tag{16.3}$$

The convection heat is calculated with the integration of Eq. (1) to the time interval of the heating [t_0, t_r]:

$$Q_c = \int_{t_0}^{t_r} F_c(t)\, dt = \int_{t_0}^{t_r} h \cdot A \cdot (T_h(t) - T(t)) \tag{17}$$

Although the absolute measurement inaccuracy of the thermo-couples is ±0.5°C, but the expected value of the measurement failure is converging to zero due to the integration in Eq. (17).

The thermo couples are well insulated from the steel coat decreasing the conduction impact from the environment. But the parasite conduction resistances of the thermo-couple wires have to be also considered between the data recorder (DR) and the Measuring Point (MP). The conduction model of the measuring system can be seen in Fig. 9, in the case of a K-type thermo-couples which materials are NiCr(90:10) and NiAl(95:5).

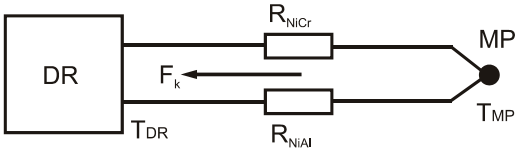

Fig. 9. Conduction model of the measuring system (illustration only for one probe).

The MP is modeled as a sphere and its conduction behavior is neglected because of the small dimensions. The thermal potential difference between the DR and MP generates the parasite conduction heat flow F_k on R_{NiCr} and R_{NiAl}:

$$\frac{dQ_k}{dt} = F_k = \frac{T_{MP} - T_{DR}}{R_{NiCr}} + \frac{T_{MP} - T_{DR}}{R_{NiAl}} \tag{18}$$

The Q_k parasite conduction heat is calculated with the integration of Eq. (18) to the time interval of the heating [t_0, t_r]:

$$Q_k = \int_{t_0}^{t_r} F_k(t) = \int_{t_0}^{t_r} \frac{T(t) - T_{DR}(t)}{R_{NiCr}} + \frac{T(t) - T_{DR}(t)}{R_{NiAl}} \tag{19}$$

The $T_{DR}(t)$ can be approximated with a liner curve which gradient depends on the circumstances of the heating (the temperature change of the data register) during the measurements:

$$T_{DR}(t) = T_0 + (T_0 - T_{DR}(t_r)) \cdot \frac{t}{t_r} \tag{20}$$

where T_0 is the initial temperature of the data register. It is supposed that the thermal capacity of the data register is infinite compared to the thermal capacity of the MP; hence the $T_{DR}(t)$ do not change doe to F_k.
The amount of absorbed thermal energy is calculated (Barbin et al., 2010):

$$Q_a = C \cdot m \cdot (T(t_r) - T(t_0)) \tag{21}$$

where C is the thermal capacity [J/kg.K] and m is the mass [kg] of the measuring point. The value of h is calculated according to Eq. (14), (17) and (21):

$$h = (Q_a + Q_k) / \int_{t_0}^{t_r} A \cdot (T_h(t) - T(t)) \quad [\mathrm{W/m^2K}] \tag{22}$$

4.3 Study of the measured heat transfer coefficients

First we present the results of the characteristics measurements of the h parameter in the case of inlet gas streams above a heated structure (Fig. 6). The applied gas was N_2; the velocity was varied between 4 and 8m/s; the distance between the heated structure and the nozzles was varied between 30 and 70mm. The change of the h parameter is illustrated in function of height (Fig. 10); each point of the characteristics was calculated by 24 measured results.
The h parameter can be considered to be constant from the entrance of the gas streams to *L/2.5*; from *L/2.5* to *L/12* the decline starts and follows a linear shape with 2.9–3.9 W/m²K/mm gradient, at *L/12* there is a cut-off point and the gradient of the decline grows. As it has been expected, the changes of h values are very high in function of the measuring height.

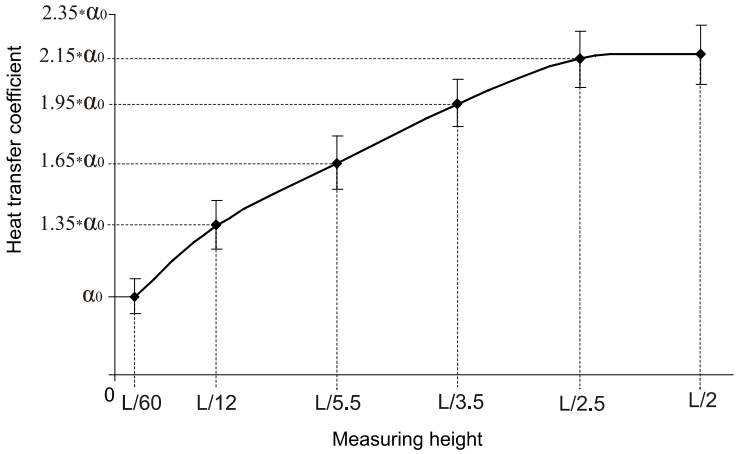

Fig. 10. Characteristics of h parameter of the inlet gas streams in function of height.

These results prove the preconceptions in Section 3.2 that the h parameters of the inlet heater gas streams depend on the height. These are nearly constant (inflowing phase) until a height where the gas flow direction begins to change (transition phase) and the radial layer formation starts. The starting of the transaction begins about at L/2.5 above the heated structure according to the measurements.
As we mentioned in Section 4.1, if the measurements are repeated at different locations under the nozzle-matrix, the distribution of the heat transfer coefficient can be determined

in the function of the height above the heated structure. An example can be seen in Fig. 11 where the efficiency of the nozzle-lines can be compared in a reflow oven at *L/2.5* measuring height (Illés, 2010). This visualization method ensures that we get sufficient view of the changes of *h* parameter in the oven.

The 15–25 % *h* parameter differences were observed between the nozzle-lines. The examined oven is six year old; therefore the differences are probably caused by the inhomogeneity of the gas circulation system (the different attrition of the fans).

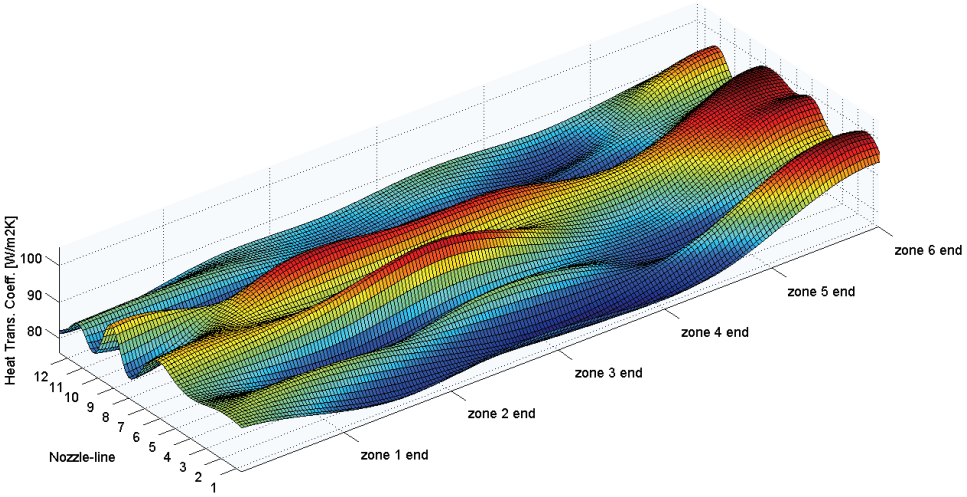

Fig. 11. Distribution of the *h* parameter in the oven at *L/2.5* measuring height.

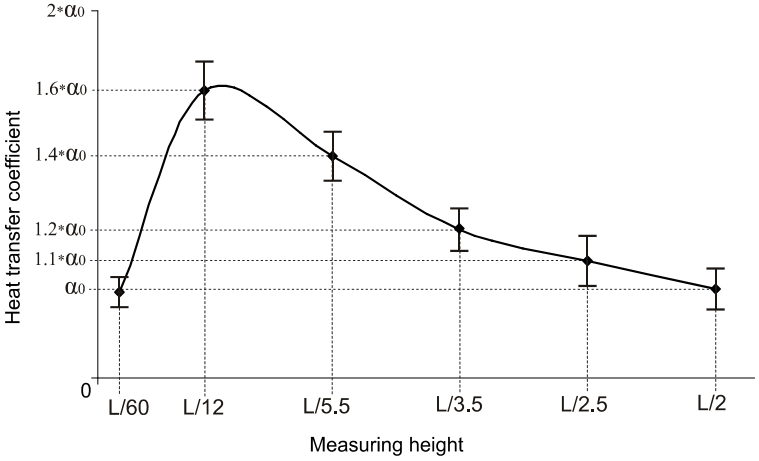

Fig. 12. Characteristics of the *h* parameter in the radial flow layer in function of height.

In Fig. 12 the results of the characteristics measurements of the *h* parameter in the radial flow layer is presented above a heated structure (Fig. 7). The gas flow parameters were the same as

the inlet gas stream measurements. The change of the h parameter is illustrated in function of height (Fig. 12); each point of the characteristics was calculated by 24 measured results.

The value of h also depends on the measuring height in the radial flow layer. This increases when getting closer to the heated structure until a given distance (peak value is near L/12 distance from the heated structure). This effect is caused by the growth of density and flow rate in the radial layer towards the heated structure, as it was discussed in Section 3.2. However, the friction becomes considerably higher at the closest ambience of the heated structure (L/60). This slows the flow rate (Illés & Harsányi, 2009; Wang et al., 2006; Cheng et al., 2008) more than the growth of the density, and this effect decreases the h parameter dramatically. It should be noted that the h parameter is near equal at the L/60 and L/2 distances.

As it was discussed in Section 4.1 we can do direction characteristics measurement in the radial flow layer. The h values measured at ML_0 – ML_{330} can be presented as 3D directional characteristics of the heat transfer coefficient. This means that we illustrate the h values above the x-y plane according to the MLs and the measuring height. The appropriate values are attached because of the better visualization: the values of a given measuring height are attached with a horizontal curve and the values of a given ML are attached with a vertical curve. In this form, our results are more expressive because the heating capability is analyzable in each direction.

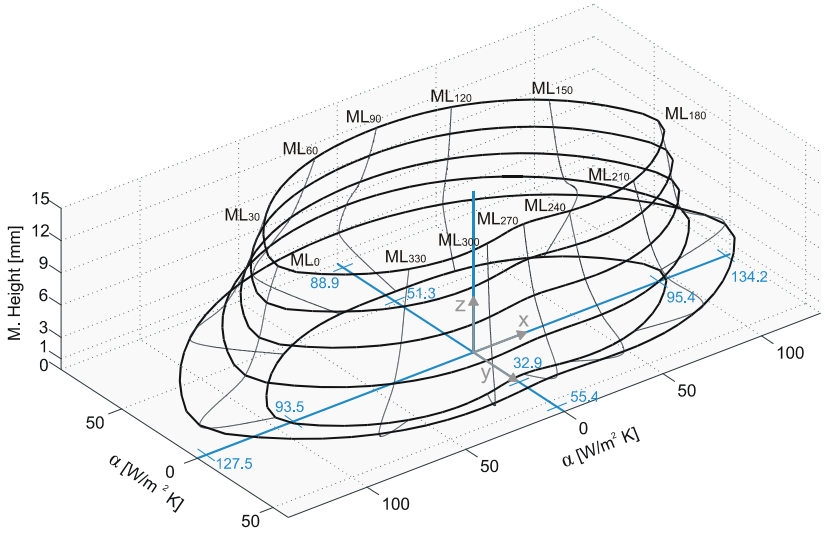

Fig. 13. 3D directional characteristics of the h parameter in a convection reflow oven.

In Fig. 13, we show an example to application of the 3D directional characteristics. This present the h parameter in the radial flow layer of a convection reflow oven (Illés & Harsányi, 2009). On the main axes (x and y), the minimum and maximum values of h are also marked.

Major heating capability differences can be observed between the directions which are caused by the construction of the oven. We can study the effect of blocking elements (such as walls; Fig. 4 in Section 4.1) on the heat transfer coefficient towards the different directions. The h parameters are much larger (80–120%) towards the directions where are no blocking oven walls, than those where these are. In addition, there are also considerable heating

capability differences (30–40%) between the directions towards the opposite oven walls (ML_{90} and ML_{270}). This is caused by the asymmetrical design of the oven (the right wall is closer to the heated structure than the left wall).

5. Modeling the heating of solid structures

In the previous sections we have discussed how the convection heat transfers to the solid structures, how the gas flow circumstances form during the convection heating and how the heat transfer coefficient can be measured. In this section, we present a 3D combined heat transfer and conduction model which can calculate the temperature distribution of the solid structure during the convection heating process. In addition we also show how the measured heat transfer coefficients can be used during the modelling.

5.1 Basics of the heating model

The model is based on the thermal or central node theory. This means that the investigated area is divided into thermal cells representing the thermal behaviour of the given material. We have defined the basic thermal cell as a cuboid (Fig 14.a). This shape is easy to handle and useful for our nonuniform grid.

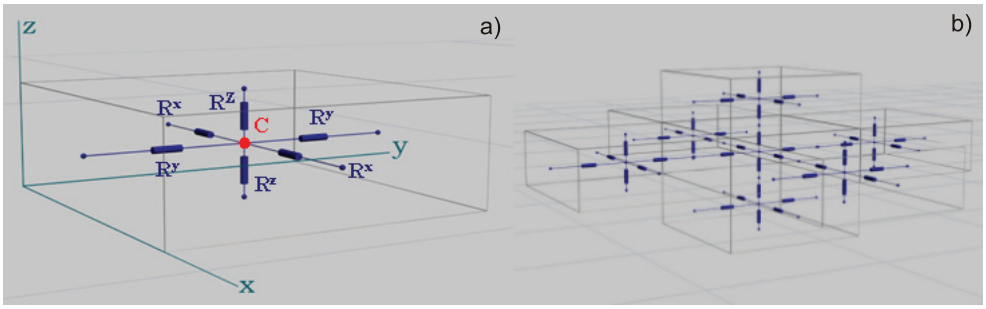

Fig. 14. a) The basic thermal cell; b) neighboring thermal cells.

All cells contain a thermal node in their geometrical centre, which represents the thermal mass of the cell as a heat capacity [J/K]:

$$C = C_S \cdot \rho \cdot V \tag{23}$$

where C_S is the specific heat capacity of the material [J/kg.K], ρ is the density of the material [kg/m^3] and V is the volume of the cell [m^3]. The thermal conduction ability of the cells is described with thermal resistances [K/W] between the node and its cell borders:

$$R^x = \frac{l_x}{2 \cdot \lambda \cdot l_y \cdot l_z} \text{ and } R^y = \frac{l_y}{2 \cdot \lambda \cdot l_x \cdot l_z} \text{ and } R^z = \frac{l_z}{2 \cdot \lambda \cdot l_x \cdot l_y} \tag{24}$$

where l_x, l_y and l_z are the dimensions of the cell [m] and λ is the specific thermal conductivity of the material [W/m.K]. The neighbouring thermal cells are in connections with the thermal resistances (Fig. 14.b).

In most of the cases the application of a non-uniform grid is the most effective; with this the resolution of the model can be refined to focus on areas of interest whilst reducing the involvement with the less important areas. The cell partition method is presented on the

example can be seen in Fig. 15.a which is a surface mounted component on a printed wiring board (Illés & Harsányi, 2008). First we have to choose the object area of the model; in our example this is only the component and its direct environment (marked by red lines around the component).
The construction of the nonuniform grid is very important due to the implementation of the model. We use a simple but very useful condition for the faces of the thermal cells in the nonuniform grid: all neighbouring faces should have the same size. It ensures that all thermal cells can be in direct connection with maximum 6 other cells (all cells can have maximum 6 neighbours). In this case, all the neighbours are known, so the model can be implemented according to the indexing of the cells. Otherwise, (if the number of the neighbours is not maximized) the direct connections between the cells would be fund by mathematical induction, so the implementation of the model would be more complicated.

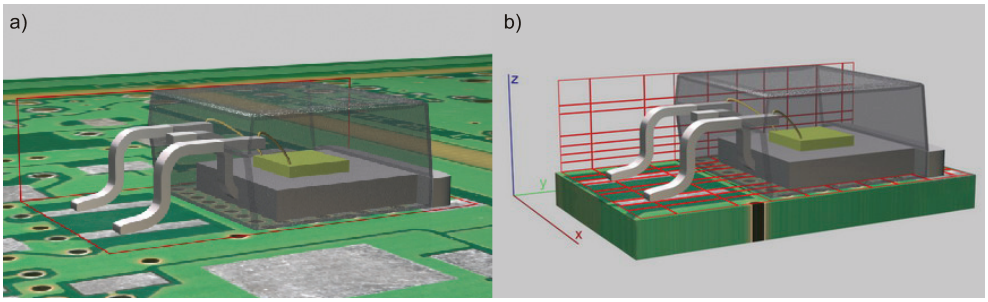

Fig. 15. a) Choose the objective area of the model; b) the nonuniform resolution.

This construction of the nonuniform grid can be achieved by the following steps: we define a basic uniform grid with section planes. The cell borders are the section lines of these planes. After this, adaptive interpolation (in the areas of interest) and decimation (in the less important areas) is done on the section planes separately along each axis. If the degrees of the interpolation and the decimation are the same then the number of cells will not change. A nonuniform grid can be seen in Fig. 15.b. In order to help a better visualization of this concept only some section lines of the section planes are visible in the picture.
According to the thermal node theory there should be thermodynamic equilibrium in all cells. Therefore during the cell partition, the borders of the different materials have to be taken into consideration.
The nonuniform grid gives as more information from the important parts than the uniform with the same cell number. This approach therefore allows to achieve a significant increase of spatial resolution of the calculated temperature distribution in some distinct areas with only a little increase of model complexity.
The cell type and the physical position of the cells can be assigned by the coordinates of the intersections. The indexing of the cells is carried out by numbering the section planes (n_x, n_y and n_z according to the axis). All cells and their cell parameters can then be identified with these numbers: the heat capacity $C(n_x, n_y, n_z)$; the thermal resistances $R^x(n_x, n_y, n_z)$, $R^y(n_x, n_y, n_z)$ and $R^z(n_x, n_y, n_z)$ which also contain the direction of the resistance (Fig. 14.a).

5.2 Model description

The model is described by common heat conduction and convection equations and these are solved by the finite difference method in order to achieve high calculation speed and easy

implementation. If the time steps are small enough then the boundary conditions and material properties can be assumed to remain constant over the time steps. The temperature change in the cells can be calculated by the backward Euler formula:

$$\frac{\mathrm{d}T_n(t)}{\mathrm{d}t} = \frac{T_n(t) - T_n(t - \mathrm{d}t)}{\mathrm{d}t} = \frac{F}{C} \tag{25}$$

where T_n is the temperature of the cell [K], t is the time [s], dt is the time step [s], F is the heat flow rate [W] and C is the heat capacity of the cell [J/K].

We use the following boundary conditions: there is only convection heat change between the solid-gas boundaries, and the convection heat always flows from the gas to the solid (the gas is always hotter than the solid). The solid-solid boundaries of the model (if we study only a part of a solid structure) are considered to be adiabatic. The heat spreads by conduction heat transport between the thermal cells in the model. As formerly, we neglect the radiation heat.

The equation of the convective heat flow rate (Eq. (1)) is used in the following form:

$$F_C(t, \underline{r}) = A_n \cdot h(\underline{r}) \cdot (T_h(\underline{r}) - T_n(t)) \tag{26}$$

where $h(\underline{r})$ is the heat transfer coefficient [W/m²K] depending on the location, A_n is the heated surface [m²] and $T_h(\underline{r})$ is the heater gas temperature [K] depending on the location. The conduction heat flow is caused by the temperature difference between the cells:

$$F_K(t) = \frac{T_{n-1}(t) - T_n(t)}{R_{n-1} + R_n} \tag{27}$$

where R_{n-1} and R_n are the thermal resistances between the adjacent cells, whilst $T_{n-1}(t)$ and $T_n(t)$ are the temperatures of the adjacent cells.

We assume the following initial condition $T_1(0) \cong T_2(0) \cong \ldots \cong T_n(0)$ meaning that, before the heating, the temperature gradient of our system is very small. This assumption is always valid for equilibrium thermodynamics systems. Therefore, between the adjacent cells $F_K(0) \cong 0$, this means that the conduction heat is generated only by convection heating. Using Eq. (25), (26) and (27), this is the general form of the differential equation which describes the temperature change of the cells in the model:

$$\frac{\mathrm{d}T}{\mathrm{d}t} = \frac{1}{C} \cdot \left[\sum_{i=0}^{k} F_{C(i)} + \sum_{j=1}^{6-k} F_{K(j)} \right] \tag{28}$$

where k is the number of the solid-gas interfaces and 6-k is the number of adjacent cells.

For the description of the whole model, a differential equation system is needed. With an appropriate selection of the cells parameters and initial assumptions, the differential equation system can be easily generated. The indexing method, shown in Section 5.1, will be our starting point. All cells have an own heat capacity, six faces and six thermal resistances from the six faces. The heat capacities can be handled as values $C(n_x, n_y, n_z)$, the surfaces and thermal resistances are stored in vectors and matrixes.

Although all cells have only three different surfaces, these are stored in 6x6 element matrixes, it will be useful for general implementation:

$$\underline{\underline{A}}(n_x,n_y,n_z)=\begin{bmatrix} A^{x}(n_x,n_y,n_z) & 0 & 0 & 0 & 0 & 0 \\ 0 & A^{-x}(n_x,n_y,n_z) & 0 & 0 & 0 & 0 \\ 0 & 0 & A^{y}(...) & 0 & 0 & 0 \\ 0 & 0 & 0 & A^{-y}(...) & 0 & 0 \\ 0 & 0 & 0 & 0 & A^{z}(...) & 0 \\ 0 & 0 & 0 & 0 & 0 & A^{-z}(...) \end{bmatrix} \tag{29}$$

where $A^{x}(n_x,n_y,n_z)=A^{-x}(n_x,n_y,n_z)$, these are opposite faces of the cell which are perpendicular to x axis, etc. For the general implementation the thermal resistances should be transformed to thermal conductances. The $\underline{G}(n_x,n_y,n_z)$ vectors have the following form:

$$\underline{G}(n_x,n_y,n_z)=\begin{bmatrix} G^{x}(n_x,n_y,n_z)\cdot G^{x}(n_x-1,n_y,n_z)/(G^{x}(n_x,n_y,n_z)+G^{x}(n_x-1,n_y,n_z)) \\ G^{x}(n_x,n_y,n_z)\cdot G^{x}(n_x+1,n_y,n_z)/(G^{x}(n_x,n_y,n_z)+G^{x}(n_x+1,n_y,n_z)) \\ G^{y}(n_x,n_y,n_z)\cdot G^{y}(n_x,n_y-1,n_z)/(G^{y}(n_x,n_y,n_z)+G^{y}(n_x,n_y-1,n_z)) \\ G^{y}(n_x,n_y,n_z)\cdot G^{y}(n_x,n_y+1,n_z)/(G^{y}(n_x,n_y,n_z)+G^{y}(n_x,n_y+1,n_z)) \\ G^{z}(n_x,n_y,n_z)\cdot G^{z}(n_x,n_y,n_z-1)/(G^{z}(n_x,n_y,n_z)+G^{z}(n_x,n_y,n_z-1)) \\ G^{z}(n_x,n_y,n_z)\cdot G^{z}(n_x,n_y,n_z+1)/(G^{z}(n_x,n_y,n_z)+G^{z}(n_x,n_y,n_z+1)) \end{bmatrix} \tag{30}$$

According to the construction of the model, multiplying by zero is carried out in the positions of solid-gas interfaces. These elements of $\underline{G}(n_x,n_y,n_z)$ are zero.
As we have proved in Section 4, the efficiency of the convection heating could be changed on the different faces of the heated structure. We apply the flowing assistant vectors:

$$\underline{h}(n_x,n_y,n_z)=\begin{bmatrix} h^{x}(n_x,n_y,n_z) \\ h^{-x}(n_x,n_y,n_z) \\ h^{y}(n_x,n_y,n_z) \\ h^{-y}(n_x,n_y,n_z) \\ h^{z}(n_x,n_y,n_z) \\ h^{-z}(n_x,n_y,n_z) \end{bmatrix} \tag{31}$$

where $h^{x}(n_x,n_y,n_z)$ is the heat transfer coefficient on $A^{x}(n_x,n_y,n_z)$ and $h^{-x}(n_x,n_y,n_z)$ is the heat transfer coefficient on $A^{-x}(n_x,n_y,n_z)$, etc. The elements of $\underline{h}(n_x,n_y,n_z)$ have to be zero at those positions where $\underline{G}(n_x,n_y,n_z)$ are not zero. This means that $\underline{h}(n_x,n_y,n_z)$ are zero on those positions where adjacent cells are located near the given cell.
The temperature differences between the heater gas and the heated cells are also stored in assistant vectors:

$$\underline{T_h}(n_x,n_y,n_z)=\begin{bmatrix} T_h^{\,x}(n_x,n_y,n_z)-T(n_x,n_y,n_z)\\ T_h^{\,-x}(n_x,n_y,n_z)-T(n_x,n_y,n_z)\\ T_h^{\,y}(n_x,n_y,n_z)-T(n_x,n_y,n_z)\\ T_h^{\,-y}(n_x,n_y,n_z)-T(n_x,n_y,n_z)\\ T_h^{\,z}(n_x,n_y,n_z)-T(n_x,n_y,n_z)\\ T_h^{\,-z}(n_x,n_y,n_z)-T(n_x,n_y,n_z)\end{bmatrix} \tag{32}$$

where $T_h^{\,x}(n_x,n_y,n_z)$ is the heater gas temperature at $A^x(n_x,n_y,n_z)$, etc. To achieve a compact description, the temperature differences between a given cell and its adjacent cells are also collected into assistant vectors:

$$\underline{T_K}(n_x,n_y,n_z)=\begin{bmatrix} T(n_x-1,n_y,n_z)-T(n_x,n_y,n_z)\\ T(n_x+1,n_y,n_z)-T(n_x,n_y,n_z)\\ T(n_x,n_y-1,n_z)-T(n_x,n_y,n_z)\\ T(n_x,n_y+1,n_z)-T(n_x,n_y,n_z)\\ T(n_x,n_y,n_z-1)-T(n_x,n_y,n_z)\\ T(n_x,n_y,n_z+1)-T(n_x,n_y,n_z)\end{bmatrix} \tag{33}$$

We need only those values of $\underline{T_K}(n_x,n_y,n_z)$ where adjacent cells exist. Therefore $\underline{T_K}(n_x,n_y,n_z)$ vectors will be filtered by the $\underline{G}(n_x,n_y,n_z)$ vectors. In those positions where the $\underline{G}(n_x,n_y,n_z)$ vector is zero, the value of the $\underline{T_K}(n_x,n_y,n_z)$ will be disregarded. The solid-gas interfaces are chosen by $\underline{h}(n_x,n_y,n_z)$. By the application of the assistant vectors and matrixes (29–33) this gives us the general expression of the differential equation system which best describes the model:

$$\frac{\mathrm{d}T(n_x,n_y,n_z)}{\mathrm{d}t}=\frac{\underline{h}(n_x,n_y,n_z)^T\cdot\underline{\underline{A}}(n_x,n_y,n_z)\cdot\underline{T_h}(n_x,n_y,n_z)+\underline{G}(n_x,n_y,n_z)^T\cdot\underline{T_K}(n_x,n_y,n_z)}{C(n_x,n_y,n_z)} \tag{34}$$

If we do not maximize the number of the cell neighbours in the model then the assistant vectors (29), (30), (31) and (33) would be matrices with *6xN* dimensions (*N* is the cell number), therefore Eq. (34) and its implementation would be more complex.

5.3 Application example

In the last section we present an application of our model which is the convectional heating of a surface mounted component (e.g. during the reflow soldering) in Fig 15. We investigate how change the temperature of the soldering surfaces of the component if the heat transfer coefficients are different around the component (see more details in (Illés & Harsányi, 2008)). The model was implemented using MATLAB 7.0 software.

We have defined a nonuniform grid with 792 thermal cells (the applied resolution is the same as in Fig 15.b), the *x-y* projection in the contact surfaces can be seen in (Fig. 16.a). In this grid, the 13 contact surfaces are described by 31 thermal cells. But the cells which represent the same contact surface can be dealt with as one. The examined cell groups are shown as squares in Fig. 16.a.

We use the following theoretical parameters: $T(0)$=175°C; T_h=225°C; h^x=40W/m.K; h^{-x}=75W/m.K; h^y= h^{-y}=100W/m.K; h^z= h^{-z}=80W/m.K. We investigate an unbalanced heating case when there is considerable heat transfer coefficient deviation between right and left faces of the component (Fig. 16.a). The applied time step was dt=10ms. In Fig. 16.b the temperature of the different contact surfaces can be seen at different times.

After 3 seconds from the starts of the heating there are visible temperature difference between the investigated thermal cells occurred by their positions (directly or non-directly heated cells) and different heat conduction abilities. The temperature of the cell groups which are heated directly (1a, 1b, 2a, 2b and 3a–3c) by the convection rises faster than the temperature of the cell groups which are located under the component (4a–4f) and the heat penetrates into them only by conduction way. This temperature differences increase during the heating until the saturation point where the temperature begins to equalize. The effect of the unbalanced heating along the x direction ($h^x \neq h^{-x}$) can also be studied in Fig. 16.b. The cell groups under the left side of the component (1a, 2a, 3a, 4a, 4c and 4e) are heated faster compared to their cell group pair (1b, 2b, 3c, 4b, 4d and 4f) from the left side.

This kind of investigations are important in the case of soldering technologies because the heating deviation results in a time difference between the starting of the melting process on different parts of the soldering surfaces. This breaks the balance of the wetting force which results in that the component will displace during the soldering. According to the industrial results, if the time difference between the starting of the melting on the different contact surfaces is larger than 0.2s the displacement of the component can occur (Warwick, 2002; Kang et al., 2005).

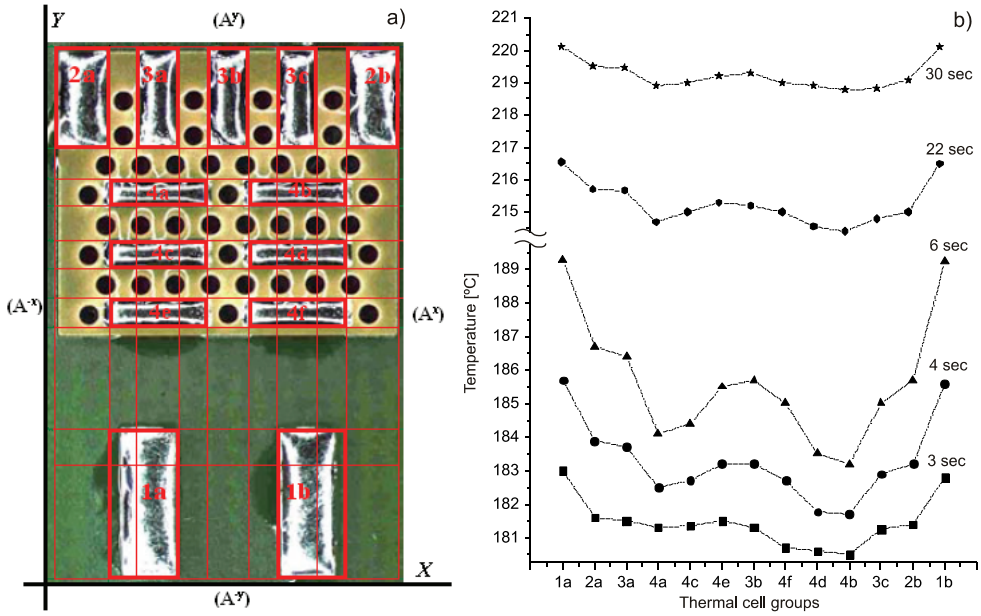

Fig. 16. a) x–y projection of the applied nonuniform grid; b) temperature distribution of the contact surfaces

Comparing the abilities of our model with a general purpose FEM system gave us the following results. The data entry and the generation of the model took nearly the same time in both systems, but the calculation in our model was much faster than in the general purpose FEM analyzer. Tested on the same hardware configuration, the calculation time was less than 3s using our model, while in the FEM analyzer it took more than 52s.

6. Summary and conclusions

In this chapter we presented the mathematical and physical basics of fluid flow and convection heating. We examined some models of gas flows trough typical examples in aspect of the heat transfer. The models and the examples illustrated how the velocity, pressure and density space in a fluid flow effect on the heat transfer coefficient. New types of measuring instrumentations and methods were presented to characterize the temperature distribution in a fluid flow in order to determine the heat transfer coefficients from the dynamic change of the temperature distribution. The ability of the measurements and calculations were illustrated with examples such as measuring the heat transfer coefficient distribution and direction characteristics in the case of free streams and radial flow layers.
We presented how the measured and calculated heat transfer coefficients can be applied during the thermal characterization of solid structures. We showed that a relatively simple method as the thermal node theory can be a useful tool for investigating complex heating problems. Using adaptive interpolation and decimation our model can improve the accuracy of the interested areas without increasing their complexity. However, the time taken for calculation by our model is very short (only some seconds) when compared with the general FEM analyzers. Although we showed results only from one investigation, the modelling approach suggested in this chapter, is also applicable for simulation and optimization in other thermal processes. For example, where the inhomogeneous convection heating or conduction properties can cause problems.

7. Acknowledgement

This work is connected to the scientific program of the " Development of quality-oriented and harmonized R+D+I strategy and functional model at BME" project. This project is supported by the New Hungary Development Plan (Project ID: TÁMOP-4.2.1/B-09/1/KMR-2010-0002).
The authors would like to acknowledge to the employees of department TEF2 of Robert Bosch Elektronika Kft. (Hungary/Hat- van) for all inspiration and assistance.

8. Reference

Barbin, D.F., Neves Filho, L.C., Silveira Júnior, V., (2010) Convective heat transfer coefficients evaluation for a portable forced air tunnel, Applied Thermal Engineering 30 (2010) 229–233.

Bilen, K., Cetin, M., Gul, H., Balta, T., (2009) The investigation of groove geometry effect on heat transfer for internally grooved tubes, Applied Thermal Engineering 29 (2009) 753–761.

Blocken, B., Defraeye, T., Derome, D., Carmeliet, J., (2009) High-resolution CFD simulations for forced convective heat transfer coefficients at the facade of a low-rise building, Building and Environment 44 (2009) 2396–2412.

Castell, A., Solé, C., Medrano, M., Roca, J., Cabeza, L.F., García, D. (2008) Natural convection heat transfer coefficients in phase change material (PCM) modules with external vertical fins, Applied Thermal Engineering 28 (2008) 1676–1686.

Cheng, Y.P., Lee, T.S., Low, H.T., (2008) Numerical simulation of conjugate heat transfer in electronic cooling and analysis based on field synergy principle, Applied Thermal Engineering 28 (2008) 1826–1833.

Dalkilic, A.S., Yildiz, S., Wongwises, S., (2009) Experimental investigation of convective heat transfer coefficient during downward laminar flow condensation of R134a in a vertical smooth tube, International Journal of Heat and Mass Transfer 52 (2009) 142–150.

Gao, Y., Tse, S., Mak, H., (2003) An active coolant cooling system for applications in surface grinding, Applied Thermal Engineering 23 (2003) 523–537.

Guptaa, P.K., Kusha, P.K., Tiwarib, A., (2009) Experimental research on heat transfer coefficients for cryogenic cross-counter-flow coiled finned-tube heat exchangers, International Journal of Refrigeration 32 (2009) 960–972.

Illés, B., Harsányi, G., (2008) 3D Thermal Model to Investigate Component Displacement Phenomenon during Reflow Soldering, Microelectronics Reliability 48 (2008) 1062–1068.

Illés, B., Harsányi, G., (2009) Investigating direction characteristics of the heat transfer coefficient in forced convection reflow oven, Experimental Thermal and Fluid Science 33 (2009) 642–650.

Illés, B., (2010) Measuring heat transfer coefficient in convection reflow ovens, Measurement 43 (2010) 1134–1141.

Incropera, F.P., De Witt, D.P. (1990) Fundamentals of Heat and Mass Transfer (3rd ed.). John Wiley & Sons.

Inoue, M., Koyanagawa, T., (2005) Thermal Simulation for Predicting Substrate Temperature during Reflow Soldering Process, IEEE Proceedings of 55th Electronic Components and Technology Conference, Lake Buena Vista, Florida, 2005, pp.1021-1026.

Kang, S.C., Kim C., Muncy J., Baldwin D.F., (2005) Experimental Wetting Dynamics Study of Eutectic and Lead-Free Solders With Various Fluxes, Isothermal Conditions, and Bond Pad Metallization. IEEE Transactions on Advanced Packaging 2005; 28 (3):465–74.

Kays, W., Crawford, M., Weigand, B., (2004) Convective Heat and Mass Transfer, (4th Ed.), McGraw-Hill Professional.

Tamás, L., (2004) Basics of fluid dynamics, (1st ed.), Műegyetemi Kiadó, Budapest.

Wang, J.R., Min, J.C., Song, Y.Z., (2006) Forced convective cooling of a high-power solid-state laser slab, Applied Thermal Engineering 26 (2006) 549–558.

Warwick, M., (2002) Tombstoning Reduction VIA Advantages of Phased-reflow Solder. SMT Journal 2002; (10):24–6.

Yin, Y., Zhang, X., (2008) A new method for determining coupled heat and mass transfer coefficients between air and liquid desiccant, International Journal of Heat and Mass Transfer 51 (2008) 3287–3297.

22

Analysis of the Conjugate Heat Transfer in a Multi-Layer Wall Including an Air Layer

Armando Gallegos M., Christian Violante C.,
José A. Balderas B., Víctor H. Rangel H. and José M. Belman F.
Department of Mechanical Engineering, University of Guanajuato, Guanajuato, México

1. Introduction

At present the design of efficient furnace is fundamental to reducing the fuel consumption and the heat losses, as well as to diminish the environment impact due to the use of the hydrocarbons. To reduce the heat losses in small industrial furnaces, a multi-layer wall that includes an air layer, which acts like a thermal insulator, can be applied. This concept is applied in the insulating of enclosures or spaces constructed with perforated bricks to maintain the comfort, without using additional thermal insulator in the walls (Lacarrière et al., 2003; Lacarrière et al., 2006). Besides it has been used to increase the insulating effect in the windows of the enclosures (Aydin, 2000; Aydin, 2006). Nevertheless, the thickness of the air layer must be such that it does not allow the movement of the air. Free movement of the air is favorable to the formation of cellular flow patterns that increase the heat transfer coefficient, provoking natural convection heat transfer through the air layer, reducing the insulating capacity of the multi-layer wall due to the transition from conduction to convection regime. A way to diminish the effect of the natural convection is to apply vertical partitions to provide a larger total thickness in the air layer (Samboua et al., 2008). In Mexico there are industrial furnaces used to bake ceramics, in which the heat losses through the walls are significant, representing an important cost of production. In order to understand this problem, a previous study of the conjugate heat transfer was made of a multi-layer wall (Balderas et al., 2007), where it was observed that a critical thickness exists which identified the beginning of the natural convection process in the air layer. This same result was obtained by Aydin (Aydin, 2006) in the analysis of the conjugate heat transfer through a double pane window, where the effect of the climatic conditions was studied. For the analysis of the multi-layer wall a model applying the volume finite method (Patankar, 1980) was developed. This numerical model, using computational fluid dynamics (Fluent 6.2.16, 2007), allowed to study the natural convection in the air layer with different thicknesses, identifying that one which provides major insulating effect in the wall.

2. Model of the multi-layer wall

Industrial furnaces have diverse forms according to the application. The furnace consists of a space limited by refractory walls which are thermally isolated. In the furnace used to bake ceramics the forms are diverse, depending on the operating conditions of the furnace, also,

the thermal isolation is inadequate requiring redesign of the furnace to adapt it to the conditions of production and operation (U.S.A. Department of Energy, 2004) and to obtain the maximum efficiency of the process. To solve this problem a multi-layer wall including an air layer to reduce the heat losses and improving the furnace efficiency is proposed.
The Figure 1(a) shows the configuration of the multi-layer wall, where the thickness of the air layer, *L*, varies while the height of the wall is constant. The materials of the multi-layer wall and H are defined according to the requirements of the furnace. When the thickness of the air layer is increased, some partitions are applied to obtain the insulating effect in the wall. The Figure 1(b) shows the air layer with partitions. The thickness of the air layer, *L*, varies from 0 to 10 cm. In each case, the heat flow towards the outside of the furnace wall is calculated to identify the thickness that allows the minimal heat losses, defined as the optimal air layer thickness.

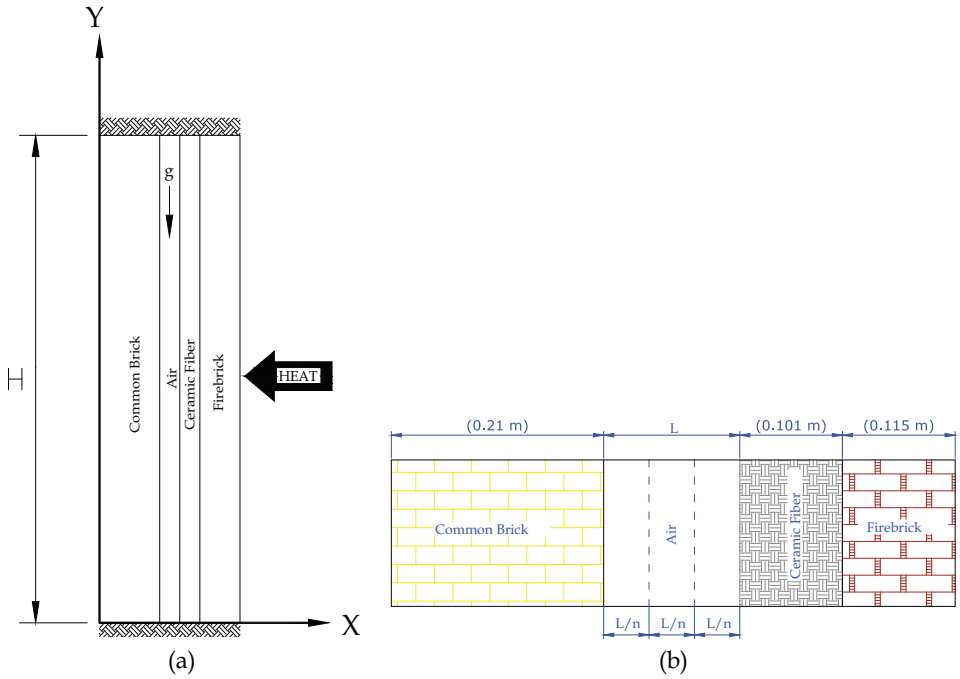

Fig. 1. Composition of the multi-layer wall.

When the thickness of the air layer is increased, the natural convection leads to the formation of cellular flow patterns that increase the heat transfer coefficient and reduce the isolation capacity (Ganguli et al., 2009). Therefore an air layer with vertical partitions in order to maintain the maximum insulation is proposed. In this air layer, each partition has a thickness near the optimal thickness, which is obtained from the analysis of the conduction and convection heat transfer. According to this analysis, a multi-layer wall with 8 and 10 cm of thickness and two, three or four partitions is applied. The configuration of the air layer with partitions is identified according to the following nomenclature.

$$\underbrace{L}_{\substack{thickness\ of \\ the\ air\ layer}} \quad \underbrace{[n]}_{\substack{partitions\ of \\ the\ air\ layer}} \tag{1}$$

where n is the partitions number and L is the thickness of the air layer.

3. Mathematical formulation

The analysis of the multi-layer wall considers the solution of the conjugate heat transfer in steady state between the solid and the air layer in a vertical cavity, which was obtained by CFD (FLUENT®), where a model in two dimensions with constant properties except density is applied, the Boussinesq and non- Boussinesq approximation (Darbandi & Hosseinizadeh, 2007) for the buoyancy effects were used. The work of compressibility and the terms of viscous dissipation in the energy equation were neglected. The thermal radiation within the air layer was neglected. In the non-Boussinesq approximation, the fluid is considered as an ideal gas. The governing equations for the model are:

Continuity equation

$$\frac{\partial u_x}{\partial x} + \frac{\partial u_y}{\partial y} = 0 \tag{2}$$

Momentum equations

component x:

$$u_x \frac{\partial u_x}{\partial x} + u_y \frac{\partial u_x}{\partial y} = \nu \left(\frac{\partial^2 u_x}{\partial x^2} + \frac{\partial^2 u_x}{\partial y^2} \right) \tag{3}$$

component y:

$$u_x \frac{\partial u_y}{\partial x} + u_y \frac{\partial u_y}{\partial y} = -\frac{\partial p}{\partial y} + \nu \left(\frac{\partial^2 u_y}{\partial x^2} + \frac{\partial^2 u_y}{\partial y^2} \right) + \rho g_y \tag{4}$$

momentum equation with Boussinesq approximation

$$u_x \frac{\partial u_y}{\partial x} + u_y \frac{\partial u_y}{\partial y} = g_y \beta \left(T - T_0 \right) + \nu \left(\frac{\partial^2 u_y}{\partial x^2} + \frac{\partial^2 u_y}{\partial y^2} \right) \tag{5}$$

Energy equation

$$u_x \frac{\partial T}{\partial x} + u_y \frac{\partial T}{\partial y} = \alpha \left(\frac{\partial^2 T}{\partial x^2} + \frac{\partial^2 T}{\partial y^2} \right) \tag{6}$$

the pressure gradient in the momentum equation in component x is not considered due to the small space between the vertical walls. The velocity in x direction is important only in the top and bottom of the cavity due to the cellular pattern forms by the natural convection (Violante, 2009).

3.1 Density model

According to the conditions of the problem, is necessary to apply a model of density. The first model applied was the Boussinesq approximation, where the difference of density is expressed in terms of the volumetric thermal expansion coefficient and the temperature difference. For this approximation, the momentum equation in y is expressed by equation 5, where the buoyancy effect depends only on the temperature. Nevertheless, this approximation is only valid for small temperature differences (Darbandi & Hosseinizadeh, 2007). According to the temperature difference in the vertical cavity, it could be possible to use the ideal gas model to calculate the density in the air layer. Therefore, a model where the density is a function of the temperature applied to the problems of natural convection in vertical cavities subject to different side-wall temperatures (Darbandi & Hosseinizadeh, 2007) is:

$$\rho = \frac{P_{op}}{\frac{R}{M_w}T} \tag{7}$$

3.2 Boundary onditions and heat flux

The temperature used in baking of ceramics is between 1123 K (850 °C) and 1173 K (900 °C), and the outside temperature of the furnace may be 300 K (27 °C). Then, the boundary conditions are: bottom and top adiabatic boundary, left and right isothermal boundary and no-slip condition in the walls (including the partitions). In the solid-gas interface, the temperature and the heat flux must be continuous. The solution can be obtained for laminar flow; this consideration is contained in the Rayleigh number and the aspect ratio, whose ranges are $1000 < Ra_L < 10^7$ and $10 < AR\ (H/L) < 110$ are applied (Ganguli et al., 2009). The Rayleigh number for thin vertical cavities is defined as (Ganguli et al., 2009):

$$10^3 < Ra_L = \frac{g\beta(T_i - T_0)L^3}{\nu\alpha} < 10^7 \tag{8}$$

To determine the heat losses, the heat flux through the multi-layer wall is calculated by applying the following equation:

$$q'' = \frac{T_i - T_o}{\frac{l_1}{k_{brick}} + \frac{l_2}{k_{iso}} + \frac{l_3}{k_{firebrick}} + \frac{L}{k_{\text{eff}}}} \tag{9}$$

where l´s is the thickness of each material used in the wall and k_{eff} is the effective conductivity obtained from the combination of the conduction and natural convection effects present in the air layer, which is define as:

$$\mathrm{k_{eff}} = \mathrm{k_{air}}\overline{\mathrm{Nu_y}} \tag{10}$$

where the average Nusselt number is related to the average of heat transfer coefficient in the vertical cavity, which is obtained numerically,

$$\overline{\mathrm{Nu_y}} = \frac{\bar{\mathrm{h}}\mathrm{H}}{\mathrm{k_{air}}} \tag{11}$$

4. Results and discussion

The results were obtained for a multi-layer wall where the inside temperature, T_i, of the furnace is 1173 K (900° C) and the outside temperature, T_o, is 300 K (27° C). The multi-layer wall is formed by four different materials; see Figure 1(b), whose properties are showed in the Table 1 (Incropera & DeWitt, 1996).

Common Brick			**Firebrick**		
ρ_{cb}	1920	kg/m^3	ρ_{fb}	2050	kg/m^3
C_{p_cb}	835	J/kg K	C_{p_fb}	960	J/kg K
k_{cb}	0.72	W/m K	k_{fb}	1.1	W/m K
Ceramic Fiber			**Air (750 K)**		
ρ_{cf}	32	kg/m^3	ρ_{air}	0.4880	kg/m^3
C_{p_cf}	835	J/kg K	C_{p_air}	1081	J/kg K
k_{cf}	0.22	W/m K	k_{air}	0.05298	W/m K
			μ_{air}	3.415x10^{-5}	kg/m s
			α_{air}	100.4x10^{-6}	m^2/s

Table 1. Properties of the materials in the multi-layer wall.

According to the properties of the fluid and assuming the film temperature of 750 K, the maximum Rayleigh number is $Ra_L = 1.37x10^6$, this value is related to the range of the equation (8), where the laminar flow governs the movement of the fluid. In order to quantify the natural convection, an analysis with both models of the density was done. For the model using the approach of Boussinesq, the equation of momentum in the y direction is equation (5). In the second model with no-Boussinesq approximation, the equations (4) and (7) are applied, where the pressure changes inside the vertical cavity are neglected. The results obtained with both density models are showed in the Table 2, where the ideal gas model is used to analyze the conjugate heat transfer through the multi-layer wall because the Boussinesq approximation fails to predict the correct behavior of the natural convection when the temperature gradient is large (Darbandi & Hosseinizadeh, 2007).

Configuration	**Heat flux (W/m2)**	
	Boussinesq approximation	Ideal gas model
8[1]	621.31	715.37
8[2]	463.94	565.86
8[3]	423.10	465.49
8[4]	463.29	429.57
10[1]	629.31	715.37
10[2]	468.28	576.42
10[3]	389.91	470.07
10[4]	458.80	**400.84**

Table 2. Heat flux to Boussinesq and ideal gas model.

The Figure 2 shows the heat flux by conduction and convection through the air layer for different thickness, obtained from equation (9). The conduction heat flux curve shows the insulating effect of the air layer without movement, with the Nusselt number equal to unity, where the heat losses through the multilayer wall continuously decrease for any thickness. The natural convection heat flux curve shows an asymptotic behavior with a constant minimal heat flux, the natural convection heat is produced by cellular flow patterns inside the air layer where the Nusselt number increases. The minimal heat flux is present in thicknesses greater than 3 cm, identifying this value as the optimal thickness to maintain the insulating capacity of the air layer inside the multi-layer wall.

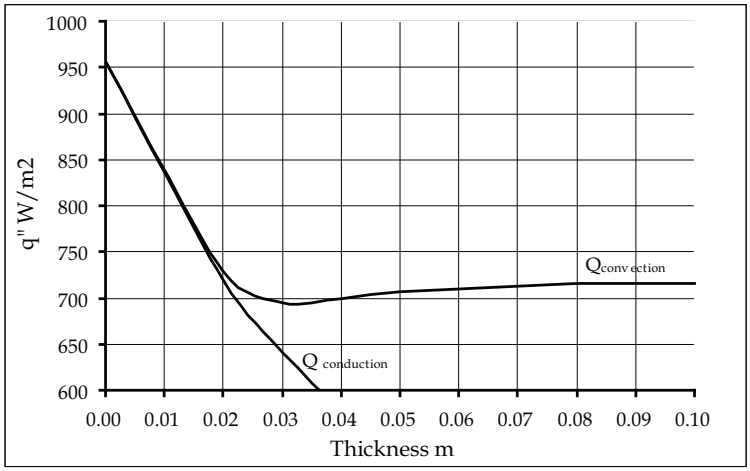

Fig. 2. Heat flow through the air layer.

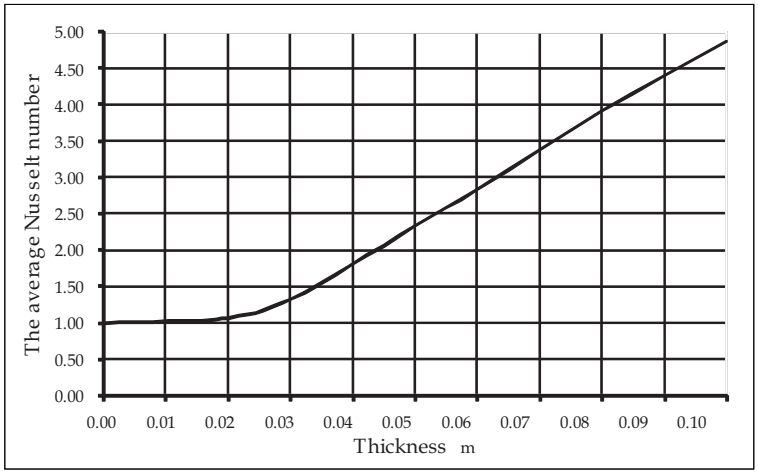

Fig. 3. Average Nusselt number in the air layer.

The average Nusselt number for each of the air layer thickness is showed in the Figure 3. For values below the optimal thickness only heat transfer by conduction is presented and the Nusselt number is equal to the unit. In agreement with equation (10), the effective conductivity is equal to the conductivity of the air. When $L > 0.02$ m the Nusselt number is bigger than unity, this result corresponds to the heat transfer by natural convection, where the cellular flow patterns produces an increase in the heat transfer coefficient due to the temperature gradient applied.

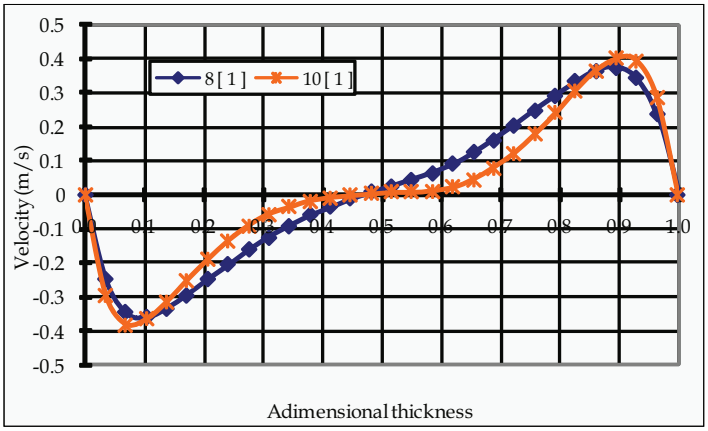

(a)

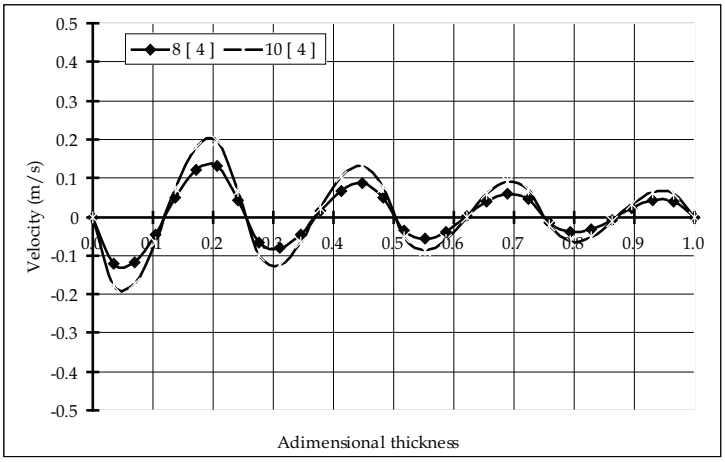

(b)

Fig. 4. Velocity profile in the air layer: (a) without partitions and (b) with four partitions.

After the optimal thickness has been determined, new thicknesses of the air layer are introduced to reduce the heat losses through multi-layer wall. These new configurations correspond to the thicknesses of 8 and 10 cm, each one with 2, 3 or 4 partitions. In each configuration the velocity profile was determined, in order to see the behavior of the cellular patterns of the air inside the cavity. The Figure 4(a) shows the velocity profiles in the vertical

direction in the air layer for the configurations *8 [1]* and *10 [1]*. According to equation (8) these configurations correspond to the air layer without partitions, where the velocity is greater near the vertical walls and practically zero in the center of the air layer, according to the unicellular flow pattern. For the same thicknesses, but with four partitions, *8 [4]* and *10 [4]*, the velocity, Figure 4(b), shows a reduction in its values where the greatest value is near to the hottest wall, which indicates that the heat flux by natural convection through the multi-layer wall it is falling. In all the configurations a unicellular flow pattern is present.

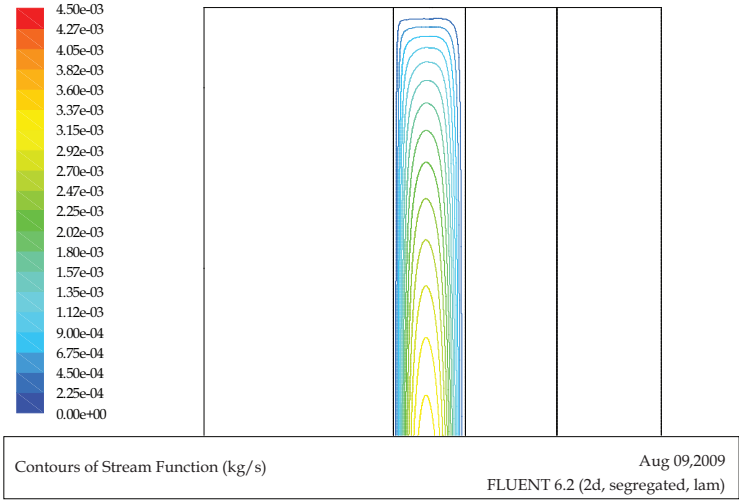

(a)

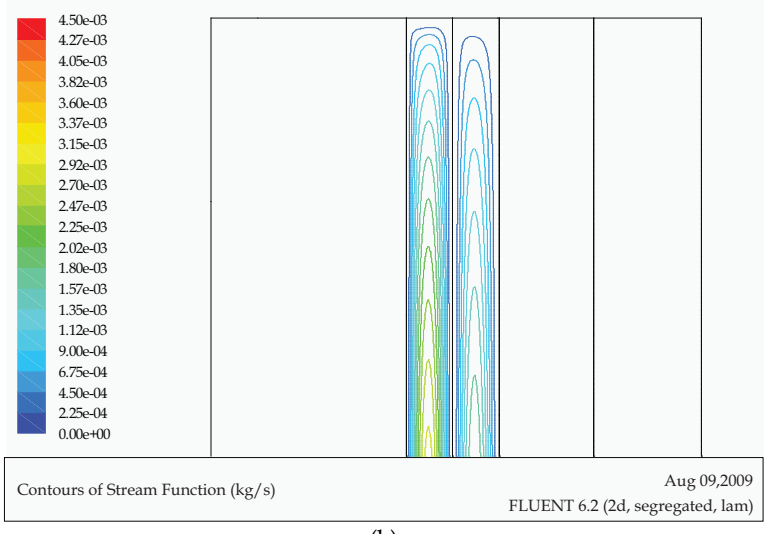

(b)

Fig. 5. (a) and (b) Streamlines in the air layer.

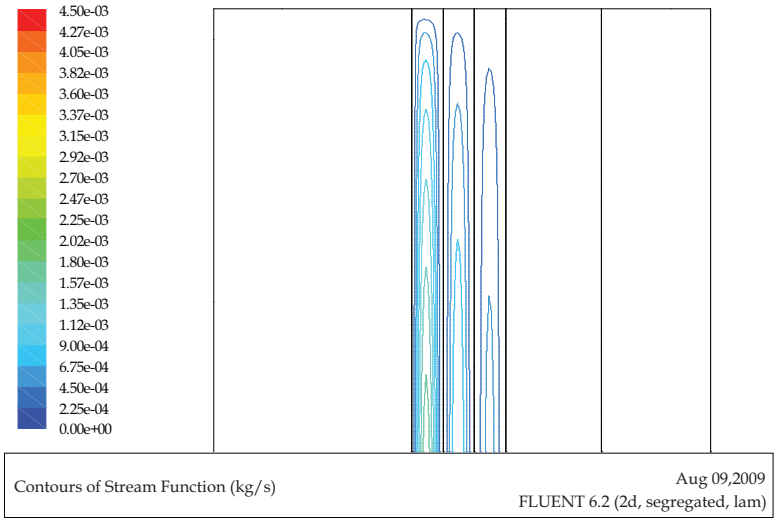

(c)

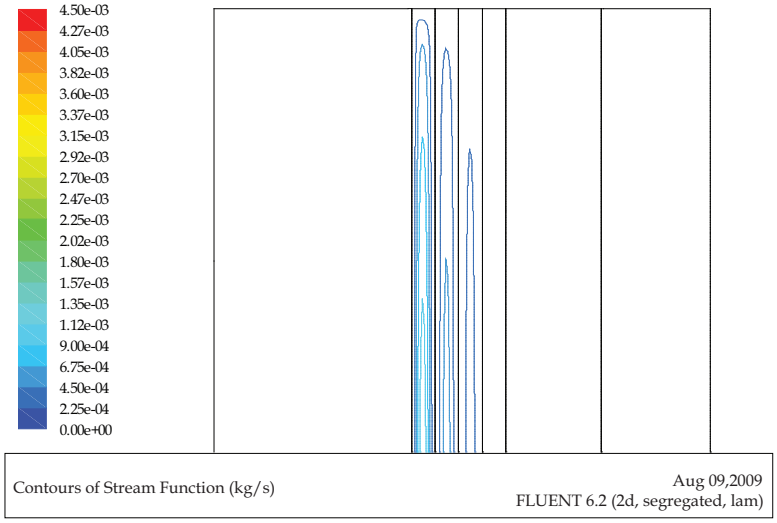

(d)

Fig. 5. (c) and (d) Streamlines in the air layer.

From these results it can be observed that when the velocity decreases, the heat transfer coefficient by convection is reduced and the overall heat losses decrease. This behavior is related to a boundary layer regime where the convection appears in the core region and the conduction is limited to a thin boundary layer near the walls (Ganguli et al., 2009). The Figures 5(a)-5(d) show the streamlines in the air layer, where the boundary layer regime with the unicellular flow pattern is identified. In each configuration we can see the flow

patterns, where it is verified that the greater velocity is in the center of the cavity and this one falls when the partitions are added in the air layer.

Nevertheless, the best parameter to identify the insulating effect of the air layer is the heat transfer through the multi-layer wall. In the table 2 are shown eight configurations where the configuration *10 [4]* shows more insulating capacity, reducing the heat losses. For this configuration each partition has a thickness near the optimal thickness. Then it is possible to deduce that continued adding partitions with thicknesses near the optimal one, the heat flow will fall significantly. This implies the increase in the total thickness of the wall, which is neither practical nor advisable economically.

Identifying the best configuration, the temperature profiles for an air layer of 10 cm and partitions from one to four are analyzed as shown in Figure 6. According to these profiles, for an air layer with a single division (10 cm) the core region does not have a temperature gradient, this behavior means that the heat transfer is controlled by the moving of the boundary layers near the walls with a flow in a laminar boundary layer regime. The heat transferred through the core is negligible. When the partitions in the air layer are placed, the temperature gradients appear indicating that the heat transfer through the multi-layer wall is present. Nevertheless, in configurations with partitions that have thicknesses bigger than the optimal, *10[2]*, the temperature profiles show small gradients, a condition similar to the air layer with a single division. When the air layer has three or four partitions, *10[3]* and *10[4]*, the temperature profile is linear which means that in the entire air layer the heat is transferred by conduction.

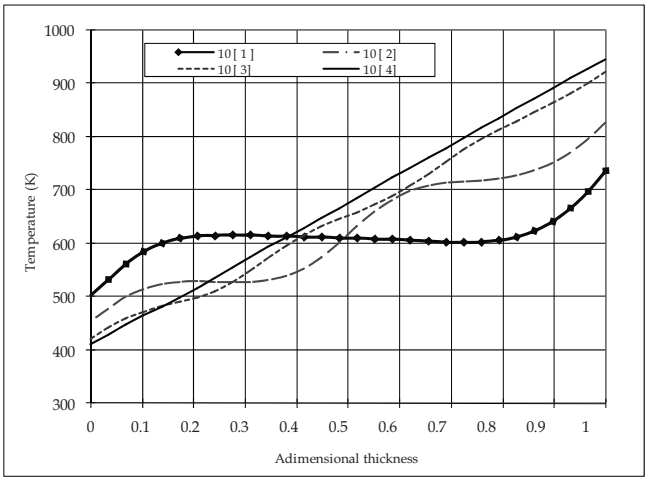

Fig. 6. Temperature profile in the air layer with different partitions.

The greatest temperature gradients appear in the air layer with four partitions, which confirms the importance to use an air layer with partitions that have thicknesses near the optimal. The Figures 7(a) to 7(d) show the temperature contours in the multi-layer wall, where it can be observed that an air layer without partitions, Figure 7(a), the core to be nearly isothermal and the heat transfer is controlled by the moving of the boundary layer near the walls (Ganguli et al., 2009). When the thickness decreases, Figures 7(b) and 7(c), a

steep vertical temperature gradient near the wall is present confirming the existence of the cellular patterns and increasing the rate of the heat transfer through the air layer. With thickness near the optimal, Figure 7(d), there is a linear temperature distribution through the air layer and the heat transfer by conduction is dominant in that region of the thin cavity; however, convection becomes important at the top and bottom corners of the cavity (Ganguli et al., 2009).

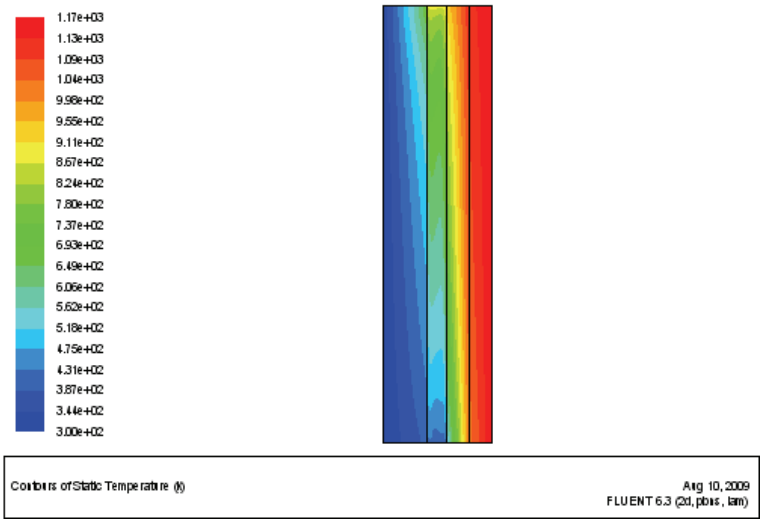

(a)

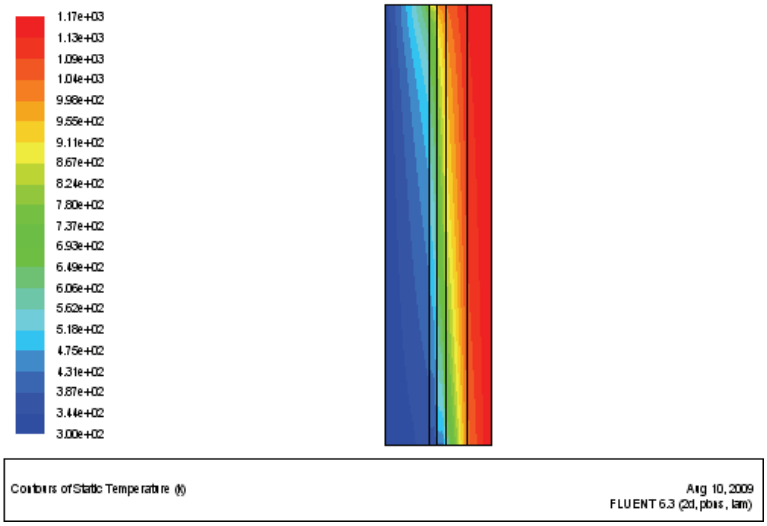

(b)

Fig. 7. (a) and (b) Temperature contours in the multi-layer wall.

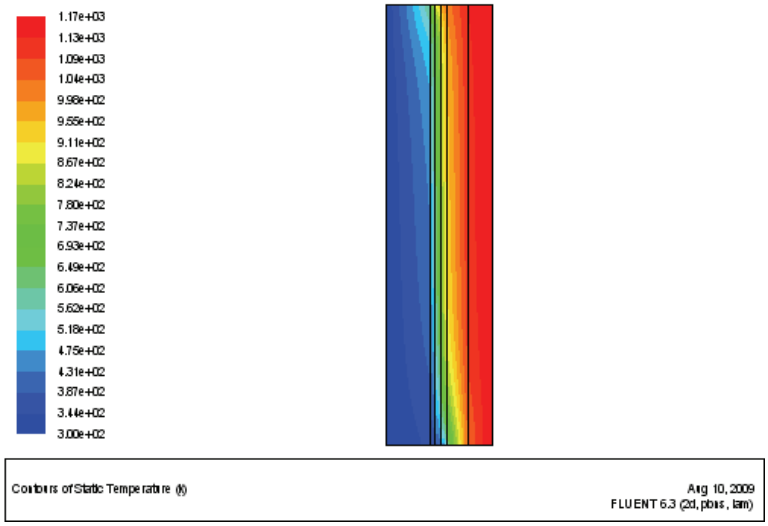

(c)

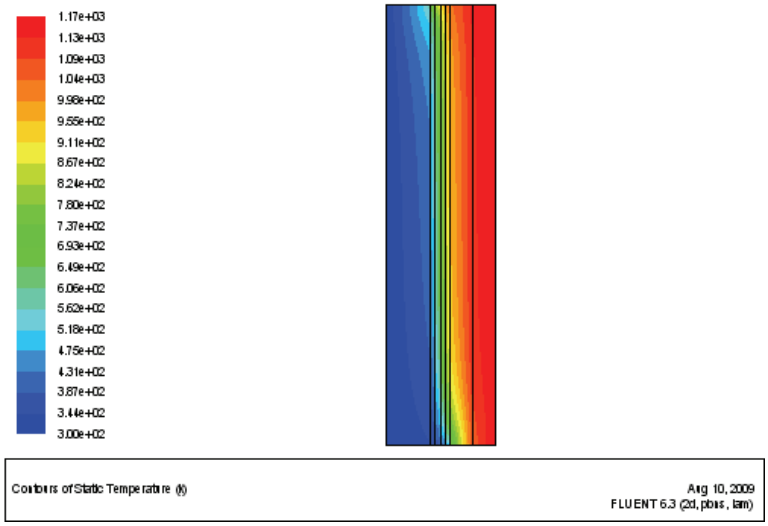

(d)

Fig. 7. (c) and (d) Temperature contours in the multi-layer wall.

5. Conclusions

In the study of the conjugate heat transfer in multi-layer walls, an optimal thickness was identified, also the number of partitions required to reduce the heat losses and obtain a greater insulating capability of the wall was determined. These walls were analyzed for operating conditions of the furnaces used to bake ceramic.

An air layer with a thickness near 3 cm allows the minimal heat transfer loss; whereas the thickness of the other components of the multi-layer wall is constant since their size depends on the commercial dimensions of the materials used.
According to the temperature gradient through the multi-layer wall in a furnace, an air layer with vertical partitions reduces heat losses when the partitions have a thickness near the optimal one; this condition reduces the fuel consumption and the pollutant emissions. For example, the air layer of 10 cm with four partitions reduces about of 44% the heat flux through the wall, with respect to a single air layer with the same thickness.
The reduction of the heat flux from the furnace is considerable and the cost that implies to have an air layer with partitions is less than the cost of using a thermal insulator. In addition, when incorporating an air layer of 10 cm with four partitions, the total thickness of the multi-layer wall is 52 cm, which is a typical thickness of the wall in the furnaces used for baking the ceramics. Also the energy savings make a significant contribution to the optimization of the baking process, reducing production costs.

6. References

Aydin O. (2000). Determination of optimum air-layer thickness in double-pane windows. *Enegy and Building*, 32, 303-308, ISSN: 0378-7788.

Aydin O. (2006). Conjugate heat transfer analysis of double pane windows. *Building and Environment*, 41, 109-116, ISSN: 0360-1323.

Balderas B. A.; Gallegos M. A.; Riesco Ávila J.M.; Violante Cruz C. & Zaleta Aguilar A. (2007). Analysis of the conjugate heat transfer in a multi-layer wall: industrial application. *Proceedings of the XIII International Annual Congress of the SOMIM*. 869-876, ISBN: 968-9173-02-2, México, September 2007, Durango, Dgo.

Darbandi M. & Hosseinizadeh S. F. (2007). Numerical study of natural convection in vertical enclosures using a novel non-Boussinesq algorithm. *Numerical Heat Transfer, Part A*, 52, 849-873, ISSN: 1040-7782.

Department of Energy U.S.A. (Energy Efficiency and Renewable Energy) (2004). Waste heat reduction and recovery for improving furnace efficiency, productivity and emissions performance. *Report DOE/GO-102004-1975,* 1-8.

Fluent 6.2.16 (2007). *User's Guide*.

Ganguli A.; Pandit A. & Joshi J. (2009). CFD simulation of the heat transfer in a two-dimensional vertical enclosure. *IChemE*, 87, 711-727, ISSN: 0263-8762.

Incropera F. & DeWitt D. (1996). *Introduction to Heat Transfer*, John Wiley, ISBN: 0-471-30458-1, New York.

Lacarrière B.; Lartigueb B. & Monchouxb F. (2003). Numerical study of heat transfer in a wall of vertically perforated bricks: influence of assembly method. *Energy and Buildings*, 35, 229-237, ISSN: 0378-7788.

Lacarrière B.; Trombe A. & Monchoux F. (2006). Experimental unsteady characterization of heat transfer in a multi-layer wall including air layers—application to vertically perforated bricks. *Energy and Buildings*, 38, 232-237, ISSN: 0378-7788.

Patankar S.V. (1980). *Numerical Heat Transfer and Fluid Flow*, Hemisphere, ISBN: 0-07-048740-5, New York.

Samboua V.; Lartiguea B.; Monchouxa F. & M. Adjb (2008). Theoretical and experimentalstudy of heat transfer through a vertical partitioned enclosure: application to the optimization of the thermal resistance. *Applied Thermal Engineering*, 28, 488-498, ISSN: 1359-4311.

Violante C. (2009). Analysis of the Conjugate Heat Transfer using CFD in Multi-Layer Walls for Brick Furnace. *Thesis*.

23

An Analytical Solution for Transient Heat and Moisture Diffusion in a Double-Layer Plate

Ryoichi Chiba
Asahikawa National College of Technology
Japan

1. Introduction

In most materials, there exists a coupling effect between heat and moisture during their transient diffusion. In particular, the coupling effect gives a significant change in the distributions of temperature and moisture concentration in some porous materials and resin composites (Chang, et al., 1991). Moreover, it is known that the absorption of moisture by hygroscopic materials under high-temperature environments causes considerable hygrothermal stresses, and meanwhile their mechanical stiffness and strength are degraded a great deal (Komai, et al., 1991). Therefore, it is important to predict accurately the coupled heat and moisture diffusion behaviour within the materials in assessing the life of moisture-conditioning building materials and resin-based structural materials such as CFRP and GFRP in hygrothermal environments.

With regard to the transient heat and moisture diffusion problems, some researchers conducted theoretical analyses using analytical (mathematical) or numerical techniques. For example, Sih et al. presented analytical or numerical solutions for the coupled heat and moisture diffusion and resulting hygrothermal stress problems (Hartranft and Sih, 1980 a) (Hartranft and Sih, 1980 b, Sih, 1983, Sih, et al., 1980) (Sih and Ogawa, 1982) (Hartranft and Sih, 1981) (Sih, 1983, Sih, et al., 1981). Chang et al. used a decoupling technique to obtain analytical solutions for the heat and moisture diffusion occurring in a hollow cylinder (Chang, et al., 1991) and a solid cylinder (Chang, 1994) subjected to hygrothermal loadings. Subsequently, using the same technique, Sugano et al. (Sugano and Chuuman, 1993 a, Sugano and Chuuman, 1993 b) obtained analytical solutions for a hollow cylinder subjected to nonaxisymmetric hygrothermal loadings. All the above-mentioned papers, however, focus on/ target a single material body.

Studies that address the coupled heat and moisture diffusion problem for composite regions (e.g., layered bodies) are limited. Chen et al. (Chen, et al., 1992) analysed the coupled diffusion problem in a double-layered cylinder using the FEM, which leads to time-consuming computation. In order to improve this disadvantage, Chang et al. (Chang and Weng, 1997) later proposed an analytical technique including Hankel and Laplace transforms, and significantly reduced the computational time compared to the FEM analysis. However, the exact continuity of moisture flux was not fulfilled at the layer interface although the coupling terms were included in the governing equations.

In this chapter, under the exact continuity condition the one-dimensional transient coupled heat and moisture diffusion problem is analytically solved for a double-layer plate subjected

to time-varying hygrothermal loadings at the external surfaces, and analytical solutions for the temperature and moisture fields are presented. The solutions are explicitly derived without complicated mathematical procedures such as Laplace transform and its inversion by applying an integral transform technique—Vodicka's method. For simplicity, the diffusion problem treated here is assumed to be a one-way coupled problem, which considers only the effect of heat diffusion on the moisture diffusion, not a fully-coupled problem, in which heat and moisture diffusions affect each other. Since, in some real cases, moisture-induced effect on the heat diffusion (i.e., the latent heat diffusion) is evaluated to be insignificant (Khoshbakht and Lin, 2010, Khoshbakht, et al., 2009), this assumption is reasonable.

Numerical calculations are performed for a double-layer plate composed of distinct resin-based composites that the temperature and moisture concentration are kept constant at the external surfaces (the 1st kind boundary condition). The effects of coupling terms included in the continuity condition of the moisture flux at the layer interface on the transient moisture distribution in the plate are quantitatively evaluated. Numerical results demonstrate that for an accurate prediction of heat and moisture diffusion behaviour, the coupling terms in the continuity condition should be taken into consideration.

Nomenclature

a: interface location, m
B: Biot number for heat transfer (= hl/λ_{ref})
B^*: Biot number for moisture transfer (= $\chi l/\Lambda_{ref}$)
c: moisture capacity, kg/(kg·°M)
h: heat transfer coefficient, W/(m²·K)
l: total thickness, m
L: Luikov number (= η/κ_{ref})
m: moisture content (= $c \cdot u$), wt.%
P: Possnov number (= $\varepsilon(T_{ref}-T_0)/(u_0-u_{ref})$)
t: time, s
T: temperature, K
$\bar{T}$: dimensionless temperature (= $(T-T_0)/(T_{ref}-T_0)$)
u: moisture potential, °M
$\bar{u}$: dimensionless moisture potential (= $(u_0-u)/(u_0-u_{ref})$)
x, y, z: coordinates, m
Z: dimensionless coordinate (= z/l)
χ: moisture transfer coefficient, kg/(m²·s·°M)
$\delta_{i,j}$: Kronecker delta
ε: thermogradient coefficient, °M/K
γ: eigenvalue for temperature field
η: moisture diffusivity, m²/s
κ: thermal diffusivity, m²/s
$\bar{\kappa}$: dimensionless thermal diffusivity (= κ/κ_{ref})
λ: thermal conductivity, W/(m·K)
μ: eigenvalue for moisture field
τ: Fourier number (= $\kappa_{ref}t/l^2$)
Λ: conductivity coefficient of moisture content, kg/(m·s·°M)

Subscripts

b: bottom surface
i: layer number
m: eigenvalue number
ref: reference value
t: top surface
0: initial
∞: surrounding medium

2. Theoretical analysis

Consider an infinite double-layer plate constructed of hygroscopic materials, which is referred to Cartesian coordinate system as shown in Fig. 1. The total thickness of the plate is represented by l. The quantities with subscript 1 or 2 denote those for the 1st or 2nd layer of the double-layer plate throughout the chapter. The coordinate value a indicates the location of the layer interface. The temperature and moisture content measured by the moisture potential in the plate are assumed to be initially T_0 and u_0, respectively. We denote the temperatures of the surrounding media by functions $T_{t\infty}(t)$ and $T_{b\infty}(t)$ and the moisture potentials of them by $u_{t\infty}(t)$ and $u_{b\infty}(t)$. The plate is subjected to these hygrothermal loadings via heat and moisture transfer coefficients h_t, h_b, χ_t and χ_b.

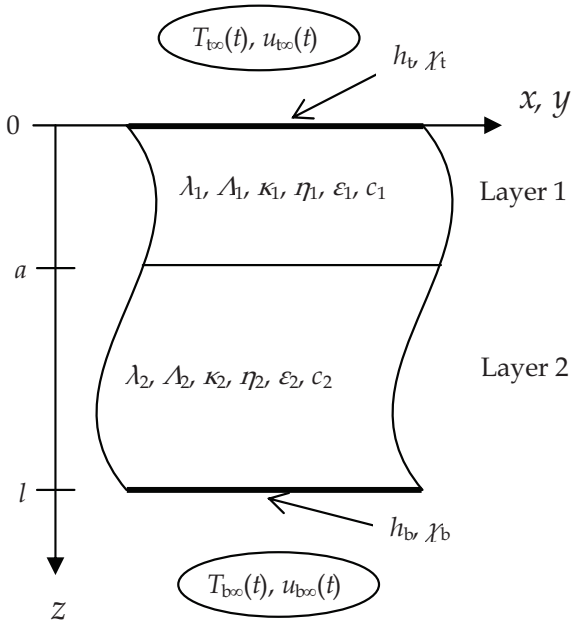

Fig. 1. Physical model and coordinate system

For the one-dimensional case shown in Fig.1, heat and moisture move along the z axis only. When the effect of the moisture content (or potential) gradient in the energy equation is

neglected, the transient heat and moisture diffusion equations for the *i*th layer (*i* = 1, 2) are written in dimensionless form as follows (Lykov and Mikhailov, 1965):

$$\frac{1}{\bar{\kappa}_i}\frac{\partial \bar{T}_i(Z,\tau)}{\partial \tau} = \frac{\partial^2 \bar{T}_i(Z,\tau)}{\partial Z^2} \quad \tau > 0, \quad i = 1, 2, \tag{1a}$$

$$\frac{1}{L_i}\frac{\partial \bar{u}_i(Z,\tau)}{\partial \tau} = \frac{\partial^2 \bar{u}_i(Z,\tau)}{\partial Z^2} - P_i\frac{\partial^2 \bar{T}_i(Z,\tau)}{\partial Z^2} \quad \tau > 0, \quad i = 1, 2. \tag{1b}$$

The one-way coupled system of equations given by Eqs. (1) is equivalent to the constant properties model presented by Fudym et al. (Fudym, et al., 2004). For constant moisture capacity, the moisture potential u_i and moisture content m_i are related by $m_i = c_i \cdot u_i$.
The initial conditions are defined as:

$$\bar{T}_i(Z,0) = 0\ ;\ \bar{u}_i(Z,0) = 0 \quad i = 1, 2. \tag{2a,b}$$

At the two sides of the plate (Z = 0 and Z = 1), the mass diffusion caused by the temperature and moisture gradients affects the mass balance (Chang and Weng, 2000 a). At the interface between two constitutive materials, the distributions of temperature and moisture potential are continuous and the moisture flux depending on both temperature and moisture potential gradients must be also continuous as well as the heat flux, provided that interfacial contact resistance is negligible. Therefore, the boundary and continuity conditions can be given as follows:

$$\frac{\partial \bar{T}_1(0,\tau)}{\partial Z} + B_t\left[\bar{T}_{t\infty}(\tau) - \bar{T}_1(0,\tau)\right] = 0\,, \tag{3a}$$

$$-\frac{\partial \bar{u}_1(0,\tau)}{\partial Z} + P_1\frac{\partial \bar{T}_1(0,\tau)}{\partial Z} - B_t^*\left[\bar{u}_{t\infty}(\tau) - \bar{u}_1(0,\tau)\right] = 0\,, \tag{3b}$$

$$\frac{\partial \bar{T}_2(1,\tau)}{\partial Z} - B_b\left[\bar{T}_{b\infty}(\tau) - \bar{T}_2(1,\tau)\right] = 0\,, \tag{3c}$$

$$-\frac{\partial \bar{u}_2(1,\tau)}{\partial Z} + P_2\frac{\partial \bar{T}_2(1,\tau)}{\partial Z} + B_b^*\left[\bar{u}_{b\infty}(\tau) - \bar{u}_2(1,\tau)\right] = 0\,, \tag{3d}$$

$$\bar{T}_1(Z_1,\tau) = \bar{T}_2(Z_1,\tau)\ ;\ \bar{u}_1(Z_1,\tau) = \bar{u}_2(Z_1,\tau)\,, \tag{4a,b}$$

$$\bar{\lambda}_1\frac{\partial \bar{T}_1(Z_1,\tau)}{\partial Z} = \bar{\lambda}_2\frac{\partial \bar{T}_2(Z_1,\tau)}{\partial Z}\,, \tag{4c}$$

$$-\bar{\Lambda}_1\frac{\partial \bar{u}_1(Z_1,\tau)}{\partial Z} + \bar{\Lambda}_1 P_1\frac{\partial \bar{T}_1(Z_1,\tau)}{\partial Z} = -\bar{\Lambda}_2\frac{\partial \bar{u}_2(Z_1,\tau)}{\partial Z} + \bar{\Lambda}_2 P_2\frac{\partial \bar{T}_2(Z_1,\tau)}{\partial Z}\,, \tag{4d}$$

where $Z_1 = a/l$, $\bar{\lambda}_i = \lambda_i / \lambda_{ref}$ and $\bar{\Lambda}_i = \Lambda_i / \Lambda_{ref}$. In existing analytical studies, the second terms of both sides of Eq. (4d) were omitted because of mathematical difficulties.

An analytical solution to the transient heat conduction problem expressed by Eqs. (1a), (2a), (3a), (3c), (4a) and (4c) has already been derived by Sugano et al. (Sugano, et al., 1993) as follows:

$$\overline{T}_i(Z,\tau)=\sum_{m=1}^{\infty}\phi_m(\tau)\left[A_{im}\cos\left(\frac{\gamma_m Z}{\sqrt{\overline{\kappa}_i}}\right)+B_{im}\sin\left(\frac{\gamma_m Z}{\sqrt{\overline{\kappa}_i}}\right)\right]+\sum_{j=1}^{2}(C_{ij}Z+D_{ij})V_j(\tau)\quad \text{for } i=1,2, \tag{5}$$

where

$$V_1(\tau)=-\overline{T}_{t\infty}(\tau)\ ;\ V_2(\tau)=\overline{T}_{b\infty}(\tau)\ , \tag{6a, b}$$

$$\phi_m(\tau)=\exp(-\gamma_m^2\tau)\left[g_m-\int_0^{\tau}\exp(\gamma_m^2 t)\sum_{j=1}^{2}f_{mj}\frac{\mathrm{d}V_j(t)}{\mathrm{d}t}\mathrm{d}t\right]. \tag{7}$$

The procedure for determining the eigenvalues γ_m (m = 1, 2,…) and the expansion coefficients g_m and f_{mj} (j = 1, 2) can be found in (Sugano, et al., 1993). The constants A_{im}, B_{im}, C_{ij} and D_{ij} in Eq. (5) are determined from the boundary and continuity conditions, Eqs. (3a), (3c), (4a) and (4c).

Rewriting Eq. (1b) with Eq. (5) yields

$$\frac{1}{L_i}\frac{\partial\overline{u}_i(Z,\tau)}{\partial\tau}=\frac{\partial^2\overline{u}_i(Z,\tau)}{\partial Z^2}+Q_i(Z,\tau)\quad \text{for } i=1,2, \tag{8}$$

where

$$Q_i(Z,\tau)=\frac{P_i}{\overline{\kappa}_i}\sum_{m=1}^{\infty}\gamma_m^2\phi_m(\tau)\left[A_{im}\cos\left(\frac{\gamma_m Z}{\sqrt{\overline{\kappa}_i}}\right)+B_{im}\sin\left(\frac{\gamma_m Z}{\sqrt{\overline{\kappa}_i}}\right)\right]. \tag{9}$$

The transient moisture diffusion problem for a composite medium represented by Eqs. (2b), (3b), (3d), (4b), (4d) and (8) is analysed by extending the ideas in an integral transform technique—Vodicka's method (Vodicka, 1955). Using this method, the solution to the moisture diffusion problem is obtained as

$$\overline{u}_i(Z,\tau)=\sum_{m=1}^{\infty}\psi_m(\tau)R_{im}(Z)+\sum_{j=1}^{3}F_{ij}(Z)W_j(\tau)\ ,\quad i=1,2, \tag{10}$$

with the following functions:

$$F_{ij}(Z)=C_{ij}^{*}Z+D_{ij}^{*}\ ,\quad j=1,2,3, \tag{11}$$

$$W_1(\tau)=\frac{P_1}{B_{\mathrm{t}}^{*}}\frac{\partial\overline{T}_1(0,\tau)}{\partial Z}-\overline{u}_{t\infty}(\tau)\ \text{ for }\ B_{\mathrm{t}}^{*}\neq 0\ ,\quad W_1(\tau)=0\ \text{ for }\ B_{\mathrm{t}}^{*}=0\ , \tag{12a}$$

$$W_3(\tau)=\frac{P_2}{B_{\mathrm{b}}^{*}}\frac{\partial\overline{T}_2(1,\tau)}{\partial Z}+\overline{u}_{b\infty}(\tau)\ \text{ for }\ B_{\mathrm{b}}^{*}\neq 0\ ,\quad W_3(\tau)=0\ \text{ for }\ B_{\mathrm{b}}^{*}=0\ , \tag{12b}$$

$$W_2(\tau) = \bar{\Lambda}_1 P_1 \frac{\partial \bar{T}_1(Z_1,\tau)}{\partial Z} - \bar{\Lambda}_2 P_2 \frac{\partial \bar{T}_2(Z_1,\tau)}{\partial Z}. \tag{12c}$$

The constants C_{ij}^* and D_{ij}^* are determined from the following relationships:

$$F_{1j}(Z_1) - F_{2j}(Z_1) = 0, \quad j = 1, 2, 3, \tag{13a}$$

$$\bar{\Lambda}_1 \frac{\mathrm{d}F_{1j}(Z_1)}{\mathrm{d}Z} - \bar{\Lambda}_2 \frac{\mathrm{d}F_{2j}(Z_1)}{\mathrm{d}Z} = \delta_{2,j} \quad j = 1, 2, 3, \tag{13b}$$

$$\frac{\mathrm{d}F_{1j}(0)}{\mathrm{d}Z} - B_{\mathrm{t}}^* F_{1j}(0) = B_{\mathrm{t}}^* \delta_{1,j}, \quad j = 1, 2, 3, \tag{13c}$$

$$\frac{\mathrm{d}F_{2j}(1)}{\mathrm{d}Z} + B_{\mathrm{b}}^* F_{2j}(1) = B_{\mathrm{b}}^* \delta_{3,j}, \quad j = 1, 2, 3. \tag{13d}$$

$R_{im}(Z)$ is the solution to the eigenvalue problem corresponding to Eqs. (3b), (3d), (4b), (4d) and (8) and is given as follows:

$$R_{im}(Z) = A_{im}^* \cos\left(\frac{\mu_m Z}{\sqrt{L_i}}\right) + B_{im}^* \sin\left(\frac{\mu_m Z}{\sqrt{L_i}}\right), \tag{14}$$

with μ_m being an eigenvalue. The conditions necessary to determine the unknown constants A_{im}^* and B_{im}^* can be obtained by substituting Eqs. (10)−(14) into Eqs. (3b), (3d), (4b) and (4d) as follows:

$$\frac{\mathrm{d}R_{1m}(0)}{\mathrm{d}Z} - B_{\mathrm{t}}^* R_{1m}(0) = 0, \tag{15a}$$

$$\frac{\mathrm{d}R_{2m}(1)}{\mathrm{d}Z} + B_{\mathrm{b}}^* R_{2m}(1) = 0, \tag{15b}$$

$$R_{1m}(Z_1) = R_{2m}(Z_1), \tag{15c}$$

$$\bar{\Lambda}_1 \frac{\mathrm{d}R_{1m}(Z_1)}{\mathrm{d}Z} = \bar{\Lambda}_2 \frac{\mathrm{d}R_{2m}(Z_1)}{\mathrm{d}Z}. \tag{15d}$$

The eigenvalues μ_m (m = 1, 2,…) are obtained from the condition under which all the A_{im}^* and B_{im}^* values are nonzero and are, therefore, positive roots of the following transcendental equation:

$$\mathbf{G} \cdot \mathbf{E} \cdot \mathbf{a} = 0, \tag{16}$$

where

$$\mathbf{G}=\begin{bmatrix}-B_{\mathrm{t}}^{*} & \dfrac{\mu_m}{\sqrt{L_1}}\end{bmatrix};\ \mathbf{E}=\mathbf{C}^{-1}\cdot\mathbf{D}, \tag{17a,b}$$

$$\mathbf{C}=\begin{bmatrix}\cos\left(\dfrac{\mu_m Z_1}{\sqrt{L_1}}\right) & \sin\left(\dfrac{\mu_m Z_1}{\sqrt{L_1}}\right)\\ -\bar{\Lambda}_1\dfrac{\mu_m}{\sqrt{L_1}}\sin\left(\dfrac{\mu_m Z_1}{\sqrt{L_1}}\right) & \bar{\Lambda}_1\dfrac{\mu_m}{\sqrt{L_1}}\cos\left(\dfrac{\mu_m Z_1}{\sqrt{L_1}}\right)\end{bmatrix}, \tag{17c}$$

$$\mathbf{D}=\begin{bmatrix}\cos\left(\dfrac{\mu_m Z_1}{\sqrt{L_2}}\right) & \sin\left(\dfrac{\mu_m Z_1}{\sqrt{L_2}}\right)\\ -\bar{\Lambda}_2\dfrac{\mu_m}{\sqrt{L_2}}\sin\left(\dfrac{\mu_m Z_1}{\sqrt{L_2}}\right) & \bar{\Lambda}_2\dfrac{\mu_m}{\sqrt{L_2}}\cos\left(\dfrac{\mu_m Z_1}{\sqrt{L_2}}\right)\end{bmatrix}, \tag{17d}$$

$$\mathbf{a}=\begin{bmatrix}\dfrac{\mu_m}{\sqrt{L_2}}\cos\left(\dfrac{\mu_m}{\sqrt{L_2}}\right)+B_{\mathrm{b}}^{*}\sin\left(\dfrac{\mu_m}{\sqrt{L_2}}\right)\\ \dfrac{\mu_m}{\sqrt{L_2}}\sin\left(\dfrac{\mu_m}{\sqrt{L_2}}\right)-B_{\mathrm{b}}^{*}\cos\left(\dfrac{\mu_m}{\sqrt{L_2}}\right)\end{bmatrix}. \tag{17e}$$

The time function $\psi_m(\tau)$ is expressed as

$$\psi_m(\tau)=\exp(-\mu_m^2\tau)\left\{g_m^{*}+\int_0^{\tau}\exp(\mu_m^2 t)\left[q_m(t)-\sum_{j=1}^{3}f_{mj}^{*}\frac{\mathrm{d}W_j(t)}{\mathrm{d}t}\right]\mathrm{d}t\right\}, \tag{18}$$

where the expansion coefficients g_m^{*}, $q_m(\tau)$ and f_{mj}^{*} are given with $Z_0 = 0$ and $Z_2 = 1$ by

$$g_m^{*}=-\frac{\displaystyle\sum_{i=1}^{2}\frac{\bar{\Lambda}_i}{L_i}\int_{Z_{i-1}}^{Z_i}\left[\sum_{j=1}^{3}F_{ij}(z)W_j(0)\right]R_{im}(z)\mathrm{d}z}{\displaystyle\sum_{i=1}^{2}\frac{\bar{\Lambda}_i}{L_i}\int_{Z_{i-1}}^{Z_i}\left[R_{im}(z)\right]^2\mathrm{d}z}, \tag{19a}$$

$$q_m(\tau)=\frac{\displaystyle\sum_{i=1}^{2}\bar{\Lambda}_i\int_{Z_{i-1}}^{Z_i}Q_i(z,\tau)R_{im}(z)\mathrm{d}z}{\displaystyle\sum_{i=1}^{2}\frac{\bar{\Lambda}_i}{L_i}\int_{Z_{i-1}}^{Z_i}\left[R_{im}(z)\right]^2\mathrm{d}z}, \tag{19b}$$

$$f_{mj}^{*}=\frac{\displaystyle\sum_{i=1}^{2}\frac{\bar{\Lambda}_i}{L_i}\int_{Z_{i-1}}^{Z_i}F_{ij}(z)R_{im}(z)\mathrm{d}z}{\displaystyle\sum_{i=1}^{2}\frac{\bar{\Lambda}_i}{L_i}\int_{Z_{i-1}}^{Z_i}\left[R_{im}(z)\right]^2\mathrm{d}z}. \tag{19c}$$

In order to obtain Eqs. (18) and (19), the following orthogonal relationship with discontinuous weight functions in terms of the eigenfunction $R_{im}(z)$ was used:

$$\sum_{i=1}^{2} \frac{\overline{\Lambda}_i}{L_i} \int_{Z_{i-1}}^{Z_i} R_{im}(z) R_{ik}(z) \mathrm{d}z = \begin{cases} \text{const.} & (m = k) \\ 0 & (m \neq k) \end{cases}. \tag{20}$$

3. Numerical results and discussion

Numerical calculations are performed for a double-layer plate composed of a T300/5208 composite (layer 1) and another hygroscopic material (layer 2). The thickness of both layers is assumed identical, that is, $Z_1 = 0.5$. The material properties are listed as follows (Chang and Weng, 2000 b, Chen, et al., 1992, Sih, et al., 1986, Yang, et al., 2006):

$$\kappa_1 = 5\kappa_2 = 2.16\times10^{-5}\ \mathrm{m^2/s}, \quad \eta_1 = \eta_2 = 2.16\times10^{-6}\ \mathrm{m^2/s},$$

$$c_1 = 5c_2 = 0.01\ \mathrm{kg/(kg{\cdot}°M)}, \quad \lambda_1 = 5\lambda_2 = 0.65\ \mathrm{W/(m{\cdot}K)},$$

$$\varepsilon_1 = \varepsilon_2 = 2.0\ \mathrm{°M/K}, \quad \Lambda_1 = \Lambda_2 = 2.2\times10^{-8}\ \mathrm{kg/(m{\cdot}s{\cdot}°M)}.$$

The material properties in the layer 1 are used as reference for the dimensionless quantities. We consider the case in which the same temperature and moisture potential values are prescribed at both external surfaces of the double-layer plate, i.e., $B_\mathrm{t} = B_\mathrm{b} = B_\mathrm{t}^* = B_\mathrm{b}^* = \infty$, $\overline{T}_{\mathrm{t}\infty} = \overline{T}_{\mathrm{b}\infty} = 1$ and $\overline{u}_{\mathrm{t}\infty} = \overline{u}_{\mathrm{b}\infty} = 1$ for $(u_0 - u_\mathrm{ref})/(T_\mathrm{ref} - T_0) = 0.82$ °M/K (Yang, et al., 2006). The number of terms in the infinite series in Eqs. (5) and (10) is taken as 100, which is used for the verification of sufficient convergence of the numerical results. Table 1 lists the specific values of up to the fifth eigenvalue for this situation.

γ_1	γ_2	γ_3	γ_4	γ_5
2.1774	3.7028	5.7323	8.0017	9.6311
μ_1	μ_2	μ_3	μ_4	μ_5
0.99344	1.9869	2.9803	3.9738	4.9672

Table 1. The first five eigenvalues for temperature and moisture fields

Figure 2 illustrates the transient behaviour of temperature and moisture potential distributions. In the moisture potential distribution, numerical results based on the simple continuity condition in which the second terms of both sides of Eq. (4d) are omitted are also shown in order to investigate the effects of the continuity condition of moisture flux. It is observed from Fig. 2(a) that the temperature distribution increases monotonously with time. The difference between temperature gradients at the layer interface in different layers increases with time in the beginning, then starting to decline at a time to vanish ultimately.

On the other hand, the variation in the moisture potential is not monotonous owing to the effect of the second derivative of temperature (see Eq. (1b)). Since the second derivative is positive throughout the plate thickness, as shown in Fig. 2(a), the temperature acts as moisture sink in the moisture potential field. Therefore, the values of moisture potential decrease from the initial state ($\overline{u} = 0$) near the thickness centre, where rapid supply of

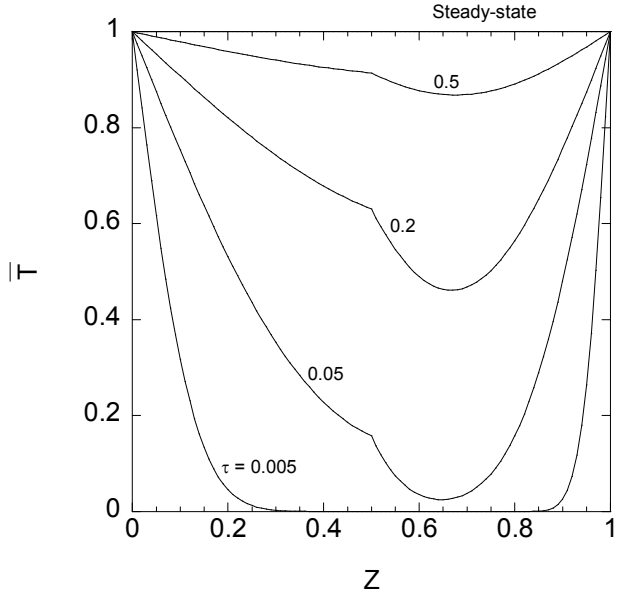

(a)

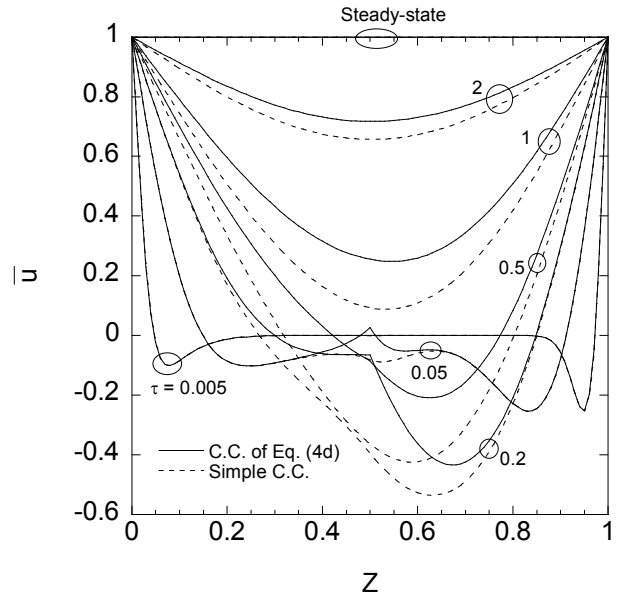

(b)

Fig. 2. Transient behaviour of (a) temperature and (b) moisture potential in a double-layer plate

moisture flux from both external surfaces is not expected. Subsequently, the strength of the moisture sink weakens as the temperature distribution approaches the steady-state one and the effect of its second derivative wanes. As a result, the moisture potential increases simply to the steady state ($\bar{u} = 1$).

The effects of the continuity condition on the moisture potential distributions are pronounced. In the case of Eq. (4d), which stipulates the exact continuity of moisture flux at the interface, the values of the moisture potential are higher than the counterparts at all the time instants. Of special note is the singular distribution adjacent to the layer interface, as observed for $\tau = 0.05$. This phenomenon, in which the sign of moisture potential gradient changes at the layer interface, can also be found by finite element analyses (Khoshbakht and Lin, 2010, Khoshbakht, et al., 2009). Figure 2(b) demonstrates that the usage of the simplified continuity condition precludes prediction of that phenomenon. It is obvious that expansion/shrinkage stresses computed based on both moisture potential distributions are substantially different from each other. Hence, for an accurate prediction of heat and moisture diffusion behaviour and resulting hygrothermal stresses, it is of great importance to take into account the coupling term in the continuity condition as well as that in the governing equation.

4. Conclusions

In this chapter, analytical solutions have been presented for the transient temperature and moisture fields in a double-layer plate subjected to time-varying hygrothermal loadings at the external surfaces. The effects of the coupling included in the continuity condition of moisture flux at the layer interface on the distribution of moisture potential (or moisture content) in the plate have been quantitatively evaluated. Numerical results have shown that, in predicting transient heat and moisture diffusion behavior in a layered body, neglecting the moisture flux component due to temperature gradient in the continuity conditions of moisture flux at layer interfaces may result in a significant error.

5. Acknowledgements

This work was financially supported by KAKENHI, a Grant-in-Aid for Encouragement of Scientists (14919018). Prof. Y. Sugano of Iwate University is gratefully acknowledged for many fruitful discussions.

6. References

Chang, W. J. (1994). Transient hygrothermal responses in a solid cylinder by linear theory of coupled heat and moisture. *Applied Mathematical Modelling* 18, 467-473.

Chang, W. J.; Chen, T. C. & Weng, C. I. (1991). Transient hygrothermal stresses in an infinitely long annular cylinder: coupling of heat and moisture. *Journal of Thermal Stresses* 14, 439 - 454.

Chang, W. J. & Weng, C. I. (1997). An analytical solution of a transient hygrothermal problem in an axisymmetric double-layer annular cylinder by linear theory of coupled heat and moisture. *Applied Mathematical Modelling* 21, 721-734.

Chang, W. J. & Weng, C. I. (2000 a). An analytical solution to coupled heat and moisture diffusion transfer in porous materials. *International Journal of Heat and Mass Transfer* 43, 3621-3632.

Chang, W. J. & Weng, C. I. (2000 b). Small time behavior of hygrothermal stresses in axisymmetric double-layer cylinders. *Journal of Thermal Stresses* 23, 15 - 46.

Chen, T. C.; Weng, C. I. & Chang, W. J. (1992). Transient hygrothermal stresses induced in general plane problems by theory of coupled heat and moisture. *Journal of Applied Mechanics* 59, S10-S16.

Fudym, O.; Batsale, J. C.; Santander, R. & Bubnovich, V. (2004). Analytical solution of coupled diffusion equations in semi-infinite media. *Journal of Heat Transfer* 126, 471-475.

Hartranft, R. J. & Sih, G. C. (1980 a). The influence of coupled diffusion of heat and moisture on the state of stress in a plate. *Mechanics of Composite Materials* 16, 44-56.

Hartranft, R. J. & Sih, G. C. (1980 b). The influence of the Soret and Dufour effects on the diffusion of heat and moisture in solids. *International Journal of Engineering Science* 18, 1375-1383.

Hartranft, R. J. & Sih, G. C. (1981). Stresses induced in an infinite medium by the coupled diffusion of heat and moisture from a spherical hole. *Engineering Fracture Mechanics* 14, 261-287.

Khoshbakht, M. & Lin, M. W. (2010). A finite element model for hygro-thermo-mechanical analysis of masonry walls with FRP reinforcement. *Finite Elements in Analysis and Design* 46, 783-791.

Khoshbakht, M.; Lin, M. W. & Feickert, C. A. (2009). A finite element model for hygrothermal analysis of masonry walls with FRP reinforcement. *Finite Elements in Analysis and Design* 45, 511-518.

Komai, K.; Minoshima, K. & Shiroshita, S. (1991). Hygrothermal degradation and fracture process of advanced fibre-reinforced plastics. *Materials Science and Engineering*: A 143, 155-166.

Lykov, A. V. & Mikhailov, Y. A. (1965). *Theory of heat and mass transfer*, Israel Program for Scientific Translations, Jerusalem.

Sih, G. C. (1983). Transient hygrothermal stresses in plates with and without cavities. *Fibre Science and Technology* 18, 181-201.

Sih, G. C.; Michopoulos, J. G. & Chou, S. C. (1986). *Hygrothermoelasticity*, Martinus Nijhoff Publishers, Dordrecht.

Sih, G. C. & Ogawa, A. (1982). Transient thermal change on a solid surface: coupled diffusion of heat and moisture. *Journal of Thermal Stresses* 5, 265 - 282.

Sih, G. C.; Ogawa, A. & Chou, S. C. (1981). Two-dimensional transient hygrothermal stresses in bodies with circular cavities: moisture and temperature coupling effects. *Journal of Thermal Stresses* 4, 193 - 222.

Sih, G. C.; Shih, M. T. & Chou, S. C. (1980). Transient hygrothermal stresses in composites: Coupling of moisture and heat with temperature varying diffusivity. *International Journal of Engineering Science* 18, 19-42.

Sugano, Y. & Chuuman, Y. (1993 a). An analytical solution of hygrothemoelastic problem in multiply connected region. *Transactions of the Japan Society of Mechanical Engineers*. A 59, 1519-1525.

Sugano, Y. & Chuuman, Y. (1993 b). Analytical solution of transient hygrothermoelastic problem due to coupled heat and moisture diffusion in a hollow circular cylinder. *Transactions of the Japan Society of Mechanical Engineers*. A 59, 1956-1963.

Sugano, Y.; Morishita, H. & Tanaka, K. (1993). An analytical solution for transient thermal stress in a functionally gradient plate with arbitrary nonhomogeneities and thermal boundary conditions: material properties determined by fuzzy inference. *Transactions of the Japan Society of Mechanical Engineers*. A 59, 2666-2673.

Vodicka, V. (1955). Linear heat conduction in laminated bodies. *Mathematische Nachrichten* 14, 47-55.

Yang, Y. C.; Chu, S. S.; Lee, H. L. & Lin, S. L. (2006). Hybrid numerical method applied to transient hygrothermal analysis in an annular cylinder. *International Communications in Heat and Mass Transfer* 33, 102-111.

24

Frictional Heating in the Strip-Foundation Tribosystem

Aleksander Yevtushenko and Michal Kuciej
Bialystok University of Technology
Poland

1. Introduction

During the process of braking the pad is pressed to the disc. As a result of friction on the contact surface the kinetic energy transforms into heat. Elements of brakes are heated and, hence, the conditions of operation of the friction pads become less favorable: their wear intensifies and the friction coefficient decreases, which may lead to emergency situations (Fasekas, 1953; Ho at al., 1974). Thus, the correct calculation of temperature is one of the most important challenges in the design of brakes (YBo at al., 2002; Chichinadze at al., 1979; Balakin and Sergienko, 1999).

The heat conduction problems of friction are nowadays formulated in two variants. In the first one, the elements of friction couple are considered separately and the heat flow intensities are set on each of the contact surfaces in such a way that their sum equals the specific power of friction (Ling, 1973; Burton, 1975; Archard and Rowntree, 1988; Kannel and Barber, 1989; Yevtushenko at al., 1995). For this purpose, the heat participation factor is introduced which is found experimentally or by empirical formulas (Block, 1937; Jaeger, 1932). It is the statement that gives the solution of the heat conduction problem of friction for the foundation with a composite strip (Matysiak at al., 2004; Yevtushenko at al., 2007a) and the heat conduction problem for the braking of a massive body coated with either a homogeneous (Evtushenko at al., 2005) or a composite (Matysiak at al., 2007) strip. The thermoelastic state resulted from the heating of the piecewise-homogeneous body consisting of a semi-infinite foundation and a strip by the heat pulse of a finite duration is studied in article (Yevtushenko at al., 2005).

Another variant of the statement of heat conduction problems of friction is based on the simultaneous solution of the heat conduction equations for both friction elements followed by the determination of the heat flows intensities on their heating (Cameron at al., 1965; Barber and Comminou, 1989; Olesiak at al., 1997; Evtushenko and Pyr'ev, 2000; Bauzin and Laraqi, 2004). In such statement the problems of transient frictional heating in cold rolling of metals (Matysiak at al., 1998), the heat transfer in friction welding of cylindrical rods with different diameters (Kahveci at al., 2005) and the fast-moving heating on the external surface of the ring due to friction of two rotating pins (Yevtushenko and Tolstoj-Sienkiewicz, 2006) were analyzed. The analytical solution of a boundary-value problem of heat conduction for tribosystem, consisting of the homogeneous semi-space, sliding uniformly on a surface of the strip deposited on a semi-infinite substrate, was obtained in paper (Yevtushenko and Kuciej, 2009a).

Heat conditions on the friction surface of two elastic bodies were formulated in the contemporary form for the first time by F. Ling (1959). He thought that in every point on the contact surfaces, the temperature of bodies being in contact is equal. Whereas the sum of heat flow intensities directed from friction surface to interior of each elements equals the power of friction (the perfect thermal contact is assumed). Such approach to statement of the contact problem with heat generation due to friction taken under consideration, assumes temperature dependence only on thermo-physical properties of friction pair materials, on cooling conditions and on power of friction.

It is well known that on friction processes, wear and heat generation, the significant influence have topographical parameters of surfaces being in contact and characteristics of so called "third body" – thin subsurface strips having properties partly physical and mechanical which differ from friction pair materials properties (Johnson, 1987; Godet, 1990; Iordanoff at al., 2002). Thermal contact of bodies, when temperature on the friction surface has jumped, is called imperfect (Barber and Comminou, 1989). The theoretical model of calculation of the contact characteristics (the temperature, the wear and the speed of sliding) during braking is based usually on the assumption that the friction elements can be treated as semi-spaces. The solution to the problem of heat generation during braking with a uniform retardation for two semi-spaces in perfect contact was obtained in articles (Grylytskyy, 1996; Yevtushenko at al., 1999), and in imperfect contact – in articles (Levitskij and Onyshkievich, 1999; Nosko and Nosko, 2006). The contact temperature, the value of wear, and the speed of sliding during braking, for general experimental dependences of the coefficients of friction and wear on the temperature were studied in article (Olesiak at al., 1997).

Solutions to the transient heat conduction problems for a massive body (the semi-space) coated with either a homogeneous, or a composite strip were suggested in articles (Yevtushenko at al., 2007a; Matysiak at al., 2007; Evtushenko at al., 2005). The thermal stresses resulted from the heating of the piecewise-homogeneous body, consisting of a semi-infinite foundation and a strip, by the heat pulse of a finite duration was studied in article (Yevtushenko at al., 2007b).

2. Evolution of the contact pressure and sliding speed during braking

The nature of change in time of the specific load on the nominal contact depends on a loading system (pneumatic, hydraulic, mechanical, electromagnetic), and a change of loading during braking (pulse braking, anti-lock braking system, automatic stability control system, etc.). Generally, the evolution of the pressure and movement during braking can be described by the equations (Chichinadze at al., 1979; Ginsburg and Chichinadze, 1978; Chichinadze, 1967)

$$p(\tau) = p_0 p^*(\tau)\ ,\ p^*(\tau) = (1 - e^{-\tau/\tau_m})[1 + a\sin(\omega_p \tau)]\ ,\ 0 \le \tau \le \tau_s\ ,\ a \ge 0\ ,\ \omega_p > 0\ , \tag{2.1}$$

$$\frac{2W_0}{V_0^2}\frac{dV(\tau)}{d\tau} = -fp(\tau)A_k\ ,\ 0 \le \tau \le \tau_s\ ,\ V(0) = V_0\ . \tag{2.2}$$

$$\tau = \frac{k_s t}{d^2}\ ,\ \tau_s = \frac{k_s t_s}{d^2} \tag{2.3}$$

where t - time; t_s - braking time; p - pressure; p_0 - nominal pressure; f - coefficient of friction; k_s - thermal diffusivity of a strip; A_k - nominal contact area; d - strip thickness; W_0 - the initial kinetic energy; V - sliding speed; V_0 - initial sliding speed; a - amplitude of pressure oscillations; ω_p - frequency of pressure oscillations.
Substituting the pressure of (2.1) to the right side of the equation (2.2), after integration we obtain

$$V^*(\tau) = V_1^*(\tau) - \frac{a}{\tau_s^0} V_2^*(\tau),\ 0 \le \tau \le \tau_s \tag{2.4}$$

where

$$V_1^*(\tau) = 1 - \frac{\tau}{\tau_s^0} + \frac{\tau_m}{\tau_s^0}(1 - e^{-\tau/\tau_m}), \tag{2.5}$$

$$V_2^*(\tau) = \frac{1}{\omega_p}[1 - \cos(\omega_p \tau)] + \frac{1}{\tau_m^{-2} + \omega_p^2}\{[\tau_m^{-1} \sin(\omega_p \tau) + \omega_p \cos(\omega_p \tau)] e^{-\tau/\tau_m} - \omega_p\}, \tag{2.6}$$

$$\tau_s^0 = \frac{k_s t_s^0}{d^2},\ \tau_m = \frac{k_s t_m}{d^2}, \tag{2.7}$$

t_m - duration of the increase of the loading from zero to maximum value p_0, t_s^0 - duration of braking in the case of constant pressure.
At the stop time moment $\tau = \tau_s$ from equations (2.4)–(2.7) we find the non-linear equation of the dimensionless time of braking τ_s in the form

$$\tau_s^0 V_1^*(\tau_s) = a V_2^*(\tau_s). \tag{2.8}$$

If the increase in pressure is monotonically without oscillations (a = 0), then the equations (2.1), (2.4) and (2.8) take the form

$$p^*(\tau) = 1 - e^{-\tau/\tau_m},\ V^*(\tau) = 1 - \frac{\tau}{\tau_s^0} + \frac{\tau_m}{\tau_s^0}(1 - e^{-\tau/\tau_m}),\ 0 \le \tau \le \tau_s. \tag{2.9}$$

If pressure reaches its maximal value p_0 immediately ($\tau_m \to 0$), then from equations (2.9) it follows that

$$p^*(\tau) = 1,\ V^*(\tau) = 1 - \frac{\tau}{\tau_s^0},\ 0 \le \tau \le \tau_s = \tau_s^0, \tag{2.10}$$

i.e. parameter τ_s^0 (2.7) may be treated as the dimensionless duration of braking at the constant deceleration.
The thermal behavior of a brake system, that consist of a shoe and a drum, for three specified braking actions: the impulse, unit step and trigonometric stopping actions was investigated in article (Naji and Al-Nimr, 2001). Most often for an analytical determination of average temperature in the pad/disc system three calculation schemes are used: two semi-spaces, a plane-parallel strip/the semi-space (the foundation), and two plane-parallel

strips. The corresponding thermal problems of friction can be formulated as one-dimensional boundary-value problems of heat conductivity of parabolic type. The temperature analysis for two homogeneous semi-spaces with the pressure increasing monotonically during braking, in accordance with equation (2.10), has been performed in the articles (Yevtushenko at al., 1999; Olesiak at al., 1997). The corresponding solution for two plane-parallel strips has been obtained in article (Pyryev and Yevtushenko, 2000).

3. Statement of the problem

In the general case, the problem of contact interaction of a pad (a plane-parallel strip) and a disc (a semi-infinite foundation) can be formulated as: the time-dependent normal pressure $p(\tau)$, $0 \le \tau \le \tau_s$ (2.1) in the direction of the z-axis of the Cartesian system of coordinates $Oxyz$ is applied to the upper surface of the strip and to the infinity in semi-space (Fig. 1). The strip slides with the speed $V(\tau)$, $0 \le \tau \le \tau_s$ (2.4)–(2.7) in the direction of the y-axis on the surface of the semi-space. Due to friction, the heat is generated on a surface of contact $z = 0$, and the elements are heated. The sum of heat fluxes, directed from a surface of contact inside each bodies, is equal to specific friction power (Barber and Comminou, 1989)

$$q(\tau) = q_0 q^*(\tau),\ q^*(\tau) = p^*(\tau)V^*(\tau),\ q_0 = fVp_0\,, \tag{3.1}$$

where f is a coefficient of friction, and the functions $p^*(\tau)$ and $V^*(\tau)$ have the form (2.1) and (2.4), respectively. Between contact surfaces of the strip and the foundation the heat transfer takes place with a coefficient of thermal conductivity of contact h. The strip surface $z = d$ is under condition of convective heat exchange with a coefficient of heat exchange h_s.

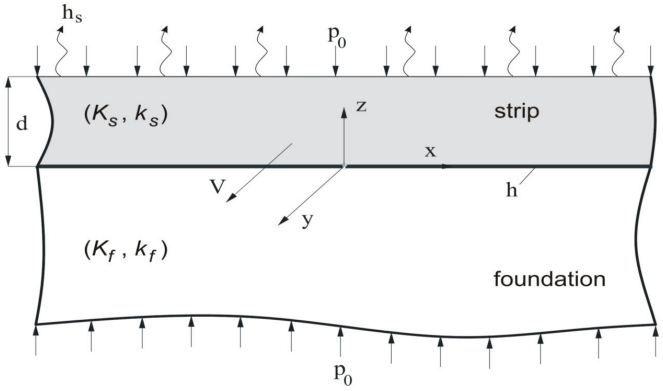

Fig. 1. Scheme of the problem

All values and the parameters concerning the strip and foundation will have bottom indexes "s" and "f", respectively.

In accordance with the above-mentioned assumptions, the heat conductivity problem at friction takes form:

$$\frac{\partial^2 T^*(\zeta,\tau)}{\partial \zeta^2} = \frac{\partial T^*(\zeta,\tau)}{\partial \tau},\quad 0 < \zeta < 1,\ 0 \le \tau \le \tau_s\,, \tag{3.2}$$

$$\frac{\partial^2 T^*(\zeta,\tau)}{\partial\zeta^2}=\frac{1}{k^*}\frac{\partial T^*(\zeta,\tau)}{\partial\tau},\ -\infty<\zeta<0,\ 0\le\tau\le\tau_s, \tag{3.3}$$

$$K^*\left.\frac{\partial T^*}{\partial\zeta}\right|_{\zeta=0-}-\left.\frac{\partial T^*}{\partial\zeta}\right|_{\zeta=0+}=q^*(\tau),\quad 0\le\tau\le\tau_s, \tag{3.4}$$

$$K^*\left.\frac{\partial T^*}{\partial\zeta}\right|_{\zeta=0-}+\left.\frac{\partial T^*}{\partial\zeta}\right|_{\zeta=0+}=\mathrm{Bi}\,[T^*(0+,\tau)-T^*(0-,\tau)],\ 0\le\tau\le\tau_s, \tag{3.5}$$

$$\left.\frac{\partial T^*}{\partial\zeta}\right|_{\zeta=1}+\mathrm{Bi}_s T^*(1,\tau)=0,\ 0\le\tau\le\tau_s, \tag{3.6}$$

$$T^*(\zeta,\tau)\to 0,\quad \zeta\to-\infty,\quad 0\le\tau\le\tau_s, \tag{3.7}$$

$$T^*(\zeta,0)=0,\quad -\infty<\zeta\le 1, \tag{3.8}$$

where

$$\zeta=\frac{z}{d},\ \mathrm{Bi}_s=\frac{h_s d}{K_s},\ K^*=\frac{K_f}{K_s},\ k^*=\frac{k_f}{k_s},\ T_0=\frac{q_0 d}{K_s},\ T^*_{s,f}=\frac{T_{s,f}}{T_0}, \tag{3.9}$$

K - coefficient of thermal conductivity; k - coefficient of thermal diffusivity; T - temperature; Z - spatial coordinate, q - has the form (3.1).

4. Heat generation at constant friction power. Perfect contact.

In this Chapter we consider the heat conduction problem of friction (3.2)-(3.8) of the plane-parallel strip and the semi-space on the following assumptions: the elements are compressed with the constant pressure $p(\tau)$ (2.1) ($p^*(\tau)$=1), the strip slides with the constant velocity $V = V_0$ (V^* = 1), and in the boundary condition (3.5) Bi→∞ (perfect thermal contact – i.e. $T_f(0,\tau)=T_S(0,\tau)$. From the assumptions above it follows that the intensity of the frictional heat fluxes directed into each component of friction pair is equal to the specific friction power $q_0 = fVp_0$ (3.1) ($q^*(\tau)$=1).

4.1 Solution to the problem

By applying the Laplace integral transform to the equations (3.2)–(3.8) with respect to the dimensionless time τ (Sneddon, 1972)

$$L[T_{s,f}(\zeta,\tau);p]\equiv\overline{T}^*_{s,f}(\zeta,p)=\int_0^\infty T^*_{s,f}(\zeta,\tau)e^{-p\tau}d\tau, \tag{4.1}$$

we obtain

$$\frac{d^2\overline{T}^*_s(\zeta,p)}{d\zeta^2}-p\overline{T}^*_s(\zeta,p)=0,\quad 0<\zeta<1, \tag{4.2}$$

$$\frac{d^2\overline{T}_f^*(\zeta,p)}{d\zeta^2}-\frac{p}{k^*}\overline{T}_f^*(\zeta,p)=0,\quad -\infty<\zeta<0, \tag{4.3}$$

$$K^*\frac{d\overline{T}_f}{d\zeta}\bigg|_{\zeta=0-}-\frac{d\overline{T}_s}{d\zeta}\bigg|_{\zeta=0+}=\frac{1}{p}, \tag{4.4}$$

$$\overline{T}_f^*(0,p)=\overline{T}_s^*(0,p), \tag{4.5}$$

$$\frac{d\overline{T}_s^*(\zeta,p)}{d\zeta}\bigg|_{\zeta=1}+\mathrm{Bi}_s\overline{T}_s^*(1,p)=0, \tag{4.6}$$

$$\overline{T}_f^*(\zeta,p)\to 0,\quad \zeta\to-\infty. \tag{4.7}$$

The solutions of the ordinary differential equations (4.2) and (4.3) at boundary conditions (4.4)–(4.7) have the form:

$$\overline{T}_s^*(\zeta,p)=\frac{\Delta_s(\zeta,p)}{p\sqrt{p}\,\Delta(p)},\quad 0\le\zeta\le 1, \tag{4.8}$$

$$\overline{T}_f^*(\zeta,p)=\frac{\Delta_f(\zeta,p)}{p\sqrt{p}\,\Delta(p)},\quad -\infty<\zeta\le 0, \tag{4.9}$$

where

$$\Delta_s(\zeta,p)=\sqrt{p}\,\mathrm{ch}[(1-\zeta)\sqrt{p}]+\mathrm{Bi}_s\,\mathrm{sh}[(1-\zeta)\sqrt{p}], \tag{4.10}$$

$$\Delta_f(\zeta,p)=[\sqrt{p}\,\mathrm{ch}(\sqrt{p})+\mathrm{Bi}_s\,\mathrm{sh}(\sqrt{p})]e^{\zeta\sqrt{\frac{p}{k^*}}}, \tag{4.11}$$

$$\Delta(p)=(\sqrt{p}+\varepsilon\,\mathrm{Bi}_s)\,\mathrm{sh}(\sqrt{p})+(\varepsilon\sqrt{p}+\mathrm{Bi}_s)\,\mathrm{ch}(\sqrt{p}), \tag{4.12}$$

$$\varepsilon=\frac{K_f}{K_s}\sqrt{\frac{k_s}{k_f}}, \tag{4.13}$$

where ε is a coefficient of thermal activity of foundation's material against strip's material.
Applying the inverse Laplace transform to equations (4.8)–(4.12), we obtain the dimensionless temperatures in the strip and in the foundation:

$$T_{s,f}^*(\zeta,\tau)=\frac{1}{2\pi i}\int_{\omega-i\infty}^{\omega+i\infty}\overline{T}_{s,f}^*(\zeta,p)e^{p\tau}\,dp,\tau\ge 0. \tag{4.14}$$

The integrals in equation (4.14) converge in semi-space Re p ≡ ω > 0. Presence $\sqrt{p}$ in exponents of equations (4.10)–(4.12) testifies that integrands (4.8) and (4.9) in solutions (4.14)

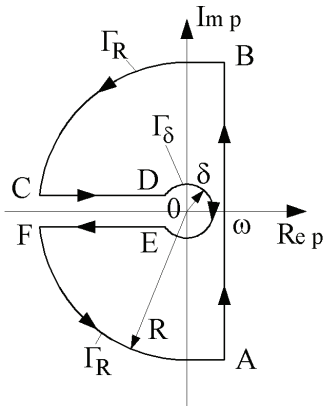

Fig. 2. Contour of integration.

and (4.15) have a branch point at the origin $p=0$. Therefore, a contour Γ of integration in formulas (4.14) and (4.15) shall be chosen as it is shown in Fig. 2. It consists of the straight line AB which is passing on distance ω parallel to imaginary axis Imp, the circles Γ_R and Γ_δ with centre O and radiuses R and δ respectively, and boundaries CD and EF a cut of a complex p-plane along negative real axis $\mathrm{Re}\,p$. Since the integrands (4.8) and (4.9) in solution (4.14) within the contour Γ have no singularities, by Cauchy's theorem (Sneddon, 1972):

$$\frac{1}{2\pi i}\oint_{\Gamma}\overline{T}_{s,f}(\zeta,p)e^{p\tau}dp\equiv\frac{1}{2\pi i}\int_{AB}+\frac{1}{2\pi i}\int_{BC}+\frac{1}{2\pi i}\int_{CD}+\frac{1}{2\pi i}\int_{\Gamma_\delta}+\frac{1}{2\pi i}\int_{EF}+\frac{1}{2\pi i}\int_{FA}=0\,. \tag{4.15}$$

On arcs BC and FA we have

$$\left|\frac{\Delta_{s,f}(p)}{p\sqrt{p}\,\Delta(p)}\right|\le\frac{const.}{p\sqrt{p}}\,, \tag{4.16}$$

and the conditions of a Jordan's lemma are carried out. Therefore, as $R\to\infty$ the corresponding integrals in equation (4.15) tend to zero and we obtain:

$$T^{*}_{s,f}(\zeta,\tau)=T^{*+}_{s,f}(\zeta,\tau)-T^{*-}_{s,f}(\zeta,\tau)-T^{*0}_{s,f}(\zeta,\tau)\,, \tag{4.17}$$

where

$$T^{*+}_{s,f}(\zeta,\tau)=\frac{1}{2\pi i}\int_{CD}\overline{T}^{*}_{s,f}(\zeta,p)e^{p\tau}\,dp\,,\ T^{*-}_{s,f}(\zeta,\tau)=\frac{1}{2\pi i}\int_{EF}\overline{T}^{*}_{s,f}(\zeta,p)e^{p\tau}\,dp\,, \tag{4.18}$$

$$T^{*0}_{s,f}(\zeta,\tau)=\frac{1}{2\pi i}\int_{\Gamma_\delta}\overline{T}^{*}_{s,f}(\zeta,p)e^{p\tau}\,dp\,. \tag{4.19}$$

In polar coordinate system $p=\rho e^{i\varphi}$ we have $p=\rho e^{i\varphi}$, $\varphi=\pi$, $p=-\rho$, $\sqrt{p}=i\sqrt{\rho}$ on upper boundary CD and $\varphi=-\pi$, $p=-\rho$, $\sqrt{p}=-i\sqrt{\rho}$ on bottom boundary EF of a cut. Therefore,

taking into account the equations (4.10)–(4.12) and the relations $\mathrm{ch}(ix)=\cos(x)$, $\mathrm{sh}(ix)=i\sin(x)$ (Abramovits and Stegun, 1979), we can write the integrals (4.18) in the form:

$$T_{s,f}^{*\pm}(\zeta,\tau)=\pm\frac{1}{2\pi i}\int_0^{\infty}\overline{T}_{s,f}^{*\pm}(\zeta,\rho)e^{-\rho\tau}\,d\rho\,, \tag{4.20}$$

where

$$\overline{T}_{s,f}^{*\pm}(\zeta,\rho)=-\frac{\Delta_{s,f}^{\pm}(\zeta,\rho)}{\rho\sqrt{\rho}\Delta^{\pm}(\rho)}\,, \tag{4.21}$$

$$\Delta_s^{+}(\zeta,\rho)=\Delta_s^{-}(\zeta,\rho)=\sqrt{\rho}\cos[(1-\zeta)\sqrt{\rho}]+\mathrm{Bi_s}\sin[(1-\zeta)\sqrt{\rho}],\ 0\le\zeta\le 1\,, \tag{4.22}$$

$$\Delta_f^{\pm}(\zeta,\rho)=[\sqrt{\rho}\cos(\sqrt{\rho})+\mathrm{Bi_s}\sin(\sqrt{\rho})]e^{\pm i\zeta\sqrt{\frac{\rho}{k^*}}},\ -\infty<\zeta\le 0\,, \tag{4.23}$$

$$\Delta^{\pm}(\rho)=(\pm i\varepsilon\,\mathrm{Bi_s}-\sqrt{\rho})\sin(\sqrt{\rho})+(\mathrm{Bi_s}\pm i\varepsilon\sqrt{\rho})\cos(\sqrt{\rho})\,. \tag{4.24}$$

Adding equations (4.21)–(4.24) at $x=\sqrt{\rho}$ we obtain:

$$T_{s,f}^{*+}(\zeta,\tau)+T_{s,f}^{*-}(\zeta,\tau)=\frac{2}{\pi}\int_0^{\infty}F(x)G_{s,f}(\zeta,x)e^{-x^2\tau}\,dx, \tag{4.25}$$

where

$$F(x)=\frac{\cos(x)+\mathrm{Bi_s}\,x^{-1}\sin(x)}{[\mathrm{Bi_s}\,\cos(x)-x\sin(x)]^2+\varepsilon^2[\mathrm{Bi_s}\,\sin(x)+x\cos(x)]^2}\,, \tag{4.26}$$

$$G_s(\zeta,x)=\varepsilon\{\cos[(1-\zeta)x]+\mathrm{Bi_s}\,x^{-1}\sin[(1-\zeta)x]\}\,,\ 0\le\zeta\le 1\,, \tag{4.27}$$

$$\begin{aligned}G_f(\zeta,x)=\varepsilon\cos\left(\zeta\frac{x}{\sqrt{k^*}}\right)[\mathrm{Bi_s}\,x^{-1}\sin(x)+\cos(x)]-\\ -x^{-1}\sin\left(\zeta\frac{x}{\sqrt{k^*}}\right)[\mathrm{Bi_s}\cos(x)-x\sin(x)],\quad -\infty<\zeta\le 0.\end{aligned} \tag{4.28}$$

Taking the formulae (4.8)–(4.12) into account, the integrals (4.19) round the small circle Γ_δ enclosing the origin for $p=\delta e^{i\varphi}$, $-\pi\le\varphi\le\pi$ and $\delta\to 0$ tends to values:

$$T_s^{*0}(\zeta,\tau)=-\frac{1+(1-\zeta)\mathrm{Bi_s}}{\mathrm{Bi_s}}\,,\ 0\le\zeta\le 1\,,\ T_f^{*0}(\zeta,\tau)=-\frac{1+\mathrm{Bi_s}}{\mathrm{Bi_s}}\,,\ -\infty<\zeta\le 0\,. \tag{4.29}$$

Substituting the results (4.25) and (4.29) into equations (4.17), we obtain the dimensionless temperatures in the strip and the foundation:

$$T_s^*(\zeta,\tau)=\frac{1+(1-\zeta)\mathrm{Bi}_s}{\mathrm{Bi}_s}-\frac{2}{\pi}\int_0^\infty F(x)G_s(\zeta,x)e^{-x^2\tau}\,dx,\quad 0\le\zeta\le 1, \tag{4.30}$$

$$T_f^*(\zeta,\tau)=\frac{1+\mathrm{Bi}_s}{\mathrm{Bi}_s}-\frac{2}{\pi}\int_0^\infty F(x)G_f(\zeta,x)e^{-x^2\tau}\,dx,\quad -\infty<\zeta\le 0, \tag{4.31}$$

where the integrands $F(x)$ and $G_{s,f}(\zeta,x)$ have the form (4.26)–(4.28).

4.2 Two particular values of the heat transfer coefficient

The boundary of the strip $z=d$ ($\zeta=1$) for $h_s\to\infty$ ($\mathrm{Bi}_s\to\infty$) is kept at zero temperature, i.e. $T_s^*(1,\tau)=0,\tau>0$. In this case, the Laplace transformed solution of the boundary-value heat conductivity problem (3.2)–(3.8), has also the form (4.8) and (4.9), where

$$\Delta_s(\zeta,p)=\mathrm{sh}[(1-\zeta)\sqrt{p}],\quad 0\le\zeta\le 1, \tag{4.32}$$

$$\Delta_f(\zeta,p)=\mathrm{sh}(\sqrt{p})e^{\zeta\sqrt{\frac{p}{k^*}}},\quad -\infty<\zeta\le 0, \tag{4.33}$$

$$\Delta(p)=\frac{1}{2}(1+\varepsilon)e^{\sqrt{p}}(1+\lambda e^{-2\sqrt{p}}), \tag{4.34}$$

$$-1<\lambda=\frac{1-\varepsilon}{1+\varepsilon}<1. \tag{4.35}$$

Taking the below relations into account

$$\frac{1}{1+\lambda e^{-2\sqrt{p}}}=\sum_{n=0}^{\infty}\Lambda^n e^{-2n\sqrt{p}}, \tag{4.36}$$

where

$$\Lambda^n=\begin{cases}(-1)^n\lambda^n, & 0\le\lambda<1\\ |\lambda|^n, & -1<\lambda\le 0\end{cases}, \tag{4.37}$$

from the equation (4.34) it can be find

$$\frac{1}{\Delta(p)}=\frac{2e^{-\sqrt{p}}}{(1+\varepsilon)}\sum_{n=0}^{\infty}\Lambda^n e^{-2n\sqrt{p}}\ . \tag{4.38}$$

Substituting equations (4.32), (4.33) and (4.38) into the solutions (4.8) and (4.9), we find the transforms for temperatures in the following form:

$$\overline{T}_s^*(\zeta,p)=\frac{1}{(1+\varepsilon)}\sum_{n=0}^{\infty}\Lambda^n\overline{T}_{s,n}^*(\zeta,p),\quad 0\le\zeta\le 1, \tag{4.39}$$

$$\bar{T}^*_{s,n}(\zeta,p)=\frac{1}{p\sqrt{p}}[e^{-(2n+\zeta)\sqrt{p}}-e^{-(2n+2-\zeta)\sqrt{p}}],\ n=0,1,2,..., \tag{4.40}$$

$$\bar{T}^*_f(\zeta,p)=\frac{1}{(1+\varepsilon)}\sum_{n=0}^{\infty}\Lambda^n\bar{T}^*_{f,n}(\zeta,p),\quad -\infty<\zeta\le 0, \tag{4.41}$$

$$\bar{T}^*_{f,n}(\zeta,p)=\frac{1}{p\sqrt{p}}[e^{-\left(2n-\frac{\zeta}{\sqrt{k^*}}\right)\sqrt{p}}-e^{-\left(2n+2-\frac{\zeta}{\sqrt{k^*}}\right)\sqrt{p}}],\ n=0,1,2,\ldots. \tag{4.42}$$

Applying the inversion formula (Bateman and Erdelyi, 1954)

$$L^{-1}\left[\frac{e^{-a\sqrt{p}}}{p\sqrt{p}};\tau\right]=2\sqrt{\tau}\ \mathrm{ierfc}\left(\frac{a}{2\sqrt{\tau}}\right),\ a>0, \tag{4.43}$$

to equation (4.39)–(4.42), we obtain the temperatures in the strip and in the foundation:

$$T^*_s(\zeta,\tau)=\frac{1}{(1+\varepsilon)}\sum_{n=0}^{\infty}\Lambda^n T^*_{s,n}(\zeta,\tau),\quad 0\le\zeta\le 1,\ \ \tau\ge 0, \tag{4.44}$$

$$T^*_{s,n}(\zeta,\tau)=2\sqrt{\tau}\left[\mathrm{ierfc}\left(\frac{2n+\zeta}{2\sqrt{\tau}}\right)-\mathrm{ierfc}\left(\frac{2n+2-\zeta}{2\sqrt{\tau}}\right)\right],n=0,1,2,..., \tag{4.45}$$

$$T^*_f(\zeta,\tau)=\frac{1}{(1+\varepsilon)}\sum_{n=0}^{\infty}\Lambda^n T^*_{f,n}(\zeta,\tau),\quad -\infty<\zeta\le 0,\ \ \tau\ge 0, \tag{4.46}$$

$$T^*_{f,n}(\zeta,\tau)=2\sqrt{\tau}\left[\mathrm{ierfc}\left(\frac{2n\sqrt{k^*}-\zeta}{2\sqrt{k^*\tau}}\right)-\mathrm{ierfc}\left(\frac{(2n+2)\sqrt{k^*}-\zeta}{2\sqrt{k^*\tau}}\right)\right],n=0,1,2,\ldots. \tag{4.47}$$

From formulas (4.44)–(4.47) it can be easily proved, that boundary and initial conditions (3.4)–(3.8), at $\mathrm{Bi_s}\to\infty$ are satisfied.

At $h_s\to 0$ ($\mathrm{Bi_s}\to 0$) the surface of the strip $\zeta=1$ is insulated:

$$\left.\frac{\partial T^*_s}{\partial\zeta}\right|_{\zeta=1}=0,\quad \tau>0. \tag{4.48}$$

The solution of the heat conduction equations (3.2) and (3.3), satisfying boundary and initial conditions (3.4)–(3.8) and (4.48), also can be found in the form of (4.44) and (4.46), when

$$T^*_{s,n}(\zeta,\tau)=2\sqrt{\tau}\left[\mathrm{ierfc}\left(\frac{2n+\zeta}{2\sqrt{\tau}}\right)+\mathrm{ierfc}\left(\frac{2n+2-\zeta}{2\sqrt{\tau}}\right)\right],n=0,1,2,..., \tag{4.49}$$

$$T^*_{f,n}(\zeta,\tau)=2\sqrt{\tau}\left[\mathrm{ierfc}\left(\frac{2n\sqrt{k^*}-\zeta}{2\sqrt{k^*\tau}}\right)+\mathrm{ierfc}\left(\frac{(2n+2)\sqrt{k^*}-\zeta}{2\sqrt{k^*\tau}}\right)\right],n=0,1,2,... \tag{4.50}$$

If the properties of materials of the strip and the foundation are the same, then from formulae (4.13), (4.25) and (4.37), that ε=1, λ=0, $\Lambda = 0$. Hence, for n=0 from solutions (4.44)–(4.47), (4.50) and (4.50) are obtained

$$T_s^*(\zeta,\tau) = \sqrt{\tau}\left[\operatorname{ierfc}\left(\frac{\zeta}{2\sqrt{\tau}}\right) \mp \operatorname{ierfc}\left(\frac{2-\zeta}{2\sqrt{\tau}}\right)\right],\ 0 \le \zeta \le 1,\ \tau \ge 0, \tag{4.51}$$

$$T_f^*(\zeta,\tau) = \sqrt{\tau}\left[\operatorname{ierfc}\left(\frac{-\zeta}{2\sqrt{\tau}}\right) \mp \operatorname{ierfc}\left(\frac{2-\zeta}{2\sqrt{\tau}}\right)\right],\ -\infty < \zeta \le 0,\ \tau \ge 0, \tag{4.52}$$

where the upper sign should be taken when the surface of the strip $z = d$ ($\zeta = 1$) is kept at zero temperature, and bottom – when this surface is insulated.
Finally, we note that the solution of the corresponding thermal problem of friction for two homogeneous semi-spaces was found in the monograph (Grylytskyy, 1996)

$$T^*(\zeta,\tau) = \frac{2\sqrt{\tau}}{(1+\varepsilon)}\begin{cases} \operatorname{ierfc}\left(\dfrac{\zeta}{2\sqrt{\tau}}\right), & 0 \le \zeta < \infty,\ \tau \ge 0, \\ \operatorname{ierfc}\left(\dfrac{-\zeta}{2\sqrt{k^*\tau}}\right), & -\infty < \zeta \le 0,\ \tau \ge 0. \end{cases} \tag{4.53}$$

The distribution of dimensionless temperature in the semi-space, which is heated up on a surface $\zeta = 0$ with a uniform heat flux of intensity q_0 has the well-known form (Carslaw and Jaeger, 1959):

$$T^*(\zeta,\tau) = 2\sqrt{\tau}\,\operatorname{ierfc}\left(\frac{\zeta}{2\sqrt{\tau}}\right),\quad 0 \le \zeta < \infty,\ \tau \ge 0. \tag{4.54}$$

5. Heat generation at constant friction power. Imperfect contact.

In this Chapter the impact of thermal resistance on the contact surface on the temperature distribution in strip-foundation system is investigated. For this purpose, we consider the heat conduction problem of friction (3.2)-(3.8) on the following assumptions: constant pressure $p(\tau)$ (2.1) ($p^*(\tau) = 1$), constant velocity $V = V_0$ ($V^* = 1$) and zero temperature on the upper surface of the strip, i.e. in the boundary condition (3.6) $\mathrm{Bi}_s \to \infty$.

5.1 Solution to the problem

Solution of a boundary-value problem of heat conduction in friction (3.2)–(3.8) by applying the Laplace integral transforms (4.1) has form

$$\overline{T}_{s,f}^*(\zeta,p) = \frac{\Delta_{s,f}(\zeta,p)}{p\,\Delta(p)}\ , \tag{5.1}$$

where

$$\Delta_s(\zeta,p) = \left(\varepsilon + \frac{\mathrm{Bi}}{\sqrt{p}}\right)\mathrm{sh}[(1-\zeta)\sqrt{p}],\ 0 \le \zeta \le 1, \tag{5.2}$$

$$\Delta_f(\zeta,p)=\left[\mathrm{ch}\sqrt{\mathrm{p}}+\frac{\mathrm{Bi}}{\sqrt{p}}\mathrm{sh}\sqrt{p}\right]e^{\zeta\sqrt{\frac{p}{k^*}}},\ -\infty<\zeta\le 0, \tag{5.3}$$

$$\Delta(p)=\varepsilon\,\mathrm{Bi}\ \mathrm{sh}\sqrt{p}+(2\varepsilon\sqrt{p}+\mathrm{Bi})\ \mathrm{ch}\sqrt{p}\,. \tag{5.4}$$

Applying the inverse Laplace transform to Eqs. (5.1)–(5.4) with integration along the same contour as in Fig. 2, we obtain the dimensionless temperatures in the strip and in the foundation:

$$T^*_{s,f}(\zeta,\tau)=T^{*0}_{s,f}(\zeta)-\frac{2}{\pi}\int_0^\infty F(x)G_s(\zeta,x)e^{-x^2\tau}\,dx,\ \tau\ge 0, \tag{5.5}$$

where

$$T^{*0}_s(\zeta)=1-\zeta,\ 0\le\zeta\le 1,\ T^{*0}_f(\zeta)=\frac{1+\mathrm{Bi}}{\mathrm{Bi}},\ -\infty<\zeta\le 0, \tag{5.6}$$

$$F(x)=\frac{\cos x+\mathrm{Bi}\,x^{-1}\sin x}{(\mathrm{Bi}\cos x)^2+\varepsilon^2(\mathrm{Bi}\sin x+2x\cos x)^2}, \tag{5.7}$$

$$G_s(\zeta,x)=\varepsilon\,\mathrm{Bi}\ x^{-1}\ \sin[(1-\zeta)x],\ 0\le\zeta\le 1, \tag{5.8}$$

$$G_f(\zeta,x)=\varepsilon\left(\frac{\mathrm{Bi}}{x}\sin x+2\cos x\right)\cos(\zeta x/\sqrt{k^*})-\frac{\mathrm{Bi}}{x}\cos x\sin(\zeta x/\sqrt{k^*}),\ -\infty<\zeta\le 0. \tag{5.9}$$

The maximum temperature is reached on the friction surface $\zeta=0$. In order to determine the maximum temperature, we use the solutions (5.5) at $T^{*0}_s(\zeta)=1$ and the integrands (5.7) as well as

$$G_s(0,x)=\varepsilon\,\mathrm{Bi}\ x^{-1}\ \sin x,\ G_f(0,x)=\varepsilon(\mathrm{Bi}\,x^{-1}\sin x+2\cos x). \tag{5.10}$$

Let us define the heat flux intensities in the strip and in semi-space as following:

$$q_s(z,t)\equiv -K_s\frac{\partial T_s(z,t)}{\partial z},\ 0\le z\le d, t\ge 0,\ q_f(z,t)\equiv K_f\frac{\partial T_f(z,t)}{\partial z},\ -\infty<z\le 0,\ t\ge 0, \tag{5.11}$$

or with taking (3.9) under consideration in the dimensionless form:

$$q^*_s(\xi,\tau)\equiv\frac{q_s(z,t)}{q}=-\frac{\partial T^*_s(\zeta,\tau)}{\partial\zeta},\ 0\le\zeta\le 1,\ \ \tau\ge 0, \tag{5.12}$$

$$q^*_f(\zeta,\tau)\equiv\frac{q_f(z,t)}{q}=K^*\frac{\partial T^*_f(\zeta,\tau)}{\partial\zeta},\ -\infty<\zeta\le 0,\ \tau\ge 0. \tag{5.13}$$

With taking solutions for dimensionless temperatures (5.5)–(5.9) under consideration, from the formulae (5.12) and (5.13) we found:

$$q_s^*(\zeta,\tau)=1-\frac{2\varepsilon}{\pi}\int_0^\infty F(x)Q_s(\zeta,x)e^{-x^2\tau}\,dx,\quad 0\le\zeta\le 1,\ \tau\ge 0, \tag{5.14}$$

$$q_f^*(\zeta,\tau)=\frac{2\varepsilon}{\pi}\int_0^\infty F(x)Q_f(\zeta,x)e^{-x^2\tau}\,dx,\quad -\infty<\zeta\le 0,\ \tau\ge 0, \tag{5.15}$$

$$Q_s(\zeta,x)=\mathrm{Bi}\cos[(1-\zeta)x],\ 0\le\zeta\le 1, \tag{5.16}$$

$$Q_f(\zeta,x)=\varepsilon(\mathrm{Bi}\sin x+2x\cos x)\sin(\zeta x/\sqrt{k^*})+\mathrm{Bi}\cos x\cos(\zeta x/\sqrt{k^*}),\ -\infty<\zeta\le 0. \tag{5.17}$$

On the friction surface $\zeta=0$ from the formulae (5.16) and (5.17) leads $Q_f(0,x)=Q_s(0,x)=\mathrm{Bi}\cos x$ and from (5.14), (5.15) we found $q_f^*(0,\tau)+q_s^*(0,\tau)=1$, $\tau\ge 0$, which means that boundary condition (3.4) is satisfied ($q^*(\tau)=1$). Spikes of temperature and heat flux intensities both on the contact surface $\zeta=0$ we found from solutions of (5.5)–(5.9) and (5.14)–(5.17) in the form:

$$T_s^*(0,\tau)-T_f^*(0,\tau)=-\frac{1}{\mathrm{Bi}}+\frac{4\varepsilon}{\pi}\int_0^\infty F(x)e^{-x^2\tau}\cos x\,dx,\ \tau\ge 0, \tag{5.18}$$

$$q_f^*(0,\tau)-q_s^*(0,\tau)=-1+\frac{4\varepsilon\,\mathrm{Bi}}{\pi}\int_0^\infty F(x)e^{-x^2\tau}\cos x\,dx,\ \tau\ge 0, \tag{5.19}$$

whence follows, that the boundary condition (3.5) is satisfied.
Dimensionless temperatures and heat flux intensities in case of perfect contact between strip and foundation ($h\to\infty$ or $\mathrm{Bi}\to\infty$) can be found from the Eqs. (5.5), (5.14) and (5.15) at $T_f^{*0}(\zeta)=1$ and the integrands in the forms:

$$F(x)=\frac{x^{-1}\sin(x)}{\cos^2(x)+\varepsilon^2\sin^2(x)}, \tag{5.20}$$

$$G_s(\zeta,x)=\varepsilon x^{-1}\sin[(1-\zeta)x],\ Q_s(\zeta,x)=\cos[(1-\zeta)x],\ 0\le\zeta\le 1, \tag{5.21}$$

$$G_f(\zeta,x)=\varepsilon\,x^{-1}\sin(x)\cos(\zeta x/\sqrt{k^*})-x^{-1}\cos(x)\sin(\zeta x/\sqrt{k^*}),\ -\infty<\zeta\le 0, \tag{5.22}$$

$$Q_f(\zeta,x)=\varepsilon\sin(x)\sin(\zeta x/\sqrt{k^*})+\cos(x)\cos(\zeta x/\sqrt{k^*}),\ -\infty<\zeta\le 0. \tag{5.23}$$

On the contact surface $\zeta=0$ from Eqs. (5.20)–(5.23) result as following

$$G_s(0,x)=G_f(0,x)=\varepsilon x^{-1}\sin x,\ Q_s(0,x)=Q_f(0,x)=\cos x. \tag{5.24}$$

The formulae (5.20)–(5.24) from the solution of the contact problem with heat generation due to friction at perfect thermal contact between strip and foundation, were obtained in Chapter four.

5.2 Asymptotic solutions

For large values of the parameter p of Laplace integral transform (4.1) the solutions (5.1)–(5.4) will take form:

$$\overline{T}_s^*(\zeta,p)\cong\frac{(\varepsilon+\mathrm{Bi}/\sqrt{p})}{2\varepsilon p(\alpha+\sqrt{p})}e^{-\zeta\sqrt{p}}\ ,\ \overline{q}_s^*(\zeta,p)\cong\frac{(\varepsilon\sqrt{p}+\mathrm{Bi})}{2\varepsilon p(\alpha+\sqrt{p})}e^{-\zeta\sqrt{p}}\ ,\ 0\le\zeta\le 1\,, \tag{5.25}$$

$$\overline{T}_f^*(\zeta,p)\cong\frac{(1+\mathrm{Bi}/\sqrt{p})}{2\varepsilon p(\alpha+\sqrt{p})}e^{\zeta\sqrt{\frac{p}{k^*}}}\ ,\ \overline{q}_f^*(\zeta,p)\cong\frac{(\sqrt{p}+\mathrm{Bi})}{2p(\alpha+\sqrt{p})}e^{\zeta\sqrt{\frac{p}{k^*}}}\ ,\ -\infty<\zeta\le 0\,, \tag{5.26}$$

where

$$\alpha=\frac{(1+\varepsilon)}{2\varepsilon}\mathrm{Bi}\,. \tag{5.27}$$

By using the relations (Bateman and Erdelyi, 1954)

$$L^{-1}\left[\frac{e^{-|\zeta|\sqrt{p}}}{\sqrt{p}(\alpha+\sqrt{p})};\tau\right]=e^{\alpha|\zeta|+\alpha^2\tau}\mathrm{erfc}\left(\frac{|\zeta|}{2\sqrt{\tau}}+\alpha\sqrt{\tau}\right), \tag{5.28}$$

$$L^{-1}\left[\frac{\alpha\,e^{-|\zeta|\sqrt{p}}}{p(\alpha+\sqrt{p})};\tau\right]=\mathrm{erfc}\left(\frac{|\zeta|}{2\sqrt{\tau}}\right)-e^{\alpha|\zeta|+\alpha^2\tau}\mathrm{erfc}\left(\frac{|\zeta|}{2\sqrt{\tau}}+\alpha\sqrt{\tau}\right), \tag{5.29}$$

$$\begin{aligned}L^{-1}&\left[\frac{e^{-|\zeta|\sqrt{p}}}{p\sqrt{p}(\alpha+\sqrt{p})};\tau\right]=\\&=\frac{2}{\alpha}\sqrt{\frac{\tau}{\pi}}e^{-\frac{\zeta^2}{4\tau}}-\left(\frac{|\zeta|}{\alpha}+\frac{1}{\alpha^2}\right)\mathrm{erfc}\left(\frac{|\zeta|}{2\sqrt{\tau}}\right)+\frac{1}{\alpha^2}e^{\alpha|\zeta|+\alpha^2\tau}\mathrm{erfc}\left(\frac{|\zeta|}{2\sqrt{\tau}}+\alpha\sqrt{\tau}\right),\end{aligned} \tag{5.30}$$

we have obtained from Eqs. (5.25), (5.26) the asymptotic formulae for dimensionless temperature and heat flux intensities both for the strip and foundation at small values of the dimensionless time $0\le\tau<<1$:

$$T_s^*(\zeta,\tau)\cong\frac{2\sqrt{\tau}}{(1+\varepsilon)}\mathrm{ierfc}\left(\frac{\zeta}{2\sqrt{\tau}}\right)-\frac{\lambda}{2\alpha}\left[\mathrm{erfc}\left(\frac{\zeta}{2\sqrt{\tau}}\right)-e^{\alpha|\zeta|+\alpha^2\tau}\mathrm{erfc}\left(\frac{\zeta}{2\sqrt{\tau}}+\alpha\sqrt{\tau}\right)\right],0\le\zeta\le 1\,, \tag{5.31}$$

$$T_f^*(\zeta,\tau)\cong\frac{2\sqrt{\tau}}{(1+\varepsilon)}\mathrm{ierfc}\left(\frac{|\zeta|}{2\sqrt{k^*\tau}}\right)+\frac{\lambda}{2\alpha\varepsilon}\left[\mathrm{erfc}\left(\frac{|\zeta|}{2\sqrt{k^*\tau}}\right)-e^{\alpha\frac{|\zeta|}{\sqrt{k^*}}+\alpha^2\tau}\mathrm{erfc}\left(\frac{|\zeta|}{2\sqrt{k^*\tau}}+\alpha\sqrt{\tau}\right)\right], \tag{5.32}$$

$$-\infty<\zeta\le 0$$

$$q_s^*(\zeta,\tau)\cong\frac{1}{(1+\varepsilon)}\mathrm{erfc}\left(\frac{\zeta}{2\sqrt{\tau}}\right)-\frac{\lambda}{2}e^{\alpha|\zeta|+\alpha^2\tau}\mathrm{erfc}\left(\frac{\zeta}{2\sqrt{\tau}}+\alpha\sqrt{\tau}\right),\ 0\le\zeta\le 1\,, \tag{5.33}$$

$$q_f^*(\zeta,\tau)\cong\frac{\varepsilon}{(1+\varepsilon)}\operatorname{erfc}\left(\frac{|\zeta|}{2\sqrt{k^*\tau}}\right)+\frac{\lambda}{2}e^{\alpha\frac{|\zeta|}{\sqrt{k^*}}+\alpha^2\tau}\operatorname{erfc}\left(\frac{|\zeta|}{2\sqrt{k^*\tau}}+\alpha\sqrt{\tau}\right),\ -\infty<\zeta\le 0\,, \tag{5.34}$$

where

$$\lambda=\frac{1-\varepsilon}{1+\varepsilon}\,. \tag{5.35}$$

The dimensionless temperatures (5.31) and (5.32) tends to zero as $\tau\to 0$, which means that initial conditions (3.8) are satisfied.

On the contact surface of the strip and foundation $\zeta=0$ we find from the solutions of (5.31)–(5.34) that:

$$\begin{aligned}T_s^*(0,\tau)&\cong\frac{2}{(1+\varepsilon)}\sqrt{\frac{\tau}{\pi}}-\frac{\lambda}{2\alpha}[1-e^{\alpha^2\tau}\operatorname{erfc}(\alpha\sqrt{\tau})],\\ T_f^*(0,\tau)&\cong\frac{2}{(1+\varepsilon)}\sqrt{\frac{\tau}{\pi}}+\frac{\lambda}{2\alpha\varepsilon}[1-e^{\alpha^2\tau}\operatorname{erfc}(\alpha\sqrt{\tau})],\end{aligned}\qquad 0\le\tau<<1\,, \tag{5.36}$$

$$q_s^*(0,\tau)\cong\frac{1}{(1+\varepsilon)}-\frac{\lambda}{2}e^{\alpha^2\tau}\operatorname{erfc}(\alpha\sqrt{\tau})\,,\ q_f^*(0,\tau)\cong\frac{\varepsilon}{(1+\varepsilon)}+\frac{\lambda}{2}e^{\alpha^2\tau}\operatorname{erfc}(\alpha\sqrt{\tau})\,,\ 0<\tau<<1\,. \tag{5.37}$$

By taking (5.27) and (5.35) into account, from the Eqs. (5.36) and (5.37) we find:

$$T_s^*(0,\tau)-T_f^*(0,\tau)=-\frac{\lambda}{\mathrm{Bi}}[1-e^{\alpha^2\tau}\operatorname{erfc}(\alpha\sqrt{\tau})]\,,\ 0\le\tau<<1\,, \tag{5.38}$$

$$q_f^*(0,\tau)+q_s^*(0,\tau)=1\,,\ q_f^*(0,\tau)-q_s^*(0,\tau)=-\lambda[1-e^{\alpha^2\tau}\operatorname{erfc}(\alpha\sqrt{\tau})]\,,\ 0<\tau<<1\,, \tag{5.39}$$

which also means that received asymptotic solution satisfies the boundary conditions (3.4) (where $q^*(\tau)=1$) and (3.5).

As results from solutions (5.31) and (5.32), at small Fourier number values τ the temperature of strip and foundation in case of perfect thermal contact ($\mathrm{Bi}\to\infty$), can be found with use of solution of the friction heat for two semi-spaces (Yevtushenko and Kuciej, 2009a)

$$\begin{aligned}T_s^*(\zeta,\tau)&\cong\frac{2\sqrt{\tau}}{(1+\varepsilon)}\operatorname{ierfc}\left(\frac{\zeta}{2\sqrt{\tau}}\right),\ 0\le\zeta<\infty,\\ T_f^*(\zeta,\tau)&\cong\frac{2\sqrt{\tau}}{(1+\varepsilon)}\operatorname{ierfc}\left(-\frac{\zeta}{2\sqrt{k^*\tau}}\right),\quad -\infty<\zeta\le 0,\quad 0\le\tau<<1.\end{aligned} \tag{5.40}$$

At small values of the parameter p from solutions (5.1)–(5.4) we obtain:

$$\overline{T}_s^*(\zeta,p)\cong\frac{(1-\zeta)}{(2+\mathrm{Bi})}\left[\frac{(2+\mathrm{Bi})\beta+\sqrt{p}}{p(\beta+\sqrt{p})}\right],\ \overline{q}_f^*(\zeta,p)\cong\frac{(\varepsilon\sqrt{p}+\mathrm{Bi})}{2\varepsilon\,p(2+\mathrm{Bi})(\alpha+\sqrt{p})},\ 0\le\zeta\le 1\,, \tag{5.41}$$

$$\overline{T}_f^*(\zeta,p)\cong\frac{(1+\mathrm{Bi})\beta}{\mathrm{Bi}}\left[\frac{1+\zeta\sqrt{p/k^*}}{p(\beta+\sqrt{p})}\right],\ \overline{q}_f^*(\zeta,p)\cong\frac{(1+\mathrm{Bi})}{(2+\mathrm{Bi})\sqrt{p}(\alpha+\sqrt{p})}\left(1+\zeta\sqrt{\frac{p}{k^*}}\right),\tag{5.42}$$

$$-\infty<\zeta\le 0\,,$$

where

$$\beta=\frac{\mathrm{Bi}}{\varepsilon(2+\mathrm{Bi})}.\tag{5.43}$$

By applying the Laplace inversion formulae (4.43) we obtain from Eqs. (5.41), (5.42) dimensionless temperatures and heat flux intensities in the strip and in the foundation at large values ($\tau>>1$) of the dimensionless time τ :

$$T_s^*(\zeta,\tau)\cong(1-\zeta)\left[1-\frac{(1+\mathrm{Bi})}{(2+\mathrm{Bi})}e^{\beta^2\tau}\mathrm{erfc}(\beta\sqrt{\tau})\right],\ 0\le\zeta\le 1\,,\tag{5.44}$$

$$T_f^*(\zeta,\tau)\cong\frac{(1+\mathrm{Bi})}{\mathrm{Bi}}\left[1-\left(1-\beta\frac{\zeta}{\sqrt{k^*}}\right)e^{\beta^2\tau}\mathrm{erfc}(\beta\sqrt{\tau})\right],\ -\infty<\zeta\le 0\,,\tag{5.45}$$

$$q_s^*(\zeta,\tau)\cong 1-\frac{(1+\mathrm{Bi})}{(2+\mathrm{Bi})}e^{\beta^2\tau}\mathrm{erfc}(\beta\sqrt{\tau})\,,\ 0\le\zeta\le 1\,,\tag{5.46}$$

$$q_f^*(\zeta,\tau)\cong\frac{(1+\mathrm{Bi})}{(2+\mathrm{Bi})}\left[\frac{\zeta}{\sqrt{\pi k^*\tau}}+\left(1-\beta\frac{\zeta}{\sqrt{k^*}}\right)e^{\beta^2\tau}\mathrm{erfc}(\beta\sqrt{\tau})\right],\ -\infty<\zeta\le 0\,.\tag{5.47}$$

From the formulae (5.44)–(5.47) the temperatures and heat flux intensities on the contact surface are found in the form:

$$T_s^*(0,\tau)\cong 1-\frac{(1+\mathrm{Bi})}{(2+\mathrm{Bi})}e^{\beta^2\tau}\mathrm{erfc}(\beta\sqrt{\tau})\,,\ T_f^*(0,\tau)\cong\frac{(1+\mathrm{Bi})}{\mathrm{Bi}}\left[1-e^{\beta^2\tau}\mathrm{erfc}(\beta\sqrt{\tau})\right],\ \tau>>1\,,\tag{5.48}$$

$$q_s^*(0,\tau)\cong 1-\frac{(1+\mathrm{Bi})}{(2+\mathrm{Bi})}e^{\beta^2\tau}\mathrm{erfc}(\beta\sqrt{\tau})\,,\ q_f^*(0,\tau)\cong\frac{(1+\mathrm{Bi})}{(2+\mathrm{Bi})}e^{\beta^2\tau}\mathrm{erfc}(\beta\sqrt{\tau})\,,\ \tau>>1\,.\tag{5.49}$$

From the formulae (5.48) and (5.49), is easy to find that boundary conditions (3.4) (where $q^*(\tau)=1$) and (3.5) are satisfied.

In addition, from (5.46) and (5.47) follows, that at fixed enough big value of Fourier number τ, the heat flux is constant along strip thickness and in foundation its value decreases linearly with distance from contact surface.

The dimensionless temperatures in the strip and in the foundation with assumption of theirs perfect thermal contact ($\mathrm{Bi}\to\infty$) can be found from solutions (5.44) and (5.45) in the form:

$$T_s^*(\zeta,\tau) \cong (1-\zeta)\left[1 - e^{\left(\frac{\sqrt{\tau}}{\varepsilon}\right)^2} \operatorname{erfc}\left(\frac{\sqrt{\tau}}{\varepsilon}\right)\right],\ 0 \le \zeta \le 1,\ \tau >> 1, \tag{5.50}$$

$$T_f^*(\zeta,\tau) \cong 1 - \left(1 - \frac{\zeta}{\varepsilon\sqrt{k^*}}\right) e^{\left(\frac{\sqrt{\tau}}{\varepsilon}\right)^2} \operatorname{erfc}\left(\frac{\sqrt{\tau}}{\varepsilon}\right),\ -\infty < \zeta \le 0,\ \tau >> 1\,.\, 1 - e^{\alpha^2\tau}\operatorname{erfc}(\alpha\sqrt{\tau})\,. \tag{5.51}$$

Setting in the above equations $\zeta = 0$, we received the equality of strip and foundation temperatures on the contact surface:

$$T_s^*(0,\tau) = T_f^*(0,\tau) \cong 1 - e^{\left(\frac{\sqrt{\tau}}{\varepsilon}\right)^2} \operatorname{erfc}\left(\frac{\sqrt{\tau}}{\varepsilon}\right),\ \tau >> 1\,. \tag{5.52}$$

6. Heat generation of braking with constant deceleration

In this Chapter we investigate the influence of the thermal resistance on the contact surface, and of the convective cooling on the upper surface of the strip (pad), with the constant pressure ($p^*(\tau) = 1$) and linear decreasing speed of sliding (breaking with constant deceleration) (2.10) taken into account. To solve a boundary problem of heat conductivity, we shall use the solutions achieved in Chapters four and five in case of constant power of friction ($q^*(\tau) = 1,\ \tau \ge 0$).

The corresponding solution to a case of braking with constant deceleration (2.10) is received by Duhamel's theorem in the form of (Luikov, 1968):

$$\hat{T}^*(\zeta,\tau) = \int_0^\tau q^*(s)\frac{\partial}{\partial s}T^*(\zeta,\tau-s)ds\,,\ -\infty < \zeta \le 1,\ 0 \le \tau \le \tau_s\,. \tag{6.1}$$

Substituting the dimensionless intensity of a heat flux $q^*(\tau)$ (3.1), (2.10) and the temperature obtained $T^*(\zeta,\tau)$ in the fourth Chapter (4.30), (4.31) to the right parts of formulae (6.1), after integration we obtain a formulae for braking with constant deceleration in case of the perfect thermal contact (between the strip and foundation), and the convective cooling on the upper surface of the strip:

$$\hat{T}^*(\zeta,\tau) = \frac{2}{\pi}\int_0^\infty F(x)G(\zeta,x)P(\tau,x)\,dx,\quad -\infty < \zeta \le 1,\ 0 \le \tau \le \tau_s\,, \tag{6.2}$$

where

$$P(\tau,x) = 1 - \frac{\tau}{\tau_s} - e^{-x^2\tau} + \frac{1-e^{-x^2\tau}}{\tau_s x^2},\ P(\tau,0) = 0\,, \tag{6.3}$$

functions $F(x)$ and $G(x)$ has the form (4.26)–(4.28) accordingly.

To determine the solution to a case of braking with constant deceleration when the thermal resistance occurs on a surface of contact ($\mathrm{Bi} \geq 0$), and the zero temperature on the upper surface of the strip is maintained ($\mathrm{Bi}_s \to \infty$), we have used the solutions obtained in Chapter five (5.5). For this case we obtain the solution in the form of (6.2), where functions $F(x)$ and $G(x)$ have the form (5.20)–(5.22) and function $P(\tau, x)$ has the form (6.3).

7. Heat generation of braking with the time-dependent and fluctuations of the pressure

In this Chapter we consider the general case of braking (3.2)-(3.8), having taken into account the time-dependent normal pressure $p(\tau)$ (2.1), the velocity $V(\tau)$, $0 \leq \tau \leq \tau_s$ (2.4)-(2.8) and the boundary condition of the zero temperature on the upper surface of the strip i.e. $\mathrm{Bi}_s \to \infty$ (3.6).

The solution $T^*(\zeta, \tau)$ to a boundary-value problem of heat conductivity (3.2)-(3.8) in the case when the bodies are compressed with constant pressure p_0, and the strip is sliding with a constant speed V_0 on a surface of foundation ($q^*(\tau) = 1$, $\tau \geq 0$), has been obtained in Chapter six in the form (5.5)–(5.9).

Substituting the temperature $T^*(\zeta, \tau)$ (5.5) to the right part of equation (6.1) and changing the order of the integration, we obtain

$$\hat{T}^*(\zeta, \tau) = \frac{2}{\pi} \int_0^\infty F(x) G(\zeta, x) P(\tau, x)\, dx, \quad -\infty < \zeta \leq 1,\ 0 \leq \tau \leq \tau_s, \tag{7.1}$$

where

$$P(\tau, x) = x^2 \int_0^\tau q^*(s) e^{-x^2(\tau - s)} ds,\ 0 \leq x < \infty, 0 \leq \tau \leq \tau_s, \tag{7.2}$$

functions $F(x)$ and $G(\zeta, x)$ take the form (5.7) and (5.8), accordingly. Taking the form of the dimensionless intensity of a heat flux $q^*(\tau)$ (3.1) into account, the function $P(\tau, x)$ (7.2) can be written as

$$P(\tau, x) = P_1(\tau, x) - \frac{a}{\tau_s^0} P_2(\tau, x), \tag{7.3}$$

where

$$P_i(\tau, x) = x^2 \int_0^\tau p^*(s) V_i^*(s) e^{-x^2(\tau - s)} ds,\ 0 \leq x < \infty, 0 \leq \tau \leq \tau_s,\ i = 1, 2. \tag{7.4}$$

Substituting in equation (7.4) the functions $p^*(\tau)$ (2.1) and $V_i^*(s)$, $i = 1, 2$ (2.4), (2.5), after integration we find

$$P_i(\tau, x) = Q_i(\tau, x) + a R_i(\tau, x),\ 0 \leq x < \infty, 0 \leq \tau \leq \tau_s,\ i = 1, 2, \tag{7.5}$$

where

$$Q_1(\tau,x)=\left(1+\frac{1}{\tau_s^0\alpha_m^2}\right)\left[J_0(\tau,x,0)-J_0(\tau,x,\alpha_m)\right]-\frac{1}{\tau_s^0}\left[J_1(\tau,x,0)-J_1(\tau,x,\alpha_m)\right]- \\ -\frac{1}{\tau_s^0\alpha_m^2}\left[J_0(\tau,x,\alpha_m)-J_0(\tau,x,\beta_m)\right], \tag{7.6}$$

$$R_1(\tau,x)=\left(1+\frac{1}{\tau_s^0\alpha_m^2}\right)\left[J_2(\tau,x,\omega,0)-J_2(\tau,x,\omega,\alpha_m)\right]-\frac{1}{\tau_s^0}\left[J_4(\tau,x,\omega,0)-J_4(\tau,x,\omega,\alpha_m)\right]- \\ -\frac{1}{\tau_s^0\alpha_m^2}\left[J_2(\tau,x,\omega,\alpha_m)-J_2(\tau,x,\omega,\beta_m)\right], \tag{7.7}$$

$$Q_2(\tau,x)=\frac{1}{\omega}\left[J_0(\tau,x,0)-J_0(\tau,x,\alpha_m)-J_3(\tau,x,\omega,0)+J_3(\tau,x,\omega,\alpha_m)\right]+ \\ +\frac{\alpha_m^2}{(\alpha_m^4+\omega^2)}\left[J_2(\tau,x,\omega,\alpha_m)-J_2(\tau,x,\omega,\beta_m)\right]+ \\ +\frac{\omega}{(\alpha_m^4+\omega^2)}\left[J_3(\tau,x,\omega,\alpha_m)-J_3(\tau,x,\omega,\beta_m)\right], \tag{7.8}$$

$$R_2(\tau,x)=\frac{1}{\omega}\left[J_2(\tau,x,\omega,0)-J_2(\tau,x,\omega,\alpha_m)\right]-\frac{1}{2\omega}\left[J_2(\tau,x,2\omega,0)-J_2(\tau,x,2\omega,\alpha_m)\right]+ \\ +\frac{\alpha_m^2}{2(\alpha_m^4+\omega^2)}\left[J_0(\tau,x,\alpha_m)-J_0(\tau,x,\beta_m)-J_3(\tau,x,2\omega,\alpha_m)+J_3(\tau,x,2\omega,\beta_m)\right]+ \\ +\frac{\omega}{2(\alpha_m^4+\omega^2)}\left[J_2(\tau,x,2\omega,\alpha_m)-J_2(\tau,x,2\omega,\beta_m)\right], \tag{7.9}$$

$$\alpha_m=\frac{1}{\sqrt{\tau_m}},\ \beta_m=\sqrt{\frac{2}{\tau_m}}. \tag{7.10}$$

The functions $J_k(\cdot)$, $k=0,1,2,3,4$ in the formulae (7.6)–(7.9) have the form (Prudnikov at al., 1989)

$$J_0(\tau,x,\alpha)\equiv x^2e^{-x^2\tau}\int_0^\tau e^{(x^2-\alpha^2)s}ds=\frac{x^2}{(x^2-\alpha^2)}(e^{-\alpha^2\tau}-e^{-x^2\tau}), \tag{7.11}$$

$$J_1(\tau,x,\alpha)\equiv x^2e^{-x^2\tau}\int_0^\tau s^k e^{(x^2-\alpha^2)s}ds=\frac{1}{(x^2-\alpha^2)}[x^2\tau\, e^{-\alpha^2\tau}-J_0(\tau,x,\alpha)], \tag{7.12}$$

$$J_2(\tau,x,\omega,\alpha)\equiv x^2e^{-x^2\tau}\int_0^\tau e^{(x^2-\alpha^2)s}\sin(\omega s)ds= \\ =\frac{x^2}{[(x^2-\alpha^2)^2+\omega^2]}\{[(x^2-\alpha^2)\sin(\omega\tau)-\omega\cos(\omega\tau)]e^{-\alpha^2\tau}+\omega e^{-x^2\tau}\}, \tag{7.13}$$

$$J_3(\tau,x,\omega,\alpha) \equiv x^2 e^{-x^2\tau}\int_0^\tau e^{(x^2-\alpha^2)s}\cos(\omega s)ds = \\ = \frac{x^2}{[(x^2-\alpha^2)^2+\omega^2]}\{[(x^2-\alpha^2)\cos(\omega\tau)+\omega\sin(\omega\tau)]e^{-\alpha^2\tau}-(x^2-\alpha^2)e^{-x^2\tau}\}, \tag{7.14}$$

$$J_4(\tau,x,\omega,\alpha) \equiv x^2 e^{-x^2\tau}\int_0^\tau s\,e^{(x^2-\alpha^2)s}\sin(\omega s)ds = \\ = \frac{x^2}{[(x^2-\alpha^2)^2+\omega^2]}\left\{\left[\left((x^2-\alpha^2)\tau-\frac{(x^2-\alpha^2)^2-\omega^2}{(x^2-\alpha^2)^2+\omega^2}\right)\sin(\omega\tau)-\right.\right. \\ \left.\left.-\left(\omega\tau-\frac{2\omega(x^2-\alpha^2)}{(x^2-\alpha^2)^2+\omega^2}\right)\cos(\omega\tau)\right]e^{-\alpha^2\tau}-\frac{2\omega(x^2-\alpha^2)}{(x^2-\alpha^2)^2+\omega^2}e^{-x^2\tau}\right\}, \tag{7.15}$$

where the parameter $\alpha \geq 0$.

If the pressure $p^*(\tau)$ (2.1) during braking increases monotonically, without oscillations ($a = 0$), then from formulae (7.3) and (7.5) it follows that $P(\tau,x) = Q_1(\tau,x)$. Taking the form of functions $Q_1(\tau,x)$ (7.6) and $J_k(\tau,x,\alpha)$, $k = 0,1$ (7.11), (7.12) into account, we obtain

$$P(\tau,x) = (1-e^{-x^2\tau})\left(1+\frac{\tau_m}{\tau_s^0}+\frac{1}{\tau_s^0 x^2}\right)-\frac{x^2(e^{-\tau/\tau_m}-e^{-x^2\tau})}{(x^2-\tau_m^{-1})}\left[1+\frac{2\tau_m}{\tau_s^0}+\frac{1}{\tau_s^0(x^2-\tau_m^{-1})}\right]+ \\ +\frac{\tau_m x^2(e^{-2\tau/\tau_m}-e^{-x^2\tau})}{\tau_s^0(x^2-2\tau_m^{-1})}+\frac{\tau\,x^2 e^{-\tau/\tau_m}}{\tau_s^0(x^2-\tau_m^{-1})}-\frac{\tau}{\tau_s^0},\ 0\leq x<\infty, 0\leq\tau\leq\tau_s. \tag{7.16}$$

In the limiting case of braking with a constant deceleration at $\tau_m \to 0$ from formula (7.16) we find the results of the Chapter six.

8. Numerical analysis and conclusion

Calculations are made for a ceramic-metal pad FMC-11 (the strip) of thickness $d = 5\,\text{mm}$ ($K_s = 34.3\,\text{Wm}^{-1}\text{K}^{-1}$, $k_s = 15.2\cdot10^{-6}\,\text{m}^2\text{s}^{-1}$), and a disc (the foundation) from cast iron CHNMKh ($K_f = 51\,\text{Wm}^{-1}\text{K}^{-1}$, $k_f = 14\cdot10^{-6}\,\text{m}^2\text{s}^{-1}$) (Chichinadze at al., 1979). Such a friction pair is used in frictional units of brakes of planes. Time of braking is equal to $t_s = 3.42\text{s}$ ($\tau_s = 2.08$) (Balakin and Sergienko, 1999). Integrals are found by the procedure QAGI from a package of numerical integration QUADPACK (Piessens at al., 1983).

From Chapter six, the results of calculations of dimensionless temperature $\hat{T}^*$ (6.2) for the first above considered variants of boundary conditions are presented in Fig. 3a–5a, and for the second – in Fig. 3b–5b. The occurrence of thermal resistance on a surface of contact leads to the occurrence of a jump of temperature on the friction surfaces of the strip and the foundation.

With the beginning of braking, the temperature on a surface of contact $(\zeta = 0)$ sharply raises, reaches the maximal value $\hat{T}^*_{\max}$ during the moment of time $\tau_{\max}$, then starts to decrease to a minimum level, and finally stops τ_s (Fig. 3a). The heat exchange with an

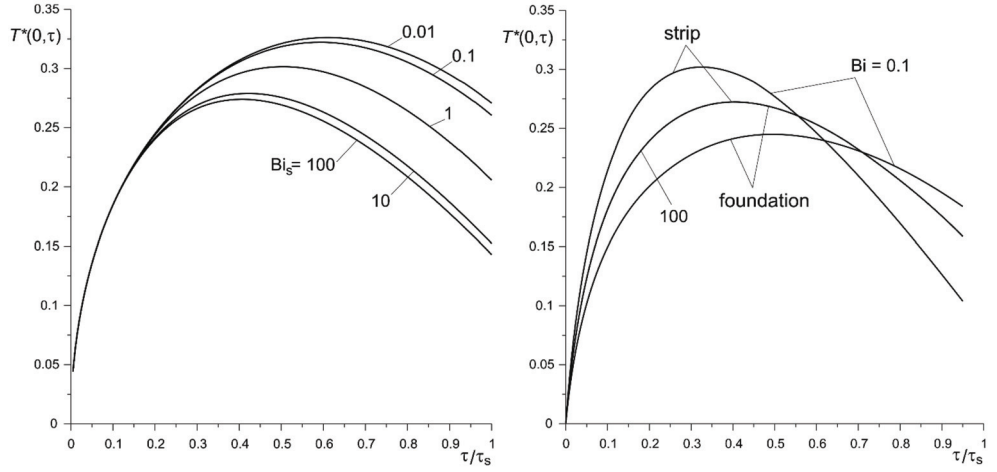

Fig. 3. Evolution of dimensionless temperature $\hat{T}^*$ on a surface of contact $\zeta = 0$ for several values of Biot numbers: a) Bi_s ; b) Bi , (Yevtushenko and Kuciej, 2010).

environment on an upper surface of a strip does not influence the temperature significantly at an initial stage of braking $0 \le \tau \le \tau_{\max}$ when the temperature increases rapidly. This influence is the most appreciable during cooling the surface of contact $\tau_{\max} \le \tau \le \tau_s$.

When the factor of thermal resistance is small ($\mathrm{Bi} = 0.1$) the strip is warmed up faster than the foundation, and it reaches the much greater maximal temperature than the maximal temperature on a working surface of the foundation (Fig. 3b). The increase in thermal conductivity of contact area results in alignment of contact temperatures on the friction surface of the bodies. For Biot number $\mathrm{Bi} = 100$ the evolutions of temperatures on contact surfaces of the strip and the foundation are identical.

The highest temperature on the surface of contact is reached in case of thermal isolation of the upper surface of the strip ($\mathrm{Bi}_s \to 0$) (Fig. 4a). While Biot number increases on the upper surface of the strip, the maximal temperature on surfaces contact decreases. From the data presented in Fig. 4a follows, that for values of Biot number $\mathrm{Bi}_s \ge 20$ to calculate the maximal temperature in considered tribosystem, it is possible to use an analytical solution to a problem, which is more convenient in practice ($\mathrm{Bi}_s \to \infty$ at the set zero temperature on the upper surface of the strip) (Yevtushenko and Kuciej, 2009b).

The effect of alignment of the maximal temperature with increase in thermal conductivity of contact surfaces is especially visible in Fig. 4b. To calculate the maximal temperature at $\mathrm{Bi} \ge 10$, we may use formulas (6.2)-(6.5), which present the solutions to the thermal problem of friction at braking in case of an ideal thermal contact of the strip and the foundation, and of maintenance of zero temperature on the upper surface of the strip.

Change of dimensionless temperature in the strip and the foundation on a normal to a friction surface for Fourier's number $\tau_s = 2.08$ is shown in Fig. 5. The temperature reaches the maximal value on the friction surface $\zeta = 0$, and decreases while the distance from it grows. The drop of temperature in the strip for small values of Biot number ($\mathrm{Bi}_s = 0.1$) has nonlinear character (Fig. 5a). If the zero temperature is maintained ($\mathrm{Bi}_s = 100$) during

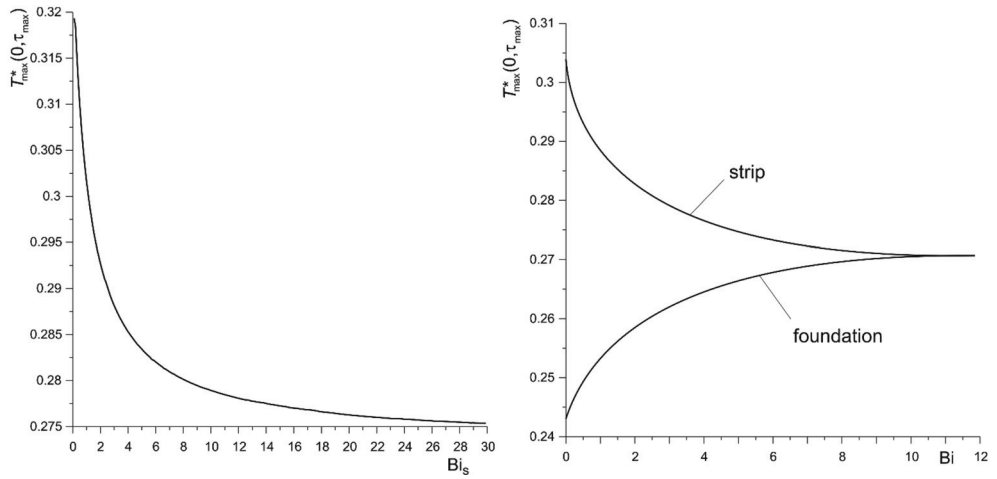

Fig. 4. Dependence of dimensionless maximal temperature $\hat{T}^*_{\max}$ on Biot numbers: a) Bi_s; b) Bi for dimensionless time of braking $\tau_s = 2.08$, (Yevtushenko and Kuciej, 2010).

braking on the upper surface of the strip, then the reduction of temperature in the strip, and while the distance from the friction surface grows, can be described by a linear function of dimensionless spatial variable ζ. The effective depth of heating up the foundation decreases with the increase in Biot number and for values $\mathrm{Bi}_s = 0.1; 100$ is equal 2.4 and 2.15 of the strip's thickness accordingly. Irrespective of size of thermal resistance, the temperature in the strip linearly decreases from the maximal value for surfaces of contact up to zero on the upper surface of the strip (Fig. 5b). The effective depth of heating up the foundation increases with the increase of thermal resistance (reduction of thermal conductivity) – for values $\mathrm{Bi} = 0.1; 100$ it is equal 2.15 and 2.7 of thickness of the strip accordingly.

From Chapter seven, the results of calculations of dimensionless temperature $\hat{T}^*$ (7.1) are presented in Figs. 5–7. First, for fixed values of the input parameters τ_m, τ_s^0, a and ω we find numerically the dimensionless time of stop τ_s as the root of functional equation (2.9). Knowing the time of braking τ_s, we can construct the dependencies of output parameters on the ratio τ / τ_s. Such dependencies for the dimensionless pressure p^* (2.1) and sliding speed V^* (2.4) are shown in Fig. 6. We see in Fig. 6a four curves for two values of the dimensionless time of pressure rise, which corresponds to instantaneous ($\tau_m = 0$) and monotonic ($\tau_m = 0.2$) increase in pressure to the nominal value, at two values of the amplitude $a = 0$ and $a = 0.1$. In Fig. 6b we see only two curves constructed at the same values of parameters τ_m and a. This is explained by the fact that the amplitude of fluctuations of pressure a practically does not influence the evolution of speed of sliding.

The evolution of the dimensionless contact temperature $\hat{T}^*(0,\tau)$ (7.2) in the pad and in the disc, for the same distributions of dimensionless pressure p^* (2.1) and velocity V^* (2.4), which are shown in Figs. 6a,b is presented in Fig. 7. Due to heat transfer through the surface of contact the temperatures of the pad (Fig. 7a) and the disk (Fig. 7b) on this surface are various. The largest value of the contact temperature is reached during braking with the

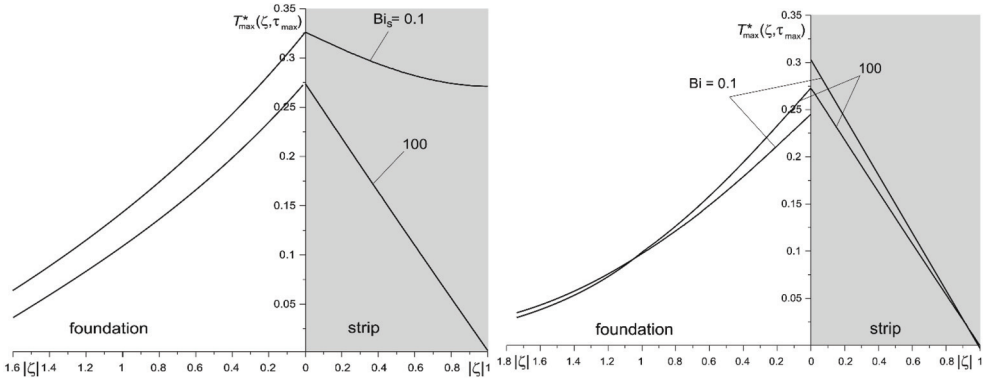

(a) (b)

Fig. 5. Distribution of dimensionless temperature $\hat{T}^*$ in the strip ($0 \le \zeta \le 1$) and the foundation ($-\infty \le \zeta \le 0$) during the dimensionless moment of time $\tau = \tau_{\max}$ of reaching the temperature of the maximal value $T^*_{\max}$ for two values of Biot numbers: a) Bi_s ; b) Bi , (Yevtushenko and Kuciej, 2010).

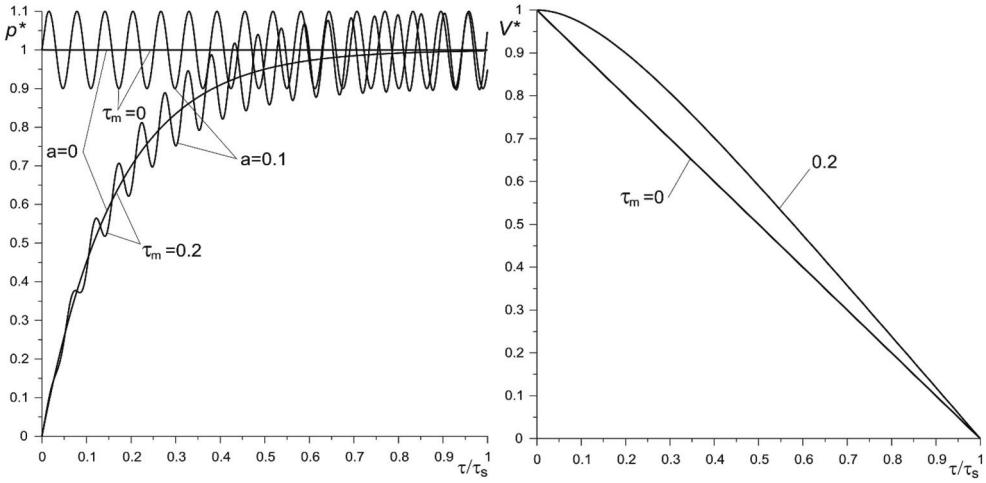

(a) (b)

Fig. 6. Evolution of the dimensionless pressure p^* (a) and sliding speed V^* (b) during braking for several values of the Fourier number τ_m and dimensionless amplitude a , (Yevtushenko at al. 2010).

constant deceleration (τ_m=0). The increase in duration of achieving the nominal value of pressure leads to a decrease in contact temperature. The maximum contact temperature in the case of braking with the constant deceleration (τ_m=0) is always larger than at the non-uniform braking. It is interesting, that the temperature at the moment of a stop is practically independent of the value of the parameter τ_m. Pressure oscillations (see Fig. 6) lead to the fact that the temperature on the contact surface also oscillates, but with a considerably lower amplitude (Fig. 7).

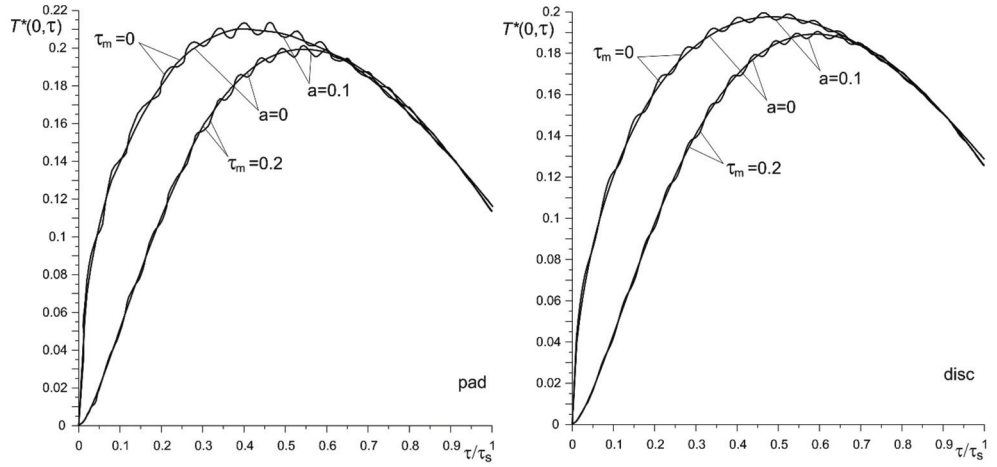

(a) (b)

Fig. 7. Evolution of dimensionless temperature $\hat{T}^*(0,\tau)$ (7.2) on the contact surface of the pad (a) and the disc (b) for two values of the Fourier number $\tau_m = 0;0.2$ and dimensionless amplitude $a = 0;0.1$ at fixed values of the dimensionless input parameters $\tau_s^0 = 1$, $\mathrm{Bi} = 5$, (Yevtushenko at al. 2010).

Evolution of dimensionless temperature $\hat{T}^*(\zeta,\tau)$ not only on a surface of contact, but also inside the pad and the disc is shown in Fig. 8. Regardless of the value of the time of pressure increase, the temperature oscillations take place in a thin subsurface layer. The thickness of this layer is about 0.2 of the thickness of the pad. Also, in these figures we see "the effect of delay" – the moment of time of achieving the temperature of the maximal value increases with the increase in distance from a surface of friction. In the pad the maximum temperature is reached before stopping at a given distance from the friction surface (Figs. 8a,c). In the disc we observe a different picture – for a depth ≥0.6*d* the temperature reaches a maximum value at the stop time moment (Figs. 8b,d).

9. Conclusions

The analytical solutions to a thermal problem of friction during braking are obtained for a plane-parallel strip/semi-space tribosystem with a constant or time-dependence friction power. In the solutions we take into account the heat transfer through a contact surface, and convective exchange on the upper surface of the pad. To solve the thermal problem of friction with time-dependent friction power we use solution to thermal problem with constant friction power and Duhamel formula (6.1).

The investigation is conducted for ceramic-metal pad (FMC-11) and cast iron disc (CHNMKh). The results of our investigation of the frictional heat generation of the pad sliding on the surface of the disc in the process of braking allow us to make the main conclusions, i.e. the temperature on the contact surface rises sharply with the beginning of braking, and at about half braking time it reaches the maximal value. Then, till the moment of stopping, the fall of temperature occurs (Fig. 3); the increase of convective exchange (Bi_s) on the outer surface of the pad, leads to the decrease of the maximal temperature on the

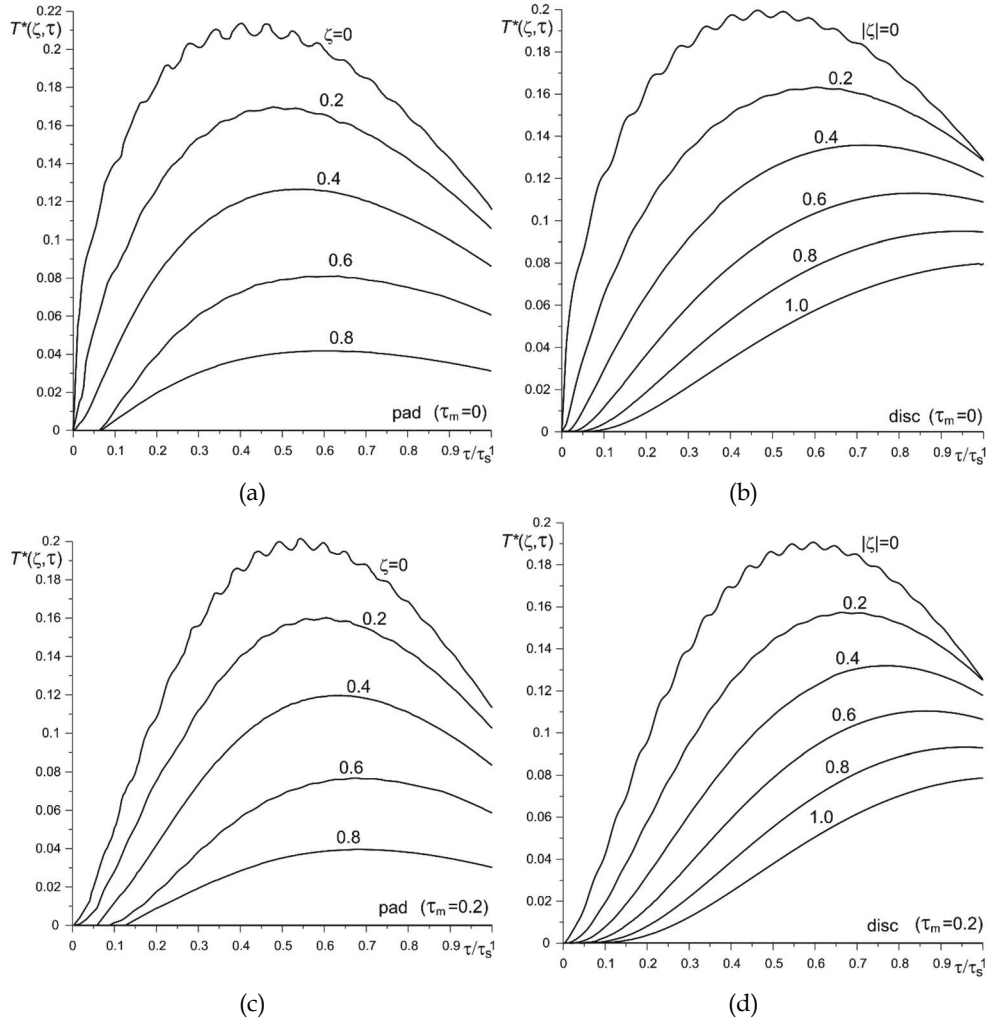

Fig. 8. Evolution of dimensionless temperature $\hat{T}^*(\zeta,\tau)$ (7.2) in the pad (a), (c) and in the disc (b), (d) for two values of the of the Fourier number $\tau_m = 0$ (a), (b) and $\tau_m = 0.2$ (c), (d) at fixed values of the dimensionless input parameters $a = 0.1$, $\tau_s^0 = 1$, Bi = 5, (Yevtushenko at al. 2010).

contact surface, while the time of reaching it gets shorter (Fig. 4a); the reduction of the thermal resistance on the contact surface (the increase of Biot's number Bi) causes the equalization of the maximal temperatures of the pad and disc's surfaces and of the time of reaching it (Fig. 4b); that the contact temperature decreases with the increase in dimensionless input parameter τ_m (duration increase in pressure from zero to the nominal value) (Figs. 7); the amplitude of the oscillations of temperature is much less than the amplitude of corresponding fluctuations of pressure ("the leveling effect") (Figs. 7, 8).

10. References

Abramovits, M., Stegun, I. (1979). Handbook of Mathematical Functions, 2 nd. edn, Dover, New York.

Archard, J. F., Rowntree, R. A. (1988). The temperature of rubbing bodies; Part 2, The distribution of temperatures, *Wear*, Vol. 128, pp. 1–17.

Balakin, V.A., Sergienko, V.P. (1999). Heat calculations of brakes and friction units, MPRI of NASB, Gomel (in Russian).

Barber, J. R., Comminou, M. (1989). Thermoelastic contact problems. In: Thermal Stresses III. Ed. R.R. Hetnarsky, Elsevier Sci. Publ., pp.1–105.

Bateman, H., Erdelyi, A. (1954). Tables of Integral Transforms, V. 1, McGraw-Hill, New York.

Bauzin, J. G., Laraqi, N. (2004). Simultaneous estimation of frictional heat flux and two thermal contact parameters for sliding contacts, *Numerical Heat Transfer; Part A: Applications*, Vol. 45, No 4, pp. 313–328.

Block, H. (1937). Theoretical studies of temperature rise at surfaces of actual contact under oiliness lubrication conditions, *Proc. General Discussion on Lubrication and Lubricants. Institute of Mechanical Engineers*, Vol. 2, pp. 222–235.

Burton, R. A. (1975). An axisymmetric contact patch configuration for two slabs in frictionally heated contact, The mechanics of the contact between deformable bodies, Proc. IUTAM Symp., ed. de Pater A. D., Kalker J. J., Delft Univ. Press.

Cameron, A., Gordon, A.N., Symm, G.T. (1965). Contact temperatures in rolling/sliding surfaces, *Proc. Roy. Soc., A*, Vol. 286, pp. 45–61.

Carslaw, H.S., Jaeger, J.C. (1959). Conduction of Heat in Solids, Clarendon Press, Oxford.

Chichinadze, A.V. (1967). Calculation and investigation of external friction during braking, Nauka, Moscow (in Russian).

Chichinadze, A.V., Braun, E.D., Ginsburg, A.G., et al., (1979). Calculation, test and selection of frictional couples, Nauka, Moscow (in Russian).

Evtushenko, A., Matysiak, S., Kutsei, M., (2005). Thermal problem of friction at braking of coated body, *J. Friction and Wear*, Vol. 26, No 2, pp. 33–40.

Evtushenko, O.O., Pyr'ev, Yu.O. (2000). Temperature and wear of the friction surfaces of a cermets patch and metal disk in the process of braking, *Materials Science*, Vol. 36, No 2, pp. 218–223.

Fasekas, G. A. G. (1953). Temperature gradients and heat stresses in brake drums, *SAE Trans.*, Vol. 61, pp. 279–284.

Ginsburg, A.G., Chichinadze, A.V. (1978). Complex estimation of performance data of frictional brakes on a design stage, In: Problems of non-stationary friction in machines, devices and apparatus, Nauka, Moscow, pp. 10-43 (in Russian).

Godet, M. (1990). Third-bodies in tribology, *Wear*, Vol. 136, No 1, pp. 29–45.

Grylytskyy, D.V. (1996) Thermoelastic contact problems in tribology, Institute of the Maintenance and Methods of Training of the Ministry of Education of Ukraine, Kiev (in Ukrainian).

Ho, T.L., Peterson, M.B., Ling, F.F. (1974). Effect of frictional heating on braking materials, *Wear*, Vol. 26, pp. 73–79.

Iordanoff, I., Berthier, Y., Descartes, S., Heshmat, H. (2002). A review of recent approaches for modeling solid third bodies, *Trans. ASME, J. Tribology*, Vol. 124, No 4, pp. 725–735.

Jaeger, J. C. (1942). Moving sources of heat and the temperatures of sliding contacts, *Proc. Roy. Soc. New South Wales*, Vol. 76, No 3, pp. 203–224.

Johnson, K. L., (1987). Contact Mechanics, Cambridge Univ. Press, Cambridge.

Kahveci, K., Can, Y., Cihan, A. (2005). Heat transfer in continuous-drive friction welding of different diameters, *Numerical Heat Transfer; Part A*, Vol. 48, No 10, pp. 1035–1050.

Kannel, J. W., Barber, S. A. (1989). Estimate of surface temperatures during rolling contact, *Tribology Trans.*, Vol. 32, No 3, pp. 305–310.

Levitskij, V.P., Onyshkievich, V.M. (1999). Investigation of influence of "third body" properties on heat generation due to friction, *Math. Methods Phys. Mech. Fields*, Vol. 42, pp. 82–86.

Ling, F. F. (1973). Surface Mechanics, Wiley, New York.

Ling, F. F., (1959). A quasi-iterative method for computing interface temperature distributions, *Zeitschrift für angewandte Mathematik und Physik (ZAMP)*, Vol. 10, No 5, pp. 461–474.

Luikov, A.V. (1968). Analytical heat diffusion theory, Academic Press, New York.

Matysiak, S., Evtushenko A., Kutsei, M. (2004). Non-stationary heating of a uniform foundation coated with a surface composite layer, *J. Friction and Wear*, Vol. 25, No 6, pp. 11–18.

Matysiak, S., Konieczny, S., Yevtushenko, A. (1998). Distribution of friction heat during cold-rolling of metals by using composite rolls, *Numerical Heat Transfer; Part A*, Vol. 34, No 7, pp. 719–729.

Matysiak, S., Yevtushenko, O., Kutsiei, M. (2007). Temperature field in the process of braking of a massive body with composite coating, *Materials Science*, Vol. 43, pp. 62–69.

Naji, M., Al-Nimr, M. (2001). Dynamic thermal behavior of a brake system, *Int. Comm. Heat Mass Trans.*, Vol. 28, pp. 835–845.

Nosko, A.L., Nosko, A.P. (2006). Solution of contact heating problem with account for heat transfer between the friction members, *J. Friction and Wear*, Vol. 27, pp. 35–40.

Olesiak, Z., Pyryev, Yu., Yevtushenko, A. (1997). Determination of temperature and wear during braking, *Wear*, Vol. 210, pp. 120–126.

Piessens, R., E. de Doncker-Kapenga, Überhuber, C.W., Kahaner, D.K. (1983). QUADPACK: A Subroutine Package for Automatic Integration, Springer-Verlag, Berlin.

Prudnikov, A.P., Brychkov, Yu. A., Marychev, O.I. (1981). Integrals and Series, Nauka, Moscow (in Russian).

Pyryev, Yu., Yevtushenko, A. (2000). The influence of the brakes friction elements thickness on the contact temperature and wear, *Heat and Mass Transfer*, Vol. 36, pp. 319–323.

Sneddon, I. N. (1972). The Use of Integral Transforms, McGraw-Hill, New York.

Yevtushenko, A. A., Ivanyk, E. G., Sykora, O. V. (1995). The transitive temperature processes in local friction contact, *Int. J. Heat Mass Transfer*, Vol. 38, No 13, pp. 2395-2401.

Yevtushenko, A., Kuciej, M. (2009a). Influence of the protective strip properties on distribution of the temperature at transient frictional heating, *Int. J. Heat Mass Transfer*, Vol. 52, No 1/2, pp. 376–384.

Yevtushenko, A.A., Kuciej, M. (2009b). Two contact problems for the strip with the frictional heating during braking, Proc. 8th Int. Congr. on Thermal Stresses, TS2009, Urbana-Champaign (Illinois, USA), June 1–4; pp. 289–293.

Yevtushenko, A., Kuciej, M. (2010). Influence of the convective cooling and the thermal resistance on the temperature of the pad/disc tribosystem, *Int. Comm. Heat Mass Transfer*, Vol. 37, pp. 337–342.

Yevtushenko, A., Kuciej, M. Yevtushenko, O. (2010). Influence of the pressure fluctuations on the temperature in pad/disc tribosystem, *Int. Comm. Heat Mass Transfer,* Vol. 37, pp. 978-983.

Yevtushenko, A., Kuciej, M., Rożniakowska, M. (2005). Thermal cleavage stresses in a piecewise-homogeneous plate, *Materials Science*, Vol. 5, pp. 581–588.

Yevtushenko, A. A., Rozniakowska, M., Kuciej, M. (2007a). Transient temperature processes in composite strip and homogeneous foundation, *Int. Comm. Heat Mass Transfer*, Vol. 34, pp. 1108–1118.

Yevtushenko, A., Rożniakowska, M., Kuciej, M. (2007b). Laser-induced thermal splitting in homogeneous body with coating, *Numerical Heat Transfer, Part. A*, Vol. 52, pp. 357–375.

Yevtushenko, A., Tolstoj-Sienkiewicz J. (2006). Temperature in a rotating ring subject to frictional heating from two stationary pins, *Numerical Heat Transfer; Part A*, Vol. 49, No 8, pp. 785–801.

Yevtushenko, A.A., Ivanyk, E.G., Yevtushenko, O.O. (1999) Exact formulae for determination of the mean temperature and wear during braking, *Heat and Mass Transfer*, Vol. 35, pp. 163–169.

Yi, YBo, Barber, J.R., Hartsock, D.L. (2002). Thermoelastic instabilities in automotive disc brakes - finite element analysis and experimental verification, In: Martins JAC and Monteiro Marques MDP, editors. Contact Mechanics, Kluwer, Dordrecht, p. 187–202.

25

Convective Heat Transfer Coefficients for Solar Chimney Power Plant Collectors

Marco Aurélio dos Santos Bernardes
CEFET-MG
Brazil

1. Introduction

This chapter deals with internal heat transfer in Solar Chimney Power Plant Collectors (SCPP), a typical symmetric sink flow between two disks. In general, specific heat transfer coefficients for this kind of flow can not be found in the literature and, consequently, most of the works employs simplified models (e.g. infinite plates, flow in parallel plates, etc.) using classical correlations to calculate the heat flow in SCPP collectors.
The extent of the chapter is limited to the analysis of the steady, incompressible flow of air including forced and natural convection. The phenomena phase change, mass transfer, and chemical reactions have been neglected. To the author' expertise, the most precise and updated equations for the Nusselt number found in the literature are introduced for use in SCPP heat flow calculations.
SCPPs consist of a transparent collector which heats the air near the ground and guides it into the base of a tall chimney coupled with it, as shown in Fig. 1. The relatively lighter air rises in the chimney promoting a flow allowing electricity generation through turbines at the base of the chimney. The literature about SCPP is extensively referred by (Bernardes 2010) at that time and there is no means of doing it here.

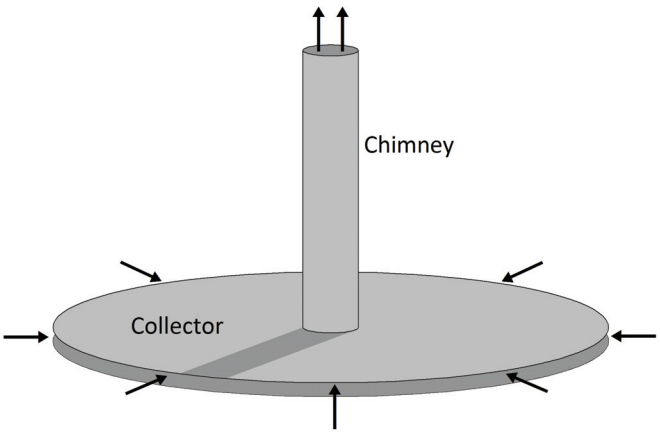

Fig. 1. Sketch of a SCPP.

The problem to be addressed here is the flow in the SCPP collector, i.e., the flow between two finite stationary disks concentrating on radially converging laminar and turbulent flow development and heat transfer. However, as a typical solar radiation dependent device, laminar, transient and turbulent and natural, mixed and forced convection, as well, may take place in the collector. Additionally, due to non uniform solar heating or ground roughness, the flow in collector should not converge axi-symmetrically. For that reason, the forced/natural convective flow in the SCPP collector can be treated as a flow:

1. between two independent flat plates in parallel flow or,
2. in a channel between parallel flat plates in parallel flow or
3. between two finite stationary disks in converging developing flow.

Moreover, collector convective heat transfers determine the rate at which thermal energy is transferred:

- between the roof and the ambient air,
- between the roof and the air inside the collector,
- between the absorber and the collector air.

It is necessary to remember that the literature for some typical heat transfer problems is extensive but scarce or even inexistent for some boundary conditions like constant heat flux, or for flow above rough surfaces like the collector ground.

1.1 Influence of the roof design in the heat transfer in collector

An important issue regarding the SCPP collector is its height as function of the radius. Some studies found in the literature (Bernardes 2004, Bernardes et al. 2003, Schlaich et al. 2005) make use of a constant height along the collector (Fig. 3). In this case, the air velocity increases continually due to the cross section decrease towards the chimney reducing the pressure in the collector, as shown in Fig. 2. Such pressure difference between the collector and surroundings allied with unavoidable slight gaps in the collector roof can result in fresh air infiltration reducing the air temperature. Furthermore, velocity variations in the collector denote different heat flows and, in this case, higher heat transfer coefficients and, consequently, a fresher collector close to the chimney. Besides, the relatively reduced collecting area in this region represents also lower heat gains harming the collector performance.

Fig. 2 also illustrates the air velocity for slight slanted roofs, evidencing a kind of 'bathtub effect'. Through this effect, the air velocity drops after the entrance region due to the cross area increasing and, especially for greater angles like 0.1° and 0.5°, remains minimal until achieves the chimney immediacy. In this region, the air velocity increases exponentially. Such air velocity profiles in collector represents lower heat transfer coefficients for a great collector area and, thus, lower heat transfer to the flowing air – predominance of natural convection – and higher losses to the ambient. Consequently, for this arrangement, the collector efficient would be inferior. (Bernardes et al. 1999) also disclose the presence of swirls when the flat collector roof is slanted.

The roof configuration for constant cross area – adopted by (Kröger & Blaine 1999, Pretorius & Kröger 2006) – leads, obviously, to constant air velocity in collector and, in terms of heat transfer, is the most appropriate for the collector. However, the roof height can achieve large values leading to higher material consumption (Fig. 3).

Lastly, the air velocity in the chimney should be taken in account. For a chimney diameter of 120 m, a collector diameter of 5000 m, an entrance collector height of 1 m and an entrance air velocity of 1 m/s, the air velocity in the chimney is 3 m/s approximately (continuity

equation). Consequently, lower collector air velocities at the chimney entry are preferably and the roof configuration for constant cross area fits relatively well this condition.

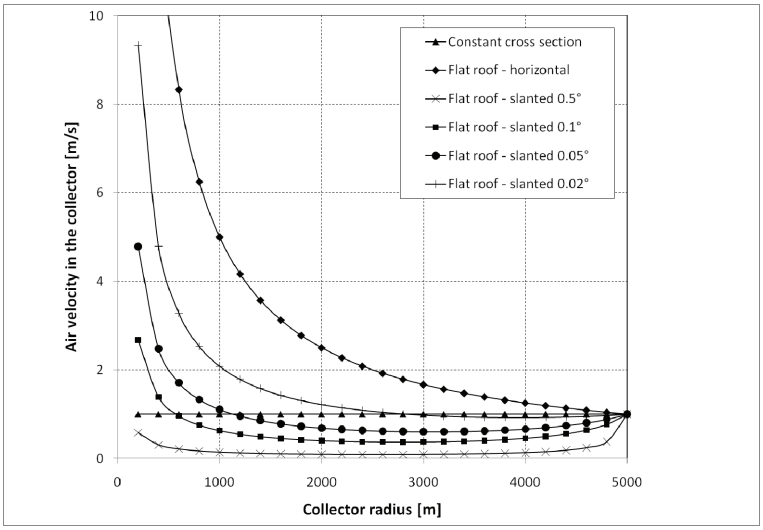

Fig. 2. Air velocity in collector for different roof arrangements.

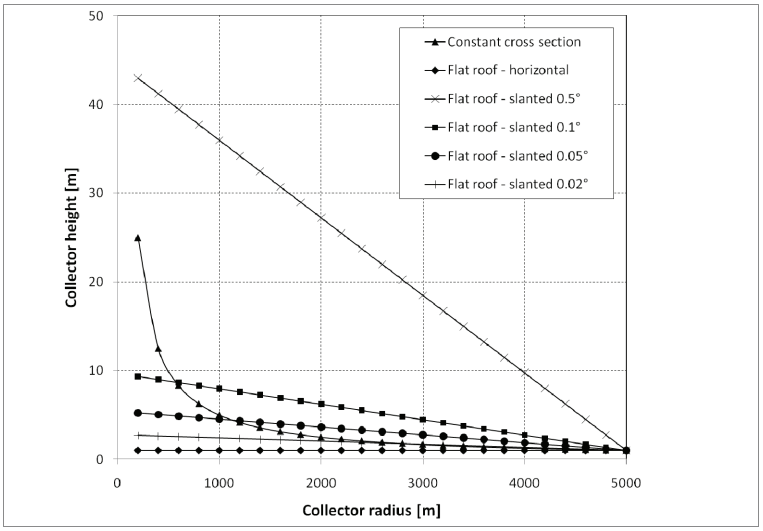

Fig. 3. Roof height for different roof arrangements.

2. Flow in collector as a flow between two independent flat plates

Due to a reasonable relative distance between the ground surface and the collector roof, the flow in a SCPP collector can be regarded as a flow involved by two independent plates, as employed be (Bernardes 2004). In this way, it is necessary to assume that the boundary layers develop indefinitely and separately.

2.1 Forced convection

The forced convection takes plate in the SCPP collector when the incident radiation is able to heat up the collector as much as necessary to promote a continuing air flow. In this condition, higher heat transfer coefficients are expected.

As represented in Fig. 4, the boundary layer flow over a flat plate regarding forced convection develops from a laminar boundary layer becoming unstable and turbulent after a certain plate length, when $Re_x = u_\infty \cdot x/\nu \approx 5 \times 10^5$. A more detailed description of this flow can be widely found in the literature, for instance, (Çengel 2007, Incropera 2007, Rohsenow et al. 1998), etc. In the following, the most important heat transfer coefficients and Nusselt numbers are introduced and their extent of application discussed.

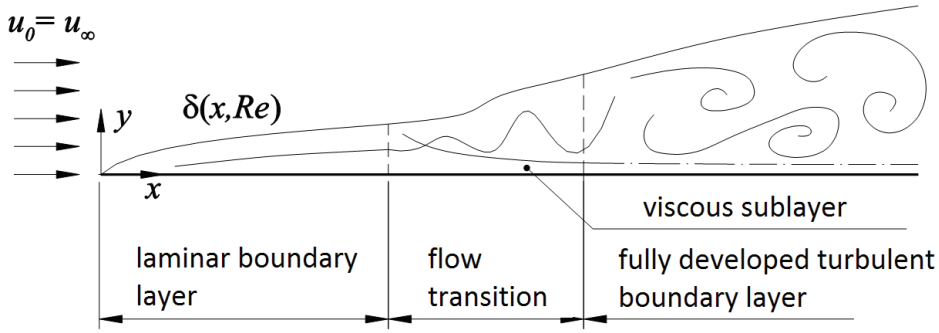

Fig. 4. Flow development in a flat plate in parallel flow.

Fundamentally, solution methodologies for the governing equations are based on the nondimensional groups and analytical means can be used to solve only a limited number of cases. Otherwise, experimental or numerical solution procedures must be employed.

Laminar flow – prescribed temperature

For two-dimensional cases, where the flow is laminar up to the point of transition to turbulent flow or flow separation, established analytical solutions can be extensively found in literature.

For the case of the laminar flow over a flat plate at uniform temperature and Pr ≈ 1 (like air, for instance), the similarity equations approach returns the local Nusselt number showed by equation (1) and the average Nusselt number by equation (2).

$$Nu_x = 0.332\,\mathrm{Re}_x^{1/2}\,\mathrm{Pr}^{1/3} \tag{1}$$

$$\overline{Nu} = 0.664\,\mathrm{Re}_L^{1/2}\,\mathrm{Pr}^{1/3} \tag{2}$$

$$Nu_x = \frac{\sqrt{\mathrm{Re}}\sqrt{\mathrm{Pr}}}{\sqrt{\pi}\left(1+1.7\,\mathrm{Pr}^{1/4}+21.36\,\mathrm{Pr}\right)^{1/6}} \qquad 0.25 \le \mathrm{Pr} \le \infty \tag{3}$$

(Baehr & Stephan 1996)

Laminar flow – Uniform wall heat flux

For a flat plate subjected to uniform heat flux instead of uniform temperature, the local and average Nusselt number are given by equations (4) and (5) respectively.

$$Nu_x = 0.453\,\mathrm{Re}_x^{1/2}\,\mathrm{Pr}^{1/3} \qquad \mathrm{Pr} > 0.6 \tag{4}$$

(Çengel 2007)

$$\overline{Nu} = 0.6795\,\mathrm{Re}_L^{1/2}\,\mathrm{Pr}^{1/3} \tag{5}$$

(Lienhard IV & Lienhard V 2008)

$$Nu_x = \frac{\sqrt{\pi}\sqrt{\mathrm{Re}}\sqrt{\mathrm{Pr}}}{2\left(1+2.09\,\mathrm{Pr}^{1/4}+48.74\,\mathrm{Pr}\right)^{1/6}} \qquad 0.25 \le \mathrm{Pr} \le \infty \tag{6}$$

(Baehr & Stephan 1996)

Turbulent flow – prescribed temperature

For the case of turbulent flows, approximate analytical solutions based on phenomenological laws of turbulence kinetics are established for local and average Nusselt numbers as introduced by equations (7), (8) and (9).

$$Nu_x = 0.032\,\mathrm{Re}_x^{0.8}\,\mathrm{Pr}^{0.43} \qquad 2\times10^5 < \mathrm{Re}_x < 5\times10^6 \tag{7}$$

(Žukauskas & Šlanciauskas 1999)

$$Nu_x = 0.0296\,\mathrm{Re}_x^{0.8}\,\mathrm{Pr}^{1/3} \qquad \begin{matrix} 5\times10^5 \le \mathrm{Re}_x \le 10^7 \\ 0.6 \le \mathrm{Pr} \le 60 \end{matrix} \tag{8}$$

(Çengel 2007)

$$\overline{Nu} = 0.037\,\mathrm{Re}_L^{0.8}\,\mathrm{Pr}^{1/3} \qquad \begin{matrix} 5\times10^5 \le \mathrm{Re}_L \le 10^7 \\ 0.6 \le \mathrm{Pr} \le 60 \end{matrix} \tag{9}$$

(Çengel 2007)

Entire plate

A relation suitable to calculate the average heat transfer coefficient over the entire plate including laminar and turbulent is given by equation (10).

$$\overline{Nu} = \left(0.037\,\mathrm{Re}_L^{0.8} - 871\right)\mathrm{Pr}^{1/3} \qquad \begin{matrix} 5\times10^5 \le \mathrm{Re}_L \le 10^7 \\ 0.6 \le \mathrm{Pr} \le 60 \end{matrix} \tag{10}$$

(Çengel 2007)

Turbulent flow – uniform wall heat flux

When the turbulent flow over a flat plate is subjected to uniform heat flux, the local and average Nusselt numbers are given by equations (11) (12) and (13).

$$Nu_x = 0.0308\,\mathrm{Re}_x^{0.8}\,\mathrm{Pr}^{1/3} \tag{11}$$

(Çengel 2007)

$$\overline{Nu} = 0.037\,\mathrm{Re}_L^{0.8}\,\mathrm{Pr}^{0.43} \qquad 2\times10^5 \le \mathrm{Re}_L \le 3\times10^7 \tag{12}$$

(Lienhard IV & Lienhard V 2008)

$$Nu = \frac{0.037\,\mathrm{Re}^{0.8}\,\mathrm{Pr}}{1+2.443\,\mathrm{Re}^{-0.1}\left(\mathrm{Pr}^{2/3}-1\right)} \quad 5\times10^5 < \mathrm{Re} < 10^7 \quad 0.6 < \mathrm{Pr} < 2000 \tag{13}$$

(Petukhov & Popov 1963)

Mixed forced convection

$$Nu = \sqrt{Nu_{lam}^2 + Nu_{turb}^2} \qquad 10 < \mathrm{Re} < 10^7 \tag{14}$$

(Baehr & Stephan 1996)

2.2 Natural convection

Natural convection at horizontal isothermal plates of various planforms with unrestricted inflow at the edges are related with the correlations presented by equations (15), (16) and (17).

$$Ra = \frac{g\beta\,\overline{\Delta T}\left(L^*\right)^3}{\nu\alpha} \tag{15}$$

$$Nu = \frac{qL^*}{A\,\overline{\Delta T}\,k} \tag{16}$$

$$L^* = A / p \tag{17}$$

Uniform Heat Flux Parallel Plates

Classical correlations:

(Lloyd & Moran 1974) presented correlations for natural convection at horizontal isothermal plates taking into account both hot side up or cold side down and hot side down or cold side up, as shown by equations (18), (19) and (20).

$$Nu = 0.54\,Ra^{1/4} \qquad 10^4 \le Ra \le 10^7 \tag{18}$$

hot side up or cold side down, (Lloyd & Moran 1974)

$$Nu = 0.15 Ra^{1/3} \qquad 10^7 < Ra \le 10^{10} \tag{19}$$

hot side up or cold side down, (Lloyd & Moran 1974)

$$Nu = 0.27 Ra^{1/3} \qquad 10^5 < Ra \le 10^{10} \tag{20}$$

hot side down or cold side up, (Lloyd & Moran 1974)

(Rohsenow et al. 1998) introduced correlations for heated upward-facing plates with uniform temperature or heat flux ($1 < Ra < 10^{10}$), namely, equations (21), (22), (23) and (24).

$$Nu = 0.835 \overline{C}_l Ra^{1/4} \qquad 1 < Ra < 10^{10} \quad \overline{C}_l = 0.515 \text{ for air} \tag{21}$$

$$Nu_{lam} = \frac{1.4}{\ln\left(1 + 1.4 / Nu\right)} \tag{22}$$

$$Nu_{turb} = C_t^U Ra^{1/3} \qquad C_t^U = 0.14 \text{ for air} \tag{23}$$

$$Nu_t = \left(Nu_{lam}^m + Nu_{turb}^m\right)^{1/m} \qquad m = 10 \tag{24}$$

On the other hand, for horizontal isothermal heated downward-facing plates, equations (25) and (26) are suggested by (Tetsu et al. 1973) for $10^3 < Ra < 10^{10}$.

$$Nu = \frac{0.527}{\left(1 + \left(1.9 / \mathrm{Pr}\right)^{9/10}\right)^{2/9}} Ra^{1/5} \qquad 10^3 < Ra < 10^{10} \tag{25}$$

$$Nu_{lam} = \frac{2.5}{\ln\left(1 + 2.5 / Nu\right)} \tag{26}$$

Mixed natural convection

$$Nu^4 = Nu_{lam}^4 + Nu_{turb}^4 \tag{27}$$

(Baehr & Stephan 1996)

Free and forced convection including radiative heat flux

The work by (Burger 2004) introduced correlations, which took into account significant natural convection mechanisms by evaluating convective and radiative heat fluxes onto or from a smooth horizontal flat plate exposed to the natural environment. As shown in equation (28), T_m is the mean temperature between the collector roof and ambient air, g is the gravitational constant and ΔT is the difference between the roof and ambient air temperature. The variables ρ, μ, c_p and k symbolize the density, dynamic viscosity, specific heat capacity and thermal conductivity of the air respectively, all of which are evaluated at the mean temperature T_m. If the collector roof temperature only marginally exceeds the ambient temperature equation (29) can be employed. Equation (30) was derived by (Kröger 2004) using Gnielinski's equation for fully developed turbulent flow, by approximating the flow in the collector as flow between variably spaced plates.

$$h = \frac{0.2106 + 0.0026v\left(\frac{\rho T_m}{\mu g \Delta T}\right)^{1/3}}{\left(\frac{\mu T_m}{g \Delta T c_p k^2 \rho^2}\right)^{1/3}} \tag{28}$$

(Burger 2004), [1]

$$h = 3.87 + 0.0022\left(\frac{v\rho c_p}{\mathrm{Pr}^{2/3}}\right) \tag{29}$$

(Burger 2004), [1]

$$h = \frac{(f/8)(\mathrm{Re}-1000)\mathrm{Pr}}{1+12.7(f/8)^{1/2}\left(\mathrm{Pr}^{2/3}-1\right)}\left(\frac{k}{D_h}\right) \tag{30}$$

(Burger 2004)

3. Flow in collector as a flow in a channel between infinite parallel plates

The development of the hydrodynamic and thermal boundary layers can produce four types of laminar flows in ducts, namely, fully developed, hydrodynamically developing, thermally developing (hydrodynamically developed and thermally developing), and simultaneously developing (hydrodynamically and thermally developing), as sketched by Fig. 5. In this case particularly, the velocity profile and dimensionless temperature profile do not change along the flow direction. On the other hand, hydrodynamically developing flow is isothermal fluid flow in which the velocity profile does not remains constant in the flow direction.

The hydrodynamic entrance length is defined as the distance over which the velocity distribution changes and the hydrodynamic boundary layer develops. (Rohsenow et al. 1998) synthesize those phenomena, as shown in Table 1.

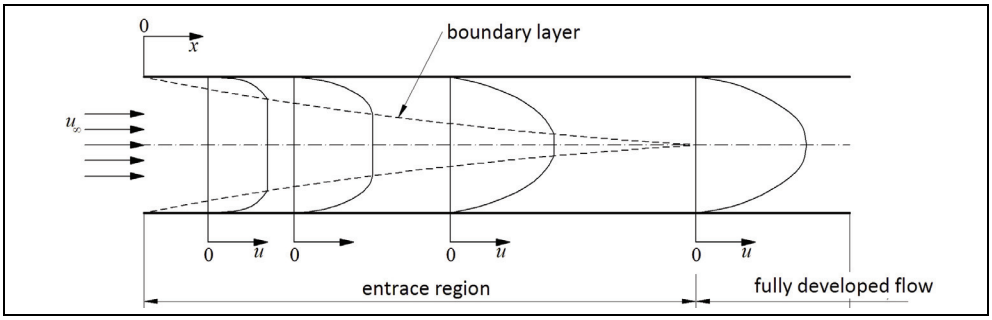

Fig. 5. Flow development in parallel plates channel.

[1] $v = v_w$ for heat transfer between roof and ambient.

Flow type	Hydrodynamic boundary layer	Velocity distribution in the flow direction	Thermal boundary layer	Dimensionless temperature distribution in the flow	Nussel number
Fully developed Flow	Developed	Invariant	Developed	Invariant	Constant
Hydrodynamically Developing flow	Developing	Variant	-	-	-
Thermally Developing flow	Developed	Invariant	Developing	Variant	Variant
Simultaneously Developing flow	Developing	Variant	Developing	Variant	Variant

Table 1. Flow types in parallel plates channel.

In general, the flow in a SCPP collector can be assumed as simultaneously developing flow. Thus, the following equations are recommended for a typical flow in a channel between infinite parallel plates.

Laminar Flow – Fully Developed Flow

For a parallel plate duct with hydraulic diameter D_h = 4t (t represents the half-distance between the plates). According to (Shah & London 1978), the following equations for the corresponding boundary conditions.
Uniform temperature, the other wall at the uniform entering fluid temperature: eq. (31)

$$Nu_1 = Nu_2 = 4 \tag{31}$$

Uniform wall heat flux at one wall; the other wall insulated: eq. (32)

$$Nu_1 = 0 \quad Nu_2 = 5.385 \tag{32}$$

Uniform temperature (different from the entering fluid temperature) at one wall; the other wall insulated: eq. (33)

$$Nu_1 = 0 \quad Nu_2 = 4.861 \tag{33}$$

Uniform wall heat flux at one wall; the other wall maintained at the entering fluid temperature: eq. (34)

$$Nu_1 = Nu_2 = 4 \tag{34}$$

Laminar Flow –Uniform temperature at each wall: eq. (35)

$$Nu_1 = Nu_2 = 7.541 \tag{35}$$

(Shah & London 1978)

Laminar Flow – Uniform temperature at one wall and uniform heat flux at the other: eq. (36)

$$Nu_1 = 4.8608 \quad Nu_2 = 0 \tag{36}$$

(Shah & London 1978)

Laminar Flow – Developing Flow – Equal and uniform temperatures at both walls: eqs. (37) and (38)

$$Nu_x = 7.55 + \frac{0.024x^{*-1.14}\left[0.0179\,\mathrm{Pr}^{0.17}\,x^{*-0.64} - 0.14\right]}{\left[1 + 0.0358\,\mathrm{Pr}^{0.17}\,x^{*-0.64}\right]^2} \tag{37}$$

(Shah & Bhatti 1987), (Hwang & Fan 1964), (Stephan 1959)

$$\overline{Nu} = 7.55 + \frac{0.024x^{*-1.14}}{1 + 0.0358\,\mathrm{Pr}^{0.17}\,x^{*-0.64}} \tag{38}$$

(Shah & Bhatti 1987), (Hwang & Fan 1964), (Stephan 1959)

Turbulent Flow

Transition Flow

The mean Nusselt number in the thermal entrance region of a parallel plate duct with uniform wall temperature at both walls in the range of 2300 < Re < 6000 is given by (Hausen 1943) as follows:

$$\overline{Nu} = 0.116\left(\mathrm{Re}^{2/3} - 160\right)\mathrm{Pr}^{1/3}\left[1 + \left(\frac{x}{D_h}\right)^{-2/3}\right] \tag{39}$$

(Hausen 1943)

Fully developed flow: eq. (40).

$$Nu_H = \frac{Nu}{1 - \gamma\theta^*} \tag{40}$$

(Hausen 1943)

γ = 0: one wall is heated and the other is insulated;
γ = 1: uniform heat fluxes of equal magnitudes are applied to both walls;
γ = -1: heat transfer into one wall and out of the other wall, while the absolute values of the heat fluxes at both walls are the same.

Nusselt Numbers and Influence Coefficients for Fully Developed Turbulent Flow - Parallel Plates Duct With Uniform Heat Flux at One Wall and the Other Wall Insulated, Pr = 0.7, (Kays & Leung 1963)

Re = 10^4		3×10^4		10^5		3×10^5		10^6	
Nu	θ*	Nu	θ*	Nu	θ*	Nu	θ*	Nu	θ*
27.8	0.220	61.2	0.192	155.0	0.170	378.0	0.156	1030.0	0.142

Natural Convection within Enclosures

The natural convection in the collector can regarded as natural convection in horizontal rectangular enclosures. Nusselt number relations for this are introduced in the following, namely, equations (41) and (42).

$$Nu = 0.195 Ra^{1/4} \qquad 10^4 < Ra < 4 \times 10^5 \tag{41}$$

(Jakob 1949)

$$Nu = 0.068 Ra^{1/3} \qquad 4 \times 10^5 < Ra < 10^7 \tag{42}$$

(Jakob 1949)

Equation (43) is suggested by (Hollands et al. 1976). Their study was based on experiments with air correlation for horizontal enclosures. The notation $[\ ]^+$ indicates that if the quantity in the bracket should be set equal to zero if it is negative.

$$Nu = 1 + 1.44\left[1 - \frac{1708}{Ra}\right]^+ + \left[\frac{Ra^{1/3}}{18} - 1\right]^+ \qquad Ra < 10^8 \tag{43}$$

4. Flow in collector as a flow between two finite stationary disks with converging flow developing

The flow between two finite stationary disks with converging flow developing and constant distance between the plates ($2t$) was investigated by (Bernardes 2003). Thermal and hydrodynamic boundary layers, friction factor, pressure development and Nusselt number were derived. For lager values of the dimensionless radii (>> 1), the velocity profile becomes parabolic and invariant and the friction factor approaches the classic value obtained for fully developed flow between infinite plates. At radii less than one a typical external boundary layer evolves close to the wall with an approximately uniform core region, the boundary layer thickness decreases from one-half the disk spacing to values proportional to the local radii as the flow accelerates. The local Nusselt number decreases with the radius and the eq.(44) is recommended for thermally developing flow. The Nusselt number for thermally fully developed flow is a straight line: $Nu \approx (r/R)$.

$$Nu = 230\left(\frac{r}{R}\right)^{0.650}\left(1 - \frac{r}{R}\right)^{-0.386} \tag{44}$$

7. Nomenclature

A	area	m²
c_p	heat capacity	J/(kg·K)
d_h	hydraulic diameter	m
k	thermal conductivity	W/(m·K)
f	friction factor	-
g	gravitational acceleration	m²/s
h	convective heat transfer coefficient	W/(m²·K)
L^*	plate length	m
L	plate length	m
Nu	Nusselt number	-
Nu_x	local Nusselt number	-
Nu_{lam}	Nusselt number for laminar flow	-

Nu_{turb}	Nusselt number for turbulent flow	-
$\overline{Nu}$	average Nusselt number	-
p	perimeter	m
Pe	Peclet number	-
Pr	Prandtl number	-
q	heat transfer rate	W
r	cylindrical coordinate	m
R	disc radius	m
Ra	Rayleigh number	-
Re	Reynolds number	-
Re_x	local Reynolds number	-
Re_L	Reynolds number for a plate with length L	-
t	half-distance between the plates	m
T	temperature	K
T_m	average temperature	K
v	velocity	m/s
x^*	dimensionless axial coordinate for the thermal entrance region, = x/D_h Pe	
α	fluid thermal diffusivity	m^2/s
β	coefficient of thermal expansion	K^{-1}
γ	ratio of heat fluxes at two walls of a parallel plate duct	-
ν	fluid kinematic viscosity	m^2/s
μ	fluid dynamic	Pa·s
ρ	density	kg/m^3

subscripts

1,2	plate 1, 2, etc.

8. References

Baehr, H. D. & Stephan, K. (1996). *Wärme- und Stoffübertragung*, Springer-Verlag, Berlin.

Bernardes, M. A. d. S. (2003). Symmetric Sink Flow and Heat Transfer Between Two Parallel Disks, *Proceedings of ASME Summer Heat Transfer Conference - Heat Transfer 2003*, pp., Las Vegas, Nevada, USA, ASME.

Bernardes, M. A. d. S. (2004). Technische, ökonomische und ökologische Analyse von Aufwindkraftwerken. In *IER*, pp. Stuttgart, Germany, Universität Stuttgart.

Bernardes, M. A. d. S. (2010). Solar Chimney Power Plants – Developments and Advancements. In: *Solar Energy,* ed. R. D. Rugescu, 432. Vukovar, Intech.

Bernardes, M. A. d. S.,Valle, R. M. & Cortez, M. F.-B. (1999) Numerical Analysis of Natural Laminar Convection in a Radial Solar Heater. *International Journal of Thermal Sciences,* Vol. 38, pp. 42-50.

Bernardes, M. A. d. S.,Voß, A. & Weinrebe, G. (2003) Thermal and Technical Analyses of Solar Chimneys. *Solar Energy,* Vol. 75, pp. 511–524.

Burger, M. (2004). Prediction of the Temperature Distribution in Asphalt Pavement Samples. In *Department of Mechanical Engineering* pp. Stellenbosch, South Africa., University of Stellenbosch.

Çengel, Y. A. (2007). *Heat and mass transfer : a practical approach*, McGraw-Hill, 0073129305, Boston.

Hausen, H. (1943) Darstellung des Wärmeüberganges in Rohren durch verallgemeinerte Potenzbeziehyngen. *VDI - Verfahrenstechnik,* Vol. 4, pp. 91-98.

Hollands, K. G. T.,Unny, T. E.,Raithby, G. D. & Konicek., L. (1976) Free Convective Heat Transfer Across Inclined Air Layers. *Journal of Heat Transfer,* Vol. 98, pp. 189–193.

Hwang, C.-L. & Fan, L.-T. (1964) Finite difference analysis of forced-convection heat transfer in entrance region of a flat rectangular duct. *Applied Scientific Research,* Vol. 13, 1, pp. 401-422.

Incropera, F. P. (2007). *Introduction to heat transfer*, Wiley, 9780471457275, Hobokenm NJ.

Jakob, M. (1949). *Heat Transfer*, Wiley, New York.

Kays, W. M. & Leung, E. Y. (1963) Heat transfer in annular passages--hydrodynamically developed turbulent flow with arbitrarily prescribed heat flux. *International Journal of Heat and Mass Transfer,* Vol. 6, 7, pp. 537-557.

Kröger, D. G. (2004). *Air-cooled Heat Exchangers and Cooling Towers*, Pennwell Corp., Tulsa, Oklahoma.

Kröger, D. G. & Blaine, D. (1999) Analysis of the Driving Potential of a Solar Chimney Power Plant. *South African Inst. of Mechanical Eng. R & D J.,* Vol. 15, pp. 85-94.

Lienhard IV, J. H. & Lienhard V, J. H. (2008). *A Heat Transfer Texbook*, Phlogiston Press, Massachussets.

Lloyd, J. R. & Moran, W. R. (1974) Natural Convection Adjacent to Horizontal Surface of Various Planforms. *Journal of Heat Transfer,* Vol. 96, pp. 443–447.

Petukhov, B. J. & Popov, N. V. (1963) Theoretical Calculation of Heat Transfer and Frictional Resistance in Turbulent Flow in Tubes of an Incompressible Fluid with Variable Physical Properties. *High Temperature,* Vol. 1, pp. 69-83.

Pretorius, J. P. & Kröger, D. G. (2006) Solar Chimney Power Plant Performance. *Transactions of the ASME,* Vol. 128, pp. 302-311.

Rohsenow, W. M.,Hartnett, J. P. & Cho, Y. I. (1998). *Handbook of heat transfer*, McGraw-Hill, 0070535558, New York.

Schlaich, J.,Bergermann, R.,Schiel, W. & Weinrebe, G. (2005) Design of Commercial Solar Updraft Tower Systems - Utilization of Solar Induced Convective Flows for Power Generation. *ASME Journal of Solar Energy Engineering,* Vol. 127, pp. 117-124.

Shah, R. K. & Bhatti, M. S. (1987). Laminar Convection Heat Transfer in Ducts. In: *Handbook of Single-Phase Convective Heat Transfer,* eds. S. Kakaç,R. K. Shah & W. Aung. New York, Wiley-Interscience, John Wiley & Sons.

Shah, R. K. & London, A. L. (1978). *Laminar Flow Forced Convection in Ducts: Supplement 1 to Advances in Heat Transfer*, Academic Press, 9780120200511, New York.

Stephan, K. (1959) Wärmeübergang und Druckabfall bei nicht ausgebildeter Laminarströmung in Rohren und in ebenen Spalten. *Chemie Ingenieur Technik,* Vol. 31, 12, pp. 773-778.

Tetsu, F.,Hiroshi, H. & Itsuki, M. (1973) A theoretical study of natural convection heat transfer from downward-facing horizontal surfaces with uniform heat flux. *International Journal of Heat and Mass Transfer,* Vol. 16, 3, pp. 611-627.

Žukauskas, A. & Šlanciauskas, A. (1999). *Heat Transfer In Turbulent Fluid Flows*, CRC Press, 089116426X.

26

Thermal Aspects of Solar Air Collector

Ehsan Mohseni Languri[1] and Davood Domairry Ganji[2]
[1]*University of Wisconsin - Milwaukee*
[2]*Noshirvani Technical University of Babol,*
[1]*USA*
[2]*Iran*

1. Introduction

The amount of solar radiation striking the earth's surface not only depends on the season, but also depends on local weather conditions, location and orientation of the surface. The average value of this radiation is about 1000 w/m^2 when the absorbing surface is perpendicular to the sun's rays and the sky is clear. There are several methods exist to absorb and use this free, clean, renewable and very long lasting source of energy [1]. The solar collectors are one of the devices which can absorb and transfer energy of the sun to a usable and/or storable form in many applications such as drying the agricultural, textile and marine products as well as the heating of building [2]. There is variety of designs for the solar thermal collectors depending on their applications. For example, parabolic trough solar air collector is widely used in solar power plants where solar heat energy is used to generate electricity [3].

Flat plate solar collectors are the most common types of solar collectors used in many applications such as solar hot water panels to provide hot water or as solar air heater for pre-heating the air in building heating or industrial HVAC systems. In the solar hot water panel, a sealed insulated box containing a black metal sheet, called absorber surface, with built-in pipes is located faced to the sun. Solar radiation heats up water inside pipes, causing it to circulate through the system by means of natural convection. Then, water is delivered to a storage tank located above the collector. Such passive solar water heating devices used widely in hotels and home especially in southern Europe.

Several models of thermal solar flat plate collector are available and generally all of them consist of four major parts:

1. A flat-plate absorber, which absorbs the solar energy
2. A transparent cover(s) that allows solar energy to pass through and reduces heat loss from the absorber
3. A heat-transport fluid (air or water) flowing through the collector (water flows through tubes) to remove heat from the absorber
4. And finally, a heat insulating backing.

The exergy of a system defined as the maximum possible useful work during a process that brings the system into equilibrium with a heat reservoir [3]. Exergy can be destroyed by irreversibility of a process. One of the powerful methods of optimizing complex thermo dynamical systems is to do an exergy analysis, which is called the second law analysis as

well. In 1956, Rant [4] proposed the term exergy that was previously developed by Gibbs [5] in 1873. One can find the details of this concept in the thermodynamics literature [6-9]. Saravanan et al. [10] used the exergy tool to analyze the performance of cooling tower. Bejan was the first person who developed and published the governing equations of exergy to solar collectors [11, 12]. Later Londono-Hurtado and Rivera-Alvarez [13] developed a model to study the behavior of volumetric absorption solar collectors and its performance. Their model is used to run a thermodynamic optimization of volumetric absorption solar collectors to maximize the energy output of heat extracted from the collector. Luminosu and Fara [14] used the thermodynamically analysis using exergy method to find out the best flow rate of the test fluid in their experiments.

Altfeld et al. [15,16] claimed that the heat transfer characteristics of the absorber are less important in case of considering a highly insulated solar air heater. Torres-Reyes et al. [17] carried out energy and exergy analysis to determine the optimal performance parameters and to design a solar thermal energy conversion system. Kurtbas and Durmuş [18] analyzed several different absorber plates for solar air heater and found that there was a reverse relationship between dimensionless exergy loss and heat transfer, as well as pressure loss.

2. Mathematical modeling

In this section, a review has been done on the theoretical modeling of several different designs of solar air heaters. Theoretical modeling of a single cover solar air collector is derived comprehensively in this section. In this case, a single air flow between absorber and glass plates assumed to convey the heat of the solar radiation, Fig.1.

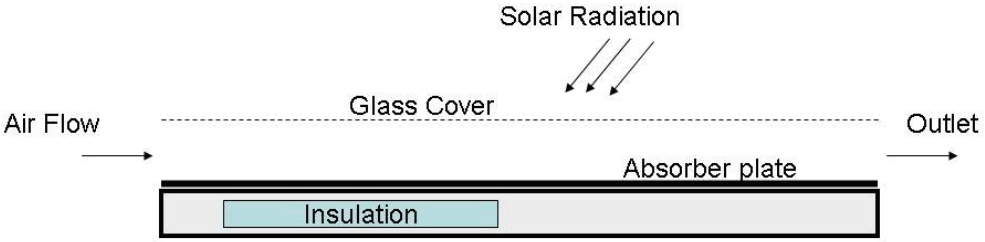

Fig. 1. Schematic view of single air flow solar air heater

The energy balance equations for cover glass, absorber plate and air flow respectively, are as following:

$$\alpha_g S = M_g C_g \frac{\partial T_g}{\partial t} + k_g \delta_g \frac{\partial^2 T_g}{\partial x^2} + h_w (T_g - T_a) + h_{rgs} (T_g - T_s) + h_{cgf} (T_g - T_f) + h_{rpg} (T_g - T_p) \quad (1)$$

$$\alpha_p \tau_p S = M_p C_p \frac{\partial T_p}{\partial t} + k_p \delta_p \frac{\partial^2 T_p}{\partial x^2} + h_{cpf} (T_p - T_f) + h_{rpg} (T_p - T_g) + U_r (T_p - T_a) \quad (2)$$

$$M_f C_f \frac{\partial T_f}{\partial t} + \frac{G_f C_f}{W} \frac{\partial^2 T_f}{\partial x^2} = h_{cgf} (T_f - T_g) + h_{cpf} (T_p - T_f) \quad (3)$$

One may assume following boundary and initial conditions for the given geometry:

$$T_f(t=0) = T_p(t=0) = T_g(t=0) = T_a(t=0) \tag{4}$$

$$\frac{\partial T_g}{\partial x}|_{x=0} = 0, \quad \frac{\partial T_g}{\partial x}|_{x=L} = 0, \quad \frac{\partial T_p}{\partial x}|_{x=0} = 0, \quad \frac{\partial T_p}{\partial x}|_{x=L} = 0 \tag{5}$$

3. Back pass solar air heater

Choudhury and Garg [19], Ong[20], Hegazy[21], Al-Kamil and Al-Ghareeb[22] investigated the heat transfer in the back pass solar air collectors. In such solar collectors, the absorber plate is placed behind the glass cover with a gap filled with static air from the glass cover. The flow of air is happens between the bottom surface of the absorber and the top surface of insulated surface, Figure 2.

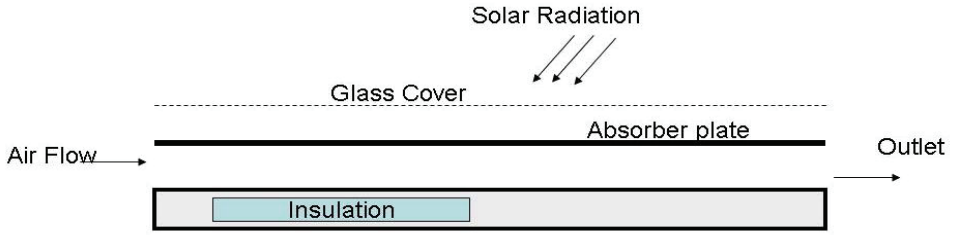

Fig. 2. Schematic view of back pass solar air heater

Garg et al. [23] developed the following mathematical modeling for the glass cover, absorber plate, air flow and the bottom plate, respectively as:

$$h_{gs}(T_s - T_g) + h_{rpg}(T_p - T_g) = U_t(T_g - T_a) \tag{6}$$

$$(\alpha\tau)S = h_{cpf}(T_p - T_{fm}) + h_{rps}(T_p - T_a) + h_{rpb}(T_p - T_b) + h_{rpg}(T_p - T_g) \tag{7}$$

$$h_{cpf}(T_p - T_{fm}) = h_{cbf}(T_{fm} - T_b) + mC_a(T_{fo} - T_a) \tag{8}$$

$$h_{rpb}(T_p - T_b) = h_{cbf}(T_b - T_{fm}) + U_b(T_b - T_a) \tag{9}$$

4. Parallel pass solar air heater

The design of the parallel pass solar air heater is to optimize the heat transfer transportation in the solar air heaters. This design consists of a glass cover, absorber plate and bottom insulated plate. There are two air flow channels which one is located between the glass cover and absorber and another one is located between the absorber and the bottom insulated plate, Figure 3.

Jha et al. [24] obtained the energy transport equations for the glass cover, channel 1, absorber plate, channel 2 and finally, bottom insulated plate as following

$$M_g C_g \frac{\partial T_g}{\partial t} = \alpha_g S + h_{rpg}(T_p - T_g) + h_{cf1g}(T_{f1} - T_g) - h_{cgw}(T_g - T_w) - h_{rga}(T_g - T_a) \tag{10}$$

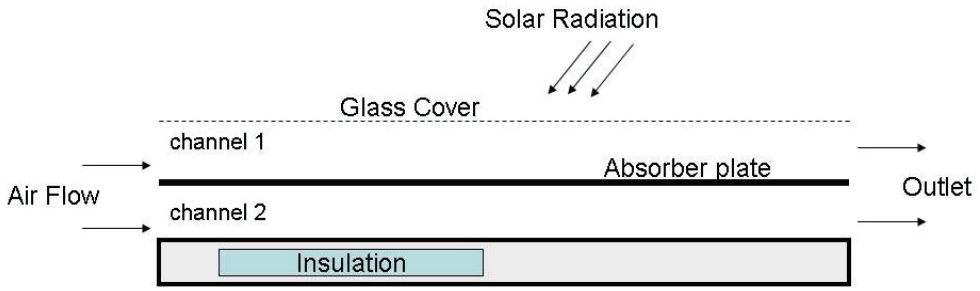

Fig. 3. Schematic view of parallel pass solar air heater

$$M_{f1}C_f\frac{\partial T_{f1}}{\partial t}=\frac{-G_1C_f}{W}\frac{\partial T_{f1}}{\partial x}+h_{cpf1}(T_p-T_{f1})-h_{cf1g}(T_{f1}-T_g) \tag{11}$$

$$M_1C_p\frac{\partial T_p}{\partial t}=\alpha_p\tau_gS-k_p\delta_p\frac{\partial^2T_p}{\partial x^2}-h_{rpg}(T_p-T_g)-h_{cpf2}(T_p-T_{f2})-h_{rpb}(T_p-T_b)-h_{cpf1}(T_p-T_{f1}) \tag{12}$$

$$M_{f2}C_f\frac{\partial T_{f2}}{\partial t}=\frac{-G_2C_f}{W}\frac{\partial T_{f2}}{\partial x}+h_{cpf2}(T_p-T_{f2})-h_{cbf2}(T_b-T_{f2}) \tag{13}$$

$$M_bC_b\frac{\partial T_b}{\partial t}=-k_b\delta_b\frac{\partial^2T_b}{\partial t}+h_{rpb}(T_p-T_b)-h_{cbf2}(T_b-T_{f2})-h_b(T_b-T_r) \tag{14}$$

Along with following boundary and initial conditions

$$\frac{\partial T_p}{\partial x}|_{x=0}=0\,,\ \frac{\partial T_p}{\partial x}|_{x=L}=0\,,\ \frac{\partial T_b}{\partial x}|_{x=L}=0 \tag{15}$$

$$T_{f1}(x=0)=T_{fi},\ \ T_{f2}(x=0)=T_{fi} \tag{16}$$

5. Double-pass solar air heater

Ho et al. [25] developed the mathematical modeling for the double pass solar air heater. In such solar collectors, the air is allowed to move faster than the simple collectors. In his mathematical modeling, following assumptions are considered:

- Temperatures of absorbing plate, bottom insulated plate and the fluid are only functions of air flow direction
- Glass cover and absorber plate do not absorb radiant energy
- The radiant energy absorbed by the outlet cover is negligible

Considering above assumptions, energy equations of cover 1, absorber plate, bottom plate, channels *a* and *b* are as following, respectively:

$$h_{rpg2}(T_p-T_{g1})+h_1'(T_b(z)-T_{g1})=U_{g1s}(T_{g1}-T_s) \tag{17}$$

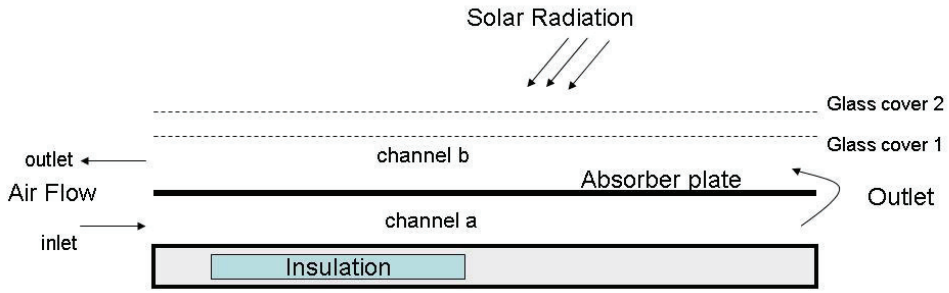

Fig. 4. Schematic view of double- pass solar air heater

$$\alpha_p \tau_{g1} \tau_{g2} S - h_T (T_p - T_s) + h_B (T_p - T_s) + h_1 (T_p - T_b(x)) + h_2 (T_p - T_a(x)) \tag{18}$$

$$h_{rpR} (T_p - T_R) + h_2' (T_a(x) - T_R) = U_{B1s} (T_p - T_s) \tag{19}$$

$$h_2 (T_p - T_a(x)) - h_2' (T_a(x) - T_R) = \left[\frac{(R+1) m C_p}{W} \right] \frac{dT_a(x)}{dx} \tag{20}$$

$$h_1 (T_p - T_b(x)) - h_1' (T_b(x) - T_{g1}) = \left[-\frac{(R+1) m C_p}{W} \right] \frac{dT_b(x)}{dx} \tag{21}$$

6. Energy analysis

According to Duffie and Beckman [26], the rate of heat received by the air from the collector is

$$\dot{Q}_f = \dot{m}_f C_p (T_o - T_i) \tag{22}$$

One can find the specific collector power by dividing of the heat by the area of the collector [26]

$$\dot{q}_f = \dot{Q}_f / A_{col} = \dot{m}_f C_p (T_o - T_i) / A_{col} \tag{23}$$

The average daily useful heat per unit area of the collector can be obtained by adding up all radiation times as

$$q_{a,d} = 3600 \sum_{i=1}^{8} \dot{q}_{a,hourly} \tag{24}$$

in which $\dot{q}_{a,hourly}$ is the useful heat per unit area of the collector for the hour i of the test day. The energy efficiency of solar energy can be obtained by the ratio of absorbed energy to the total energy of the sun [14].

$$\eta_{en} = \dot{q}_f / G_{col} \tag{25}$$

where G_c is the solar radiation captured by the collector in w / m^2

7. Exergy analysis

According to Bejan et al. [11] and Bejan [12], there are two main sources of entropy generation in a solar air collector, one due to the friction of passing fluid, and the other one due to the thermal heat transfer or temperature change of air. Esens's [22] considered following assumptions to derive the exergy balance equations:

1. The process is steady state and steady flow.
2. The potential and kinetic energies are negligible.
3. Air is an ideal gas, so its specific heat is constant.
4. The humidity of air is negligible.

The general exergy balance for a steady state and steady flow process is

$$\dot{I} = \dot{E}x_{heat} - \dot{E}x_{work} + \dot{E}x_i - \dot{E}x_o \tag{26}$$

Considering above assumptions, following relations are defined for the mentioned terms:

$$\dot{E}x_{heat} = \sum (1 - \frac{T_0}{T_s})\dot{Q}_s \tag{27}$$

$$\dot{E}x_{work} = 0 \tag{28}$$

$$\dot{E}x_i = \sum \dot{m}_{in}[(h_{in} - h_0) - T_0(s_{in} - s_0)] \tag{29}$$

$$\dot{E}x_o = \sum \dot{m}_{out}[(h_{out} - h_0) - T_0(s_{out} - s_0)] \tag{30}$$

Eq (28) comes from the fact that there is no work has done during the process. From mass balance we have

$$\sum \dot{m}_i = \sum \dot{m}_o = \dot{m}_a \tag{31}$$

Upon substitution of Eqs (27) to (31) in Eq (26), one can find the rate of irreversibility as

$$\dot{I} = (1 - \frac{T_a}{T_s})\dot{Q}_s - \dot{m}_f[(h_o - h_i) - T_a(s_o - s_i)] \tag{32}$$

$\dot{Q}_s$ is the total rate of the exergy received by the collector absorber area from the solar radiation and is evaluated by this relation

$$\dot{Q}_s = G_c.A_{col}.\tau\alpha \tag{33}$$

where $\tau\alpha$ is absorbance-transmittance product of the covering glass and the absorber plate. The changes in enthalpy and entropy of test liquid, air, in the collector can be obtained using following two expressions:

$$h_o - h_i = C_p(T_o - T_i) \tag{34}$$

$$s_o - s_i = C_p \ln(\frac{T_o}{T_i}) - R \ln(\frac{P_o}{P_i}) \tag{35}$$

One can find the final form of irreversibility expression by substituting Eqs (33) to (35) in Eq (32) as

$$\dot{I} = (1 - \frac{T_a}{T_s}) G_{col}.A_{col}.\tau\alpha - \dot{m}_f C_p (T_o - T_i) + \dot{m}_f T_a C_p \ln(\frac{T_o}{T_i}) - \dot{m}_f T_a R \ln(\frac{P_o}{P_i}) \tag{36}$$

T_s is apparent temperature of sun surface, which considered to be 6000 K. In this equation the first term comes from the entropy generated due to heat transfer; second and third terms are related to the temperature change of air and last term is related to the entropy generated due to the friction of fluid. By definition, irreversibility is the total entropy generated times the ambient temperature [8]

$$\dot{I} = \dot{S}_{gen} T_a \tag{37}$$

Therefore, the total entropy generated during the process will be

$$\dot{S}_{gen} = \frac{1}{T_a}[(1 - \frac{T_a}{T_s}) G_{col}.A_{col}.\tau\alpha - \dot{m}_f C_p (T_o - T_i)] + \dot{m}_f C_p \ln(\frac{T_o}{T_i}) - \dot{m}_f R \ln(\frac{P_o}{P_i}) \tag{38}$$

According the second law of thermodynamics, the exergy efficiency defined as [17]

$$\eta_{ex} = 1 - \frac{\dot{I}}{\dot{E}x_{heat}} = 1 - \frac{\dot{S}_{gen} T_a}{(1 - T_a / T_s)\dot{Q}_s} \tag{39}$$

8. Error analysis

There are two types of errors in doing the energy and exergy analysis;
One group comes from direct measurement, such as ΔG_c , ΔT , ΔP and $\Delta \dot{m}$

The second group of errors comes from indirect measurement, which are $\Delta \eta_{en}$ and $\Delta \eta_{ex}$. Luminosu and Fara [14] proposed following relations for error analysis:

$$\Delta \eta_{ex} = \Delta \dot{I} / \dot{E}x_{heat} + \dot{I} \Delta \dot{E}x_{heat} / \dot{E}x_{heat}^2 \tag{40}$$

$$\Delta \eta_{en} = \Delta \dot{q}_a / G_c + \dot{q}_f \Delta G_{col} / G_{col}^2 \tag{41}$$

where each error term may be computed as following:

$$\Delta \dot{E}x_{heat} = (\Delta T / T_s + T_a \Delta T / T_s^2) A_{col} (\tau\alpha) G_{col} + (1 - T_a / T_s) A_{col} (\tau\alpha) \Delta G_{col} \tag{42}$$

$$\Delta \dot{I} = T_a \Delta \dot{S}_{gen} + \dot{S}_{gen} \Delta T \tag{43}$$

$$\begin{aligned} \Delta \dot{S}_{gen} = {} & [R \ln(P_o / P_i) + C_p \ln(T_i / T_o) + C_p (T_o + T_i) / T_a] \Delta \dot{m} + G_{col} A_{col} (\tau\alpha) \Delta T / T_a^2 \\ & + \dot{m} C_p [1 / T_o + 1 / T_i + 2 / T_a + (T_o + T_i) / T_a^2] \Delta T + \dot{m} R [1 / P_o + 1 / P_i] \Delta P \\ & + A_{col} (\tau\alpha) [1 / T_s + 1 / T_a] \Delta G_{col} \end{aligned} \tag{44}$$

$$\Delta\dot{q}_a = C_p[\Delta\dot{m}(T_o + T_i) + 2\dot{m}\Delta T] / A_{col} \quad (45)$$

9. Nomenclature

A	Absorbing area [m^2]
C	Specific heat [kJ/kg.K]
$\dot{E}x$	Rate of exergy [kJ/s]
G	Solar radiation flux [kw / m^2]
h	Enthalpy [kJ/kg]
$\dot{I}$	Irreversibility [kw]
$\dot{m}$	Mass flow rate [kg/s]
p	pressure [Pa]
$\dot{Q}$	Rate of heat energy received [kw]
$\dot{q}$	Ratio of heat energy received by the unit area [kw / m^2]
R	Gas constant for carrier fluid [kJ/kg.K]
$\dot{S}$	Rate of entropy generated [kw/K]
T	Temperature [K]

Greek Letters

η	Efficiency (dimensionless)
$\tau\alpha$	Absorbance-transmittance product (dimensionless)
Δ	Error in measuring or calculation

Subscripts

a	Ambient
f	Carrier fluid (air)
c	convection
col	Collector
g	Glass cover
d	Daily
en	Energy
ex	Exergy
gen	Generated
heat	Heat energy
hourly	Hourly
i	Inlet flow of carrier fluid
o	Outlet flow of carrier fluid
p	Absorber plate
s	Sun
work	Work

10. References

[1] E, Mohseni Languri, H. Taherian, R. Masoodi, J. Reisel, An exergy and energy study of a solar thermal air collector, Thermal Science, 2009; 13(1):205-216.

[2] Rene Tchinda, A review of the mathematical models for predicting solar air heaters systems, Renewable and Sustainable Energy Reviews 13 (2009) 1734–1759.
[3] Perrot, Pierre, A to Z of Thermodynamics, Oxford University Press, Oxford, 1998.
[4] Rant, Z., Exergy, a new word for technical available work, Forschung auf dem Gebiete des Ingenieurwesens 22, (1956), pp. 36–37.
[5] Gibbs, J. W. ,A method of geometrical representation of thermodynamic properties of substances by means of surfaces: reprinted in Gibbs, Collected Works, ed. W. R. Longley and R. G. Van Name, Transactions of the Connecticut Academy of Arts and Sciences, 2, (1931), pp. 382–404 .
[6] Moran, M. J. and Shapiro, H. N., Fundamentals of Engineering Thermodynamics, 6th Edition, 2007.
[7] Van Wylen, G.J., Thermodynamics, Wiley, New York, 1991.
[8] Wark, J. K., Advanced Thermodynamics for Engineers, McGraw-Hill, New York, 1995.
[9] Bejan, A., Advanced Engineering Thermodynamics, 2nd Edition, Wiley, 1997.
[10] Saravan , M. Saravan, R and Renganarayanan, S. , Energy and Exergy Analysis of Counter flow Wet Cooling Towers, Thermal Science, 12, (2008), 2, pp. 69-78.
[11] Bejan, A., Kearney, D. W., and Kreith, F., Second Law Analysis and Synthesis of Solar Collector Systems, Journal of Solar Energy Engineering, 103, (1981), pp. 23-28.
[12] Bejan, A. , Entropy Generation Minimization, New York, CRC press, 1996.
[13] Londono-Hurtado, A. and Rivera-Alvarez, A., Maximization of Exergy Output From Volumetric Absorption Solar Collectors, Journal of Solar Energy Engineering , 125, (2003) ,1 , pp. 83-86.
[14] Luminosu, I and Fara, L., Thermodynamic analysis of an air solar collector, International Journal of Exergy, 2, (2005), 4, pp. 385-408.
[15] Altfeld, K,. Leiner, W., Fiebig, M., Second law optimization of flat-plate solar air heaters Part I: The concept of net exergy flow and the modeling of solar air heaters, Solar Energy 41, (1988), 2, pp. 127-132.
[16] Altfeld, K., Leiner, W., Fiebig, M., Second law optimization of flat-plate solar air heaters Part 2: Results of optimization and analysis of sensibility to variations of operating conditions, Solar Energy, 41, (1988),4 , pp. 309-317.
[17] Torres-Reyes, E., Navarrete-Gonzàlez, J. J., Zaleta-Aguilar, A., Cervantes-de Gortari, J. G., Optimal process of solar to thermal energy conversion and design of irreversible flat-plate solar collectors, Energy 28, (2003), pp. 99–113.
[18] Kurtbas, I., Durmuş, A., Efficiency and exergy analysis of a new solar air heater, Renewable Energy, 29, (2004), pp. 1489-1501.
[19] Choudhury C, Chauhan PM, Garg HP. Design curves for conventional solar air heaters. Renewable energy 1995;6(7):739–49.
[20] Ong KS. Thermal performance of solar air heaters: mathematical model and solution procedure. Solar Energy 1995;55(2):93–109.
[21] Hegazy AA. Thermohydraulic performance of heating solar collectors with variable width, flat absorber plates. Energy Conversion and Management 2000;41:1361–78.
[22] Al-Kamil MT, Al-Ghareeb AA. Effect of thermal radiation inside solar air heaters. Energy Conversion and Management 1997;38(14):1451–8.
[23] Garg HP, Datta G, Bhargava K. Some studies on the flow passage dimension for solar air testing collector. Energy Conversion and Management 1984;24(3):181–4.

[24] Forson FK, Nazha MAA, et Rajakaruna H. Experimental and simulation studies on a single pass, double duct solar air heater. Energy Conversion and Management 2003;44:1209–27.

[25] Ho CD, Yeh HM, Wang RC. Heat-transfer enhancement in double-pass flatplate solar air heaters with recycle. Energy 2005;30:2796–817.

[26] Duffie J.A, Beckman W.A, Solar engineering of thermal processes, 2nd ed. New York, John Wiley, 1991.

27

Heat Transfer in Porous Media

Ehsan Mohseni Languri[1] and Davood Domairry Ganji[2]
[1]*University of Wisconsin - Milwaukee*
[2]*Noshirvani Technical University of Babol,*
[1]*USA*
[2]*Iran*

1. Introduction

Heat transfer phenomena play a vital role in many problems which deals with transport of flow through a porous medium. One of the main applications of study the heat transport equations exist in the manufacturing process of polymer composites [1] such as liquid composite molding. In such technologies, the composites are created by impregnation of a preform with resin injected into the mold's inlet. Some thermoset resins may undergo the cross-linking polymerization, called curing reaction, during and after the mold-filling stage. Thus, the heat transfer and exothermal polymerization reaction of resin may not be neglected in the mold-filling modeling of LCM. This shows the importance of heat transfer equations in the non-isothermal flow in porous media.

Generally, the energy balance equations can be derived using two different approaches: (1) two-phase or thermal non-equilibrium model [2-6] and (2) local thermal equilibrium model [7-18]. There are two different energy balance equations for two phases (such as resin and fiber in liquid composite molding process) separately in the two-phase model, and the heat transfer between these two equations occur via the heat transfer coefficient. In the thermal equilibrium model, we assume that the phases (such as resin and fiber) reach local thermodynamic equilibrium. Therefore, only one energy equation is needed as the thermal governing equation, [3,5]. Firstly, we consider the heat transfer governing equation for the simple situation of isotropic porous media. Assume that radioactive effects, viscous dissipation, and the work done by pressure are negligible. We do further simplification by assuming the thermal local equilibrium that $T_s = T_f = T$ where T_s and T_f are the solid and fluid phase temperature, respectively. A further assumption is that there is a parallel conduction heat transfer taking place in solid and fluid phases.

Taking the average over an REV of the porous medium, we have the following for solid and fluid phases,

$$(1-\varphi)(\rho c)_s \frac{\partial < T_s >^s}{\partial t} = (1-\varphi)\nabla.(k_s \nabla < T_s >^s) + (1-\varphi) q_s''' \tag{1}$$

$$\varphi(\rho c_P)_f \frac{\partial < T_f >^f}{\partial t} + (\rho c_P)_f v.\nabla < T_f >^f = \varphi \nabla.(k_f \nabla < T_f >^f) + \varphi q_f''' \tag{2}$$

where c is the specific heat of the solid and c_p is the specific heat at constant pressure of the fluid, k is the thermal conductivity coefficient and q''' is the heat production per unit volume. By assuming the thermal local equilibrium, setting $T_s = T_f = T$, one can add Eqs. (1) and (2) to have:

$$(\rho c)_m \frac{\partial < T >}{\partial t} + (\rho c)_f \, v.\nabla < T >= \nabla.(k_m \nabla < T >) + q'''_m \tag{3}$$

where $(\rho c)_m$, k_m and q'''_m are the overall heat capacity, overall thermal conductivity, and overall heat conduction per unit volume of the porous medium, respectively. They are defined as follows:

$$(\rho c)_m = (1-\varphi)(\rho c)_s + \varphi(\rho c_p)_f \tag{4}$$

$$k_m = (1-\varphi)k_s + \varphi k_f \tag{5}$$

$$q'''_m = (1-\varphi)q'''_s + \varphi q'''_f \tag{6}$$

2. Governing equations

2.1 Macroscopic level

Pillai and Munagavalasa [19] have used volume averaging method with the local thermal equilibrium assumption to derive a set of energy and species equations for dual-scale porous medium. The schematic view of such volume is presented in the figure 1. Unlike the single scale porous media, there is an unsaturated region behind the moving flow-front in the dual-scale porous media. The reason for such partially saturated flow-front can be mentioned as the flow resistance difference between the gap and the tows where the flow goes faster in the gaps rather than the wicking inside the tows. Pillai and Munagavalasa [19] have applied the volume averaging method to the dual-scale porous media. Using woven fiber mat in the LCM, they considered the fiber tows and surrounding gaps as the two phases.

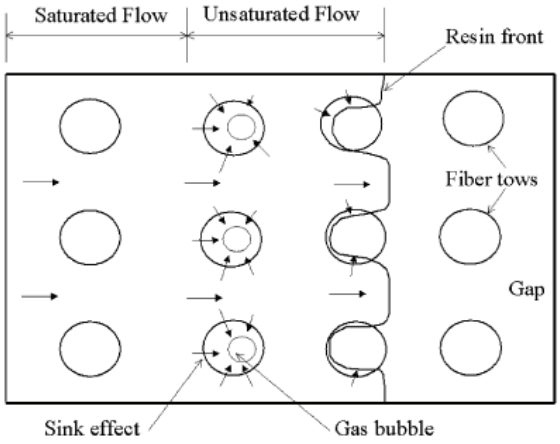

Fig. 1. Schematic view of dual-scale porous-medium [19]

The pointwise microscopic energy balance and species equations for resin inside the gap studied at first, and then the volume average of these equation is taken. Finally, they came up with the macroscopic energy balance and species equations.
The macroscopic energy balance equation in dual-scale porous medium is given by

$$\rho_g C_{P,g}\left[\varepsilon_g \frac{\partial}{\partial t}\left\langle T_g\right\rangle^g + \left\langle v_g\right\rangle.\nabla\left\langle T_g\right\rangle^g\right] = \nabla.\mathrm{K}_{th}.\nabla\left\langle T_g\right\rangle^g + \varepsilon_g\rho_g H_R f_c + Q_{conv} - Q_{cond} \tag{7}$$

where the ρ_g and $C_{P,g}$ are the resin density and specific heat respectively. T_g is the temperature of resin in the gap region, ε_g is gap fraction, H_R is the heat reaction and f_c is the reaction rate. The $\varepsilon_g\rho_g H_R f_c$ term represents the heat source due to exothermic curing reaction. The term K_{th} is the thermal conductivity tensor for dual-scale porous medium defined as

$$K_{th} = k_g\varepsilon_g\delta + \frac{k_g}{\mathrm{V}}\int_{A_{gt}} n_{gt}bdA - \frac{\rho_g C_{P,g}\varepsilon_g}{\mathrm{V}_g}\int \hat{v}_g bdV \tag{8}$$

where k_g, δ and $\hat{v}_g$ are thermal conductivity of the resin, a unit tensor and the fluctuations in the gap velocity with respect to the gap averaged velocity respectively. The vector b relates temperature deviations in the gap region to the gradient of gap-averaged temperature in a closure. Considering the temperature closure formulation as $\hat{T}_g = b.\nabla < T_g >^g$, the local temperature deviation is related to the gradient of the gap-averaged temperature through the vector b , [19].
Q_{conv} in the Eq. (8) is the heat source term due to release of resin heat prior to the absorption of surrounding tows given by

$$Q_{conv} = \rho_g C_{P,g} S_g[\left\langle T_g\right\rangle^g - \left\langle T_g\right\rangle^{gt}] \tag{9}$$

where Sg , the sink term and areal average of temperature on the tow-gap interface are expressed as following respectively

$$S_g = \frac{1}{\varepsilon_g V}\int v_g.n_{gt}dA \tag{10}$$

and

$$\left\langle T_g\right\rangle^{gt} = \frac{1}{A_{gt}}\int T_g dA \tag{11}$$

and Q_{cond} is the heat sink term caused by conductive heat loss to the tows given by

$$Q_{cond} = \frac{1}{V}\int k_g(-\nabla T_g).n_{gt}dA \tag{12}$$

Using the analogy between heat and mass transfer to derive the gap-averaged cure governing equation following the Tucker and Dessenberger [6] approach, one can derive the following equation

$$\varepsilon_g \frac{\partial}{\partial t}\left\langle c_g \right\rangle^g + \left\langle v_g \right\rangle.\nabla\left\langle c_g \right\rangle^g = \nabla.D.\nabla\left\langle c_g \right\rangle^g + \varepsilon_g f_c + M_{conv} - M_{diff} \tag{13}$$

where c_g is the degree of cure in a resin which value of 0 and 1 correspond to the uncured and fully cured resin situation, D is diffusivity tensor for the gap flows and is given by

$$D = D_1\varepsilon_g\delta + \frac{D_1}{\mathbf{V}}\int n_{gt} b\, d\mathbf{A} - \frac{\varepsilon_g}{\mathrm{V}_g}\int \hat{v}_g b \,\mathrm{dV} \tag{14}$$

where D_1 is the molecular diffusivity of resin. In the Eq. (13), M_{conv} is the convective source due to release of resin cure when absorbing into tows as a results of sink effect, given by

$$\mathrm{M}_{conv} = \mathrm{S}_g[\left\langle c_g \right\rangle^g - \left\langle c_g \right\rangle^{gt}] \tag{15}$$

where $\left\langle c_g \right\rangle^{gt}$ is the areal average of temperature on the tow-gap interface, expressed as

$$\left\langle c_g \right\rangle^{gt} = \frac{1}{A_{gt}}\int_{A_{gt}} c_g dA \tag{16}$$

and M_{diff} is the cure sink term as a result of the diffusion of cured resin into the tows, given by

$$M_{diff} = \frac{1}{V}\int D_1(-\nabla c_g).n_{gt} dA \tag{17}$$

It should be noted that the only way to compute the Q_{conv}, Q_{cond}, M_{conv} and M_{diff} is solving for flow and transport inside the tows.

2.2 Microscopic level

Phelan et al. [20] showed that the conventional volume averaging method can be directly used to derive the transport equation for thermo-chemical phenomena inside the tows for single-scale porous media. The final derivation for microscopic energy equation is

$$[\varepsilon_t\left(\rho C_p\right)_l + \left(1-\varepsilon_t\right)\left(\rho C_P\right)_f]\frac{\partial T_t}{\partial t} + \left(\rho C_P\right)_l v_t.\nabla T_t = \nabla.K_{th,t}.\nabla T_t + \varepsilon_t\rho_l H_R f_c \tag{18}$$

where the subscript t refer to tows. The microscopic species equation is given by

$$\varepsilon_t\frac{\partial c_t}{\partial t} + v_t.\nabla c_t = \nabla.\varepsilon_t D_t.\nabla c_t + \varepsilon_t f_c \tag{19}$$

The complete set of microscopic and macroscopic energy and species equations as well as the flow equation should be solved to model the unsaturated flow in a dual-scale porous medium.

3. Dispersion term

In some cases, a further complication arises in the thermal governing equation due to thermal dispersion [21]. The thermal dispersion happens due to hydrodynamic mixing of fluid at the pore scale. The mixings are mainly due to molecular diffusion of heat as well as

the mixing caused by the nature of the porous medium. The mixings are mainly due to molecular diffusion of heat as well as the mixing caused by the nature of the porous medium. Greenkorn [22] mentioned the following nine mechanisms for most of the mixing;

1. Molecular diffusion: in the case of sufficiently long time scales
2. Mixing due to obstructions: The flow channels in porous medium are tortuous means that fluid elements starting a given distance from each other and proceeding at the same velocity will not remain the same distance apart, Fig. 2.
3. Existence of autocorrelation in flow paths: Knowing all pores in the porous medium are not accessible to the fluid after it has entered a particular fluid path.
4. Recirculation due to local regions of reduced pressure: The conversion of pressure energy into kinetic energy gives a local region of low pressure.
5. Macroscopic or megascopic dispersion: Due to nonidealities which change gross streamlines.
6. Hydrodynamic dispersion: Macroscopic dispersion is produced in capillary even in the absence of molecular diffusion because of the velocity profile produced by the adhering of the fluid wall.
7. Eddies: Turbulent flow in the individual flow channels cause the mixing as a result of eddy migration.
8. Dead-end pores: Dean-end pore volumes cause mixing in unsteady flow. The main reason is as solute rich front passes the pore, diffusion into the pore occurs due to molecular diffusion. After the front passes, the solute will diffuse back out and thus, dispersing.
9. Adsorption: It is an unsteady-state phenomenon where a concentration front will deposit or remove material and therefore tends to flatten concentration profiles.

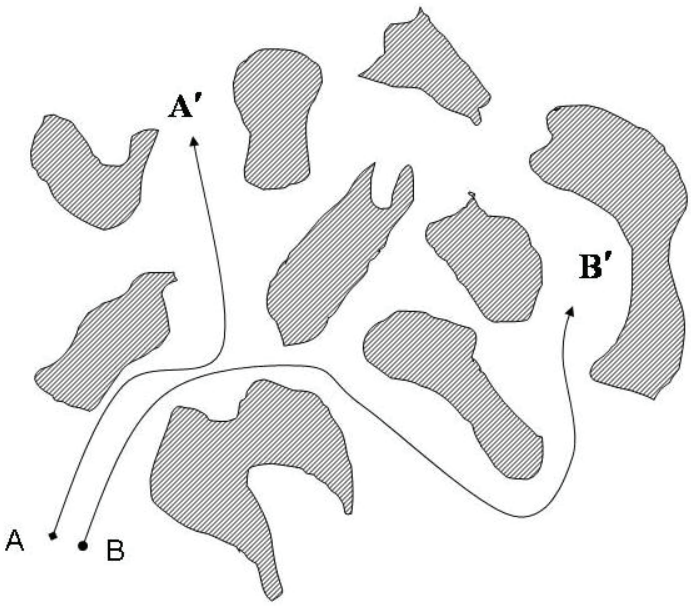

Fig. 2. Mixing as a result of obstruction

Rubin [23] generalized the thermal governing equation

$$(\rho c)_m \frac{\partial T}{\partial t} + (\rho c)_f \, v.\nabla T = \nabla.(k_m \nabla T) + q'''_m \tag{20}$$

where K is a second-order tensor called dispersion tensor.

Two dispersion phenomena have been extensively studied in the transport phenomena in porous media are the mass and thermal dispersions. The former involves the mass of a solute transported in a porous medium, while the latter involves the thermal energy transported in the porous medium. Due to the similarity of mass and thermal dispersions, they can be described using the dimensionless transport equations as

$$\frac{\partial \langle \Omega \rangle}{\partial \theta} + \langle U_i \rangle \frac{\partial \langle \Omega \rangle}{\partial X_i} = \frac{1}{Pe} \frac{\partial}{\partial X_i} \left(D_{ij} \frac{\partial \langle \Omega \rangle}{\partial X_j} \right) \tag{21}$$

where $\langle \Omega \rangle$ is either averaged concentration for mass dispersion or averaged dimensionless temperature for thermal dispersion, θ is dimensionless time, $\langle U_i \rangle$ is averaged velocity vector, Pe is Peclet number, D_{ij} is dispersion tensor of 2nd order. It should be noted that $Pe = \frac{uL}{\mathcal{D}}$ in mass dispersion and $Pe = \frac{uL}{\alpha}$ in thermal dispersion where u and L are characteristic velocity and length, respectively. $\mathcal{D}$ and α are molecular mass and thermal diffusivities, respectively.

3.1 Dispersion in porous media

Most studies on dispersion tensor so far have been focusing on the isotropic porous media. Nikolaveskii [24] obtained the form of dispersion tensor for isotropic porous media by analogy to the statistical theory of turbulence. Bear [25] obtained a similar result for the form of the dispersion tensor on the basis of geometrical arguments about the motion of marked particles through a porous medium. Bear studied the relationship between the dispersive property of the porous media as defined by a constant of dispersion, the displacement due to a uniform field of flow, and the resulting distribution. He used a point injection subjected to a sequence of movements. The volume averaged concentration of the injected tracer, C_0, around a point which is displaced a distance $L = ut$ in the direction of the uniform, isotropic, two dimensional field of flow from its original position is considered in his research.

$$C(x,y;x_0,y_0) = \frac{C_0}{2\pi\sigma_x^{\,2}\sigma_y^{\,2}} . \exp\left\{ -\frac{m^2}{2\sigma_x^{\,2}} - \frac{n^2}{2\sigma_y^{\,2}} \right\} \tag{22}$$

where L is the distance of mean displacement, u is the uniform velocity of flow, t is the time of flow, σ_x and σ_y are standard deviations of the distribution in the x and y directions, respectively and, finally m and n are the coordinates of the point (x,y) in the coordinate system centered at (ξ, η) given by $m = x - (x_0 + L)$ and $n = y - y_0$, figure 3. This figure shows a point injection as a result of subsequence movement where initially circle tracer gets an elliptic shape at $L = ut$.

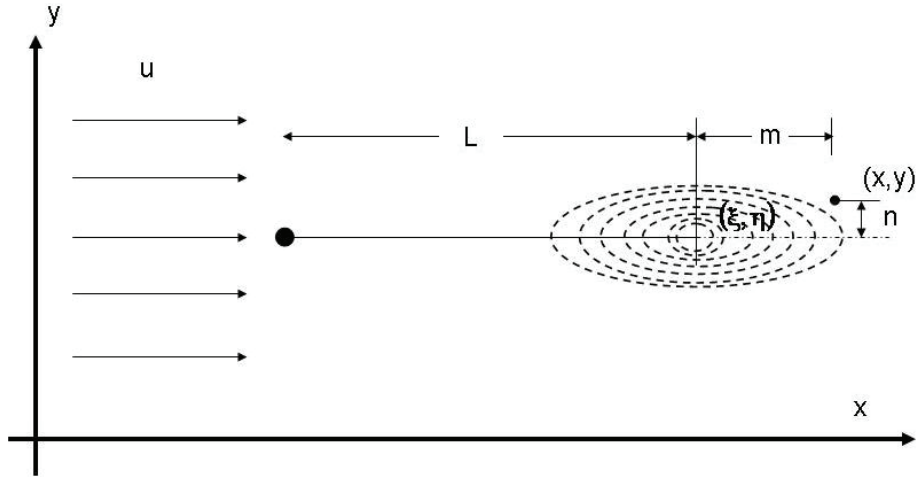

Fig. 3. Dispersion of a point injection displaced a distance L

Standard deviations are defined by $\sigma_x = (2D_I L)^{0.5}$ and $\sigma_y = (2D_{II} L)^{0.5}$ where D_I and D_{II} are the longitudinal and transverse constants of dispersion in porous media, respectively. One should note that the D_I and D_{II} used in the Bear work depend only upon properties of the porous medium such as porosity, grain size, uniformity, and shape of grains. From Eq. (22), it follows that, after a uniform flow period, lines of the similar concentration resulting from the circular point injection of the tracer take the ellipse shape centered at the displaces mean point and oriented with their major axes in the direction of the flow.

$$\frac{x^2}{\sigma_x{}^2} + \frac{y^2}{\sigma_y{}^2} = 1 \tag{23}$$

Bear conjectured that the property which is defined by the constant of dispersion, D_{ijkl}, depends only upon the characteristics of porous medium and the geometry of its pore-channel system. In a general case, this is a fourth rank tensor which contains 81 components. These characteristics are expressed by the longitudinal and lateral constants of dispersion of the porous media. Scheidegger [26] used the dispersion tensor D_{ij} in the following form

$$D_{ij} = a_{ijkm} \frac{v_k v_m}{|v|} \tag{24}$$

where v is the average velocity vector, v_k is the k_{th} component of velocity vector, a_{ijkm} is a fourth rank tensor called geometrical dispersivity tensor of the porous medium. Bear demonstrated how the dispersion tensor relates to the two constants for an isotropic medium: $a_{||}$ = longitudinal dispersion[1], and $a_{\perp}$ = transversal dispersion[2]. Scheidegger [26] has shown that there are two symmetry properties for dispersivity tensor

[1] The longitudinal direction is along the mean flow velocity in porous media, whereas the transverse direction is perpendicular to the mean flow velocity.

$$a_{ijkm} = a_{jikm} \quad \text{and} \quad a_{ijkm} = a_{ijmk} \tag{25}$$

Therefore, only 36 of 81 components of fourth rank tensor a_{ijkl} is independent. For an isotropic porous medium, the dispersivity tensor must be isotropic. An isotropic fourth rank tensor can be expressed as

$$a_{ijkm} = \alpha\delta_{ij}\delta_{km} + \beta\delta_{ik}\delta_{jm} + \gamma\delta_{im}\delta_{jk} \tag{26}$$

where α, β, γ are constants and δ_{ij} is Kronecker symbol. Because of symmetry properties expressed by Eq.(23), we get

$$\beta = \gamma \tag{27}$$

So the dispersivity tensor can be written as

$$a_{ijkm} = \alpha\delta_{ij}\delta_{km} + \beta\left(\delta_{ik}\delta_{jm} + \delta_{im}\delta_{jk}\right) \tag{28}$$

On substituting Eq. (26) into Eq. (22), we can obtain the dispersion tensor as

$$D_{ij} = \alpha|v|\delta_{ij} + \frac{2\beta}{|v|}v_i v_j \tag{29}$$

If we define $a_\perp = \alpha|v|$, $a_{||} - a_\perp = 2\beta|v|$ and $n_i = v_i/|v|$ (n_i is the mean flow direction), then dispersion tensor D_{ij} can be written as

$$D_{ij} = a_\perp\delta_{ij} + \left(a_{||} - a_\perp\right)n_i n_j \tag{30}$$

From Eq. (28), it is quite clear that the three principle directions of dispersion tensor D are orthogonal to each other (due to the symmetry of D_{ij}), and one principle direction is along the mean flow direction (**n**) and the other two are perpendicular to the mean flow direction. Therefore, for isotropic medium, the dispersion tensor can be expressed by longitudinal and transverse dispersion coefficients. If we consider the mean flow is along x-axis, D_{ij} can be written as

$$D = \begin{bmatrix} a_{||} & 0 & 0 \\ 0 & a_\perp & 0 \\ 0 & 0 & a_\perp \end{bmatrix} \tag{31}$$

Therefore, transport equation can be written as

$$\frac{\partial\langle\Omega\rangle}{\partial\theta} + \langle U_1\rangle\frac{\partial\langle\Omega\rangle}{\partial X_1} = \frac{1}{Pe}\left(a_{||}\frac{\partial^2\langle\Omega\rangle}{\partial X_1^2} + a_\perp\frac{\partial^2\langle\Omega\rangle}{\partial X_2^2} + a_\perp\frac{\partial^2\langle\Omega\rangle}{\partial X_3^2}\right) \tag{32}$$

It has been shown that one of the principle axes of the dispersion tensor in isotropic porous medium is along the mean flow direction. Unlike the isotropic media, there are nine independent components in the dispersion tensor for the case of anisotropic porous media. Bear [25] noted that the dispersion problem in a nonisotropic material still remains unsolved. He suggested to distinguishing between various kinds of anisotropies and doing

statistical analysis with different frequency functions for the spatial distribution of channels in each case. Unless some specific types of porous media, like axisymmetric or transversely isotropic, it is not possible to simplify the form of dispersion tensor. In 1965, Poreh [27] used the theory of invariants to give a dispersion tensor for axisymmetric porous media. The average properties of axisymmetric porous medium which affecting the macroscopic dispersion pattern are invariants to rotaion about given line. He establish the general form of D_{ij} with two arbitrary vectors **R** and **S** as following

$$D_{ij}R_iS_j = B_1\delta_{ij}R_iS_j + B_2v_iv_jR_iS_j + B_3\lambda_i\lambda_jR_iS_j + B_4v_iR_i\lambda_jS_j + B_5\lambda_iR_iv_jS_j \tag{33}$$

where **λ** is the axis of symmetry, B_1, B_2, B_3, B_4, and B_5 are arbitrary functions of v^2 and $v_k\lambda_k$. For arbitrary **R** and **S** and symmetric D_{ij}, one can have

$$D_{ij} = B_1\delta_{ij} + B_2v_iv_j + B_3\lambda_i\lambda_j + B_4\left(v_i\lambda_j + \lambda_iv_j\right) \tag{34}$$

The dimensionless form of Eq. (32) is obtained as

$$\frac{D_{ij}}{D_0} = G_1\delta_{ij} + G_2\left(\frac{l^2}{D_0^2}\right)v_iv_j + G_3\lambda_i\lambda_j + G_4\left(\frac{l}{D_0}\right)\left(v_i\lambda_j + \lambda_iv_j\right) \tag{35}$$

where G_1, G_2, G_3 and G_4 are dimensionless functions of $(vl/D_0)^2$, $(vl/\upsilon)^2$, and D_0 is molecular diffusivity coefficient, l is length characterizing the size of the pores, υ is kinematic viscosity. Finally, the dispersion tensor for axisymmetric porous media is

$$\frac{D_{ij}}{D_0} = \left(\beta_1 + \beta_2\frac{v^2l^2}{D_0^2}\right)\delta_{ij} + \beta_3\left(\frac{l^2}{D_0^2}\right)v_iv_j + \left(\beta_4 + \beta_5\frac{v^2l^2}{D_0^2}\right)\lambda_i\lambda_j + \beta_6\left(\frac{vl^2}{D_0^2}\right)\left(v_i\lambda_j + \lambda_iv_j\right) \tag{36}$$

where β_1 and β_4 are dimensionless numbers, β_2, β_3 and β_5 are even functions of $\cos\omega$, and β_6 is an odd function of $\cos\omega$.

By assuming no motion within an axisymmetric medium, D_{ij} is simplify to

$$\frac{D_{ij}}{D_0} = \beta_1\delta_{ij} + \beta_4\lambda_i\lambda_j \tag{37}$$

Eq.(37) indicating that one of the principal axes of D_{ij} is, in this case, co-directional with **λ**. He followed these arguments that for sufficiently large Reynolds number, the dispersivity tensor for axisymmetric porous medium can be expressed as

$$\frac{D_{ij}}{lv} = \varepsilon_1\delta_{ij} + \frac{\varepsilon_2v_iv_j}{v^2} + \varepsilon_3\lambda_i\lambda_j + \frac{\varepsilon_4\left(v_i\lambda_j + v_j\lambda_i\right)}{v} \tag{38}$$

where ε_1, ε_2, ε_3, and ε_4 are parameters determined by the dimensionless geometry of the medium and depends slightly on the Reynolds number and value of $\cos\omega$. On should note that the above derivation, primarily based on symmetry considerations, can not reveal the scalar nature of general dispersivity tensor. Bear [25] also noted that his analysis was based on an unproved assumption that D_{ij} may be expanded in a power series. In 1967, Whitaker [28] applied pointwise volume-averaging method for transport equation in anisotropic porous media and obtained following dispersion tensor D_{ij}

$$D_{ij} = D_0\left(\delta_{ij} + RB_{ij}\right) + C_{ikj}v_k + E_{ikmj}v_k v_m \tag{39}$$

where second order tensor B_{ij} is a function of tortuosity vector

$$\tau_j = \int_S \Omega n_j ds \tag{40}$$

The third-order tensor C_{ikj} is given by

$$C_{ikj} = \frac{\partial^2 \left\langle \tilde{\Omega}\tilde{v}_i \right\rangle}{\partial \left\langle v_k \right\rangle \partial \left(\frac{\partial \left\langle \Omega \right\rangle}{\partial x_j} \right)} \tag{41}$$

And the fourth-order tensor E_{ikmj} is introduced as

$$E_{ikmj} = \frac{\partial^3 \left\langle \tilde{\Omega}\tilde{v}_i \right\rangle}{\partial \left\langle v_k \right\rangle \partial \left\langle v_m \right\rangle \partial \left(\frac{\partial \left\langle \Omega \right\rangle}{\partial x_j} \right)} \tag{42}$$

where $\tilde{\Omega}$ is deviation of concentration or temperature from the average and $\tilde{v}_i$ is velocity deviation given respectively as

$$\tilde{\Omega} = \Omega - \left\langle \Omega \right\rangle^f \text{ and } \tilde{v}_i = v_i - \left\langle v_i \right\rangle^f \tag{43}$$

One should keep in mind that from Eqs. (41) and (42), we know that C_{ikj} and E_{ikmj} are completely symmetrical.

On comparing Eq. (38) with Eq. (24), one can note that there are both third- and fourth-order symmetric tensors associated with velocity in the Whitaker's derivation, while Nikolaveskii [24], Bear [25], and Scheidegger's [26] derivations only contain fourth-order symmetric tensor. Patel and Greenkorn [29] suggested that Whitaker's expression for dispersion tensor is the correct one for anisotropic media. There are two distinct components of dispersion tensor for isotropic medium while Whitaker's expression of dispersion tensor resulted in only one component for isotropic medium.

The diffusion term becomes less important at higher velocities which gives

$$D_{ij} \approx C_{ikj}v_k + E_{ikmj}v_k v_m \tag{44}$$

For isotropic media, the tensors C_{ikj} and E_{ikmj} must be isotropic. Hence, C_{ikj} =0, and E_{ikmj} is a linear combination of the Kronecker deltas as expressed in Eq. (26). Since E_{ikmj} is completely symmetric, Eq. (42), the tensor E_{ikmj} can be shown as

$$E_{ikmj} = \alpha\left(\delta_{ik}\delta_{mj} + \delta_{im}\delta_{kj} + \delta_{ij}\delta_{km}\right) \tag{45}$$

Therefore Eq. (39) reduces to

$$D_{ij} = \alpha\left(2v_i v_j + \delta_{ij}\left|v\right|^2\right) \tag{46}$$

Assuming 1-D flow in Cartesian coordinate frame where

$$v_1 = u \quad v_2 = v_3 = 0 \tag{47}$$

then, Eq. (46) can be written as

$$D = \alpha u^2 \begin{bmatrix} 3 & 0 & 0 \\ 0 & 1 & 0 \\ 0 & 0 & 1 \end{bmatrix} \tag{48}$$

Equation (48) shows that the longitudinal coefficient of dispersion tensor in this case, is three times the transverse coefficient. This equation clearly indicates the huge difference between the isotropic and anisotropic porous media. Greenkorn [29] showed experimentally that the ratio $D_{||} / D_{\perp}$ varies approximately from lower value of 3 to the higher value of 60. He showed that this ration is a function of the flow velocity.

Experimental results by Patel and Greenkorn [29] show that the ratio $D_{||} / D_{\perp}$ varies from a lower value of about 3 to a high value of about 60. This ratio of longitudinal to transverse dispersion coefficients is shown to be actually a function of the velocity of flow. Although the Whitaker's method is at variance with Greenkorn experimental results, it still do give the correct lower limit result for a homogeneous, uniform, isotropic medium.

4. References

[1] Rudd CD, Long AC, Kendall KN, Mangin CGE. Liquid molding technologies. Woodhead Publishing Ltd; 1997.

[2] Chan, A.W. and S.-T. Hwang, Modeling Nonisothermal Impregnation of Fibrous Media with Reactive Polymer Resin, Polymer Engineering & Science, 1992. 32(5):p. 310-318.

[3] Chiu, H.-T., B. Yu, S.C. Chen, et al., Heat Transfer During Flow and Resin Reaction through Fiber Reinforcement. Chemical Engineering Science, 2000. 55(17): p. 3365-3376.

[4] Lee, L.J., W.B. Young, and R.J. Lin, Mold Filling and Cure Modeling of RTM and Srim Processes. Composite Structures, 1994. 27(1-2): p. 109-120.

[5] Lin, R.J., L.J. Lee, and M.J. Liou, Mold Filling and Curing Analysis Liquid Composite Molding. Polymer Composites, 1993. 14(1): p. 71-81.

[6] Tucker, C.L. and R.B. Dessenberger, Governing Equations for Flow through Stationary Fiber Beds, in Flow and Rheology in Polymer Composites Manufacturing, S.G. Advani, Editor. 1994, Elsevier.

[7] Lam, Y.C., S.C. Joshi, and X.L. Liu, Numerical Simulation of the Mould-Filling Process in Resin-Transfer Moulding. Composites Science and Technology, 2000. 60(6): p. 845-855.

[8] Wu, C.H., H.-T. Chiu, L.J. Lee, et al., Simulation of Reactive Liquid Composite Molding Using an Eulerian–Lagrangian Approach. International Polymer Processing, 1998(4): p. 398-397.

[9] Bruschke, M.V. and S.G. Advani, Numerical Approach to Model Non-Isothermal Viscous Flow through Fibrous Media with Free Surfaces. International Journal for Numerical Methods in Fluids, 1994. 19(7): p. 575-603.

[10] Dessenberger, R.B. and C.L. Tucker, Thermal Dispersion in Resin Transfer Molding. Polymer Composites, 1995. 16(6): p. 495-506.

[11] Kang, M.K., W. Lee, II, J.Y. Yoo, et al., Simulation of Mold Filling Process During Resin Transfer Molding. Journal of Materials Processing and Manufacturing Science, 1995. 3(3): p. 297-313.
[12] Liu, B. and S.G. Advani, Operator Splitting Scheme for 3-D Temperature Solution Based on 2-D Flow Approximation. Computational Mechanics, 1995. 16(2): p. 74-82.
[13] Mal, O., A. Couniot, and F. Dupret, Non-Isothermal Simulation of the Resin Transfer Moulding Process. Composites - Part A: Applied Science and Manufacturing, 1998. 29(1-2): p. 189-198.
[14] Ngo, N.D. and K.K. Tamma, Non-Isothermal '2-D Flow/3-D Thermal' Developments Encompassing Process Modeling of Composites: Flow/Thermal/Cure Formulations and Validations. American Society of Mechanical Engineers, Applied Mechanics Division, AMD, 1999. 233: p. 83-102
[15] Shojaei, A., S.R. Ghaffarian, and S.M.H. Karimian, Simulation of the Three- Dimensional Non-Isothermal Mold Filling Process in Resin Transfer Molding. Composites Science and Technology, 2003. 63(13): p. 1931-1948.
[16] Shojaei, A., S.R. Ghaffarian, and S.M.H. Karimian, Three-Dimensional Process Cycle Simulation of Composite Parts Manufactured by Resin Transfer Molding. Composite Structures, 2004. 65(3-4): p. 381-390.
[17] Young, W.-B., Three-Dimensional Nonisothermal Mold Filling Simulations in Resin Transfer Molding. Polymer Composites, 1994. 15(2): p. 118-127.
[18] Young, W.-B., Thermal Behaviors of the Resin and Mold in the Process of Resin Transfer Molding. Journal of Reinforced Plastics and Composites, 1995. 14(4): p. 310.
[19] Pillai, K.M. and M.S. Munagavalasa, Governing Equations for Unsaturated Flow through Woven Fiber Mats. Part 2. Non-Isothermal Reactive Flows. Composites Part A: Applied Science and Manufacturing, 2004. 35(4): p. 403-415.
[20] Phelan, F.R., Jr. Modeling of Microscale Flow in Fibrous Porous Media. 1991. Detroit, MI, USA: Publ by Springer-Verlag New York Inc., New York, NY, USA.
[21] Donald A. Nield and Adrinan Bejan, Convection in Porous Media, Springer, 3rd edition.
[22] Robert A. Greenkorn, Flow phenomena in porous media, Marcel Dekker, INC., New York and Besel, 1983.
[23] Rubin, H., Heat dispersion effect on thermal convection in a porous medium layer. J. Hydrol. 21, 1074,P: 173–184.
[24] Nikolaevskii, V.N., Convective diffusion in porous media, Journal of applied mathematics and mechanics, 23, 6, 1492-1503, 1959.
[25] Bear, J., On the Tensor Form of Dispersion in Porous Media. Journal of Geophysical Research, 1961. 66: p. 1185-1197.
[26] Scheidegger, A.E., General Theory of Dispersion in Porous Media. Journal of Geophysical Research, 1961. 66(10): p. 3273-3278.
[27] Poreh, M., The Dispersivity Tensor in Isotropic and Axisymmetric Mediums. Journal of Geophysical Research, 1965. 70: p. 3909-3913.
[28] Whitaker, S., Diffusion and Dispersion in Porous Media. AIChE Journal, 1967. 13(3): p. 420-427.
[29] Patel, R.D. and R.A. Greenkorn, On Dispersion in Laminar Flow through Porous Media. AIChE Journal, 1970. 16(2): p. 332-334.
[30] Beavers, G.S. and Joseph D.D., Boundary condition at a naturally permeable wall, J. Fluid Mech,. Vol. 30, pp. 197-207, 1967.
[31] Sahraoui, M. and Kaviany, M., Slip and no-slip boundary condition at interface of porous plain media, Int. J. Heat Mass Transfer, Vol. 35, pp. 927-943, 1992.